

EXPERIMENTAL AND NUMERICAL INVESTIGATION OF MOVING LOADS ON HULL STRUCTURES

by

© Bruce W. T. Quinton, B.Eng., M.Eng.

A thesis submitted to the School of Graduate Studies

in partial fulfillment of the requirements for the degree of

Doctor of Philosophy

Faculty of Engineering and Applied Science

Memorial University of Newfoundland

October 2015

St. John's

Newfoundland and Labrador

Canada

Abstract

Regulations and design codes for ships and offshore structures operating in ice infested waters consider only stationary loads for hull structural design. This implies that the effects of movement of a load along the hull are negligible. Real hull structures most often experience operational ice loads in a way that would be better modelled as a moving load.

Previous work (Quinton 2008) predicted a significant decrease in the structural capacity of a steel grillage (hull) structure subjected to moving loads that cause plastic damage, when compared with similar stationary loads. In particular, the previous work predicted a decrease in the structural capacity of both hull plating and hull frames. For hull frames, it was noticed that plastic buckling of the frame webs occurred at a much lower load level for moving loads, than for stationary loads.

This thesis explores the effects of moving loads causing plastic damage on hull structures using experiments and subsequent numerical models. The results of this work identify a loss of hull structural capacity directly attributable to plastic damage caused by lateral load movement for both plates and frames. It explores the structural response phenomena underlying the observed capacity losses. In particular, this thesis presents: results of laboratory experiments carried out using a novel moving load apparatus involving steel and ice indenters acting on steel plates and frames; a discussion of the design and capabilities of the novel moving load apparatus; a discussion of the structural response phenomena present during moving loads based on a calibrated numerical model of the moving load experiments; and general guidelines for conducting numerical models of moving loads.

Acknowledgements

This research was supported by funding through the STePS² project and its government and industry partners. Specifically: the Atlantic Canada Opportunities Agency (ACOA) through its Atlantic Innovation Fund (AIF), Research & Development Corporation (RDC) through its Collaborative R&D program, the American Bureau of Shipping, BMT Fleet Technology Ltd., Husky Energy, Rolls-Royce, Samsung Heavy Industries, National Research Council of Canada - Ocean, Coastal, River Engineering (formerly the Institute for Ocean Technology), MITACS through their Accelerate program, and through Memorial University of Newfoundland's Offshore Technology Research – an NSERC CREATE program.

Dr. Claude G. Daley, Professor – my graduate supervisor. Thank you for your outstanding supervision, confidence, support, enthusiastic discussions, reality checks, and for inspiring me.

Dr. Robert E. Gagnon, Research Council Officer – my graduate co-supervisor. Thank you for your excellent direction, encouragement to pay careful attention to detail, and vast knowledge of ice mechanics.

Dr. D. Bruce Colbourne, Professor – my graduate co-supervisor. Thank you for your pragmatism, logic, management, and enthusiasm, and sound practical advice.

Technical Services – Billy Bidgood, David Snook, Paul Sullivan, Gerry Smith, and everyone else who worked on fabricating the moving load apparatus. Your talent and expertise brought the moving load apparatus to life and made this thesis possible.

Technical Staff – Matthew Curtis, Craig Mitchell, Shawn Organ, and Mark Pope. Thank you for your expertise, patience with my questions, and willingness to help.

Engineering Computing Services (ECS) Staff – Tony Kearsey and Shannon March for their assistance, patience and willingness to help.

Engineering Graduate Studies Office Staff – Moya Crocker, Colleen Mahoney and Nicole Parisi for always being there to help.

Jennifer Mersereau of The National Research Council of Canada - Canada Institute for Scientific and Technical Information (NRC-CISTI) for your kind and generous help and support.

The National Research Council of Canada – Oceans, Coastal and River Engineering (NRC-OCRE; formerly the Institute for Ocean Technology (NRC-IOT)) for hosting me for one year and providing support services.

My parents, Judy and Terry Quinton, for showing me that anyone can do anything.

Finally and most importantly, I would like to thank my very patient and supportive wife, Melissa, and my lovely young daughters, Isabelle and Leah, for all the time together that we sacrificed in order for this thesis to be possible. I could not have accomplished this without your support and blessing.

Table of Contents

Abstract	ii
Acknowledgements	iii
Table of Contents	v
List of Tables	xv
List of Figures	xviii
List of Symbols, Nomenclature or Abbreviations	xxix
List of Appendices	xxxvi
Chapter 1 Introduction	1
1.1 A Note on Capacity	1
1.2 Background	2
1.3 Applicability of Moving Load Effects	7
1.4 Methodology	8
1.5 Thesis Organization	9
Chapter 2 Literature Review	11
2.1 Ice	11
2.1.1 Introduction	11
2.1.2 Ice mechanics	12

2.1.2.1	Continuum mechanics.....	13
2.1.2.2	Fracture mechanics	14
2.1.2.3	Combined continuum and fracture mechanics.....	15
2.1.3	Scale.....	16
2.1.4	Confinement.....	17
2.1.5	Numerical modeling of ice.....	18
2.2	Collision (or Allision) and Grounding Loads	21
2.2.1	Introduction.....	21
2.2.2	Collision physics.....	22
2.2.3	Methods for assessment of collision and grounding of ships	23
2.2.4	Types of collision loads	24
2.2.4.1	Rupture-type loads.....	24
2.2.4.2	Non-rupture type loads	25
2.3	Moving Loads	27
2.4	Progressive Damage.....	30
2.5	Strain Rate and Temperature Effects	31
2.5.1	Temperature effects	32
2.5.2	Strain-rate effects	32
2.6	Literature Review Summary	33

Chapter 3	Moving Load Experiments	35
3.1	Research Approach	35
3.2	Scope and Objectives	35
3.3	A Note on Directions	36
3.4	Design, Capabilities and Operation of the Moving Load Apparatus	38
3.4.1	Incorporating existing infrastructure.....	39
3.4.2	Introduction to the moving load apparatus	39
3.4.3	Design of the moving load apparatus.....	42
3.4.3.1	Vertical load.....	44
3.4.3.2	Horizontal load.....	46
3.4.3.3	General structure	47
3.5	Indenters.....	48
3.5.1	Steel wheel indenter	49
3.5.2	Ice indenter.....	50
3.6	Plate and Frame Test Specimens	55
3.6.1	Frames.....	55
3.6.1.1	Frame test specimen installation procedure	59
3.6.2	Plates	61
3.6.2.1	Plate test specimen installation procedure	63

3.7	Data Acquisition	63
3.7.1.1	MTS data channels.....	63
3.7.1.2	Imaging technologies	64
3.7.1.3	Spatial digitizing technology	67
3.7.2	Control equipment	67
3.8	Methodology	67
3.8.1	Sample type.....	68
3.8.2	Load path	69
3.8.3	Load type	70
3.8.4	Indenter type	70
3.8.5	Normal indentation depth	70
3.8.6	Normal loading / indentation rate	72
3.8.7	Lateral indenter starting location	74
3.8.8	Lateral travel length	74
3.8.9	Lateral travel speed	75
3.8.10	Temperature	75
3.8.11	Friction.....	76
3.9	Test regime.....	76
3.10	Experimental Procedure.....	78

3.10.1	General procedure	78
Chapter 4	Experimental Results	80
4.1	$\frac{1}{4}$ " Plates with Steel Wheel Indenter at Room-temperature	83
4.1.2	Strain-rate mitigation effects.....	86
4.1.3	Further discussion	87
4.2	$\frac{1}{2}$ " Plates with Steel Wheel Indenter at Room-temperature	90
4.2.2	Strain-rate mitigation effects.....	93
4.2.3	Further discussion	95
4.3	Frames with Steel Wheel Indenter at Room-temperature.....	95
4.3.2	Strain-rate mitigation effects.....	99
4.3.3	Further discussion	100
4.4	$\frac{1}{4}$ " Plates with Steel Wheel Indenter at -10°C: 2 cm Indentation..	103
4.4.2	Strain-rate mitigation effects.....	106
4.4.3	Further discussion	106
4.5	$\frac{1}{4}$ " Plates with Steel Wheel Indenter at -10°C: 4 cm Indentation..	107
4.5.2	Strain-rate mitigation effects.....	110
4.5.3	Further discussion	110
4.6	$\frac{1}{2}$ " Plates with Steel Wheel Indenter at -10°C	111
4.6.2	Strain-rate mitigation effects.....	114

4.6.3	Further discussion	114
4.7	Frames with Steel Wheel Indenter at -10°C	115
4.7.2	Strain-rate mitigation effects.....	118
4.7.3	Further discussion	119
4.8	Force controlled Experiments at -10°C	120
4.8.1	Results.....	121
4.8.2	Further discussion	126
4.9	Ice Cone Tests.....	127
4.9.1	Load path	127
4.9.2	Elastic structural ice tests without pressure film.....	128
4.9.2.1	Slow – MovingLoad30 and MovingLoad31	128
4.9.2.2	Slow – MovingLoad38 and MovingLoad39.....	135
4.9.2.3	Fast – MovingLoad34	139
4.9.3	Elastic structural ice tests with pressure film.....	141
4.9.3.1	Slow – MovingLoad32	142
4.9.3.2	Slow – MovingLoad33	143
4.9.3.3	Slow – MovingLoad35	144
4.9.4	Plastic structural ice tests	145
4.9.4.1	Slow – MovingLoad40	145

4.9.4.2	Fast – MovingLoad41	149
4.9.5	Results of moving ice cone indenter tests.....	153
4.10	Summary of Results and Discussion.....	155
4.10.1	Capacity loss and strain-rate effects gains	156
4.10.2	Force controlled experiments.....	158
4.10.3	Verification of early onset of plastic buckling.....	160
4.10.4	Effect of temperature	162
4.10.5	Effect of starting location on lateral moving load capacity	162
4.11	Experiment Conclusions	163
Chapter 5	Numerical Simulations	165
5.1	Scope and Objectives	165
5.2	Methodology	166
5.2.1	Finite element code capability requirements	168
5.2.2	Indenter motion.....	169
5.2.3	DOE determination of undefined variables	169
5.2.3.1	Factors level determination.....	170
5.2.3.2	Responses measured	173
5.2.3.3	RSM design summary.....	174
5.2.3.4	½” plate specimen DOE analysis and predictions	176

5.2.3.5	¼” plate specimen DOE analysis and predictions	181
5.2.3.6	Frame specimen DOE analysis and predictions.....	185
5.2.3.7	A note about vertical compliance	189
5.3	Numerical Model	190
5.3.1	Precision.....	190
5.3.2	Geometry modeled.....	191
5.3.2.1	Test specimen geometries	191
5.3.2.2	Indenter geometry	195
5.3.3	Boundary conditions	196
5.3.3.1	Evolution by trial-and-error and final boundary conditions	197
5.3.3.2	Indenter boundary conditions	198
5.3.3.3	Guidance on interfacing solid and shell elements.....	198
5.3.3.4	Summary of boundary conditions	203
5.3.4	Finite element meshes.....	204
5.3.4.1	Plate specimen mesh	205
5.3.4.2	Framed specimen meshes	210
5.3.4.3	Indenter mesh.....	210
5.3.4.4	Mesh convergence study	212
5.3.5	Material model	212

5.3.5.1	Material constants	214
5.3.6	Section definitions	215
5.3.7	Part definition.....	218
5.3.8	Contact	219
5.3.8.1	Penalty method.....	219
5.3.8.2	Element grouping.....	220
5.3.8.3	SOFT parameter.....	221
5.3.9	Loading	221
5.3.10	Hourglassing	221
5.3.11	Solution controls	222
5.3.12	Output of Results	223
5.4	Validation Simulations.....	224
5.4.1	¼” Plate simulation validation.....	224
5.4.2	½” Plate simulation validation.....	228
5.4.3	Frame simulation validation	231
5.5	A First Investigation of Indenter Path.....	235
5.5.1	Model parameters.....	235
5.5.2	Results.....	237
5.6	Guidelines for Modeling Moving Loads on Hull Structures	241

5.7	Discussion of Numerical Simulations.....	243
5.8	Numerical Modeling Conclusions	244
Chapter 6	Overall Conclusions, Novel Contributions and Recommendations for Future Work.....	246
6.1	Novel Contributions.....	247
6.2	Recommendations for Further Work	249
Bibliography	252
Appendices	259

List of Tables

Table 3.1: Indentation Rates for displacement-controlled experiments.	73
Table 3.2: Test Regime* - green rows indicate that the run is a repeat, and orange rows indicate that pressure film was used to record the maximum pressures.	76
Table 4.1: Actual experiment parameters for room-temperature tests with steel wheel indenter.	80
Table 4.2: Actual experiment parameters for -10°C tests with steel wheel indenter.....	81
Table 4.3: Actual experiment parameters for -10°C force controlled tests with steel wheel indenter.	81
Table 4.4: Actual experiment parameters for -10°C tests with ice cone indenter and elastic plate response.	82
Table 4.5: Actual experiment parameters for -10°C tests with ice cone indenter and plastic plate response.	82
Table 4.6: ¼” plate normal (vertical) force capacity results at room-temperature.	84
Table 4.7: ½” plate normal (vertical) force capacity results at room-temperature.	92
Table 4.8: Frame normal (vertical) force capacity results at room-temperature.	97
Table 4.9: ¼” plate normal (vertical) force capacity results at -10°C: 2 cm indentation.	104
Table 4.10: ¼” plate normal (vertical) force capacity results at -10°C: 4 cm indentation.	108
Table 4.11: ½” plate normal (vertical) force capacity results at -10°C.	112
Table 4.12: Frame normal (vertical) force capacity results at -10°C.....	116

Table 4.13: Friction coefficients for moving ice load on elastic steel plate with ice-polyester sliding interface.	142
Table 4.14: Summary of friction coefficients for moving ice indenter experiments.	155
Table 4.15: Summary of moving load % capacity loss and strain-rate effects % capacity gains for the plate and frame specimens.	158
Table 4.16: Increase in plate and frame indentation for force controlled moving load experiments.	160
Table 4.17: Temperature effects gains relative to room-temperature for all three test specimen types.	162
Table 5.1: Material Properties of 44W and 40W steels.	170
Table 5.2: Response surface factor level summary.	173
Table 5.3: RSM factor levels and runs for all three specimen types.	176
Table 5.4: RSM run results for ½” plate case.	178
Table 5.5: RSM Design Summary for ½” plate case.	178
Table 5.6: DOE optimized factors for experimental response values for ½” plate case.	181
Table 5.7: RSM run results for ¼” plate case.	182
Table 5.8: RSM Design Summary for ¼” plate case.	183
Table 5.9: DOE optimized factors for experimental response values for ¼” plate case.	184
Table 5.10: RSM run results for frame case.	187
Table 5.11: RSM Design Summary for frame case.	187
Table 5.12: DOE optimized factors for experimental response values for frame case.	189
Table 5.13: Summary of global finite element boundary conditions.	204
Table 5.14: Summary of internal connections between finite element parts.	204

Table 5.15: Relative position of outermost point for Gaussian integration for shell elements.	
.....	209
Table 5.16: Summary of shell element attributes.	209
Table 5.17: Plastic-kinematic material model inputs by specimen type.....	214
Table 5.18: Rigid material model inputs.....	215
Table 5.19: Inputs for SECTION_SHELL cards.	218
Table 5.20: Summary of effect of load path on normal force for ¼” plate.....	240
Table 5.21: Summary of effect of load path on resultant force for ¼” plate.	241

List of Figures

Figure 1-1: IACS PC6 grillage model from Quinton (2008) – plating (green) and stiffener webs (yellow) are transparent to show indenter (brown).....	3
Figure 1-2: Normal force versus lateral displacement (data from Quinton (2008)) of a moving 2 cm imposed indentation on the plating of the grillage shown in Figure 1-1 – the initial drop in normal force occurs once lateral motion of the load commences.	3
Figure 1-3: Normal force versus lateral displacement (data from Quinton (2008)) of a moving 2 cm imposed indentation on the central frame of the grillage shown in Figure 1-1 – the initial drop in normal force occurs once lateral motion of the load commences.	4
Figure 1-4: IACS PC6 grillage model from Quinton (2008) – this fringe plot of y-direction displacement illustrates the plastic buckling of the central frame under a 2 cm moving indentation.....	4
Figure 2-1. Example concentrated moving load on a rigid-plastic plate where damage due to the passage of the load is ignored.	29
Figure 2-2. Example concentrated moving load on a rigid-plastic plate showing line of damage in red.	30
Figure 3-1: Longitudinally framed hull sections showing normal (green arrow) and lateral (red arrow) directions in undeformed (left) and deformed (right) states. This figure illustrates that the <i>normal</i> direction always refers to the original (i.e. undeformed) normal direction, despite hull deformation.	37
Figure 3-2: Partial schematic of the moving load apparatus showing the horizontal ram, and the directions of motion*.	38

Figure 3-3: Moving load apparatus schematic highlighting the carriage, roller rail system, swing arm, indenter, vertical ram, MTS test frame and support structure.....	41
Figure 3-4: Moving load apparatus housed in a cold room.	42
Figure 3-5: Components of moving load apparatus.....	43
Figure 3-6: Moving load apparatus: vertically loaded components.....	45
Figure 3-7: Moving load apparatus: horizontally loaded components (closest rail support, rail and linear bearings not shown for clarity).	47
Figure 3-8: Remaining general structure.	48
Figure 3-9: Rigid indenter (left) mounted on pillow-block bearings (blue) (right).	49
Figure 3-10: Ice cone sample: (top) showing ice and steel ice holder and (bottom) showing relevant dimensions of ice (yellow) and ice holder (grey).....	50
Figure 3-11: Example ice cone indenter mounted to swing-arm (red) using a stilt (box shaped object between swing arm and ice cone indenter) prior to a test.	51
Figure 3-12: Example ice cone indenter after test – crushed surface (truncating surface of the ice cone) and extruded ice (snow like substance on the surface of the ice cone and indenter) are apparent.....	52
Figure 3-13: Cross-section of apparatus to control freezing of ice indenters.	54
Figure 3-14: Special purpose ice-shaping turntable.....	54
Figure 3-15: Frame test specimen showing plating, stiffener and stiffener end plates.....	56
Figure 3-16: End view of frame test specimen (units are inches; bracketed units are mm).	57
Figure 3-17: Plan view of frame test specimen (units are inches; bracketed units are mm).	58

Figure 3-18: Side view of frames test specimen showing omitted welds.....	58
Figure 3-19: Exploded view of how frame test specimens are installed on the test carriage.	60
Figure 3-20: Lug nut torqueing pattern.....	61
Figure 3-21: ¼” plate test specimen –bolt holes and keyways are apparent.	62
Figure 4-1: Normal (vertical) force versus lateral (horizontal) displacement for rigid indenter acting on room-temperature ¼” plates.....	84
Figure 4-2: Lateral (horizontal) force versus lateral (horizontal) displacement for rigid indenter acting on room-temperature ¼” plates.....	85
Figure 4-3: Moving load apparatus components: left – “Swing arm” (red) attached to load cells (black); right – swing arm shown with steel wheel indenter shown mounted to moving load apparatus.	90
Figure 4-4: Lateral (horizontal) moving load capacities of “slow centre” and “slow end” ¼” plate cases – “slow end” case (green) shown again translated by +550 mm (red).	90
Figure 4-5: Normal (vertical) force versus lateral (horizontal) displacement for room-temperature ½” plates.	91
Figure 4-6: Lateral (horizontal) force versus lateral (horizontal) displacement for room-temperature ½” plates.	92
Figure 4-7: Lateral (horizontal) moving load capacities of “slow centre” and “slow end” ½” plate cases with red line translated by +550 mm.	95
Figure 4-8: Normal (vertical) force versus lateral (horizontal) displacement for room-temperature frames.....	97

Figure 4-9: Lateral (horizontal) force versus lateral (horizontal) displacement for room-temperature frames.....	98
Figure 4-10: Magnification of Figure 4-9.....	98
Figure 4-11: Lateral (horizontal) moving load capacities of “slow centre” and “slow end” frame cases with red line translated by +550 mm.....	103
Figure 4-12: Normal (vertical) force versus lateral (horizontal) displacement for -10°C ¼” plates: 2 cm indentation.	104
Figure 4-13: Lateral (horizontal) force versus lateral (horizontal) displacement for -10°C ¼” plates: 2 cm indentation.	105
Figure 4-14: Lateral (horizontal) moving load capacities of “slow centre” and “slow end” ¼” plate cases: 2 cm indentation with red line translated by +550 mm.	107
Figure 4-15: Normal (vertical) force versus lateral (horizontal) displacement for -10°C ¼” plates: 4 cm indentation.	108
Figure 4-16: Lateral (horizontal) force versus lateral (horizontal) displacement for -10°C ¼” plates: 4 cm indentation.	109
Figure 4-17: Lateral (horizontal) moving load capacities of “slow centre” and “slow end” ¼” plate cases: 4 cm indentation with red line translated by +550 mm.	111
Figure 4-18: Normal (vertical) force versus lateral (horizontal) displacement for -10°C ½” plates.	112
Figure 4-19: Lateral (horizontal) force versus lateral (horizontal) displacement for -10°C ½” plates.	113
Figure 4-20: Lateral (horizontal) moving load capacities of “slow centre” and “slow end” ½” plate cases with red line translated by +550 mm.	115

Figure 4-21: Normal (vertical) force versus lateral (horizontal) displacement for -10°C frames.....	116
Figure 4-22: Lateral (horizontal) force versus lateral (horizontal) displacement for -10°C frames.....	117
Figure 4-23: Lateral (horizontal) moving load capacities of “slow centre” and “slow end” frame cases with red line translated by +550 mm.....	119
Figure 4-24: Normal (vertical) displacement vs. lateral (horizontal) displacement for a force controlled ¼” plate experiment at -10°C.	122
Figure 4-25: Normal (vertical) displacement vs. lateral (horizontal) displacement for a force controlled ½” plate experiment at -10°C.	123
Figure 4-26: Normal (vertical) displacement vs. lateral (horizontal) displacement for a force controlled frame experiment at -10°C.	124
Figure 4-27: Lateral (horizontal) force vs. lateral (horizontal) displacement for force controlled ¼” plate.....	125
Figure 4-28: Lateral (horizontal) force vs. lateral (horizontal) displacement for force controlled ½” plate.....	125
Figure 4-29: Lateral (horizontal) force vs. lateral (horizontal) displacement for force controlled frame.	126
Figure 4-30: Normal (vertical) force versus time for “slow” experiments ML30 and ML31 (ice cone on elastic plate) showing “chatter” phenomenon at about a 20 kN load level.	130
Figure 4-31: Lateral (horizontal) force versus time for “slow” experiments ML30 and ML31 (ice cone on elastic plate) showing “chatter” phenomenon at about a 1 kN load level.	131

Figure 4-32: Normal (vertical) and lateral (horizontal) force versus time for “slow” experiments MovingLoad30 and MovingLoad31.	131
Figure 4-33: Magnification of part of the lateral (horizontal) force versus normal (vertical) force for ML30.	132
Figure 4-34: Friction factor for “slow” experiment ML30 (i.e. Total Horizontal Force divided by Vertical Force).	132
Figure 4-35: Friction factor for “slow” experiment ML31 (i.e. Total Horizontal Force divided by Vertical Force).	133
Figure 4-36: Photograph of the ice cone indenter for “slow” experiment ML30 after the test – magnified section shows dark “deposits”	134
Figure 4-37: Normal (vertical) force versus time for “slow” experiments ML38 and ML39 (ice cone on elastic plate) showing “chatter” phenomenon beginning at 5 [kN] for ML38 and 9 [kN] for ML39.	137
Figure 4-38: Lateral (horizontal) force versus time for “slow” experiments ML38 and ML39 (ice cone on elastic plate) showing “chatter” phenomenon beginning at <0.5 [kN].	137
Figure 4-39: Friction factor for “slow” experiment ML38 (i.e. Total Horizontal Force divided by Vertical Force).	138
Figure 4-40: Friction factor for “slow” experiment ML39 (i.e. Total Horizontal Force divided by Vertical Force).	139
Figure 4-41: Normal (vertical) force versus time for “fast” experiment ML34 (ice cone on elastic plate) showing sawtooth loading.	140

Figure 4-42: Lateral (horizontal) force versus time for “fast” experiment ML34 (ice cone on elastic plate) showing sawtooth loading.	140
Figure 4-43: Friction factor for “fast” experiment ML34 (i.e. Total Horizontal Force divided by Vertical Force).	141
Figure 4-44: Friction factor for “slow” “pressure film” experiment ML32 (i.e. Total Horizontal Force divided by Vertical Force).	143
Figure 4-45: Friction factor for “fast” “pressure film” experiment ML33 (i.e. Total Horizontal Force divided by Vertical Force).	144
Figure 4-46: Friction factor for “pseudo in-along load path” “pressure film” experiment ML35 (i.e. Total Horizontal Force divided by Vertical Force).	145
Figure 4-47: Picture of ice cone indenter for experiment MovingLoad40 after the test was completed – the crushed surface of the ice cone is visible as the dark spot at the apex of the cone.	147
Figure 4-48: Normal (vertical) force versus time for “slow” experiment ML40 (ice cone on plastic plate) showing “chatter” phenomenon beginning at 5 [kN].	148
Figure 4-49: Lateral (horizontal) force versus time for “slow” experiment ML40 (ice cone on plastic plate) showing “chatter” phenomenon beginning at 0.5 [kN].	148
Figure 4-50: Friction factor for “slow” “plastic” experiment ML40 (i.e. Total Horizontal Force divided by Vertical Force).	149
Figure 4-51: Picture of ice cone indenter for experiment MovingLoad41 after the test was completed – the crushed surface of the ice cone resembles the shape the plastically deformed plate on which it was acting.	150

Figure 4-52: Normal (vertical) force versus time for “fast” experiment ML40 (ice cone on plastic plate).	151
Figure 4-53: Lateral (horizontal) force versus time for “fast” experiment ML40 (ice cone on plastic plate).	152
Figure 4-54: Friction factor for “fast” “plastic” experiment ML41 (i.e. Total Horizontal Force divided by Vertical Force).	153
Figure 4-55: Fish-eye lens side view of frame’s web under full stationary load.....	161
Figure 4-56: Side view of frame’s web under moving load.	161
Figure 5-1: Plot of final numerical model geometries for the $\frac{1}{4}$ ” and $\frac{1}{2}$ ” plate cases (top left) and for the frame case (top right). Also shown, underneath, are renders of the physical specimens these numerical models represent.	166
Figure 5-2: Transparent view of design simulation of carriage, framed sample, bolted connections, sandwich ring, and rigid indenter.....	167
Figure 5-3: Mesh for simulation shown in Figure 5-2.	168
Figure 5-4: Normal direction load response measuring points.	173
Figure 5-5: Lateral direction load response measuring points.	174
Figure 5-6: Normal Capacity for a Frame with varying tangent modulus.....	188
Figure 5-7: Transparent view of geometry for plate test specimens: plate and rigid indenter.	191
Figure 5-8: Transparent view of frame test specimen geometry: plate, “T” stiffener and rigid indenter.	192
Figure 5-9: Framed specimen geometry shown with stiffener end plates.	193
Figure 5-10: Final plate test specimen geometry (shown transparent).	194

Figure 5-11: Final frame test specimen geometry (shown transparent).....	194
Figure 5-12: Indenter: hollow sphere section (dimensions in inches).	195
Figure 5-13: Indenter: final geometry (dimensions in inches).....	196
Figure 5-14: Plan view of plating boundary conditions (half of plate specimen shown).	198
Figure 5-15: Internal “shell to solid” CNRB connection (yellow).	200
Figure 5-16: Shell reference surfaces (black) with zero offset (left) and with full offset to one side (upper right “flange”).....	201
Figure 5-17: Plating showing cut-out for stiffener end plate.	202
Figure 5-18: Internal connection for plating and stiffener end plate.	202
Figure 5-19: CNRB (blue) with added nodes to simulate rigid weld geometry.	203
Figure 5-20: Final shell element mesh for plate sample types.....	206
Figure 5-21: Final framed specimen mesh.....	210
Figure 5-22: Rigid indenter mesh.	211
Figure 5-23: Numerical and experimental normal force results for ¼” plate specimen.	225
Figure 5-24: Numerical and experimental normal force results for ¼” plate specimens with and without normal direction compliance.....	227
Figure 5-25: Numerical and experimental lateral force results for ¼” plate specimen.	228
Figure 5-26: Numerical and experimental normal force results for ½” plate specimen.	229
Figure 5-27: Numerical and experimental normal force results for ½” plate specimens with and without normal direction compliance.....	230
Figure 5-28: Numerical and experimental lateral force results for ½” plate specimen.	231
Figure 5-29: Numerical and experimental normal force results for frame specimen.	232

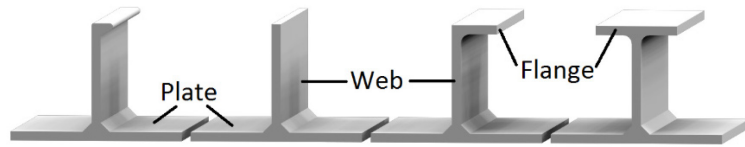
Figure 5-30: Numerical and experimental normal force results for frame specimens with and without normal direction compliance.....	233
Figure 5-31: Numerical and experimental lateral force results for frame specimen.	234
Figure 5-32: y-displacement fringe plot of frame numerical model illustrating plastic buckling.....	234
Figure 5-33: Visualization of load path for “shallow” simulation. Indenter moves simultaneously in normal and lateral directions, starting at the end position and finishing at the centre of the plate.	236
Figure 5-34: Visualization of load path for “steep” simulation. Indenter moves simultaneously in normal and lateral directions, starting at the quarter position and finishing at the centre of the plate.	236
Figure 5-35: Visualization of load path for “steep” simulation. Indenter first moves in normal direction only, and then in the lateral direction only; starting at the “centre” position and finishing at the “end” position.....	237
Figure 5-36: Plot of load paths for each of the three “load path” simulations. The vertical axis is normal displacement, the horizontal axis is lateral displacement.....	238
Figure 5-37: Normal (vertical) force results versus time for load path simulations – (A-red) experiment results of ML10, (B-green) ¼” plate numerical model calibration results from Chapter 5.4.1 for experiment ML10, (C-blue) steep simulation results, (D-cyan) shallow simulation results.....	239
Figure 5-38: Resultant force results versus time for load path simulations – (A-red) experiment results of ML10, (B-green) ¼” plate numerical model calibration results from	

Chapter 5.4.1 for experiment ML10, (C-blue) steep simulation results, (D-cyan) shallow simulation results.	240
---	-----

List of Symbols, Nomenclature or Abbreviations

Plastic buckling	The <i>plastic</i> structural mechanism through which a <i>frame's</i> <i>web</i> predominantly deforms in the vicinity of a moving load causing plastic damage.
Design load	A <i>design load</i> is the load applied to a <i>hull</i> that is meant to be representative of the largest expected <i>environmental load</i> to be encountered in the <i>hull's</i> service life. The <i>design load</i> is usually prescribed by a regulatory body.
Elastic deformation	Response of a hull as it deforms within its elastic region. This type of deformation is temporary (i.e. completely recoverable) and no permanent damage occurs.
Environmental load	For the purposes of this thesis, an <i>environmental load</i> is any load that a <i>hull</i> may be subject to through normal operation in its design environment.
Frame	The <i>framing</i> of a <i>grillage</i> structure provides stiffness to the <i>plating</i> and serves to transmit environmental loads shed from the <i>plating</i> to the primary <i>hull</i> structure. The stiffness is provided by a <i>stiffener</i> . When analysing a <i>frame</i> , it is common to include a portion of the <i>plating</i> adjacent to the <i>stiffener</i> ; thus a <i>frame</i> consists of the <i>stiffener</i> and part of the

adjacent *plating*. Each of the four structures show in the following figure are *frames*.



Horizontal load

This term refers to a *lateral load* as measured during the moving load experiments. As motion in the *lateral direction* was applied with a hydraulic ram orientated perpendicular to gravity, the terms *lateral load* and *horizontal load* are sometimes used interchangeably throughout this thesis.

Hourglassing

Hourglassing is a nonphysical, zero energy mode of vibration for underintegrated shell and solid finite elements. It produces zero strain and no stress.

Hull

For the purposes of this thesis, a *hull* is the exterior load bearing structure of a ship/offshore-structure which is comprised of a steel *grillage* that is designed to withstand environmental loads such that the hull remains intact and the ship/offshore-structure remains operational.

Grillage

A grillage is a structure consisting of contiguous *plates* supported by underlying *frames*. The plating sheds load to the underlying framing, which sheds load to the primary hull structure.

Lateral direction	<p>Any direction aligned with the plane of the <i>hull plating</i>.</p> <p>Please note: during the moving load experiments, the term <i>lateral</i> implies the direction aligned with the long axis of the specimen's plating. Throughout this thesis, the terms <i>lateral</i> and <i>horizontal</i> are used synonymously, as the horizontal direction in the moving load experiments corresponds with the lateral direction of the hull plating.</p>
Lateral load	<p>A load aligned with any direction in the plane of the <i>hull plating</i>. Please note: during the moving load experiments, any reference to a <i>lateral load</i> implies load in the direction aligned with the long axis of the specimen's plating. As motion in the lateral direction was applied with a hydraulic ram orientated perpendicular to gravity, the terms <i>lateral load</i> and <i>horizontal load</i> are sometimes used interchangeably throughout this thesis.</p>
Moving load	<p>Any <i>hull</i> load (e.g. design load or accidental overload) that includes lateral motion along <i>hull's</i> exterior (i.e. plating). The term <i>moving load</i> does not relate to the magnitude of the load; it refers only to location with respect to time.</p>
Moving load capacity	<p>The structural capacity of a hull to withstand a <i>moving load</i>.</p>

Moving load effects	For the purposes of this thesis, this term refers to the phenomena associated with the reduction in structural capacity of a hull <i>plate</i> or <i>frame</i> attributed to the <i>lateral</i> movement of a load causing <i>plastic hull damage</i> , compared with the structural capacity for a <i>stationary load</i> of equal magnitude. Further when considering a <i>frame</i> , it also includes the early onset (compared with stationary loads) of <i>plastic buckling</i> in a <i>frame's web</i> .
Normal direction	The direction perpendicular to the hull plating in its undeformed condition. Throughout this thesis, the terms <i>normal</i> and <i>vertical</i> are used synonymously, as the vertical direction in the moving load experiments corresponds with the normal direction of the hull plating.
Normal load	A load acting perpendicular to the hull plating in its undeformed condition. Please note: during the moving load experiments, motion in the <i>normal direction</i> was applied with a hydraulic ram orientated vertically (i.e. aligned with gravity), and the terms <i>normal load</i> and <i>vertical load</i> may be used interchangeably throughout this thesis.
Plastic damage	Permanent (i.e. non-recoverable) hull structure deformation resulting from <i>plastic deformation</i> .

Plastic deformation	Response of a hull as it deforms past its elastic threshold (i.e. non-recoverable deformation resulting in <i>plastic damage</i>).
Plate	The <i>plate</i> (or <i>plating</i>) of a <i>grillage</i> structure comprises the exterior of a <i>hull</i> and consists of a series of welded contiguous thin shells supported by underlying <i>frames</i> . The <i>plating</i> is required to remain intact in order to prevent the ingress of water or, if it is adjacent to a tank, the outflow of the contents of the tank. A <i>plate</i> is illustrated in the figure given in the definition of <i>frame</i> above.
Pseudo-elastic response	For the purposes of this thesis, <i>pseudo-elastic response</i> refers to a type of hull structural response resulting from a <i>moving load</i> that causes very low levels of <i>plastic damage</i> (in the vicinity of the load), where the hull structure grossly behaves as if no permanent damage occurs.
Stationary load	Any <i>hull</i> load that acts upon a single location on the <i>hull</i> . <i>Design loads</i> , as presently defined by classification and regulatory rules, are <i>stationary loads</i> . The term <i>stationary load</i> does not relate to the magnitude of the load; it refers only to location with respect to time. Any analysis of a hull structure that ignores the history of the lateral position of a load with respect to time assumes the load to be a <i>stationary load</i> .

Stationary load capacity	The structural capacity of a hull to withstand a <i>stationary load</i> (e.g. the structural capacity of a hull to withstand a <i>design load</i>). Any analysis of a hull structure that ignores the history of the lateral position of a load with respect to time is implicitly determining the <i>stationary load capacity</i> .
Stiffener	For the purposes of this thesis, a <i>stiffener</i> provides stiffness to a <i>plating</i> , and consists of a <i>web</i> , and usually a <i>flange</i> as well. A <i>stiffener</i> is illustrated in the figure given in the definition of <i>frame</i> above.
Three Hinge Collapse	A clamped beam or plate supporting a distributed load has the highest stresses present at the supports. If the load large enough, the stresses will be above the yield strength of the beam/plate material. If elastic/perfectly-plastic stress-strain behaviour is assumed, plastic hinges will form at these locations (i.e. one plastic hinge at each of the supports). Subsequently, if the load is large enough, another plastic hinge will form at the centre of the beam/plate. Once three hinges exist, the structure can no longer support itself and collapses (theoretically).
Ultimate limit state	This term generally refers to the practice of designing a structure so that its design point is the onset of some theoretical structural collapse mechanism (e.g. three-hinge

collapse for fixed beam that is free to pull in). It is important to note that setting the design point at a theoretical point of collapse is generally conservative as the theory itself is generally conservative. I.e. the practical point of collapse generally requires a far greater energy input due to ignored energy storage mechanisms in the theory.

Vertical load

This term refers to a *normal load* as measured in the moving load experiments. During the moving load experiments, *normal loads* were applied with a hydraulic ram orientated in the vertical direction (i.e. aligned with gravity) and the terms *normal load* and *vertical load* may be used interchangeably throughout this thesis.

Web

A *web* is the portion of a *stiffener* (or also a *frame*) that consists of a thin shell affixed to the *plating* so as to maximize bending stiffness (e.g. perpendicular to *plating* in the case of wall sided ship). A *web* is illustrated in the figure given in the definition of *frame* above.

List of Appendices

Appendix A – Moving Load Apparatus Equipment Specifications	260
Appendix A1 – MTS Test Frame Specifications	261
Appendix A2 – MTS Vertical Hydraulic Ram Specifications.....	265
Appendix A3 – MTS Flextest GT Specifications	267
Appendix A4 – MTS Load Cell Specifications	268
Appendix A5 – MTS LVDT Specifications	269
Appendix A6 – Horizontal Load Cell Specifications	272
Appendix A7 – Horizontal Linear Position Transducer Specifications.....	274
Appendix A8 – Linear Roller-Rail System Specifications	275
Appendix A9 – Horizontal Hydraulic Cylinder Specifications	278
Appendix A10 – Indenter Bearing Specifications	280
Appendix A11 – Steel Mill Certifications for Carriage Steel and W-Beams	282
Appendix B – Other Apparatus Specifications	285
Appendix B1 – High-speed Camera Specifications.....	286
Appendix B2 – GoPro HD Hero 2 & Hero 3 Specifications	287
Appendix B3 – Canon EOS60D Specifications.....	289
Appendix B4 – Flir Thermal Cameras Specifications	290
Appendix B5 – Fujifilm Prescale™ Pressure Film.....	293

Appendix B6 – Microscribe Specifications	294
Appendix C – Moving Load Experimental Results Plots	295
Appendix C1 – Room-temperature Tests.....	297
Appendix C1.1 – Quarter Inch Plate – 4 cm (1.575 in.) Indentation	298
Appendix C1.1.1 – Summary Plots for Experiments ML 9, 10 and 11.....	299
Appendix C1.1.2 – MovingLoad9	303
Appendix C1.1.3 – MovingLoad10	310
Appendix C1.1.4 – MovingLoad11	317
Appendix C1.2 – Half Inch Plate – 3 cm (1.181 in) Indentation	325
Appendix C1.2.1 – Summary Plots for Experiments ML 6, 7 and 8	326
Appendix C1.2.2 – MovingLoad6	330
Appendix C1.2.3 – MovingLoad7	337
Appendix C1.2.4 – MovingLoad8	344
Appendix C1.3 – Frame – 2.5 cm (0.984 in.) Indentation	350
Appendix C1.3.1 – Summary Plots for Experiments ML 14, 15 and 16	351
Appendix C1.3.2 – MovingLoad14	354
Appendix C1.3.3 – MovingLoad15	361
Appendix C1.3.4 – MovingLoad16	368
Appendix C2 – -10°C (14° F) Tests.....	375

Appendix C2.1 – Quarter Inch Plate – 2 cm (0.787 in.) Indentation	376
Appendix C2.1.1 – Summary Plots for Experiments ML 17, 18 and 19	377
Appendix C2.1.2 – MovingLoad17	380
Appendix C2.1.3 – MovingLoad18	387
Appendix C2.1.4 – MovingLoad19	394
Appendix C2.2 – Quarter Inch Plate – 4 cm Indentation.....	401
Appendix C2.2.1 – Summary Plots for Experiments ML 23, 24 and 25	402
Appendix C2.2.2 – Fast – MovingLoad23.....	406
Appendix C2.2.3 – MovingLoad24	413
Appendix C2.2.4 – Full Length – Slow - MovingLoad25	420
Appendix C2.3 – Half Inch Plate – 3 cm Indentation.....	427
Appendix C2.3.1 – Summary Plots for Experiments ML 20, 21 and 22	428
Appendix C2.3.2 – MovingLoad20	432
Appendix C2.3.1 – MovingLoad21	439
Appendix C2.3.2 – MovingLoad22	446
Appendix C2.4 – Frame – 2.5 cm Indentation.....	453
Appendix C2.4.1 – Summary Plots for Experiments ML 26, 27 and 28	454
Appendix C2.4.2 – MovingLoad26	458
Appendix C2.4.3 – MovingLoad27	465

Appendix C2.4.4 – MovingLoad28	472
Appendix C2.5 – Force Controlled Tests.....	479
Appendix C2.5.1 – Summary Plots for Experiments ML 29, 36 and 37	480
Appendix C2.5.2 – Force Controlled – MovingLoad29	483
Appendix C2.5.3 – Force Controlled – MovingLoad36	491
Appendix C2.5.4 – Force Controlled – MovingLoad37	499
Appendix C3 – Ice Cone Tests	507
Appendix C3.1 – Ice Cone Tests Inducing Frictionless Elastic Plate Response	508
Appendix C3.1.1 – Summary Plots for Experiments ML 32, 33, and 35	509
Appendix C3.1.2 – MovingLoad32	513
Appendix C3.1.3 – MovingLoad33	525
Appendix C3.1.4 – MovingLoad35	535
Appendix C3.2 – Ice Cone Tests Inducing Elastic Plate Response	546
Appendix C3.2.1 – Summary Plots for Experiments ML 30, 31, 34, 38, and 39	547
Appendix C3.2.2 – MovingLoad30	551
Appendix C3.2.3 – MovingLoad31	562
Appendix C3.2.4 – MovingLoad34	573
Appendix C3.2.5 – MovingLoad38	584
Appendix C3.2.6 – MovingLoad39	594

Appendix C3.3 – Ice Cone Tests Inducing Plastic Plate Deformation	604
Appendix C3.3.1 – Summary Plots for Experiments ML 40, 41 and 42	605
Appendix C3.3.2 – MovingLoad40	609
Appendix C3.3.3 – MovingLoad41	620
Appendix C3.3.4 – MovingLoad42	631
Appendix D – Custom Data Analysis and Plotting Script.....	642

Chapter 1 Introduction

All current regulations and design codes for icebreaking/ice-strengthened ships and offshore structures consider only *stationary loads* for hull structural design. This implies that the effects of movement of a load along the hull are negligible. It is well known that ice loads are most often applied – particularly to ship hulls – in a way that would be better modelled as a *moving load*.

(Quinton 2008), using a calibrated numerical model, found that there were no appreciable effects of load movement for moving loads inciting an elastic hull response; but when the moving loads caused plastic damage, the effects were dramatic – the structural capacities of both plate and frame hull structures were predicted to be significantly less than for a stationary load of equal magnitude applied at the same location.

This thesis tests the hypothesis that the structural capacity of a hull subject to a moving load causing plastic damage is significantly less than when subject to a stationary, but otherwise equivalent, load. This hypothesis is investigated using a combination of novel laboratory experiments and corresponding calibrated numerical models.

1.1 A Note on Capacity

The capacity of a structure is a function of the condition under which it is loaded. It is improper to say that the capacity of a structure is a single value, without specifying the load condition associated with that capacity; however, given that current regulations and design codes for Arctic ships and offshore structures consider only stationary design loads, we tend to think of a hull as having a particular structural capacity (i.e. the capacity to withstand

the stationary design load). The term *reduced structural capacity* is used throughout this thesis when referring to the effects of load movement for loads causing plastic damage. Whenever this term is used herein, it may be assumed to be referring to a comparison with the structural capacity of the same structure subject to a stationary load of equivalent magnitude.

1.2 Background

A reduced structural capacity to moving loads that cause plastic damage was predicted in (Quinton 2008), where a numerical model calibrated against laboratory experiments on a full-scale IACS PC6 classed steel grillage (see Figure 1.1) under stationary loading (Daley, Hermanski 2008a, 2008b) was extrapolated to investigate moving loads. Moving loads are loads that act not only normal to the hull, but at the same time translate laterally along the hull's surface. In particular, the previous work predicted a decrease in the structural capacity of both hull plating (see Figure 1.2) and hull frames (see Figure 1.3) compared to the stationary loading condition. For hull frames, it was further noticed that *plastic buckling* of the frame webs (see Figure 1.4) occurred at a much lower load level for moving loads, than for stationary loads. These behaviours will be collectively referred to as *moving load effects* throughout this thesis.

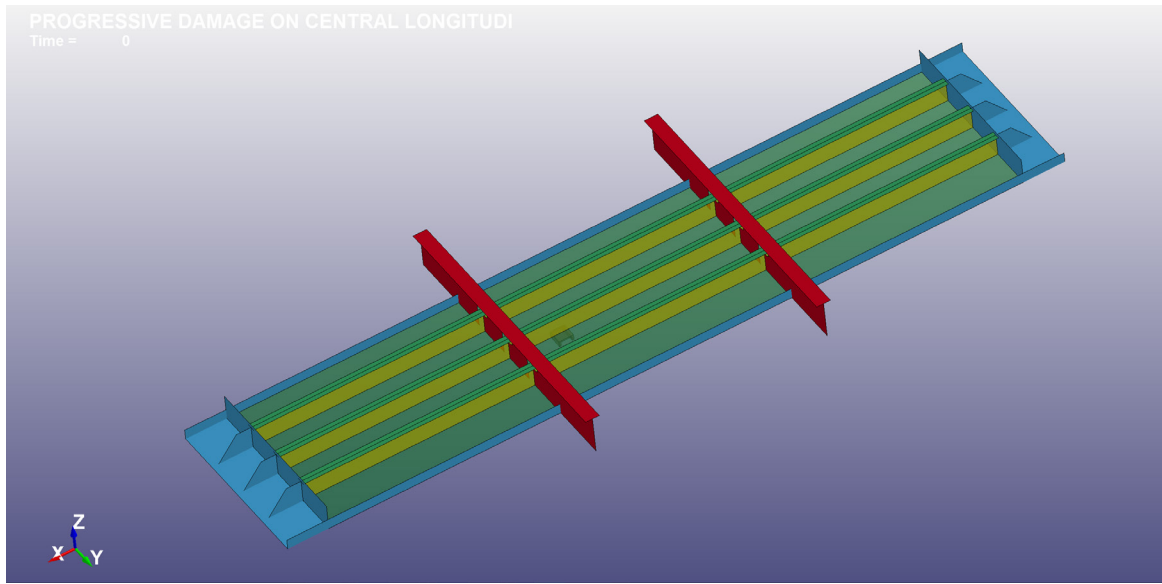


Figure 1.1: IACS PC6 grillage model from Quinton (2008) – plating (green) and stiffener webs (yellow) are transparent to show indenter (brown).

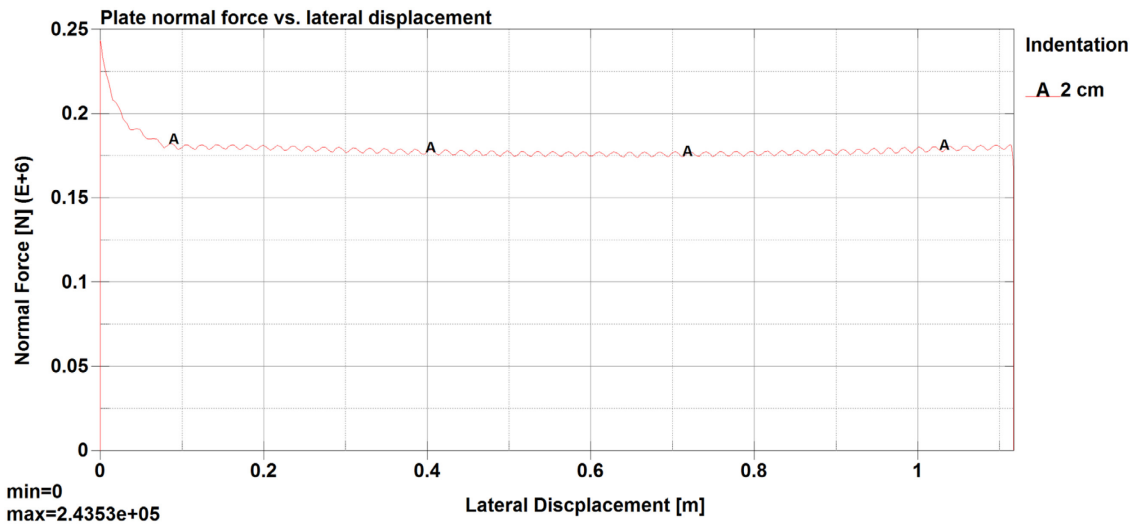


Figure 1.2: Normal force versus lateral displacement (data from Quinton (2008)) of a moving 2 cm imposed indentation on the plating of the grillage shown in Figure 1.1 – the initial drop in normal force occurs once lateral motion of the load commences.

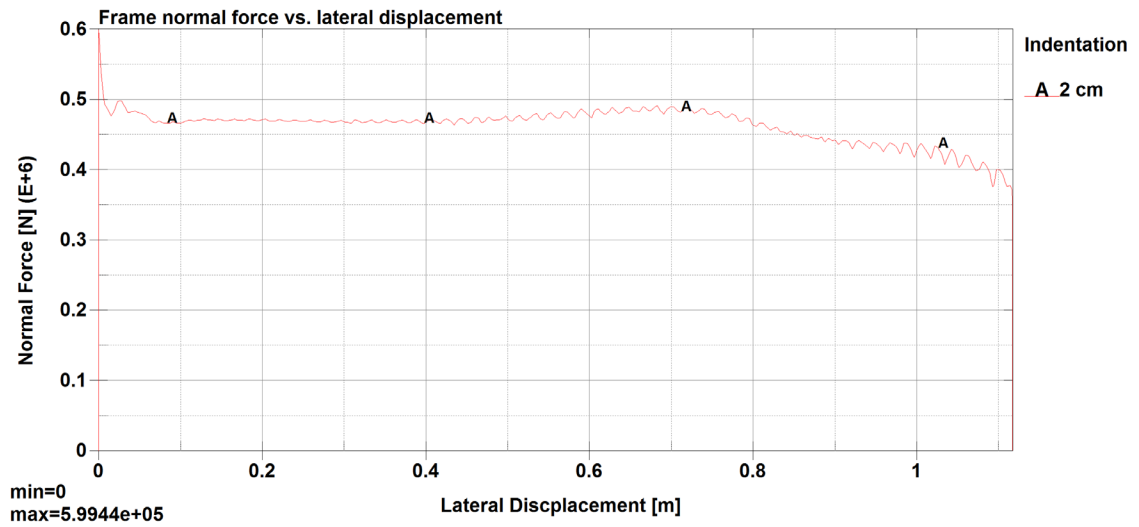


Figure 1.3: Normal force versus lateral displacement (data from Quinton (2008)) of a moving 2 cm imposed indentation on the central frame of the grillage shown in Figure 1.1 – the initial drop in normal force occurs once lateral motion of the load commences.

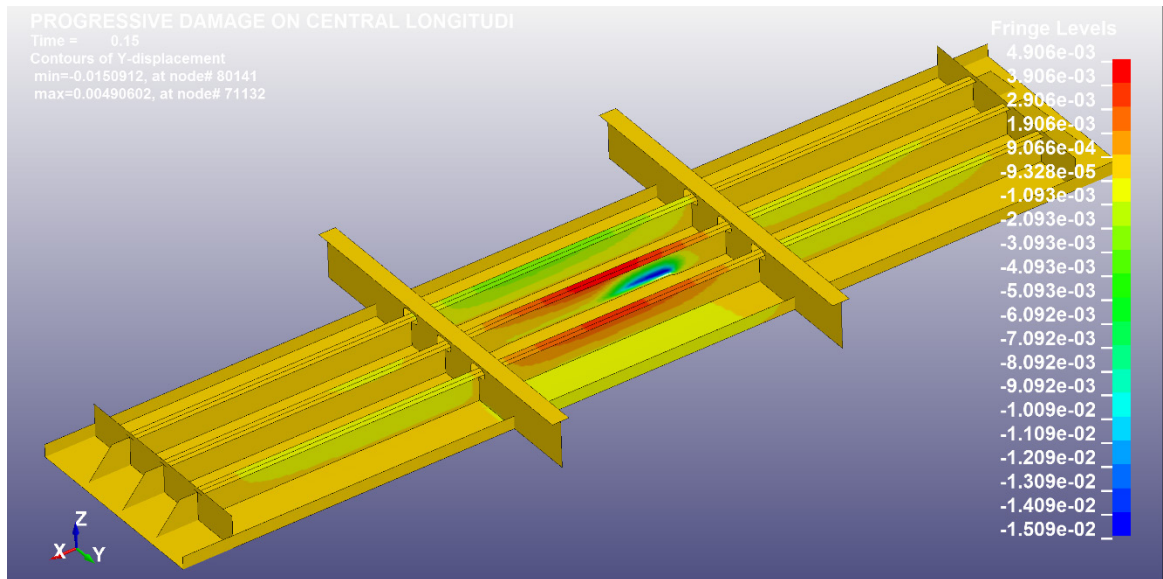


Figure 1.4: IACS PC6 grillage model from Quinton (2008) – this fringe plot of y-direction displacement illustrates the plastic buckling of the central frame under a 2 cm moving indentation.

A review of the publically available literature on the subject of moving loads on ship hulls reveals that the research has concentrated on the tearing response of hull plating in collision and grounding scenarios (see Chapter 2.2). There is very little treatment of the scenario where a moving load causes plastic damage that does not result in puncture and subsequent tearing of the hull steel. The most notable of this work is the numerical and analytical work of Hong and his co-authors (Hong 2008, Hong, Amdahl 2012). They numerically investigated the response of a ship hull's double-bottom to *sliding loads* during grounding on a *shoal* (which is defined as a large seabed surface) and developed a simplified semi-empirical method for predicting the structural response (see Chapter 2.2.4.2).

The scenario of moving loads causing plastic damage without hull tearing is important for ships and offshore structures operating in ice, as these vessels are generally designed or *classed* to withstand a certain level of ice load, and rarely (even under accidental overload) experience hull fracture, puncture or tearing of the hull plating¹; although such vessels are regularly dented. This scenario is also important for non-ice-strengthened ships that encounter ice, as these ships are much more likely to experience plastic damage during ice impacts.

The investigation of moving loads causing plastic damage is particularly relevant at this point given two recent developments: 1. the recent shift in design practice of Arctic going ships and offshore structures towards *ultimate limit states design*, and 2. the recent increase in Arctic activity.

¹ No references are provided here as this contention is explored in more detail below.

On March 1, 2008, the International Association of Classification Society's (IACS) *Unified Rules for Polar Class* (IACS 2011) came into effect. This new international standard precipitated a shift in the design of Arctic going ships from an elastic design regime to ultimate limit states design. The ultimate limit state design point for these rules is the theoretical onset of three-hinge collapse for both plating and framing² (Daley 2002, Daley, Kendrick et al. 2001). Given the plastic design point, it is reasonable to expect some plastic hull damage in today's polar class vessels upon sustaining their hull design load.

The recent increase in Arctic activity is important because of increased activity: raises the probability of occurrence of accidental loads (i.e. loads greater than the design load); and it increases the likelihood of non-ice-classed ships venturing into ice infested waters. The latter is due to the lack of support infrastructure in most Arctic areas. It is conceivable that an incident (e.g. search and rescue, oil spill cleanup, etc...) in the Arctic may require the support of non-ice-strengthened ships. Therefore, there is a need to understand the effect of moving loads causing plastic damage on these vessels.

Despite the move to recognize the onset of plasticity as a design point, the design load for all present day standards (classification society rules³, government regulations⁴, and international guidelines⁵) is a stationary load, and therefore does not consider any possible effects of the lateral movement of the load on the hull structure. If the lateral movement of a load does in fact significantly reduce the plastic structural capacity (as is shown in this

² This is a slight oversimplification, but sufficiently valid for the present discussion.

³ For example American Bureau of Shipping: Steel Vessel Rules 2015 – Part 6, and others.

⁴ For example the Canadian Arctic Shipping Pollution Prevention Regulations (ASPPR).

⁵ For example the International Association of Classification Societies (IACS): e.g. Requirements Concerning Polar Class; and International Organization for Standardization (ISO): e.g. ISO 19906.

thesis), then it is important to consider this in the design of icebreaking ships, and especially when deciding whether to send a non-ice-classed ship into ice infested waters.

1.3 Applicability of Moving Load Effects

To further qualify the need for examination of these moving load effects, their scope of consequences should be discussed. Quinton (2008), as well as experiments presented in this thesis, verify the implicit assumption in existing design standards that there is no reduction in hull structural capacity due to lateral load movement of loads that only lead to elastic deformations. That is, any movement of these lower level loads may be safely ignored (i.e. at any instant in time, they may be treated as stationary loads). Further, Quinton (2008) predicted that the effect of lateral movement of loads inciting a *pseudo-elastic* hull response is minimal; and may also be treated as stationary loads. Pseudo-elastic hull response occurs when a moving load incites minimal localized plastic damage, and the hull structure grossly behaves as if it had remained elastic (which the vast majority of it does). Further, additional work by (Quinton, Daley et al. 2013, and unpublished) suggest that the effects of lateral movement of the design load (which should not lead to significant plastic deformation) for all IACS polar class structures (i.e. PC1-7) – while not insignificant – is not detrimental. As discussed above, the design point for IACS hull structures is the onset of three-hinge collapse. This is based on a theory that ignores many practically occurring energy sinks (e.g. strain hardening and plastic membrane stress). This “builds in” a high degree of conservatism, not only against three-hinge collapse, but against large structural deformations at the design load. Please note, this work regarding movement of

the IACS design load is preliminary, and requires more study before any solid conclusions can be drawn.

The above suggests that the effects of moving loads on IACS polar class ships are not particularly significant up to the theoretical initial onset of three-hinge collapse (i.e. the design point). The question, then, is “When are the effects of moving loads significant?” They are significant in accidental overload scenarios. As will be shown below, moving load laboratory experiments indicate that an indentation of just 5% of the frame spacing is enough to incite a significant loss in capacity of the hull structure due to lateral load movement. This number is not an upper boundary, but represents the smallest indentation carried out in the experiments. Determination of the specific point where moving load effects become significant was not within the scope of these experiments, however prior numerical simulations (Quinton 2008) suggest that these effects become significant at an indentation of 1.5-2% of the frame spacing for both plates and frames; discounting the mitigating effect of strain-rate.

1.4 Methodology

In order to investigate moving load effects (as defined above) with a higher degree of confidence than that provided by the purely numerical previous studies, it was decided to conduct a series of laboratory experiments. These experiments would provide insight into conditions leading to moving load effects, conditions that mitigate moving load effects, and provide a basis for further calibrated numerical investigations.

1.5 Thesis Organization

This thesis is organized into the following chapters:

1. Introduction – Introduces the topic of moving loads causing plastic damage, and discusses the need to investigate the effects of load movement on the structural capacity of ship hulls subjected to ice loads and accidental loads.
2. Literature Review – Identifies the literature pertaining directly to moving ice loads causing plastic damage, discusses the background information, identifies the knowledge gaps, and identifies the current state-of-the-art techniques for modeling similar scenarios.
3. Moving Load Experiments – Discusses the design and capabilities of the novel moving load apparatus, as well as the experimental test regime.
4. Experimental Results – Presents the results and discussion of the experiments described in Chapter 3.
5. Numerical Simulations – Uses three representative experimental cases (i.e. $\frac{1}{4}$ " plate, $\frac{1}{2}$ " plate and frame) to calibrate a numerical model of moving loads causing plastic damage to plates and frames. Begins with a discussion of the design of experiments analysis used to determine certain material and physical parameters that were unknown during the experiments and were required for the numerical models. Discusses the calibration of the numerical models. Finishes with guidelines for numerically modeling moving loads on hull structures.
6. Overall Conclusions, Novel Contributions and Recommendations for Future Work.

Finally, the Appendices include specifications for all of the experimental apparatus employed in this research (Appendix A and Appendix B), plots of all recorded experimental data for each experiment (Appendix C), and the code for the custom data analysis software employed during this research (Appendix D).

Chapter 2 Literature Review

Other than limited work by (Quinton 2008, Quinton, Daley et al. 2010, 2012, Quinton, Daley et al. 2013), there is no publically available literature on moving ice loads on the hulls of ships and offshore structures. What follows is a review of the relevant parent topics that contribute to the subject of moving ice loads on the hulls of ships and offshore structures. These topics are: ice, collision and grounding loads, moving loads, progressive damage, and strain rate and temperature effects.

2.1 Ice

One of the goals of this research is to observe the behaviour of ice as it is permanently damaging a structure during a moving load scenario. Another goal is to determine if lateral movement (i.e. sliding of the ice along the hull) changes the behaviour of the ice, relative to the case of no lateral movement, when there is no permanent deformation. In order to observe any phenomena unique to moving load scenarios, it was necessary to conduct a general review of the existing literature on ice behaviour. The following general review provides the background necessary to design and conduct the novel laboratory experiments involving ice presented in this thesis. Further, the last section “Numerical modeling of ice” will provide background information for future work.

2.1.1 Introduction

Glaciology (the study of ice) is a wide field. To narrow the scope of the review of relevant literature, a description of the ice used in the experiments presented in this thesis is given here. The ice used in the moving load experiments was laboratory scale, pure freshwater

granular ice. This type of ice is similar to glacial ice in that both have fine (small) grain sizes with randomly oriented c-axes. Additionally both have entrapped bubbles, however the bubbles in glacial ice are usually subject to compression from the surrounding ice, whereas the bubbles in laboratory ice are not; or are compressed to a much lesser degree. This is because glacial ice is formed from compressed snow. The characteristics of glacial ice have been summarized in Gagnon and Gammon (1995a, 1995b, 1997). The durations of time the laboratory ice samples were under load covers from approximately one second to one-hundred fifty seconds (i.e. two and a half minutes). The durations of these tests have implications on the response of the ice samples from both a continuum mechanics and a fracture mechanics point of view; as will be discussed below. Depending on the experiment, the behaviour exhibited by the ice samples was either primarily crushing (i.e. tiny fractures coupled with comminution of the crushed ice), or crushing with large fractures and spalls.

In 1988, Sanderson published a very highly regarded book (Sanderson 1988) on the state-of-the-art of ice mechanics. This literature review, relies heavily on his work in describing the relevant literature up to 1988, but supplements his presentation as necessary with newer works. Other relevant summary type works are Hobbs (1974), Petrenko and Whitworth (1999), and Schulson and Duval (2009). The first two deal with the physics of ice as a general material. The later deals specifically with the creep and fracture of ice.

2.1.2 Ice mechanics

At laboratory scale, the mechanical properties of pure freshwater ice are well understood, and once corrections for brine inclusions are made, the results of experiments performed

with freshwater ice provide good estimates for the behaviour of sea ice (Sanderson 1988). There are many facets of ice that make it very hard to classify from an engineering standpoint. Ice creeps at all stresses and shows no yield point (Sanderson 1988). From a mechanical perspective relevant to icebreaking, it behaves as both a continuum prior to fracture and as discontinuous media after fracture. Ice is extremely brittle at high strain rates and fractures readily under these conditions (Sanderson 1988). To further complicate the matter, ice exhibits a scale effect (Dempsey, Defranco et al. 1999, Dempsey, Adamson et al. 1999, Mulmule, Dempsey 1999) that can be explained by brittle fracture mechanics and leads to relatively higher failure loads at smaller scales. Thus if operational ice loads were extrapolated from laboratory experiments without considering the scale effects, then the extrapolated loads would be far higher than for actual operational scale ice.

2.1.2.1 Continuum mechanics

Ice may be classified as *columnar* or *granular* based on the shape and orientation of its grains. In order to be treated as a continuum, the grain size of an ice sample must be small compared with its dimensions. This topic is discussed in Chapter 2.1.3.

Columnar ice will not be discussed, as the laboratory ice cone samples used in this research are composed of granular ice; which has randomly oriented c-axes and therefore exhibits isotropic material properties. When stressed, ice will initially deform in three distinct and simultaneous ways: immediate elastic strain, transient time-dependent delayed elastic strain (i.e. primary creep), and time-dependent non-linear viscous creep strain (i.e. secondary creep) (Sanderson 1988). The constitutive laws for this behaviour for granular ice may be found in Jacka (1984). As time progresses past the instant of applied load, the

primary creep ceases and the secondary creep strain continues to increase. After sufficient time, secondary creep gives way to tertiary creep.

The immediate elastic strain component follows Hooke's Law, with an elastic modulus of approximately 9.5 GPa, and is not strongly dependent on temperature or grain size; but is strongly dependent on porosity (Sanderson 1988). Poisson's ratio is reported in Sanderson's book to be 0.33 ± 0.03 . The primary creep strain component commences immediately and decreases at a variable rate. Primary creep is elastic and recoverable; given enough time upon release of the load (Sanderson 1988). The secondary creep strain component begins to dominate as the primary creep strain-rate approaches zero, and can be viewed as a minimum creep-rate in the transition from primary creep to tertiary creep (Sanderson 1988). Sanderson reports this type of creep to be independent of grain size. The beginning of the tertiary creep strain stage is marked by an increase in strain-rate after the minimum strain-rate of the secondary creep stage.

2.1.2.2 Fracture mechanics

In addition to the above continuum mechanics, once ice reaches a sufficient stress, strain-rate, or strain level, it fractures (Sanderson 1988). Currier and Schulson (1982) show that the fracture strength, σ_f , decreases with increasing grain size, d ; at least for aggregates slowly strained (10^{-6} s^{-1}) at high temperatures (-10°C or $0.96 T_m$). Their analysis suggests that the strength is controlled by the propagation, in a brittle manner, of micro-cracks nucleated through dislocation pile-ups at grain boundaries. It is important to distinguish between crack nucleation and propagation. Micro-cracks may nucleate under a given load, or they may pre-exist before a load was applied to the ice. The ice will not fail unless the

load level is sufficient to cause the cracks to propagate (Sanderson 1988). Two types of fracture have been reported by Sanderson: *nucleation-controlled* and *propagation-controlled*. The former occurs when the applied load induces the nucleation of cracks that are large enough to immediately propagate. The latter occurs when the nucleated (or pre-existing) cracks are too small to immediately propagate, and propagation requires an increased load (Sanderson 1988).

The fracture behaviour of ice for pure tension and pure compression cases are different; compression incites stable crack propagation, while tension crack propagation is unstable (Sanderson 1988). For the moving ice load scenario, the stress state is complex (i.e. not pure compression or tension) due to the motion of the load.

Much theoretical work on ice fracture, fracture toughness, and the applicability of linear elastic fracture mechanics to laboratory experiments has been done by Dempsey et al. (1999, 1999) and Mulmule and Dempsey (1999).

2.1.2.3 Combined continuum and fracture mechanics

Dutta, Cole, Schulson and Sodhi (2004) performed high strain-rate compressive tests on laboratory grown columnar ice. They tested at two temperatures, -10°C and -40°C , and varied strain-rate between 10 and 15 s^{-1} , with an additional control strain rate at $3 \times 10^{-4}\text{ s}^{-1}$. They observed that most failures occurred by splitting; and final failure by collapse of the columns during the passage of the stress wave⁶. They found that most failures occurred at around 1000 micro strain, and that failure begins with a crack, followed by progressive

⁶ They used Hopkinson pressure bar tests for the high strain rate tests.

failure with multiple peaks in the stress time history. They noted that the initial fracture was brittle in nature, but that final failure was affected by the time it took for the ejection of the failed ice fragments; thereby giving the appearance of visco-elastic failure. Similar findings are found in Mulmule and Dempsey (1999). While these findings are for columnar ice, and not the granular ice used in the experiments presented herein, it is expected that the final failure load of granular ice is also time-dependent.

Gagnon (1998, 1999) analysed the video data from the Hobson's Choice ice island medium-scale indenter tests of May, 1990. He found that the forward motion of the indenter coincided with spall events (where large chunks of intact ice would break away from the contact area) and that "hard blue zones" of relatively intact ice supported the load in between spall events. He reported that this repetition of increasing load supported by the hard zones, and subsequent load release through spalling events, is the basis for the sawtooth load-time histories observed.

2.1.3 Scale

The works of Dempsey et al. (1999, 1999) and Mulmule and Dempsey (1999) show that the scale of the ice affects its structural behaviour (and therefore its developed loads) through how it fractures. They suggest that for laboratory scale experiments, experimenters often give little or no thought to the size of the sample compared with its grain size. Further they show that the nominal tensile strength of ice decreases with increasing test specimen size. Linear elastic fracture mechanics (LEFM) suggests that the decrease should be on the scale of $1/\sqrt{L}$. This has been shown to be too large for smaller scale specimens, but larger samples tend toward this limit.

2.1.4 Confinement

Confinement exists when crushed ice at the contact interface is prevented from being extruded, and escaping the contact zone. This can occur when a small indenter is crushed in to a large piece of ice, or when the geometric shape of the structure confines the ice at the contact interface. The latter is of concern for these experiments. For the case of a moving ice cone indenter inducing plastic damage in a steel plate, it is conceivable that the steel plate would deform around the ice cone, applying a confining pressure.

Confinement of ice at the crushing interface can increase contact pressures by preventing flaking and spalling of the intact ice (Croasdale 2001). Because the crushed ice is prevented from leaving the contact zone, it exerts a confining pressure on the adjacent intact ice. This confining pressure tends to prevent cracks from propagating in the solid ice, and therefore prevents spalls (or flakes) from breaking off. This serves to increase the overall load at the contact interface.

Kim (2014) studied the effect of crushing ice into non-planar surfaces. In particular, he crushed ice cones into a concave conical shaped surface (receptacle), as well as a concave wedge. He determined that circumferential confinement from the conical surface caused an increase in overall load, while the confinement effects of crushing into the concave wedge were negligible. He explains that while the crushed ice appeared to be partially confined by the wedge, it was able to escape easily via each of the unconfined sides. These results are of particular importance to the moving ice cone experiments involving plastic deformation of steel plates in this research.

2.1.5 Numerical modeling of ice

Ice-structure interaction is a highly non-linear transient dynamic problem. Ice exhibits a myriad of behaviours, including: creep; elasticity; plasticity; crushing; fracture (spalling); extrusion/comminution of crushed/spalled material; melting/re-freezing; and cohesion. To date, it has not been possible, to capture all of these behaviours in a single omnibus numerical ice model. Creep, elasticity and plasticity are fairly easy to model using either implicit or explicit finite element codes, however these behaviours are only dominant at very low to low rates of strain. Melting/refreezing and cohesion are difficult to model numerically, but again these behaviours generally do not dominate the interaction of ice with ship hull structures. The remaining behaviours - i.e. crushing, spalling, and extrusion/comminution - generally do dominate, and are difficult to model numerically. These mechanisms are highly non-linear transient dynamic processes, which are not suited for modeling in an implicit finite element simulation environment. Furthermore, ice-structure interactions often occur over very short periods of time (e.g. bow-shoulder impacts). Such scenarios are better suited to explicit finite element codes.

Various aspects of ice-structure interaction have been numerically modeled, with good results. These include: impact with glacial ice, flexural failure, hail impacts, and application of recorded ice pressure data directly to structures. To date, there is no numerical ice model that can incorporate all salient features of ice-structure interaction simultaneously.

Gagnon and Derradji-Aouat (2006) proposed a finite element model composed of solid elements in order to simulate impacts between ships and glacial ice. It was implemented

in LS-Dyna® (Livermore Software Technology Corp.) and requires that the ice be modeled using solid finite elements that employ a crushable-foam material model. Ice loads are transmitted to a separate finite element mesh (e.g. grillage structure) via a contact algorithm. The material model inputs were derived by Gagnon based on measured field (Gagnon, Cumming et al. 2008) and laboratory experiments involving ice tank model tests and ice crushing experiments (Gagnon 2004a, 2004b, 2004c). This model does not involve spalling, but handles crushing and produces the high and low pressure zones observed in ice crushing experiments. This model was later extended by Gagnon (2011) to include predefined spall events.

Derradji-Aouat (2005) developed a novel failure criterion and employed element erosion (i.e. deletion of an element when it reaches a certain failure strain). This method was used successfully to model ice fracture for ice covers exhibiting flexural response to imposed loads. It involves modelling the ice cover with solid elements that are far smaller than would normally be practical, therefore when the failure strain in a very small element is exceeded, it erodes (i.e. disappears), instigating crack propagation. The elements need to be small so that the mass loss due to the disappearing elements is negligible. A major downside is the time it takes to solve the model, as the time step size in an explicit simulation is directly proportional to the size of the smallest elements.

Likely the most complete numerical material model implemented in commercial finite element codes today is that of Carney et al (2006). This model was developed by NASA in response to the *Columbia* shuttle crash of 2003, implemented in LS-Dyna, and used to assess hail impacts on shuttles (i.e. high strain rates). The hail was modeled as an Eulerian

(ALE) body which impacted a Lagrangian structure. Others (Anghileri, Castelletti et al. 2007, Keegan, Nash, D., Stack, M. 2013) have used this material model in smoothed particle hydrodynamics (SPH) simulations of hail impacts. These models do not incorporate ice fracture.

Quinton, Daley and Gagnon (2012) proposed a method for applying real-time/real-space variable pressures to finite element models, called the *4D Pressure Method*. This method was subsequently used (Quinton, Daley et al. 2013) to apply ice loads recorded during the 1982-86 USCGS *Polar Sea* ice trials (Daley, St. John et al. 1990, Minnick, St. John 1990), to IACS URI (IACS 2011) polar classed ship structures. It is worth noting that the pressure data garnered from laboratory experiments or field trials should be applied in the context in which it was recorded. For example, if the hull structure in a field trial responded elastically to an ice pressure event, then any post-yield behaviour observed in a numerical model resulting from application of that field trial pressure event should be viewed with skepticism, as the effect of plastic deformation on ice-structure interaction pressures is as yet unknown, and would not be captured in the field trial data.

The *4D Pressure Method* is a novel, non-contact loading method that may be used in explicit finite element analyses to apply ice pressure loads that vary in both time, and 3-dimensional space. The required input for this method is of the form of $(x, \Delta x, y, \Delta y, P(t))$. $P(t)$ is the magnitude of the pressure at time, t ; x and y pinpoint the location of $P(t)$ on a given surface; and Δx and Δy define the pressure's spatial extent.

2.2 Collision (or Allision) and Grounding Loads

The goal of this section of the literature review is to ascertain the state of the art for understanding/modeling collision and grounding events; theoretically, analytically and numerically. This literature was reviewed in order to better understand the behaviours observed in the experiments and numerical models conducted for this thesis, and facilitates the numerical modeling work through providing an understanding of the state-of-the-art techniques employed in other similar analyses.

2.2.1 Introduction

Collision generally refers to the collision of a ship with another ship⁷, or with another structure (e.g. a pier). *Grounding* generally refers to a sliding impact with a submerged object (e.g. a rock) or a sloping sea bed. Much research has been done to predict the outcome of ship collisions/groundings; particularly regarding oil tankers and oil outflow since the Exxon Valdez oil spill in Alaska in March 23, 1989 resulting in the U.S. Oil Pollution Act (1990) and the subsequent International Maritime Organisation (IMO) regulations. Paik (1995, 2003, 2007), Pedersen (1995, 2000), Simonsen (1997a, 1997b, 2000), Kitamura (1997, 2002), Brown (2002b, 2002a), Sajdak (2004), and Zhang (2002) have all recently contributed to the current state-of-the-art of the mechanics and modeling of collision and grounding.

⁷ The term *allision* is used if one of the ships is stationary.

2.2.2 Collision physics

Analysis of the physics of ship impact/collision is usually divided into two parts: external mechanics and internal mechanics (Pedersen 1995). External mechanics deal with the rigid body motion of the ship during impact, as well as the hydrodynamic pressures over its wetted surface. Internal mechanics encompass the ship's structural response during an impact/collision and subsequent deformation. External and internal collision mechanics can be treated separately or coupled, depending on the analysis. The research presented herein entirely neglects external mechanics, and concentrates solely on the structural response (internal mechanics) to moving ice loads. The reasons for this are twofold:

1. The experimental moving load apparatus developed for this study does not account for external mechanics.
2. Explicit inclusion of the external mechanics would unnecessarily complicate the development of the numerical model at this point in the research. Including them could viably be part of a larger, subsequent analysis that explicitly accounts for external mechanics, or implicitly includes them through modification of the moving load magnitude and direction (or some other means (e.g. the 4D Pressure Method (Quinton, Daley et al. 2012))).

When considering the impact of a ship with an object, internal collision mechanics usually consider the structural response of the ship in terms of shell membrane tension; shell rupture; web frame bending; shear and compression loads; yield strength; failure-strain; friction; and crushing and tearing of decks, bottoms, and stringers. Literature suggests that plastic bending of the shell plating is considered negligible, and that it is safe to assume

that plastic membrane tension is the primary mechanism of shell energy absorption and is the first mechanism that takes place in a collision (i.e. before bending/buckling of transverse web stiffeners) (Brown 2002a). Plastic shell membrane tension actually accounts for the greatest fraction of all structural energy absorption during a collision (Kitamura 1997). It should be noted that these results are based on ships that are not ice-strengthened. Plastic bending may play more of a role for ice strengthened ships, because the plating thickness is generally much greater, and the frame span much smaller. For the majority of the experiments presented herein, the plastic bending component is not insignificant.

2.2.3 Methods for assessment of collision and grounding of ships

To date, four main methods are used to assess the collision and grounding of ships (Wang, Ji et al. 2006); they are: simple formulae, simple analytical models, simplified finite element models (FEM), and nonlinear FEM. Simple formulae involve hand calculations and are used to estimate the initial energy absorption. Simple analytical models utilise more complex calculations, but offer more accurate energy and load predictions. Simplified FEM provide relatively fast energy and load predictions and are applicable in situations where computing power is limited, or where the problem is extremely large (e.g. simulation of a ship-ship collision where both ships are entirely modeled, and they are both deformable). Nonlinear FEM are the norm for collision analyses (Wang, Ji et al. 2006), and they represent the most accurate methods of predicting collision energy, loads, and stresses. They also have the ability to model structural and material failure.

2.2.4 Types of collision loads

For the purposes of this thesis, collision and grounding loads may be broadly classified into two categories: those that cause hull rupture (e.g. tearing through hull plating) and those that do not. This research is concerned only with the latter type – *non-rupturing* loads – as ice-strengthened ships and offshore structures are expected to survive impacts with ice (within their operational capacity) without tearing of the hull plating. To support this concentration on plastic deformation, Hänninen (2004), in his statistical analysis of damages to ships in ice in the Baltic Sea for the 2002-2003 winter shipping season, suggests that "The most typical hull ice damage is that where the ship plating has a permanent deformation" (p. 32) and that "Most of the fractures were located on the bow area. These ships were already initially in bad condition (a lot of corrosion, abrasion and denting) or there was inadequate ice strengthening" (p. 33). While these statements only represent Baltic Sea statistics for a single shipping season, it is not a stretch to assume that they may be generally extrapolated to all ice-strengthened ships and offshore structures. The following sections discuss the relevance of each type of load to the topic of this thesis, as well as the state-of-the-art where applicable.

2.2.4.1 Rupture-type loads

Hull rupture occurs when the impactor (e.g. another ship or a rock) penetrates the ship's hull. There is a wealth of literature available on *rupture* type loads; good reviews of which are presented in MSL Engineering Ltd. (2000) and Paik et al (2003). Analytical, empirical and numerical techniques have been used with great success to predict the behaviour of ship hulls in collision and grounding scenarios. With one notable exception (discussed

below), all of these methods involve rupture and tearing of the hull plating, and are thus not applicable to this research.

The pioneering method for estimating the damage to a ship structure in a collision/grounding incident is Minorsky's method (1959). This empirical method relates the kinetic energy of a ship lost during a collision with the volume of indentation for the side of the ship. This method was successively developed and expanded upon by others. One of the drawbacks of the Minorsky based methods is that they assume hull rupture, and therefore fail to model low energy impacts well. This is because they do not account for the membrane stresses developed in the hull plating prior to rupture (MSL Engineering Ltd. 2000). Work by Rosenblatt and McDermott (discussed in the next section) addresses this shortcoming and provides a method for dealing with low energy impacts (i.e. non-rupturing loads).

These rupture-type methods are not applicable to the subject of this research and hence will not be discussed further.

2.2.4.2 Non-rupture type loads

The work of Rosenblatt (1975) and McDermott (1974) address the shortcomings of the Minorsky method regarding its inability to assess hull behaviour for low energy impacts; i.e. non-rupturing impacts where membrane stresses in the hull plating are significant. In the development of their method, they consider many different ship collision scenarios including rigid bow, non-rigid bow, and normal and oblique collisions. They introduced the concept of *progressive plastic deformation*, which McDermott defines as "... plastic deformation of backup structure, together with plastic membrane stretching of side shell

structure, until the ductility of the side shell is exhausted, rather than by an initial cutting of the struck ship's side and subsequent tearing and/or shearing of shell and bow plating.”

Note: this progressive plastic deformation is not to be confused with the concept of *progressive damage* presented in (Quinton 2008) and discussed in Chapter 2.4. The major downfall regarding application of this method to this research is that it does not consider the case where the load is moving laterally along the hull, and thus does not address *moving load effects*.

The works of Hong (2008) and Hong and Amdahl (2012) do investigate a scenario involving a moving load causing plastic damage. It is important to note that these works are based on numerical models, and the majority of the work is significantly different than that presented in this thesis. They investigated the behaviour of a double-hull structure; which is significantly different in both form and structural response from the single-hull structures investigated in this work. Hong (2008) numerically investigated the scenario where a ship's double bottom is subjected to a moving load causing plastic damage from a grounding incident with a *shoal* (which is defined as a large subsea contact surface). The numerical indenter used in the simulations was a truncated pyramid. Hong identified three important structural responses: deformation of longitudinal girders, deformation of transverse floors, and deformation of hull plating. The numerical behaviour observed in the longitudinal girders is significantly different than that predicted in Quinton (2008), and is characterised by a repetitive deformation pattern in which the web is crushed both horizontally and vertically such that it attains a sinusoidal out-of-plane deformation (with the sine wave switching from one side of the web to the other). Later, Hong and Amdahl

(2012) provided a simplified semi-empirical method for predicting the behaviour of Hong's three structural responses. One area that is comparable with this work is their semi-empirical simplified method for predicting the response of hull plating to their grounding scenario (Hong, Amdahl 2012). A comparison of the experimental results of this research with their simplified method is beyond the scope of this thesis, however this exercise is recommended for future work (see Chapter 6.2).

2.3 Moving Loads

Moving loads, as their name suggest, vary in both time and space. They are loads that act not only normal to the hull, but at the same time translate laterally along the hull's surface. Regarding, *non-rupture* type moving loads, further sub-classification is necessary: moving loads inciting an elastic response, and moving loads inciting an inelastic (or plastic) response.

As the focus of this research is on non-rupture type loads, any subsequent reference to moving loads may be assumed to be referring to this load type.

The study of moving loads seems to have begun in the mid-nineteenth century with the advent of wrought iron railway bridges. The failure, resulting in casualties, of the Dee Bridge on May 24, 1847 (Walker, Simmons 1847) - less than a year after it was completed in September of 1846 - on the Chester and Holyhead railway in the United Kingdom sparked an investigation into the principles of the application of iron to railway structures (Wrottesley, Willis et al. 1849). Timoshenko (1953) reports that there were two schools of thought on the effects of a moving load on a beam: "that a load moving with high speed

acts like a suddenly applied load and may produce deflections larger than those corresponding to static action," and "that at very high speeds there was insufficient time for the load to drop through the distance of the expected dynamical deflection." Experiments were carried out where a loaded carriage passed over steel rails and the resulting deflection was measured (Appendix B, Wrottesley, Willis et al. 1849). It was found that the dynamic deflection was up to three times greater than the static deflection at higher speeds; and that the greater the speed, the worse the effect (Timoshenko 1953). One of the experimenters, Willis, developed an analytical theory for a moving load on an elastic beam where the mass of the beam was considered small compared to the mass of the load (Appendix B, Wrottesley, Willis et al. 1849).

From there, other authors developed analytical models for the various permutations of load type (e.g. massless, sprung, patch, harmonic, etc...), structure type (elastic beam, elastic infinite plate, rigid-plastic plate, etc...), and so on. A highly cited compendium on the subject of moving loads is Frýba's *Vibration of Solids and Structures under Moving Loads* (1999). In it may be found the majority of the work done to date on the subject, including an analytical model of a rigid-plastic beam subject to a moving load.

Quinton (2008) reported a numerical model that showed moving loads causing progressive plastic damage aligned with stiffeners ("T" shaped beams), caused the web of the stiffeners to buckle plastically at a much lower load than for stationary loads.

One of the items not covered in Frýba (1999) is the inelastic theory of a moving load on plate. Sokol-Supel (1985) has made an attempt to develop the theory for rigid-plastic plates under a concentrated moving load. In this work only the plastic-bending response of plates

is considered; plastic membrane response is ignored. This choice would likely be valid for thick plates, however the theory developed does not consider the damage in the wake of the moving concentrated load (see Figure 2.1). This implies that the damaged material on the trailing side of the moving load (shown in red in Figure 2.2) instantaneously recovers to an elastic undamaged state. This formulation is the reason that the author claims that a rigid-plastic plate can sustain a *larger* moving load than a quasi-static (or stationary) load; and that the higher the speed (up to some critical speed), the larger the sustainable load before plastic collapse. Evidence that this work has been validated was not presented in the paper.

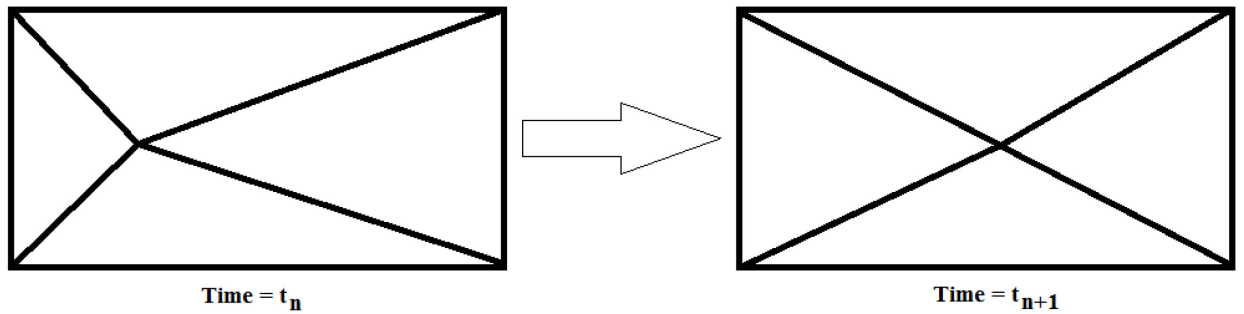


Figure 2.1. Example concentrated moving load on a rigid-plastic plate where damage due to the passage of the load is ignored.

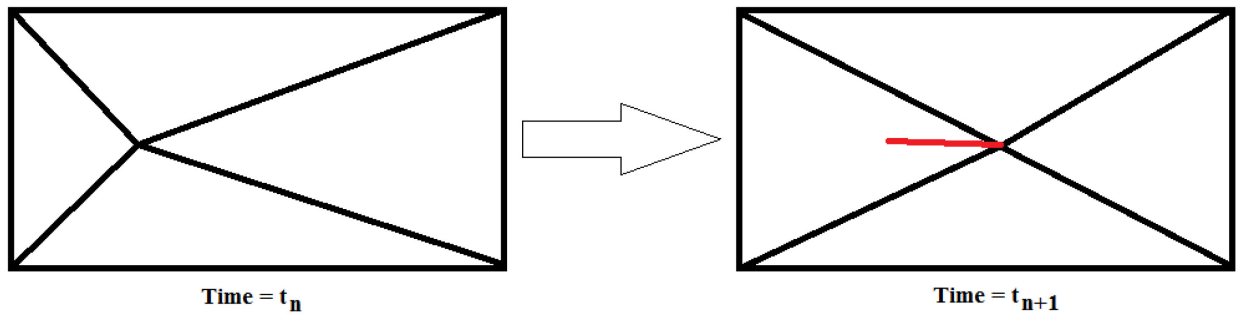


Figure 2.2. Example concentrated moving load on a rigid-plastic plate showing line of damage in red.

These findings are in conflict with the results of the numerical model presented in Quinton (2008), where it is shown that moving loads causing plastic damage incite a *reduced* structural capacity when compared with stationary loads.

2.4 Progressive Damage

Given a moving load, *progressive damage* is the idea that any contiguous plastic strain that was caused by the moving load at an earlier point in time (i.e. at a different location), affects the structure's response to the load at the present time. In this regard, during the impact of a hull structure with ice, progressive damage occurs after the initial ice impact and can be viewed as plastic structural damage due to the scoring/raking action of ice as it scrapes along the hull. This type of structural interaction generally happens in the vicinity of the waterline or below. Waterline damage may result from collision with pack ice, glacial ice of various size (from growler to iceberg), or level-ice during ice-channel navigation

(assisted or unassisted). Damage below the waterline may occur from collision with glacial ice, ridge ramming, or if a ship strikes a submerged ice ridge (e.g. *anchor ice*⁸).

Progressive damage is similar to *raking damage*⁹; however, the tearing and subsequent curling of the hull steel (see Zhang (2002)) is not treated because ice-strengthened ships are expected to survive such impacts (within their operational capacity) without tearing of the hull plating. Progressive damage occurs when there is enough compliance in the ice, or the structure, or both to extend the damage past the point of collision; provided that the geometry of the impacted area allows for the sliding of the ice along the hull.

2.5 Strain Rate and Temperature Effects

In addition to exploring moving load effects, it was decided to investigate related phenomena that may play a role in mitigating the loss in structural capacity (when compared with stationary loads). These phenomena are material effects related to strain-rate and temperature. These factors are known to influence the strength of steel, but are not explicitly included in current design practice for icebreaking ships; although both factors may be evident in real-life ice loading scenarios.

⁸ *Anchor ice* is defined as "submerged ice attached or anchored to the bottom, irrespective of the nature of its formation" (WMO/IOC 2004).

⁹ *Raking damage* is commonly understood to refer to the damage resulting from a grounding incident when a ship traveling at a non-trivial speed strikes a rock, resulting in damage in the form of torn and curled hull steel.

2.5.1 Temperature effects

It is generally accepted that a reduction in temperature is associated with a slight increase in the yield strength of steel. It is desired to see if this yield strength increase has a noticeable mitigating effect on moving load effects.

2.5.2 Strain-rate effects

It is well known that the material properties of steel (and many other metals¹⁰) are generally highly sensitive to strain-rate (Jones 1983). The physics of why strain rate influences yield strength is a subject of materials science, and is beyond the scope of this literature review. The practical function of strain-rate effects are best summarized in the following quote from “Metallic materials – Tensile testing at high strain rates – Part 2: Servo-hydraulic and other test systems” (ISO 26203-2 2011):

The deformation behaviour of many technical materials shows a positive strain-rate effect up to ductile failure, i.e. with increasing strain rate, an increase of yield stress and strain to failure can be observed.

The generally accepted method for accounting for strain-rate effects in analytical and numerical models is through the use of an empirical regression equation; with parameters determined by laboratory material tests at various known strain-rates. Published empirical parameters for various specific alloys and grades are available in literature. Two of the most common models used in accounting for strain-rate effects are the Cowper-Symonds (Jones 1983) and the Johnson-Cook models (Johnson, Cook 1983).

¹⁰ With the notable general exception of aluminum.

The Cowper-Symonds model (Equation [1]) explicitly accounts for strain and strain rate:

$$\sigma_y = \sigma_o \left[1 + \left(\frac{\dot{\epsilon}}{C} \right)^{\frac{1}{p}} \right] \quad [1]$$

where: σ_y is the yield stress
 σ_o is the initial yield strength (i.e. static value)
 $\dot{\epsilon} = \sqrt{\dot{\epsilon}_{ij}\dot{\epsilon}_{ij}}$ is strain rate
 p, C are constants

In addition to strain and strain-rate, the Johnson-Cook model (Equation [2]) explicitly accounts for temperature:

$$\sigma_y = (A + B\bar{\epsilon}^p)(1 + c \ln \dot{\epsilon}^*)(1 - T^{*m}) \quad [2]$$

where: σ_y is the von Mises flow (i.e. yield) stress
 $\bar{\epsilon}^p$ is the equivalent plastic strain
 $\dot{\epsilon}^* = \frac{\dot{\epsilon}}{\dot{\epsilon}_o}$ is the dimensionless plastic strain rate for $\dot{\epsilon}_o = 1.0s^{-1}$
 $T^* = \frac{T - T_{room}}{T_{melt} - T_{room}}$ is the homologous temperature
 A, B, c, n, m are constants

These strain-rate models are implemented in LS-Dyna and thus provide a method for their inclusion in numerical models.

2.6 Literature Review Summary

This chapter summarizes the literature relevant to the subject of moving loads causing plastic damage. The lack of literature on the subject of moving ice loads on ship structures

is apparent, and the present international movement toward the plastic design of ship structures necessitates a need to understand how moving load effects associated with non-rupture type moving loads causing plastic damage affect our notions of ship structural capacity.

Chapter 3 Moving Load Experiments

3.1 Research Approach

Quinton (2008) predicted that the structural capacities of steel plates and frames are significantly less for moving loads causing plastic damage than for similar stationary loads. In particular, it was predicted that the onset of plastic buckling in a frame's web would occur at a much lower load magnitude for moving loads than for stationary loads.

Given the lack of available literature on experiments involving moving loads causing plastic damage (without hull tearing), coupled with the detrimental effects predicted in Quinton (2008), it was decided to test, using laboratory experiments, whether or not these moving load effects exist in reality. If indeed they did exist (which is shown in this thesis), then it was desired to develop a simple method for numerically modeling these effects for future design and analysis exercises.

3.2 Scope and Objectives

The scope and objectives of the laboratory experiments were to:

- Investigate the existence of moving load effects, as predicted in Quinton (2008);
- Investigate the structural response of plates and frames to a rigid moving load;
- Investigate the structural response of plates to a deformable moving load (i.e. ice);
- Investigate the influence of indentation depth, indentation speed, lateral location, temperature, and plate thickness on moving load effects;

- Investigate the effects of lateral load movement and indentation speed coupled with elastic structural deformation on the behaviour of ice;
- Investigate the effects of lateral load movement and indentation speed coupled with plastic structural deformation on the behaviour of ice;
- Provide suitable data for the calibration of numerical models to be employed in further investigation of moving load effects.

Many of these objectives involve determining the structural capacity (i.e. structural response to a particular load scenario). This is accomplished through the accurate measurement of applied load and resulting structural displacement, as well as through various forms of image capture.

3.3 A Note on Directions

Throughout this thesis, when referring to a ship's hull, the term *normal* refers to the direction perpendicular to the undeformed orientation of the hull plating (regardless of the state of deformation of the plating). Similarly, the term *lateral* generally refers to any direction in the plane of the undeformed orientation of the hull plating; but when referring to the experiments or numerical models presented in Chapters 3, 4, and 5, it specifically means motion in the direction of the long axis of the specimens' plating (see Chapter 3.6 for descriptions of the test specimens). These directions (normal shown with a green arrow and lateral shown with a red arrow) are illustrated with respect to undeformed (left) and deformed (right) longitudinally framed sections of a hull structure in Figure 3.1.

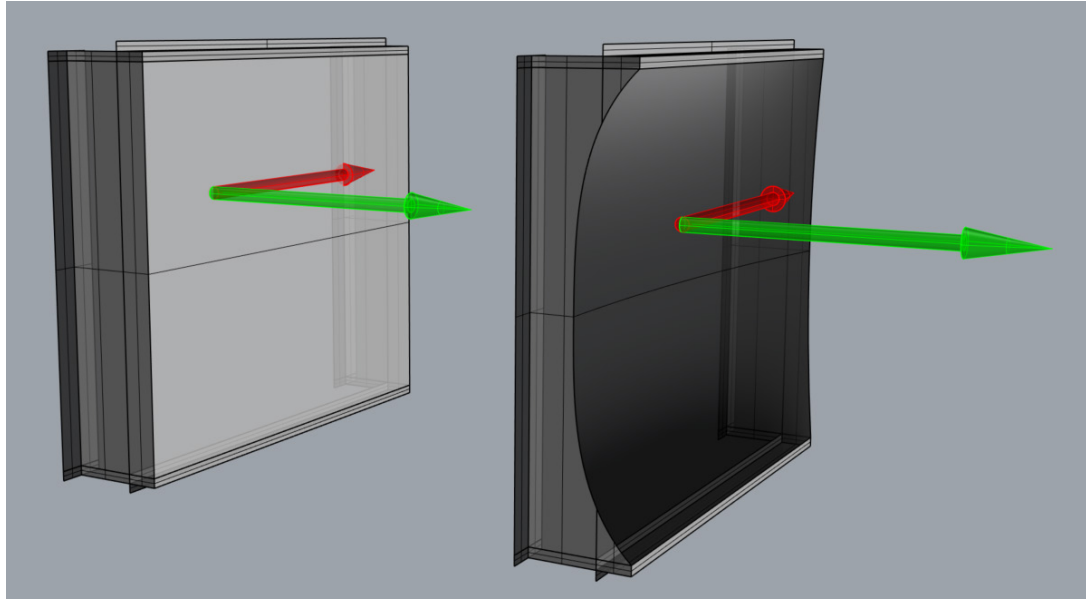


Figure 3.1: Longitudinally framed hull sections showing normal (green arrow) and lateral (red arrow) directions in undeformed (left) and deformed (right) states. This figure illustrates that the *normal* direction always refers to the original (i.e. undeformed) normal direction, despite hull deformation.

Additionally (see Figure 3.2), the normal direction corresponds with the vertical direction in the laboratory experiments (i.e. opposite to gravity), and the lateral direction corresponds with the direction of motion of the horizontal ram (which is orthogonal with the vertical direction). The terms *normal* and *vertical*, are used interchangeably throughout this thesis, as are *lateral* and *horizontal*.

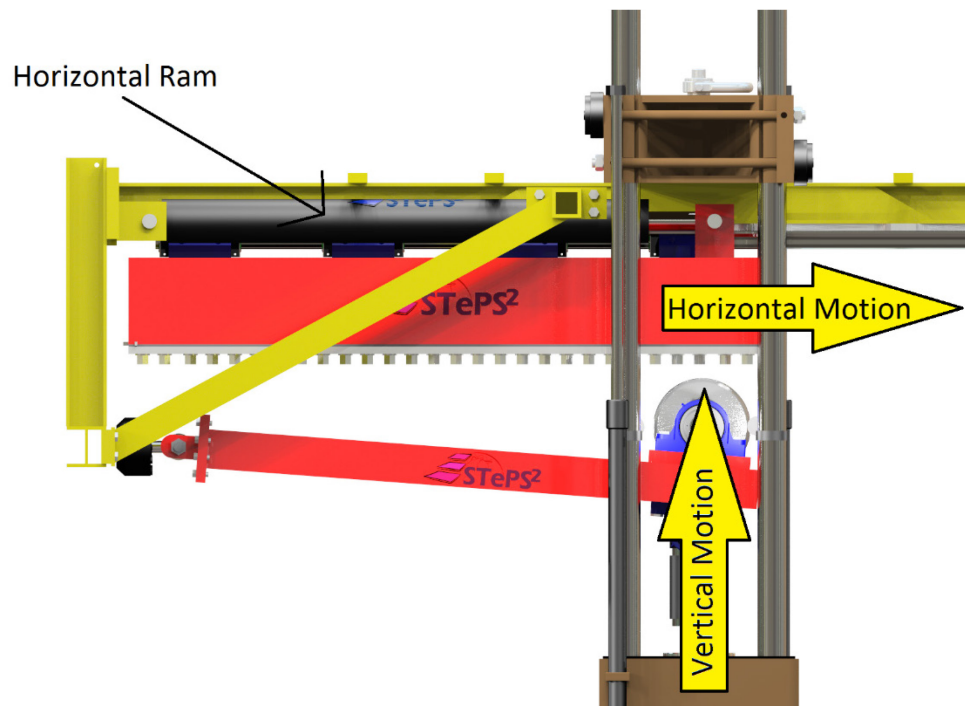


Figure 3.2: Partial schematic of the moving load apparatus showing the horizontal ram, and the directions of motion*.

*Note: motion in the normal direction corresponds with motion in the vertical direction for the moving load apparatus, and similarly, motion in the lateral direction corresponds with motion in the horizontal direction.

3.4 Design, Capabilities and Operation of the Moving Load Apparatus

Given that the main objective of the study was to explore the problem of moving loads experimentally, and as there was no evidence in the literature of any previous lab scale experimental work on the subject of moving loads on plate structures, it was necessary to devise a novel experimental apparatus in order to carry out the investigation. This section discusses the design, capabilities and operation of the moving load apparatus. This moving load apparatus was designed to meet the research objectives identified in Chapter 3.2.

3.4.1 Incorporating existing infrastructure

The moving load apparatus was designed to take advantage of relevant existing facilities available at Memorial University of Newfoundland. Specifically, it was desired to utilise the cold room and the MTS test frame contained therein. Incorporating the former allowed for control and variation of the ambient temperature during the experiments; and the latter provided an ideal instrument with which to precisely apply and measure loads. The MTS test frame is ideal because it is a self-reacting frame (i.e. it does not transmit any force to its surroundings) and it is capable of applying and measuring up to 500 kN (110 kip) in a manner precise enough to perform uniaxial material tests. Further, in its existing configuration it was able to record five data channels at up to 4096 Hz each; which again, was ideal for these experiments. The specifications for the MTS test frame and its relevant components are given in Appendices A1 through A5.

3.4.2 Introduction to the moving load apparatus

Figure 3.3 shows the moving load apparatus and highlights its main parts. With reference to this figure, a high level description of the apparatus and operational procedure is as follows: a test sample is bolted to the bottom of the carriage, which provides fixed boundary conditions for the sample; an indenter is mounted on the swing-arm; the vertical ram (which is part of the MTS test machine) pushes on a bearing attached to the swing arm underneath the indenter; this causes the swing arm to rotate slightly as the vertical displacement of the indenter increases (note the maximum angle of rotation of the swing arm for the moving load experiments was 3.4° ; starting at -1.7° and sweeping through 0° (horizontal) to $+1.7^\circ$); the swing arm and bearing are necessary to release the vertical ram

from any horizontal load generated during the test; the indenter makes contact with the test specimen and continues to apply load to the test specimen either through force or displacement control; subsequent to the vertical motion (or simultaneous with it, depending on the nature of the test) the vertical ram (not shown in Figure 3.3) pushes the carriage attached to the linear roller rail system using displacement control (force control is not possible); the carriage (and with it the test specimen) move horizontally along the rails, causing the indenter to impart a lateral load on the test specimen; the test is over when the motions of the vertical and horizontal rams cease.

The various parts of the moving load apparatus and their functions are discussed in greater detail below.

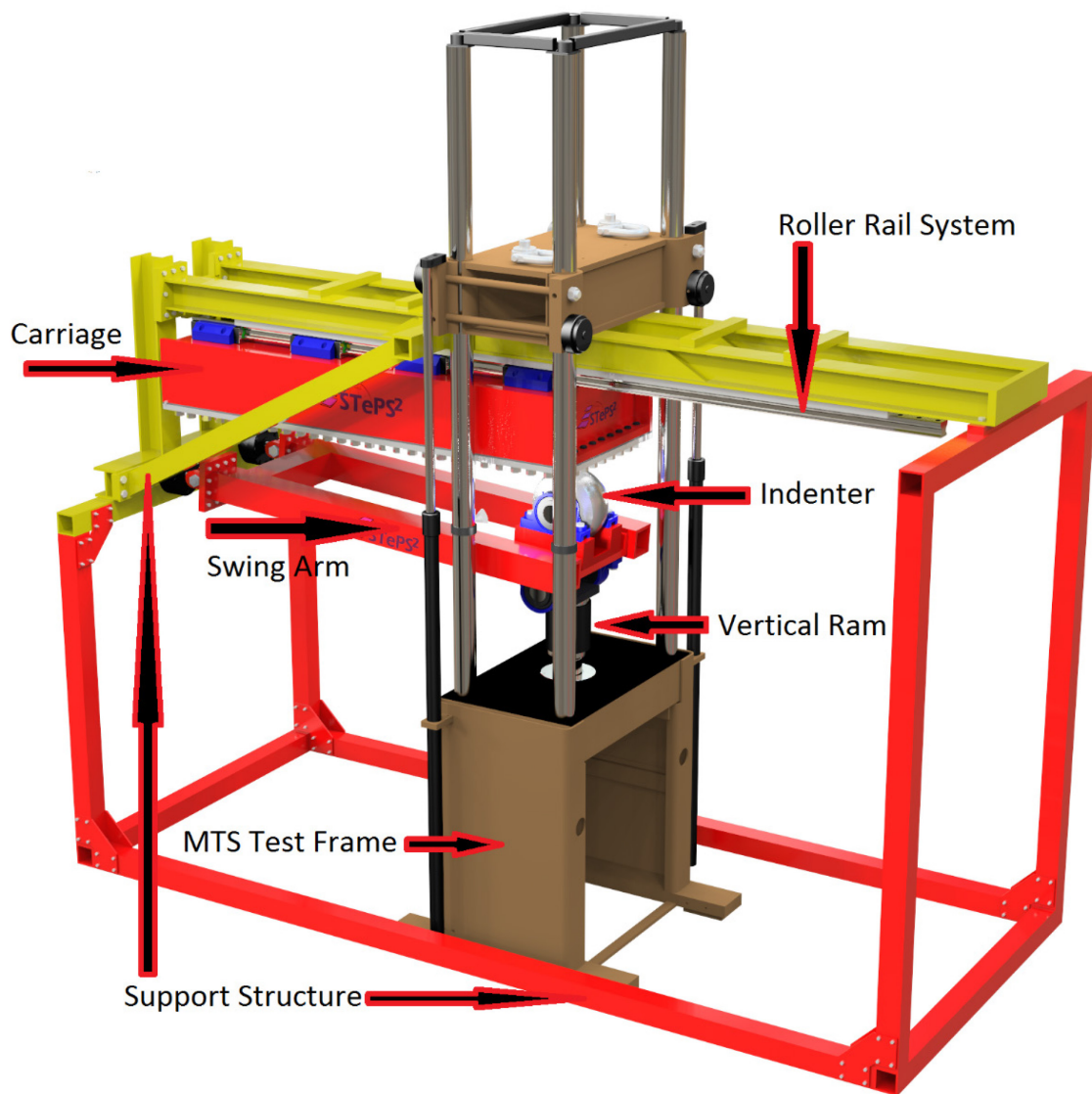


Figure 3.3: Moving load apparatus schematic highlighting the carriage, roller rail system, swing arm, indenter, vertical ram, MTS test frame and support structure.

A picture of the actual moving load apparatus housed in a cold room is given in Figure 3.4.



Figure 3.4: Moving load apparatus housed in a cold room.

3.4.3 Design of the moving load apparatus

Referring to Figure 3.5, the moving load apparatus consists of a carriage suspended by a linear roller-rail system (specifications given in Appendix A8) that is actuated by a horizontal hydraulic ram (specifications given in Appendix A9); and relies on an MTS® test frame to provide vertical load and vertical load resistance.

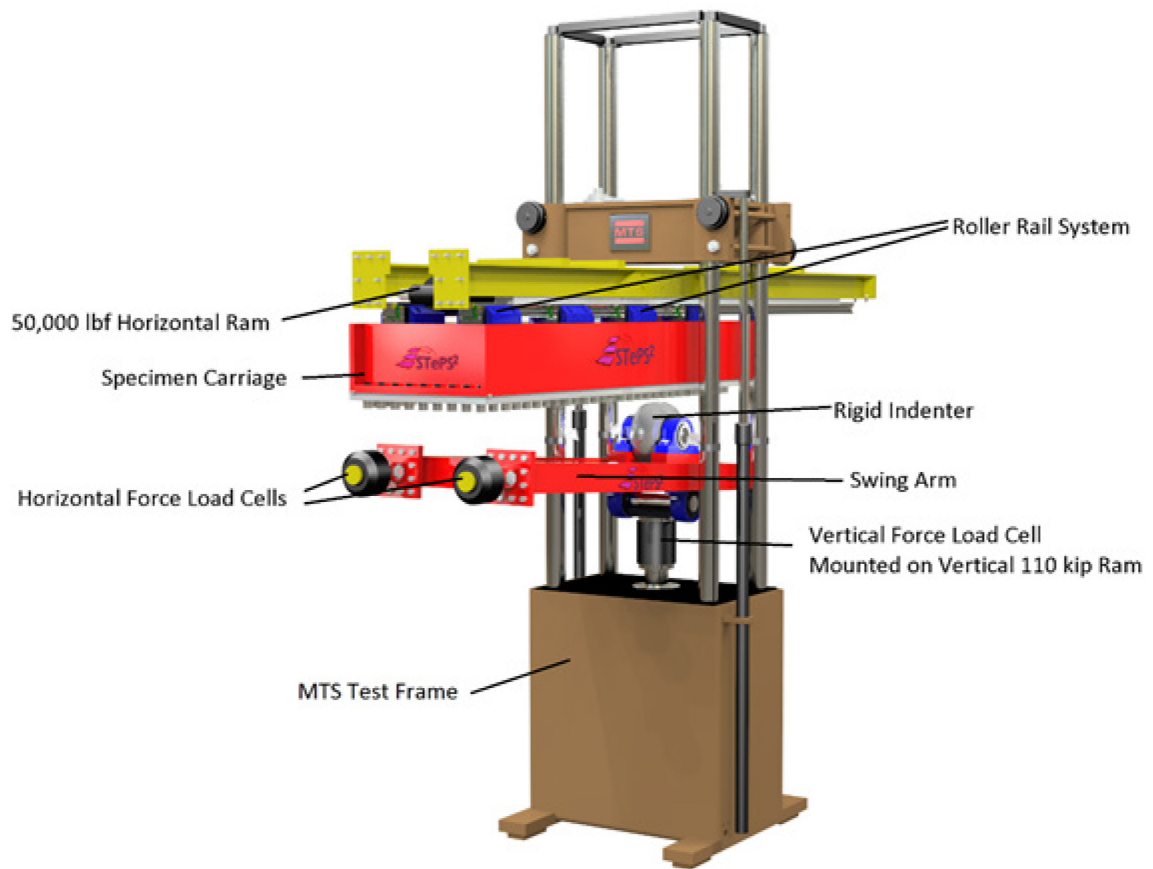


Figure 3.5: Components of moving load apparatus.

It should be noted that while the moving load apparatus was commissioned expressly for these experiments, it was decided to make the apparatus as general as possible in its functionality in order to accommodate many different types of experiments that involve loads on structures in two orthogonal directions¹¹. To this end the load capacity of the moving load apparatus matches that of the MTS test frame (i.e. application of the full force capability of the MTS test frame will not damage the apparatus) and the various components of the apparatus have been designed to be modular. Specifically, the indenter

¹¹ Indeed this apparatus was used soon after these moving load experiments by other researchers to study the effects of ice collision and adhesion on concrete surfaces (Tijssen, Bruneau et al. 2015).

(i.e. the body inducing load on the test specimen) may be replaced with anything that geometrically fits on the apparatus; and the carriage, while inherently versatile in its own right, may also be replaced with anything that geometrically fits; or may be adapted to suit another purpose (as with the work of Tijssen et al (2015)).

3.4.3.1 Vertical load

Vertical load originates from the vertically orientated 500 kN (110 kip) hydraulic ram (specifications given in Appendix A2) mounted in the MTS test frame's base. Referring to Figure 3.6, the load passes through the MTS load cell (specifications given in Appendix A4), an attached hardened plate¹², the swing-arm bearing, the swing-arm indenter mount, the steel wheel indenter, the test specimen, the carriage, the linear roller-rail system, the rail supports and into the MTS test frame's crosshead. The crosshead is attached to the base of the MTS test frame via the MTS frame supports, which completes the self-reacting vertical load loop. In this configuration, the vertical hydraulic ram stroke is approximately 75 mm (3 in.).

¹² The plate was hardened to an estimated hardness of 55-58 on the Rockwell scale. This was done to minimize any indentation into the plate under load by the swing arm roller bearing in contact with it, and therefore minimize any transmission of horizontal load to the vertical ram.

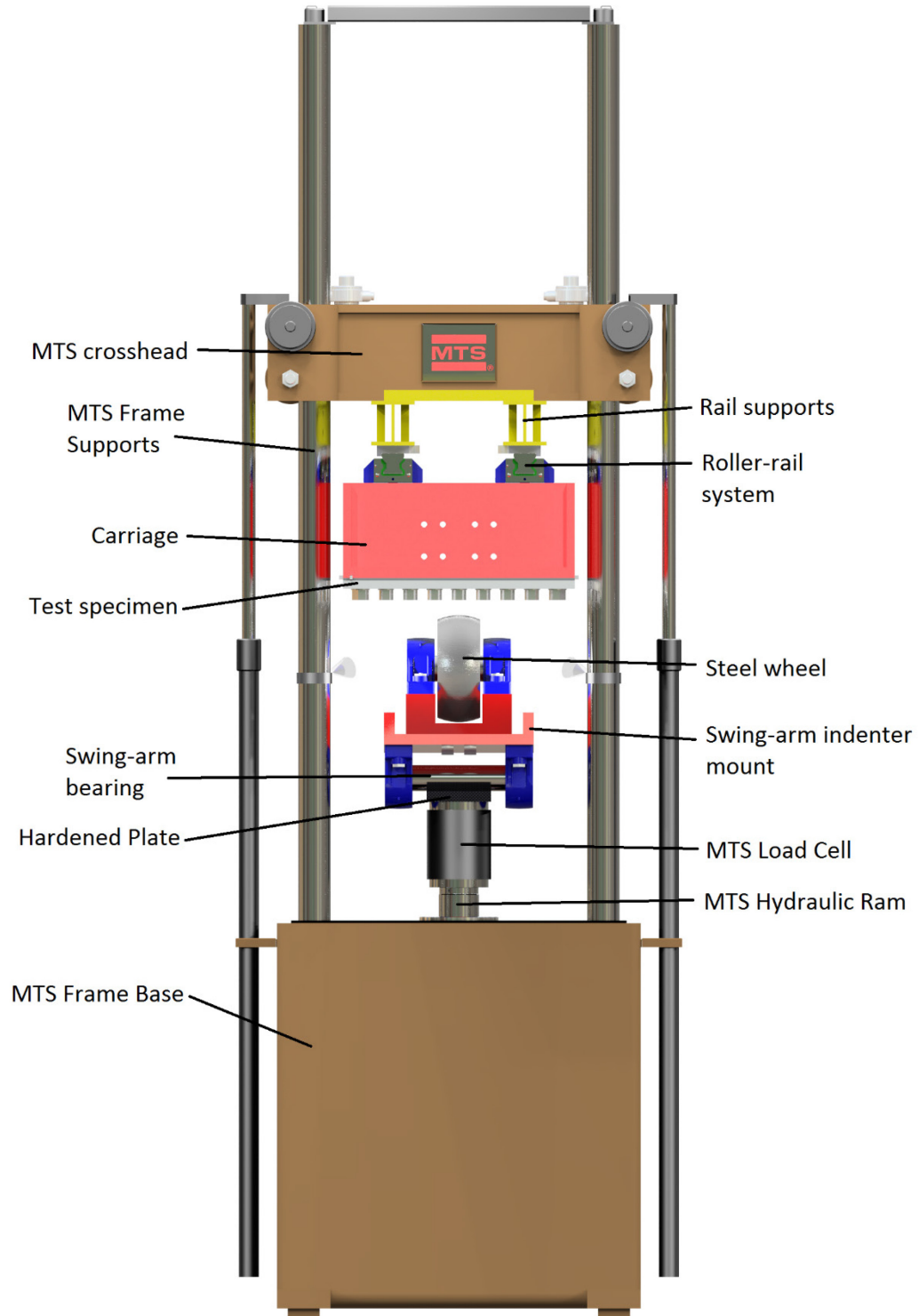


Figure 3.6: Moving load apparatus: vertically loaded components.

3.4.3.2 Horizontal load

Horizontal load originates from the 225 kN (50 kip) horizontally orientated ram (specifications given in Appendix A9), which has a stroke of approximately 1.2 m (48 in.). For the following description of the horizontal load members, please refer to Figure 3.7. The ram's base is connected to a baseplate, which is also connected to the rail-supports (yellow). The ram's head is connected to the carriage. Horizontal load is primarily resisted by the indenter (when it is in contact with the test specimen), which is attached to the end of the swing-arm. This resisted load is transmitted through the swing-arm, through the horizontal load cells (specifications given in Appendix A6), and into a heavy "leg" structure that is attached to the aforementioned baseplate. This structure alone is self-reacting, however it is too flexible; as there is a significant moment about the baseplate generated by the point of action of the swing-arm load on the leg. This moment is resisted, on either side of the carriage, by a truss member that connects the end of the leg to the rail mount; forming a truss structure. While the apparatus will work with the swing-arm in compression, it was designed such that the swing-arm is placed in tension under load movement. This pulls the swing-arm so that it does not try to "wander". Further, the horizontal hydraulic ram is orientated so that it's maximum force and speed places the swing-arm in tension.

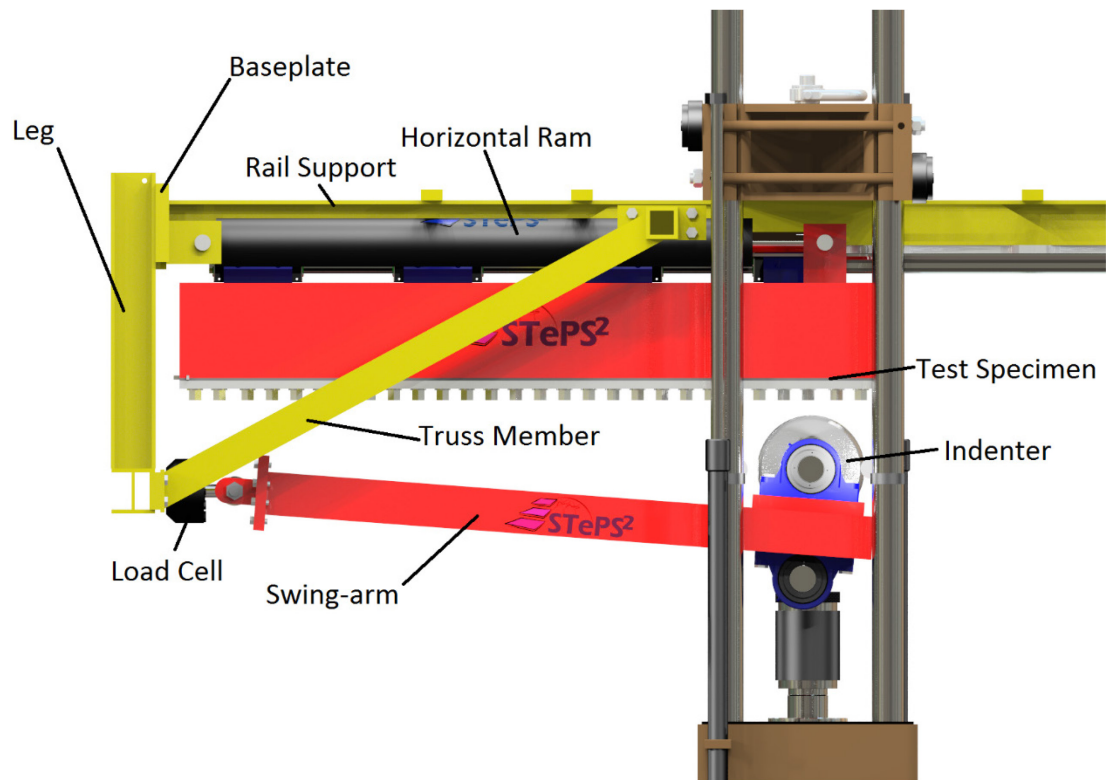


Figure 3.7: Moving load apparatus: horizontally loaded components (closest rail support, rail and linear bearings not shown for clarity).

3.4.3.3 General structure

The remaining frame structure (see Figure 3.8) supports and aligns the components described in 3.4.3.1 and 3.4.3.2. As each of the vertical and horizontal load systems described above are self-reacting, the remaining frame structure simply supports the apparatus weight. The points of alignment exist to allow the longitudinal axes of the swing-arm and the carriage to be aligned.

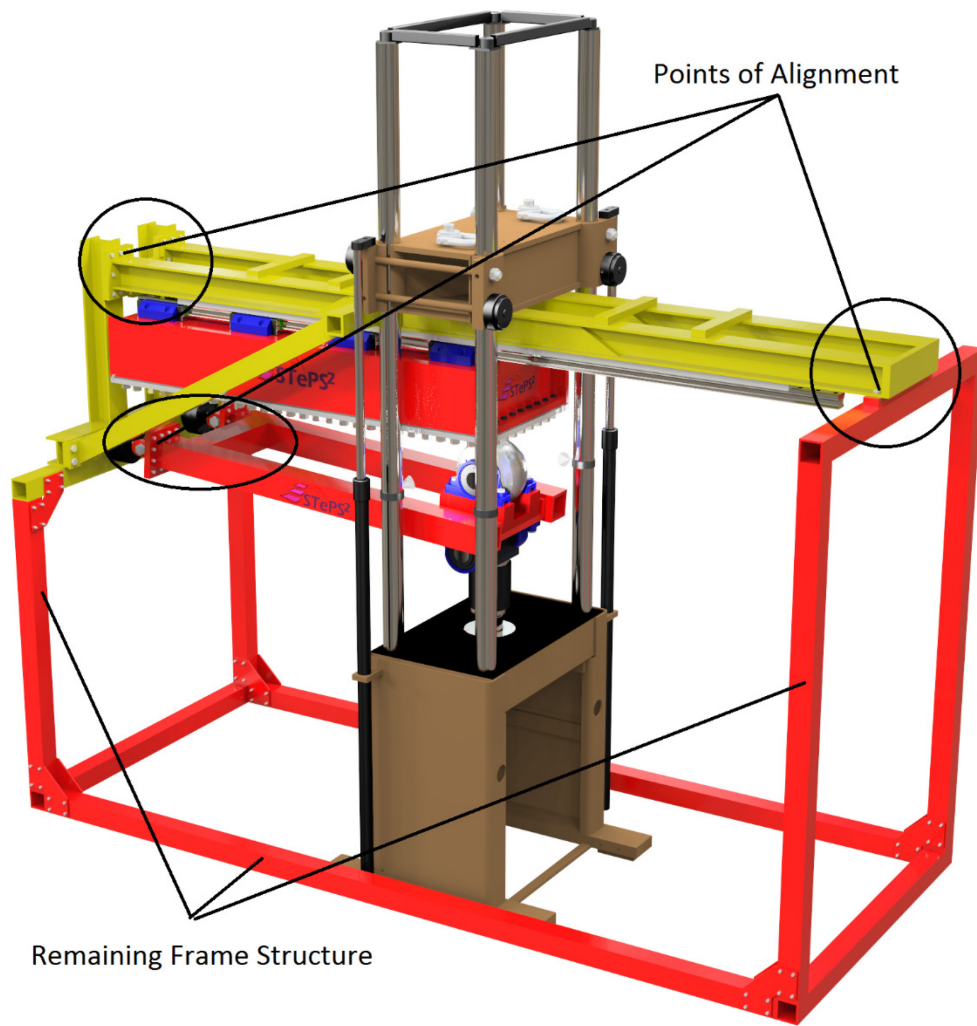


Figure 3.8: Remaining general structure.

3.5 Indenters

As the objective was to study the problem at a fundamental level it was decided to start with a simple scenario in which only the structure was subject to deformation. Thus it was necessary to examine the response of plates and frames to a “rigid” load; that is, an indenter that does not appreciably deform during its interaction with a structure. Later as a more

complex case, the effects on plates, frames and the ice itself, for moving loads involving ice (instead of a rigid indenter) were examined.

3.5.1 Steel wheel indenter

As mentioned above, an indenter that would not appreciably deform under load (i.e. is essentially rigid) was required for these experiments. Further, as moving load effects are not well understood, it was decided to conduct these experiments in this first instance without sliding friction between the rigid indenter and the specimen plating.

A rigid indenter was created from QT100 steel¹³ in the shape of a 10.16 cm (4 in.) thick segment of a 25.4 cm (10 in.) diameter sphere cut about the sphere's centreline. It was made frictionless by mounting it on a shaft supported by two pillow-block bearings.

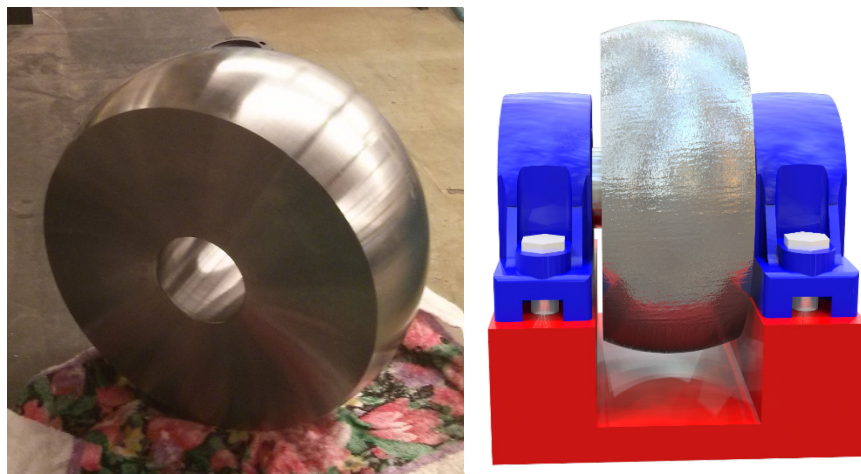


Figure 3.9: Rigid indenter (left) mounted on pillow-block bearings (blue) (right).

¹³ 690 MPa (100 ksi) yield strength.

3.5.2 Ice indenter

Bruneau et al. (2012) devised a standard method for the production of 25 cm (9.84 in.) diameter ice cones (see Figure 3.10) for laboratory testing of ship collisions with ice. This method has evolved with time. For example, ice chips are now made with a special purpose device, instead of an ice auger. The updated procedure is presented in Manuel (2012). It was decided to adhere to the evolved standard for the experiments described herein. All experiments used ice cones shaved to a base angle of 30° .

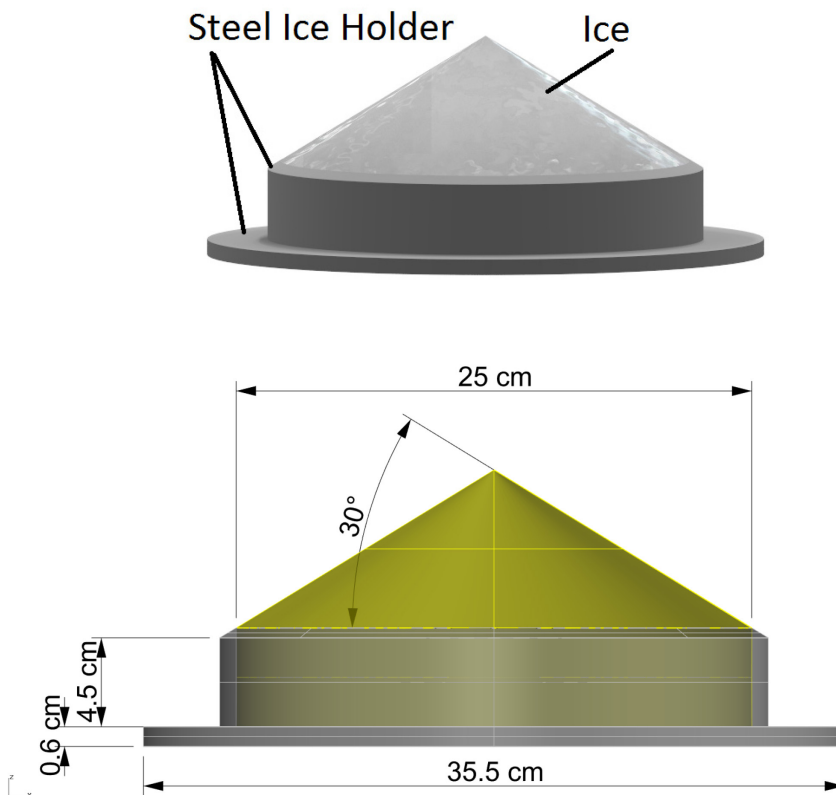


Figure 3.10: Ice cone sample: (top) showing ice and steel ice holder and (bottom) showing relevant dimensions of ice (yellow) and ice holder (grey).

As can be seen in Figures 3.10, 3.11, and 3.12 the ice cone samples are contained by a steel ice holder consisting of a vertical ring containing the ice and a horizontal ring. When

affixed to the moving load apparatus, the horizontal ring is bolted to another round steel plate which is fixed to the swing arm of the moving load apparatus.

Because of the nature of the moving load apparatus, the difference in the height of the rigid indenter and the ice indenter required that the ice samples be placed on a stilt so that the tip of the ice cone was at the same elevation as the top of the rigid indenter. The stilt is shown under the ice indenter in Figure 3.11. Figures 3.11 and 3.12 show examples of actual ice indenters before and after testing (respectively).

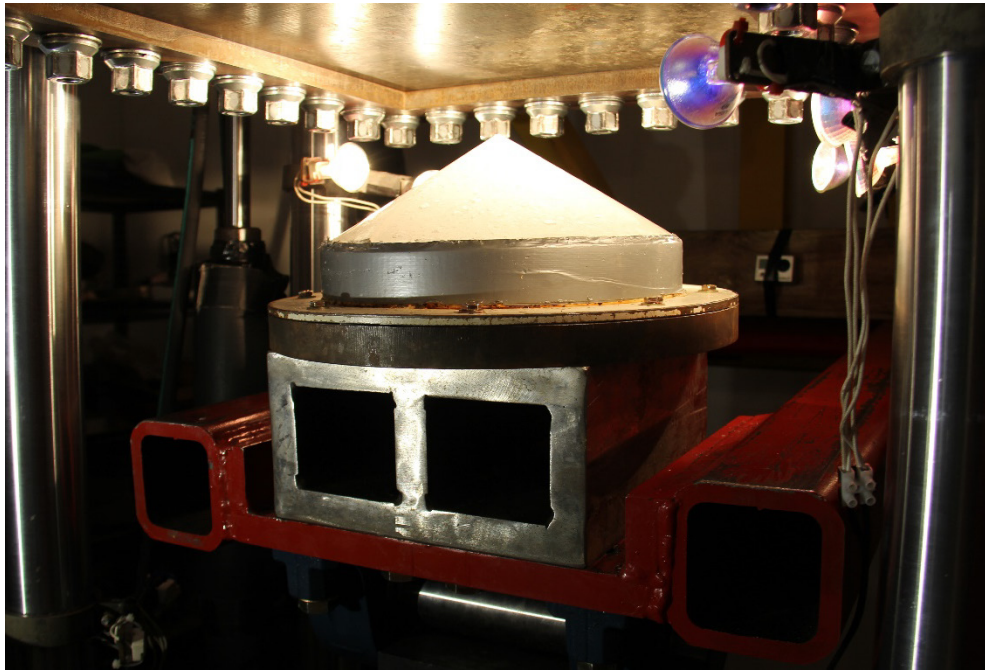


Figure 3.11: Example ice cone indenter mounted to swing-arm (red) using a stilt (box shaped object between swing arm and ice cone indenter) prior to a test.



Figure 3.12: Example ice cone indenter after test – crushed surface (truncating surface of the ice cone) and extruded ice (snow like substance on the surface of the ice cone and indenter) are apparent.

As mentioned below, these ice cones were seeded with ice chips of approximately 4-10 mm (0.157-0.394 in.). This implies a specimen size to grain size ratio of approximately 20 to 60; accounting for slight growth of grains during freezing. According to Dempsey (1991), the crack size and unbroken ligament size of a fracture specimen must be around 12 times the average grain size so that homogeneity requirements are satisfied. The dimensions of these samples generally agree with this recommendation.

A summary of the process used in creating and shaping the ice cone indenters is as follows: Type I reagent water (ASTM¹⁴ D1193, ISO¹⁵ 3696, and CLSI®-CLRW¹⁶ standards), which is distilled and multi-stage filtered water, is deaerated and chilled to just above freezing.

¹⁴ American Society for Testing and Materials

¹⁵ International Organization for Standardization

¹⁶ Clinical and Laboratory Standards Institute-Clinical Laboratory Reagent Water

Commercial ice cubes are pulverised and sieved to exclude ice chips smaller than 4.0 mm (0.157 in.). The largest chips are approximately 10 mm (0.394 in.). Plastic buckets are placed over the rim of steel ice holders (shown in Figure 3.13) creating a water-tight seal. They are then placed in slots in a specially designed chest freezer lid and insulating rings are placed around the buckets' sides. The buckets are first filled with the ice chips, followed by the chilled water. The mixture is then stirred to remove any entrapped air, and compacted to ensure that ice chips are not floating above the bottom of the bucket. An insulated lid is placed over the slot. The bottom of the bucket is left uninsulated as this allows controlled, directional freezing of the ice chip slurry. Freezing from the bottom toward the top is necessary to avoid residual stresses in the ice arising from boundary confinement due to the expansion of the ice during the freezing process; as well as the large-scale and inhomogeneous entrapment of air. As the top of the bucket is unconfined, the ice is free to expand upwards. When the mixture is frozen (approximately 2-3 days) the ice-holder/buckets are removed from the freezer slots, the insulation is removed, and the buckets are taken off the ice holders. Care must be taken during this process so as not to crack the ice samples. The ice sample is then placed on a special purpose turntable (see Figure 3.14) that allows precise shaping of the ice sample into a cone of the required cone angle. The blade on the device shaves ice from the ice sample as the turn table turn the ice. The actuator moves the blade about the blade arm pivot point. Shaping is finished once the blade reaches the predetermined, calibrated angle markings (e.g. 30°).

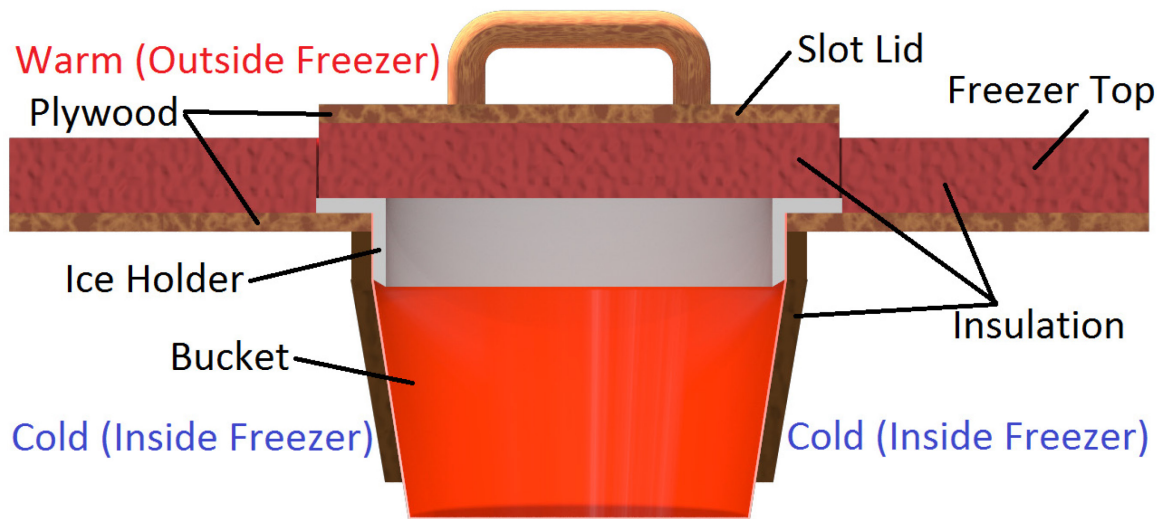


Figure 3.13: Cross-section of apparatus to control freezing of ice indenters.

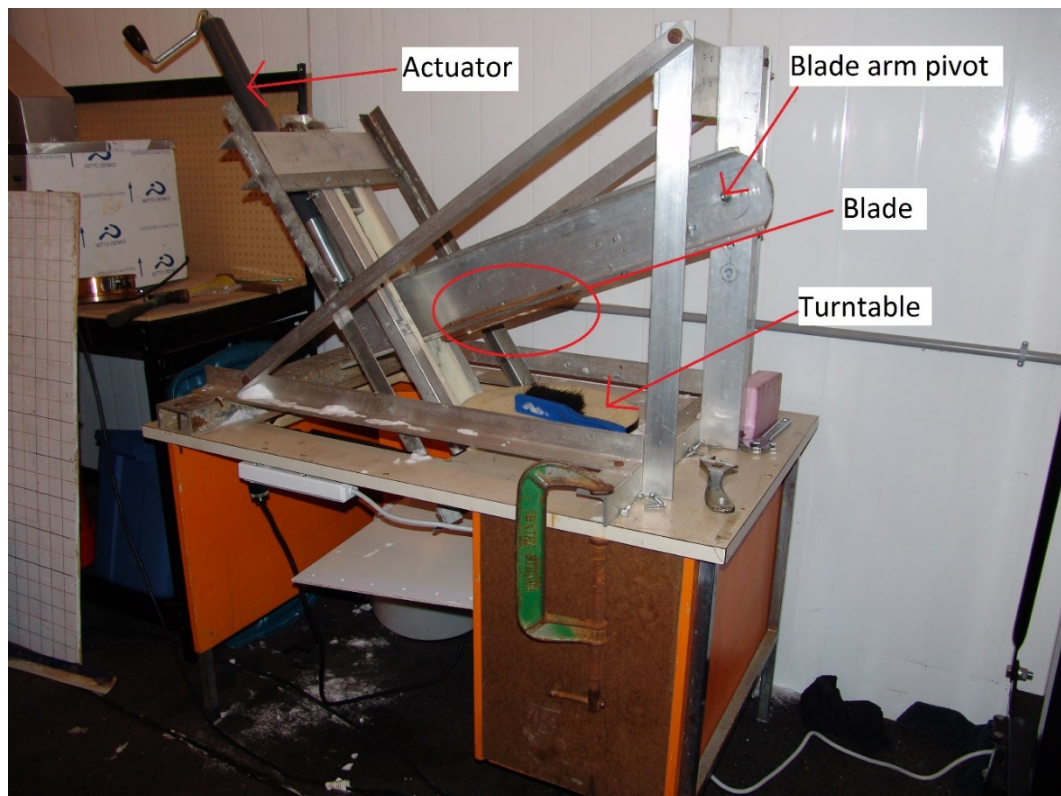


Figure 3.14: Special purpose ice-shaping turntable.

The ice specimen holders were bolted down when installed on the moving load apparatus so that they could not translate or rotate relative to the swing-arm.

3.6 Plate and Frame Test Specimens

One of the defined objectives was to examine the effects of moving loads causing plastic damage on both plates and frames. It was further desired to maximize the scale of the structure, so as to take full advantage of the load capabilities of the MTS test frame. To this end, the author conducted preliminary numerical modelling to determine the appropriate thicknesses for the plate and frame scantlings. It was desired to deform the plate in the normal direction by 5 cm (1.97 in.), as Quinton (2008) predicted that this was well into the level of plastic damage that would induce the moving load effects. It was predicted that the MTS machine could withstand the load generated by a 5 cm (1.97 in.) deflection into a 12.7 mm (0.5 in.) thick steel plate with a 350 MPa yield strength; where the plate dimensions were as large as would fit between the MTS crosshead legs and be practical to manipulate with a long stroke hydraulic ram. This contributed significantly to the design condition for the entire moving load apparatus.

3.6.1 Frames

The frame test specimens consist of three essential components: the plating, the stiffener and the stiffener end plates (shown in Figure 3.15). The plating is analogous to the external plate on the hull of a ship. The stiffener is welded to the plate to provide support against normal and in-plane plate loads. The stiffener end plates have no direct analog with an actual hull structure and exist only to provide a means with which to fix the end of the stiffener to the carriage in order to provide a fixed boundary condition.

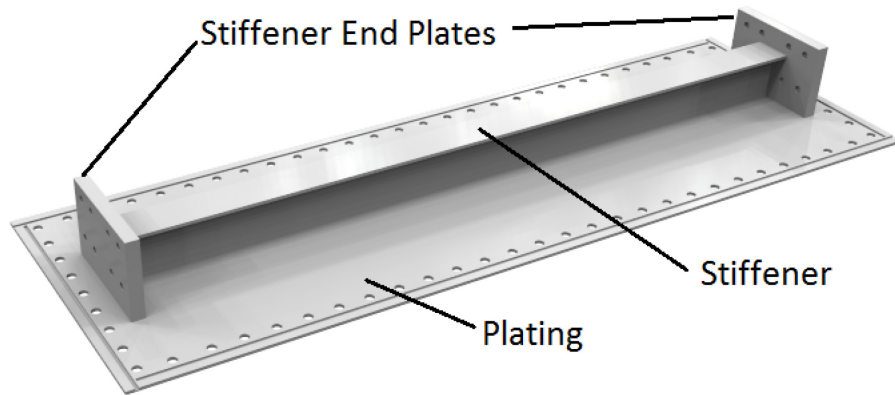


Figure 3.15: Frame test specimen showing plating, stiffener and stiffener end plates.

The frame test specimen scantlings contributed significantly to the design of the carriage, as the carriage depth (vertical direction) had to accommodate both the height of the frame and the frame's deformation resulting from a 5 cm (1.97 in.) indentation. Correspondingly, the height of the frame web was essentially driven by design of the carriage because of the trade-off between the thickness of the steel plate used to construct the carriage, and the overall depth of the carriage. To explain, it was necessary to ensure that the carriage was stiff enough to provide a rigid boundary condition to the test specimens. To this end it was decided to limit the overall deflection of the carriage side walls to 1 mm (0.039 in.) under maximum vertical load. The side-wall deflection depended on the overall height of the carriage, the thickness of the steel comprising the side-walls, and the design of the internal reinforcing structure. The iterative design process, including numerous preliminary numerical simulations, produced the following frame scantlings (see Figures 3.16 and 3.17): the plate is 6.35 mm (1/4 in.) thick and has dimensions 550 mm (21.65 in.) by 1650 mm (64.96 in.); the attached stiffener is a “T-stiffener” with web dimensions of 101.6x6.35

mm (4x1/4 in.), and face flat dimensions of 76.2x6.35 mm (3x1/4 in). The stiffener end plates are 228.6 mm (9 in.) wide, by 152.4 mm (6 in.) tall by 25.4 mm (1 in.) thick. All components are fillet welded at all component interfaces, with one exception: the stiffener end plates are only welded on three sides where they join to the plating. It was necessary to omit the long weld on the side adjacent to the carriage as otherwise the weld would interfere with the carriage wall.

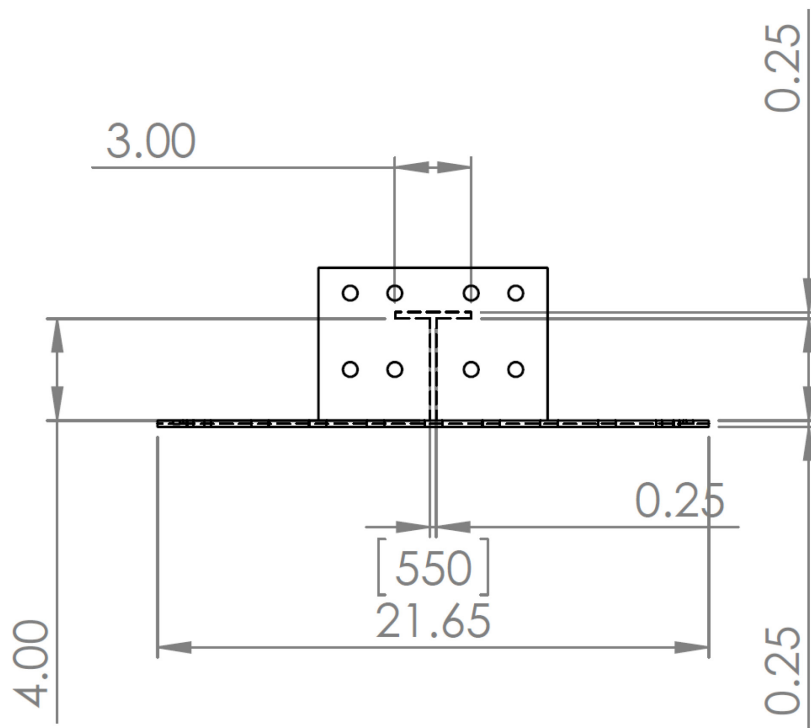


Figure 3.16: End view of frame test specimen (units are inches; bracketed units are mm).

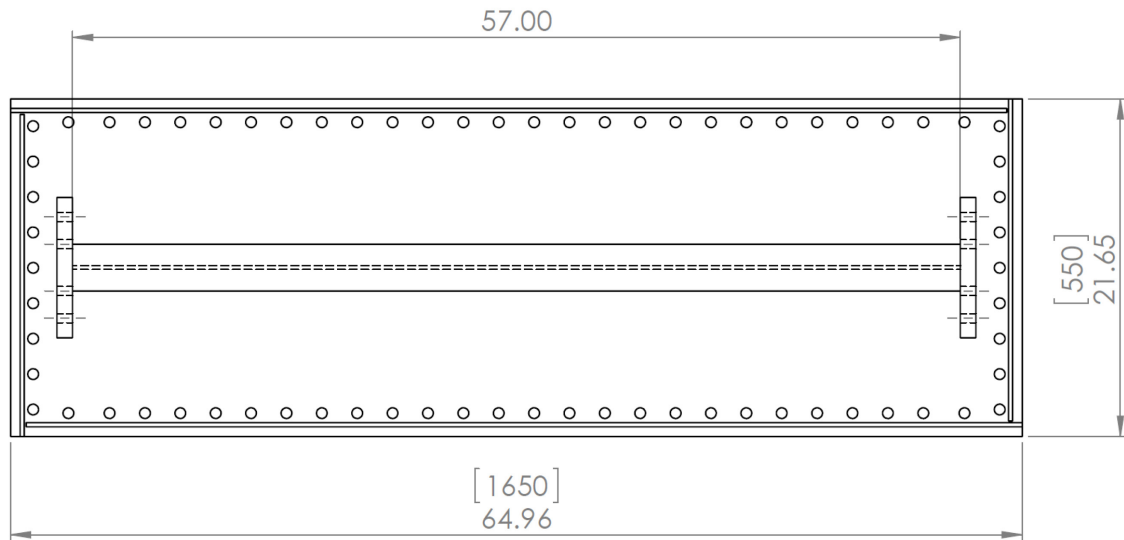


Figure 3.17: Plan view of frame test specimen (units are inches; bracketed units are mm).

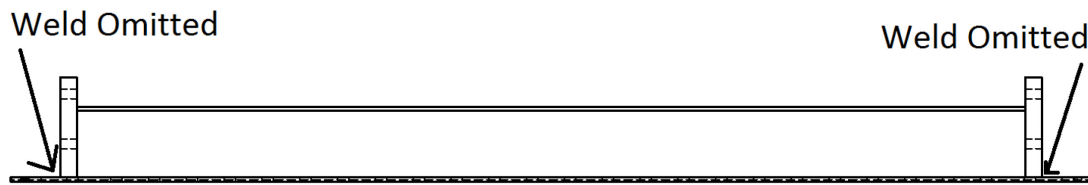


Figure 3.18: Side view of frames test specimen showing omitted welds.

The supporting edge of the carriage incorporates a combination of a sandwich ring, a keyway and bolts (see Figure 3.19) to provide a “fixed-fixed” boundary condition for the plate (i.e. motion in all translational and rotational degrees of freedom (DOF) is restricted). Therefore the portion of the plating sandwiched between the sandwich plate and the carriage does not partake in the overall plate behaviour. Thus the effective plating dimensions do not consider the area of the sandwich ring. The effective plating dimensions are therefore 400 mm (15.75 in.) by 1500 mm (59.06 in.). End conditions for the stiffener

were essentially fixed-fixed as the stiffener end plates were bolted to the carriage in such a way as to resist translation and rotation in all DOF. It should be noted that in order to fit the frame test specimen into the carriage, there must necessarily be a small gap between the stiffener end plates and the ends of the carriage. This gap was nominally less than 1 mm (0.039 in.).

3.6.1.1 Frame test specimen installation procedure

A frame test specimen is installed on the carriage (please refer to Figure 3.19) by lifting it up into the carriage so that the threaded studs pass through the corresponding holes in the test specimen plating. Bolts are then inserted through the holes in the end of the carriage and screwed into the corresponding threaded holes in the test specimen's frame end plates. Next, the sandwich ring is installed snug against the test specimen's plating and several nuts are installed to hold it in place. Next the keystock is inserted into the keyways that are cut in both the bottom of the carriage support edge and the top of the test specimen's plating. Inserting the keystock has the added benefit of precisely aligning the test specimen with the carriage. Once the keystock is in place, the remaining nuts are installed and all nuts are torqued to 325 Nm (240 ft-lbf). The lug nut torque was chosen such that the frictional force between the test specimen plating and the bottom of the carriage would be sufficient to resist any lateral slippage of the test specimen plating when loaded. It was later decided to add the keyways and keystock for the same purpose. In order to ensure minimum slippage, the keystock was used, and the lug nuts were torqued to specification for every test using the torqueing pattern shown in Figure 3.20. This "three ahead, two back" method insured that the plate was free to flatten out progressively as the lug nuts

were tightened, thus avoiding locked in stresses between the bolts. Also, it insured that all lug nuts were torqued twice. This was necessary as lug nuts would appear to loosen slightly as their neighbours were tightened.

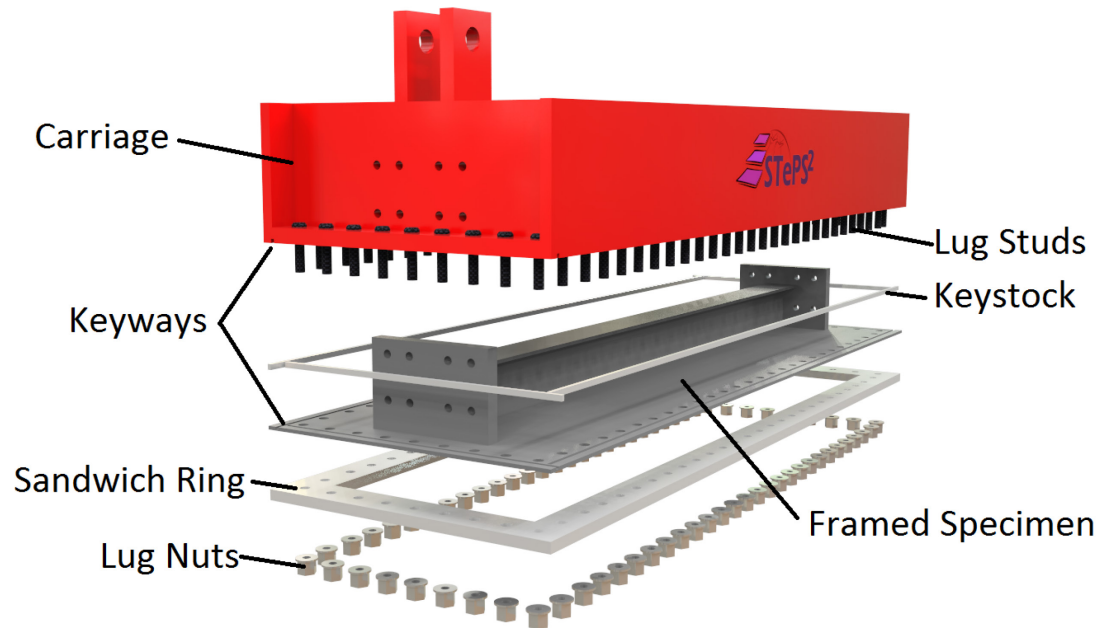


Figure 3.19: Exploded view of how frame test specimens are installed on the test carriage.

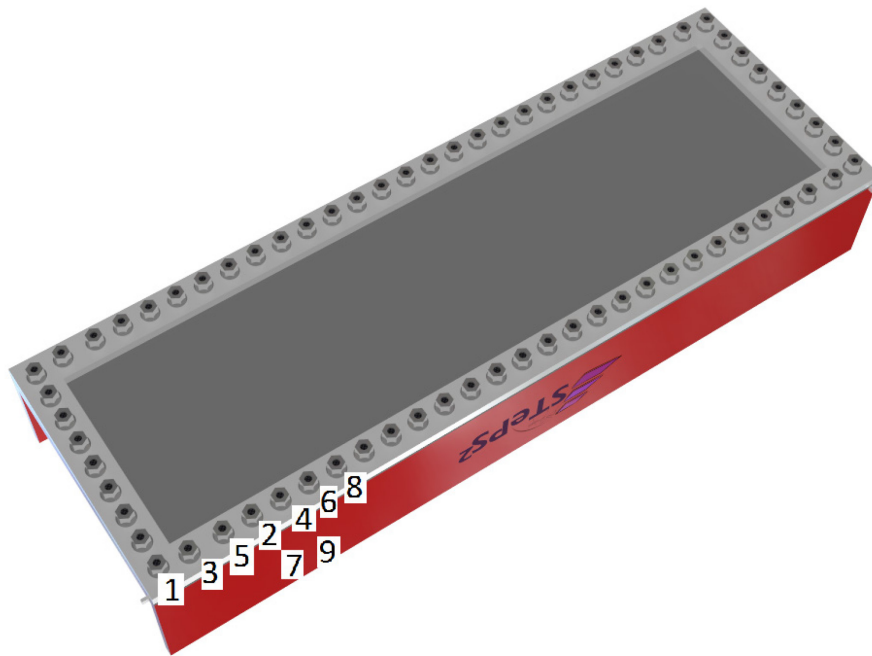


Figure 3.20: Lug nut torquing pattern.

3.6.2 Plates

The plate test specimens (see Figure 3.21) are similar to the frame test specimens except: that they do not have attached stiffeners (and therefore do not need the stiffener end plates); they were tested in three thicknesses: 12.7 mm (1/2 in.), 6.35 mm (1/4 in.) and 3.175 mm (1/8 in.)¹⁷; and the keyway depths were different for each thickness. The bolt holes and keyway locations are identical to the frame test specimens.

¹⁷ There were only two 3.175 mm (1/8 in.) plate specimens tested, and those used ice indenters.

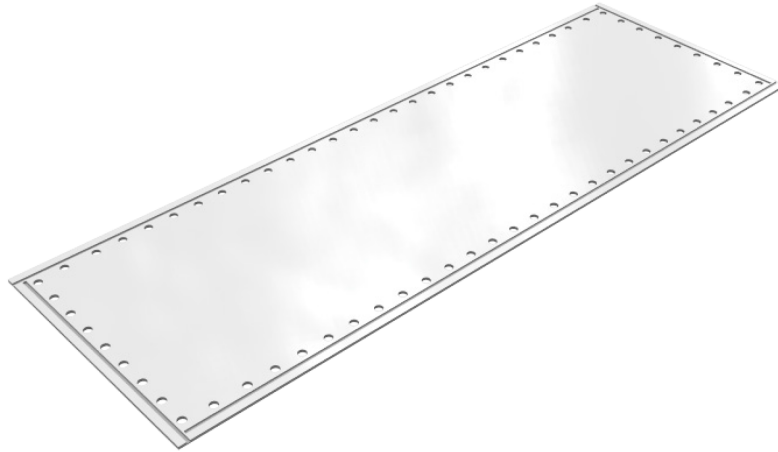


Figure 3.21: 1/4" plate test specimen –bolt holes and keyways are apparent.

The boundary conditions of these plates are identical to those of the plating of the framed specimens. Regarding the keyway depths the 1/4" (6.35 mm) plates had the same keyway depth machined into them as the frame test specimens; that is 1/8" (3.175 mm), or half the thickness of the plate; and the 1/2" plates had a 1/4" (6.35 mm) keyway depth. The 1/8" (3.175 mm) were too thin to machine keyways into them, and therefore the boundary conditions relied solely on frictional force generated by the lug nuts/bolts (as described in 3.6.1.1).

Because the effective dimensions of these plates are $b = 400$ mm (15.75 in.) by $a = 1500$ mm (59.06 in.), their length to width ratio is $a/b = 3.75$. According to Hughes and Caldwell (Hughes, Paik et al. 2010), a plate may be considered a *long plate* if its $a/b \geq 3$ and it is simply supported; or if its $a/b > 2$ and it is clamped. Since these plates are clamped, they are well into the long plate range. Long plates undergo cylindrical (1D) bending for the central portion, b , away from either end. Although there are end effects,

the long plate assumption allows the central portion of the plate to be analysed as if it was an infinitely long plate.

3.6.2.1 Plate test specimen installation procedure

Installation of the plate specimens on the moving load apparatus is identical to that for the frame specimens (described in 3.6.1.1) except that no bolts are used through the carriage ends as there are no stiffener end plates on the plate specimens.

3.7 Data Acquisition

Sensor and visual data was acquired during each test, or shortly after. Each of these is described in the sections following. Data was recorded via the MTS test frames internal data acquisition system, various imaging technologies, and a 3D spatial digitizer.

3.7.1.1 MTS data channels

As mentioned above, the MTS test frame was configured with five general purpose digital/analog conditioned data recording channels. These were employed as follows:

1. MTS linear variable differential transducer (LVDT) – analog signal recorded at 2048 Hz (4096 Hz for experiments involving ice). Recorded the displacement of the MTS hydraulic ram (and hence the displacement of the indenter in the test specimen plating's normal direction). See Appendix A5 for specifications.
2. MTS load cell – Model: 661.21E-01 – digital signal recorded at 2048 Hz (4096 Hz for experiments involving ice). Recorded the load applied in the test specimens plating's normal direction. See Appendix A4 for specifications.

3. Tovey load cell 1 – Model: SW20-50K – digital signal recorded at 2048 Hz (4096 Hz for experiments involving ice). Recorded, in combination with Tovey load cell 2, part of the lateral load resulting from the horizontal motion of the test specimens. Together, both load cells recorded the entire horizontal load. See Appendix A6 for specifications.
4. Tovey load cell 2 - Model: SW20-50K – digital signal recorded at 2048 Hz (4096 Hz for experiments involving ice). Recorded, in combination with Tovey load cell 1, part of the lateral load resulting from the horizontal motion of the test specimens. Together, both load cells recorded the entire horizontal load. See Appendix A6 for specifications.
5. Horizontal Linear Position Transducer (yo-yo pot) – digital signal recorded at 2048 Hz (4096 Hz for experiments involving ice). Recorded the horizontal displacement of the test carriage (and hence the test specimens). See Appendix A7 for specifications.

3.7.1.2 Imaging technologies

Four different imaging technologies were employed for these experiments: a digital high-speed camera, four conventional digital video cameras, two digital thermal imaging cameras, and Fujifilm Prescale pressure measurement film.

1. High-speed digital camera – Brand: MegaSpeed® Model: MS55K black and white imaging. See Appendix B1 for specifications. The high-speed camera was used for the experiments involving ice only, to record the behaviour of the ice. As the camera has limited memory with which to store video, the frame-rate at which

videos were taken depended on the duration of the test. Shorter duration tests were recorded at a higher frame rate than longer duration tests.

2. Four conventional digital video cameras were used: two GoPro Hero 2® cameras (see Appendix B2 for specifications), one GoPro Hero 3® camera (see Appendix B2 for specifications), and a Canon® EOS60D digital SLR camera (see Appendix B3 for specifications). The GoPro Hero 2 cameras are small, battery powered high-definition cameras with an extremely wide-angle lens (up to 170°). The GoPro Hero 3 camera is similar to the GoPro Hero 2 cameras, except it is a slightly newer version. The placement of the GoPro Hero cameras depended on the experiment. For experiments involving the rigid indenter, all three were placed inside the carriage to record the deformation of the specimen. For experiments involving ice, one GoPro Hero camera was placed outside the carriage, mounted to the swing-arm and pointed at the ice sample; recording its behaviour. 12VDC LED light strips were placed inside the carriage to provide ambient light for the GoPro Hero cameras. All GoPro Hero videos were shot in 1080p resolution at 30 frames per second. The GoPro Hero 2 videos were shot at a 127° field of view, and the GoPro Hero 3 videos at 170° field of view. The Canon DSLR camera records uncompressed high-definition video and in most cases was used to film the test from a location that had the most general view. All Canon videos were recorded at 1080p at 30 frames per second at various fields of view.
3. Two thermal cameras were used: a FLIR® Ax5 model suitable for laboratory testing and a FLIR T450sc handheld model (see Appendix B4 for specifications for both). The Ax5 model was placed inside the carriage for the experiments involving

plate specimens. There was no room to place it in the carriage with the frame test specimens. The T450sc model was used for the experiments involving ice, to record the thermal behaviour of the ice.

4. The Fujifilm PrescaleTM pressure measurement film (see Appendix B5 for specifications) is a special film used to determine the magnitude of static pressure developed between two mating surfaces. It consists of tiny glass beads that break under pressure, releasing a chemical that reacts with the film to dye the vicinity red. The shade of red in a particular area of the film is indicative of the pressure at that location. The shades are calibrated to specific pressure ranges. After an experiment, the film is optically scanned, and software converts the red shades to numeric values. Pressure film is available to measure different ranges of pressure. As ice is capable of generating pressure over a very wide range, three levels of pressure film (i.e. low, medium and high) were employed simultaneously in a layered fashion between the ice cone indenter and a ½ in. moving steel plate. The low pressure film measured the range of 2.5-10 MPa; medium 10-50 MPa; and high 50-100 MPa. This layering technique was developed and tested by Kim et al (2012) and was subsequently used in several studies, including Ulan-Kvitberg (2012), Kim (2014) and Kim et al (2014). This pressure measurement technique will not give a time-history of pressure, rather it will record the maximum pressures exerted on it.

3.7.1.3 Spatial digitizing technology

A Microscribe®, model G2LX, which is a 3D spatial digitizer was used to record the location of specific points on the loaded surface of the test specimen's plating. Centre-punched points at predefined locations on each specimen were measured before and after each test. Specifications for the Microscribe are given in Appendix B6.

3.7.2 Control equipment

One other important apparatus were used in these experiments: the hydraulic control table for the horizontal hydraulic ram. The table consisted of a pressure compensated flow control valve that allowed the speed of the horizontal ram's motion to be controlled. Prior to each test, trials were performed to set the valve position so that the required horizontal ram speed was attained during the experiment.

It is worth mentioning here that subsequent to these experiments, the table controlling the horizontal ram was replaced by computerized electronic servo-control similar to that controlling the MTS® vertical ram. It is now possible to program the desired speed and displacement profile directly using a computer.

3.8 Methodology

As part of the study objectives and given that there have been no previous experiments of this nature, these experiments were kept as simple as possible. The factors considered are:

- Sample type
- Load path
- Load type

- Indenter type
- Normal indentation depth
- Normal loading / indentation rate
- Lateral indenter starting location
- Lateral travel length
- Lateral travel speed
- Temperature
- Friction

3.8.1 Sample type

Regarding plates, it was desired to examine cases where the bending response of the plate was significant (i.e. thick plates) as well as cases where the membrane stresses were more significant (thin plates). After preliminary numerical analyses coupled with overall design of the moving load apparatus, it was decided to choose 6.35 mm (1/4 in.) and 12.7 mm (1/2 in.) plate thicknesses for testing with the rigid indenter. 12.7 mm (1/2 in.) and 3.175 mm (1/8 in.) plates were tested with the ice cone indenters).

Regarding frames, choice of stiffener and attached plating scantlings was a combination of the design of the moving load apparatus (as there was a space restriction in the direction of the height of the frame) and maximizing frame height. A reasonable frame height solution was attained and subsequent numerical simulations were performed to determine suitable dimensions for the remaining scantlings, to suit the load/displacement capacity of the moving load apparatus. It was decided to construct the frames entirely from 6.35 mm (1/4 in.) plate.

3.8.2 Load path

In real ship-icebreaking scenarios, the path through space of a moving load varies greatly with respect to contact with a ship's hull. It is complex due to the local and global response of both the ship and ice feature.

For these experiments, the simplest load path for the steel wheel indenter is to break the load path into three phases: normal loading phase, lateral motion phase, and unloading phase. The normal loading phase consists of load only in the normal direction, without any lateral motion of the indenter. The lateral motion phase consists of holding the vertical load (from the first phase) steady, and moving the indenter laterally along the plating of the test specimen. Once the lateral motion from the second phase ceases, the unloading phase consists of removing the vertical load (applied in the first phase).

While it could be argued that the simplest load path for the steel wheel indenter would be applicable to the ice indenter as well, it was desired to investigate the effects of load motion on the crushing behaviour of ice. The simplest load path to accomplish this consists of two phases. The first phase consists of simultaneous displacement control in the normal and lateral directions; where the velocities have to be coupled such that the normal and lateral displacements of the indenter will reach their maximum extent simultaneously. The second phase is the unloading phase; similar to above.

It should be noted that an investigation of the effect of varying load path was conducted numerically and described in Chapter 5.5.

3.8.3 Load type

The majority of the experiments were performed using *displacement control*; that is, the position of the base of the indenter in space was controlled at all times, and the resulting load was variable. It was desired to examine moving load behaviour using *force control* as well; that is, the force applied by the indenter on the test specimen was controlled at all times, and the resulting displacement was variable. Three force controlled experiments were performed using the steel wheel indenter. No force controlled experiments were performed using ice cone indenters, as force control with ice is more difficult to achieve than displacement control (due to the load drops associated with spalling events), and achieving force control was outside the scope of these preliminary moving ice load experiments.

3.8.4 Indenter type

As previously discussed, two types of indenters were used: a steel wheel indenter and an ice cone indenter. The steel wheel indenter allowed the experimentation on the plate and frame test specimens without regard for the behaviour of the indenter; thus the response of the plates and frames were essentially decoupled from the indenter. The ice indenter's deformation was coupled with the deformation of the plates. Please see Chapters 3.5.1 and 3.5.2 for further discussion.

3.8.5 Normal indentation depth

The depth of the indentation into the plating (normal direction) impacts the response of the test specimen. Small indentations induce an elastic response while larger indentations induce a plastic response. Plastic response may be a combination of several types of plastic

behaviours (e.g. plastic bending response only, or plastic bending and plastic membrane responses).

For the experiments involving the steel wheel indenter, the highest level of plastic damage that was *practical* to achieve was generally applied to the test specimens. The “practicality” was a function of how difficult the damaged test specimen was to remove from the test apparatus after the test was completed, and whether the edges of the steel wheel indenter scored the plate or not. Too much plastic damage meant that the test specimens had to be cut and pried off the carriage. This added considerably to the time required to perform a single test, and risked damaging some of the more sensitive equipment housed inside the test carriage (e.g. thermal camera). Additionally, it was not desirable to have the edges of the steel wheel indenter score the plating, as this introduced structural effects that were beyond the scope of this study. Despite these limitations it was generally practical to indent the plating to the following extent of the plating’s width: 10% for the $\frac{1}{4}$ ” plates; 7.5% for the $\frac{1}{2}$ ” plates; and 6.25% for the frames.

Three tests were conducted on $\frac{1}{4}$ ” plates, using the steel wheel indenter, where the indentation in the normal direction was reduced to 5% of the plate width in order to examine the plate behaviour at lower levels of plastic damage.

For experiments involving ice cones, indentation depth became a function of the behaviour of the ice (instead of the behaviour of only the test specimen, as for the steel wheel experiments). As the ice cones are contained within a steel ring, they may be subject to confinement effects as the crushed surface of the ice approaches the top of the vertical steel ring. These confinement effects are artificial in the sense that they are a function of the

necessity for the ice cones to be held in place in order to conduct laboratory testing; and not necessarily present for real-world ice loads. Artificial confinement tends to strengthen the ice when compared with unconfined ice loads. It was desired to minimize these confinement effects, so a limit was placed on displacement of the base of the ice cone indenter such that the maximum possible distance from the tip of the undamaged ice cone to the deepest crushed surface was 3.0 cm (1.18 in.). This depth is approximately half the total height of the ice cone (above the top of the ring of the ice holder), experience has shown that this level of indentation generally does not promote confinement effects from the ice holder.

3.8.6 Normal loading / indentation rate

For the three force controlled experiments, the loading rate was somewhat arbitrarily chosen to be 10 kN/s (1 long-ton/s). As only one rate was used, loading rate was essentially not a variable for these three tests. The choice of 10 kN/s allowed the tests to be conducted in a reasonable timeframe (up to 3 minutes for the ¼” plate).

For the remaining displacement-controlled experiments, indentation rate was a variable. Indentation rate directly impacts the strain-rate experienced by each test specimen during the application of the load. As discussed above, strain-rate affects the general behaviour of the test specimens, and therefore it was desirable to examine the effects of strain-rate on moving loads causing plastic damage. Two levels of indentation rate were used as shown in Table 3.1. The “Fastest Possible” entry is a function of the fact that the speed of the MTS (vertical) hydraulic ram is a function of the resistance of the structure it is pushing

on, as well as the demand on the pump¹⁸ supplying hydraulic oil to the ram. As the hydraulic supply pump was shared between this apparatus, and other high-demand applications (e.g. wave-maker in a tow-tank) that may have been operating simultaneously, it was impossible to set an upper limit in advance of the experiments.

Table 3.1: Indentation Rates for displacement-controlled experiments.

Indenter	Low Level	High Level
Steel Wheel	1 mm/s	Fastest Possible
Ice Cone	0.25 mm/s	10 mm/s

For the experiments utilising the ice cone indenters, indentation rate not only affected the behaviour of the test specimen, it also affected the ice cone's behaviour. As discussed in Chapter 2, ice is sensitive to strain-rate in various ways. Dillenburg (2012) has shown that the low level of 0.25 mm/s (0.00984 in./s) for these scale ice cones corresponds to a rate at which ductile response will dominate the ice behaviour. At this rate creep effects are minimal and large spalling events are not common. The high rate of 10 mm/s (0.394 in./s) corresponds with ice behaviour that exhibits both crushing and large spalling events. As well, because the load path for these tests requires that this speed be coupled with the lateral travel speed, 10 mm/s corresponds with the maximum speed possible from the horizontal hydraulic ram¹⁹ so that the normal and lateral indenter motions cease at the desired location.

¹⁸The hydraulic pump was pressure-compensated such that high demand did not affect the pressure; only the flow-rate.

¹⁹ Unlike the vertical hydraulic ram, it is possible to reliably predict the maximum speed of the horizontal hydraulic ram in this case as it is loaded at only a fraction of its load capacity.

3.8.7 Lateral indenter starting location

Lateral indenter starting location is the position of the point of contact of the indenter (i.e. the top of the steel wheel or the tip of the ice cone) with respect to the test specimen's plating. As the response of plates and frames vary with position relative to their extents, lateral starting location is important. It was desired to examine their behaviour when the load was initially applied at the centre of the plating, and when it was applied near one longitudinal end. With reference to the test regime shown in Table 3.2, "Centre" implies that the tip of the indenter was initially placed at a point half-way along the length and width of the plate. "20 cm from End" implies that the tip was initially placed 20 cm (7.87 in.) from the end of the plate along the longitudinal centreline. "Absolute End" is similar to the above, except that the tip was placed as close to the end of the plate as the apparatus would allow; that is, 13.5 cm (5.31 in.).

The "20 cm from End" level was chosen to allow the steel wheel to indent the plate without interfering with the sandwich plate or carriage. It was not necessary to account for this interference with the ice cone experiments as the load path allowed the starting position to be at the absolute end of the test specimen.

3.8.8 Lateral travel length

Lateral travel length is less of a variable and more of a consequence of the lateral starting position. However, it is important to account for the travel distance explicitly when examining moving load effects. There were two levels of lateral travel length: a low level of approximately 550 mm (21.65 in.), and a high level of approximately 1100 mm (43.3 in.). The low level corresponds to the distance between the centre starting position and the

“20 cm from End” position. The high level corresponds to the distance between the “20 cm from End” lateral starting position and the position symmetrically opposite to it. It is important to distinguish lateral end position as symmetrically opposite to the start position because it allows direct comparison of the *stationary capacity* of the test specimen with the *moving load capacity* at essentially the same position (due to symmetry).

3.8.9 Lateral travel speed

Lateral travel speed is analogous to the “normal indentation rate” variable; that is, it is the lateral speed at which the indenter moves along the plating.

For all experiments except three, there were two levels for this variable: a low value of 10 mm/s (0.394 in./s) and a high value of 185 mm/s (7.28 in./s). 185 mm/s is the maximum speed of the horizontal hydraulic ram.

The three experiments where the high value was not 185 mm/s were “one-off” ice cone tests, and are explained below.

It should be noted that force control in the lateral (i.e. horizontal ram) direction is not presently possible with this apparatus because of the presence of two load cells measuring lateral load and inability of the control software to sum them to form a feedback signal on which to base the force control.

3.8.10 Temperature

As temperature is known to affect the behaviour of steel, it was desired to conduct experiments at two ambient temperatures: room-temperature of 20°C and -10°C. Room-temperature was chosen because of its facility, and because it allows results of these tests

to be compared with other laboratory tests. -10°C was chosen for a number of reasons: 1. it is a good approximation for average Arctic conditions as cold Arctic air temperatures are tempered by -2°C Arctic sea water adjacent to a ship's hull; 2. it provides a 30°C temperature difference from room-temperature, which is significant; 3. -10°C is a common temperature at which many laboratory ice behaviour experiments have been carried out (allowing for future comparison); and 4. much of the equipment used in the moving load apparatus is only rated to function down to -10°C .

3.8.11 Friction

While sliding friction was practically eliminated for the rigid wheel indenter (by placing it on a shaft supported by pillow block bearings), this was not possible for the ice cone indenters. Note: the low-pressure film – which is the type of pressure film (in the stack of three layers of pressure film) adjacent to the ice – is composed of two thin polyester sheets.

3.9 Test regime

The test regime for these experiments is given in Table 3.2. This schedule of experiments allows exploration of each of the above variables at their high and low values. Time and resources restraints contributed to the lack of repetition for each run; with the exception of two experiments involving moving ice loads on an elastic plate, where one repetition each was performed (shown as green rows in Table 3.2). Note that the orange rows in Table 3.2 indicate tests in which Fujifilm PrescaleTM pressure film was used to get an indication of the maximum pressures present during the experiment.

Table 3.2: Test Regime* - green rows indicate that the run is a repeat, and orange rows indicate that pressure film was used to record the maximum pressures.

Room Temperature Tests							
Sample Type	Run Type	Indenter Type	Location	Vertical Indentation	Vertical Speed	Horizontal Travel	Horizontal Speed
1/4"	In-Along-Out	Steel	Centre	4 cm	1 mm/s	55+ cm	10 mm/s
1/4"	In-Along-Out	Steel	20 cm from end	4 cm	1 mm/s	110+ cm	10 mm/s
1/4"	In-Along-Out	Steel	Centre	4 cm	Fastest	55+ cm	Fastest
1/2"	In-Along-Out	Steel	Centre	3 cm	1 mm/s	55+ cm	10 mm/s
1/2"	In-Along-Out	Steel	20 cm from end	3 cm	1 mm/s	110+ cm	10 mm/s
1/2"	In-Along-Out	Steel	Centre	3 cm	Fastest	55+ cm	Fastest
Frame	In-Along-Out	Steel	Centre	2.5 cm	1 mm/s	55+ cm	10 mm/s
Frame	In-Along-Out	Steel	20 cm from end	2.5 cm	1 mm/s	110+ cm	10 mm/s
Frame	In-Along-Out	Steel	Centre	2.5 cm	Fastest	55+ cm	Fastest
-10 °C Tests							
Sample Type	Run Type	Indenter Type	Location	Vertical Indentation	Vertical Speed	Horizontal Travel	Horizontal Speed
1/4"	In-Along-Out	Steel	Centre	4 cm	1 mm/s	55+ cm	10 mm/s
1/4"	In-Along-Out	Steel	20 cm from end	4 cm	1 mm/s	110+ cm	10 mm/s
1/4"	In-Along-Out	Steel	Centre	4 cm	Fastest	55+ cm	Fastest
1/4"	In-Along-Out	Steel	Centre	2 cm	1 mm/s	55+ cm	10 mm/s
1/4"	In-Along-Out	Steel	20 cm from end	2 cm	1 mm/s	110+ cm	10 mm/s
1/4"	In-Along-Out	Steel	Centre	2 cm	Fastest	55+ cm	Fastest
1/2"	In-Along-Out	Steel	Centre	3 cm	1 mm/s	55+ cm	10 mm/s
1/2"	In-Along-Out	Steel	20 cm from end	3 cm	1 mm/s	To End	10 mm/s
1/2"	In-Along-Out	Steel	Centre	3 cm	Fastest	55+ cm	Fastest
Frame	In-Along-Out	Steel	Centre	2.5 cm	1 mm/s	55+ cm	10 mm/s
Frame	In-Along-Out	Steel	20 cm from end	2.5 cm	1 mm/s	110+ cm	10 mm/s
Frame	In-Along-Out	Steel	Centre	2.5 cm	Fastest	55+ cm	Fastest
1/4"	In&Along-Out	Steel	20 cm from end	125 kN	10 kN/s	110+ cm	10 mm/s
1/2"	In&Along-Out	Steel	20 cm from end	250 kN	10 kN/s	110+ cm	10 mm/s
Frame	In&Along-Out	Steel	20 cm from end	250 kN	10 kN/s	110+ cm	10 mm/s
Elastic Plate Response Ice Tests (-10°C)							
Sample Type	Run Type	Indenter Type	Location	Vertical Indentation	Vertical Speed	Horizontal Travel	Horizontal Speed
1/2"	In&Along-Out	Ice Cone	Absolute End	3 cm	0.25 mm/s	110+ cm	10 mm/s
1/2"	In&Along-Out	Ice Cone	Absolute End	3 cm	0.25 mm/s	110+ cm	10 mm/s
1/2"	In&Along-Out	Ice Cone	Absolute End	3 cm	0.25 mm/s	110+ cm	10 mm/s
1/2"	In&Along-Out	Ice Cone	Absolute End	3 cm	3.5 mm/s	90+ cm	100 mm/s
1/2"	In&Along-Out	Ice Cone	Absolute End	3 cm	3.5 mm/s	90+ cm	100 mm/s
1/2"	In&Along-Out	Ice Cone	Absolute End	3 cm	83.0 mm/s	110+ cm	83.0 mm/s
1/2"	In&Along-Out	Ice Cone	Absolute End	3 cm	0.25 mm/s	110+ cm	10 mm/s
1/2"	In&Along-Out	Ice Cone	Absolute End	3 cm	0.25 mm/s	110+ cm	10 mm/s
Plastic Plate Response Ice Tests (-10°C)							
Sample Type	Run Type	Indenter Type	Location	Vertical Indentation	Vertical Speed	Horizontal Travel	Horizontal Speed
1/8"	In&Along-Out	Ice Cone	Absolute End	3 cm	0.25 mm/s	110+ cm	10 mm/s
1/8"	In&Along-Out	Ice Cone	Absolute End	6.4 cm	10 mm/s	110+ cm	Fastest

*Note: Regarding “Run Type”: “In-Along-Out” refers to the sequential application of motions; “In&Along-Out” refers to the In (normal) and Along (lateral) motions occurring simultaneously.

3.10 Experimental Procedure

3.10.1 General procedure

For all experiments, the general procedure was:

1. Activate the carriage's internal cameras and LED lights.
2. Install the test specimen.
3. Get initial external plating geometry using the Microscribe.
4. Calibrate horizontal hydraulic ram speed.
5. Check MTS test frame cross head position and adjust as necessary.
6. Exercise hydraulic rams for 10 minutes to bring hydraulic system up to operating temperature.
7. If ice cone test, install new ice cone.
8. Update test log with experiment details.
9. Move horizontal hydraulic ram to starting position.
10. Bring vertical ram up to touch the specimen's plating.
11. Set data acquisition rate (2048 Hz for rigid indenter tests; 4096 for ice indenter tests).
12. Set vertical hydraulic ram "load" displacement profile.
13. Set vertical hydraulic ram "unload" displacement profile.

14. Activate other video (e.g. high-speed, conventional or thermal).
15. Do test.
16. Take post-test (i.e. unloaded/deformed state) specimen plating Microscribe points.
17. Take post-test pictures and in the case of ice-cone tests, measurements of the deformed ice cone.
18. Remove the test specimen.

Chapter 4 Experimental Results

The actual experiment parameters (e.g. normal indenter speed, lateral displacement, etc...) are presented in groups of related tests below. Tables 4.1 through 4.5 provide a summary of the test parameters for each of the experiment groups, which respectively are: room-temperature tests with steel wheel indenter; -10°C tests with steel wheel indenter; -10°C force controlled tests with steel wheel indenter; -10°C ice cone tests on an elastically deforming plate; and -10°C ice cone tests on plastically deforming plates.

Results of the experiments relevant to the subject of this thesis are presented in the following subsections. Please note that the *datatips* (i.e. boxes showing the values of some of the points on the curves in the figures) may obscure part of the curves in the figures. Every attempt was made to minimize this, however it was unavoidable in some cases. All data recorded for each experiment are given in Appendix C, and are presented unobscured.

Table 4.1: Actual experiment parameters for room-temperature tests with steel wheel indenter.

Room Temperature Tests										
Sample	Date	Sample Type	Run Type	Indenter Type	Location [mm]	Vertical Indentation [mm]	Vertical Speed [mm/s]	Horizontal Travel [mm]	Horizontal Speed [mm/s]	Notes
MovingLoad10	March 27, 10:15am	1/4"	In-Along-Out	Steel	0	40.0	1.00	569.1	10.02	Stationary & slow 4 cm moving load
MovingLoad11	March 27, 4:10pm	1/4"	In-Along-Out	Steel	-550	40.0	1.00	1120.4	9.60	Stationary & slow 4 cm moving load
MovingLoad9	March 26, 3:40pm	1/4"	In-Along-Out	Steel	0	40.0	83.75	593.0	186.40	Stationary & fast 4 cm moving load
MovingLoad7	March 25, 4:40pm	1/2"	In-Along-Out	Steel	0	30.0	1.00	573.7	8.64	Stationary & slow 3 cm moving load
MovingLoad8	March 26, 12:00pm	1/2"	In-Along-Out	Steel	-550	30.0	1.00	1121.2	9.86	Stationary & slow 3 cm moving load
MovingLoad6	March 24, 2:10pm	1/2"	In-Along-Out	Steel	0	30.0	71.69	589.8	185.64	Stationary & fast 3 cm moving load
MovingLoad15	April 2, 3:00pm	Frame	In-Along-Out	Steel	0	25.0	1.00	564.3	8.79	Stationary & slow 2.5 cm moving load
MovingLoad16	April 3, 2:45pm	Frame	In-Along-Out	Steel	-550	25.0	1.00	1114.4	9.52	Stationary & slow 2.5 cm moving load
MovingLoad14	April 1, 3:55pm	Frame	In-Along-Out	Steel	0	25.0	71.03	602.0	185.06	Stationary & fast 2.5 cm moving load

Table 4.2: Actual experiment parameters for -10°C tests with steel wheel indenter.

-10° Tests										
Sample	Date	Sample Type	Run Type	Indenter Type	Location [mm]	Vertical Indentation [mm]	Vertical Speed [mm/s]	Horizontal Travel [mm]	Horizontal Speed [mm/s]	Notes
MovingLoad18	April 7, 3:50pm	1/4"	In-Along-Out	Steel	0	40.0	1.00	562.3	10.32	Stationary & slow 4 cm moving load
MovingLoad19	April 8, 3:00pm	1/4"	In-Along-Out	Steel	-550	40.0	1.00	1107.4	10.25	Stationary & slow 4 cm moving load
MovingLoad17	April 4, 4:25pm	1/4"	In-Along-Out	Steel	0	40.0	84.01	595.9	185.92	Stationary & fast 4 cm moving load
MovingLoad24	April 15, 2:55pm	1/4"	In-Along-Out	Steel	0	20.0	1.00	567.3	11.27	Stationary & slow 2 cm moving load
MovingLoad25	April 16, 12:00pm	1/4"	In-Along-Out	Steel	-550	20.0	1.00	1106.4	11.09	Stationary & slow 2 cm moving load
MovingLoad23	April 15, 11:20am	1/4"	In-Along-Out	Steel	0	20.0	91.81	594.8	188.96	Stationary & fast 2 cm moving load
MovingLoad20	April 9, 1:20pm	1/2"	In-Along-Out	Steel	0	30.0	1.00	558.7	9.05	Stationary & slow 3 cm moving load
MovingLoad21	April 10, 1:00pm	1/2"	In-Along-Out	Steel	-550	30.0	1.00	1106.6	9.14	Stationary & slow 3 cm moving load
MovingLoad22	April 14, 1:20pm	1/2"	In-Along-Out	Steel	0	30.0	67.90	597.1	186.46	Stationary & fast 3 cm moving load
MovingLoad27	April 22, 2:15pm	Frame	In-Along-Out	Steel	0	25.0	1.00	565.2	8.06	Stationary & slow 2.5 cm moving load
MovingLoad28	April 23, 4:15pm	Frame	In-Along-Out	Steel	-550	25.0	1.00	1111.9	8.62	Stationary & slow 2.5 cm moving load
MovingLoad26	April 16, 4:10pm	Frame	In-Along-Out	Steel	0	25.0	69.02	593.5	178.07	Stationary & fast 2.5 cm moving load

Table 4.3: Actual experiment parameters for -10°C force controlled tests with steel wheel indenter.

Force Controlled -10 °C Tests										
Sample	Date	Sample Type	Run Type	Indenter Type	Location [mm]	Vertical Force [kN]	Vertical Rate [N/s]	Horizontal Travel [mm]	Horizontal Speed [mm/s]	Notes
MovingLoad 36	May 1, 3:50pm	1/4"	In&Along-Out	Steel	-550	125	10356	1111.4	9.33	Force Controlled
MovingLoad 29	April 24, 12:10pm	1/2"	In&Along-Out	Steel	-550	250	10029	1117.3	8.78	Force Controlled
MovingLoad 37	May 5, 3:00pm	Frame	In&Along-Out	Steel	-550	250	9976	1116.8	8.70	Force Controlled

Table 4.4: Actual experiment parameters for -10°C tests with ice cone indenter and elastic plate response.

Elastic Plate Response Ice Tests (-10°C)										
Sample	Date	Sample Type	Run Type	Indenter Type	Location [mm]	Vertical Indentation [mm]	Vertical Speed [mm/s]	Horizontal Travel [mm]	Horizontal Speed [mm/s]	Notes
MovingLoad30	April 25, 1:00pm	1/2"	In&Along-Out	Ice Cone	-550	30.0	0.25	1121.3	10.91	constant ramp
MovingLoad31	April 28, 11:45pm	1/2"	In&Along-Out	Ice Cone	-550	30.0	0.25	1100.2	10.64	constant ramp
MovingLoad32	April 28, 3:30pm	1/2"	In&Along-Out	Ice Cone	-550	30.0	0.25	1105.3	10.76	constant ramp - With Pressure Film
MovingLoad33	April 29, 12:00pm	1/2"	In&Along-Out	Ice Cone	-615	30.0	3.50	950.1	96.60	constant ramp - With Pressure Film
MovingLoad34	April 29, 2:40pm	1/2"	In&Along-Out	Ice Cone	-615	30.0	3.50	915.5	97.02	constant ramp
MovingLoad35	April 29, 4:00pm	1/2"	In&Along-Out	Ice Cone	-615	30.0	83.23	1197.7	83.03	constant ramp then hold - With Pressure Film
MovingLoad38	May 14, 2:45pm	1/2"	In&Along-Out	Ice Cone	-615	30.0	0.25	1215.3	10.55	constant ramp
MovingLoad39	May 16, 10:50pm	1/2"	In&Along-Out	Ice Cone	-615	30.0	0.25	1215.8	10.42	constant ramp

Table 4.5: Actual experiment parameters for -10°C tests with ice cone indenter and plastic plate response.

Plastic Plate Response Ice Tests (-10°C)										
Sample	Date	Sample Type	Run Type	Indenter Type	Location [mm]	Vertical Indentation [mm]	Vertical Speed [mm/s]	Horizontal Travel [mm]	Horizontal Speed [mm/s]	Notes
MovingLoad40	May 16, 2:45pm	1/8"	In&Along-Out	Ice Cone	-615	30.0	0.25	1215.8	10.44	constant ramp
MovingLoad41	May 20, 12:00pm	1/8"	In&Along-Out	Ice Cone	-615	64.0	10.01	1147.2	186.85	constant ramp

It should be noted that all data manipulation, analysis and plotting was performed using a custom Matlab® script. The script a screenshot of its associated graphical user interface are provided in Appendix D.

4.1 1/4" Plates with Steel Wheel Indenter at Room-temperature

Three displacement-controlled experiments were performed on 6.35 mm (1/4 in.) plate test specimens at room-temperature using the steel wheel indenter. All plates were indented 4 cm (1.575 in.) in the normal direction. Table 4.1 lists the actual experimental parameters for these experiments. Two of the experiments have the indenter starting at the “Centre” of the plate (i.e. half-way along the plate in the longitudinal direction) and the other has the starting position 20 cm (7.874 in.) from one end; this latter position is referred to as the “End” position. For all three experiments, the lateral travel of the indenter passes the opposite “End” mark on the far side of the plate. The two “Centre” tests are conducted at different speeds (i.e. vertical and horizontal ram speeds). This allows for investigation of strain-rate effects, and their mitigating potential on moving load effects. The “End” test is conducted at the same speed as the slower “Centre” test. This allows direct comparison of the “stationary capacity” and “moving load capacity” of the “End” and “Centre” positions. Figures 4.1 and 4.2 and Table 4.6 present the experimental results relevant to this discussion. All data collected for these experiments is presented in Appendix C1.1.

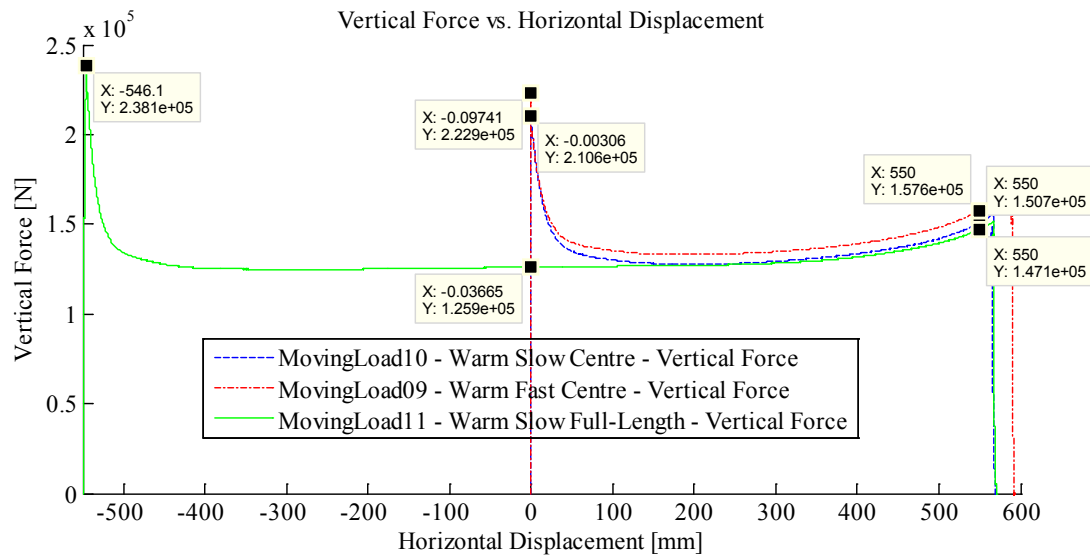


Figure 4.1: Normal (vertical) force versus lateral (horizontal) displacement for rigid indenter acting on room-temperature $\frac{1}{4}$ " plates.

Table 4.6: $\frac{1}{4}$ " plate normal (vertical) force capacity results at room-temperature.

Experiment	Speed	End "Stationary Capacity" [kN]	End "Moving Capacity" [kN]	Centre "Stationary Capacity" [kN]	Centre "Moving Capacity" [kN]
Centre	Slow	N/A	150.7	210.6	N/A
Centre	Fast	N/A	157.6	222.9	N/A
End	Slow	238.1	147.1	N/A	125.9

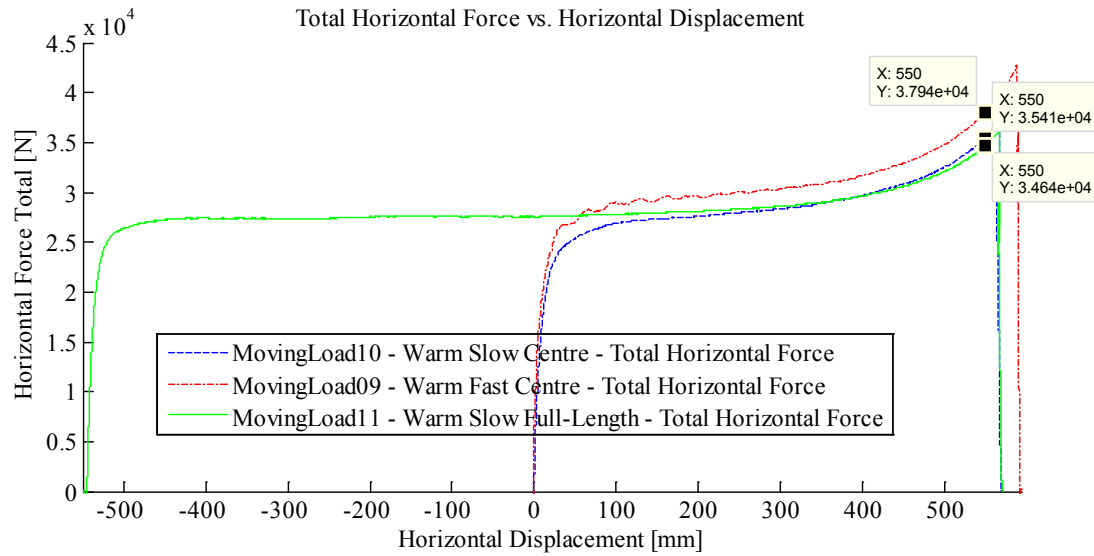


Figure 4.2: Lateral (horizontal) force versus lateral (horizontal) displacement for rigid indenter acting on room-temperature $\frac{1}{4}$ " plates.

4.1.1 Moving load capacity vs. stationary capacity

Figure 4.1 shows the normal reaction force of the $\frac{1}{4}$ " plates versus lateral displacement of the steel wheel indenter. Note that 0 mm on the "Horizontal Displacement" axis aligns with the geometric centre of the test specimen, and is the start location for all "Centre" experiments. The -550 mm position is the start location for all "End" experiments. Table 4.6 lists the key results from these experiments.

Figure 4.1 shows three highlighted values at 0 mm horizontal displacement. They are: the "slow" "normal stationary capacity" of 210.6 kN; the "fast" "normal stationary capacity" of 222.9 kN, and the "slow" "normal moving capacity" of 125.9 kN. Both of the "slow" capacities can be compared directly as they occur at the same lateral location. The "slow" "normal stationary capacity", 210.6 kN, represents the structural capacity of the plate to a stationary normal indentation of 4 cm. The "slow" "normal moving capacity", 125.9 kN,

represents the normal structural capacity of the plate to a laterally moving indentation of 4 cm. These results show that the “normal moving capacity” is just 60% of the “normal stationary capacity”. Regarding strain-rate effects, the strain-rates for the stationary and moving loads at the “Centre” location may not have been identical, but the strain-rate for the moving load would likely have been higher due to two components of motion versus the stationary load’s one. This implies that any difference in the tests due to strain-rate effects would only serve to increase the “moving capacity”, and thus mitigate the associated capacity loss.

The normal direction capacity loss may be assessed at the “End” position, using only the “slow End” experiment. Symmetry in the plate and the loading condition implies that the location symmetrically opposite the indenter’s starting position (about the short axis of the plate) would give an identical structural response as the starting position to the same load. Therefore the “End” “normal stationary capacity” is the response at the “End” starting location, and the “End” “normal moving capacity” is the response at the symmetrically opposite point (i.e. +550 mm). The “End” “normal stationary capacity” is 238.1 kN, and the “End” “normal moving capacity” is 147.1 kN (i.e. 62% of the “normal stationary capacity”).

4.1.2 Strain-rate mitigation effects

Regarding Figure 4.1 and comparing the “slow” normal “stationary capacity”, 210.6 kN, and the “fast” normal “stationary capacity”, 222.9 kN, at the plate’s centre shows an increase in normal “stationary capacity” of 5.8% due most likely to the difference in loading

rate (i.e. strain-rate effects). It is possible however that this difference may be experimental error due primarily to different material properties of the test specimens.

A similar comparison may be made for the lateral force curves (see Figure 4.2). As there is no lateral force during the “stationary load” for the “slow centre” and “fast centre” experiments, this entire plot presents the lateral “moving capacity” for each test. We can compare the “fast centre” and “slow centre” curves at any location along their length to determine the increase in structural capacity in the lateral direction due to strain-rate effects. Choosing the “End” position as a convenient location shows that the “slow moving capacity” for this location is 35.4 kN and the “fast moving capacity” is 37.9 kN; an increase of 7%. Further examination shows this to be a constant increase over the length of both curves. Again, it is possible that this increase is due, at least in part, to slightly different material properties between the plate specimens.

4.1.3 Further discussion

Regarding Table 4.6, the End “Moving Capacity” values for both of the “slow” tests should be equal. Instead they are 147.1 kN for the “End” case and 150.7 kN for the “Centre” case (a difference of 2.5%). To explain this discrepancy, we first look at the minimum moving load over the length of the plate for case.

As will be seen in all following plate experiments, the minimum “moving load” capacity was observed to occur over the central portion of the plate. This is the portion of the plate not subject to “end effects”; or equivalently, is the section of the plate that may be treated as an “infinitely long plate”. Further, the “moving load capacity” for this “infinite plate” portion is essentially constant (along the longitudinal centreline) when compared with the

magnitude of the initial “stationary capacity” and the “End” region “moving load capacity”. This allows direct comparison between the minimum moving loads for each case. The “Centre” case’s minimum moving load is 127.6 kN; the “End” case’s is 124.7 kN. As with the “End” location, the minimum “moving load” capacity of the “Centre” case is 2.3% higher than the end case. This implies that the difference between the two experiments is relatively constant. There are two potential reasons for this offset: experimental error in the form of lateral travel speed (i.e. rate-effects) and slight differences in material properties. The former is unlikely as the “Centre” case was travelling laterally only 0.4 mm/s faster than the “End” case and it is unlikely that a 0.4mm/s difference is large enough by itself to cause this discrepancy. The latter is always a possibility; and can affect the former as well, but the difference can mainly be considered to be within the resolution of the experiment. Additionally, experimental error may play a role as lateral displacement was measured with a string-pot. These devices are subject to several shortcomings. Specifically, any misalignment between the string and the carriage rails induces an error that increases with increasing string length. As the lateral displacement for the “Centre” experiment was 550 mm, and 1100 mm for the “End” experiment, any error in these readings due to string misalignment would be double for the “End” experiment. Further, given that the slope of the curve in the far location of both experiments is rapidly increasing, any error in this region is magnified when extracting a corresponding force value.

Also, regarding Figure 4.2, the lateral “moving capacity” at the “End” location for both “slow” experiments should be equal. As with the normal stationary capacity, these too are offset by 2.2%; and likely for the same reasons.

Some decaying vibration is evident in the lateral force results for the “fast centre” experiment shown in Figure 4.2. This is due to a mismatch in the length of both arms of the “swing arm” (shown in Figure 4.3) resulting in a slight misalignment of the steel wheel indenter with the longitudinal axis of the plate. This misalignment was noticed partway through experiments and was subsequently corrected. It does not appear that this misalignment affected the “Total Horizontal Force” measured by the two load cells together – and tests were performed to verify this – however the ratio of load sharing between the two load cells was affected, and for the higher speed tests, some vibration was induced.

Finally, Figure 4.4 shows the “slow centre” case (blue line) and the “slow end” case plotted twice (red and green lines). The green line shows the “End” case at its proper starting location of -550 mm. The red line, shows the “End” case translated 550 mm forward. This arrangement of “End” case curves makes it easy to compare the lateral moving capacity of the start and finish of the “End” case with the start and finish of the “Centre” case. It is interesting to note that for this room-temperature $\frac{1}{4}$ ” plate, the lateral location of the starting position seems independent of the lateral moving capacity response; as the blue and red lines agree very well at their start, and the blue and green lines agree very well at their end.

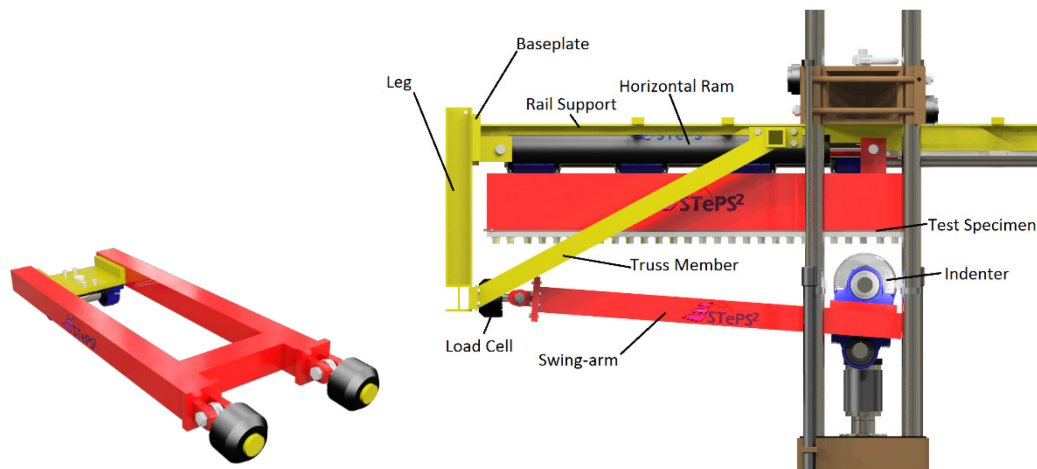


Figure 4.3: Moving load apparatus components: left – “Swing arm” (red) attached to load cells (black); right – swing arm shown with steel wheel indenter shown mounted to moving load apparatus.

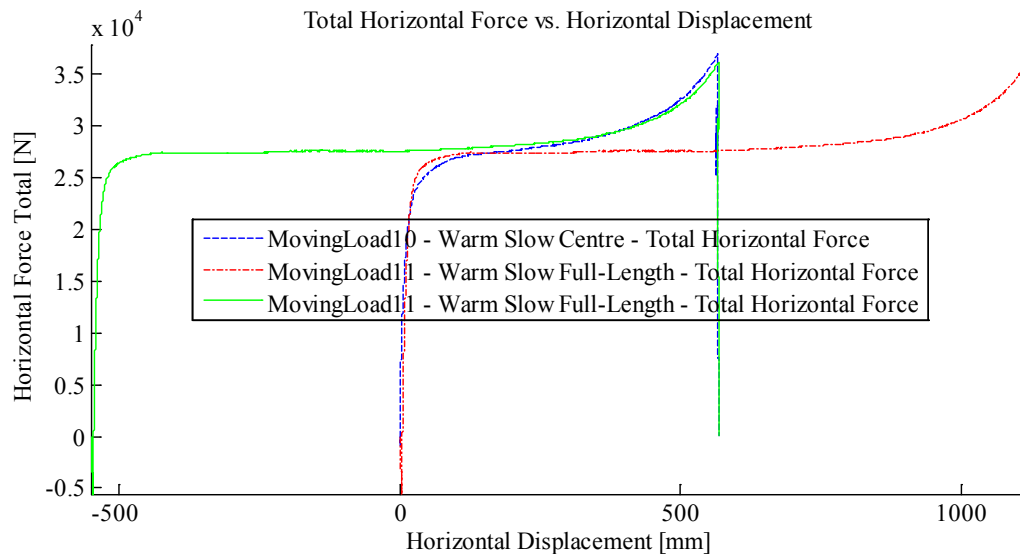


Figure 4.4: Lateral (horizontal) moving load capacities of “slow centre” and “slow end” $\frac{1}{4}$ ” plate cases – “slow end” case (green) shown again translated by +550 mm (red).

4.2 $\frac{1}{2}$ ” Plates with Steel Wheel Indenter at Room-temperature

Three experiments were performed on 12.7 mm ($\frac{1}{2}$ in.) plate test specimens at room-temperature using the steel wheel indenter. All plates were indented 3 cm (1.181 in.) in the

normal direction. The rest of the experimental parameters are the same as other displacement-controlled steel wheel indenter tests, and are given in Table 4.1 and discussed in the first paragraph of Chapter 4.1.

Figures 4.5 and 4.6 and

Table 5.14 present the experimental results relevant to this discussion. All data collected for these experiments is presented in Appendix C1.2.

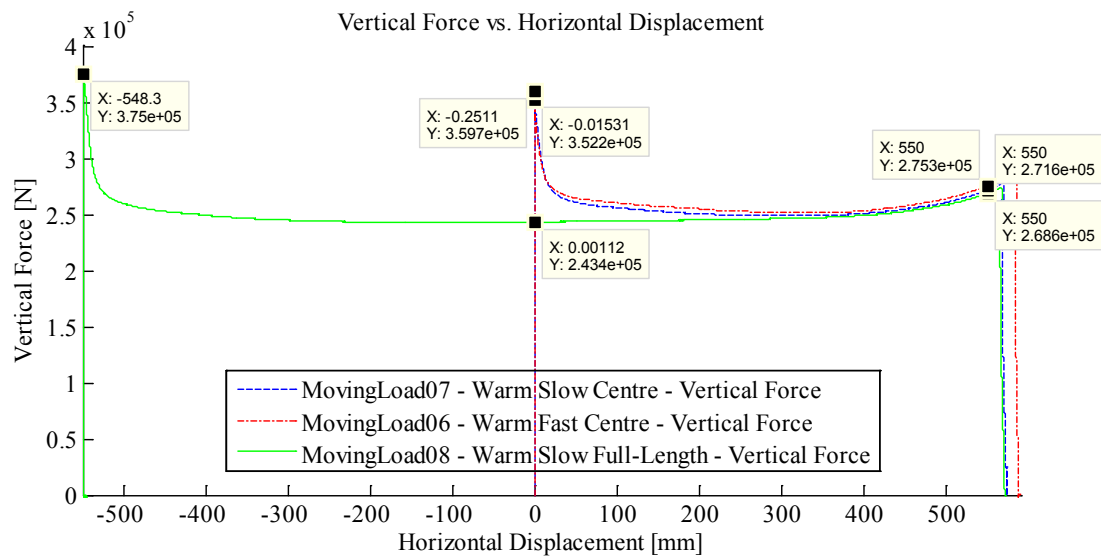


Figure 4.5: Normal (vertical) force versus lateral (horizontal) displacement for room-temperature 1/2" plates.

Table 4.7: ½” plate normal (vertical) force capacity results at room-temperature.

Experiment	Speed	End "Stationary Capacity" [kN]	End "Moving Capacity" [kN]	Centre "Stationary Capacity" [kN]	Centre "Moving Capacity" [kN]
Centre	Slow	N/A	271.6	352.2	N/A
Centre	Fast	N/A	275.3	359.7	N/A
End	Slow	375.0	268.6	N/A	243.4

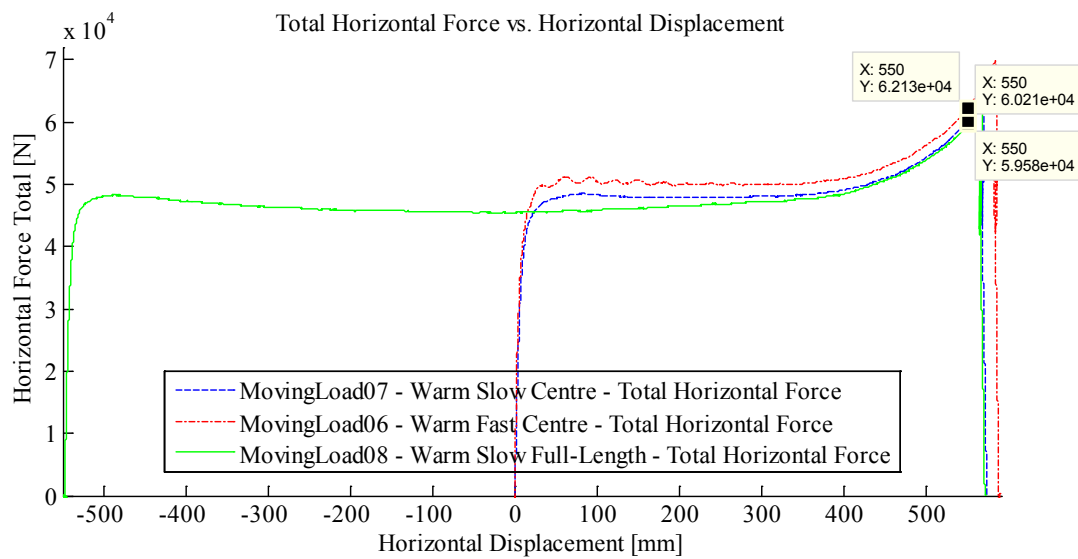


Figure 4.6: Lateral (horizontal) force versus lateral (horizontal) displacement for room-temperature ½” plates.

4.2.1 “Moving load capacity” vs. “stationary capacity”

Figure 4.5 shows the normal reaction force of the ½” plates versus lateral displacement of the steel wheel indenter.

Table 4.7 lists the key results from these experiments. At the “Centre” position, the “slow” “stationary capacity” is 352.2 kN for a stationary indentation of 3 cm. The “slow” “moving capacity” for a 3 cm indentation at this location is 243.4 kN. Therefore, the “moving capacity” at the “Centre” position is 69% of the “stationary capacity”. As with the ¼” plates, any difference in the tests due to differences in strain-rate would likely only serve to increase the “moving capacity”, and thus mitigate any capacity loss due to load movement.

Regarding the “End” position, the “stationary capacity” is 375.0 kN, and the “moving capacity” is 268.6 kN; therefore the “moving capacity” is 72% of the “stationary capacity”.

4.2.2 Strain-rate mitigation effects

Regarding Figure 4.5 and comparing the “slow” normal “stationary capacity”, 352.2 kN, and the “fast” normal “stationary capacity”, 359.7 kN, at the plate’s centre shows an increase in “stationary capacity” of 2.1%. This is likely due primarily to strain-rate effects, but may be experimental error. This increase is not as dramatic as for the ¼” plate case. If in fact this slight increase is due to strain-rate effects, this lower increase (versus the ¼” plate case) makes sense, because the normal velocity for the “fast” case was lower for the ½” plate than for the ¼” plate; and therefore the strain-rate effects would not be as significant. From Table 4.1 we can see that the normal (i.e. vertical) speed for the ¼” “fast” case (i.e. MovingLoad9) is 83.75 mm/s, and the corresponding value for the ½” plate test (i.e. MovingLoad6) is 71.69 mm/s. This is a difference of 12 mm/s (or 12%). This difference is present because the load on the MTS vertical ram was much higher for the ½” plate experiments than the ¼” plate experiments, and the hydraulic supply pump could not

produce the same flow-rate²⁰. Another factor is that membrane stretching played much less of a role for the ½” plate case than for the ¼” plate case. Membrane stresses tend to involve the whole plate, meaning that a much greater area is under strain, and therefore subject to strain-rate effects. With bending stresses being much more important in this thicker ½” plate, there was substantially less membrane stretching, and therefore less area subject to strain-rate effects.

From Figure 4.6 we can see that the strain-rate related mitigation of capacity loss for the lateral “moving capacity” at the “End” position (see similar discussion above for the ¼” plate) is 3.2%; as the “moving capacity” for the “fast” case is 62.13 kN, and 60.21 kN for the “slow” case. This value is lower than the 7% observed above for the comparable ¼” plates. From Table 4.1 we can see that the lateral (i.e. horizontal) travel speeds are nearly identical at 186.4 mm/s for the ¼” plate and 185.64 mm/s for the ½” plate. The difference between the two cases is likely still explained by a difference in strain-rate; although it is within the realm of experimental error. The ¼” plate normal indentation was 4 cm, and the ½” plate normal indentation was 3 cm. So as strain requires a 2nd order tensor of type (1, 1) to describe its state in three dimensions, so too does strain-rate. As the normal indentation was 1 cm greater for the ¼” plate case, the strain-rate was necessarily greater too; despite the fact that the indenter was travelling at the same lateral speed. In other words, if the normal indentation for both cases had been the same, the strain-rates would have been similar.

²⁰ There may also have been additional demand on the hydraulic supply pump from an external source.

4.2.3 Further discussion

Aside from the issues regarding flow-rate from the hydraulic supply pump discussed above in this section, similar issues arose for these $\frac{1}{2}$ " plate tests as for the $\frac{1}{4}$ " plate tests above. The discussion of these issues is the same and the reader is referred to Chapter 4.1.3.

Regarding Figure 4.7, as with the $\frac{1}{4}$ " plate case above, the lateral moving load response seems to be independent of the lateral starting location as the start and end of the “slow end” case matches the start and end of the “slow centre” case very well.

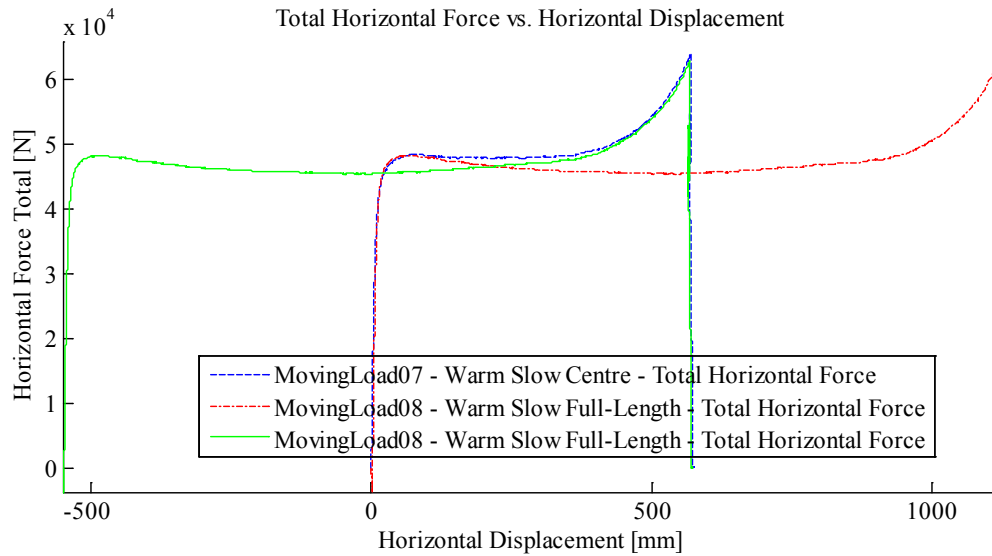


Figure 4.7: Lateral (horizontal) moving load capacities of “slow centre” and “slow end” $\frac{1}{2}$ " plate cases with red line translated by +550 mm.

4.3 Frames with Steel Wheel Indenter at Room-temperature

Three experiments were performed on “frame” test specimens at room-temperature using the steel wheel indenter. All frames were indented 2.5 cm (0.984 in.) in the normal

direction. The rest of the experimental parameters are the same as other displacement-controlled steel wheel indenter tests, and are given Table 4.1 and discussed in the first paragraph of Chapter 4.1.

A comment should be made at this point on the potential for error in these frame experiments versus the previous plate experiments. There are more sources of error/variability for the frame experiments due to one or more of the following possibilities: slight geometric and material inconsistencies in the welding used to attach the stiffener to the plating; the fact that load movement incites plastic buckling and post-buckling behaviours in the stiffener web; and the compliant end conditions for the stiffener web. As mentioned previously, a small gap (slightly less than 1 mm) is present between the stiffener end plates and the carriage ends, when the frame specimen is installed in the carriage. This gap is practically necessary, as it allows the frame test specimens to be installed in the carriage. The stiffener end plates are subsequently bolted to the carriage ends, but the gap is not completely closed. When the stiffener goes into compression during the experiment, the stiffener's end condition is not truly "fixed" until there is enough deformation of the stiffener such that the stiffener end plate contacts the carriage end. Even then, the stiffener end plate is capable of losing contact with the carriage end given the proper conditions.

Figures 4.8 and 4.9 and Table 4.8 present the experimental results relevant to this discussion. All data collected for these experiments is presented in Appendix C1.3.

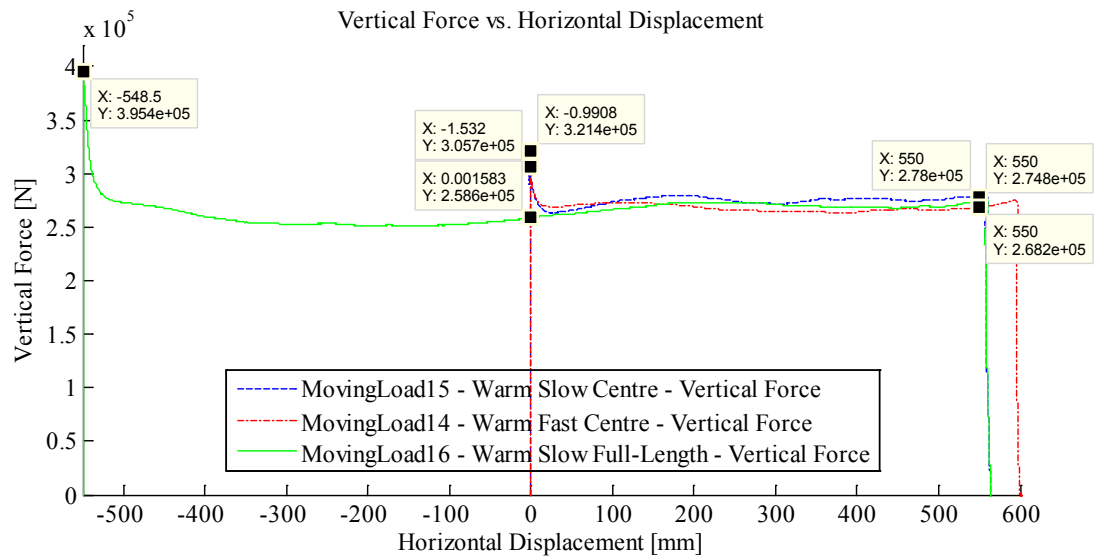


Figure 4.8: Normal (vertical) force versus lateral (horizontal) displacement for room-temperature frames.

Table 4.8: Frame normal (vertical) force capacity results at room-temperature.

Experiment	Speed	End "Stationary Capacity" [kN]	End "Moving Capacity" [kN]	Centre "Stationary Capacity" [kN]	Centre "Moving Capacity" [kN]
Centre	Slow	N/A	278.0	305.7	N/A
Centre	Fast	N/A	268.2	321.4	N/A
End	Slow	395.4	274.8	N/A	258.6

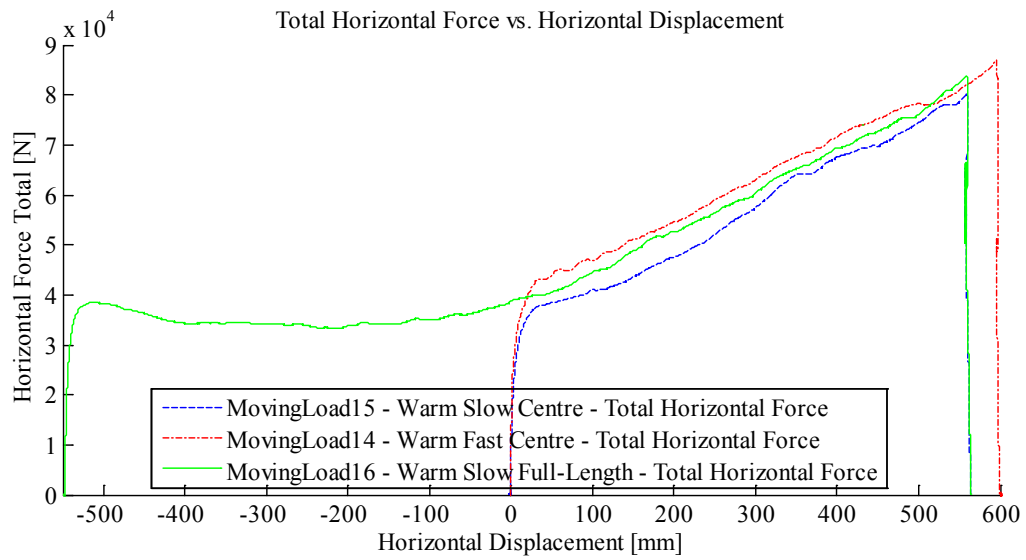


Figure 4.9: Lateral (horizontal) force versus lateral (horizontal) displacement for room-temperature frames.

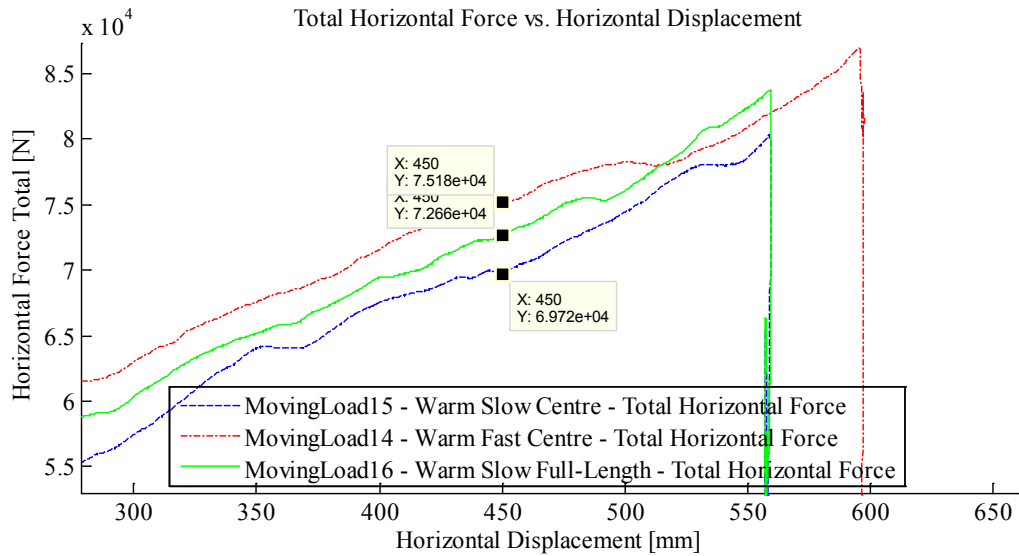


Figure 4.10: Magnification of Figure 4.9.

4.3.1 “Moving load capacity” vs. “stationary capacity”

Figure 4.8 shows the normal reaction force of the frames versus lateral displacement of the steel wheel indenter. Table 4.8 lists the key results from these experiments. At the “Centre” position, the “slow” “stationary capacity” is 305.7 kN for a stationary indentation of 2.5 cm. The “slow” “moving capacity” for a 2.5 cm indentation at this location is 258.6 kN. Therefore, the “moving capacity” at the “Centre” position is 85% of the “stationary capacity”. As with the other cases explored above, any difference in the tests due to differences in strain-rate likely would only serve to increase the “moving capacity”, and thus mitigate any capacity loss due to load movement.

Regarding the “End” position, the “stationary capacity” is 395.4 kN, and the “moving capacity” is 274.8 kN; therefore the “moving capacity” is 69% of the “stationary capacity”.

4.3.2 Strain-rate mitigation effects

Regarding Figure 4.8 and comparing the “slow” normal “stationary capacity”, 305.7 kN, and the “fast” normal “stationary capacity”, 321.4 kN, at the plate’s centre shows an increase in “stationary capacity” of 5.1% due most likely to strain-rate effects. Similar to the 1/2” plate case above, the normal indenter speed was approximately 12.72 mm/s less than the 1/4” case, and the lateral indenter speed was identical at 185.06 mm/s, however the increase in structural capacity due to strain-rate effects is of a similar magnitude with the 1/4” case. As the plating of the frame was 1/4” plate, membrane stresses most likely played a similar role. Further, the frame has a much more complex geometry than a simple plate and there is more steel in the vicinity of the load that is also subject to strain-rate effects. It is likely that had the normal ram velocity been equal to the 1/4” plate case, the increase in

normal “stationary capacity” due to strain-rate effects would have been larger, due to the extra steel in the vicinity of the indenter.

When evaluating the strain-rate effect on the lateral “moving capacity” of the test specimens, the “End” position has been chosen thus far, for the point of interrogation. This has been a somewhat arbitrary choice as the relative difference between the “slow” and “fast” lateral force curves is fairly constant throughout the various test specimen types. From Figure 4.9 we can see that at the “End” position (i.e. 550 mm), an unusual decrease is evident for the “fast” curve. The other curves exhibit local anomalies similar to this at other locations, but in general the curves tend to be scaled versions of each other (which agrees with the above findings). For this reason, the “end position” is not used to evaluate the strain-rate effects on the lateral “moving capacity” for these experiments. Instead, 450 mm is used as the three curves are free of these “anomalies” at this point.

From Figure 4.10, the lateral “moving capacity” for the “fast” case is 75.18 kN, and 96.72 kN for the “slow centre” case; which is a 7.8% increase. As with the normal direction strain-rate related effects, this value is comparable with the increase observed in the $\frac{1}{4}$ ” plate case above.

4.3.3 Further discussion

These three experiments exhibit both expected and unexpected behaviours. As expected, the “fast centre” normal “stationary capacity” is higher than the “slow centre” normal “stationary capacity”; further, the “slow end” normal “stationary capacity” is larger than both (see Figure 4.8). This behaviour is consistent with the other experiments. Additionally as expected, the “slow end” and “slow centre” normal force curves agree fairly

well with each other from about 30 mm to 550 mm horizontal displacement (which is the “moving load” portion where the indenter is in similar locations for both experiments).

It is unexpected that the normal “moving load capacity” for the “fast centre” is lower than the “slow centre” curve for the locations between 30 mm and 550 mm. This is anomalous because strain-rate effects would be expected to increase this capacity for the “fast centre” case. Indeed, Figure 4.9 shows that the lateral force for the “fast centre” case is higher than both the “slow centre” and “slow end” cases; as expected. It is believed that subsequent to the commencement of lateral motion for MovingLoad14 (i.e. the “fast centre” case), something anomalous occurred during the experiment. As no experimental repetitions were performed, it is difficult to say for certain that this was experimental error.

It was additionally unexpected that the lateral “moving capacity” (see Figure 4.9) was consistently higher for the “slow end” case than for the “slow centre” case. At the “End” location, the “slow centre” “moving capacity” is 69.72 kN, and the “slow end” “moving capacity” is 72.66 kN; a difference of 4.2%. This is a much greater offset than observed for the ¼” and ½” plate experiments. Like the other experiments, it was expected that the portions of curves between approximately 100 mm and 550 mm would be very similar. Please note, that it is not expected that the curves be identical between 0 mm and somewhere up to 100 mm because this section would include the transient development of plastic buckling in the stiffener’s web for the “Centre” case, while it would already be well developed at 0 mm for the “End” case. As the normal and lateral indenter speeds were nearly identical for both experiments, the difference is not attributable to strain-rate effects as they relate to indenter speed. Further, because the frame specimens were constructed

(requiring a jig), and not simply cut-out using a computer controlled water-jet, it is possible that the two framed specimens (ML14 and ML15) were slightly different in their manufacturing and/or material properties. Indeed, the frame specimen used in the MovingLoad14 experiment was the only one that did not have the “bevels” in the stiffener end plates. It was subsequent to testing this frame specimen that it was decided to add “bevels” to the stiffener end plates to aid in installing and removing the frame specimens. It is extremely likely that the lack of these bevels increased the stiffness of the boundary conditions of the stiffener portion of the frame, leading to the anomalous results. This conjecture is supported by finding from the numerical model (Chapter 5.4.1) where it is discovered that stiffer boundary conditions cause a greater decrease in a structures capacity to sustain moving loads.

As with the above $\frac{1}{4}$ ” and $\frac{1}{2}$ ” plate cases, Figure 4.11 suggests that lateral moving load capacity is independent of starting location. While the blue and green curves do not match up as well as the other specimen types, this is not surprising for these frame tests as other unexpected behaviours occurred as described above.

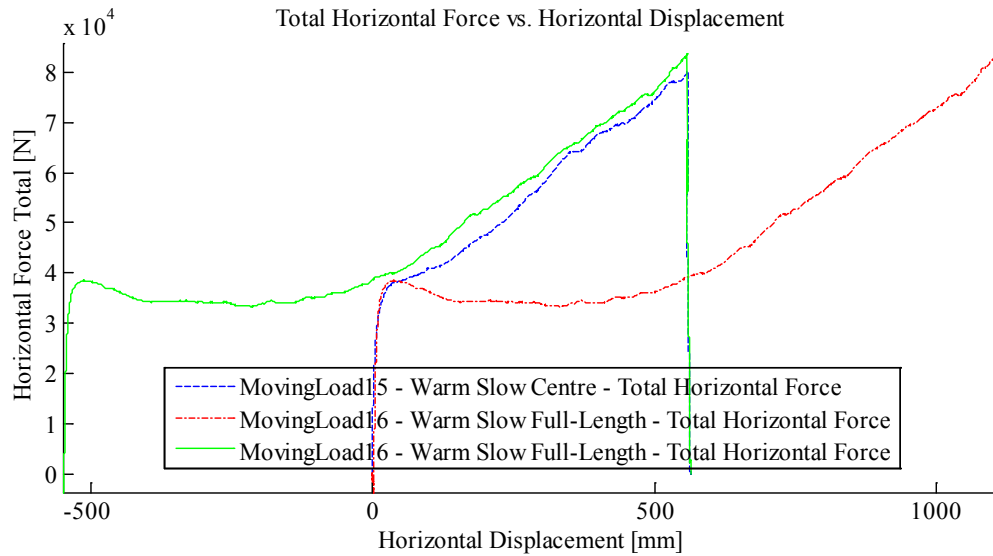


Figure 4.11: Lateral (horizontal) moving load capacities of “slow centre” and “slow end” frame cases with red line translated by +550 mm.

4.4 ¼” Plates with Steel Wheel Indenter at -10°C: 2 cm Indentation

Three experiments were performed on ¼” plate test specimens at -10°C using the steel wheel indenter at an indentation of 2.0 cm (0.787 in.) in the normal direction. The reason these tests were performed was to probe the lower bound of when “moving load effects” begin. The rest of the experimental parameters are the same as other displacement-controlled steel wheel indenter tests, and are given Table 4.2 and discussed in the first paragraph of Chapter 4.1.

Figures 4.12 and 4.13 and Table 4.9 present the experimental results relevant to this discussion. All data collected for these experiments is presented in Appendix C2.1.

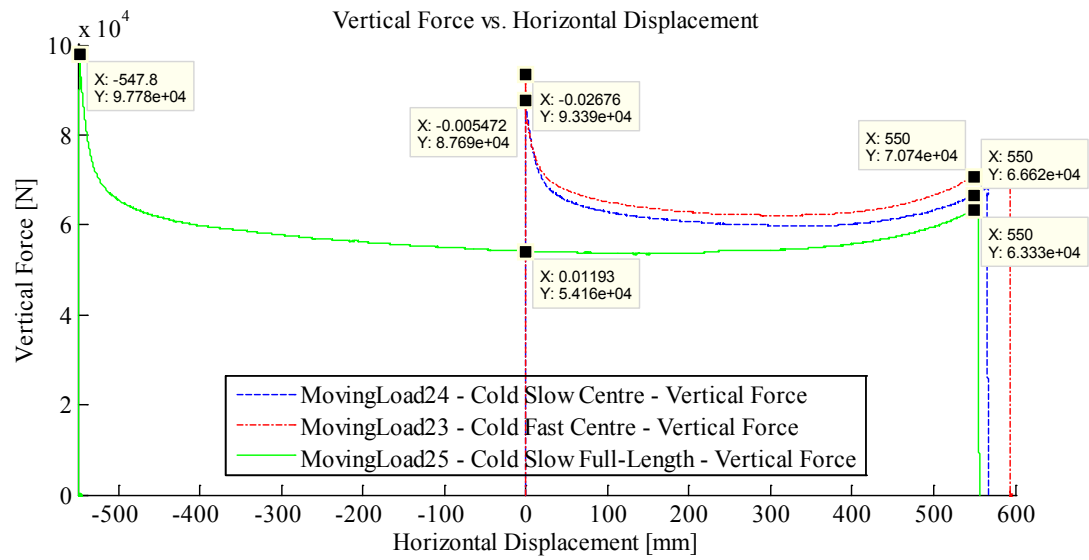


Figure 4.12: Normal (vertical) force versus lateral (horizontal) displacement for -10°C $\frac{1}{4}$ " plates: 2 cm indentation.

Table 4.9: $\frac{1}{4}$ " plate normal (vertical) force capacity results at -10°C : 2 cm indentation.

Experiment	Speed	End "Stationary Capacity" [kN]	End "Moving Capacity" [kN]	Centre "Stationary Capacity" [kN]	Centre "Moving Capacity" [kN]
Centre	Slow	N/A	66.62	87.69	N/A
Centre	Fast	N/A	70.74	93.39	N/A
End	Slow	97.78	63.33	N/A	54.16

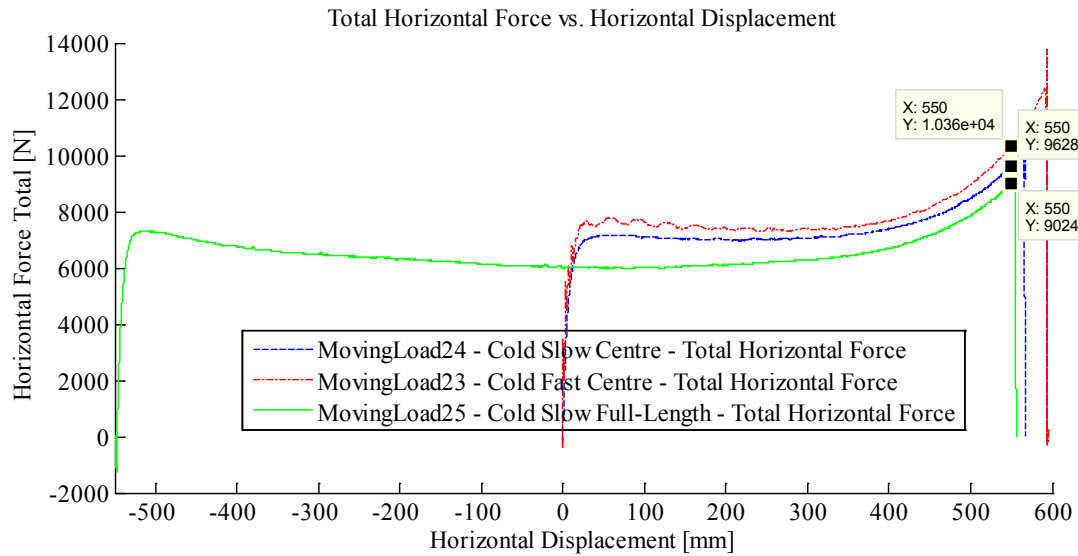


Figure 4.13: Lateral (horizontal) force versus lateral (horizontal) displacement for -10°C $\frac{1}{4}$ " plates: 2 cm indentation.

4.4.1 "Moving load capacity" vs. "stationary capacity"

Figure 4.12 shows the normal reaction force of the frames versus lateral displacement of the steel wheel indenter. Table 4.9 lists the key results from these experiments. At the "Centre" position, the "slow" "stationary capacity" is 87.69 kN for a stationary indentation of 2.0 cm. The "slow" "moving capacity" for a 2.0 cm indentation at this location is 54.16 kN. Therefore, the "moving capacity" at the "Centre" position is 62% of the "stationary capacity". As with the other cases explored above, any difference in the tests due to differences in strain-rate would only serve to increase the "moving capacity", and thus mitigate any capacity loss due to load movement.

Regarding the "End" position, the "stationary capacity" is 97.78 kN, and the "moving capacity" is 63.33 kN; therefore the "moving capacity" is 65% of the "stationary capacity".

4.4.2 Strain-rate mitigation effects

Regarding Figure 4.12 and comparing the “slow” normal “stationary capacity”, 87.69 kN, and the “fast” normal “stationary capacity”, 93.39 kN, at the plate’s centre shows an increase in “stationary capacity” of 6.5% due most likely to strain-rate effects. As the overall load for these 2 cm indentations into $\frac{1}{4}$ ” plates is much lower than the other experiments, the normal indenter speed (i.e. vertical ram speed) was slightly higher than for the other tests, at 91.81 mm/s. This greater speed is likely the greatest contributor to these experiments having the highest “rate-effects gain” for the centre position.

From Figure 4.13 we can see that at the “End” position, the lateral “moving capacity” of the “slow centre” curve is 9.628 kN, and the “fast centre” curve is 10.36 kN. This is a 7.6% gain due to strain-rate effects for the lateral “moving load capacity”.

4.4.3 Further discussion

It is evident from these experiments that “moving load effects” are just as significant at in indentation of 5% of the frame spacing (i.e. 2 cm) as they are for 10% (see next section) for $\frac{1}{4}$ ” plates.

Unexpectedly, the “End” case showed a lower “moving load capacity” throughout the entire test for both normal and lateral loads. As detailed above, it was expected that the moving load capacities for both normal and lateral force would be similar between 100 mm and 550 mm displacement.

Like the other experiments above, Figure 4.14 shows that the lateral moving capacity is independent of the starting location, at the starting location. Unlike the other experiments

above (except the room-temperature frame experiments), the behaviour of the “slow centre” and “slow end” curves do not match near the “End” position. As will be seen below, this behaviour is not consistent with the other -10°C plate experiments. It is unclear at this point what caused this behaviour.

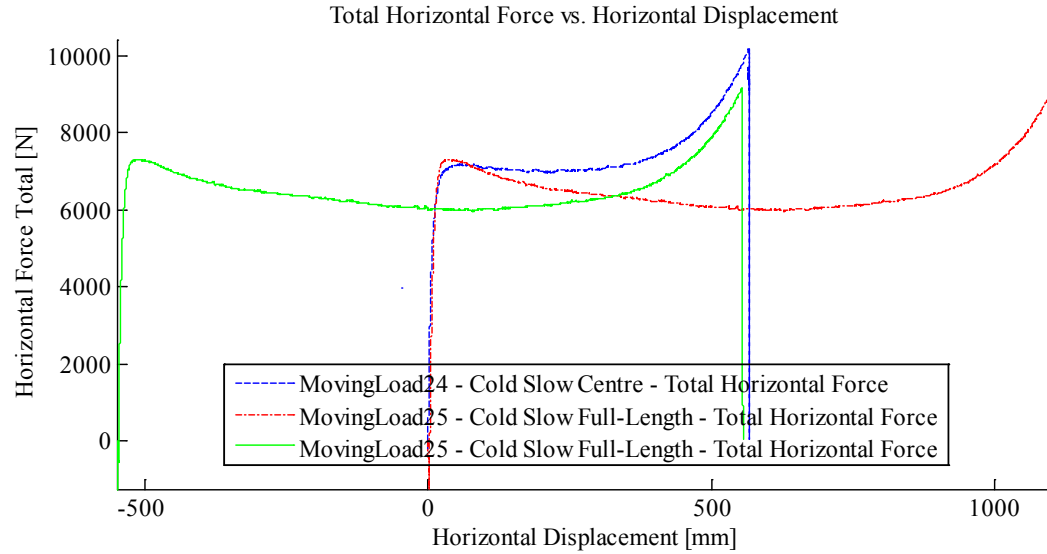


Figure 4.14: Lateral (horizontal) moving load capacities of “slow centre” and “slow end” $\frac{1}{4}$ ” plate cases: 2 cm indentation with red line translated by +550 mm.

4.5 $\frac{1}{4}$ ” Plates with Steel Wheel Indenter at -10°C: 4 cm Indentation

Three more experiments were performed on $\frac{1}{4}$ ” plate test specimens at -10°C using the steel wheel indenter; this time at an indentation equal to that of the $\frac{1}{4}$ ” plate room-temperature experiments: 4.0 cm (1.575 in.). The rest of the experimental parameters are the same as other displacement-controlled steel wheel indenter tests, and are given in Table 4.2 and discussed in the first paragraph of Chapter 4.1.

Figures 4.15 and 4.16 and Table 4.10 present the experimental results relevant to this discussion. All data collected for these experiments is presented in Appendix C2.2.

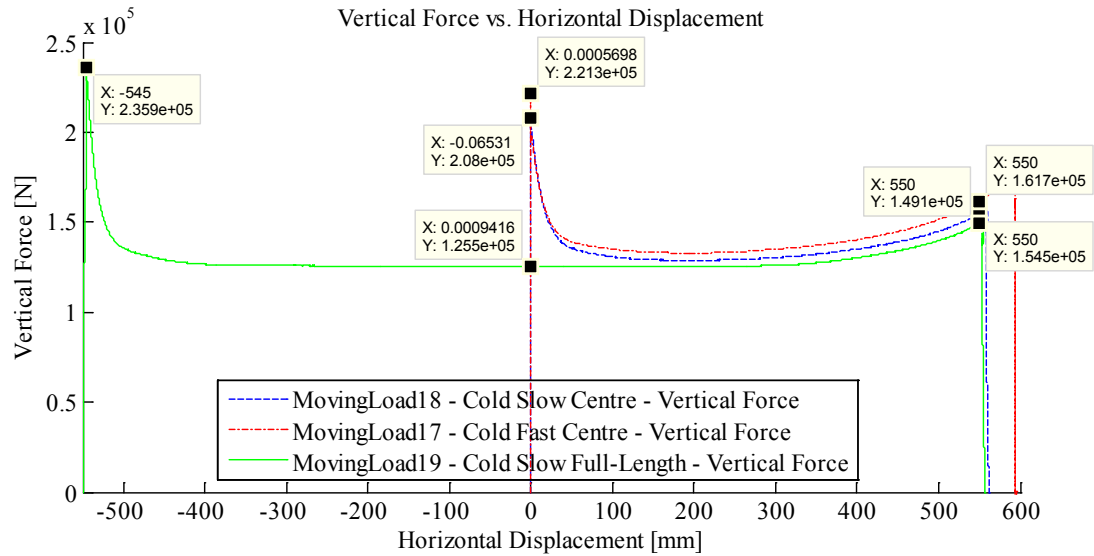


Figure 4.15: Normal (vertical) force versus lateral (horizontal) displacement for -10°C $\frac{1}{4}$ " plates: 4 cm indentation.

Table 4.10: $\frac{1}{4}$ " plate normal (vertical) force capacity results at -10°C : 4 cm indentation.

Experiment	Speed	End "Stationary Capacity" [kN]	End "Moving Capacity" [kN]	Centre "Stationary Capacity" [kN]	Centre "Moving Capacity" [kN]
Centre	Slow	N/A	149.1	208.0	N/A
Centre	Fast	N/A	161.7	221.3	N/A
End	Slow	235.9	154.5	N/A	125.5

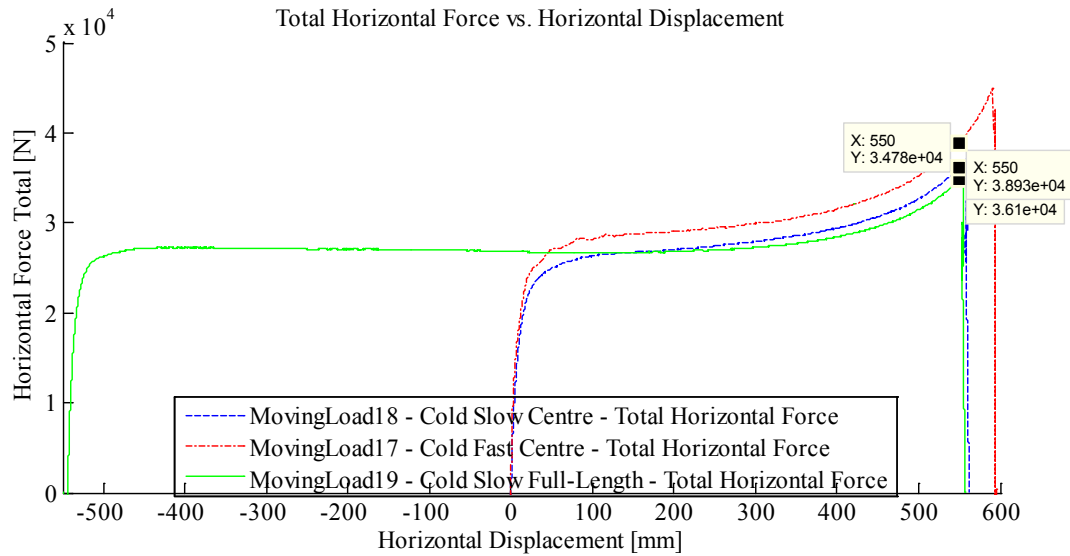


Figure 4.16: Lateral (horizontal) force versus lateral (horizontal) displacement for -10°C $\frac{1}{4}$ " plates: 4 cm indentation.

4.5.1 “Moving load capacity” vs. “stationary capacity”

Figure 4.15 shows the normal reaction force of the frames versus lateral displacement of the steel wheel indenter. Table 4.10 lists the key results from these experiments. At the “Centre” position, the “slow” “stationary capacity” is 208.0 kN for a stationary indentation of 4.0 cm. The “slow” “moving capacity” for a 4.0 cm indentation at this location is 125.5 kN. Therefore, the “moving capacity” at the “Centre” position is 60% of the “stationary capacity”. As with the other cases explored above, any difference in the tests due to differences in strain-rate would only serve to increase the “moving capacity”, and thus mitigate any capacity loss due to load movement.

Regarding the “End” position, the “stationary capacity” is 235.9 kN, and the “moving capacity” is 154.5 kN; therefore the “moving capacity” is 65% of the “stationary capacity”.

4.5.2 Strain-rate mitigation effects

Regarding Figure 4.15 and comparing the “slow” normal “stationary capacity”, 208.0 kN, and the “fast” normal “stationary capacity”, 221.3 kN, at the plate’s centre shows an increase in “stationary capacity” of 6.4% due primarily to strain-rate effects. The rate-effect gain from the similar room-temperature tests presented above is 5.9%. As the normal and lateral indenter velocities are nearly identical for both the room-temperature and cold experiments, the only significant difference between the two is a temperature difference of approximately 30°C. It is possible that the slight increase in normal rate-effects gain is due to the stiffening effect lower temperatures have on steel material properties; however the difference is practically negligible.

From Figure 4.16 we can see that at the “End” position, the lateral “moving capacity” of the “slow centre” curve is 34.78 kN, and the “fast centre” curve is 38.93 kN. This is a 12% gain due to strain-rate effects for the lateral “moving load capacity”. As with the normal direction, this represents a small increase over the similar room-temperature experiments.

4.5.3 Further discussion

These experiments generally behaved as expected, except that – similar to above – the “slow end” case produced “moving load” results that were slightly less than the “slow centre” case.

Regarding Figure 4.17 below, as with the above plate experiments (excepting the 2 cm $\frac{1}{4}$ ” experiments) this plot supports the theory that the lateral moving load is independent of the starting location.

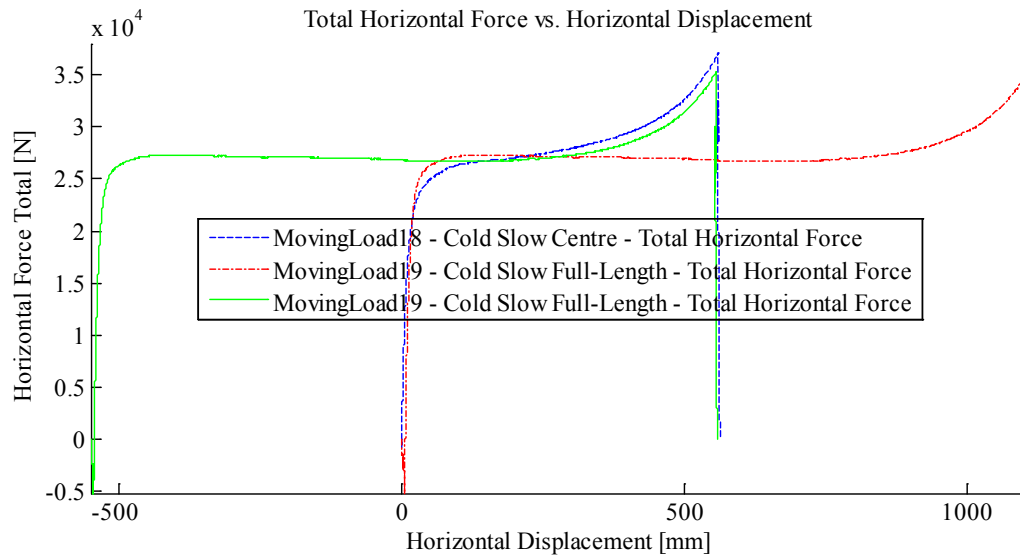


Figure 4.17: Lateral (horizontal) moving load capacities of “slow centre” and “slow end” $\frac{1}{4}$ ” plate cases: 4 cm indentation with red line translated by +550 mm.

4.6 $\frac{1}{2}$ ” Plates with Steel Wheel Indenter at -10°C

Three experiments were performed on 12.7 mm ($\frac{1}{2}$ in.) plate test specimens at -10°C using the steel wheel indenter. All plates were indented 3 cm (1.181 in.) in the normal direction. The rest of the experimental parameters are the same as other displacement-controlled steel wheel indenter tests, and are given Table 4.2 and discussed in the first paragraph of Chapter 4.1.

Figures 4.18 and 4.19 and Table 4.11 present the experimental results relevant to this discussion. All data collected for these experiments are presented in Appendix C2.3.

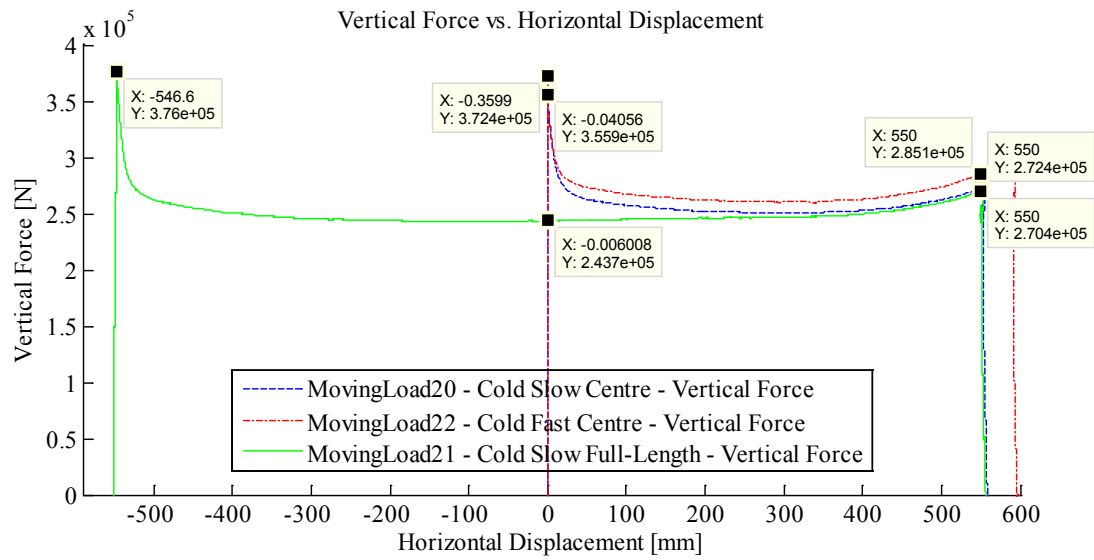


Figure 4.18: Normal (vertical) force versus lateral (horizontal) displacement for -10°C $\frac{1}{2}$ '' plates.

Table 4.11: $\frac{1}{2}$ '' plate normal (vertical) force capacity results at -10°C .

Experiment	Speed	End "Stationary Capacity" [kN]	End "Moving Capacity" [kN]	Centre "Stationary Capacity" [kN]	Centre "Moving Capacity" [kN]
Centre	Slow	N/A	149.1	208.0	N/A
Centre	Fast	N/A	161.7	221.3	N/A
End	Slow	235.9	154.5	N/A	125.5

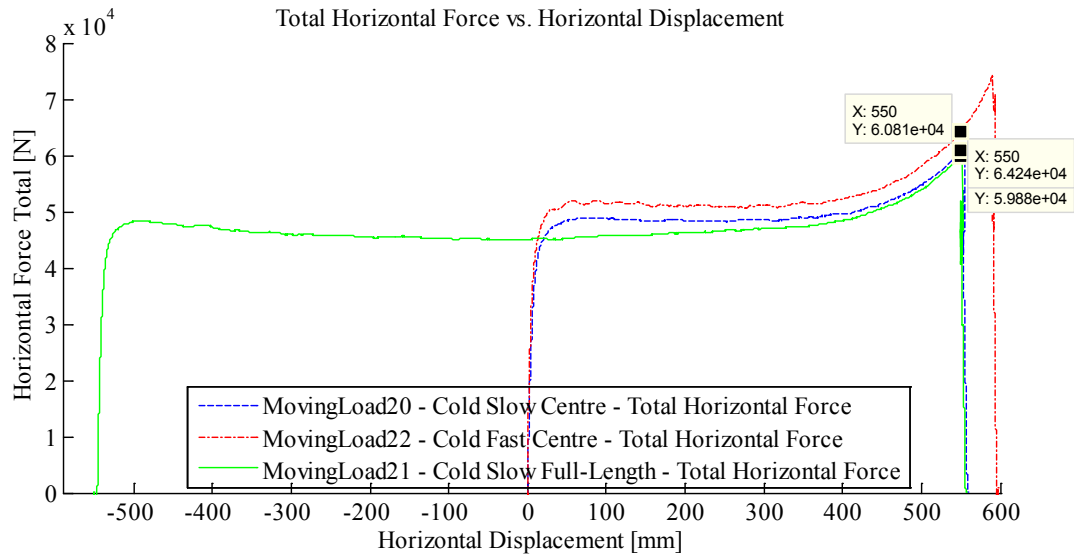


Figure 4.19: Lateral (horizontal) force versus lateral (horizontal) displacement for -10°C $\frac{1}{2}$ " plates.

4.6.1 "Moving load capacity" vs. "stationary capacity"

Figure 4.18 shows the normal reaction force of the frames versus lateral displacement of the steel wheel indenter. Table 4.11 lists the key results from these experiments. At the "Centre" position, the "slow" "stationary capacity" is 355.9 kN for a stationary indentation of 3.0 cm. The "slow" "moving capacity" for a 3.0 cm indentation at this location is 243.7 kN. Therefore, the "moving capacity" at the "Centre" position is 68% of the "stationary capacity". As with the other cases explored above, any difference in the tests due to differences in strain-rate would only serve to increase the "moving capacity", and thus mitigate any capacity loss due to load movement.

At the "End" position, the normal "stationary capacity" is 376.0 kN, and the "moving capacity" is 270.4 kN; therefore the normal "moving capacity" is 72% of the "stationary capacity".

4.6.2 Strain-rate mitigation effects

Regarding Figure 4.18 and comparing the “slow” normal “stationary capacity”, 355.9 kN, and the “fast” normal “stationary capacity”, 372.4 kN, at the plate’s centre shows an increase in “stationary capacity” of 4.6% due primarily to strain-rate effects.

From Figure 4.19 we can see that at the “End” position, the lateral “moving capacity” of the “slow centre” curve is 60.81 kN, and the “fast centre” curve is 64.24 kN. This is a 5.6% gain due to strain-rate effects for the lateral “moving load capacity”.

4.6.3 Further discussion

These experiments generally behaved as expected, except that – similar to above – the “slow end” case produced “moving load” results that were slightly less than the “slow centre” case.

Regarding Figure 4.20 below, as with the above plate experiments (excepting the 2 cm $\frac{1}{4}$ ” experiments) this plot supports the theory that the lateral moving load is independent of the starting location.

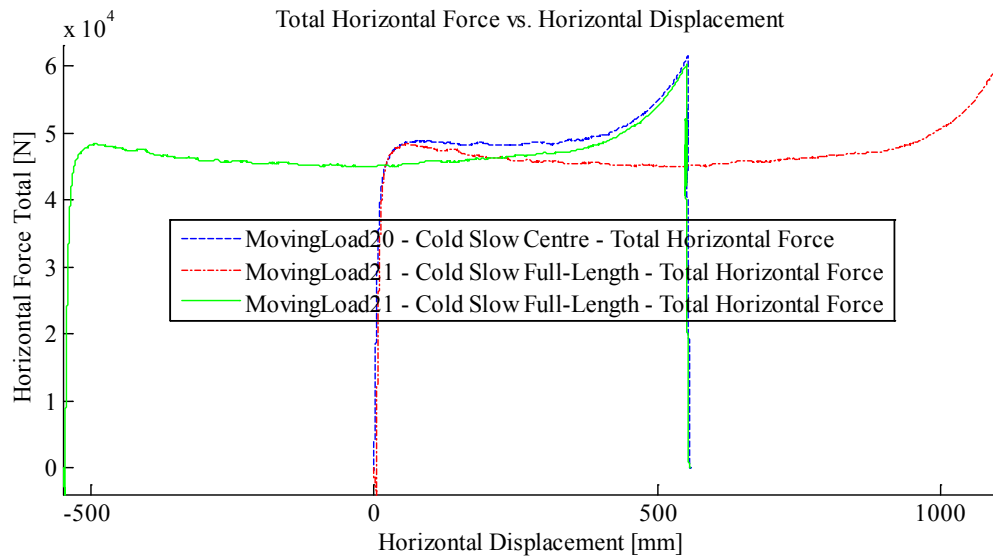


Figure 4.20: Lateral (horizontal) moving load capacities of “slow centre” and “slow end” $\frac{1}{2}$ ” plate cases with red line translated by +550 mm.

4.7 Frames with Steel Wheel Indenter at -10°C

Three experiments were performed on “frame” test specimens at -10°C using the steel wheel indenter. All frames were indented 2.5 cm (0.984 in.) in the normal direction. The rest of the experimental parameters are the same as other displacement-controlled steel wheel indenter tests, and are given Table 4.2 and discussed in the first paragraph of Chapter 4.1.

Figures 4.21 and 4.22 and Table 4.12 present the experimental results relevant to this discussion. All data collected for these experiments is presented in Appendix C2.4.

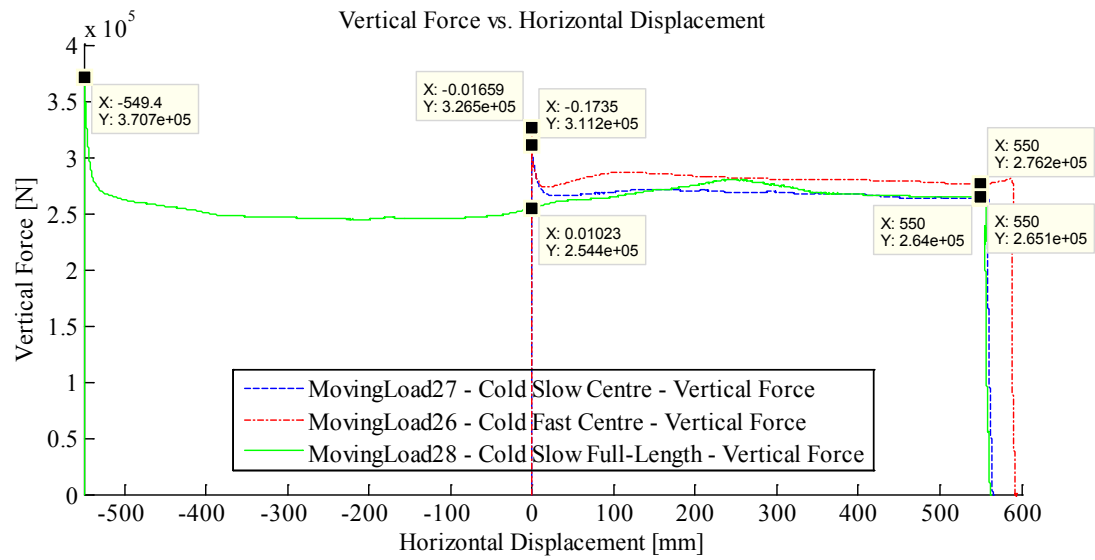


Figure 4.21: Normal (vertical) force versus lateral (horizontal) displacement for -10°C frames.

Table 4.12: Frame normal (vertical) force capacity results at -10°C.

Experiment	Speed	End "Stationary Capacity" [kN]	End "Moving Capacity" [kN]	Centre "Stationary Capacity" [kN]	Centre "Moving Capacity" [kN]
Centre	Slow	N/A	264.0	311.2	N/A
Centre	Fast	N/A	276.2	326.5	N/A
End	Slow	370.7	265.1	N/A	254.4

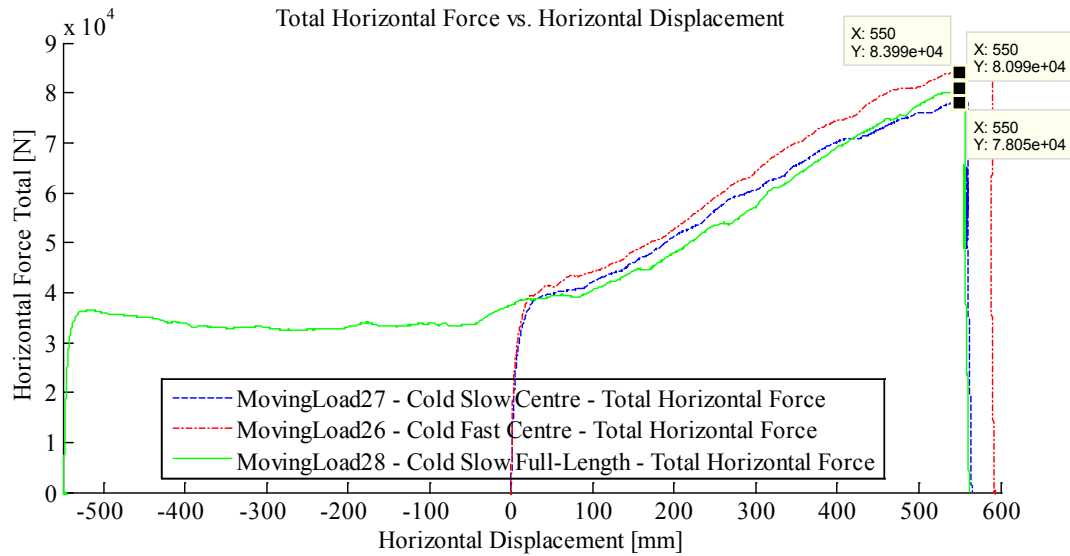


Figure 4.22: Lateral (horizontal) force versus lateral (horizontal) displacement for -10°C frames.

4.7.1 “Moving Load Capacity” vs. “Stationary Capacity”

Figure 4.21 shows the normal reaction force of the frames versus lateral displacement of the steel wheel indenter. Table 4.12 lists the key results from these experiments. At the “Centre” position, the “slow” “stationary capacity” is 311.2 kN for a stationary indentation of 2.5 cm. The “slow” “moving capacity” for a 2.5 cm indentation at this location is 254.4 kN. Therefore, the normal “moving capacity” at the “Centre” position is 82% of the “stationary capacity”. As with the other cases explored above, any difference in the tests due to differences in strain-rate would only serve to increase the “moving capacity”, and thus mitigate any capacity loss due to load movement.

Regarding the “End” position, the normal “stationary capacity” is 370.7 kN, and the “moving capacity” is 265.1 kN; therefore the “moving capacity” is 72% of the “stationary capacity”.

4.7.2 Strain-rate mitigation effects

Regarding Figure 4.21 and comparing the “slow” normal “stationary capacity”, 311.2 kN, and the “fast” normal “stationary capacity”, 326.5 kN, at the plate’s centre shows an increase in “stationary capacity” of 4.9% due primarily to strain-rate effects. Similar to the $\frac{1}{2}$ ” plate case above, the normal indenter speed was approximately 12.72 mm/s less than the $\frac{1}{4}$ ” case, and the lateral indenter speed was nearly identical at 185.06 mm/s, however the increase in structural capacity due to strain-rate effects is of a similar magnitude with the $\frac{1}{4}$ ” case. As the plating of the frame was $\frac{1}{4}$ ” plate, membrane stresses played a similar role. Further, the frame has a much more complex geometry than a simple plate and there is more steel in the vicinity of the load subject to strain-rate effects. It is likely that, had the normal ram velocity been equal to the $\frac{1}{4}$ ” plate case, the increase in normal “stationary capacity” due to strain-rate effects would have been larger, due to the extra steel in the vicinity of the indenter.

From Figure 4.22 we can see that the strain-rate related mitigation of capacity loss for the lateral “moving capacity” at the “End” position (see similar discussion above for the other cases above) is 7.6%; as the “moving capacity” for the “fast” case is 83.99 kN, and 78.05 kN for the “slow centre” case. As with the normal direction strain-rate related effects, this value is comparable with the increase observed in the $\frac{1}{4}$ ” plate case above. It should be noted that the relative difference between the “End” “moving capacities” of the “slow centre” case, at 78.05 kN, and the “slow end” case, at 80.99 kN is higher at 3.8% than for the $\frac{1}{4}$ ” and $\frac{1}{2}$ ” plate experiments above. Observing both curves (i.e. MovingLoad27 and MovingLoad28) in Figure 4.22 shows that overall they agree fairly well from the centre of

the plate onwards, however they occasionally diverge by up to 9%, and cross each other twice. Not only is the frame more complex geometrically than a plate, it is subject to much more manufacturing in the form of welding. The discrepancies between these two curves are likely primarily a function slight manufacturing differences between the two samples.

4.7.3 Further discussion

These tests exhibited similar issues to those presented above, with the exception of a greater disagreement between the “End” position values of both “slow” lateral force vs. horizontal displacement curves.

Regarding Figure 4.23 below, as with the above frame experiments, this plot does not support the theory that the lateral moving load is independent of the starting location, as the lateral moving capacity at the “End” starting location is not similar to that at the “Centre” starting location.

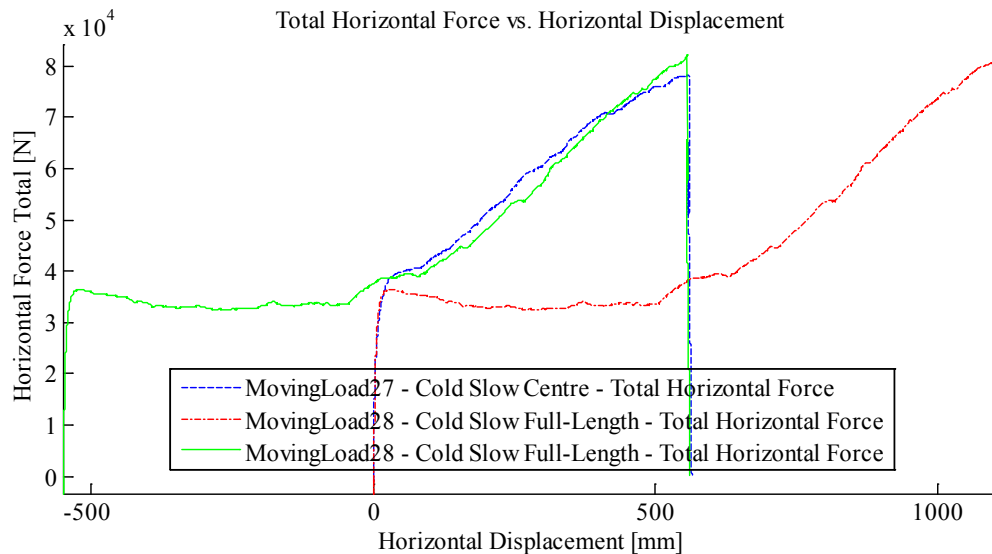


Figure 4.23: Lateral (horizontal) moving load capacities of “slow centre” and “slow end” frame cases with red line translated by +550 mm.

4.8 Force controlled Experiments at -10°C

To investigate whether “moving load effects” are present for force- (or load-) controlled scenarios, three experiments were conducted; one on each of the three test specimen types: ¼” plate, ½” plate, and frame. The steel wheel indenter was used for all three tests. Normal force on the test specimen’s plating was prescribed, and normal displacement was measured. As lateral force control was not possible with the moving load apparatus, lateral displacement control was utilised to apply lateral motion during the experiments.

The hypothesis for these three experiments is: If normal force drops upon commencement of lateral load displacement for normal displacement controlled experiments, then under normal force control, the normal displacement should increase.

The first experiment was conducted on a ¼” plate specimen. Based on the above normal displacement controlled experiments on ¼” plates, a load of 125 kN was selected for this test. A load rate of 10 kN/s was also used. The load path was like the other tests: stationary load, followed by lateral motion while holding the stationary load, followed by unloading. The lateral speed was equal to the “slow” experiments discussed above, and the indenter starting position was at the “End” (i.e. -550 mm). A summary of the experimental parameters is given in Table 4.3.

The second experiment was conducted on a ½” plate specimen. Based on the above normal displacement controlled experiments on ½” plates, a load of 250 kN was selected for this test. All other experimental parameters are identical to the force controlled ¼” plate experiment, and are given in Table 4.3.

The third experiment was conducted on a frame specimen. Based on the above normal displacement controlled experiments on frames, a load of 250 kN was selected for this test. All other experimental parameters are identical to the force controlled ¼” plate experiment above, and are given in Table 4.3.

4.8.1 Results

Plots of normal displacement versus horizontal displacement for all three experiments are given in Figures 4.24 through 4.26. Plots of lateral force versus horizontal displacement are given in Figures 4.27 through 4.29. All other experimental data is provided in Appendix C2.5.

Figure 4.24 shows the indenter’s normal (i.e. vertical ram) displacement versus indenter horizontal displacement for the ¼” plate force controlled experiment. During the stationary load portion of the experiment, a 125 kN normal load induced a 25.1 mm indentation in the ¼” plate. Immediately upon commencement of lateral indenter motion the normal displacement began to increase, until it reached its maximum, 39.5 mm (an increase of 57% the original value), near the centre of the plate (as expected).

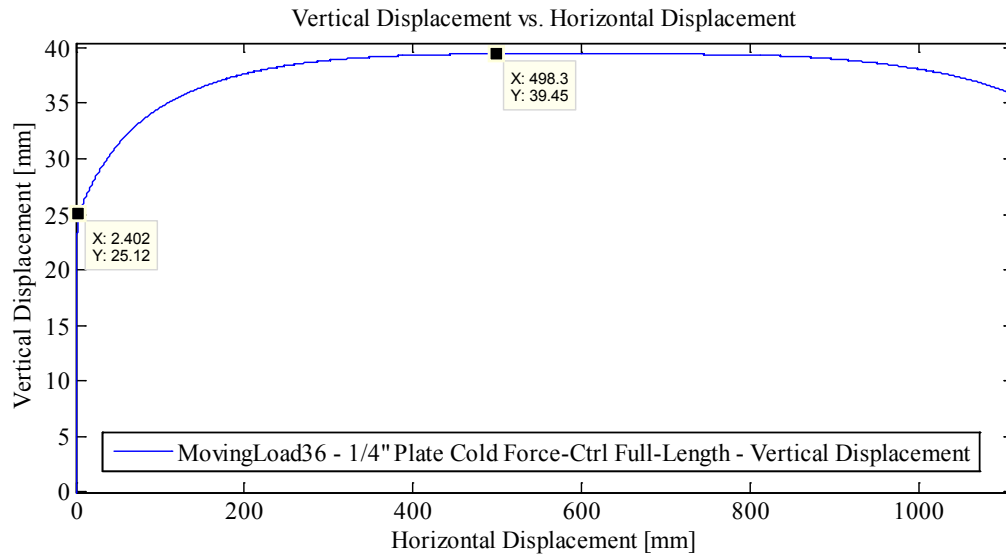


Figure 4.24: Normal (vertical) displacement vs. lateral (horizontal) displacement for a force controlled $\frac{1}{4}$ " plate experiment at -10°C .

Figure 4.25 shows the indenter's normal (i.e. vertical ram) displacement versus indenter horizontal displacement for the $\frac{1}{2}$ " plate force controlled experiment. During the stationary load portion of the experiment, a 250 kN normal load induced a 20.6 mm indentation in the $\frac{1}{2}$ " plate. Immediately upon commencement of lateral indenter motion the normal displacement began to increase, until it reached its maximum, 30.5 mm (an increase of 48% the original value), near the centre of the plate (as expected).

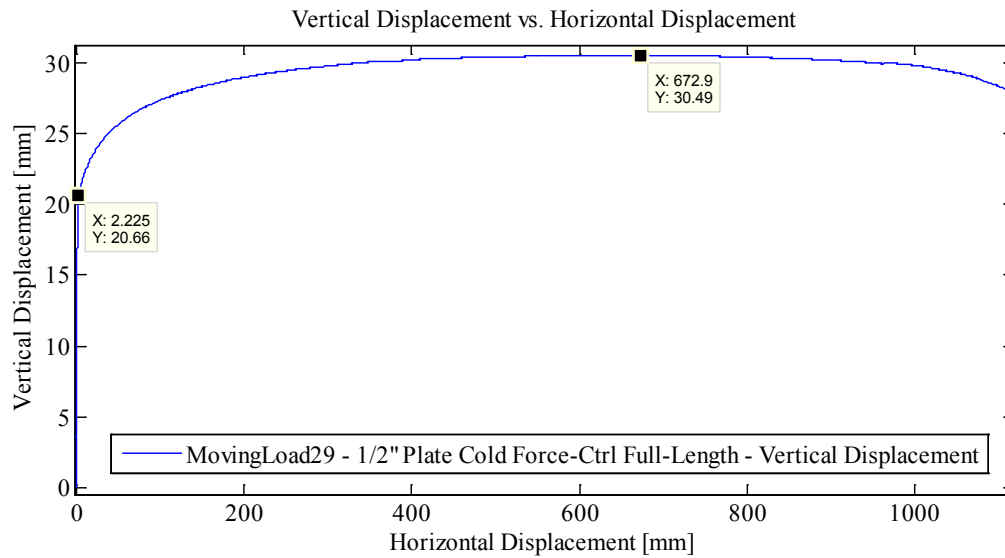


Figure 4.25: Normal (vertical) displacement vs. lateral (horizontal) displacement for a force controlled 1/2" plate experiment at -10°C.

Figure 4.26 shows the indenter's normal (i.e. vertical ram) displacement versus indenter horizontal displacement for the frame force controlled experiment. During the stationary load portion of the experiment, a 250 kN normal load induced a 12.9 mm indentation in the frame. Immediately upon commencement of lateral indenter motion the normal displacement began to increase, until it reached its maximum, 23.4 mm (an increase of 81% the original value), near the centre of the plate (as expected).

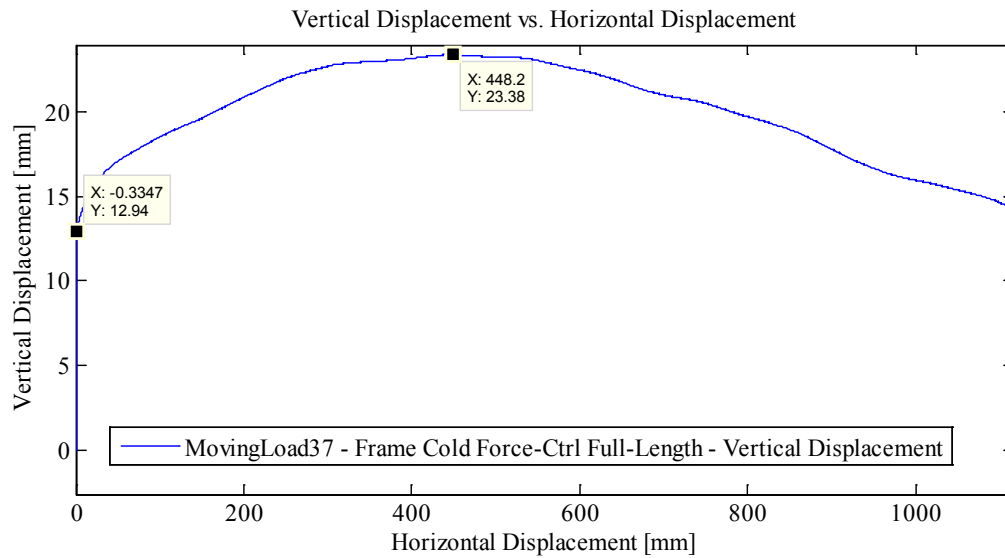


Figure 4.26: Normal (vertical) displacement vs. lateral (horizontal) displacement for a force controlled frame experiment at -10°C .

Figures 4.27 through 4.29 show the lateral force versus horizontal displacement plot for the force controlled frame experiments. Their overall shape is similar to their corresponding displacement-controlled experiments, except that the force rises over a longer lateral displacement (and hence time).

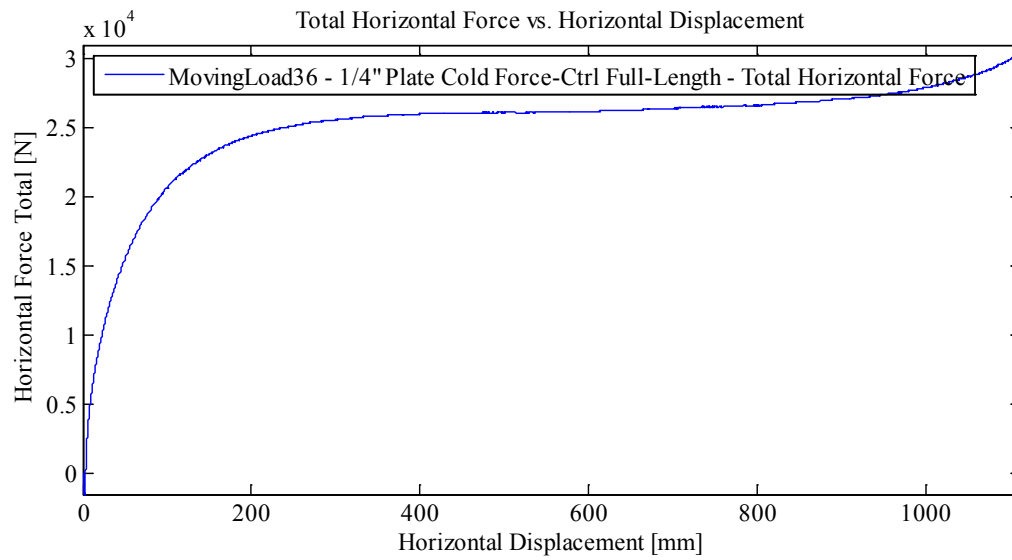


Figure 4.27: Lateral (horizontal) force vs. lateral (horizontal) displacement for force controlled $\frac{1}{4}$ " plate.

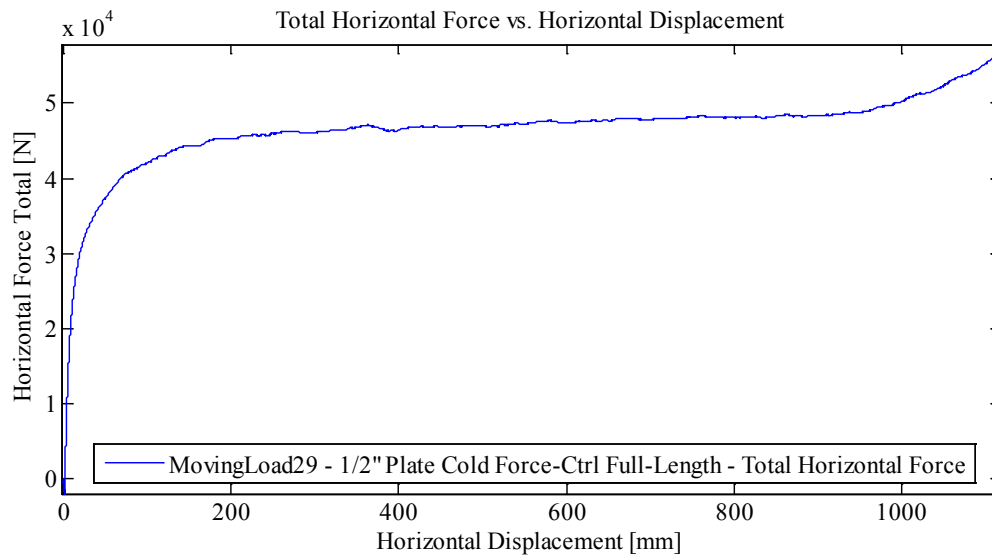


Figure 4.28: Lateral (horizontal) force vs. lateral (horizontal) displacement for force controlled $\frac{1}{2}$ " plate.

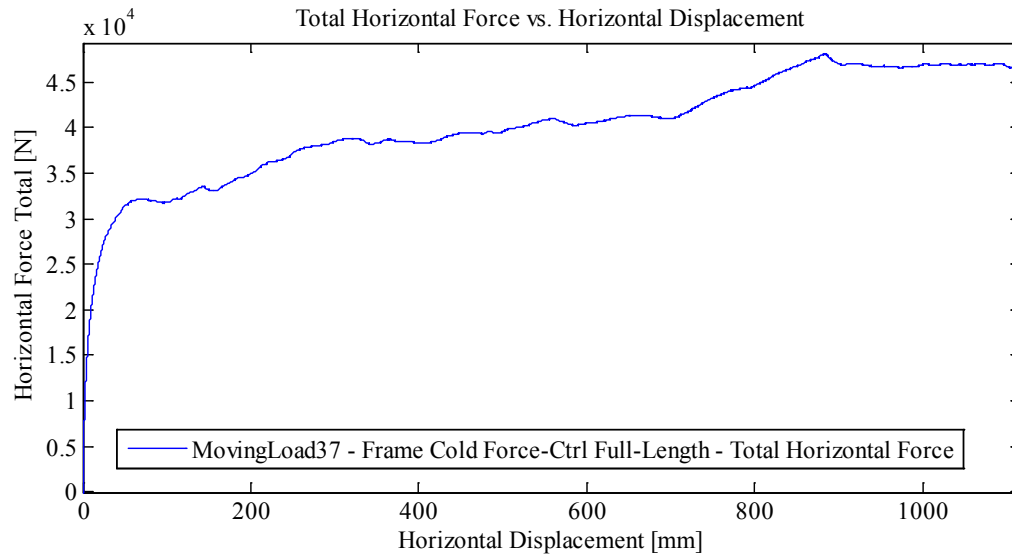


Figure 4.29: Lateral (horizontal) force vs. lateral (horizontal) displacement for force controlled frame.

The structural behaviour observed in these experiments was exactly as predicted, showing that “moving load effects” are equally present under force control.

4.8.2 Further discussion

The force controlled frame experiment warrants further discussion. During the stationary load phase of the experiment, the plating (and attached stiffener) deformed approximately half as much as the ½” plate under the same load. Considering that the plating portion of the frame is a ¼” plate (which deformed twice as much under half the load), the stiffener was primarily responsible for the load-deflection behaviour of the frame. As would be expected, this suggests that T-stiffened panels are very efficient at resisting stationary loads. During the lateral load phase, however, the frame exhibited an 81% increase in normal deformation. This occurred because load movement triggered a plastic buckling

event that does not occur in frames for similar stationary loads. This suggests that it is not such an efficient design for resisting moving loads.

4.9 Ice Cone Tests

The ice cone experiments were divided into two major groups: ice inciting an elastic plate response (referred to from this point on as *elastic structural ice tests*), and ice inciting a plastic plate response (referred to from now on as *plastic structural ice tests*). Regarding the elastic structural ice tests, they are further subdivided into two groups: tests involving Fujifilm PrescaleTM pressure film and tests that do not (i.e. ice directly acting on steel plate).

Please note, the elastic structural ice tests involving the pressure film were conducted in a joint effort with Hyunwook Kim, and are the subject of another paper (Kim, Quinton 2015). As such, only the relevant differences due to sliding friction between these and the elastic structural ice tests without the pressure film will be discussed here. The data for all ice cone tests are given in Appendix C3.

4.9.1 Load path

As discussed in 3.8.2, the load path for all ice cone indenter tests involves simultaneous vertical and lateral motions. This load path was chosen to allow any potential changes in the behaviour of the ice cones resulting from lateral load movement to develop while the ice was being crushed (instead of crushing vertically, followed by lateral motion; as with the rigid wheel indenter).

4.9.2 Elastic structural ice tests without pressure film

For these experiments, a ½” thick steel plate was the crushing surface. The plate was mounted on the carriage of the moving load apparatus, similar to the procedure for the rigid wheel indenter experiments, except that it was not removed after each ice cone indenter test. This is because the ½” steel plate remained elastic during each test, and was subsequently reused.

4.9.2.1 Slow – MovingLoad30 and MovingLoad31

Note: MovingLoad31 is a repetition of MovingLoad30.

Starting position:	End
Lateral travel:	1100 mm
Lateral speed:	10 mm/s
Vertical Travel:	30 mm
Vertical speed:	0.25 mm/s

These are “slow” speed tests. The vertical indentation is at a rate where steady state crushing without the dramatic drops in load associated with large spalling (i.e. flaking) events should occur.

One of the interesting phenomena that appeared during these ice cone on elastic plate experiments was a “chattering”, or “stick-slip” phenomenon that began partway through each “slow” test and decreased in frequency as the load increased. This stick-slip phenomena is evident in Figures 4.30 and 4.31, and in Figure 4.32. For MovingLoad30 the “chatter” begins at about time = 60 [s]; and for MovingLoad31 at about time = 70 [s].

Figure 4.30 is a plot of the normal force versus time, and Figure 4.31 is a plot of lateral force versus time. Despite the fact that the two curves in Figure 4.30 are significantly different in their load response, the onset of this “stick-slip” phenomena occurs at about the same vertical load level of about 20 [kN] (4.5 [kip]). The curves in Figure 4.31 are more alike, and the “chatter” begins at a horizontal load level of about 1 [kN] (0.25 [kip]). Figure 4.32 plots the normal and lateral forces versus time for both MovingLoad30 and MovingLoad31 on the same scale. It is apparent from this figure that the amplitude of force vibration of the “chatter” is comparable in all cases, however inspection of the lateral force versus normal force curve for MovingLoad30 found in Figure 4.33 shows that the frequency of vibration is significantly higher for the normal direction than for the lateral direction. Similar results are observed for MovingLoad31.

It presently unknown whether this “stick-slip” phenomena is a result of a misalignment in the swing arm, which may have caused the response, or if this is a behaviour associated with moving ice loads. It is unlikely that this chatter is the result of a “lock-in” phenomena that is a result of some resonant mode of vibration of the moving load apparatus. This is because the frequency of vibration in both the horizontal and vertical directions decreases with time. This is discussed more in the following section, where evidence appears that supports the “stick-slip” phenomenon as being inherent to slow moving ice loads.

The vertical forces developed by the moving ice indenters were compared with similar cones crushing against a “rigid” surface. Dillenburg (2012) reported values for an indentation speed of 0.3 mm/s in the range of 67-80 kN. The vertical force results (taking

the mean of the “chatter”) for both ML30 (i.e. 62.5 kN) and ML31 (i.e. 46 kN) are below this range.

Regarding friction, for MovingLoad30 the maximum horizontal force is 20 times less than the maximum vertical force; indicating a friction factor of 0.05 for the highest load. A plot of Total Horizontal Force divided by Vertical Force is given in Figure 4.34. For MovingLoad31, the maximum friction factor is approximately 0.07 (see Figure 4.35).

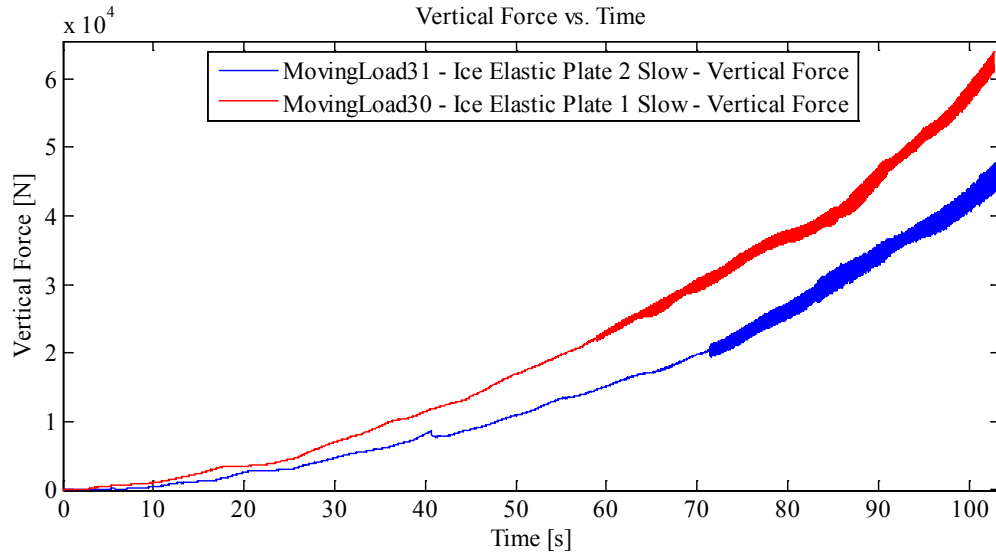


Figure 4.30: Normal (vertical) force versus time for “slow” experiments ML30 and ML31 (ice cone on elastic plate) showing “chatter” phenomenon at about a 20 kN load level.

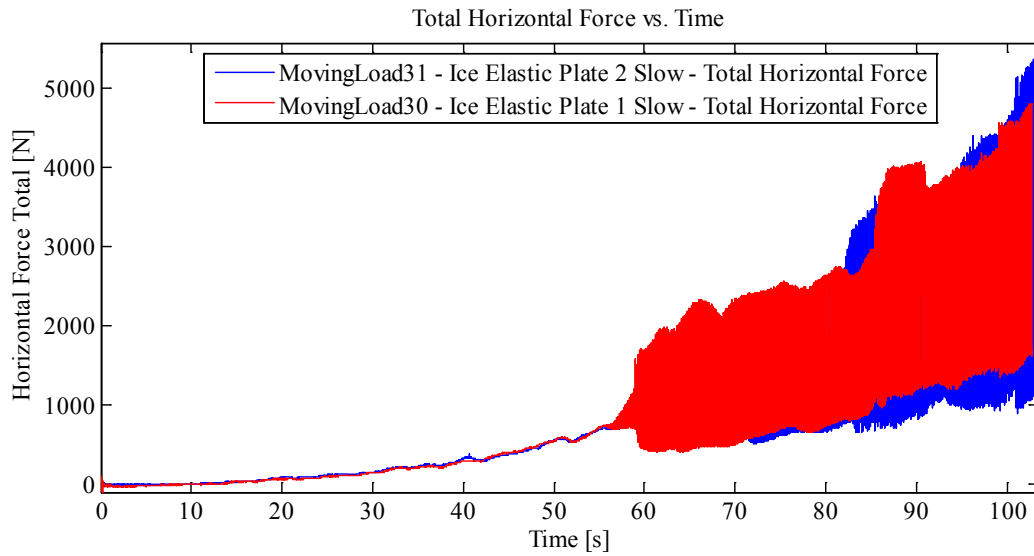


Figure 4.31: Lateral (horizontal) force versus time for “slow” experiments ML30 and ML31 (ice cone on elastic plate) showing “chatter” phenomenon at about a 1 kN load level.

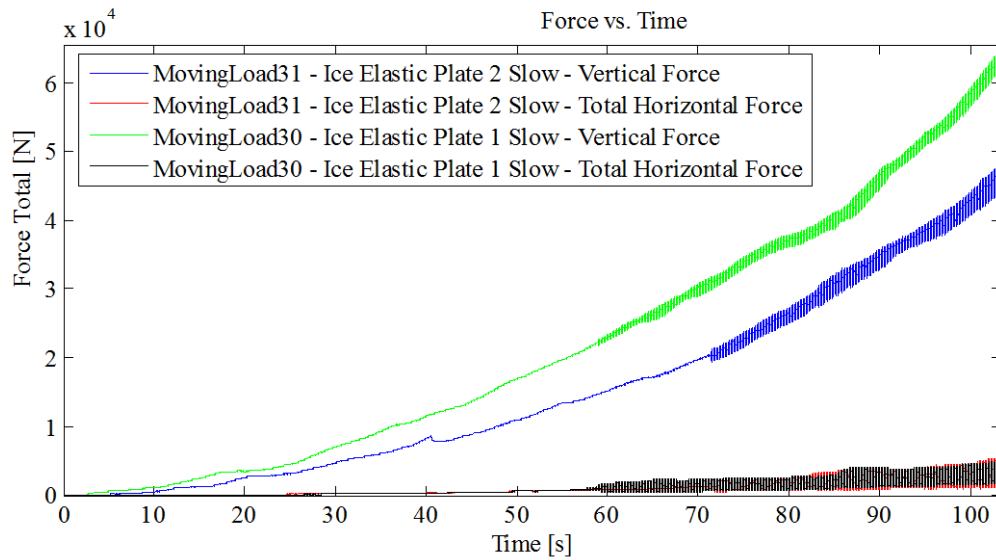


Figure 4.32: Normal (vertical) and lateral (horizontal) force versus time for “slow” experiments MovingLoad30 and MovingLoad31.

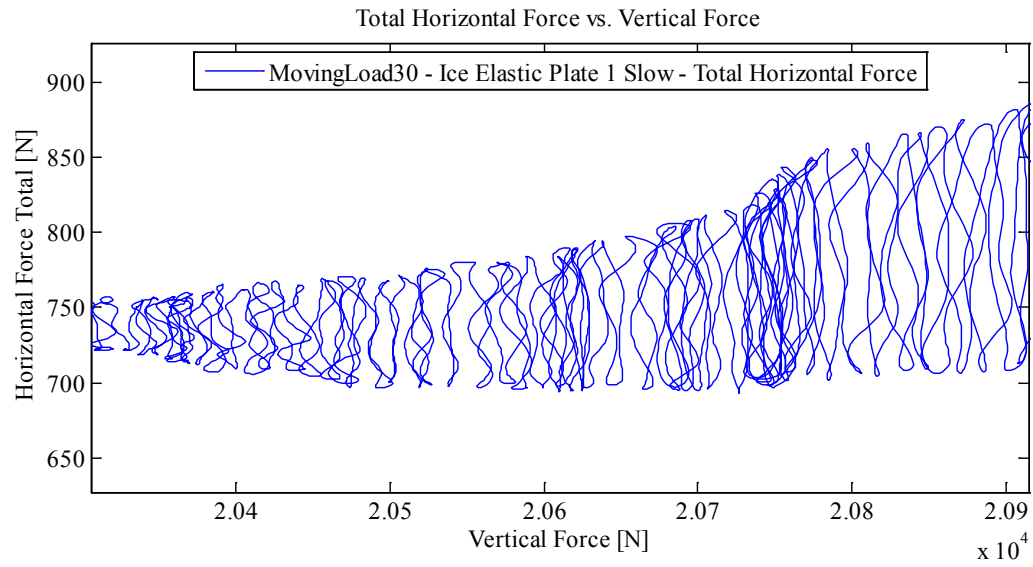


Figure 4.33: Magnification of part of the lateral (horizontal) force versus normal (vertical) force for ML30.

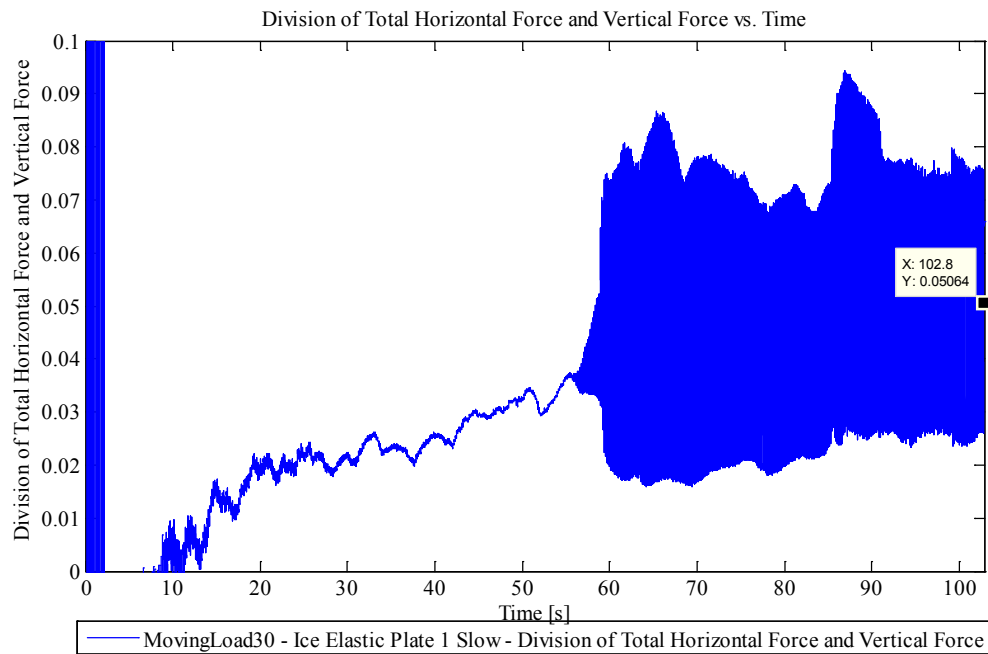


Figure 4.34: Friction factor for “slow” experiment ML30 (i.e. Total Horizontal Force divided by Vertical Force).

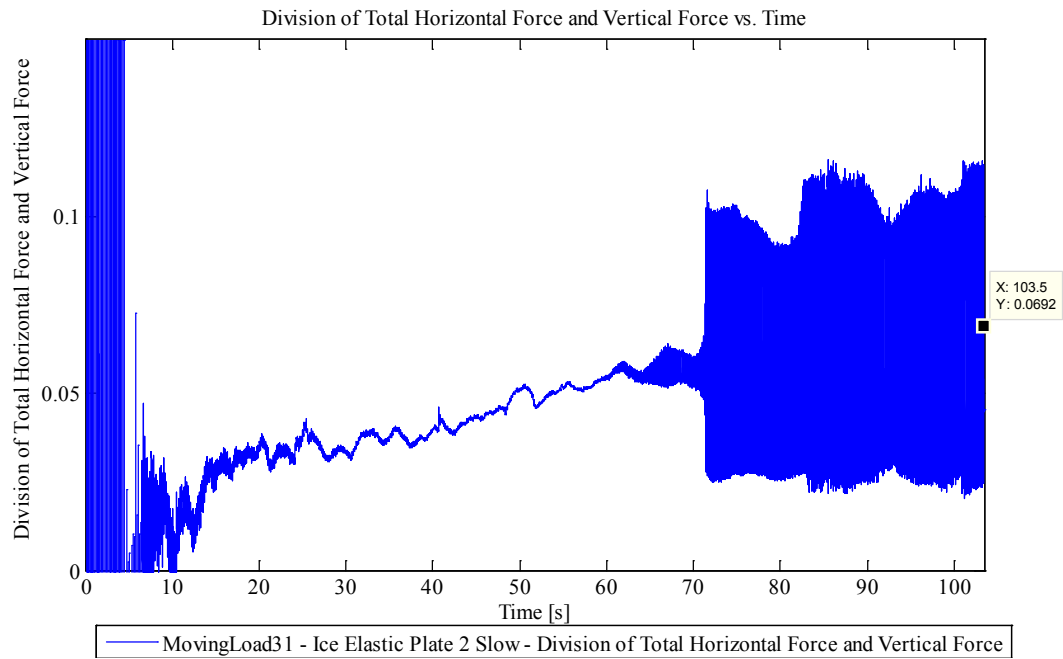


Figure 4.35: Friction factor for “slow” experiment ML31 (i.e. Total Horizontal Force divided by Vertical Force).

Regarding other behaviours observed the following is noted:

- In both ML30 and ML31 spalls (or flakes) were evident around most of the circumference of the crushed surface. There did not seem to be a preferential spalling location induced by the lateral movement.
- In both ML30 and ML31, spider-web like dark markings appeared on the contact surface near the edges. These markings are shown magnified in Figure 4.36. These deposits may be displaced oil residue that was present on the surface of the plate prior to the test.

- For both ML30 and ML31, a “grid” like imprint is visible on the crushed surface of the ice cone. This is the result of the ice conforming to the surface texture of the steel plate on which it was crushed.

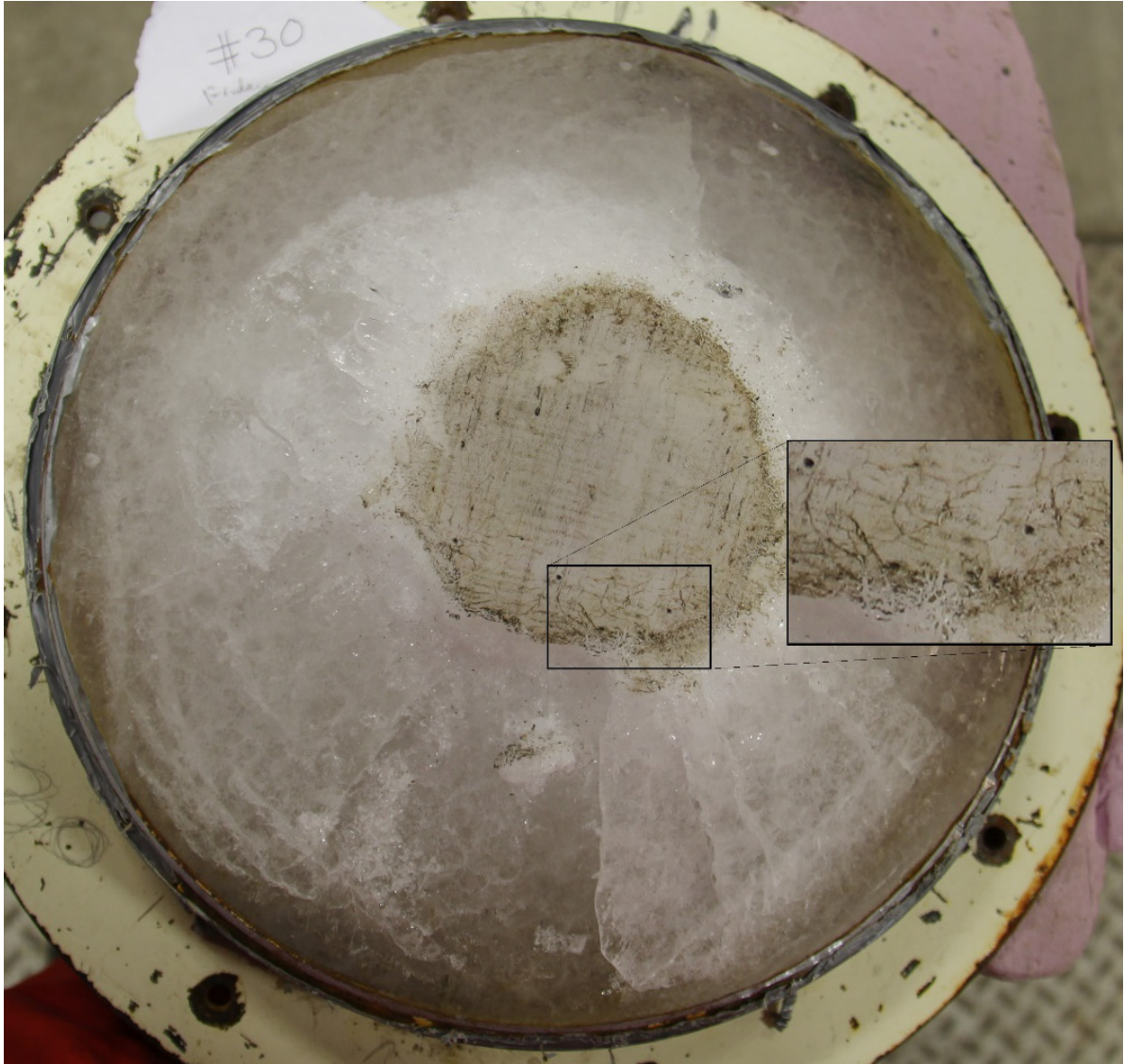


Figure 4.36: Photograph of the ice cone indenter for “slow” experiment ML30 after the test – magnified section shows dark “deposits”.

4.9.2.2 Slow – MovingLoad38 and MovingLoad39

Starting position: Absolute End

Lateral travel: 900 mm

Lateral speed: 1200 mm/s

Vertical Travel: 30 mm

Vertical speed: 0.25 mm/s

These are more “slow” speed tests. They are essentially identical to the above MovingLoad30 and MovingLoad31 tests, except that they have a slightly different starting point. These tests start 65 mm closer to the short edge of the plate, and therefore experience a slightly different structural stiffness at the start of the experiment. It may be argued that as the force is small, and because the plate is a “long plate” that there is practically little difference in stiffness of the crushing surface by the time any appreciable load arises. This is likely the case, and comparisons with the previous two tests will be made.

Like the previous two tests, these tests also exhibit the “chatter” noted above; evident in Figures 4.37 and 4.38. This time however, the onset of chatter happens much earlier in the test (for both tests); at a vertical force value of approximately 5 [kN] (1.12 [kip]). A major difference between these tests and the previous two tests is that the swing arm was realigned prior to these two tests; in order to fix a prior misalignment. Misalignment of the swing arm for the previous two tests, may have acted to stabilize this “chatter” vibration in the previous tests, and the removal of that misalignment may have freed the “chatter” to start at a lower load for these two tests. More work is needed to ascertain the origins of this

“chatter” (including a comparison of the frequency at which the servo-motor that controls the flow of oil to the vertical hydraulic ram with the chatter frequencies).

Figure 4.37 is a plot of the normal force versus time, and Figure 4.38 is a plot of lateral force versus time. The normal force curves in Figure 4.37 agree very well until about time = 80 [s], when a large spall event occurs in MovingLoad39. It should be noted that the drop in load at time = 120 [s] is due to the vertical motion of the indenter ceasing prior to the horizontal motion.

As above, the normal force values for these tests were compared with similar results reported in Dillenburg (2012) (i.e. 67-80 kN). The peak force for MovingLoad38, 76 kN (taking the mean of the “chatter”), falls within this range. The peak force for MovingLoad39, 56 kN (taking the mean of the “chatter”), is below this range. These values are higher than the results of the previous two tests (considering that MovingLoad39 experienced a spall event that the others did not).

The average friction values for MovingLoad38 and MovingLoad39 are 0.06 and 0.07 respectively; as seen in Figures 4.39 and 4.40.

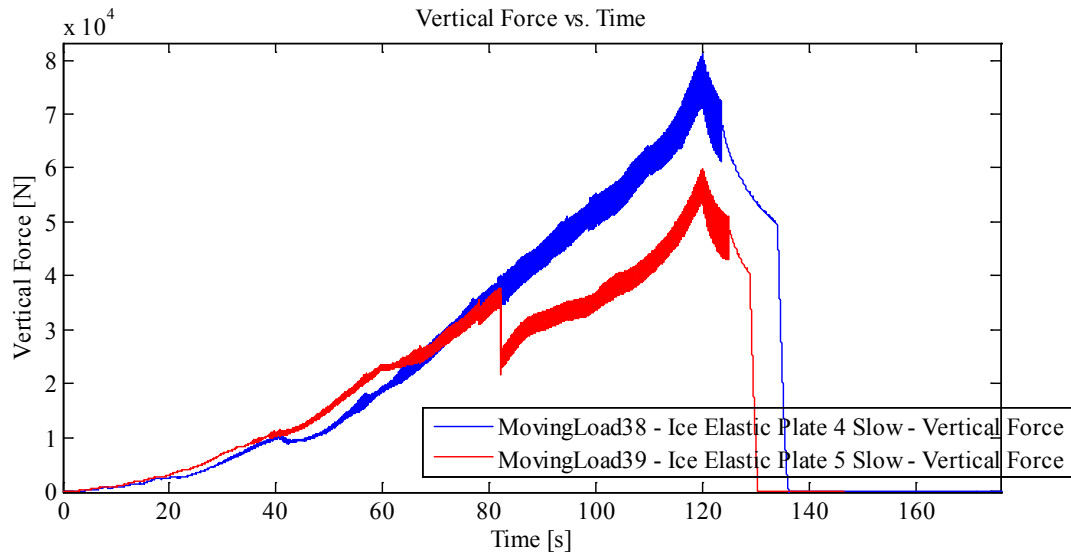


Figure 4.37: Normal (vertical) force versus time for “slow” experiments ML38 and ML39 (ice cone on elastic plate) showing “chatter” phenomenon beginning at 5 [kN] for ML38 and 9 [kN] for ML39.

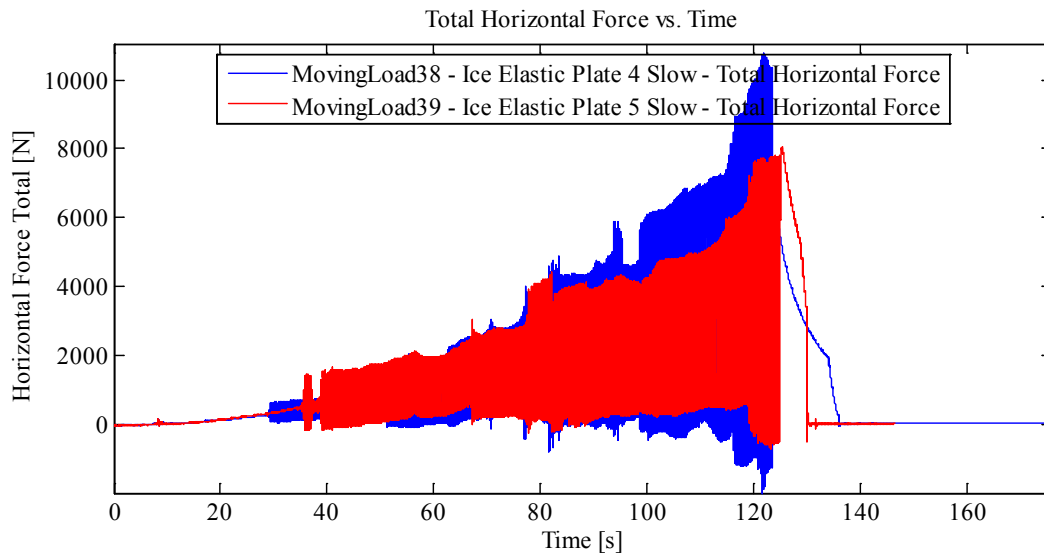


Figure 4.38: Lateral (horizontal) force versus time for “slow” experiments ML38 and ML39 (ice cone on elastic plate) showing “chatter” phenomenon beginning at <0.5 [kN].

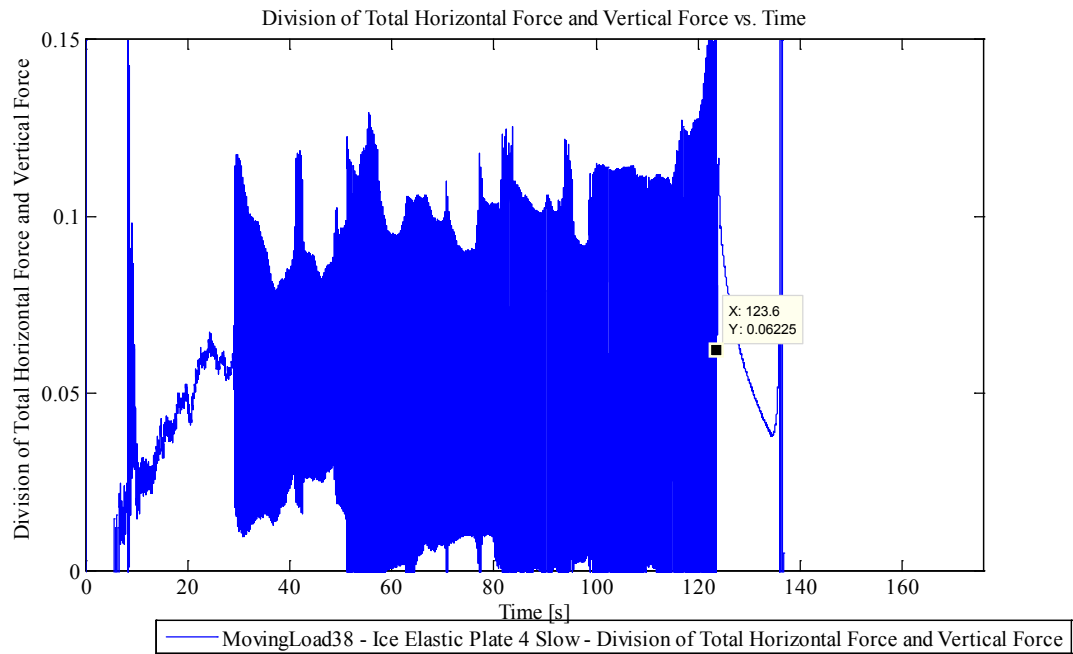


Figure 4.39: Friction factor for “slow” experiment ML38 (i.e. Total Horizontal Force divided by Vertical Force).

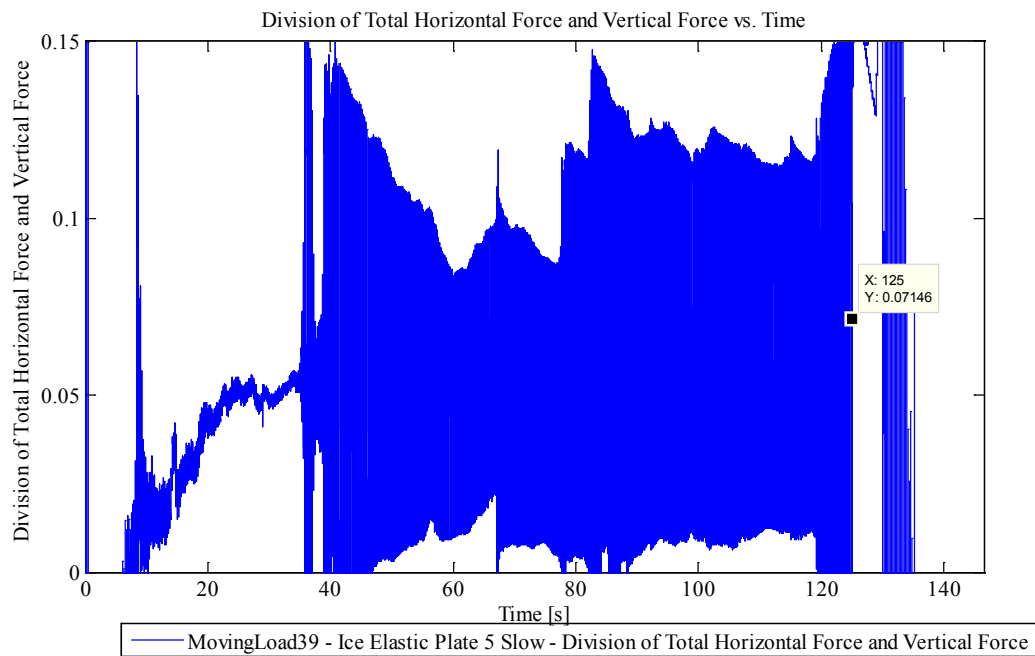


Figure 4.40: Friction factor for “slow” experiment ML39 (i.e. Total Horizontal Force divided by Vertical Force).

4.9.2.3 Fast – MovingLoad34

Starting position: Absolute End

Lateral travel: 900 mm

Lateral speed: 100 mm/s

Vertical Travel: 30 mm

Vertical speed: 3.5 mm/s

This is a “high” speed test. The vertical indentation is at a rate where large spalling (i.e. flaking) events should occur, inducing a saw-tooth load response in the ice. Indeed this is the case as can be seen for the vertical force in Figure 4.41 and the horizontal force in Figure 4.42. “The chattering” was not evident in this test, suggesting that it is alleviated by successive large spalling events.

Dillenburg (2012) reported values, for similar cones crushed against a rigid surface at a speed of 100 mm/s, in the range of 18-32 kN. The vertical force results for ML34 (i.e. 43.7 kN) are well beyond this range.

Regarding friction, for MovingLoad34 the average friction coefficient was 0.03, as can be seen in Figure 4.43.

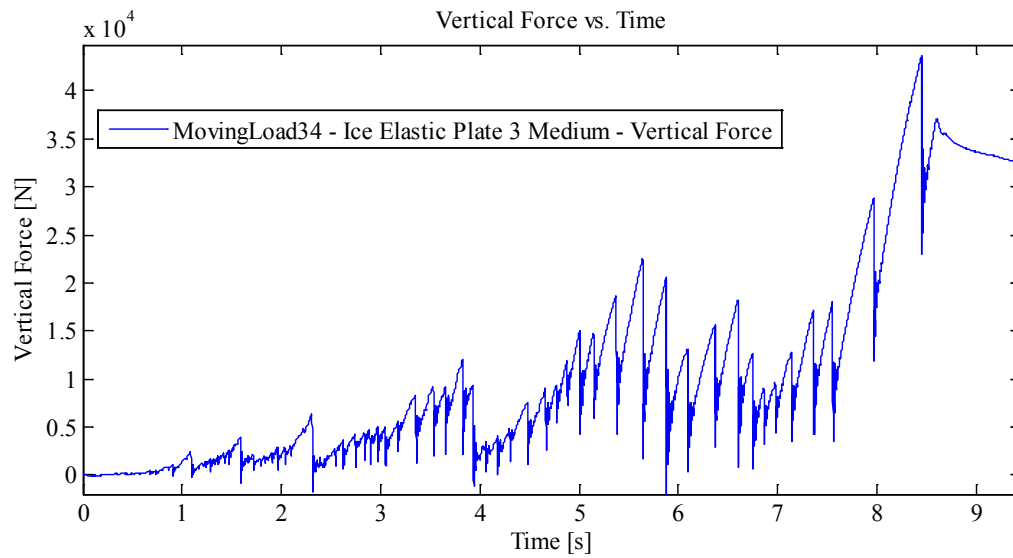


Figure 4.41: Normal (vertical) force versus time for “fast” experiment ML34 (ice cone on elastic plate) showing sawtooth loading.

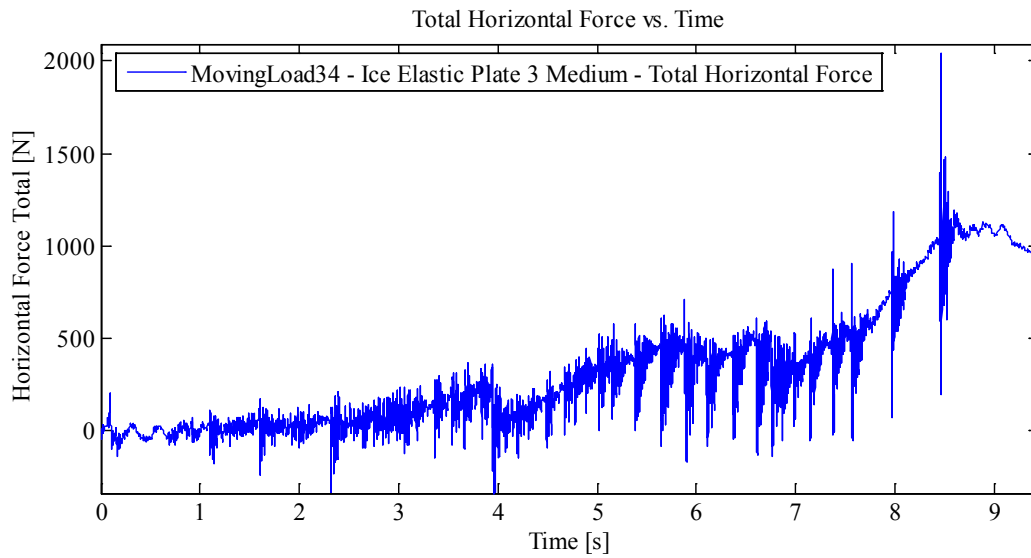


Figure 4.42: Lateral (horizontal) force versus time for “fast” experiment ML34 (ice cone on elastic plate) showing sawtooth loading.

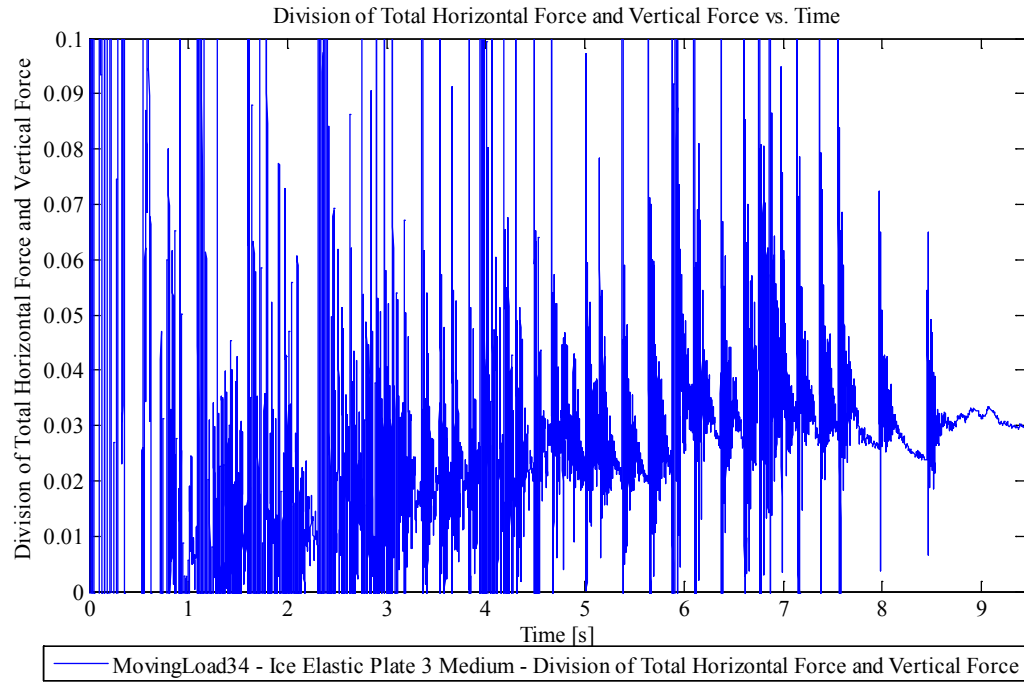


Figure 4.43: Friction factor for “fast” experiment ML34 (i.e. Total Horizontal Force divided by Vertical Force).

4.9.3 Elastic structural ice tests with pressure film

As mentioned above, a detailed account of these experiments will be published by Kim, H. and Quinton, B. in the near future. What follows is a summary of the friction coefficients for moving ice loads on an elastic steel plate with an ice-polyester sliding interface, given in Table 4.13. Figures 4.44, 4.45, and 4.46 show the friction factor (i.e. Total Horizontal Force divided by Vertical Force) curves for MovingLoad experiments 32, 33, and 35.

Table 4.13: Friction coefficients for moving ice load on elastic steel plate with ice-polyester sliding interface.

ML32	slow-elastic-pressure film	polyester	0.02
ML33	fast-elastic-pressure film	polyester	0.03
ML35	pseudo in-along-elastic-pressure film	polyester	0.04

4.9.3.1 Slow – MovingLoad32

Starting position: End

Lateral travel: 1100 mm

Lateral speed: 10 mm/s

Vertical Travel: 30 mm

Vertical speed: 0.25 mm/s

Notes: With pressure film.

MovingLoad32 is similar to MovingLoad experiments 30 and 31, except with the use of pressure film.

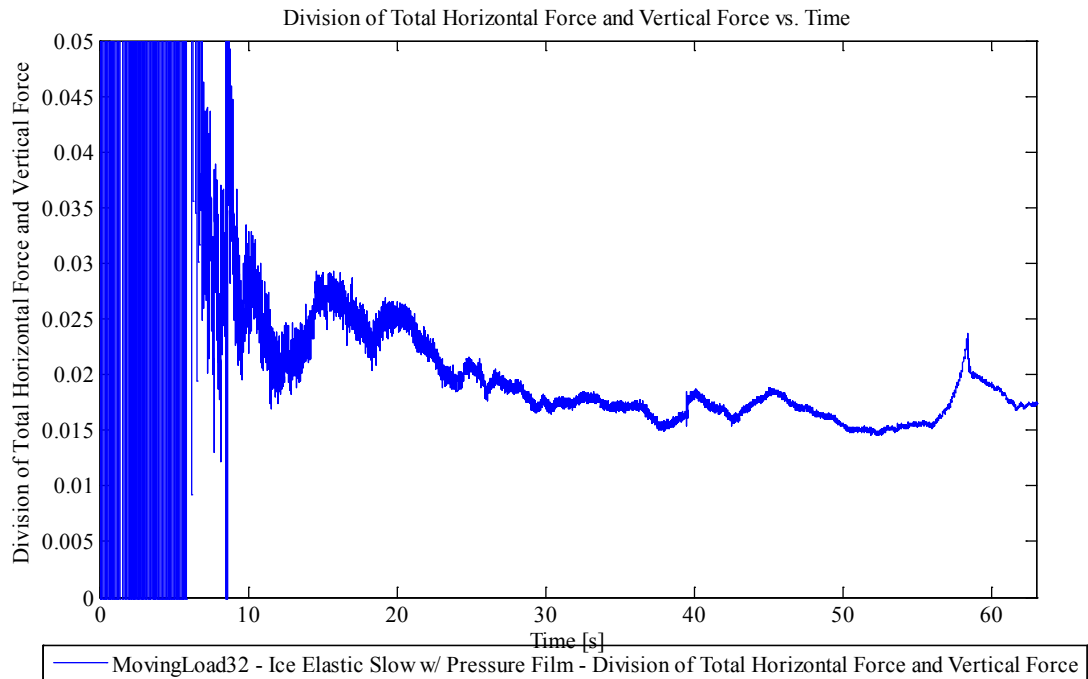


Figure 4.44: Friction factor for “slow” “pressure film” experiment ML32 (i.e. Total Horizontal Force divided by Vertical Force).

4.9.3.2 Slow – MovingLoad33

Starting position: Absolute End

Lateral travel: 1100 mm

Lateral speed: 10 mm/s

Vertical Travel: 30 mm

Vertical speed: 0.25 mm/s

Notes: With pressure film.

MovingLoad33 is similar to experiments MovingLoad34, except with the use of pressure film. Note in determining the friction factor, the average value was calculated.

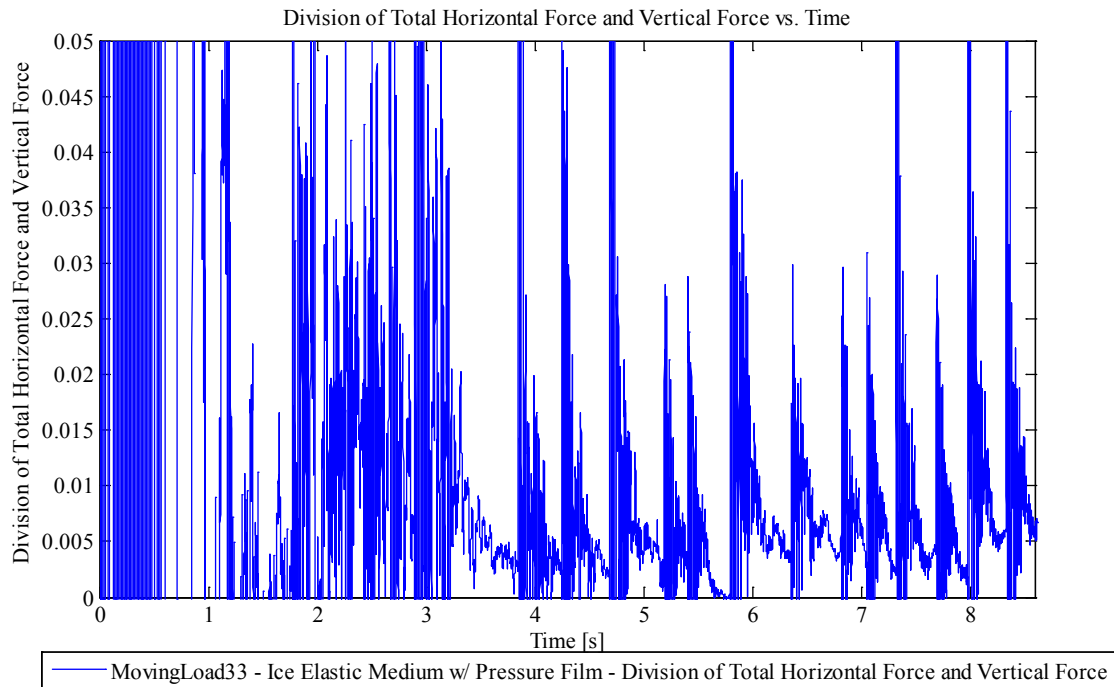


Figure 4.45: Friction factor for “fast” “pressure film” experiment ML33 (i.e. Total Horizontal Force divided by Vertical Force).

4.9.3.3 Slow – MovingLoad35

Starting position: Absolute End

Lateral travel: 1200 mm

Lateral speed: 83 mm/s

Vertical Travel: 30 mm

Vertical speed: 83 mm/s

Notes: With pressure film.

MovingLoad35 is a unique ice cone indenter test. No attempt was made to have the vertical and horizontal motions cease simultaneously. Instead, the vertical indentation is completed

within 0.4 [s] and the horizontal motion continues for 14 [s]. This provides a load path very similar to the sequential load path used in the rigid wheel indenter tests.

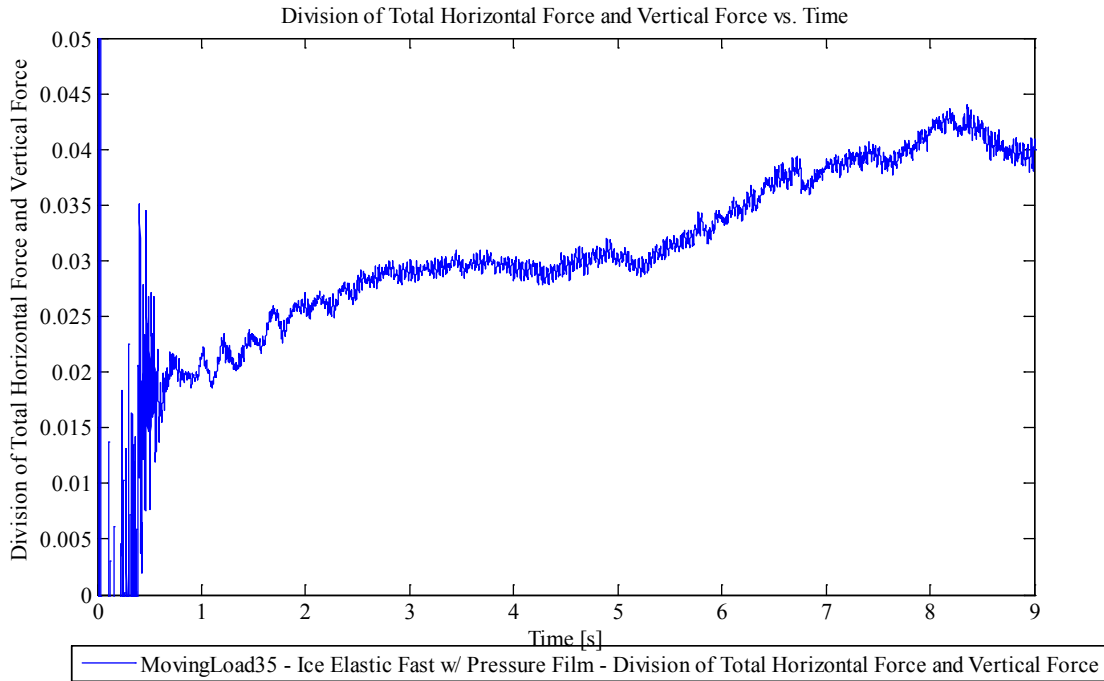


Figure 4.46: Friction factor for “pseudo in-along load path” “pressure film” experiment ML35 (i.e. Total Horizontal Force divided by Vertical Force).

4.9.4 Plastic structural ice tests

Two tests were done where moving ice cone indenters induced a plastic response in 1/8 in. steel plates.

4.9.4.1 Slow – MovingLoad40

Starting position: Absolute End

Lateral travel: 1200 mm

Lateral speed: 10 mm/s

Vertical Travel: 30 mm

Vertical speed: 0.25 mm/s

This test is similar to MovingLoad38 and MovingLoad39, except it is performed on a 1/8 in. thick plate (instead of a 1/2 in. thick plate). This test was a first attempt at plastically damaging a steel plate with a moving ice cone indenter. Unfortunately, the vertical travel of 30 mm was not enough to incite much plastic damage as, due to the plate deformation, the depth of crushing into the ice cone was much less than 30 mm (see Figure 4.47).

The “chatter” phenomenon is evident for this test, beginning at a normal (vertical) force level of 5 [kN] (1.12 [kip]) and a lateral (horizontal) force of 0.5 [kN] (0.11 [kip]) (see Figures 4.48 and 4.49).

Comparison of the normal (vertical) peak force level for this experiment, 20 kN (4.5 [kip]) (taking the mean of the “chatter”), with similar results from Dillenburg (2012) (i.e. 67-80 kN) shows that this force level is very low. This is to be expected because the deformation in the plate accounted for much of the 30 mm vertical travel imposed on the ice cone during the test. Assuming that this experiment fits with Dillenburg’s dataset, a peak vertical force of 20 kN would correspond with an indentation of approximately 14 mm on a rigid surface.

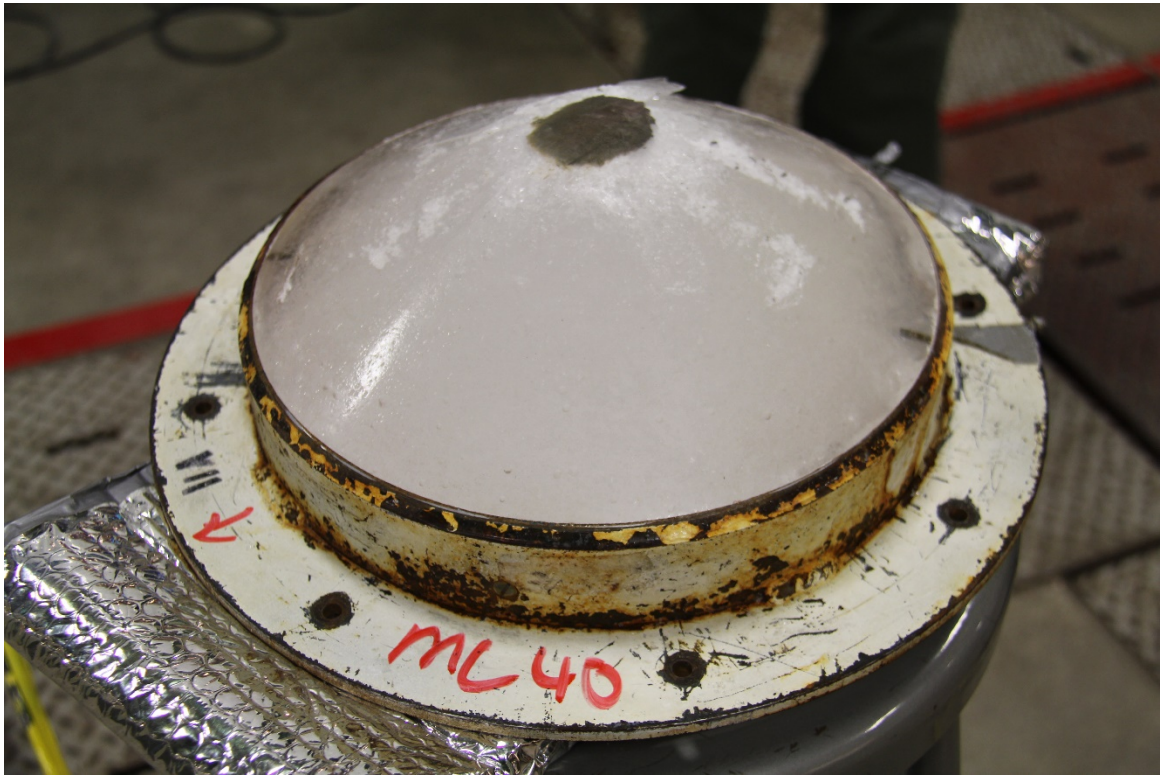


Figure 4.47: Picture of ice cone indenter for experiment MovingLoad40 after the test was completed – the crushed surface of the ice cone is visible as the dark spot at the apex of the cone.

The friction factor, 0.19, for this experiment was extremely high compared with the elastic structural ice tests. This is undoubtedly due to the excessive deformation of this plate in comparison.

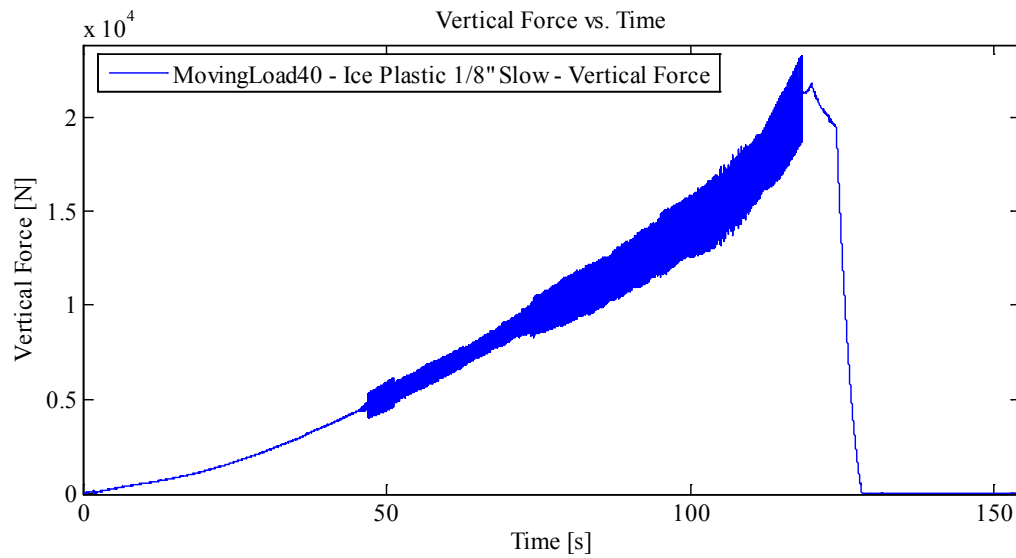


Figure 4.48: Normal (vertical) force versus time for “slow” experiment ML40 (ice cone on plastic plate) showing “chatter” phenomenon beginning at 5 [kN].

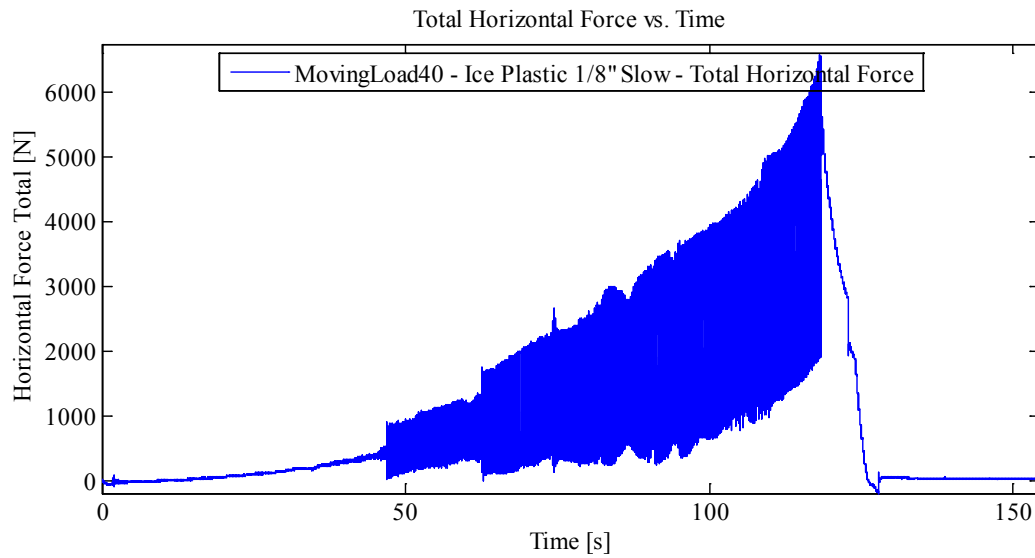


Figure 4.49: Lateral (horizontal) force versus time for “slow” experiment ML40 (ice cone on plastic plate) showing “chatter” phenomenon beginning at 0.5 [kN].

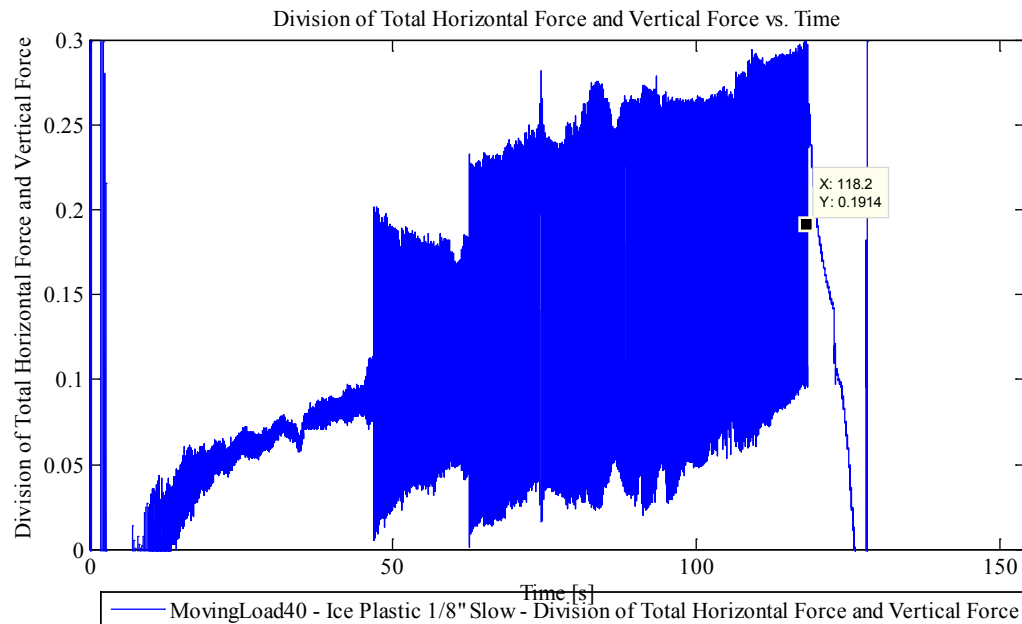


Figure 4.50: Friction factor for “slow” “plastic” experiment ML40 (i.e. Total Horizontal Force divided by Vertical Force).

4.9.4.2 Fast – MovingLoad41

Starting position: Absolute End

Lateral travel: 1150 mm

Lateral speed: 185 mm/s

Vertical Travel: 64 mm

Vertical speed: 10.0 mm/s

The vertical and horizontal speeds for this test were increased from the previous test. At 10 mm/s vertical indentation rate, we would expect to see large spall events and sudden drops in load. Based on experience from the previous test, a vertical travel of 64 mm was chosen. This value maximizes the ice crushing while minimizing artificial confinement from the ice holder (crushed ice cone shown in Figure 4.51).

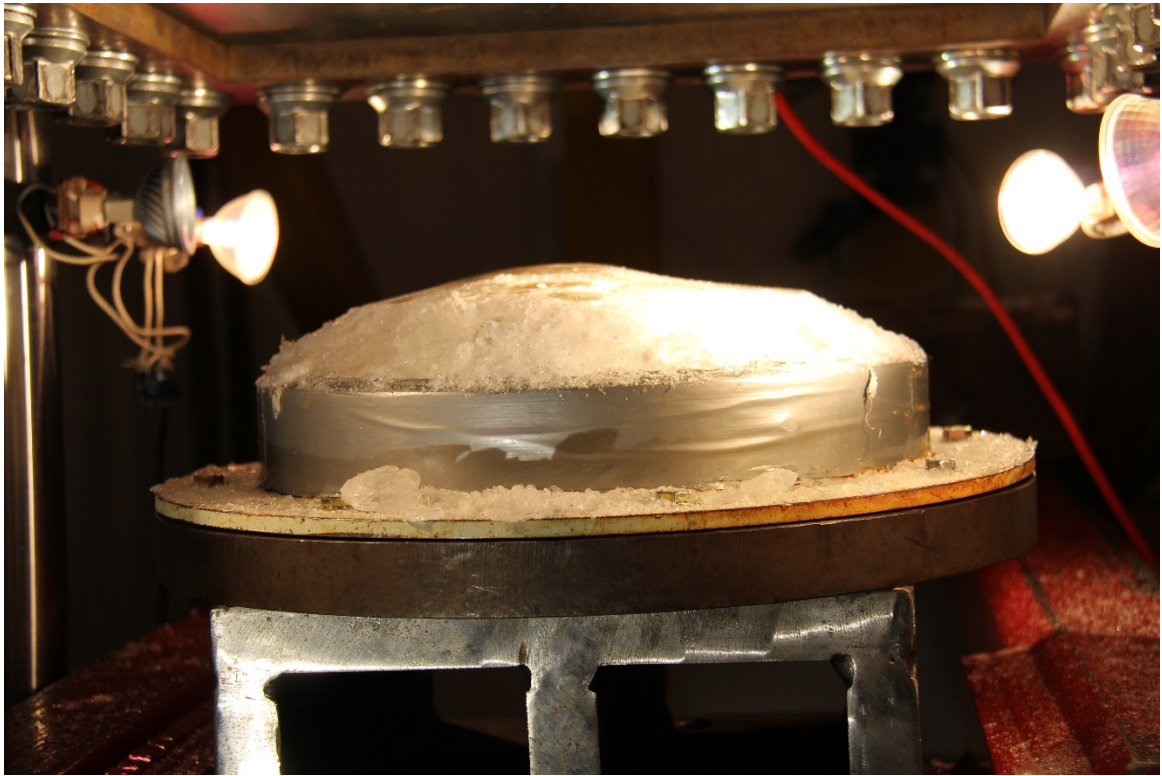


Figure 4.51: Picture of ice cone indenter for experiment MovingLoad41 after the test was completed – the crushed surface of the ice cone resembles the shape the plastically deformed plate on which it was acting.

As with the fast elastic plate test above (MovingLoad34) the “chatter” phenomenon was not present for this fast experiment.

Regarding peak normal and lateral forces (see Figures 4.52 and 4.53 respectively), the peak normal force is 59 [kN] (13.2 [kip]) and the peak lateral force is 6.8 [kN] (1.5 [kip]). If the assumption is made that that this experiment fits with Dillenburg’s (2012) dataset, this would correspond with an indentation of somewhere between 35-45 mm on a rigid surface. This may not be a good assumption due to the level of plastic deformation present in the plate. It is undetermined at this point whether confinement from the plastically deformed plate was a factor, or not. It is likely however, based on Kim’s (2014) experiments of

crushing ice cones into concave wedge shaped crushing surfaces, that confinement is not a significant factor due to the lateral movement of the ice cone indenter. As the ice cone indenter plastically damages the plate, it is essentially creating an elongating wedge shape. The difference between this case and Kim's case is that the wedge on the leading side of the moving ice load is not open (i.e. crushed ice may not freely escape this way). The only viable route for crushed ice to escape is on the trailing side of the ice cone indenter. Further study is required to see if this scenario contributes to the confinement of crushed ice at contact interface.

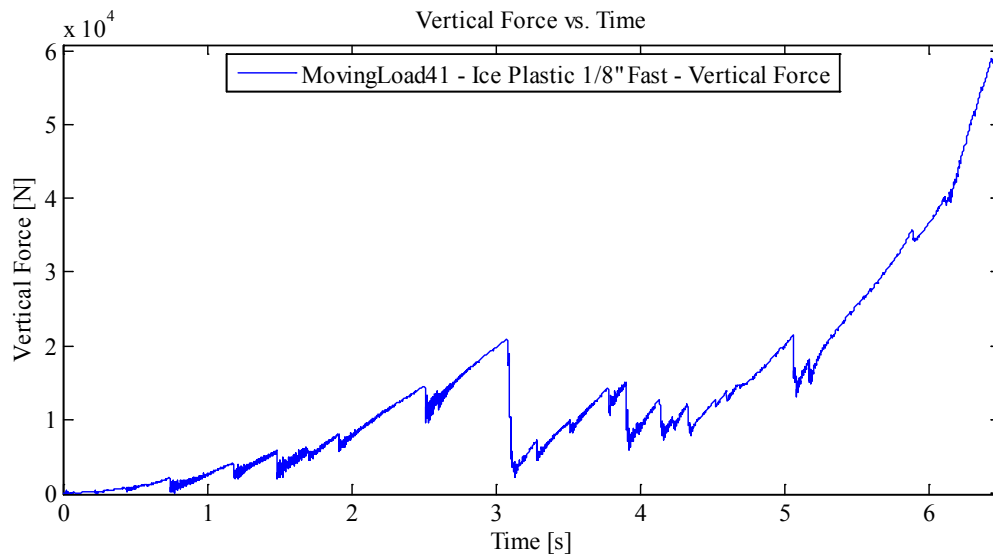


Figure 4.52: Normal (vertical) force versus time for “fast” experiment ML40 (ice cone on plastic plate).

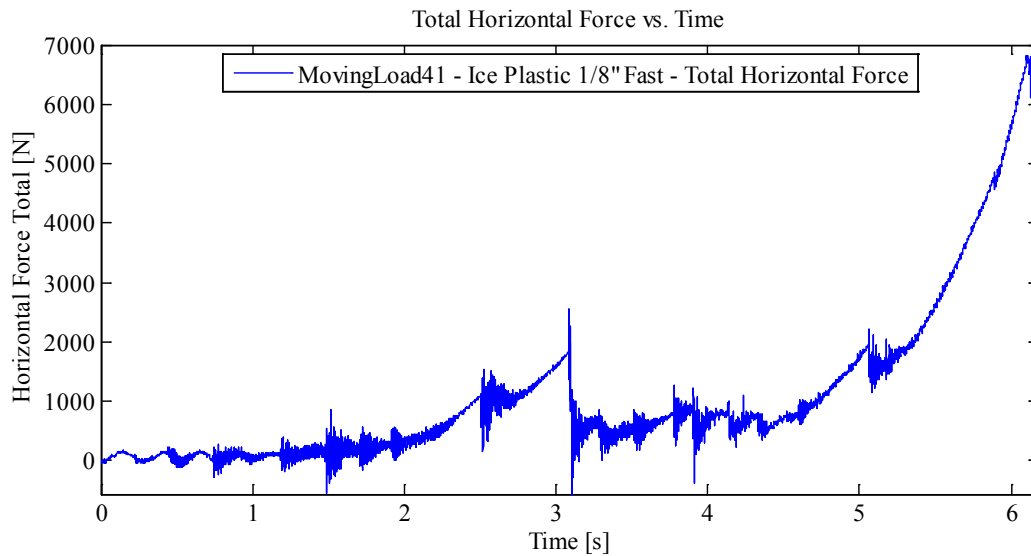


Figure 4.53: Lateral (horizontal) force versus time for “fast” experiment ML40 (ice cone on plastic plate).

Regarding the friction factor, the average of the data shown in Figure 4.54 yields a friction factor of 0.17. This is very high, and like the previous experiment incorporates the effects of gross plastic deformation of the sliding surface (i.e. it is not purely the result of surface friction, but arises mostly from the action of the ice “plowing” through the steel in the lateral direction).

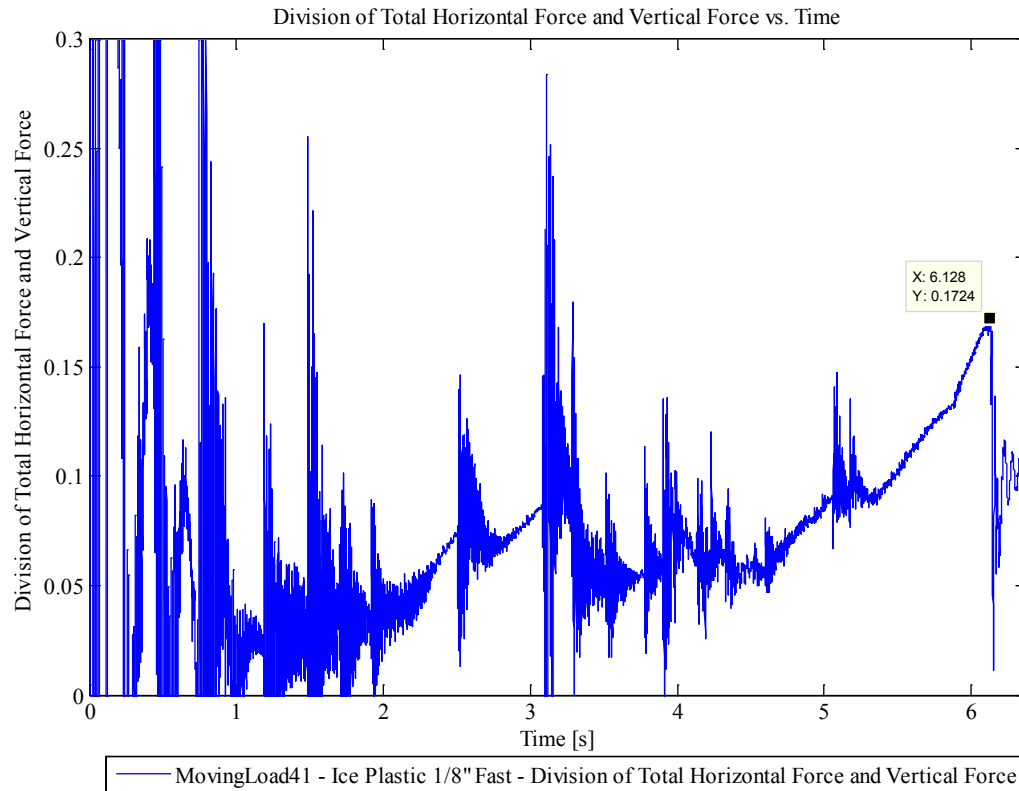


Figure 4.54: Friction factor for “fast” “plastic” experiment ML41 (i.e. Total Horizontal Force divided by Vertical Force).

4.9.5 Results of moving ice cone indenter tests

These experiments represent the first tests involving a moving ice cone acting on elastically, and plastically, deforming plates. This section presents a cursory overview of the collected data.

There is not enough evidence from the present study to say whether or not there is an appreciable effect, due to load movement, on the behaviour of ice acting on an elastic plate. Of the four slow speed “elastic plate response” tests (i.e. MovingLoad tests 30, 31, 38, and 39), only the vertical force for MovingLoad39 was comparable in magnitude to similar

published data (Dillenburg 2012) for stationary ice loads on a rigid surface. The other three tests showed lower magnitudes. The vertical force for the single fast speed “elastic plate response” ice cone test (MovingLoad34) was higher than Dillenburg’s results. More study is required before anything definitive can be determined.

Regarding moving ice loads on plastically deforming plates, it is also not possible with this limited data set to make any sort of generalisation. One of the key issues with making use of the data from these experiments is determining how much of the imposed deflections on the ice cone holder go into deforming the plate, and how much go into deforming the ice. Without this data, it is impossible to benchmark the ice load against published stationary ice loads (e.g. Dillenburg (2012)), and it is also not possible to quantify the extent of the effect of ice load lateral movement on plate structural capacity. Another key issue is determining the effect of confinement due to plastic deformation. A new confinement scenario, similar to Kim’s (2014) concave wedge, has been identified, and requires further investigation.

A “chatter” (or “stick-slip”) phenomenon was observed in the “slow” experiments for both the elastically and plastically deforming plates. It is not clear whether this is a phenomenon of moving ice loads in general, or if it is a spurious effect of the test apparatus. The data suggests the former. This phenomenon, if valid, is worth investigation due to the amplitude and frequency ranges of the vibrations experienced by the moving load apparatus, which could be potentially dangerous to the integrity of hull structures at larger scale.

Regarding friction, the following table, Table 4.14, summarizes the calculated friction coefficients for each of the experiments.

Table 4.14: Summary of friction coefficients for moving ice indenter experiments.

Test	Category	Material	Max. Friction Coefficient
ML30	slow - elastic	steel	0.05
ML31	slow - elastic	steel	0.07
ML38	slow - elastic	steel	0.06
ML39	slow - elastic	steel	0.07
ML34	fast - elastic	steel	0.03
ML40	slow - plastic	steel	0.19
ML41	fast - plastic	steel	0.17
ML32	slow-elastic-pressure film	polyester	0.02
ML33	fast-elastic-pressure film	polyester	0.03
ML35	Pseudo in-along-elastic-pressure film	polyester	0.04

4.10 Summary of Results and Discussion

Generally, the moving load experiments went well and the moving load apparatus behaved as it was designed to do. The results of one experiment in particular are questionable: MovingLoad14. This is a “fast” frame experiment conducted at room-temperature. Expectations based on the rest of the “fast” experiments indicate that the moving load capacity for this experiment should have been higher than the corresponding “slow” experiments. There is one particular difference between this experiment and the rest of the frame experiments that could explain this discrepancy. The frame specimen used in the MovingLoad14 experiment was the only one that did not have the “bevels” in the stiffener end plates. It is extremely likely that the lack of these bevels increased the stiffness of the boundary conditions of the stiffener portion of the frame, leading to the anomalous results. This conjecture is supported by findings from the numerical model (Chapter 5.4.1) where

it is discovered that stiffer boundary conditions cause a greater decrease in a structures capacity to sustain moving loads.

Also, the ice cone tests are summarized in Chapter 4.9.54.9.5, and are not repeated in this section.

4.10.1 Capacity loss and strain-rate effects gains

The moving load experiments show definitively that a significant structural capacity loss exists for plates and frames subject to moving loads causing plastic damage, versus similar stationary loads.

Table 4.15 summarizes this percentage capacity loss for the moving load experiments, as well as the capacity gains associated with the fast experiments – most likely due to strain-rate effects – in the normal and lateral directions. The moving load capacity losses are significant, ranging from 14% to 40% depending on the scenario. The strain-rate effects capacity gains range from 2.1% to 6.5% in the normal direction, and 3.2% to 7.8% in the lateral direction.

Table 4.15: Summary of moving load % capacity loss and strain-rate effects % capacity gains for the plate and frame specimens.

	Specimen Type														
	1/4 Plate						1/2 Plate				Frame				
	Indentation														
	2 cm		4 cm				3 cm				2.5 cm				
	Temperature														
	-10°C		20°C		-10°C		20°C		-10°C		20°C		-10°C		
	Starting Location														
	Centre	End	Centre	End	Centre	End	Centre	End	Centre	End	Centre	End	Centre	End	Centre
Normal Capacity Loss at Starting Location	38%	35%	40%	38%	40%	35%	31%	28%	32%	28%	15%	31%	18%	28%	
Normal Rate-effects Gain at Starting Location	6.5%	N/A	5.8%	N/A	6.4%	N/A	2.1%	N/A	4.6%	N/A	5.1%	N/A	4.9%	N/A	
Lateral Moving Rate-effects Gain at End Location	7.6%	N/A	7.0%	N/A	7.6%	N/A	3.2%	N/A	5.6%	N/A	7.8%	N/A	7.6%	N/A	

4.10.2 Force controlled experiments

In addition to verification that moving load effects exist for displacement-controlled scenarios, these experiments confirmed their existence for force controlled scenarios too.

As would be expected by comparison with their displacement-controlled counterparts, when a force causing plastic damage is held constant and lateral motion begins, the indentation made by the initial stationary load increases dramatically. The percentage increase in indentation for each specimen type is given in

Table 4.16.

Table 4.16: Increase in plate and frame indentation for force controlled moving load experiments.

	Specimen Type		
	1/4" Plate	1/2" Plate	Frame
Indentation increase	57%	48%	81%

Regarding the lateral moving load capacity during the force controlled experiments, it is worth noting that the overall shape of the lateral moving load response curve is similar to the corresponding displacement-controlled experiments, except that the force rises over a longer lateral displacement (and hence time). With the displacement-controlled curves the force rises much more quickly.

The force controlled frame experiment provided surprising results as the moving load indentation was 181% of the stationary indentation. This suggests that a T-stiffener is not a very efficient design for resisting moving loads.

4.10.3 Verification of early onset of plastic buckling

Quinton (2008) predicted that plastic buckling behaviour would occur in the web of a ship's frame at a much lower load for moving loads causing plastic damage than for stationary loads. This has been verified through the use of cameras mounted inside the specimen test carriage. Figures 4.55 and 4.56 are frames from a video; the former is a side view of the frame's web under full stationary load. No evidence of plastic buckling is present. Figure 4.56 shows the frame later in time, after the moving load has passed. While the distortion from the fish-eye lens make it difficult to discern, a severely buckled shape is evident on the left side of the figure in the stiffener's web, above the weld.

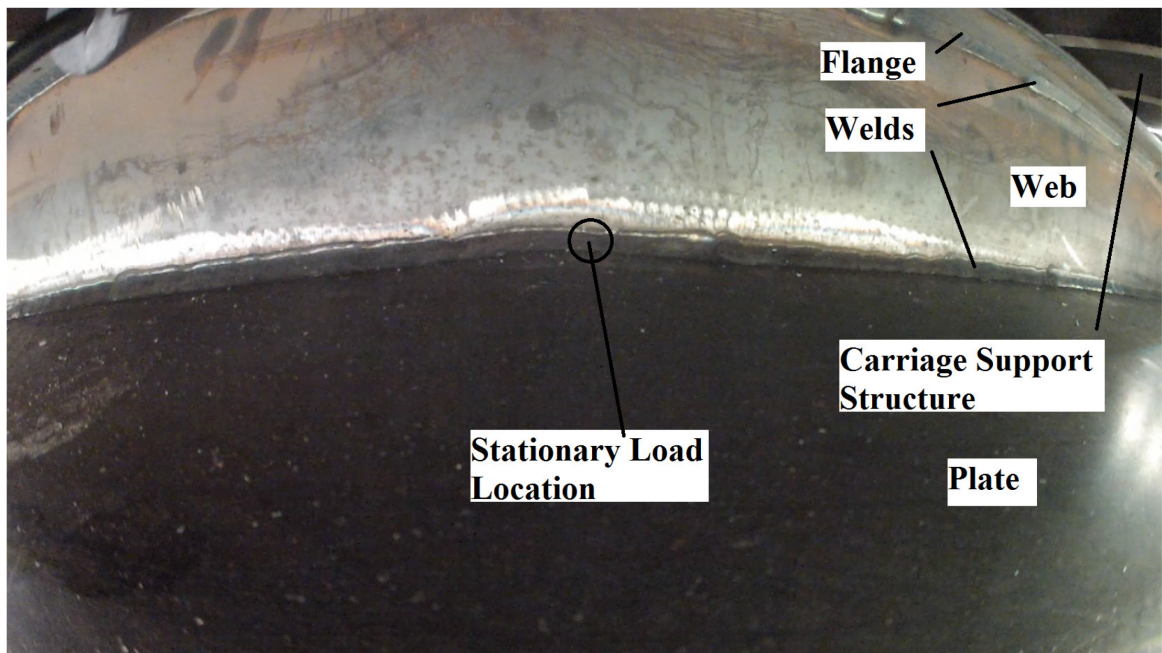


Figure 4.55: Fish-eye lens side view of frame's web under full stationary load.

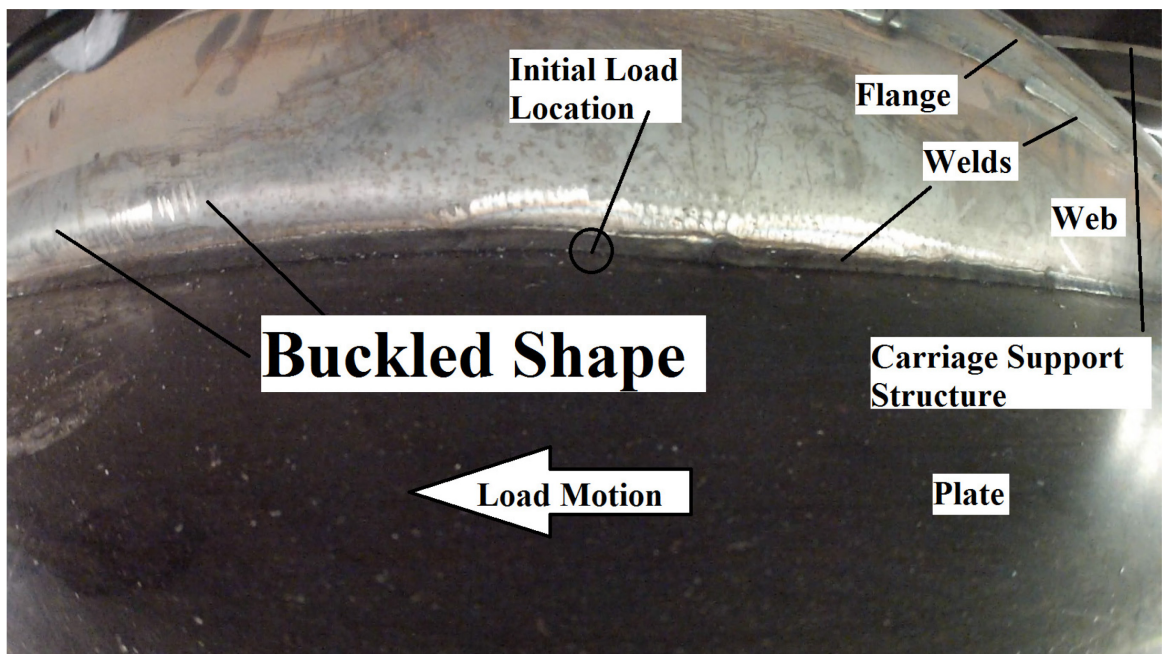


Figure 4.56: Side view of frame's web under moving load.

4.10.4 Effect of temperature

Table 4.17 presents the percentage difference in structural capacity at -10°C versus room-temperature (a difference of approximately 30°C). There is no apparent benefit or loss overall, as the data is scattered about 0%; and excepting the frame specimen, only ranging up to approximately $\pm 5\%$. The frame specimen appeared to benefit from a 12% increase in lateral structural capacity at the “End” position, but this value is an outlier and should be viewed with caution. Further, this value was calculated from comparison with the MovingLoad14 frame experiment, which has been identified above as likely having different boundary conditions than the rest of the experiments.

Table 4.17: Temperature effects gains relative to room-temperature for all three test specimen types.

	Temperature Effects Gains Relative to Room Temperature								
	Run Type								
	Slow Centre			Fast Centre			Slow End		
	Specimen Type			Specimen Type			Specimen Type		
	1/4 Plate	1/2 Plate	Frame	1/4 Plate	1/2 Plate	Frame	1/4 Plate	1/2 Plate	Frame
Normal Stationary at -550 mm	N/A	N/A	N/A	N/A	N/A	N/A	-1%	0%	-6%
Normal Stationary at 0 mm	-1%	1%	2%	-1%	4%	2%	N/A	N/A	N/A
Normal Moving at 0 mm	N/A	N/A	N/A	N/A	N/A	N/A	0%	0%	-2%
Normal Moving at 550 mm	3%	0%	-5%	3%	4%	3%	1%	1%	-4%
Lateral Moving at 550 mm	2%	1%	12%	3%	3%	12%	0%	1%	11%

4.10.5 Effect of starting location on lateral moving load capacity

With the notable exceptions of the frame experiments and, to a lesser extent the -10°C 2 cm indentation ¼” plate experiments, the lateral moving load capacity appears to be independent of the lateral indenter starting location for the ¼” plates and ½” plates.

4.11 Experiment Conclusions

Large structural capacity losses (i.e. moving load effects) were shown to exist for both controlled normal displacements and controlled normal forces causing plastic damage in plates and frames. This implies that moving load effects have very real consequences for hull structures, and that the design and analyses of the hulls of ships and offshore structures operating in conditions where they could be damaged plastically should explicitly account for moving load effects.

Strain-rate was shown to provide limiting mitigating effects against this capacity loss. This lends weight to the argument that strain-rate effects should be explicitly accounted for in the design and analyses of the hulls of ships and offshore structures.

A temperature differential of 30°C (between room-temperature and -10°C) appears to have little to no effect on the behaviour of plates or frames concerning moving load effects. Therefore, this suggests that changes in the yield strength and post-yield strength of hull steels due to changes in temperature are slight and need not be explicitly considered in the design and analyses of the hulls of ships and offshore structures. Note: this conclusion does not consider notch toughness or transition temperature.

Regarding the ice cone experiments, the most definitive result is the evidence of “chatter” (also known as “stick-slip” phenomenon) present in all slow speed tests. This phenomenon consisted of oscillations in both the horizontal and vertical planes. The frequency of each appeared to decrease with increasing load magnitude. Aside from this result, there is not enough evidence provided by the limited number of experiments

conducted to make any generalizations about the effect of lateral movement on the behaviour of ice. Vertical force results for the slow speed ice cone experiments involving elastic plate response were generally below comparable published values (as described above), while the single fast test was well above. Due to the variability inherent in ice loads, this data is not conclusive, and many more experiments are required in order to detect any trends. Regarding the experiments involving ice cones acting on plastically deforming plates, it was not possible to measure the deflection of the plates during the experiment. This makes it impossible to determine the relative deformation of the ice and the plate, compared with the imposed displacement on the ice cone holder. More experiments of this type are needed (with measurement of the deflection of the plate under load at various locations), so that the effects of load movement on both the ice, as well as the plastically deforming structure may be ascertained.

Results of the room temperature experiments on plates and frames are used in the following chapter to develop a numerical model with which to further study/predict moving load effects on hull structures.

Chapter 5 Numerical Simulations

Numerical simulations of three of the moving load experiments (geometries shown in Figure 5.1) were performed for the purposes of validating that the observed experimental effects can be simulated using the finite element method, as well as to provide insight into the phenomena leading to the loss of structural capacity observed for moving loads causing plastic damage versus similar stationary loads. One simulation was performed for each of the three specimen types: $\frac{1}{4}$ " plate, $\frac{1}{2}$ " plate and frame. The "slow" tests were used to benchmark the simulation cases so that the influence of strain-rate effects would be minimized (and thus yield strength becomes a constant, instead of a variable). At this stage in the research, neglecting strain-rate effects greatly simplifies the validation of the numerical simulations.

5.1 Scope and Objectives

The scope and objectives of the numerical simulations were to:

- Create and calibrate (using data from the experiments) a numerical model with which to replicate the room-temperature moving load experiments;
- Investigate the structural behaviour underlying the moving load effects;
- In particular, investigate the very early onset of plastic buckling of frame webs;
- Develop a robust bottom-up modeling strategy that can easily be replicated in order to assess/investigate moving load effects.

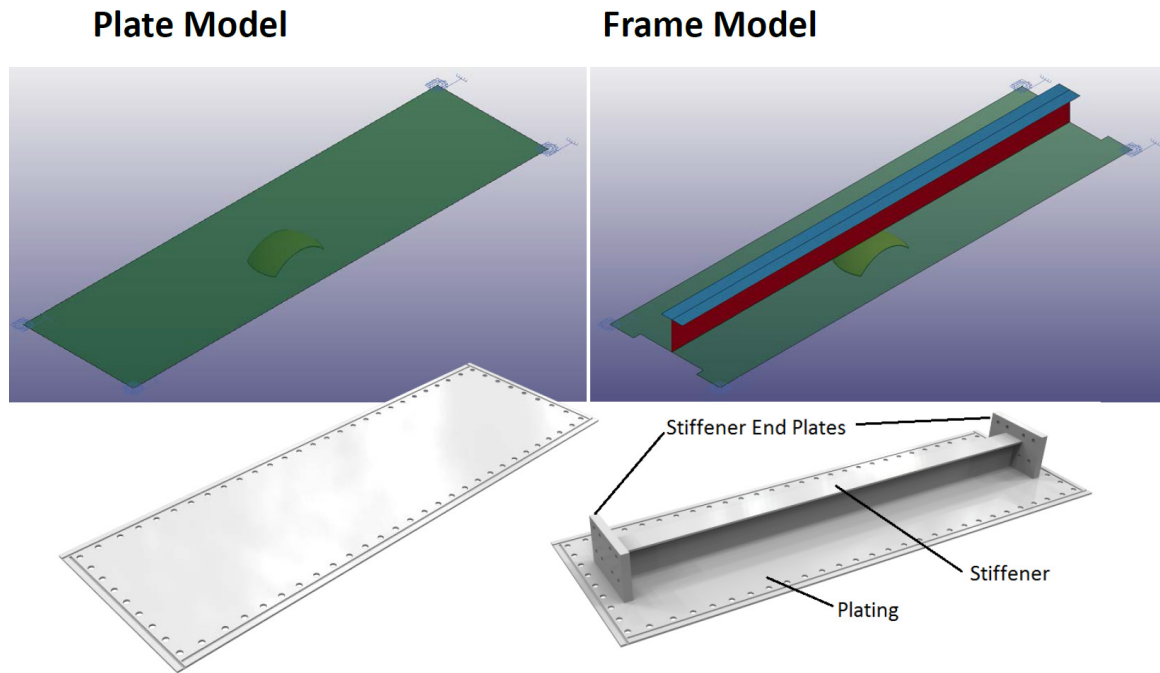


Figure 5.1: Plot of final numerical model geometries for the $\frac{1}{4}$ " and $\frac{1}{2}$ " plate cases (top left) and for the frame case (top right). Also shown, underneath, are renders of the physical specimens these numerical models represent.

5.2 Methodology

The objective of these simulations is to employ simple, standard and robust finite element techniques in order to adequately reproduce the behaviour observed in the moving load experiments discussed above. This methodology implies that solution times are minimized, and that the method is transferrable across similar finite element packages. This methodology is essentially a “bottom-up” approach²¹. As will be shown below, past experience with similar simulations and trial-and-error were used to optimize the simulations. Complexity was added only as necessary to capture the general behaviours

²¹ Here the term “bottom-up” refers to the process of adding complexity to the numerical model. Approach starts off with the most basic assumptions, and adds complexity as is needed in order to capture the behaviour of the experiments.

observed in the experiments. The following modelling approach was not developed without context however; as many numerical simulations were conducted during the design of the moving load apparatus in which it was often necessary to model components of the apparatus at a high level of detail. One example of this is the carriage, which was modeled entirely including a frame test specimen, bolted connections, the sandwich ring, and the rigid indenter. The experience gained from this and other detailed design simulations implicitly guided the numerical simulations presented herein.

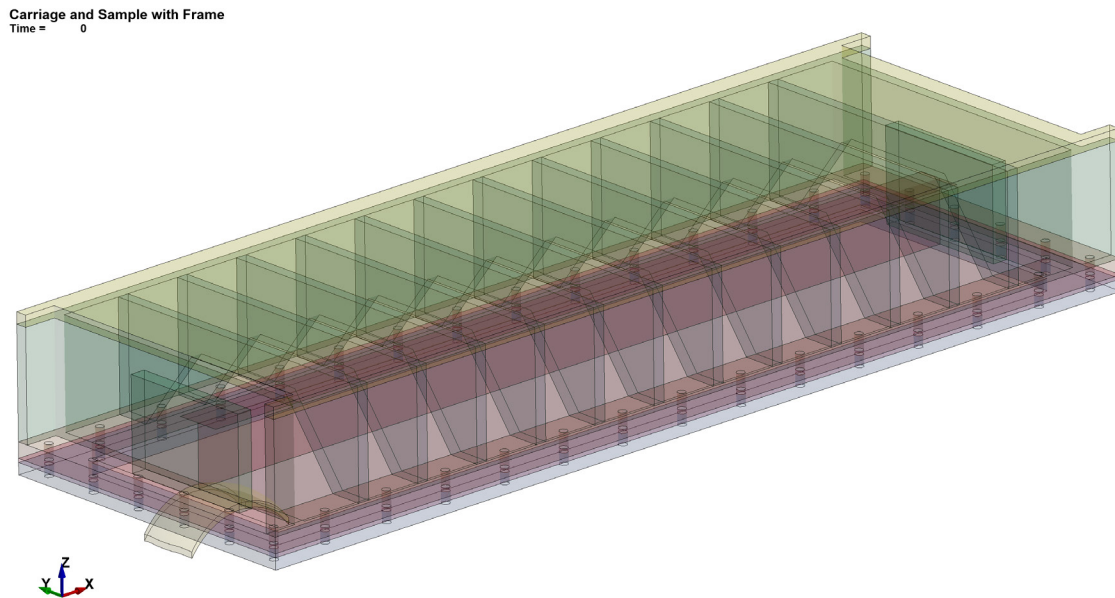


Figure 5.2: Transparent view of design simulation of carriage, framed sample, bolted connections, sandwich ring, and rigid indenter.

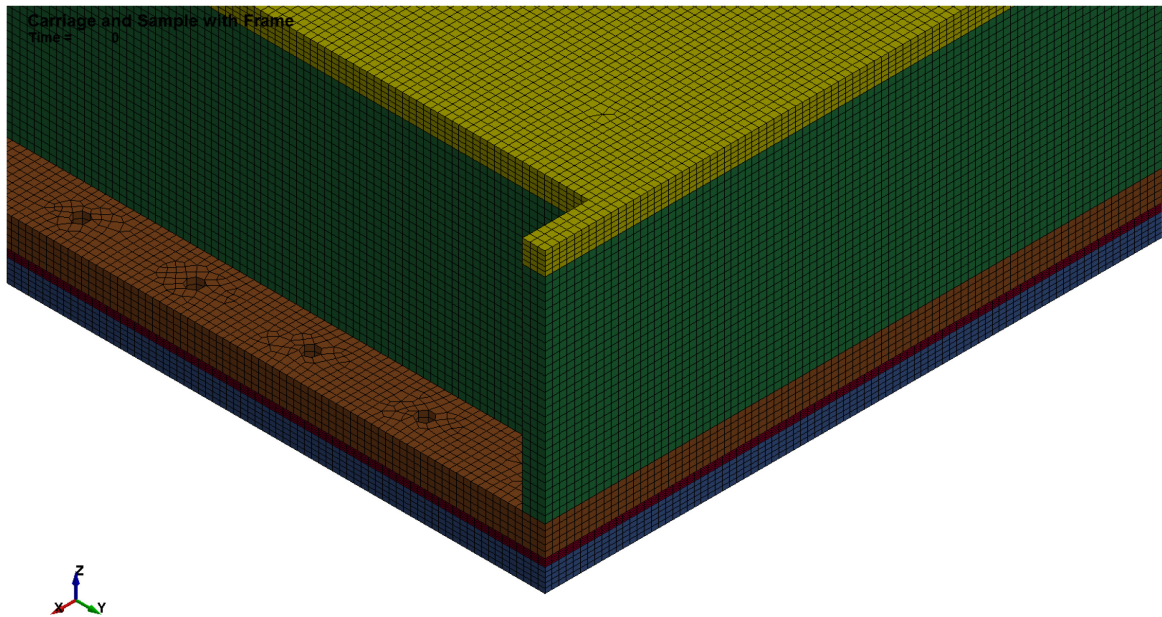


Figure 5.3: Mesh for simulation shown in Figure 5.2.

5.2.1 Finite element code capability requirements

Given that the moving load experiments exhibit highly nonlinear structural behaviour, contact between two bodies and generally transient behaviour, a transient finite element code with nonlinear geometric, material, and constraint capabilities was required for these simulations. Further, due to the large degree of deformation attained in the moving load experiments, it was decided to employ *explicit* time integration. LS-Dyna® was favoured for these simulations because it was originally created to solve highly nonlinear, transient dynamic finite element analyses using explicit time integration, and it incorporates extremely robust contact algorithms. Further, LS-Dyna is highly scalable on distributed memory computing platforms. This is a very attractive feature if one has access to a high performance computing (HPC) cluster, as the solution times of simulations are greatly reduced while the potential for numerical modelling accuracy through added detail and

enhanced ability to “fine-tune” is greatly increased. The author was able to use Memorial University of Newfoundland’s STePS² HPC cluster to leverage this capability in LS-Dyna.

5.2.2 Indenter motion

In order to benchmark these numerical models against the moving load experiments, it was decided to extract the indenter motions from the appropriate experiments and import them directly in the simulations as discussed in Chapter 5.3.9.

5.2.3 DOE determination of undefined variables

Three variables important to the successful numerical simulation of the moving load experiments were unknown: yield strength, tangent modulus, and the vertical compliance of the moving load apparatus. Regarding yield strength and tangent modulus, the type of steel used in the fabrication of the test specimens was known, and therefore the minimum values acceptable for that steel grade was known; however while the minimum values may be appropriate for design simulations, they are not accurate enough for accurate post-experiment analyses. Regarding the vertical compliance of the moving load apparatus, it is not possible to accurately determine this value after the experiments have been concluded.

The main purpose of this response surface analysis was to ascertain appropriate values for the yield strength, the tangent modulus and the moving load apparatus’s vertical compliance. Interaction effects between these three factors are not explored.

As the response of the test specimens was assumed to be dependent on these three unknowns, and the three unknowns were assumed to interact, a design of experiments

(DOE) (Montgomery 2008) central-composite response surface method (RSM) (Myers, Montgomery et al. 2009) was used to estimate their values and determine their overall impact on the response of the test specimens.

The central-composite response surface method was chosen because it excels at determining factor levels that simultaneously satisfy a set of desired specifications, as well as exploring the effect of changes in the factor levels over specified ranges. This is the type of optimization required as the *desired specifications* are the results of the moving load experiments, and the factor ranges are either known, or able to be estimated. It also provides guidance on the relative importance of each factor to the responses examined.

5.2.3.1 Factors level determination

The documentation that accompanied the steel used in all three test specimen types specified that the steel grade was “44W/50W”. This is not a single steel grade, but two separate steel grades: 44W(300W) and 50W(350W). The terms in brackets are the SI grade names, while the terms outside the brackets are the Imperial grade names). Both of these steel types comply with the Canadian Standard CSA G40.21 and have nominal material properties given in Table 5.1.

Table 5.1: Material Properties of 44W and 40W steels.

Mechanical Properties 44W/300W:	Mechanical Properties 50W/350W:
Tensile: 448 to 586 MPa [65 to 85 ksi]	Tensile: 448 to 655 MPa [65 to 95 ksi]
Minimum Yield: 303 MPa [44 ksi]	Minimum Yield: 345 MPa [50 ksi]
Elongation: 20% min in 8” 23% min in 2”	Elongation: 19% min in 8” 22% min in 2”
Source: www.chapelsteel.com	

These properties provide the ranges for the yield strength and tangent modulus factors. Regarding yield strength, the values given in Table 5.1 are guaranteed minimums. In practice, the values are likely to be very much higher. As it is not known whether the steel plate is 44W or 50W, the yield strength range's minimum was selected to be lesser of the two steel types: 300 MPa (44 ksi). The maximum was chosen to be 448 MPa (65 ksi) as this spans the range of both steels up to their guaranteed minimum tensile strength.

The ranges for the tangent modulus were initially determined via the following method.

Tangent modulus may be defined with the following equation:

$$E_t = \frac{\sigma_{tens} - \sigma_y}{\varepsilon_f - \varepsilon_y} \quad [3]$$

where: σ_{tens} is the true tensile strength
 σ_y is the yield strength
 ε_f is the failure strain
 ε_y is the yield strain

Note: use of the failure strain, ε_f , from Table 5.1 does not imply that material fracture was modeled in these simulations. This value was only used to define E_t for the strain hardening portion of the material curve. As no failure strain was input into the numerical model, infinite plastic strains are theoretically possible.

The minimum and maximum true tensile strengths were taken from Table 5.1, and are respectively 448 MPa (65 ksi) and 655 MPa (95 ksi). For the purposes of this analysis, the minimum elongation is assumed to be the failure strain, and is assumed to occur at the true

tensile strength. This value was chosen to be 20%. The yield strain is a function of the following equation:

$$\varepsilon_y = \frac{\sigma_y}{E} \quad [4]$$

where: E is Young's modulus and is assumed at 207 GPa

Therefore the minimum tangent modulus is given by:

$$E_{t,min} = \frac{\sigma_{tens,min} - \sigma_{y,max}}{\varepsilon_f - \left(\frac{\sigma_y}{E}\right)} = \frac{448 - 448}{0.20 - \left(\frac{303}{207000}\right)} = 0 \text{ MPa} \quad [5]$$

This minimum value of 0 is unrealistic; therefore the next highest value was substituted:

$$E_{t,min} = \frac{\sigma_{tens,min} - \sigma_{y,min}}{\varepsilon_f - \left(\frac{\sigma_y}{E}\right)} = \frac{448 - 303}{0.20 - \left(\frac{303}{207000}\right)} = 730 \quad [6]$$

The maximum tangent modulus is given by:

$$E_{t,max} = \frac{\sigma_{tens,max} - \sigma_{y,min}}{\varepsilon_f - \left(\frac{\sigma_y}{E}\right)} = \frac{655 - 303}{0.20 - \left(\frac{303}{207000}\right)} = 1773 \text{ MPa} \quad [7]$$

Subsequent analysis with values from Equations [6] and [7] did not yield satisfactory results. Therefore the range was modified to $E_{t,min} = 585 \text{ MPa}$ and $E_{t,max} = 976 \text{ MPa}$.

Regarding compliance of the moving load apparatus in the normal direction, this was the subject of a numerical sensitivity analysis, from which it was determined a valid range would be 1.0E-8 mm/N to 2.5E-8 mm/N. As will be discussed below, the normal compliance was implemented using four discrete linear springs in parallel, therefore the spring constant range for each individual spring was 1.0E7 N/mm to 2.5E7 N/mm. All factor levels are summarized in Table 5.2.

Table 5.2: Response surface factor level summary.

Yield low	Etan low	Spring Rate per spring low
303 MPa	585 MPa	1.0E7 N/mm
Yield high	Etan high	Spring Rate per spring high
448 MPa	976 MPa	2.5E7 N/mm

5.2.3.2 Responses measured

In order to quantify the influence of the above factors, four responses were monitored.

They are: peak normal stationary load, normal moving load at centre of plate, lateral moving load at centre of plate, and peak lateral moving load. Examples of the former two responses are shown in Figure 5.4 and the latter two responses in Figure 5.5.

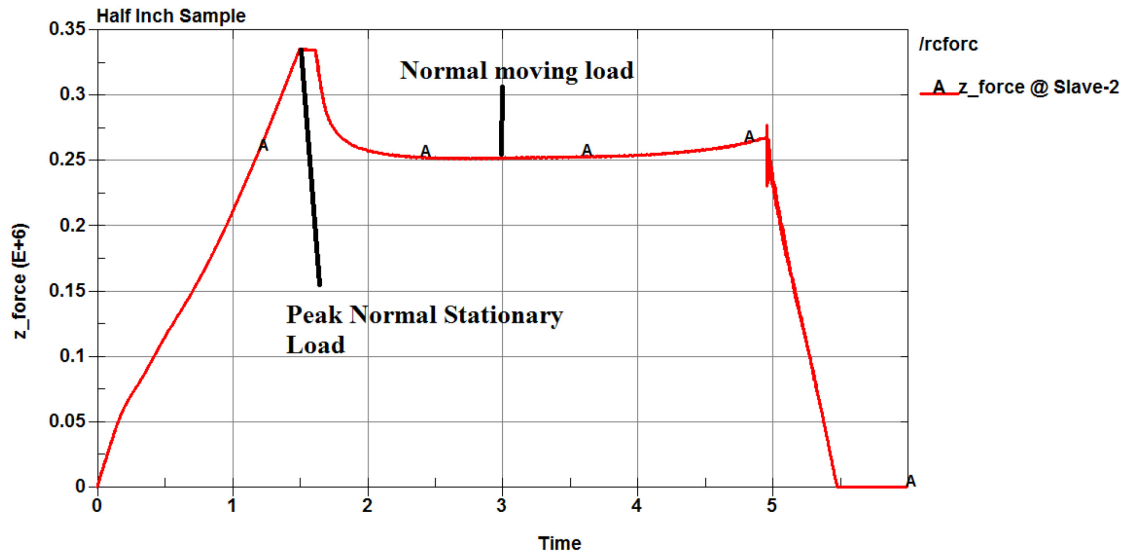


Figure 5.4: Normal direction load response measuring points.

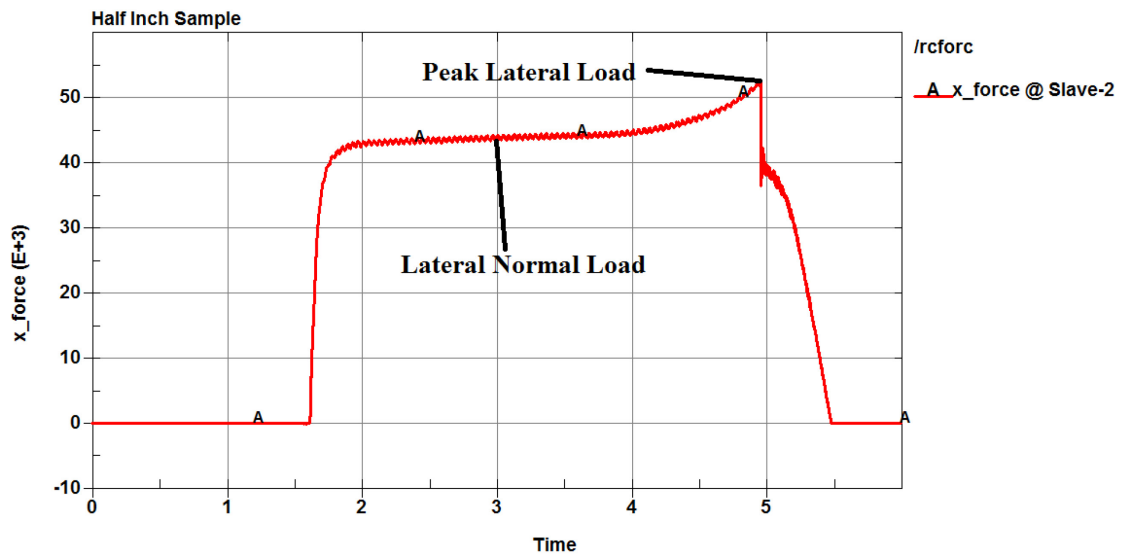


Figure 5.5: Lateral direction load response measuring points.

5.2.3.3 RSM design summary

For a normal central composite RSM analysis with three factors, there would be nineteen runs. Five centre-point runs and fourteen others. As the results for this RSM analysis come from a deterministic computer program, the centre point will always have the same response; therefore it is unnecessary to repeat the centre run. This brings the total number runs to fifteen.

Table 5.3 lists the factor levels for all fifteen runs.

Table 5.3: RSM factor levels and runs for all three specimen types.

Std. Run	Run	Factor 1: Yield	Factor 2: Etan	Factor 3: k
4	1	448.0	976.0	10000000
5	2	303.0	585.0	25000000
7	3	303.0	976.0	25000000
10	4	497.4	780.5	17500000
13	5	375.5	780.5	4886500
9	6	253.6	780.5	17500000
8	7	448.0	976.0	25000000
6	8	448.0	585.0	25000000
12	9	375.5	1109.3	17500000
3	10	303.0	976.0	10000000
2	11	448.0	585.0	10000000
1	12	303.0	585.0	10000000
14	13	375.5	780.5	30113000
15	14	375.5	780.5	17500000
11	15	375.5	451.7	17500000

5.2.3.4 ½” plate specimen DOE analysis and predictions

The results for the ½” plate case are given in

Table 5.4 and the design summary is given in Table 5.5.

Table 5.4: RSM run results for ½” plate case.

Std. Run	Run	Factor 1: Yield	Factor 2: Etan	Factor 3: k	Response 1: Ns	Response 2: Nm	Response 3: Ls	Response 4: Lm
4	1	448.0	976.0	10000000	336000	252000	43800	52500
5	2	303.0	585.0	25000000	308000	200000	42900	50100
7	3	303.0	976.0	25000000	317000	209000	44200	51900
10	4	497.4	780.5	17500000	416000	295000	54300	65900
13	5	375.5	780.5	4886500	232000	188000	29400	34800
9	6	253.6	780.5	17500000	261000	173000	36900	43200
8	7	448.0	976.0	25000000	420000	287000	35900	67800
6	8	448.0	585.0	25000000	413000	278000	55100	66500
12	9	375.5	1109.3	17500000	351000	244000	47600	57200
3	10	303.0	976.0	10000000	267000	191000	37000	43500
2	11	448.0	585.0	10000000	332000	246000	43500	52100
1	12	303.0	585.0	10000000	261000	184000	36200	42700
14	13	375.5	780.5	30113000	377000	247000	51500	60900
15	14	375.5	780.5	17500000	345000	237000	46800	56300
11	15	375.5	451.7	17500000	330000	219000	45000	53500

Table 5.5: RSM Design Summary for ½” plate case.

Study Type	Response Surface		Runs	15							
Design Type	Central Composite		Blocks	No Blocks							
Design Model	Quadratic										
Factor	Name	Units	Type	Subtype	Minimum	Maximum	Mean	Std. Dev.			
A	Yield	MPa	Numeric	Continuous	254	497	376	72			
B	ETan	MPa	Numeric	Continuous	452	1109	781	193			
C	k	N/m	Numeric	Continuous	4886500	30113000	17499967	7407468			
Response	Name	Units	Obs	Analysis	Minimum	Maximum	Mean	Std. Dev.	Ratio	Trans	Model
R1	Peak V Stationary	MPa	15	Polynomial	232000	420000	331067	59179	2	None	RQuadratic
R2	V mid H	MPa	15	Polynomial	173000	295000	230000	38881	2	None	RQuadratic
R3	H mid H	MPa	15	Polynomial	29400	55100	43340	7277	2	None	RLinear
R4	H end H	MPa	15	Polynomial	34800	67800	53260	9607	2	None	RQuadratic

An analysis of variance (ANOVA) for the Peak Normal Stationary Load response suggests that the model is significant (F value is 175.23), and that Factors A, C, AC and C² are significant (see Table 5.5 to relate factor letter code to factor name); implying the response is non-linear. Please note that while factor B, tangent modulus, was not considered significant, it was not removed from the response surface model; so the subsequent

optimization of the factor levels to attain the desired responses still depends on B for the peak normal stationary capacity.

ANOVA for the Normal Moving Load response suggests that the model is significant (F value is 204.10), and that Factors A, C, AC and C^2 are significant; implying the response is non-linear. It is interesting to note that tangent modulus is not considered a significant factor for the stationary normal load.

ANOVA for the Lateral Moving Load response suggests that the model is significant (F value is 6.42), and that Factors A and C, are significant; implying the response is linear. It is interesting to note that tangent modulus is not considered a significant factor for the stationary normal load.

ANOVA for the Lateral Peak Moving Load response suggests that the model is significant (F value is 204.10), and that Factors A, C, AC and C^2 are significant; implying the response is non-linear. As with the peak stationary capacity, tangent modulus was not significant, but not removed from the optimization.

Optimizing the factor levels for the experimental response value results provides the predictions shown in

Table 5.6.

Table 5.6: DOE optimized factors for experimental response values for ½” plate case.

Response	Experimental Result
Peak Stationary Normal Load	352000
Moving Normal Load	249000
Moving Lateral Load	47900
Peak Moving Lateral Load	64100
Factor	Optimized Value
Yield Strength	433
Etan	585
k	1.42E+07

5.2.3.5 ¼” plate specimen DOE analysis and predictions

The run results for the ¼” plate case are given in Table 5.7 and the design summary is given in

Table 5.8.

Table 5.7: RSM run results for ¼” plate case.

Std. Run	Run	Factor 1: Yield	Factor 2: Etan	Factor 3: k	Response 1: Ns	Response 2: Nm	Response 3: Ls	Response 4: Lm
12	1	375.5	1109.3	17500000	265000	142000	36100	41200
1	2	303	585	10000000	200000	107000	28000	31800
11	3	375.5	451.7	17500000	253000	133000	34200	39500
10	4	497.4299802	780.5	17500000	321000	175000	43100	49400
7	5	303	976	25000000	231000	120000	31200	35800
5	6	303	585	25000000	223000	113000	30200	34500
15	7	375.5	780.5	17500000	259000	154000	35100	40300
6	8	448	585	25000000	306000	161000	40600	47100
14	9	375.5	780.5	30113000	274000	141000	36400	42100
8	10	448	976	25000000	314000	167000	41600	48100
4	11	448	976	10000000	271000	171000	37600	42700
2	12	448	585	10000000	265000	165000	36800	41900
9	13	253.5700198	780.5	17500000	191000	110000	26200	29900
3	14	303	976	10000000	206000	125000	29000	32700
13	15	375.5	780.5	4886600	197000	118000	28700	32500

Table 5.8: RSM Design Summary for ¼” plate case.

Study Type	Response Surface		Runs	15							
Design Type	Central Composite		Blocks	No Blocks							
Design Model	Quadratic		Build Tim	2							
Factor	Name	Units	Type	Subtype	Minimum	Maximum	Mean	Std. Dev.			
A	Yield	MPa	Numeric	Continuous	254	497	376	72			
B	ETan	MPa	Numeric	Continuous	452	1109	781	193			
C	k	N/m	Numeric	Continuous	4886600	30113000	17499973	7407456			
Response	Name	Units	Obs	Analysis	Minimum	Maximum	Mean	Std. Dev.	Ratio	Trans	Model
R1	Peak V Stationary	MPa	15	Polynomial	191000	321000	251733	42763	2	None	RQuadratic
R2	V mid H	MPa	15	Polynomial	107000	175000	140133	23991	2	None	RQuadratic
R3	H mid H	MPa	15	Polynomial	26200	43100	34320	5258	2	None	RQuadratic
R4	H end H	MPa	15	Polynomial	29900	49400	39300	6215	2	None	RQuadratic

An analysis of variance (ANOVA) for the Peak Normal Stationary Load response suggests that the model is significant (F value is 264.18), and that Factors A, B, C, AC and C² are significant (see

Table 5.8 to relate factor letter code to factor name); implying the response is non-linear.

ANOVA for the Normal Moving Load response suggests that the model is significant (F value is 33.83), and that Factors A, C, AC and C^2 are significant; implying the response is non-linear. Like the 1/2" plate case, it is interesting to note that tangent modulus is not considered a significant factor for the stationary normal load. Despite its apparent insignificance, tangent modulus (factor B) was not excluded from the response surface fit of the data.

ANOVA for the Lateral Moving Load response suggests that the model is significant (F value is 251.12). Unlike the 1/2" plate case where only Factors A and C are significant, Factors A, B, C, AC and C^2 are significant for the 1/4" plate case; implying the response is non-linear. It should be pointed out that while the tangent modulus was not a significant factor for the normal moving load response, the RSM model predicts that it is significant for the lateral moving load response.

ANOVA for the Lateral Peak Moving Load response suggests that the model is significant (F value is 313.53), and that Factors A, B, C, AC and C^2 are significant; implying the response is non-linear.

Optimizing the factor levels for the experimental response value results provides the predictions shown in Table 5.9. It should be noted that the vertical spring rate predicted is less than the low factor level; therefore the RSM model is extrapolating this value.

Table 5.9: DOE optimized factors for experimental response values for 1/4" plate case.

Response	Experimental Result
Peak Stationary Normal Load	211000
Moving Normal Load	128000
Moving Lateral Load	27500
Peak Moving Lateral Load	37000
Factor	Optimized Value
Yield Strength	378.8
Etan	585
k	6.3380E+06

5.2.3.6 Frame specimen DOE analysis and predictions

The run results for the frame case are given in

Table 5.10 and the design summary is given in Table 5.11.

Table 5.10: RSM run results for frame case.

Std. Run	Run	Factor 1: Yield	Factor 2: Etan	Factor 3: k	Response 1: Ns	Response 2: Nm	Response 3: Ls	Response 4: Lm
4	1	448	976	1.00E+07	292000	227000	50500	65400
5	2	303	585	2.50E+07	258000	160000	45900	51900
7	3	303	976	2.50E+07	265000	177000	49300	57500
10	4	497.43	780.5	1.75E+07	347000	240000	59600	75500
13	5	375.5	780.5	4.89E+06	214000	193000	34100	47100
9	6	253.57	780.5	1.75E+07	227000	147000	41800	48000
8	7	448	976	2.50E+07	344000	234000	59300	74000
6	8	448	585	2.50E+07	343000	217000	59500	68300
12	9	375.5	1109.3	1.75E+07	295000	208000	51800	66300
3	10	303	976	1.00E+07	234000	171000	43300	54600
2	11	448	585	1.00E+07	289000	211000	50600	64200
1	12	303	585	1.00E+07	230000	156000	40100	49900
14	13	375.5	780.5	3.01E+07	314000	199000	55000	63600
15	14	375.5	780.5	1.75E+07	291000	196000	51400	62800
11	15	375.5	451.71	1.75E+07	282000	195000	49400	60000*

* This value was estimated because the simulation failed to run to completion as the 451.71 MPa tangent modulus level caused an instability.

Table 5.11: RSM Design Summary for frame case.

Study Type	Response Surface		Runs	15							
Design Type	Central Composite		Blocks	No Blocks							
Design Model	Quadratic										
Factor	Name	Units	Type	Subtype	Minimum	Maximum	Mean	Std. Dev.			
A	Yield	MPa	Numeric	Continuous	254	497	376	72			
B	ETan	MPa	Numeric	Continuous	452	1109	781	193			
C	k	N/m	Numeric	Continuous	4886500	30113000	17499967	7407468			
Response	Name	Units	Obs	Analysis	Minimum	Maximum	Mean	Std. Dev.	Ratio	Trans	Model
R1	Peak V Stationary	MPa	15	Polynomial	214000	347000	281667	43698	2	None	RQuadratic
R2	V mid H	MPa	15	Polynomial	147000	240000	195400	28595	2	None	Linear
R3	H mid H	MPa	15	Polynomial	34100	59600	49440	7443	2	None	RQuadratic
R4	H end H	MPa	15	Polynomial	47100	75500	60607	8946	2	None	RQuadratic

An analysis of variance (ANOVA) for the Peak Normal Stationary Load response suggests that the model is significant (F value is 154.86), and that Factors A, C, AC and C² are significant (see Table 5.11 to relate factor letter code to factor name); implying the response is non-linear. It is interesting to note that tangent modulus is not considered significant with respect to normal peak stationary capacity.

ANOVA for the Normal Moving Load response suggests that the model is significant (F value is 253.75), and that Factors A, B, and C are significant; implying the response is linear. It is interesting to note that tangent modulus is considered a significant factor for the stationary normal load for the frames; where it was not for either of the plate cases. Figure 5.6 shows the results for four simulations where tangent modulus was varied between 1.0 GPa to 2.0 GPa. As predicted by the RSM, there is a much more pronounced effect on the normal moving load capacity than on the normal peak stationary capacity.

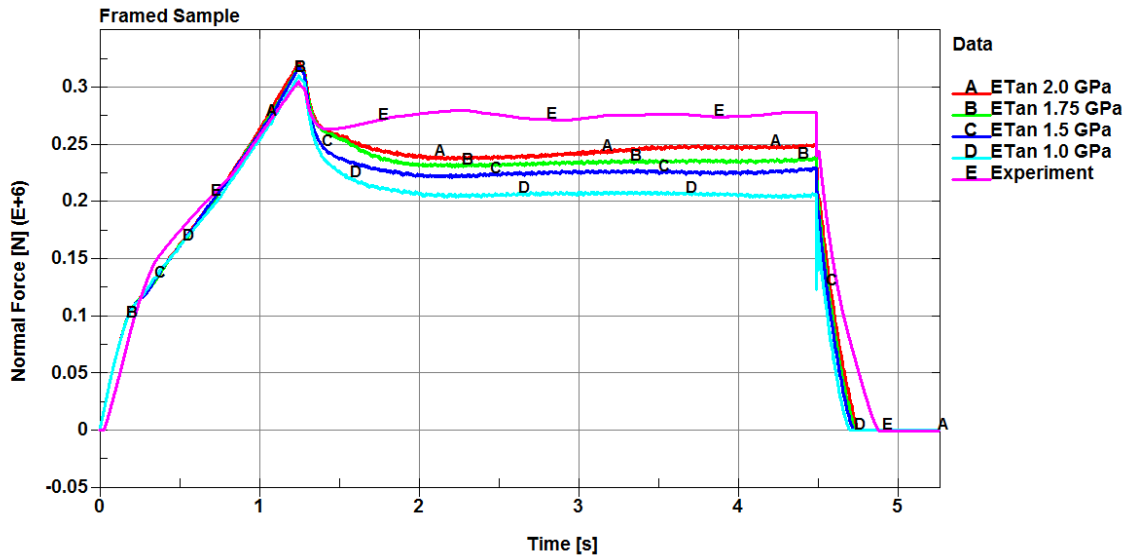


Figure 5.6: Normal Capacity for a Frame with varying tangent modulus.

ANOVA for the Lateral Moving Load response suggests that the model is significant (F value is 42.45), and that Factors A, C, and C^2 , are significant; implying the response is non-linear. Tangent modulus is not significant here (but left in the response optimization model).

ANOVA for the Lateral Peak Moving Load response suggests that the model is significant (F value is 58.73), and that Factors A, B, C, and C^2 are significant; implying the response is non-linear.

It should be noted that the factor optimization for the frame case required extrapolation for all response variables except peak normal stationary capacity. Optimizing the factor levels for the experimental response value results provides the predictions shown in Table 5.12.

Table 5.12: DOE optimized factors for experimental response values for frame case.

Response	Experimental Result
Peak Stationary Normal Load	306000
Moving Normal Load*	272000
Moving Lateral Load*	60100
Peak Moving Lateral Load*	80300
Factor	Optimized Value
Yield Strength	378.8
Etan	976
k	2.5800E+07

* These responses required extrapolation during the optimization.

As the steel used in the ¼” plate test specimens is the same steel used in the frame specimens, the RSM optimization for the frame case used 378.8 MPa as a target value for the yield strength factor (i.e. the value from the results of the ¼” RSM optimization). According to the two RSM models, the tangent modulus was more significant for the frame specimen than for the ¼” plate specimen, so it was not subject to a targeted value.

5.2.3.7 A note about vertical compliance

The vertical compliance factor, implemented as a linear spring in the numerical model, is meant to account for the fact that the experimental moving load apparatus is not perfectly

rigid. The outcome of the RSM DOE analyses yielded three different spring constants; one for each of the $\frac{1}{4}$ " plate, $\frac{1}{2}$ " plate and frame cases. These values were 6.338 [MN/m] for the $\frac{1}{4}$ " plate, 15.8 [MN/m] for the $\frac{1}{2}$ " plate, and 14.2 [MN/m] for the frame. One might expect that this value should be constant; implying a linear vertical compliance. Linearity may not be a good assumption in this case, as there are many nonlinearities in the physical system. Some examples are: a slight gap between the MTS crosshead and the beams supporting the linear roller-rail system; a small leak in the hydraulic system operating the locks keeping the MTS crosshead in place; and the fact that the hydraulic pump was powering more than just the moving load apparatus. Additionally, the magnitude of force applied to the $\frac{1}{4}$ " plates was significantly less than that applied to both the $\frac{1}{2}$ " plates and frames. If the vertical spring constant was indeed nonlinear (as the DOE analysis suggests) than the fact that it is higher for the $\frac{1}{2}$ " plate and frame cases, than for the $\frac{1}{4}$ " plate case, is plausible.

5.3 Numerical Model

The following sections describe the required inputs with which to numerically model moving loads, as well as the factors and decisions leading up to their implementation.

5.3.1 Precision

All simulations were solved in *single precision*. The level of *precision* refers to either single or double floating-point format. LS-Dyna recommends using *single precision* for structural simulations of this type. It was verified for these simulations that there was no significant change in the results when the simulations were solved in *double precision*.

5.3.2 Geometry modeled

Given the rigidity of the moving load apparatus's carriage and vertical load supporting structure, initial application of the bottom-up approach implies that only the geometry of the test specimens and the rigid indenter need be modeled; as the test specimen would absorb the vast majority of the energy put into the system by the hydraulic rams.

5.3.2.1 Test specimen geometries

Initially, the geometries shown in Figures 5.7 and 5.8 were simulated. Note the plating is divided into two sections. The green section is the part that is free to deform while the yellow part is clamped between the moving load apparatus's sandwich ring and carriage, and is restrained horizontally by the bolt holes.

Carriage and Sample with Frame

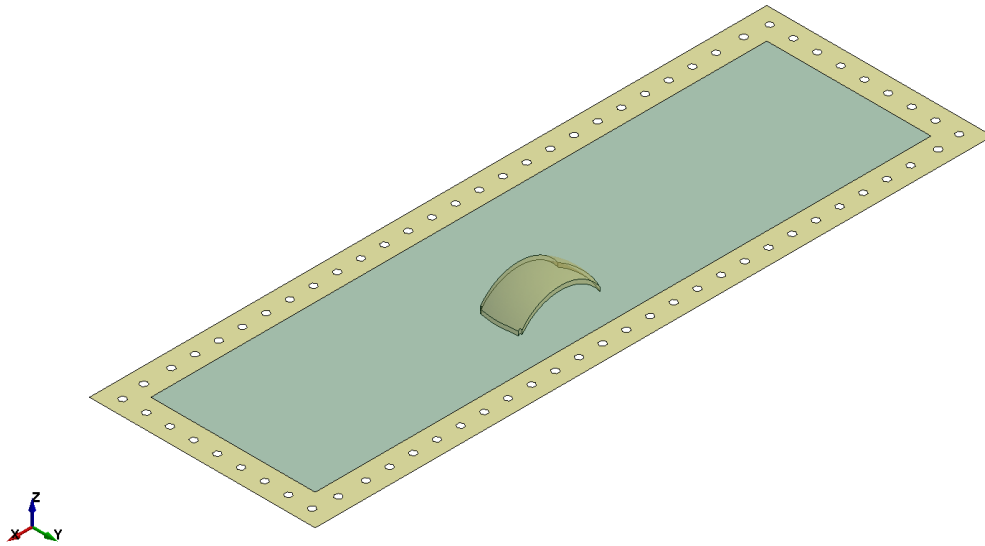


Figure 5.7: Transparent view of geometry for plate test specimens: plate and rigid indenter.

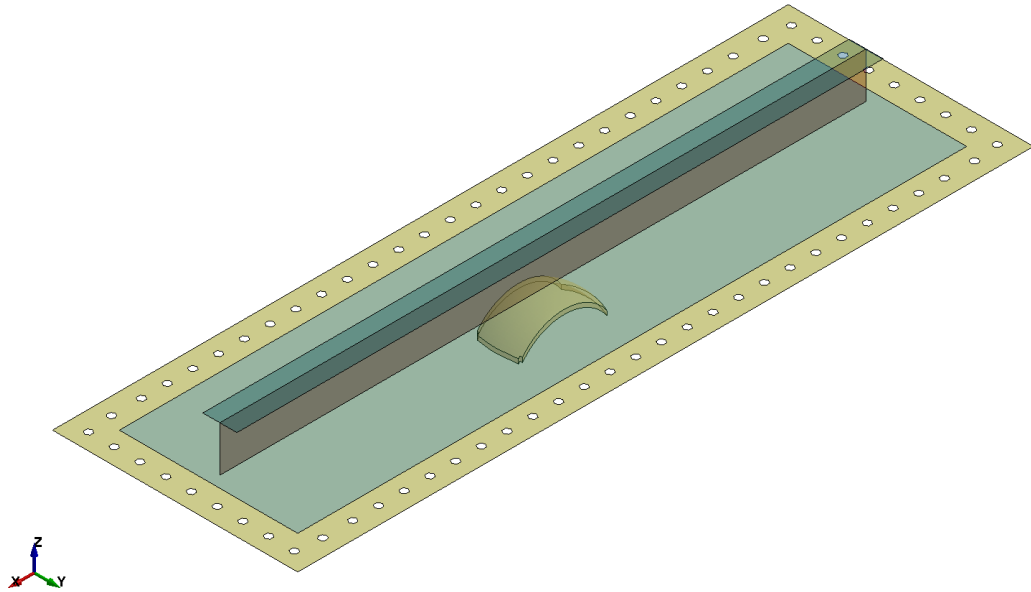


Figure 5.8: Transparent view of frame test specimen geometry: plate, “T” stiffener and rigid indenter.

Trial-and-error showed that there was negligible difference in the results if the yellow portion of the plating was omitted (for both plate and frame test specimens); and instead the edges of the green section were fixed on all degrees of freedom. Additionally, for the framed specimens, it was determined that it was not necessary to model the portion of the plate under the stiffener end plates (shown in Figure 5.9). The stiffener end plates existed to provide boundary conditions for the stiffener during the moving load experiments, and it was unnecessary to model the plating underneath them as that portion of the plate was also fixed by the stiffener end plates.

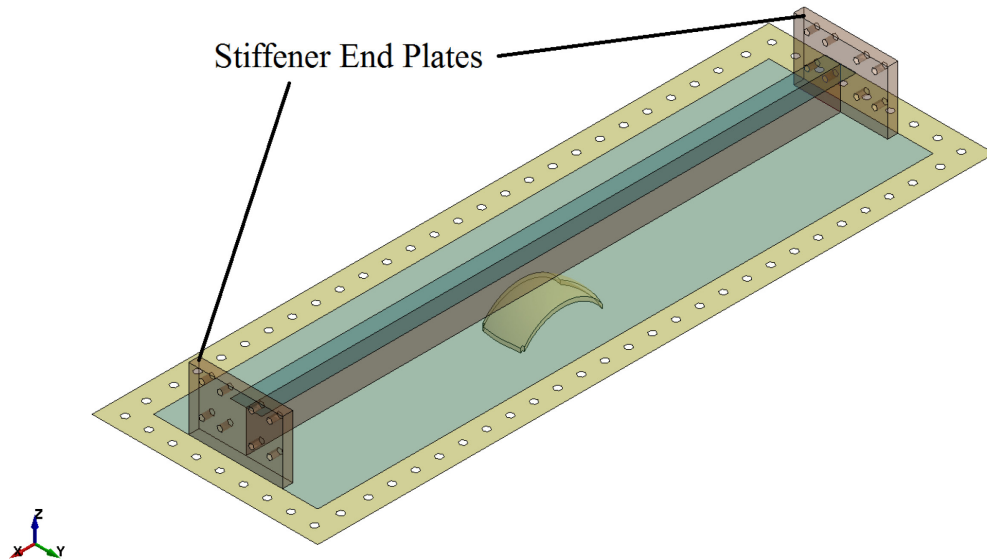


Figure 5.9: Framed specimen geometry shown with stiffener end plates.

Figures 5.10 and 5.11 show the final geometries for each specimen type. Because the test specimens' plating was modeled with shell elements, plate thickness is a parameter of the shell element and therefore this thickness is not reflected in the geometry. This allows the same geometry to be used for plate test specimens of all thicknesses.

Half Inch Plate

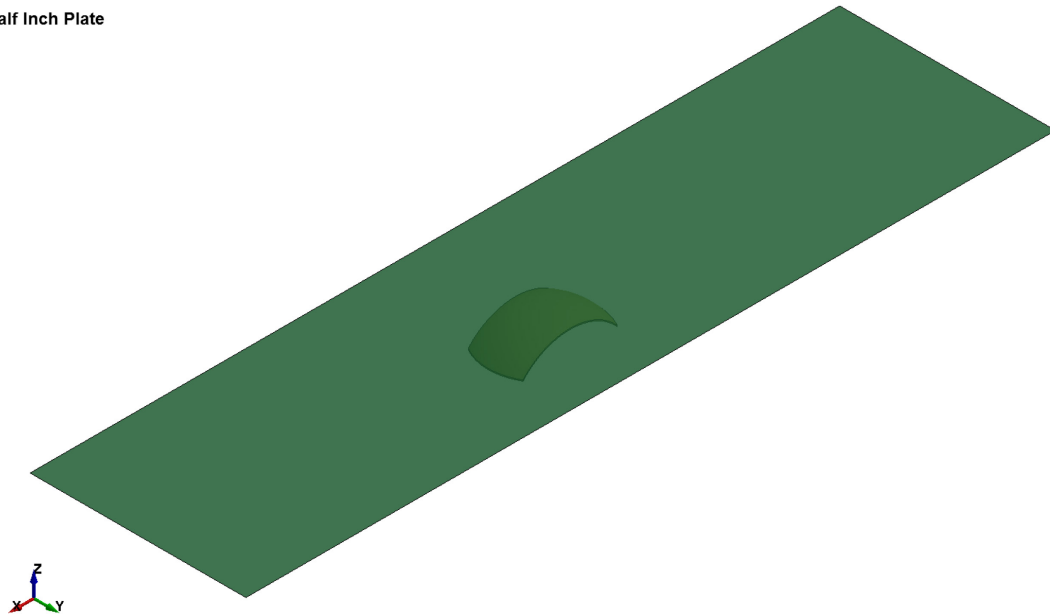


Figure 5.10: Final plate test specimen geometry (shown transparent).

Framed Sample

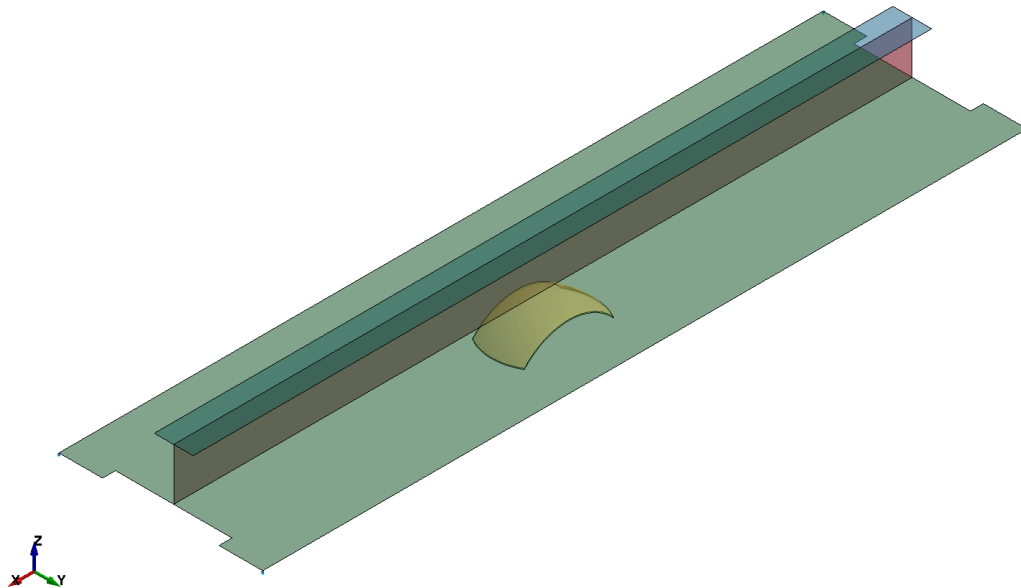


Figure 5.11: Final frame test specimen geometry (shown transparent).

5.3.2.2 Indenter geometry

The steel wheel indenter used in the moving load experiments is a 10.16 cm (4 in.) wide section of a 25.4 cm (10 in.) diameter sphere centred on the sphere's equator. To get the geometry for these simulations, a hollow sphere (i.e. a shell) of these dimensions was modeled in a CAD (computer aided design) program, then the appropriate sections were trimmed away leaving the desired 10.16 cm (4 in.) section (see Figure 5.12).

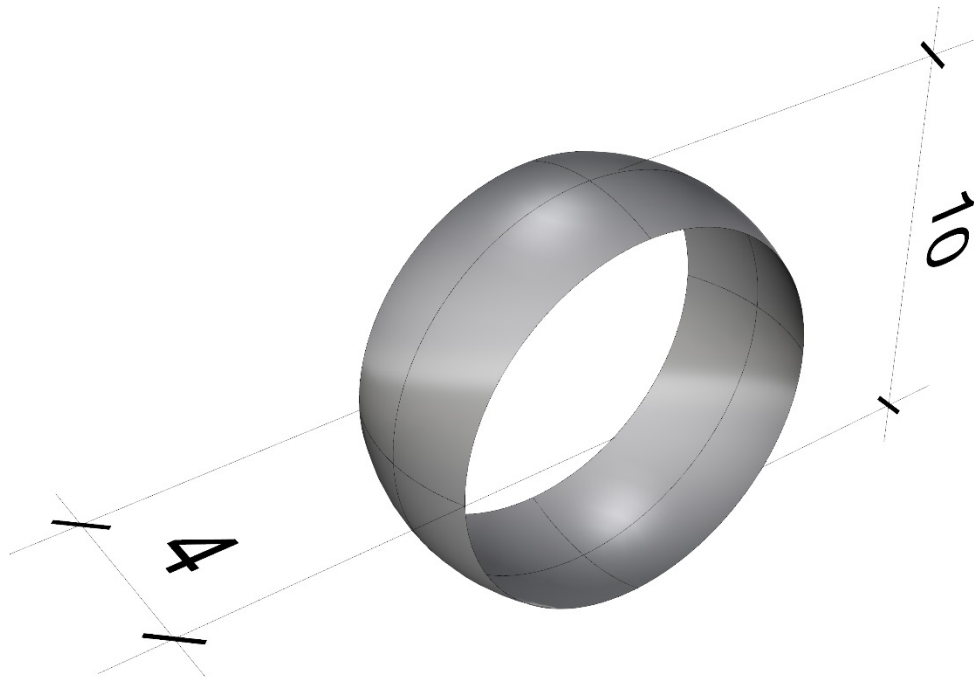


Figure 5.12: Indenter: hollow sphere section (dimensions in inches).

The largest indentation normal to the plating for any of the moving load experiments was 4 cm (1.575 in.). Also, because the moving load experiments involving the rigid indenter were frictionless, and sliding friction was not modeled in these simulations, it was not necessary to complicate these simulations by having the indenter spin about its centreline.

Instead a wedge of the indenter 5 cm (2 in.) in depth was trimmed out and used as the steel wheel indenter geometry (see Figure 5.13).

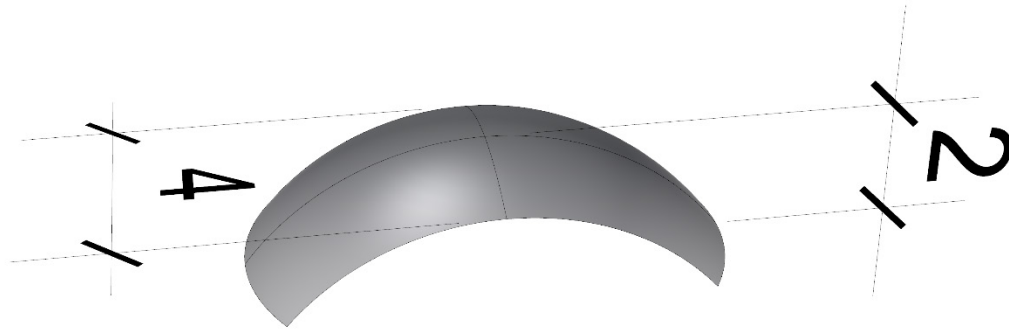


Figure 5.13: Indenter: final geometry (dimensions in inches).

5.3.3 Boundary conditions

The following sections present a description of the boundary conditions employed in the numerical simulations carried out for this thesis, as well as guidance for simulations outside their scope.

As discussed below, the simulations in this thesis exclusively employ shell elements for the deformable structure. During the development of these “final” simulations, trial simulations were carried out where the stiffener end plates were explicitly modeled; using solid elements. While it was determined that modeling the stiffener end plates was unnecessary for the final simulations, it was discovered that mating shell and solid elements is not trivial. As it is likely that combinations of shell and solid elements might be used for various reasons when modeling ship structures, guidance, based on the experience of this work, is provided in this section for interfacing solid and shell elements.

5.3.3.1 Evolution by trial-and-error and final boundary conditions

From initial trial-and-error numerical simulations, it was discovered that the “bottom-up” assumption that most of the energy would be absorbed by the test specimen was not valid. With the initially fixed boundary conditions in the vertical (i.e. normal) direction the stationary loads were too high, and the moving loads were too low. This is a significant result that implies that the normal boundary stiffness has a significant result on the moving load behaviour of a plate or frame. It is believed that a small but noticeable amount of energy was being directed into recoverable elastic deformation of the vertical supporting structure and the hydraulics system; or in other words, the moving load apparatus has a noticeable compliance in the vertical (i.e. normal) direction.

It was decided to numerically model this recoverable vertical compliance using discrete linear springs. To accomplish this, the nodes on the boundaries of the plating were converted into a “constrained nodal rigid body” (CNRB); implying that they move together as a rigid body, and that their positions relative to each other are fixed. The horizontal (x- and y-direction) translations and all rotations were then fixed; while vertical translation was left free. Four discrete linear springs (one at each corner of the plating) were then applied. The spring constant was deduced by a design of experiments (DOE) central-composite response surface analysis (along with other factors) as outlined in Chapter 5.2.3. Figure 5.14 depicts the CNRB boundary (brown) with attached linear springs (blue) for a plate specimen. Please note, the lines connecting all nodes to one node in particular are inconsequential to the behaviour of the nodes as a system and exist as part of how the nodal rigid body is defined internally in LS-Dyna.

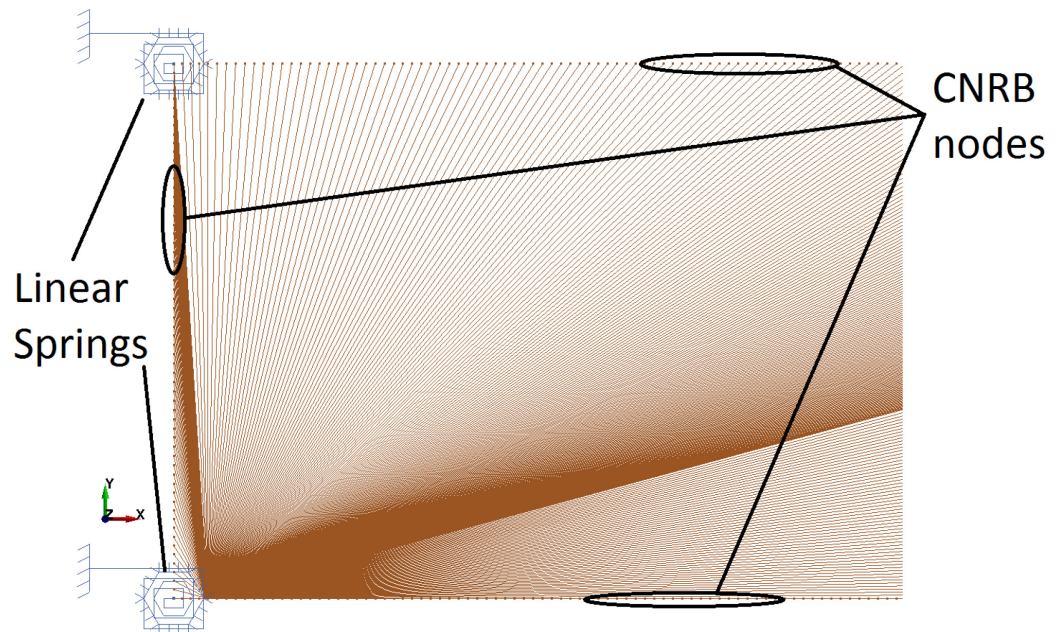


Figure 5.14: Plan view of plating boundary conditions (half of plate specimen shown).

5.3.3.2 Indenter boundary conditions

The rigid wheel indenter's motion is restricted in the y-direction, and in rotations about x, y, and z. Its translation in the x and z directions are prescribed as outlined in Chapter 5.3.9. Contact between the test specimen's plating and the indenter is detected as detailed below. The fact that the rigid wheel indenter is restricted in rotation is inconsequential from the viewpoint of interface forces because friction is not included in the contact interface definition. The two bodies slide past each other without friction.

5.3.3.3 Guidance on interfacing solid and shell elements

As discussed in section 5.3.3, the stiffener end plates were modeled during the evolution of these numerical models. Although they are not present in the final numerical models, this section details a method for mating solid and shell elements, and a rudimentary method to include welds between them.

The “T” stiffener and plating were modeled using shell elements and the stiffener end plates were modeled with solid elements. Defining connections between solid elements and shell elements is not trivial as thickness is a parameter for two dimensional shell elements, while it is explicitly geometrically defined for three dimensional solid elements. There are at least two methods to connect shell elements to solid elements in LS-Dyna: implementation of the *CONSTRAINED_SHELL_TO_SOLID card, or through the use of constrained nodal rigid bodies (CNRB). The latter method was chosen for these simulations due to its efficacy in this case. Essentially, given a body comprised of shell elements that shares an edge interface with a body comprised of solid elements, but without coincident nodes (i.e. the meshes are not connected; which is the recommended situation) both of the above methods allow the nodes at the interface to be “tied” such that motion of a shell node at the interface will induce motion in nodes of the solid body that fall within the thickness parameter of the shell element. Figure 5.15 depicts the connection of the stiffener flange (blue shell elements) and the stiffener web (red shell elements) to the stiffener end plate (brown solid elements) using a CNRB (yellow).

It should be noted that a shell element’s “reference surface” must be considered when mating solid and shell elements. The reference surface for the web’s shell elements (red) lies half way along their “thickness” (i.e. zero reference surface offset). As such, the neutral axes of these shells coincide with their “reference surface”. Unlike the web, the reference surface for the flange’s shell elements is offset to the negative vertical extent of the shell “thickness”, implying that the shell’s neutral axes are half their thickness above their reference surfaces. The reference surfaces were chose this way so that the “thicknesses”

of the perpendicular shells do not overlap (see Figure 5.16). These offsets are important for how the shell-to-solid interfaces are defined. Figure 5.15 shows that the nodes of the flange (blue) have been tied to the horizontally adjacent solid element nodes of the stiffener end plate, as well as the solid element nodes one shell thickness above. The nodes of the web have been tied to adjacent solid element nodes within half the shell thickness to either side of the shell.

Quarter Inch Plate with Frame

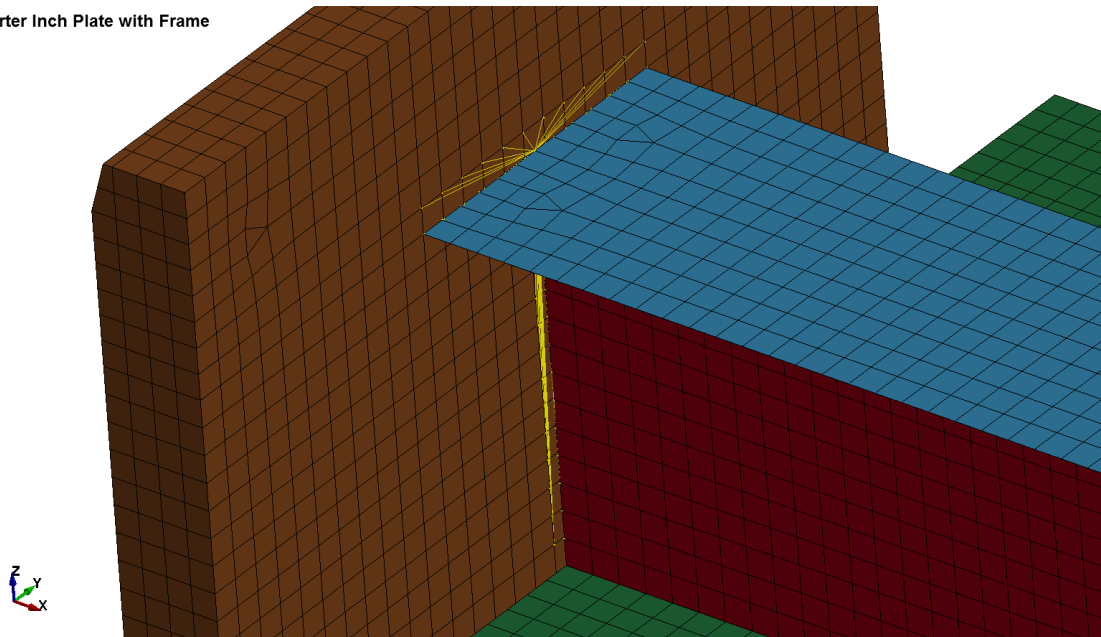


Figure 5.15: Internal “shell to solid” CNRB connection (yellow).

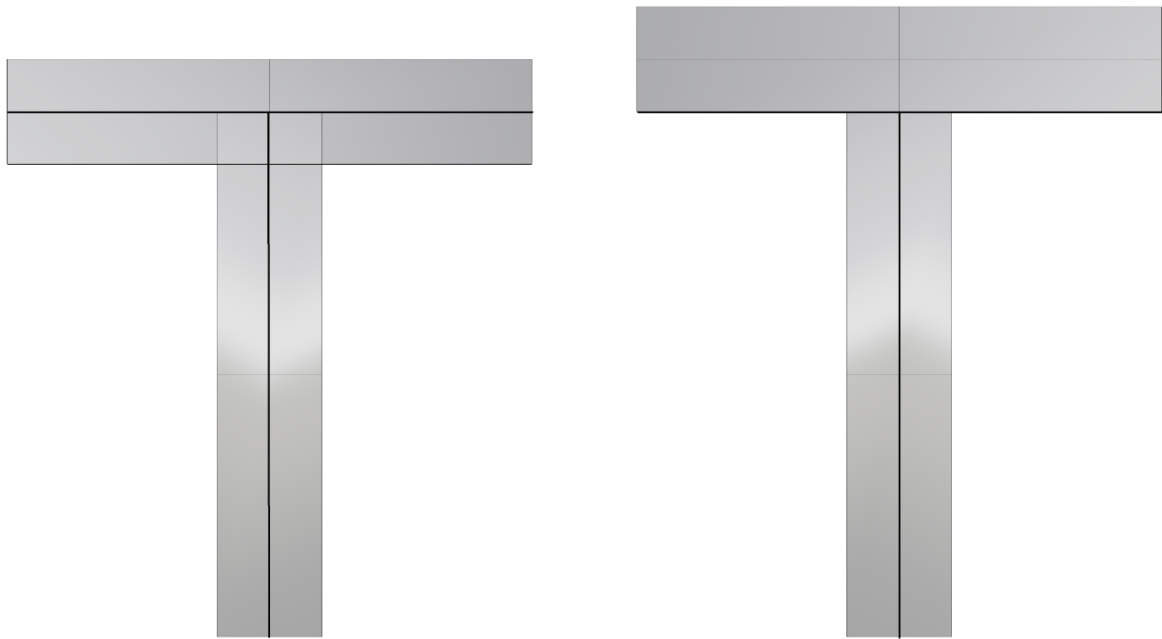


Figure 5.16: Shell reference surfaces (black) with zero offset (left) and with full offset to one side (upper right “flange”).

The nodes of the plating are attached to the stiffener end plates in a similar manner. The reference surface for the plating shell elements are offset away from the stiffener web (i.e. negative z -direction). Rather than have overlapping plate and solid elements, and to facilitate the shell to solid transition, it was decided to extend the stiffener end plate material through the plating (see Figures 5.17 and 5.18). The resulting structure is no different than the experimental test specimens as the same volume of steel is present; and it responds in the same way.

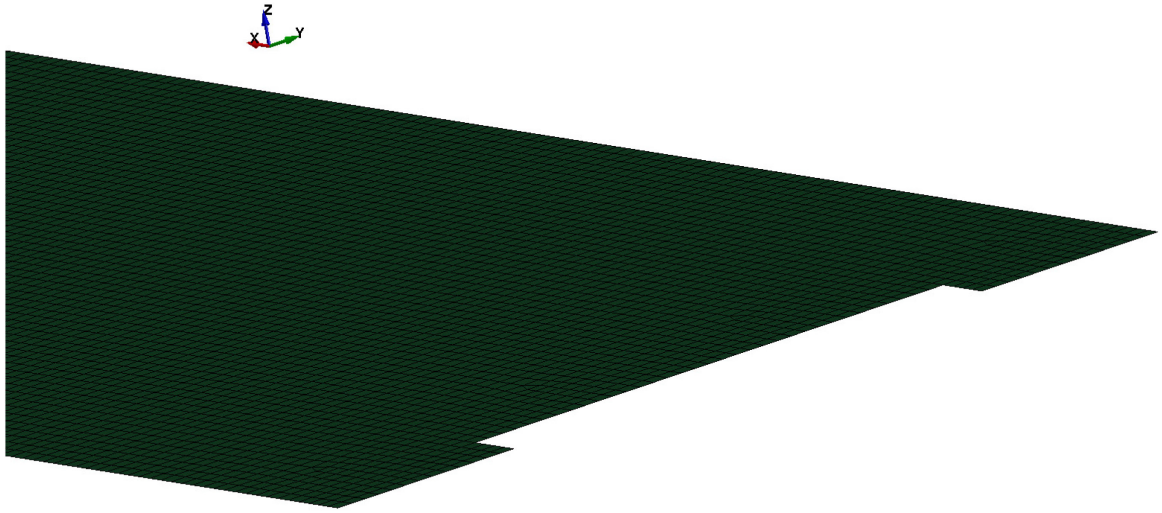


Figure 5.17: Plating showing cut-out for stiffener end plate.

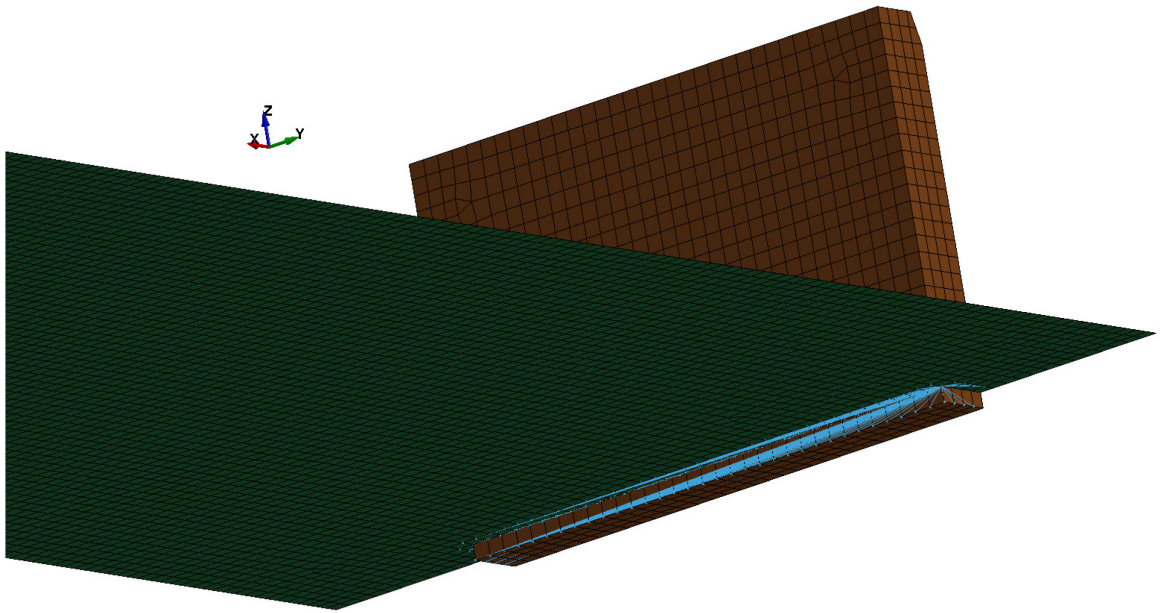


Figure 5.18: Internal connection for plating and stiffener end plate.

Additionally, it was a simple matter to capture the weld toe between the stiffener end plates and the plating by including extra elements at the appropriate locations in the CNRB definition. Figure 5.19 depicts a CNRB (blue) that joins the solid elements of the stiffener end plate to the shell elements of the plating. The nodes immediately adjacent to the solid-shell interface nodes were positioned at the location on the plate where the weld toe would be. These nodes were included in the CNRB definition, and thus the weld geometry was included in the model as a rigid body.

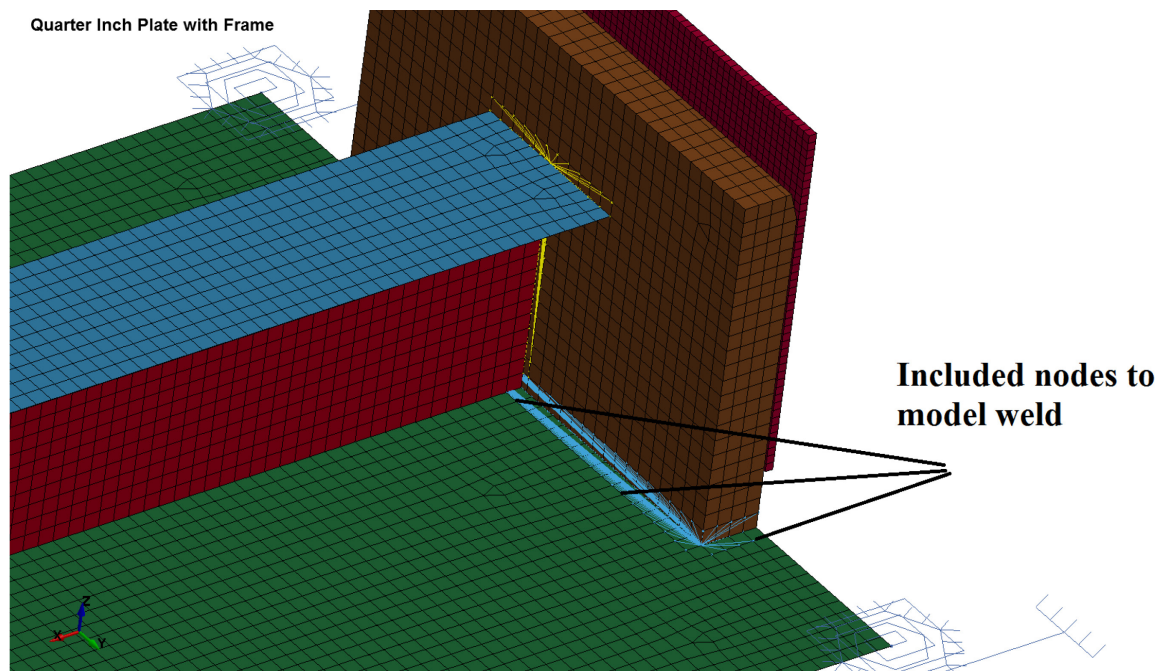


Figure 5.19: CNRB (blue) with added nodes to simulate rigid weld geometry.

5.3.3.4 Summary of boundary conditions

Tables 5.13 and 5.14 summarize the global and internal finite element boundary conditions, respectively. Please note that these tables reflect the final numerical model boundary

conditions, as presented in Chapters 5.3.3.1 and 5.3.3.2. Boundary conditions described in Chapter 5.3.3.3 were not included in the final numerical model.

Table 5.13: Summary of global finite element boundary conditions.

Part	X-Translation	Y-Translation	Z-Translation	X-Rotation	Y-Rotation	Z-Rotation
Plate	CNRB	CNRB	Vertical Linear Springs	CNRB	CNRB	CNRB
Stiffener Ends	CNRB	CNRB	Free	CNRB	CNRB	CNRB
Rigid Indenter	Prescribed Motion	Fixed	Prescribed Motion	Fixed	Fixed	Fixed

Table 5.14: Summary of internal connections between finite element parts.

Part Connections	Plating	Stiffener Web	Stiffener Flange
Plating	-	Continuous Mesh	Continuous Mesh
Stiffener Web	Continuous Mesh	-	Continuous Mesh
Stiffener Flange	Continuous Mesh	Continuous Mesh	-

5.3.4 Finite element meshes

Shell elements were used exclusively to model the test specimens. Solid elements were used for the steel wheel indenter mesh. Solid elements are not recommended for modeling plates or frames for several reasons. Reduced integration solid elements do not capture plate bending properly unless there are at least five layers of solid elements through-thickness. Implementing a minimum of five solid element layers through-thickness either leads to solid elements that are much thinner in one direction, and hence not well formed; or excessively small, well-formed solid elements. Either way, the single small dimension will drastically decrease the simulation's stable time-step size. This coupled with the added expense of utilising solid elements leads to excessively long run times with little to no

benefit in accuracy over shell elements. Fully-integrated solid elements would alleviate this bending problem somewhat (e.g. only two to three layers may be required), but these element types suffer from shear and/or volumetric locking as Poisson's ratio nears the incompressible limit (i.e. 0.5), limiting their effective use to linear-elastic or small-strain plastic problems.

Beam elements are not recommended for modelling moving loads causing plastic damage either. A possible application for beam elements may be to model the stiffener attached to the plating for the frame test specimens. This is not recommended for this purpose where large deformations occur, because beam elements generally do not incorporate membrane stretching; which plays an important role not only in the plating, but also in the frame's stiffener.

5.3.4.1 Plate specimen mesh

The finite element mesh for the plating of both plate sample types ($\frac{1}{4}$ " and $\frac{1}{2}$ " plates) is shown in Figure 5.20. The geometry is meshed entirely with 12,255 quadrilateral shell elements, which have an average edge length of 7 mm (0.276 in.).

Plate Samples Mesh

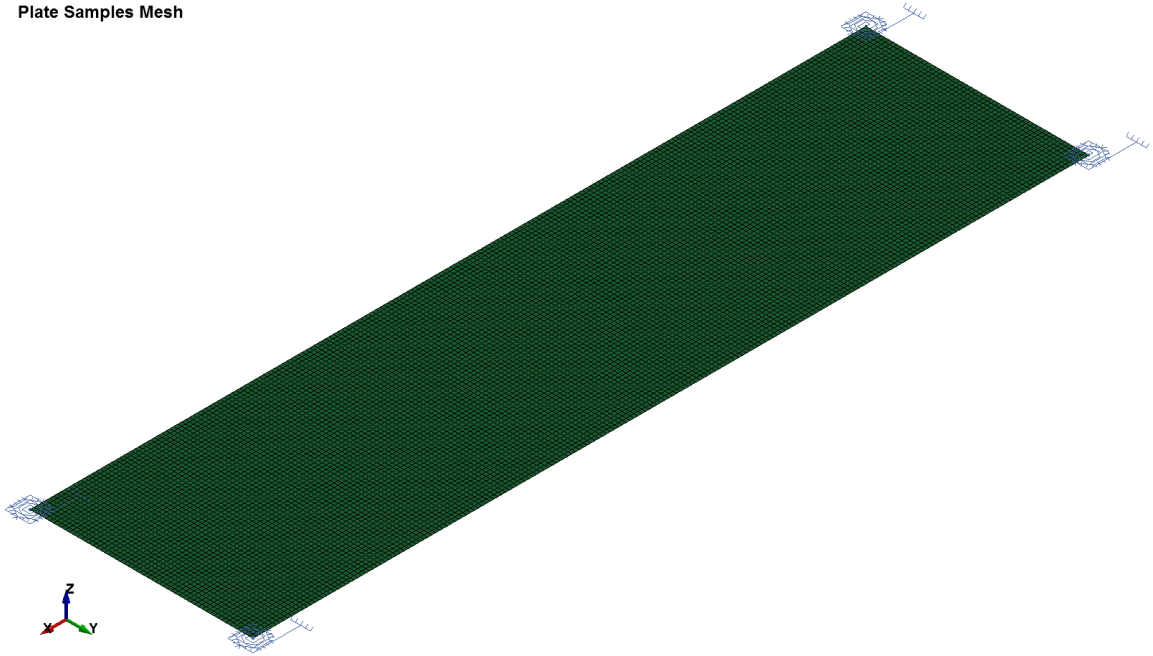


Figure 5.20: Final shell element mesh for plate sample types.

For the $\frac{1}{4}$ " plates (6.35 mm thick), the average shell element edge length is approximately 7.5 mm (0.3 in.). This implies a very fine mesh. The same mesh was used for the $\frac{1}{2}$ " plates (12.7 mm thickness); which implies an extremely fine mesh. Caution is advised when using elements with edge lengths less than their thickness for two reasons: 1. Depending on the shell formulation used, this may violate the formulation of the shell element and impact the bending response of the shell; and 2. when used with *automatic* contact algorithms in LS-Dyna, the program will assume the larger of either the element edge length, or the thickness to be the *contact thickness*. In this case, contact between bodies will occur too soon unless a specific contact thickness is explicitly defined. The contact thickness was explicitly set for these numerical simulations by defining the plate with a PART_CONTACT card and setting the *contact thickness* with option *OPTT*, in Card 2.

Shell sensitivity study

The shell element formulation used in these simulations is LS-Dyna's default: type 2 – Belytschko-Lin-Tsay. Shell element formulation was the subject of an extensive sensitivity study, where all of LS-Dyna's compatible shell element types were trialed to correctly model the behaviour of the web of the framed specimens under moving loads. The other shell formulations investigated were *type 1* – Hughes-Liu shells, *type 16* – Fully Integrated shells, *type 10* – Belytschko-Wong-Chiang shells, *type 8* – Belytschko-Leviathan shells, *type 6* – selectively reduced (S/R) Hughes-Liu shells, *type 25* – Belytschko-Lin-Tsay shells with thickness stretch, and *type 26* – Fully Integrated with thickness stretch. The criteria for selecting the best shell element type was (in descending order of importance): structural behaviour compared with the results of the moving load experiments, energy ratio, and solution time. Energy ratio is defined by the following equation:

$$E.R. = \frac{E_{total}}{E_{total}^0 + W_{ext}} = \frac{E_{kin} + E_{int} + E_{si} + E_{rw} + E_{damp} + E_{hg}}{E_{kin}^0 + E_{int}^0 + W_{ext}} \quad [8]$$

where:

E_{kin} is the kinetic energy

E_{int} is the internal energy

E_{si} is the sliding interface energy (including friction)

E_{rw} is the rigid wall energy

E_{damp} is the damping energy

E_{hg} is the hourglass energy

E_{kin}^0 is the initial kinetic energy (i.e. at time $t = 0$)

E_{int}^0 is the initial internal energy (i.e. at time $t = 0$)

W_{ext} is the external work

This ratio should be close to 1, and variations away from unity may indicate various problems (including contact issues, hourglassing, etc...). Simulation time is the length of real time it takes for a simulation to run to completion. The various shell element formulations model various behaviours and treat some behaviours in different ways; and therefore require different numbers of calculations (per timestep) to implement.

In addition to the various shell element formulations, various shell control parameters were also part of the sensitivity study, specifically: warping stiffness, shell thinning, full iterative plasticity, various numbers of through thickness integration points, and through thickness integration method (Gaussian versus Lobatto). Shell thinning may be modeled explicitly as a shell undergoes membrane stretching. Shell thinning was found to have no benefit for these simulations. Full iterative plasticity refers to how the stress-strain curve is utilised during plastic deformation. It is particularly effective at utilising noisy experimental stress-strain curves, but had no appreciable benefit for a standard bilinear material model. On the surface, this option would appear to be a material option, however is only applicable to shell elements in LS-Dyna. The number of through thickness integration points (NIP) directly affects the accuracy of the shell results as strains are assumed to be linear through the shell thickness. No benefit was found from adding more than 5 NIP in these simulations. There are two options for through thickness integration method: Gaussian and Lobatto. The former places the outermost integrations at the location relative to the shells outer surface as given in Table 5.15. Lobatto integration places the outermost integration points at the shell surface. Lobatto integration was tried for these simulations,

but negatively affected the structural behaviour. Gaussian integration was subsequently used in the final simulations.

Table 5.15: Relative position of outermost point for Gaussian integration for shell elements.

		Midplane (0.0)
Outermost Point	2 NIP	0.5774
	3 NIP	0.7746
	4 NIP	0.8611
	5 NIP	0.9062
		Outer Surface (1.0000)

The CONTROL_SHELL option CNTCO, which is meant to account for shell reference surface offsets in the treatment of contact between bodies, caused some very strange behaviour in these models, and its use was abandoned (LS-Dyna version 971R7.1.1 was used for these simulations).

In summary shell elements with the following attributes were selected for these numerical simulations:

Table 5.16: Summary of shell element attributes.

Attribute	Value
Type	Belytschko-Lin-Tsay
Shear Factor	5/6
Through Thickness Integration Points	5
Through Thickness Integration Method	Gaussian
Shell Thinning	No
Warping Stiffness	Yes
Projection method for warping stiffness	Full

5.3.4.2 Framed specimen meshes

The parameters of the mesh for the framed specimen are identical to those of the plate specimen meshes except that are 17,168 quadrilateral, and 24 degenerate triangular shells. The framed specimen mesh is shown in Figure 5.21.

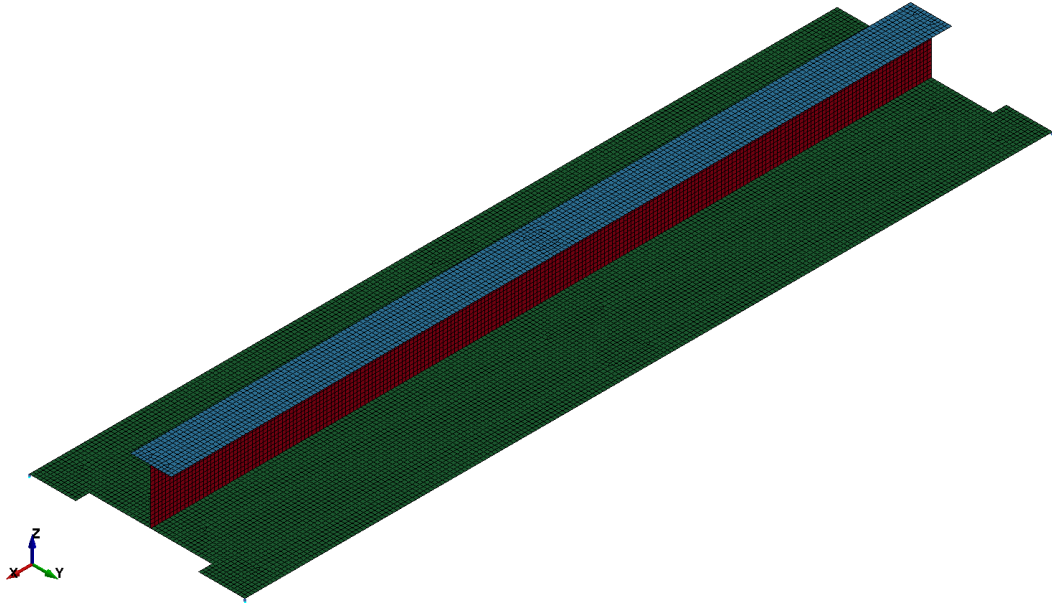


Figure 5.21: Final framed specimen mesh.

5.3.4.3 Indenter mesh

While the indenter geometry is a surface (as defined in 5.3.2) it was desired to have the indenter meshed with solid elements, as solid to shell contact is more robust than shell to shell contact (Hallquist 2006, ANSYS Inc. 2011). Shell to shell contact is slightly more complicated than shell to solid contact because shell thickness is considered in the contact algorithm employed. The contact interface has to be inferred from two “pseudo” surfaces for shell to shell contact, instead of one “pseudo” surface and one geometric surface for the case of shell to solid contact. Any error in detection of the nodes near the contact surface

can lead to penetration of nodes through the contact surface. This can be a problem for rigid shells, which would be the case for these simulations if shells were used for the indenter mesh.

In order to mesh the indenter with solid elements, the surface geometry was temporarily meshed with shell elements, and these shells were then extruded into solid elements (and the shells subsequently deleted). The extrusion distance was equal to the average edge length of the shell elements (see Figure 5.22).

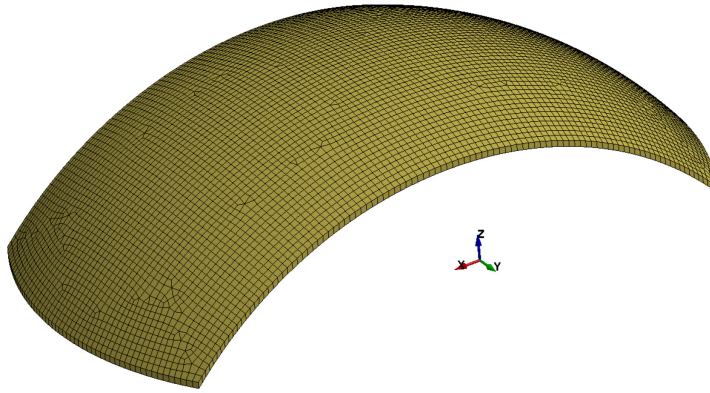


Figure 5.22: Rigid indenter mesh.

An average element edge length of 2 mm (0.079 in.) was chosen, as it is smaller than the average edge length of the mesh of the plating, and it captures the curvature of the steel wheel indenter very well. Further, increasing mesh density for rigid bodies is usually recommended by LS-Dyna, as it not only improves the discretization of the bodies shape, it improves the inertial properties of the rigid body as well.

5.3.4.4 Mesh convergence study

A mesh convergence study identifies the ideal point between simulation efficiency and accuracy. Several mesh sizes were examined: 5 mm, 7 mm, and 10 mm edge lengths. They all converged to a similar solution for the plate samples, but the 7 mm mesh was found to be optimal for the framed samples as it took considerably less time to run the simulations to completion.

5.3.5 Material model

The bottom up modelling approach, implies that the simplest material models that capture the required phenomena be initially chosen. They are PLASTIC_KINEMATIC (Mat_3) (Hallquist 2006, LSTC 2014) and MAT_RIGID (Mat_20) (Hallquist 2006, LSTC 2014). Mat_3 was used to model the deformable structure and Mat_20 was used to model the rigid indenter.

The Mat_3 material is properly titled *Elastic Plastic with Kinematic Hardening*. It is capable of modelling bilinear elasto-plastic behaviour; including strain-rate effects and element failure (in the form of element erosion at a specified strain). The inputs for Mat_3 are: density, Young's modulus, Poisson's ratio, yield strength, tangent modulus, beta, C , p , failure strain, and rate effects formulation. Density, Young's modulus, Poisson's ratio, and yield strength need no explanation. Tangent modulus is slope of the plastic hardening curve. Beta is the value defining the ratio between completely kinematic hardening (i.e. migration of the centre of the yield surface with a fixed yield radius), 1.0, and completely isotropic hardening (i.e. fixed centre of yield surface with yield radius as a function of plastic strain), 0.0. A sensitivity study showed that a beta value of 1.0 provided the best

results for these numerical simulations. C and p are the Cowper-Symonds parameters used in implementing strain-rate effects as discussed in Chapter 2.5.2. Strain-rate effects were not included in these simulations as they were deemed not to be a factor for the “slow” moving load experiments utilised in the benchmarking of these models. Failure strain is simply a finite strain at which an element disappears (including its mass) from the simulation. Failure strain was not employed in these simulations. Finally rate effects formulation is a switch that defines whether the Cowper-Symonds model uses the “total strain-rate” (i.e. including elastic strain-rate), 0.0, or the “plastic strain-rate” (excluding the elastic strain-rate), 1.0. A sensitivity study showed that the structural response for these simulations was more accurate when the plastic strain-rate was used (i.e. $VP=1$).

Mat_3 is commonly used for modeling metals that may (or may not) exhibit kinematic hardening as it is a very mature and efficient material model.

The Mat_20 rigid material model is a convenient way of turning a part into a rigid body. Rigid bodies are extremely efficient because rigid elements are bypassed in the element solving, and no storage is allocated for saving their history variables (Hallquist 2006). Inputs for Mat_20 include inertia properties, Young’s Modulus, and Poisson’s ratio. The latter two inputs are used for determining sliding interface parameters for contact with other bodies. Another convenience of using Mat_20 is that it allows for explicit definition of the degrees of freedom (DOF) for the rigid body. The user can choose a local or global coordinate system and is able to restrict all 6 DOF independently. Mat_20 was used to model the steel wheel indenter because the steel wheel indenter itself was designed to approximate a rigid body.

5.3.5.1 Material constants

The exact material properties are not known for the steel used in these moving load experiments. The type of steel is known, and therefore the normal range of material properties for this class of steel is known. A significant hurdle in benchmarking these numerical models was determination of the proper material constants. This was accomplished – in tandem with determining the vertical compliance of the moving load apparatus – by employing *design of experiments*. A “central-composite” “response surface analysis” with three factors was employed, as described in Chapter 5.2.3.

The inputs for these material models are given in Tables 5.18 and 5.17.

Table 5.17: Plastic-kinematic material model inputs by specimen type.

Mat_3			Plastic Kinematic		
Specimen Type					
1/4" Plate and Frame			1/2" Plate		
Density	Young's Modulus	Poisson's Ratio	Density	Young's Modulus	Poisson's Ratio
7850 kg/m ²	207 GPa	0.3	7850 kg/m ²	207 GPa	0.3
Yield Strength	Tangent Modulous	Beta	Yield Strength	Tangent Modulous	Beta
379	plate: 585 frame: 976	1	433	585	1
C	p	Failure Strain	C	p	Failure Strain
0	0	0	0	0	0
VP			VP		
1			1		

Table 5.18: Rigid material model inputs.

Mat_20	Rigid Material	
Density	Young's Modulus	Poisson's Ratio
7850 kg/m ²	207 GPa	0.3
Global/Local	Translations Fixed	Rotations Fixed
Global	y	x,y,z

5.3.6 Section definitions

Element formulations, element constants and certain controlling parameters for the various elements are input using SECTION cards.

The SECTION_SHELL cards used required the following inputs: ELFORM, SHRF, NIP, thickness, and NLOC. ELFORM defines the shell element formulation used in the simulation. ELFORM=2 (i.e. Belytschko-Lin-Tsay) was used for all simulations. SHRF is the “shear correction factor” and is set at the LS-Dyna recommended value of 5/6 for all simulations. NIP is the number of through-thickness integration points (as discussed in Chapter 5.3.4.1), and it is set at 5 for all simulations. Thickness is the plate thickness of the various test specimens (and web and flange thicknesses for the framed specimens). It is set appropriately as defined in

Table 5.19. NLOC defined the position of the shell element reference surface with respect to its mid-plane as discussed in 5.3.3.3. It is set to 0 (i.e. at the mid-plane) for the two plate specimens, and set as defined in

Table 5.19 for the framed specimen.

Table 5.19: Inputs for SECTION_SHELL cards.

1/4" Plate Specimen Section Parameters				
ELFORM	SHRF	NIP	Thickness	NLOC
2	5/6	5	0.00635	0
1/2" Plate Specimen Section Parameters				
ELFORM	SHRF	NIP	Thickness	NLOC
2	5/6	5	0.0127	0
Frame Specimen Section Parameters				
ELFORM	SHRF	NIP	Thickness	
2	5/6	5	0.00635	
NLOC Web	NLOC Flange	NLOC Plate		
0	1	-1		

5.3.7 Part definition

LS- Dyna applies element parameters and material models to elements by collecting them into groups called *parts*. There is very little restriction on how parts may be defined; in fact to separate bodies may be the same *part*. It was convenient to define two *parts* in the plate simulations: the plate and the rigid indenter. For the frame simulations, the *parts* are: the plate, the web, the flange (note that the web and flange together are defined in this thesis as the *stiffener*), and the rigid indenter.

It should be pointed out that the CNRBs discussed above are also considered *parts* in LS-Dyna.

Specifically a *part* definition combines an element formulation, element properties (as defined in a SECTION card (discussed below)) and a material model (as defined in a MAT card (discussed above)); and other cards that are not relevant to these simulations. Each element, in its definition, is tied to a *part*, thus inheriting the parameters defined in the SECTION and MAT cards.

5.3.8 Contact

The contact algorithms in LS-Dyna are very robust and very little effort was spent fine tuning the contact. The contact algorithm employed was AUTOMATIC_SINGLE_SURFACE, which is a penalty contact formulation with automatic contact surface detection²². When using this contact card, it is necessary to employ another card in order to extract the contact force. The FORCE_TRANSDUCER_PENALTY card was employed for this purpose. This card does not affect the contact in any way, it simply measures the forces on the master and slave surfaces.

5.3.8.1 Penalty method

The penalty method expressly makes use of slave node penetration into the master surface. The penalty method consists of identifying the slave nodes that penetrate the master surface and placing discrete springs normal to the surface between the master surface and slave nodes (Hallquist 2006). A given spring exerts a force on its slave node that is proportional to the slave node's penetration through the master surface (Hallquist 2006). Each spring's modulus is unique and depends on the bulk moduli of the slave and master surfaces. Drastic differences in material bulk moduli at the interface can cause problems and several algorithms are available to address these issues; however, for these simulations, both the test specimens and the indenter are composed of similar steel; negating the need to employ other than the standard algorithm. Because of this, the standard algorithm provides spring

²² As discussed above, this automatic contact detection breaks down when the shell element edge length is smaller than its thickness.

moduli approximately equal to the material moduli at the contact interface. An added benefit of having approximately equal spring and material moduli is that the explicit time step is not affected by the contact algorithm (Hallquist 2006).

Further explanation of the penalty method is necessary. The time steps of explicit structural simulations are sufficiently small (on the order of 10^{-6} seconds for these simulations) such that the slave node penetration for each time step is also very small. During a single time step, the relative position of the slave and master surfaces are calculated without considering contact between them. The contact algorithm is then employed (Belytschko, Liu et al. 2000) and if a contact interface is found, slave nodes that penetrate the master surface are “pushed” back to the surface by a force equal to the nodal penetration times the interface spring modulus.

Some of the major benefits of using the penalty method include: little to no excitement of hourglassing; exact conservation of momentum without imposing impact and release conditions; and no special treatment of intersecting interfaces is required (Hallquist 2006).

5.3.8.2 Element grouping

For these simulations, the shell elements that were expected to come into contact with the indenter were grouped into a SET_SEGMENT, which is a collection of “faces”; each defined by the nodes of the element that was selected²³. The top faces of the solid elements on the rigid indenter were grouped into another SET_SEGMENT. The contact algorithm

²³ Allowing an entire shell element, or just a single face of a solid element to be addressed.

was then instructed to only consider contact between the “faces” in these sets. This step was not necessary, but was done to make the simulations more efficient.

5.3.8.3 SOFT parameter

A parameter available in the CONTACT cards is SOFT. SOFT=1 is the penalty formulation, SOFT=1 is a soft constraint formulation, and SOFT=2 is segment-based contact (LSTC 2014). SOFT=1 is available to treat potential problems when bodies having dissimilar elastic bulk moduli come into contact (LSTC 2014), and is sometimes otherwise recommended. SOFT=2 is an alternate option for general shell to solid contact (LSTC 2014). A sensitivity study was conducted across these three values and it was determined that SOFT=1 provided the best results.

5.3.9 Loading

The rigid wheel indenter’s motion was prescribed in the normal and lateral directions for each simulation. The curves describing these motions were extracted from the experimental results. The experimental data was recorded at 2048 Hz. This was filtered at 256Hz and input directly into the simulations.

BOUNDARY_PRESCRIBED_MOTION_RIGID cards were used to move the rigid wheel indenter according to the paths described in the curves drawn from the experiments.

5.3.10 Hourglassing

Hourglassing is a nonphysical, zero energy mode of vibration for underintegrated shell and solid finite elements. It produces zero strain and no stress. Hourglassing was not an issue

for these simulations and thus required no special attention. The hourglassing energy was typically less than 2% of the total energy.

5.3.11 Solution controls

Solution controls modify the default behaviour of LS-Dyna. For these numerical models, four solution controls were utilized: `CONTROL_ACCURACY`, `CONTROL_ENERGY`, `CONTROL_SHELL`, and `CONTROL_TERMINATION`.

`CONTROL_ACCURACY` may be used to improve the accuracy of the simulations calculations (LSTC 2014). For these simulations, the INN option was invoked for all shell and solid element (i.e. `INN=4`). INN is an acronym for invariant node numbering, and it is used to realign the local element coordinate system (which is defined by the node input order (and the shell normal vector for shells) for irregularly shaped elements in the event that the node number in is permuted during the simulation (LSTC 2014).

`CONTROL_ENERGY` defines the types of energies computed and included in the energy balance (see Equation [8]). For these simulations, all types of energy were computed; they are: hourglass energy, Stonewall energy (default), sliding interface energy (default if contact is employed), and Rayleigh energy (damping energy).

`CONTROL_SHELL` was used to modify the default behaviour of the shell elements. Specifically, the options `ESORT`, `BWC`, and `PROJ` were invoked. `ESORT=1` improves the behaviour of degenerate triangular elements by automatically switching them to more suitable triangular shell formulations (LSTC 2014). `BWC` and `PROJ` are used in conjunction with the Belytschko-Lin-Tsay shell element formulation to invoke “warping

stiffness”. Most shell formulations undergoing warping (akin to beam torsion) are too soft, and require additional, and somewhat expensive, calculations to properly respond (Hallquist 2006, LSTC 2014). BWC=1 invokes the Belytschko-Won-Chiang warping stiffness calculations, and PROJ=1 invokes the “full projection method” instead of the default “drill projection method”; which is inappropriate for highly warped shells (LSTC 2014).

CONTROL_TERMINATION defines the point in *simulation time* that the simulation of the problem terminates. This value changes depending on the *simulation time* required by each simulation.

5.3.12 Output of Results

Results are recorded in LS-Dyna via two databases: an ASCII database and a binary database. The output frequency (i.e. the amount of *simulation time* between output of results) may be specified separately for each database. Results from the ASCII database may be plotted versus time, or cross-plotted against other results. Results from the binary database may also be plotted thus; however, it also contains information that may be plotted in fringe plots overlaying the elements in the numerical model. The latter implies that it requires significantly more data storage than the ASCII database, especially because nearly all types of data calculated are stored in there. For the purposes of these simulations data was stored in the binary database at 40 Hz. The ASCII database was used to store specific data (contact force, global statistics, rigid body data, etc...) at higher resolution of 1000 Hz.

Additionally the SHGE option in the DATABASE_EXTENT_BINARY card was invoked. This option outputs shell hourglass energy into the binary database, allowing for fringe plots to be created.

5.4 Validation Simulations

The following sub-sections compare the numerical simulations of the “warm slow centre” experiments for each of the three specimen types: ¼” plate, ½” plate and frame. These experiments took in excess of 120 seconds to run. This is a considerable amount of time to simulate using explicit time integration. As strain-rate effects are assumed to be negligible, time has been scaled by a factor of 1/20 for these numerical simulations. Despite this, inertial effects are assumed to be negligible because the accelerations are still quite low, at 0.0133 m/s² in the normal direction and 0.171 m/s² in the lateral direction.

5.4.1 ¼” Plate simulation validation

Using the numerical modelling techniques discussed above and the material constants determined from the RSM analysis (Chapter 5.3.5.1) a simulation of MovingLoad10 was carried out (see Appendix C1.1.3 for plots of all experimental data collected for MovingLoad10). Figures 5.23 and 5.25 plot the normal and lateral reaction forces respectively, for both the numerical simulation and the experiment. The agreement between the simulation and the experimental results is very good for the normal reaction force, except near the end of the simulation. This discrepancy near the end is likely due to strain-rate effects; which were not modeled in the simulation, but of course were present in the experiments. To explain, imagine the indent is at the “Centre” location. At this location the plate behaves as if it is an “infinite plate”. As the indenter moves laterally, the

indentation is dragged along with it, and there is nothing restricting the plate on the leading side of the indenter from lifting in advance of the indenter getting there. As the indenter nears the end of the plate, the end fixed boundary condition now prevents the plate ahead of the indenter from lifting, but the normal indentation does not change. This implies that the plate near the end is stretching faster than the plate at the centre; and thus strain-rate effects would cause increasing structural capacity as the indenter neared the end of the plate. It is also possible that the difference between the “ideal” fixed boundary condition in the numerical model and the “practical” fixed boundary condition in the experiment plays a role.

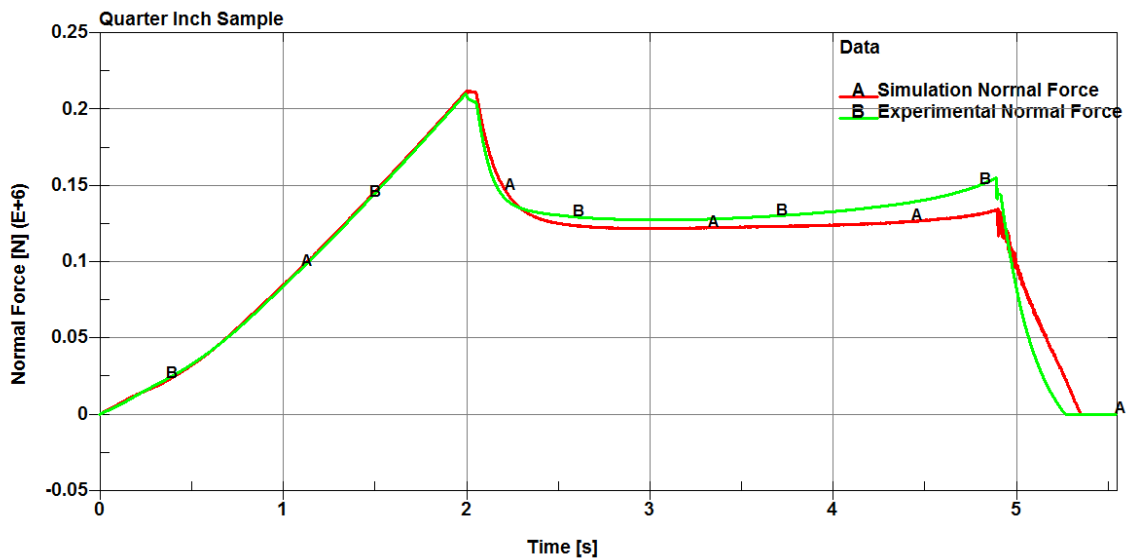


Figure 5.23: Numerical and experimental normal force results for ¼” plate specimen.

Further, regarding the capacity loss immediately after the indenter begins lateral motion (i.e. at time=2 seconds) and the subsequent moving load capacity, it is apparent that the fixity in the normal direction has a dramatic effect on the prediction of these quantities. Figure 5.24 presents the same results as in Figure 5.23, except it also presents the normal

force results for a similar simulation without normal direction compliance (i.e. the plate is fixed in the normal direction). From this figure we can see that the initial stationary capacity of the fixed plate is much higher than for the compliant plate. This is to be expected. What is unexpected is that drop in normal moving load capacity for the fixed case is much larger than for the compliant case. This is an important result for two reasons. First, it is counter intuitive. Generally, increasing the stiffness of a structure increases its capacity (for stationary loads). The opposite is true, in the normal direction, for moving loads. The other reason this result is important is that in design and analysis simulations, it is common to fix ship structures at the boundaries. Of course this is a valid method for standard analysis of ship structures, but when designing for, or analysing moving loads, a careful estimate of the normal compliance of the structure should be made; otherwise actual moving load capacity of the structure will be underestimated. The only change in the lateral moving load response to normal fixity is in increase in capacity.

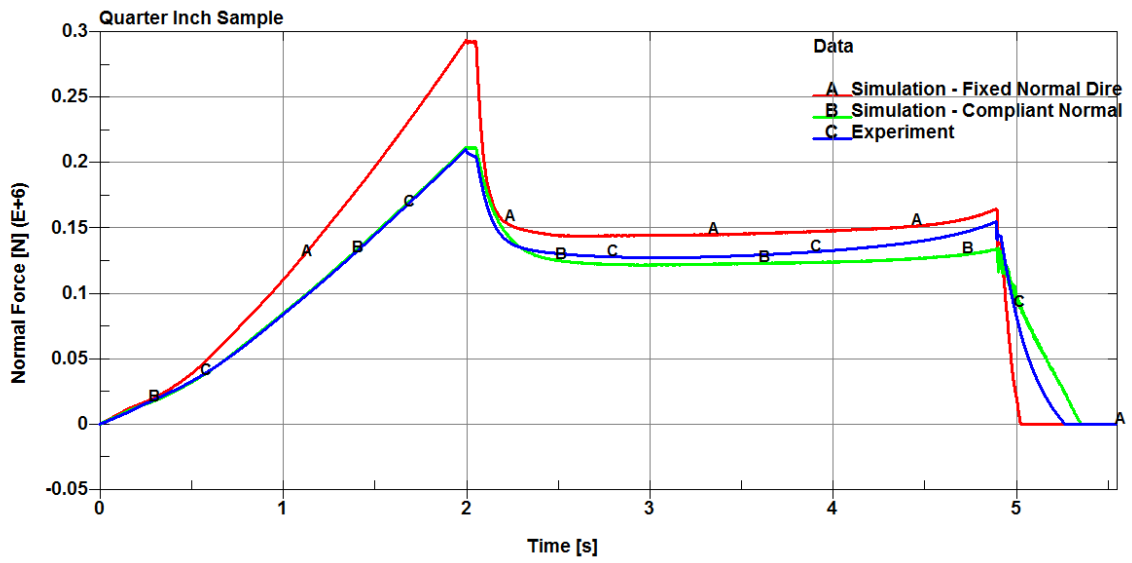


Figure 5.24: Numerical and experimental normal force results for 1/4" plate specimens with and without normal direction compliance.

The lateral force results shown in Figure 5.25 do not appear to agree as well as the normal results; however scale must be considered. At time=3 seconds, the simulation predicts a normal capacity of $1.22\text{E}5$ [N], while the experimental capacity is $1.28\text{E}5$ [N]; a difference of approximately 5%. At time=3 seconds, the simulation (over) predicts a lateral force of $3.05\text{E}4$ [N], while the experimental value is $2.75\text{E}4$ [N]; a difference of approximately 10%. The difference in prediction accuracy in both cases most likely has to do with the value chosen for the tangent modulus of steel for these simulations. The RSM model for this case (see section 5.2.3.5) predicted that the tangent modulus was not significant for the normal moving load response, but that it was for the lateral moving load response. This suggests that any error in the value of the tangent modulus would not impact the normal moving load response prediction, but would for the lateral.

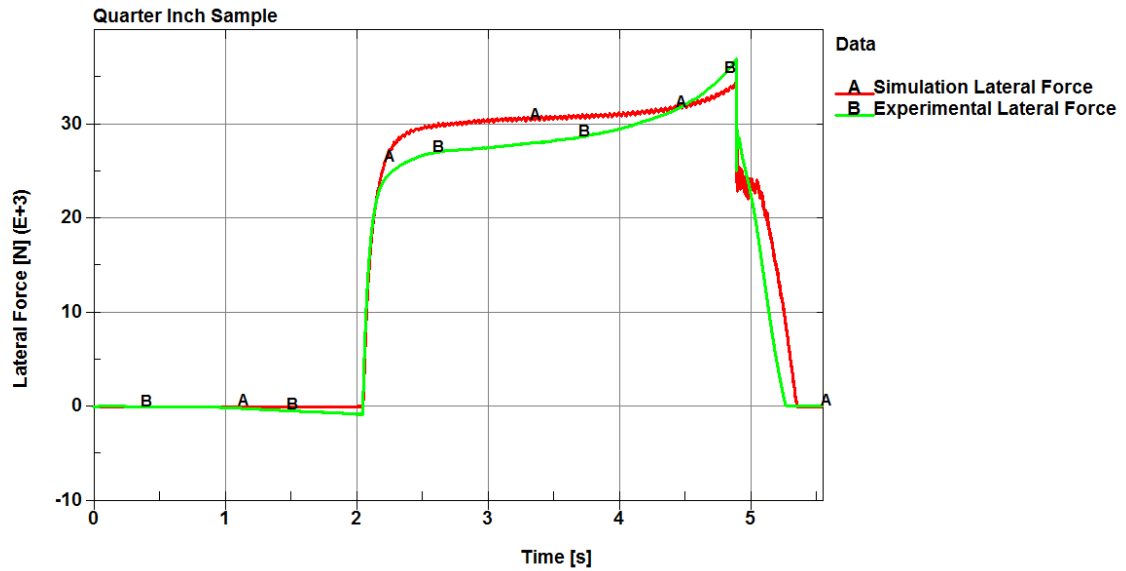


Figure 5.25: Numerical and experimental lateral force results for 1/4" plate specimen.

5.4.2 1/2" Plate simulation validation

Using the numerical modelling techniques discussed above and the material constants determined from the RSM analysis (Chapter 5.3.5.1) a simulation of MovingLoad7 was carried out (see Appendix C1.2.3 for plots of all experimental data collected for MovingLoad7). Figures 5.26 and 5.28 plot the normal and lateral reaction forces respectively, for both the numerical simulation and the experiment. The agreement between the simulation and the experimental results is very good throughout the simulation. This lends weight to the hypothesis that strain-rate effects are the reason for the increase in capacity observed near the end for the 1/4" plate experimental results discussed above. As in the 1/2" plate moving load experiments (see section 4.2.2) it is likely a comparable lack of membrane stretching and a lesser indentation that contribute to the reduced strain-rate effects in this case.

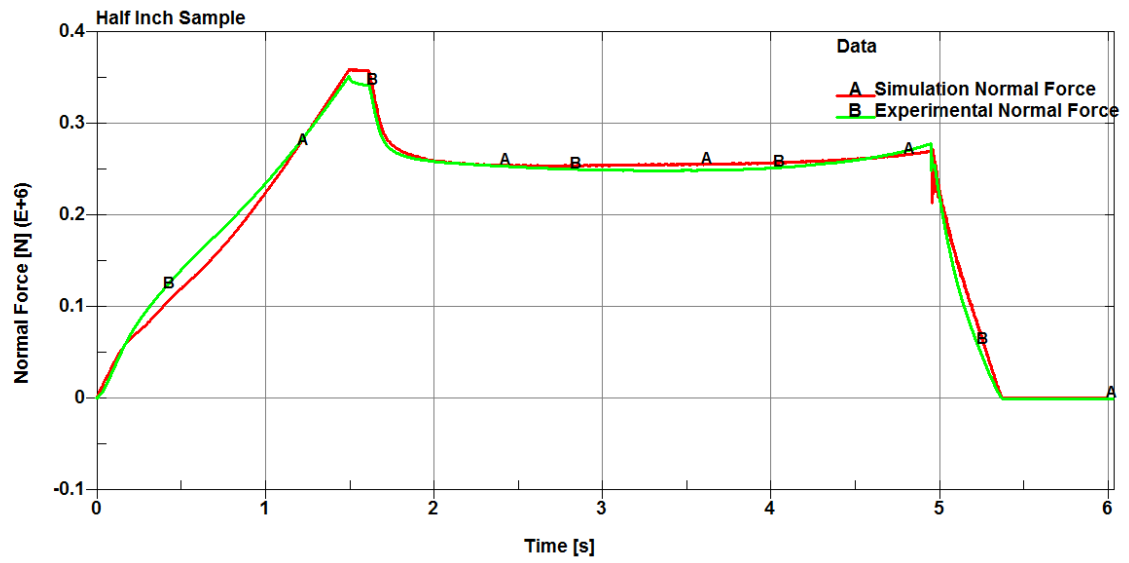


Figure 5.26: Numerical and experimental normal force results for $\frac{1}{2}$ " plate specimen.

Similar to the discussion above for the fixity of the $\frac{1}{4}$ " plate, Figure 5.27 presents the same results as in Figure 5.26, except it also presents the normal force results the fixed case.

Similar behaviour regarding in increased drop in structural capacity for the fixed simulation is evident.

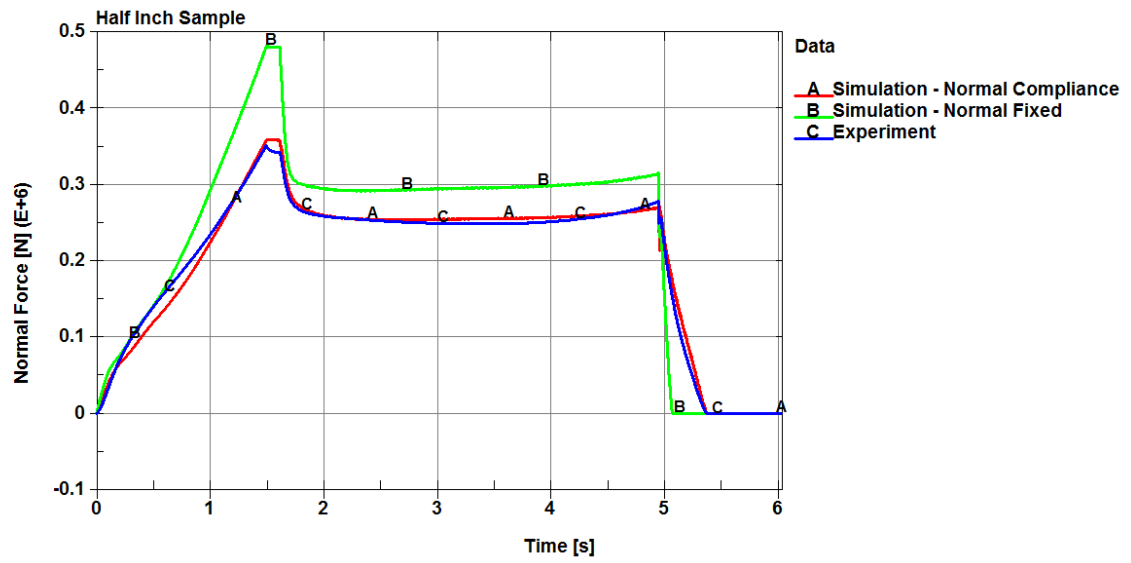


Figure 5.27: Numerical and experimental normal force results for 1/2" plate specimens with and without normal direction compliance.

The lateral force results shown in Figure 5.28 agree very well too, except again near the end where either strain-rate effects become evident, and/or the “ideal” boundary condition in the numerical model restricts the structural response more than the “practical” experimental boundary condition.

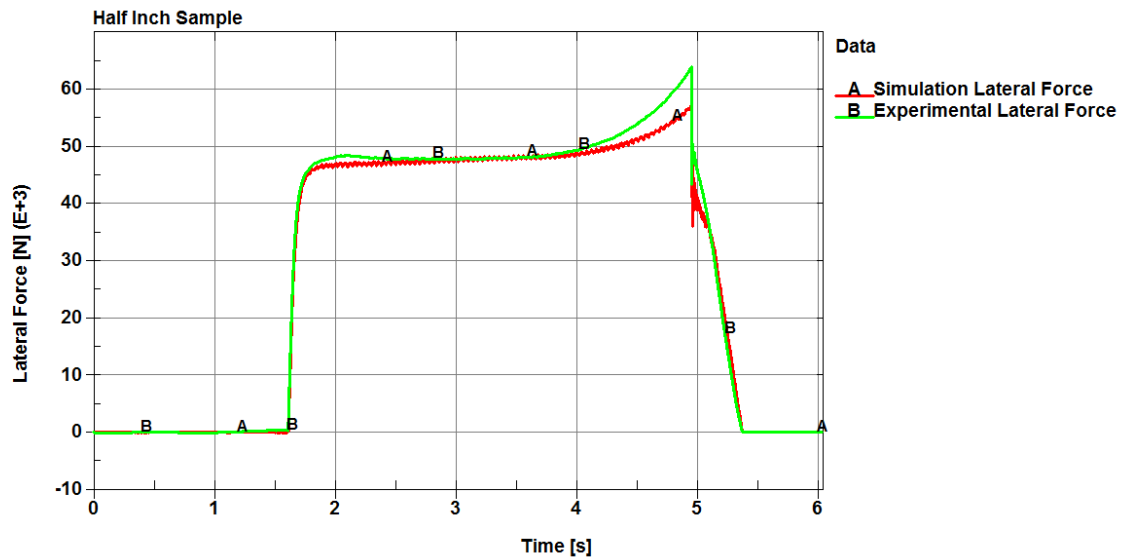


Figure 5.28: Numerical and experimental lateral force results for 1/2" plate specimen.

5.4.3 Frame simulation validation

Using the numerical modelling techniques discussed above and the material constants determined from the RSM analysis (Chapter 5.3.5.1) a simulation of MovingLoad15 was carried out (see Appendix C1.3.3 for plots of all experimental data collected for MovingLoad15). Figures 5.29 and 5.31 plot the normal and lateral reaction forces respectively, for both the numerical simulation and the experiment. The results agree fairly well during the stationary load, but as soon as the lateral motion begins, the simulation under-predicts the normal moving load capacity. Based on the RSM analysis, it would seem that this is the result of either a poor choice for tangent modulus, or that a more sophisticated plastic model is required. It is more likely however that the experimental boundary conditions for the stiffener (as provided by the stiffener end plate and its connection to the carriage via bolts) were far from the ideal “fixed” case assumed in the

numerical model (please refer to Chapter 4.3 for a discussion of the experimental stiffener boundary conditions).

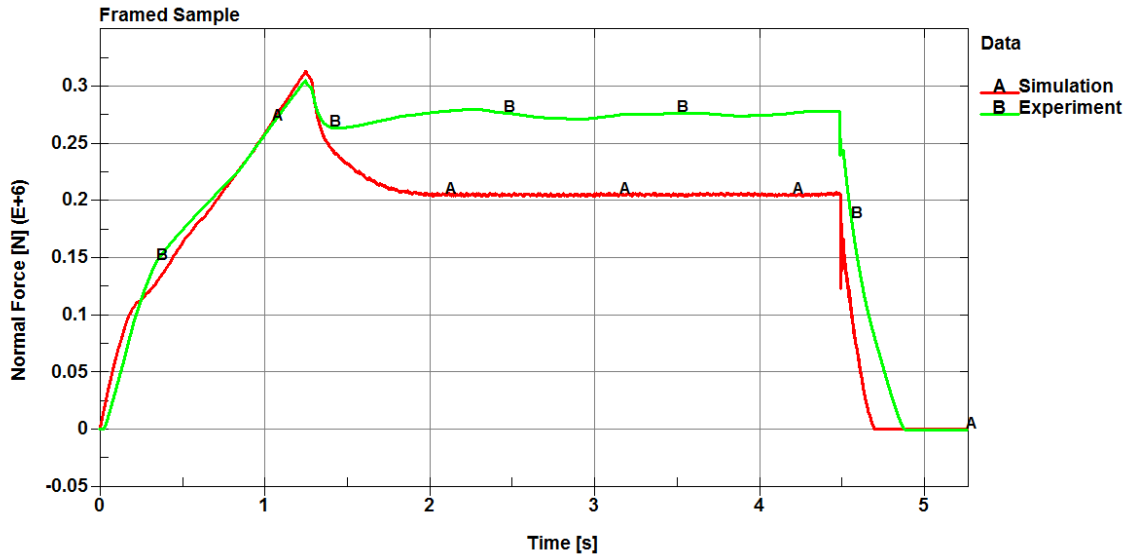


Figure 5.29: Numerical and experimental normal force results for frame specimen.

Similar to the discussion above for the vertical fixity of the $\frac{1}{4}$ " and $\frac{1}{2}$ " plates, Figure 5.30 presents the same results as in Figure 5.29, except it also presents the normal force results of the fixed case.

Similar behaviour regarding in increased peak stationary load and increased drop in structural capacity for the fixed simulation is evident.

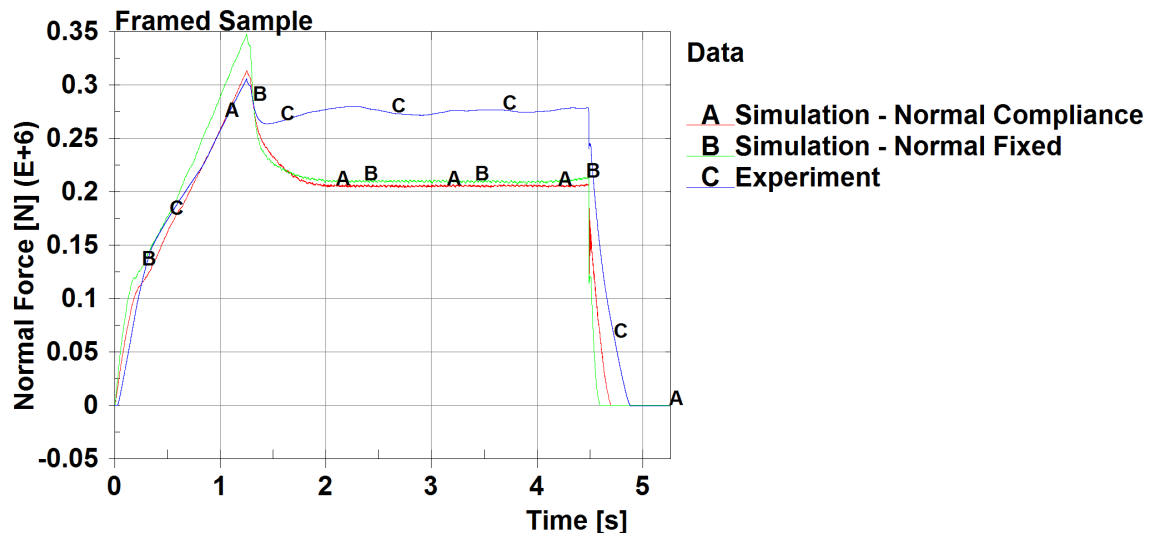


Figure 5.30: Numerical and experimental normal force results for frame specimens with and without normal direction compliance.

The lateral force results shown in Figure 5.31 agree well initially, but as the lateral motion progresses, the frame's web plastically buckles too much compared with the experiment, and so lateral capacity of the frame is under-predicted by the simulation. Figure 5.32 depicts the frame numerical model and shows the location and extent of the plastic buckling of the frame's web.

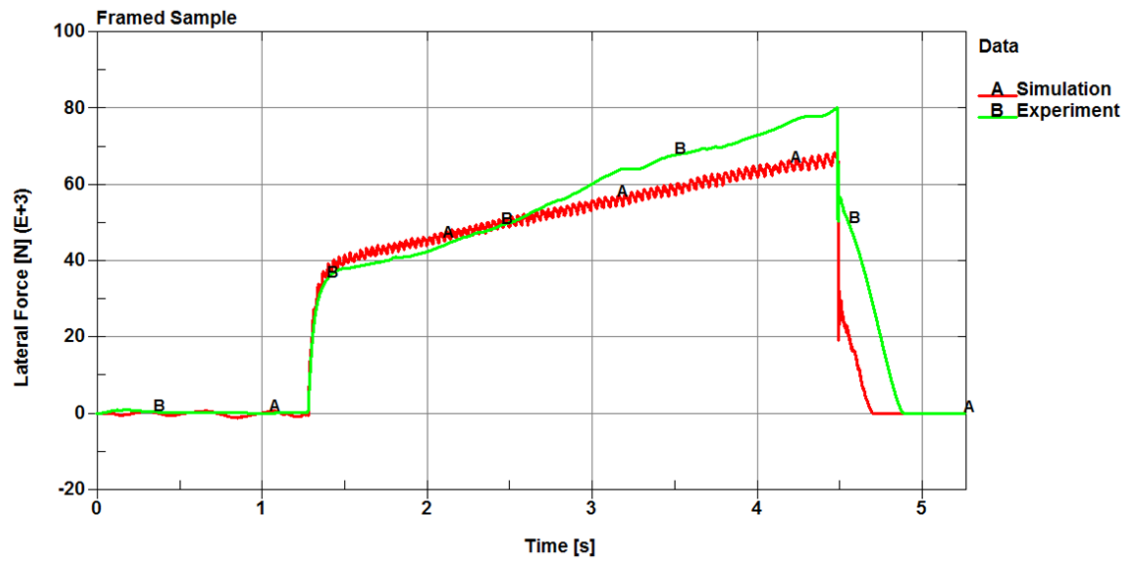


Figure 5.31: Numerical and experimental lateral force results for frame specimen.

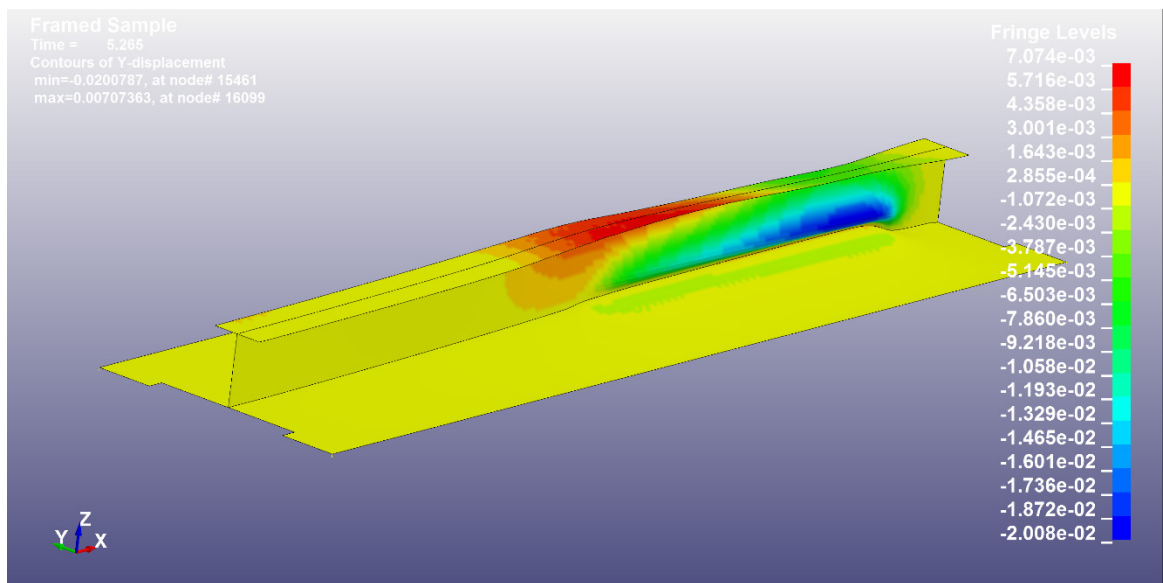


Figure 5.32: y-displacement fringe plot of frame numerical model illustrating plastic buckling.

5.5 A First Investigation of Indenter Path

As load path (see Chapter 3.8.2) was not a variable in these experiments, a preliminary examination of the effect of simultaneous vertical (normal) and horizontal (lateral) indentation was carried out numerically. It was hypothesised that the sequential “in-along-out” path of the rigid indenter in the experiments would incite the weakest structural response, because membrane stretching of the plating had already been maximized by the time the horizontal motion began. The goal of these simulations is to ascertain if moving load effects exist for load paths causing increasing membrane response (i.e. simultaneous vertical and horizontal indentation).

5.5.1 Model parameters

For this study, the calibrated ¼” plate numerical model presented in Chapter 5.4.1 was utilised. Two new simulations were conducted with the following load path parameters (all other parameters are identical to Chapter 5.4.1, including the starting position of the rigid wheel indenter):

Simulation 1 – Shallow load path:

- Indenter vertical motion: 0 [cm] (0 [in.]) at time = 0 [s] increasing steadily to 40 [cm] (15.75 [in.]) at time=2 [s].
- Indenter horizontal motion: “End” position at time = 0 [s] increasing steadily to the “Centre” position at time = 2 [s]. This represents a total horizontal travel distance of 55.0 [cm] (21.65 [in.]).

- The simultaneous vertical and horizontal displacements create a load path that is 36° from horizontal (i.e. $\text{atan}(40/55)$).

Figure 5.33 shows a time sequence depicting the path of the indenter.

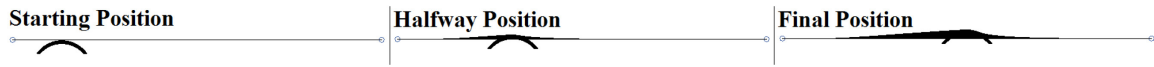


Figure 5.33: Visualization of load path for “shallow” simulation. Indenter moves simultaneously in normal and lateral directions, starting at the end position and finishing at the centre of the plate.

Simulation 2 – steep load path:

- Indenter vertical motion: 0 [cm] (0 [in.]) at time = 0 [s] increasing steadily to 40 [cm] (15.75 [in.]) at time=2 [s].
- Indenter horizontal motion: “Quarter” position²⁴ at time = 0 [s] increasing steadily to the “Centre” position at time = 2 [s]. This represents a total horizontal travel distance of 27.5 [cm] (10.83 [in.]).
- The simultaneous vertical and horizontal displacements create a load path that is 55° from horizontal (i.e. $\text{atan}(40/27.5)$).

Figure 5.34 shows a time sequence depicting the path of the indenter.

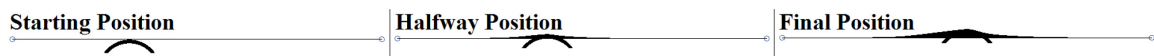


Figure 5.34: Visualization of load path for “steep” simulation. Indenter moves simultaneously in normal and lateral directions, starting at the quarter position and finishing at the centre of the plate.

²⁴ The “quarter” position is half way between the “End” position and the “Centre” position.

Chapter 5.4.1 calibration simulation – in-along-out load path:

- Indenter vertical motion: 0 [cm] (0 [in.]) at time = 0 [s] increasing steadily to 40 [cm] (15.75 [in.]) at time=2 [s].
- Indenter horizontal motion: “Centre” position at time = 0 [s]; remaining stationary at “Centre” position until time = 2 [s]; increasing steadily and achieving “End” position at time = 4.9 [s]. This represents a total horizontal travel distance of 55.0 [cm] (21.65 [in.]).
- The simultaneous vertical and horizontal displacements create a load path that is vertical (i.e. stationary portion), and then horizontal (i.e. moving portion).

Figure 5.35 shows a time sequence depicting the path of the indenter.

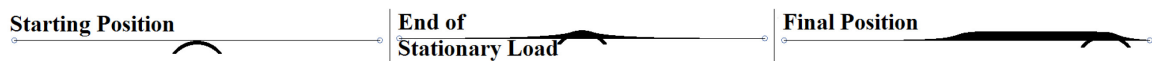


Figure 5.35: Visualization of load path for “steep” simulation. Indenter first moves in normal direction only, and then in the lateral direction only; starting at the “centre” position and finishing at the “end” position.

5.5.2 Results

The results of these two simulations were compared with the “in-along-out” simulation results from Chapter 5.4.1, as well as the experiment that Chapter 5.4.1 is based on. Figure 5.36 summarized the load paths for each of the three simulations.

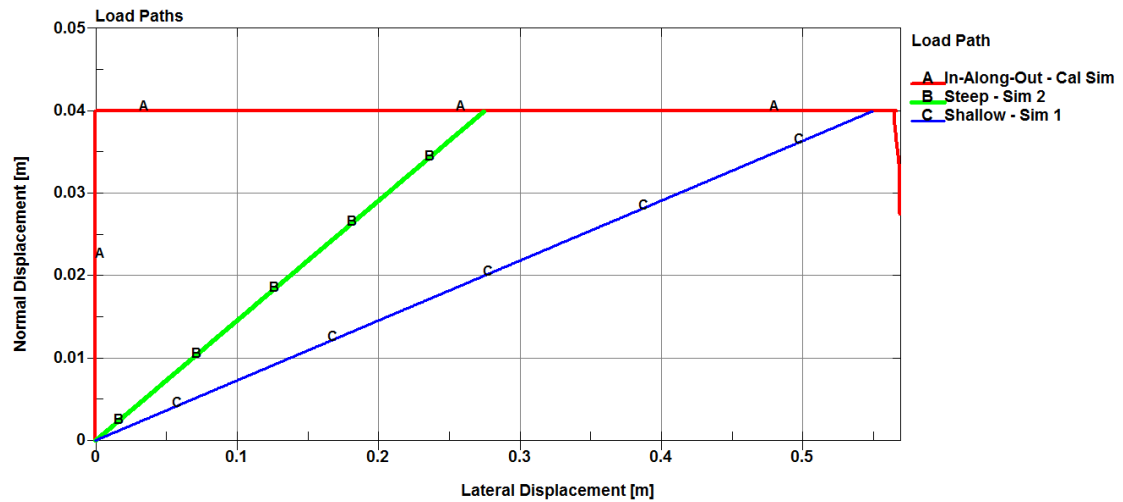


Figure 5.36: Plot of load paths for each of the three “load path” simulations. The vertical axis is normal displacement, the horizontal axis is lateral displacement.

Figure 5.37 shows the normal (vertical) force versus time for the load path simulations. The experiment results of ML10, on which the ¼” numerical model calibration is based, is shown as curve A (red). The calibration simulation from Chapter 5.4.1 are shown as curve B (green). The steep simulation result (Simulation 2) is shown as curve C (blue) and the shallow simulation result (Simulation1) is curve D (cyan). What this graph indicates with respect to load path is not immediately obvious. Regarding curves A and B, the uncoupled (i.e. sequential) vertical and horizontal vertical force results are very obvious. At time = 0 [s], the rigid wheel indenter begins to move vertically (and the “Centre” plate location), and at time = 2 [s], the vertical motion has stopped (after travelling 40 cm). This peak value (point A1 in Figure 5.37) of 212 [kN] (47.66 [kip]) represents the stationary load capacity at the “Centre” location. At time = 2 [s], the horizontal motion these curves begins. Shortly after, at approximately time = 3 [s], the normal force reached a local minimum (point A2 in Figure 5.37) of 122 [kN] (27.43 [kip]) for the numerical simulation (or 128 [kN] (28.87

[kip] for the experiment) due to moving load effects. This is a reduction of approximately 42%. Because these plates are “long plates”, and this minimum value occurs far from the boundary of the plate, this minimum value is representative of the moving load capacity at the “Centre” location for this load path. At time = 2 [s] for curve C, the steep simulation, the indenter has finished its simultaneous vertical and horizontal motion at the “Centre” location; therefore point C1, with value 154 [kN] (34.62 [kip]), represents the moving load capacity at the “Centre” for the 55° load path. Similarly, point D1, with value 137 [kN] (30.8 [kip]), represents the moving load capacity at the “Centre” position for the 36° load path.

Table 5.20 summarizes these results, and shows the capacity reduction for this ¼” plate as a function of load path.

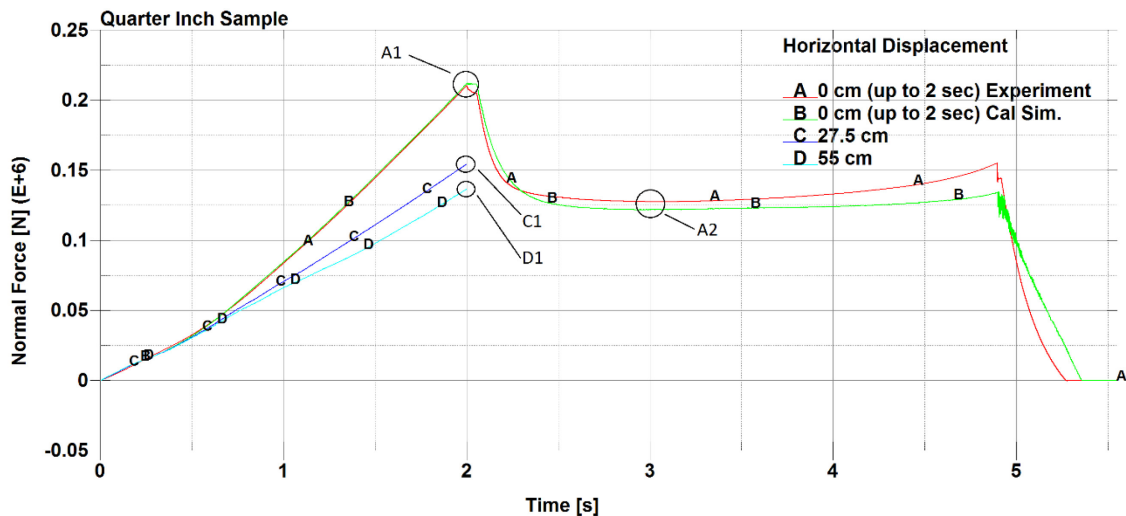


Figure 5.37: Normal (vertical) force results versus time for load path simulations – (A-red) experiment results of ML10, (B-green) ¼” plate numerical model calibration results from Chapter 5.4.1 for experiment ML10, (C-blue) steep simulation results, (D-cyan) shallow simulation results.

Table 5.20: Summary of effect of load path on normal force for ¼” plate.

Run	Load Path	Stationary Capacity [kN]	Moving Load Capacity [kN]	Capacity Reduction
Experiment	vertical then horizontal	212	122	42%
Calibration Experiment	vertical then horizontal		128	40%
Steep Simulation	55°		154	27%
Shallow Simulation	36°		137	35%

Figure 5.38 is similar to Figure 5.37, except that resultant force is plotted (instead of normal force). Similar behaviour is observed, and analogous results are given in Table 5.21. It is obvious from comparing the capacity between the normal and resultant loads that lateral (horizontal) force plays a negligible role in moving load effects in this case.

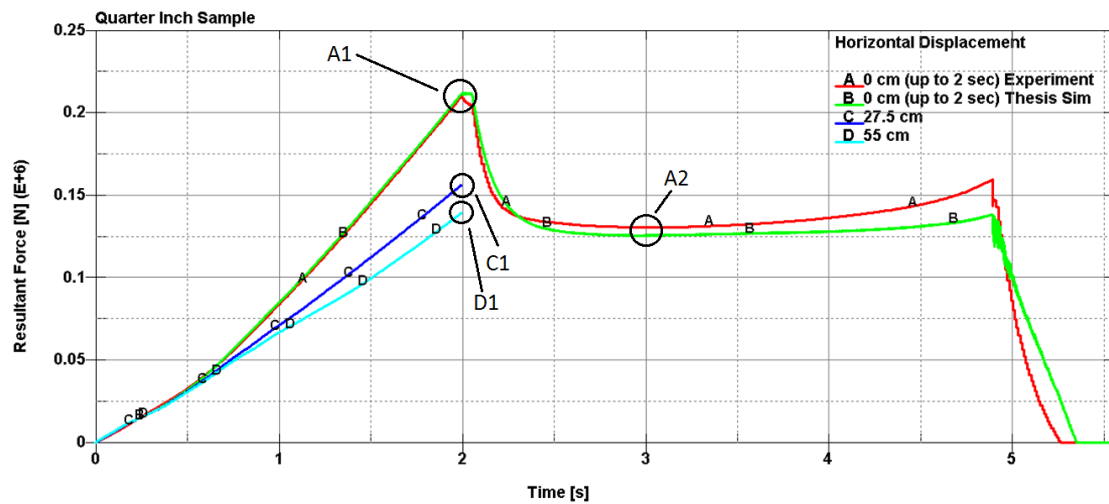


Figure 5.38: Resultant force results versus time for load path simulations – (A-red) experiment results of ML10, (B-green) ¼” plate numerical model calibration results from Chapter 5.4.1 for experiment ML10, (C-blue) steep simulation results, (D-cyan) shallow simulation results.

Table 5.21: Summary of effect of load path on resultant force for ¼” plate.

Run	Load Path	Stationary Capacity [kN]	Moving Load Capacity [kN]	Capacity Reduction
Experiment	vertical then horizontal	212	131	38%
Calibration Experiment	vertical then horizontal		126	41%
Steep Simulation	55°		156	26%
Shallow Simulation	36°		139	34%

5.6 Guidelines for Modeling Moving Loads on Hull Structures

As shown in Chapter 5.4, the numerical modelling method outlined in this section works very well for modeling moving loads causing plastic damage on hull plating. It appears to be not so accurate for modelling moving load effects on frames, where it tends to underestimate the stiffener capacity (at least compared with the experimental results of this research). It is unclear whether the greatest error regarding the response of frames lies with the experimental stiffener boundary conditions (as discussed in Chapter 4.3), or with this numerical modelling method. Further work is required to better understand this discrepancy.

For clarity and simplicity, the following modelling guidelines are condensed from the above:

FE Code: Non-linear with explicit time integration.

Floating-point precision: Single precision is generally sufficient.

Geometry: Depends the structure being modeled.

Mesh:	<p>Shell elements with warping stiffness and five through-thickness integration points. Solid elements and beam elements are not recommended.</p> <p>Care should be taken regarding the shell reference surface offset from the mid-plane.</p> <p>Care should be taken if shell edge length is less than shell thickness.</p>
Boundary Conditions:	<p>Depends on the structure being modeled; however care should be taken regarding the fixity in the direction normal to the hull plating. Zero compliance in the normal direction will lead to underestimating the structures moving load capacity.</p> <p>Care should be taken when mating shell and solid elements. Constrained nodal rigid bodies are sufficient.</p>
Material Model:	<p>A bilinear kinematic elasto-plastic material model is sufficient for thick plates. Thinner plates exhibiting plastic membrane stretching and frames in general may require a more sophisticated plasticity model.</p> <p>Strain-rate effects may (and should) be included.</p> <p>Rigid material is sufficient if ignoring behaviour of impacting object.</p>

Contact:	Penalty formulation is sufficient. Caution: the effect of friction on moving loads causing plastic damage is presently unknown. SOFT=1 is sufficient.
Load:	Depends on the situation being modelled.
Solution Controls:	Invariant node numbering for all elements is sufficient.

These guidelines were determined based on a “bottom-up” approach (i.e. only get as complicated as necessary) coupled with sensitivity analyses, past experience, and validation against experiments.

5.7 Discussion of Numerical Simulations

The previous section, 5.6 Guidelines for Modeling Moving Loads on Hull Structures effectively summarizes and discusses the numerical modelling methodology.

Regarding the RSM analysis of the three specimen types, yield strength and vertical compliance were always significant factors. Tangent modulus was shown not to be significant for any of the ½” responses, and the validation simulation for this specimen type is very good. Tangent modulus was a factor in many cases for the ¼” and frame specimens. It is hypothesized that this is because plastic membrane stretching was more significant in these specimens, and the tangent modulus directly impacts this behaviour.

Membrane effects are not so important for the ½” plate specimens. As the validation was the best for the ½” plate model, it is possible that the tangent modulus was a significant factor in the other validation tests. This may be a function of the simple bilinear material

model employed. Future work is required to determine if better results are attainable for situations involving membrane stretching using a more sophisticated (i.e. multilinear) plasticity model.

Regarding the validation simulations in Chapter 5.4, the numerical models of the plate experiments captured the moving load effects very well. One area for improvement is the response of the model as the indenter nears the plates fixed boundary. It is likely that this discrepancy is due to the combination of a lack of including strain rate effects, and the difference between the lateral compliance of the fixed boundary condition with that of the “practical” experimental boundary. The validation of the frame experiments was not as successful. The peak stationary load was modeled well, but the post plastic buckling behaviour was not. This is likely due to an insufficient model of post-yield constitutive behaviour, coupled with a lack of modeling the compliance in the stiffener boundary conditions; a compliance that was present in experiments out of practical necessity. As discussed in Chapter 4.3, a gap between the stiffener end plate and the carriage wall was practically necessary in order to enable the test specimens to be installed in the carriage.

5.8 Numerical Modeling Conclusions

Moving load effects on plates may be successfully modeled using the approach outlined in Chapter 5.6. The use of this method for moving loads on frames may under-predict the post moving load induced plastic buckling capacity. It is undetermined at this point how much of a role the complexity of the material model has in the post-buckling behaviour of the frame’s web, and it is also unclear at this point how the end conditions of the frame affect this behaviour.

It appears that a simple bilinear plasticity model may not be sufficient to describe moving load effects in general. In particular, plastic membrane stretching and plastic buckling behaviour of the stiffener webs were not modeled adequately. Further work is required to determine if a more sophisticated plasticity model would yield better results.

The response surface method provided important insights into the significant factors for modeling moving loads on plates and frames. For $\frac{1}{2}$ " plates, the significant factors are yield strength, boundary compliance and the interaction of the two. For $\frac{1}{4}$ " plates, the significant factors are the same as for $\frac{1}{2}$ " plates, except the in the case of lateral response to moving loads, tangent modulus became significant. For frames, yield strength, tangent modulus and boundary compliance were all important.

Finally, when modeling moving load effects the stiffness of the boundary plays a very important role. If the boundary is non-compliant (i.e. ideally fixed) in the vicinity of the moving load, then the structural capacity loss associated with movement of the load will be over-predicted. It is critical to either have the boundary conditions far from the moving load (this can be expensive for complicated numerical models) or to add compliance (which can be difficult to estimate).

Chapter 6 Overall Conclusions, Novel Contributions and

Recommendations for Future Work

The scope and objectives this research as defined above (Chapters 3.2 and **Error! Reference source not found.**) were accomplished and discussed in this thesis. The moving load effects as predicted in Quinton (2008) were found to exist in the laboratory through experimentation involving a novel moving load apparatus designed by the author. The structural response of plates and frames subject to rigid moving loads causing plastic damage, as well as plates subject to moving ice loads inciting both elastic and plastic structural responses were investigated. The effects of moderate strain rate and temperature changes were also investigated. From the perspective of ice, these experiments are a first attempt to investigate the effects of load movement and plastic structural damage on the ice load, and the first publication of experimental friction factors for moving ice loads causing plastic damage.

A numerical model for moving load effects on hull structures was created and calibrated against these experiments. The significant factors – yield strength, tangent modulus and boundary compliance – required to model the various responses to moving load effects were identified, and a bottom-up modeling strategy that can easily be replicated in order to assess/investigate moving load effects on plates was created.

The single largest uncertainty of this research is the degree of fixity of the stiffener boundary conditions for the frame test specimens. The necessary gap between the stiffener end plates and the carriage wall (discussed in Chapter 4.3) gave rise to a complex boundary condition which: was compliant up to the point where the stiffener end plate contacted the

carriage wall; was essentially non-compliant (i.e. fixed) while the contact was maintained; but compliant again if the contact was broken (as would be the case if the stiffener attained a significant state of membrane tension). It is believed that this gap contributed to the unexplained behaviour in the experiments, and the inability to reproduce the frame test experiments numerically.

In summary, the effects of moving loads causing plastic damage to hull plating and framing were clearly demonstrated through experimental work, and with numerical simulations. It has been established that a moving load causes increased plastic damage both in lateral extent (from the motion) and in depth, due to a loss of structural capacity (over what would be expected from a similar stationary load) that effectively arises from the previous (upstream) damage. Thus for designs or analyses where the extent of plastic damage is a consideration and a moving load is a likely scenario, it is inadequate to analyse the situation as a simple stationary load. The numerical modeling guidelines presented in Chapter 6 may be used to aid in numerical analyses of hull plating subject to moving loads.

6.1 Novel Contributions

- The author was unable to identify any literature pertaining to experiments of moving loads causing plastic hull damage without hull tearing. As such, the following two items are novel contributions:
 - Novel experimental apparatus for conducting moving load experiments (see Chapter 0).

- Definitive experiments demonstrating “reduced structural capacity” for force- and displacement-controlled moving loads on plates and frames (see Chapter 4).
- The author was unable to identify any literature pertaining to experiments of moving *ice* loads causing both elastic and plastic damage. As such, the following two items are novel contributions:
 - First investigation of moving ice loads inciting both elastic and plastic structural responses in plates (see Chapter 4.9).
 - First publication of ice-steel friction factors for plastically deforming plates subject to moving ice loads (4.9.5).
- Simplified “bottom-up” numerical modeling methodology for simulation of moving loads on ship structures (see Chapter 5.6).
- Discovery of parameters important for the design and analysis structures against moving load effects (see Chapter 5.7).
- First investigation of the effects of indenter path on moving load effects (see Chapter 5.5).
- Results of the moving load experiments invalidate Sokol-Supel’s (1985) theory of moving loads on rigid-plastic plates.
- Recommendations for future work on the subject of moving loads causing plastic damage (see Chapter 6.2).

6.2 Recommendations for Further Work

Further work is possible on many of the aspects of the research presented herein; in particular on the following topics:

- Friction: friction was not explicitly a factor in the rigid indenter moving load experiments. In a real collision involving an indenter sliding along a hull, friction will be present. It is expected that friction will play a major role in the behaviour of the hull structure to moving loads causing plastic damage.
- Due to lack of time and resources, no attempt was made to isolate the point at which (i.e. load level) a moving load begins to incite moving load effects in the hull structure. Determination of this point is an important design consideration, and may shed further light on the structural phenomena responsible for moving load effects.
- An attempt to create a numerical model of the moving load experiments involving the ice indenters was not made in this research. This data is available and should be used to calibrate such a numerical model.
- A limited design of experiments analysis was conducted in this research in order to identify values for some parameters for which little or no data was available. This analysis proved useful in the subsequent analysis of the behaviour of moving loads causing plastic damage. A much more detailed design of experiments analysis on the subject is possible, and should be performed.
- A simple bilinear strain-hardening material model was used in the numerical model for this research. It is likely that this material model was insufficient to capture

plastic membrane behaviour of thin plates as well as post plastic buckling behaviour of frame webs. A more appropriate material model should be employed.

- Only standard 4-node shell elements were used for the numerical models in this research. Due to the level of mesh refinement necessary to capture the geometric behaviour of frame webs during plastic buckling, the shell element edge length was close to its thickness. A more appropriate element for this case may be a *thick shell element*. The author has re-run several simulations presented in this thesis using thick shell elements, and the results are very promising. Further investigation as to their applicability in modeling moving load effects should be conducted.
- Regarding the “chatter” or “stick-slip” phenomenon observed some of the moving ice cone indenter tests, more work needs to be done to ascertain whether or not it is a phenomenon of moving ice loads, or was simply a spurious effect of the test apparatus. Due to the magnitude and frequency of vibrations experienced by the moving load apparatus, this could be a potentially dangerous loading condition at larger scale.
- Further experimentation involving lateral movement of ice cones acting on plastically deforming structures, in order to ascertain any structural capacity loss due to moving ice loads.
- Regarding the confinement of ice, the experiments presented in this thesis involving the plastic deformation of plates with moving ice indenters has uncovered a scenario where the ice is confined essentially for 270° around the contact surface, but free to escape out the remaining 90°. This case is similar to Kim’s (2014) concave wedge,

except with one of the open sides of the wedge closed off. Further work is required to determine the effect of this scenario on the confinement of ice at the contact surface.

- The results of the experiments involving moving loads on plates should be compared with the predictions of Hong and Amdahl's (2012) simplified semi-empirical method for sliding loads on plates.

Bibliography

ANGHILERI, M., CASTELLETTI, L., MILANESE, A. and SEMBOLONI, A., 2007. Modeling Hailstone Impact onto Composite Material Panel Under a Multi-axial State of Stress, *6th European LS-DYNA Conference* 2007.

ANSYS INC., 2011. ANSYS LS-DYNA User's Guide. *Release 14.0 ANSYS Help System*. Version 14.0 edn. USA: ANSYS Inc., .

BELYTSCHKO, T., LIU, W. and MORAN, B., 2000. *Nonlinear Finite Elements for Continua and Structures*. Chichester, England: John Wiley & Sons, Ltd.

BROWN, A.J., 2002a. Collision scenarios and probabilistic collision damage. *Marine Structures*, **15**(4),.

BROWN, A.J., 2002b. *Modeling Structural Damage in Ship Collisions*. SSC - 1400 Draft Report. Washington, D.C.: Ship Structure Committee.

BRUNEAU, S.E., DILLENBURG, A.K. and RITTER, S., 2012. Ice Sample Production Techniques and Indentation Tests for Laboratory Experiments Simulating Ship Collisions with Ice, *The Proceedings of the 22nd (2012) International Offshore and Polar Engineering Conference* 2012.

CARNEY, K.S., BENSON, D.J., DUBOIS, P. and LEE, R., 2006. A phenomenological high strain rate model with failure for ice. *International Journal of Solids and Structures*, **43**(25-26), pp. 7820.

CROASDALE, K., 2001. *Local Ice Load Data Relevant to Grand Banks Structures*. PERD/CHC Report 20-61. National Research Council of Canada.

CURRIER, J.H. and SCHULSON, E.M., 1982. The tensile strength of ice as a function of grain size. *Acta Metallurgica*, **30**(8), pp. 1511-1514.

DALEY, C., ST. JOHN, J.W., BROWN, R. and GLEN, I., 1990. *Ice Loads and Ship Response to Ice - Consolidation Report*. SSC-340. Ship Structure Committee.

DALEY, C.G., 2002. Derivation of plastic framing requirements for polar ships. *Marine Structures*, **15**(6), pp. 543-559.

DALEY, C.G. and HERMANSKI, G., 2008a. *Ship Frame Research Program - An Experimental Study of Ship Frames and Grillages Subjected to Patch Loads, Volume 1 - Data Report*. SSC Project SR 1442 - Final Report; OERC Report 2008-001; NRC-IOT Report TR-2008-11. Ship Structure Committee.

DALEY, C.G. and HERMANSKI, G., 2008b. *Ship Frame Research Program - An Experimental Study of Ship Frames and Grillages Subjected to Patch Loads, Volume 2 - Theory and Analysis Reports*. SSC Project SR 1442 - Final Report; OERC Report 2008-001; NRC-IOT Report TR-2008-11. Ship Structure Committee.

DALEY, C., KENDRICK, A. and APPOLONOV, E., 2001. Plating and framing design in the unified requirements for polar class ships, 2001, pp. 779-791.

DEMPSEY, J.P., 1991. The Fracture Toughness of Ice. , pp. 109-145.

DEMPSEY, J.P., ADAMSON, R.M. and MULMULE, S.V., 1999. Scale effects on the in-situ tensile strength and fracture of ice. Part II: First-year sea ice at Resolute, N.W.T. *International Journal of Fracture*, **95**(1), pp. 347-366.

DEMPSEY, J.P., DEFRANCO, S.J., ADAMSON, R.M. and MULMULE, S.V., 1999. Scale effects on the in-situ tensile strength and fracture of ice Part I: Large grained freshwater ice at Spray Lakes Reservoir, Alberta. *International Journal of Fracture*, **95**(1), pp. 325-345.

DERRADJI-AOUAT, A., 2005. Explicit FEA and constitutive modelling of damage and fracture on polycrystalline ice - simulations of ice loads on offshore structures , *Proceedings of the 18th International Conference on Port and Ocean Engineering Under Arctic Conditions (POAC 2005)*, June 26-30 2005.

DILLENBURG, A.K., 2012. *Rate Dependency in Conical Ice Indenter Failure*, Universität Duisburg-Essen.

DUTTA, P.K., COLE, D.M., SCHULSON, E.M. and SODHI, D.S., 2004. A fracture study of ice under high strain rate loading. *International Journal of Offshore and Polar Engineering*, **14**(3), pp. 182-188.

FRÝBA, L., 1999. *Vibration of solids and structures under moving loads / Ladislav Frýba*. London: Thomas Telford.

GAGNON, R.E., 2004a. Analysis of laboratory growler impact tests. *Cold Regions Science and Technology*, **39**(1),.

GAGNON, R.E., 2004b. Physical model experiments to assess the hydrodynamic interaction between floating glacial ice masses and a transiting tanker. *Journal of Offshore Mechanics and Arctic Engineering*, **126**(4),.

GAGNON, R.E. and GAMMON, P.H., 1997. In situ thermal profiles and laboratory impact experiments on iceberg ice. *Journal of Glaciology*, **43**, pp. 569-582.

GAGNON, R.E. and GAMMON, P.H., 1995a. Characterization and flexural strength of iceberg and glacier ice. *Journal of Glaciology*, **41**(137), pp. 103-111.

GAGNON, R.E. and GAMMON, P.H., 1995b. Triaxial experiments on iceberg and glacier ice. *Journal of Glaciology*, **41**(139), pp. 528-540.

GAGNON, R.E., 2011. A numerical model of ice crushing using a foam analogue. *Cold Regions Science and Technology*, **65**(3), pp. 335-350.

GAGNON, R.E., 2004c. Side-viewing high-speed video observations of ice crushing, *17th International Symposium on Ice - International Association of Hydraulic Engineering and Research (IAHR)*, June 21-25 2004c.

GAGNON, R.E., 1999. Consistent observations of ice crushing in laboratory tests and field experiments covering three orders of magnitude in scale, *Proceedings of the 15th International Conference on Port and Ocean Engineering under Arctic Conditions, POAC-99 1999*, pp. Vol. 2, 858-869.

GAGNON, R.E., 1998. Analysis of visual data from medium scale indentation experiments at Hobson's Choice Ice Island. *Cold Regions Science and Technology*, **28**(1), pp. 45-58.

GAGNON, R.E. and DERRADJI-AOUAT, A., 2006. First results of numerical simulations of bergy bit collisions with the CCGS Terry Fox icebreaker, 2006, NRC Institute for Ocean Technology.

GAGNON, R., CUMMING, D., RITCH, R., BROWNE, R., JOHNSTON, M., FREDERKING, R., MCKENNA, R. and RALPH, F., 2008. Overview accompaniment for papers on the bergy bit impact trials. *Cold Regions Science and Technology*, **52**(1),.

HALLQUIST, J.O., 2006. *LS-DYNA Theory Manual*. Livermore, California: Livermore Software Technology Corporation.

HÄNNINEN, S., 2004. *INCIDENTS AND ACCIDENTS IN WINTER NAVIGATION IN THE BALTIC SEA, WINTER 2002 – 2003*. Research Report 54. Winter Navigation Research Board, Finnish Maritime Administration.

HOBBS, P.V., 1974. *Ice Physics*. Clarendon Press.

HONG, L., 2008. *Simplified Analysis and Design of Ships subjected to Collision and Grounding*, Norwegian University of Science and Technology (NTNU).

HONG, L. and AMDAHL, J., 2012. Rapid assessment of ship grounding over large contact surfaces. *Ships and Offshore Structures*, **7**(1), pp. 5-19.

HUGHES, O.F., PAIK, J.K., BÉGHIN, D., CALDWELL, J.B., PAYER, H.G. and SCHELLIN, T.E., 2010. *Ship structural analysis and design*. Jersey City, N.J: Society of Naval Architects and Marine Engineers.

IACS, 2011. *Requirements Concerning Polar Class*. London: International Association of Classification Societies.

ISO 26203-2, 2011. *Metallic materials — Tensile testing at high strain rates — Part 2: Servo-hydraulic and other test systems*. Corrected version 2012-03-15 edn. Geneva: International Organization for Standardization.

JACKA, T.H., 1984. The time and strain required for development of minimum strain rates in ice. *Cold Regions Science and Technology*, **8**(3), pp. 261-268.

JOHNSON, G.R. and COOK, W.H., 1983. A Constitutive Model and Data for Metals Subjected to Large Strains, High Strain Rates, and High Temperatures, *Proceedings of the 7th International Symposium on Ballistics*, April 1983.

JONES, N., 1983. Structural aspects of ship collisions. In: N. JONES and T. WIERZBICKI, eds, *Structural Crashworthiness*. London: Butterworths, pp. 308.

KEEGAN, M.H. and NASH, D., STACK, M., 2013. Numerical modelling of hailstone impact on the leading edge of a wind turbine blade, *EWEA Annual Wind Energy Event 2013*, 4/02/13 - 7/02/13 2013.

KIM, H., 2014. *Ice crushing pressure on non-planar surface*, Memorial University of Newfoundland.

KIM, H., DALEY, C.G. and ULAN-KVITBERG, C.A., 2012. Reappraisal of Pressure Distribution Induced by Ice-Structure Interaction Using High-Precision Pressure Measurement Film, *International Conference and Exhibition of Performance of Ships and Structures in Ice (ICETECH)* 2012.

KIM, H. and QUINTON, B.W.T., 2015. *Moving Ice Loads on an Elastic Plate*. Unpublished.

KIM, H., ULAN-KVITBERG, C.A. and DALEY, C.G., 2014. Evaluation of spatial pressure distribution during ice-structure interaction using pressure indicating film. *International Journal of Naval Architecture and Ocean Engineering*, **6**(3), pp. 578.

KITAMURA, O., 1997. Comparative Study on Collision Resistance of Side Structure. *Marine Technology*, **24**(4),.

KITAMURA, O., 2002. FEM approach to the simulation of collision and grounding damage. *Marine Structures*, **15**.

LSTC, 2014. *LS-Dyna Keyword User's Manual*. Livermore, California: Livermore Software Technology Corporation.

MANUEL, A., 2012. *Steps2: Manual of Laboratory Procedures*. St. John's, NL: Memorial University of Newfoundland.

MCDERMOTT, J.F., KLINE, R.G., JONES, E.L., MANIAR, N.M. and CHIANG, W.P., 1974. Mcdermott J F; Kline R G; Jones E L; Maniar N M; Chiang W P. *SNAME Transactions*, .

MINNICK, P. and ST. JOHN, J., 1990. *Global Ice Forces and Ship Response to Ice - A Second Season*. SSC-343. Washington, D.C.: Ship Structure Committee.

MINORSKY, V.U., 1959. An Analysis of Ship Collisions with Reference to Protection of Nuclear Power Plants. *Journal of Ship Research*, .

MONTGOMERY, D.C., 2008. *Design and Analysis of Experiments*. John Wiley & Sons.

MSL ENGINEERING LTD., 2000. *Collision resistance of ship-shaped structures to side impact*. 2000/O53. Sudbury, Suffolk: HSE Books.

MULMULE, S.V. and DEMPSEY, J.P., 1999. Scale effects on sea ice fracture. *Mechanics of Cohesive-frictional Materials*, **4**(6), pp. 505-524.

MYERS, R.H., MONTGOMERY, D.C. and ANDERSON-COOK, C.M., 2009. *Response Surface Methodology: Process and Product Optimization Using Designed Experiments*. Wiley.

PAIK, J.K., 2007. Practical techniques for finite element modelling to simulate structural crashworthiness in ship collisions and grounding (Part II: Verification). *Ship and Offshore Structures*, **2**(1),.

PAIK, J.K., AMDAHL, J., BARLTROP, N., DONNER, E.R., GU, Y., ITO, H., LUDOLPHY, H., PEDERSEN, P.T., ROHR, U. and WANG, G., 2003. Committee V.3: Collision and Grounding, *15th International Ship and Offshore Structures Congress (ISSC) 2003*.

PAIK, J.K. and LEE, T.K., 1995. Damage and Residual Strength of Double-Hull Tankers in Grounding. *International Journal of Offshore and Polar Engineering*, **5**(4),.

PEDERSEN, P.T., 1995. Collision and Grounding Mechanics, *Proceedings of the West European Confederation of Maritime Technology Societies (WEMT)* 1995, pp. Vol. 1 P. 125-157.

PEDERSEN, P.T. and ZHANG, S., 2000. Effect of ship structure and size on grounding and collision damage distributions. *Ocean Engineering*, **27**, pp. 1161.

PETRENKO, V.F. and WHITWORTH, R.W., 1999. *Physics of Ice*. Oxford: Oxford University Press.

QUINTON, B.W.T., 2008. *Progressive Damage to a Ship's Structure Due to Ice Loading*, Memorial University of Newfoundland.

QUINTON, B.W.T., DALEY, C.G. and GAGNON, R.E., 2013. Response of IACS URI Ship Structures to Real-time Full-scale Operational Ice Loads. *SNAME Transactions* 2012, **120**, pp. 203-209.

QUINTON, B.W.T., DALEY, C.G. and GAGNON, R.E., 2012. Realistic Moving Ice Loads and Ship Structural Response, *The Proceedings of the 22nd (2012) International Offshore and Polar Engineering Conference (ISOPE)*, 17-22 June 2012.

QUINTON, B.W.T., DALEY, C.G. and GAGNON, R.E., 2010. Effect of Moving Ice Loads on the Plastic Capacity of a Ship's Structure, *Proceedings of the 9th International Conference and Exhibition on Performance of Ships and Structures in Ice (ICETECH 2010)*, 20-23 September 2010, SNAME.

ROSENBLATT (M) & SON, INC., 1975. *Tanker Structural Analysis for Minor Collisions*. CG-D-72-76. Springfield, VA: National Technical Information Service.

SAJDAK, J.A.W. and BROWN, A.J., 2004. *Modeling Longitudinal Damage in Ship Collisions*. SR-1426. Washington, D.C.: Ship Structure Committee.

SANDERSON, T.J.O., 1988. *Ice mechanics : risks to offshore structures*. London, UK; Boston: Graham & Trotman.

SCHULSON, E.M. and DUVAL, P., 2009. *Creep and Fracture of Ice*. Cambridge, UK: Cambridge University Press.

SIMONSEN, B.C., 1997a. Ship Grounding on Rock - I. Theory. *Marine Structures*, **10**, pp. 519.

SIMONSEN, B.C., 1997b. Ship Grounding on Rock - II. Validation and Application. *Marine Structures*, **10**, pp. 563.

SIMONSEN, B.C. and HANSEN, P.F., 2000. Theoretical and Statistical Analysis of Ship Grounding Accidents. *Transactions of the American Society of Mechanical Engineers*, **122**, pp. 200.

SOKOL-SUPEL, J., 1985. Rigid Plastic Plates under a Concentrated Moving Load. *Journal of structural mechanics*, **13**(1), pp. 77-93.

TIJSEN, J., BRUNEAU, S. and COLBOURNE, B., 2015. Laboratory Examination of Ice Loads and Effects on Concrete Surfaces from Bi-axial Collision and Adhesion Events, *Proceedings of the 23rd International Conference on Port and Ocean Engineering under Arctic Conditions (POAC 2015)* 2015.

TIMOSHENKO, S., 1953. *History of strength of materials*. New York: McGraw-Hill.

ULAN-KVITBERG, C.A., 2012. *Adapting Pressure Films to Measure Pressure Patterns in Ice-Steel Interaction Experiments*, Memorial University of Newfoundland.

WALKER, J. and SIMMONS, C.J., 1847. *Report to the Commissioners of Railways, on the fatal Accident on the 24th day of May 1847, by the falling of the Bridge over the River Dee, on the Chester and Holyhead Railway*. London: .

WANG, G., JI, C., KUJALA, P., LEE, S.-., MARINO, A., SIRKAR, J., SUZUKI, K., PEDERSEN, P.T., VREDEVELDT, A.W. and YURIY, V., 2006. Committee V.1: Collision and Grounding, *16th International Ship and Offshore Structures Congress (ISSC)* 2006.

WMO/IOC, 2004. *JCOMM expert team on sea ice (ETSI), Second Session, Steering group for the global digital sea ice data bank (GDSIDB), Tenth Session*. JCOMM Meeting Report No. 28. Hamburg: World Meteorological Organization & Intergovernmental Oceanographic Commission (of UNESCO).

WROTTESELEY, J., WILLIS, R., JAMES, H., RENNIE, G., CUBITT, W. and HODGKINSON, E., 1849. *Report of the Commissioners Appointed to Inquire into the Application of Iron to Railway Structures*. London: William Clowes and Sons.

ZHANG, S., 2002. Plate tearing and bottom damage in ship grounding. *Marine Structures*, **15**(2),.

Appendices

Appendix A – Moving Load Apparatus Equipment Specifications

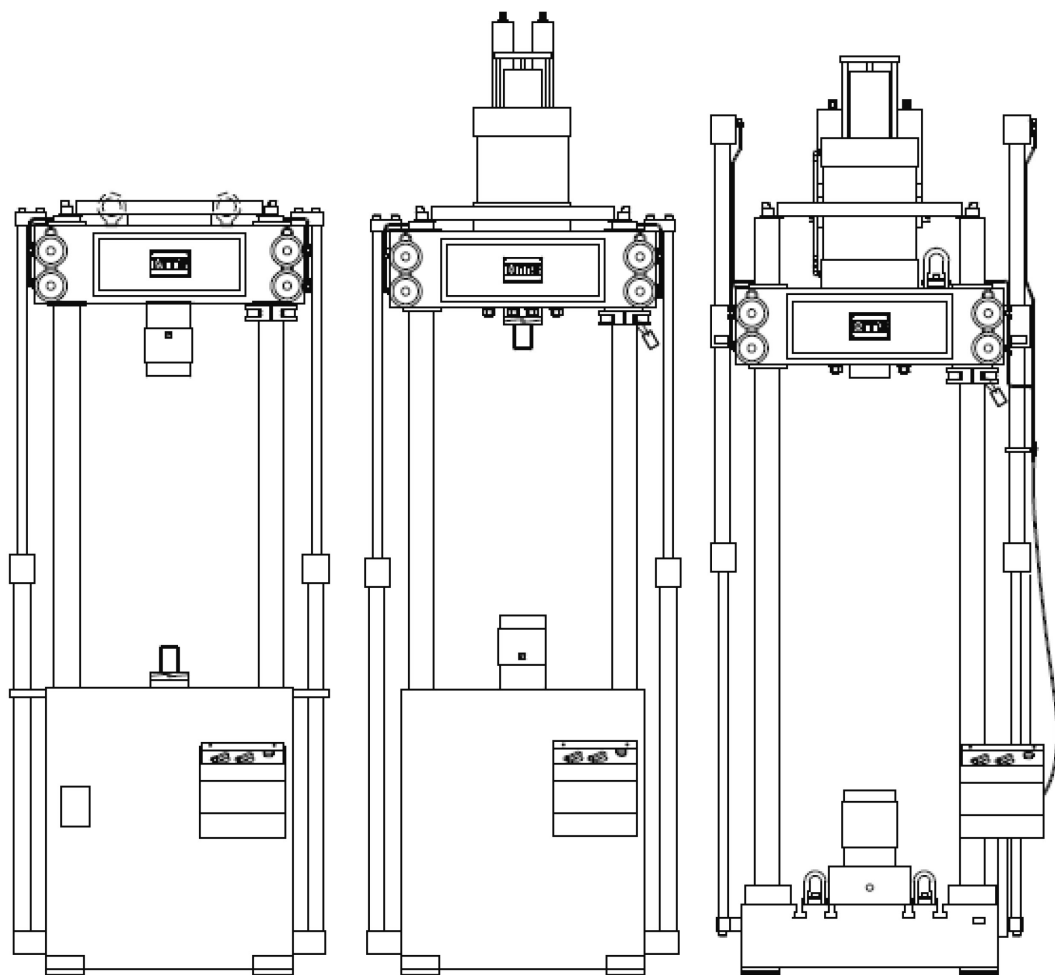
Appendix A1 – MTS Test Frame Specifications

Test frame model 311.21

Introduction

The Series 311 Load Frames are designed to perform high-velocity tension or compression testing, high-frequency fatigue testing, as well as other tests. The load frame must be configured with optional actuators, servovalves, force transducers, grips, and other components from MTS Systems Corporation.

Contents	Component Identification	15
	Functional Description	17
	Specifications	19



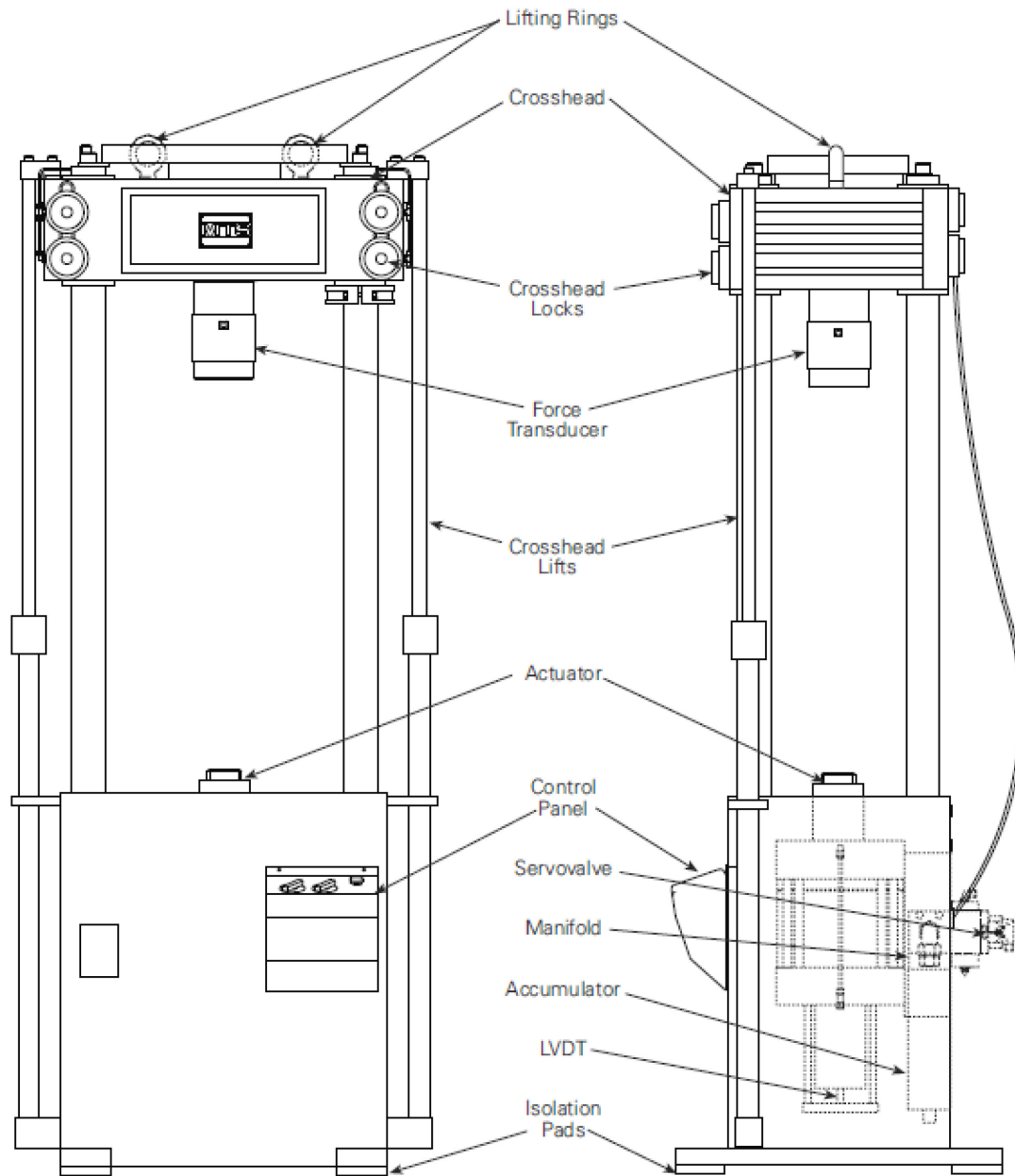
Base Mounted Actuator

Crosshead Mounted Actuator

Custom T-Slot Baseplate

Model 311.31 Load Frame

Component Identification



Specifications

This section provides some of the specifications of the Series 311 Load Frame. Other specifications can be found on the assembly drawings specific to each load frame.

Parameter	Specification
Force rating	
311.11	250 kN (55 kip)
311.21	500 kN (110 kip)
311.31	1000 kN (220 kip)
311.41	2500 kN (550 kip)
311.51	5000 kN (1100 kip)
311.61	7500 kN (1650 kip)
311.71	10,000 kN (2200 kip)
Crosshead weight	
311.11	180 kg (400 lb)
311.21	320 kg (700 lb)
311.31	680 kg (1500 lb)
311.41	1680 kg (3700 lb)
311.51	3175 kg (7000 lb)
311.61	5450 kg (12,000 lb)
311.71	7300 kg (16,000 lb)
Total weight*	
311.11	900 kg (2000 lb)
311.21	2000 kg (4500 lb)
311.31	3500 kg (8000 lb)
311.41	8500 kg (19,000 lb)
311.51	16,000 kg (36,000 lb)
311.61	27,000 kg (60,000 lb)
311.71	36,000 kg (80,000 lb)

* The weight specification is for lifting and moving purposes. The weight includes a typical actuator, force transducer, and grips. The actual shipping weight must be determined by a scale.

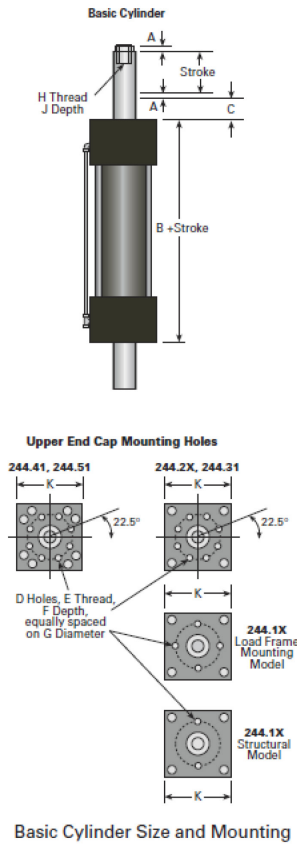
Appendix A2 – MTS Vertical Hydraulic Ram Specifications

Model: 244.41

Specifications

The specifications for the Series 244 Hydraulic Actuator models are shown on the following pages. To determine the overall dimensions of an actuator equipped with swivels, refer to the Series 249 Swivels

Product Specification and add the swivel height to the closed housing LVDT height. Similarly, the overall length of a pedestal base actuator is determined by adding the pedestal base height to the closed housing LVDT height.



Specifications for Basic Cylinder Size and Mounting

Model	Force Rating*		Rod Diameter		Piston Area		Cushions (A)	
	kip	kN	in.	mm	in. ²	cm ²	in.	mm
244.11	3.3	15	1.75	44.5	1.17	7.50	0.60	15.2
244.12	5.5	25	1.75	44.5	2.10	13.50	0.60	15.2
244.21	11	50	2.75	69.9	3.90	25.16	0.40	10.2
244.20	15	68	2.75	69.9	5.22	33.68	0.40	10.2
244.22	22	100	2.75	69.9	7.57	48.84	0.30	7.6
244.23	35	150	2.75	69.9	12.73	82.13	0.25	6.4
244.31	55	250	3.75	95.3	19.63	126.65	0.20	5.1
244.41	110	500	5.25	133.4	38.48	248.28	None	None
244.51	220	1000	6.00	152.4	75.60	487.70	None	None

Model	B		C†		D#	E	F		G	
	in.	mm	in.	mm			in.	mm	in.	mm
244.11	9.38	238.3	1.00	25.4	2 or 4	3/8-16	0.75	19.1	3.20	81.3
244.12	9.38	238.3	1.00	25.4	2 or 4	3/8-16	0.75	19.1	3.20	81.3
244.21	9.70	246.4	1.00	25.4	8	1/2-13	0.75	19.1	4.10	104.1
244.20	9.70	246.4	1.00	25.4	8	1/2-13	0.75	19.1	4.10	104.1
244.22	9.20	233.7	1.00	25.4	8	1/2-13	0.75	19.1	4.10	104.1
244.23	9.20	233.7	1.00	25.4	8	1/2-13	0.75	19.1	4.10	104.1
244.31	10.10	256.5	1.00	25.4	8	5/8-11	1.00	25.4	5.50	139.7
244.41	12.27	311.6	1.12	28.4	8	1-8	1.75	44.5	10.37	263.4
244.51	13.49	342.6	1.50	38.1	8	1-8	1.75	44.5	10.37	263.4

Model	H		J‡		K	
	U.S. Customary	SI Metric	in.	mm	in.	mm
244.11	1/2-20	M12 x 1.25 mm	1.75	44.5	4.00	101.6
244.12	1/2-20	M12 x 1.25 mm	1.75	44.5	4.00	101.6
244.21	1-14	M27 x 2 mm	2.25	57.2	5.00	127.0
244.20	1-14	M27 x 2 mm	2.25	57.2	5.50	139.7
244.22	1-14	M27 x 2 mm	2.25	57.2	6.00	152.4
244.23	1-14	M27 x 2 mm	2.25	57.2	6.50	165.1
244.31	1 1/2-12	M36 x 2 mm	2.75	69.9	8.50	215.9
244.41	2-12	M52 x 2 mm	2.75	69.9	11.75	298.5
244.51	3-12	M76 x 2 mm	4.50	114.3	15.25	387.4

* Dynamic force achieved with 3000 psi (21.0 MPa) hydraulic pressure.

† Length of piston rod that extends from the cylinder with the rod is fully retracted. Load frame extensions are greater.

‡ Dimension from end of piston rod to bottom of internal threads. The 244.51 does not use a threaded rod insert.

Must specify structural or load frame model for specific mounting requirements.

Specifications are subject to change. Contact MTS for verification of specifications critical to your needs.

LVDT and Pedestal Base Assemblies

Typical Actuator Configurations

Series 244 Hydraulic Actuators are used every day in labs throughout the world for rigorous testing of materials, structures, and components. Some of the most common configurations are listed below:

Structural Actuator

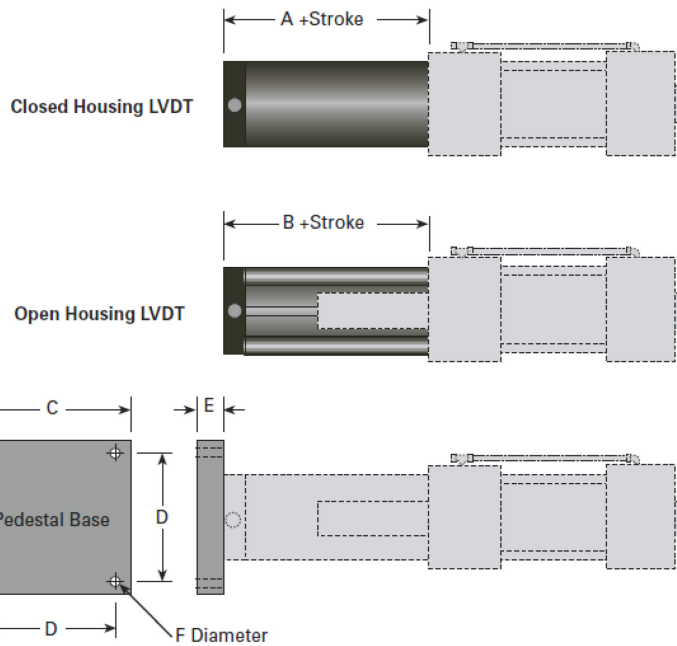
► The most common configuration for the Series 244 Actuator is as a component in a structural testing system. By adding a swivel rod end, load cell, closed housing LVDT, and swivel base to the basic actuator assembly, you can mount the actuator in any position. The pivoting ability of the swivels, lightweight materials, and rugged construction make this configuration a competitive alternative to more complex hydrostatic bearing actuators.

Load Frame Actuator

► The compact size, high sideload tolerance, and high force capacity of the Series 244 Actuators make them ideal for load frame applications. If you are designing your own fixturing and need an actuator configuration with extra stroke or rod length, the 244 may be just what you need. If you prefer a proven load frame design, MTS 318 and 322 Load Units incorporate Series 244 Actuators into a complete, versatile testing system.

Pedestal Base Actuator

► Although most applications profit from at least a small degree of pivotal freedom, others require rigid actuator fixturing. Pedestal bases are available for all actuator models to handle these situations. Vibration testing, seismic tables, and horizontal cantilever installations are common applications for pedestal bases. Check with your sales representative for help in determining the effect of sideloading on pedestal base installations.



Specifications for LVDT and Pedestal Base

Model	A		B		C		D		E		F	
	in.	mm	in.	mm	in.	mm	in.	mm	in.	mm	in.	mm
244.11	3.18	80.8	2.70	68.6	5.50	139.7	4.50	114.3	1.50	38.1	0.56	14.2
244.12	3.18	80.8	2.70	68.6	5.50	139.7	4.50	114.3	1.50	38.1	0.56	14.2
244.21	2.76	70.1	2.70	68.6	7.38	187.4	5.75	146.0	1.75	44.4	0.68	17.3
244.20	2.76	70.1	2.70	68.6	7.38	187.4	5.75	146.0	1.75	44.4	0.68	17.3
244.22	2.76	70.1	2.70	68.6	7.38	187.4	5.75	146.0	1.75	44.4	0.68	17.3
244.23	2.76	70.1	2.70	68.6	7.38	187.4	5.75	146.0	1.75	44.4	0.68	17.3
244.31	2.36	59.9	2.70	68.6	9.00	228.6	7.25	184.2	2.50	63.5	0.94	23.9
244.41	1.96	49.8	2.70	68.6	13.88	352.6	11.00	279.4	2.50	63.5	1.31	33.3
244.51	3.88	98.6	2.70	68.6	14.00	355.6	11.00	279.4	3.00	76.2	1.56	39.6

Specifications are subject to change. Contact MTS for verification of specifications critical to your needs.

Appendix A3 – MTS Flextest GT Specifications

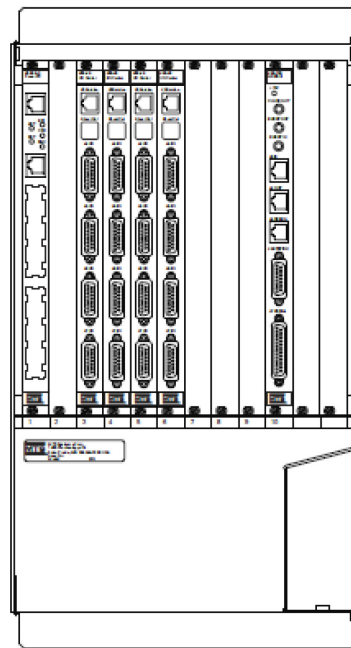
Model 493.10 Chassis

FlexTest GT Controllers

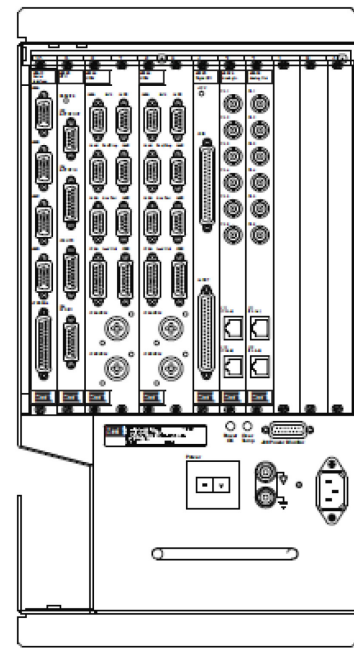
MTS FlexTest GT Controllers are fully digital Proportional, Integral, Derivative, Feedforward (PIDF) servocontrollers which use an identical chassis configuration. They provide complete control of up to eight channels distributed among up to eight stations. Optional station configurations are available (see “Hydraulic Configurations” on page 243).

Model 493.10 Chassis

FlexTest GT Controllers use the Model 493.10 Chassis. The Model 493.10 Chassis is a multi-station, multi-channel VMEbus chassis which houses up to ten MTS VMEbus modules in its front panel and up to ten transition modules in its rear panel.



Front Panel
(with VMEbus Modules)



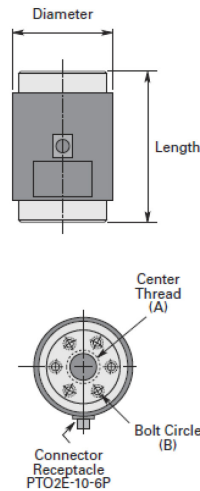
Rear Panel
(with Transition Modules)

Appendix A4 – MTS Load Cell Specifications



Series 661 High Capacity Force Transducers

SPECIFICATIONS



Static Overload Capacity

- ▶ 150% of rated force capacity

Temperature Coefficient Of Zero

- ▶ 0.0025% of full scale/°F
- ▶ 0.0045% of full scale/°C

Temperature Coefficient Of Output

- ▶ 0.003% of reading/°F
- ▶ 0.0055% of reading/°C

Compensated Temperature Range

- ▶ +50°F (+10°C) to +150°F (+66°C)

Useable Temperature Range

- ▶ -50°F (-46°C) to +200°F (+93°C)

Nominal Output Sensitivity

At Full Scale Load

- ▶ 2 mV/V

Bridge Resistance

- ▶ 661.22C/D-01, 661.23E/F-01, 661.31E/F-01, 661.34E/F-01; 700 ohms
- ▶ 661.36C/D-03, 661.38A/B-01; 350 ohms

Hysteresis (% of full scale)

- ▶ 661.22C/D-01, 661.23E/F-01; 0.15
- ▶ 661.31E/F-01, 661.34E/F-01, 661.36C/D-03, 661.38A/B-01; 0.20

Non-linearity (% of full scale)

- ▶ 661.22C/D-01, 661.23E/F-01, 661.31E/F-01, 661.34E/F-01; 0.15
- ▶ 661.36C/D-03, 661.38A/B-01; 0.20

Maximum Excitation

- ▶ 661.22C/D-01, 661.23E/F-01, 661.31E/F-01, 661.34E/F-01; 20 volts
- ▶ 661.36C/D-03, 661.38A/B-01; 15 volts

Calibration

- ▶ Each force transducer ordered may be calibrated by MTS using our automated calibration system at our factory or on-site by MTS Field Service. In addition, the force transducer and associated conditioning electronics may be returned to MTS for repair and recalibration.

Bolt Circle (B)

- ▶ 661.22 and 661.23 Models; none
- ▶ 661.31E-01; 1-14 UNS x 1.75 in. deep, 8 holes on a 6 in. diameter bolt circle
- ▶ 661.34E-01; 1 1/4-12 UNF x 2.50 in. deep, 8 holes on 7.00 in. diameter bolt circle.
- ▶ 661.36C-01; 1 1/2-12 UNF x 3 in. deep, 8 holes on a 10 in. diameter bolt circle
- ▶ 661.38A-01; 1 1/2-12 UNF x 3 in. deep, 16 holes on a 14 in. diameter bolt circle
- ▶ 661.31F-01; M27 x 2 mm x 44 mm deep, 8 holes on a 152.4 mm diameter bolt circle
- ▶ 661.34F-01; M30 x 2 mm x 63.5 mm deep, 8 holes on a 177.8 mm diameter bolt circle.
- ▶ 661.36D-01; M36 x 2 mm x 76.2 mm deep, 8 holes on a 254 mm diameter bolt circle
- ▶ 661.38B-01; M36 x 2 mm x 76.2 mm deep, 16 holes on a 355.6 mm diameter bolt circle

Model	Force Capacity (lb)/ Deflection at Rated Force Capacity (in)	Spring Rate (10 ⁶ lb/in)	Diameter (in)	Length (in)	Center Thread* (A)
661.22C-01	55,000/0.0025	22	5	8	1 1/2-12 UNF x 2.35 in
661.23E-01	110,000/0.003	36	6	8	2-12 UN x 2.00 in
661.31E-01	220,000/0.004	55	8.75	12	3-12 UNF x 3.00 in
661.34E-01	330,000/0.005	64	10.25	14	3 1/2-12 UN x 3.5 in
661.36C-03	550,000/0.006	92	13.75	17.25	4 1/2-8 UN x 6.00 in
661.38A-01	1,100,000/0.008	138	18.25	22	5-8 UN x 7.50 in

Model	Force Capacity (kN)/ Deflection at Rated Force Capacity (mm)	Spring Rate (10 ⁶ N/mm)	Diameter (mm)	Length (mm)	Center Thread* (A)
661.22D-01	250/0.064	3.9	127	203	M36 x 2 mm x 60 mm
661.23F-01	500/0.08	6.2	152	203	M52 x 2 mm x 51 mm
661.31F-01	1,000/0.10	10	222	305	M76 x 2 mm x 76 mm
661.34F-01	1,500/0.13	11.2	260	356	M90 x 2 mm x 89 mm
661.36D-03	2,500/0.15	17	349	438	M125 x 4 mm x 152 mm
661.38B-01	5,000/0.20	25	464	559	M125 x 4 mm x 190 mm

*Center thread information is for both ends of the unit.

MTS Systems Corporation
14000 Technology Drive
Eden Prairie, MN 55344-2290
952-937-4555, Fax 952-937-4515

ISO 9001:2000 CERTIFIED QMS

Specifications Subject to Change Without Notice
©Copyright MTS Systems Corporation 6/1996
Part Number 300143-01 661-02 Printed in U.S.A.

Appendix A5 – MTS LVDT Specifications

The MTS test frame uses a modified version of the 0219 model highlighted on the following pages.

Series 210-220

Long Stroke AC LVDTs

The Series 210-220 AC LVDTs offer precision linear displacement measurements for applications with strokes from 0.5 to 60 inches. The transducers have been designed with an extremely low temperature coefficient, and non-linearity of less than $\pm 0.25\%$ F.S. Variable pitch secondary windings are incorporated into the design with computer controlled winding machines to minimize package length to stroke ratio, and assure a uniform product.



KEY FEATURES

- Ranges from $\pm 0.25''$ to $60''$
- Non-linearity $\leq 0.25\%$
- Low Temperature Coefficient
- Stainless Steel Construction
- High Sensitivity
- Splashproof

TRANSDUCER SPECIFICATIONS

MODEL	FULL STROKE \pm Inches (mm)	MAX. USABLE STROKE \pm Inches (mm)	BODY LENGTH L Inches (mm)	CORE P/N	CORE LENGTH Lc Inches (mm)	CORE MASS Grams	INPUT IMPEDANCE Ohms	DC INPUT RESISTANCE Ohms	OUTPUT IMPEDANCE Ohms	PHASE ANGLE Degrees
0215-0000	0.25 (6.4)	0.65 (16.5)	2.50 (63.5)	C005-0108	1.00 (25.4)	5.1	205	22	265	13
0216-0000	0.50 (12.7)	0.95 (24.1)	3.25 (82.6)	C005-0108	1.00 (25.4)	5.1	235	31	310	17
0217-0000	1.00 (25.4)	1.45 (36.8)	4.50 (114.3)	C005-0113	1.25 (31.8)	6.6	195	36	205	19
0218-0000	2.00 (50.8)	2.70 (68.9)	7.50 (190.5)	C005-0107	1.50 (38.1)	8.1	200	46	255	22
0219-0000	3.00 (76.2)	3.80 (96.5)	10.00 (254.0)	C005-0106	1.90 (48.3)	10.9	225	57	285	25
0220-0000	5.00 (127.0)	5.95 (151.1)	15.00 (381.0)	C005-0105	2.50 (63.5)	14.7	360	89	460	31
0221-0000	7.50 (190.5)	8.45 (214.6)	21.50 (546.1)	C005-0104	4.00 (101.6)	24.5	235	55	235	30
0222-0000	10.00 (254.0)	11.00 (279.4)	28.00 (711.2)	C005-0103	5.50 (139.7)	34.4	330	72	285	31
0223-0000	15.00 (381.0)	16.40 (416.6)	40.00 (1016)	C005-0100	7.00 (177.8)	44.4	450	57	395	25
0224-0000	20.00 (508.0)	21.30 (541.0)	50.00 (1270)	C005-0100	7.00 (177.8)	44.4	660	100	580	30
0225-0000	25.00 (635.0)	26.20 (665.5)	60.00 (1524)	C005-0100	7.00 (177.8)	44.4	210	41	355	28
0226-0000	30.00 (762.0)	31.30 (795.0)	70.00 (1778)	C005-0100	7.00 (177.8)	44.4	200	45	410	30

(Specifications at reference frequency)

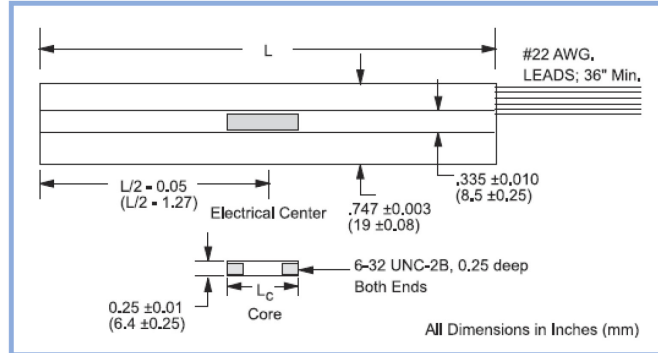
NON-LINEARITY	$\leq \pm 0.25\%$ FS (Best Fit Straight Line)
REFERENCE FREQUENCY	Models 0215-0000 thru 0222-0000, 7.0 KHz; Models 0223-0000 thru 0226-0000, 3.0 KHz
SENSITIVITY	0.50 V/V $\pm 10\%$ at FULL SCALE
INPUT VOLTAGE	20 VRMS, Max.
NULL VOLTAGE	$< 1.0\%$ Excitation Voltage
TEMPERATURE COEFFICIENTS	$< \pm 0.001\%$ FS/ $^{\circ}$ F Zero, $< \pm 0.01\%$ Reading/ $^{\circ}$ F Span
TEMPERATURE RANGE	-67 $^{\circ}$ F to +257 $^{\circ}$ F (-55 $^{\circ}$ C to +125 $^{\circ}$ C) Operating -67 $^{\circ}$ F to +275 $^{\circ}$ F (-55 $^{\circ}$ C to +135 $^{\circ}$ C) Storage
OUTER HOUSING AND BORE LINER	300 Series Stainless Steel
CORE	Chrome Plated Iron/Nickel Alloy

Tel: 800-828-3964 Fax: 860-872-4211
860-872-8351 Web: www.transtekinc.com

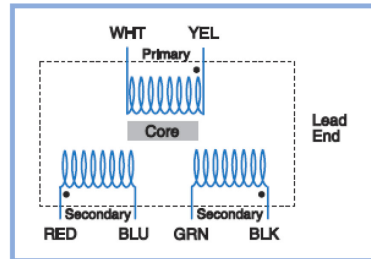
SERIES 210-220

Long Stroke AC LVDTs

DIMENSIONAL DIAGRAM



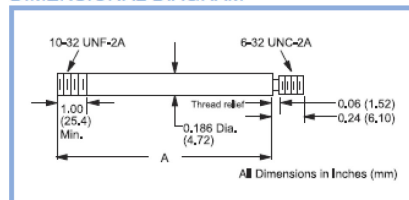
SCHEMATIC



CORE EXTENSION RODS *(Sold Separately)*

The recommended core extension rods are made of nonmagnetic stainless steel and are sized to allow the transducers to operate over their full range. Extension rods from models with longer strokes may be used to facilitate installation. Using extension rods shorter than recommended may reduce the LVDT's usable measurement range.

DIMENSIONAL DIAGRAM



MODEL	RECOMMENDED CORE EXTENSION ROD	DIMENSION A Inches (mm)
0215-0000	C006-0174	3.00 (76.2)
0216-0000	C006-0175	3.60 (91.4)
0217-0000	C006-0176	4.70 (119.4)
0218-0000	C006-0177	7.20 (182.8)
0219-0000	C006-0178	9.30 (236.2)
0220-0000	C006-0179	13.70 (348.0)
0221-0000	C006-0180	19.00 (482.6)
0222-0000	C006-0181	24.20 (614.7)
0223-0000	C006-0182	35.00 (889.0)
0224-0000	C006-0183	45.50 (1156)
0225-0000	C006-0184	56.00 (1422)
0226-0000	C006-0185	66.50 (1689)

TRANS-TEK
INCORPORATED

Appendix A6 – Horizontal Load Cell Specifications

Two Tovey Engineering SW20 50K shear web load cells were used.

SHEAR WEB (SW) SERIES LOAD CELLS

FEATURES

- First Choice for Structural and Materials Testing
- Low Height
- Guaranteed Maximum Off-Center Load & Moment Error
- Low Creep
- Low Susceptibility to Magnetic Fields
- Barometric Pressure Compensation
- Output to 4mV/V
- 5pt Tension & Compression Calibration
- Proprietary Modulus Compensated Strain Gages



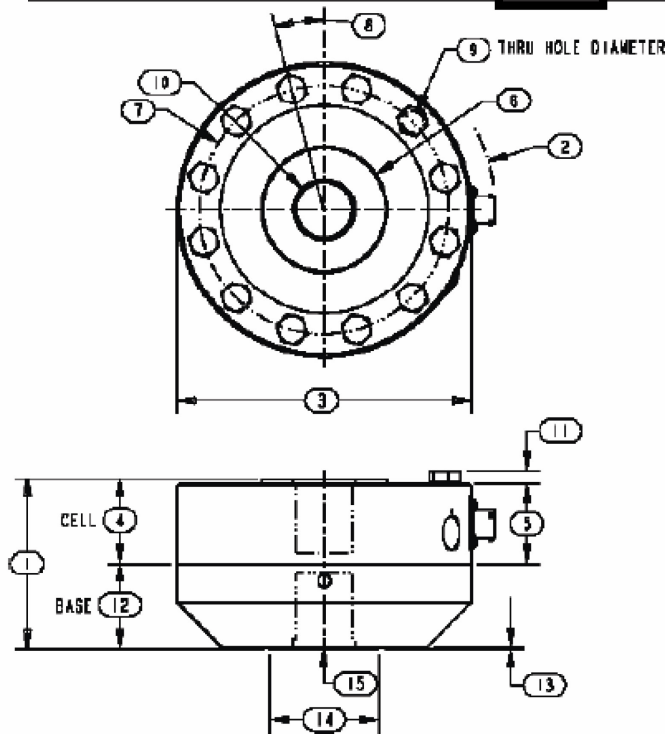
SPECIFICATIONS

Model	SW10 300, 500, 1K, 2K	SW10 5K, 10K	SW20 25K, 50K	SW22 60K	SW30 100K
Capacity U.S. lbf.	1.5, 2.5, 5, 10	25, 50	100, 250	270	300, 500
Capacity Metric kN	1.5, 2.5, 5, 10	25, 50	100, 250	270	300, 500
PARAMETERS					
ACCURACY					
Static Error Band, % Rated Output	+/-0.040	+/-0.040	+/-0.040	+/-0.050	+/-0.050
Nonlinearity, % Rated Output	+/-0.040	+/-0.040	+/-0.040	+/-0.050	+/-0.050
Hysteresis, % Rated Output	+/-0.030	+/-0.040	+/-0.050	+/-0.050	+/-0.050
Nonrepeatability, % Rated Output	+/-0.010	+/-0.010	+/-0.010	+/-0.010	+/-0.010
Creep, % in 20 minutes	+/-0.025	+/-0.025	+/-0.025	+/-0.025	+/-0.025
Off-Center Load Sensitivity, %/inch	+/-0.250	+/-0.250	+/-0.250	+/-0.250	+/-0.250
Side Load Sensitivity, %	+/-0.250	+/-0.250	+/-0.250	+/-0.250	+/-0.250
Zero Balance, % Rated Output	+/-1.0	+/-1.0	+/-1.0	+/-1.0	+/-1.0
TEMPERATURE					
Range, Compensated, °F	+15 to +115	+15 to +115	+15 to +115	+15 to +115	+15 to +115
Range, Compensated, °C	-10 to +45	-10 to +45	-10 to +45	-10 to +45	-10 to +45
Range, Operating, °F	-65 to +200	-65 to +200	-65 to +200	-65 to +200	-65 to +200
Range, Operating, °C	-55 to +90	-55 to +90	-55 to +90	-55 to +90	-55 to +90
Effect on Sensitivity, % Rdg/ °F	+/-0.0008	+/-0.0008	+/-0.0008	+/-0.0008	+/-0.0008
Effect on Sensitivity, % Rdg/ °C	+/-0.0015	+/-0.0015	+/-0.0015	+/-0.0015	+/-0.0015
Effect on Zero, % Rated Output/ °F	+/-0.0008	+/-0.0008	+/-0.0008	+/-0.0008	+/-0.0008
Effect on Zero, % Rated Output/ °C	+/-0.0015	+/-0.0015	+/-0.0015	+/-0.0015	+/-0.0015
ELECTRICAL					
Rated Output, mV/V, Nominal	2	4	4	4	4
Excitation Voltage, VDC Maximum	20	20	20	20	20
Input Resistance, Ohms	350	350	350	350	350
Output Resistance, Ohms	350	350	350	350	350
Insulation Resistance, Megohm	5000	5000	5000	5000	5000
Bayonet Connector	PT02E-10-6P (MS3112E-10-6P)				
MECHANICAL					
Safe Overload Range, % Rated Capacity	+/-150	+/-150	+/-150	+/-150	+/-150
Weight lb	1.0	2.9	9.1	13.5	23.5
Weight kg	0.5	1.3	4.1	6.1	10.7
Weight w/base lb	2.5	6.5	21.5	27.5	52.5
Weight w/base kg	1.1	3.0	9.8	12.5	23.8
Flexure Material	Aluminum	Steel	Steel	Steel	Steel

SHEAR WEB (SW) SERIES LOAD CELLS

DIMENSIONS

Model	SW10	SW10M	SW10	SW10M	SW20	SW20M	SW22	SW22M	SW30	SW30M
Capacity	300, 500, 1K, 2K lbf	1.5, 2.5, 5, 10 kN	5K, 10K lbf	25, 50 kN	25K, 50K lbf	100, 250 kN	60K lbf	270 kN	100K lbf	300, 500 kN
Dimensions	inch	mm	inch	mm	inch	mm	inch	mm	inch	mm
1.	2.51	63.5	2.51	63.5	3.51	88.9	4.50	114.3	4.50	114.3
2.	R 2.53	R 64.3	R 2.53	R 64.3	R 3.50	R 88.9	R 3.50	R 88.9	R 4.50	R 114.3
3.	4.12	104.8	4.12	104.8	6.06	154.0	6.06	154.0	8.00	203.2
4.	1.38	34.9	1.38	34.9	1.75	44.5	2.25	57.2	2.50	63.5
5.	1.25	31.8	1.25	31.8	1.63	41.3	2.13	54.1	2.25	57.2
6.	1.29	32.8	1.29	32.8	2.34 25K 2.58 50K	59.4 100kN 65.6 250kN	2.58	65.6	3.76	95.6
7.	3.50	88.9	3.50	88.9	5.13	130.3	5.13	130.3	6.50	165.1
8.	22.5°	22.5°	22.5°	22.5°	15°	15°	15°	15°	11.25°	11.25°
9.	28 8 Places	7.1 8 Places	28 8 Places	7.1 8 Places	41 12 Places	10.3 12 Places	47 12 Places	11.9 12 Places	53 16 Places	13.5 16 Places
10.	1/2-20 1.12 Deep	M12 x 1.25 28.5 Deep	5/8 - 18 1.12 Deep	M16 x 2 28.5 Deep	1 1/4 - 12 1.50 Deep	M33x 2 38.1 Deep	1 1/2 - 12 2.0 Deep	M36x 2 50.8 Deep	1 3/4-12 2.20 Deep	M42 x 2 55.9 Deep
11.	0.18	4.7	0.18	4.7	0.29	7.5	0.31	7.9	.40	10.2
12.	1.13	28.6	1.13	28.6	1.75	44.5	2.25	57.2	2.00	50.8
13.	0.03	0.8	0.03	0.8	0.03	0.8	0.03	0.8	0.03	0.8
14.	1.25	31.8	1.25	31.8	2.25	57.2	3.00	76.2	3.00	76.2
15.	1/2-20 .88 Deep	M12 x 1.25 22.4 Deep	5/8 - 18 .88 Deep	M16 x 2 22.4 Deep	1 1/4 - 12 1.50 Deep	M33 x 2 38.1 Deep	1 1/2 - 12 2.00 Deep	M36 x 2 50.8 Deep	1 3/4-12 1.75 Deep	M42 x 2 44.5 Deep



OPTIONS

- Additional bridges
- Output adjustment to standard
- Compression overload protection
- Integral cable
- Custom connectors
- Connector Protectors
- Base

ACCESSORIES

- Mating connector
- Loading fixtures
- Interconnect cable
- Shunt calibration resistor
- Instrumentation

Appendix A7 – Horizontal Linear Position Transducer Specifications

Celeco
P/N: PT101-0075-111-2120
Range: 1905mm
Sen: .5 mV/V/mm

PT101

Instrument Grade • Voltage Divider

Absolute Linear Position • Classic Stringpot Design
Stroke Range Options: 0–2 to 0–100 inches
Powder Painted & Anodized Aluminum Enclosure
Industrial Automation & Testing Applications

GENERAL

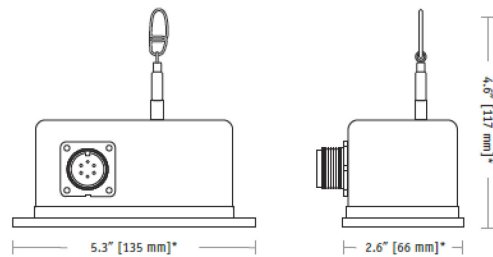
Full Stroke Range Options	0-2 to 0-100 Inches
Output Signal Options	voltage divider (potentiometer)
Accuracy	see ordering information
Repeatability	± 0.02% full stroke
Resolution	essentially infinite
Measuring Cable	see ordering information
Enclosure Material	powder-painted and anodized aluminum
Sensor	plastic-hybrid precision potentiometer
Potentiometer Cycle Life	see ordering information
Maximum Retraction Acceleration	see ordering information
Weight	2 lbs. max.

ELECTRICAL

Input Resistance Options	500, 1K, 5K, 10K or bridge
Maximum Input Voltage	see ordering information
Power Rating	see ordering information
Output Signal Change Over Full Stroke Range	94% ±4% of input voltage

ENVIRONMENTAL

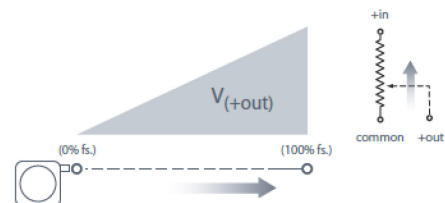
Enclosure	IP50, NEMA 1
Temperature Coefficient of Sensing Element	88 PPM/°F
Humidity	100% RH @ 90°F (32° C)
Operating Temperature	-40° to 200°F (-40° to 90°C)
Vibration	up to 10 g to 2000 Hz maximum



Based on Celeco's original string pot design dating back to the late 1960's, the PT101 has become a standard throughout the years for literally thousands of applications including aircraft structural testing, hydraulic cylinder control, valve stem opening, and factory automation.

Available in full stroke ranges up to 100-inches, the PT101 provides a voltage feedback signal linearly proportional to the position of its traveling stainless steel measuring cable. Additionally the PT101 installs in minutes and doesn't require perfect parallel alignment. Simply secure the base to a fixed surface and attach the measuring cable to your moving object.

Electrical Output Signal



— bridge circuit option available, see ordering information

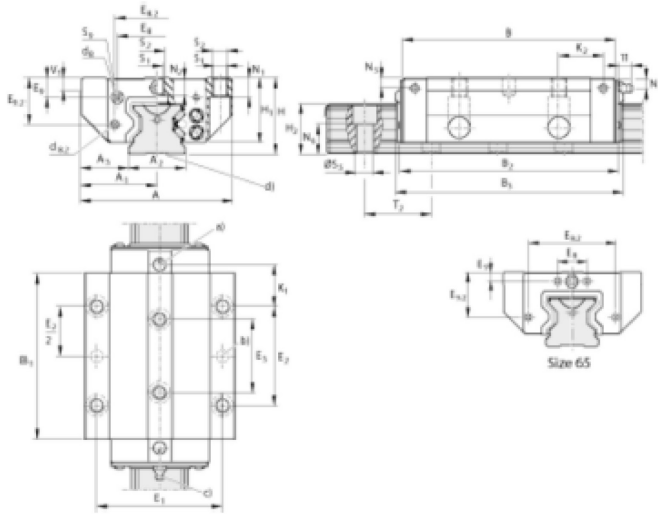
Appendix A8 – Linear Roller-Rail System Specifications

Note: The following two pages are the specifications for the eight roller-bearings used on the carriage.

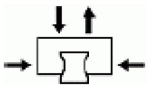
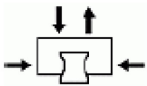




Resist CR - Standard
Size 55

[Click to enlarge picture.](#)

Rexroth
Bosch Group



Part numbers (TNR)	R1853 523 60
Accuracy class	H
Preloading	0,08 C
A [mm]	140
A₁ [mm]	70
A₂ [mm]	53
A₃ [mm]	43.5
B [mm]	205.5
B₁ [mm]	162.1
B₂ [mm]	209.5
B₃ [mm]	216
d₈ [mm]	10
d_{8.2} [mm]	6
E₁ [mm]	116
E₂ [mm]	95
E₃ [mm]	70
E₈ [mm]	74.2
E_{8.2} [mm]	81.6
E₉ [mm]	18.85
E_{9.2} [mm]	40.75

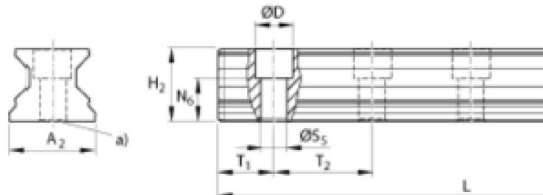
H [mm]	70	
H ₁ [mm]	58	
H ₂ with rail seal cover strip [mm]	47.85	
H ₂ without rail seal cover strip [mm]	47.55	
K ₁ [mm]	41.25	
K ₂ [mm]	44.4	
N ₁ [mm]	18	
N ₂ [mm]	13.7	
N ₅ [mm]	9	
N ₆ ±0,5 [mm]	28.7	
S ₁ [mm]	12.5	
S ₂ [mm]	M14	
S ₅ [mm]	16	
S ₉ [mm]	M5-8 deep	
T ₂ [mm]	60	
V ₁ [mm]	12	
weight [kg]	7.7	
C [N] ¹⁾	165000	
C ₀ [N] ¹⁾	345300	
M _l [Nm] ¹⁾	4837	
M _{t0} [Nm] ¹⁾	10122	
M _L [Nm]	4030	
M _{L0} [Nm] ¹⁾	8440	
Product group info		
	Runner block FLS	
	R1853 ... 6.	
	Flanged, long, standard height	
Product family info		
	Note on dynamic load capacities and moments	
	The dynamic load capacities and moments are based on 100,000 m travel. However, a travel of just 50,000 m is often taken as a basis.	
	If this is the case, for comparison purposes:	
	Multiply values C, M _l und M _L from the table by 1.23.	

The following page is the specifications for the two 2800mm long linear rails.

**Guide rails with plastic mounting hole plugs R1845.0...
end faces coated**

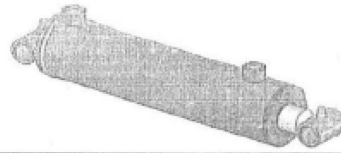
Click to enlarge picture.

Rexroth
Bosch Group



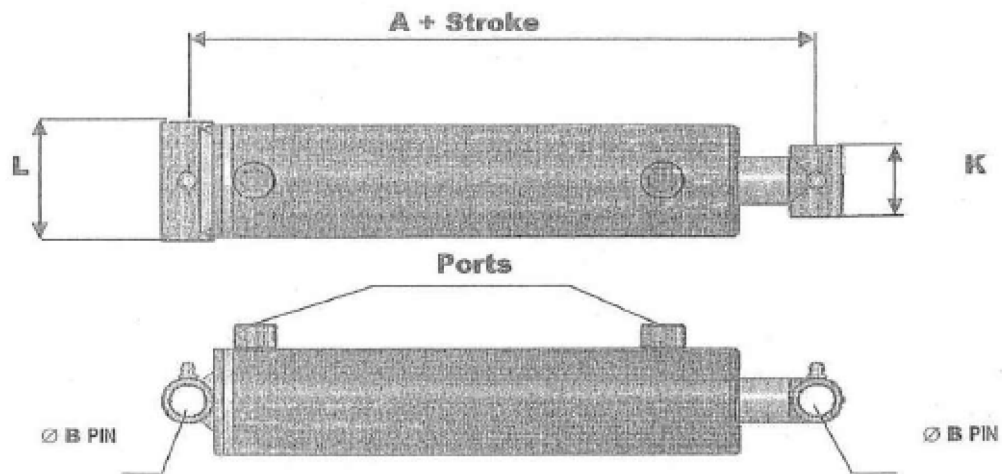
Configuration	Please click here for configuring the product and putting it into the shopping basket!	
Part numbers (TNR)	R1845 503 41	Composite guide rails on request
Size	55	
Accuracy class	H	Accuracy classes SP and P on request
one-part / composite	one-piece	
Recommended rail lengths	$L = n_B \cdot T_2 - 4$ (up to 66/3956 max.)	
A₂ [mm]	53	
D [mm]	24	
H₂ [mm]	47.55	
L_{max} [mm]	4000	
N₆ ±0,5 [mm]	28.7	
S₅ [mm]	16	
T_{1 min} [mm]	18	
T_{1S} [mm]	28	Preferred dimension T _{1S} with tolerances +0.75/-1.0
T₂ [mm]	60	
Mass [kg/m]	13.1	
Product group info	*UNDEFINED TEXT*	
Product family info	Caution! Please read the general notes on guide rails in Resist CR! Notes Plastic mounting hole plugs are also available as accessories.	

Appendix A9 – Horizontal Hydraulic Cylinder Specifications



MODEL	BORE X STROKE (inches)	ROD DIA. (inches)	PIN DIA. (inches)	CENTER TO CENTER OF PIN (inches)		PORTS	WEIGHT (lbs)
				retracted	extended		
HYS 30MAL12-10	3 X 12	1-1/2	1	20	32	SAE-8	29
HYS 30MAL14-10	3 X 14			22	36		31
HYS 30MAL16-10	3 X 16			24	40		32
HYS 30MAL18-10	3 X 18			26	44		36
HYS 30MAL20-10	3 X 20			28	48		39
HYS 30MAL24-10	3 X 24			32	56		42
HYS 30MAL28-10	3 X 28			36	64		48
HYS 30MAL30-10	3 X 30			38	68		52
HYS 30MAL32-10	3 X 32			40	72		56
HYS 30MAL36-10	3 X 36			44	80		60
HYS 30MAL40-10	3 X 40			48	88		65
HYS 30MAL48-10	3 X 48			56	104		71
HYS 35MAL08-10	3 1/2 X 8	1-3/4	1-1/4	16	22	SAE-8	31
HYS 35MAL08-10	3 1/2 X 8			18	26		33
HYS 35MAL10-10	3 1/2 X 10			20	30		36
HYS 35MAL12-10	3 1/2 X 12			22	34		39
HYS 35MAL14-10	3 1/2 X 14			24	38		41
HYS 35MAL16-10	3 1/2 X 16			26	42		45
HYS 35MAL18-10	3 1/2 X 18			28	46		48
HYS 35MAL20-10	3 1/2 X 20			30	50		51
HYS 35MAL24-10	3 1/2 X 24			34	58		56
HYS 35MAL28-10	3 1/2 X 28			38	66		60
HYS 35MAL30-10	3 1/2 X 30			40	70		64
HYS 35MAL32-10	3 1/2 X 32			42	74		68
HYS 35MAL36-10	3 1/2 X 36			46	82		77
HYS 35MAL40-10	3 1/2 X 40			50	90		81
HYS 35MAL48-10	3 1/2 X 48			58	106		85
HYS 40MAL08-10	4 X 8	2	1-1/2 can be converted to 1-3/4	18	26	SAE-8	41
HYS 40MAL10-10	4 X 10			20	30		45
HYS 40MAL12-10	4 X 12			22	34		48
HYS 40MAL14-10	4 X 14			24	38		52
HYS 40MAL16-10	4 X 16			26	42		55
HYS 40MAL18-10	4 X 18			28	46		59
HYS 40MAL20-10	4 X 20			30	50		63
HYS 40MAL24-10	4 X 24			34	58		68
HYS 40MAL28-10	4 X 28			38	66		77
HYS 40MAL30-10	4 X 30			40	70		81
HYS 40MAL32-10	4 X 32			42	74		84
HYS 40MAL36-10	4 X 36			46	82		92
HYS 40MAL40-10	4 X 40			50	90		99
HYS 40MAL48-10	4 X 48			58	106		114

Note: Model HYS 40MAL48-10 was used.



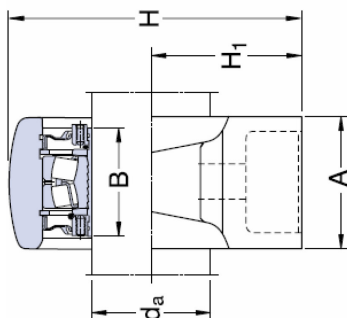
Pressure (PSI)	
Operating	Testing
3000	8000

MAL CYLINDER DIMENSIONS

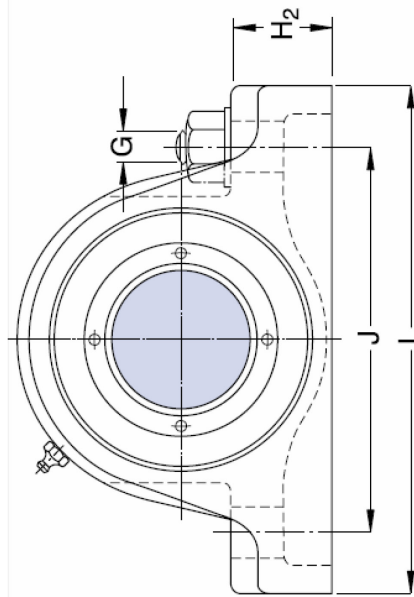
	TUBE DIA.	A	ØB PIN	K	L	PORTS (SAE)
in	1.50	8.00	0.75	2.00	2.25	6
mm	38.1	203.2	19.05	50.80	57.15	
in	2.00	8.00	1.00	2.25	2.75	6
mm	50.8	203.2	25.4	57.15	69.85	
in	2.50	8.00	1.00	2.25	3.25	8
mm	63.5	203.2	25.4	57.15	82.55	
in	3.00	8.00	1.00	2.25	3.75	8
mm	76.2	203.2	25.4	57.15	95.25	
in	3.50	10.00	1.25	2.25	4.25	8
mm	88.9	254	37.5	57.15	107.95	
in	4.00	10.00	1.50	2.50	4.75	8
mm	101.6	254	38.1	63.50	120.65	
in	5.00	12.00	1.75	3.25	6.00	12
mm	127	304.8	44.45	82.55	152.40	

LIFETIME WARRANTY AGAINST ALL MANUFACTURING DEFECTS

ConCentra roller bearing units SYR .. N for inch shafts

$$d_a = 1\frac{7}{16} - 4\text{ in}$$


Shaft diameter	Bearing unit Dimensions											Mass	Designation ¹⁾ Non-locating unit with Tri-Gard seals	
	A	B	H	H ₁	H ₂	J	L	N	N ₁	G				
d _a														
in/mm	in/mm												lb/kg	-
2 7/16 65.1	2 9/16 65.1	2 37/64 65.5	5 11/16 144.5	2 3/4 69.8	1 3/4 44.4	7 1/8 181	9 1/4 235	1 1/16 27	3/4 19	5/8 16.0	SYR 2.7/16 N			
11 9/12											7.25			



Unit Designation	Bearing Basic design- nation	Basic load ratings dynamic C	static C ₀	Calculation factors e	Y ₁	Y ₂	Y ₀	Speed ratings for units with Tri-Gard seals	labyrinth seals	Grease quantity Relubrication
-	-	lbf/kN		-				r/min		oz/g
SYR 2.7/16 N	22213	43 000 193	48 000 216	0,24	2,8	4,2	2,8	1 800	5 300	0,70 20

Appendix A11 – Steel Mill Certifications for Carriage Steel and W-Beams

6/14/13 7:36:28

EMAIL COVER PAGE

=====
Company: Russel Metals Inc

6/14/13 7:36:28

Document Summary:

Cover Page: 1

Subject: MILL TEST CERTIFICATE

Order Number :03328167

Customer PO# :REQ # 033371

City : MEM. UNIV OF NEFD, S State/Province : NL

The order of the printed MTRs is as follows:

Item Description:	Heat	MTR
.750 (3/4) HR PLT 44W	A2K284	020055649

4 X 13 WF BEAM A572 50/50W/A992 55027172 020058232



Test Certificate


Form TC1: Revision 1: Date 31 Oct 2000

1770 Bill Sharp Boulevard, Muscatine, IA 52761-9412

Customer: RUSSEL METALS 28TH LAKESIDE PARK DRIVE LAKESIDE NS B3T1A3		Customer P.O.No.: M02073085 & 41-34599 Product Description: CSA G40.21(2004)44W/300W / ASTM A36(08) A709(01A)36/ASME SA36(01ED)		Mill Order No. 41-34599-07		Shipping Manifest: MR185691															
		Ship Date: 01 Dec 12 Cert Date: 01 Dec 12		Ship Date: 01 Dec 12 Cert Date: 01 Dec 12		Cert No: 061360617 (Page 1 of 1)															
		Size: 0.750 X 96.00 X 240.0 (IN)																			
Tested Pieces:		Tensiles:		Charpy Impact Tests																	
Heat Id	Piece Id	Tested Thickness	YS (KSI)	UTS (KSI)	%RA	Elong % 2in 8in	Average Hardness	Abs. Energy (FTLB)	% Shear	1	2	3	Avg	1	2	3	Avg	Tst Tmp	Tst Dir	Tst Siz (mm)	BDWTT Tmp %Shr
A2K284	D11	0.749 (DISCRT)	L 49	72		30															
A2K284	D14	0.749 (DISCRT)	L 50	74		30															
A2K301	B20	0.625 (DISCRT)	L 51	75		31															
A2K301	B23	0.751 (DISCRT)	L 51	74		28															
Chemical Analysis																					
Heat Id	C	Mn	P	S	Si	Tot Al	Cu	Ni	Cr	Mo	Cb	V	Ti	B	N	ORGN					
A2K284	.18	.86	.013	.002	.16	.029	.30	.16	.12	.04	.001	.005	.012	.0002	.0084	USA					
A2K301	.20	1.01	.010	.004	.04	.025	.26	.16	.12	.05	.002	.007	.019	.0001	.0078	USA					
<p>MERCURY IS NOT A METALLURGICAL COMPONENT OF THE STEEL AND NO MERCURY WAS INTENTIONALLY ADDED DURING THE MANUFACTURE OF THIS PRODUCT</p> <p>MTR EN 10204:2004 INSPECTION CERTIFICATE 3.1 COMPLIANT</p> <p>PRODUCTS SHIPPED:</p> <p>A2K284 D13 PCES: 11, WGT: 54138 A2K301 B24 PCES: 2, WGT: 9842</p>																					
(P)		Cust Part #:		WE HEREBY CERTIFY THAT THIS MATERIAL WAS TESTED IN ACCORDANCE WITH, AND MEETS THE REQUIREMENTS OF, THE APPROPRIATE SPECIFICATION																	
				B. H. Wales SENIOR METALLURGIST - PRODUCT																	

020055649

CERTIFIED MATERIAL TEST REPORT

 GERDAU US-ML-CARTERSVILLE 384 OLD GRASSDALE ROAD NE CARTERSVILLE, GA 30121 USA		CUSTOMER SHIP TO RUSSEL METALS INC 28 LAKESIDE PARK DR LAKESIDE, NS B3T 1A3 Canada		CUSTOMER BILL TO RUSSEL METALS INC 28 LAKESIDE PARK DR LAKESIDE, NS B3T 1A3 Canada		GRADE A992/A572-50		SHAPE / SIZE Wide Flange Beam / 4 X 13#		HEAT / BATCH 5502717202	
CUSTOMER PURCHASE ORDER NUMBER 02073968EW1		SALES ORDER 267328/000001		BILL OF LADING 1322-0000002386		DATE 03/30/2013		LENGTH 40'00"		WEIGHT 18,720 LB	
SPECIFICATION / DATE OF REVISION 1-ASTM A6/AGM-11 2-A992/A992M-11 3-A572/A572M-07											

CHEMICAL COMPOSITION											
C	%	0.13	P	%	0.013	S	%	0.027	Si	%	0.24
Mn	%	0.92	Cu	%	0.24	Ni	%	0.14	C	%	0.04
Sn	%	0.012	Mo	%	0.031	V	%	0.017	Nb	%	0.002
									N	%	0.0090
									P	%	0.0070

CHEMICAL COMPOSITION											
Sn	%	0.012									

MECHANICAL PROPERTIES											
Elong.	%	22.80	G/L	inch	8.000	UTS	MPa	512	UTS	MPa	512
		22.60					PSI	74209		PSI	57700
								76600			

MECHANICAL PROPERTIES											
YS / UTS	%	0.800	YS	0.2%	PSI	59000	YS	MPa	407		
		0.760				57700			398		

COMMENTS / NOTES	020058232
------------------	-----------

The above figures are certified chemical and physical test records as contained in the permanent records of company. This material, including the billets, was melted and manufactured in the USA. We certify that these data are correct and in compliance with specified requirements. CMTR complies with EN 10204 3.1.

Bhaskar
 BHASKAR VALAMANCHILI
 QUALITY DIRECTOR

Yan Wang
 YAN WANG
 QUALITY ASSURANCE MGR.

Appendix B – Other Apparatus Specifications

Appendix B1 – High-speed Camera Specifications

Model: MS55K

- The MS55K camera is a mid-level high speed camera.
- Typical uses are medium speed applications from 25 fps to 3000 fps.
- Maximum image size is 1280 x 1020 with recording speeds of over 1000 fps at this resolution.
- Minimum image size is 32 x 8.
- Maximum camera speed is 100,000 fps
- On board memory storage.
 - Does not stream the high speed image files back to the PC.
 - Saves the high speed image file inside the camera's RAM, operator then downloads the image file to their PC.
- Sends back real time, pre-view images when the camera is recording via a gigabit Ethernet connection through a CAT 6 cable.
- Can be used in a “stand alone” application without a PC connection.

Please note: the above specifications were taken from MegaSpeed's website for the MS55K model camera on November 17, 2014.

http://www.megaspeed.ca/index.php?option=com_content&view=article&id=10&Itemid

=9

Appendix B2 – GoPro HD Hero 2 & Hero 3 Specifications

FEATURES		HD HERO 2
PHOTO – FEATURES + FOV		
MEGAPIXELS		5 MP
MODES		Single 3 photos in 1 sec Time Lapse every 1, 2, 10, 30, 60 Self-Timer
VIDEO – RESOLUTION + FOV		
1080p		1920×1080 wide (127°) FOV 30fps
960p		1280×960 FOV Wide (170°) 30fps
720p		1280×720 Wide (170°) FOV 30fps 60fps
WVGA		848×480 Wide (170°) FOV 60fps
USABILITY		
Inputs		Component port, Composite port, USB, SD, HERO Port
Battery Life (in 720p/60 mode)		2.5 hrs
Simultaneous record + charge when plugged into USB power source		yes

FEATURES	HERO 3
Optics + Lens	Ultra-sharp <i>f</i> /2.8 - 6 element lens, Ultra wide angle with reduced distortion
PHOTO FEATURES	
Megapixels	5MP
Modes	Photo
	Burst Photo
	Time Lapse
VIDEO FEATURES + FOV	
1080p (16:9)	30, 25 fps
	Medium FOV
960P (16:9)	30, 25 fps
	Ultra Wide FOV
720P (16:9)	60, 50, 30, 25 fps
	Ultra Wide FOV
WVGA (16:9)	60, 50 fps
	Ultra Wide FOV
PHOTO SPECS	
Megapixels + FOV	5MP (Wide)
Time Lapse Intervals	0.5, 1, 2, 5, 10, 30, 60 seconds
Burst Photo (Frames/sec)	3/1
ADVANCED FEATURES	
Wi-Fi Built-in	Yes
Looping Video	Yes
High Video Bitrate Capture (H.264)	Up to 15/Mbs
Mode dependent, highest bitrates supported in Protune	
AUDIO SPECS	
Mono Mic, AAC compression w/ AGC	No
USABILITY	
Inputs	Micro-HDMI port, mini USB, microSD, HERO Port, composite A/V (via adapter, optional accessory), 3.5mm stereo mic (via adapter, optional accessory)
Battery	1050mAh rechargeable lithium-ion

Appendix B3 – Canon EOS60D Specifications

- Megapixel CMOS sensor and DIGIC 4 Imaging Processor.
- ISO 100 – 6400.
- Improved EOS HD Video mode.
- Enhanced iFCL 63-zone, Dual-layer metering system; and 9-point AF system utilizing a high-precision, f/2.8 cross-type centre point.
- Compatibility with SD/SDHC/SDXC memory cards.
- Compatible with the full line of Canon EF and EF-S lenses.

See: http://www.canon.ca/inetCA/en/products/method/gp/pid/4714#_030 for more details.

Appendix B4 – Flir Thermal Cameras Specifications

Model: Ax5-A35sc

Detector	A5sc	A15sc	A35sc
Detector Type	Uncooled VOx microbolometer		
Spectral Range	7.5 μm to 13.0 μm		
Resolution	80 × 64	160 × 128	320 × 256
Detector Pitch	50 μm	25 μm	25 μm
NETD	<50 mK		
Imaging			
Time Constant	Typical 12 ms		
Frame Rate (Full Window)	60 Hz		
Dynamic Range	14-bit		
Digital Data Streaming	Gigabit Ethernet		
Command and Control	Gigabit Ethernet		
Measurement			
Standard Temperature Range	-40 to +160°C (-40 to 320°F) -40 to +550°C (-40 to +1022°F).		
Accuracy	±5°C (±9°F) or ±5% of reading		
Optics			
Available Lenses	5 mm	9 mm	9 mm
Focus	Fixed		
Image Presentation			
Digital Data	Via PC Using FLIR R&D Software or GigE Vision Protocols		
General			
Operating Temperature Range	-15°C to 50°C (5°F to 122°F)		
Storage Temperature Range	-40°C to 70°C (-40°F to 158°F)		
Encapsulation	IP 40 (IEC 60527)		
Bump / Vibration	5 g (IEC 60068-2-27) / 2 g (IEC 60068-2-6)		
Power	12/24 VDC, TBA W absolute max		
Weight	0.2 kg (0.44 lb)		
Size (L × W × H) w/o Lens	106 × 40 × 43 mm (4.2 × 1.6 × 1.7 in.)		
Tripod Mounting	UNC 1/4"-20 via Base Support Accessory		
Base Mounting	4 × M3 thread mounting holes (on bottom)		

Model: T450sc

Detector	T450sc
Detector Type	Uncooled Microbolometer
Spectral Range	7.5 – 13.0 μm
Resolution	320 \times 240
Detector Pitch	25 μm
NETD	<30 mK
Electronics / Imaging	
Time Constant	<12 ms
Frame Rate	60 Hz
Dynamic Range	14-bit
Digital Data Streaming	Real-time Radiometric = USB to PC Real-time Non-radiometric = MPEG via USB to PC
On-Camera Radiometric Recording	Real-time Temperature Calibrated Movie Recording at 30Hz to SD card
Analog Video	Composite Video / RCA connector
Command & Control	USB, WiFi
Measurement	
Standard Temperature Range	-20°C to 1500°C (-4°F to 2732°F)
Accuracy	$\pm 1^\circ\text{C}$ or $\pm 1\%$ (limited range)
Optics	
Camera f/#	f/1.3
Integrated Lens	18 mm (25°)
Available Lenses	76 mm (6°), 30 mm (15°), 10 mm (45°), 4 mm (90°)
Close-up Lenses / Microscopes	Close-up (25 μm), (50 μm), (100 μm)
Focus	Automatic or Manual (Motorized)
Image Presentation	
On-Camera Display	Touch Screen/3.5 in LCD Display (320 \times 240)
Auto-Orientation	Keeps Onscreen Temperature Data Upright in Portrait or Landscape
Automatic Gain Control	Manual, Linear, Histogram, DDE
Image Analysis	Spot Meters, Areas, Auto Hot / Cold Detection, Difference Temp, Isotherms, Alarms, Line Profile
Image Annotations	60 Sec Voice, Text, 4 x Markers, Sketch
Zoom	8 \times Digital Continuous
Visible Image	3.1 Megapixel from Integrated Visible Camera
MSX® Enhancement/ Picture in Picture	Adds Visible Detail to Thermal/ P-i-P Overlays Thermal on Visible Image

MSX® Enhancement/ Picture in Picture	Adds Visible Detail to Thermal/ P-i-P Overlays Thermal on Visible Image
General	
Operating Temperature Range	-15°C to 50°C (5°F to 122°F)
Storage Temperature Range	-40°C to 70°C (-40°F to 158°F)
Encapsulation	IP 54 (IEC 60529)
Bump / Vibration	25 g (IEC 60068-2-29) / 2 g (IEC 60068-2-6)
Power	AC Adapter 90-260 VAC, 50/60 Hz or 12 V from a Vehicle
Battery System	Li Ion, 4 Hours Operating Time
Weight w/ Battery	0.88 kg (1.94 lb)
Size (L × W × H)	106 × 201 × 125 mm (4.2 × 7.9 × 4.9 in)
Mounting	¼"-20

Appendix B5 – Fujifilm Prescale™ Pressure Film

Specifications and Operational Environment

Accuracy: $\pm 10\%$ or less (measured by densitometer at 23°C, 65% RH)

Recommended service temperature: 20°C~35°C (68 °F~ 95°F) *

Recommended service humidity: 35% RH ~ 80% RH**

Thickness: mono-sheet type(S): 100μm

two-sheet type(W): 100μm x2

For more information please visit:

<http://www.fujifilm.com/products/prescale/prescalefilm/#specifications>

Appendix B6 – Microscribe Specifications

Model: Microscribe G2LX



MicroScribe® G2 Desktop Digitizing Systems

In developing the MicroScribe G2 system, it was Immersion's goal to provide graphic artists, animators, video game developers, industrial designers, engineers, and scientists a 3D digitizer with the best combination of functionality and affordability. The result is a highly refined product that looks and feels at home on the desktop while providing the performance of a precision industrial instrument. The USB port provides both a high speed data connection and power for the system, producing a highly portable digitizing solution when combined with a laptop computer. The MicroScribe G2 system is constructed from the highest quality components using precise aluminum housings, lightweight graphite links, and state-of-the-art electronics to provide years of trouble-free digitizing. The mechanical arm is carefully counter-balanced to allow effortless manipulation.

The Fastest Way to Create in 3D

MicroScribe technology provides a fast, reliable, and easy-to-use method for creating accurate 3D computer models. Just trace over the contours of a physical object and build complex 3D datasets in a matter of minutes. MicroScribe systems work with physical objects of any shape, size, and material. A variety of software packages provide the solutions you need to get up and running in no time.

Software Support

To take advantage of MicroScribe technology, you can either use a dedicated digitizing software application or use one of many software drivers that link the MicroScribe G2 system to existing 3D graphics applications. Each of these options allows you to create complex 3D models using points, lines, polygons, splines, NURBS, or other standard geometric entities. Graphical datasets can be saved as dxf, IGES, obj, txt, 3ds, and nearly any other file format your software can export. You can even use the MicroScribe G2 system to control camera views, set light source locations, and define animation trajectories in real-time.

Compatible Software

3D Modeling/Animation/Rendering Software

- 3ds max
- LightWave 3D
- Autodesk VIZ
- Maya
- form • Z

CAD/CAM/Inspection Software

- SolidWorks
- Pro/ENGINEER
- AutoCAD
- solidThinking
- Delcam PowerSHAPE
- Mastercam
- CADKEY
- Rhino 3D

Immersion Software

- MicroScribe Utility Software
- Software Development Kit (PC and Mac)

Specifications

Workspace:

MicroScribe G2	50" sphere
MicroScribe G2X	50" sphere
MicroScribe G2L	66" sphere
MicroScribe G2LX	66" sphere

Accuracy (100 point ANSI sphere):

MicroScribe G2	0.015" (0.38 mm)
MicroScribe G2X	0.009" (0.23 mm)
MicroScribe G2L	0.017" (0.43 mm)
MicroScribe G2LX	0.012" (0.30 mm)

Footprint: 6" x 6"

Interface: RS-232 / USB 1.1

Requirements:

Available serial or USB port on any PC or USB port on any Mac

Versatile Base:

Sits on a desk, mounts on a tripod, or attaches to any surface.

Immersion also offers the MicroScribe MX product line providing higher accuracy at an affordable price.

About Immersion Corporation

Founded in 1993, Immersion Corporation develops hardware and software technologies that improve the way people interact with digital devices. The Immersion digitizing products enable engineers and animators to quickly create 3D models of physical objects.

Please contact:

Solution Technologies, Inc.

Toll-free 800-731-3038

www.3d-microscribe.com



Appendix C – Moving Load Experimental Results Plots

Notes:

1. The following data plots were created using a custom data analysis and plotting script written by the author in Matlab®. The script and its associated graphical user interface are presented in Appendix D.
2. For all figures including “Horizontal Displacement”: horizontal displacement was zeroed at the indenter’s starting position for each experiment. Therefore any plot showing multiple experiments may show data with different x-origins plotted together. Specifically the starting positions of the “Centre” and “End” experiments are 550 mm apart, therefore the x-origin for an “End” experiment is 550 mm less than the x-origin for a “Centre” experiments. Plots with both “End” and “Centre” experiments involving “Horizontal Displacement” should be viewed as if the “End” curves are 550 mm less than shown.
3. The descriptors used in the legends of the following plots are defined as follows:

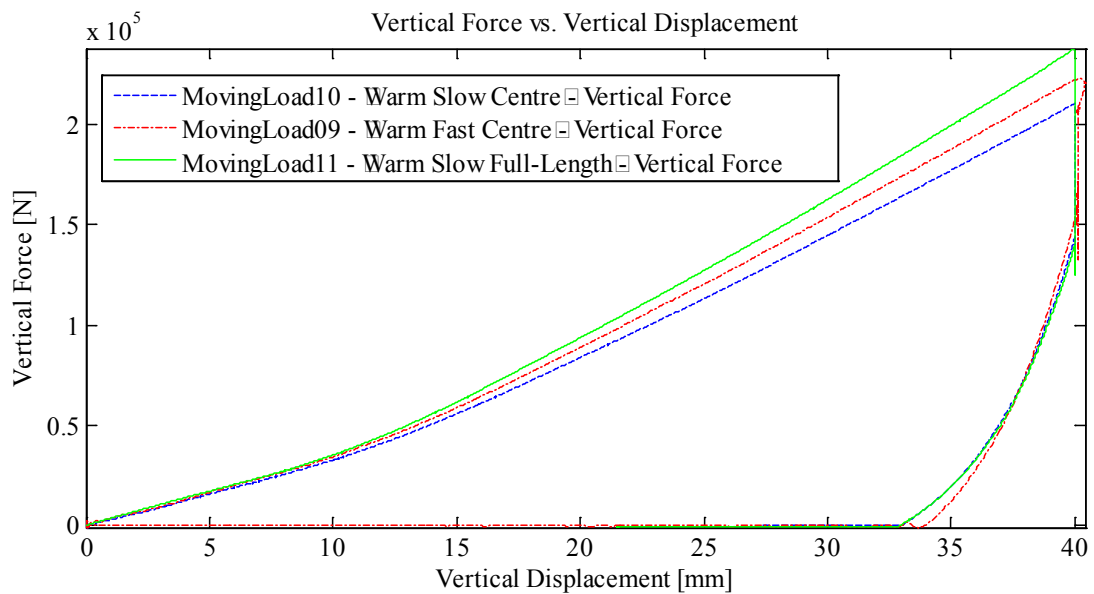
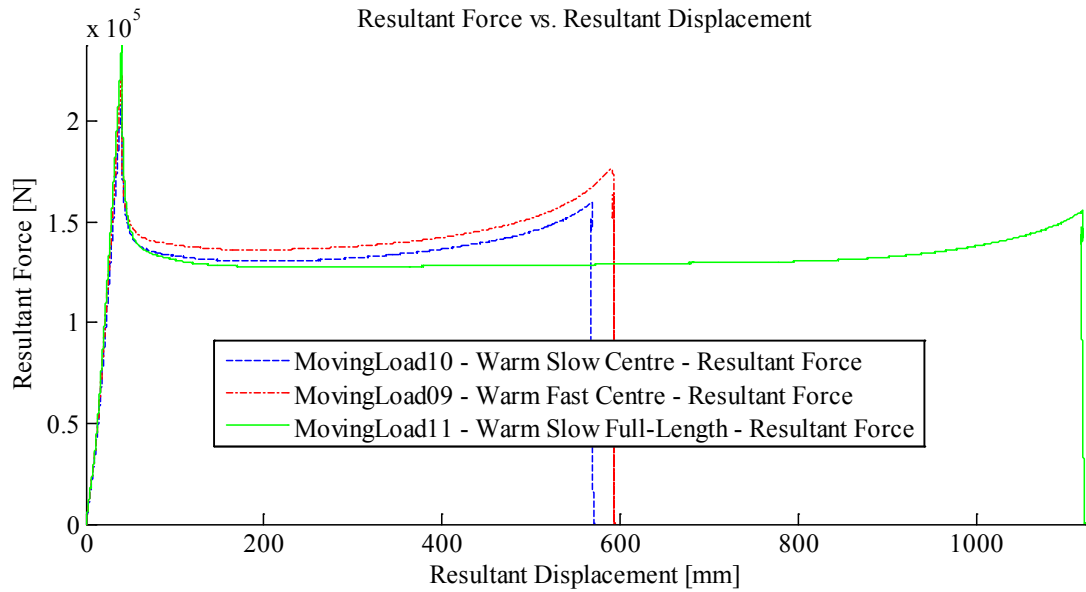
Warm	Specimen at room-temperature (20°C (68°F) nominal)
Cold	Specimen temperature -10 °C (14°F) nominal
Slow	Nominal Vertical Indentation Rate of 1 mm/s (0.039 in./s); Nominal Horizontal Travel Rate of 10 mm/s (0.394 in./s)

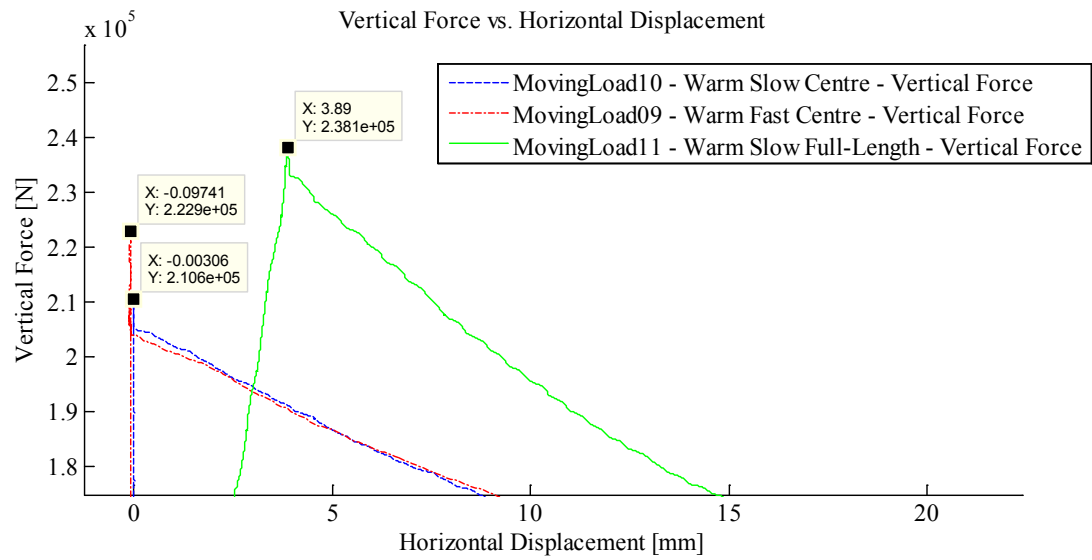
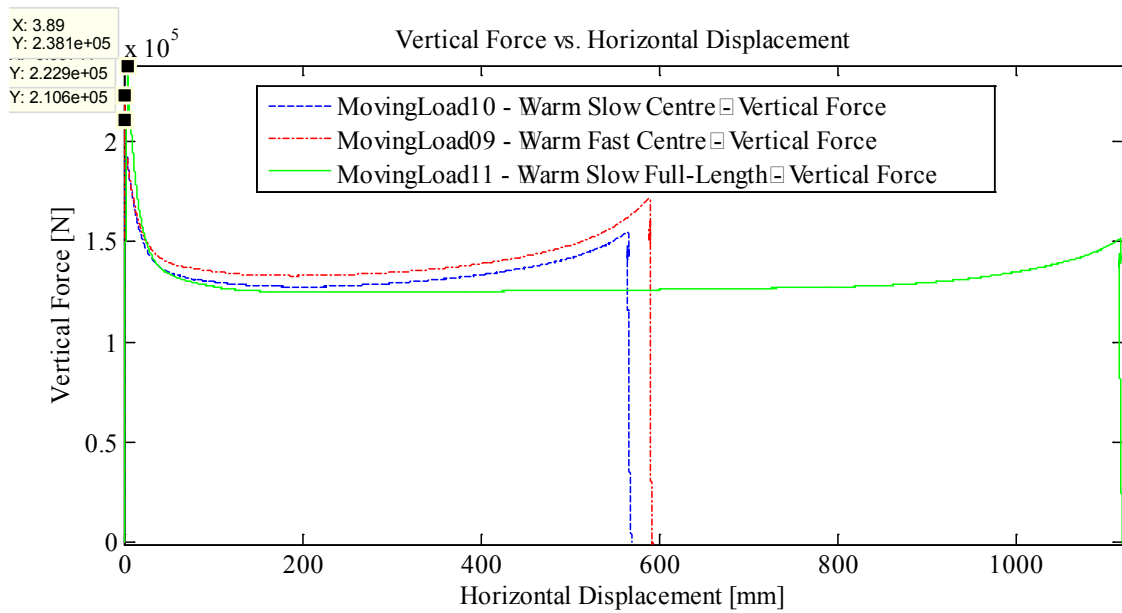
Fast	Maximum Possible Vertical Indentation Rate and Maximum Possible Horizontal Travel Rate
Centre	Indenter starting point at geometric centre of plating, horizontal travel over rest of plate along longitudinal centreline.
Full-Length	Indenter starting point 25 cm (9.84 in.) from end of plate along longitudinal centreline, horizontal travel over rest of plate along longitudinal centreline to opposite end.
Force-Ctrl	Force Control – Signifies that experiment was carried out by controlling the force applied by the vertical hydraulic ram.
Ice	Uses ice cone indenter (not steel wheel indenter)
Elastic	With respect to experiments using the ice cone indenter, “Elastic” implies that the test specimen was <u>not</u> permanently damaged by the ice.
Plastic	With respect to experiments using the ice cone indenter, “Plastic” implies that the test specimen was permanently damaged by the ice.

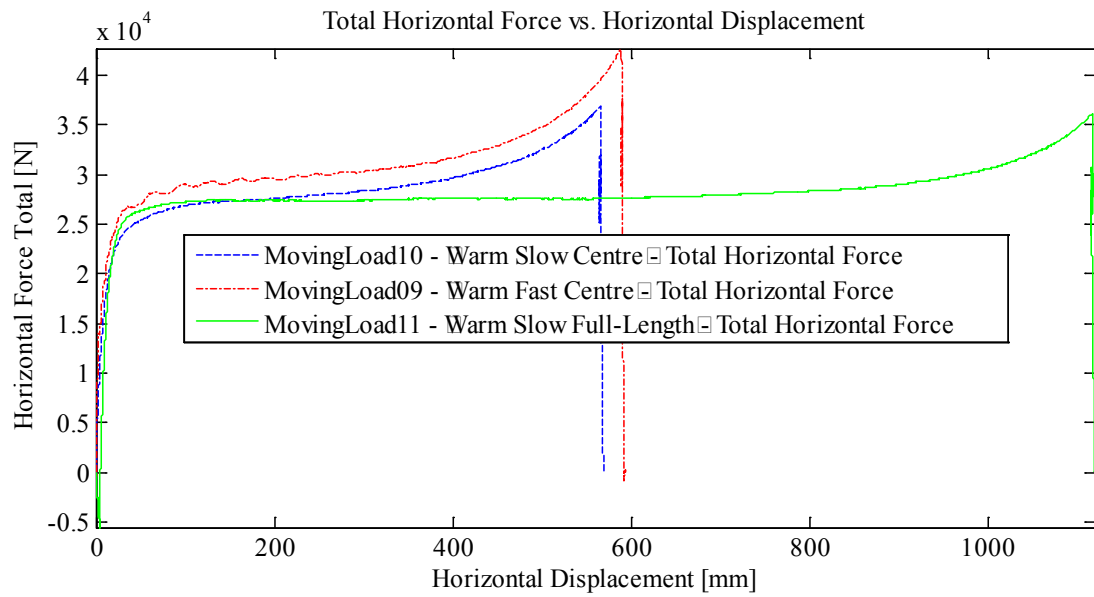
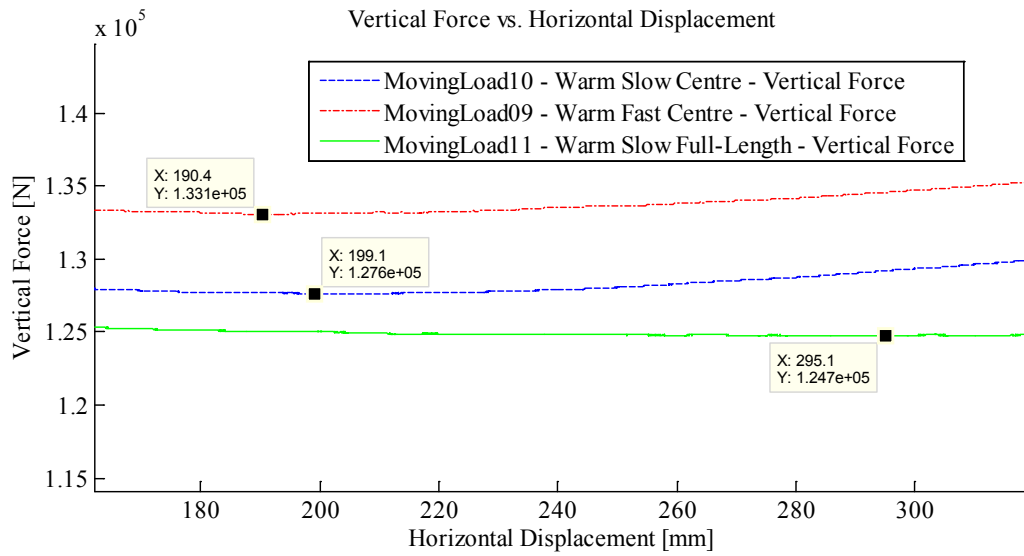
Appendix C1 – Room-temperature Tests

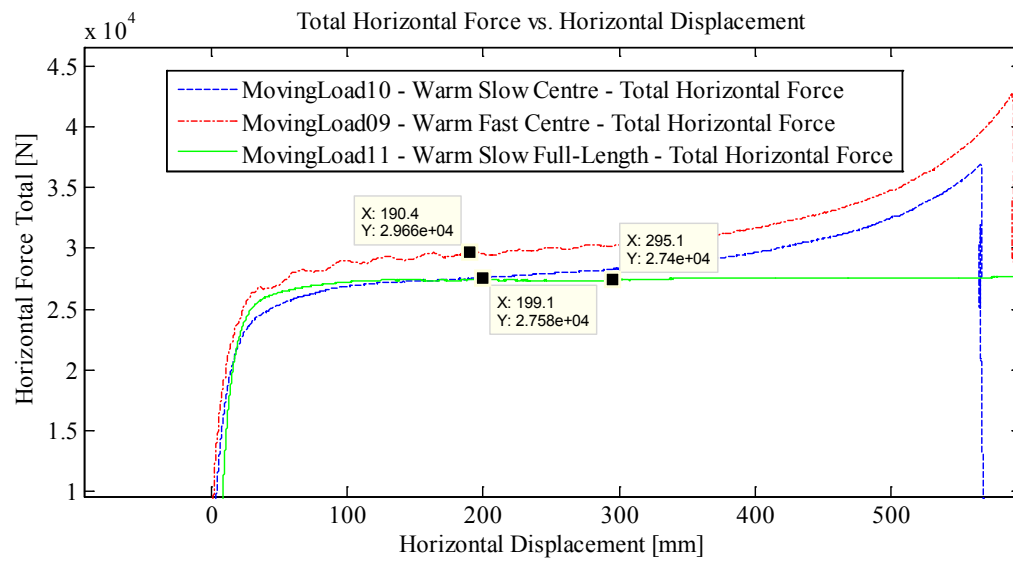
Appendix C1.1 – Quarter Inch Plate – 4 cm (1.575 in.) Indentation

Appendix C1.1.1 – Summary Plots for Experiments ML 9, 10 and 11.









Appendix C1.1.2 – MovingLoad9

March 26, 2014 at ~3:40 p.m.

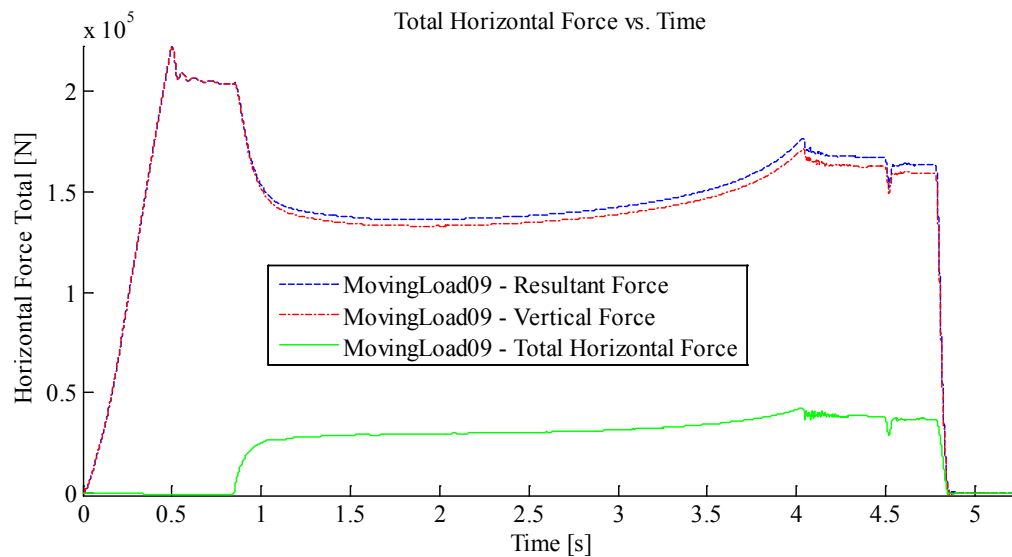
Run #: 4
Run Type: Fast
Room-temperature: ~20°C
Sample Type: 1/4"
Test Type: In-Along-Out Centre to End

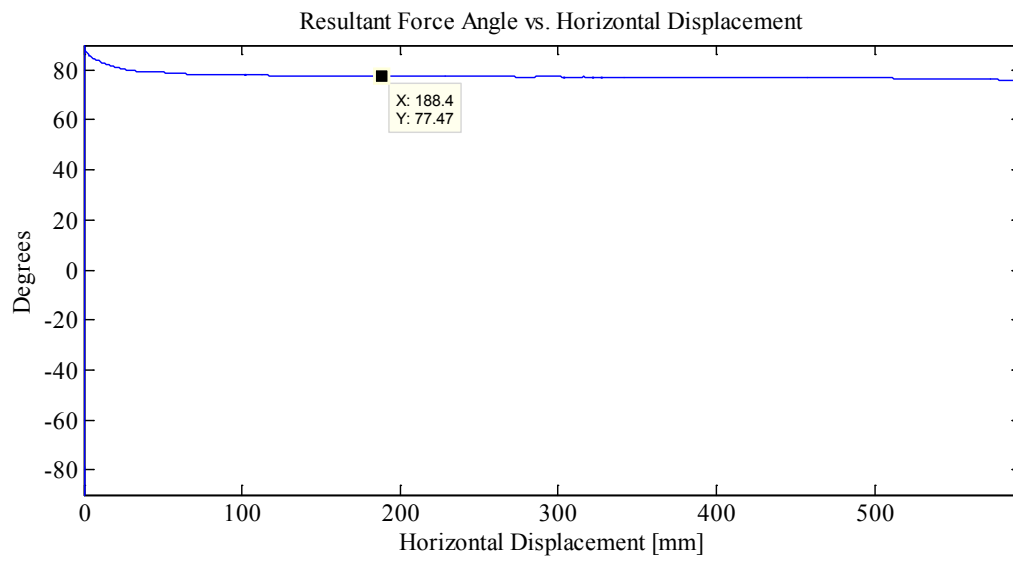
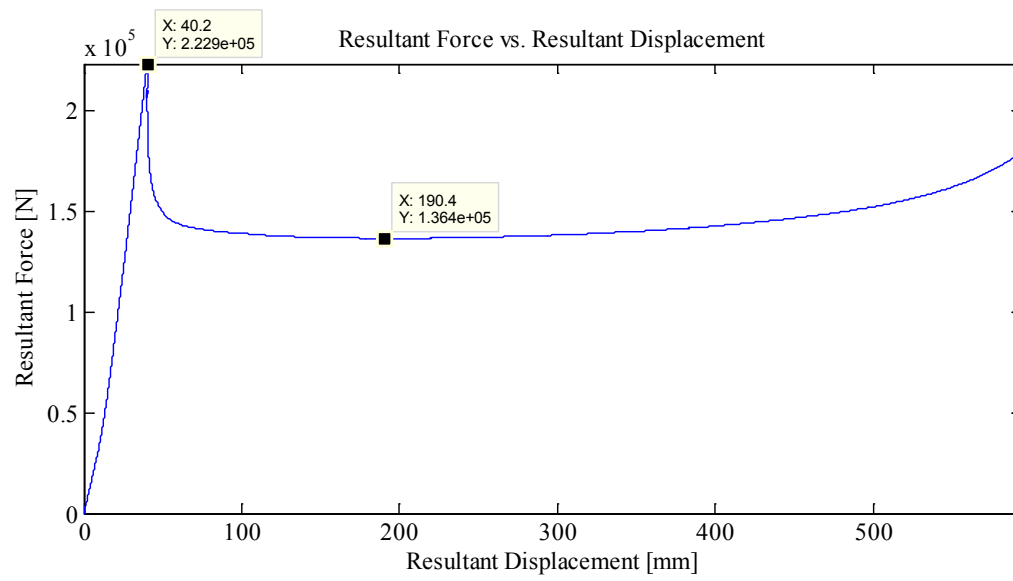
HStarting Point: Centre
HSpeed: Fastest
H Travel: Centre to End (55+ cm)

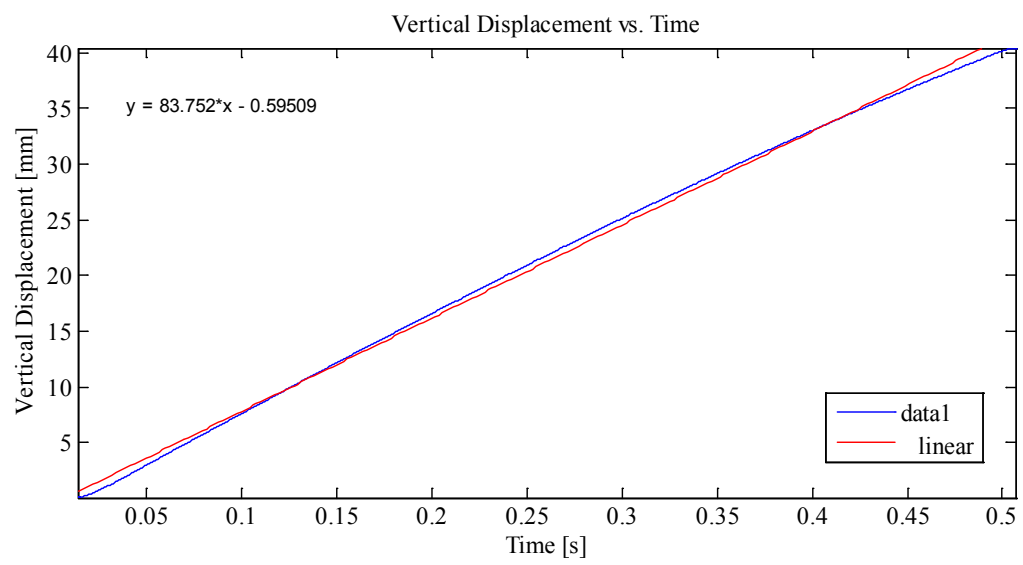
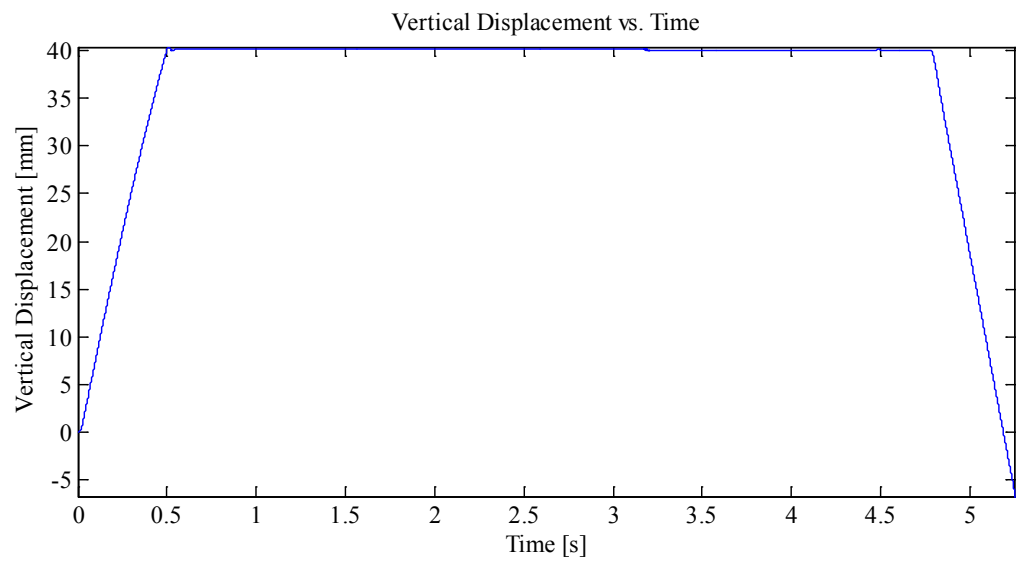
Vstarting Point: -2.20 mm
VSpeed: Fastest
V Travel: 40 mm

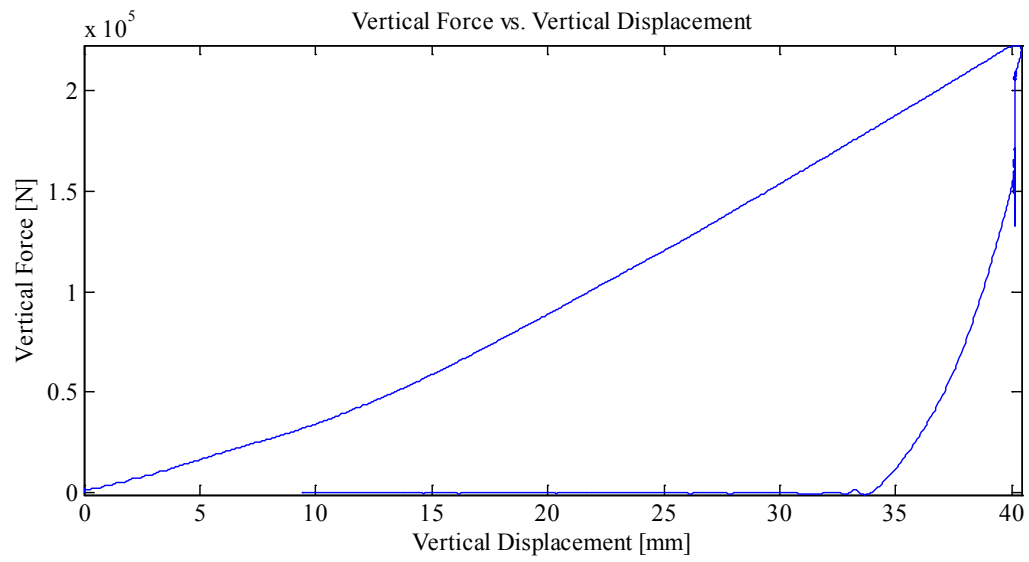
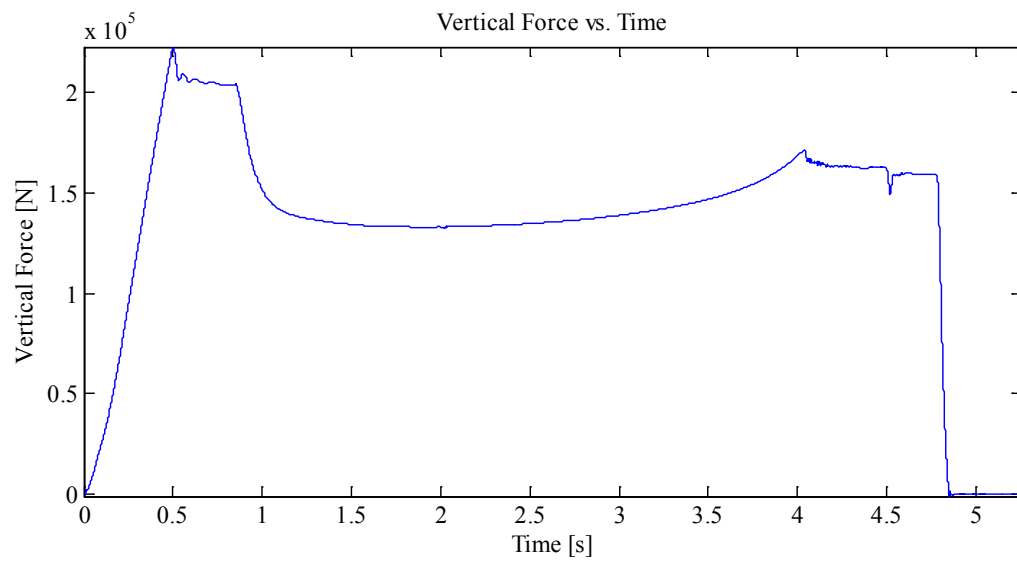
Indentation 1: ~30 mm, In-Along-Out - Centre to End
Data from Indentation 1 saved as MovingLoad09

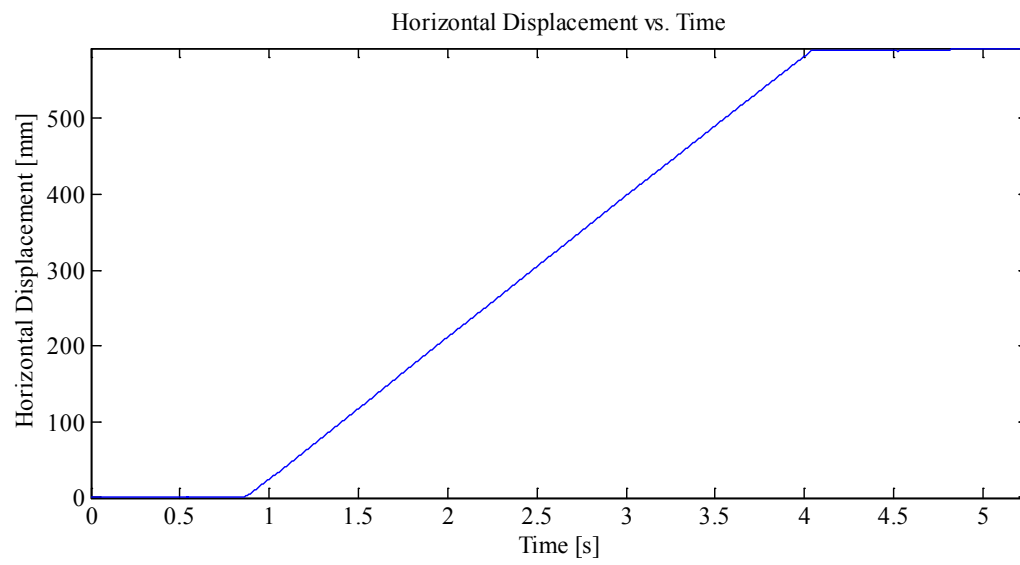
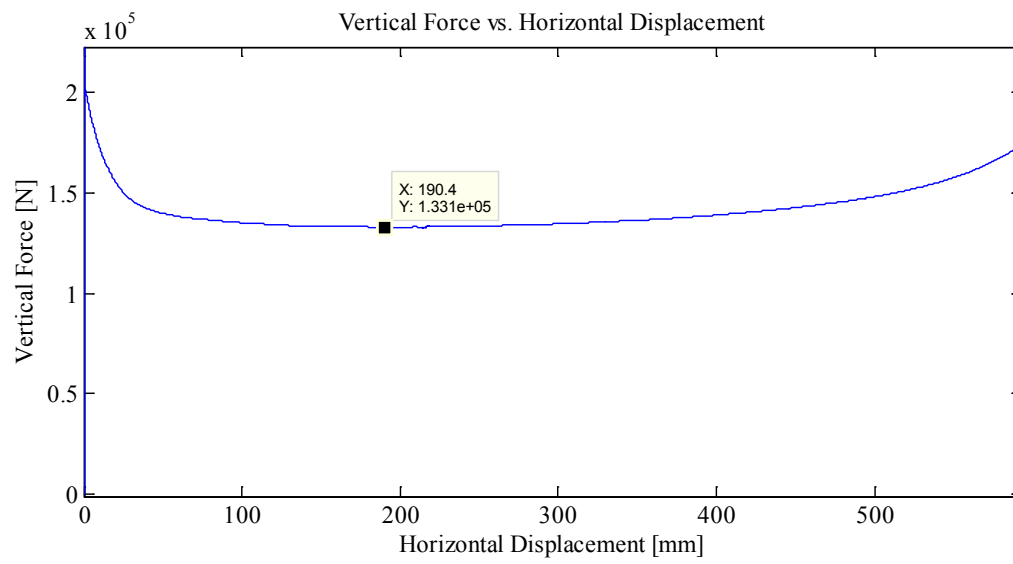
Plots:

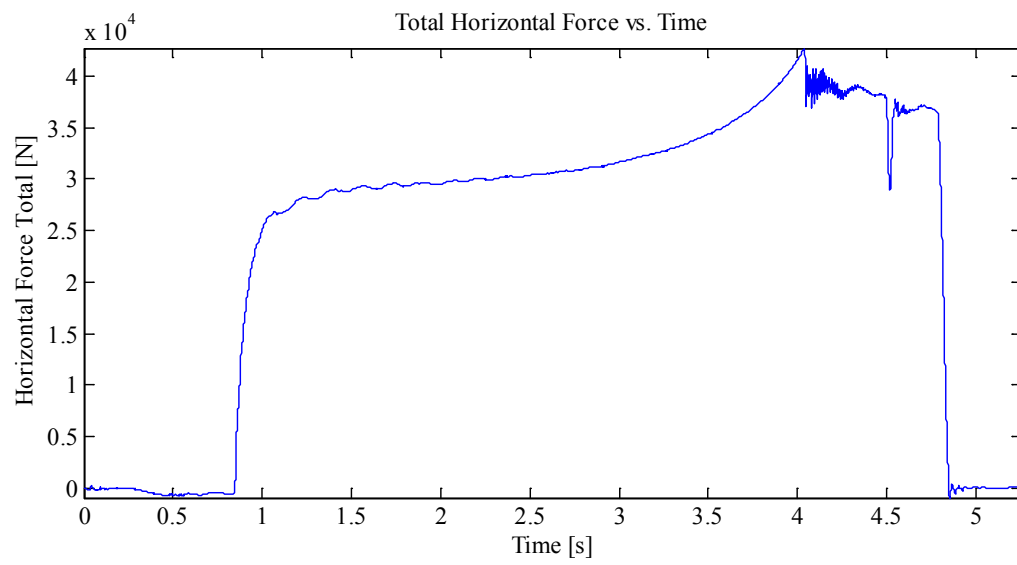
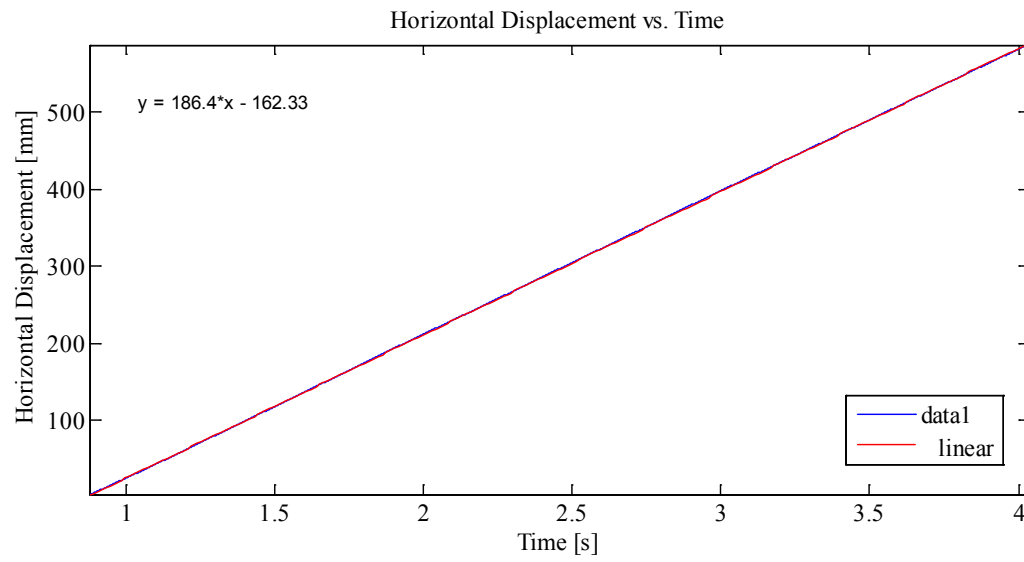


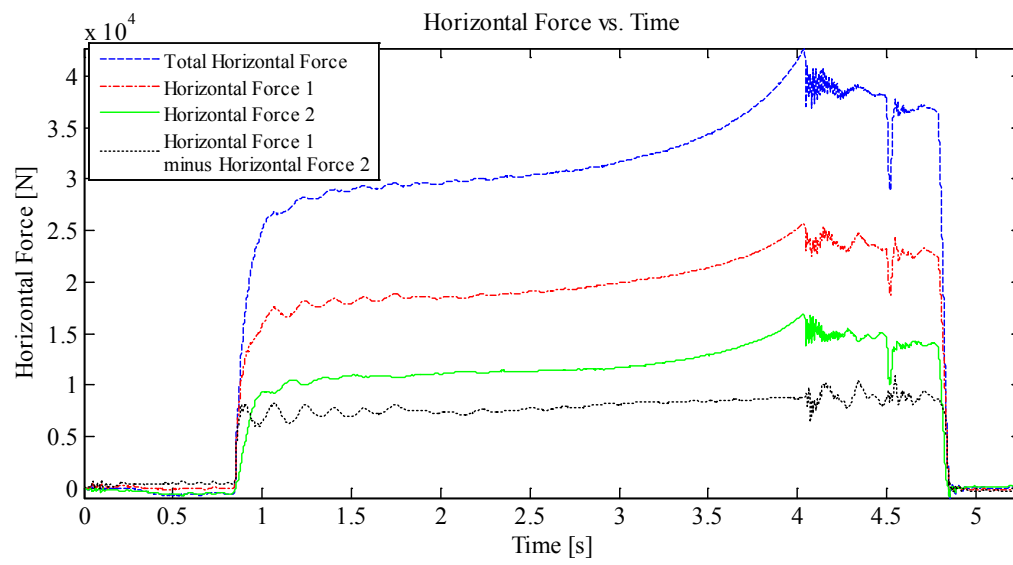
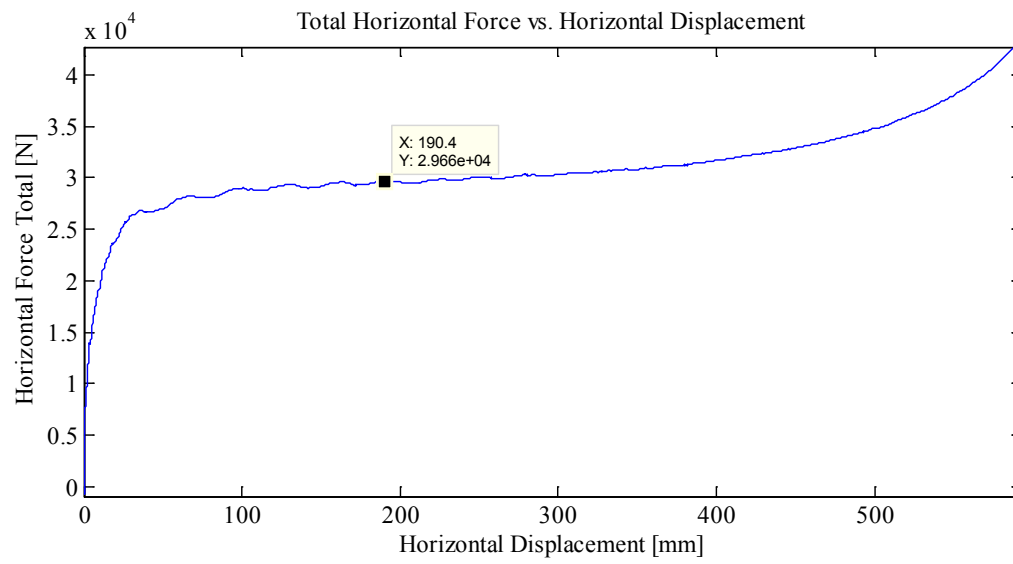












Appendix C1.1.3 – MovingLoad10

March 27, 2014 at ~10:15 a.m.

Run # 5
Run Type: Slow
Room-temperature: ~20°C
Sample Type: 1/4"
Test Type: In-Along-Out Centre to End

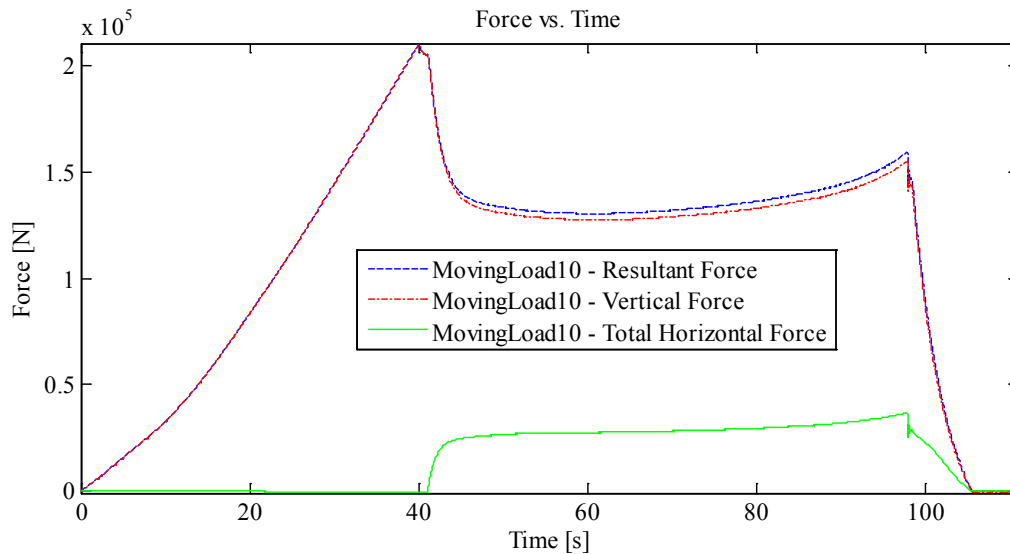
HStarting Point: Centre
HSpeed: ~10 mm/s
H Travel: Centre to End (55+ cm)

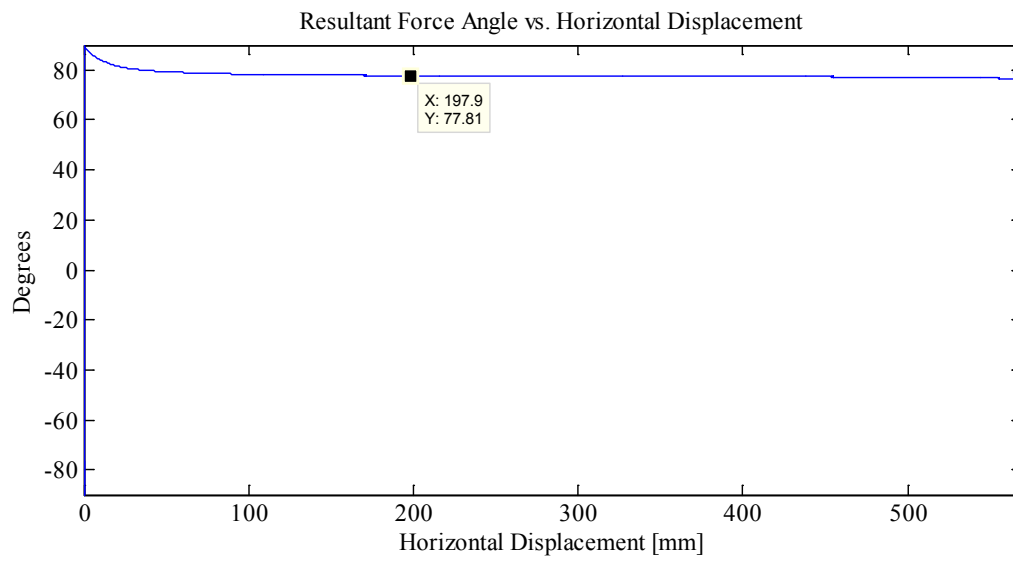
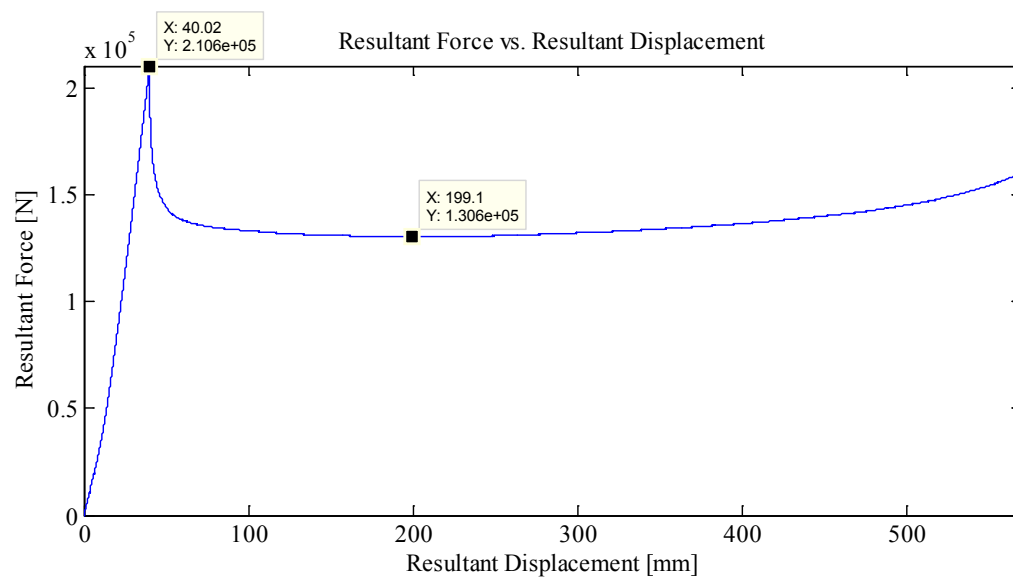
Vstarting Point: -2.29 mm
VSpeed: 1.0mm/s
V Travel: 40 mm

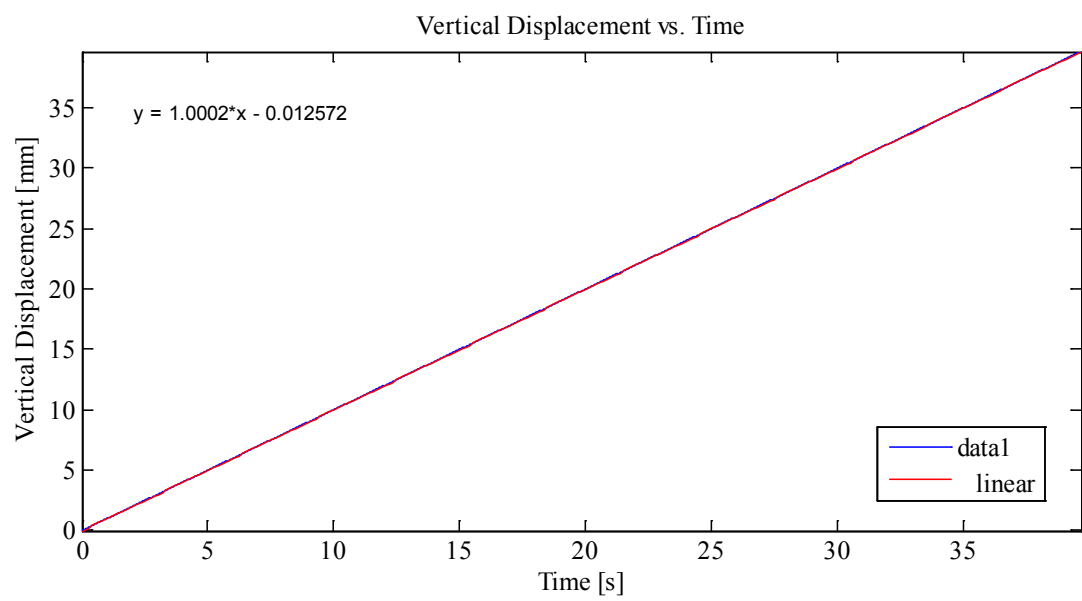
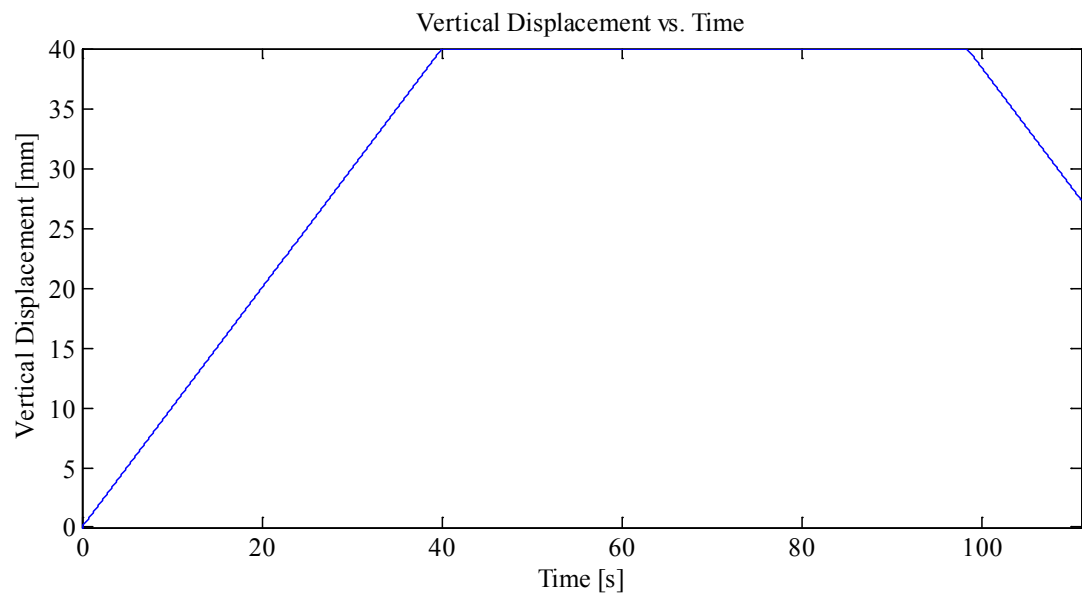
Notes:

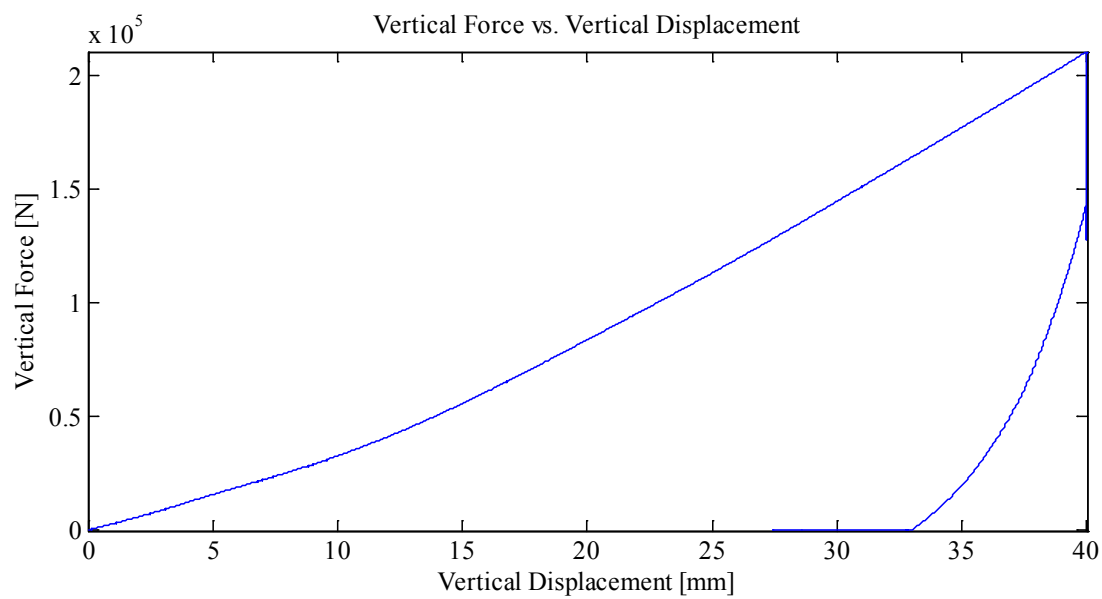
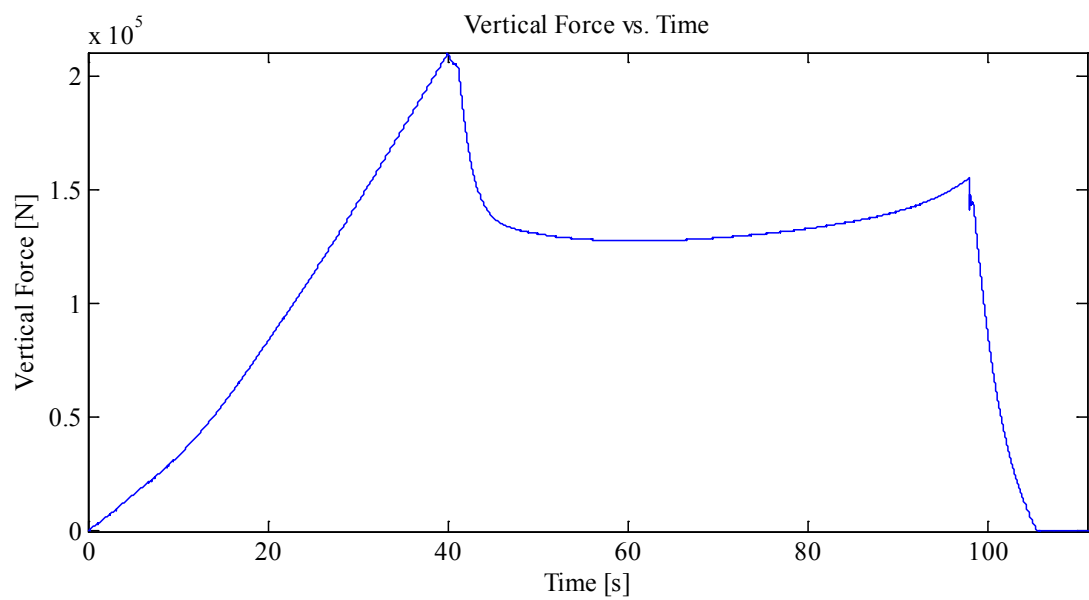
Indentation 1: ~40 mm, In-Along-Out - Centre to End
Data from Indentation 1 saved as MovingLoad10

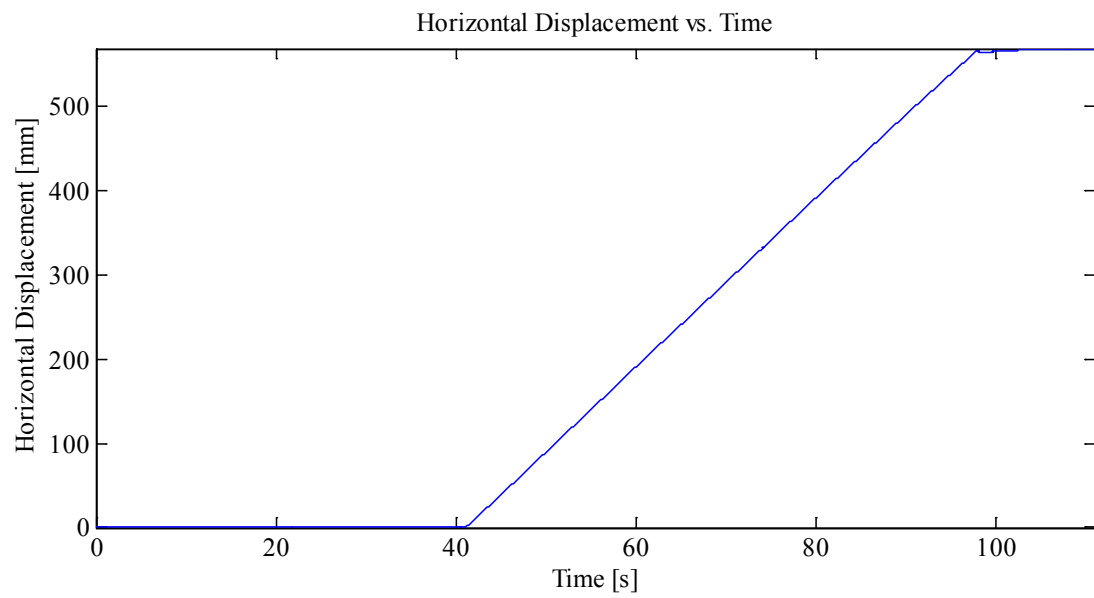
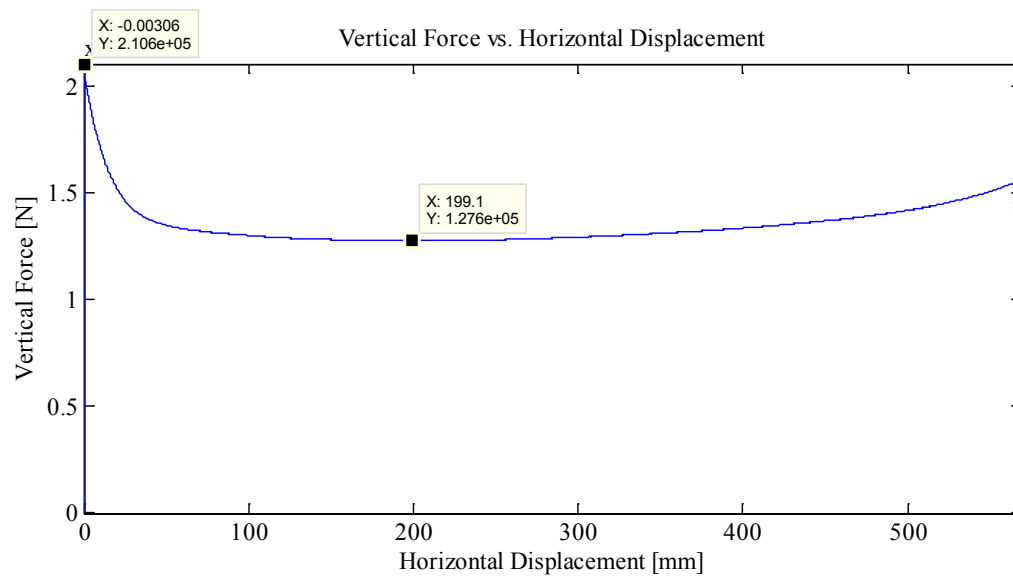
Plots:

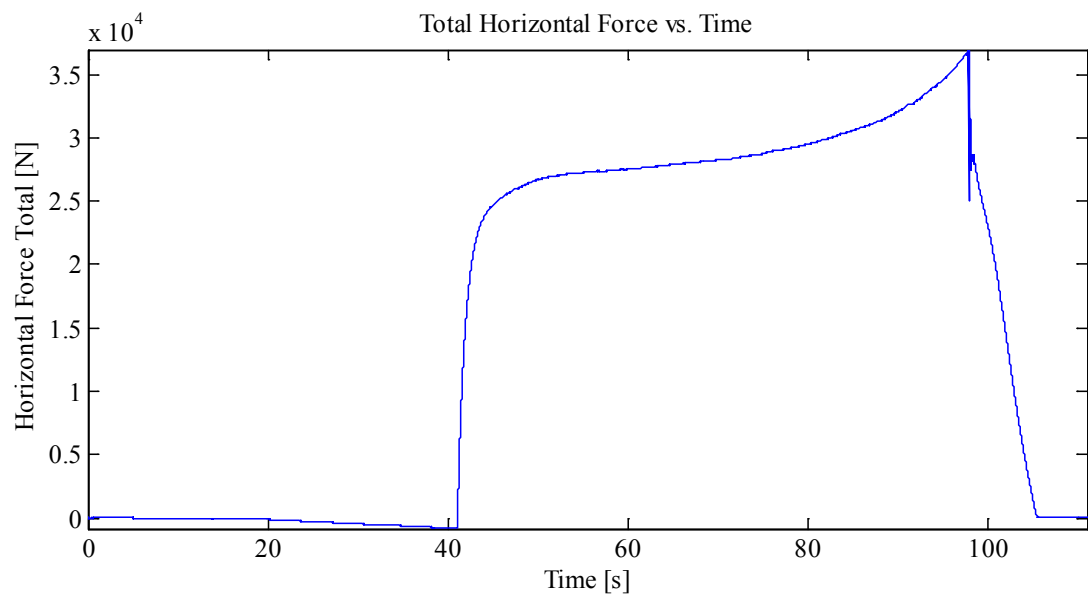
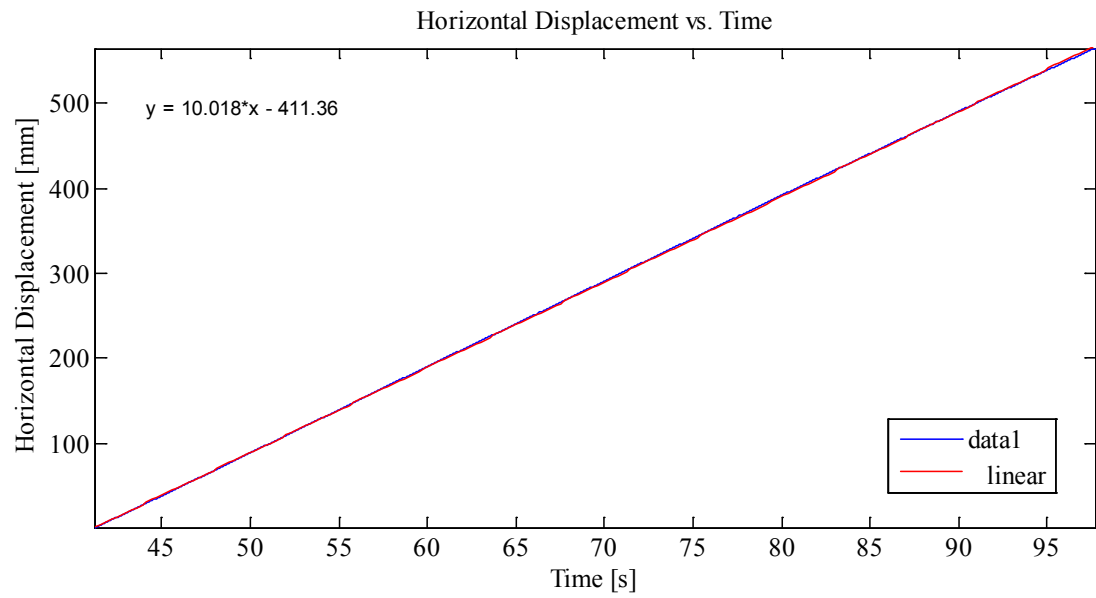


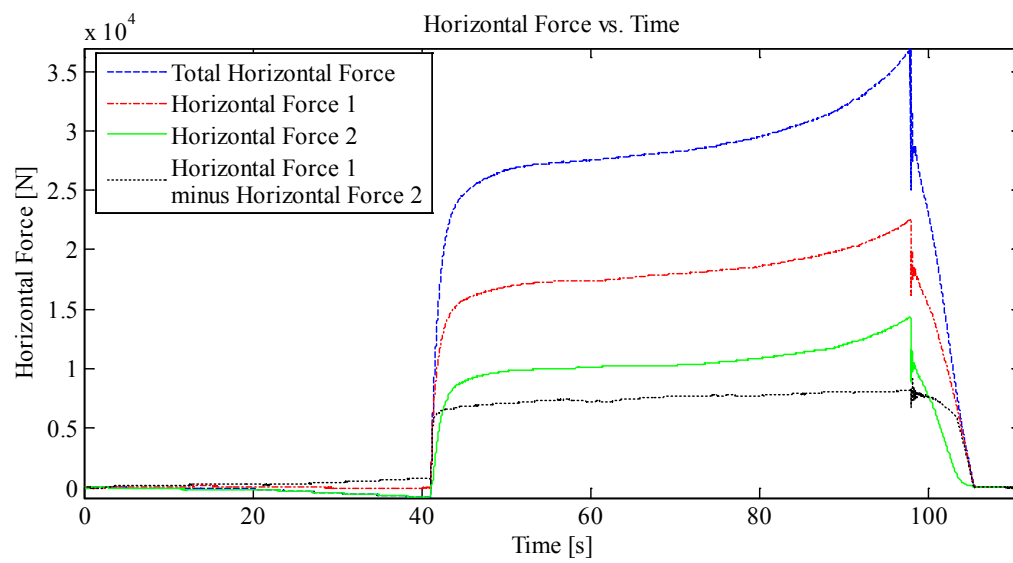
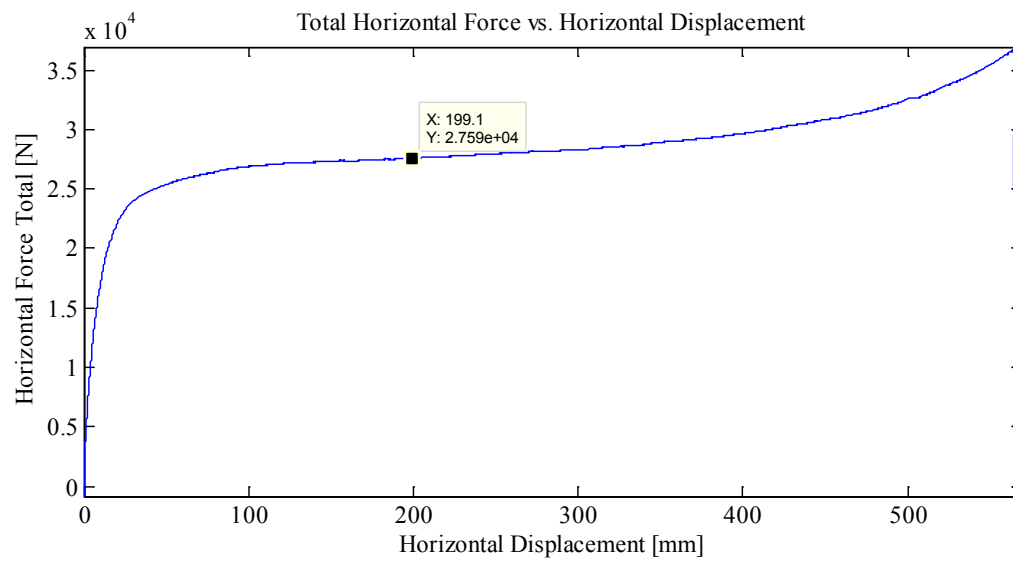












Appendix C1.1.4 – MovingLoad11

March 27, 2014 at ~4:10 p.m.

Run # 6
Run Type: Slow & Full length
Room-temperature: ~20°C
Sample Type: 1/4"
Test Type: In-Along-Out End to End

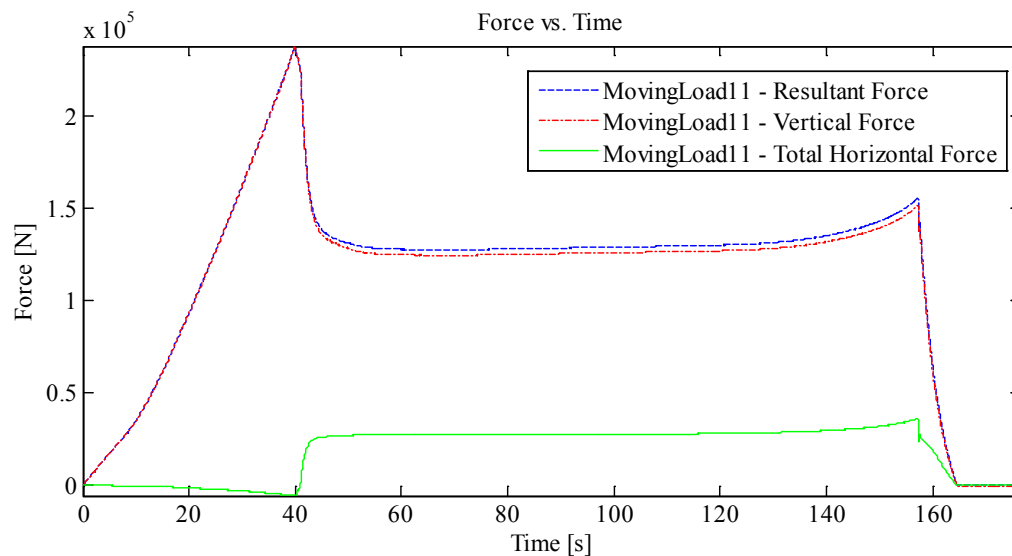
HStarting Point: End
HSpeed: 10mm/s nominal
H Travel: End to End (110+ cm)

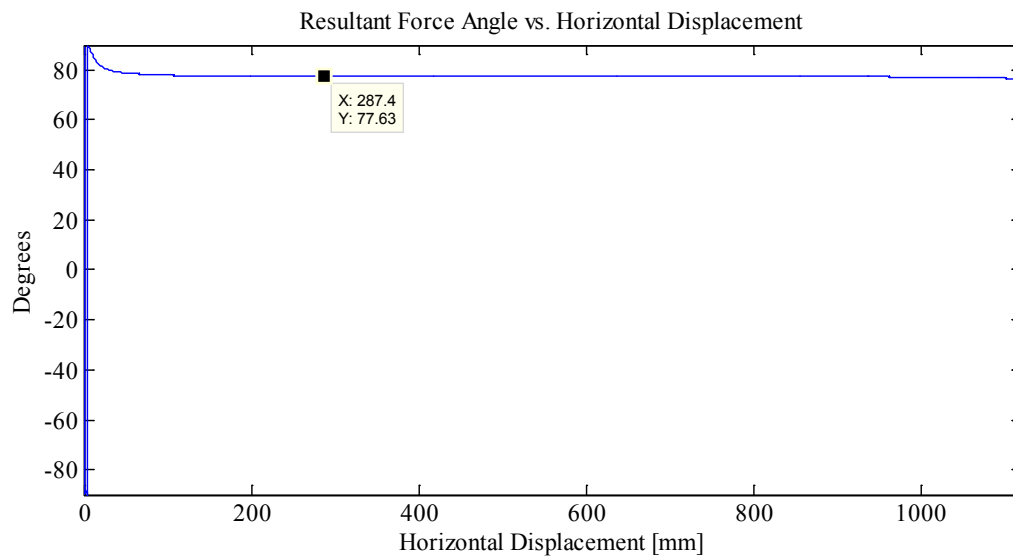
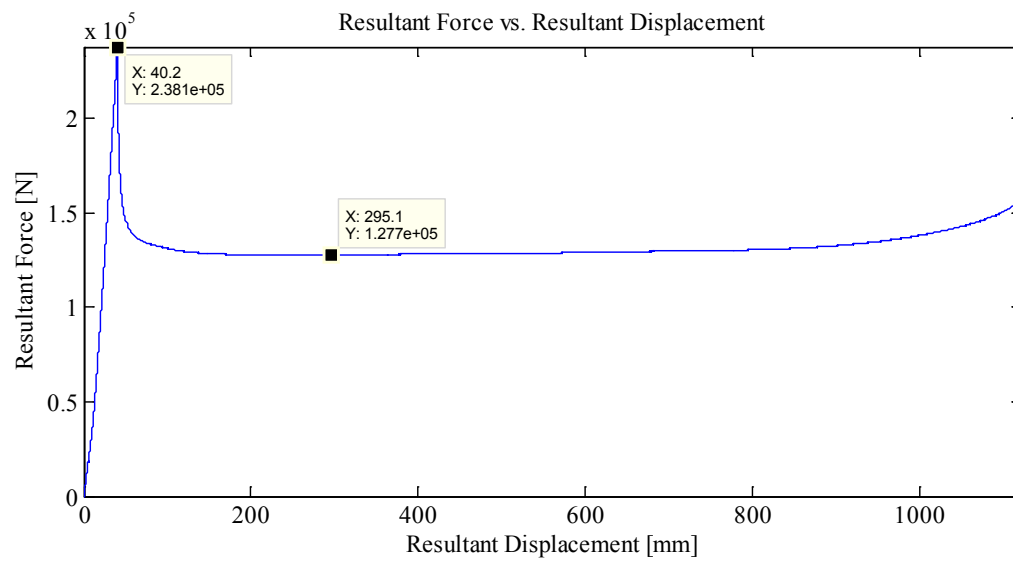
Vstarting Point: mm
VSpeed: 1.0mm/s (Nominal)
V Travel: 40 mm

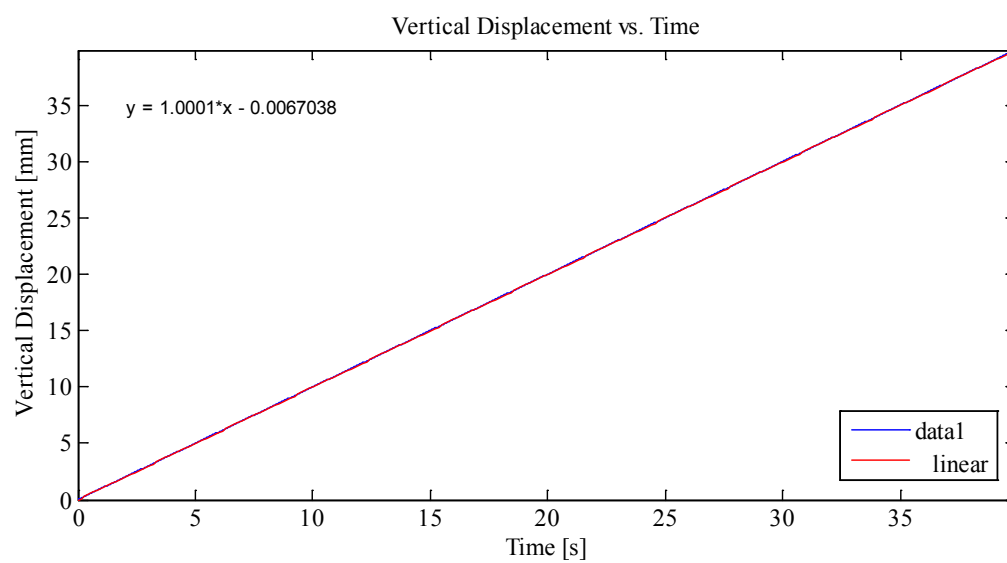
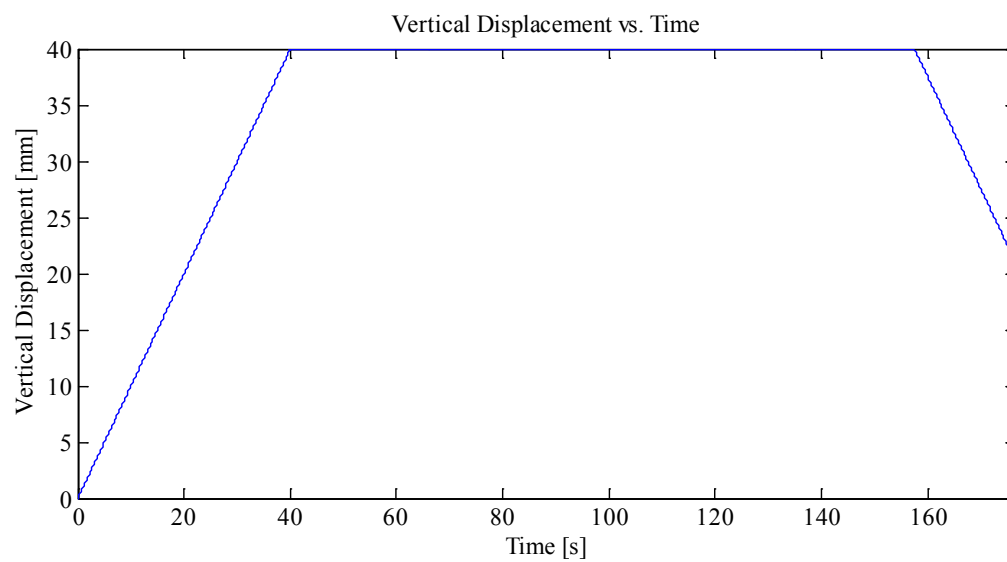
Notes:

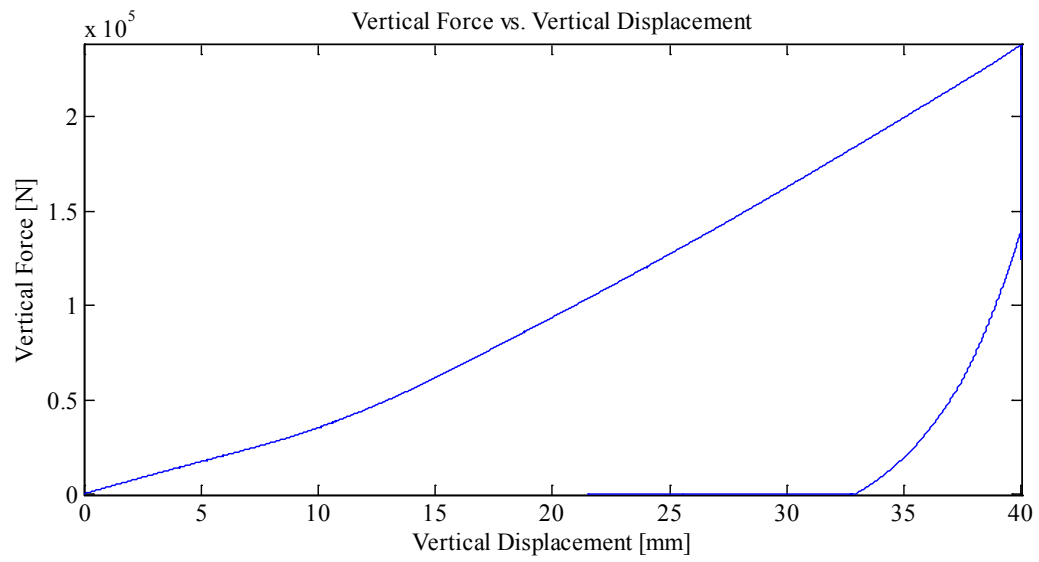
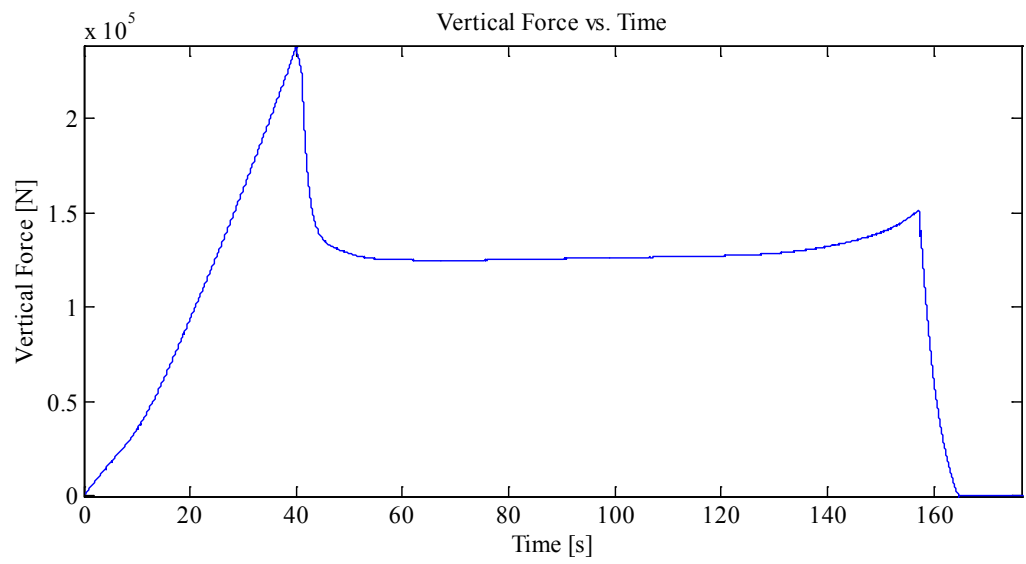
Indentation 1: ~40 mm, In-Along-Out - End to End
Data from Indentation 1 saved as MovingLoad11

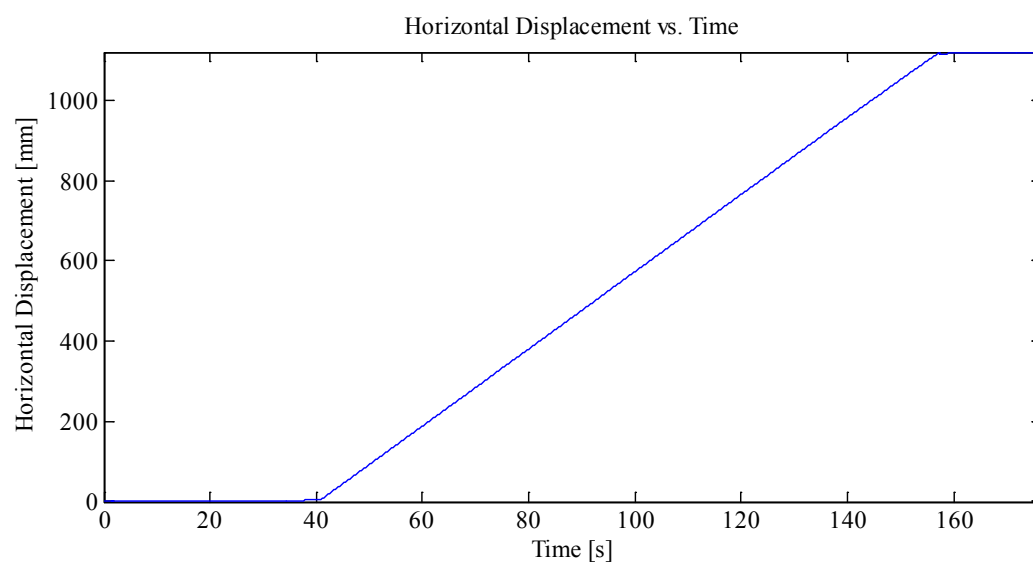
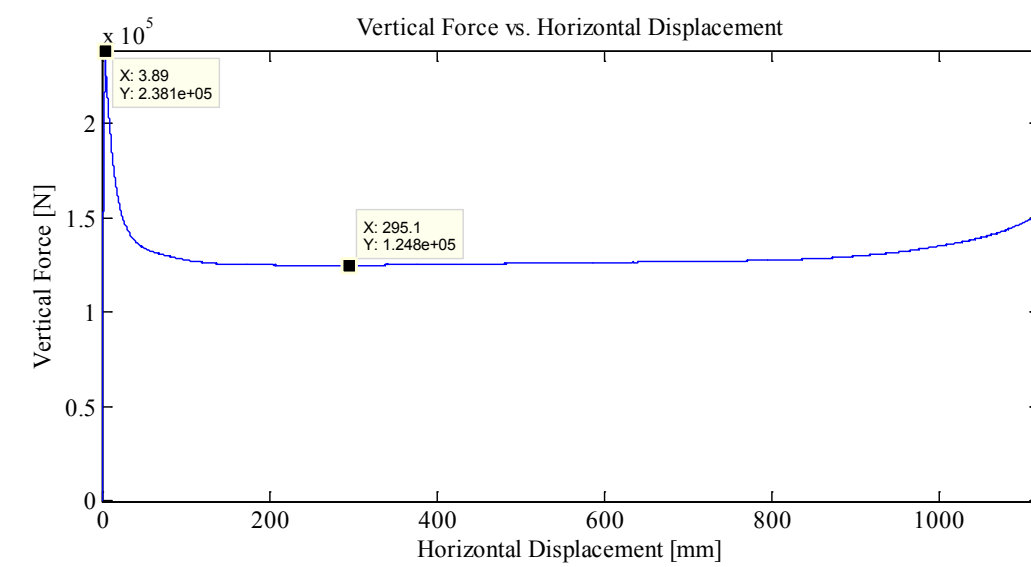
Plots:

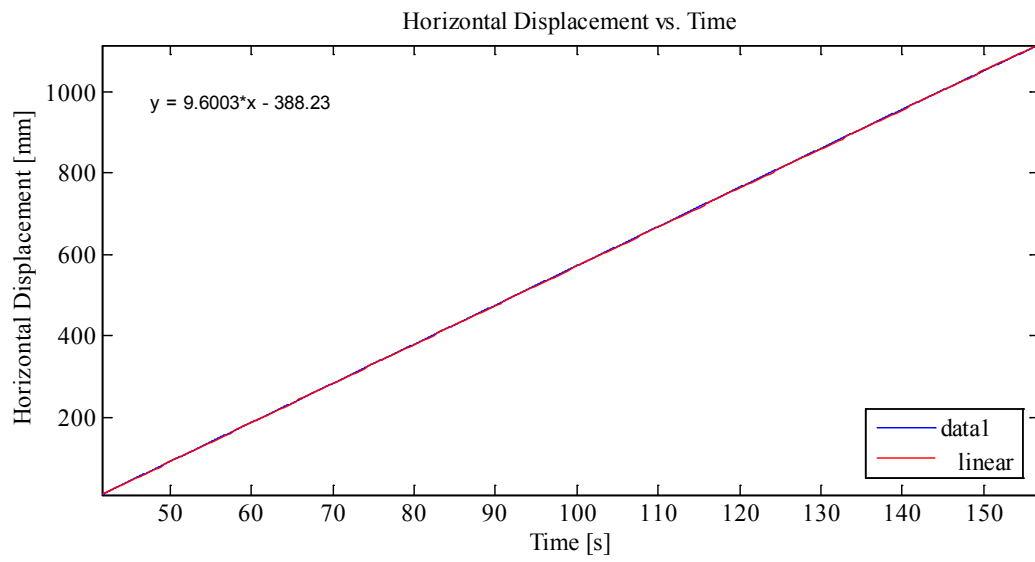
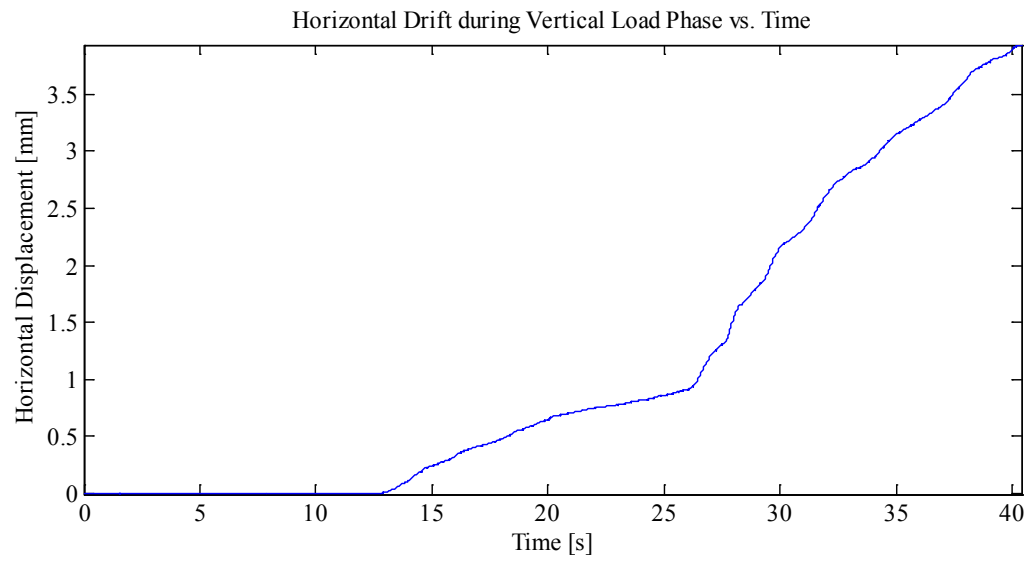


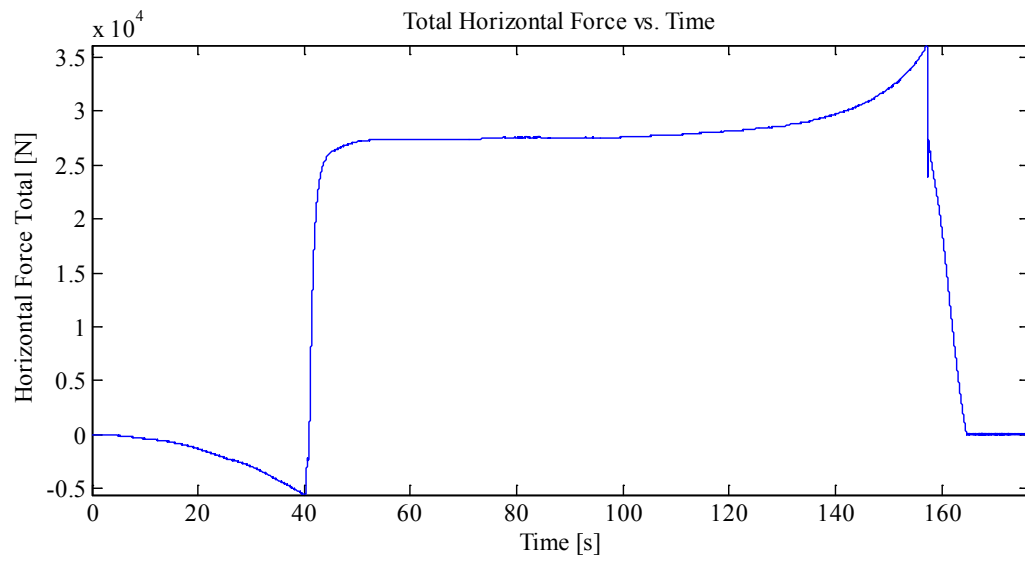
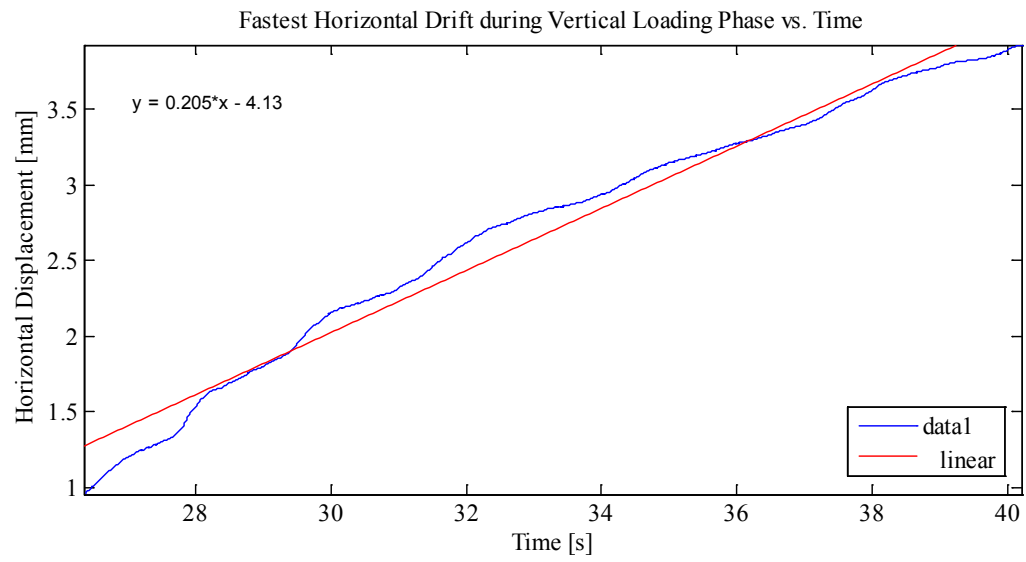


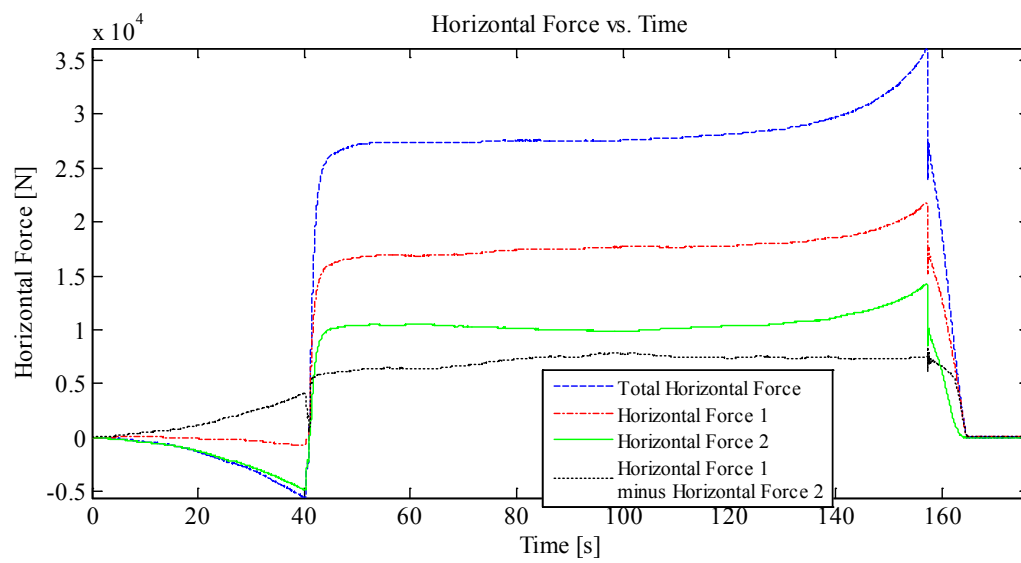
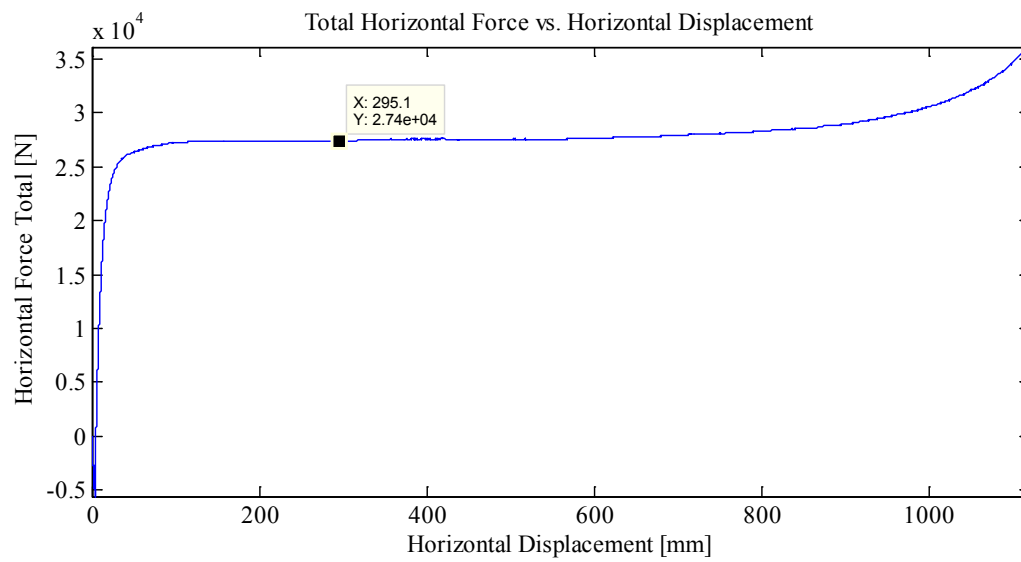






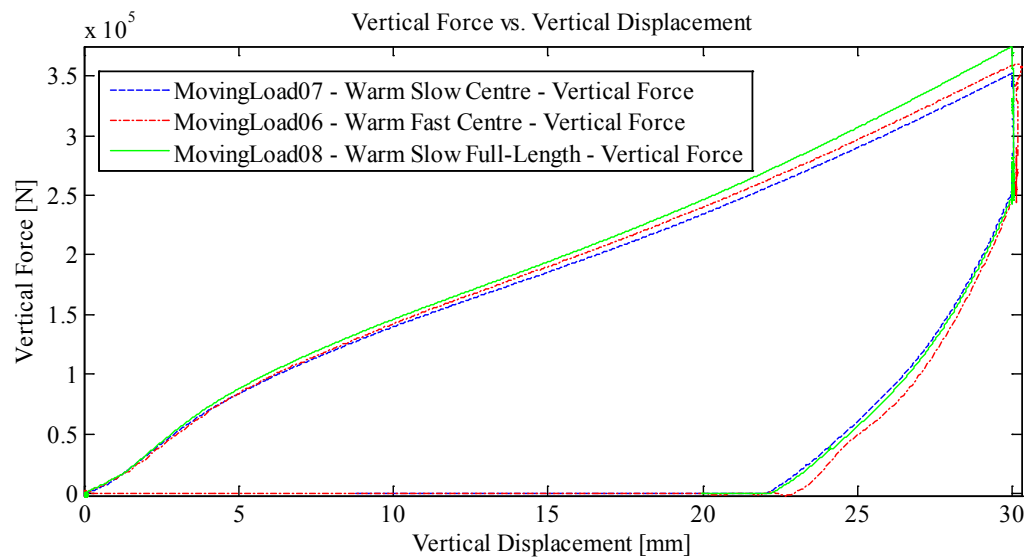
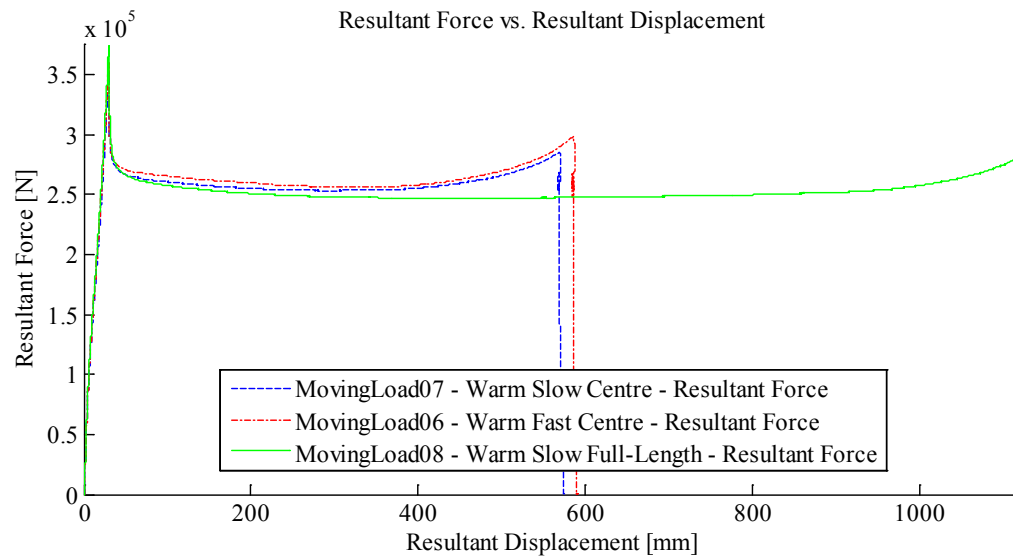


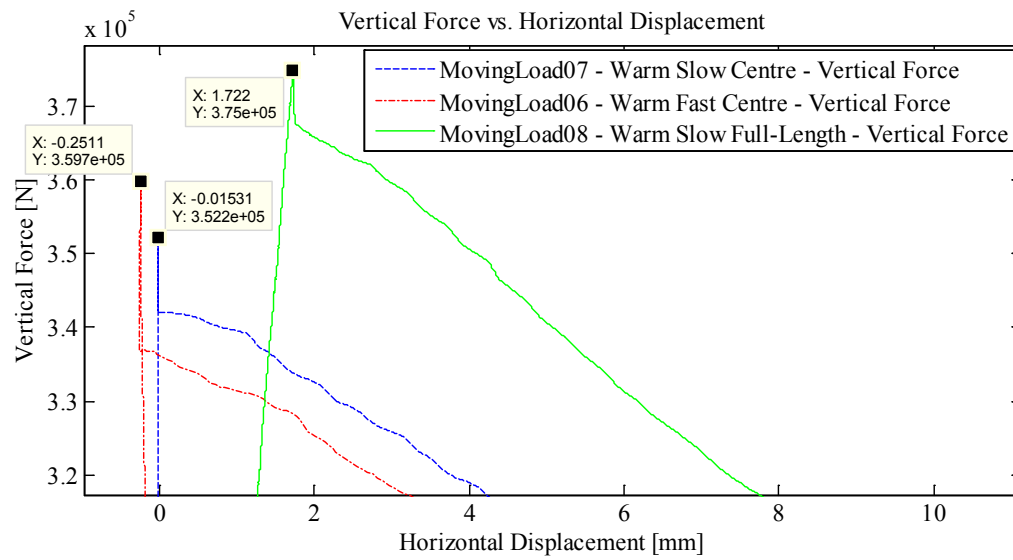
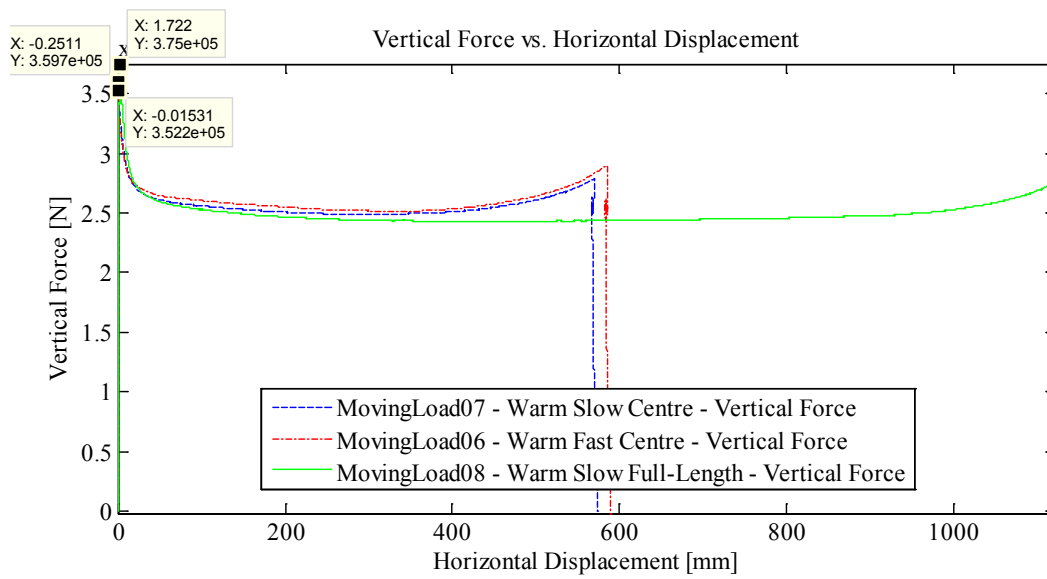


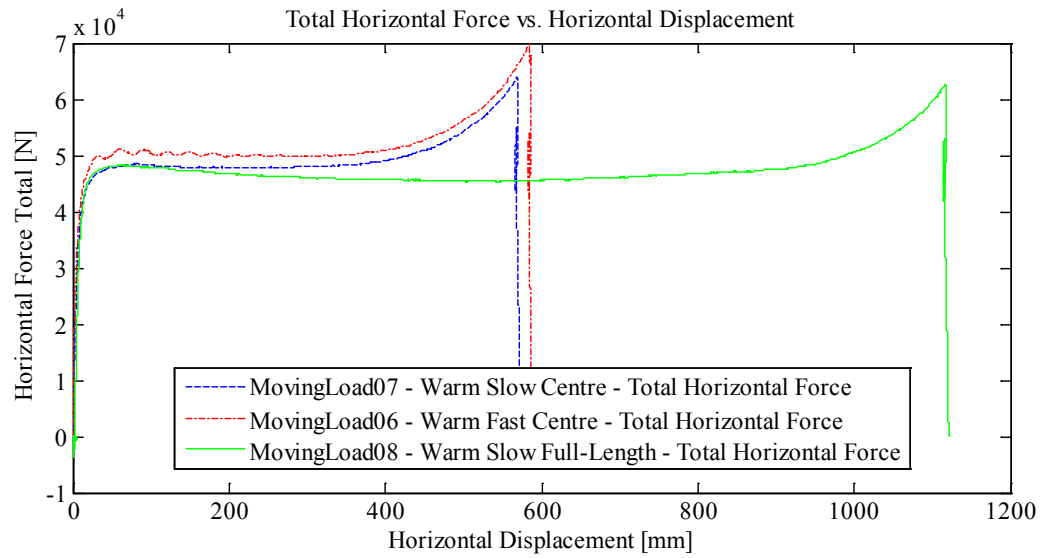
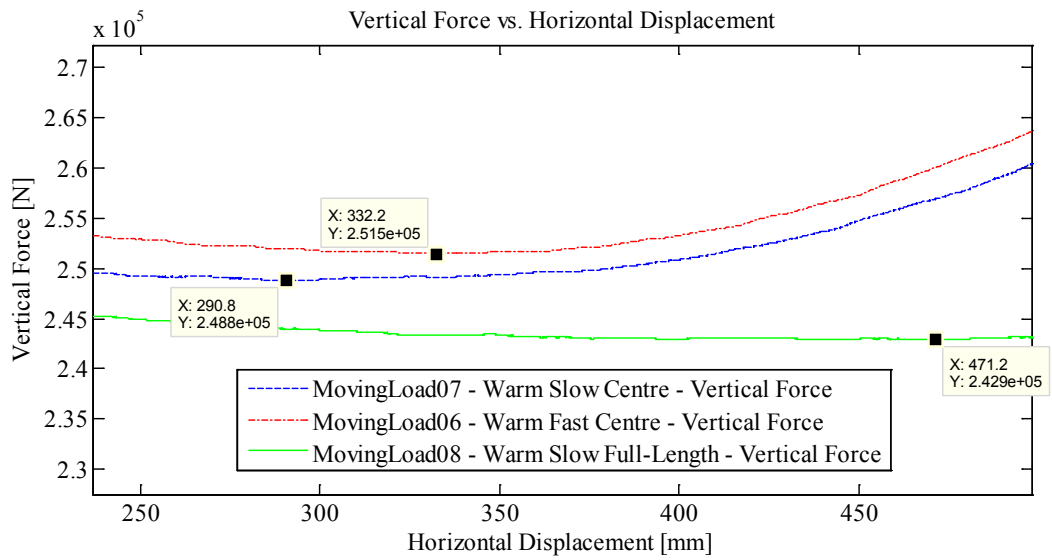


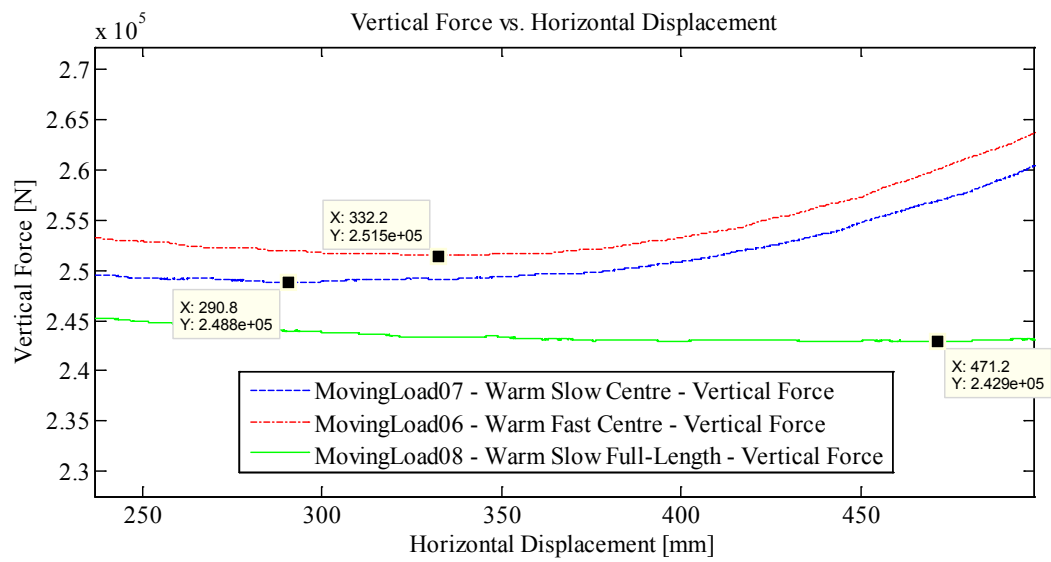
Appendix C1.2 – **Half Inch Plate – 3 cm (1.181 in) Indentation**

Appendix C1.2.1 – Summary Plots for Experiments ML 6, 7 and 8









Appendix C1.2.2 – MovingLoad6

March 25, 2014 at ~2:10 p.m.

Run #: 1
Run Type: Fast
Room-temperature ~20°C
Sample Type: 1/2"
Test Type: In-Along-Out Centre to End

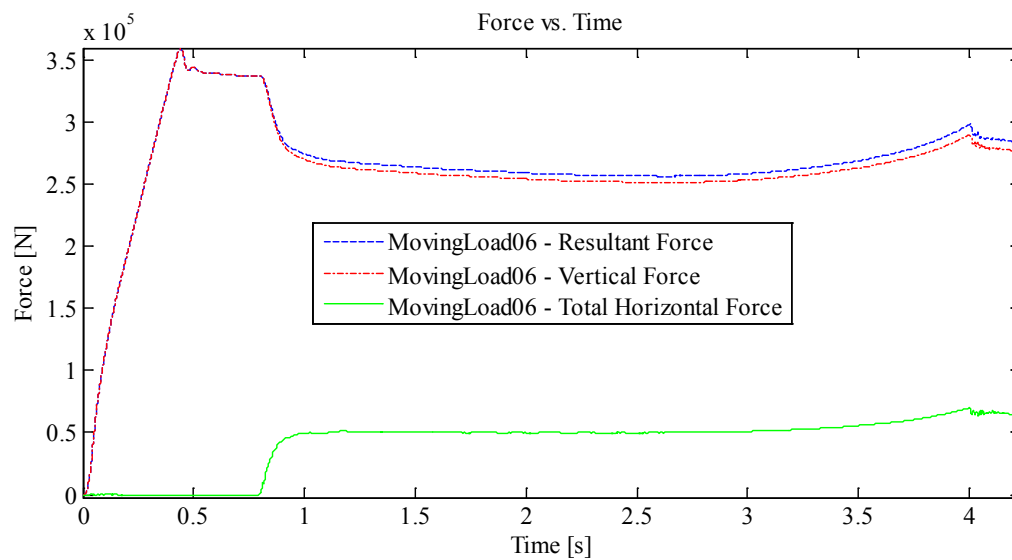
HStarting Point: Centre
HSpeed: Fastest Possible
H Travel: Centre to End

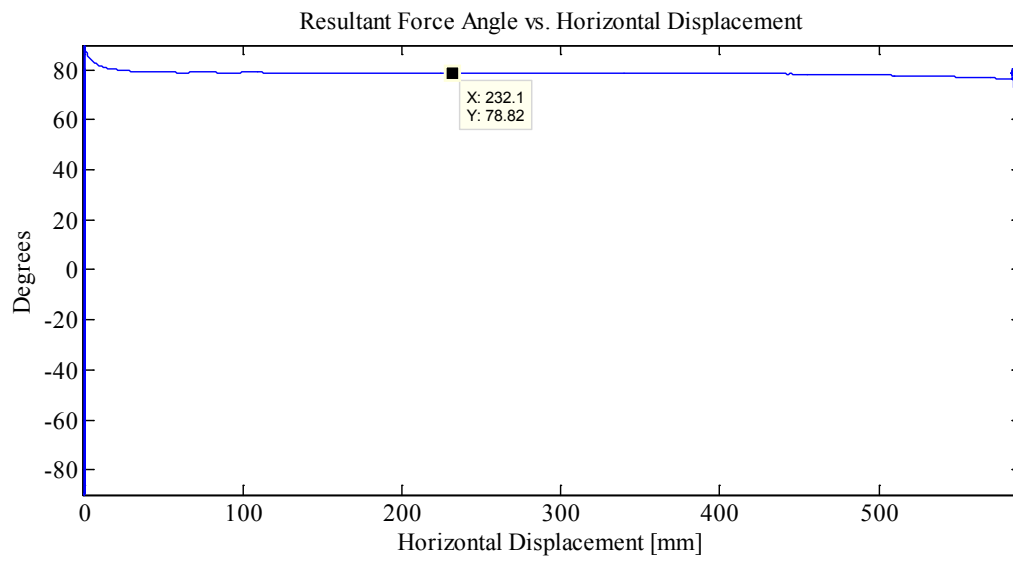
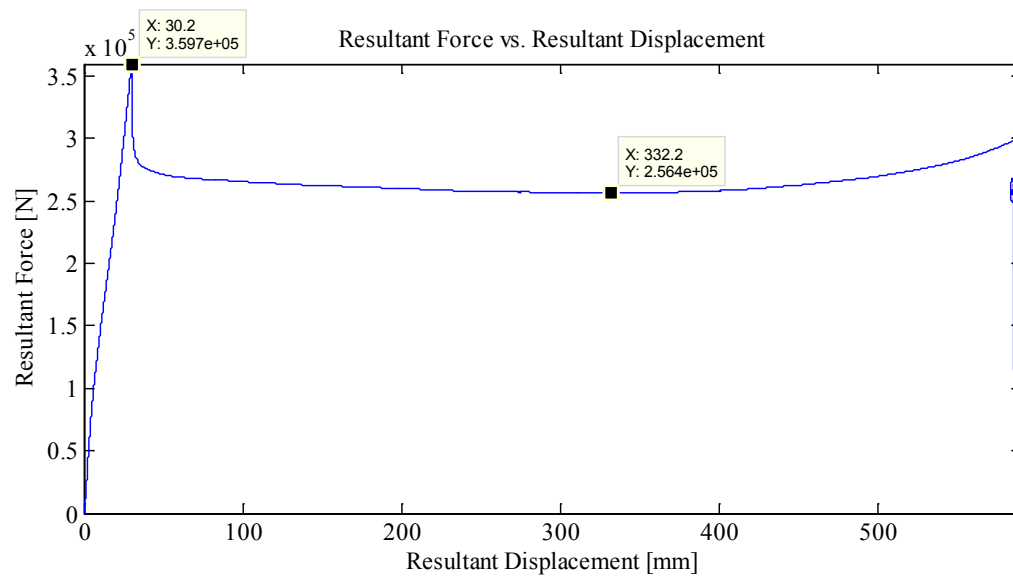
Vstarting Point: 8.855 mm
VSpeed: Fastest Possible
V Travel: 30 mm

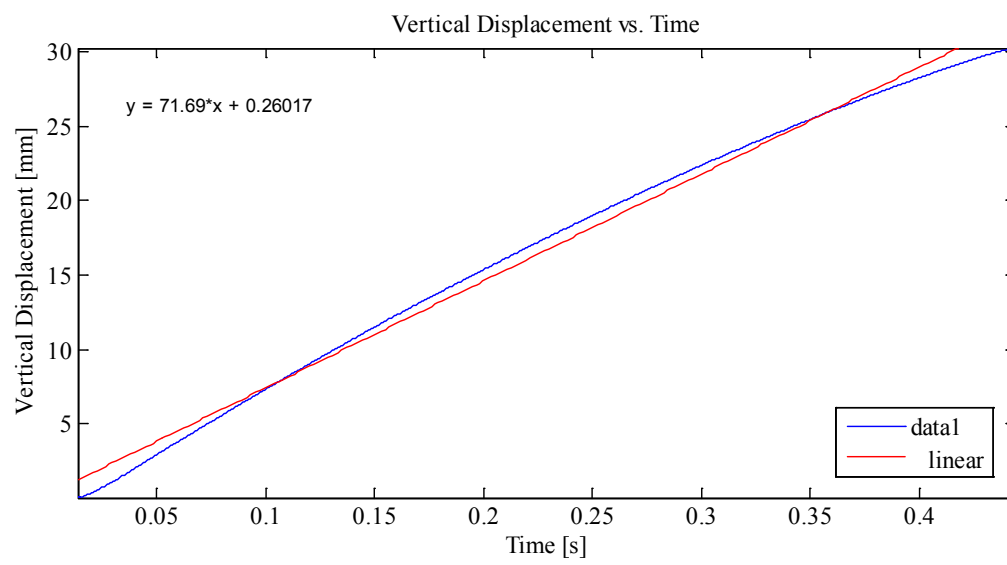
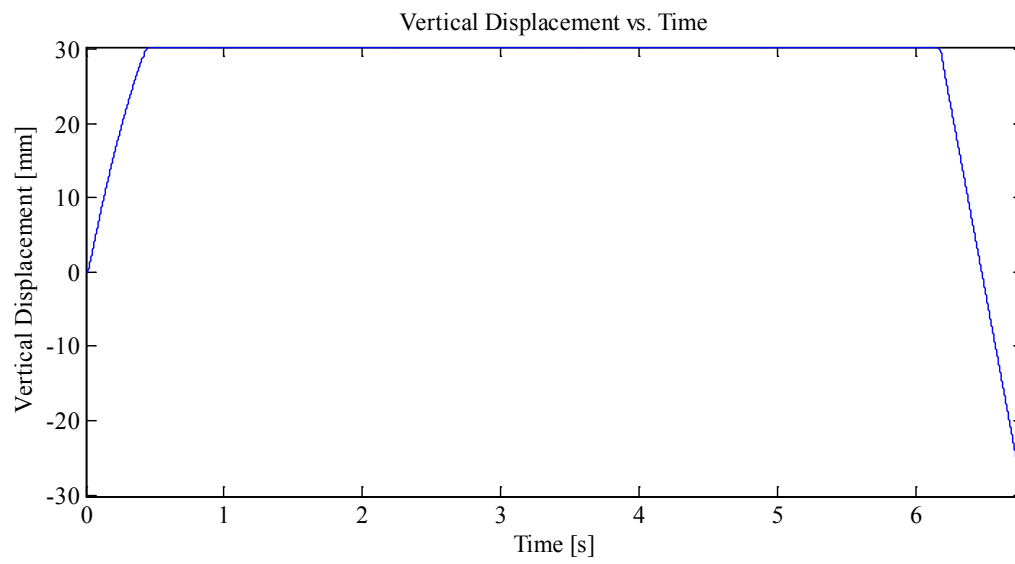
Indentation 1: ~30 mm, In-Along-Out - Centre to End
Data from Indentation 1 saved as MovingLoad06

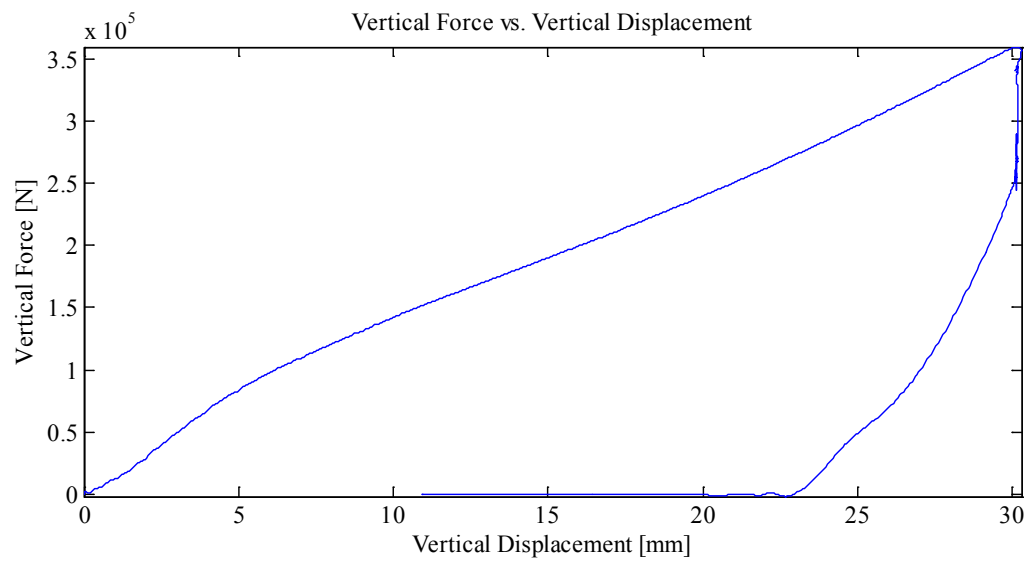
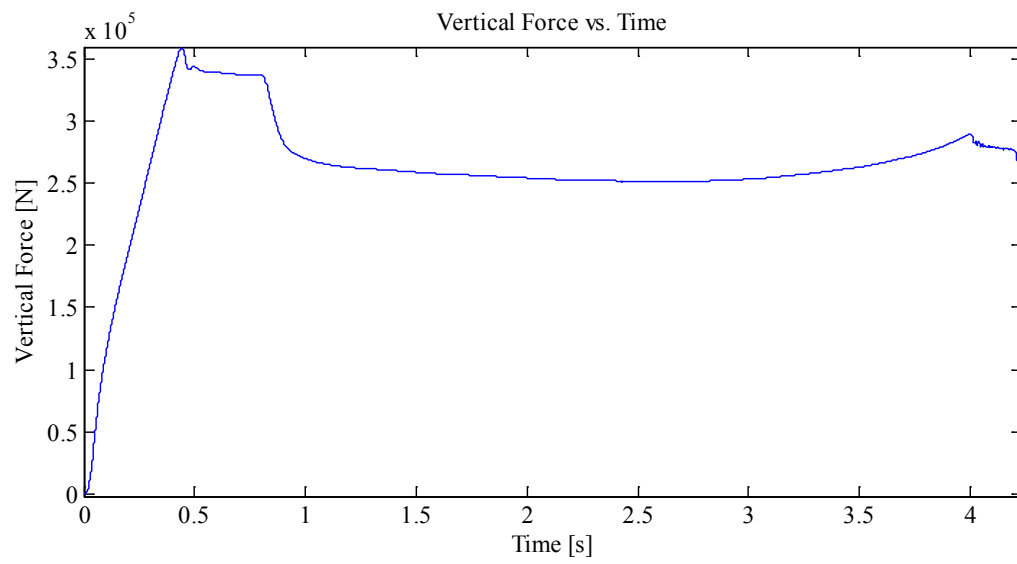
Note: Microscribe not bolted to table (bolted for run 3 onwards).

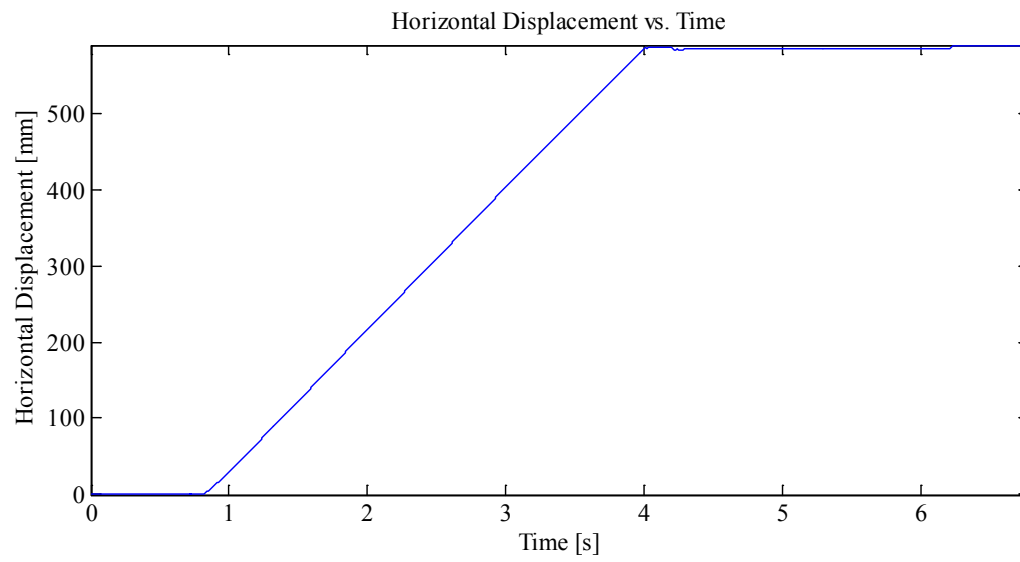
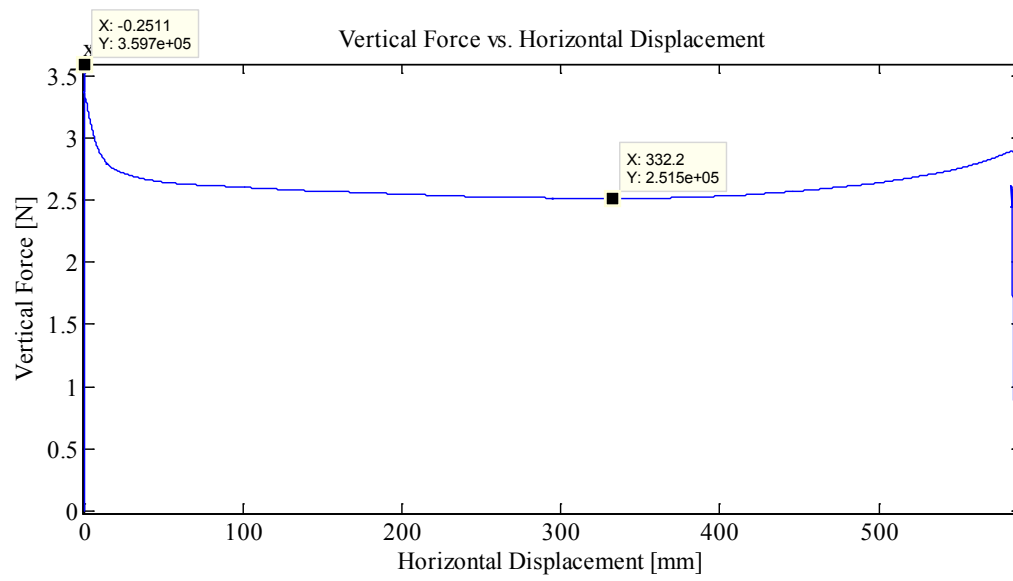
Plots:

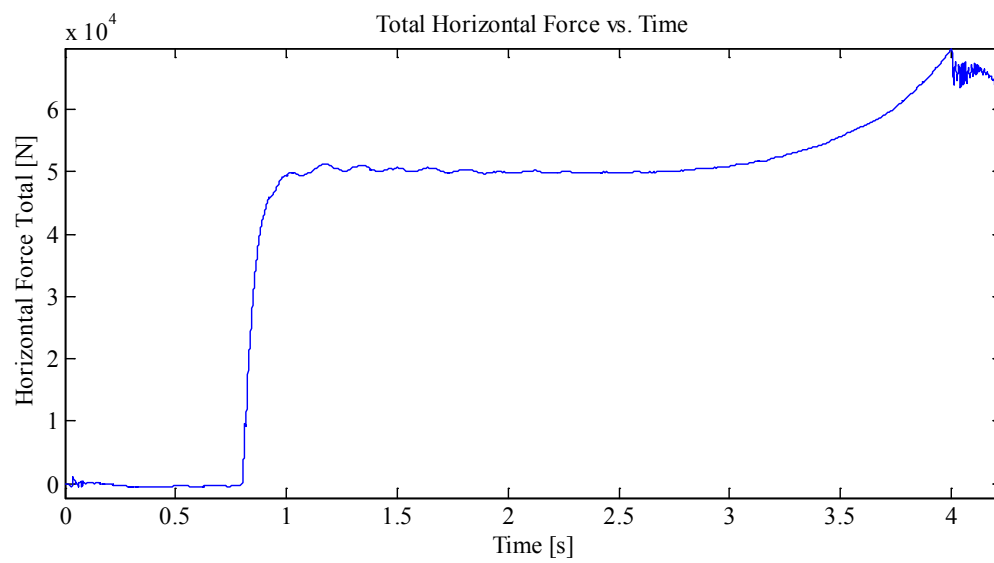
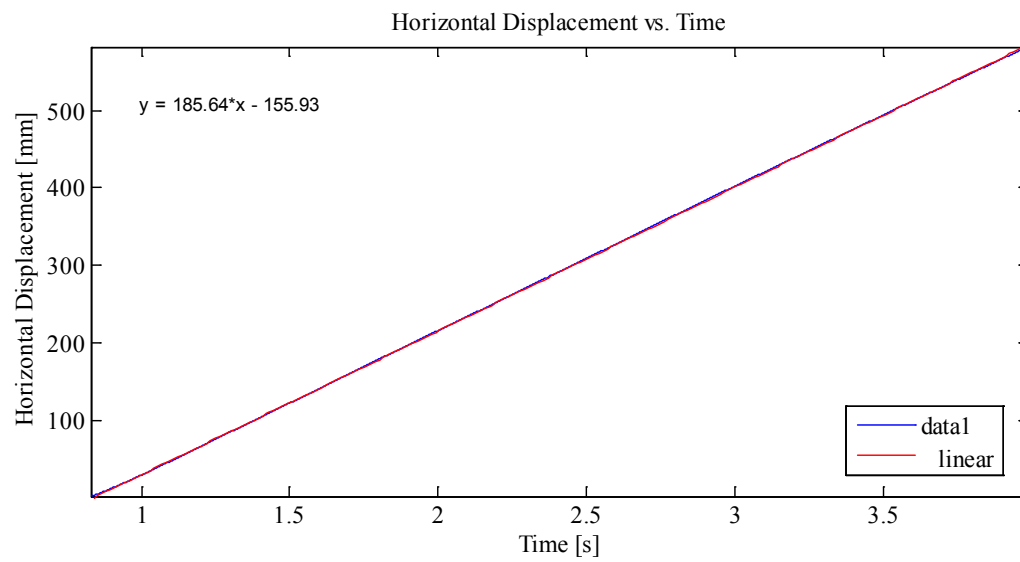


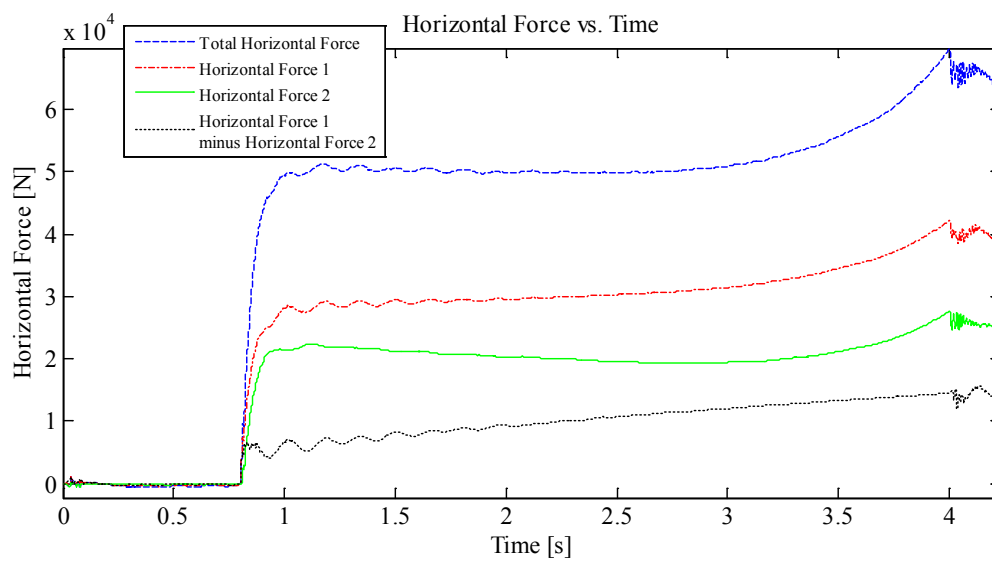
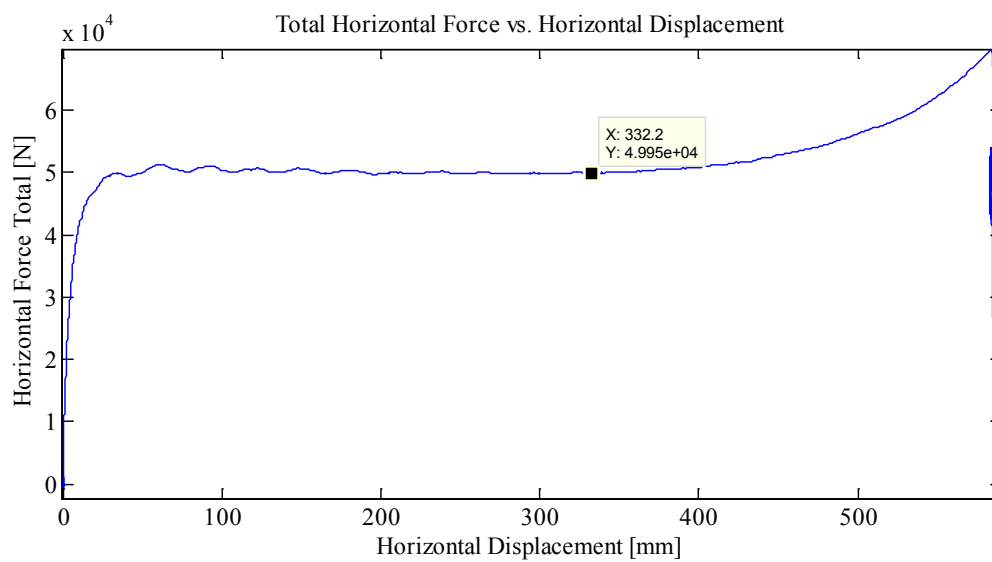












Appendix C1.2.3 – MovingLoad7

March 25, 2014 at ~4:40 p.m.

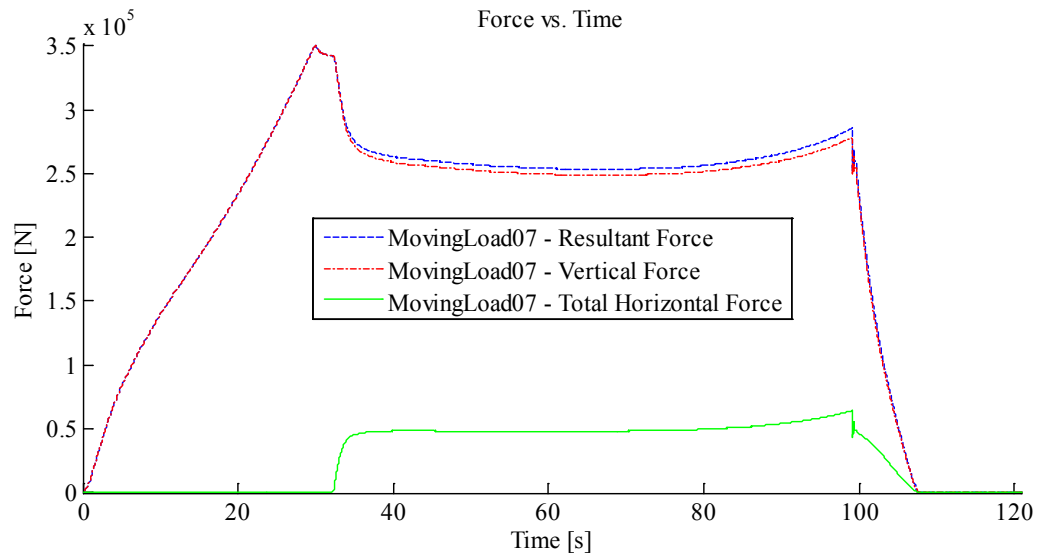
Run #: 2
Run Type: Slow
Room-temperature ~20°C
Sample Type: 1/2"
Test Type: In-Along-Out Centre to End

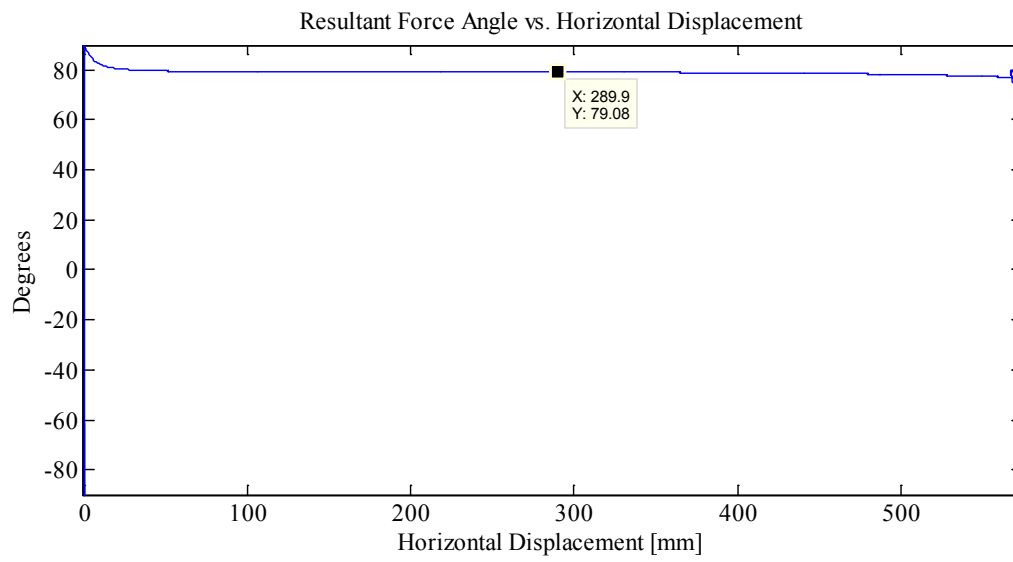
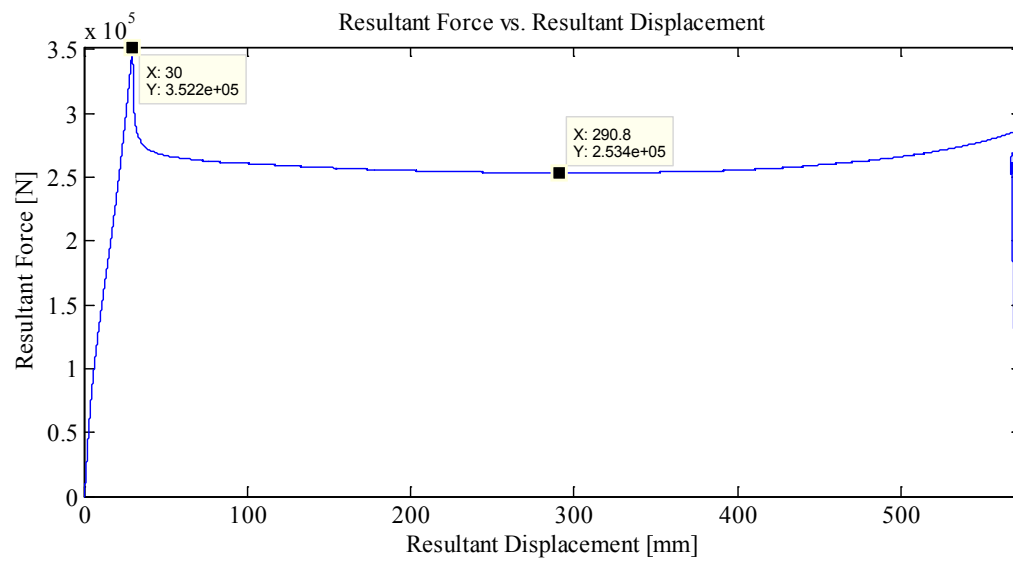
HStarting Point: Centre
HSpeed: 10 mm/s (Nominal)
H Travel: Centre to End

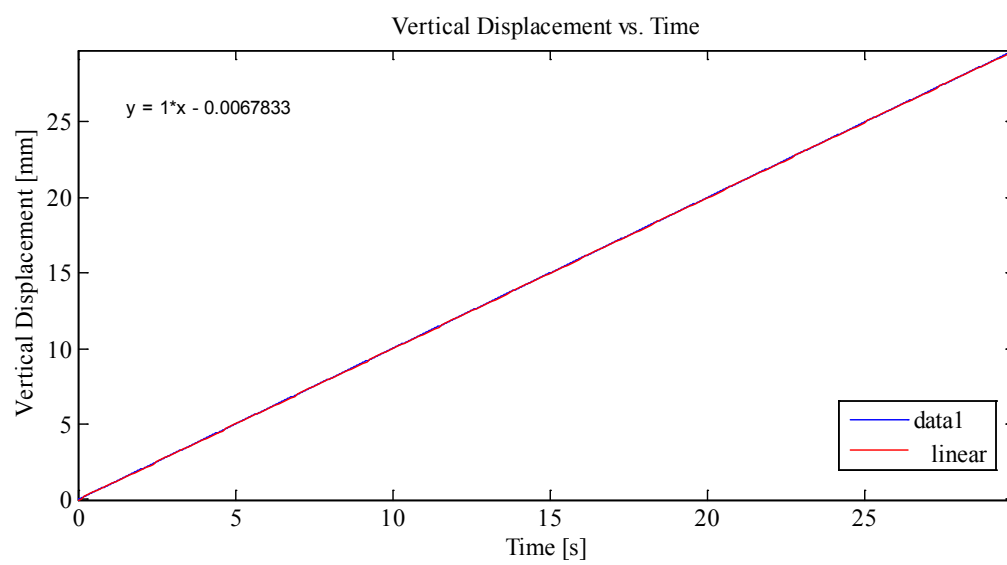
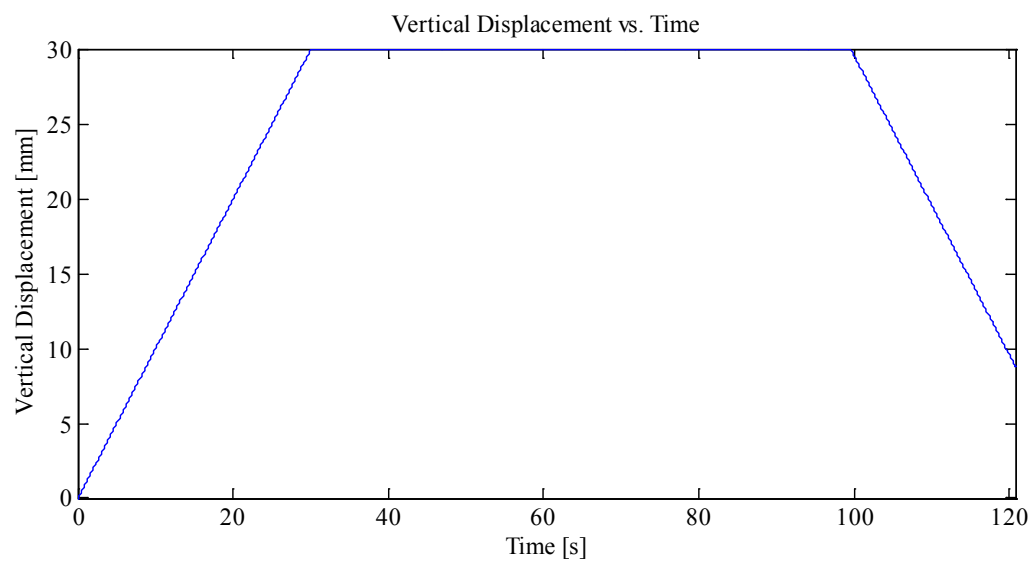
Vstarting Point: -8.7 mm
VSpeed: 1.0mm/s (Nominal)
V Travel: 30 mm

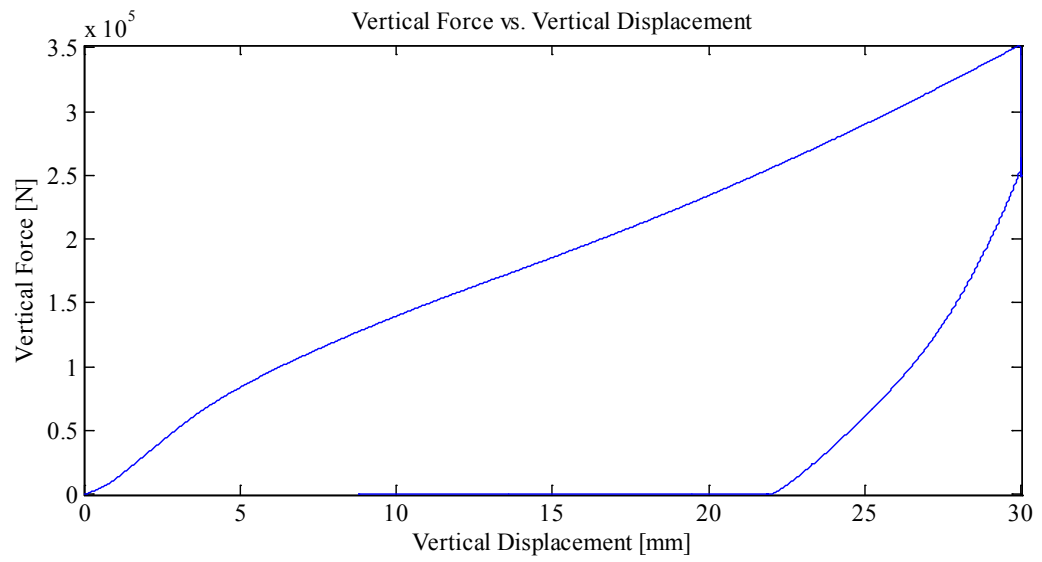
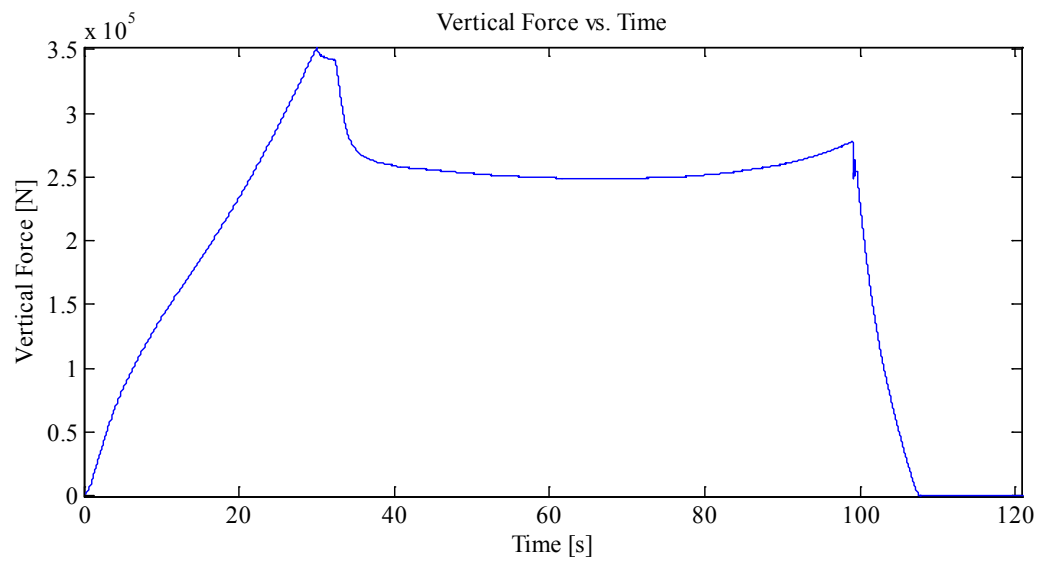
Indentation 1: ~30 mm, In-Along-Out - Centre to End
Data from Indentation 1 saved as MovingLoad07

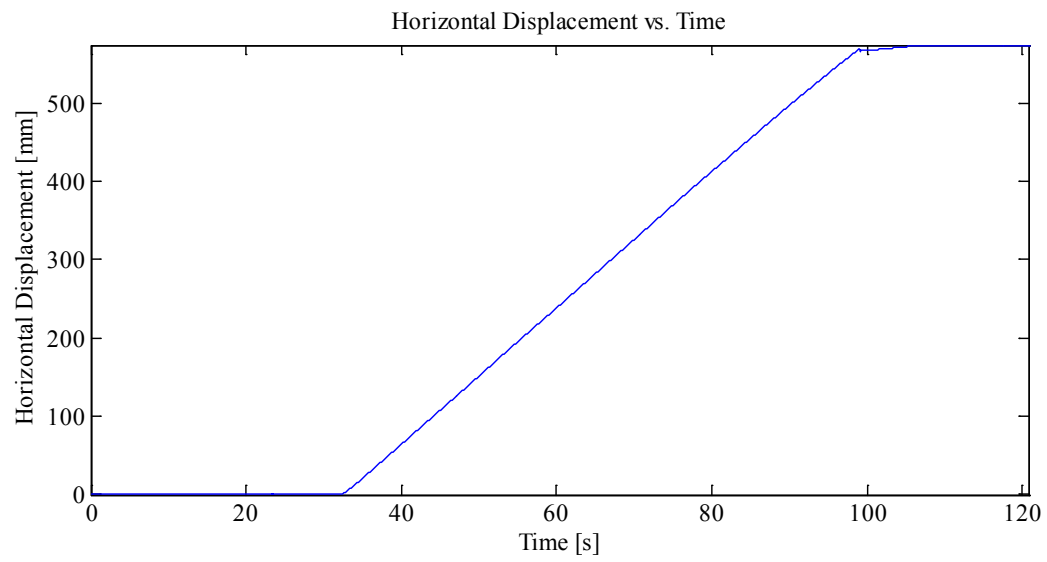
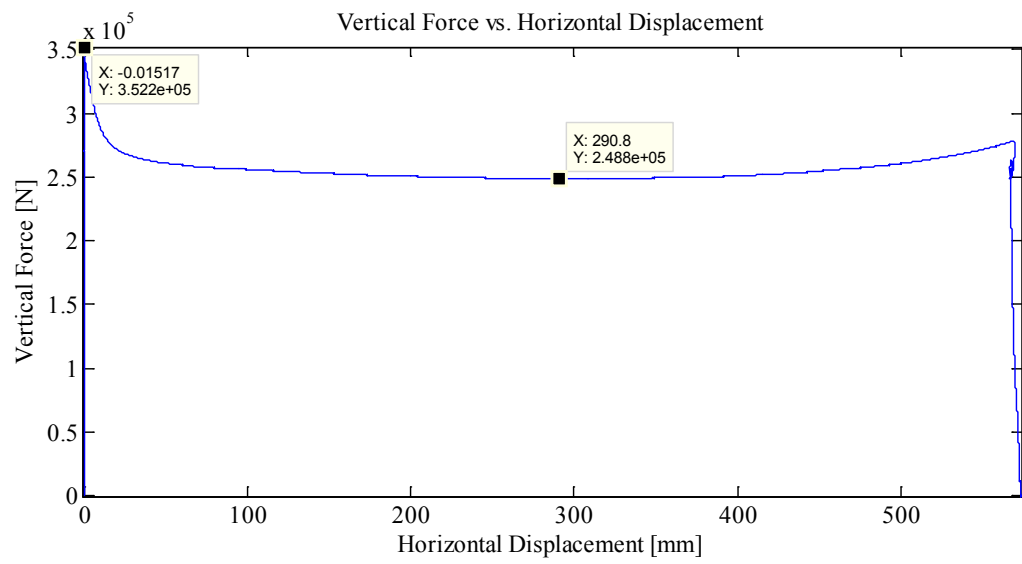
Note: Microscribe not bolted to table (bolted for run 3 onwards).

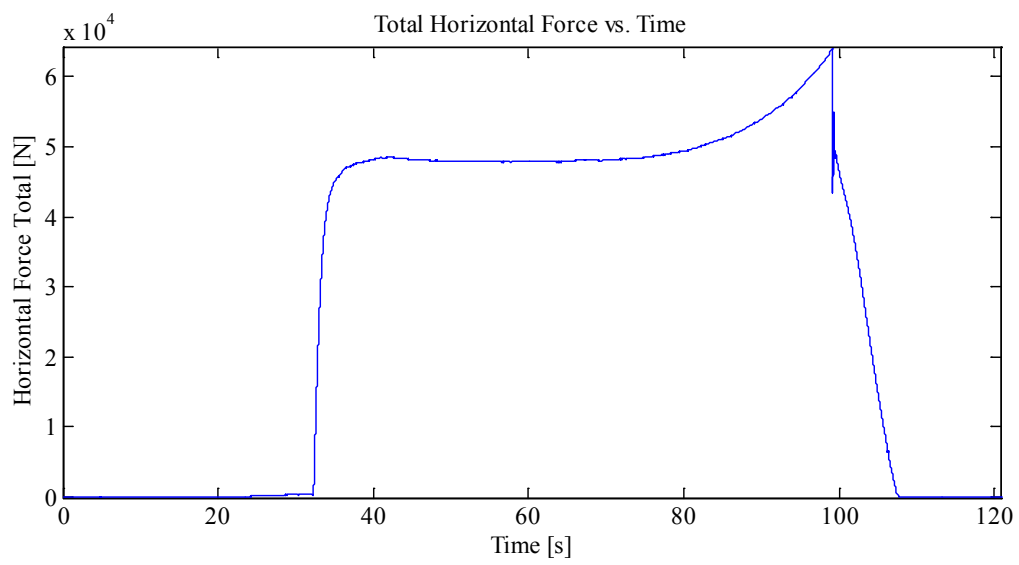
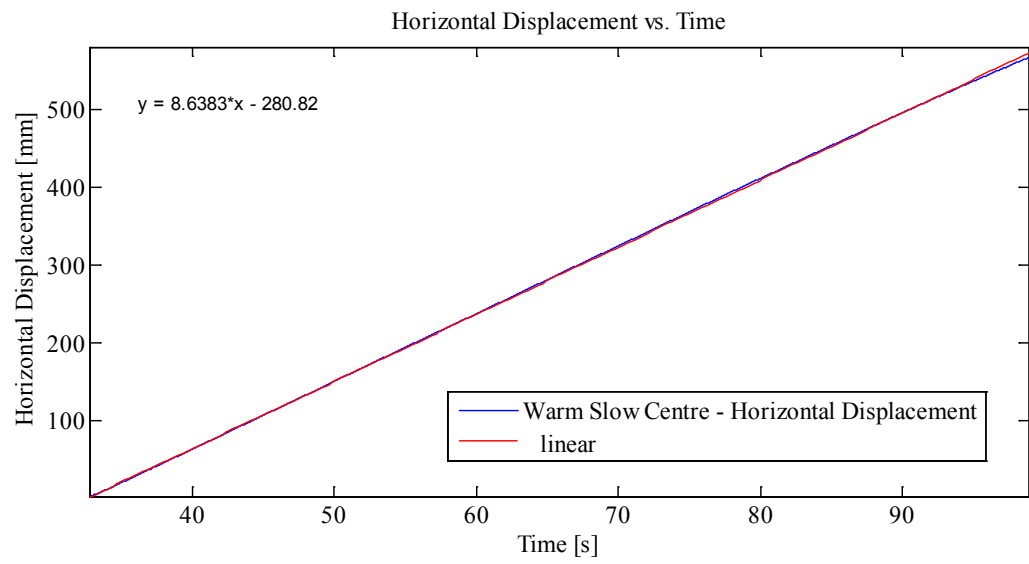


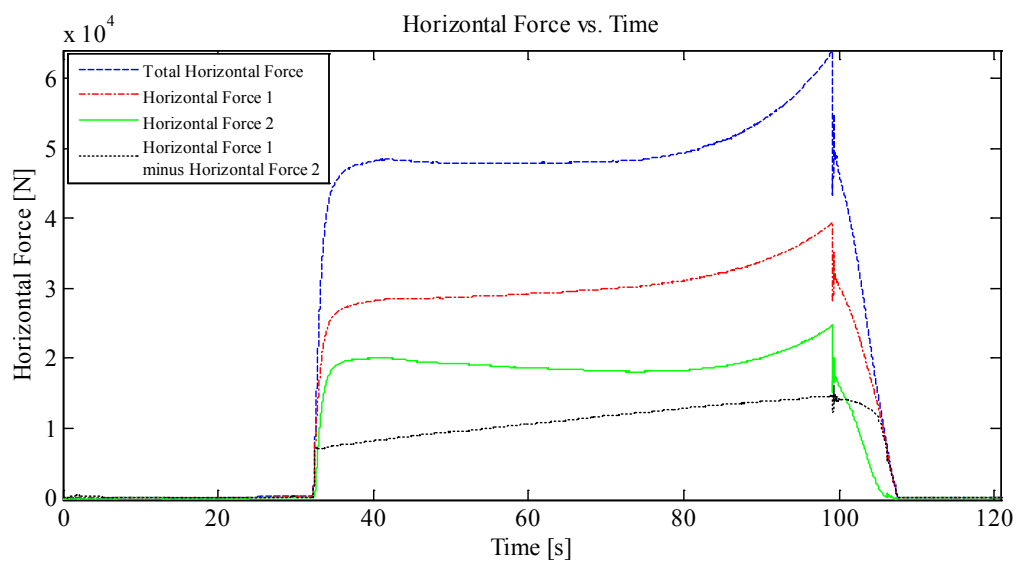
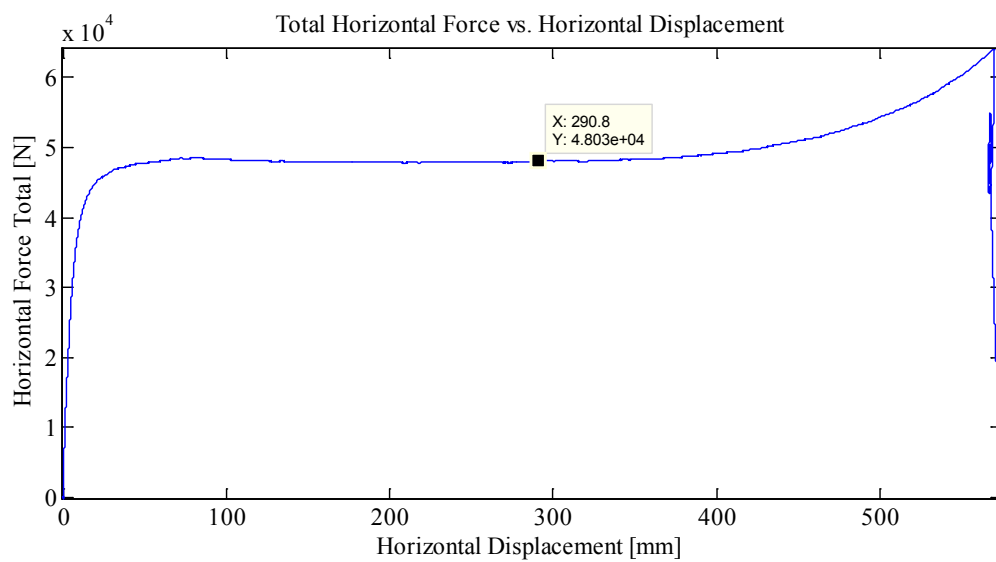












Appendix C1.2.4 – MovingLoad8

March 26, 2014 at ~12:00 p.m.

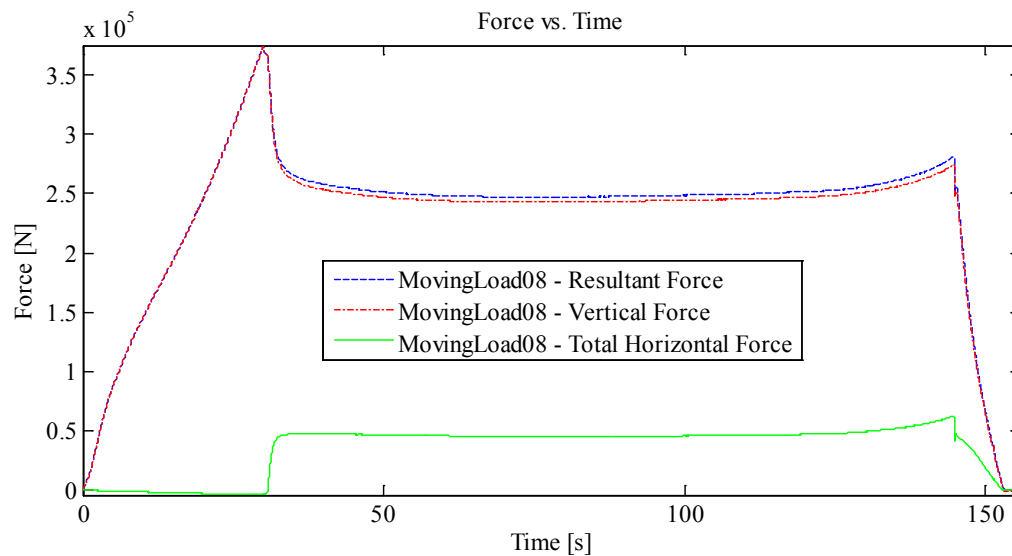
Run #: 3
Run Type: Full Length – Slow
Room-temperature ~20°C
Sample Type: 1/2"
Test Type: In-Along-Out End to End

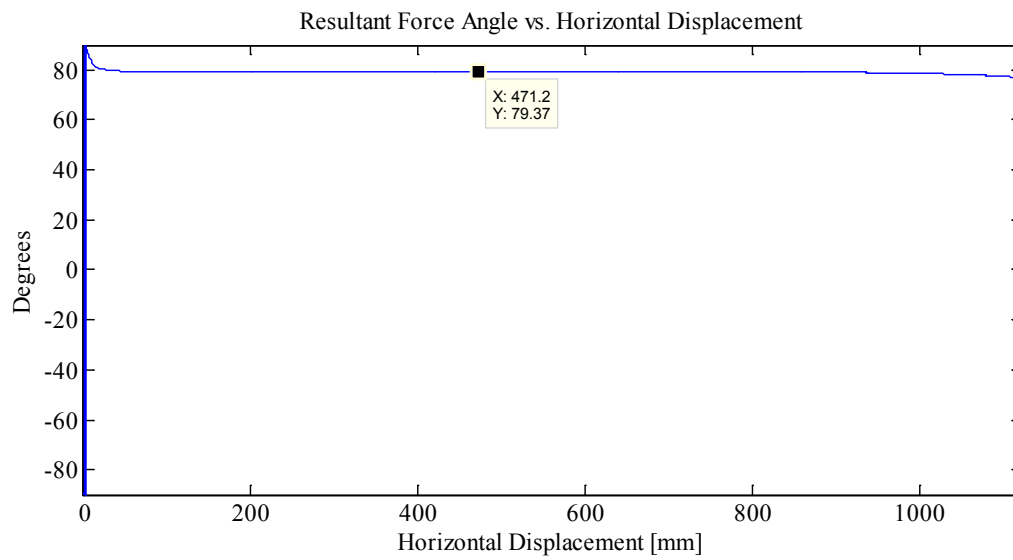
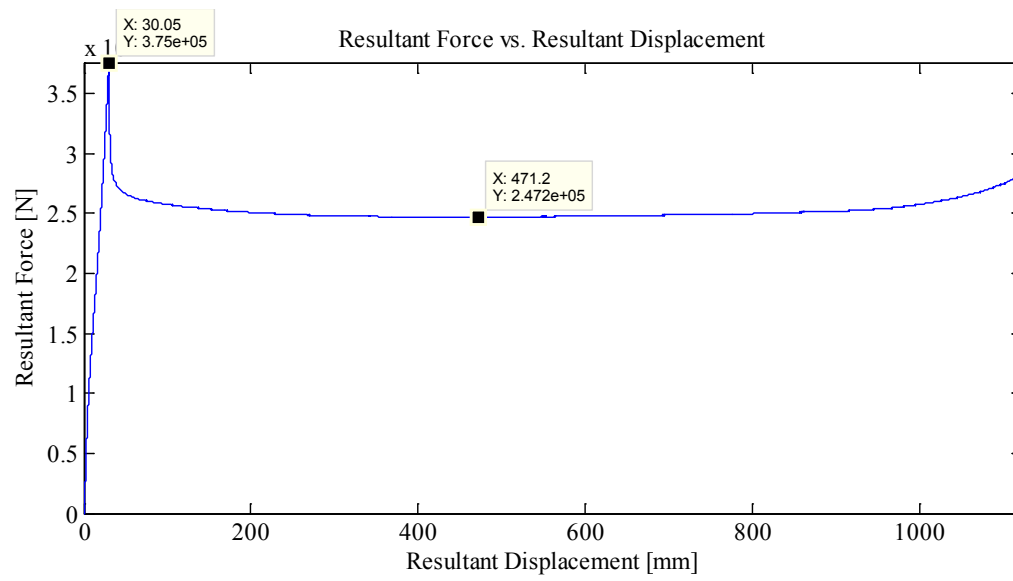
HStarting Point: End (20 cm from Edge)
HSpeed: 10 mm/s Nominal
H Travel: End to End (110+ cm)

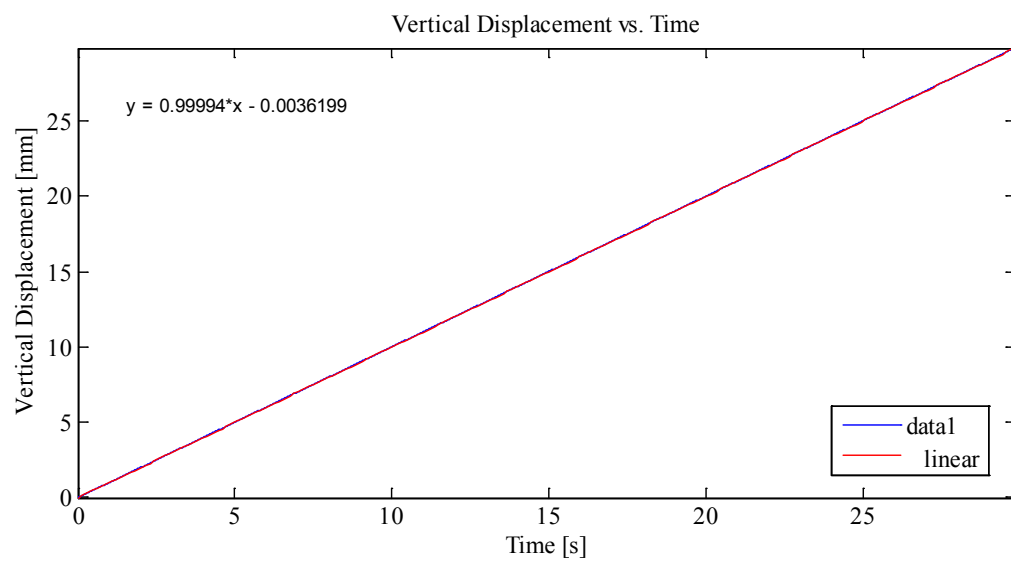
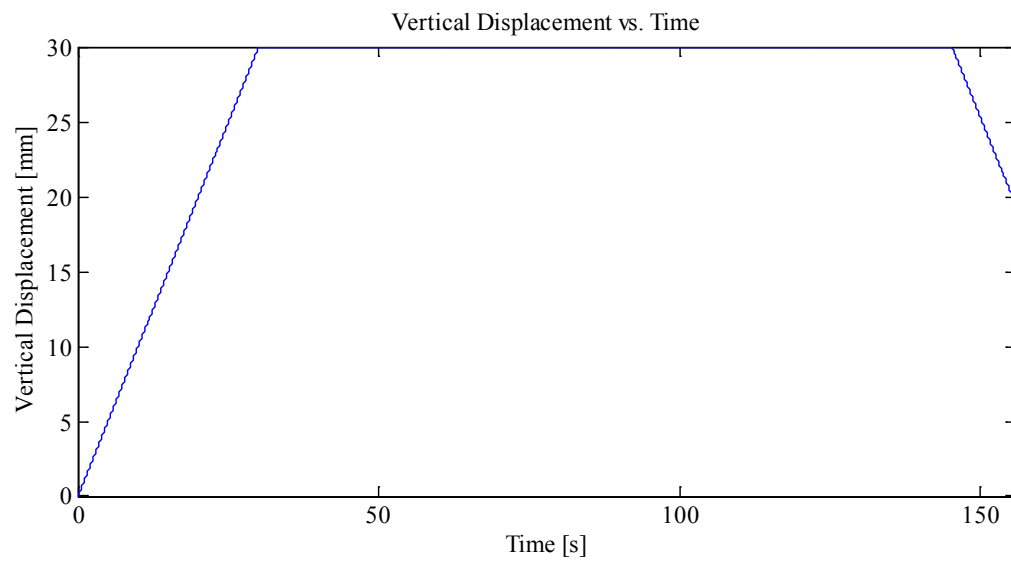
Vstarting Point: mm
VSpeed: 1.0mm/s (Nominal)
V Travel: 30 mm

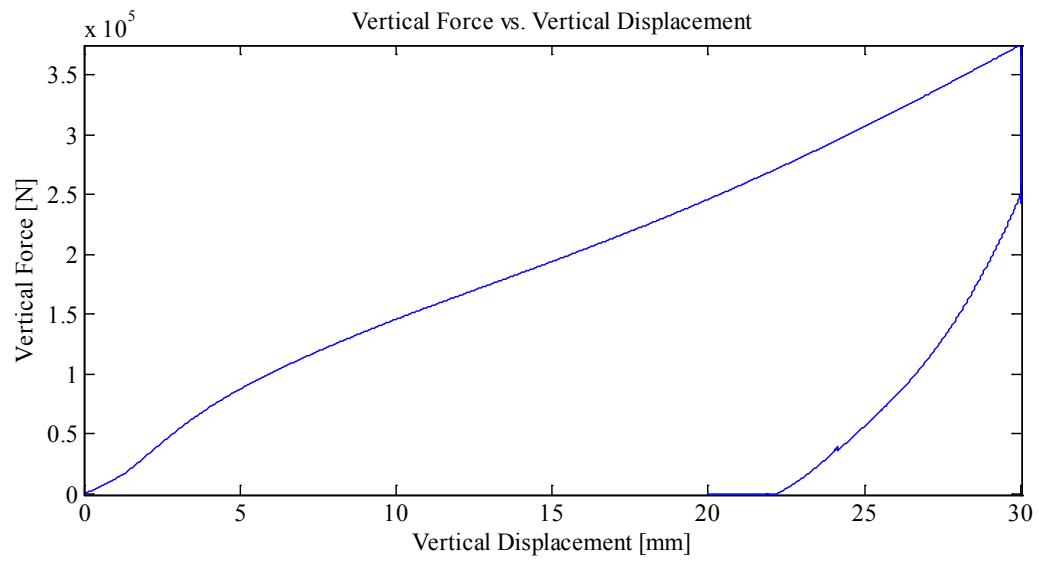
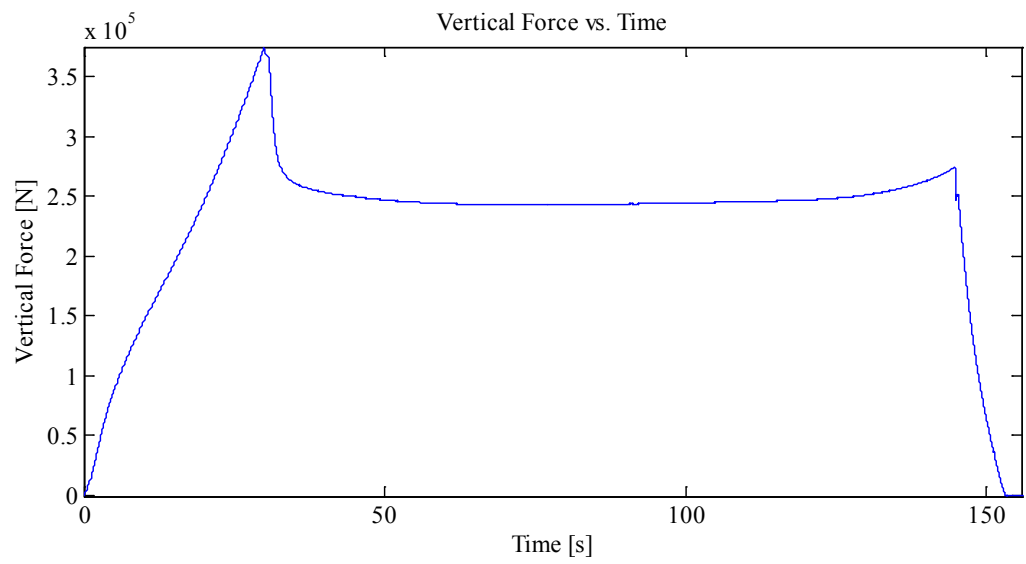
Indentation 1: ~30 mm, In-Along-Out - Centre to End
Data from Indentation 1 saved as MovingLoad08

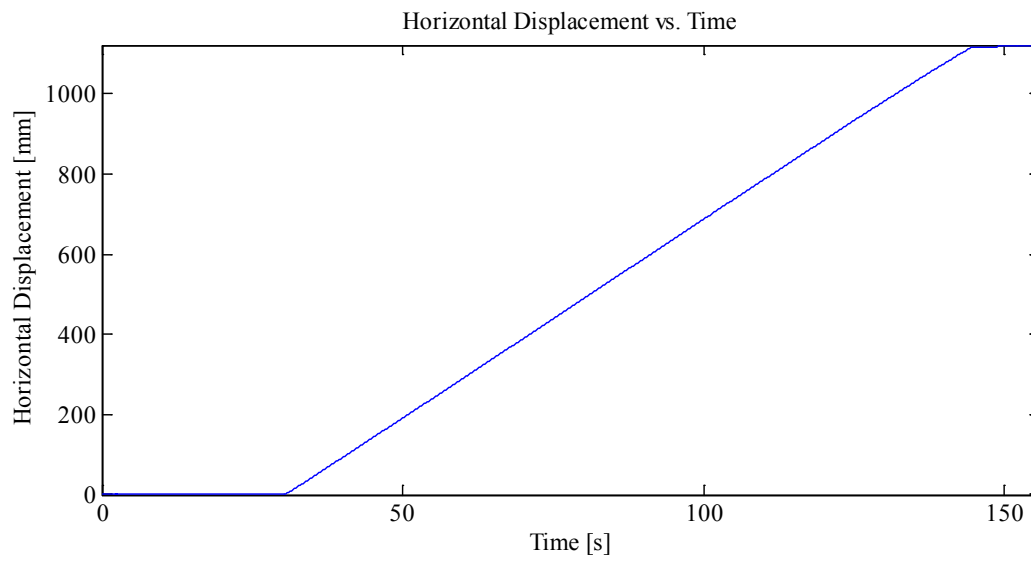
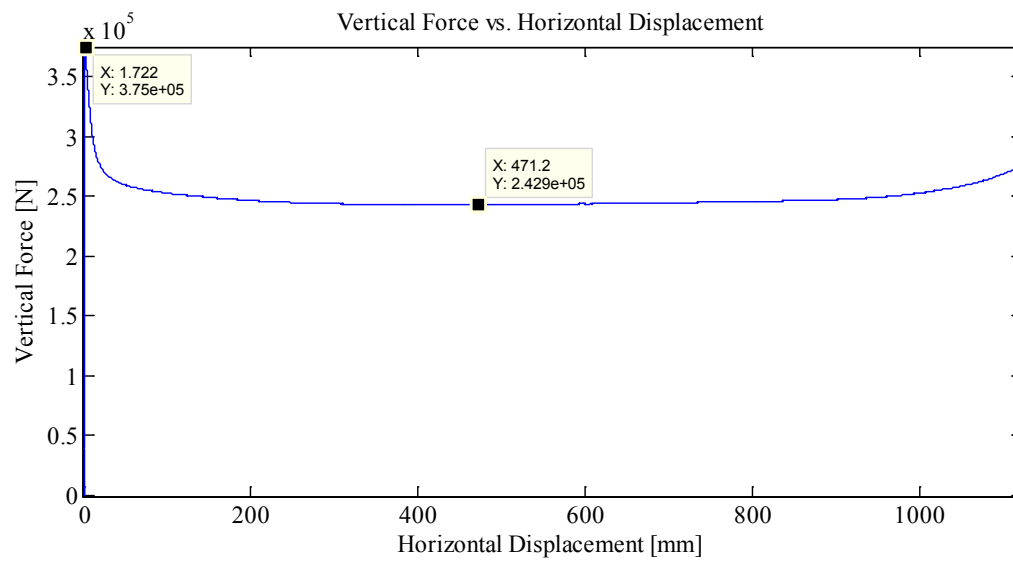
Note:
Bolted Microscribe to table for more accurate readings.

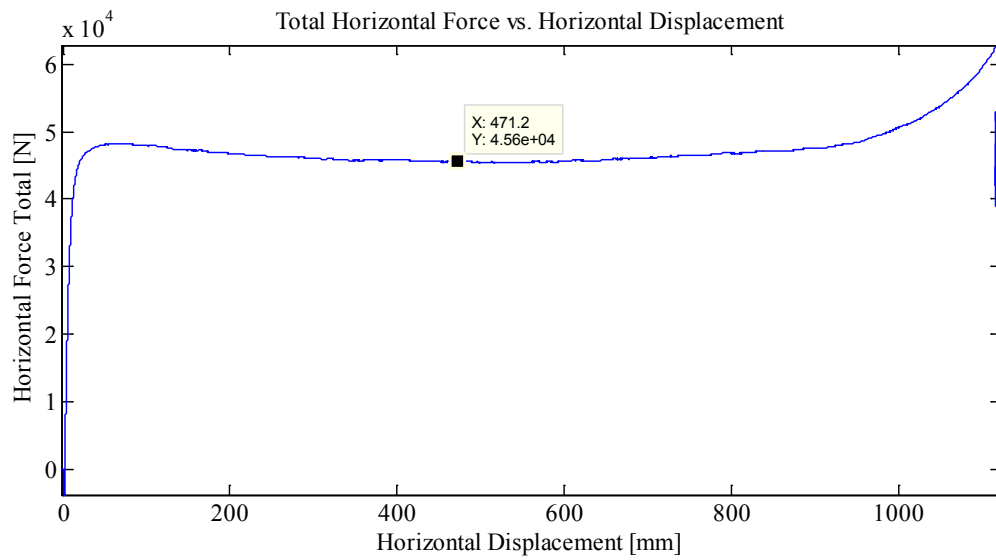
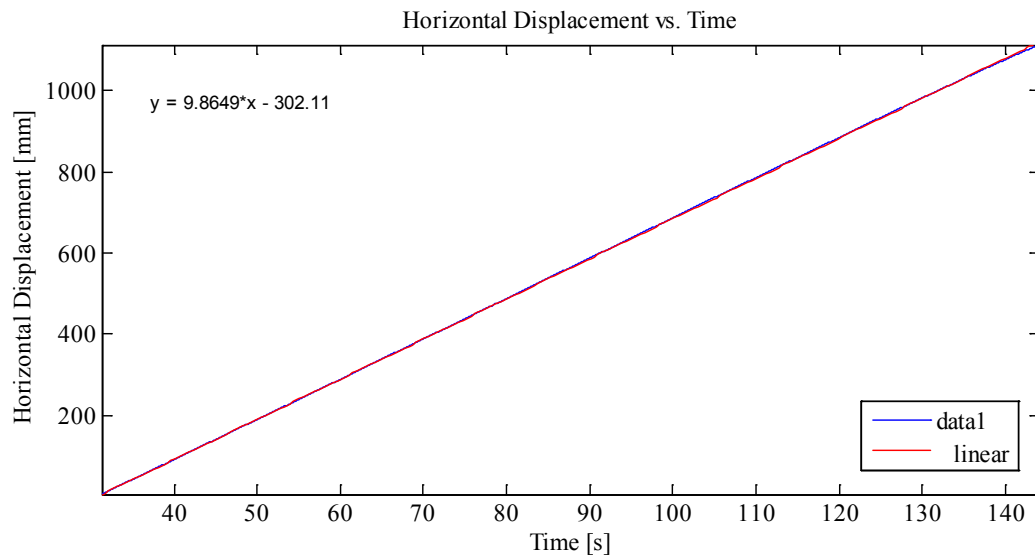








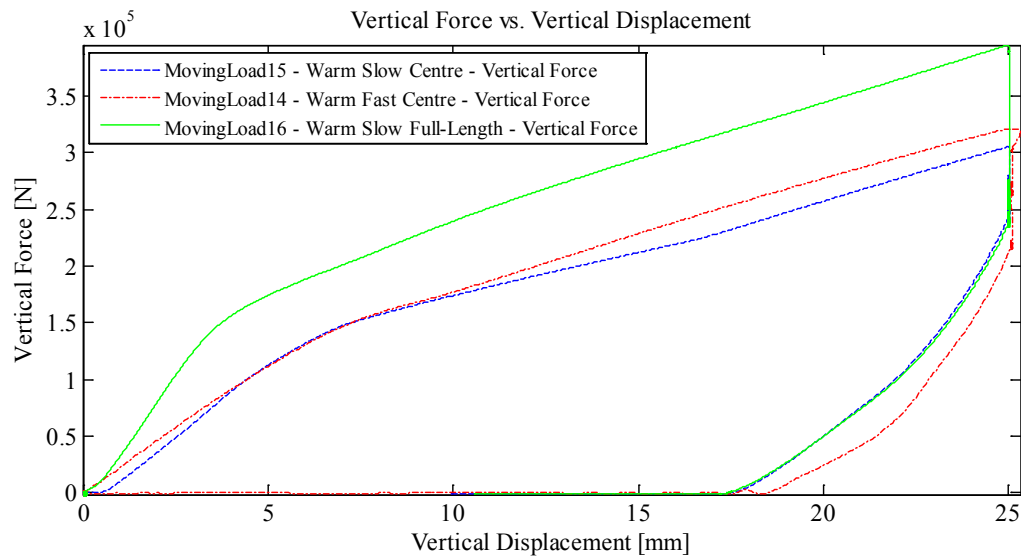
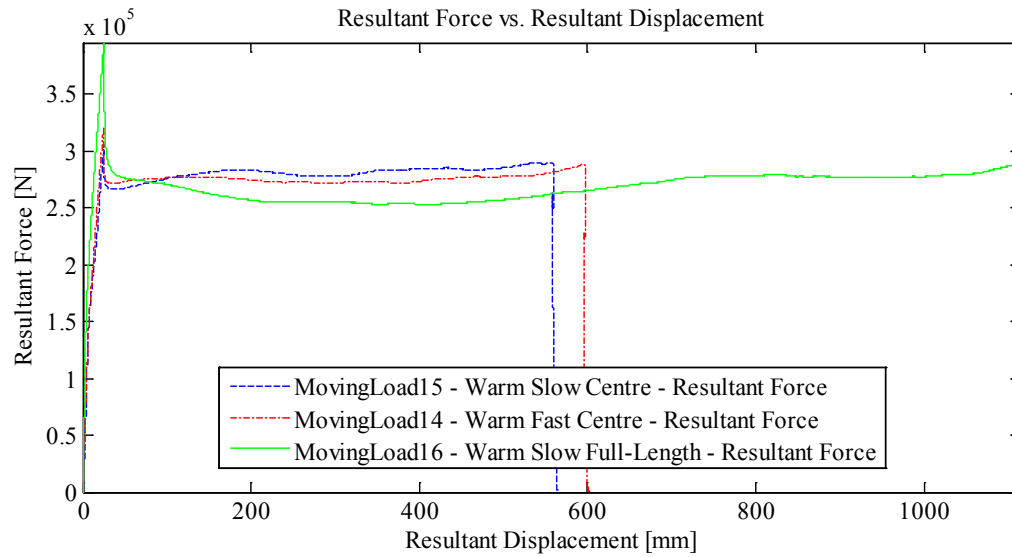


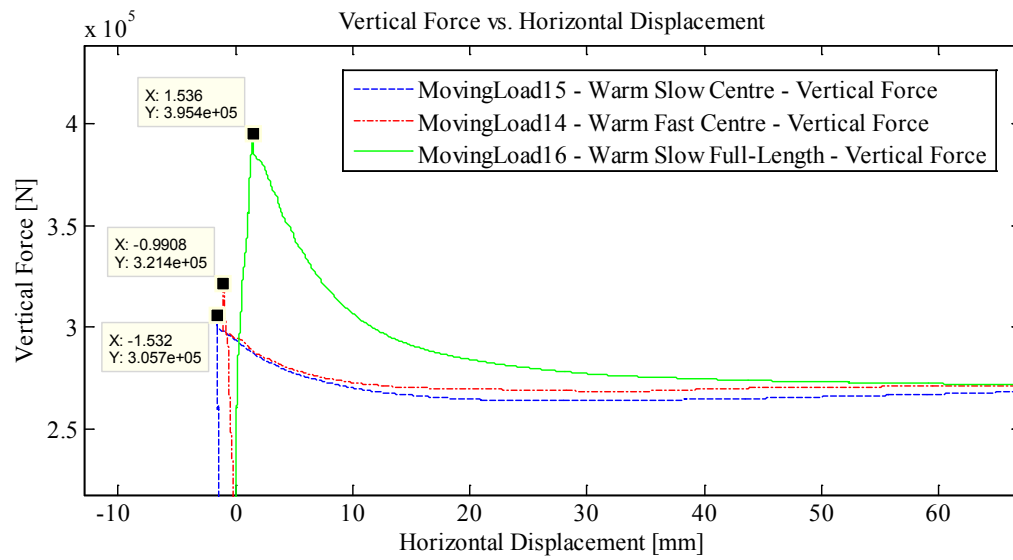
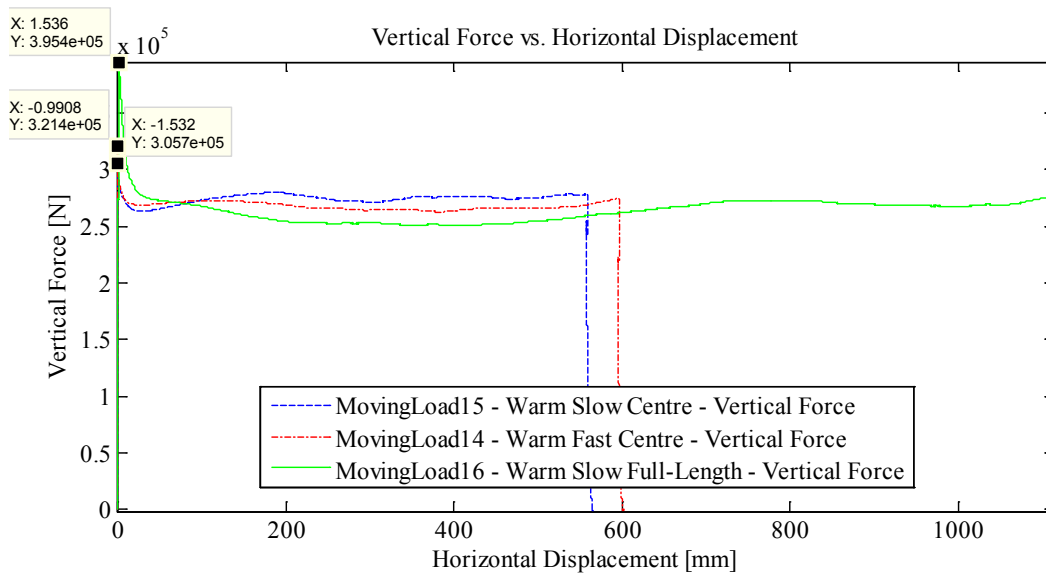


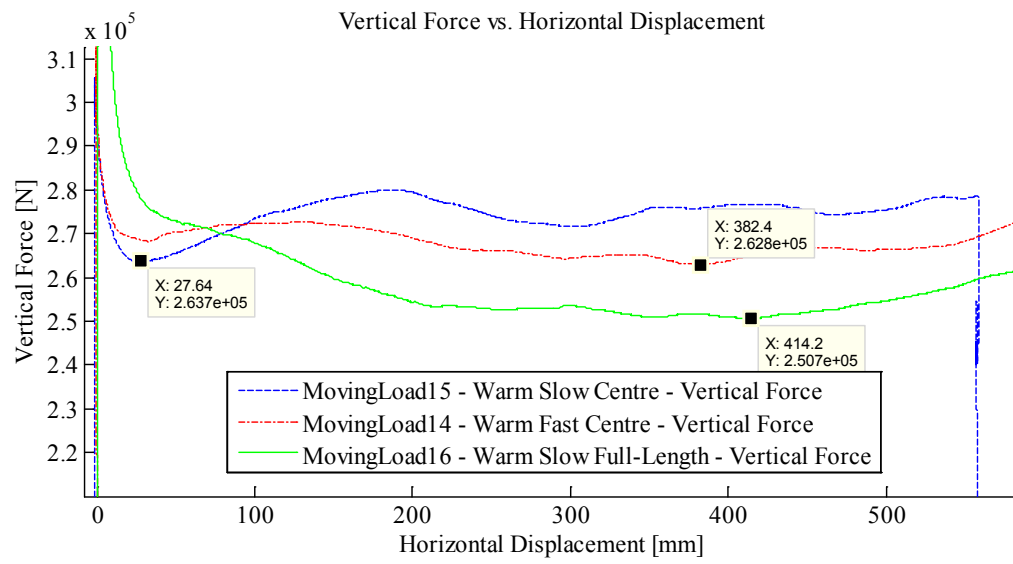
Appendix C1.3 – **Frame – 2.5 cm (0.984 in.) Indentation**

Appendix C1.3.1 – Summary Plots for Experiments ML 14, 15 and

16







Appendix C1.3.2 – MovingLoad14

April 1, 2014 at ~3:55 p.m.

Run # 7
Run Type: Fast
Room-temperature: ~20°C
Sample Type: Frame
Test Type: In-Along-Out Centre to End

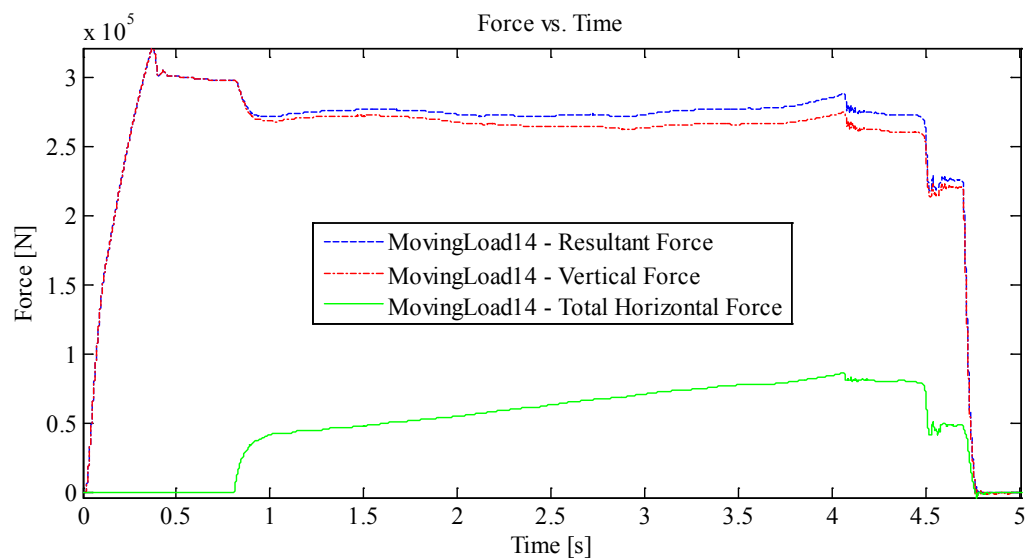
HStarting Point: Centre
HSpeed: 100.0 mm/s (Nominal)
H Travel: Centre to End (55+ cm)

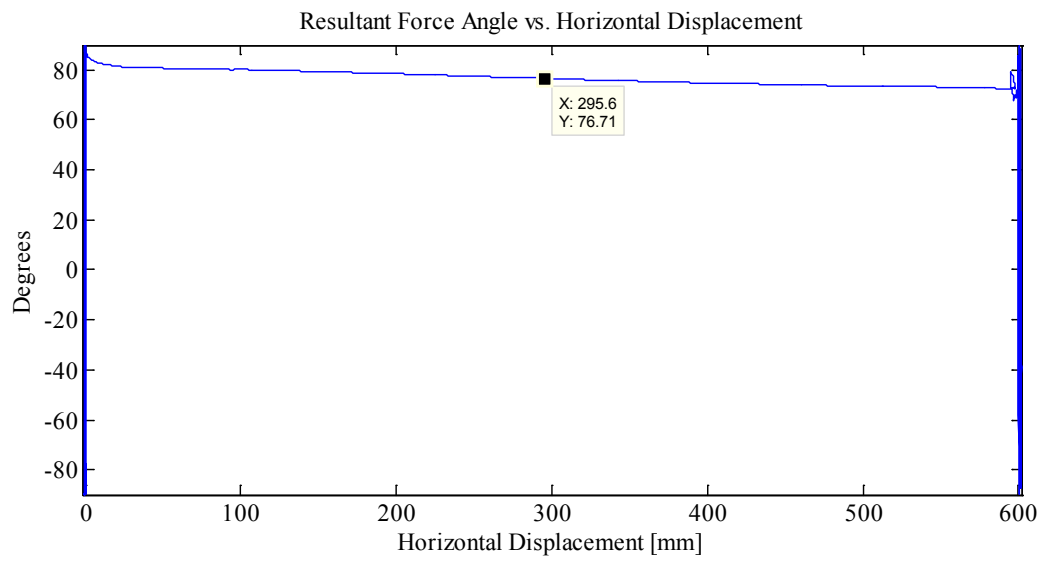
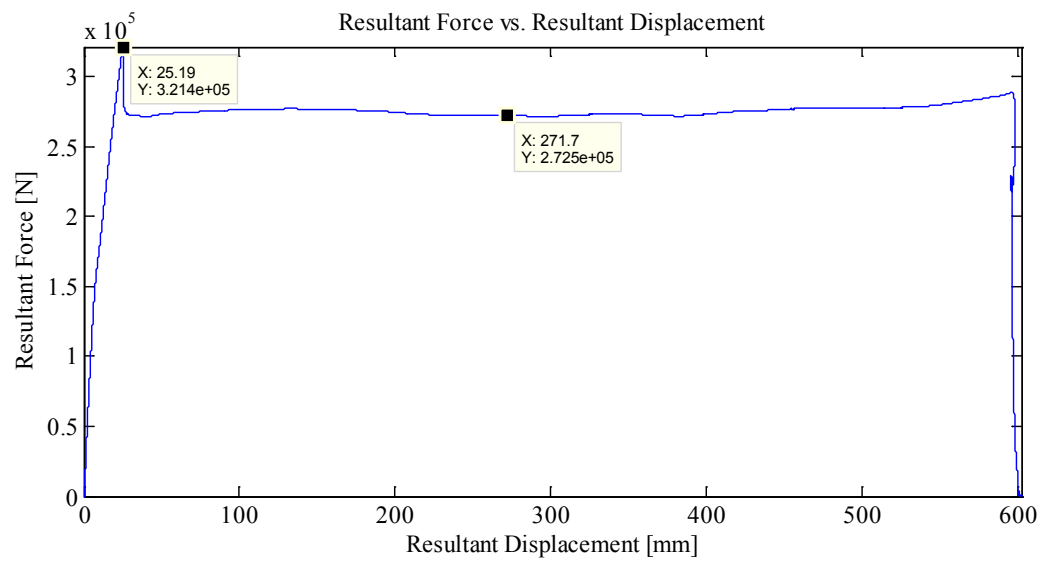
Vstarting Point: 3.63 mm
VSpeed: Max (Nominal)
V Travel: 25 mm
V Stopping Point: -21.37 mm

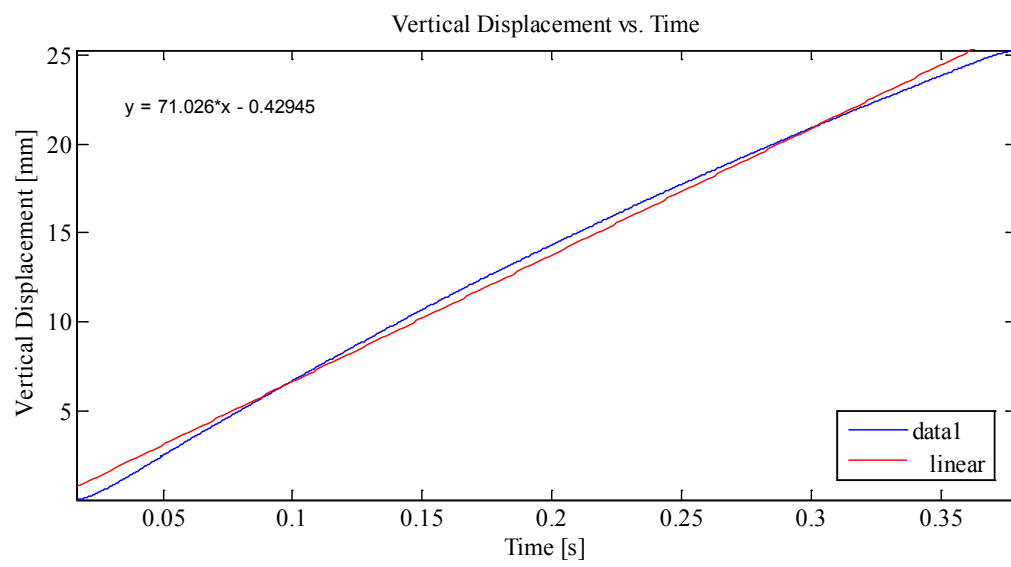
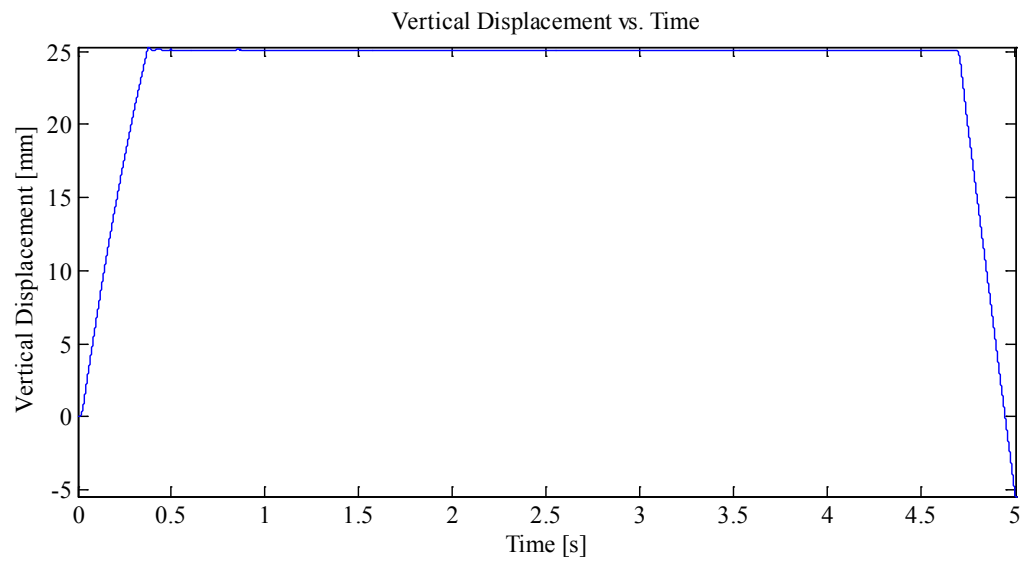
Notes:

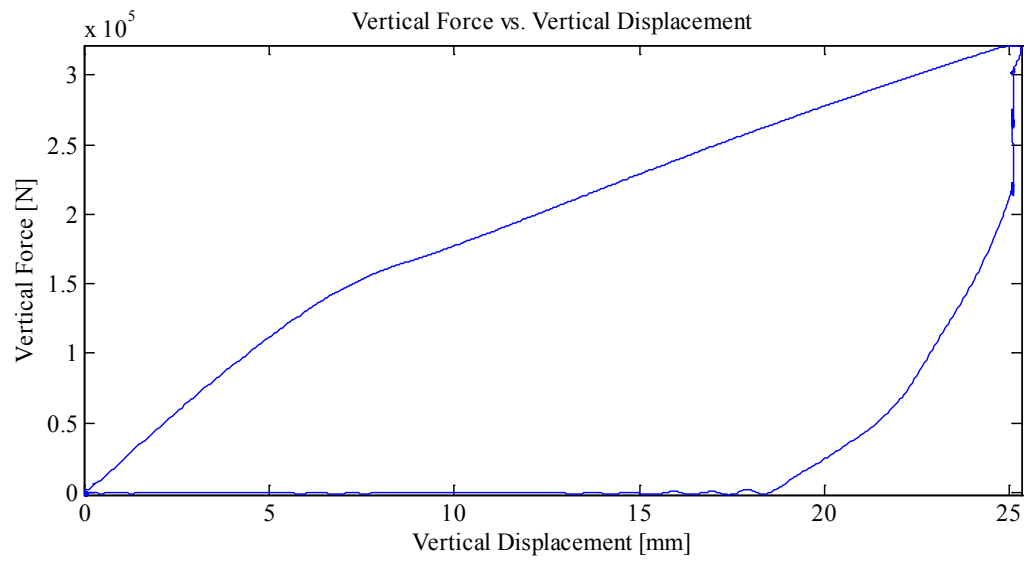
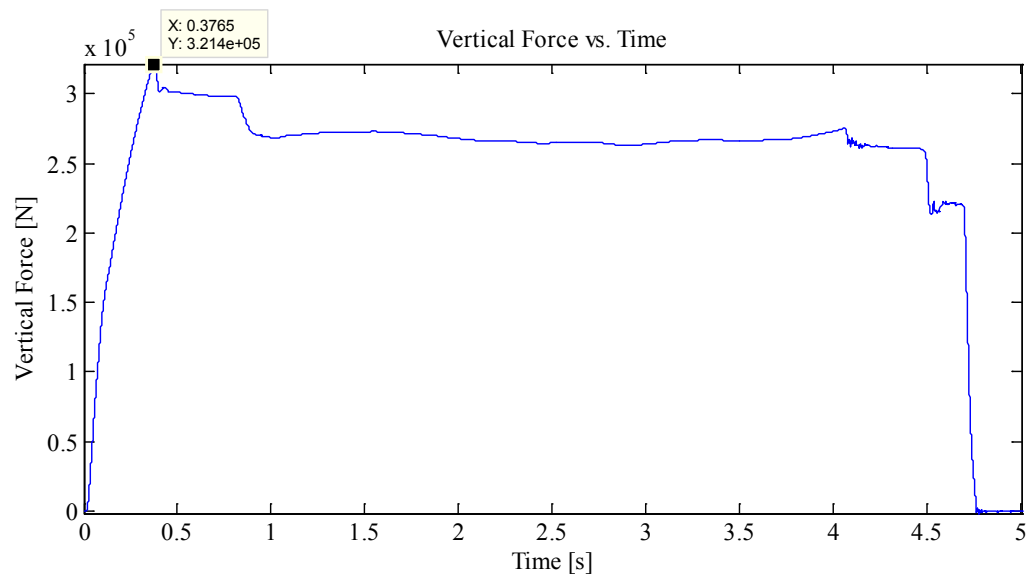
Indentation 1: ~25 mm, In-Along-Out - Centre to End
Data from Indentation 1 saved as MovingLoad14.

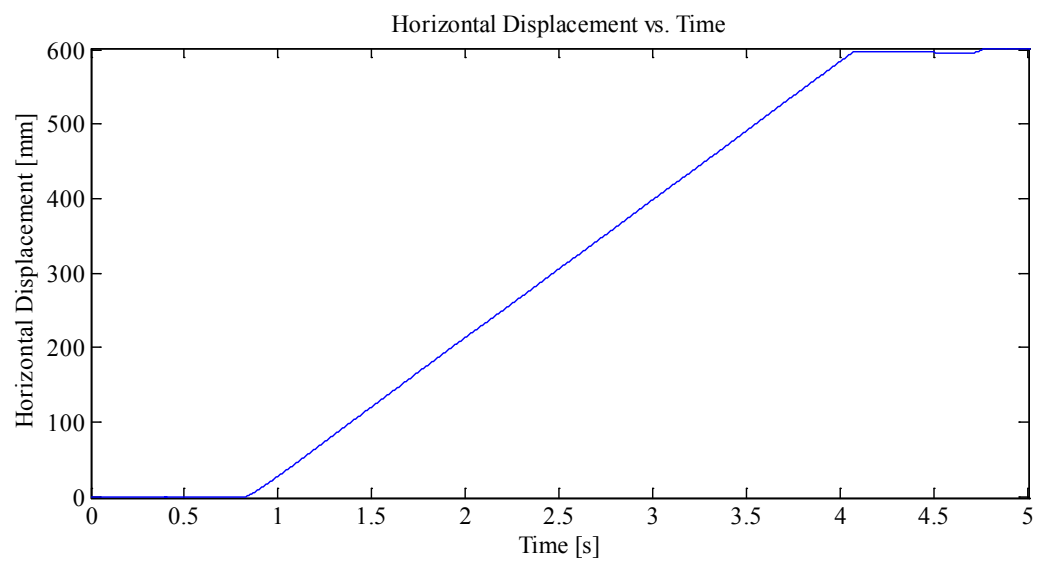
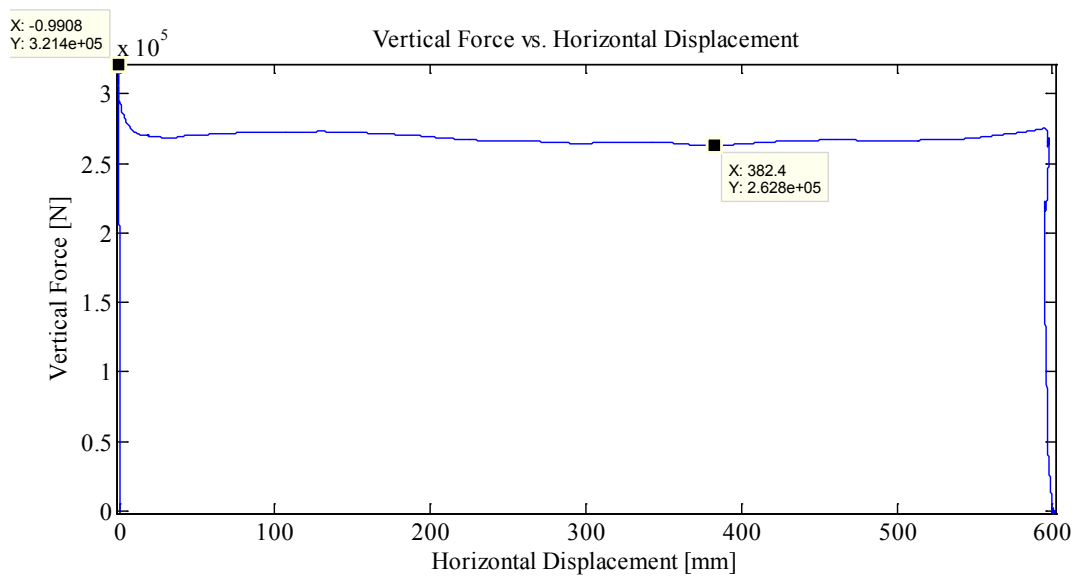
Plots:

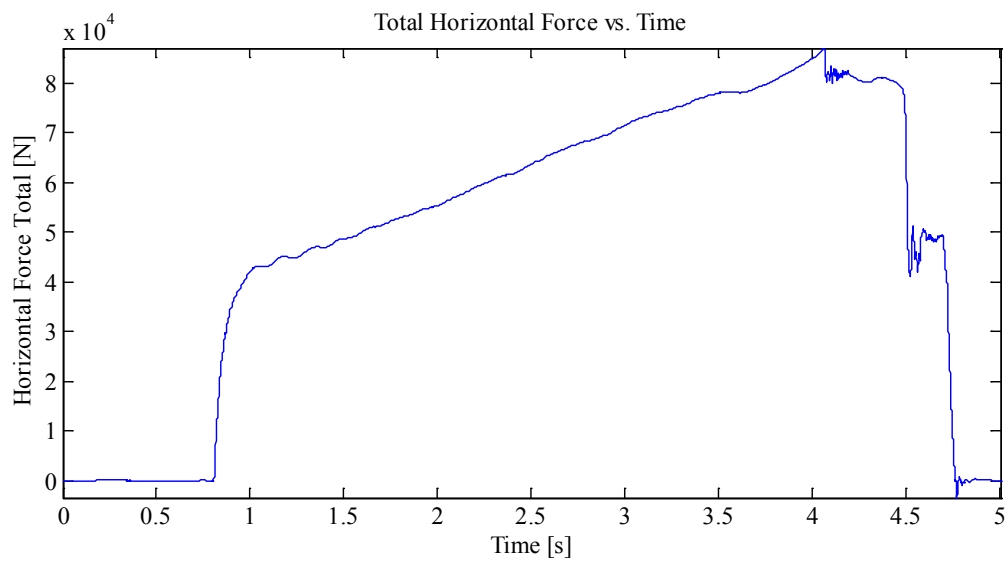
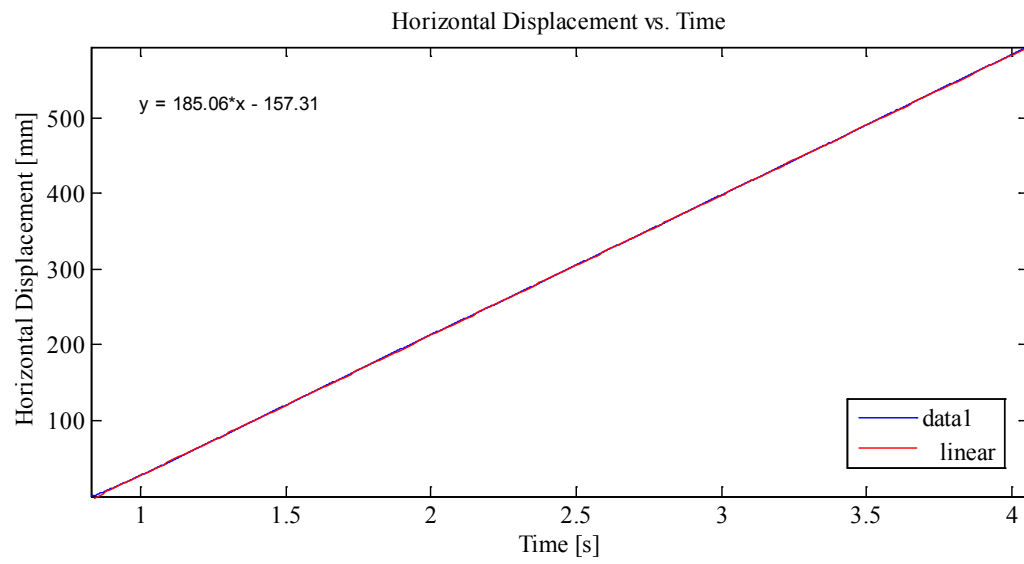


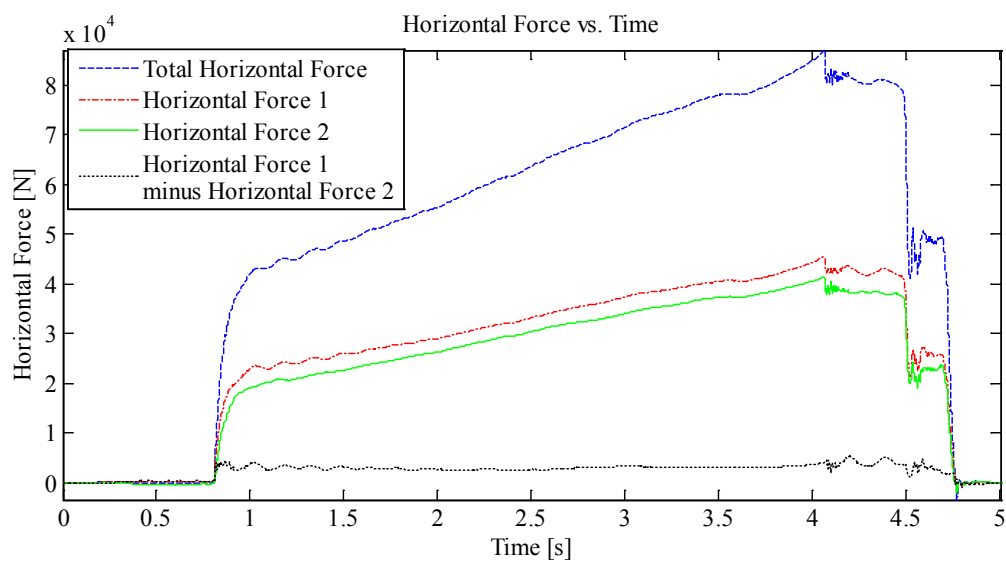
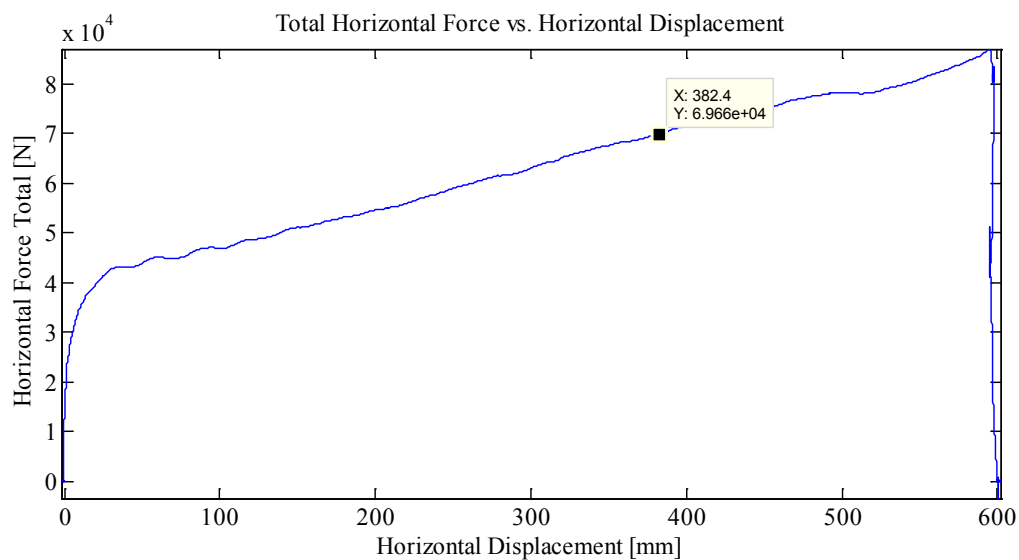












Appendix C1.3.3 – MovingLoad15

April 2, 2014 at ~3:00 p.m.

Run # 8
Run Type: Slow
Room-temperature: ~20°C
Sample Type: Frame
Test Type: In-Along-Out Centre to End

HStarting Point: Centre
HSpeed: 1.0 mm/s (Nominal)
H Travel: Centre to End (55+ cm)

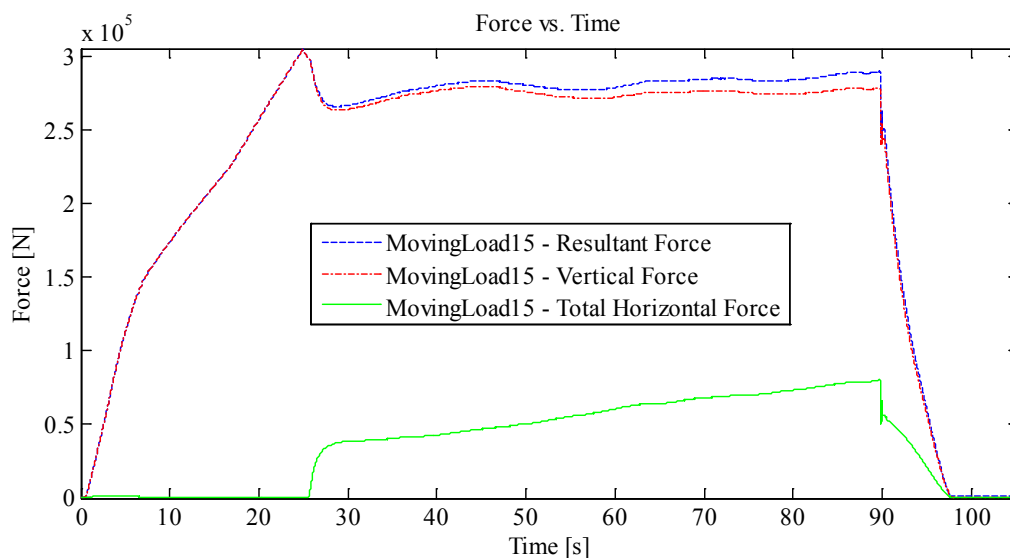
Vstarting Point: 3.51 mm
VSpeed: 10 mm/s (Nominal)
V Travel: 25 mm
V Stopping Point: -21.49 mm

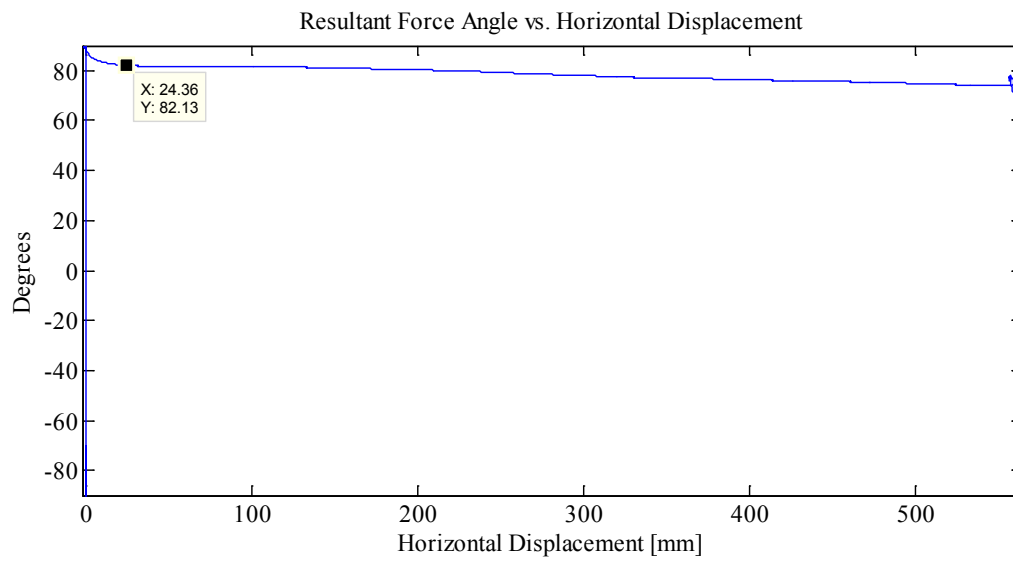
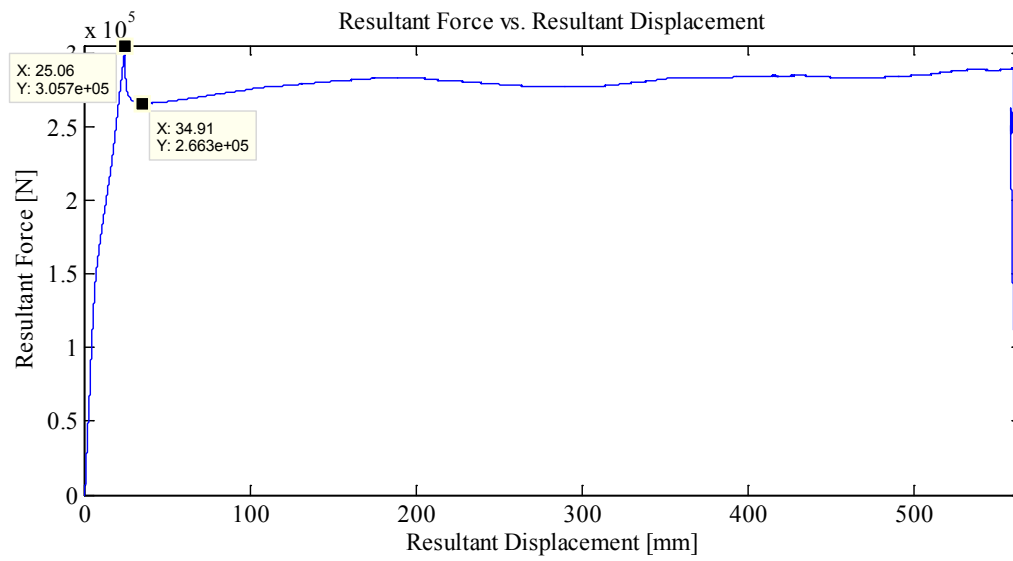
Notes:

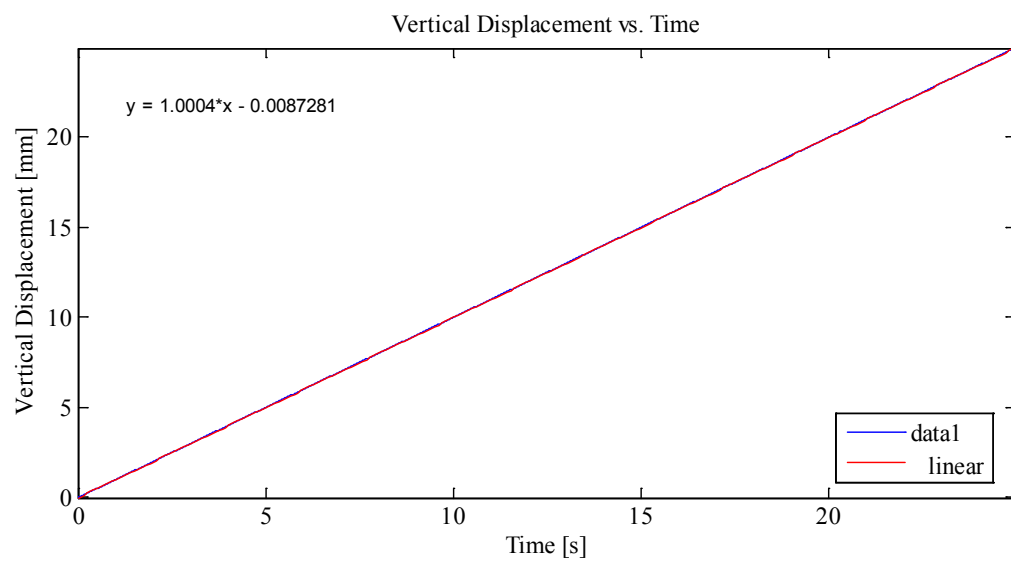
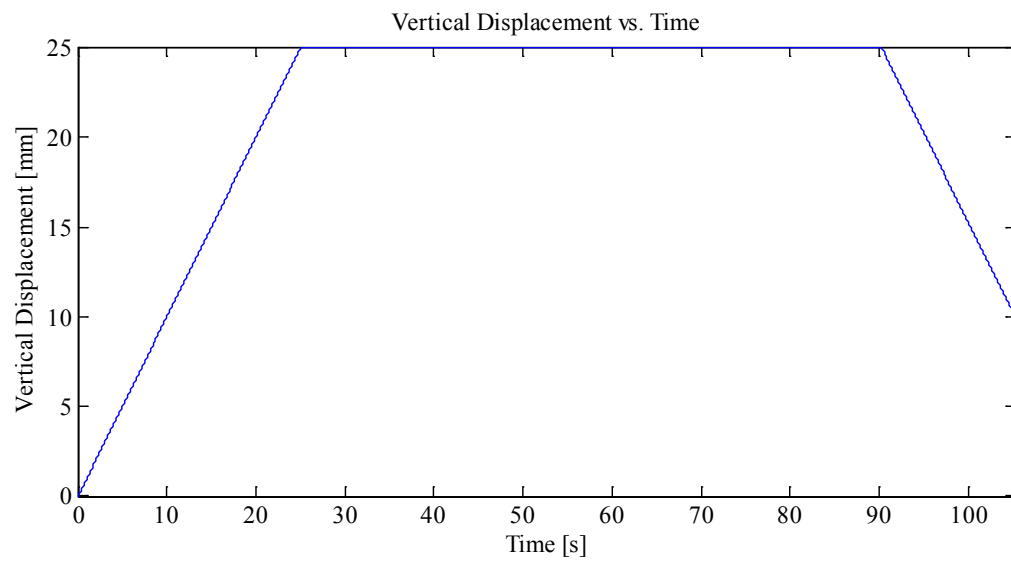
Accidentally indented ~2mm into plate at centre before test. ~30kN (no big deal).
Centre is at 2.7 mm from last centre (for some reason, probably the yoyo pot).

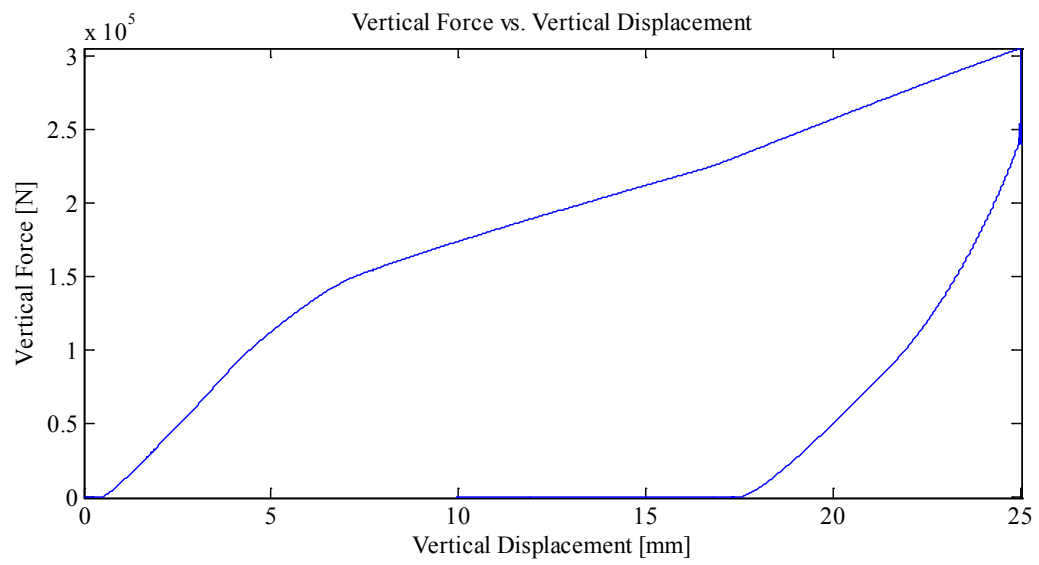
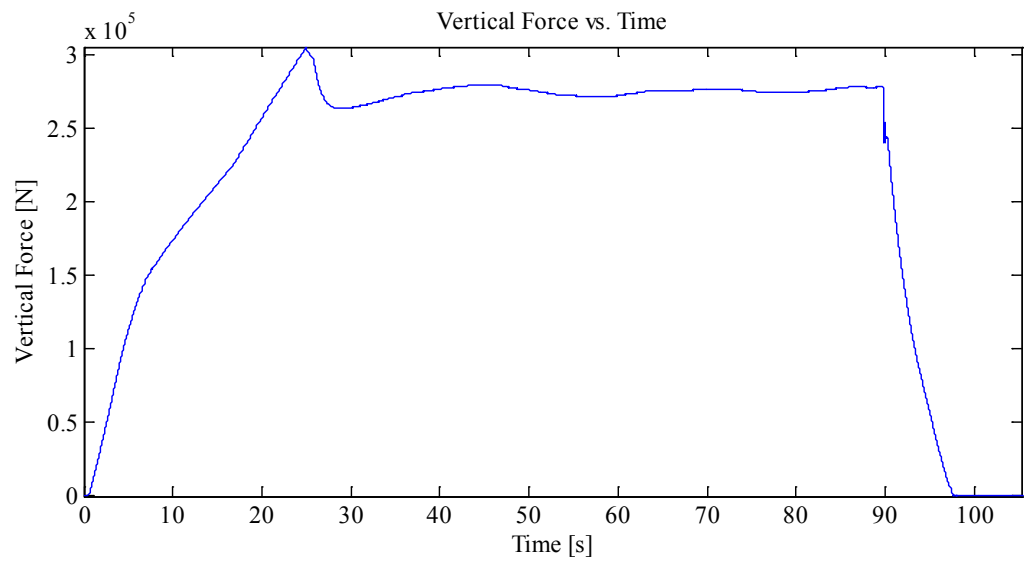
Indentation 1: ~25 mm, In-Along-Out - Centre to End
Data from Indentation 1 saved as MovingLoad15

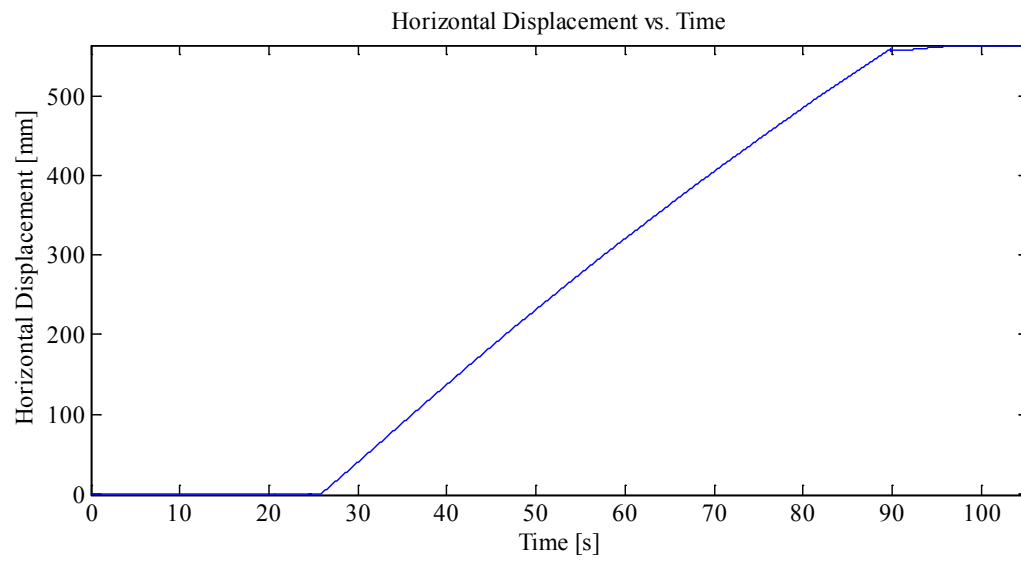
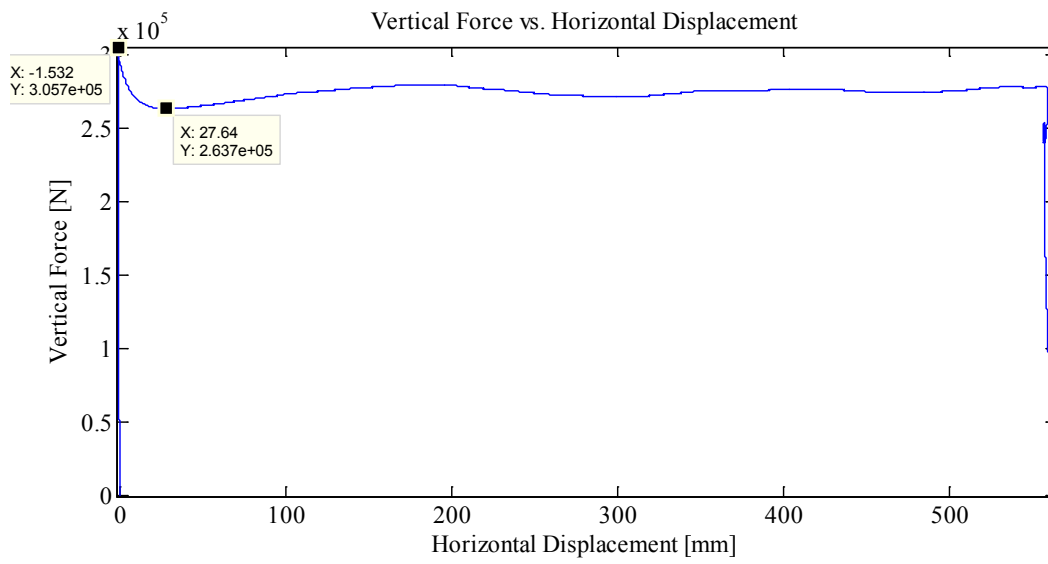
Plots:

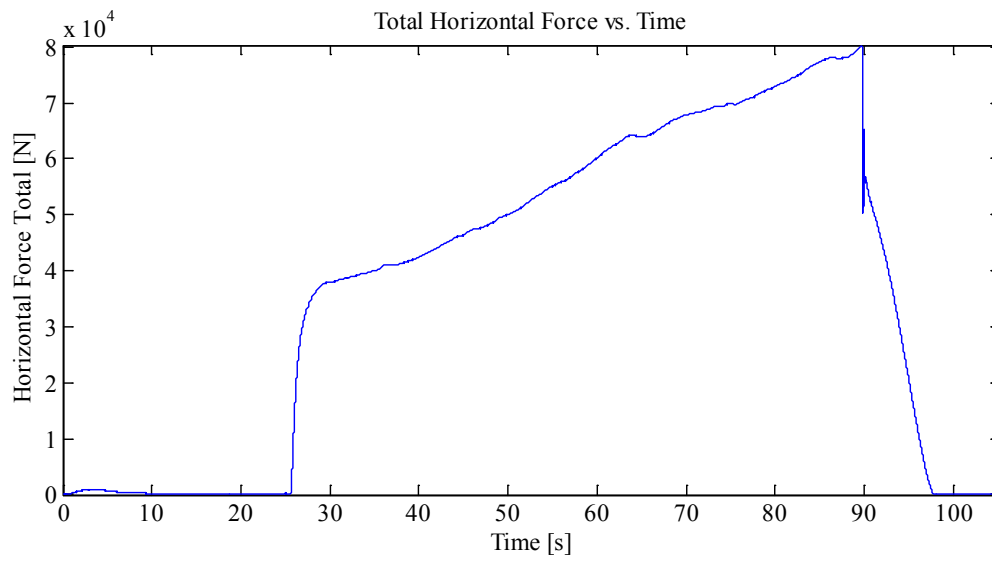
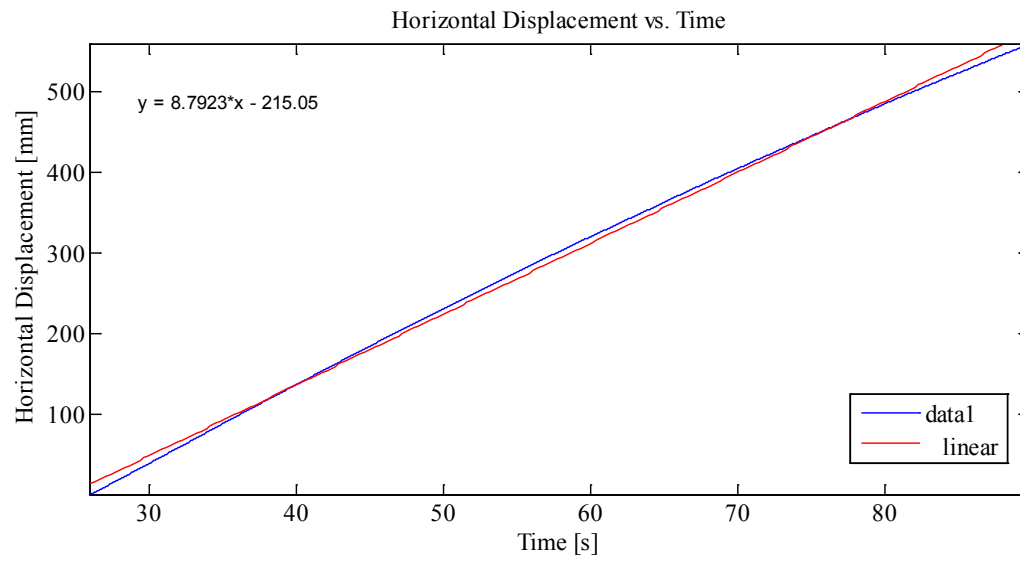


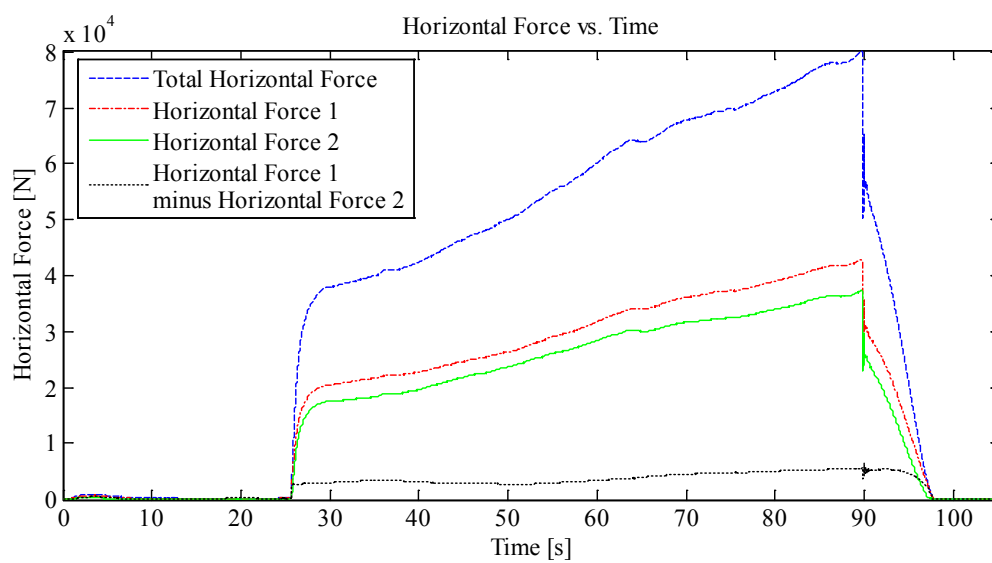
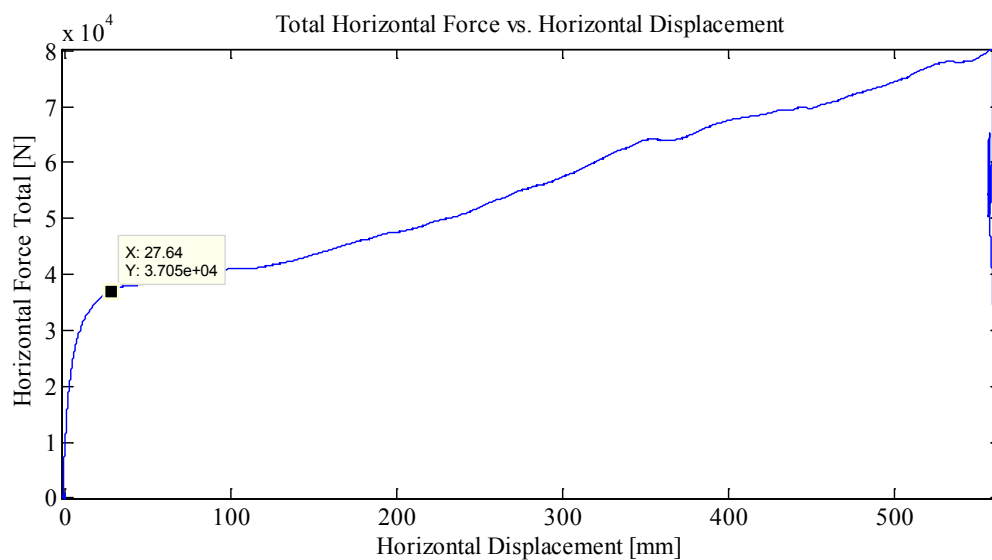












Appendix C1.3.4 – MovingLoad16

April 3, 2014 at ~2:45 p.m.

Run # 9
Run Type: Full Length – Slow
Room-temperature: ~20°C
Sample Type: Frame
Test Type: In-Along-Out End to End

HStarting Point: End (-54.7 cm (-55 cm nominal))
HSpeed: 10 mm/s (Nominal)
H Travel: End to End (110+ cm)

Vstarting Point: 3.36 mm
VSpeed: 1.0 mm/s (Nominal)
V Travel: 25 mm
V Stopping Point: -21.64 mm

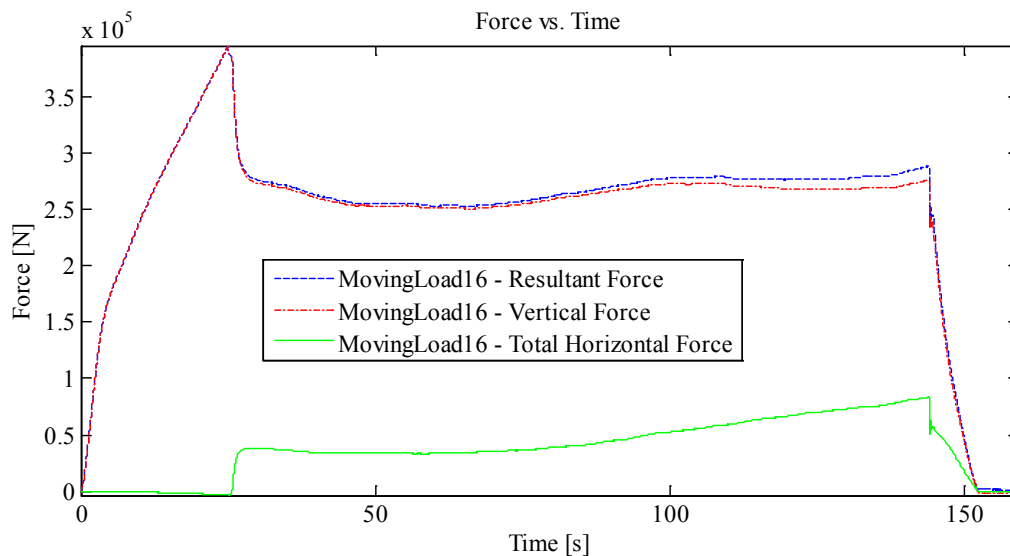
Notes:

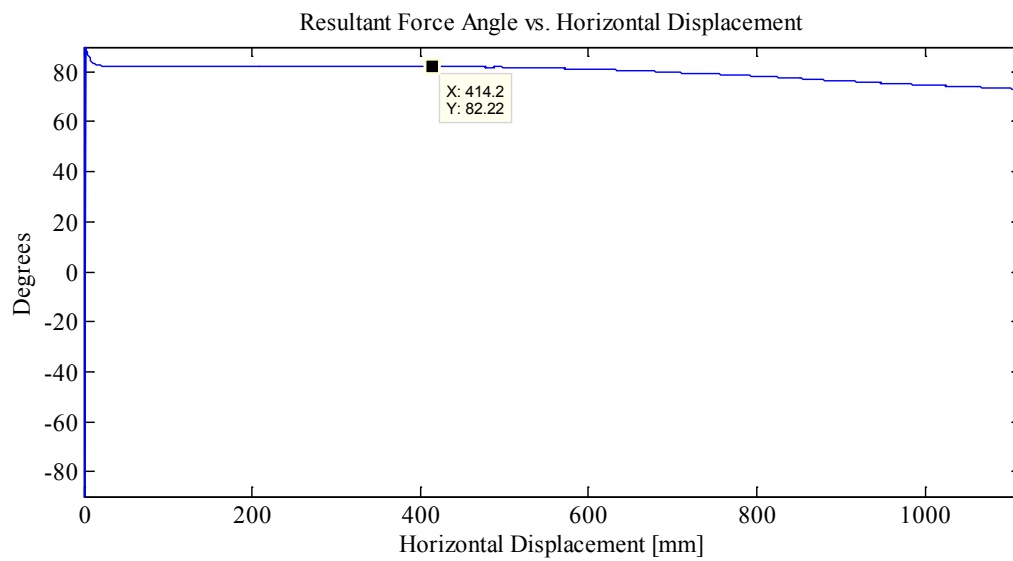
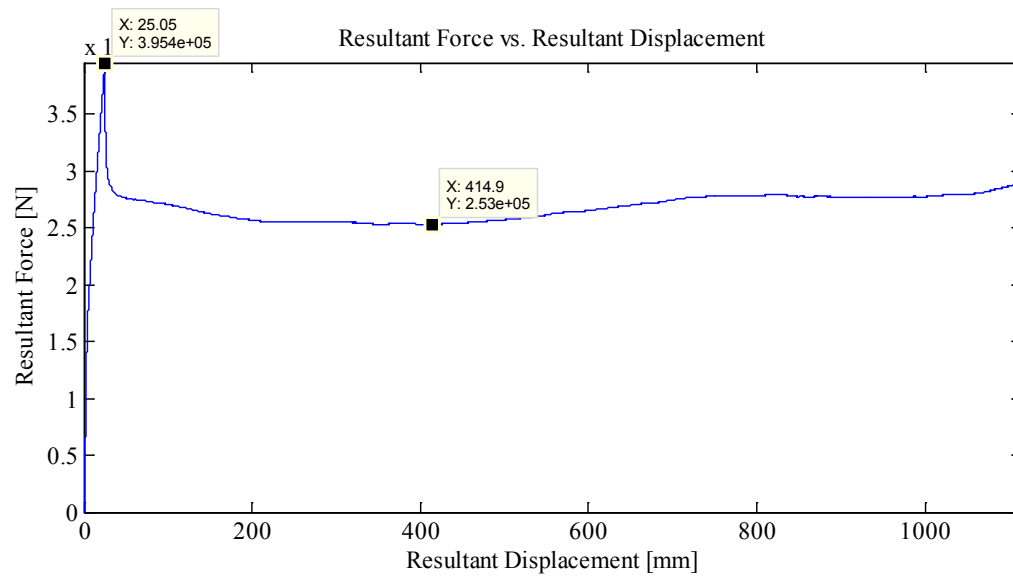
HDisp Offset: -613.3 mm

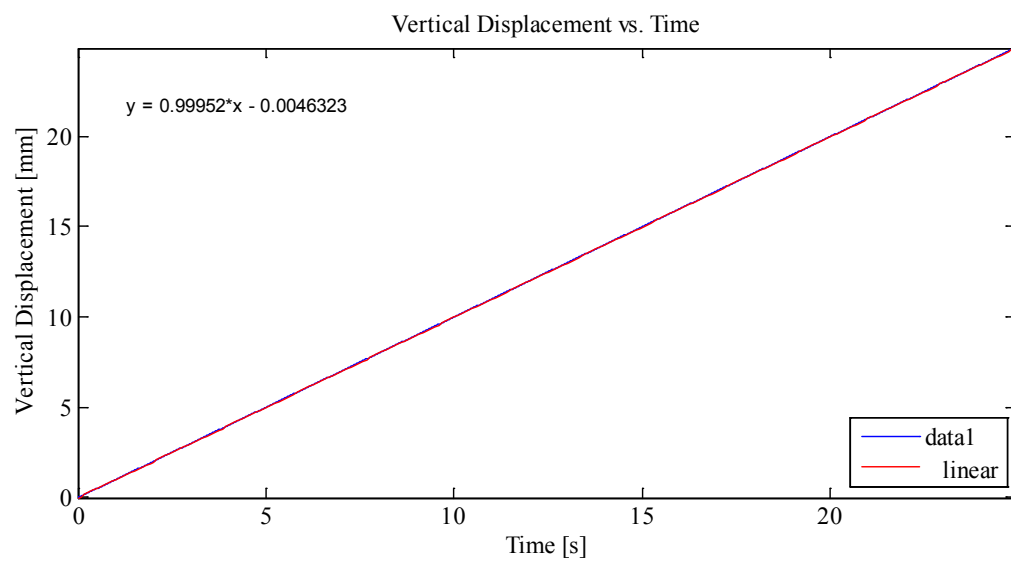
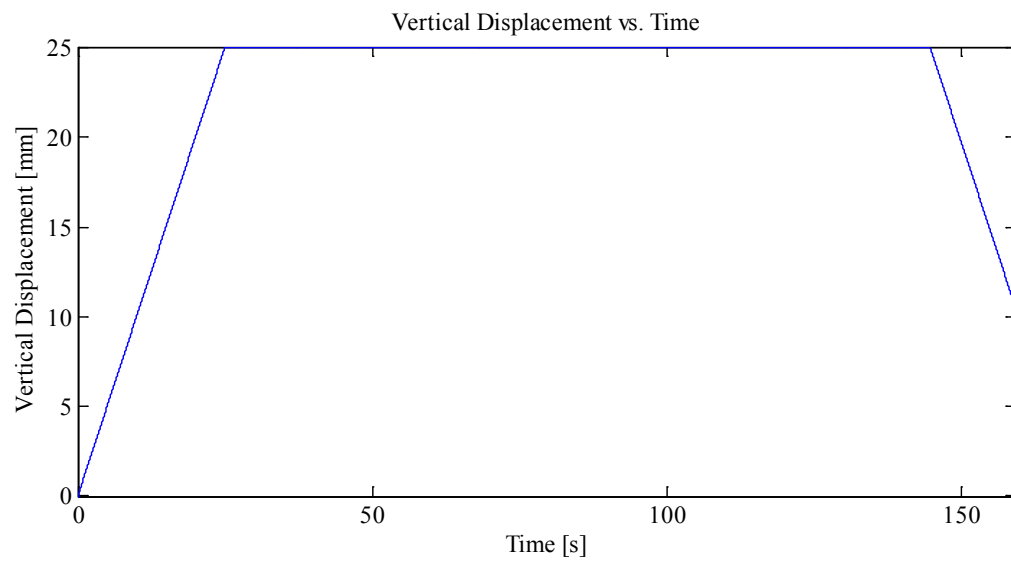
Indentation 1: ~25 mm, In-Along-Out - End to End

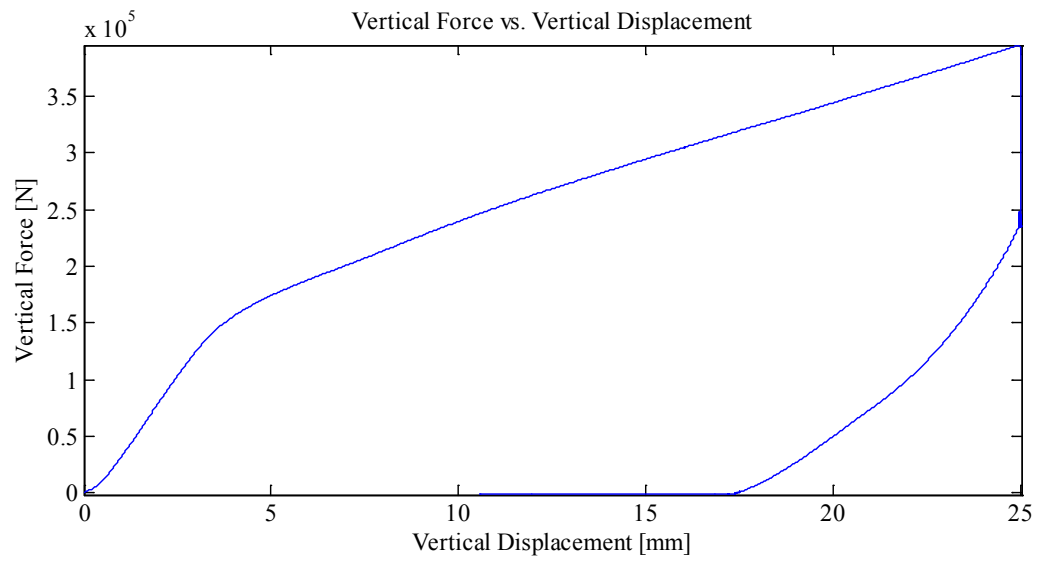
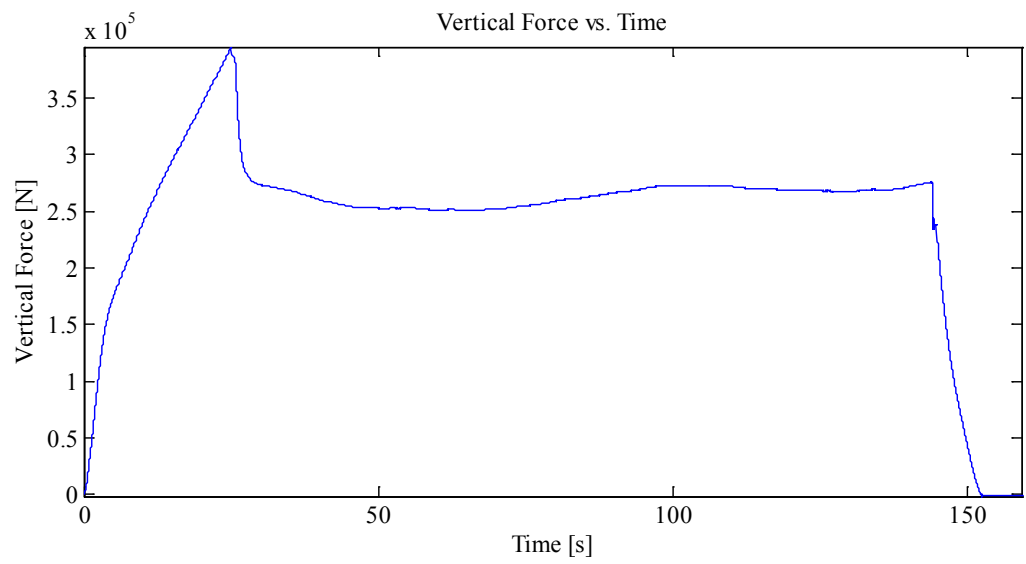
Data from Indentation 1 saved as MovingLoad16

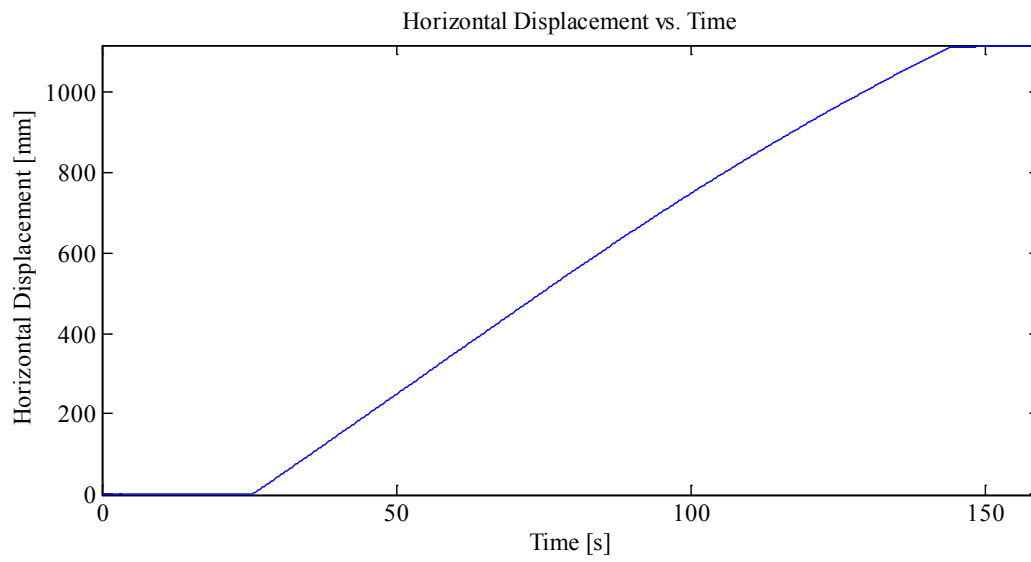
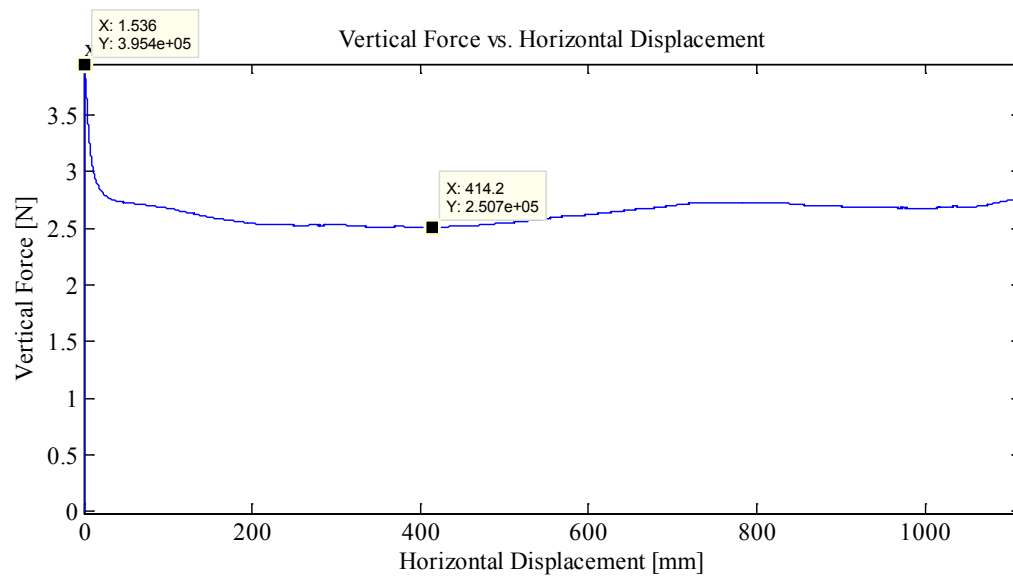
Plots:

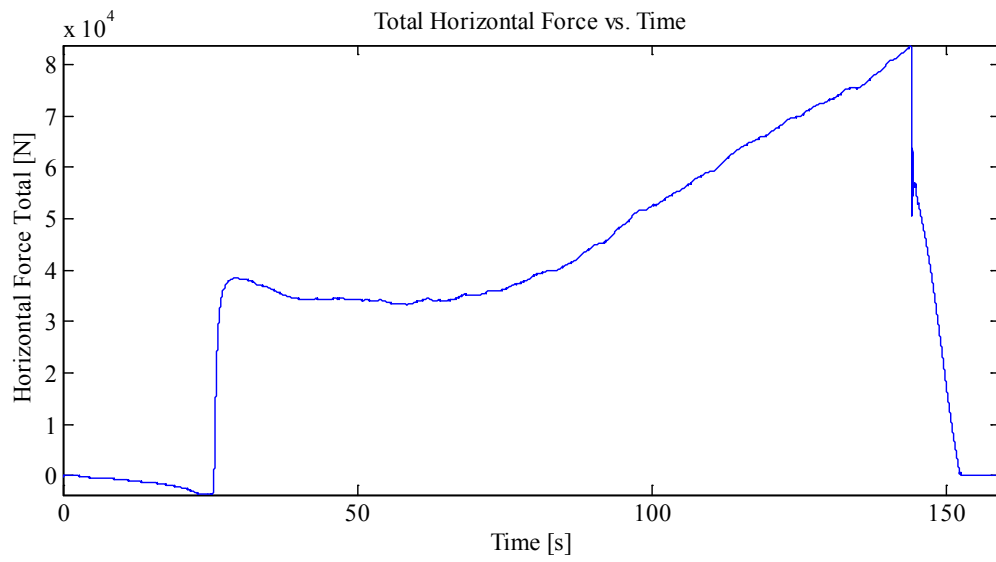
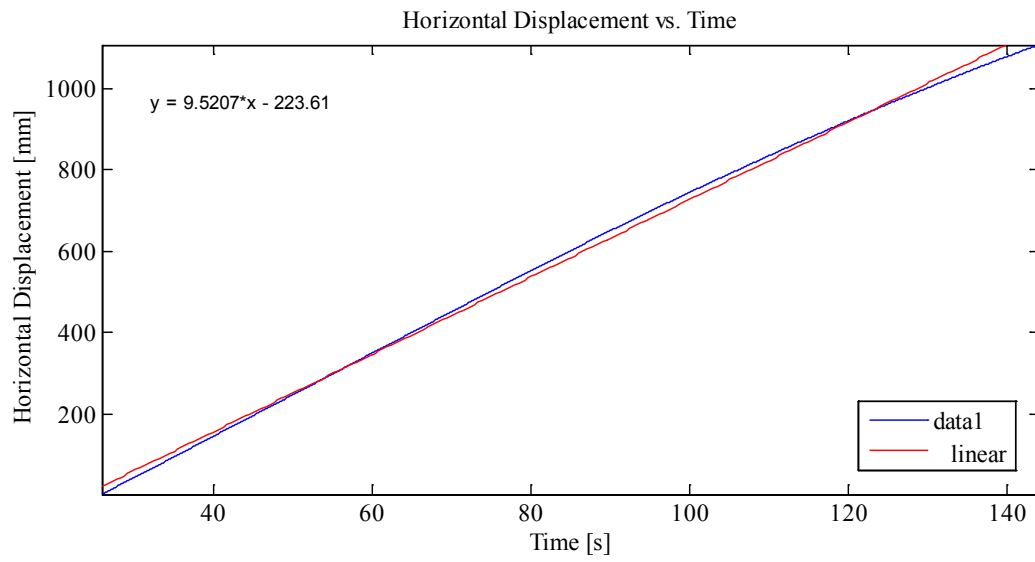


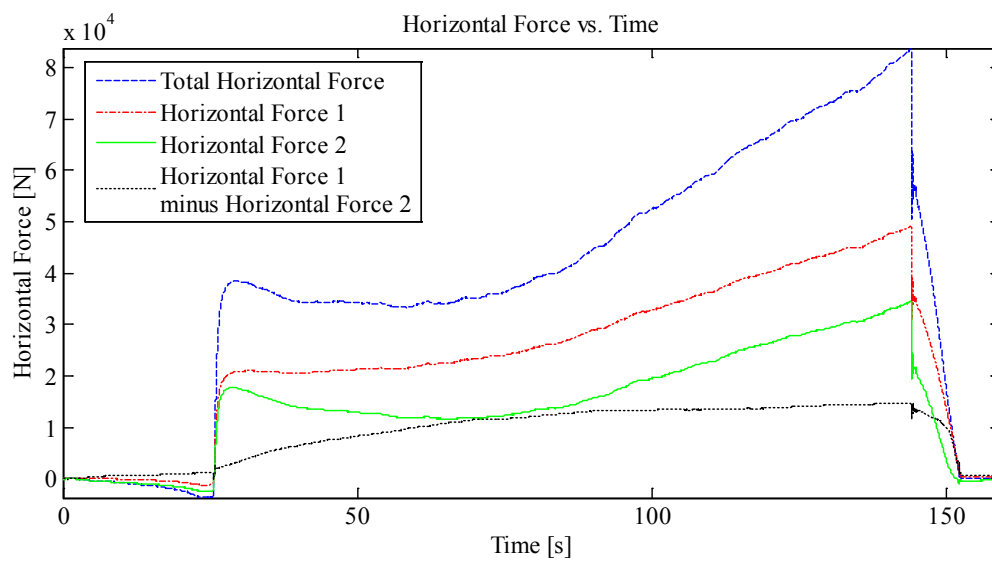
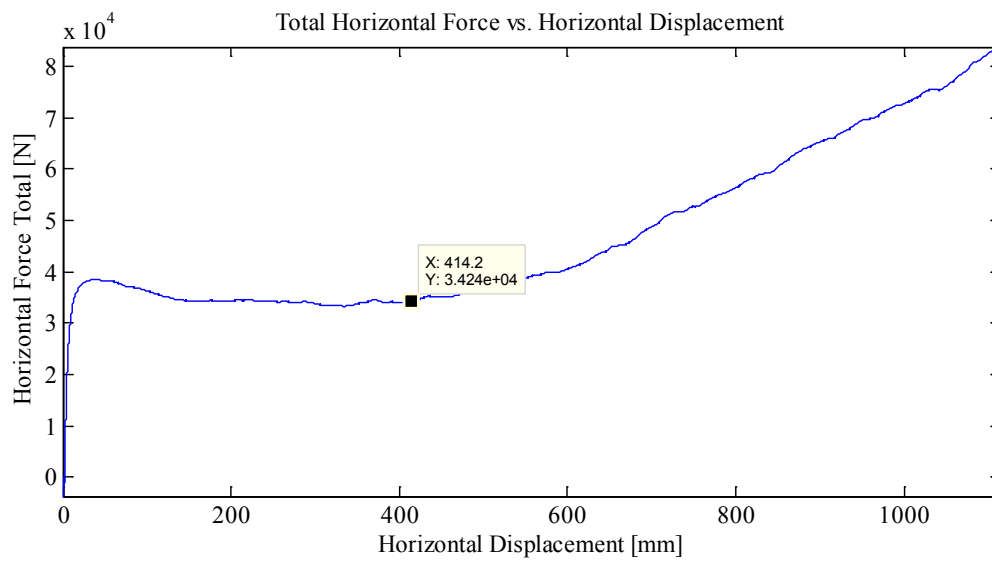










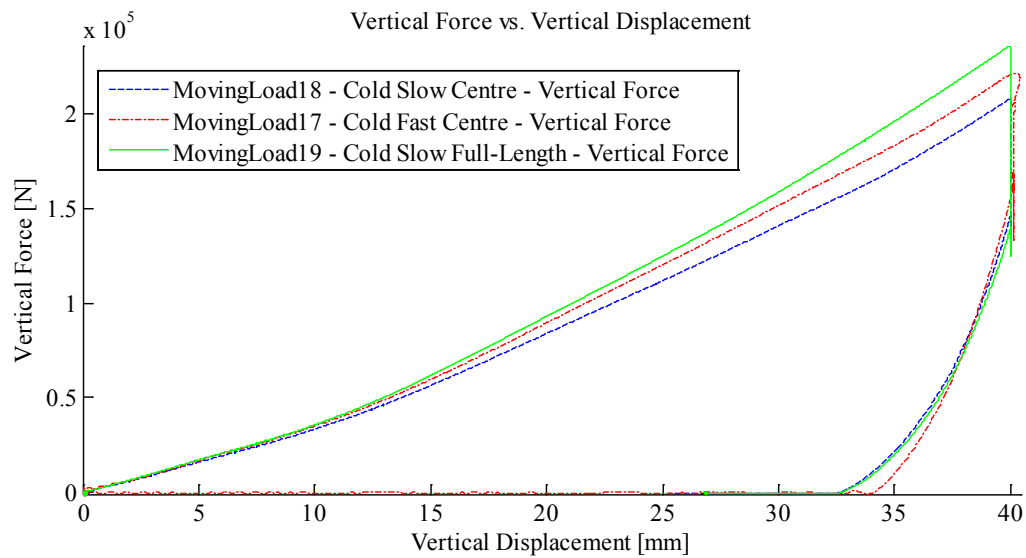
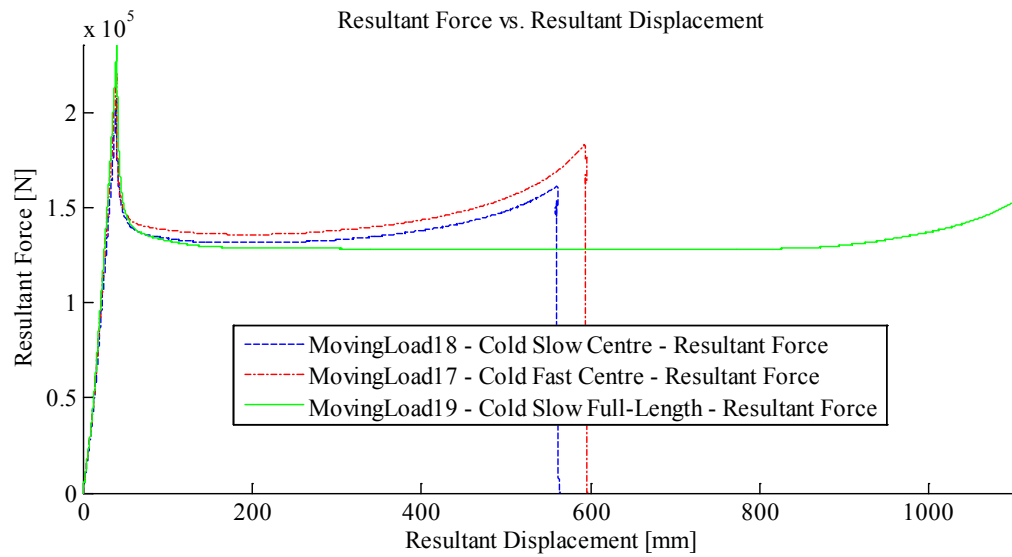


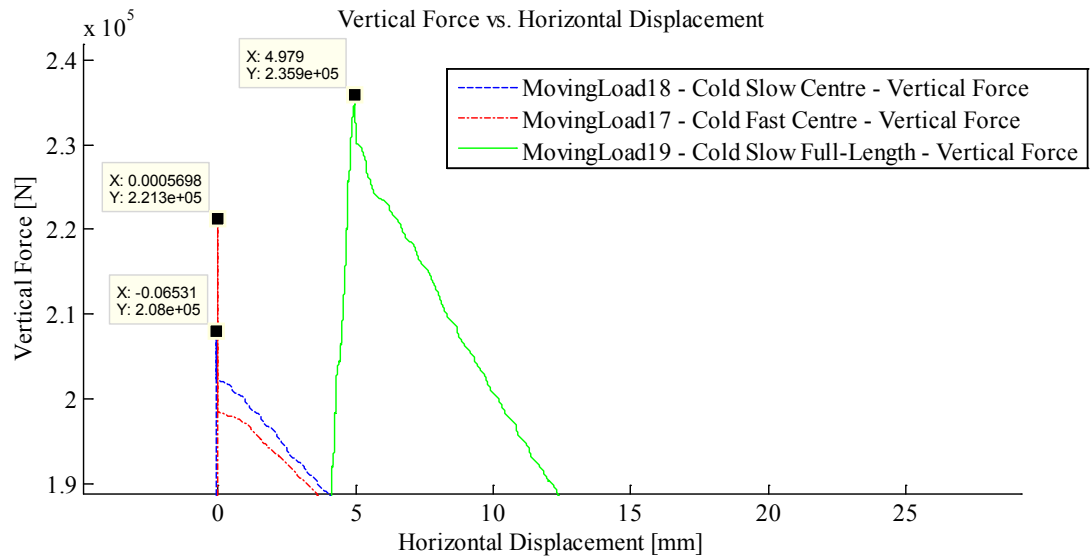
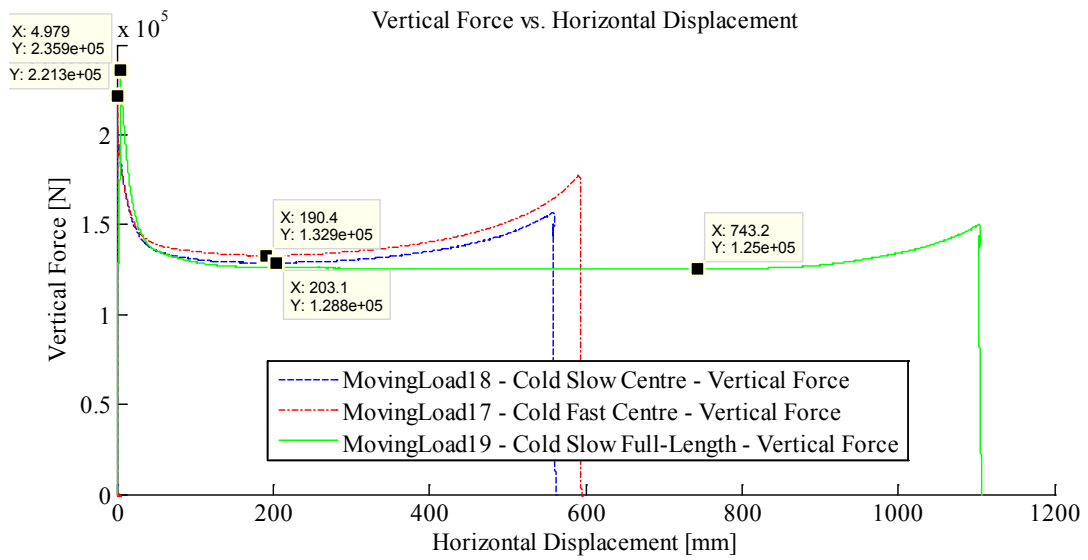
Appendix C2 – -10°C (14° F) Tests

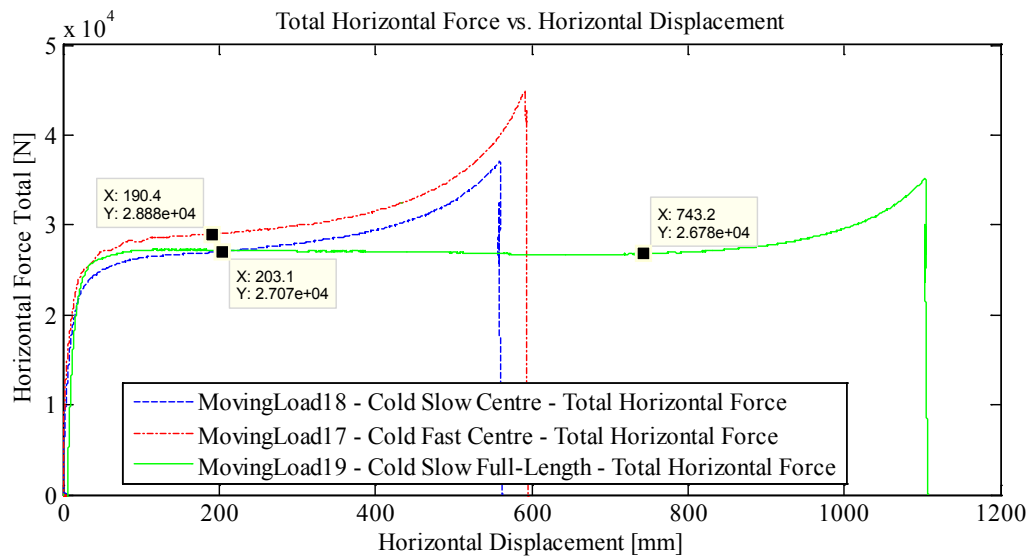
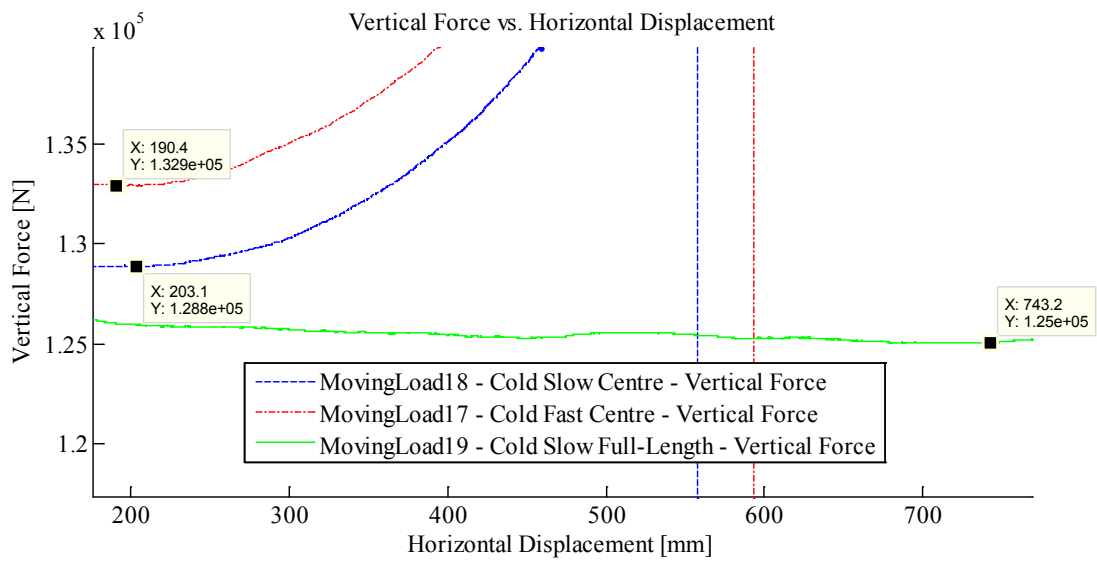
Appendix C2.1 – Quarter Inch Plate – 2 cm (0.787 in.) Indentation

Appendix C2.1.1 – Summary Plots for Experiments ML 17, 18 and 19

19







Appendix C2.1.2 – MovingLoad17

April 4, 2014 at ~4:25 p.m.

Run # 10
Run Type: Fast
Room-temperature: -10°C
Sample Type: 1/4" Plate
Test Type: In-Along-Out Centre to End

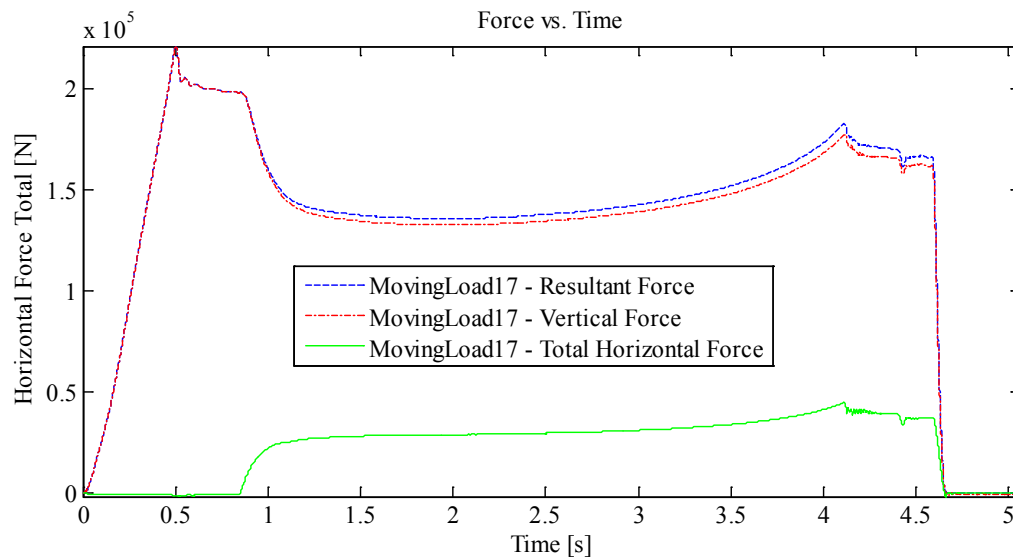
HStarting Point: Centre (0 cm nominal)
HSpeed: Fastest mm/s (Nominal)
H Travel: Centre to End (55+ cm)

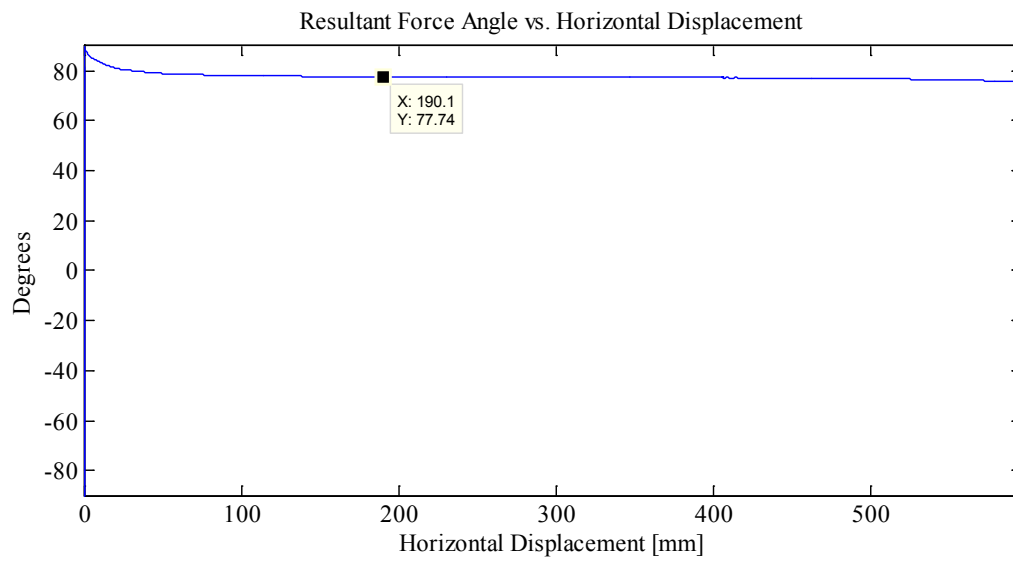
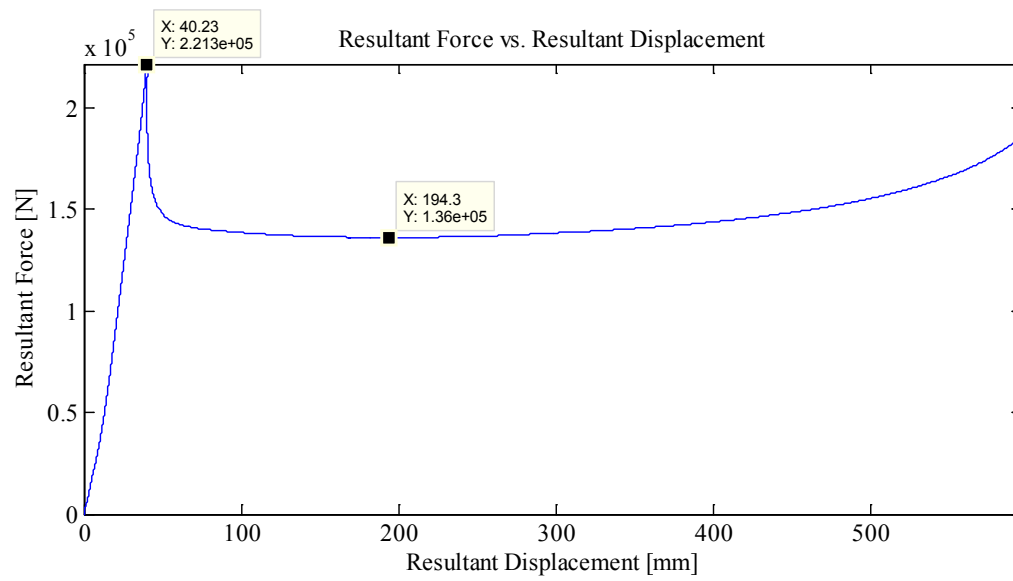
Vstarting Point: 2.25 mm
VSpeed: 100.0 mm/s (nominal)
V Travel: 40 mm
V Stopping Point: -37.75 mm

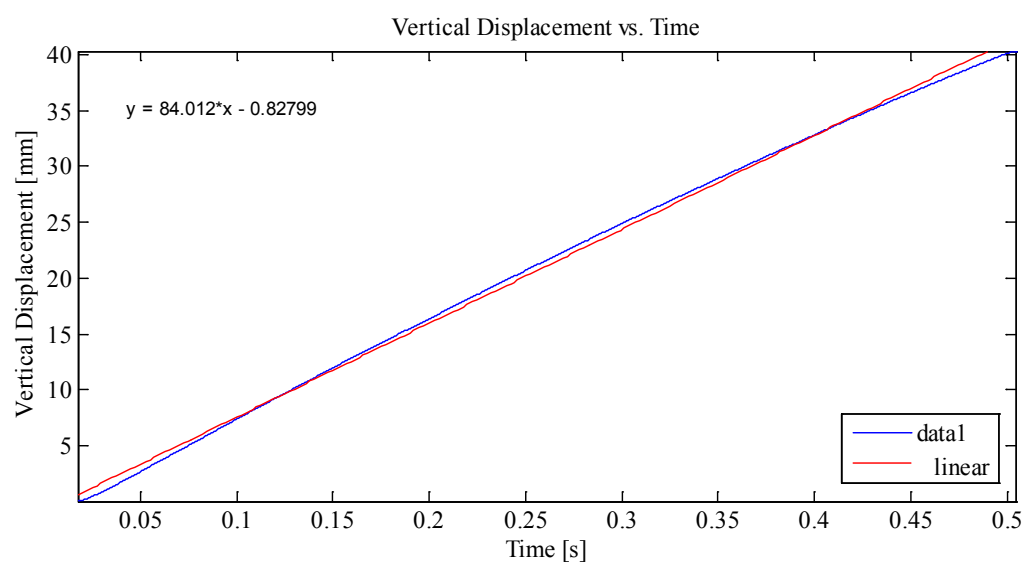
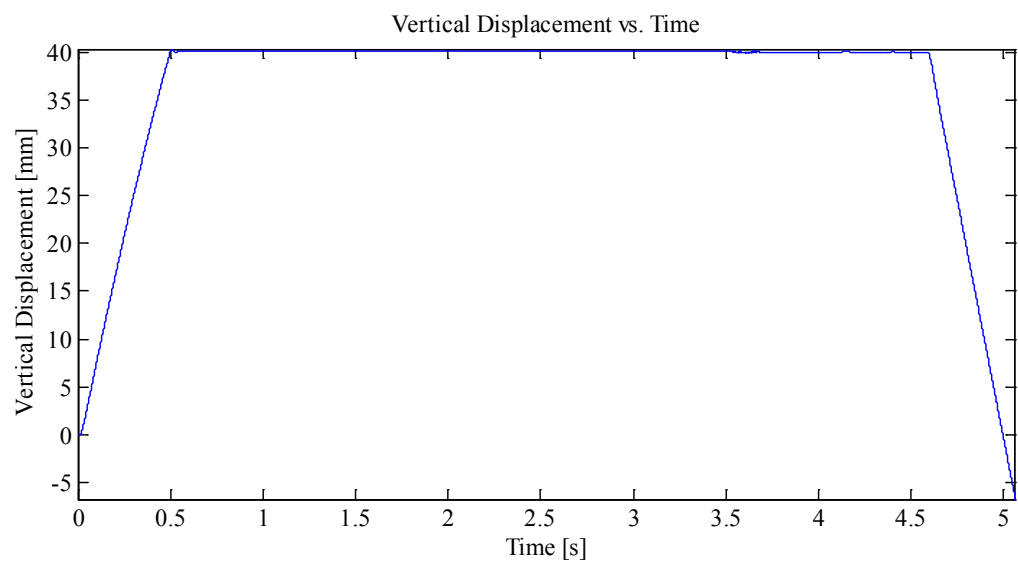
Notes:

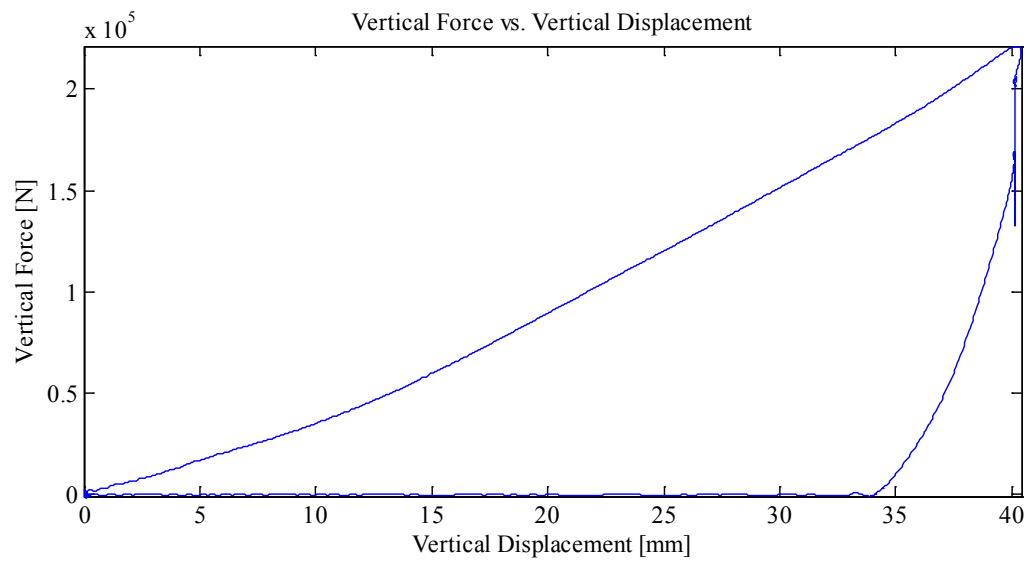
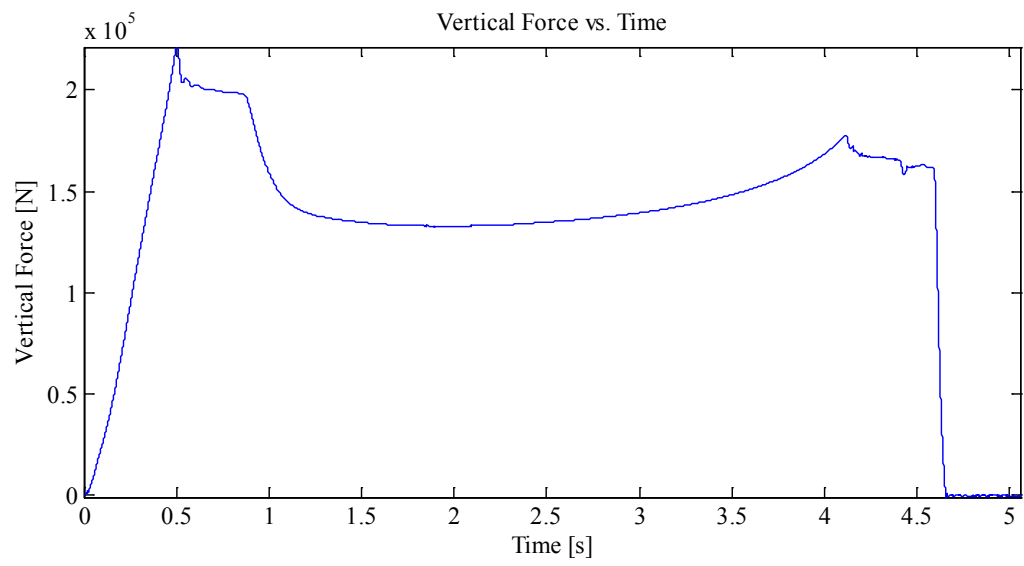
Indentation 1: ~40 mm, In-Along-Out - Centre to End
Data from Indentation 1 saved as MovingLoad17

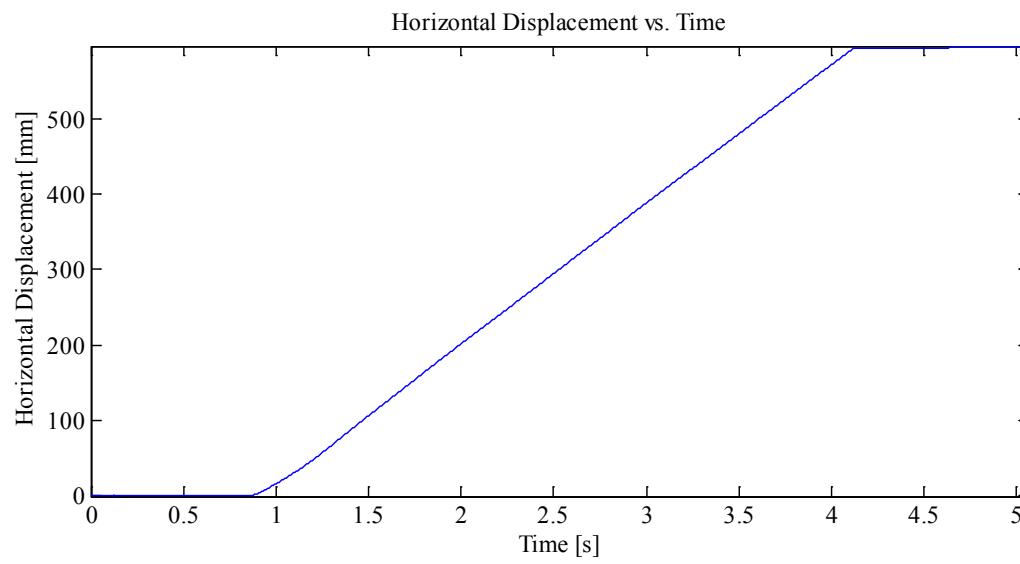
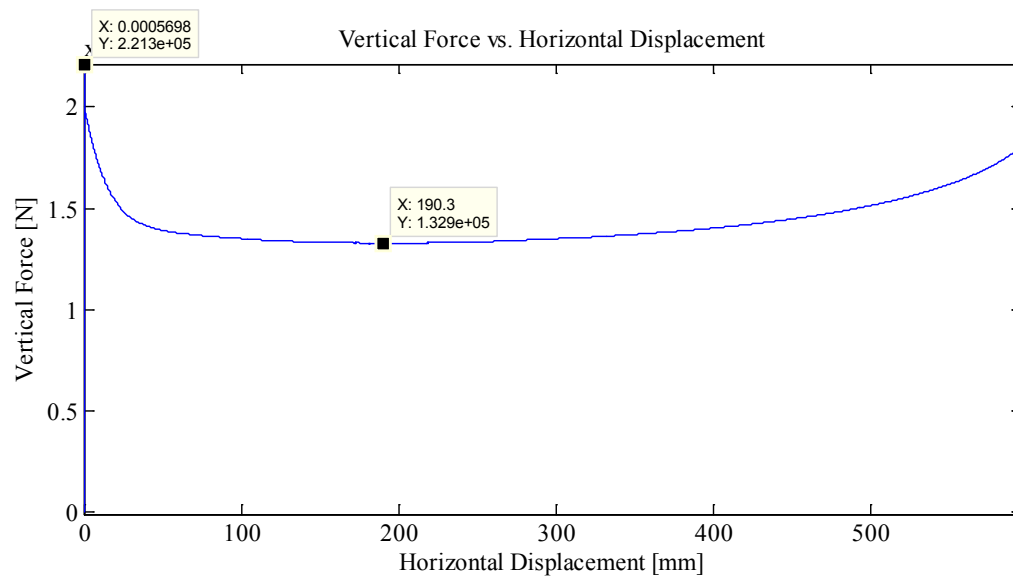
Plots:

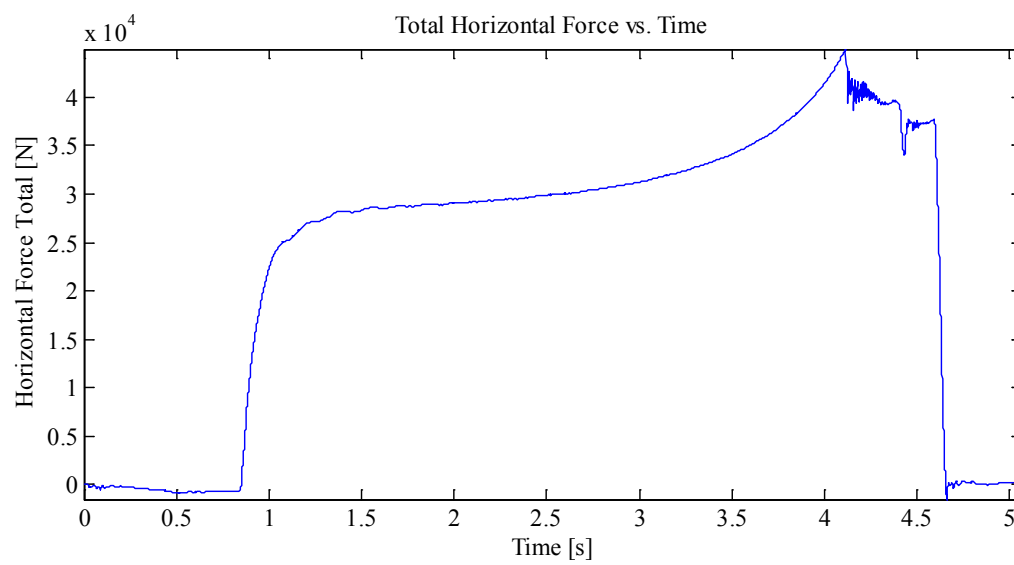
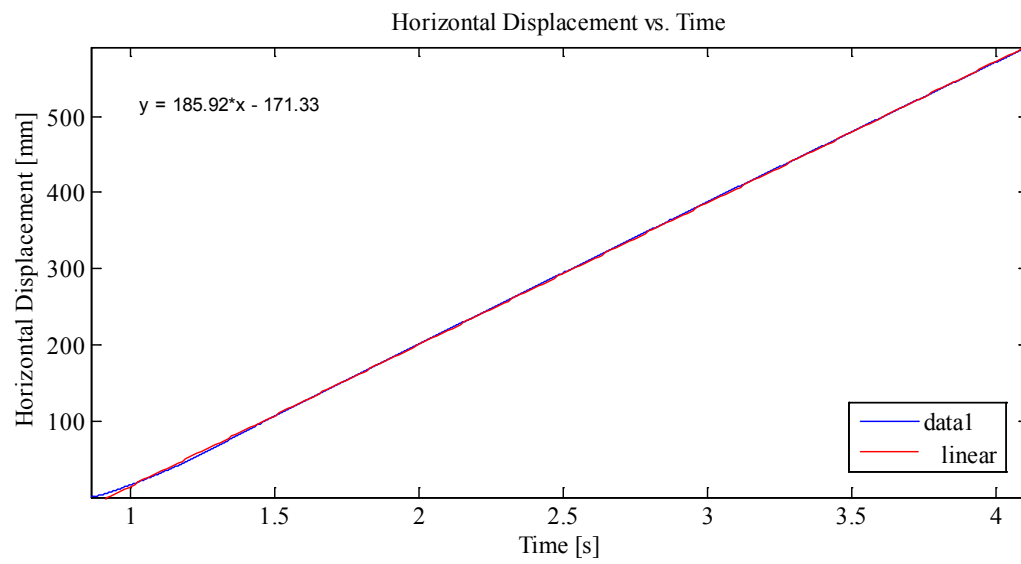


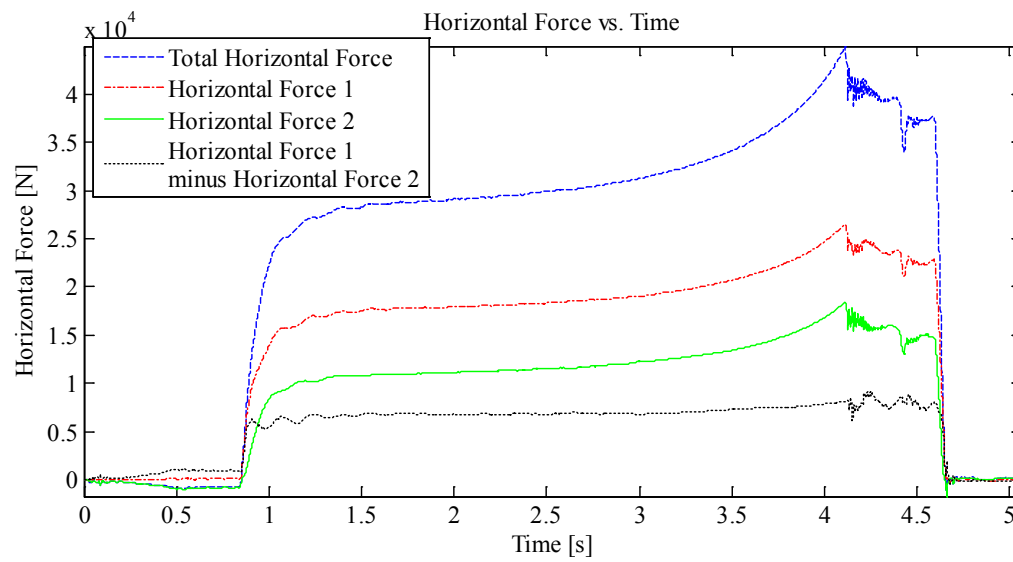
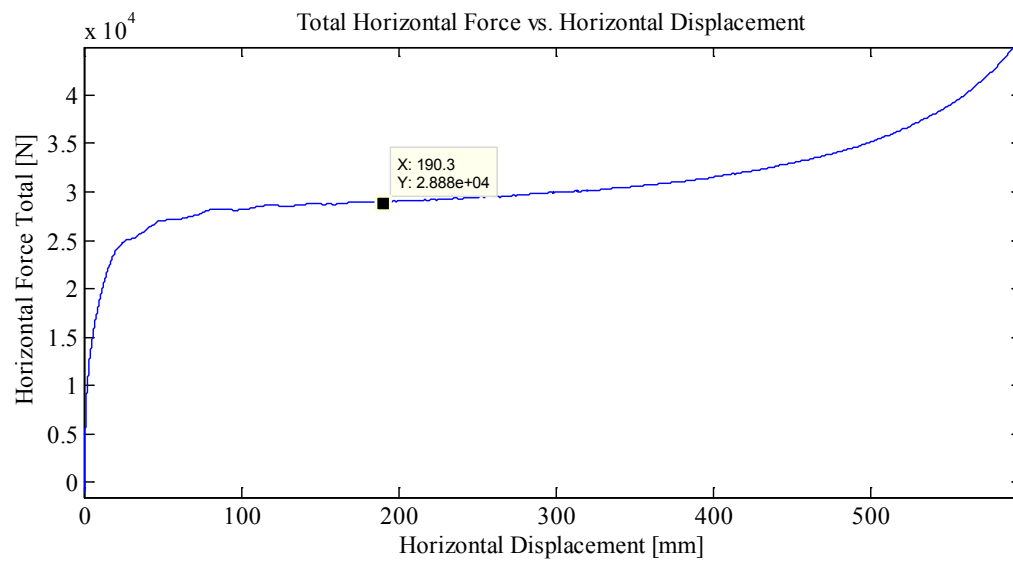












Appendix C2.1.3 – MovingLoad18

April 7, 2014 at 3:50 p.m.

Run # 11
Run Type: Slow
Room-temperature: -10°C
Sample Type: 1/4" Plate
Test Type: In-Along-Out Centre to End

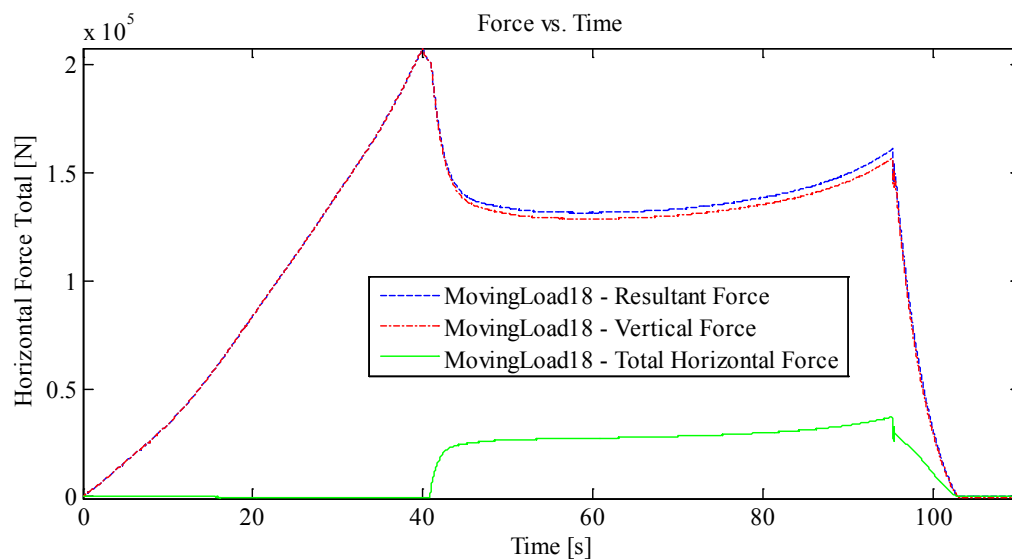
HStarting Point: Centre (+.50 cm (0 cm nominal))
HOffset(from -613.3 mm): 0.41 cm
HSpeed: ~11 mm/s (Nominal)
H Travel: Centre to End (55+ cm)

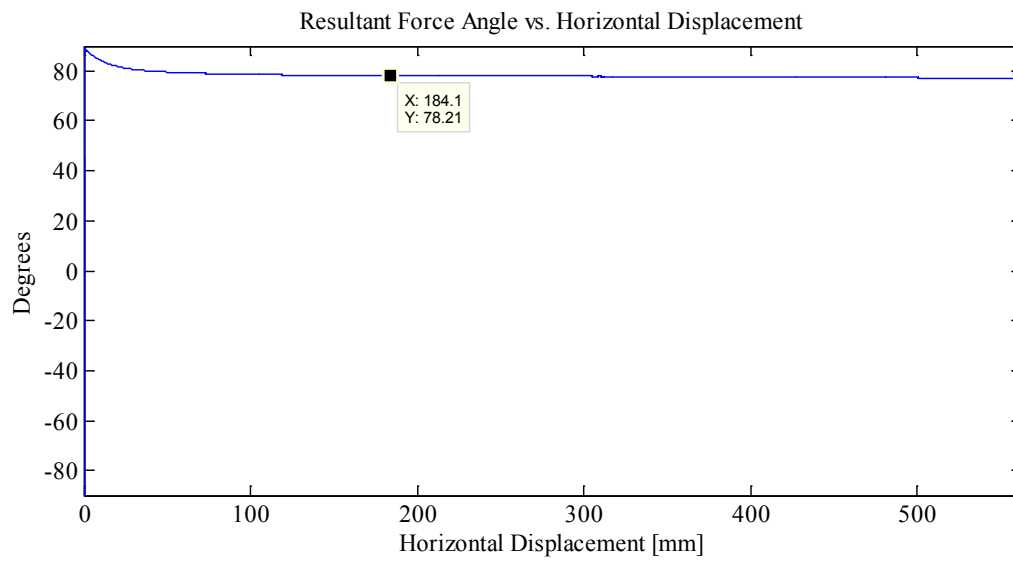
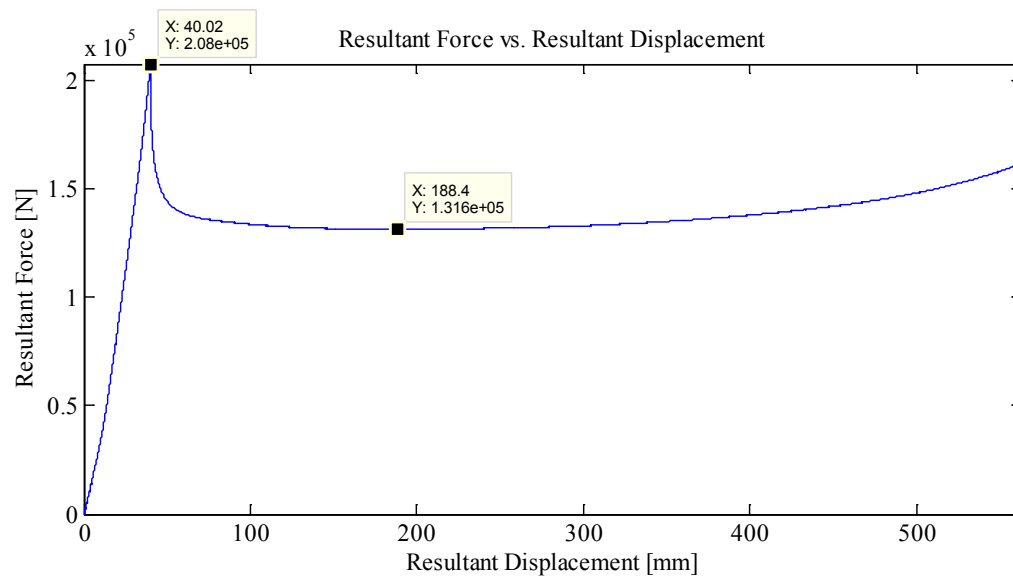
Vstarting Point: 2.40 mm
VSpeed: 1.0 mm/s (nominal)
V Travel: 40 mm
V Stopping Point: -37.6 mm

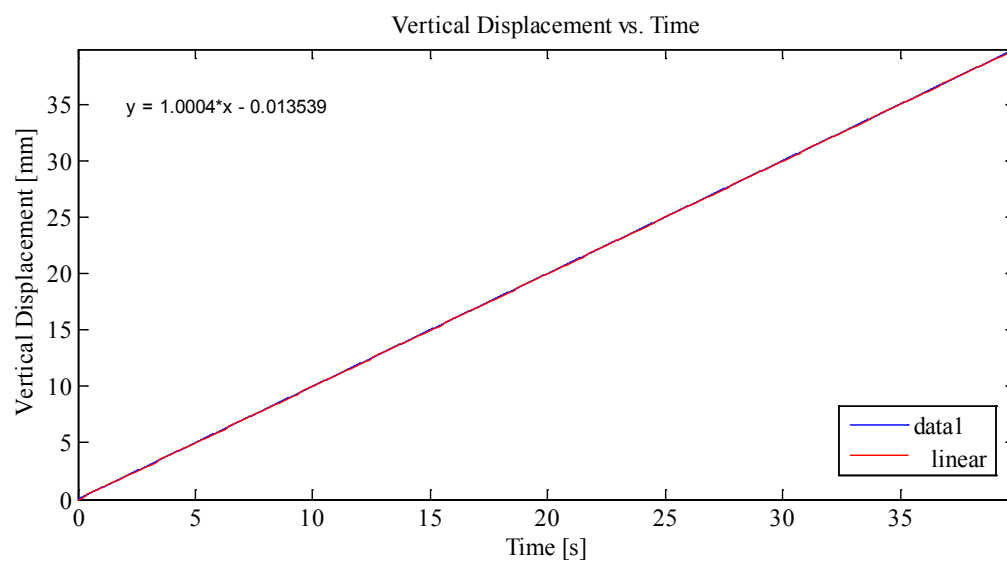
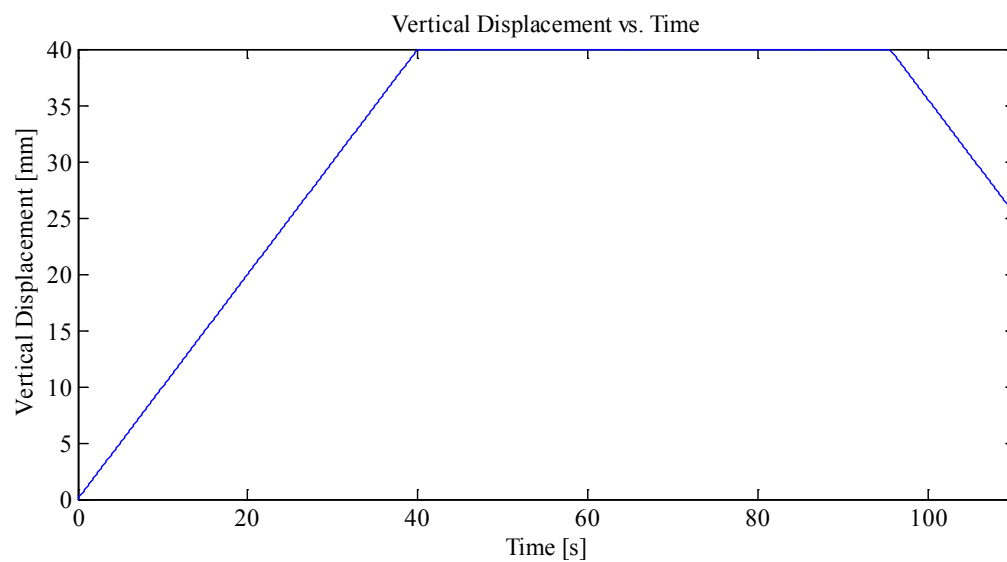
Notes:

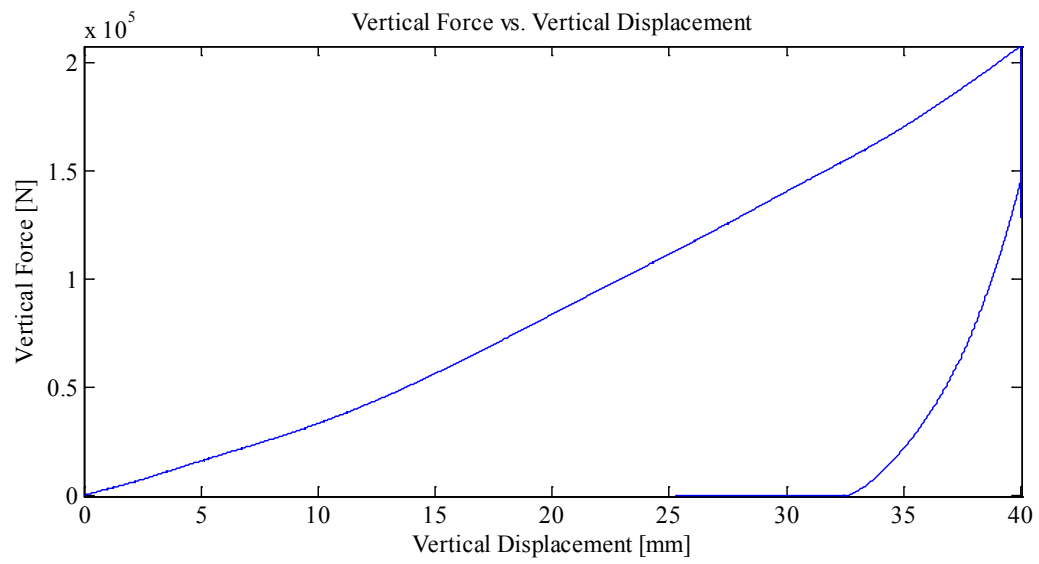
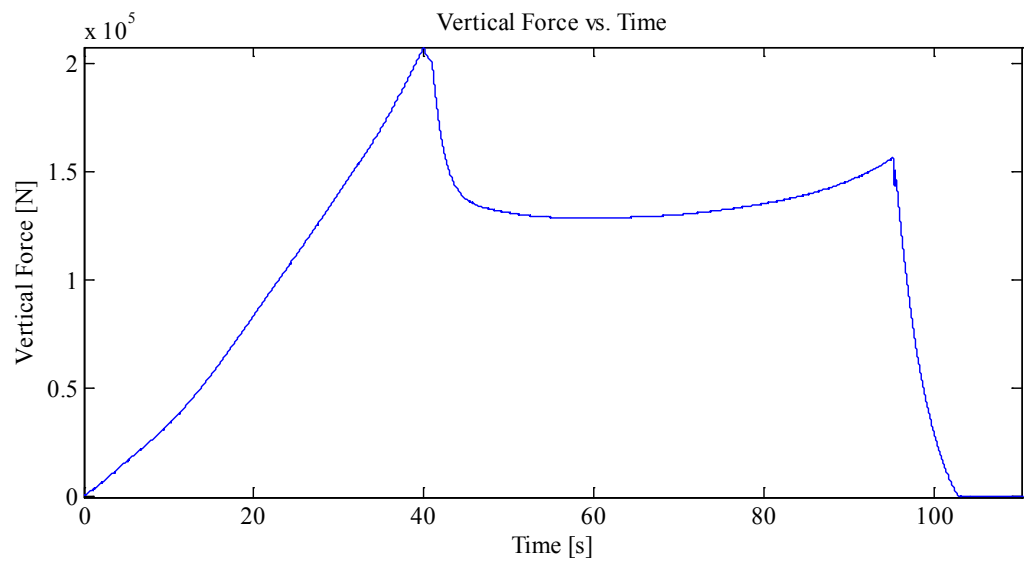
Indentation 1: ~40 mm, In-Along-Out - Centre to End
Data from Indentation 1 saved as MovingLoad18

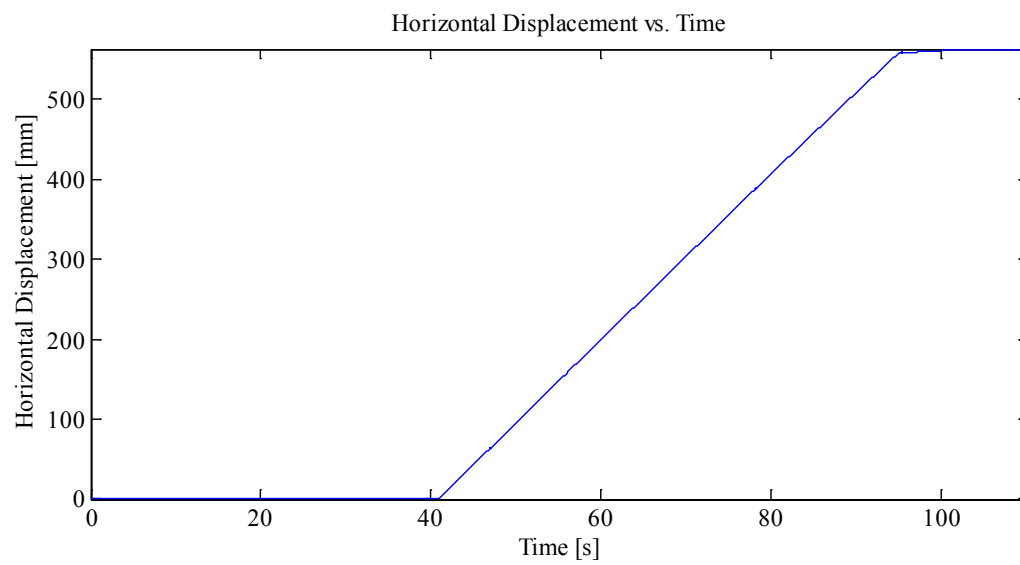
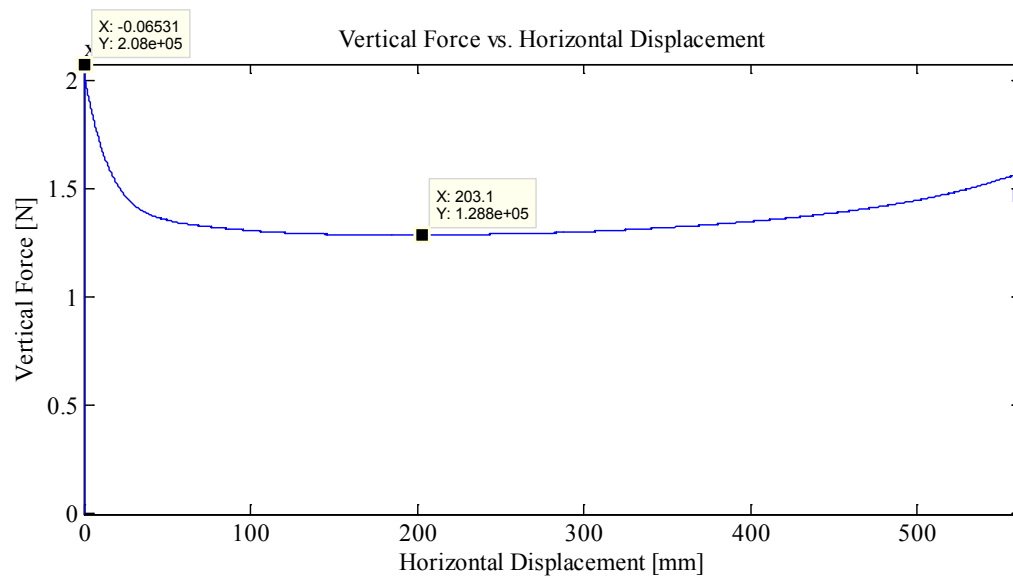
Plots:

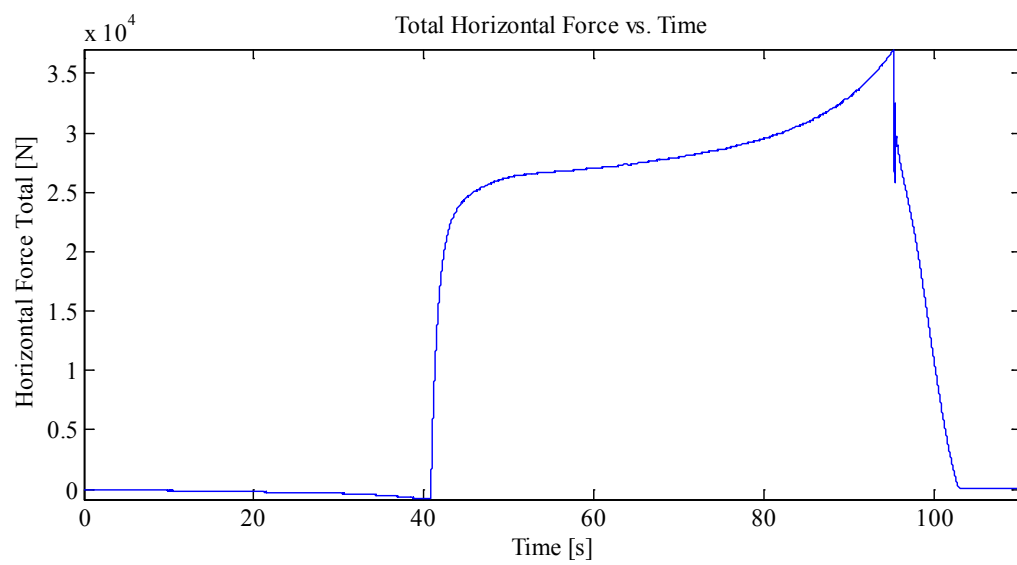
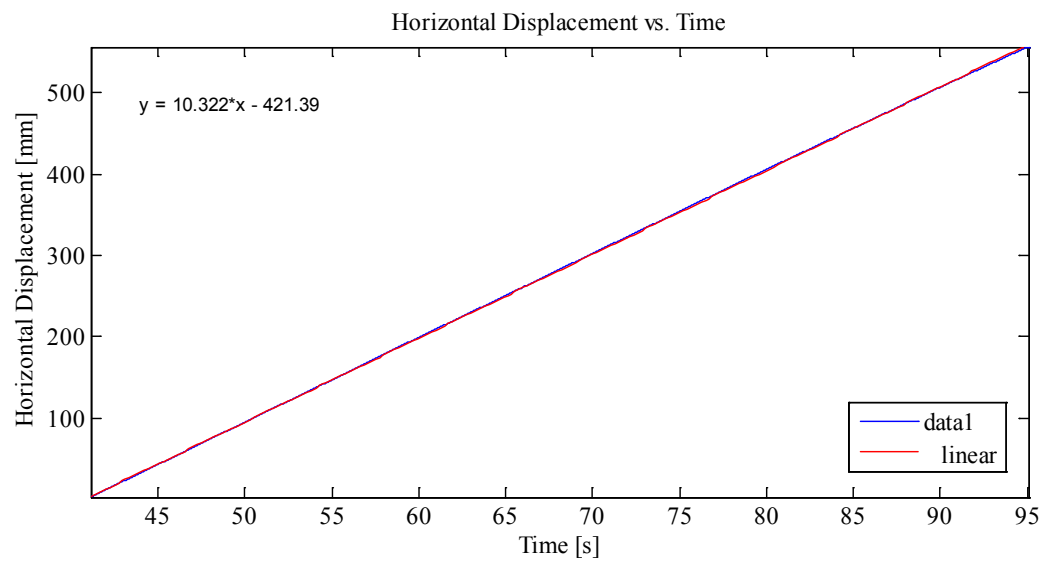


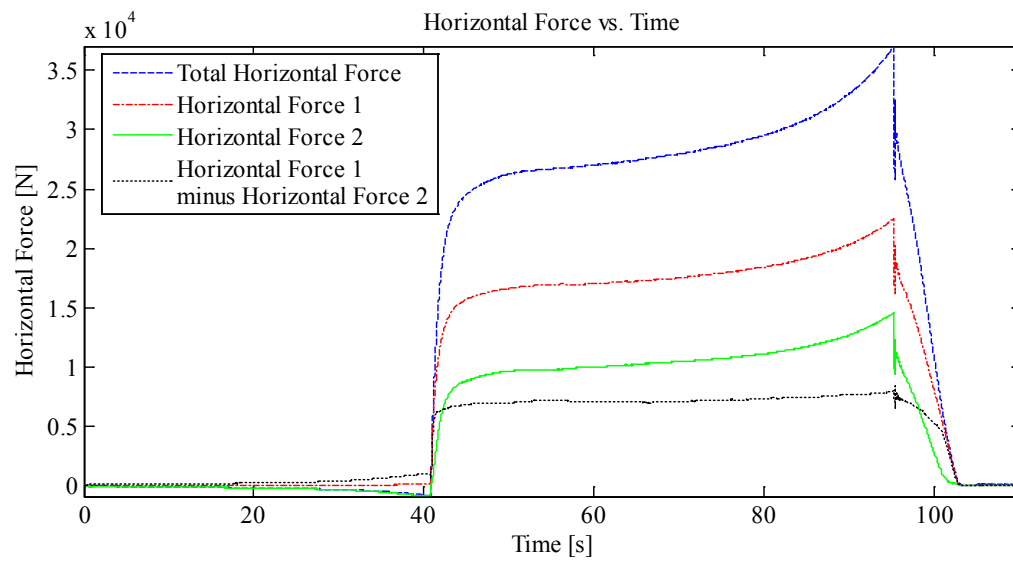
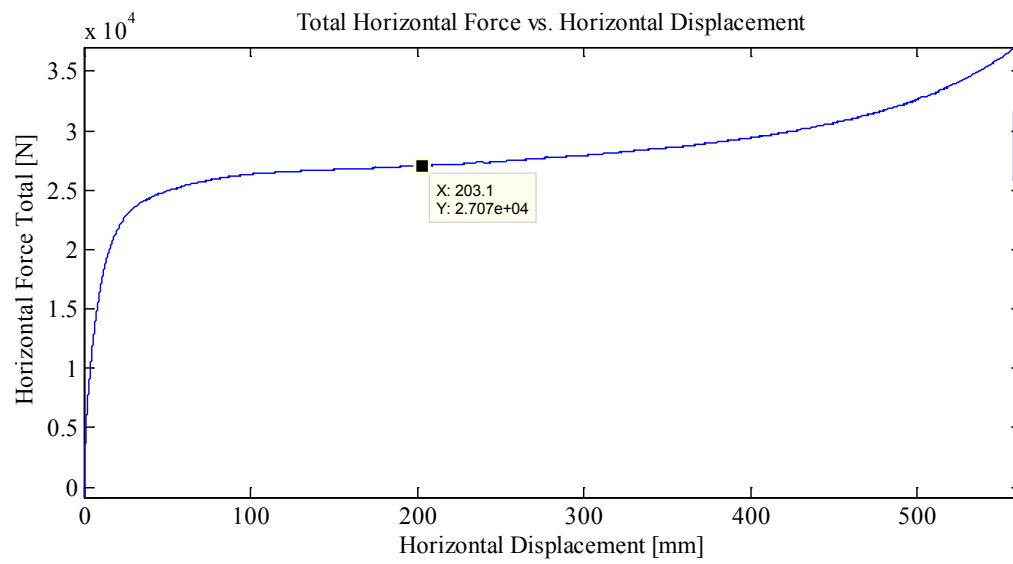












Appendix C2.1.4 – MovingLoad19

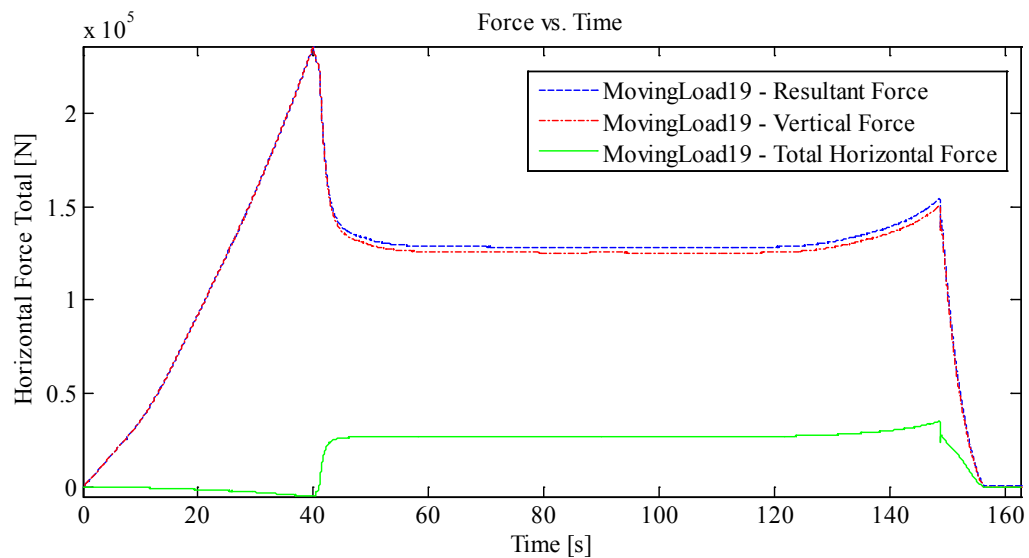
April 8, 2014 at ~3:00 p.m.

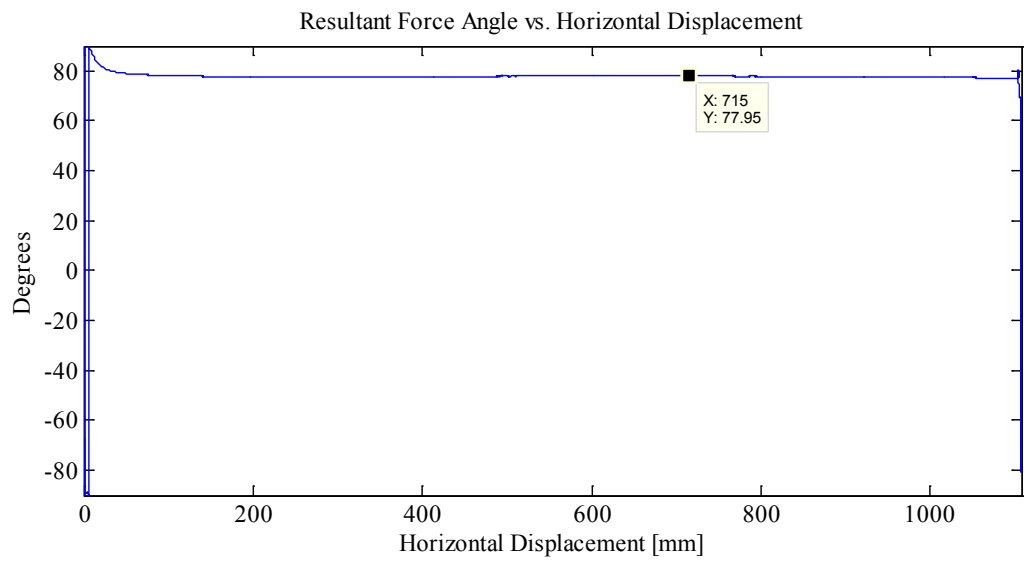
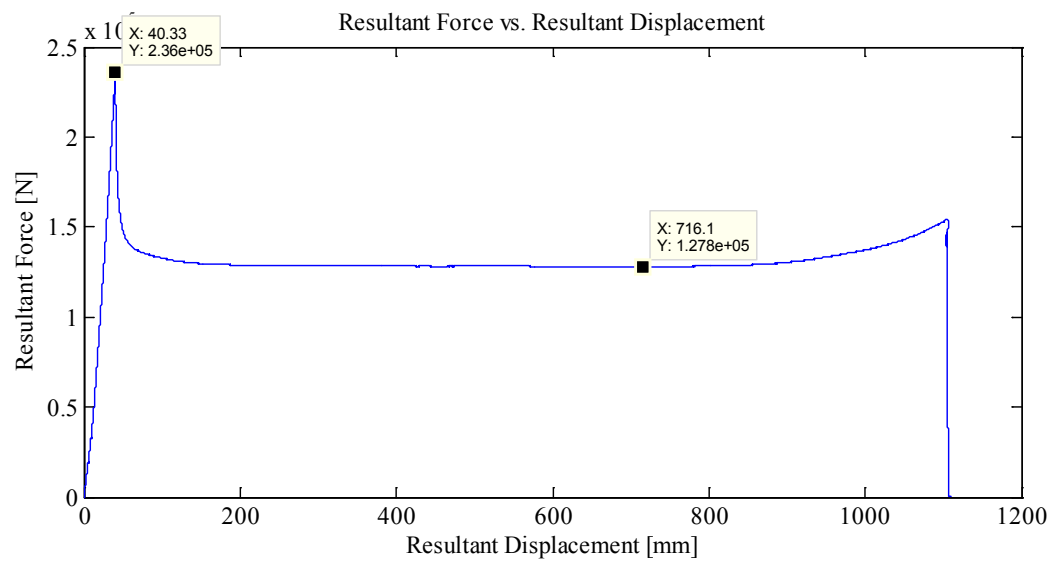
Run #	12
Run Type:	Full Length – Slow
Room-temperature:	-10°C
Sample Type:	1/4" Plate
Test Type:	In-Along-Out End to End
HStarting Point:	End (-54.19 cm (-55 cm nominal))
HSpeed:	~10 mm/s (Nominal)
H Travel:	End to End (110+ cm)
Vstarting Point:	3.15 mm
VSPEED:	1.0 mm/s (nominal)
V Travel:	40 mm
V Stopping Point:	-36.85 mm

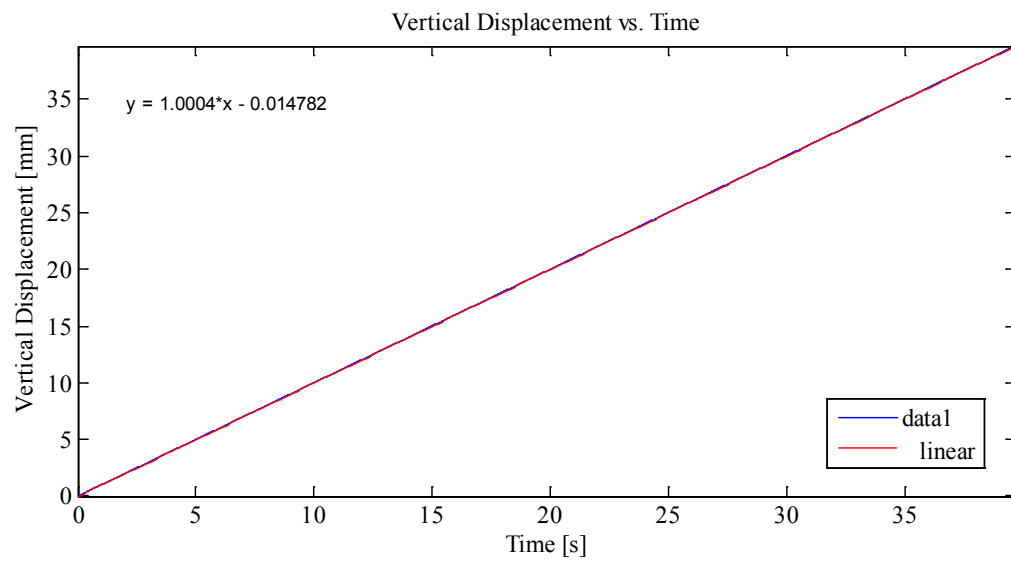
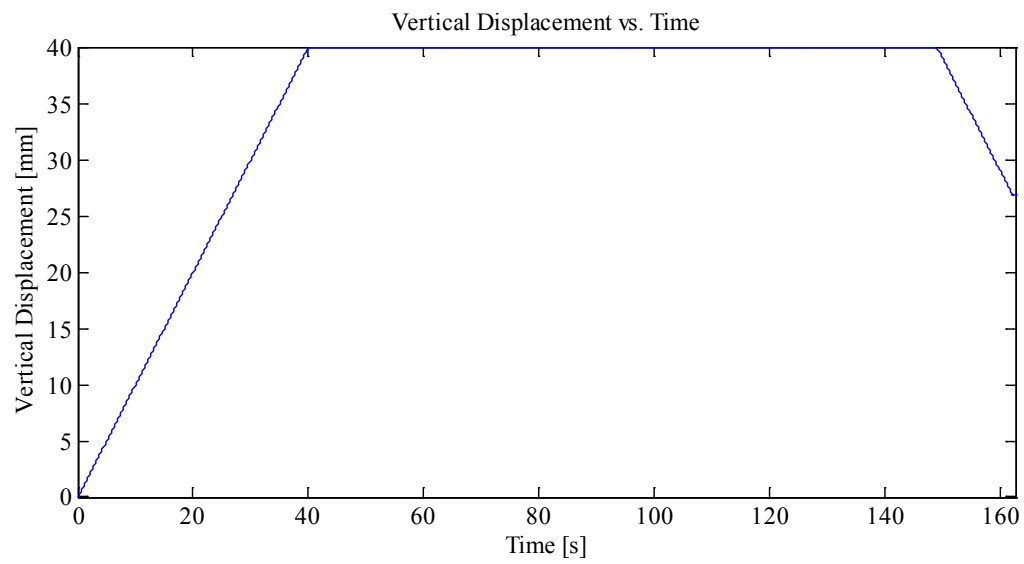
Notes:

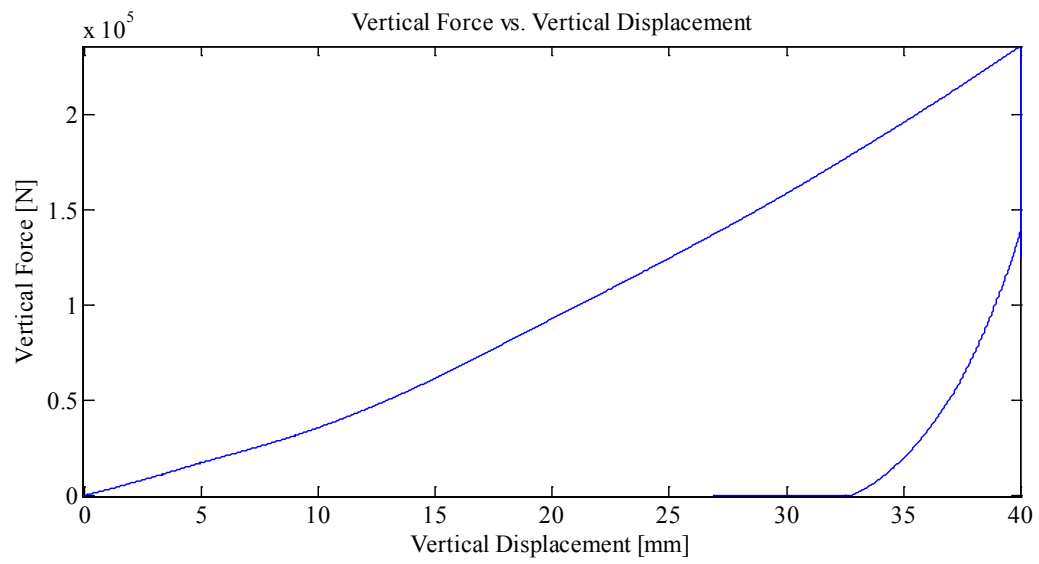
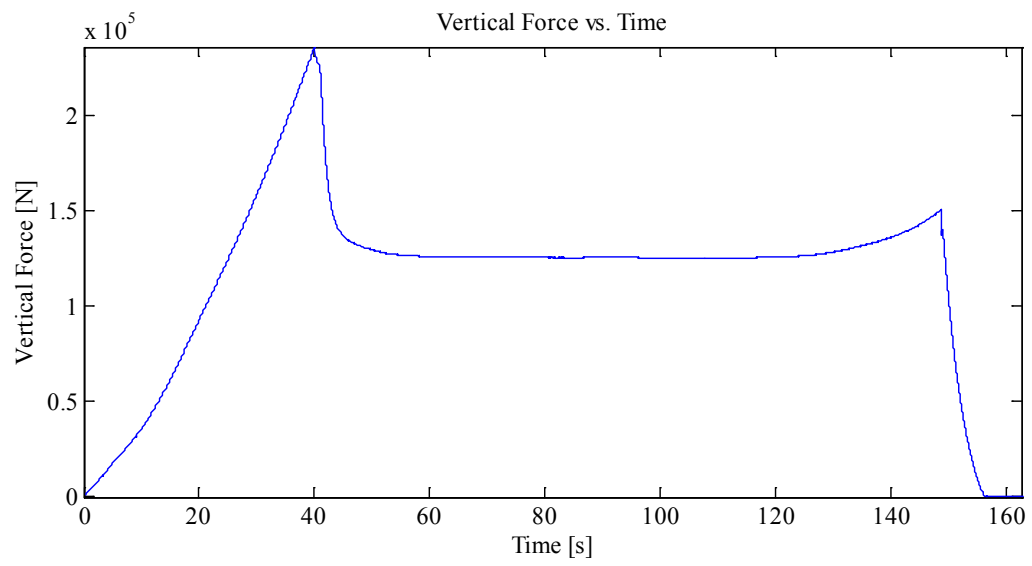
Indentation 1: ~40 mm, In-Along-Out - End to End
Data from Indentation 1 saved as MovingLoad19

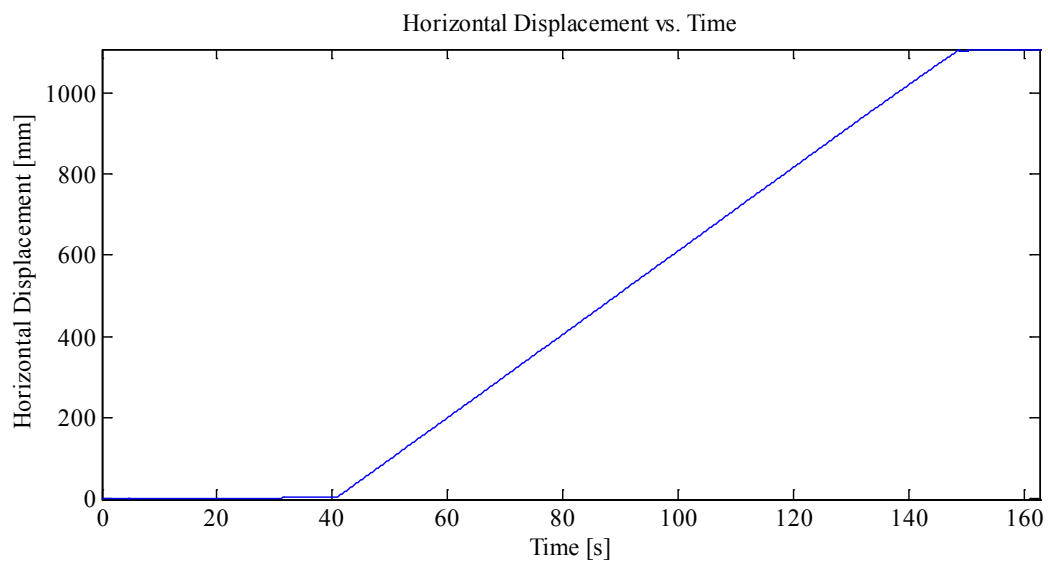
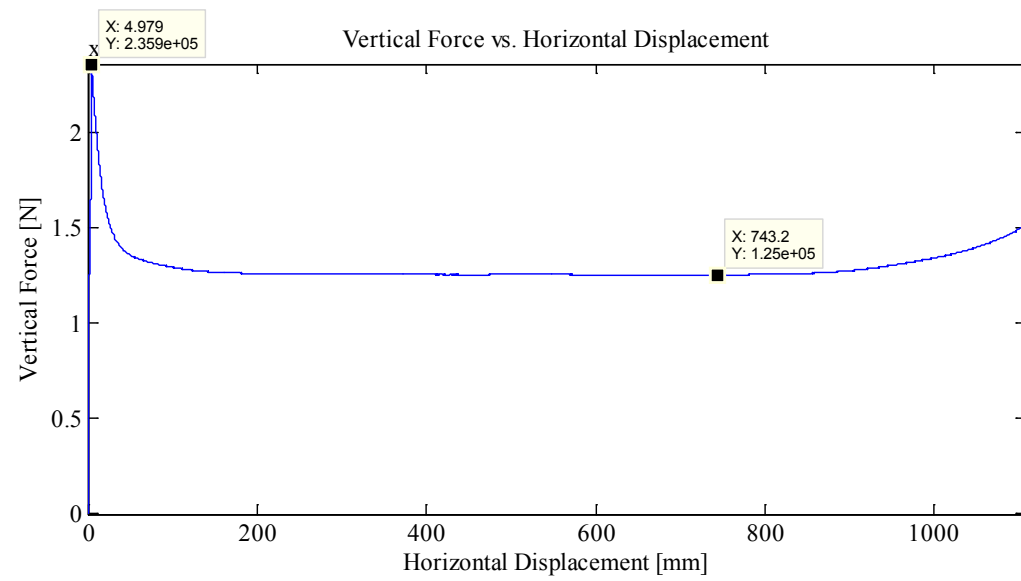
Plots:

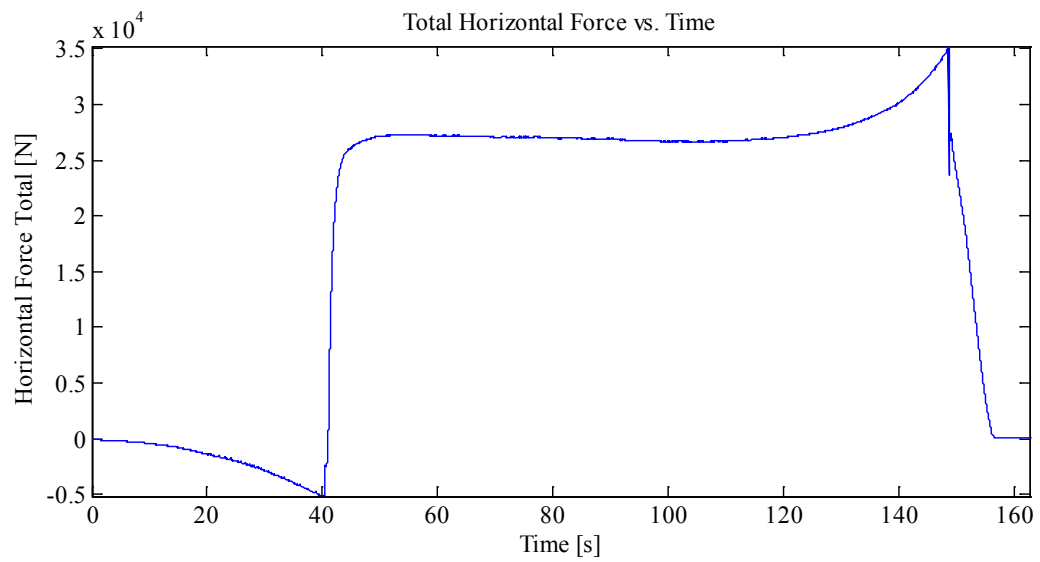
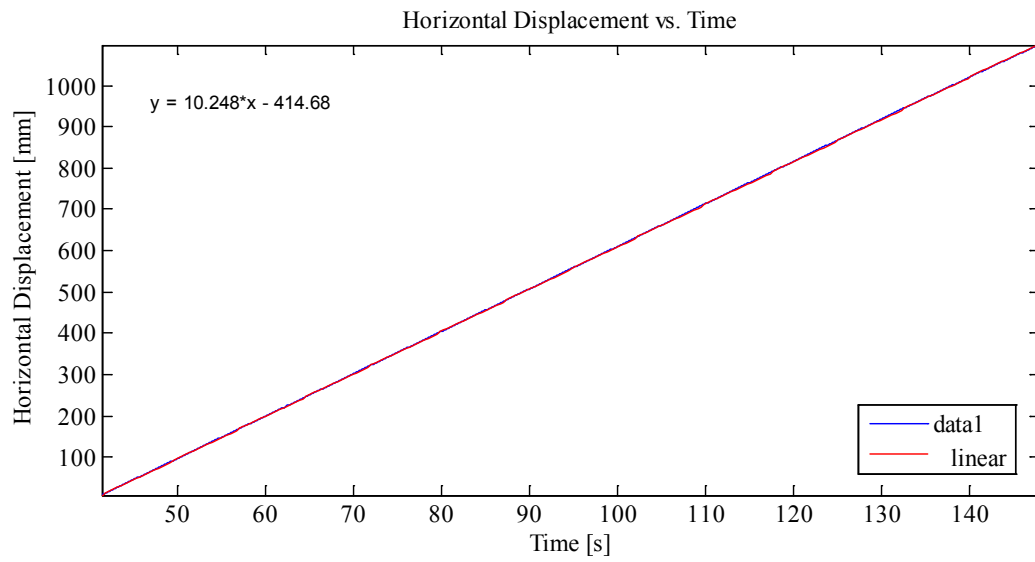


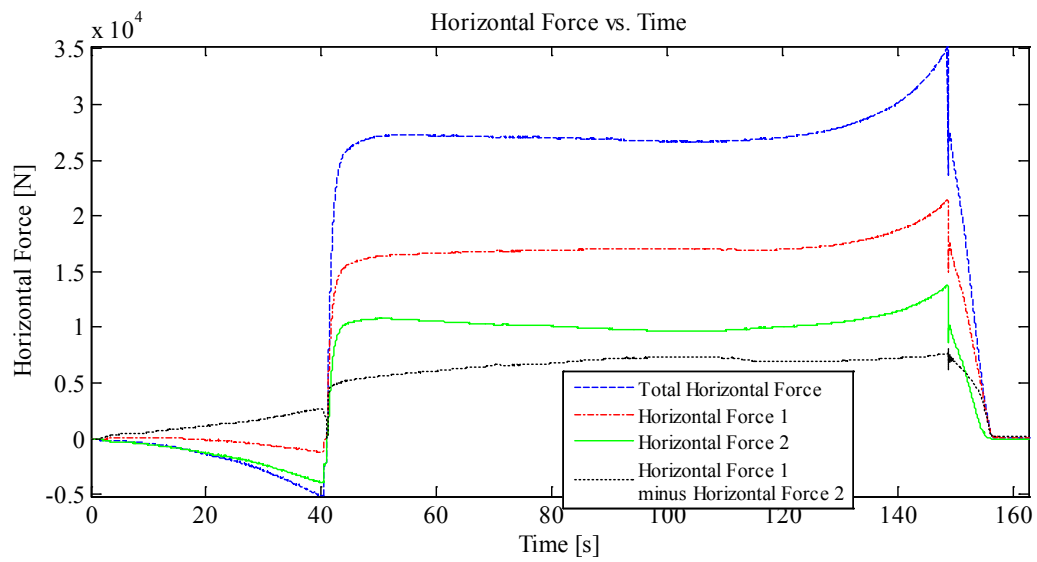
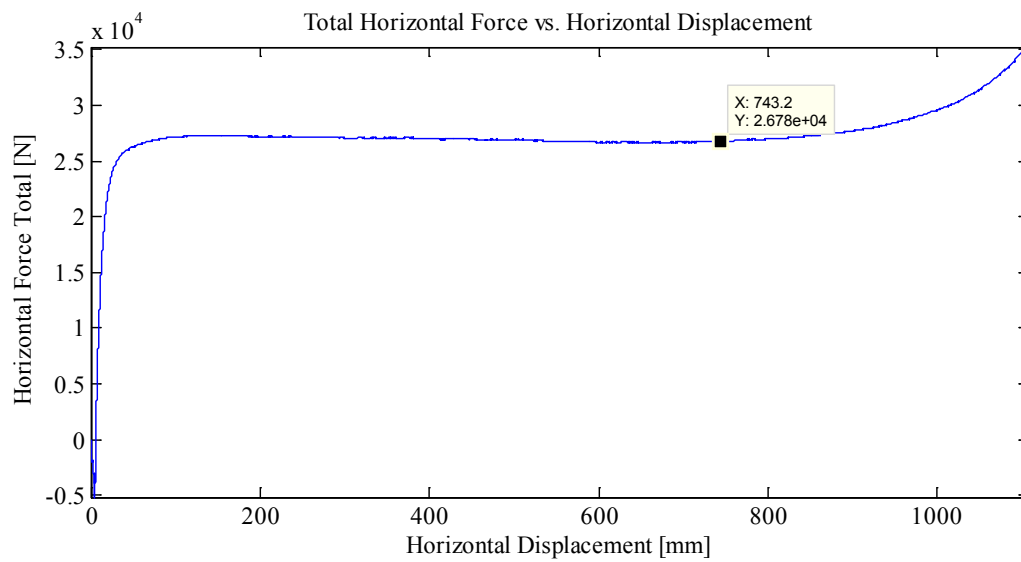








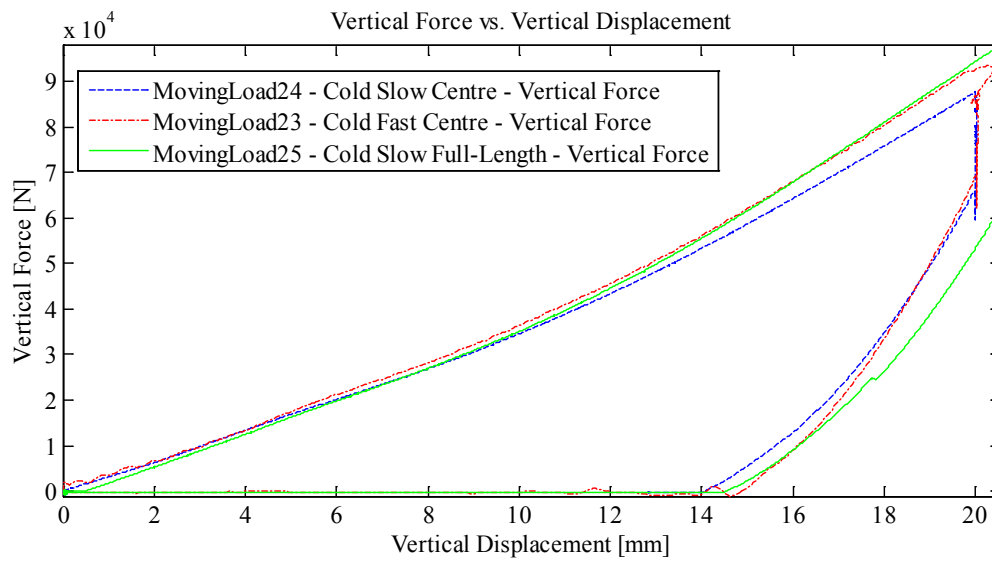
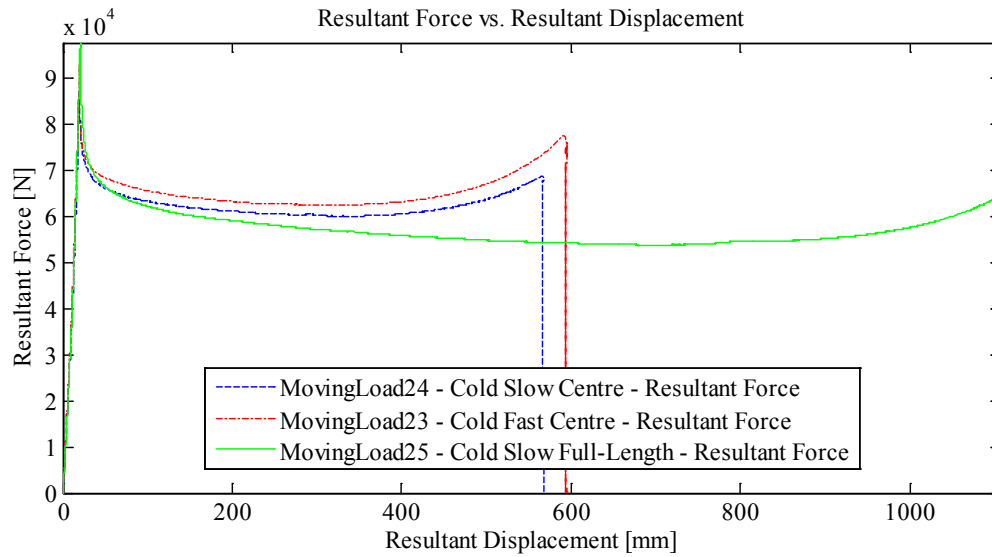


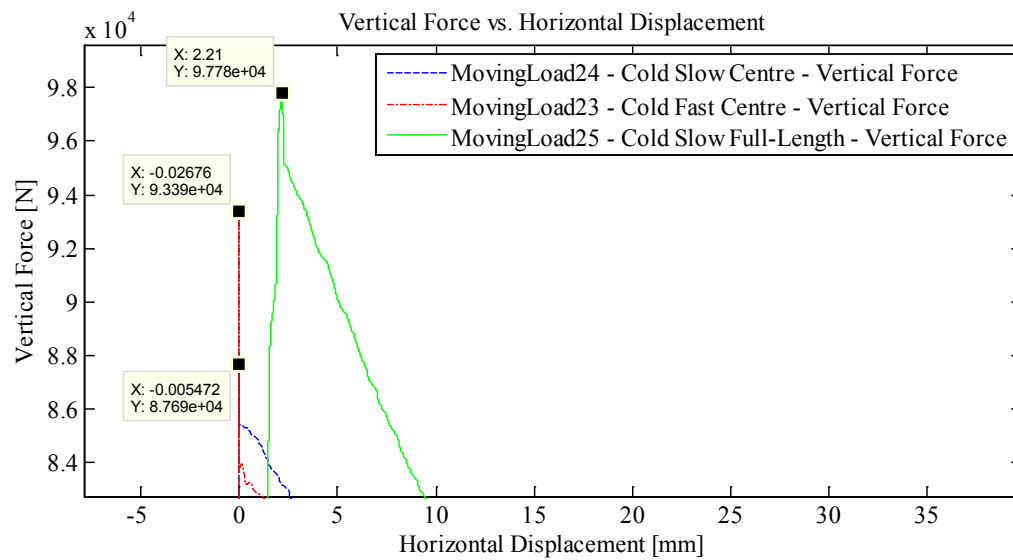
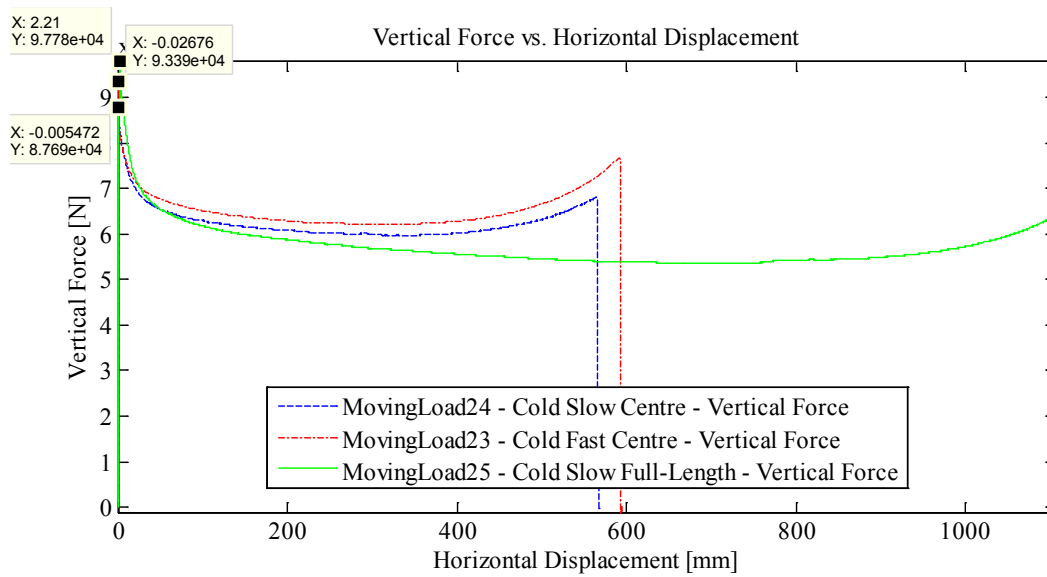


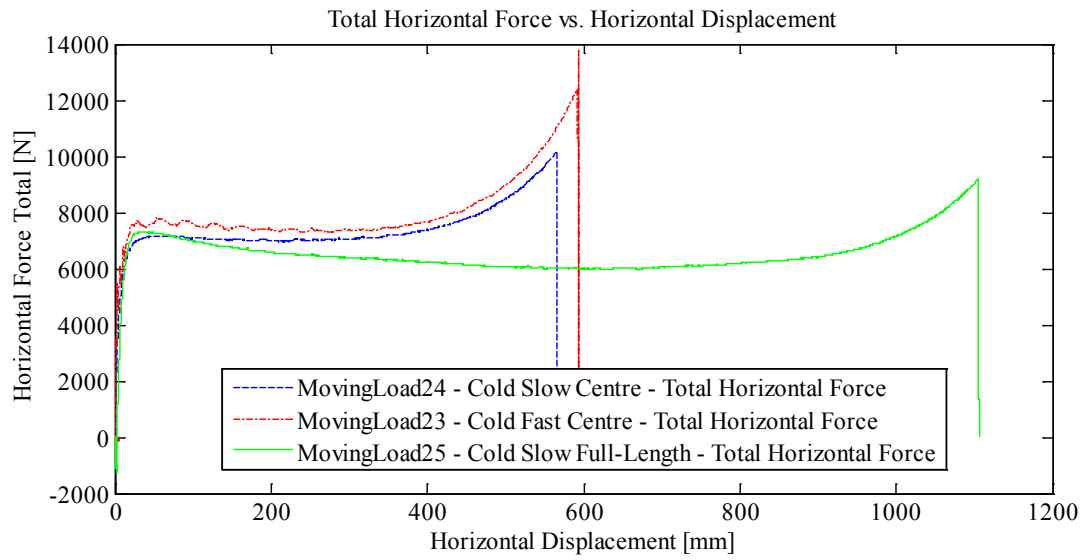
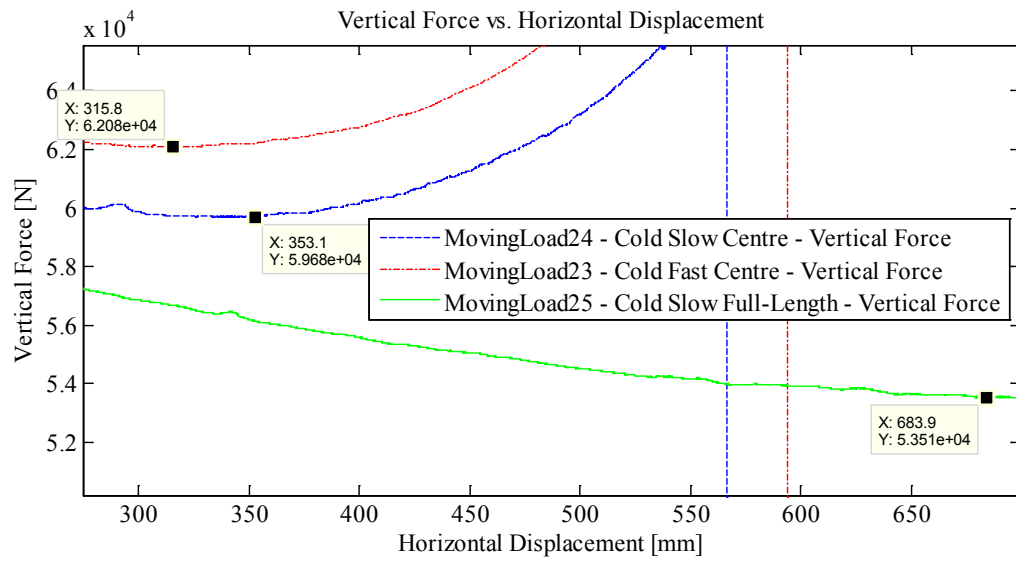
Appendix C2.2 – Quarter Inch Plate – 4 cm Indentation

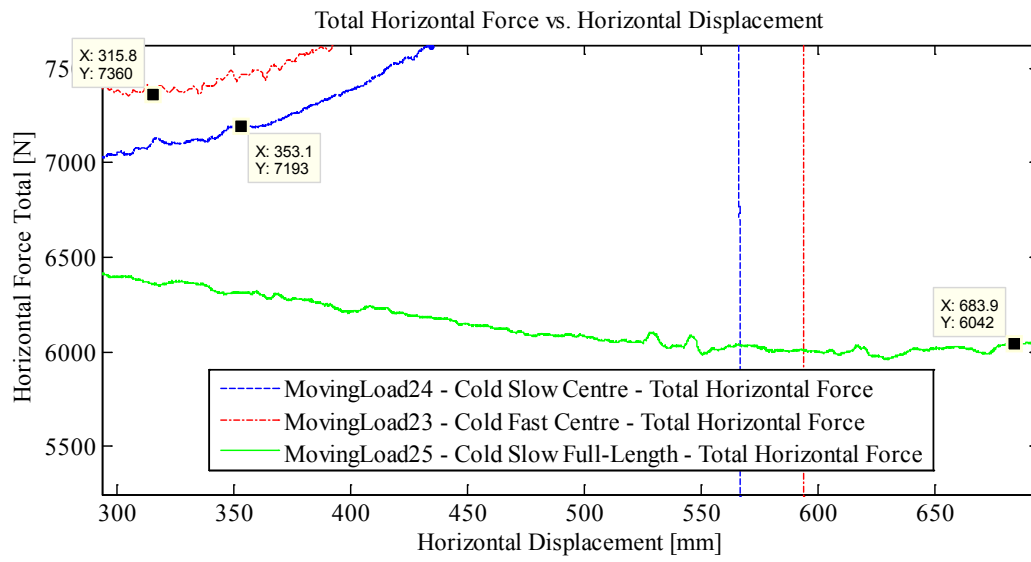
Appendix C2.2.1 – Summary Plots for Experiments ML 23, 24 and 25

25









Appendix C2.2.2 – Fast – Movin1gLoad23

April 15, 2014 at ~11:20 a.m.

Run # 16
Room-temperature: -10°C
Sample Type: 1/4" Plate
Test Type: In-Along-Out Centre to End

HStarting Point: Centre (0.62 cm (0 cm nominal))
HSpeed: Fastest mm/s
H Travel: Centre to End (55+ cm)

Vstarting Point: 2.5 mm
VSpeed: Fastest mm/s
V Travel: 20 mm
V Stopping Point: -17.5 mm

Notes:

May be slightly damaged on far end by accidental drop on steel wheel indenter before test.

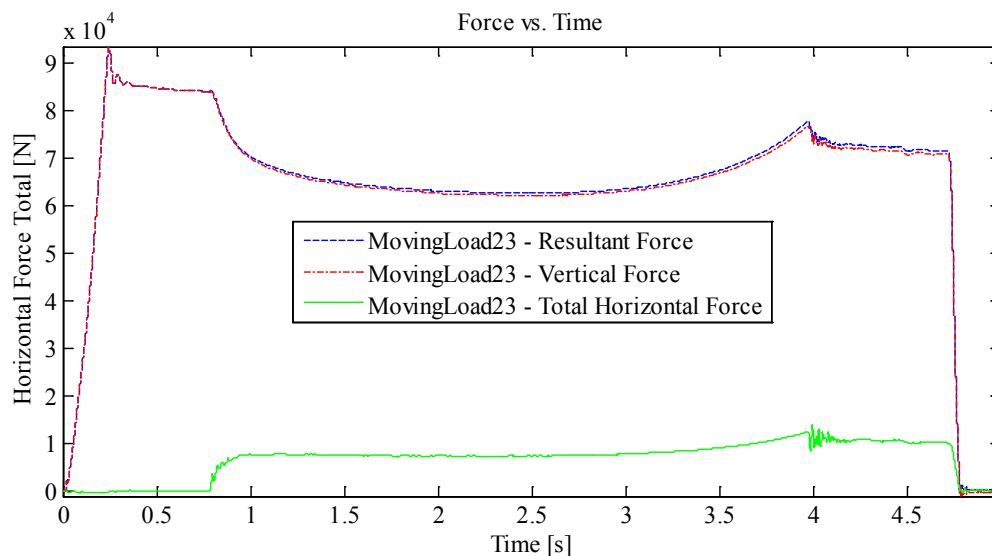
Indentation 1: ~20 mm, In-Along-Out - Centre to End

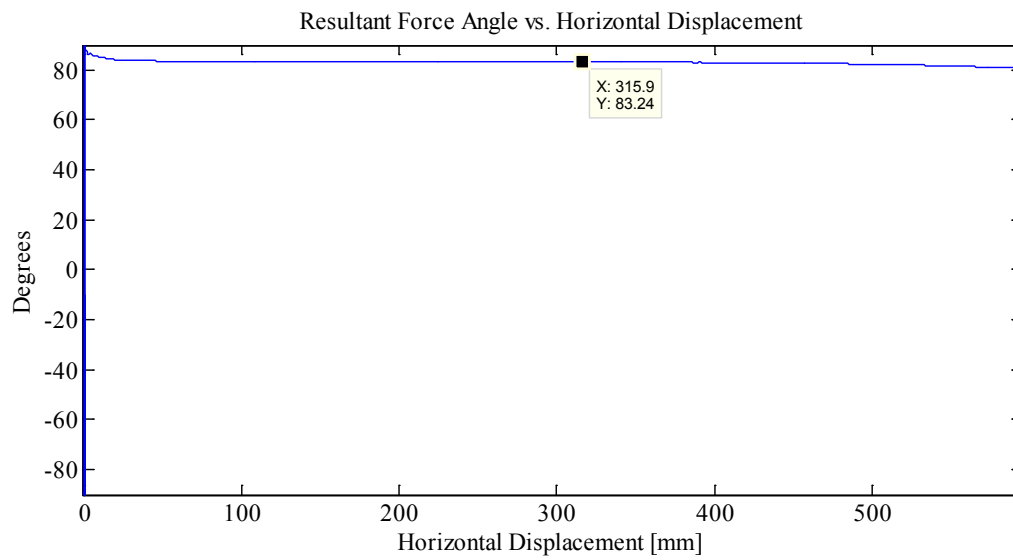
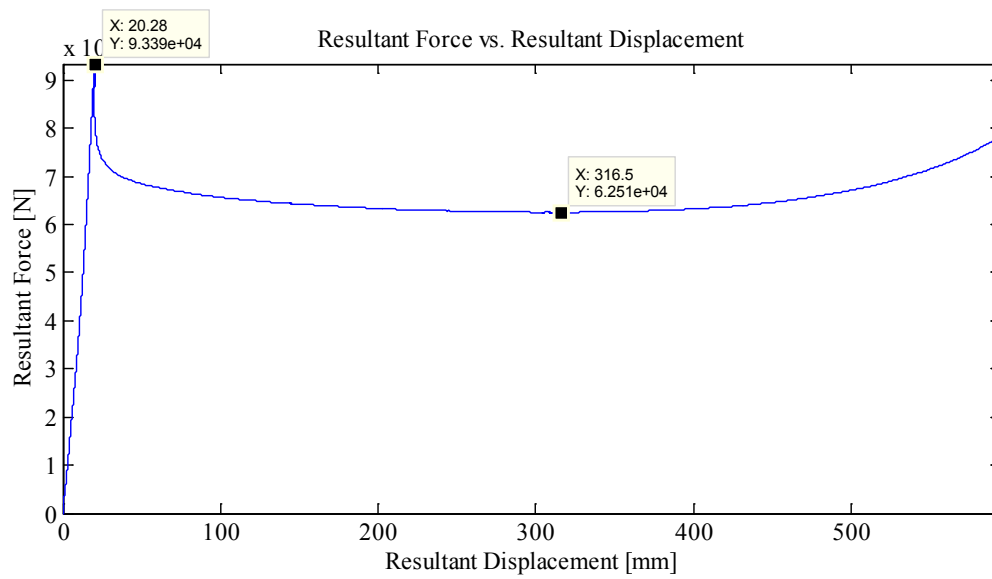
Data from Indentation 1 saved as MovingLoad23

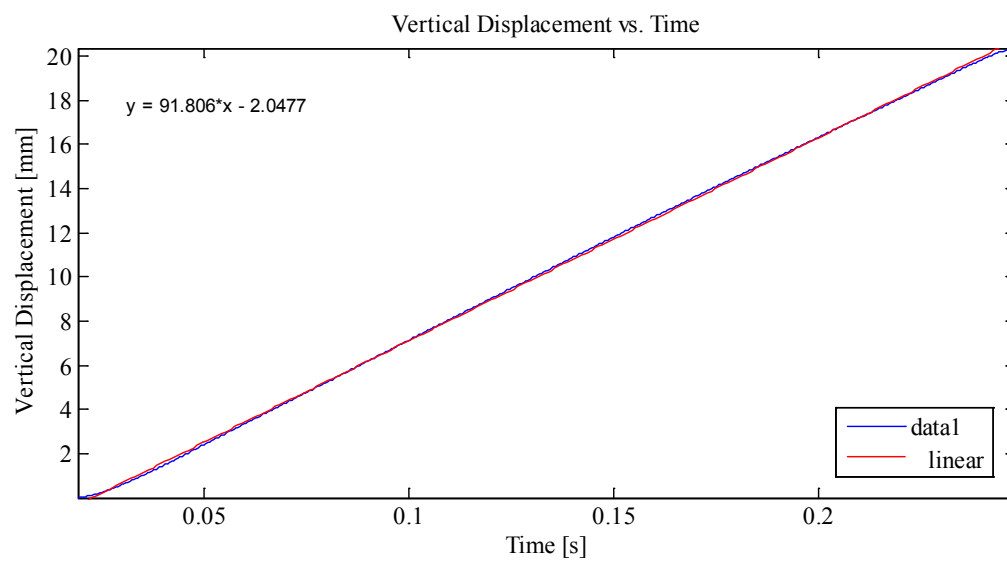
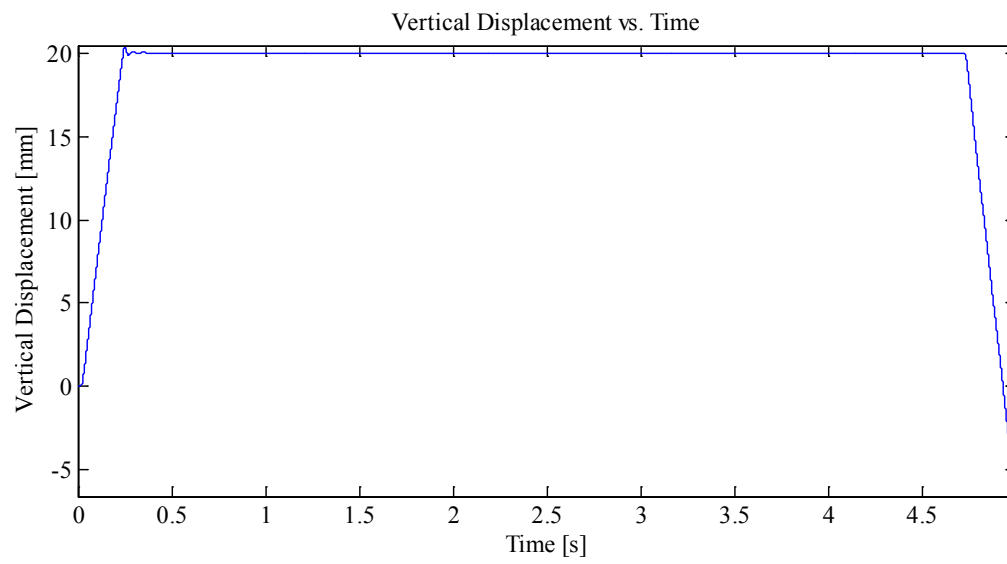
With Thermal Video

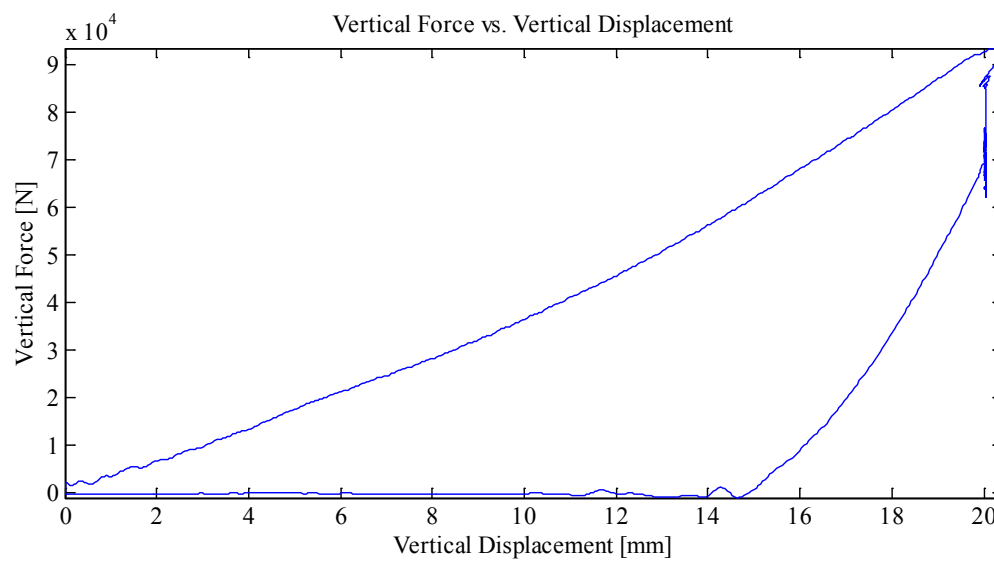
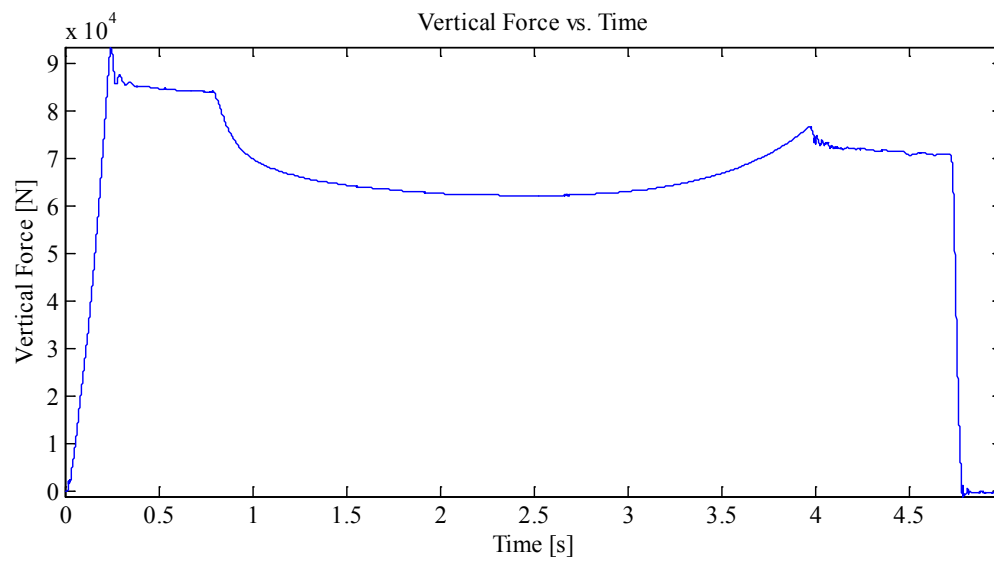
No Microscribe Tests for this sample.

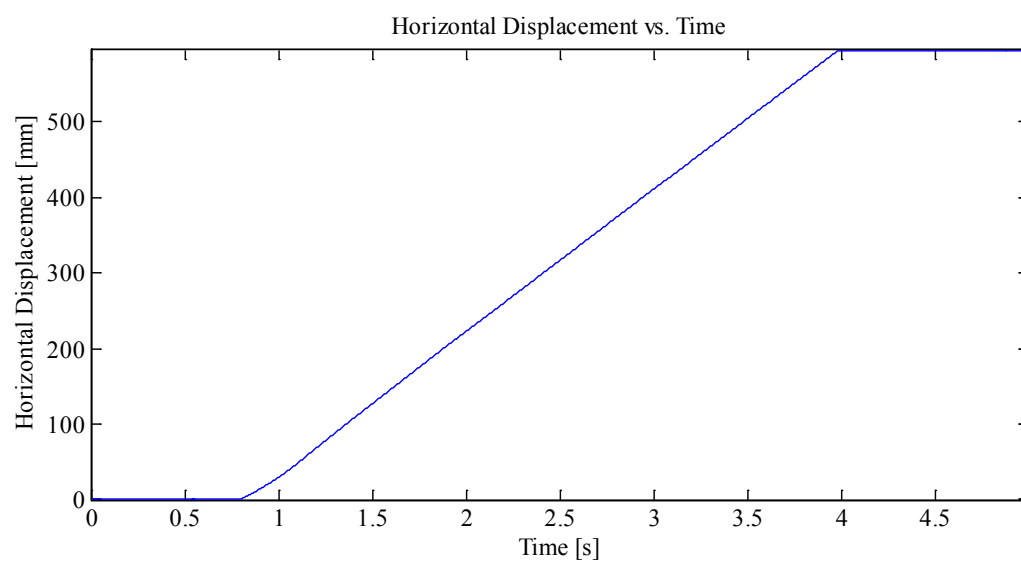
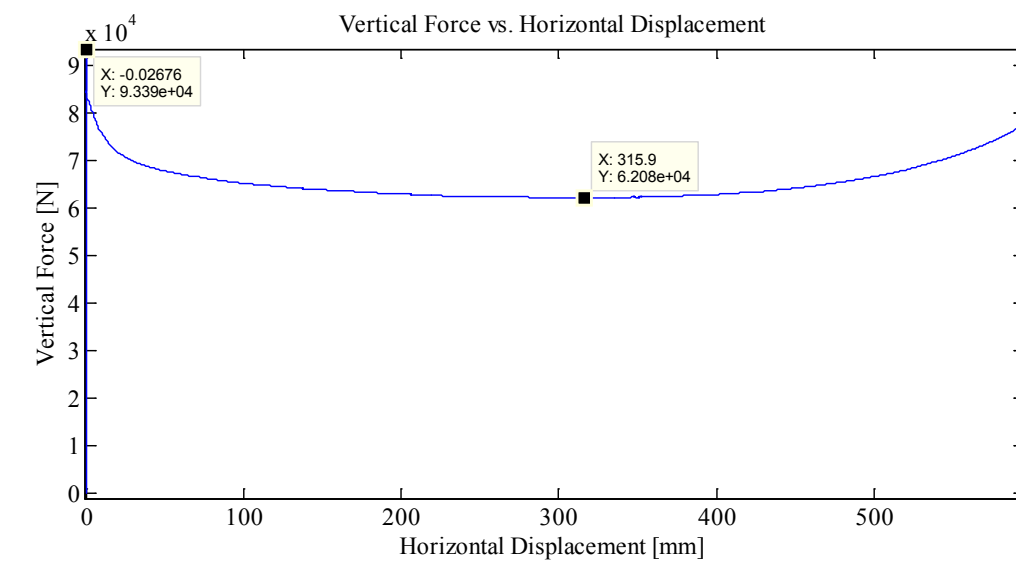
Plots:

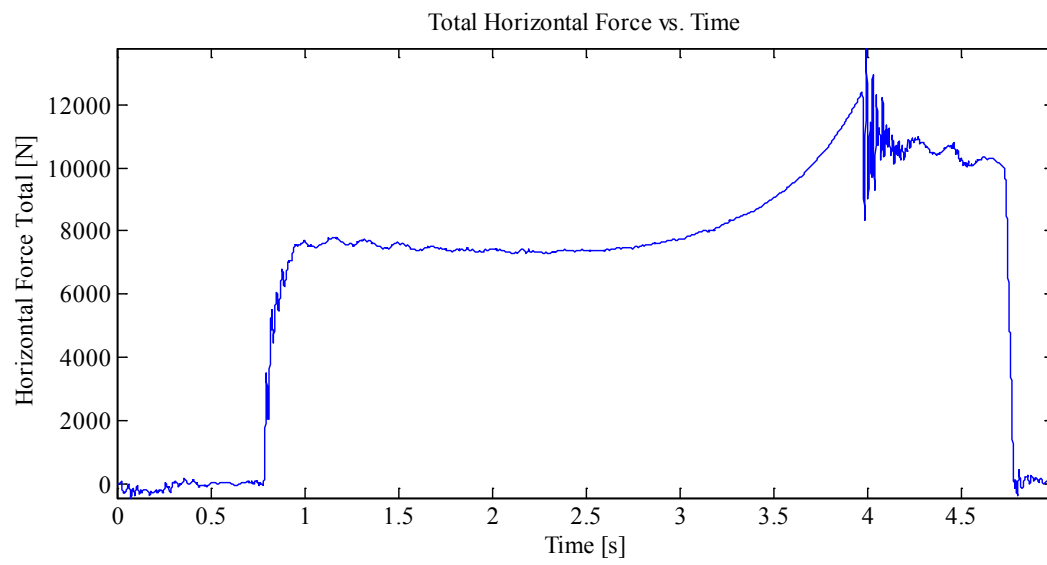
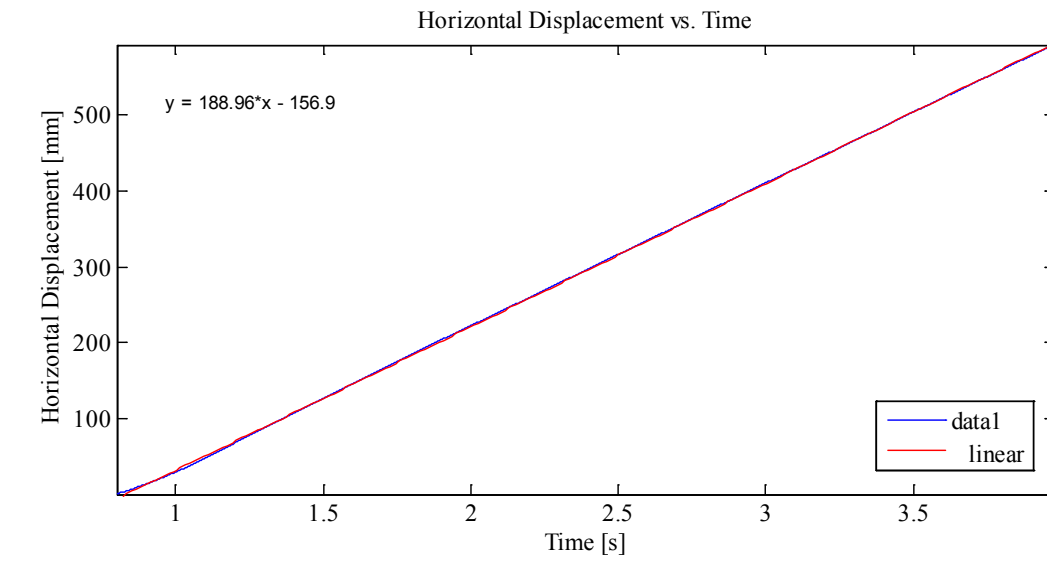


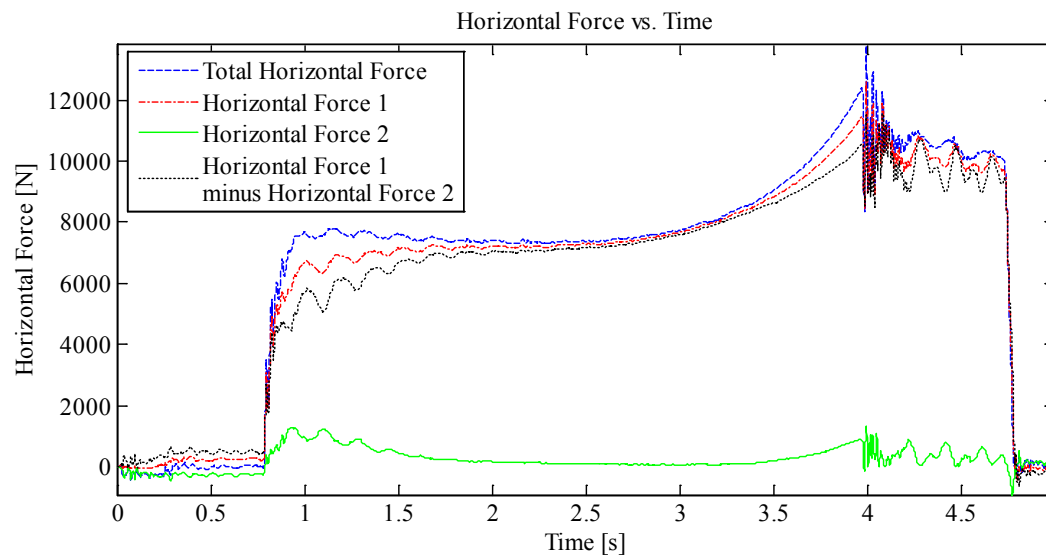
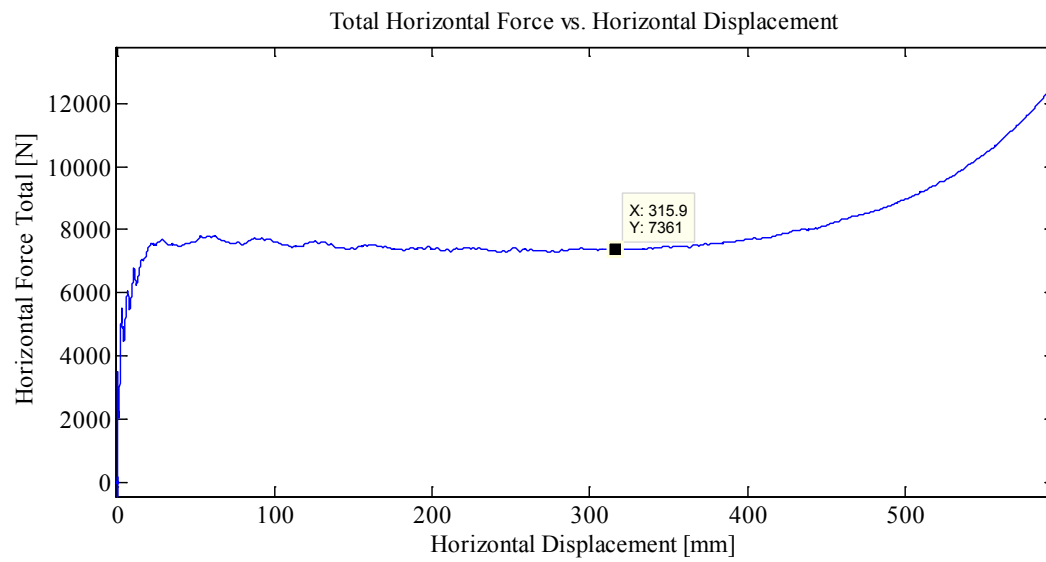












Appendix C2.2.3 – MovingLoad24

April 15, 2014 at ~2:55 p.m.

Run # 17
Run Type: Slow
Room-temperature: -10°C
Sample Type: 1/4" Plate
Test Type: In-Along-Out Centre to End

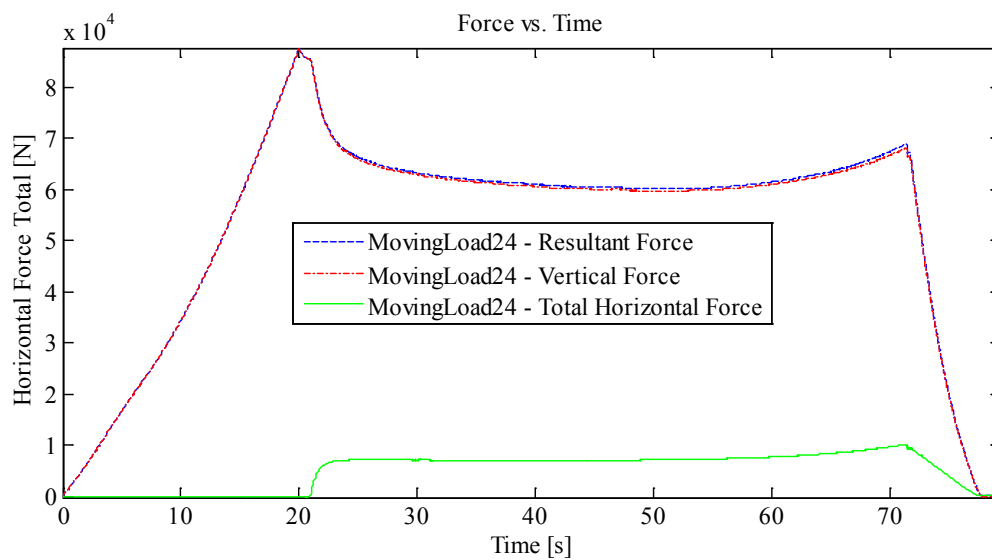
HStarting Point: Centre (0.0 (0 cm nominal))
HSpeed: 10 mm/s (Nominal)
H Travel: Centre to End (55+ cm)

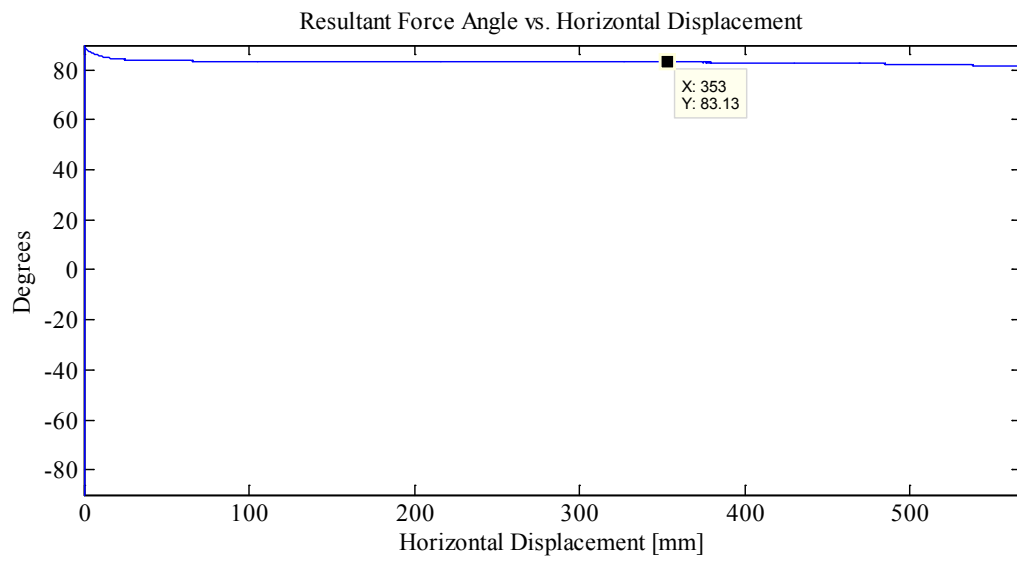
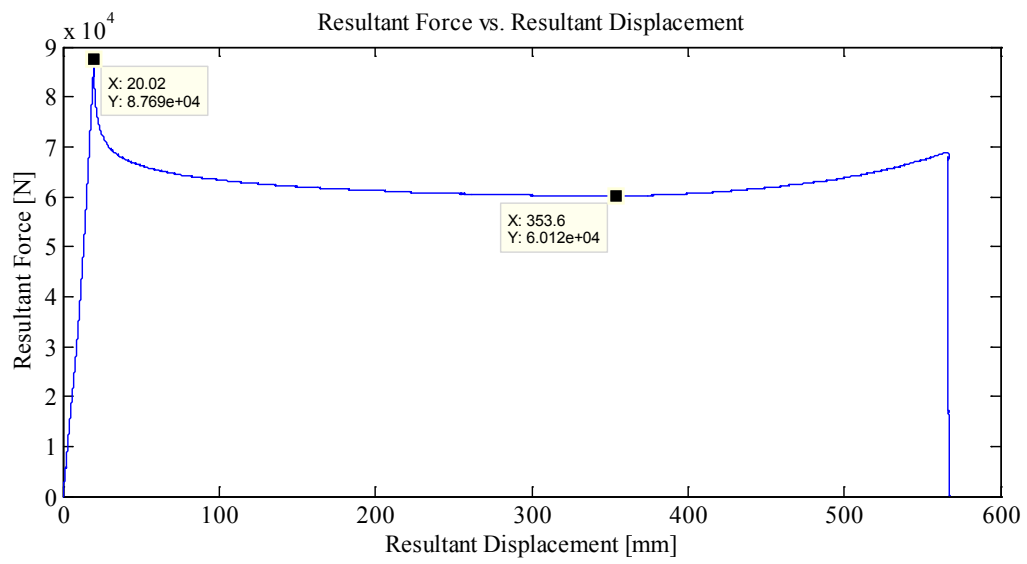
Vstarting Point: 2.45 mm
VSpeed: 1.0 mm/s (nominal)
V Travel: 20 mm
V Stopping Point: -17.55 mm

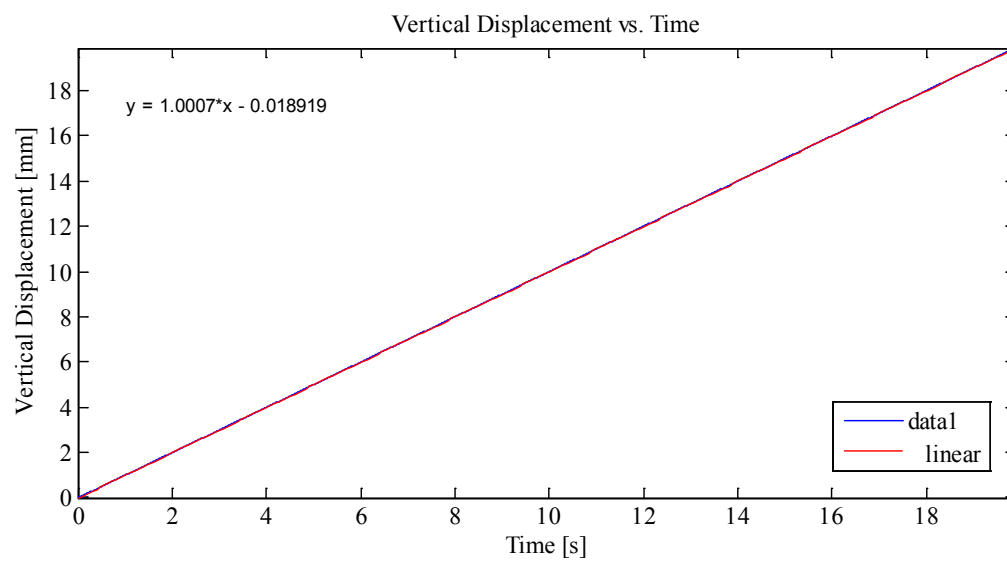
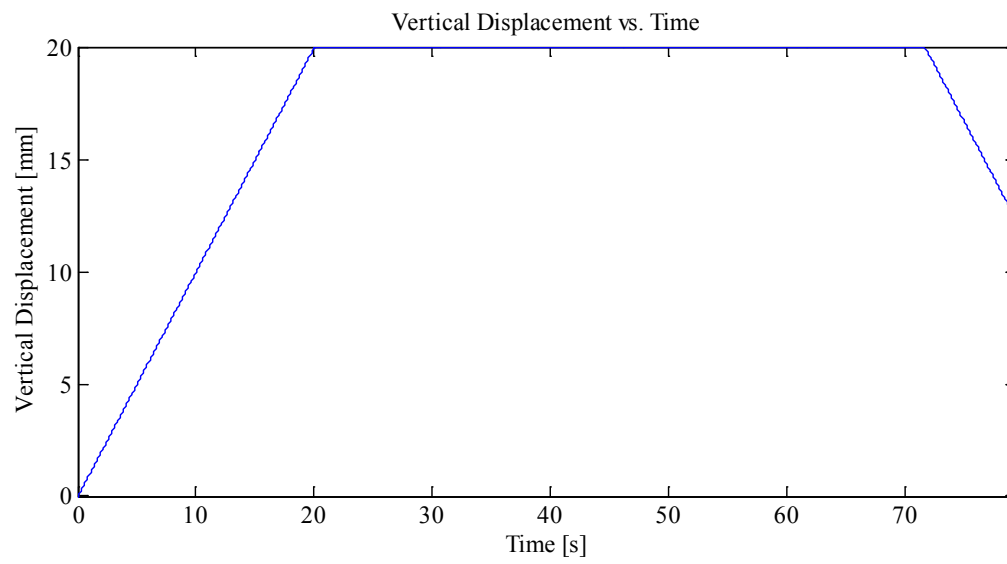
Notes:

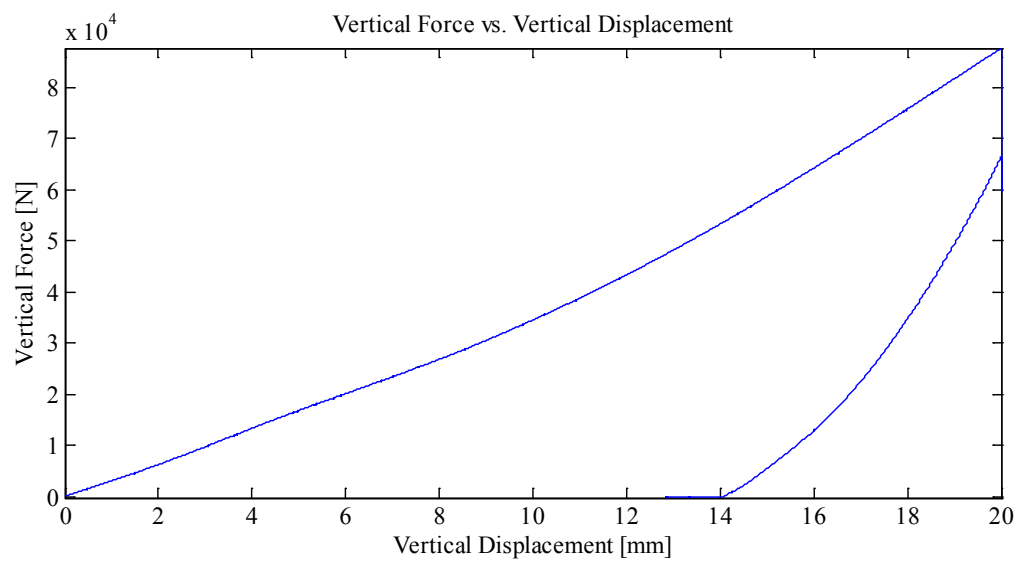
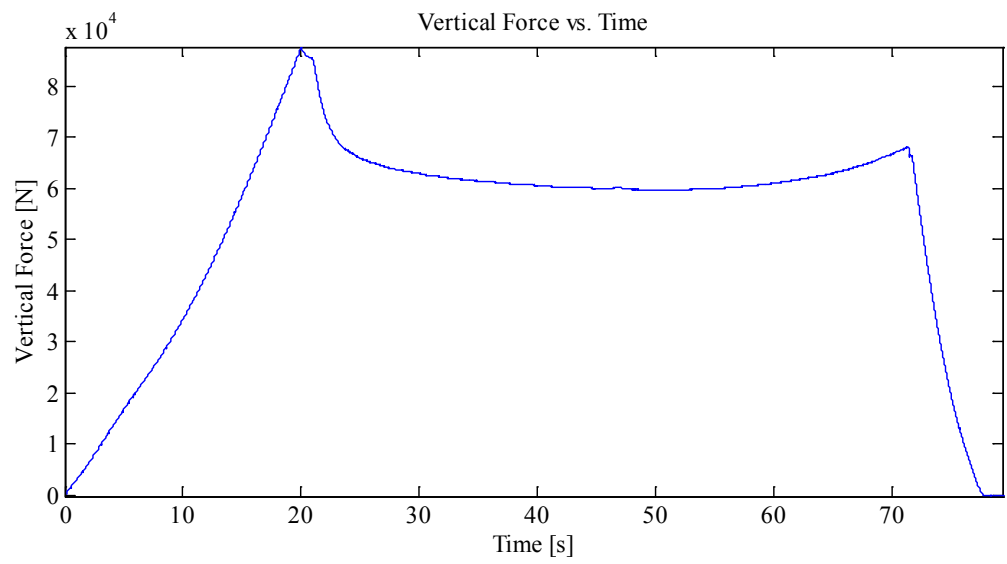
Indentation 1: ~20 mm, In-Along-Out - Centre to End
Data from Indentation 1 saved as MovingLoad24
With Thermal Video

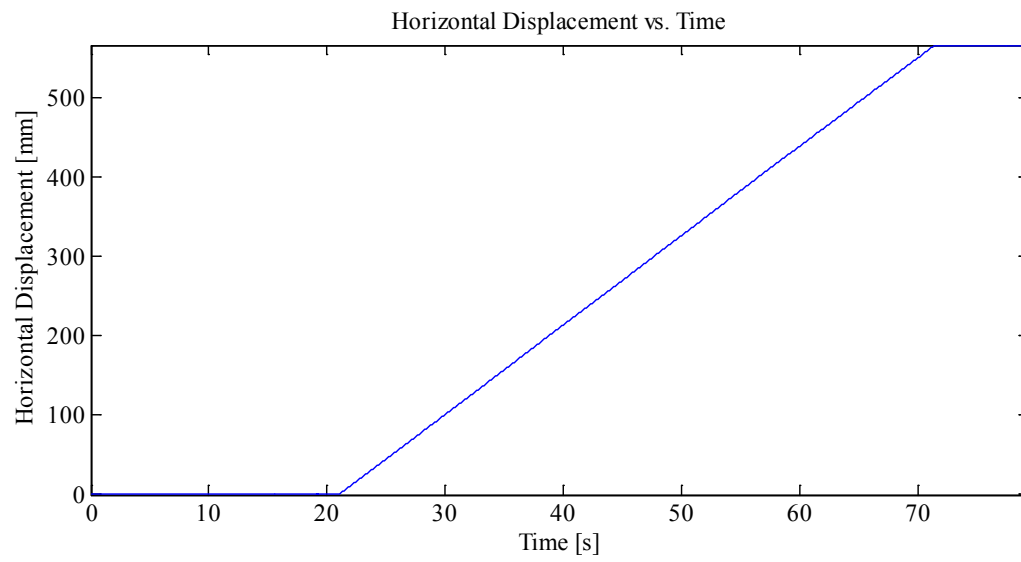
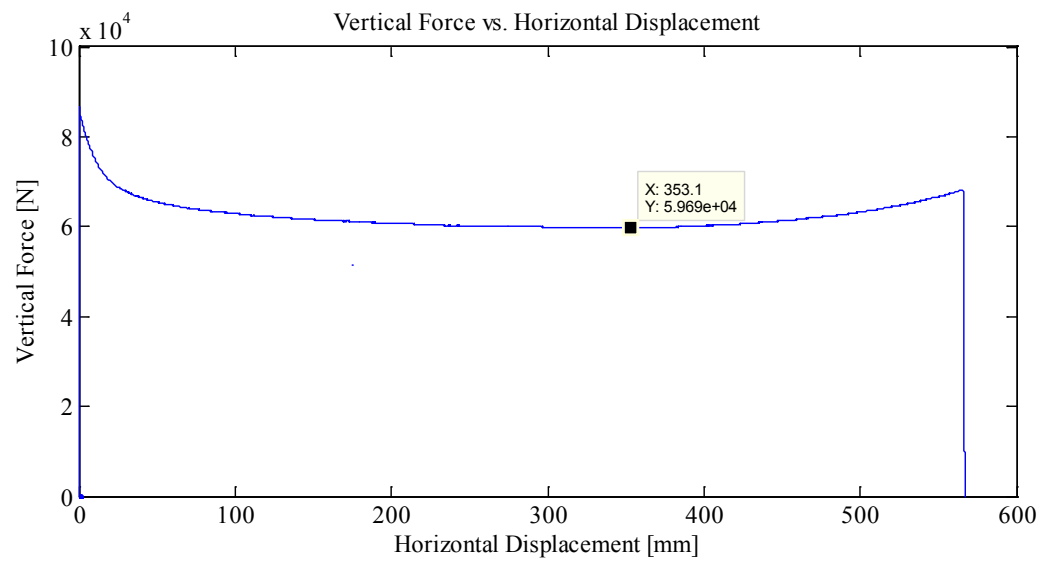
Plots:

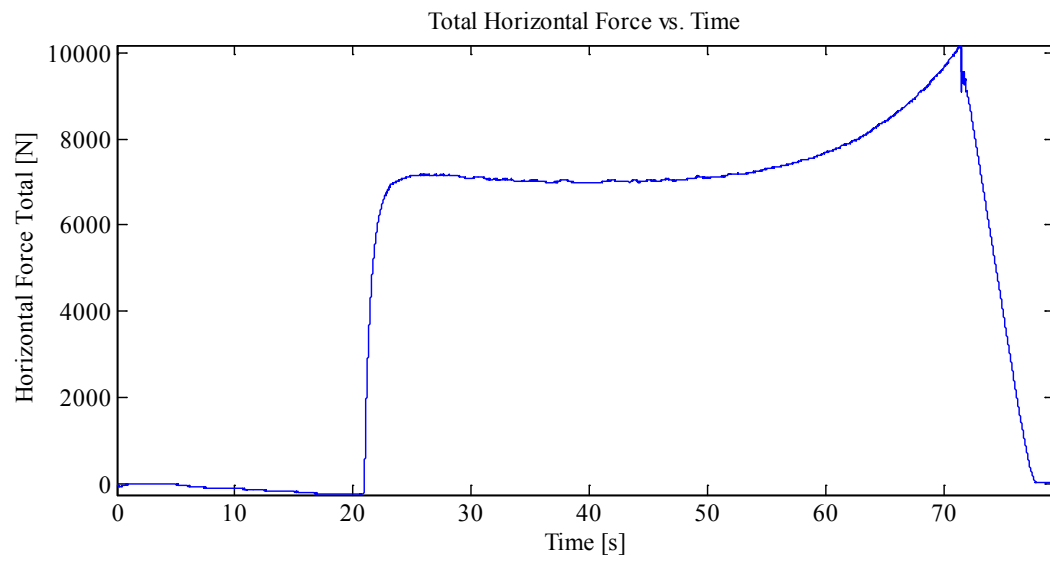
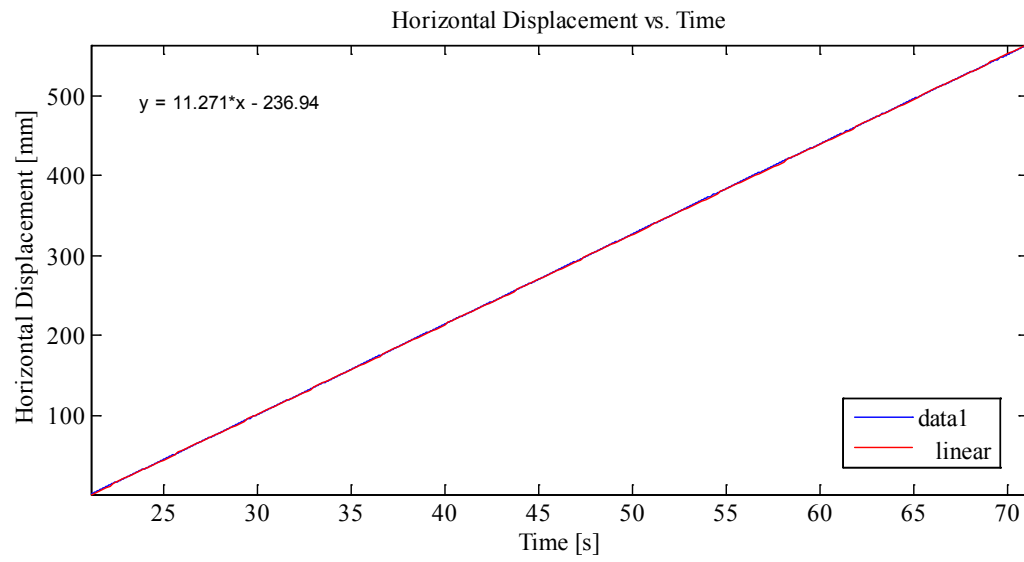


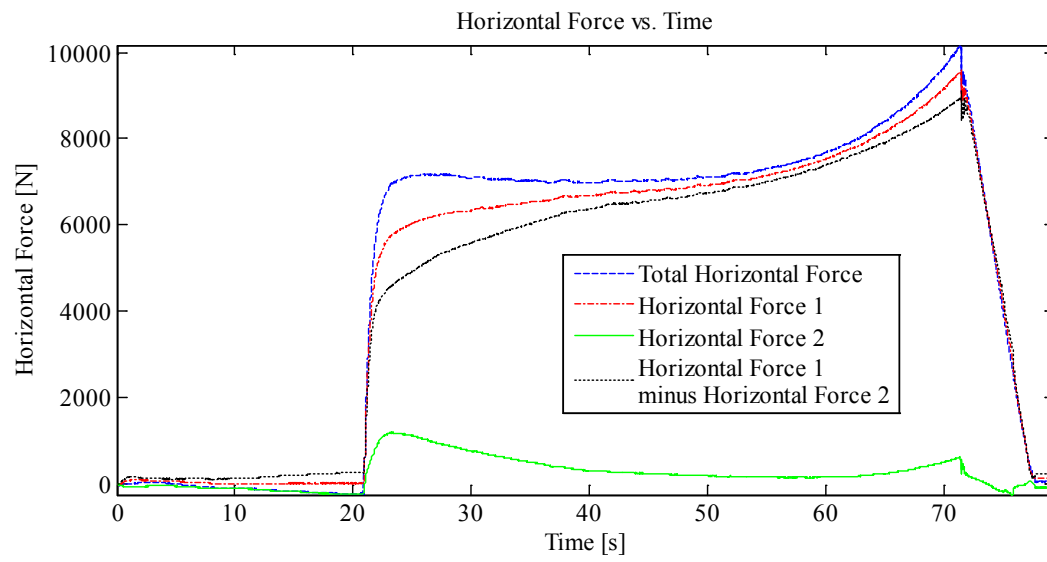
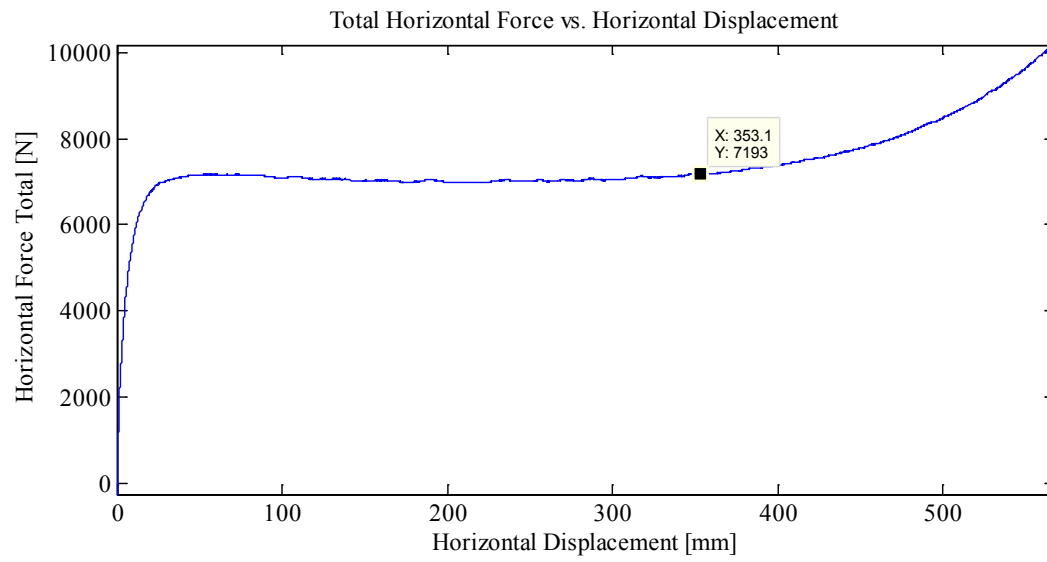












Appendix C2.2.4 – Full Length – Slow - MovingLoad25

April 16, 2014 at 12:00p.m

Run # 18
Room-temperature: -9.4°C (Started measuring with thermocouple)
Sample Type: 1/4" Plate
Test Type: In-Along-Out End to End

HStarting Point: End (-54.69 (-55 cm nominal))
HSpeed: 10mm/s (nominal)
H Travel: End to End (110+ cm)

Vstarting Point: 3.05 mm
VSpeed: 1.0 mm/s (nominal)
V Travel: 20 mm
V Stopping Point: -16.95 mm

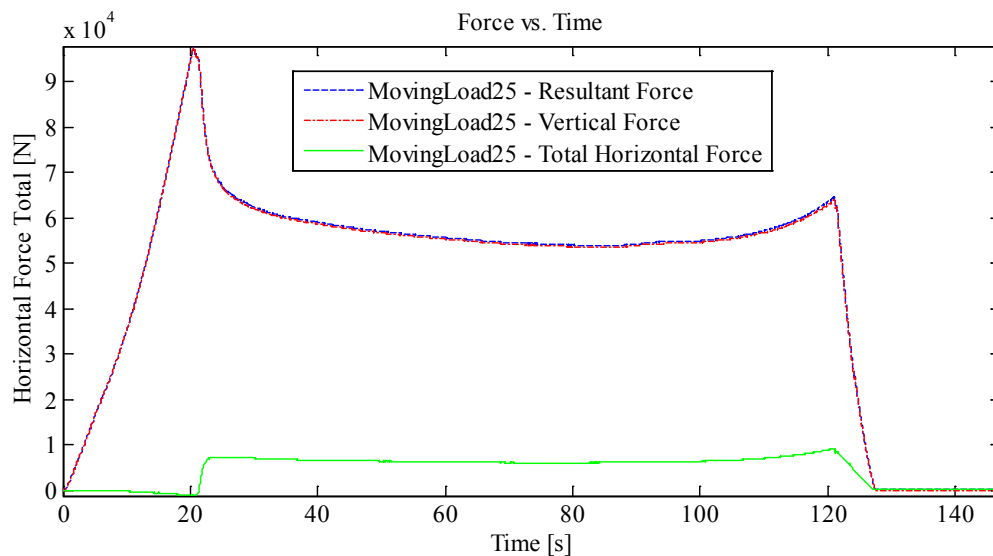
Notes:

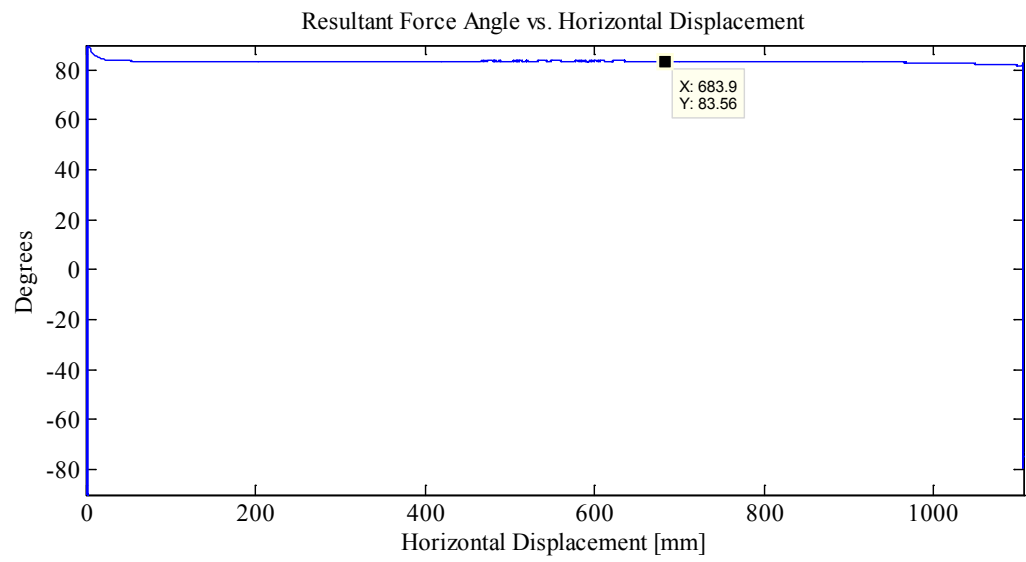
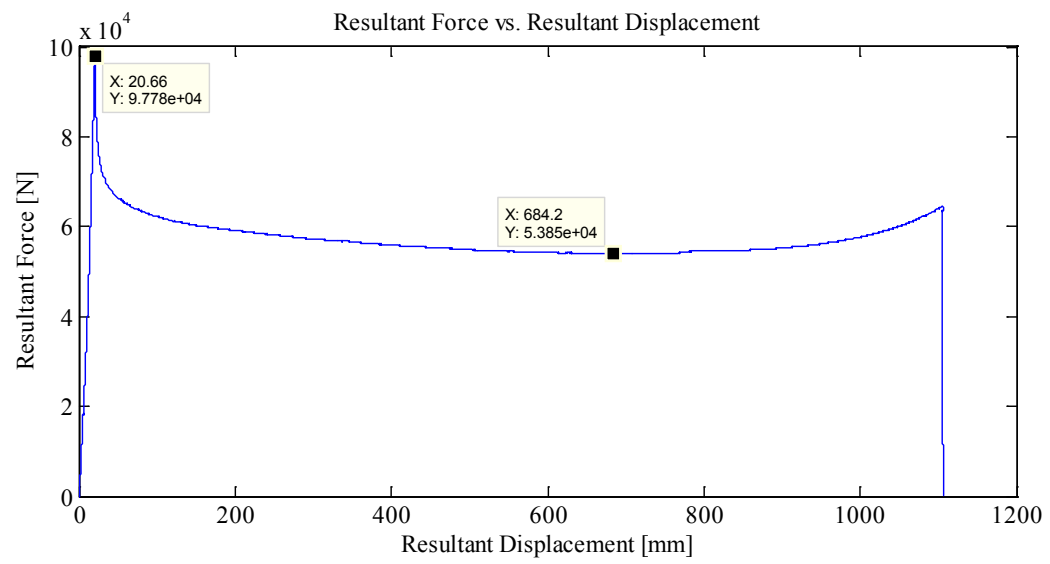
Indentation 1: ~20 mm, In-Along-Out - End to End

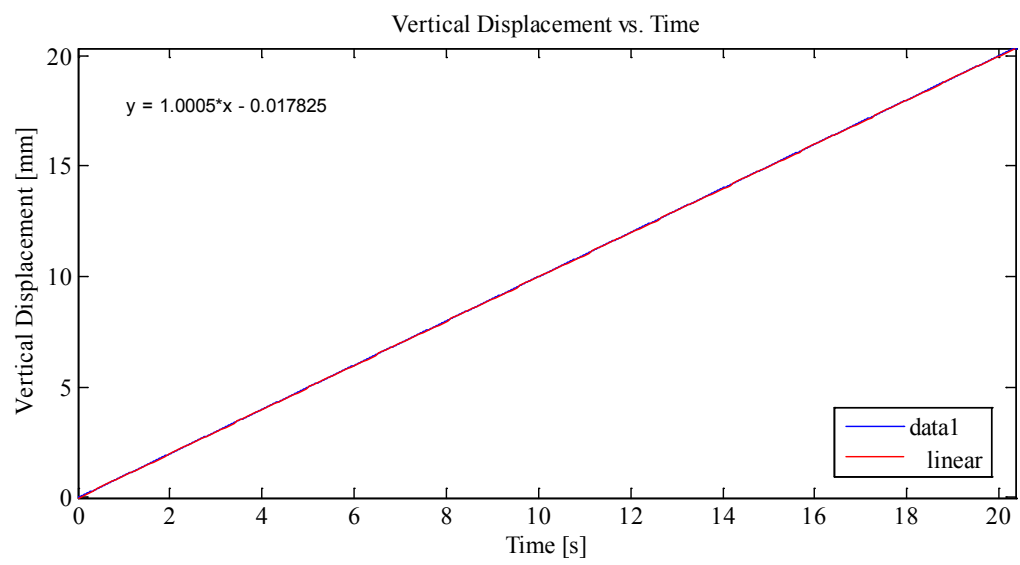
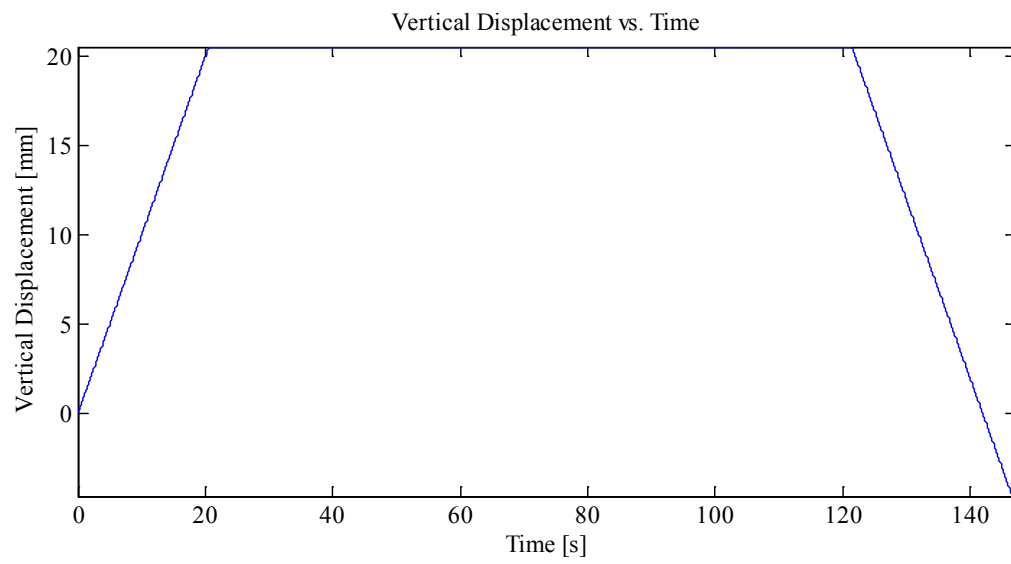
Data from Indentation 1 saved as MovingLoad25

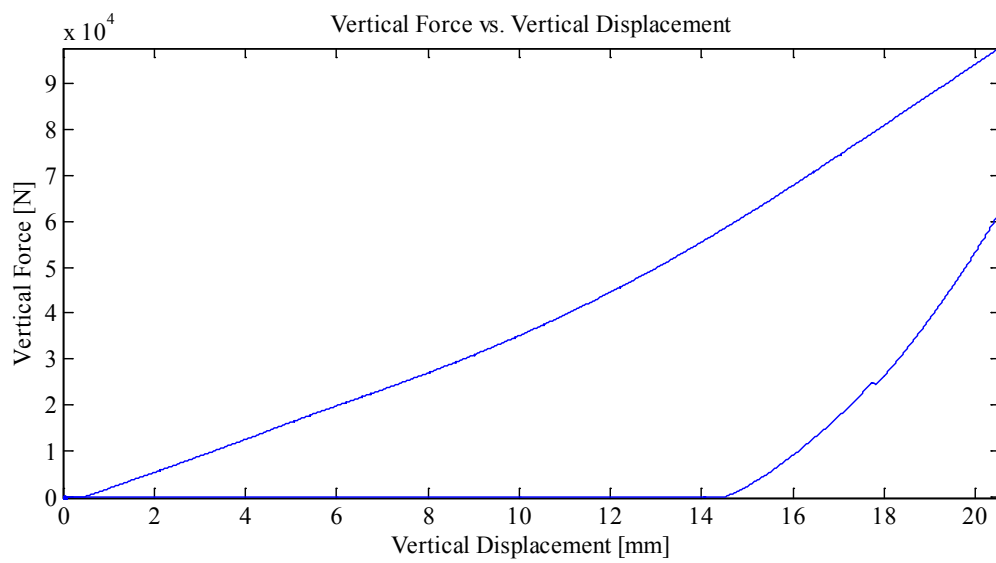
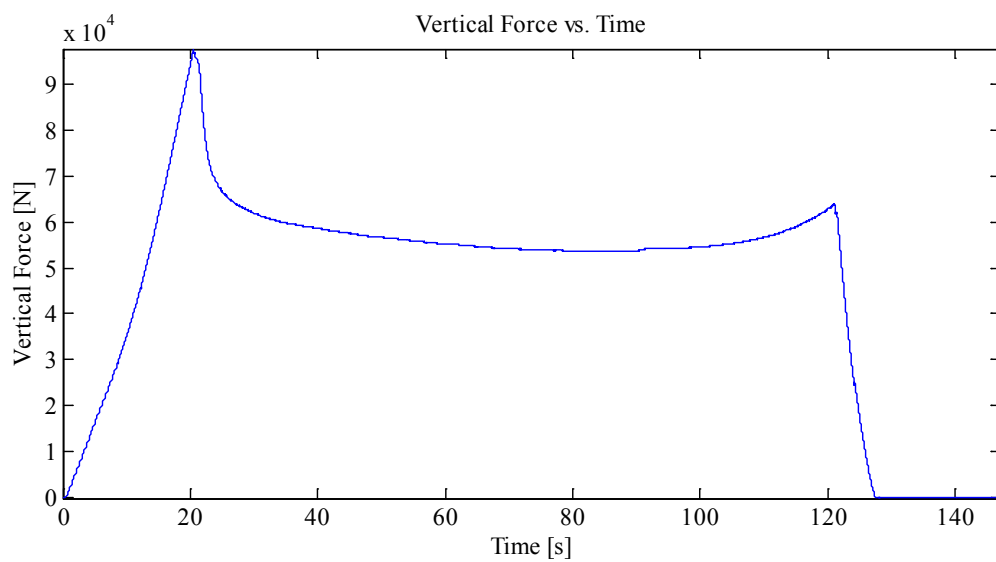
With Thermal Video

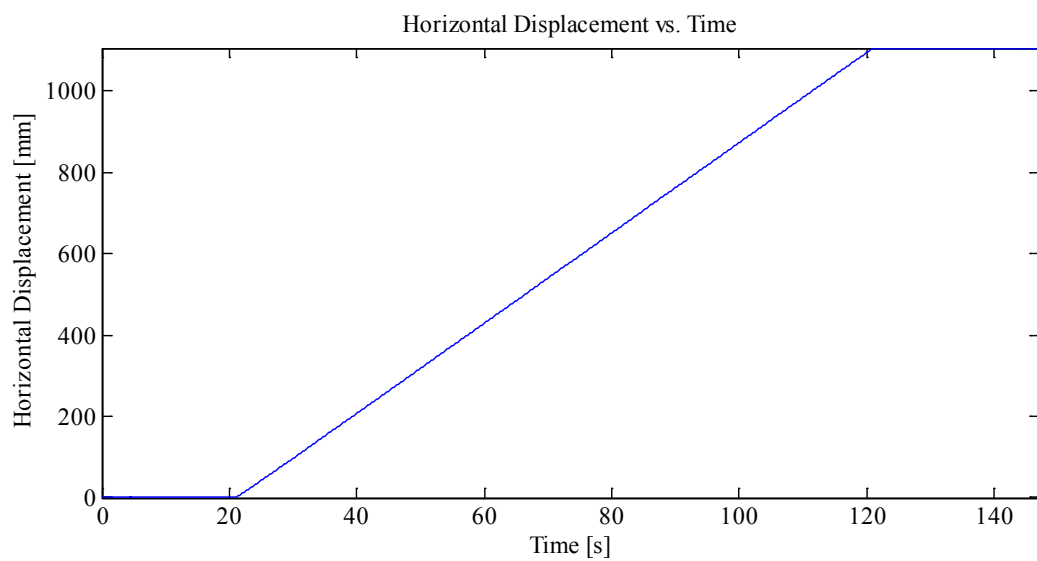
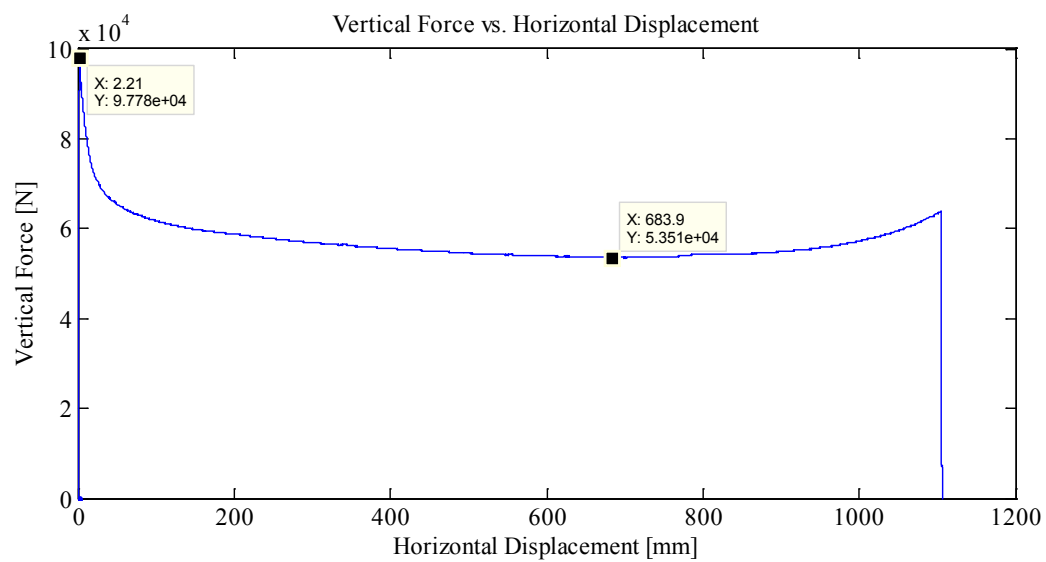
Plots:

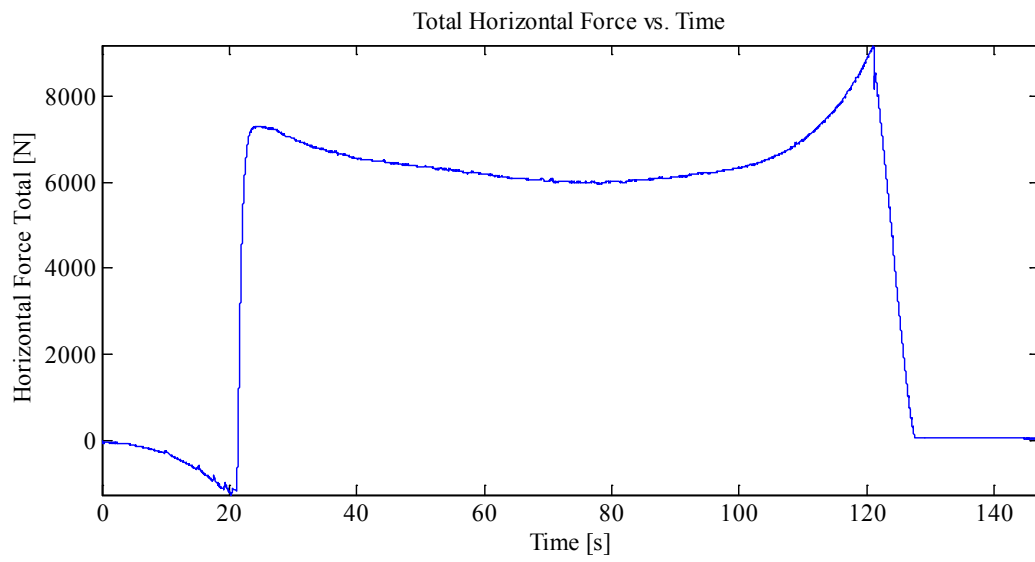
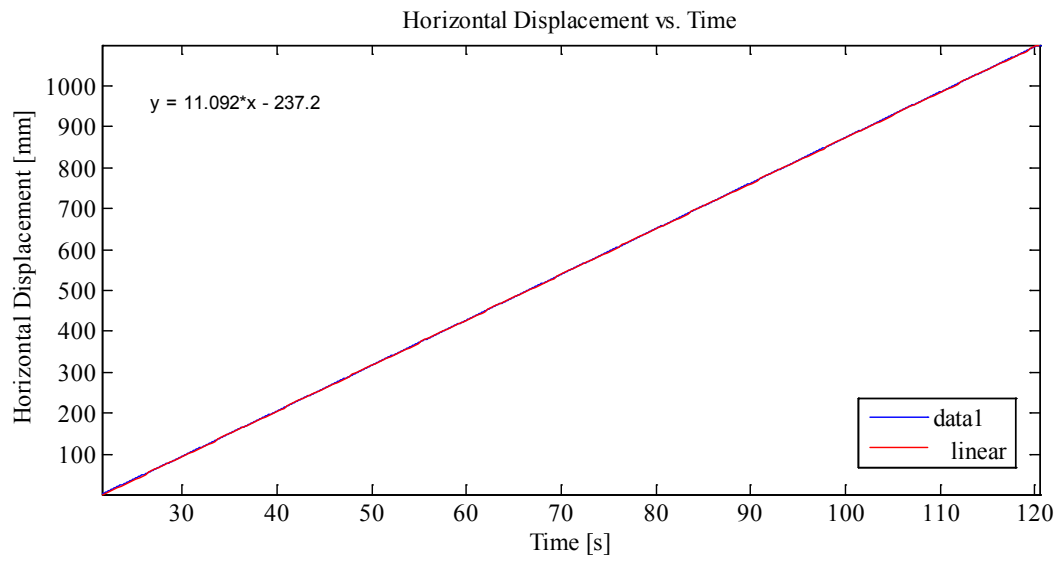


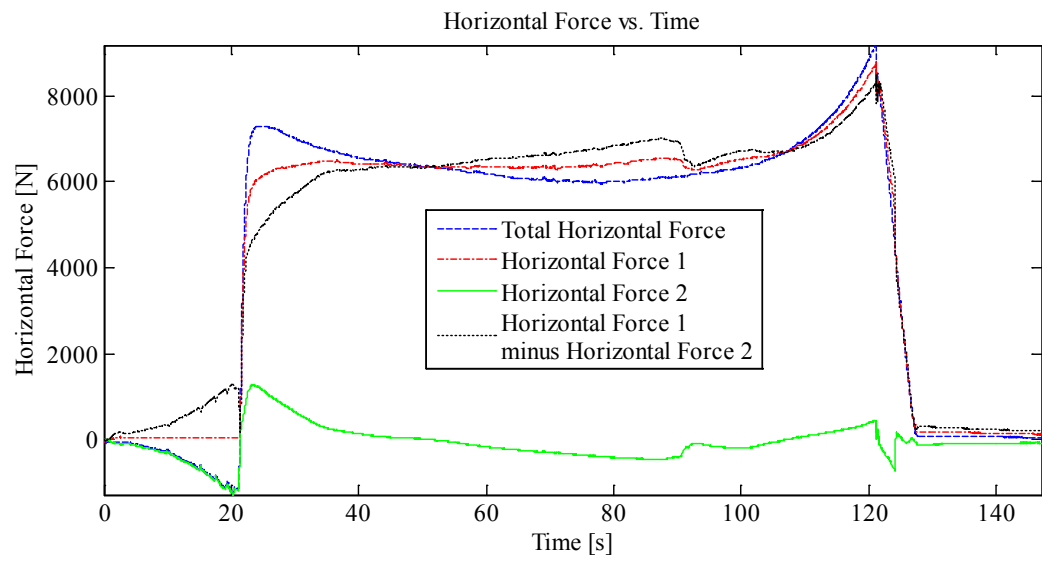
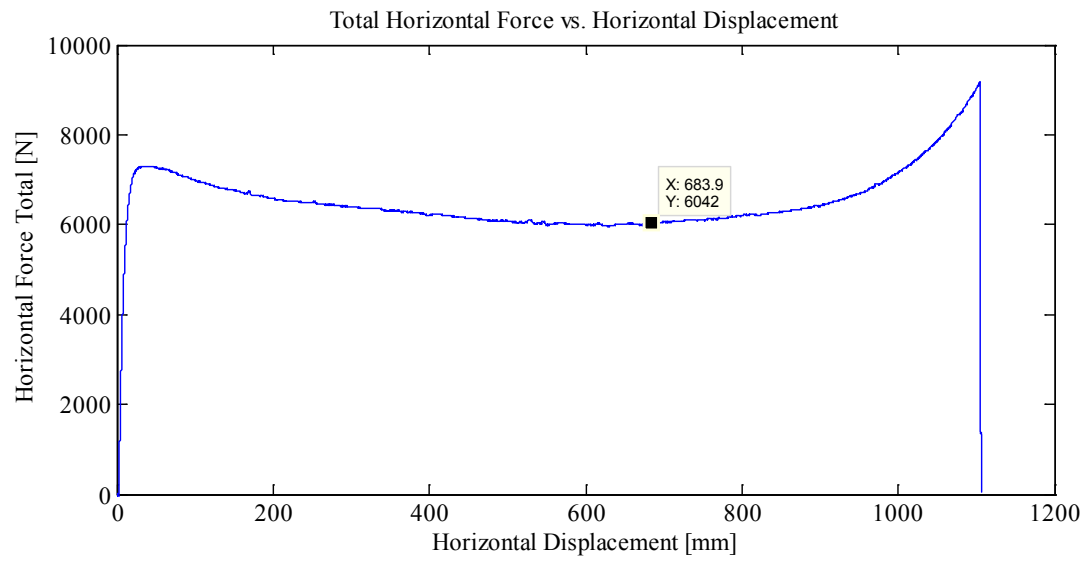








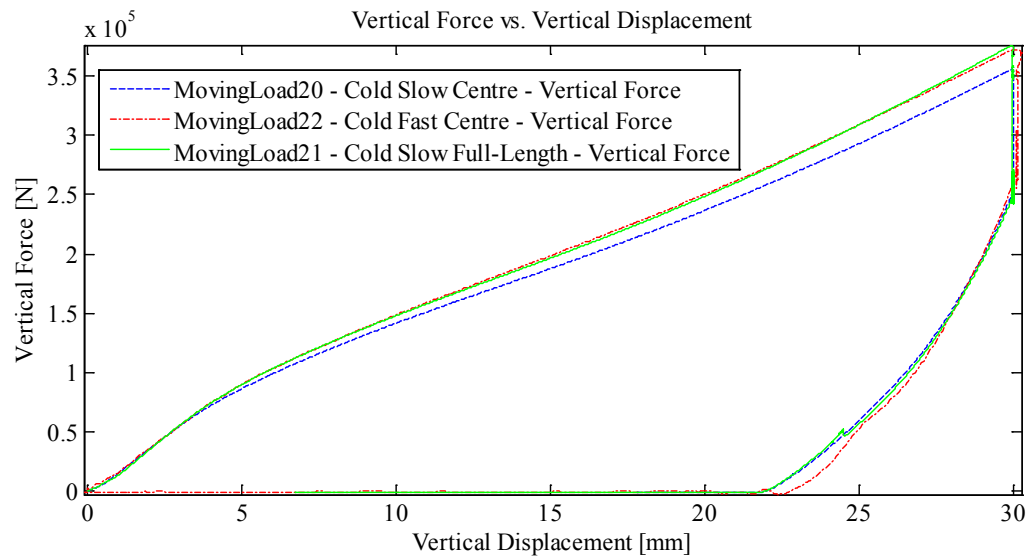
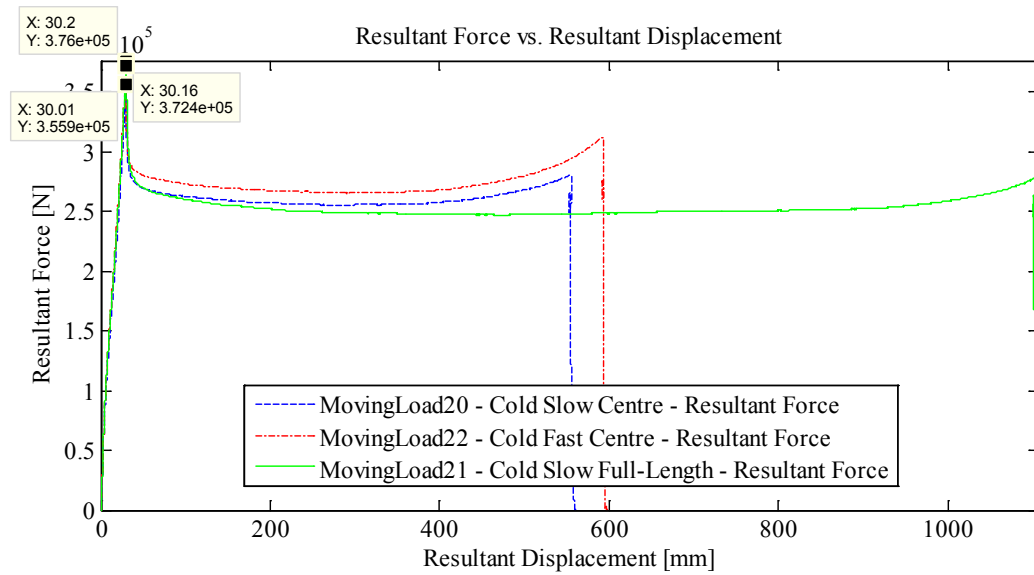


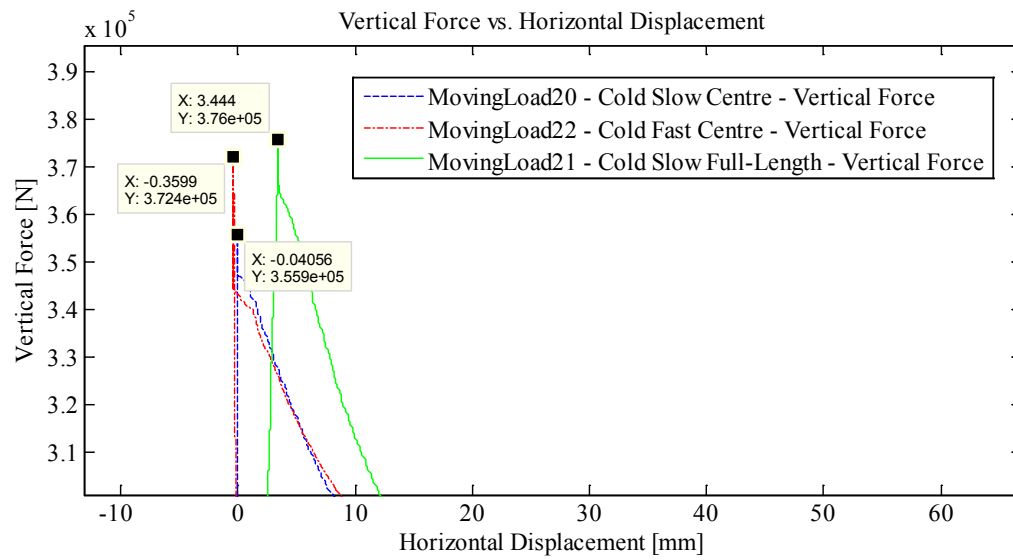
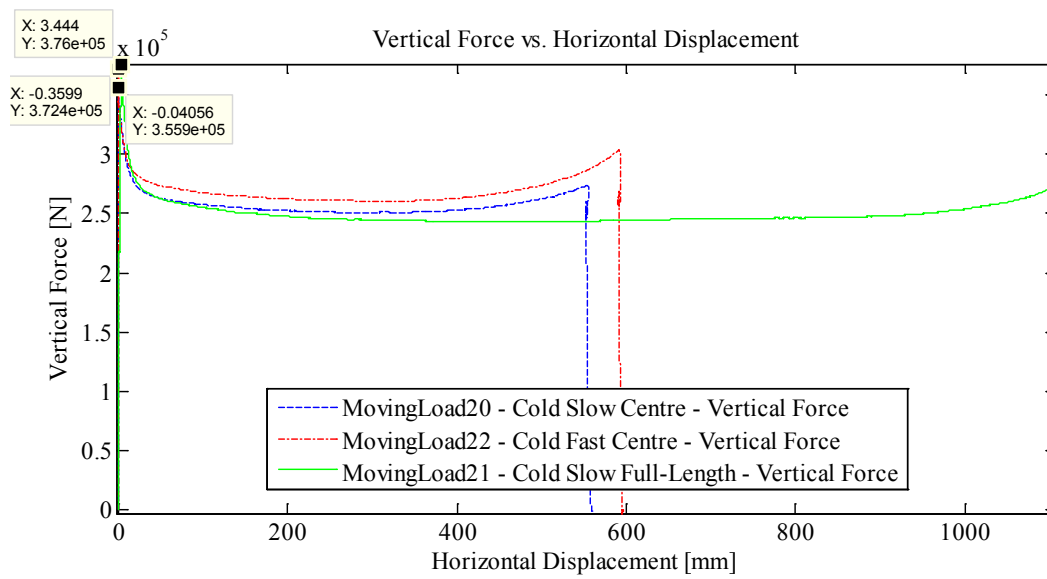


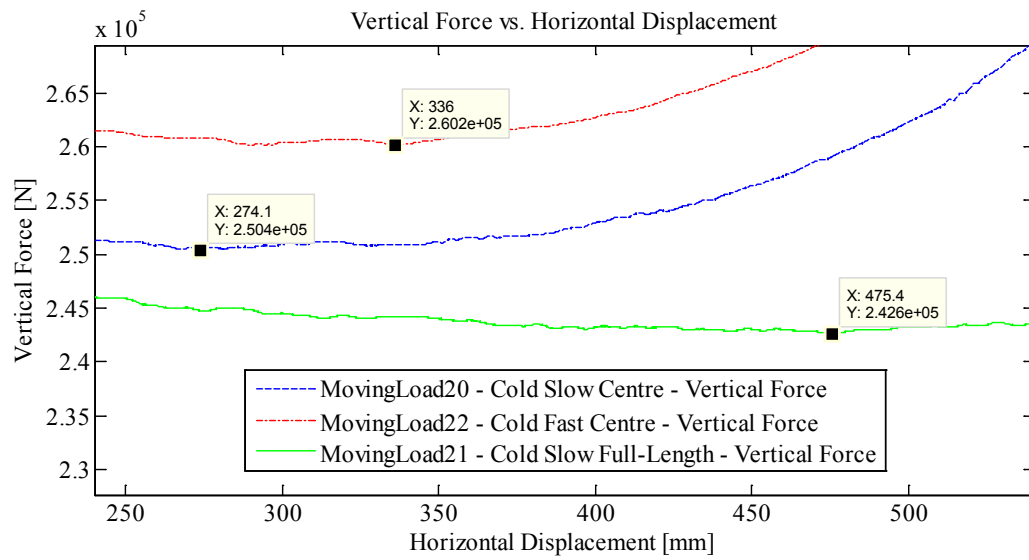
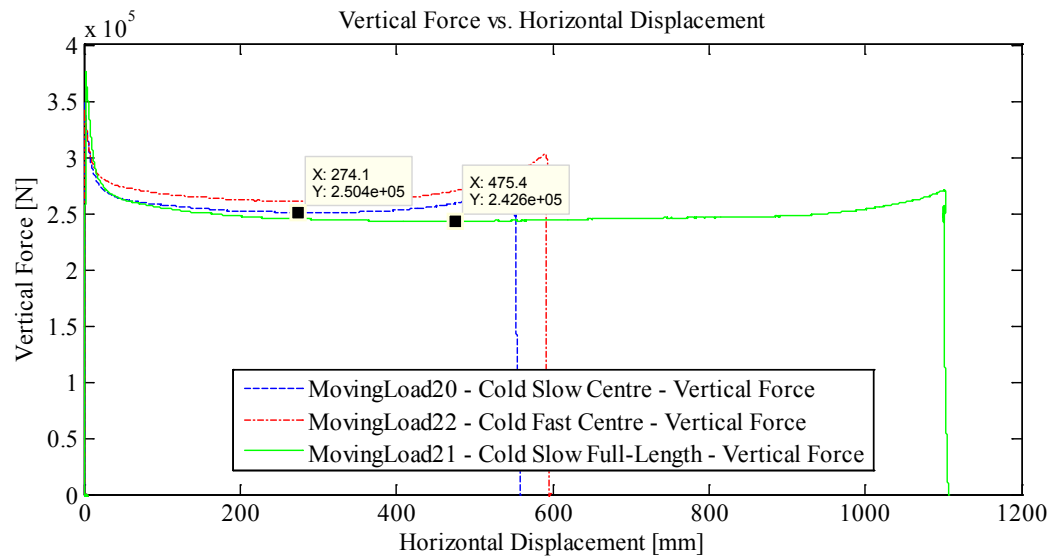
Appendix C2.3 – **Half Inch Plate – 3 cm Indentation**

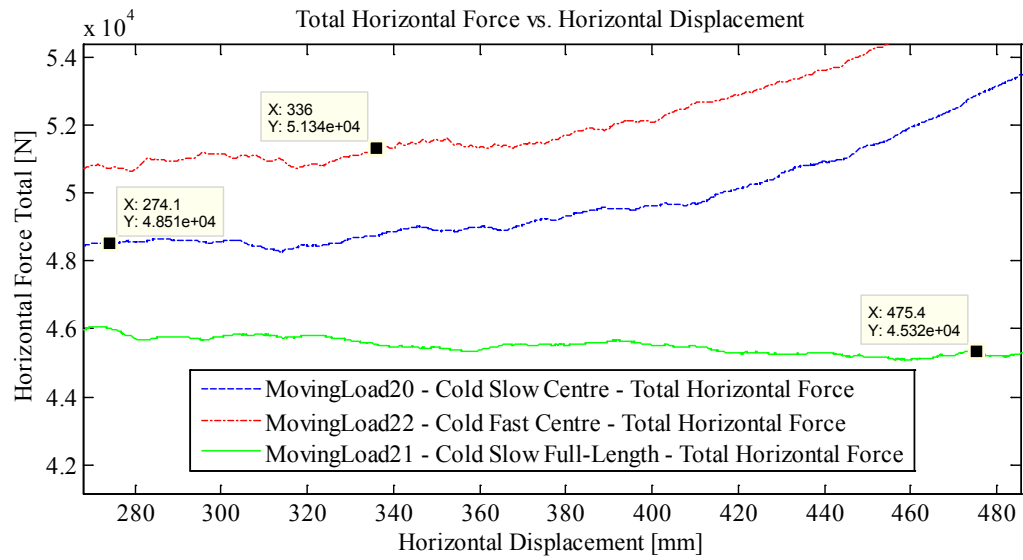
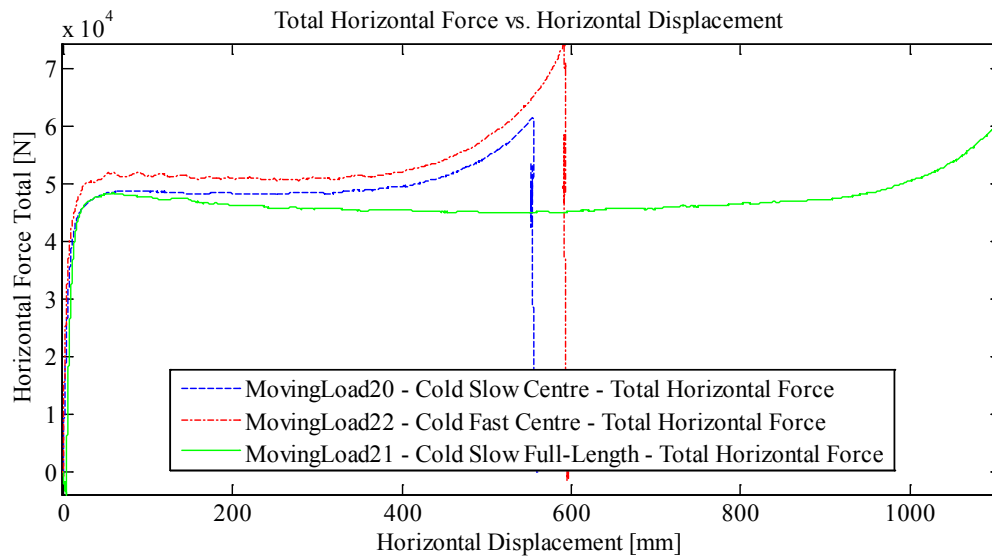
Appendix C2.3.1 – Summary Plots for Experiments ML 20, 21 and

22









Appendix C2.3.2 – MovingLoad20

April 9, 2014 at ~1:15 p.m.

Run # 13
Run Type: Slow
Room-temperature: -10°C
Sample Type: 1/2" Plate
Test Type: In-Along-Out Centre to End

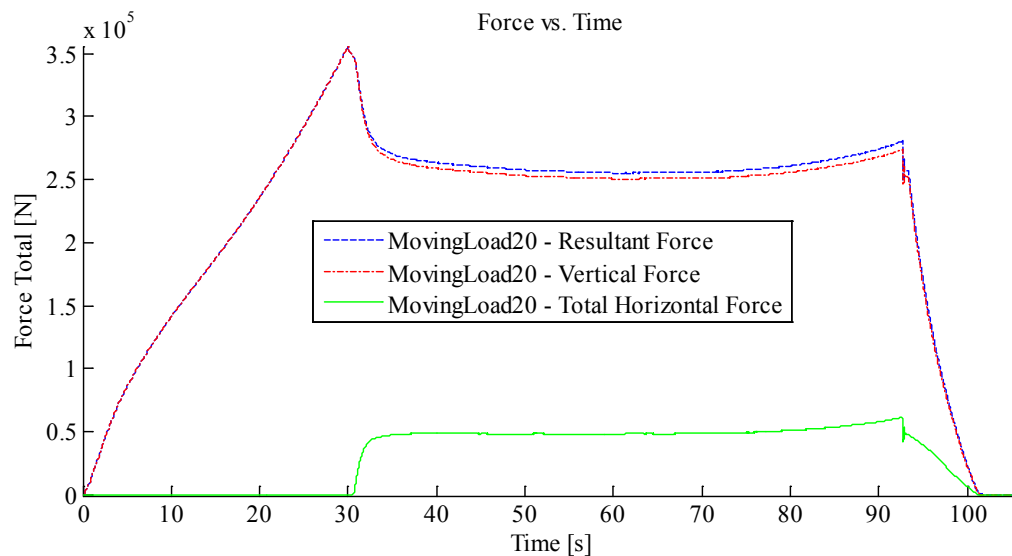
HStarting Point: Centre (.46 cm (0 cm nominal))
HSpeed: ~10 mm/s (Nominal)
H Travel: Centre to End (55+ cm)

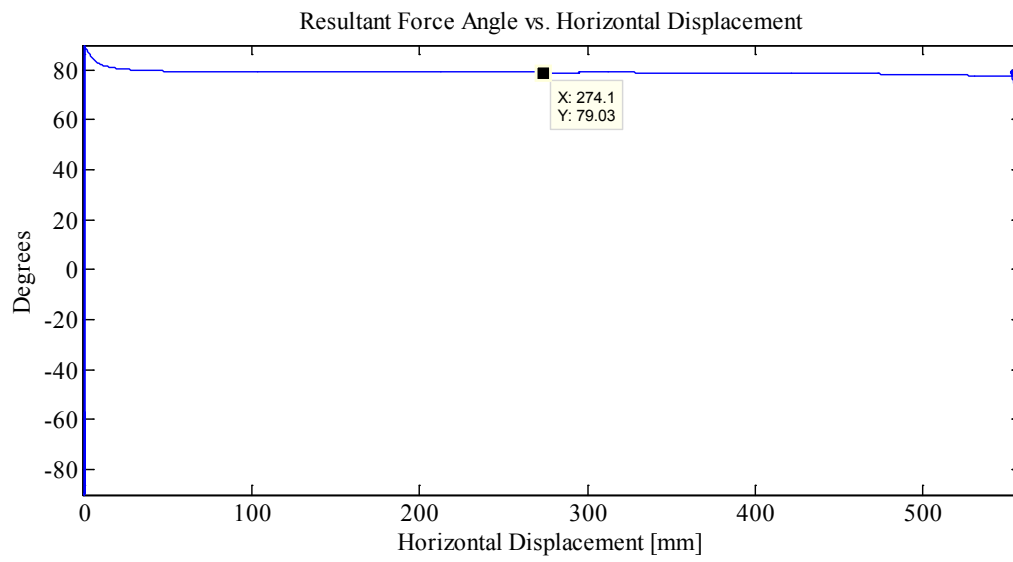
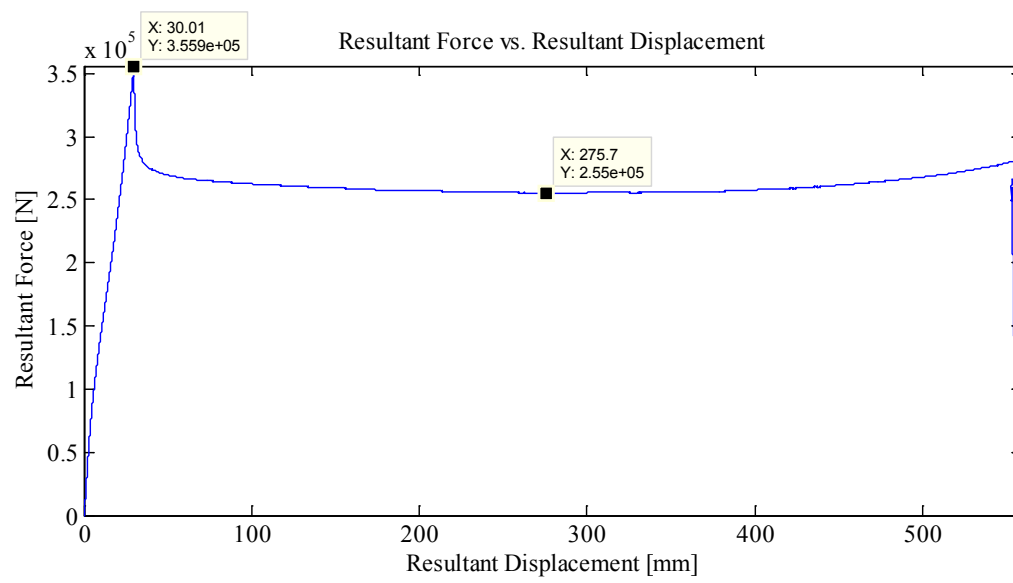
Vstarting Point: 8.90 mm
VSpeed: 1.0 mm/s (nominal)
V Travel: 30 mm
V Stopping Point: -21.1 mm

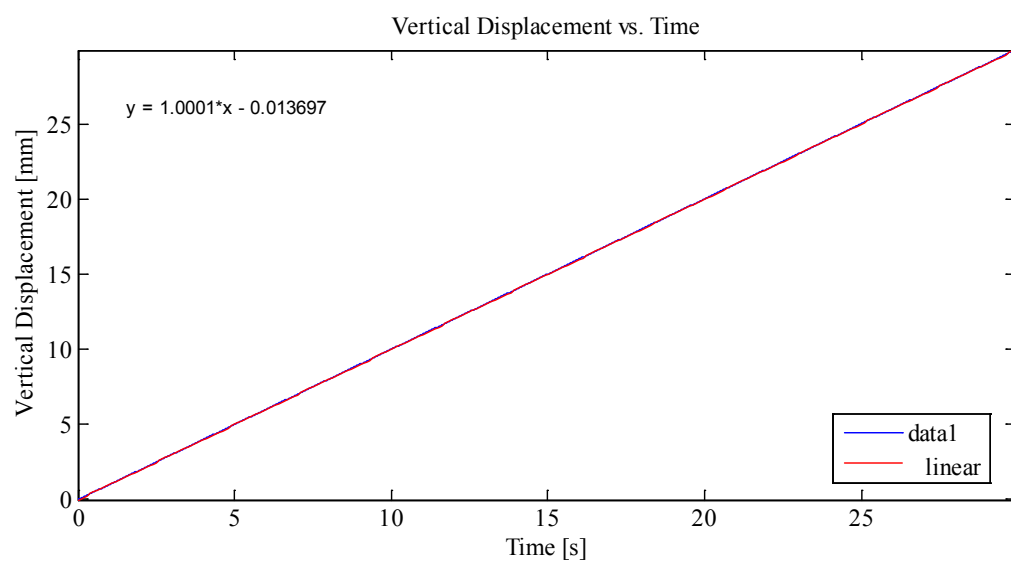
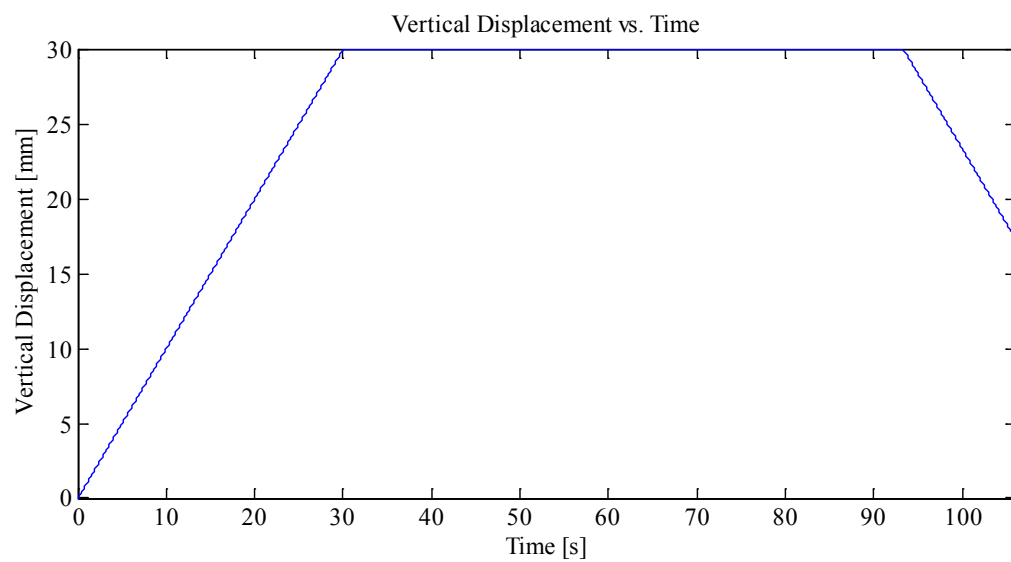
Notes:

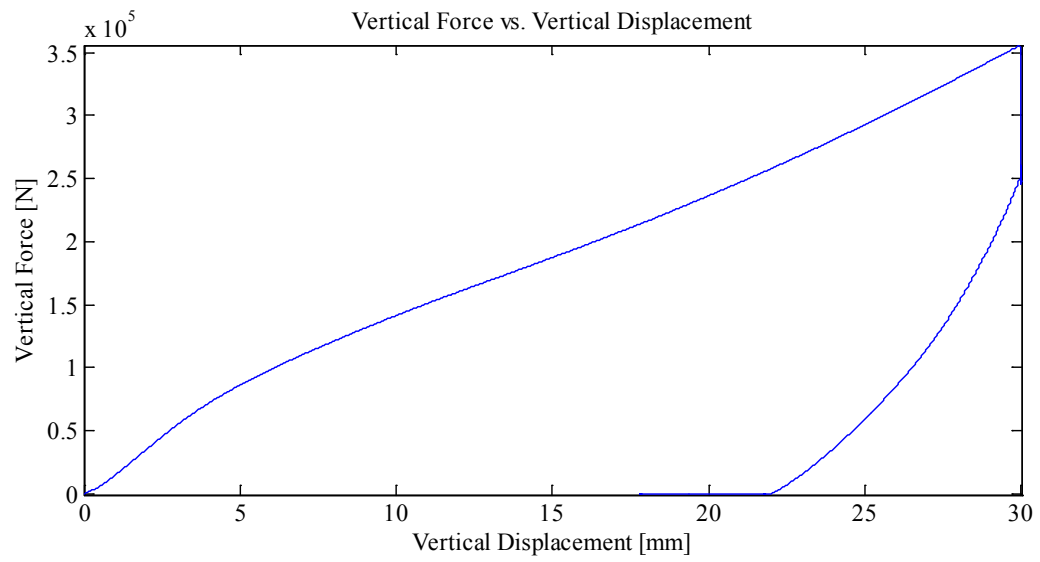
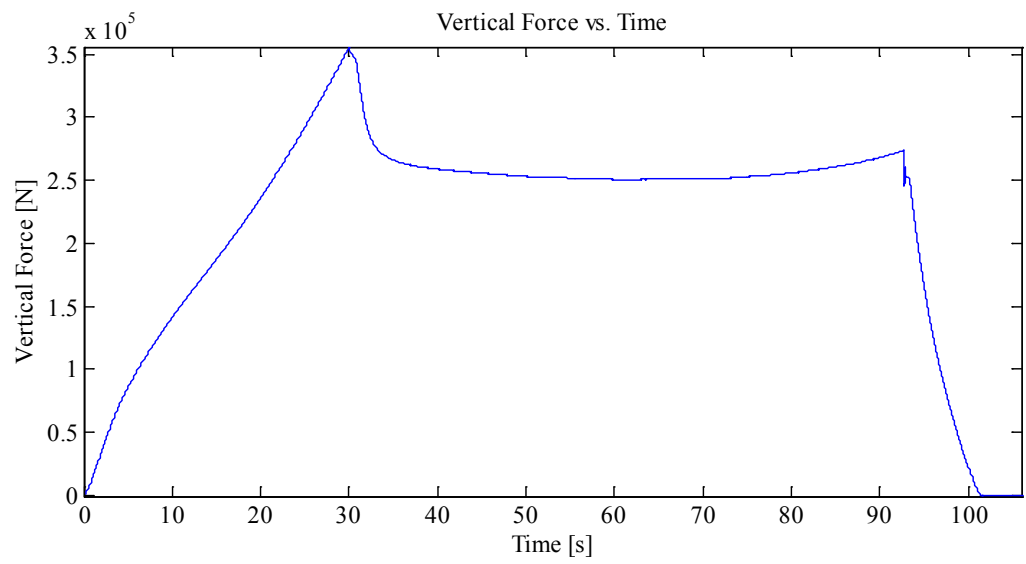
Indentation 1: ~30 mm, In-Along-Out - Centre to End
Data from Indentation 1 saved as MovingLoad20

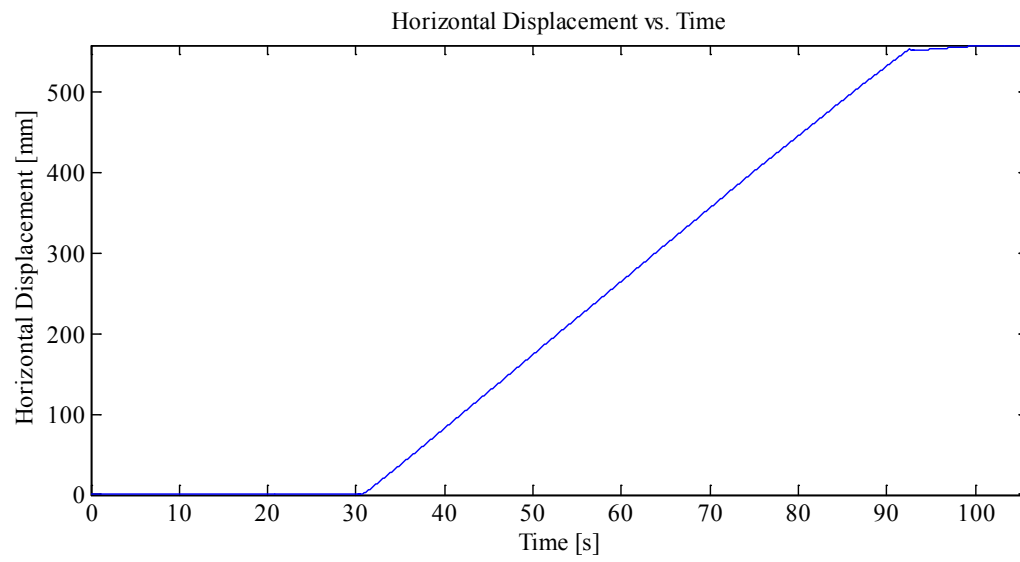
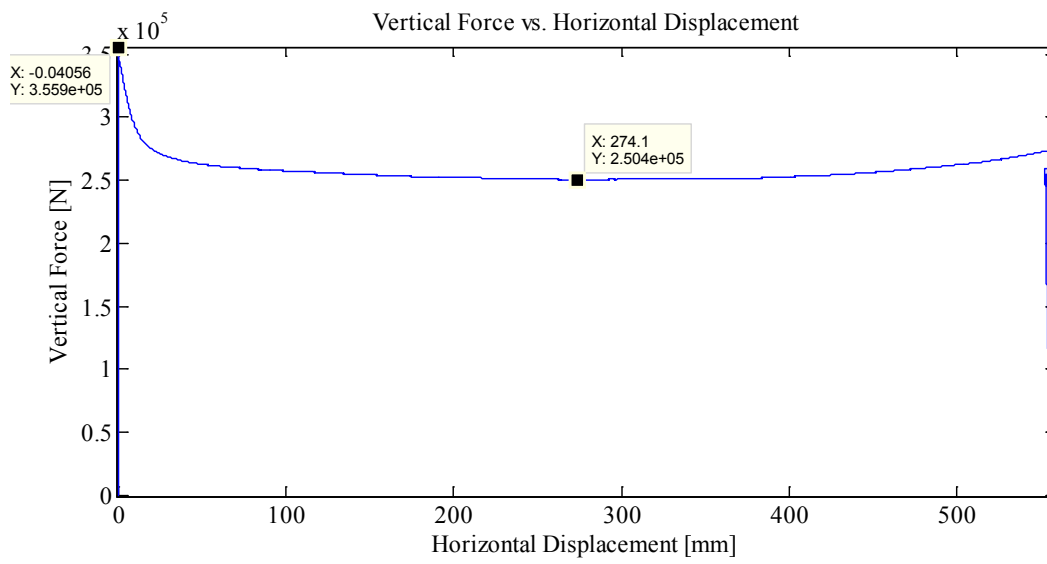
Plots:

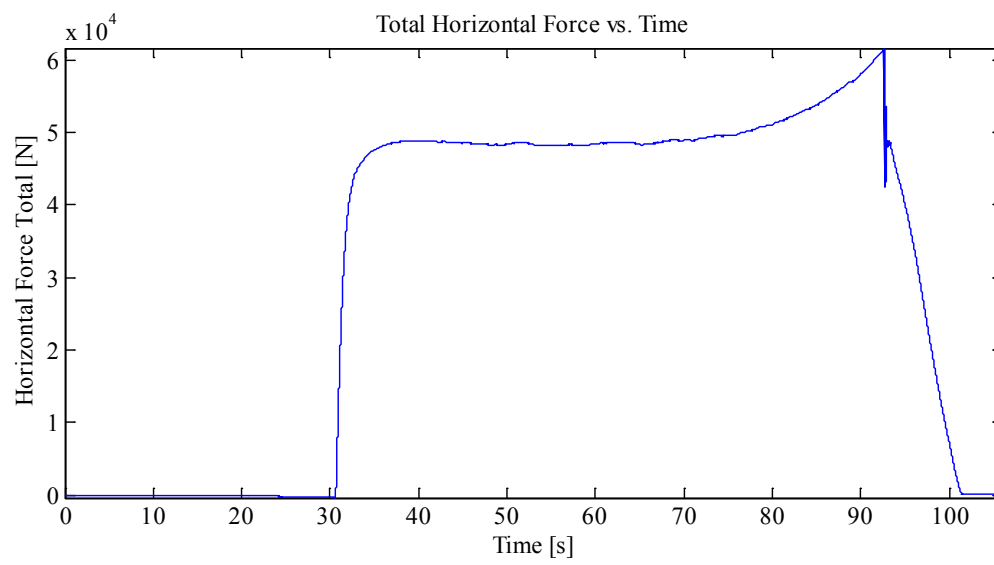
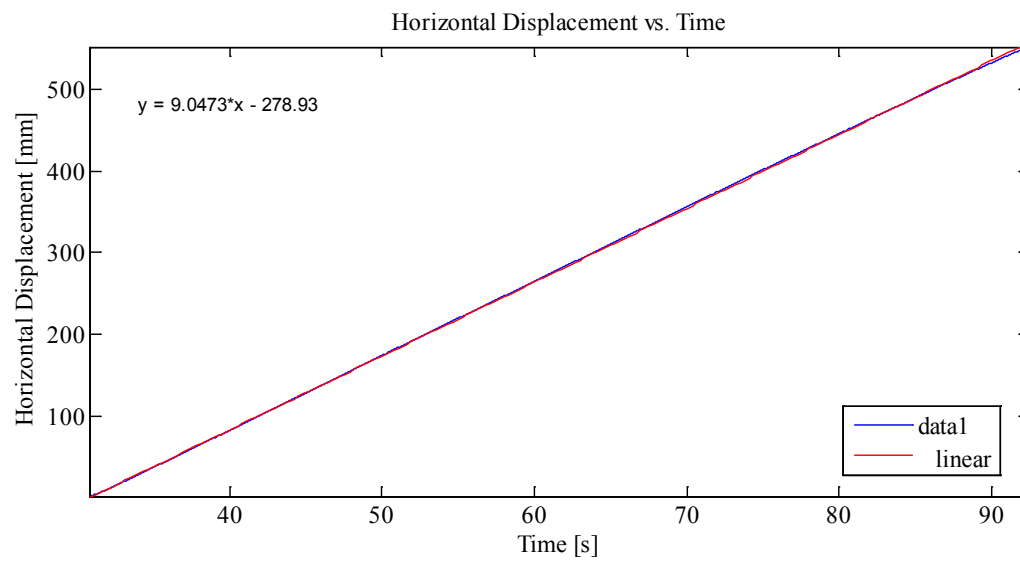


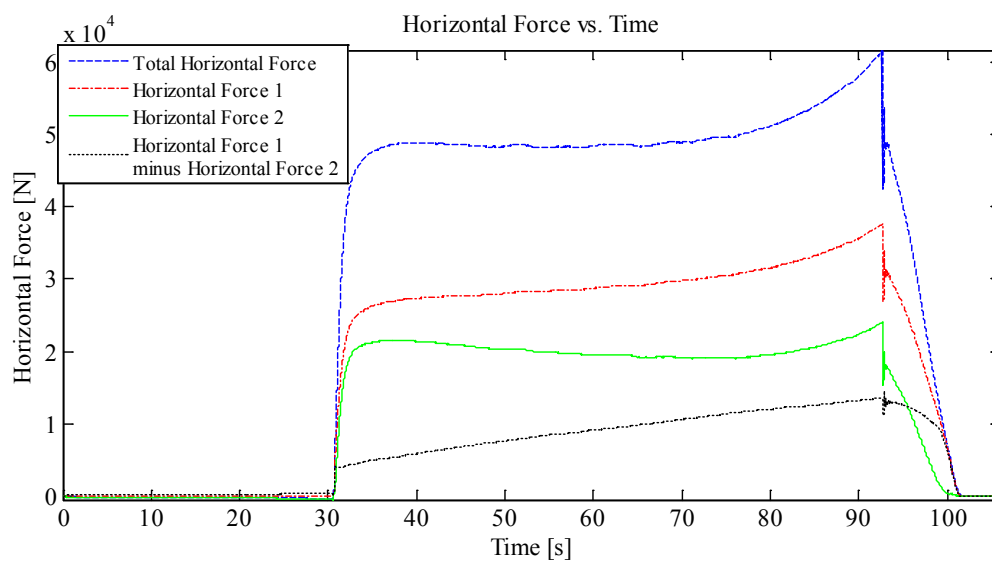
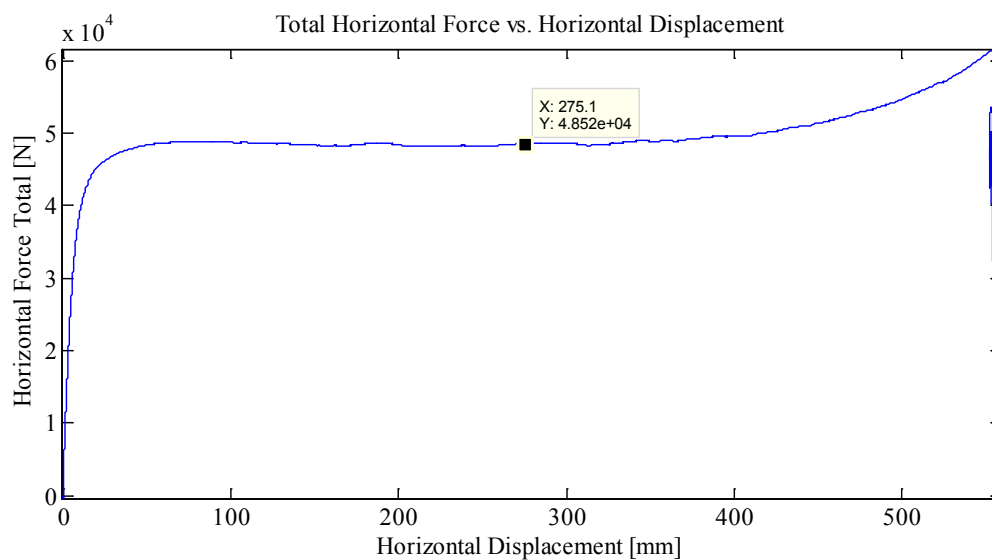












Appendix C2.3.1 – MovingLoad21

April 10, 2014 at ~1:00 p.m.

Run # 14
Run Type: Full Length – Slow
Room-temperature: -10°C
Sample Type: 1/2" Plate
Test Type: In-Along-Out End to End

HStarting Point: End (-54.21 cm (-55 cm nominal))
HSpeed: 10 mm/s (Nominal)
H Travel: End to End (110+ cm)

Vstarting Point: 9.6 mm
VSpeed: 1.0 mm/s (Nominal)
V Travel: 30 mm
V Stopping Point: -20.4 mm

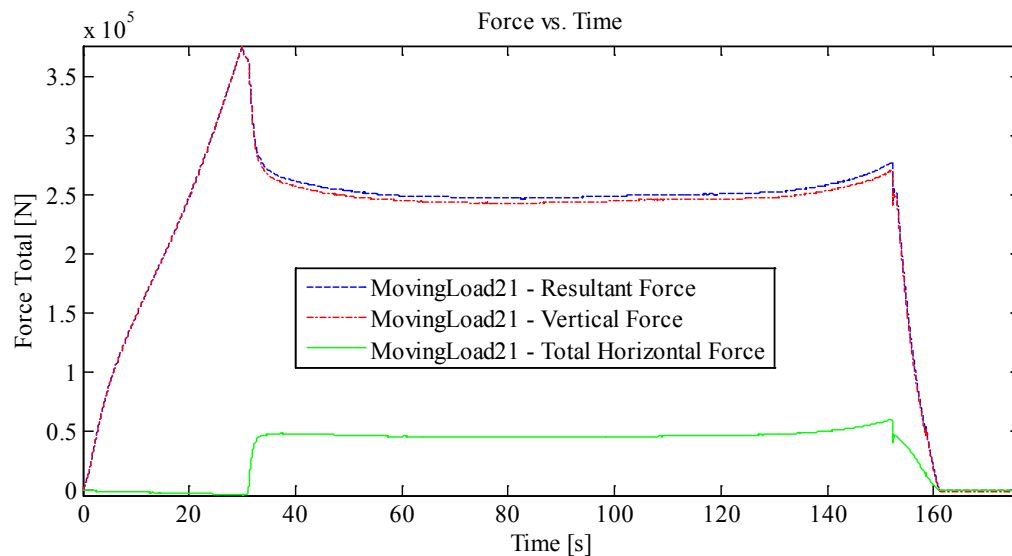
Notes:

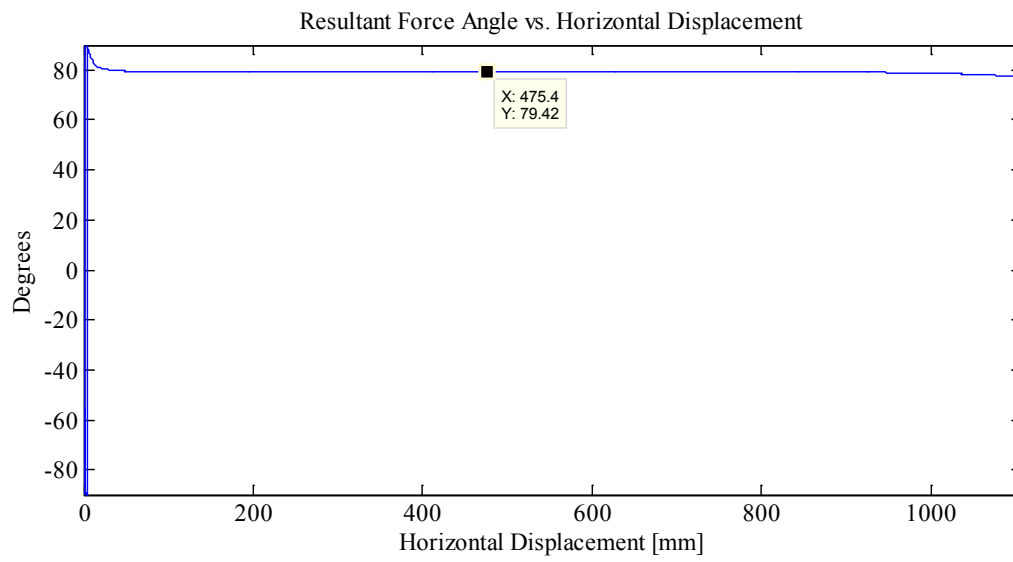
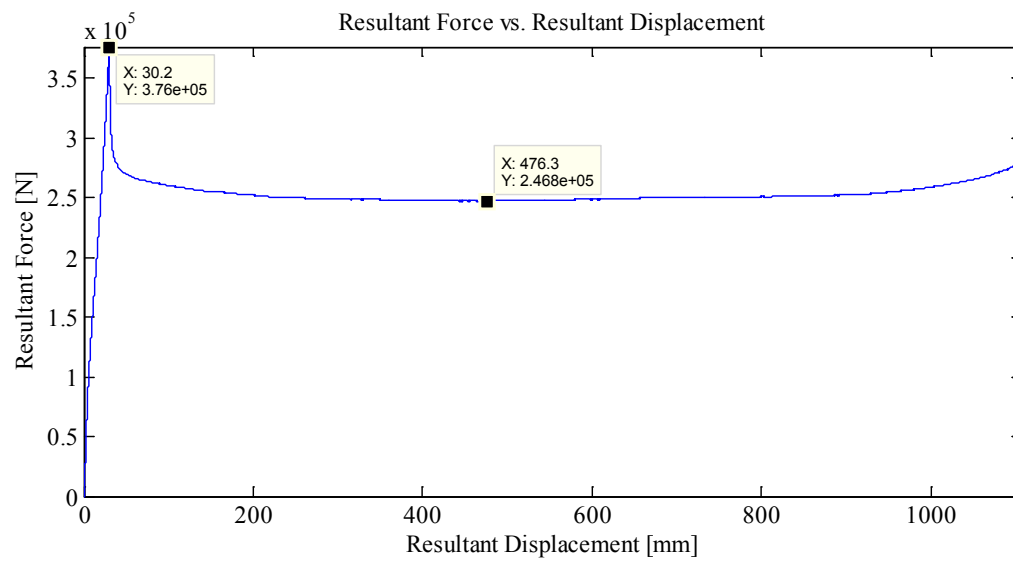
- Indentation 1: ~30 mm, In-Along-Out - End to End

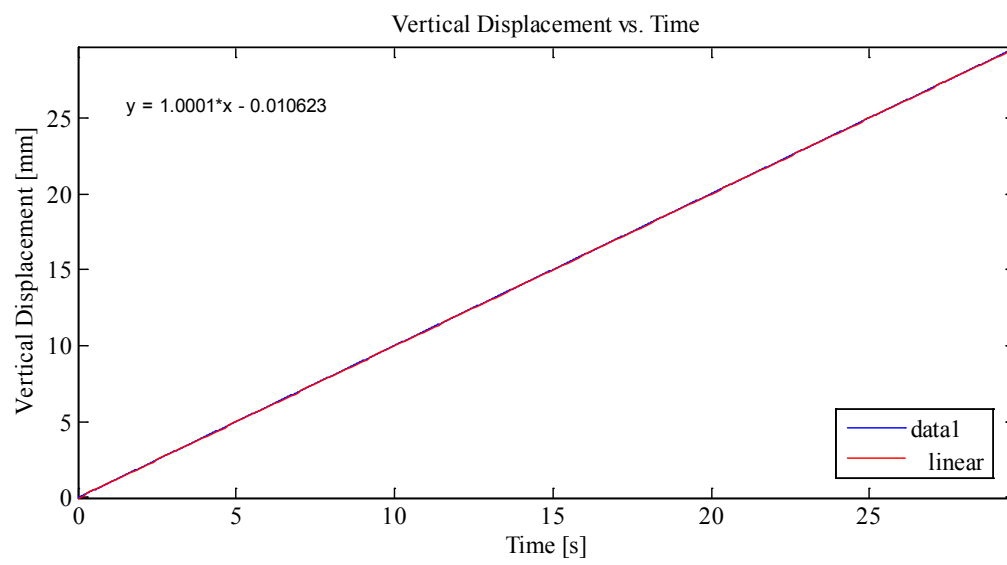
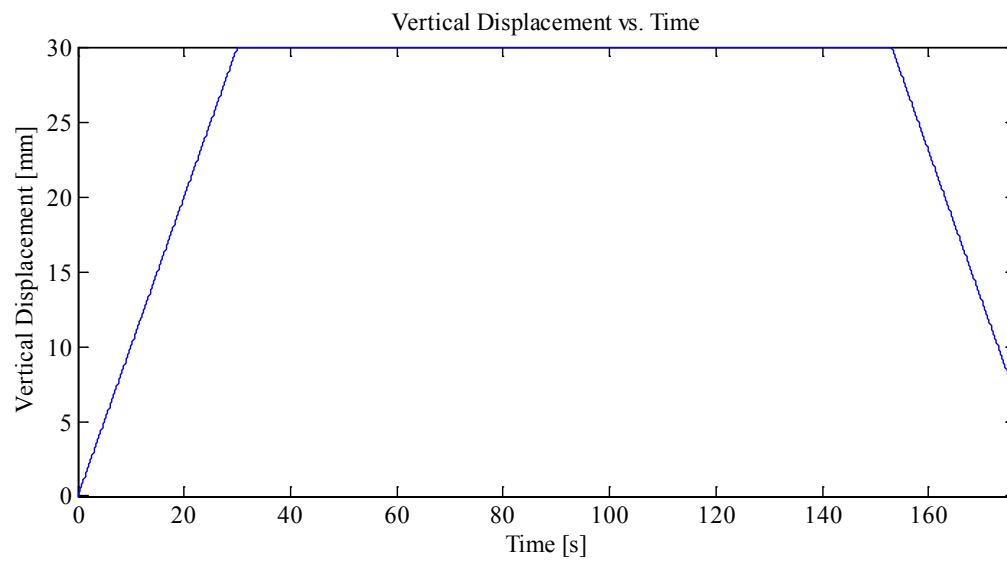
Data from Indentation 1 saved as MovingLoad21

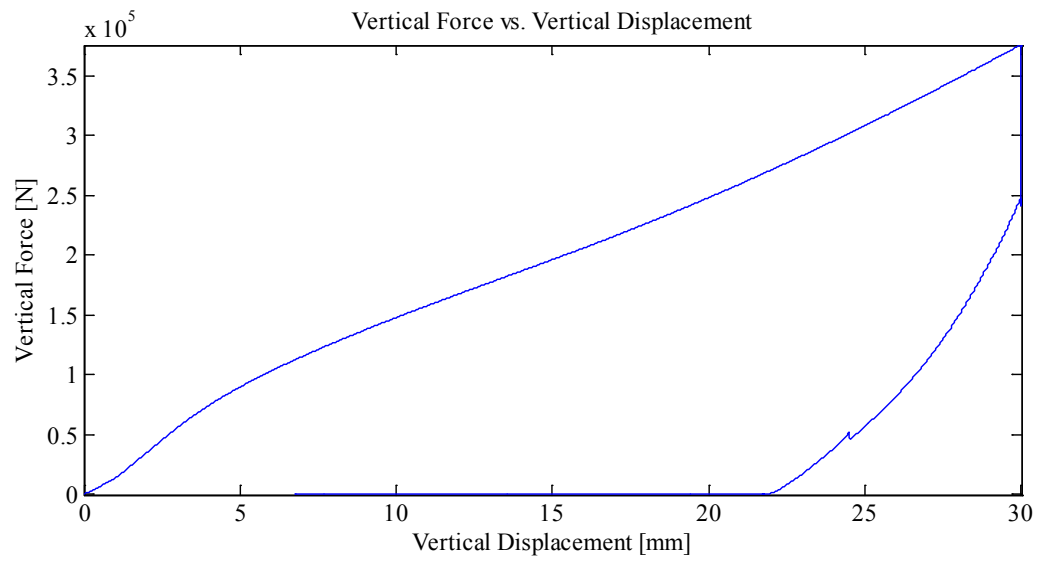
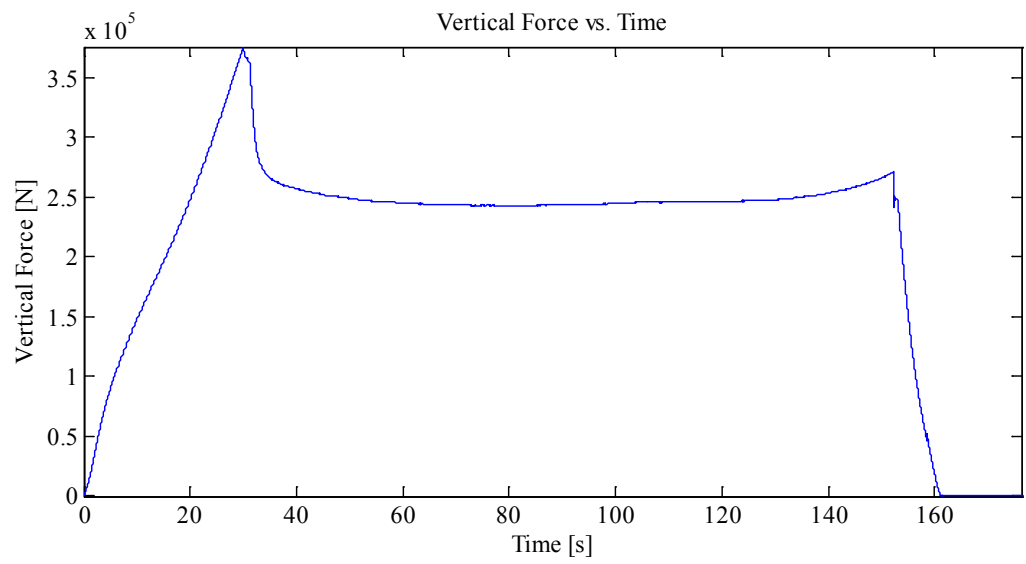
- Temperature varied between -8.5°C and -7.8°C due to just entering defrost mode.
Steel probably colder than air temperature.

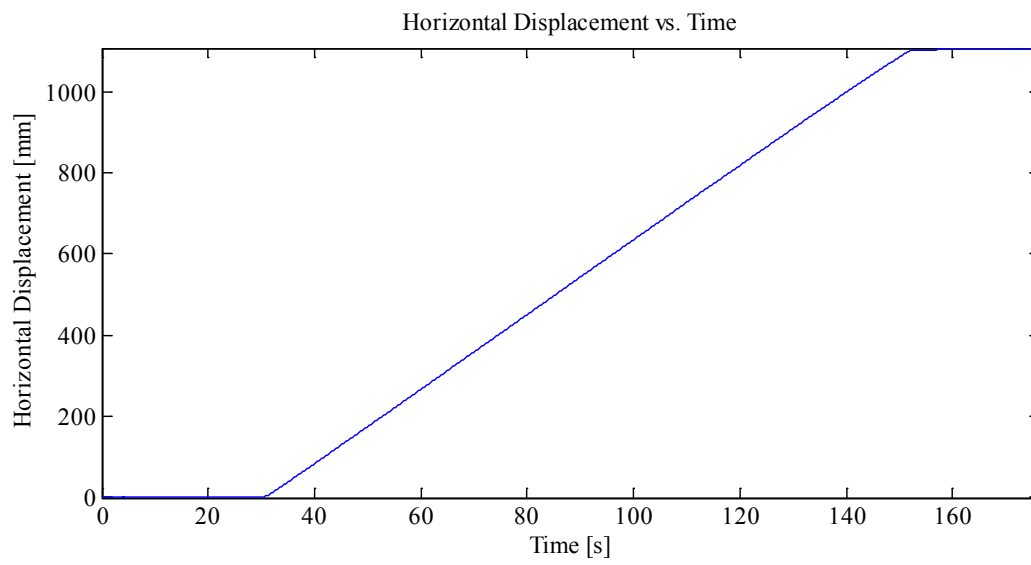
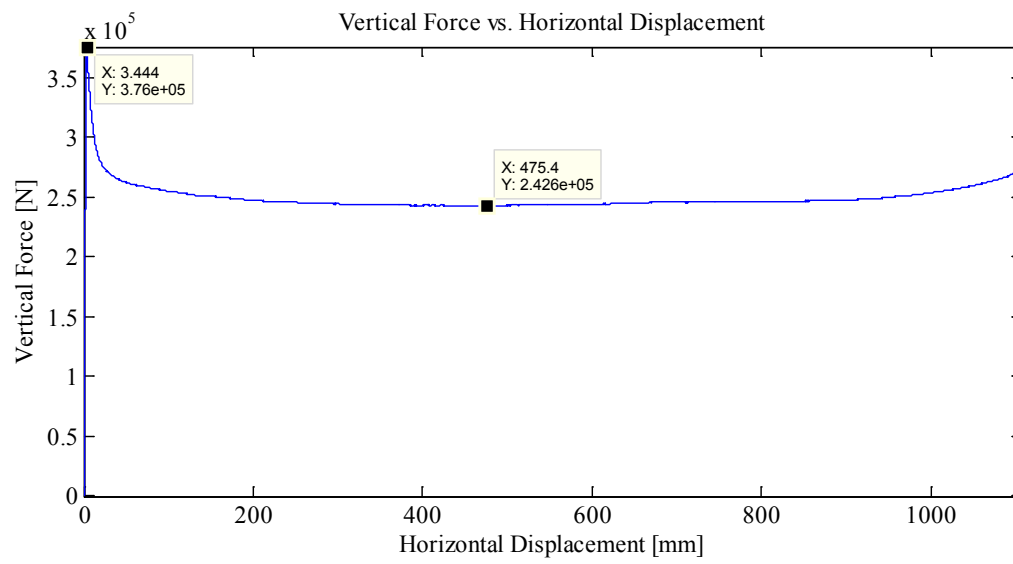
Plots:

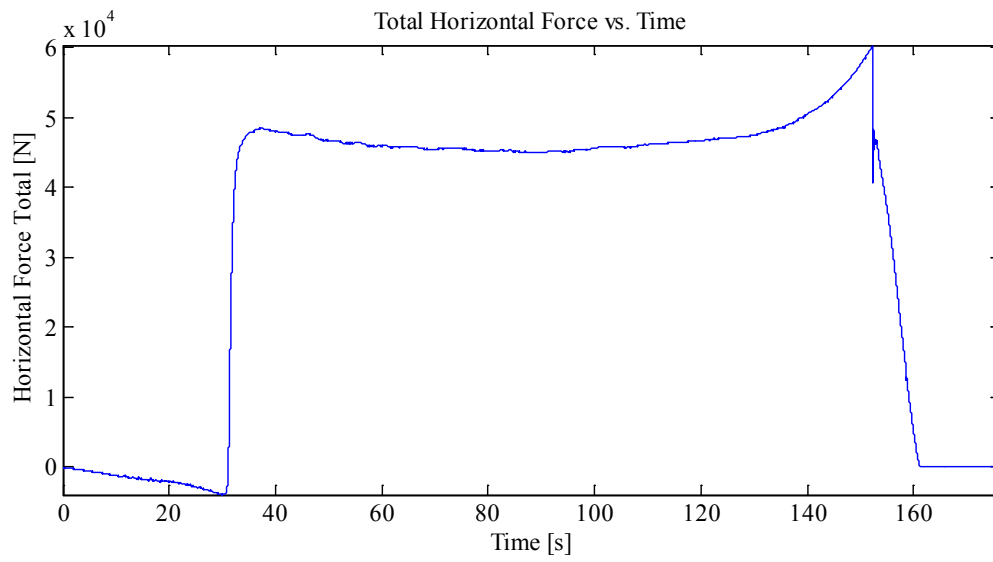
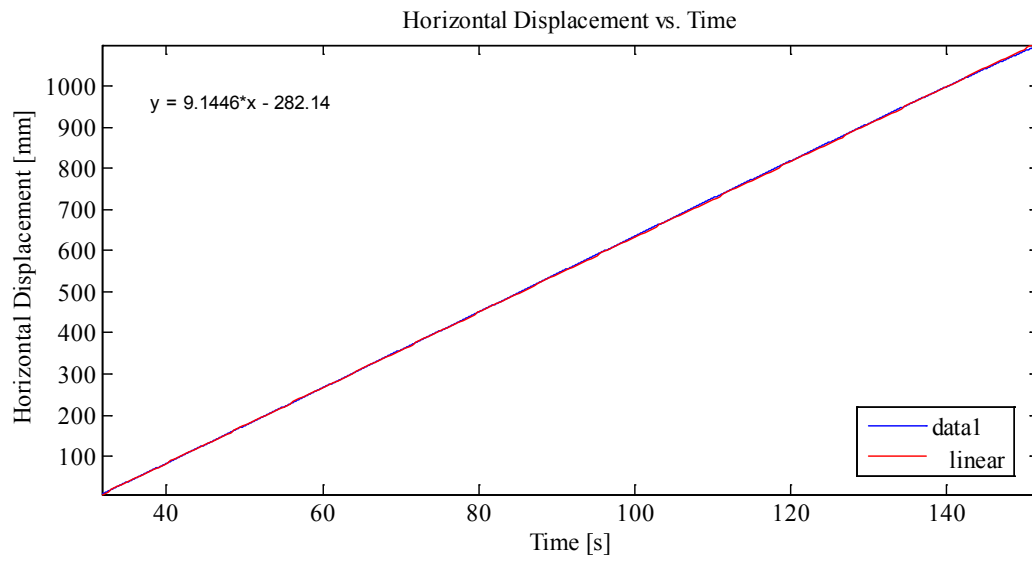


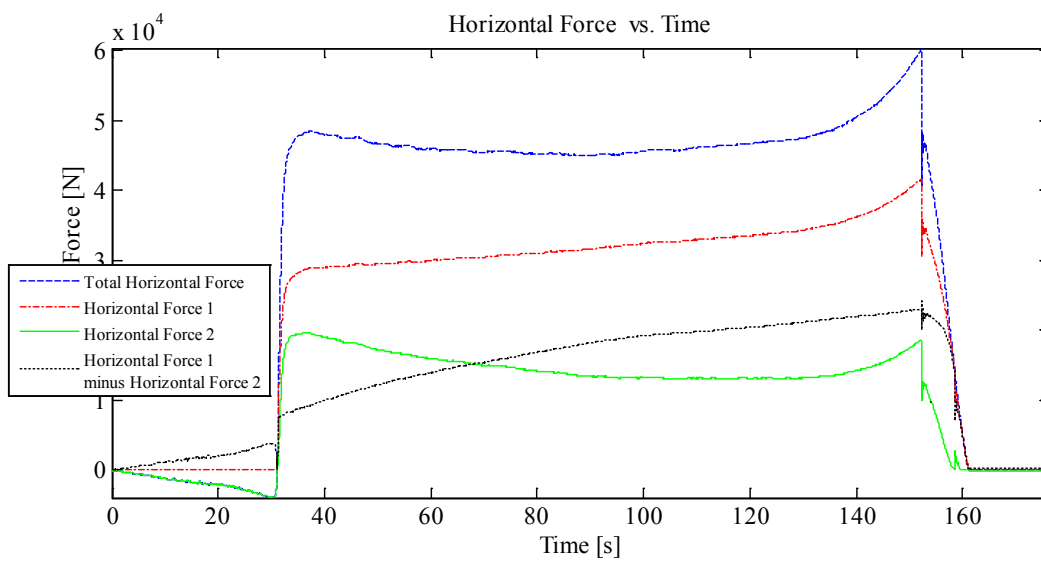
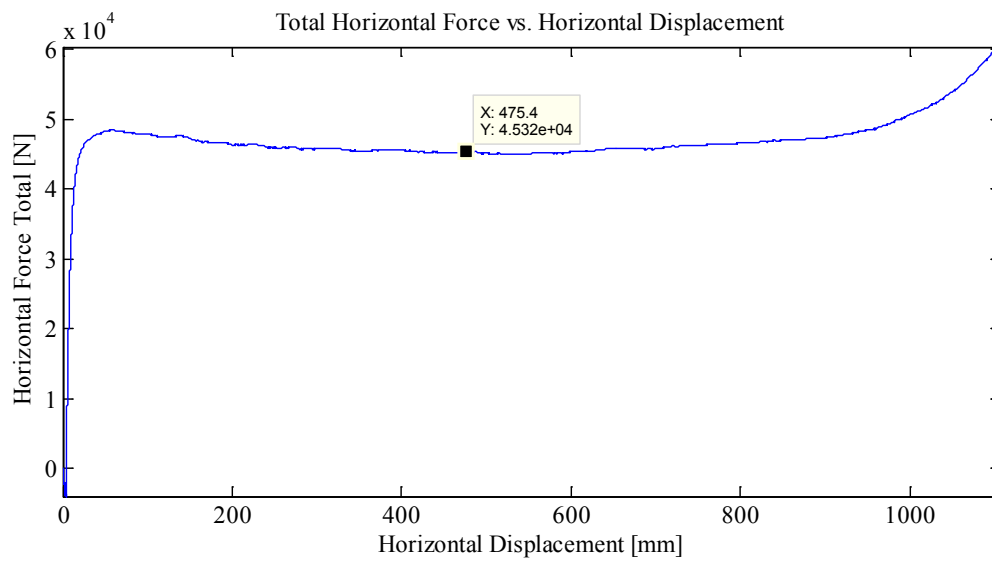












Appendix C2.3.2 – MovingLoad22

April 14, 2014 at ~1:20 p.m.

Run # 15
Run Type: Fast
Room-temperature: -10°C
Sample Type: 1/2" Plate
Test Type: In-Along-Out Centre to End

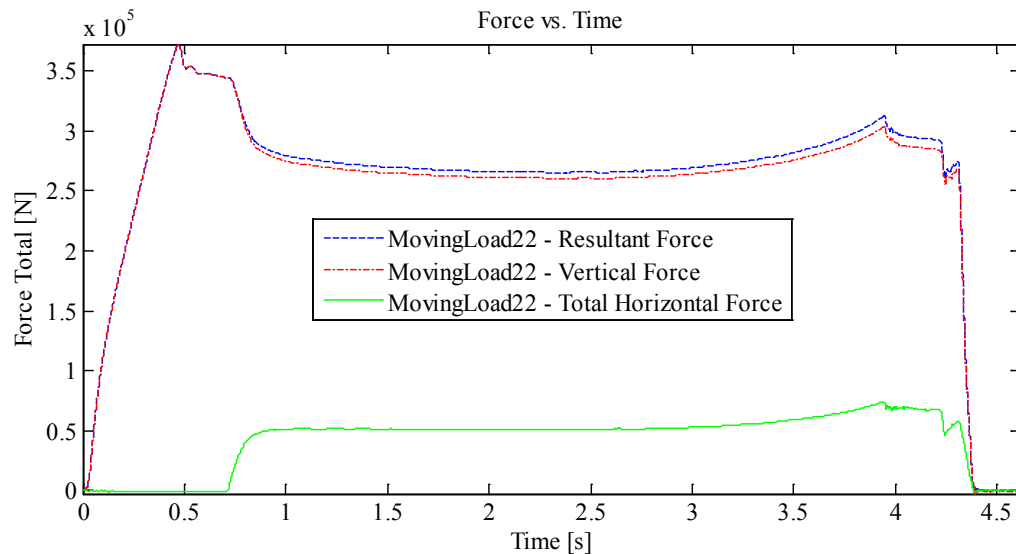
HStarting Point: Centre (0.5 cm (0 cm nominal))
HSpeed: Fastest (Nominal)
H Travel: Centre to End (55+ cm)

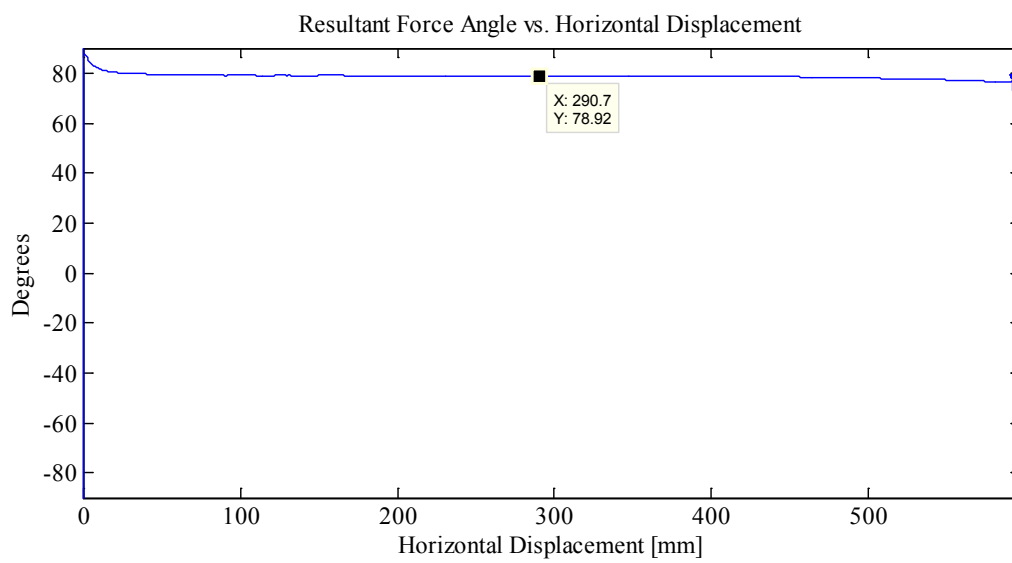
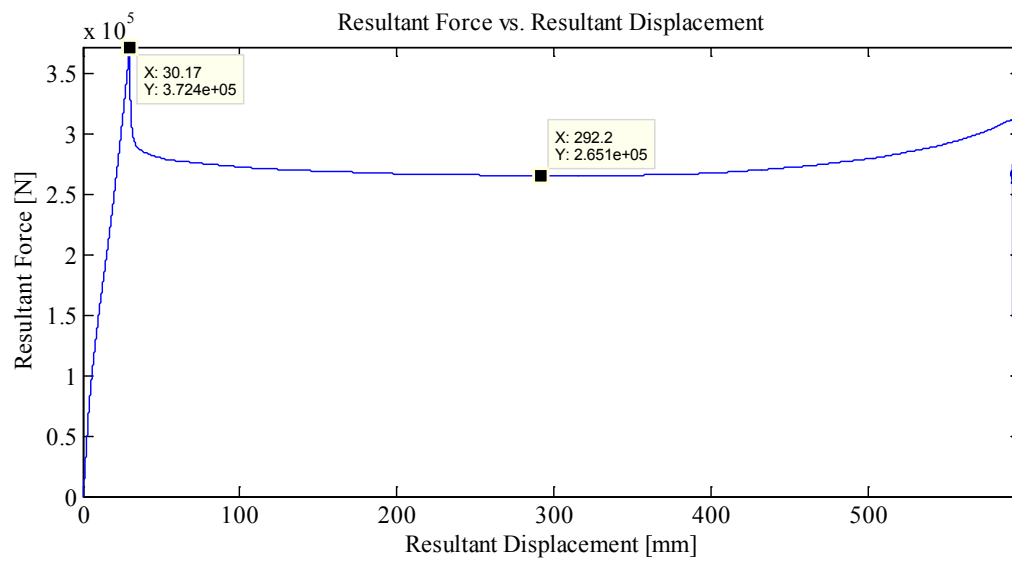
Vstarting Point: 8.91 mm
VSpeed: Fastest mm/s (nominal)
V Travel: 30 mm
V Stopping Point: -21.09 mm

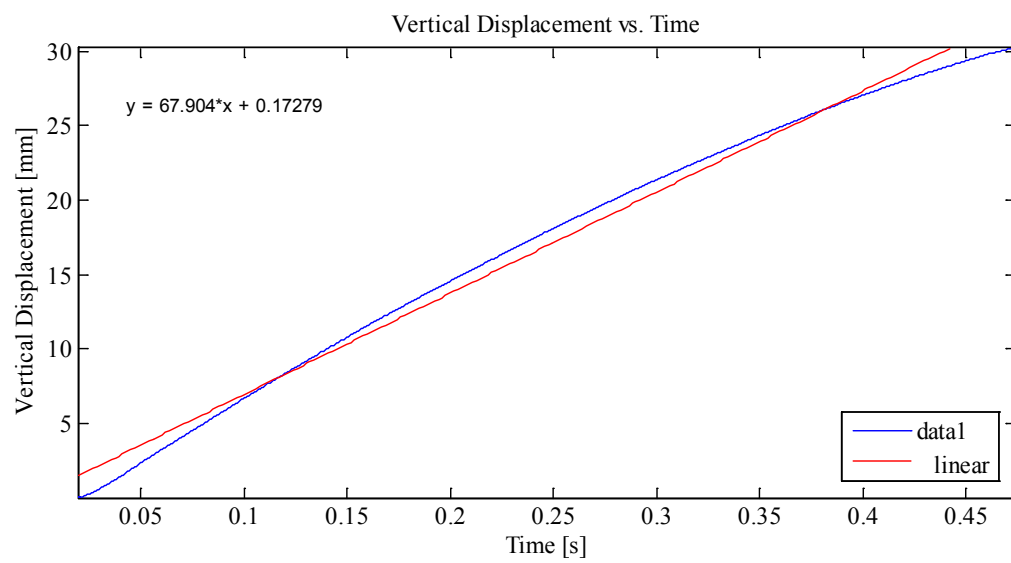
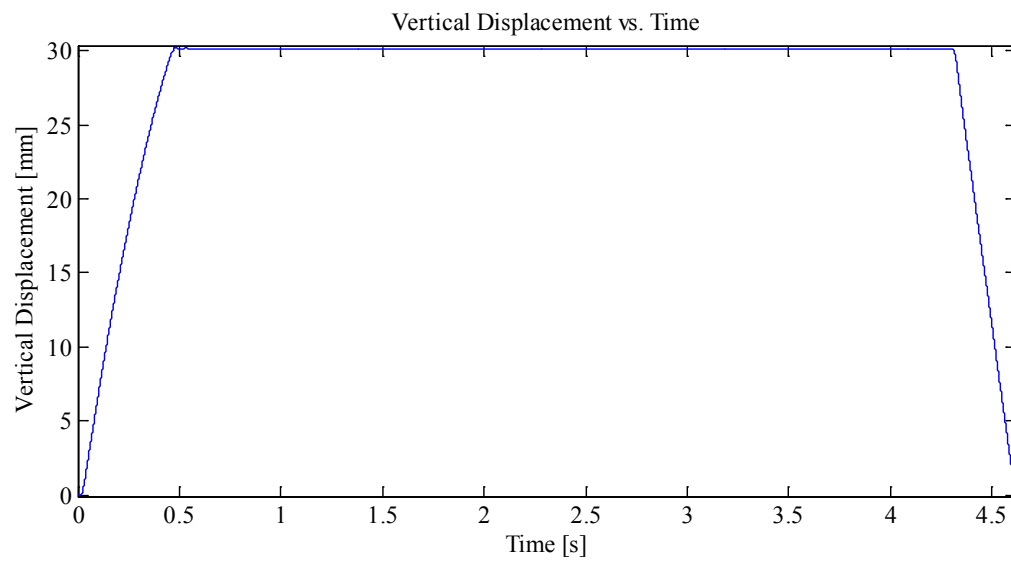
Notes:

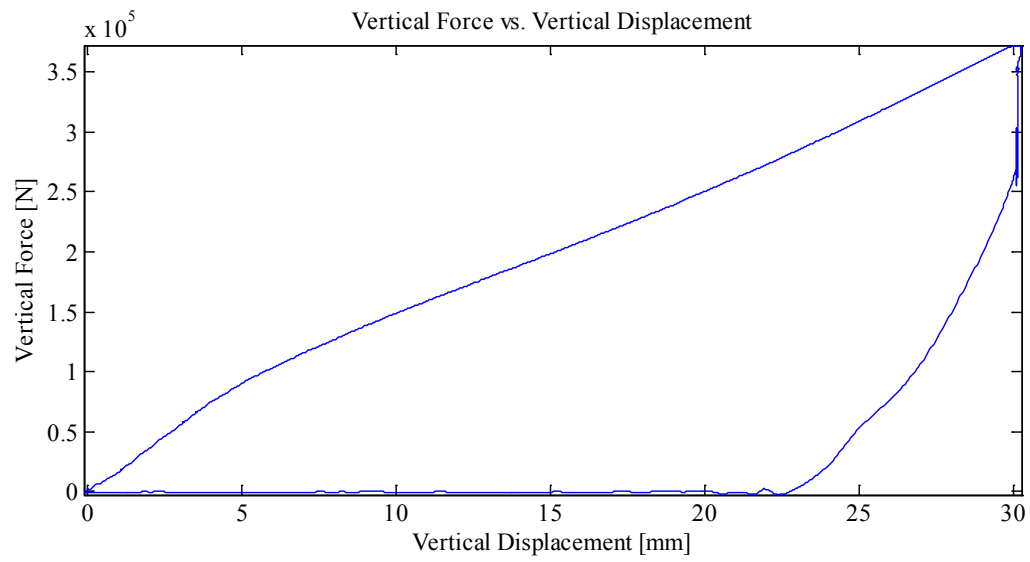
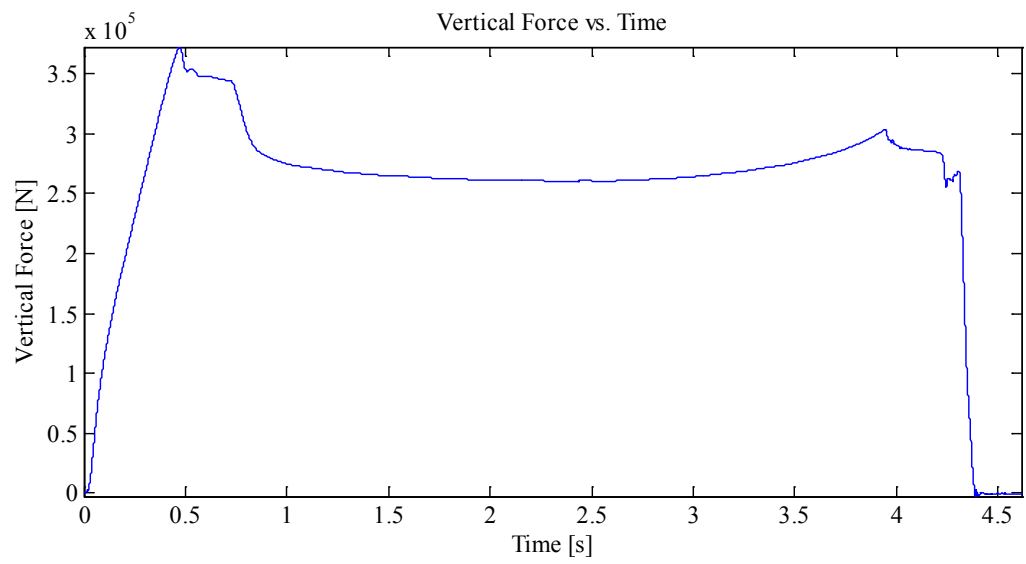
Indentation 1: ~30 mm, In-Along-Out - Centre to End
Data from Indentation 1 saved as MovingLoad22

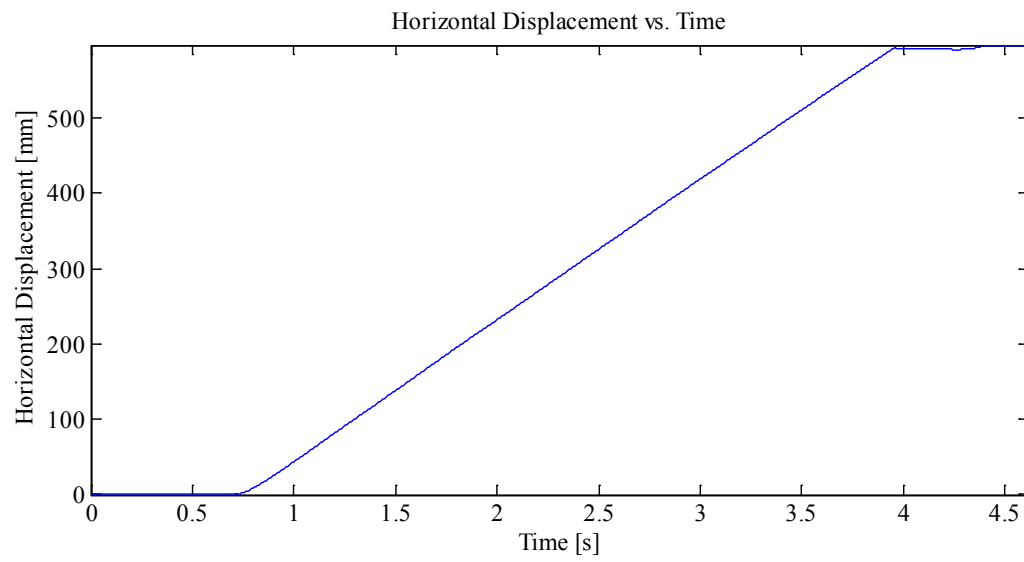
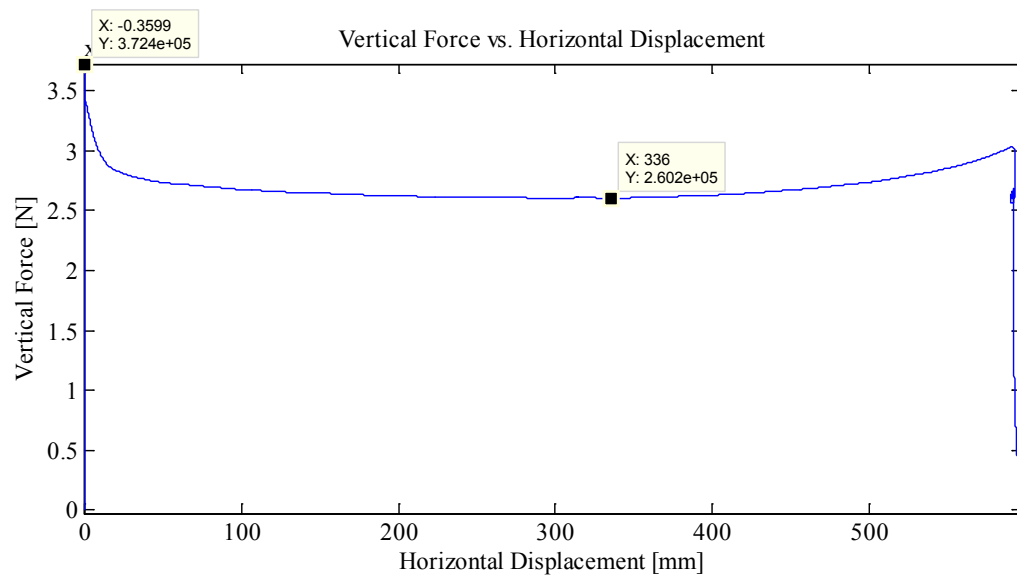
Plots:

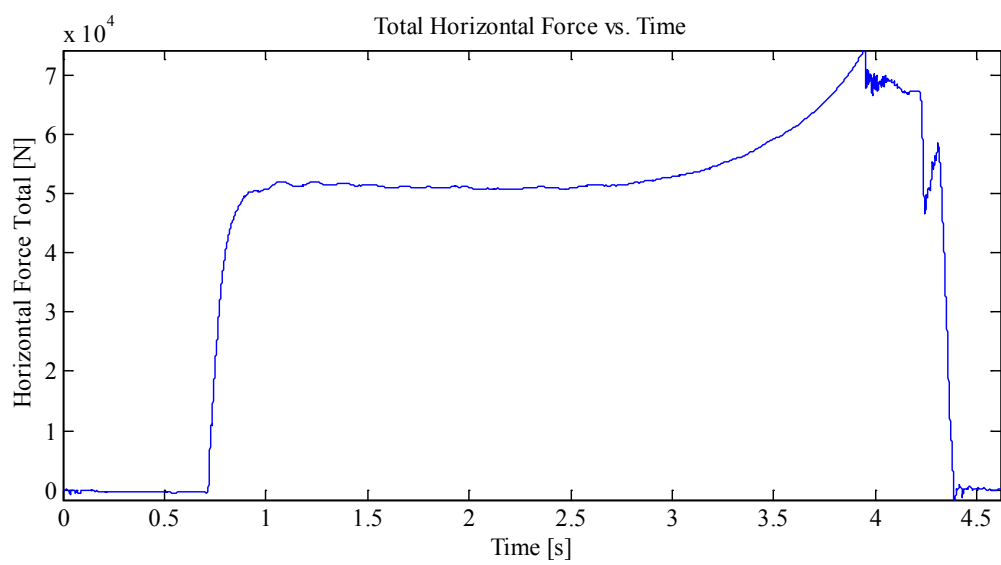
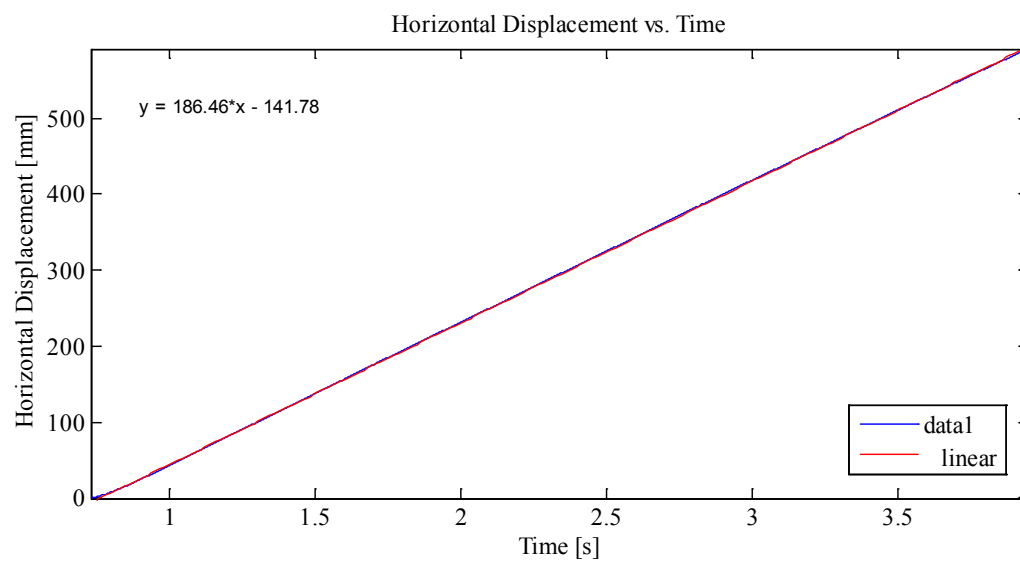


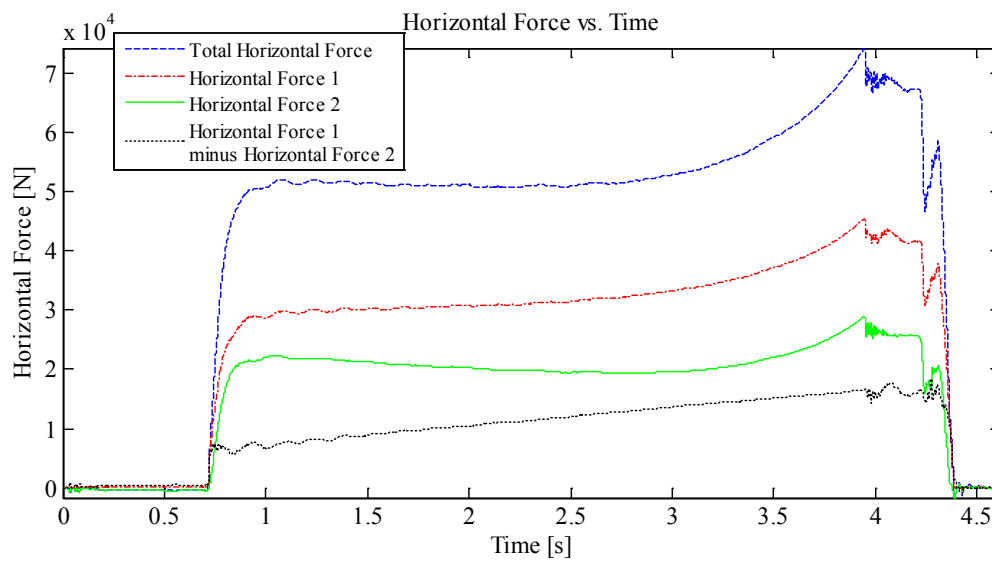
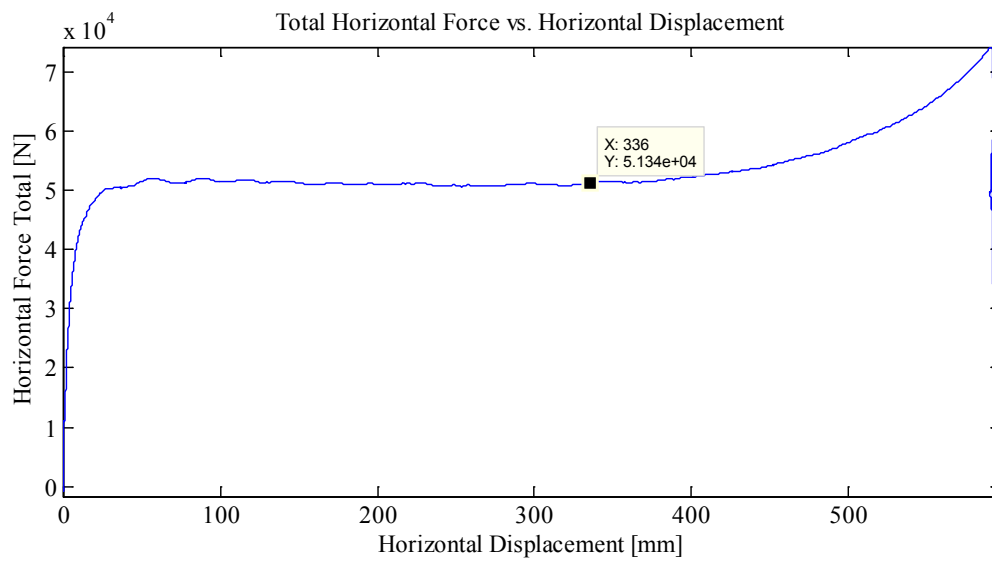








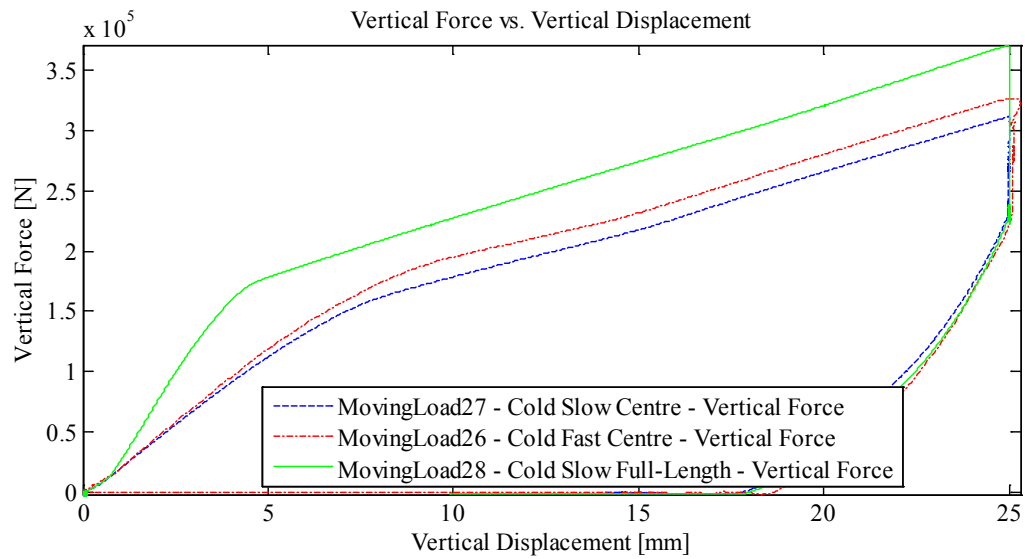
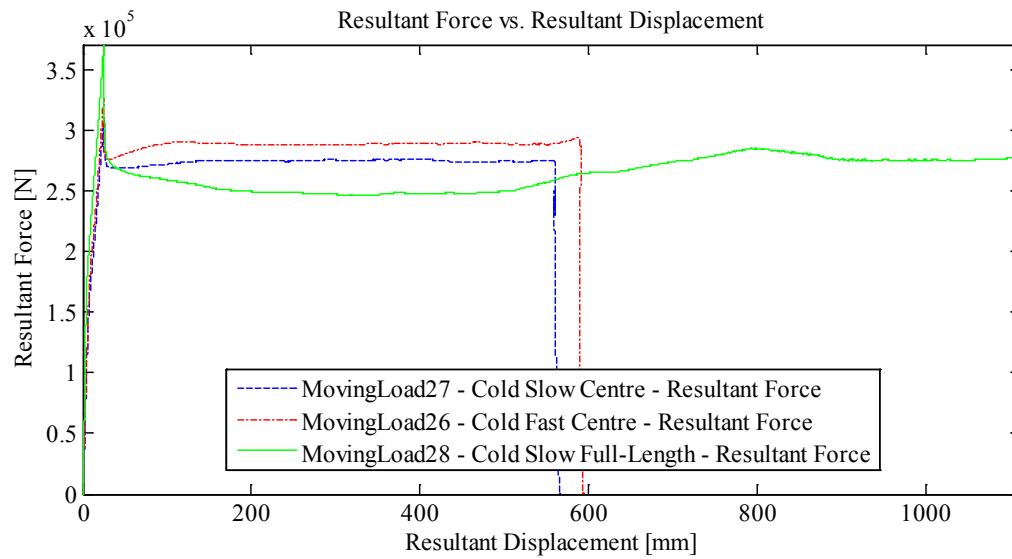


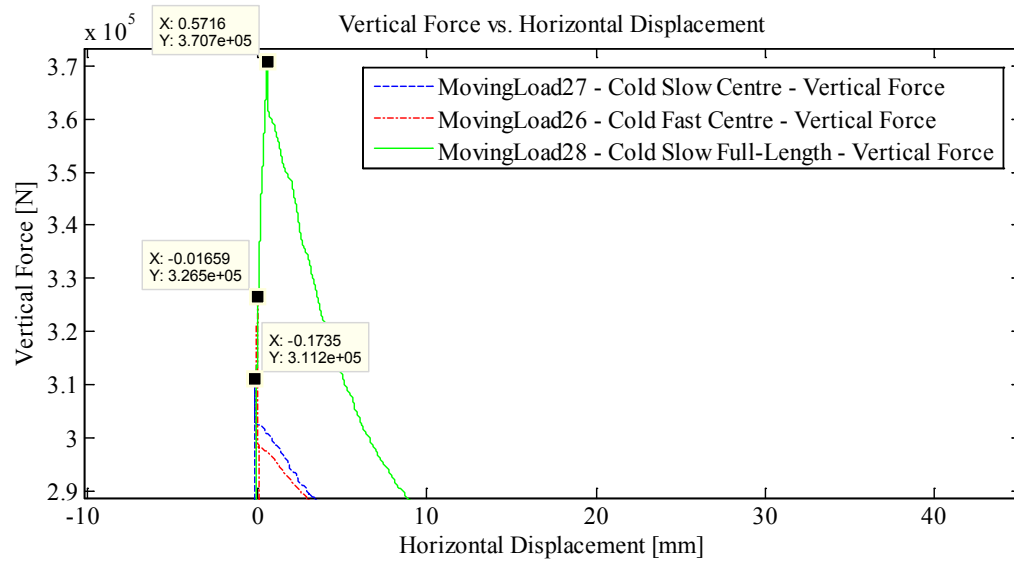
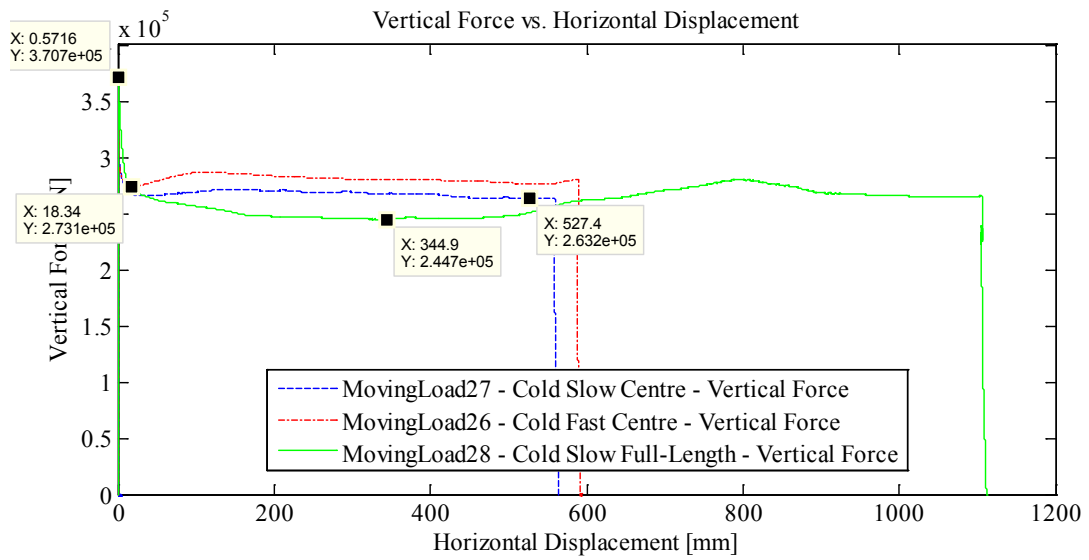


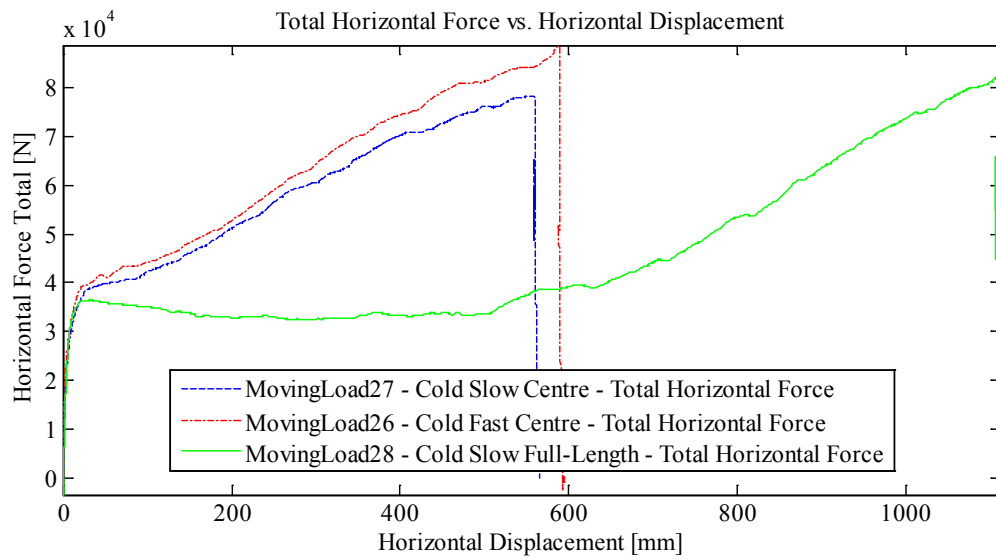
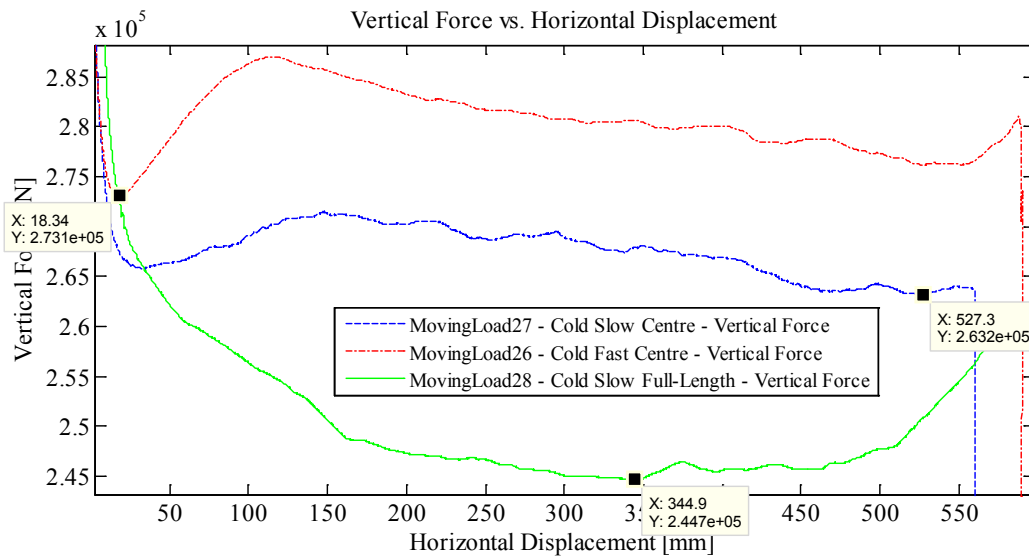
Appendix C2.4 – Frame – 2.5 cm Indentation

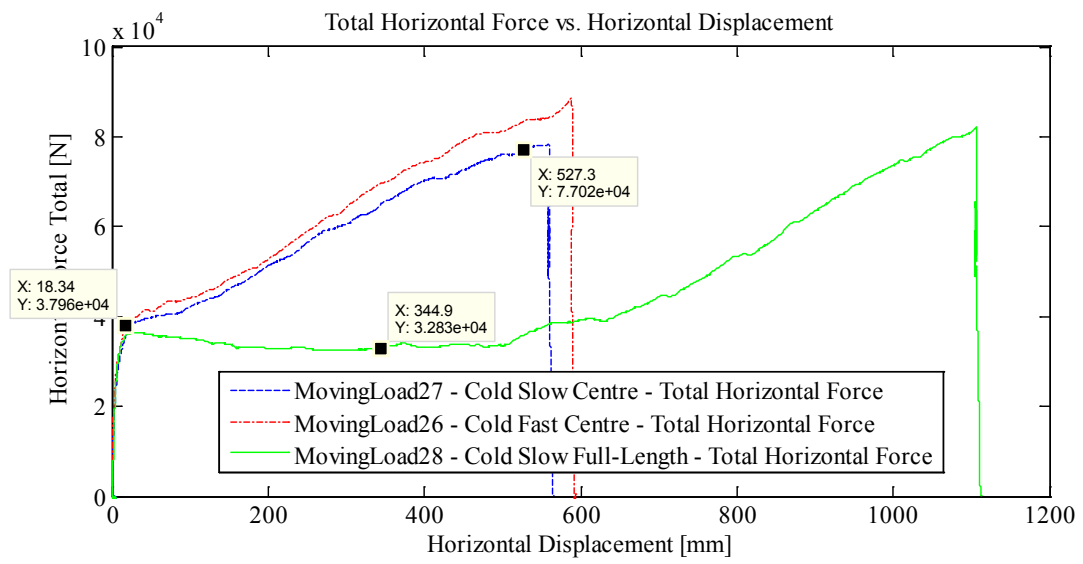
Appendix C2.4.1 – Summary Plots for Experiments ML 26, 27 and

28









Appendix C2.4.2 – MovingLoad26

April 16, 2014 at 4:10p.m.

Run # 19
Run Type: Fast
Room-temperature: -9.6°C (Measured with thermocouple)
Sample Type: Frame
Test Type: In-Along-Out Centre to End

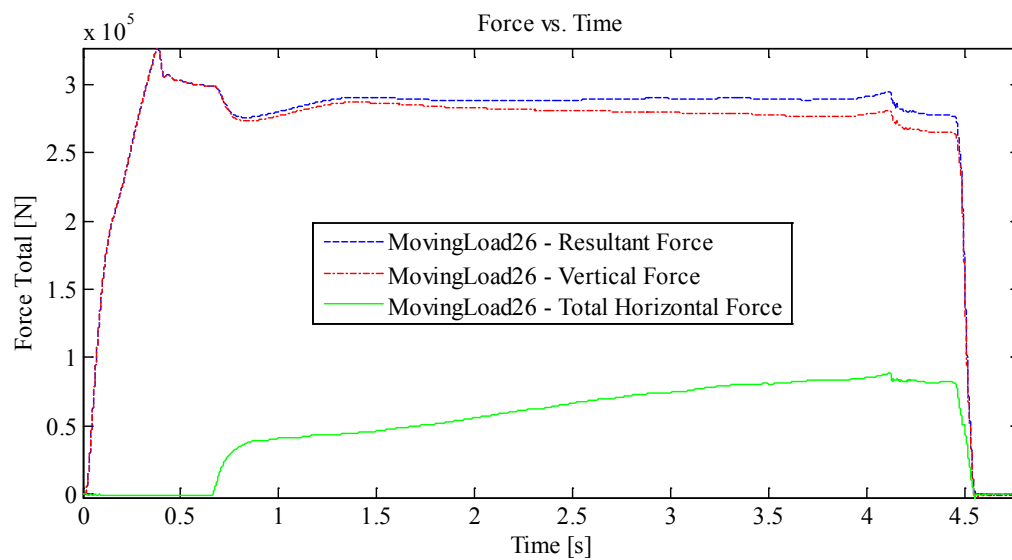
HStarting Point: Centre (0.70 cm (0 cm nominal))
HSpeed: Fastest
H Travel: Centre to End (55+ cm)

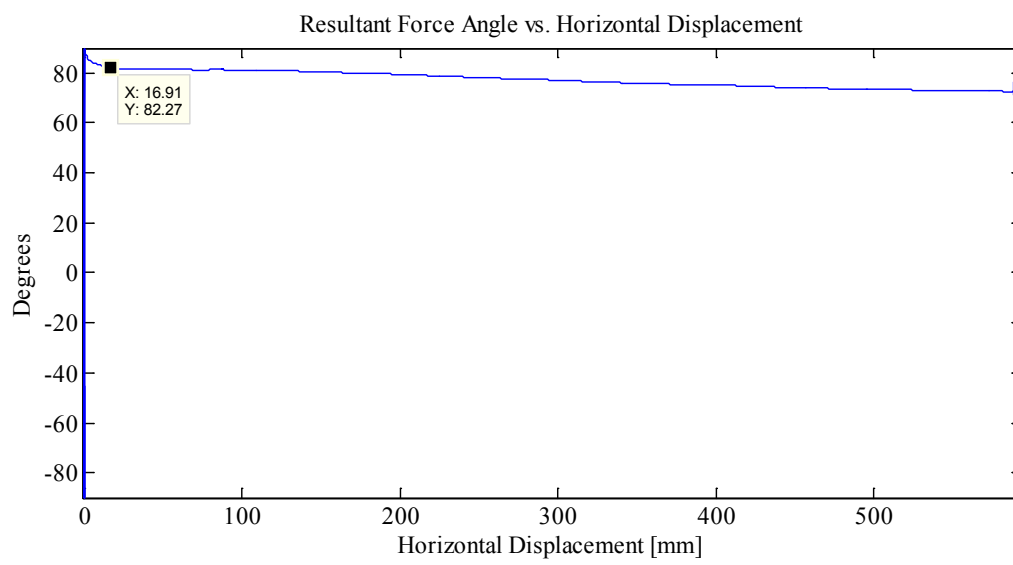
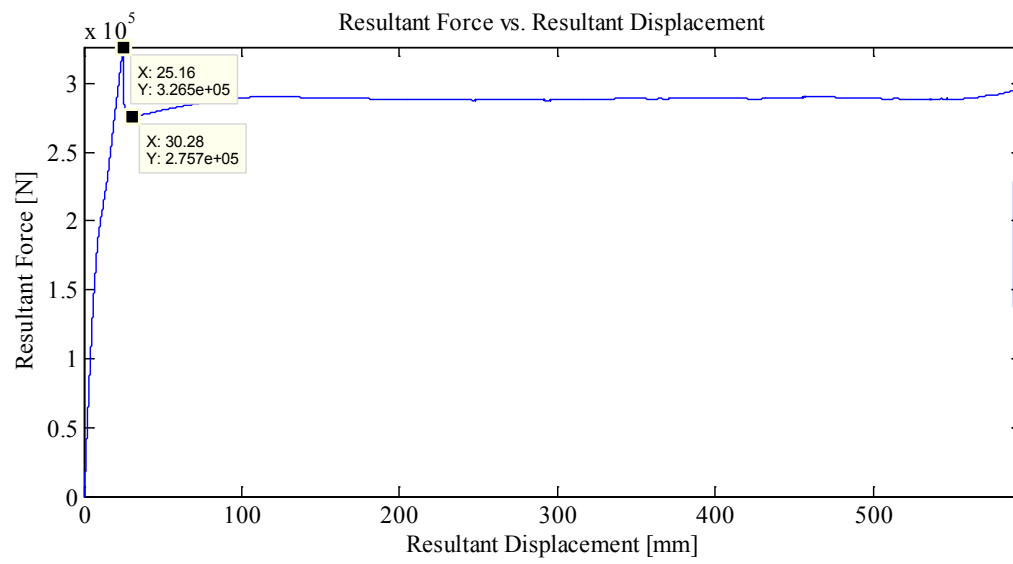
Vstarting Point: 4.01 mm
VSpeed: Fastest (nominal)
V Travel: 25 mm
V Stopping Point: -20.99 mm

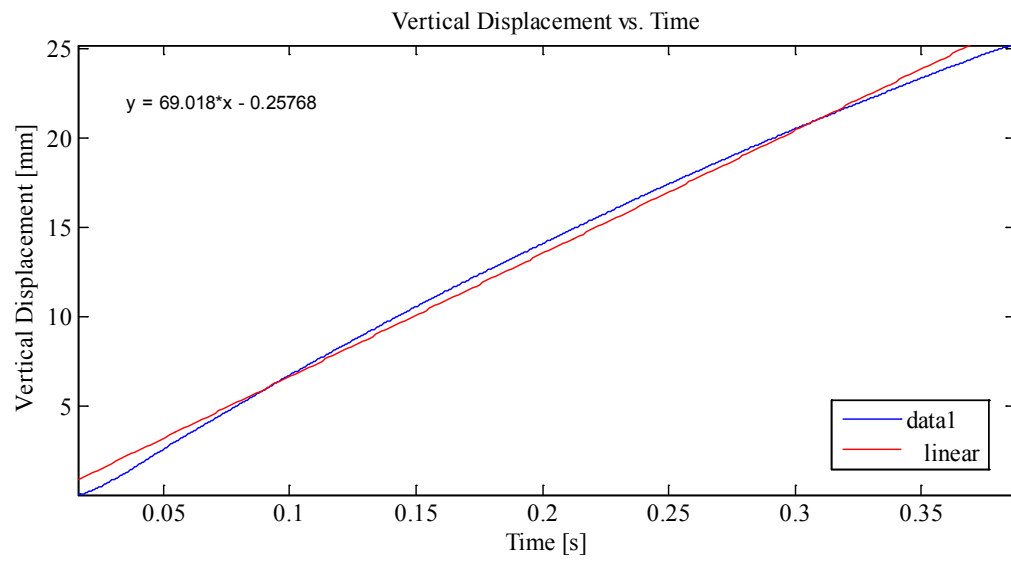
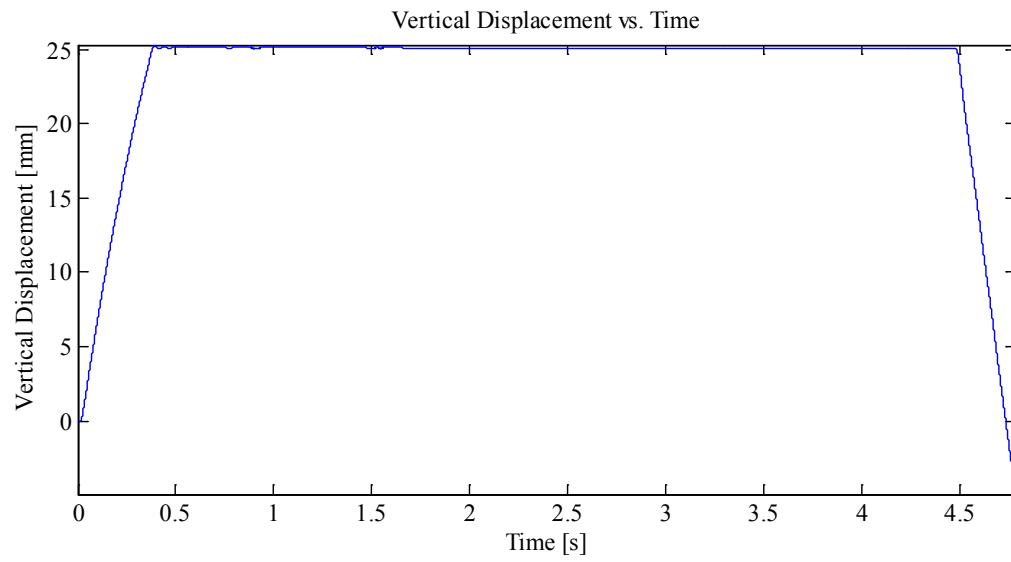
Notes:

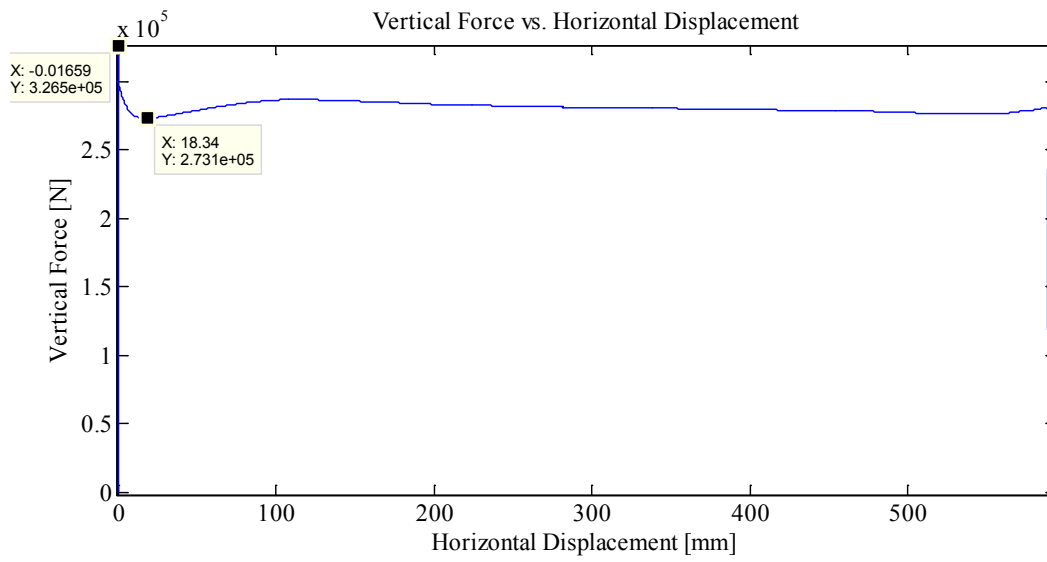
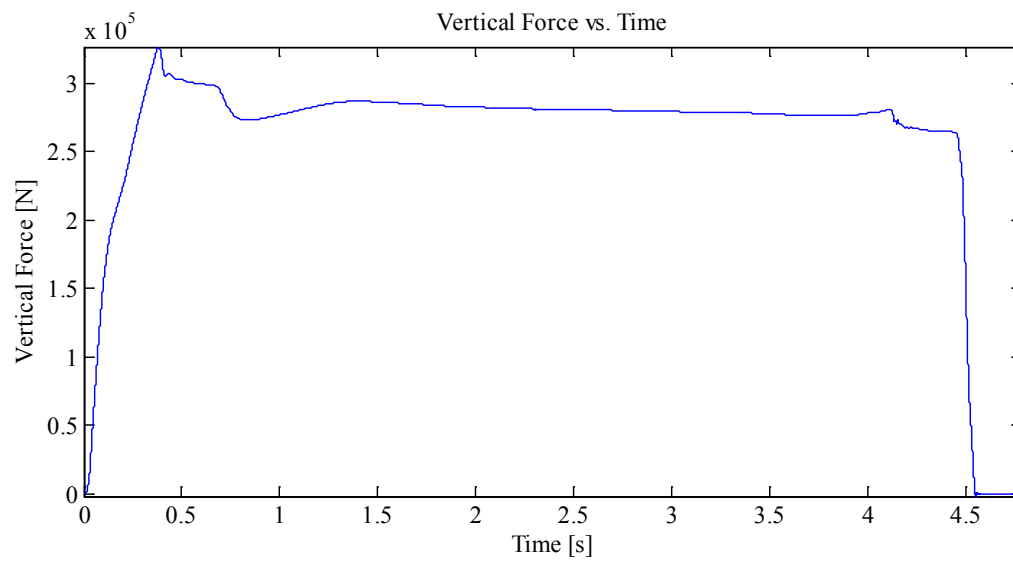
Indentation 1: ~25 mm, In-Along-Out - Centre to End
Data from Indentation 1 saved as MovingLoad26
With Thermal Video

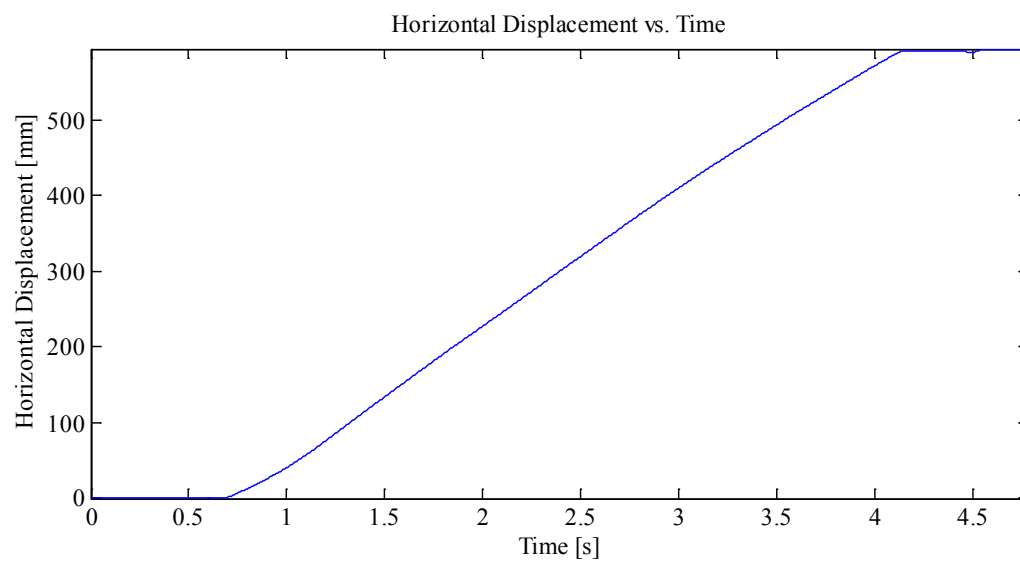
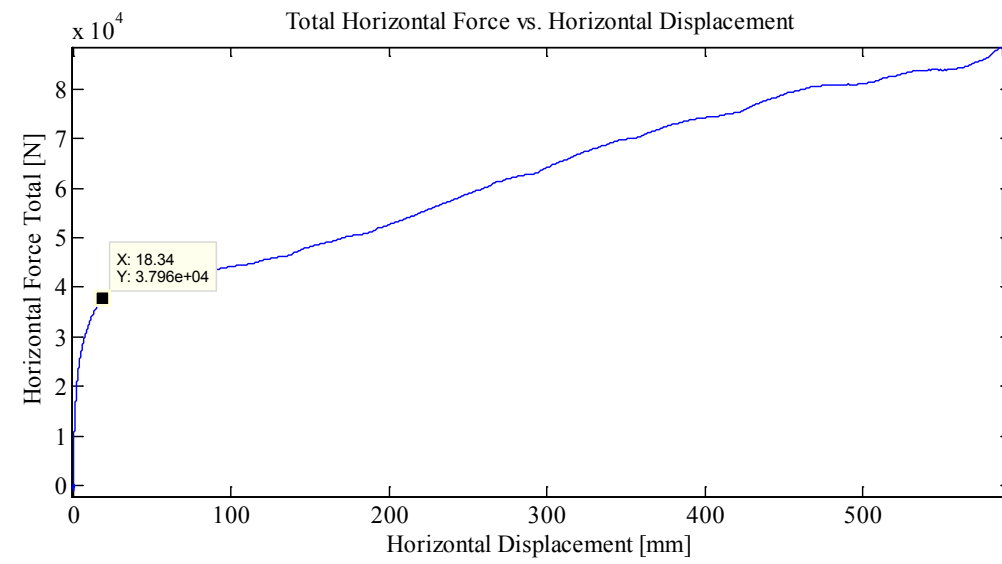
Plots:

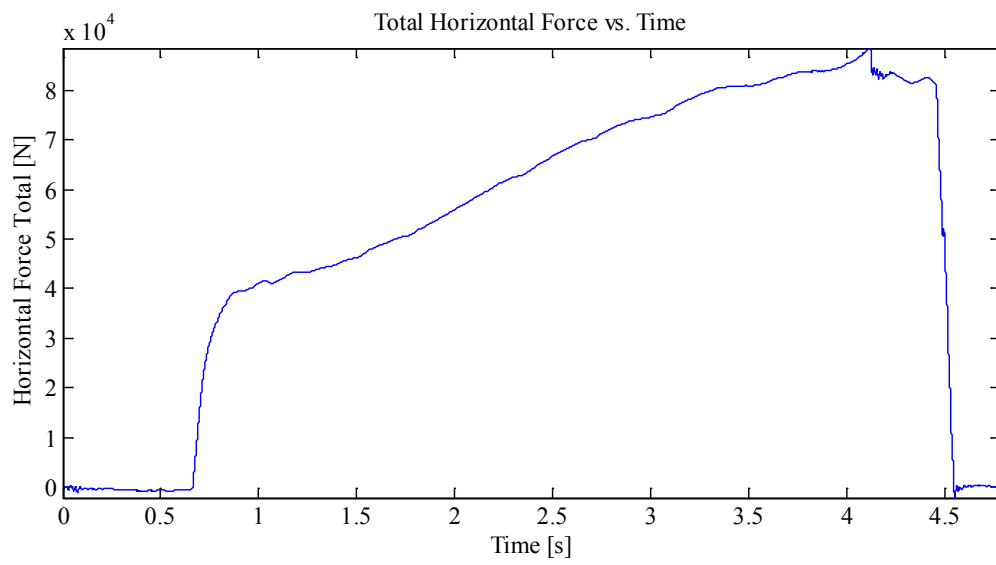
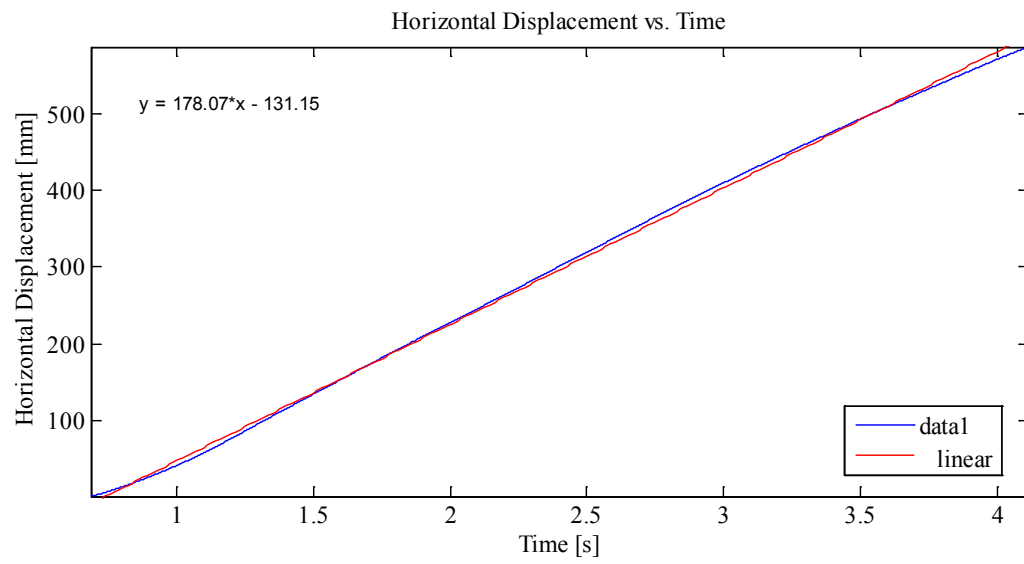


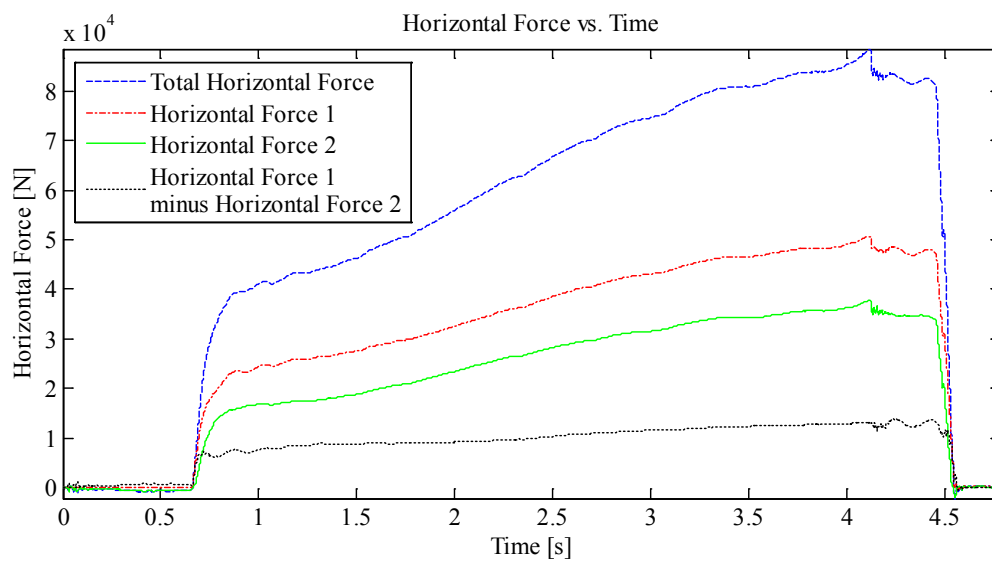












Appendix C2.4.3 – MovingLoad27

April 22, 2014 at ~2:15 a.m.

Run # 20
Run Type: Slow
Room-temperature: -9.8°C (Measured with thermocouple)
Sample Type: Frame
Test Type: In-Along-Out Centre to End

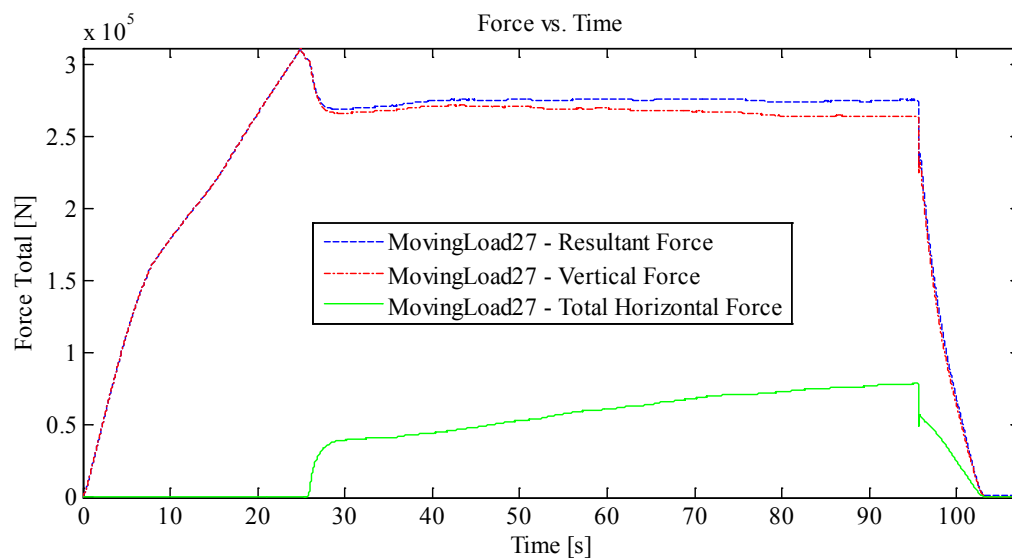
HStarting Point: Centre (0.27 cm (0 cm nominal))
HSpeed: 10 mm/s (Nominal)
H Travel: Centre to End (55+ cm)

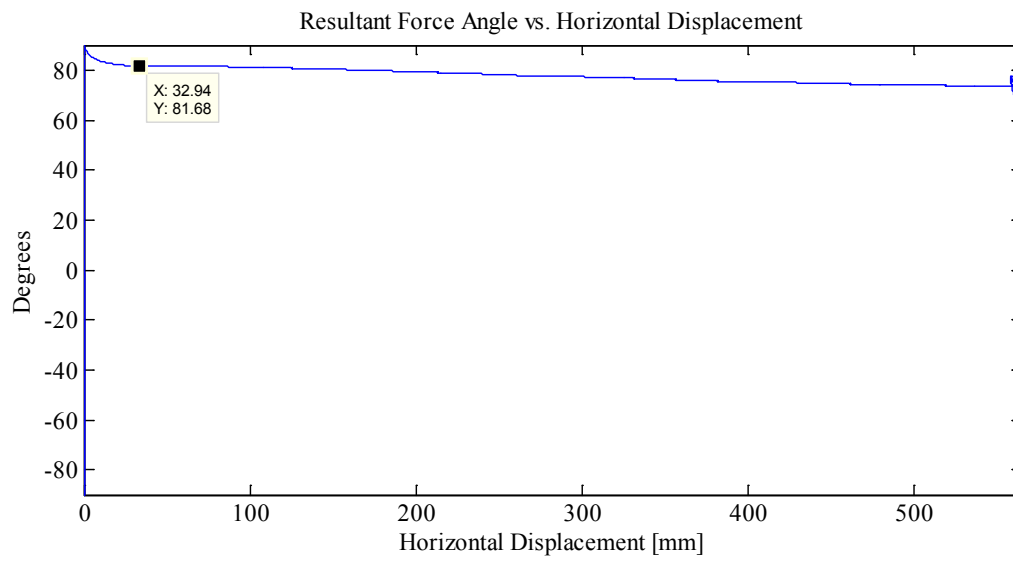
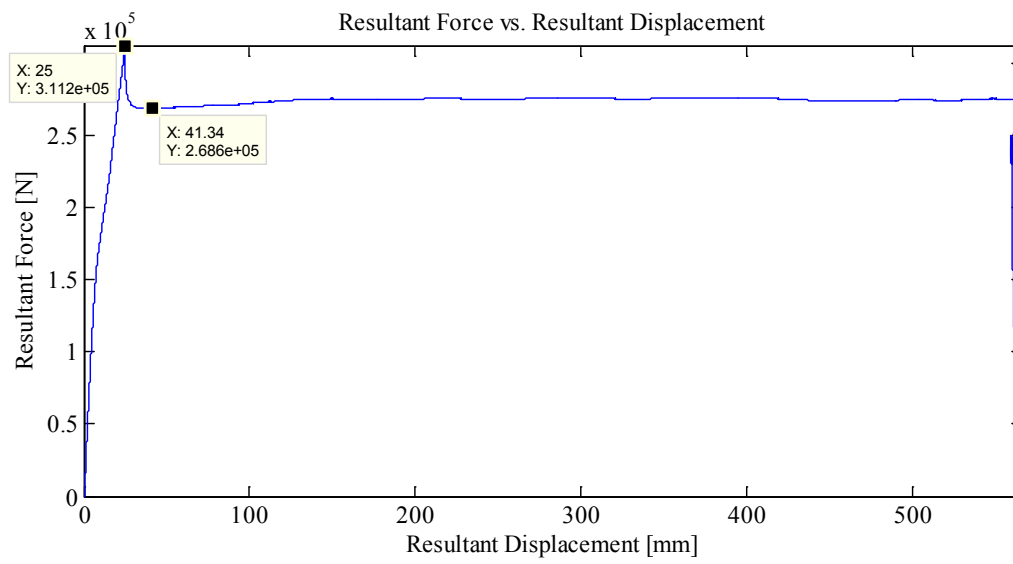
Vstarting Point: 4.25 mm
VSpeed: 1.0 mm/s (Nominal)
V Travel: 25 mm
V Stopping Point: -20.75 mm

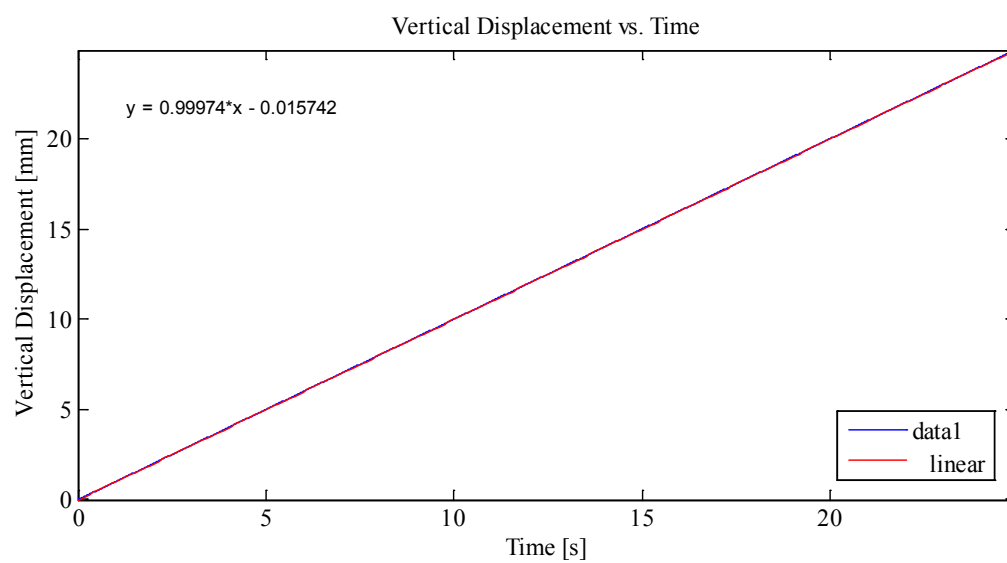
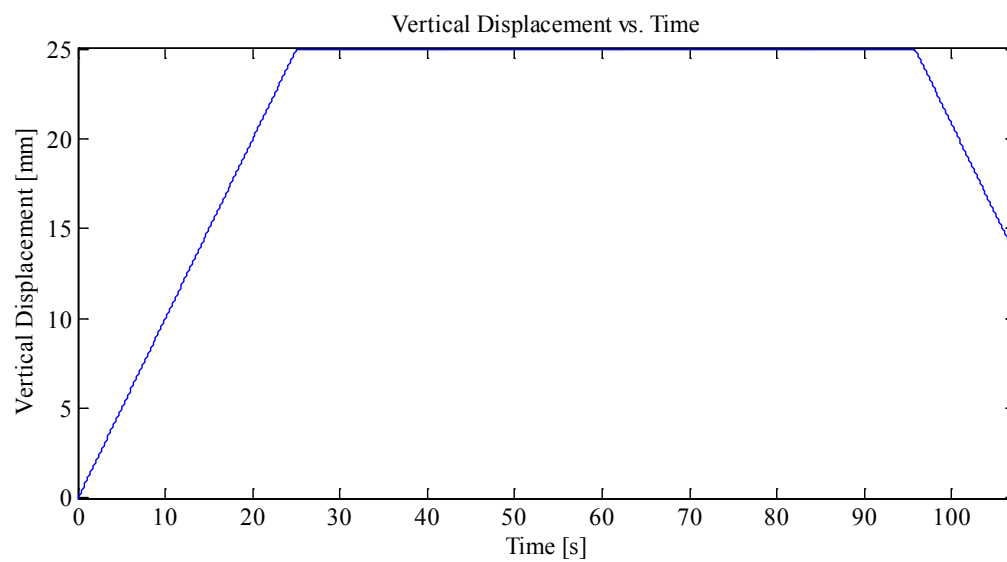
Notes:

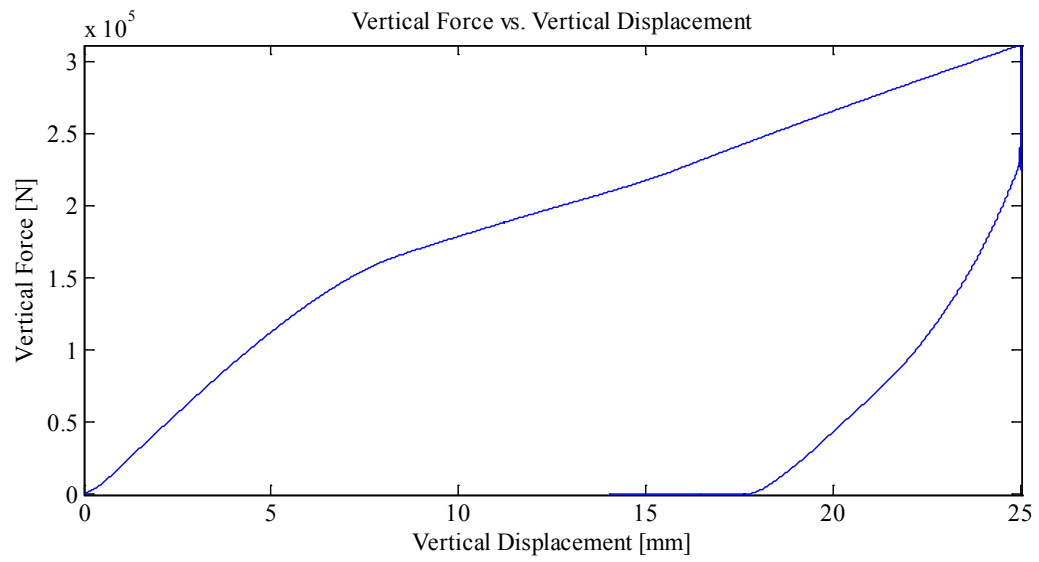
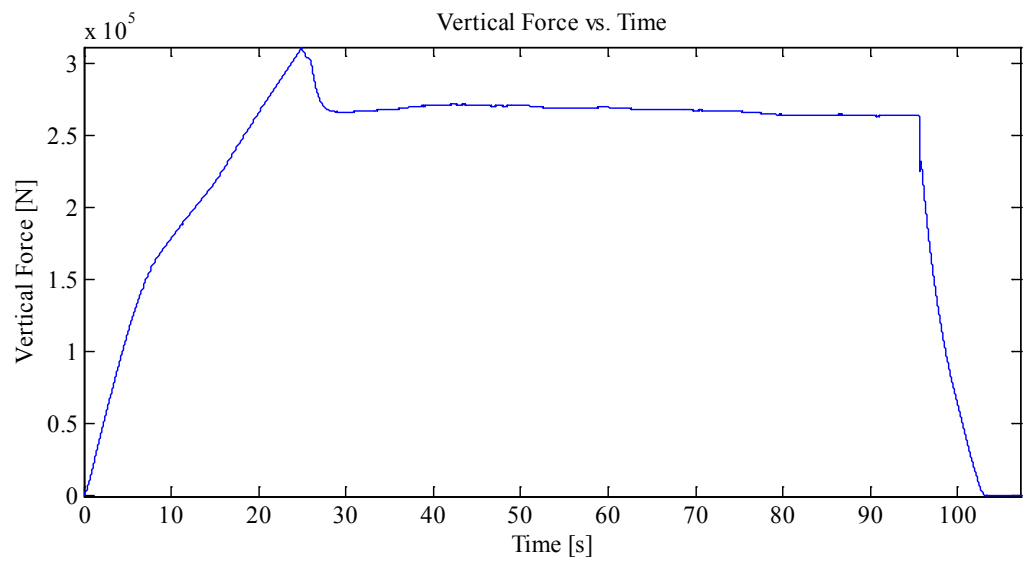
Indentation 1: ~25 mm, In-Along-Out - Centre to End
Data from Indentation 1 saved as MovingLoad27
With Thermal Video

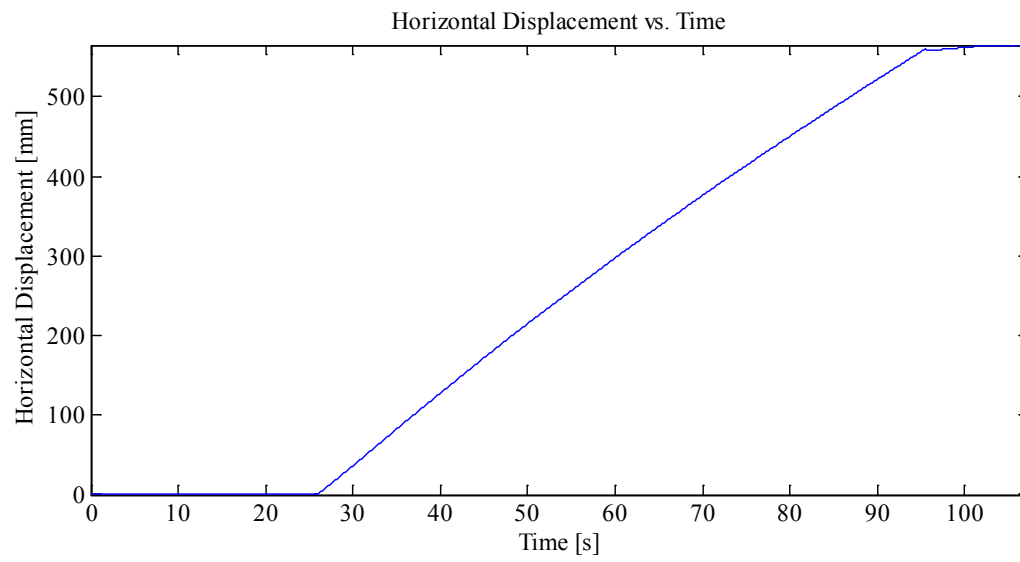
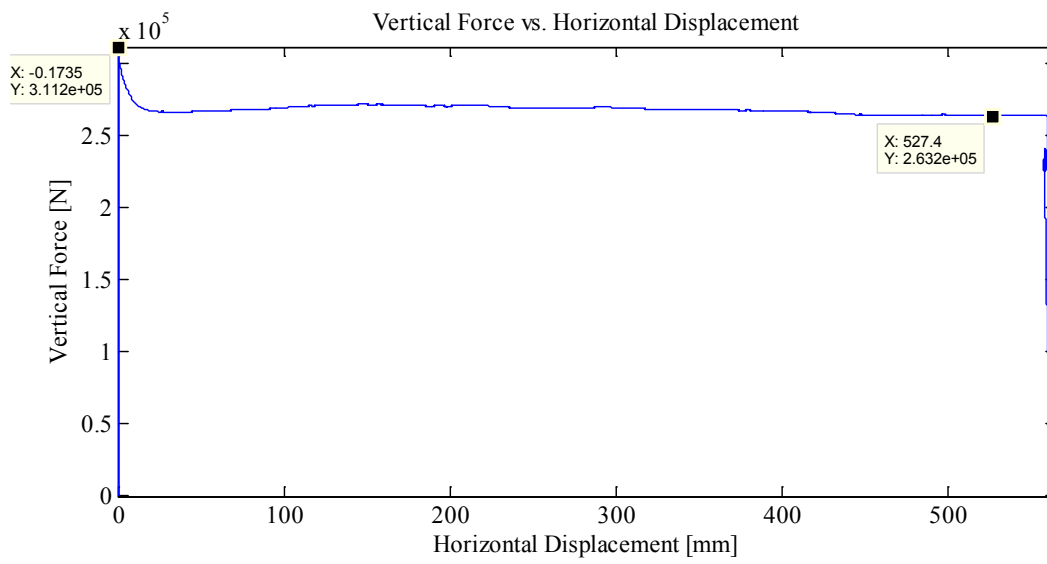
Plots:

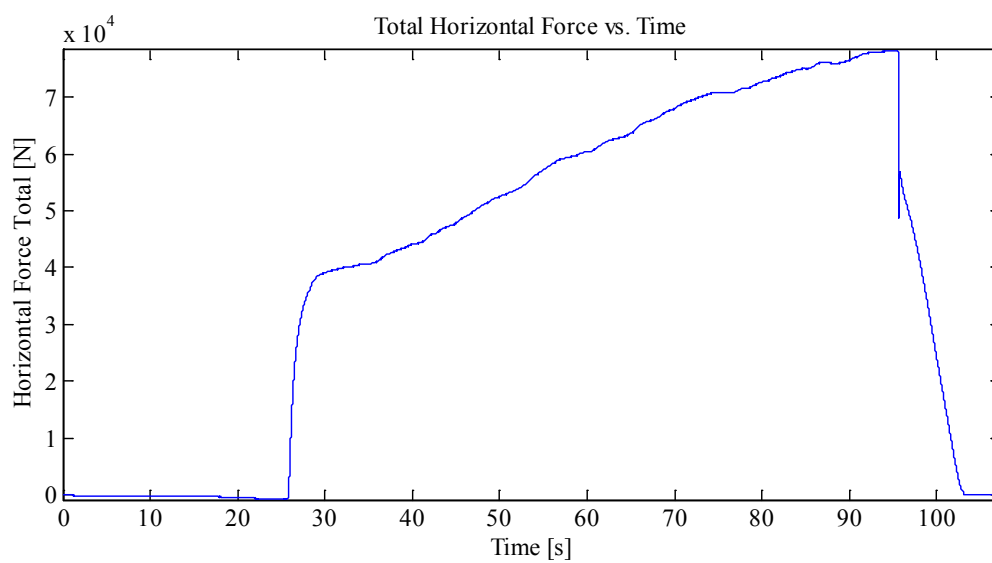
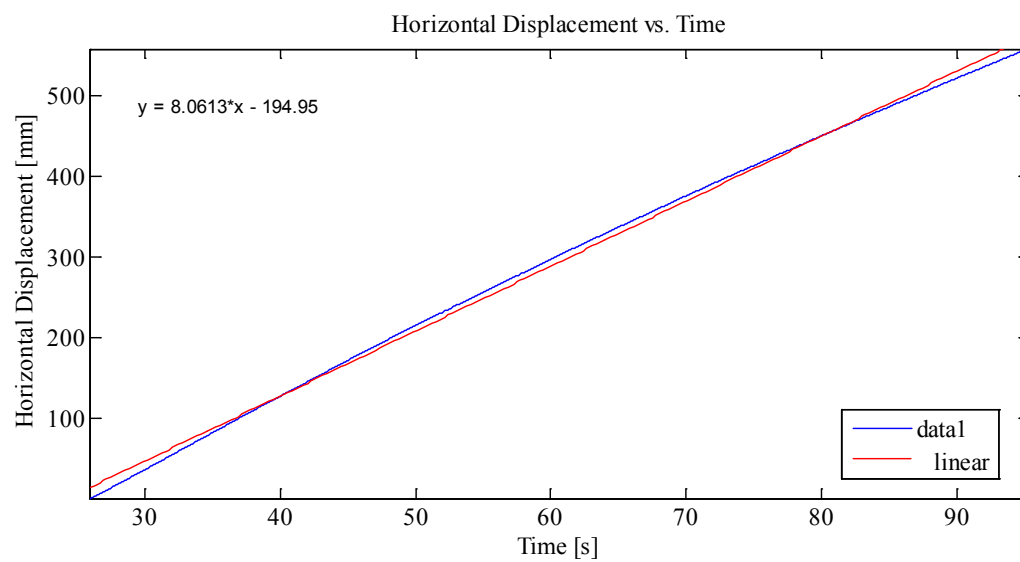


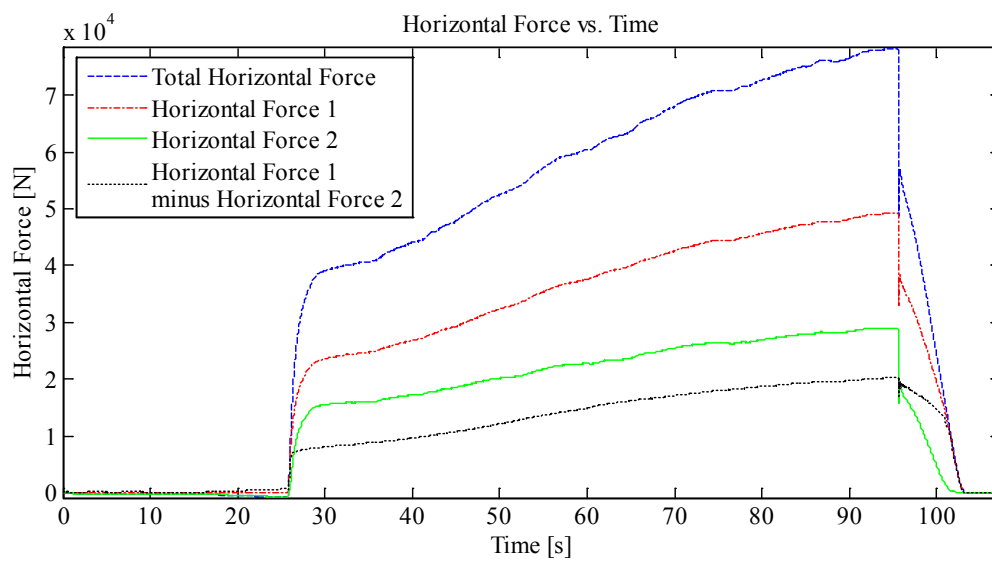
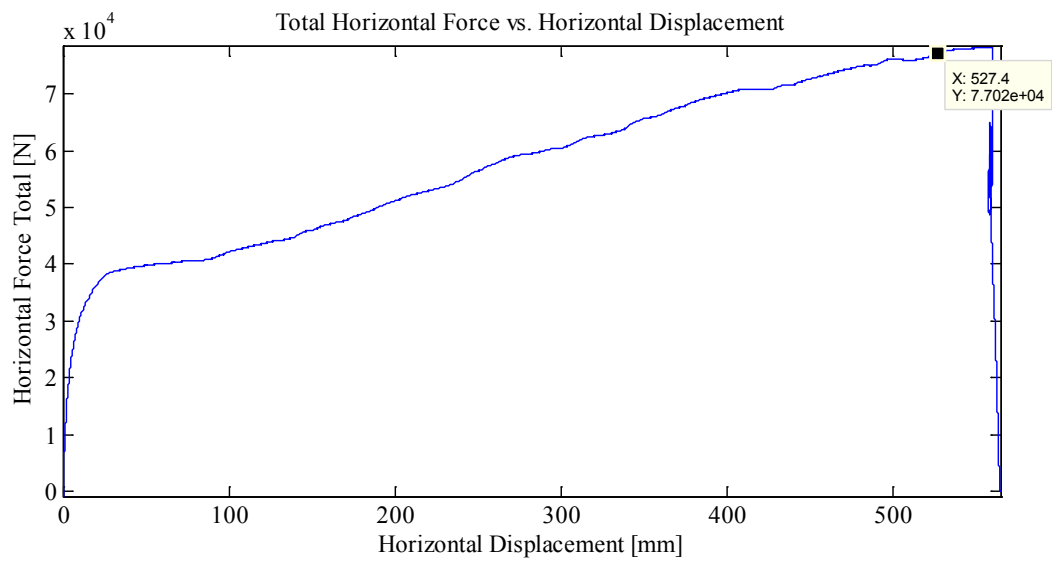












Appendix C2.4.4 – MovingLoad28

April 23, 2014 at ~4:15p.m.

Run # 21
Run Type: Full Length – Slow
Room-temperature: -9.7°C (Measured with thermocouple)
Sample Type: Frame
Test Type: In-Along-Out End to End

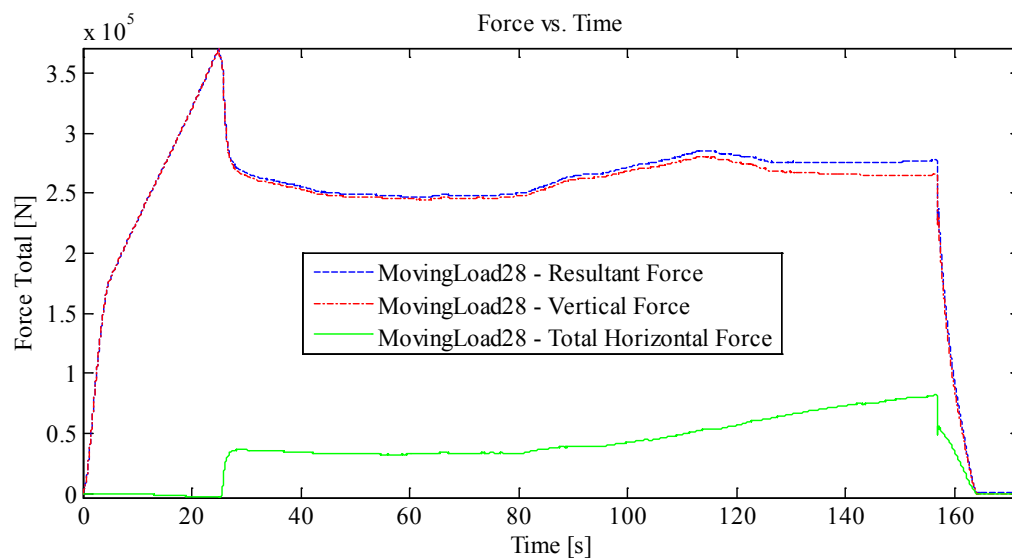
HStarting Point: End (-54.44 cm (-55 cm nominal))
HSpeed: 10mm/s (Nominal)
H Travel: End to End (110+ cm)

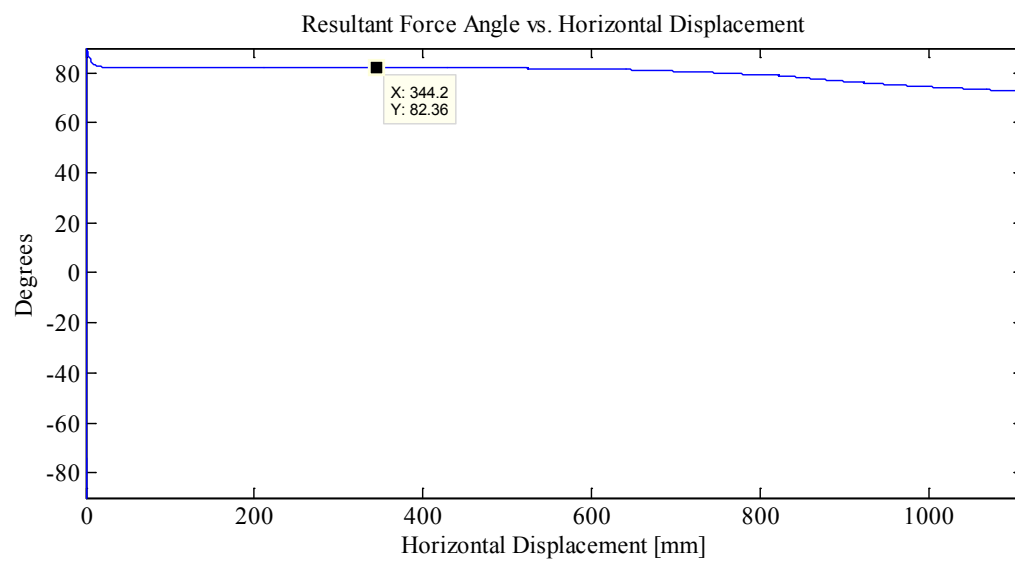
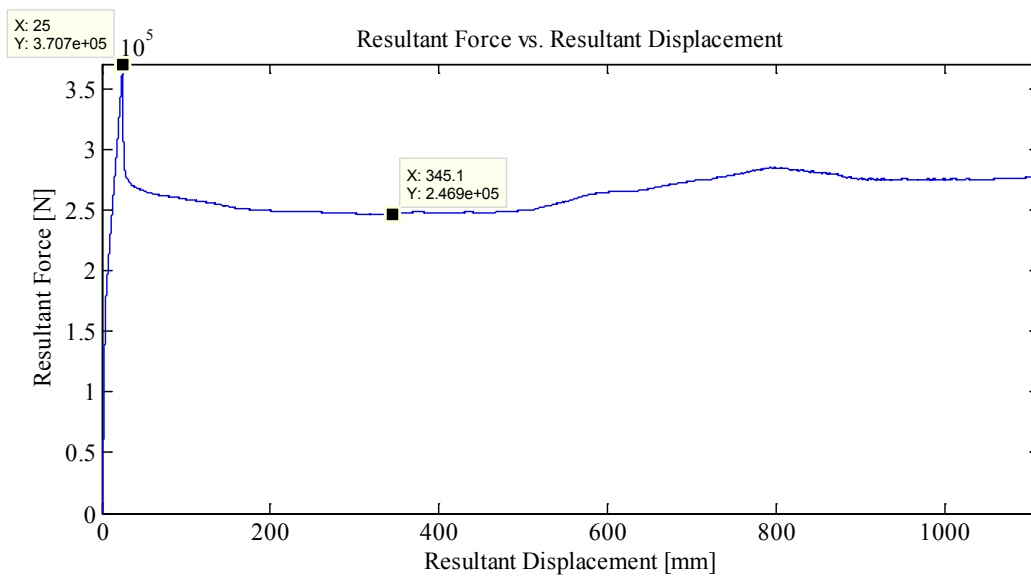
Vstarting Point: 4.26 mm
VSpeed: 1.0 mm/s (nominal)
V Travel: 25 mm
V Stopping Point: -20.74 mm

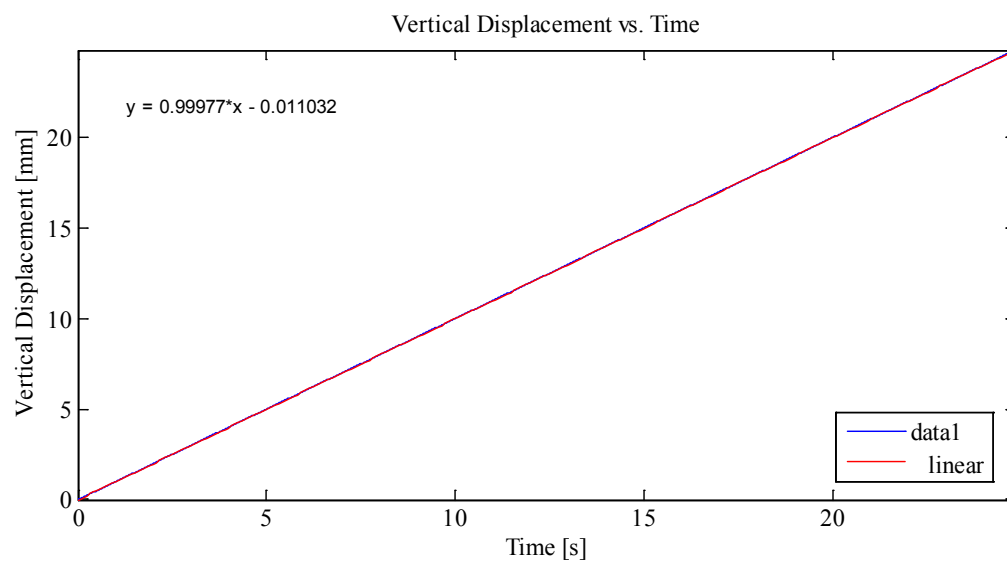
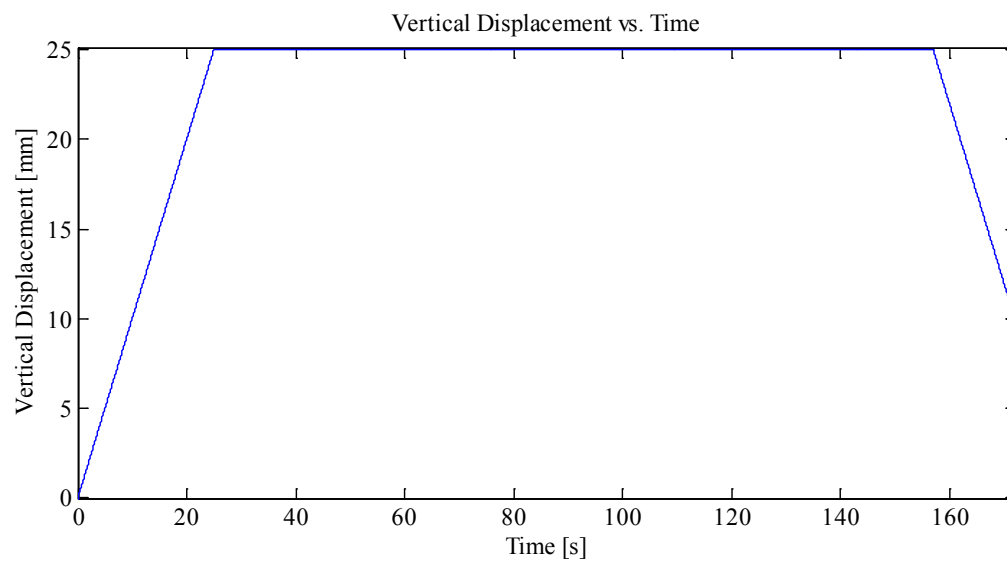
Notes:

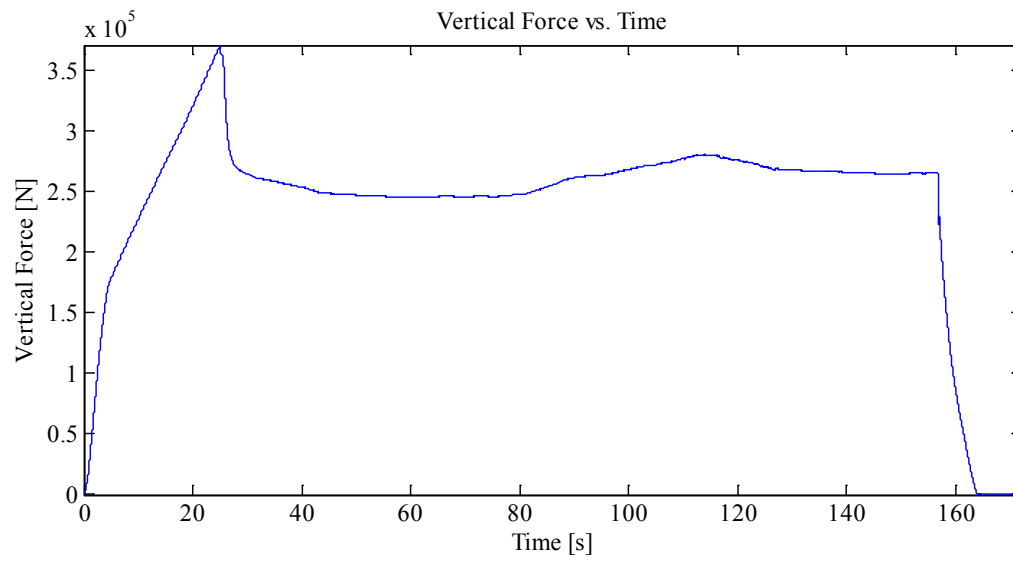
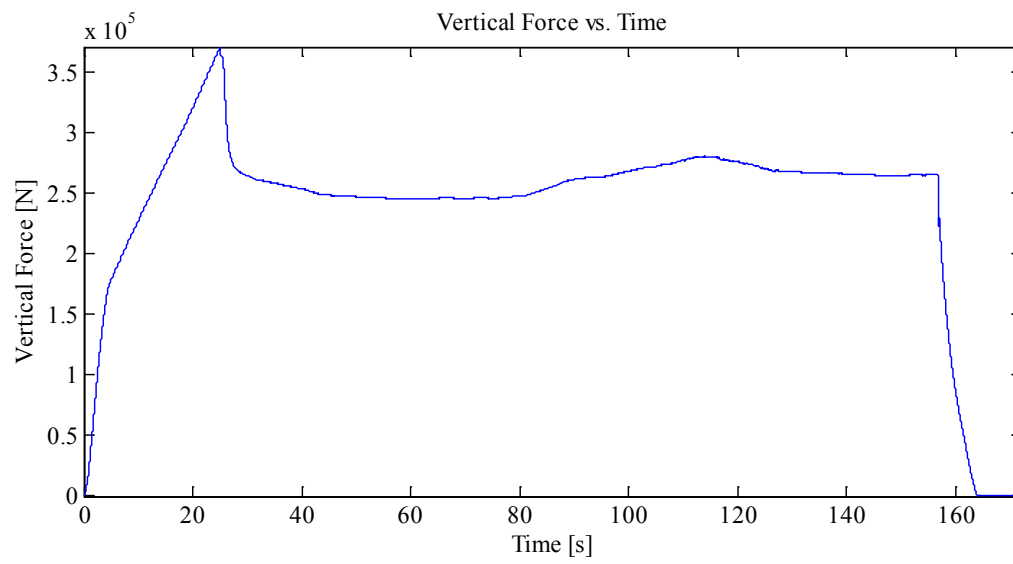
Indentation 1: ~25 mm, In-Along-Out - End to End
Data from Indentation 1 saved as MovingLoad28
With Thermal Video

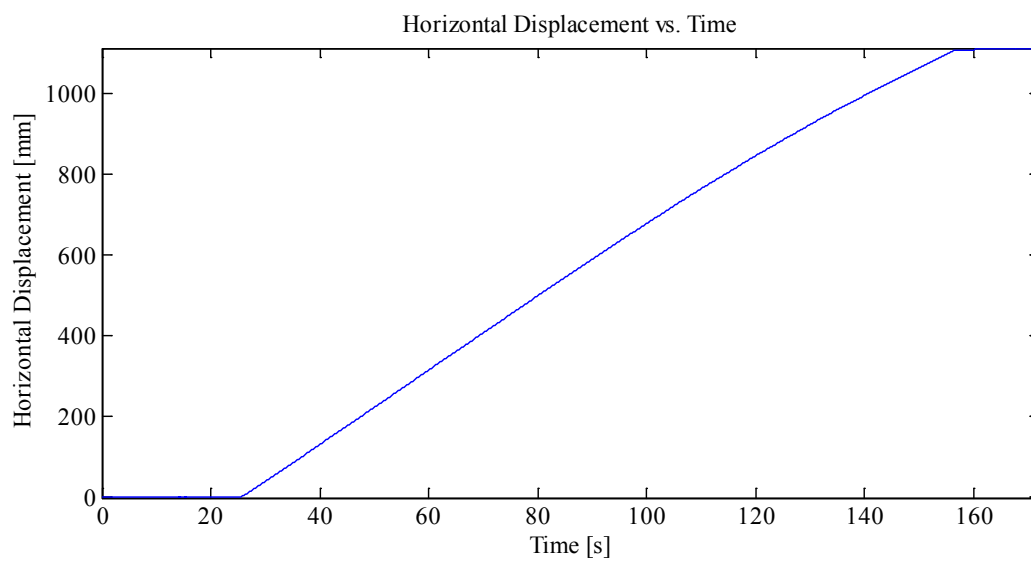
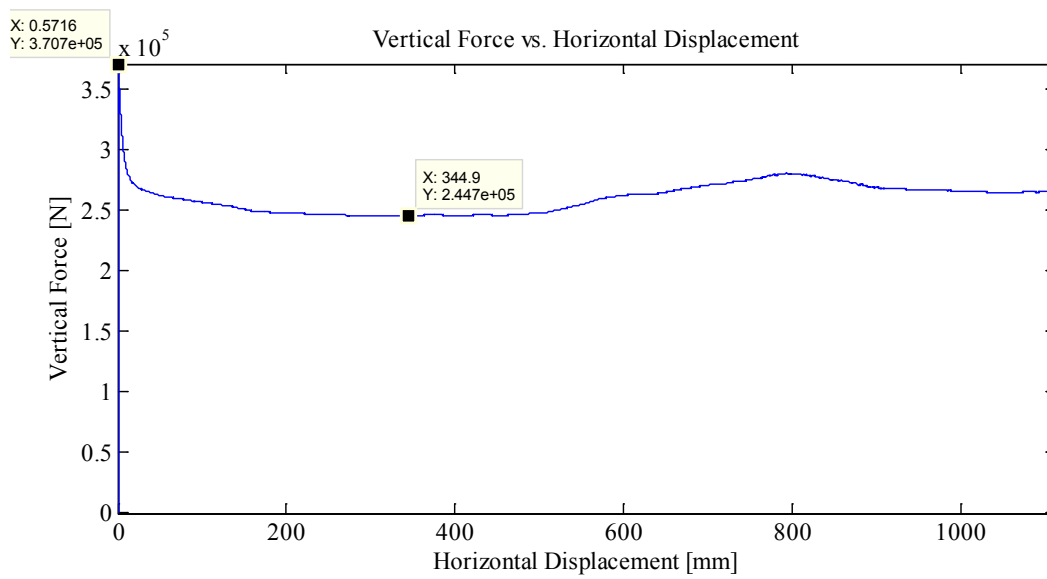
Plots:

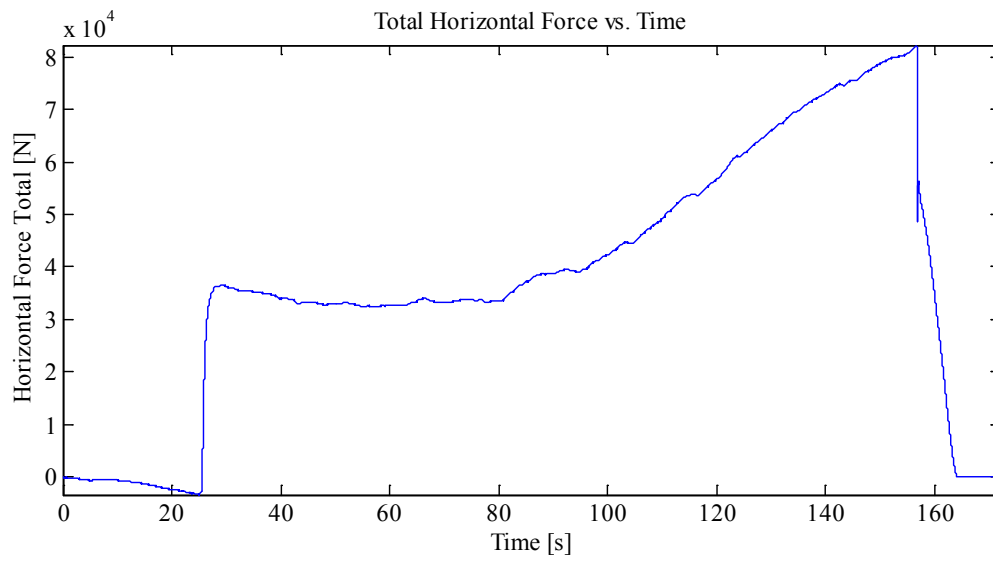
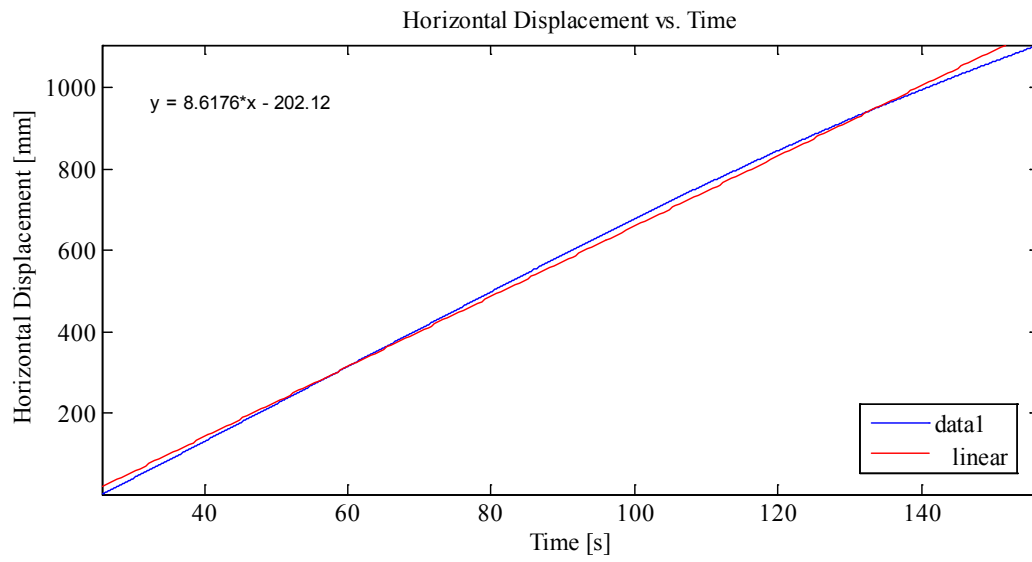


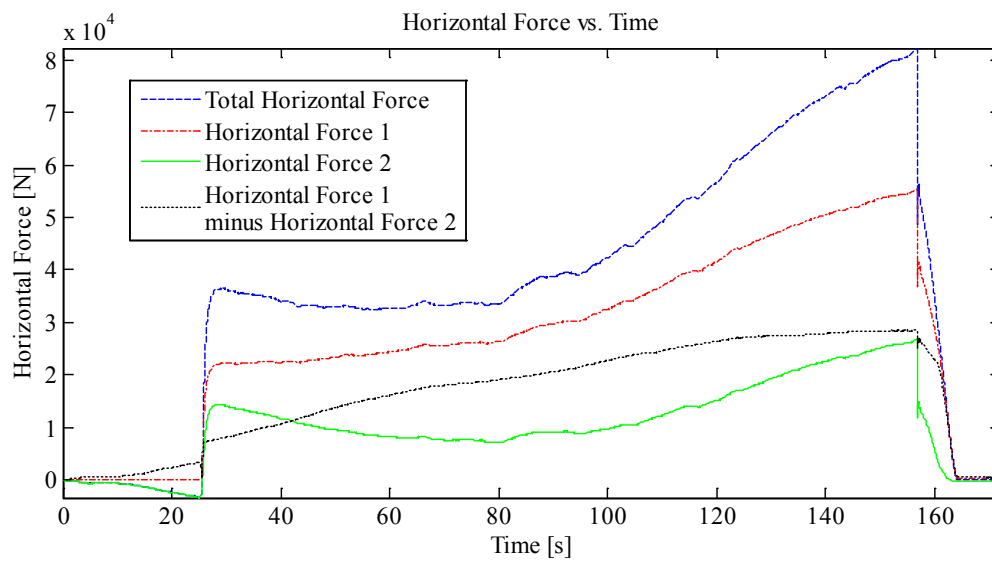
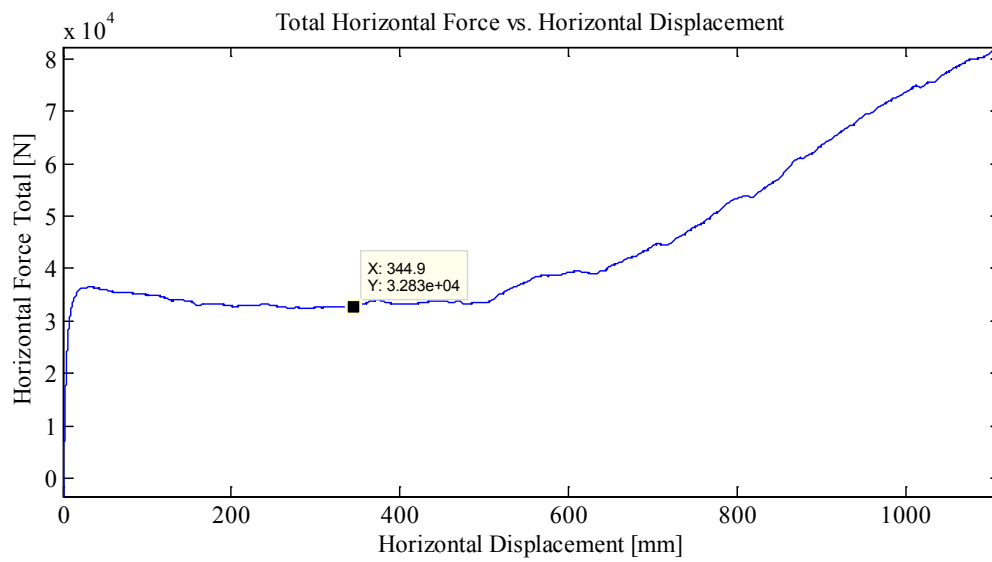








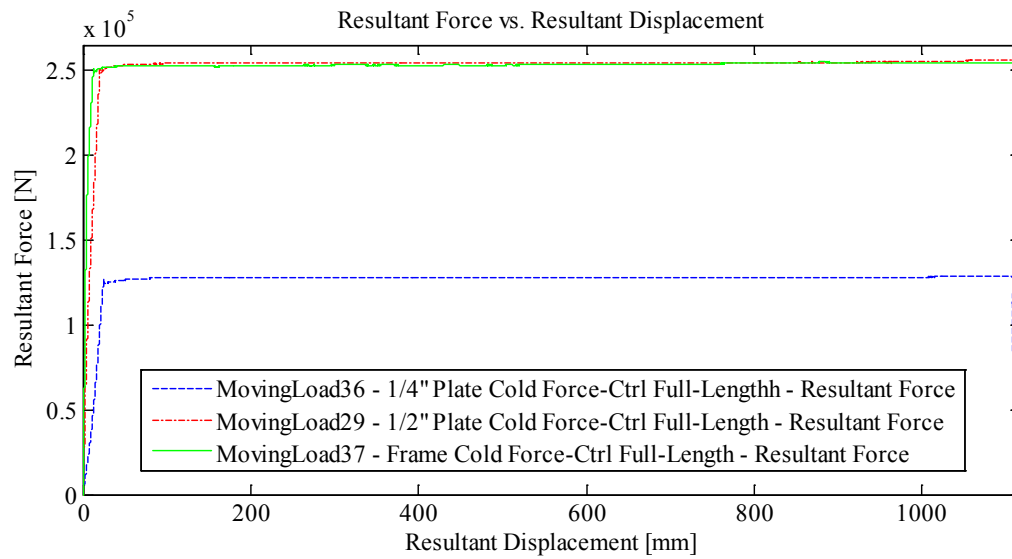
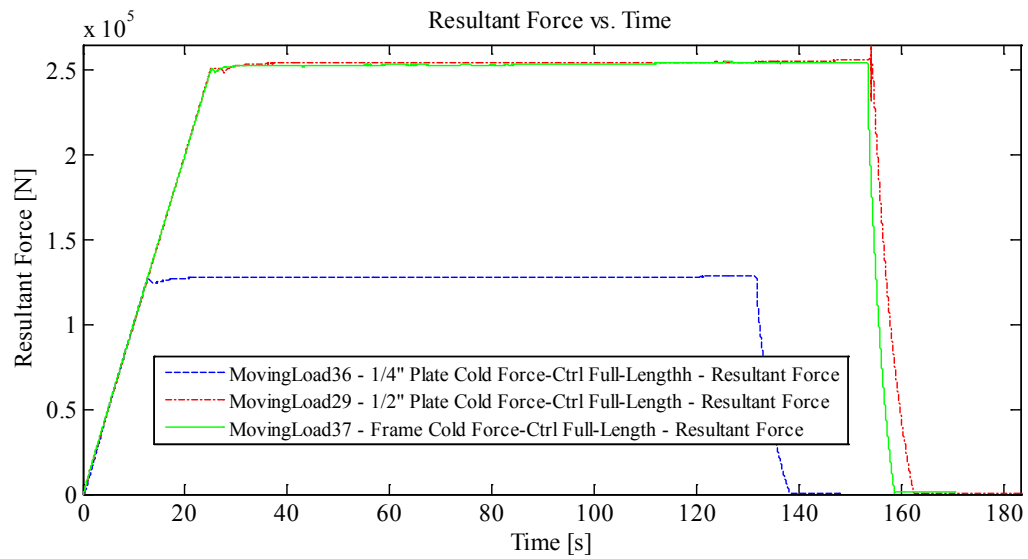


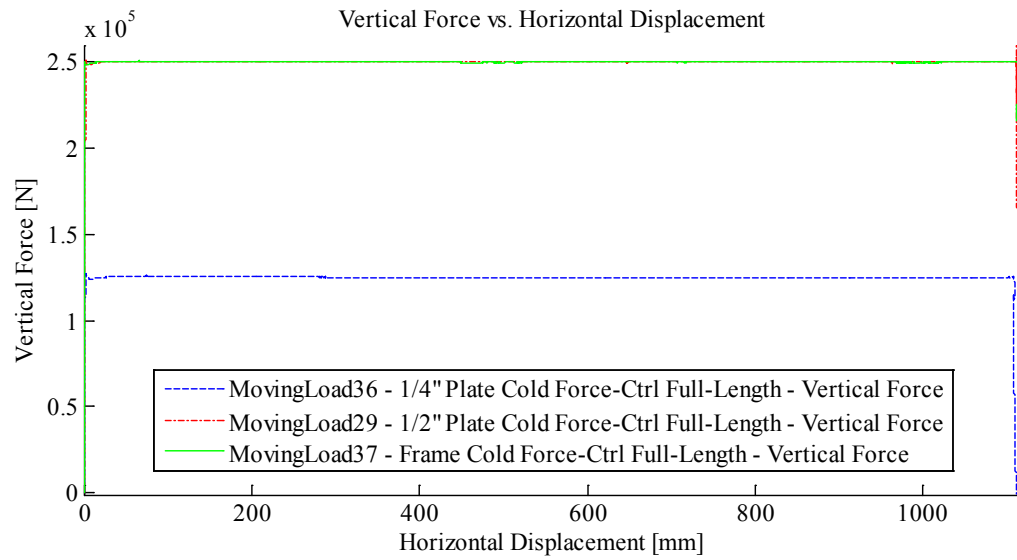
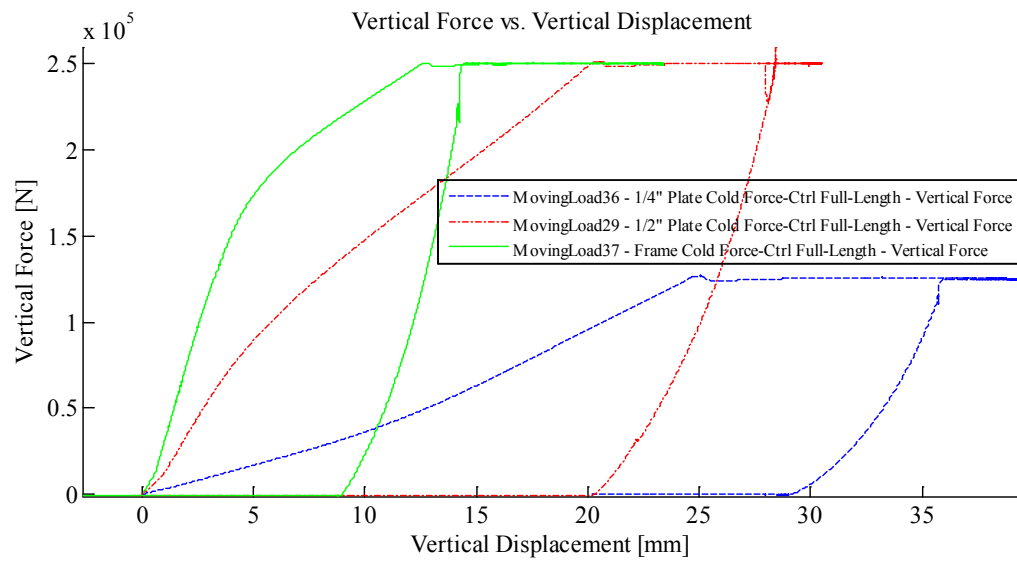


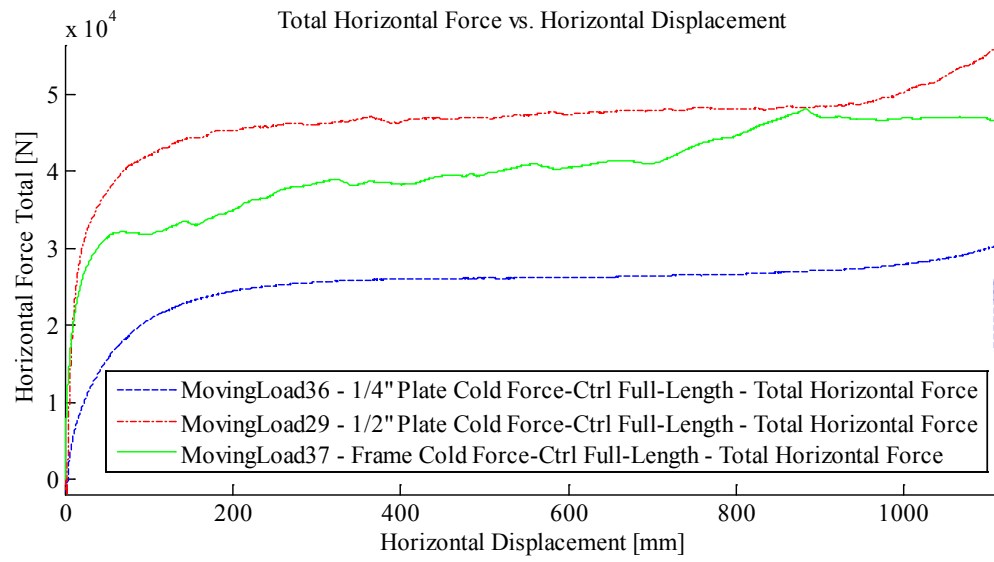
Appendix C2.5 – **Force Controlled Tests**

Appendix C2.5.1 – Summary Plots for Experiments ML 29, 36 and

37







Appendix C2.5.2 – Force Controlled – MovingLoad29

April 24, 2014 at ~12:10p.m.

Run # 22
Run Type: Force Control - Half Inch Plate - Full Length
Room-temperature: -9.5°C (Measured with thermocouple)
Sample Type: 1/2" Plate
Test Type: In-Along-Out End to End

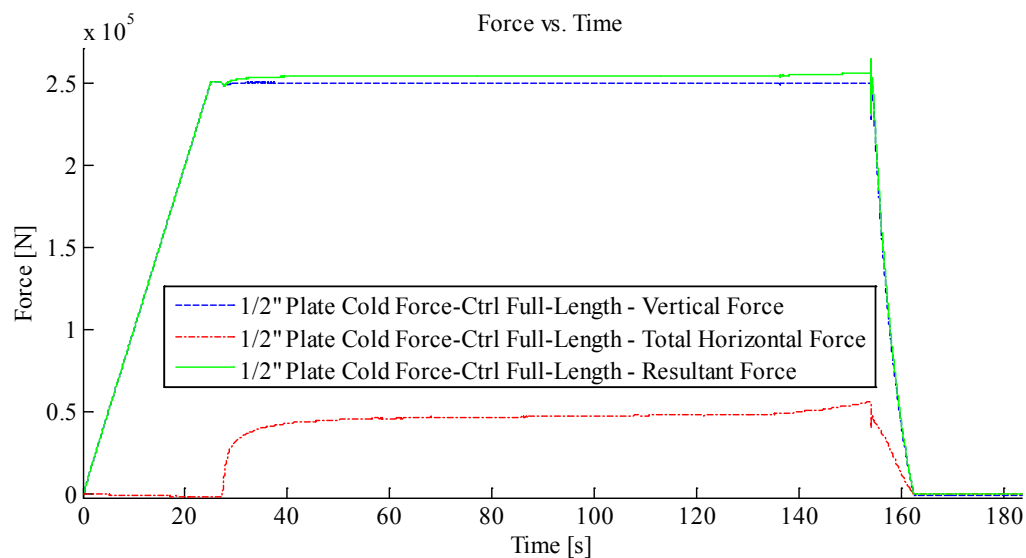
HStarting Point: End (-54.42 cm (-55 cm nominal))
HSpeed: 10mm/s (Nominal)
H Travel: End to End (110+ cm)

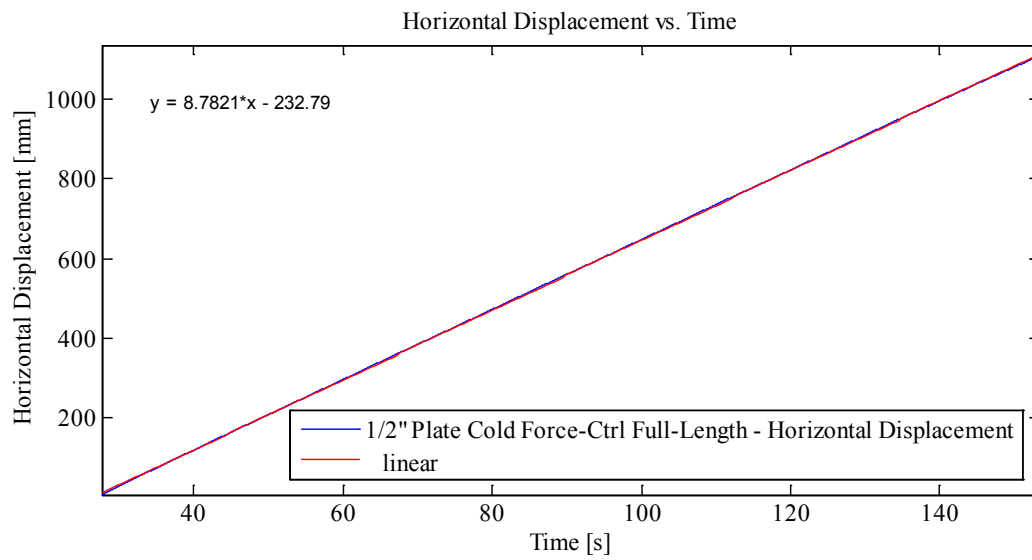
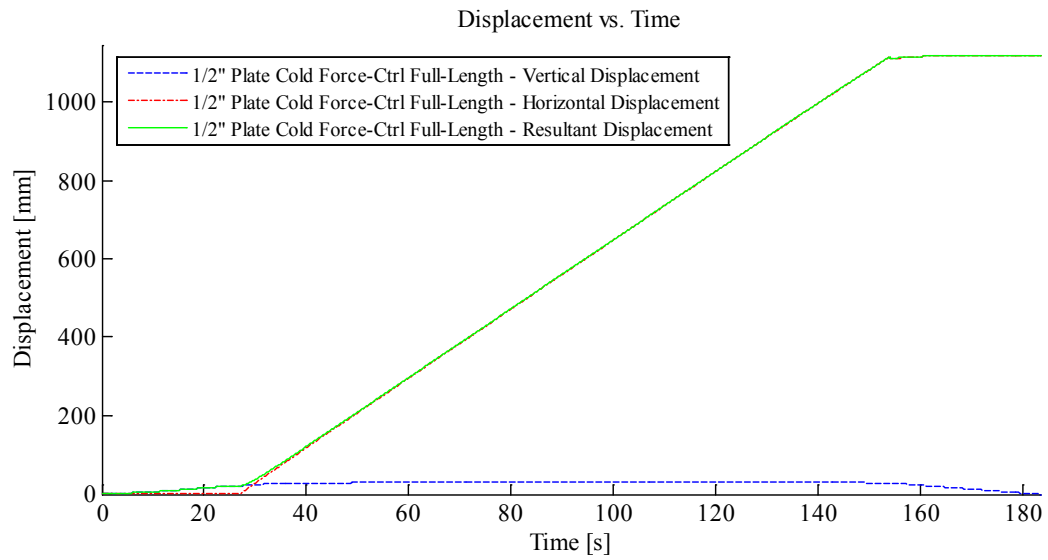
Vstarting Point: 9.49 mm
VSpeed: 10 kN/s
V Force Target: 250 kN
V Disp Limit: -35 mm

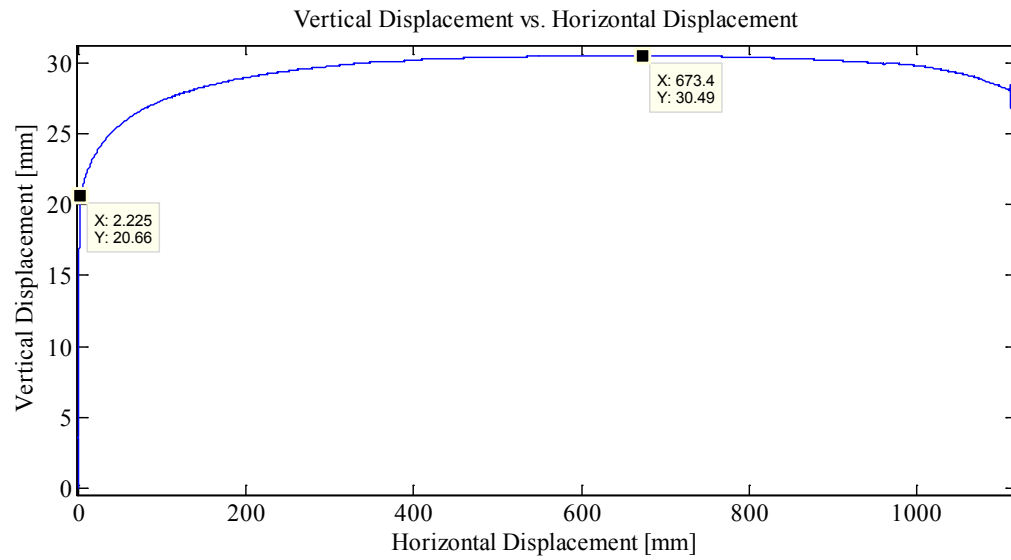
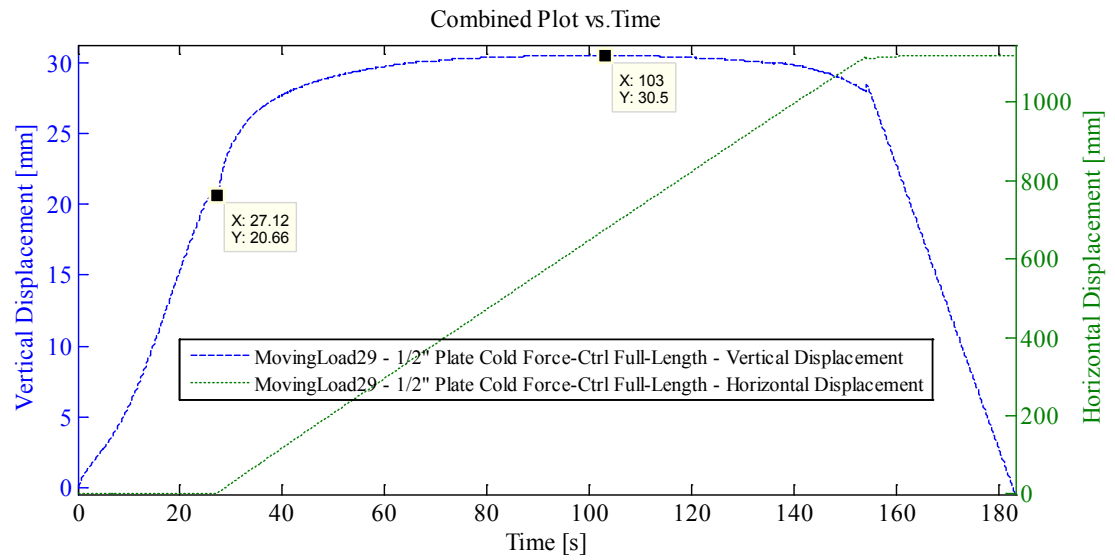
Notes:

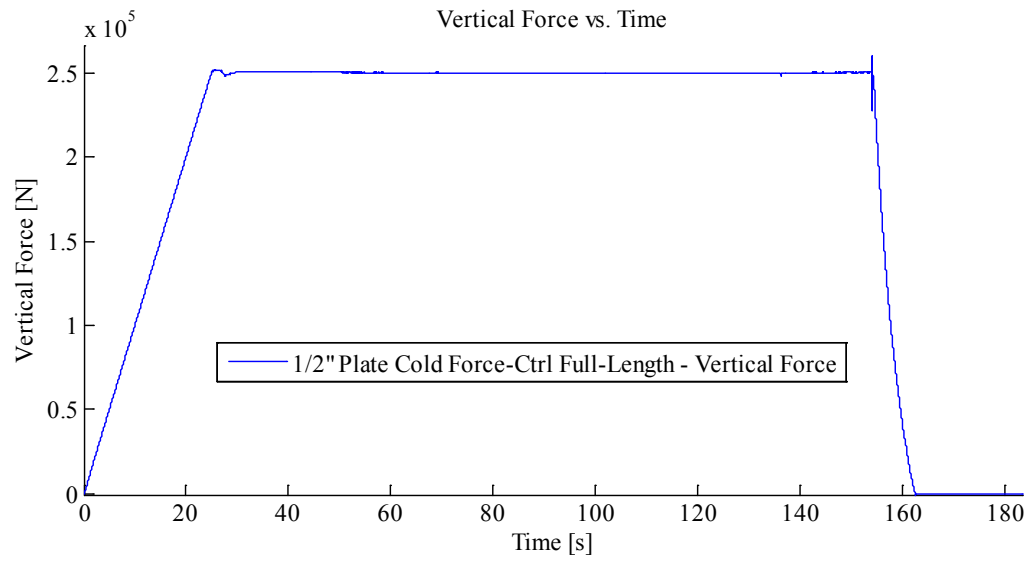
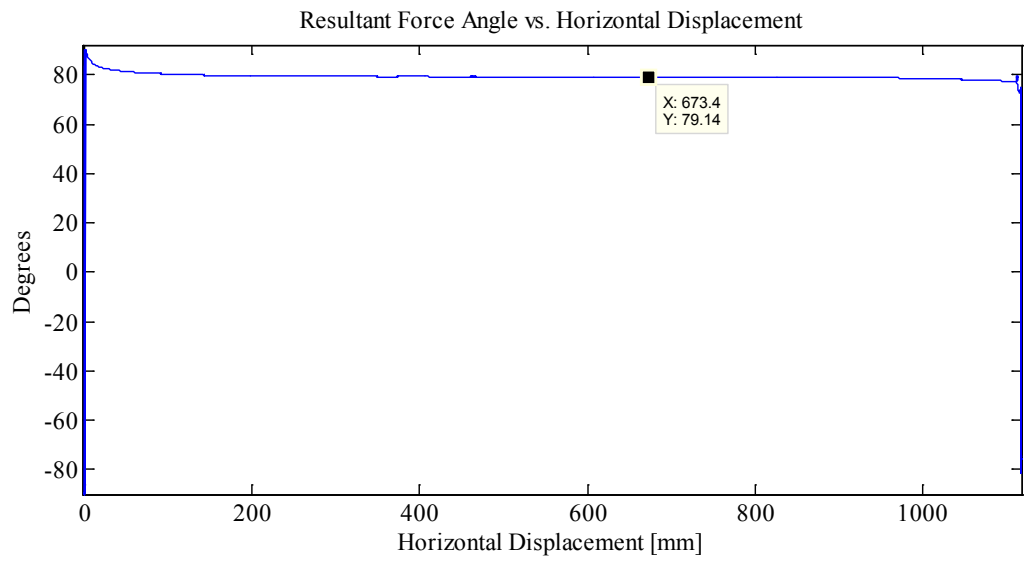
Force 1: 250 kN In-Along-Out - End to End
Data from Indentation 1 saved as MovingLoad29
With Two Thermal Video Cameras

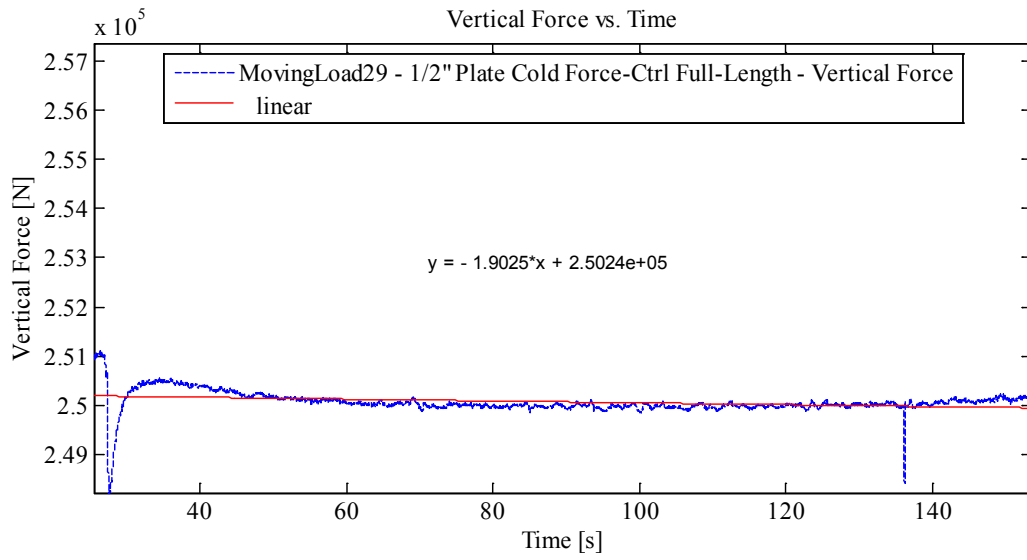
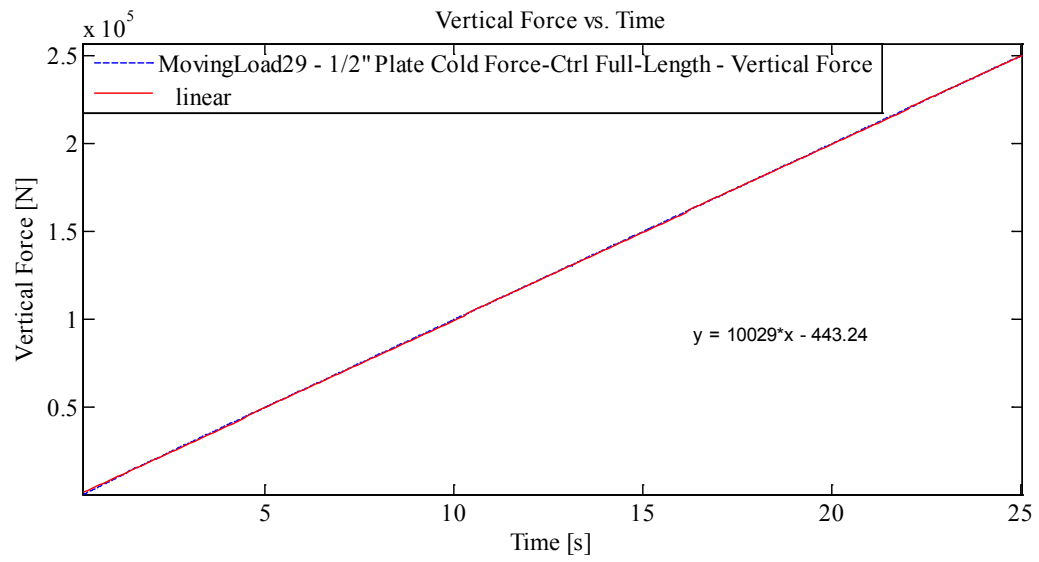
Plots:

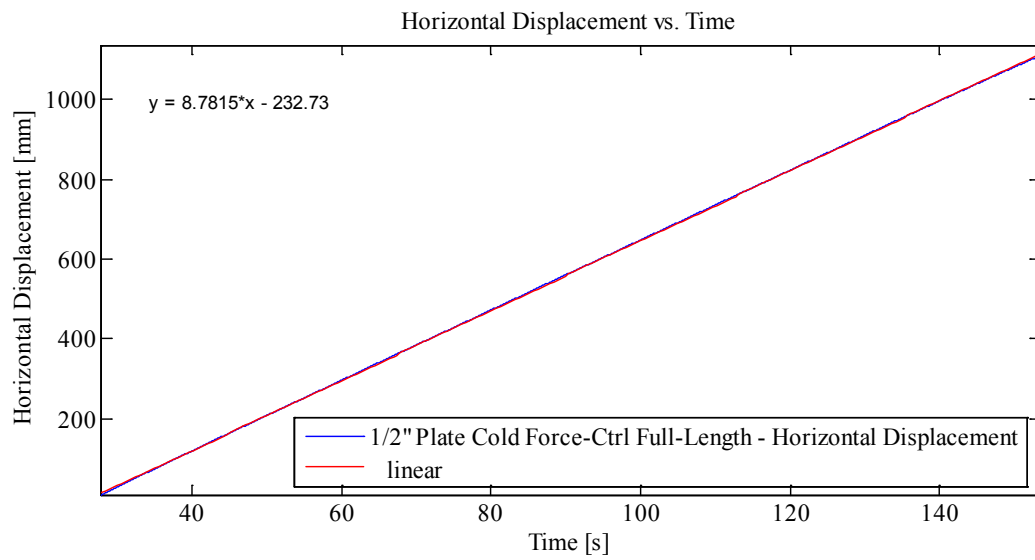
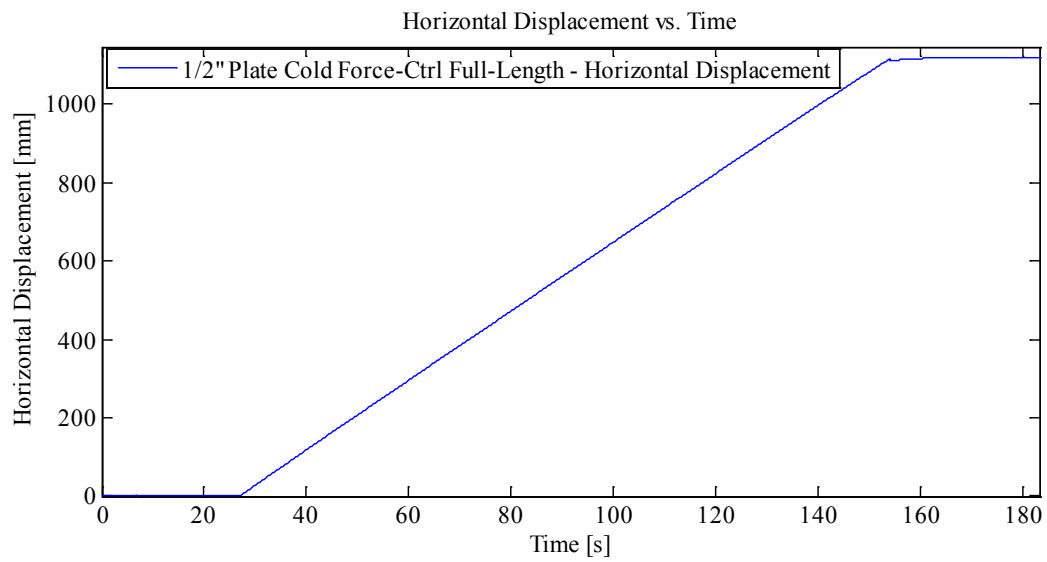


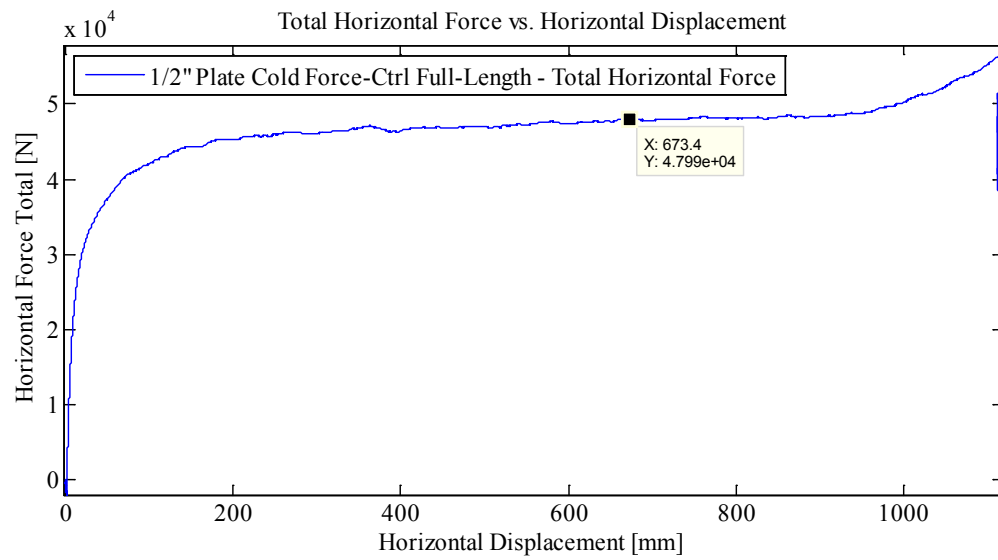
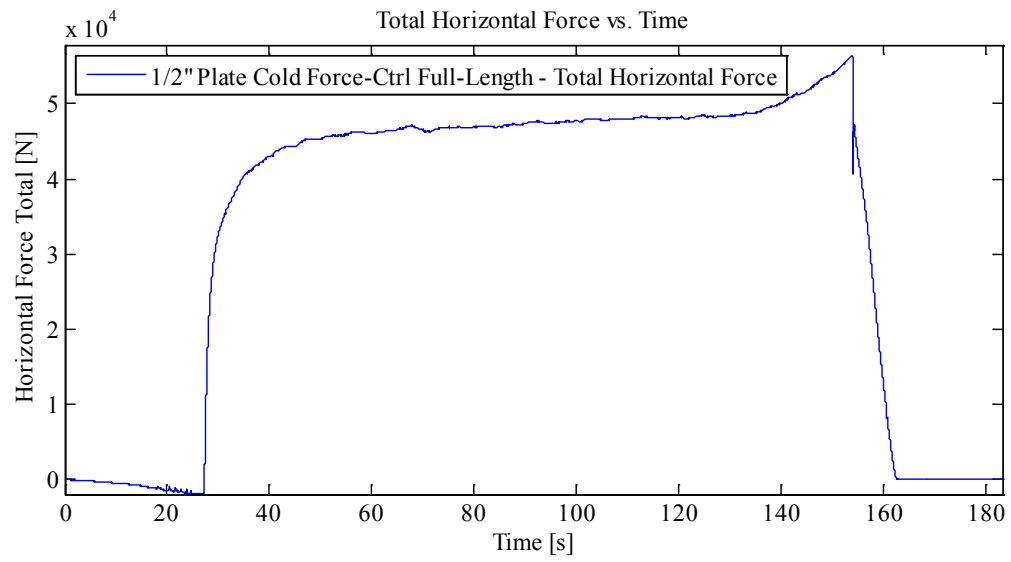


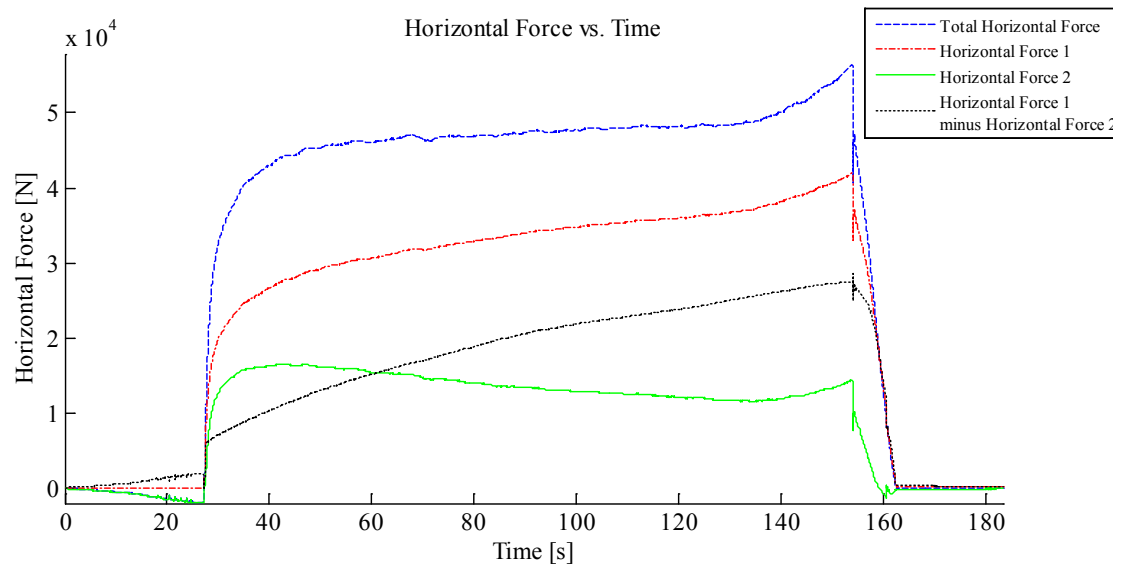












Appendix C2.5.3 – Force Controlled – MovingLoad36

May 1, 2014 at ~3:50p.m.

Run # 24
Run Type: Force Control - Quarter Inch Plate - Full Length
Room-temperature: -9.3°C (Measured with thermocouple)
Sample Type: 1/4" Plate
Test Type: In-Along-Out End to End

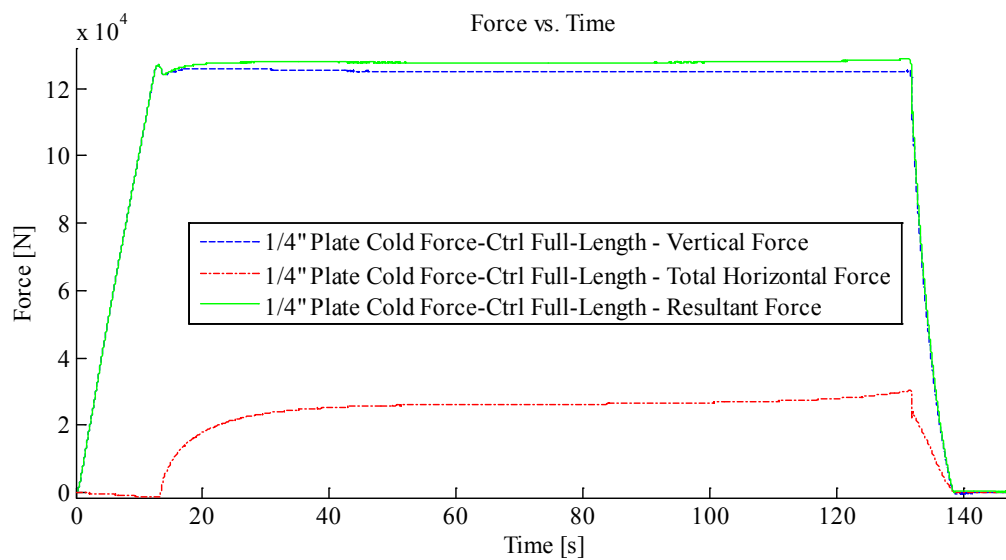
HStarting Point: End (-54.21 cm (-55 cm nominal))
HSpeed: 10mm/s (Nominal)
H Travel: End to End (110+ cm)

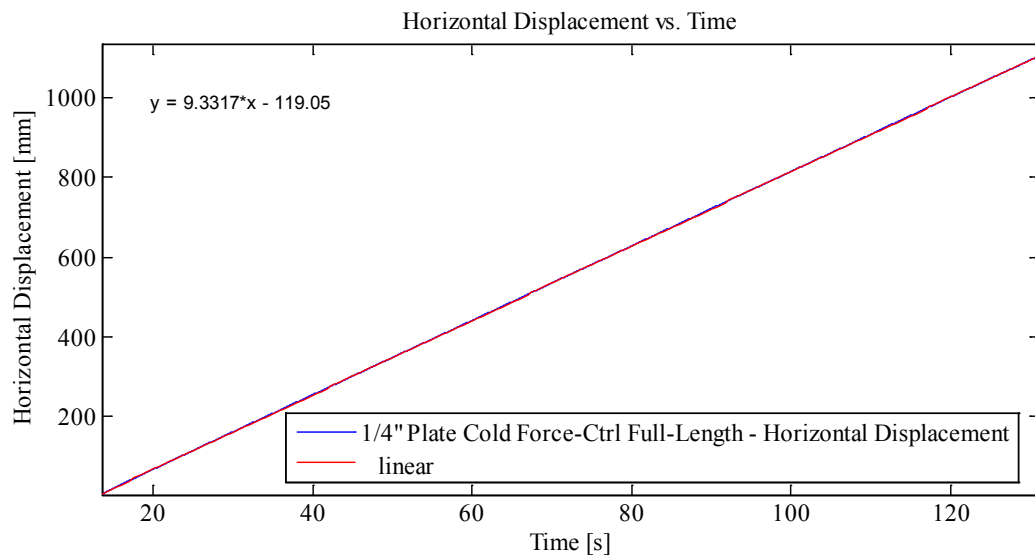
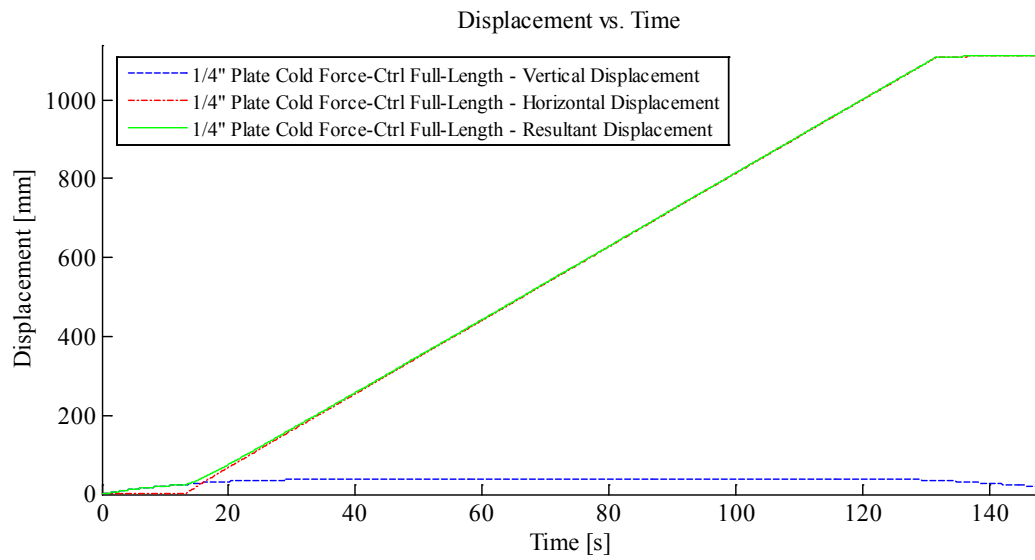
Vstarting Point: 3.1 mm
VSpeed: 10 kN/s (Nominal)
V Force Target: 125 kN
V Disp Limit: -50 mm

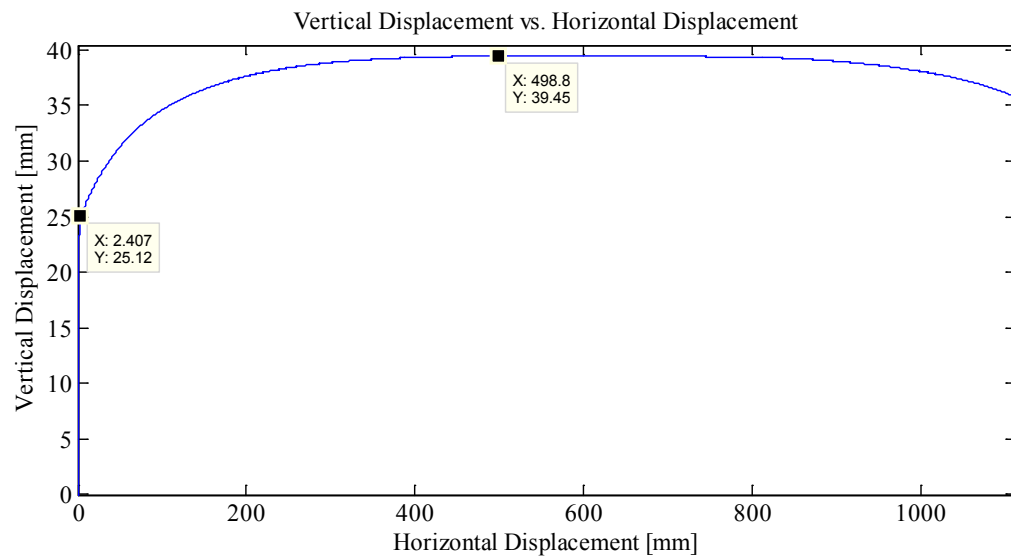
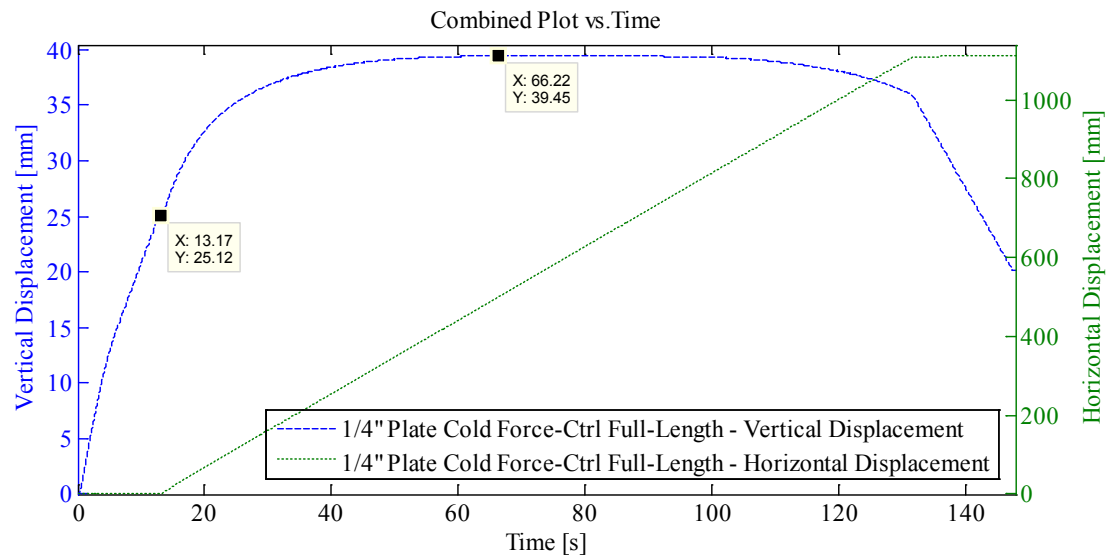
Notes:

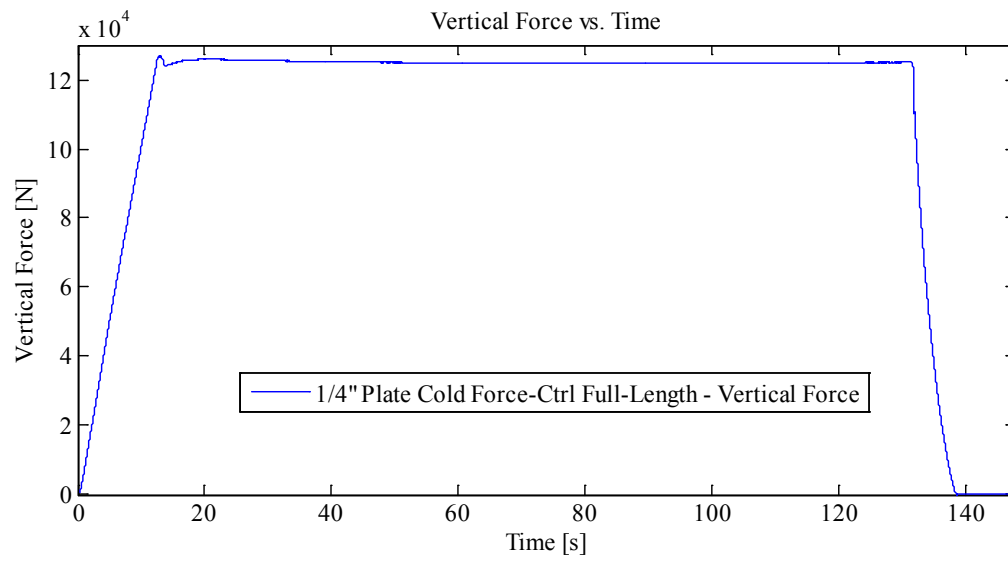
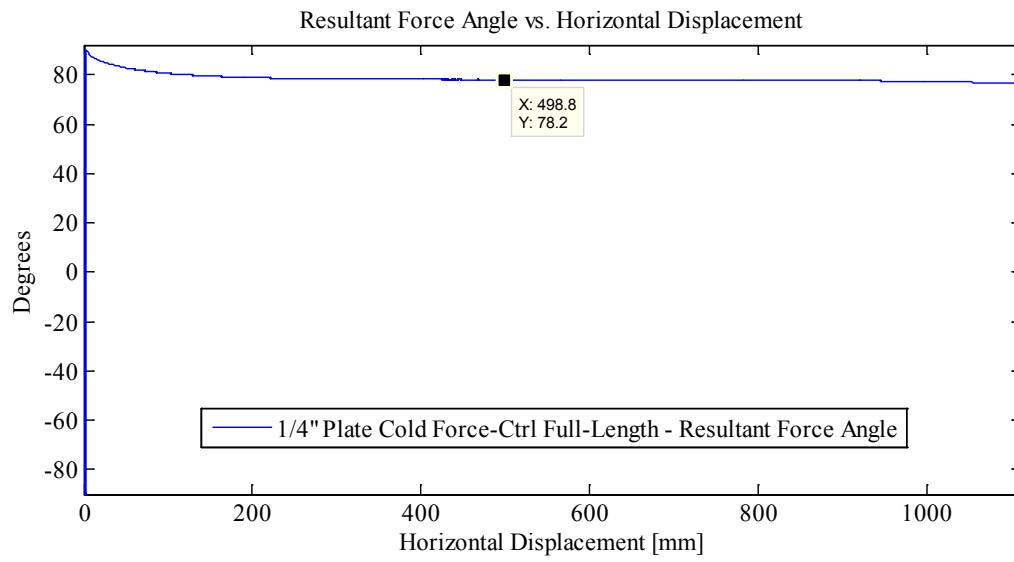
Force 1: 125 kN In-Along-Out - End to End
Data from Indentation 1 saved as MovingLoad36
With Two Thermal Video Cameras

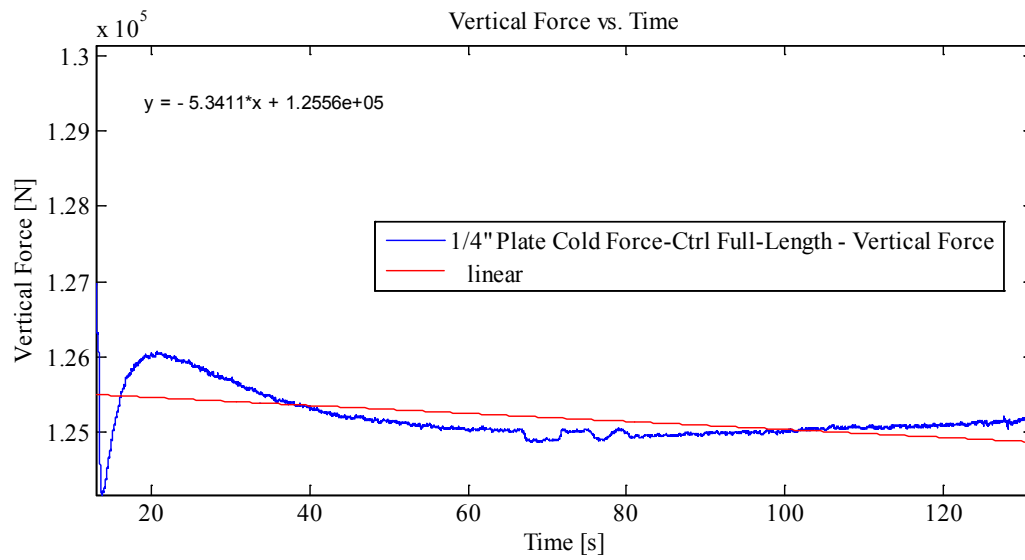
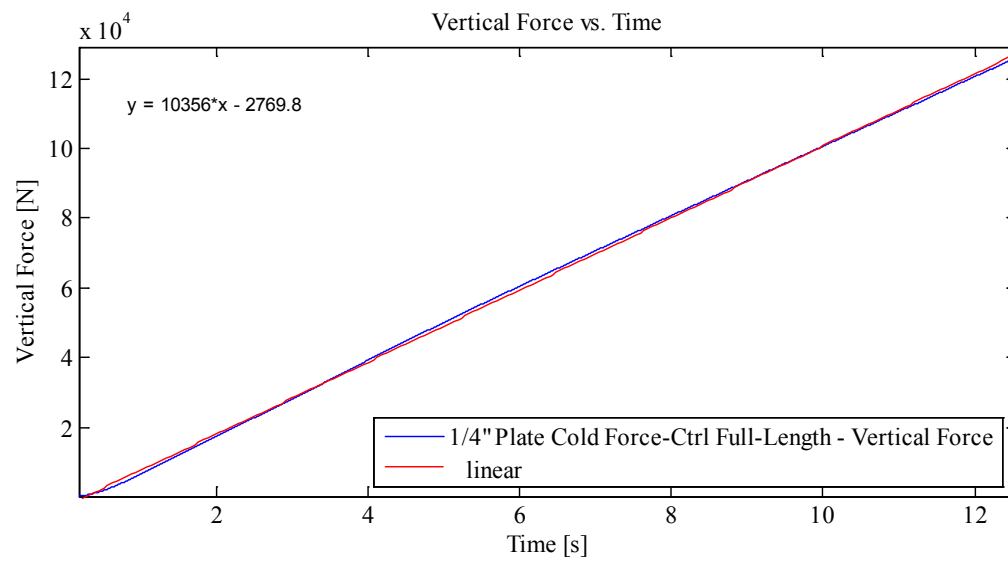
Plots:

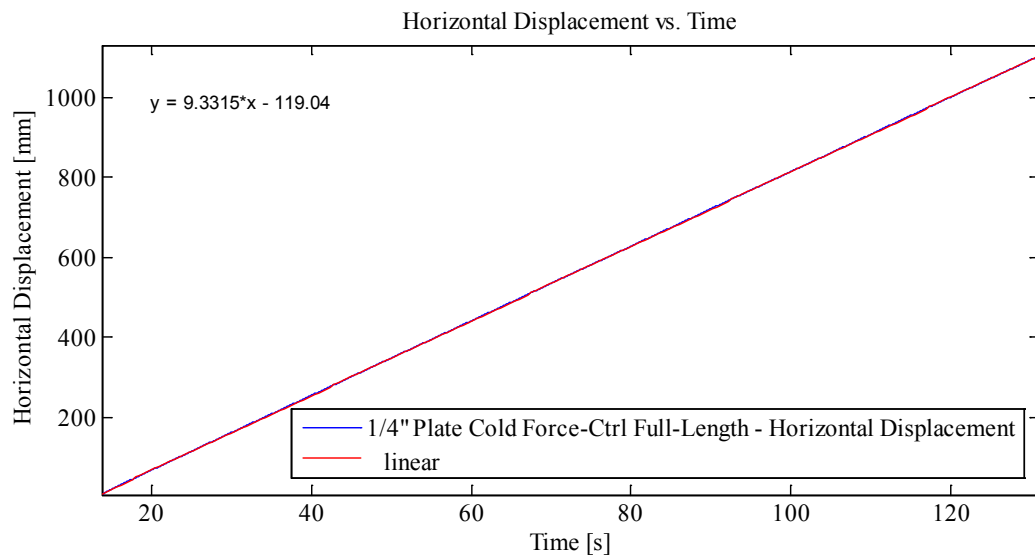
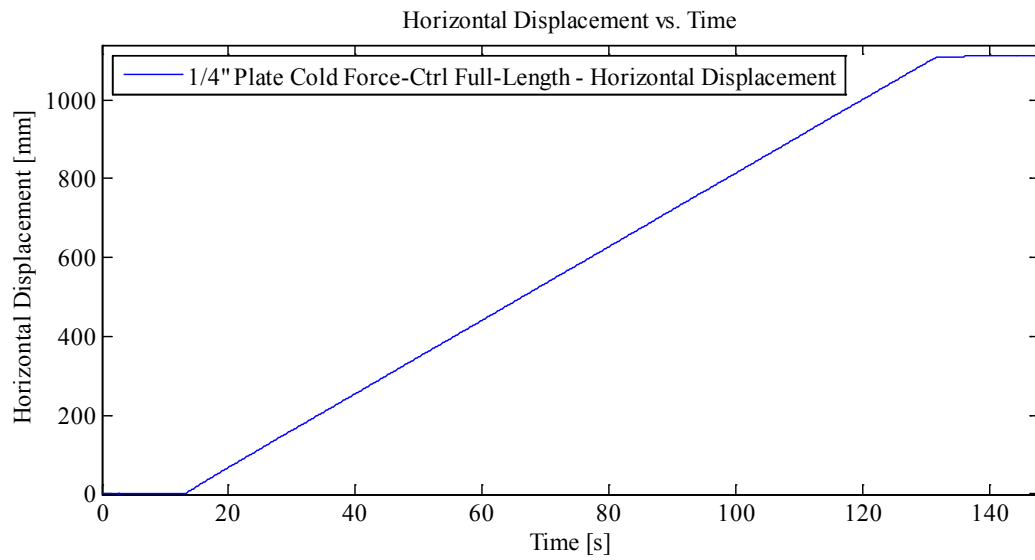


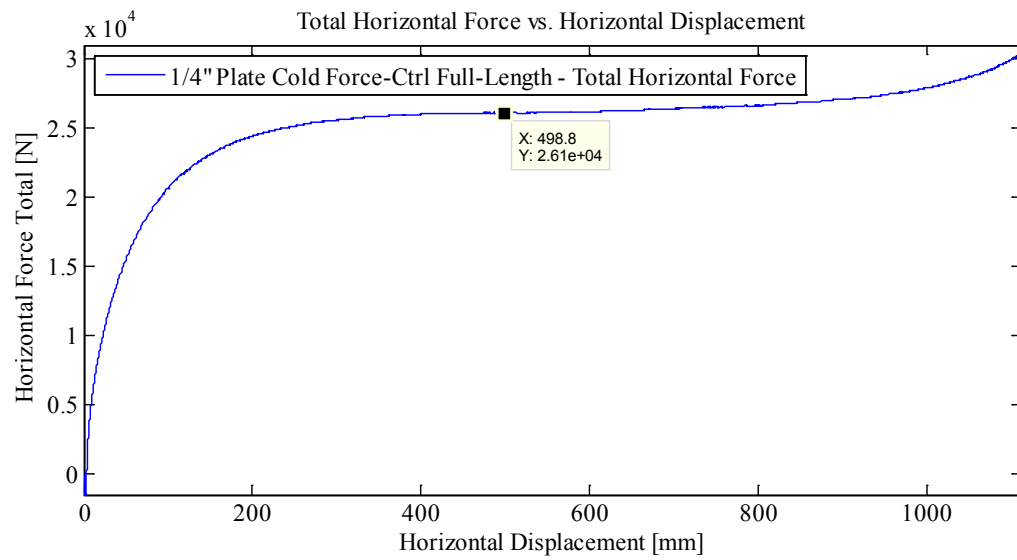
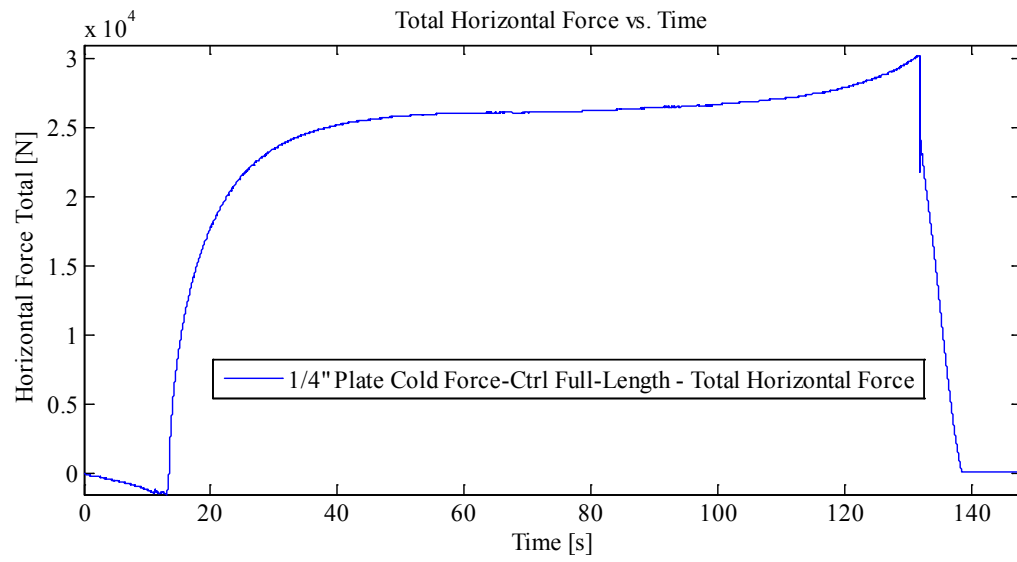


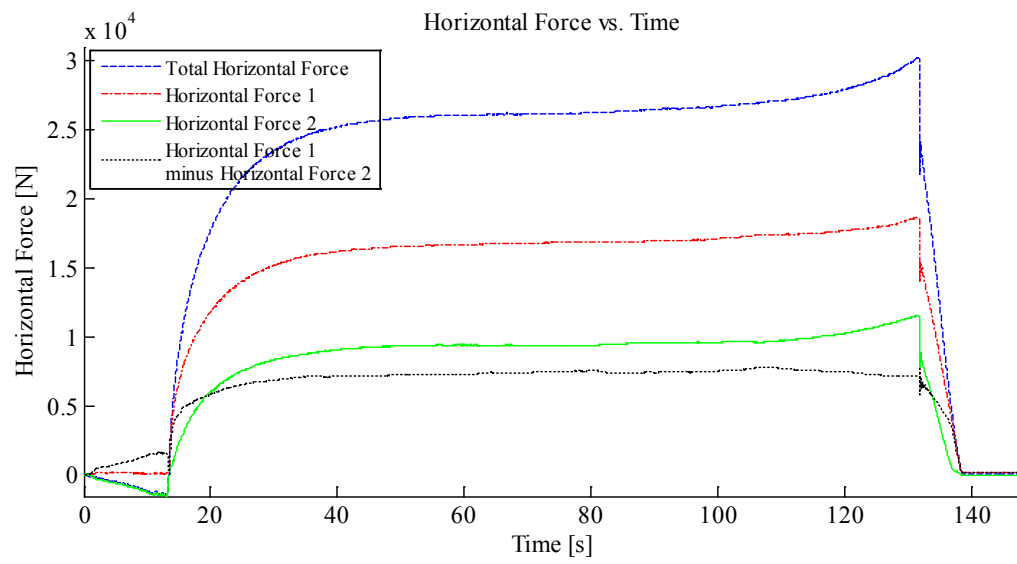












Appendix C2.5.4 – Force Controlled – MovingLoad37

May 5, 2014 at ~3:00p.m.

Run # 25
Run Type: Frame - Force Controlled - Full Length
Room-temperature: -9.9°C (Measured with thermocouple)
Sample Type: Frame
Test Type: In-Along-Out End to End

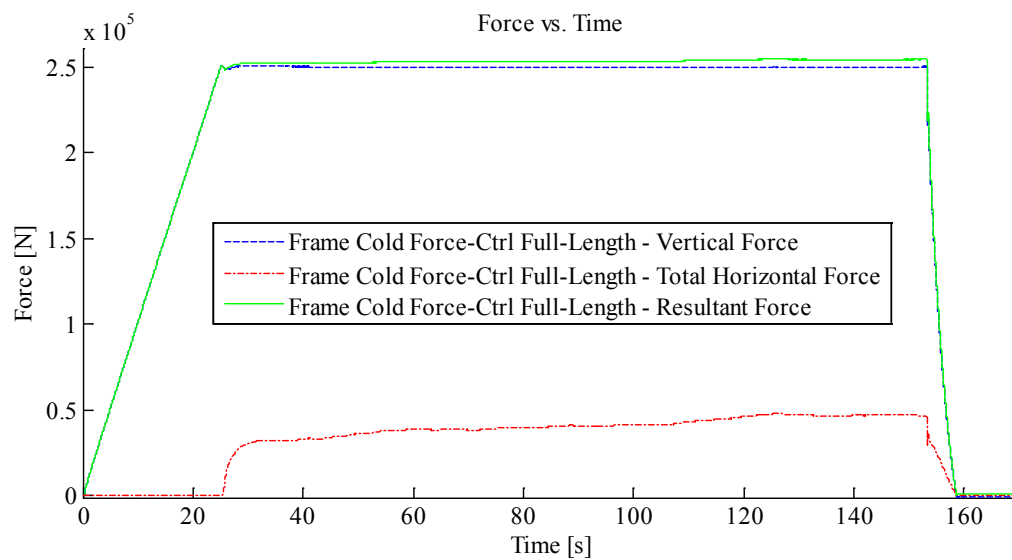
HStarting Point: End (-54.61 cm (-55 cm nominal))
HSpeed: 10mm/s (Nominal)
H Travel: End to End (110+ cm)

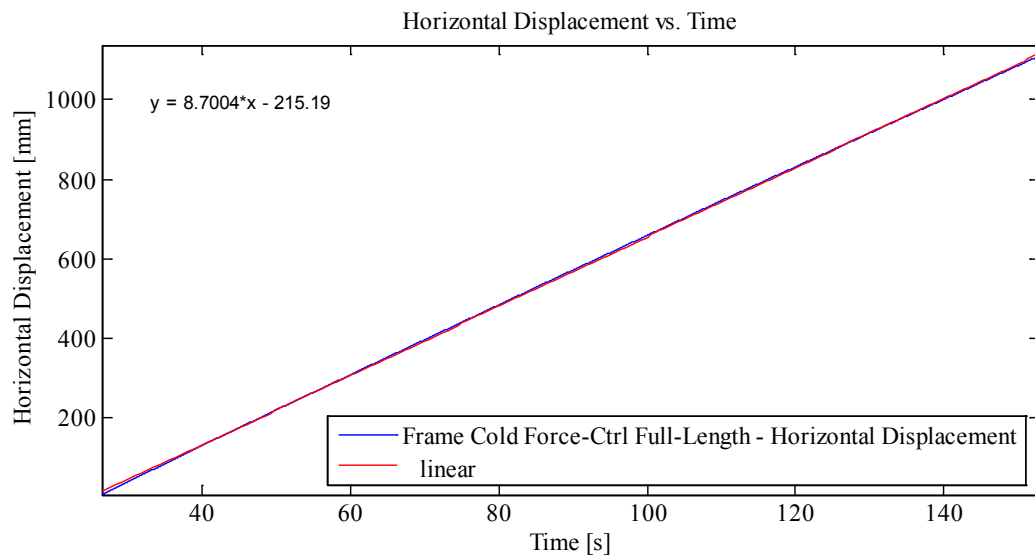
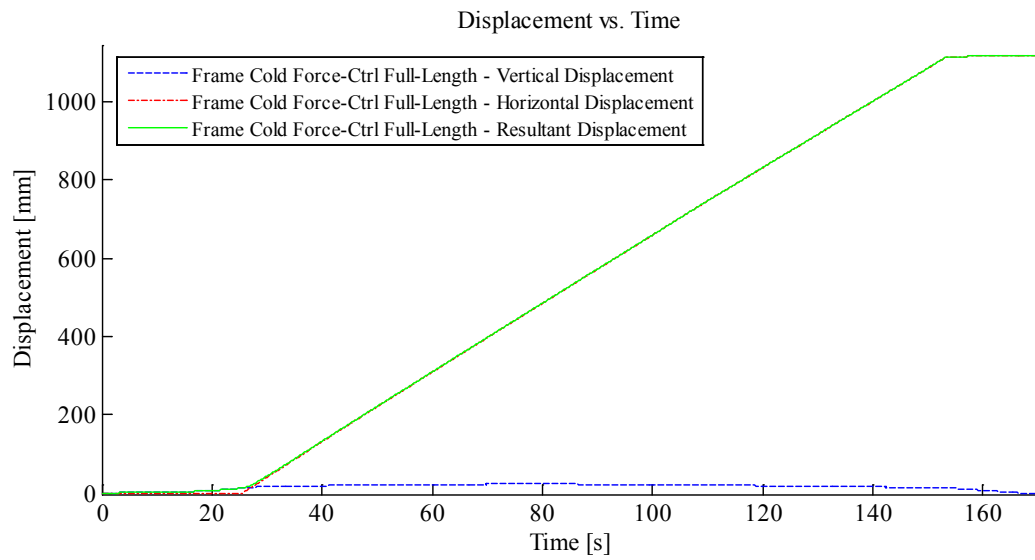
Vstarting Point: 3.35 mm
VSpeed: 10 kN/s
V Force Target: 250 kN
V Disp Limit: -40 mm

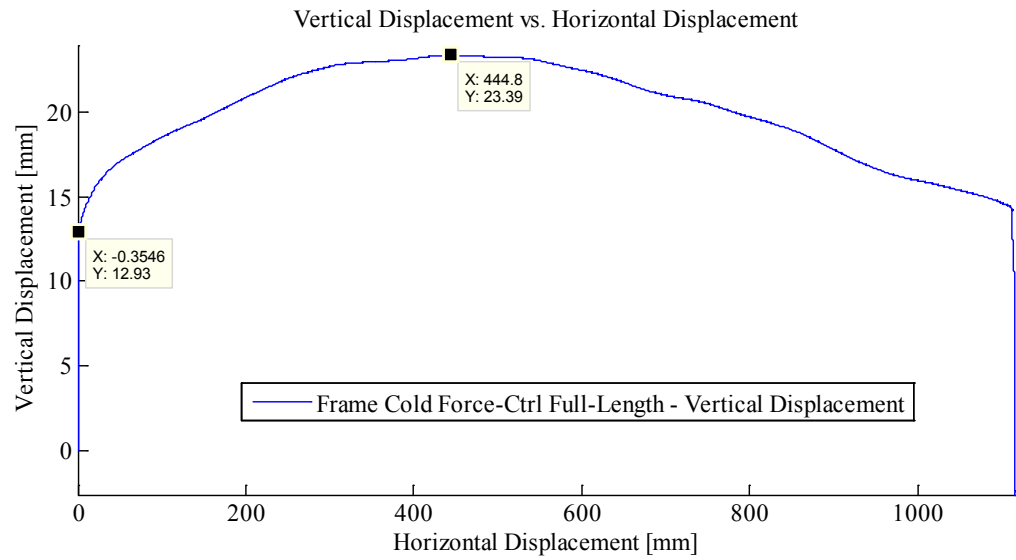
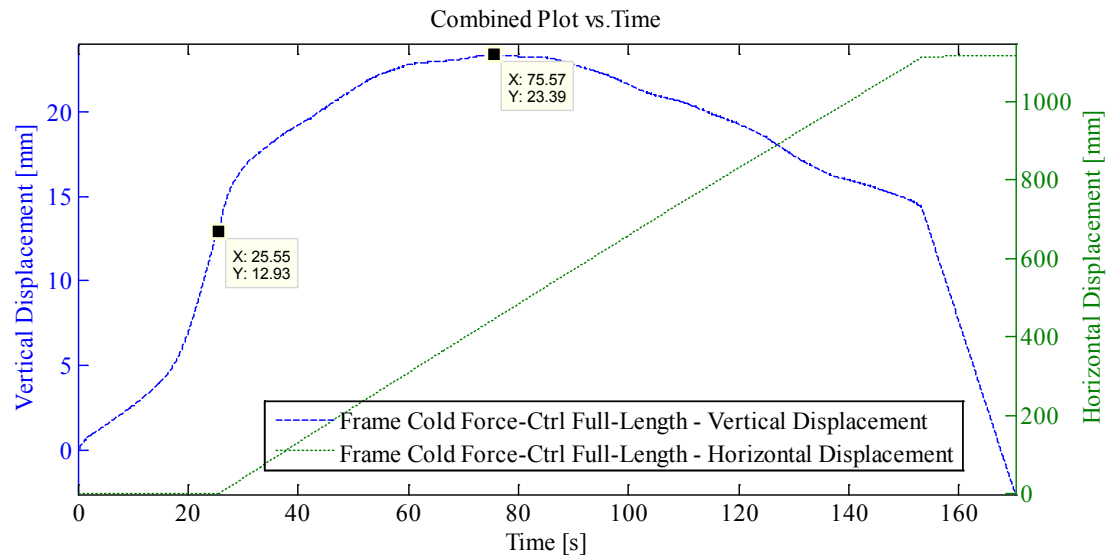
Notes:

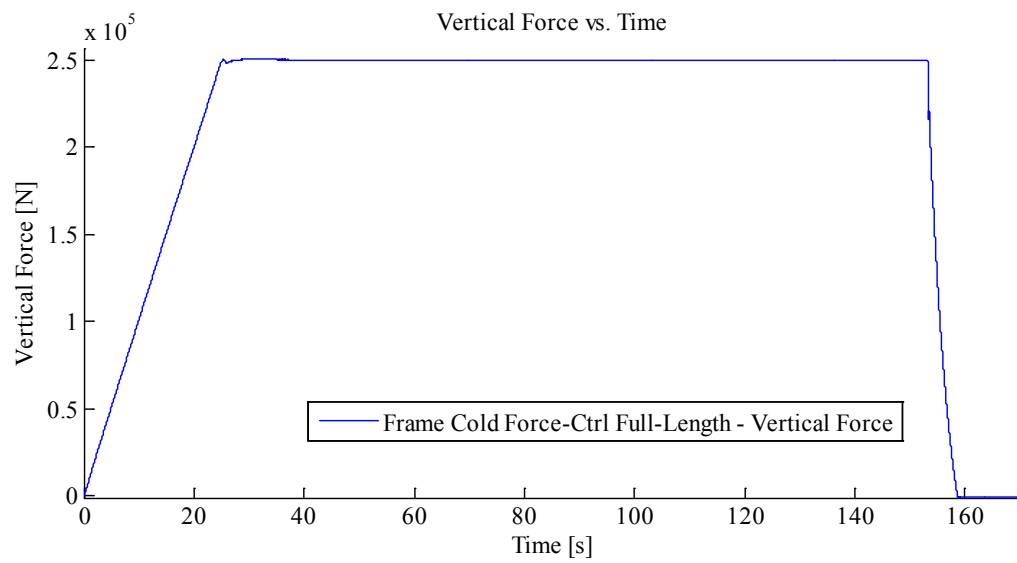
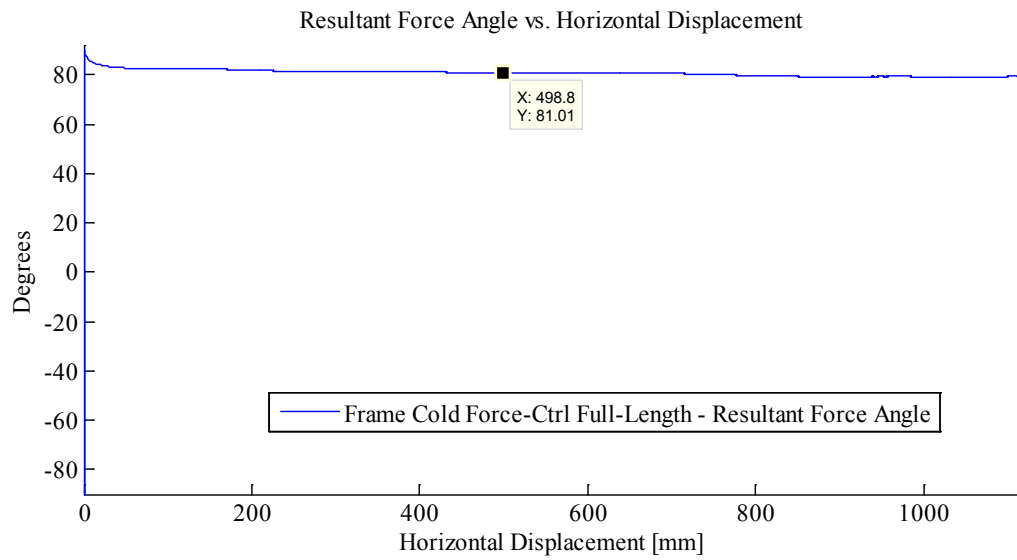
Force 1: 250 kN In-Along-Out - End to End
Data from Indentation 1 saved as MovingLoad37
With one Thermal Video Cameras

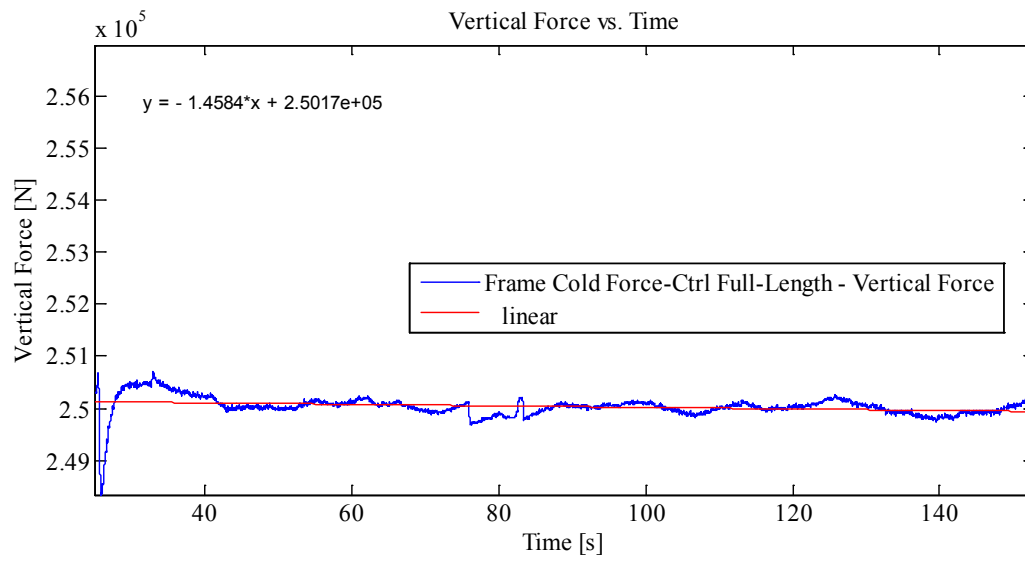
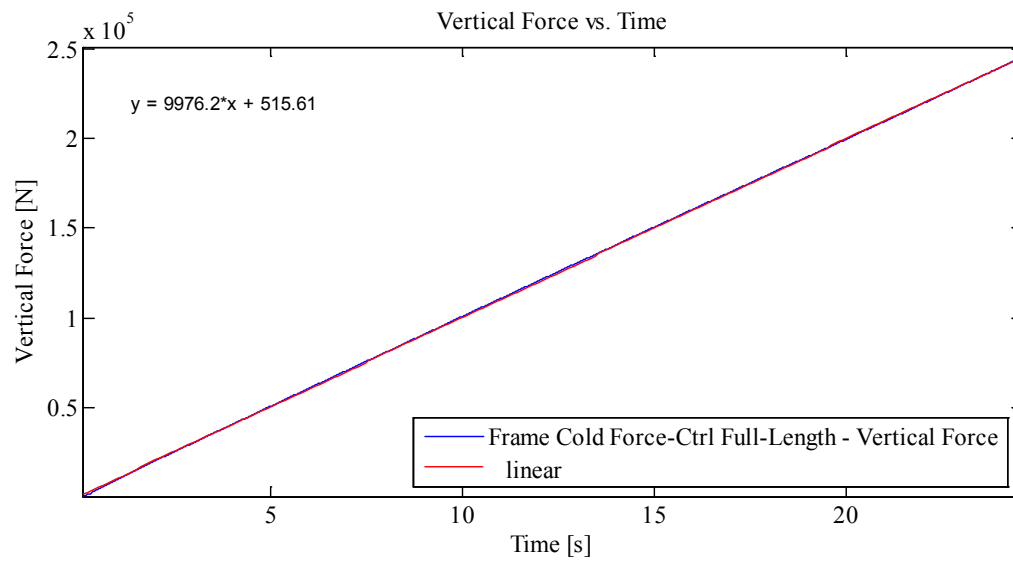
Plots:

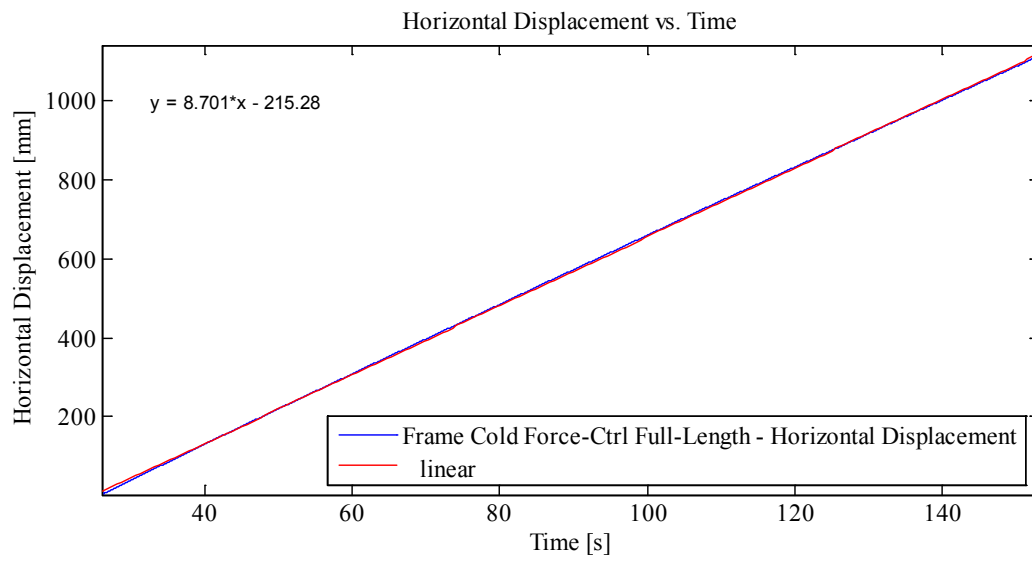
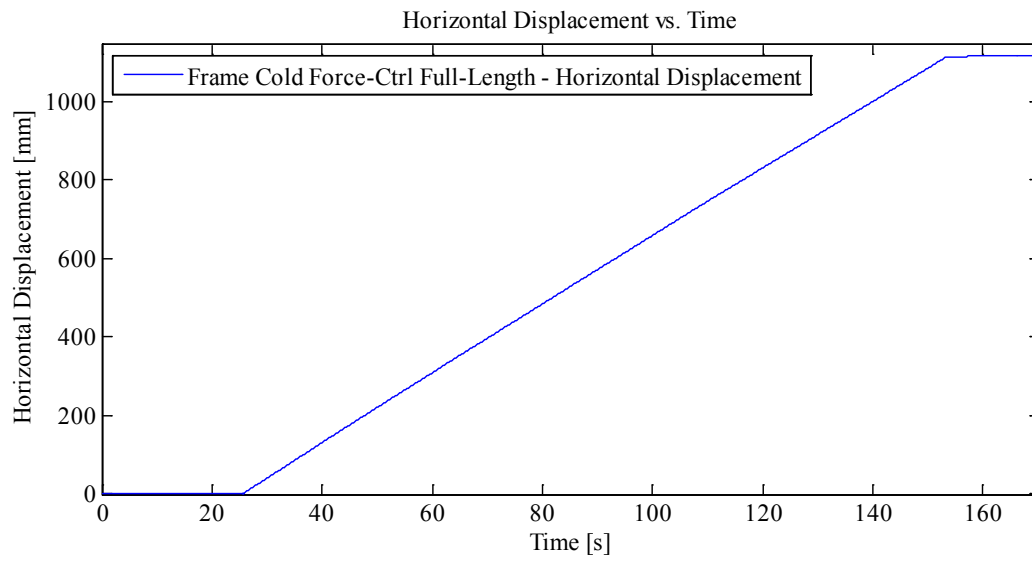


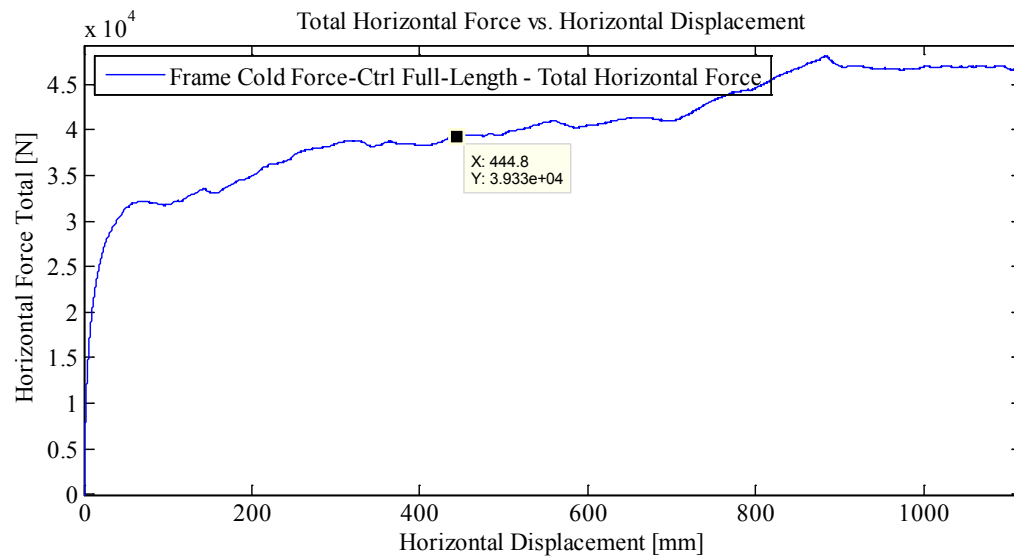
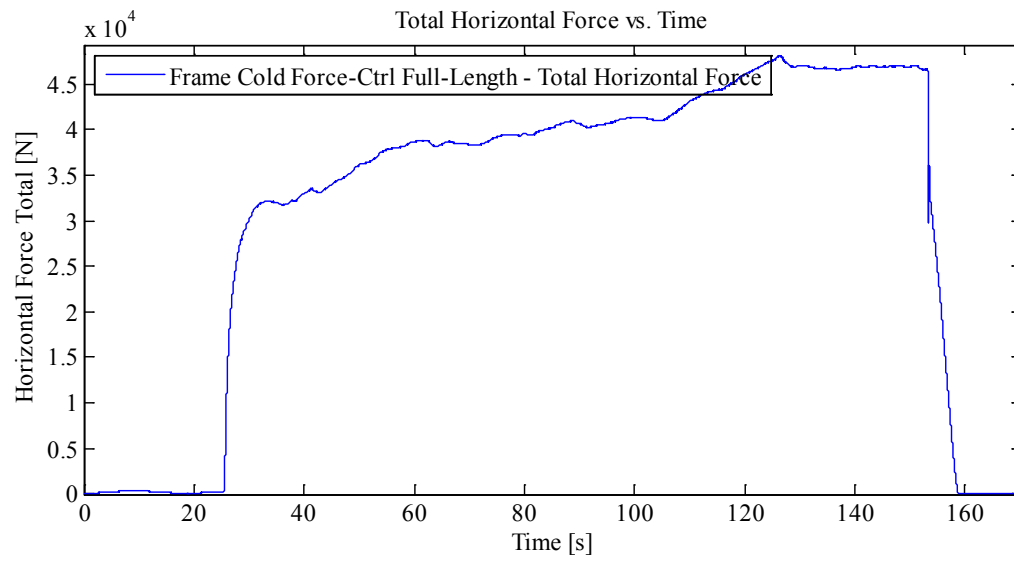


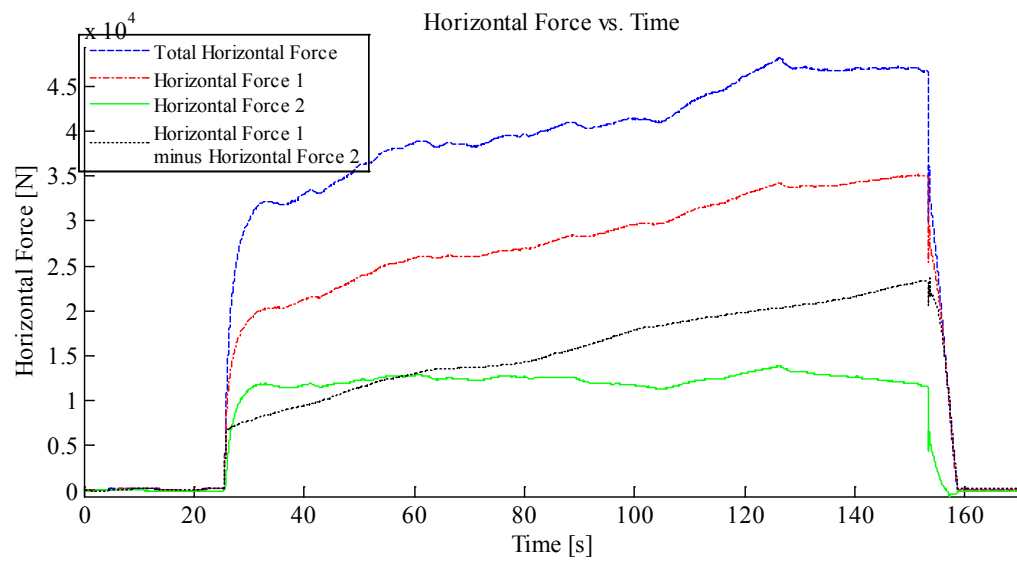












Appendix C3 – Ice Cone Tests

Appendix C3.1 – Ice Cone Tests Inducing Frictionless Elastic Plate

Response

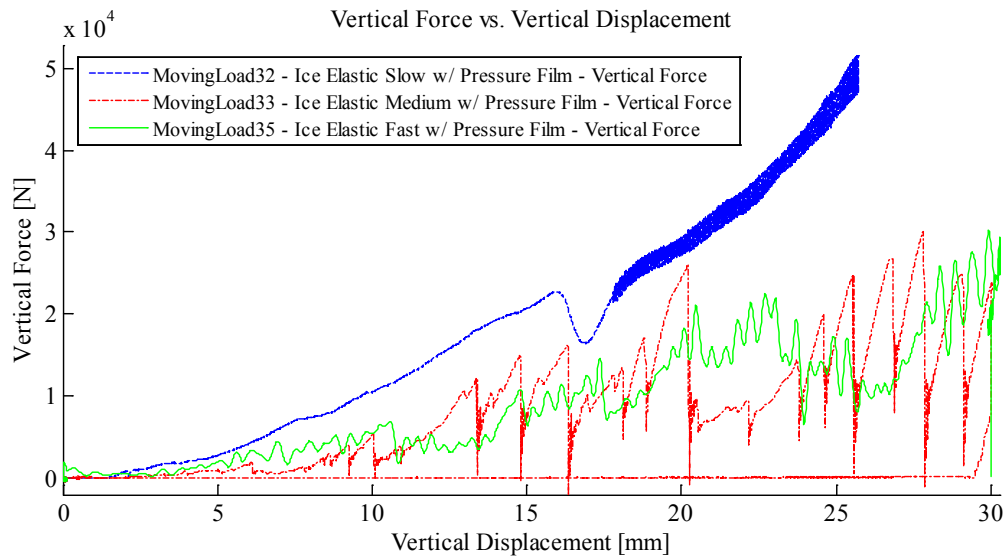
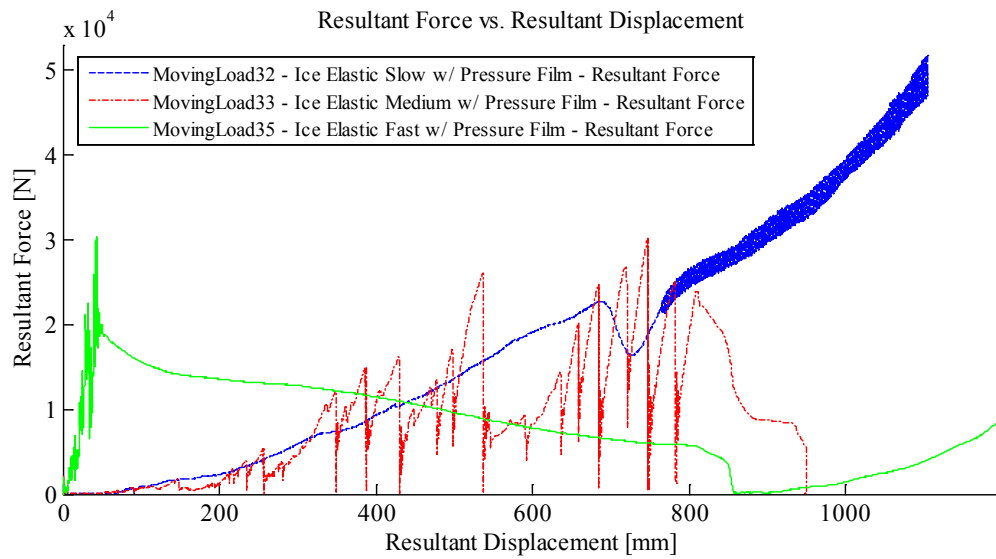
Acknowledgment: The experiments conducted in this section (Appendix C3.1) were a joint effort between Hyunwook Kim and myself. Pressure film was overlaid on the elastic plate test specimen, which did not move relative to the plate. The pressure film recorded the aggregate pressure between the ice cone and the plate as the ice cone moved laterally along the plate. The pressures recorded during these experiments are not included in this thesis, and are as yet unpublished.

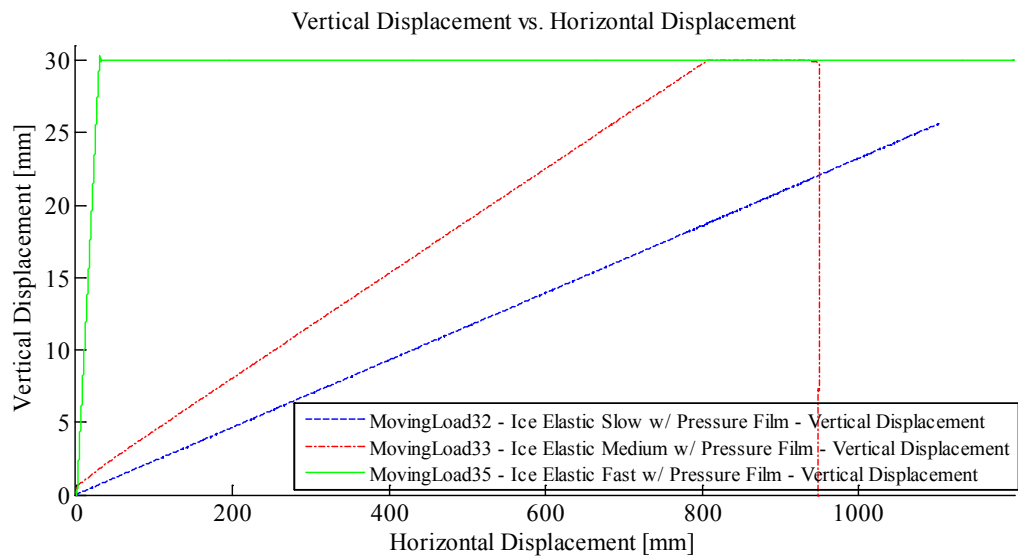
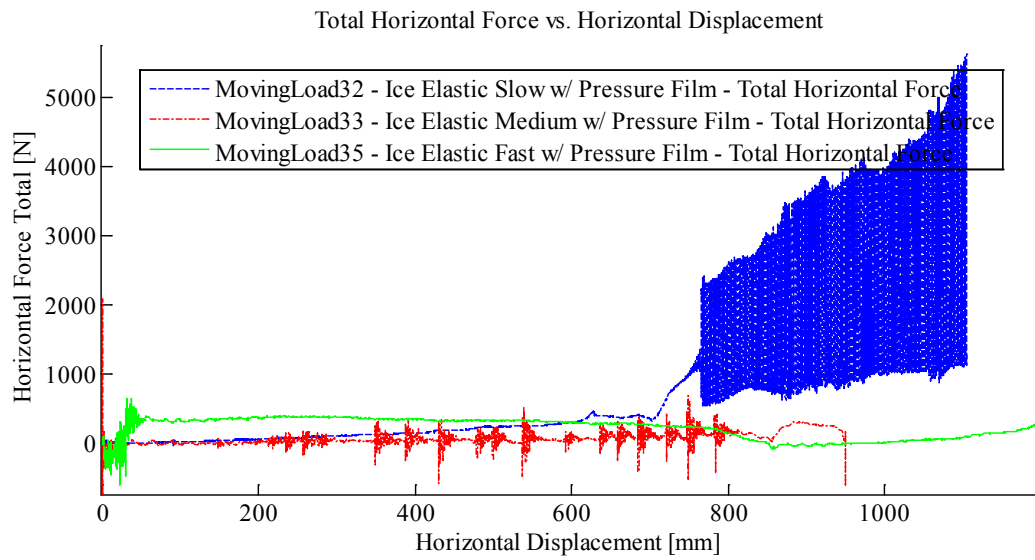
In addition to recording the ice pressure, the pressure film was very smooth, and essentially provided a frictionless surface for the ice to slide along. The results in this appendix may be thought of as practically frictionless, and provide a basis for comparison with the ice cone tests in the following appendix (Appendix C3.2), which are the analog of these tests, but without the pressure film (and hence with normal ice-steel friction).

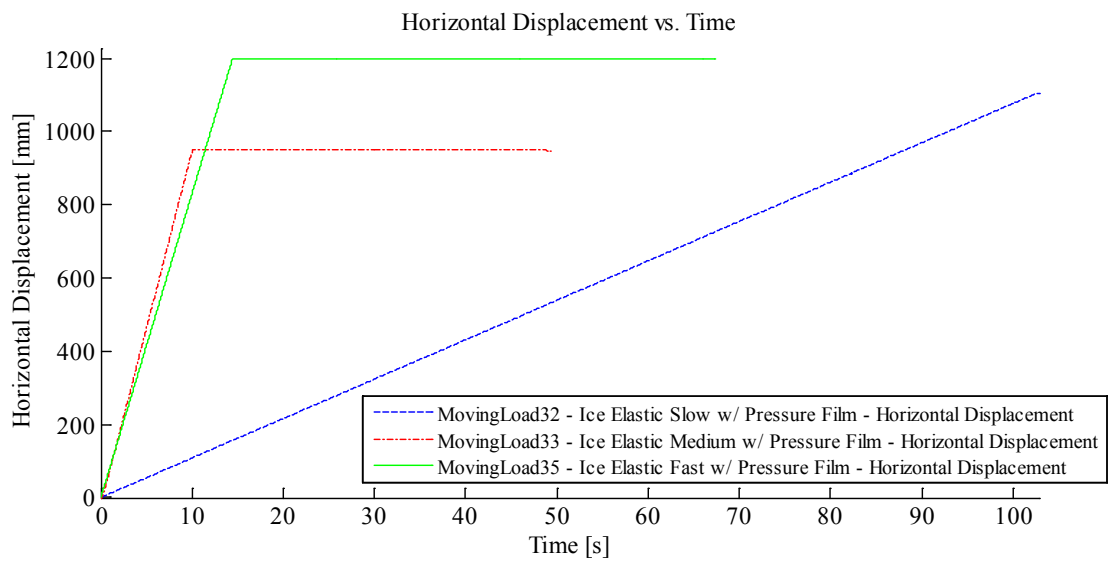
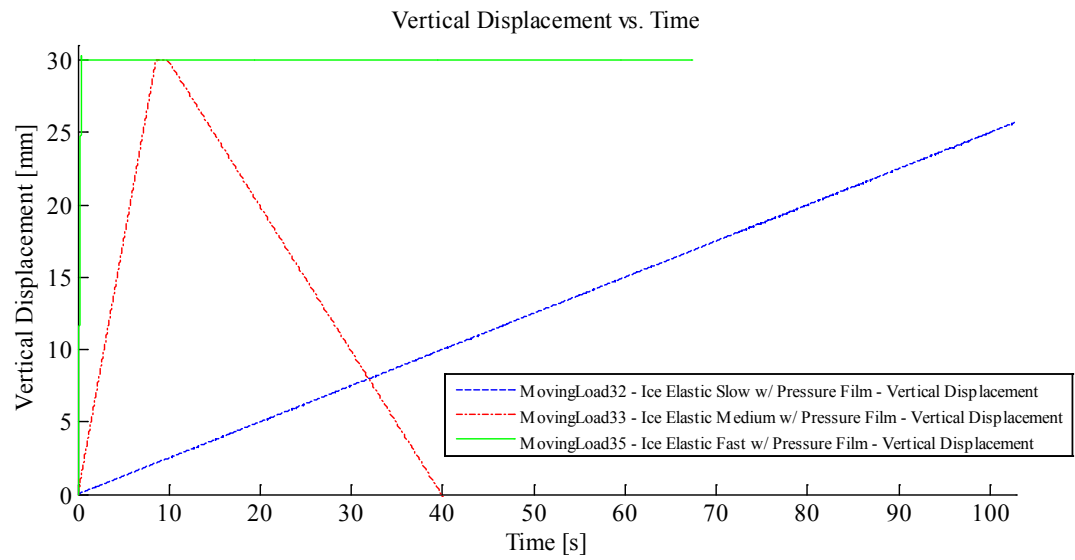
It should further be noted that the longitudinal extent pressure film did not cover the entire plate for each test, therefore there is a “frictionless section” while the ice is sliding along the pressure film; then abruptly returns to a standard ice-steel frictional surface as the ice transitions onto the bare steel plate. This can be observed plainly in the following plots as significant “stick-slip” phenomena begins at the point of transition.

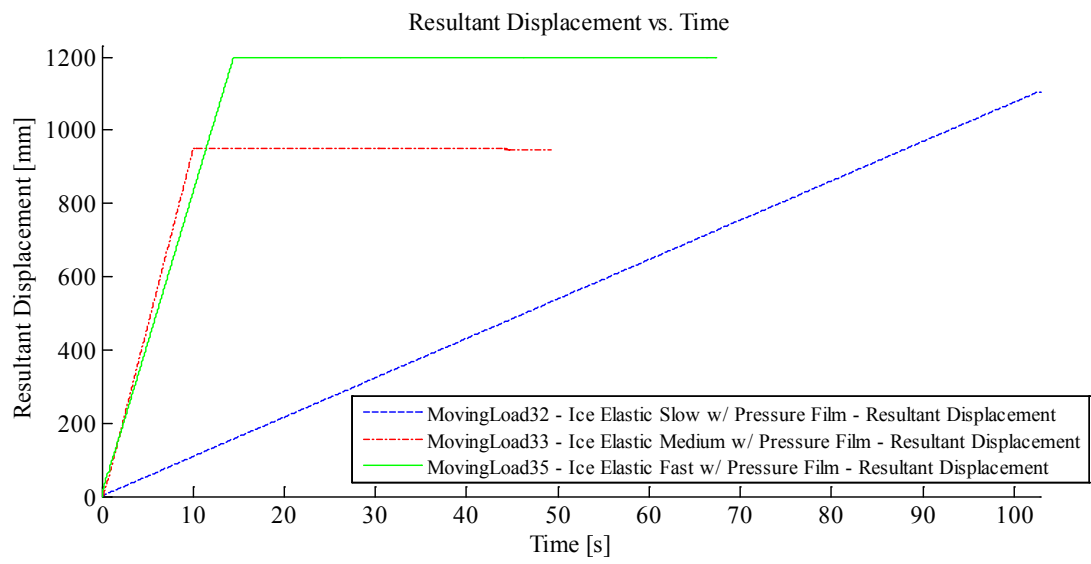
Appendix C3.1.1 – Summary Plots for Experiments ML 32, 33, and 35

35









Appendix C3.1.2 – MovingLoad32

April 28, 2014 at ~3:30p.m.

Run #

Run Type: Ice Cone – Pressure Film 1

Room-temperature: -8.9°C (Measured with thermocouple)

Sample Type: 1/2" Plate with Ice

Test Type: In-Along-Out End to End

HStarting Point: End (-54.84 cm (-55 cm nominal))

HSpeed: 10mm/s (Nominal)

H Travel: End to End (110+ cm)

Vstarting Point: -0.60 mm

VSPEED: 0.25 mm/s

V Target: -30.6 mm

V Travel: 30.0 mm

Notes:

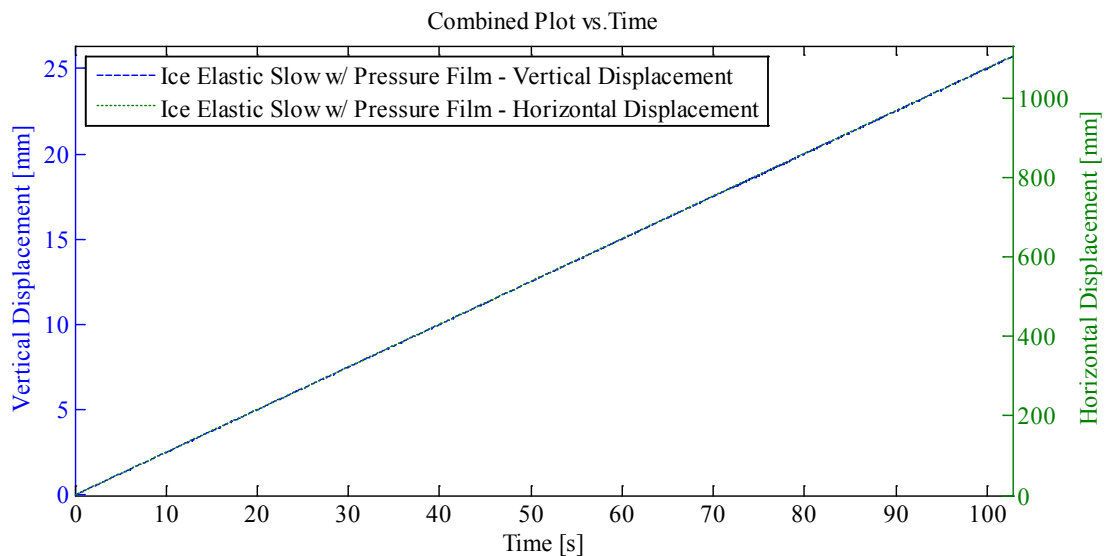
Force 1: 3 cm Ice Indentation In-Along-Out - End to End

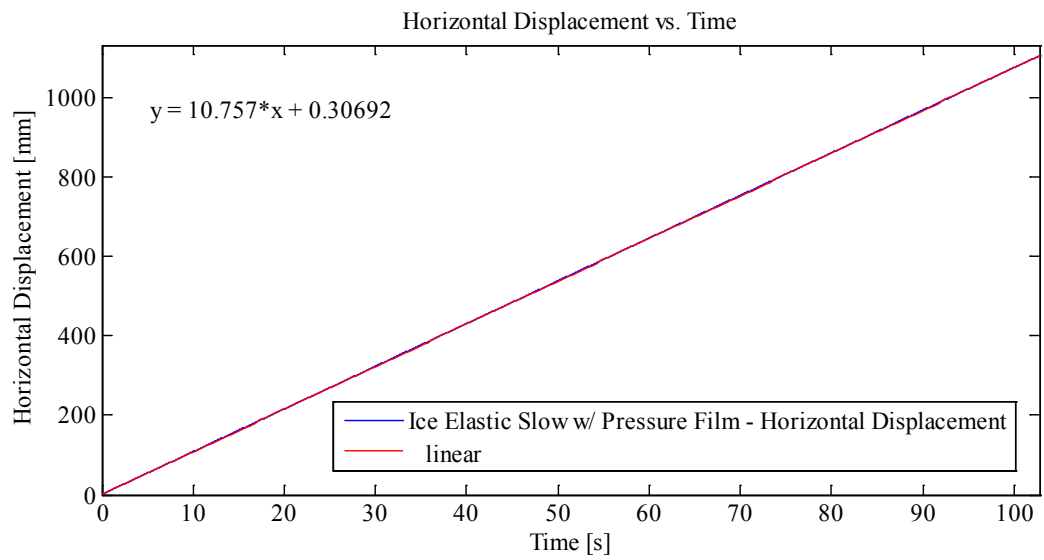
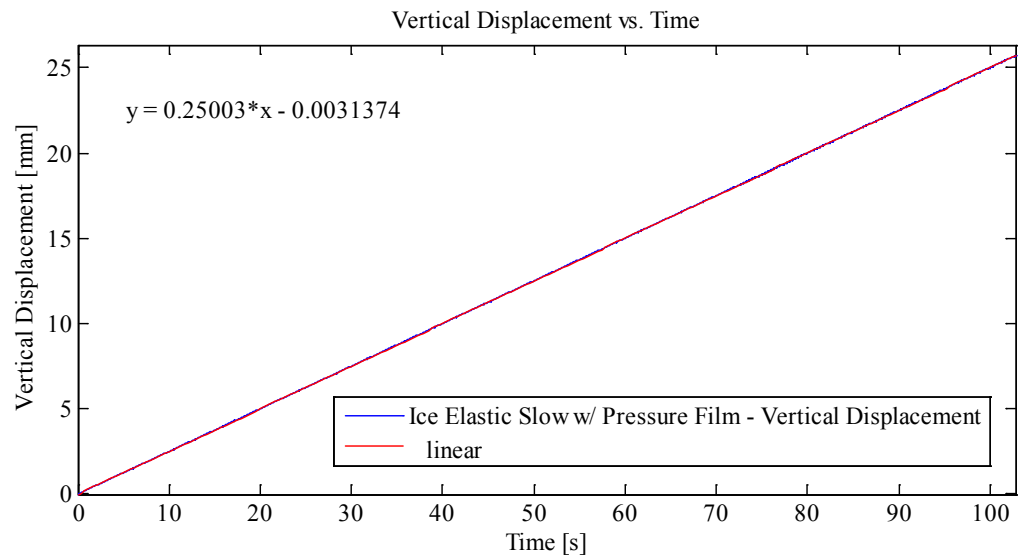
Data from Indentation 1 saved as MovingLoad32

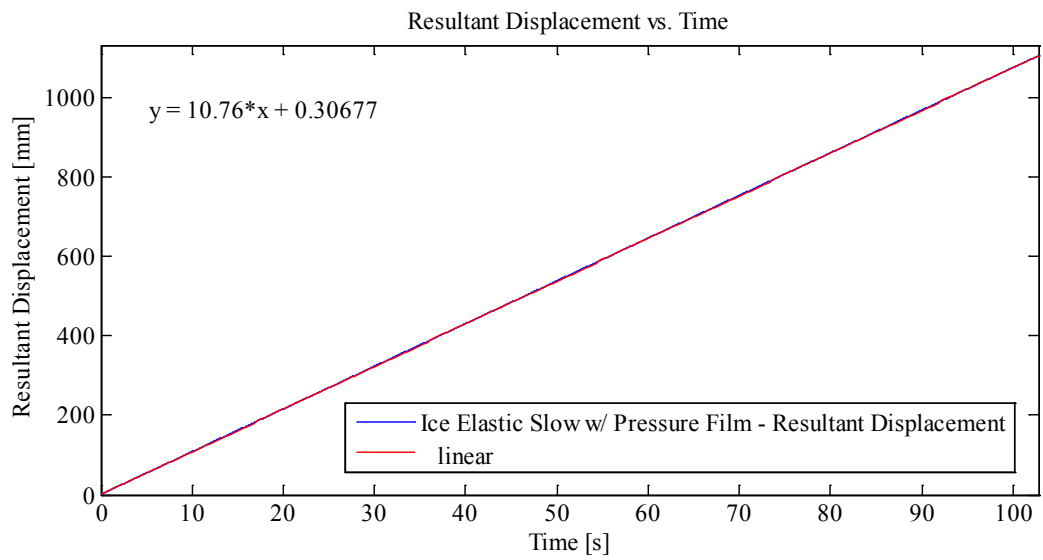
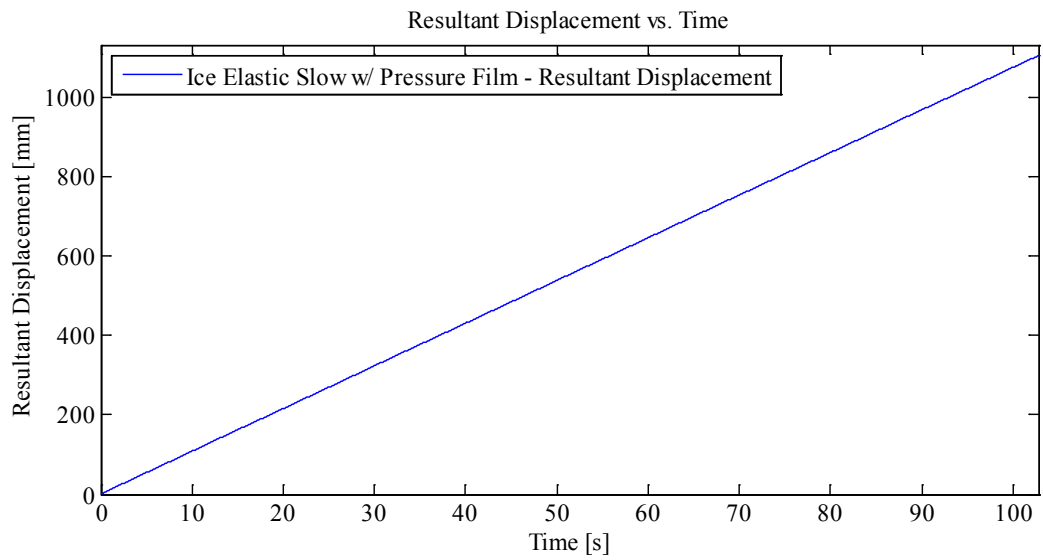
With Two Thermal Video Cameras and High Speed

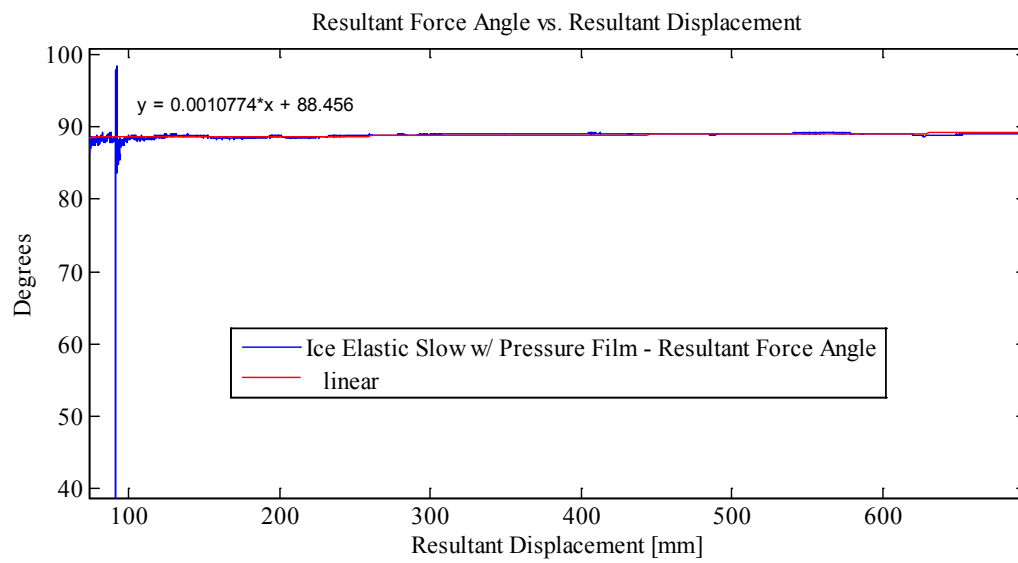
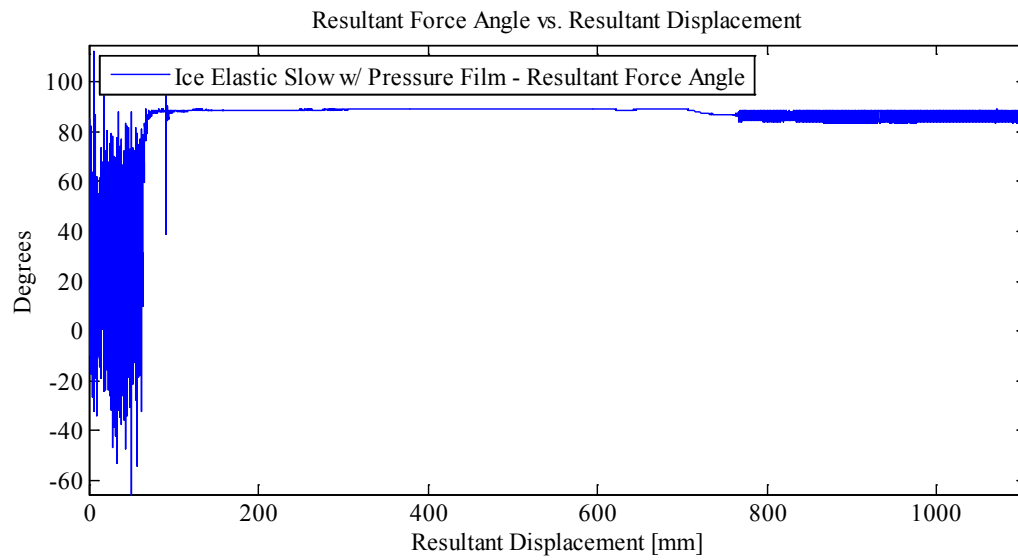
With Pressure Film

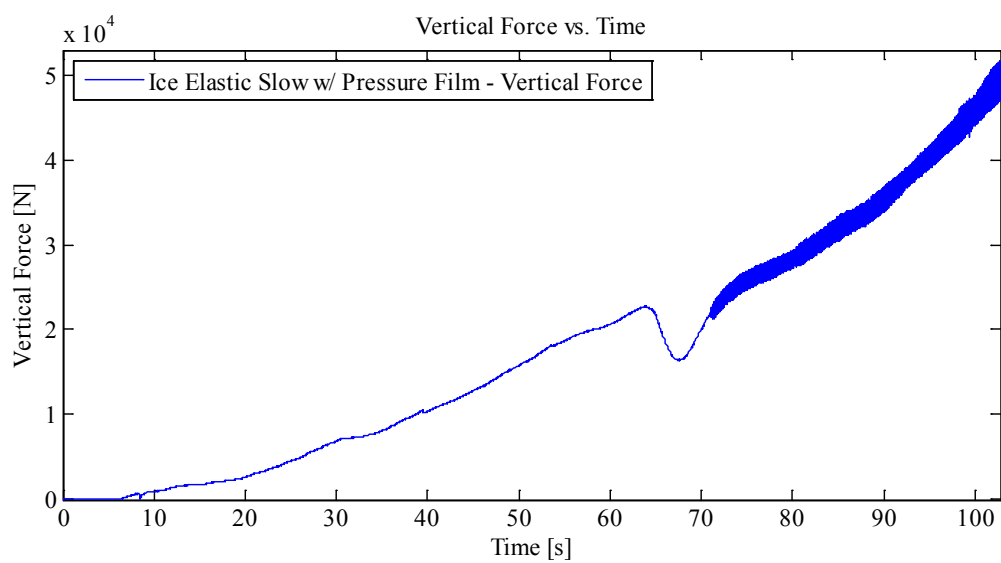
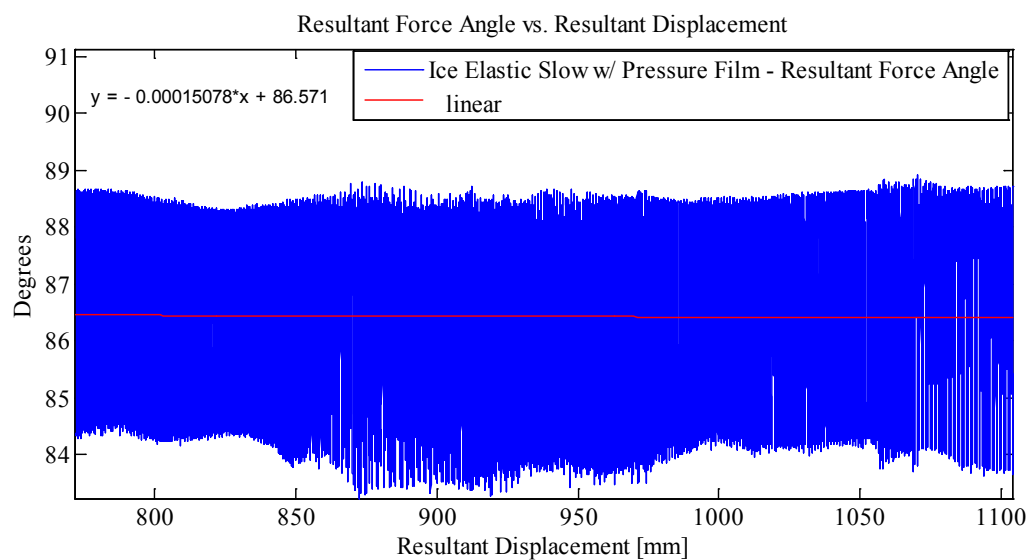
Plots:

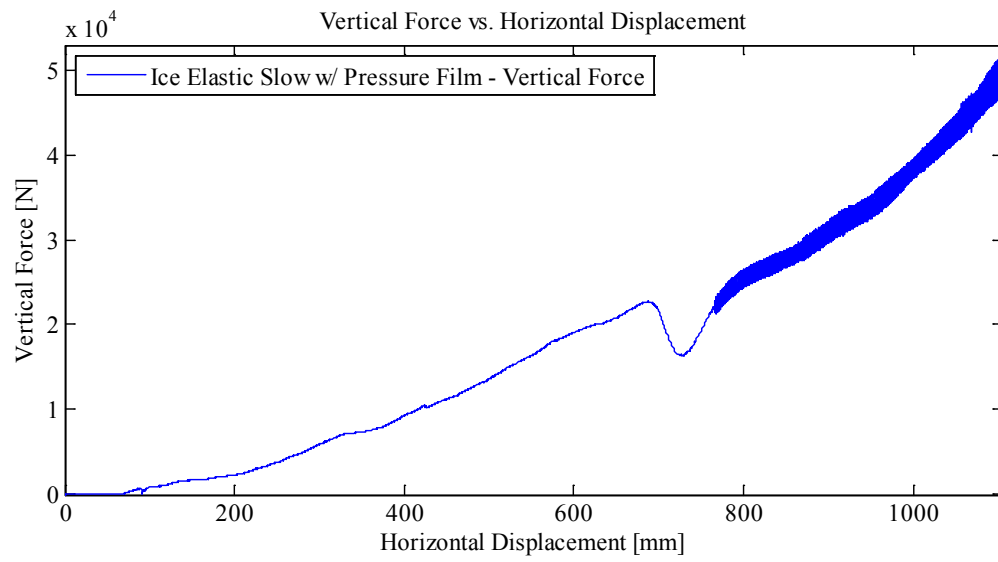
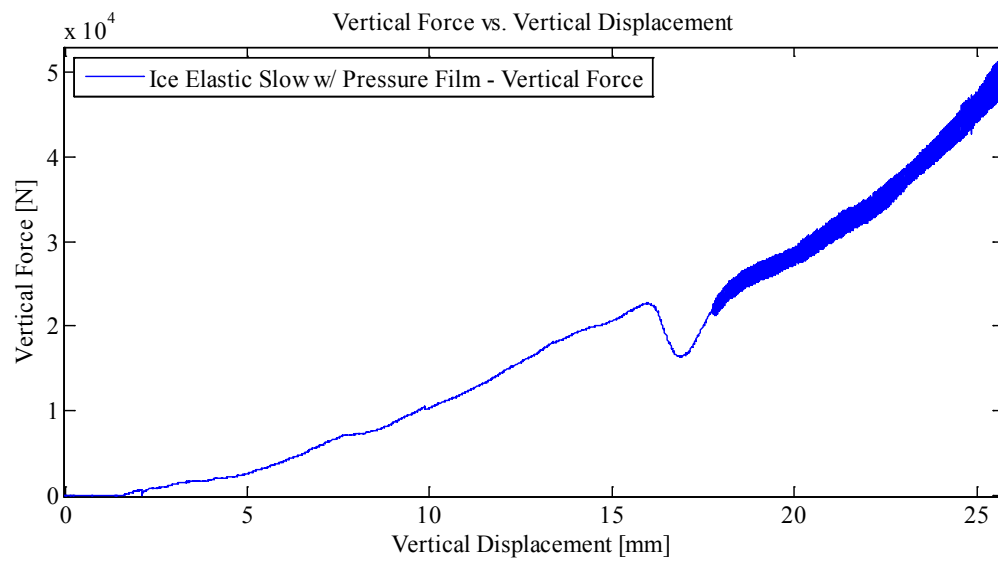


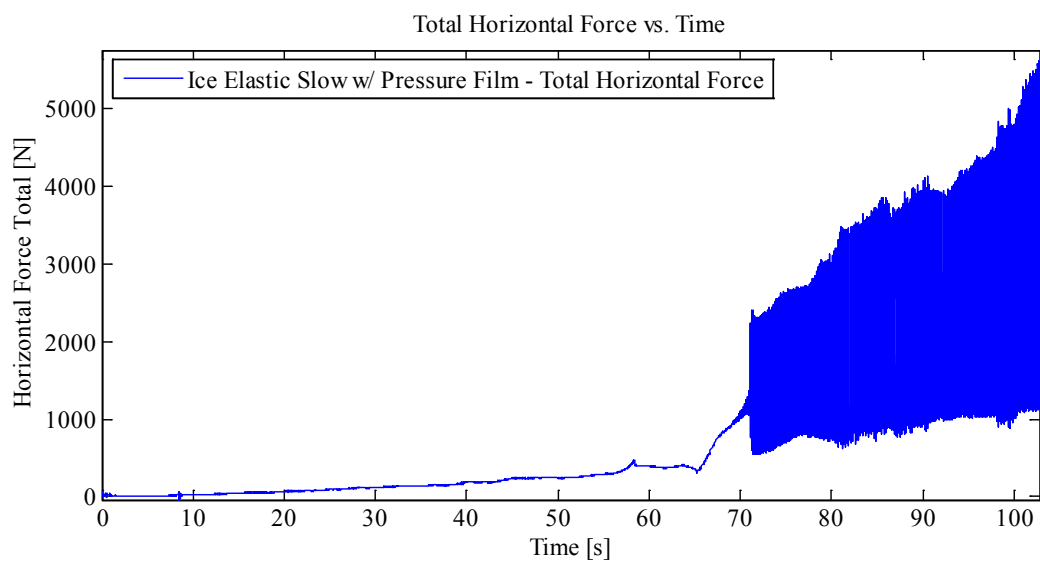
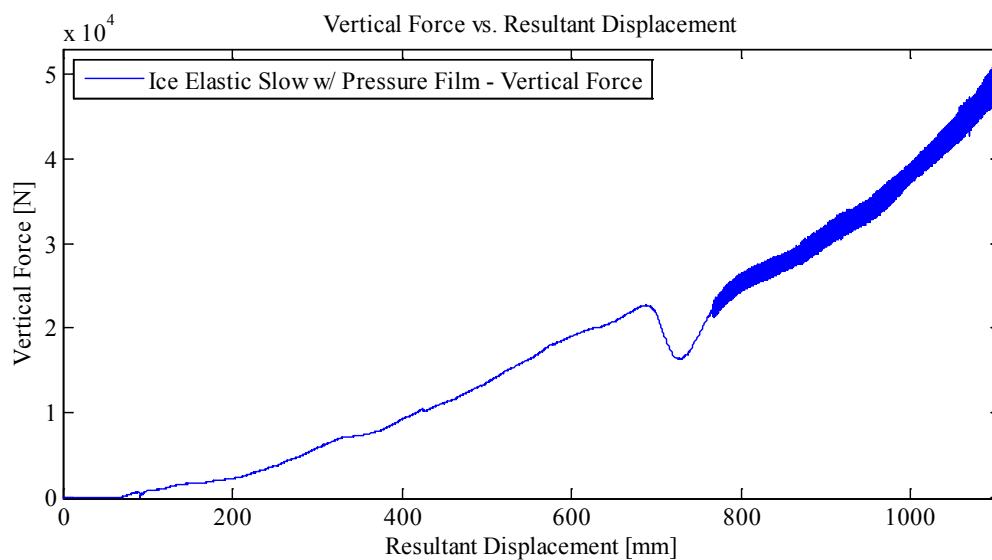


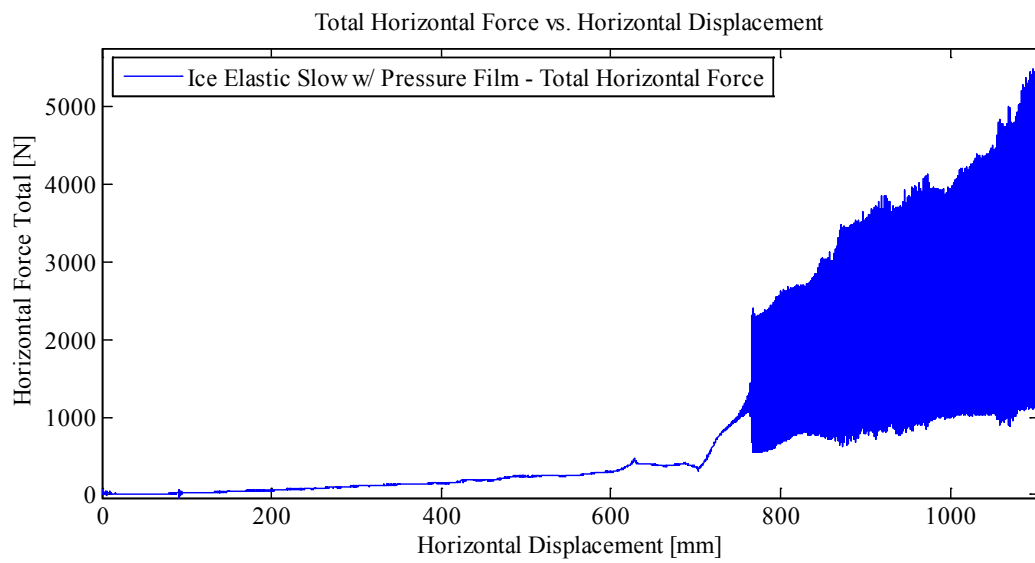
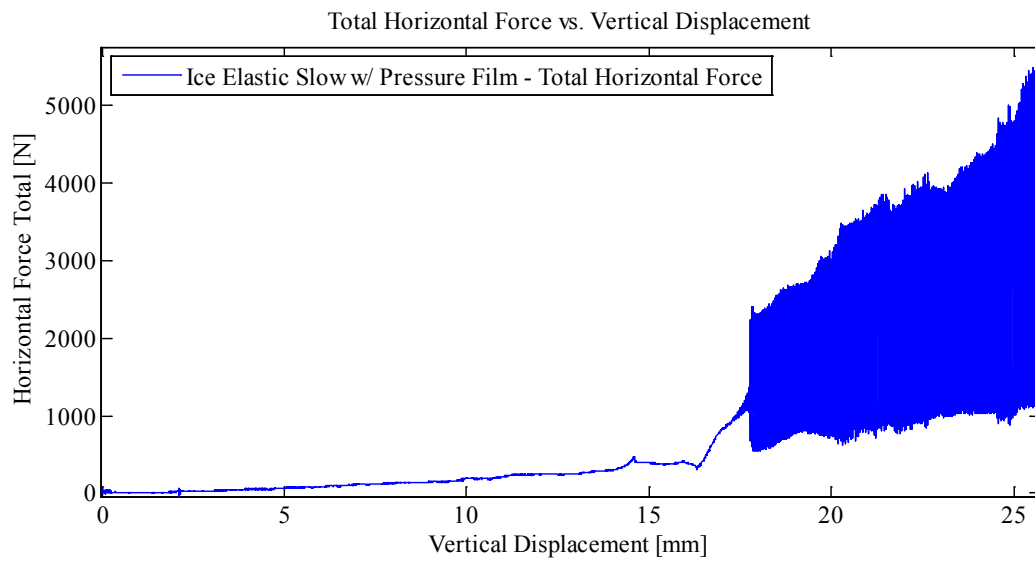


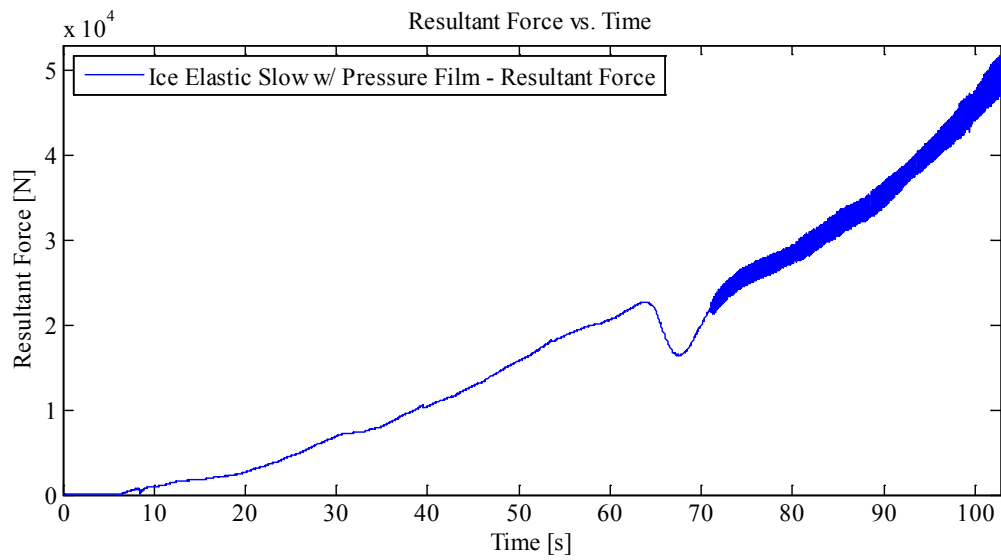
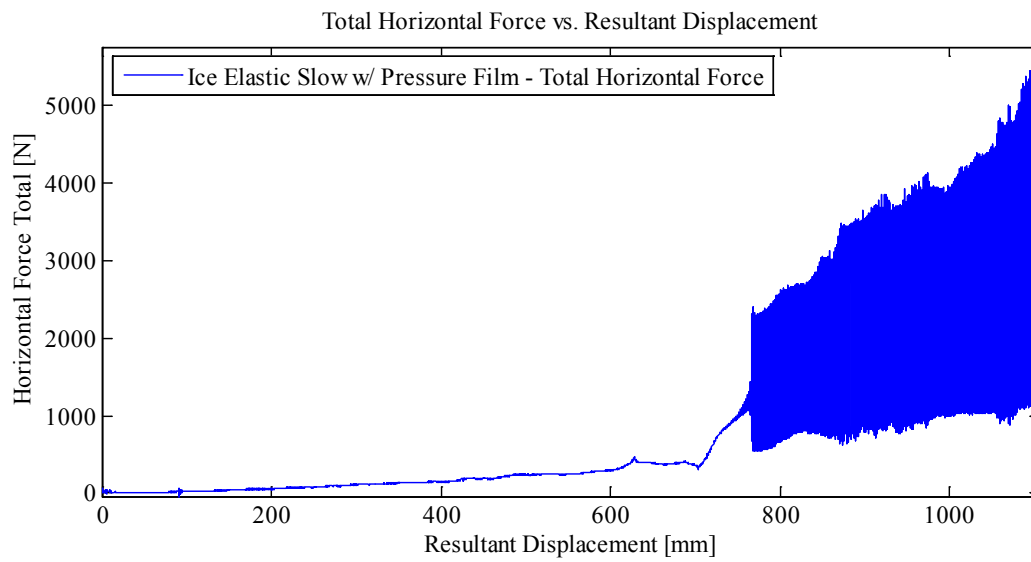


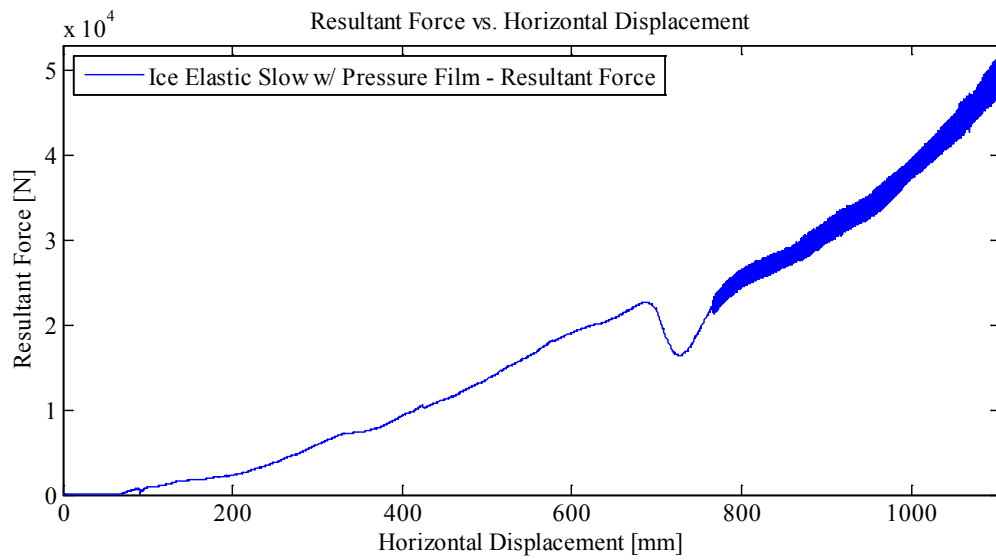
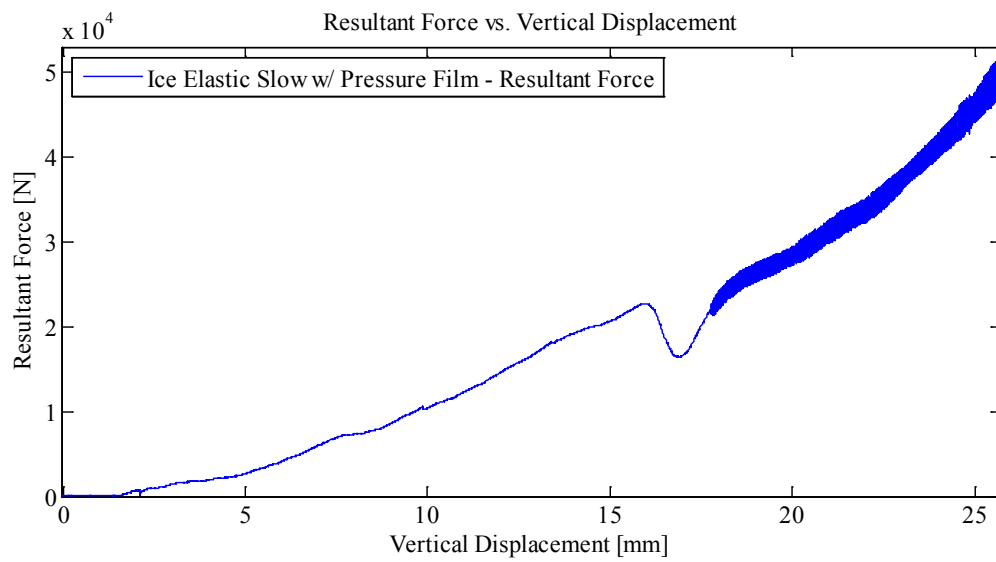


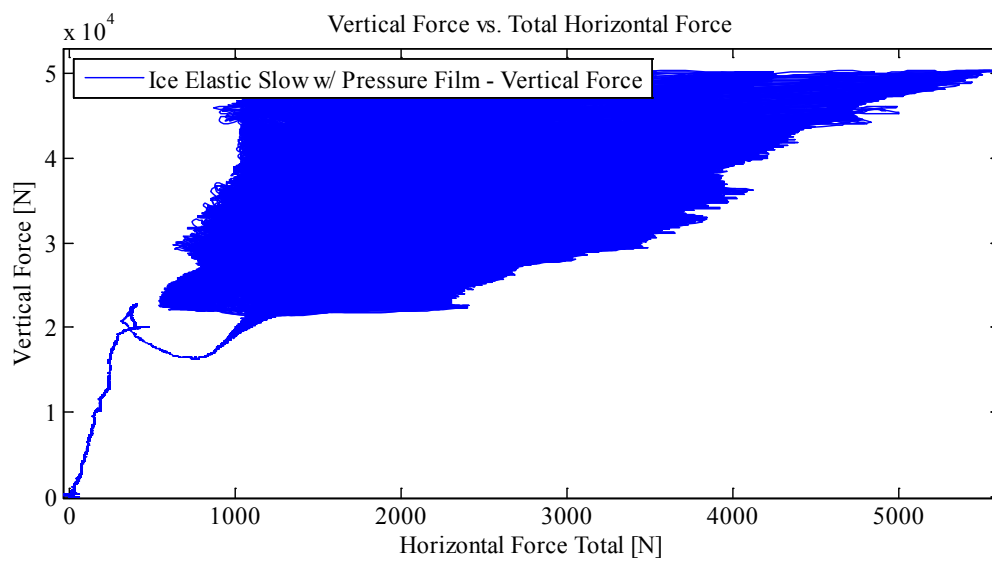
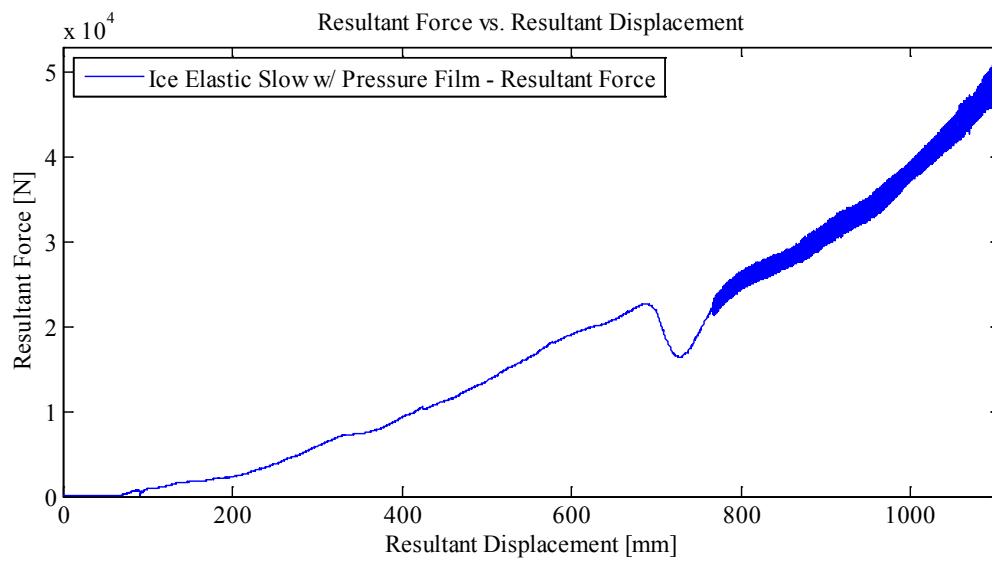


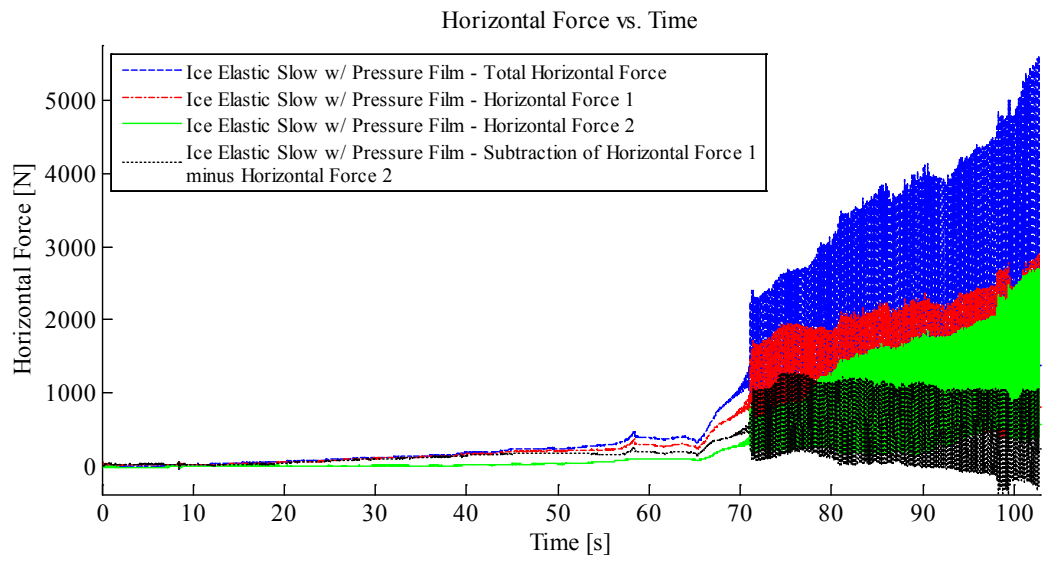












Appendix C3.1.3 – MovingLoad33

April 29, 2014 at ~12:00p.m.

Run #

Run Type: Ice Cone – Pressure Film 2

Room-temperature: -8.9°C (Measured with thermocouple)

Sample Type: 1/2" Plate with Ice

Test Type: In-Along-Out End to end of pressure film (85 cm)

HStarting Point: End (-61.49 cm (absolute end))

HSpeed: 100mm/s (Nominal)

H Travel: Abs. End to end of pressure film (85 cm)

Vstarting Point: 0.60 mm

VSpeed: 3.5 mm/s

V Target: -29.4 mm

V Travel: 30.0 mm

Notes:

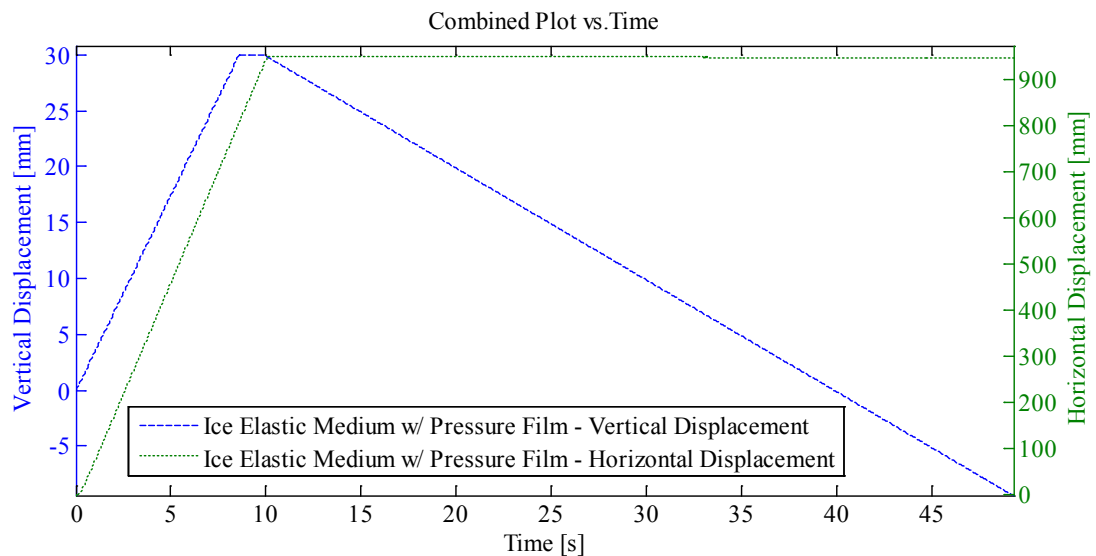
Force 1: 3 cm Ice Indentation In-Along-Out - End to End

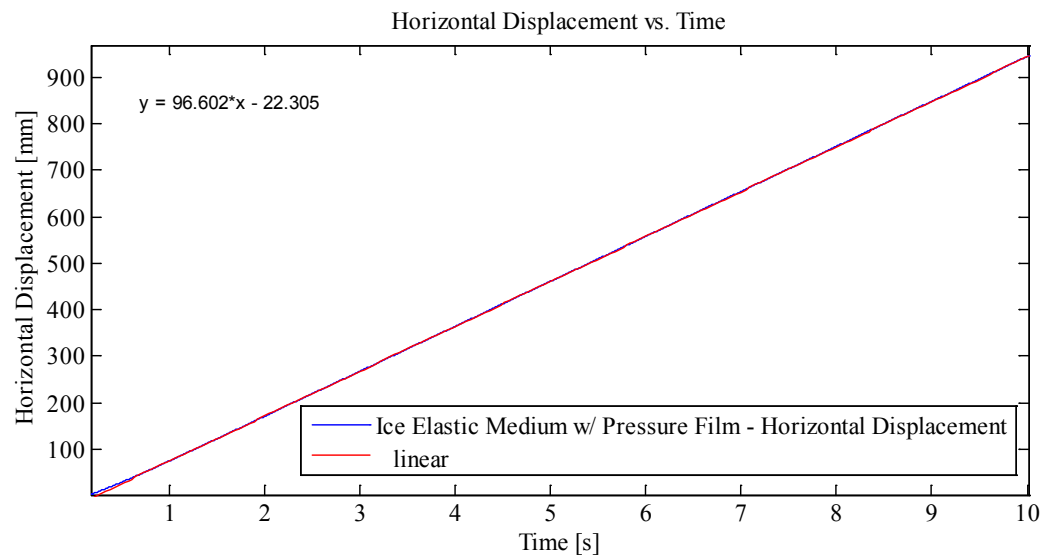
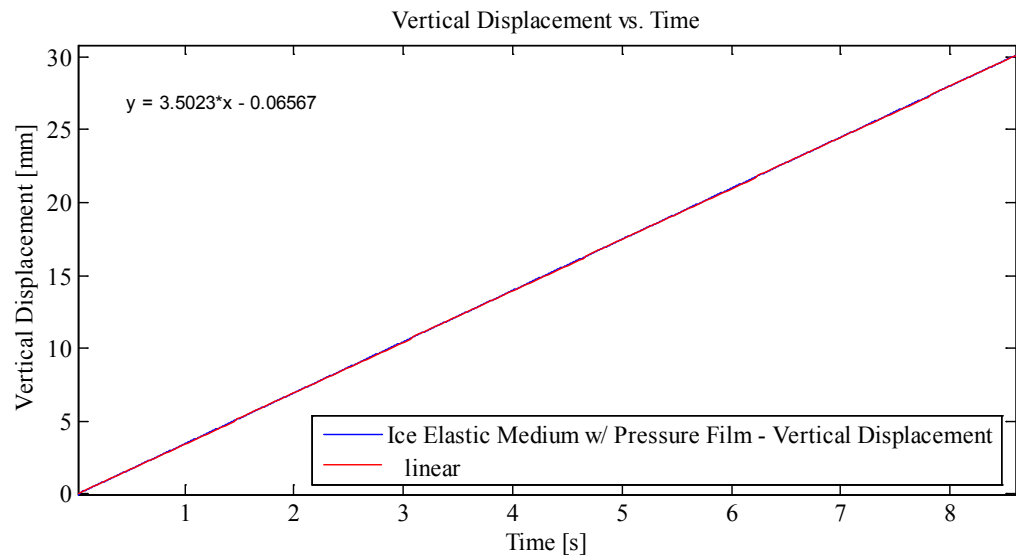
Data from Indentation 1 saved as MovingLoad33

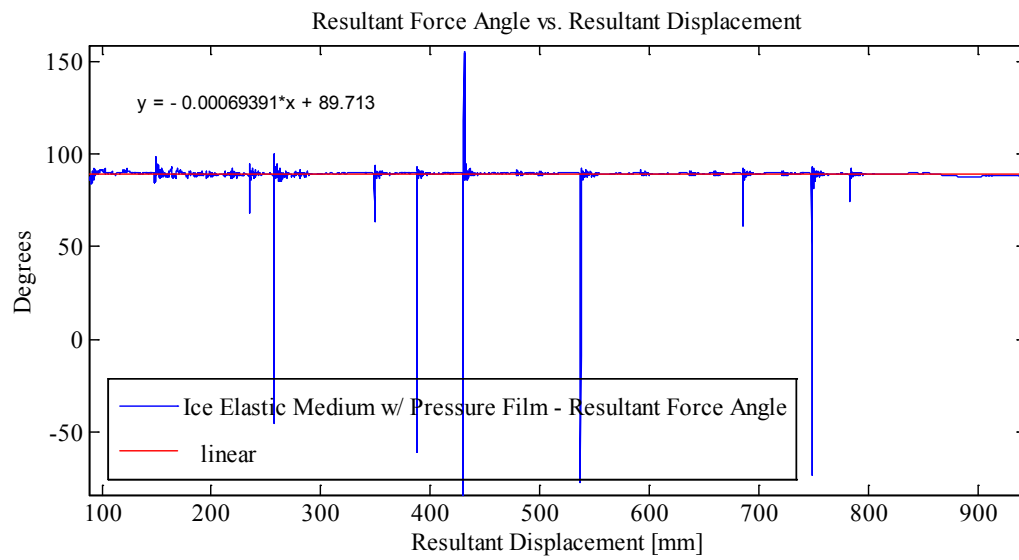
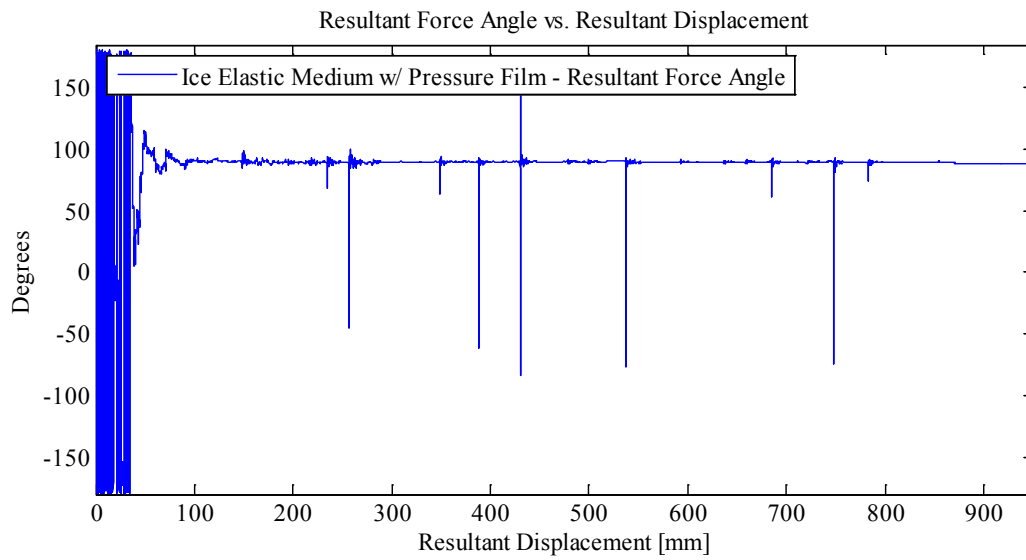
With Two Thermal Video Cameras and High Speed

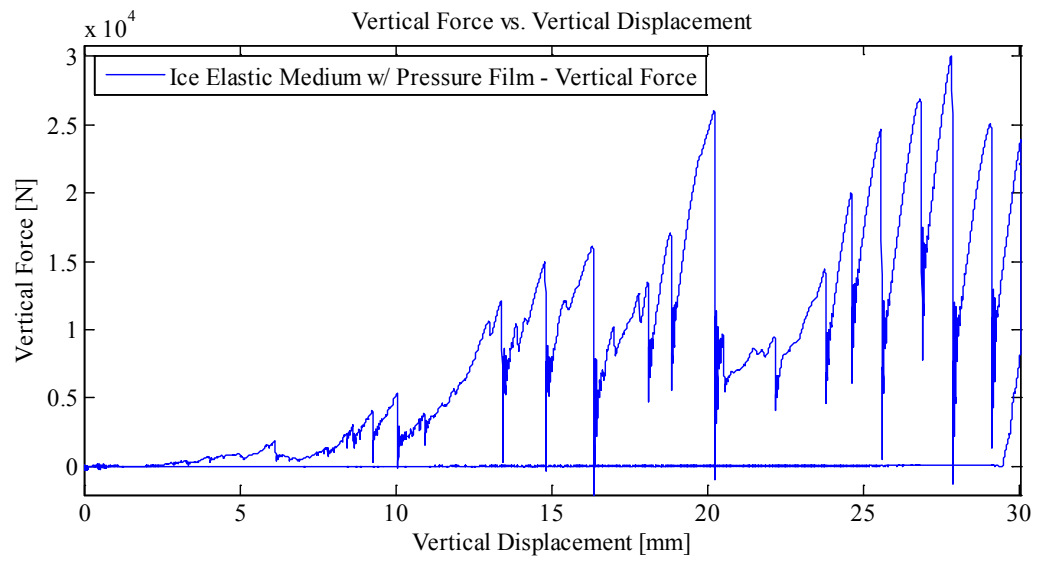
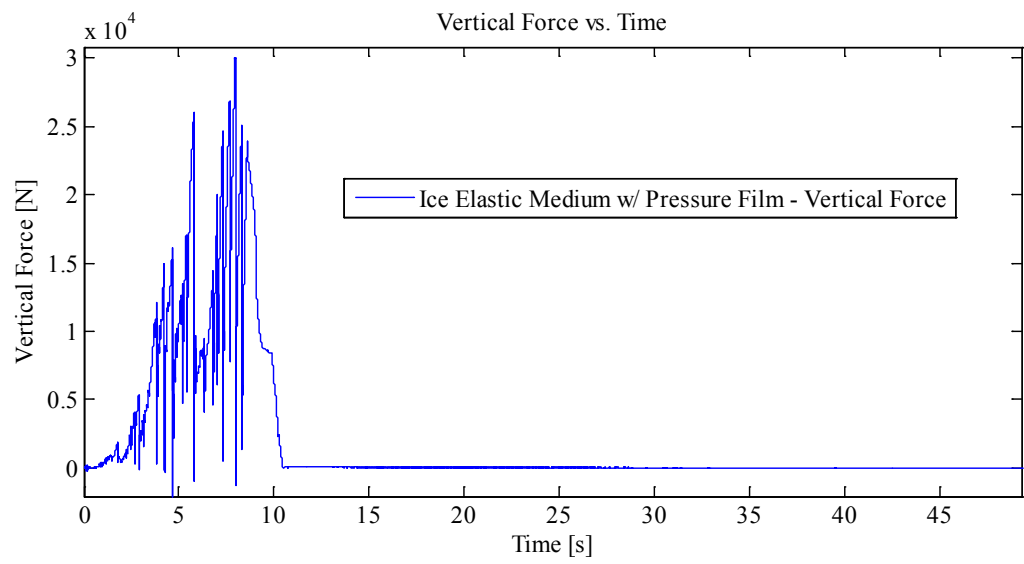
With Pressure Film

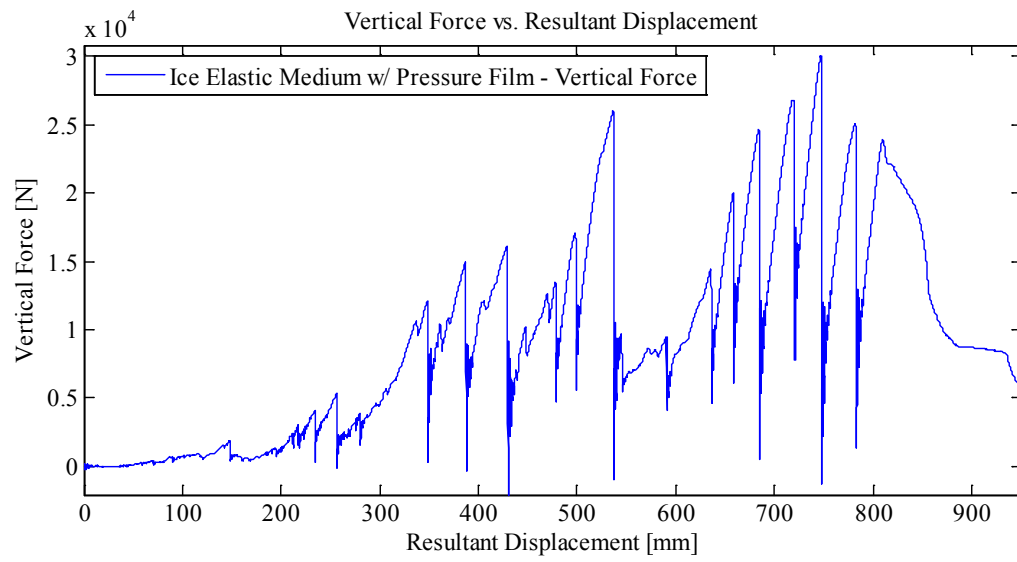
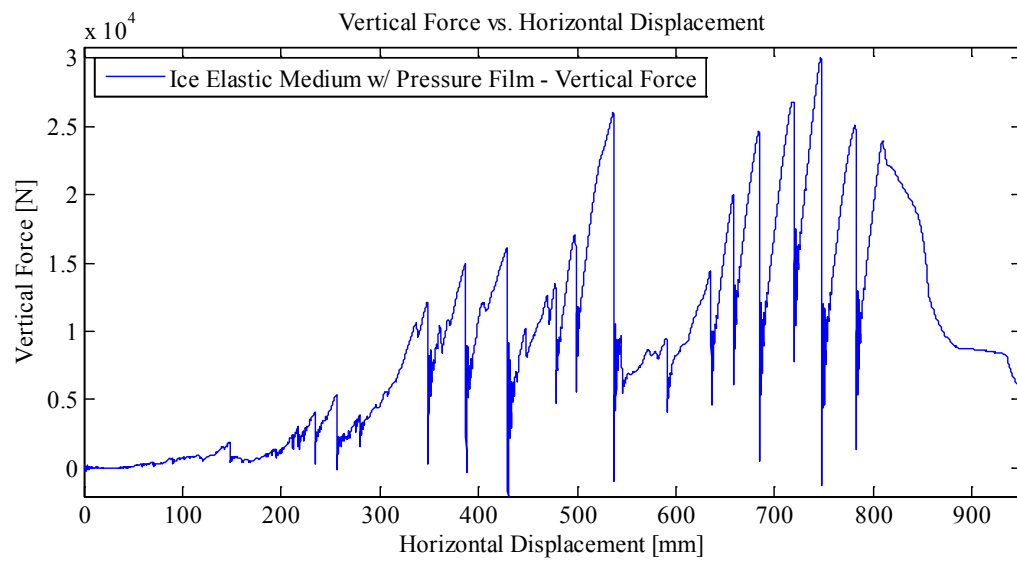
Plots:

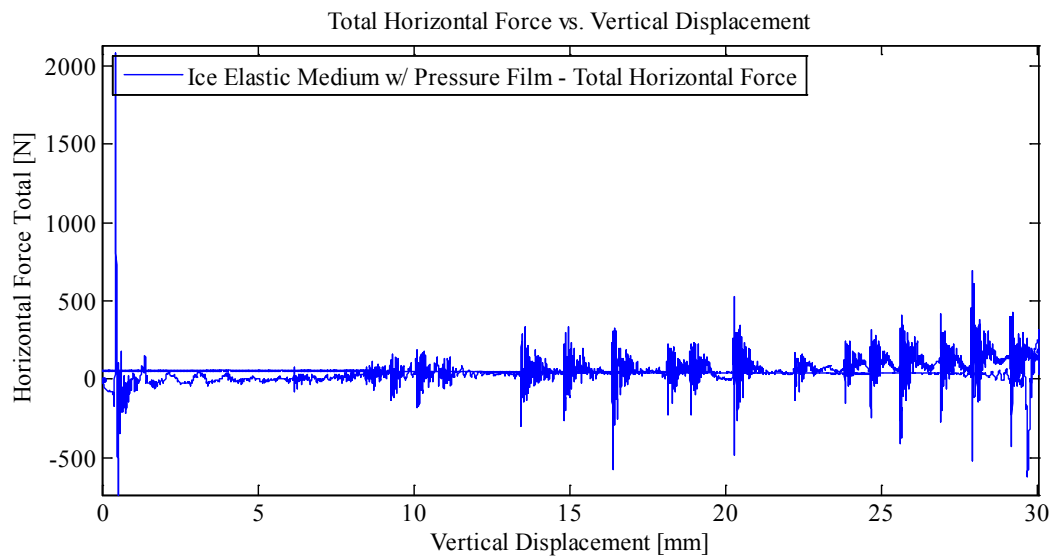
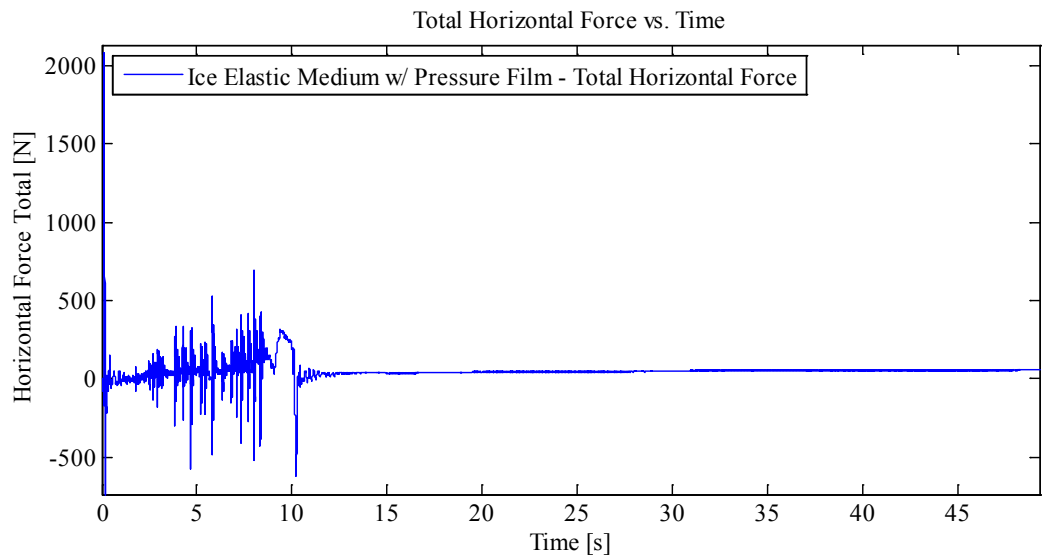


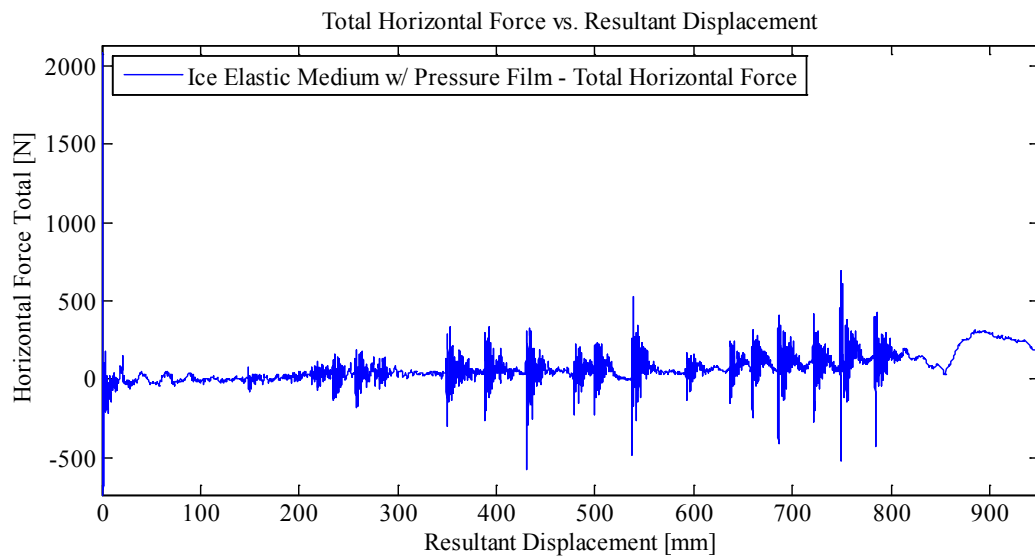
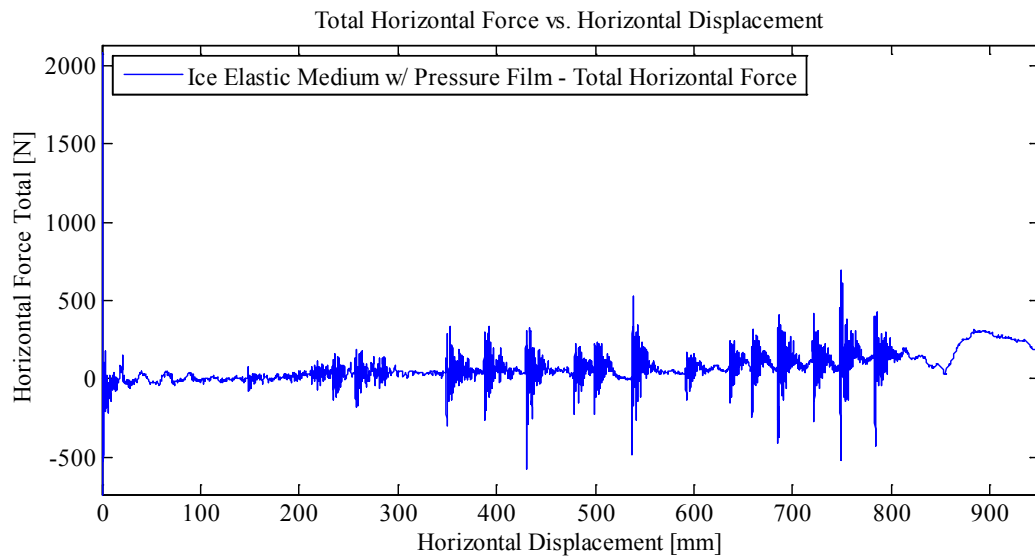


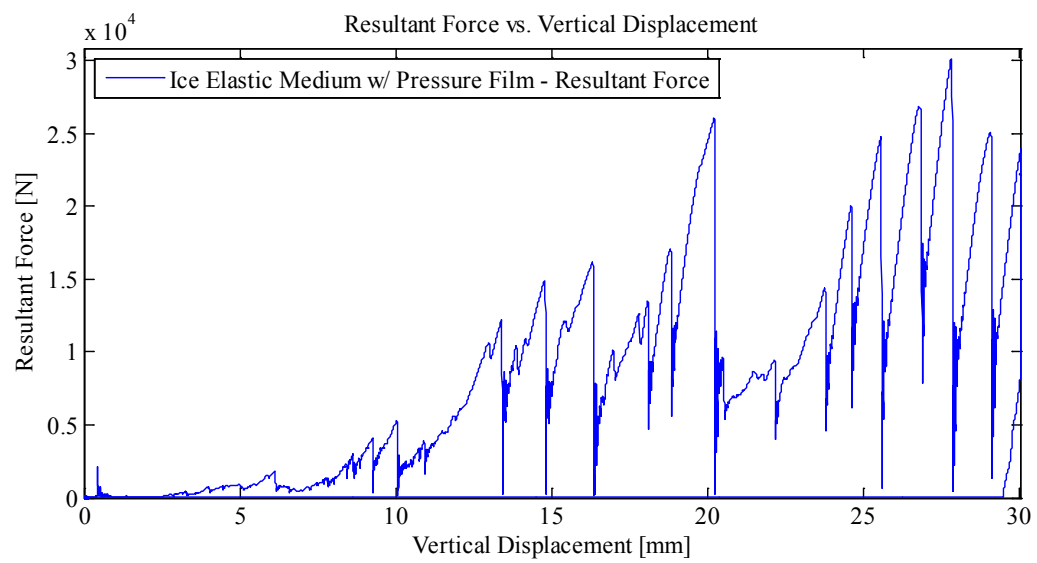
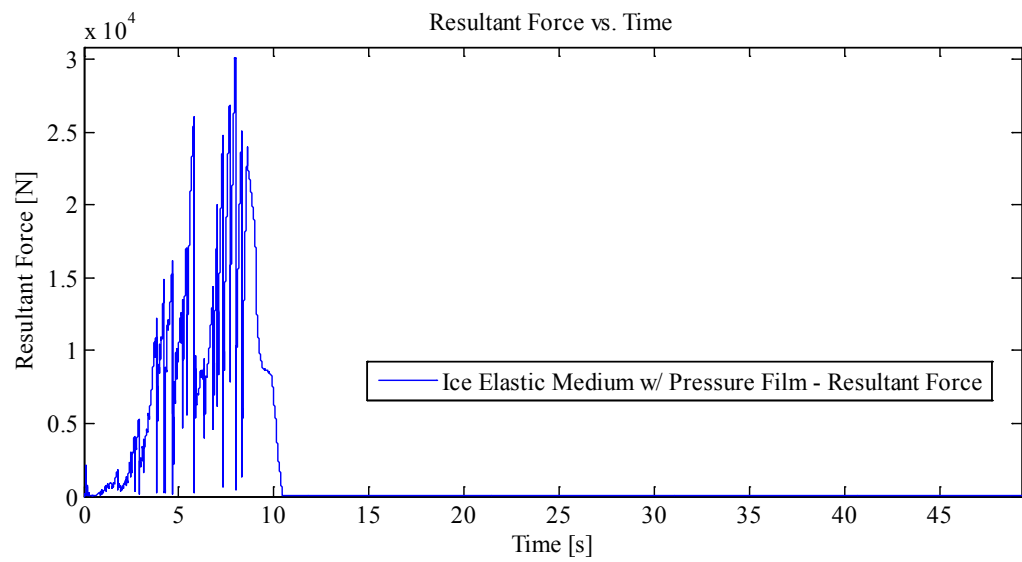


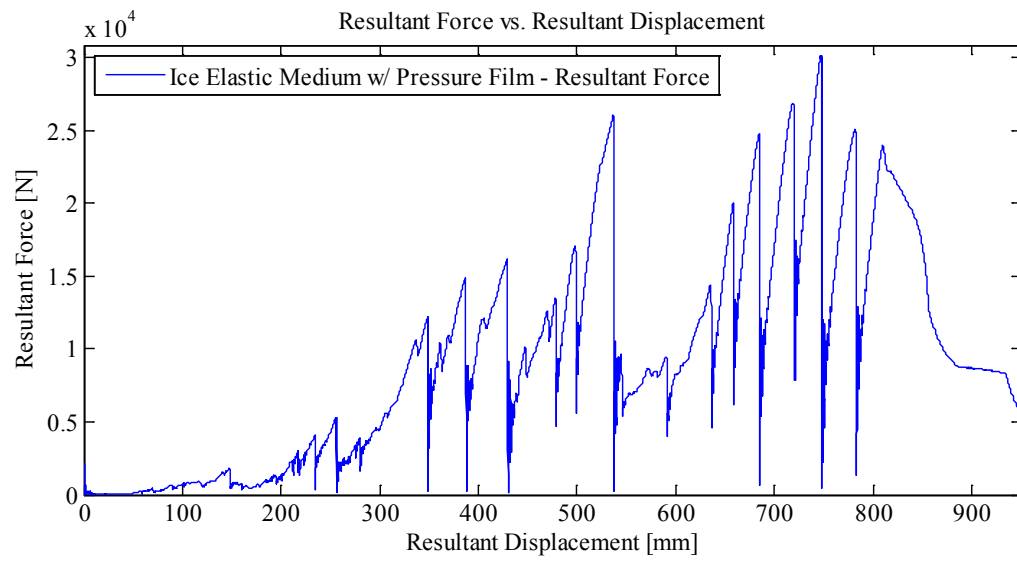
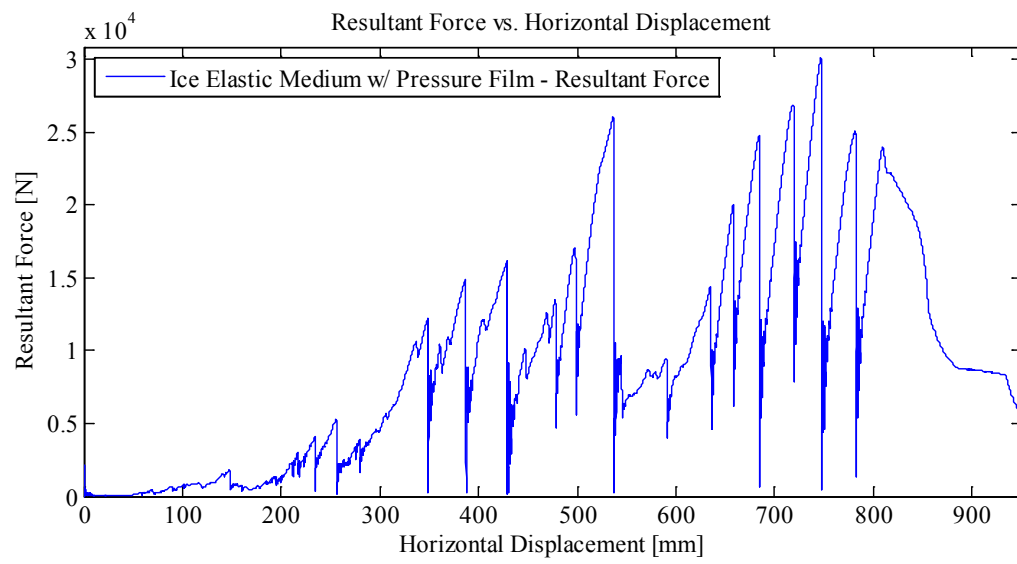


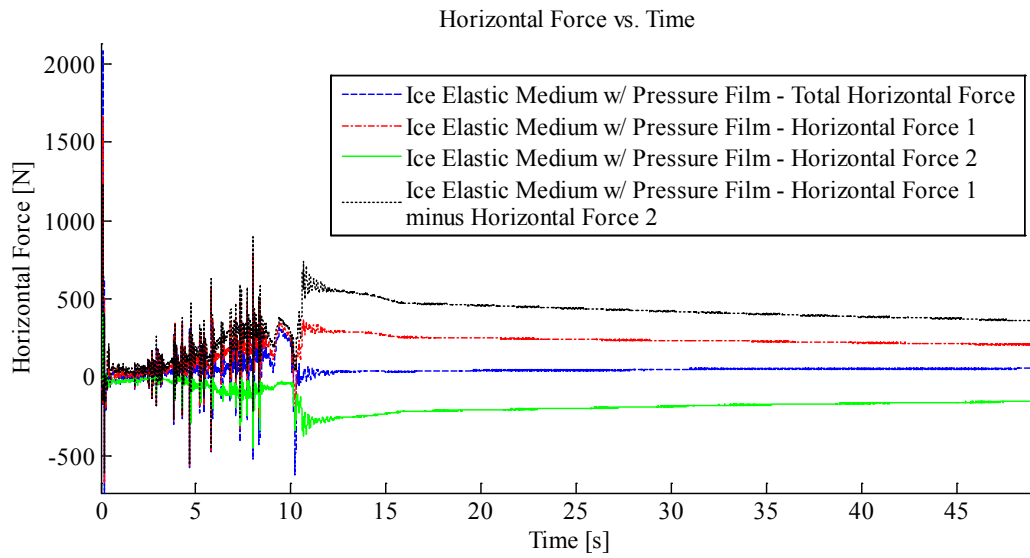
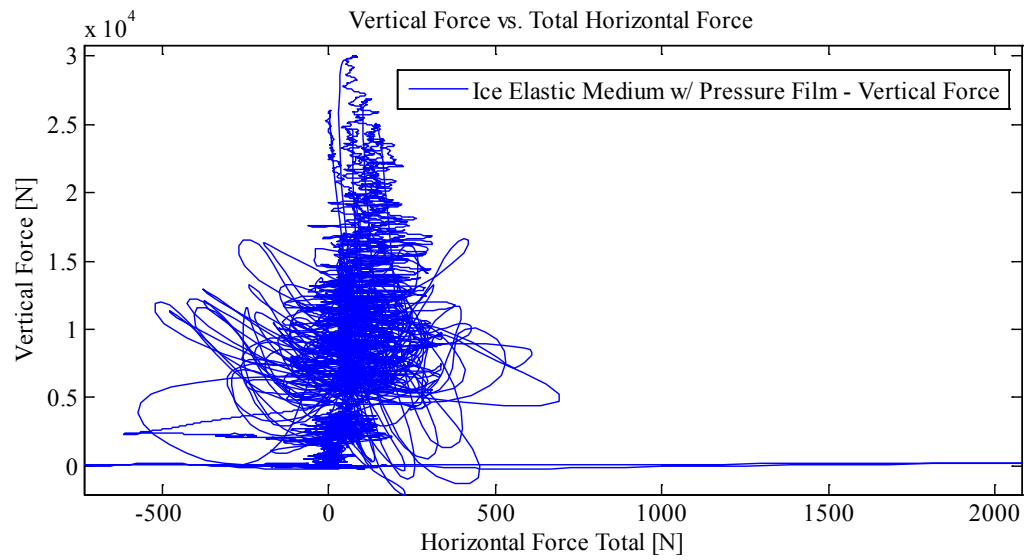












Appendix C3.1.4 – MovingLoad35

April 29, 2014 at ~4:00p.m.

Run #

Run Type: Ice Cone – Pressure Film 3

Room-temperature: -8.4°C (Measured with thermocouple)

Sample Type: 1/2" Plate with Ice

Test Type: In-Along-Out End to End

HStarting Point: End (-61.49 cm (absolute end))

HSpeed: 82.963 mm/s (Nominal)

H Travel: Abs. End to end of pressure film (85 cm)

Vstarting Point: 2.43 mm

VSpeed: 82.963 mm/s

V Target: -27.57 mm

V Travel: 30.0 mm

Notes:

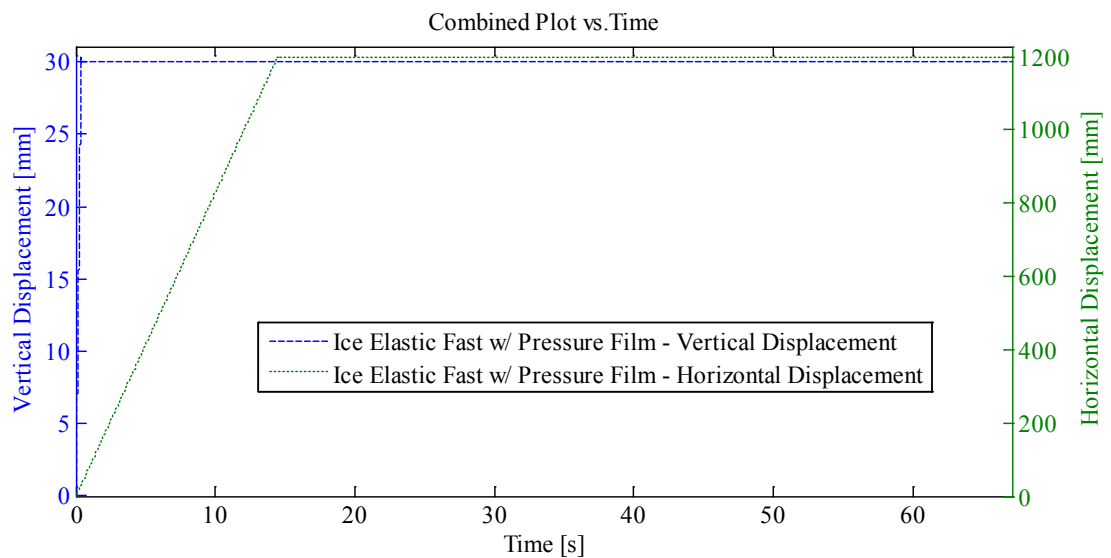
Force 1: 3 cm Ice Indentation In-Along-Out - End to End

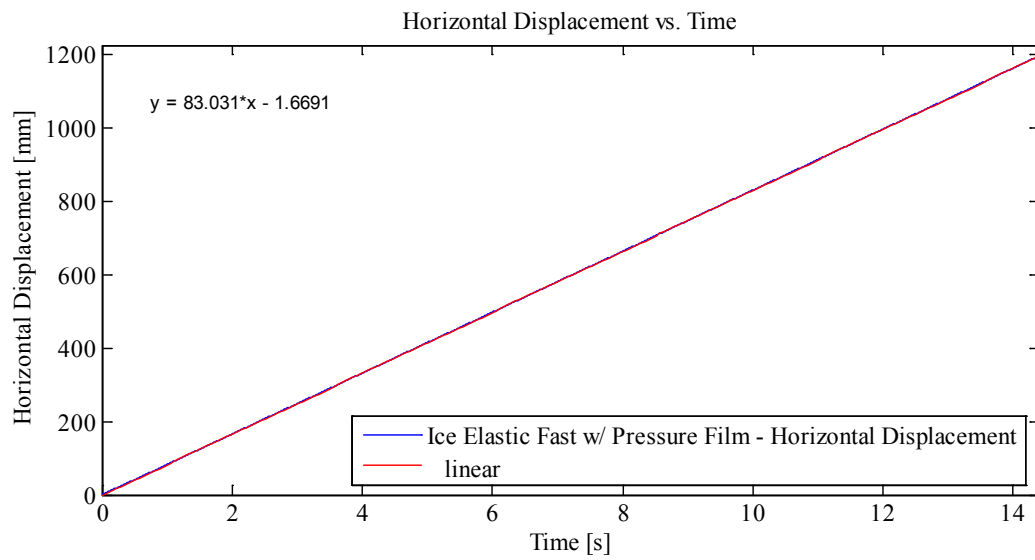
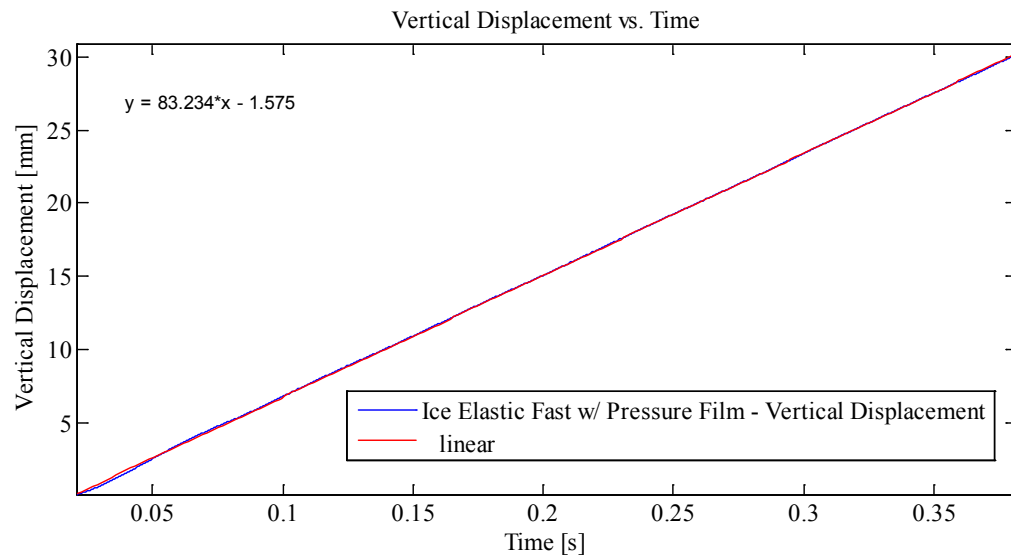
Data from Indentation 1 saved as MovingLoad35

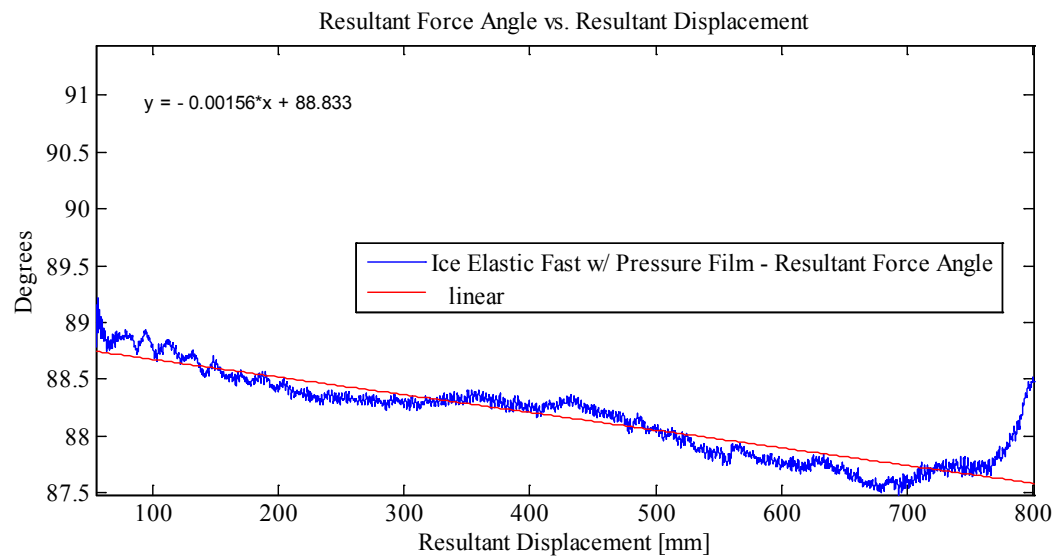
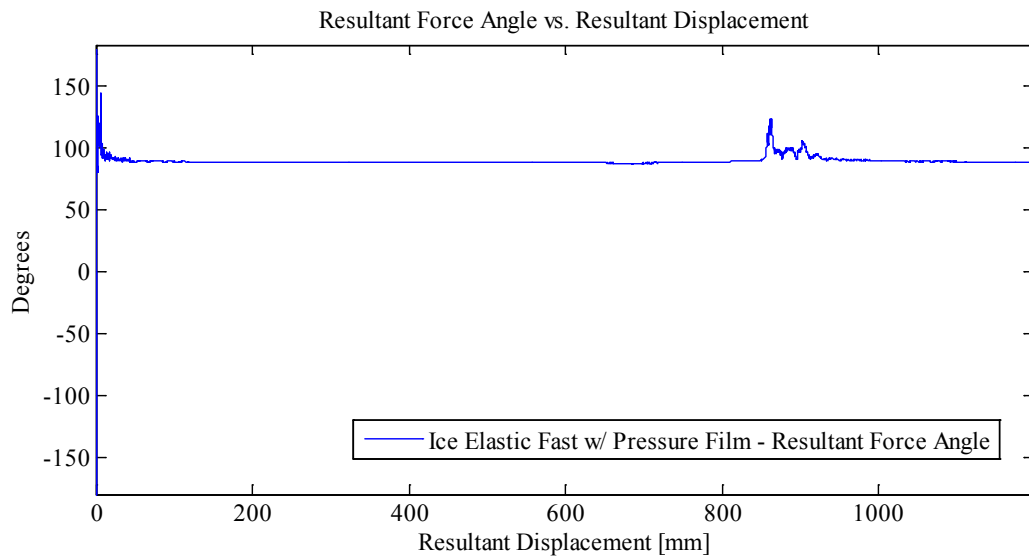
With Two Thermal Video Cameras and High Speed

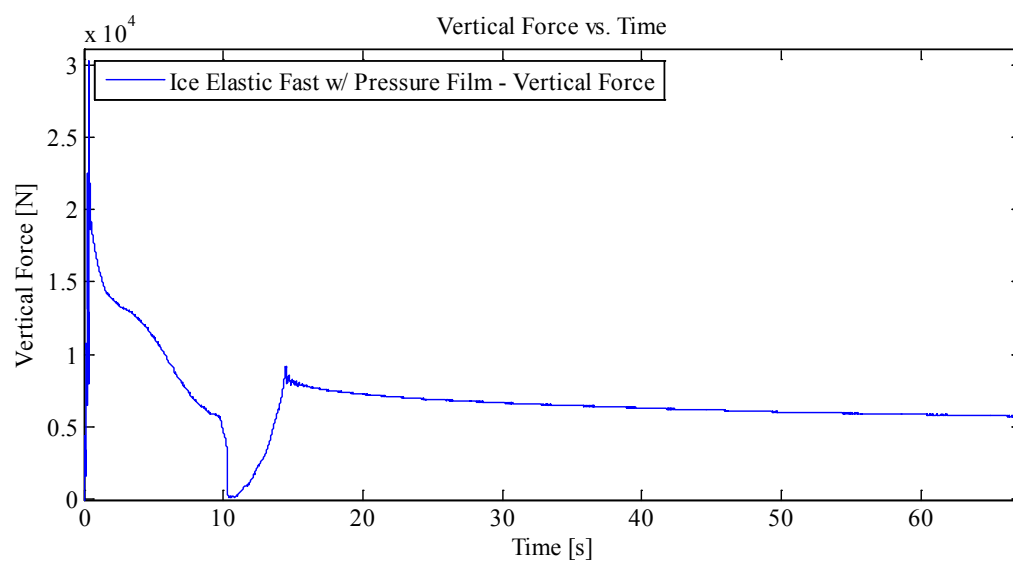
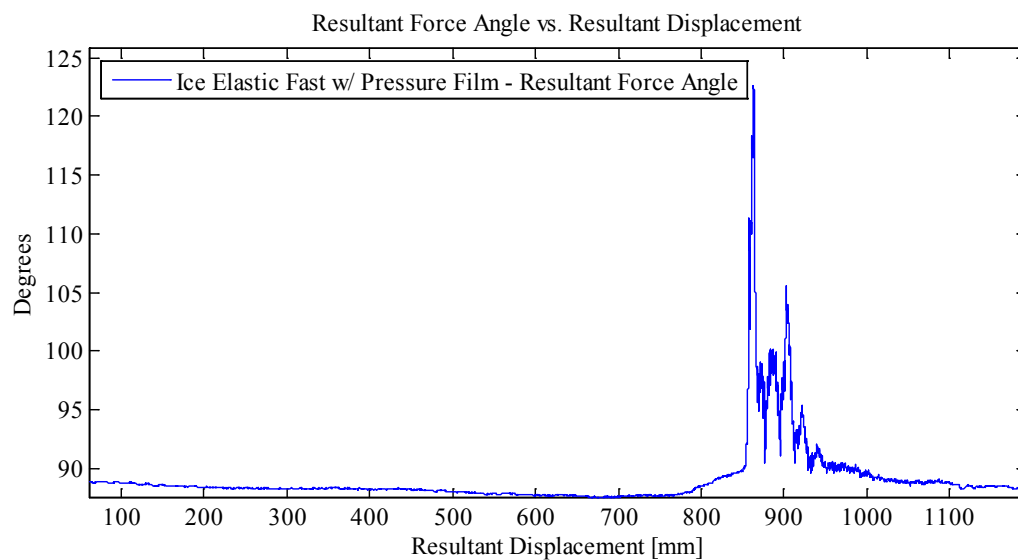
With Pressure Film

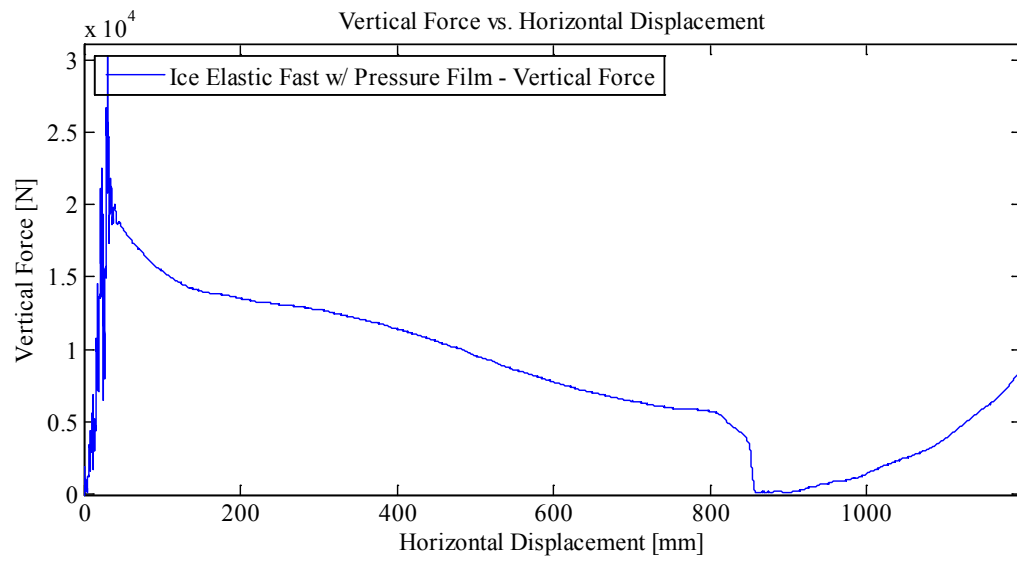
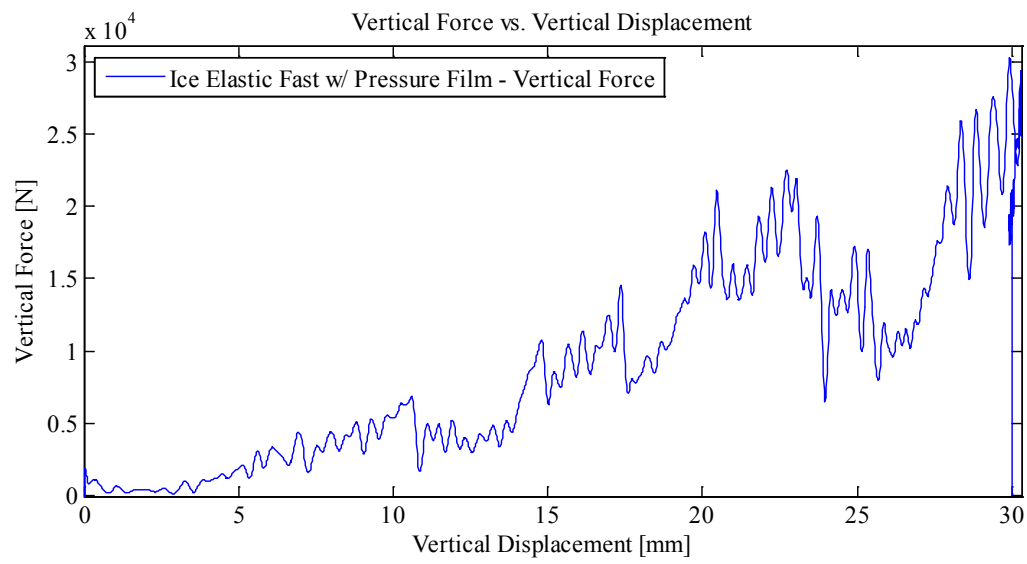
Plots:

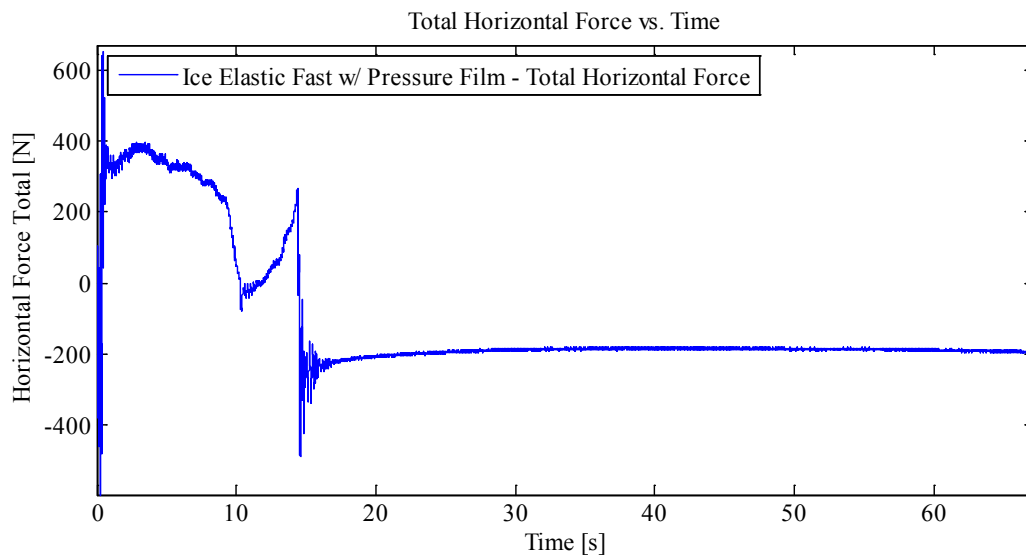
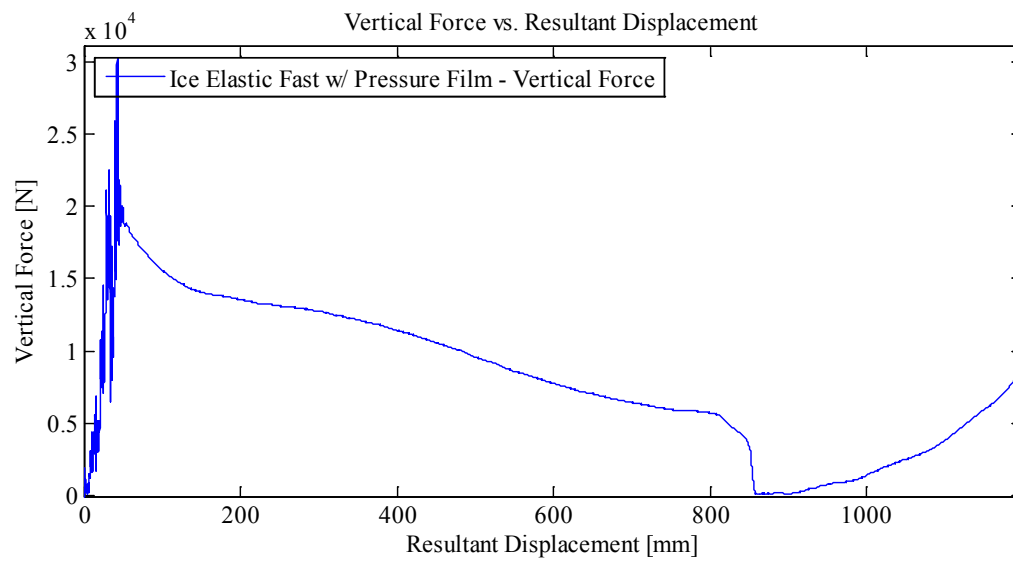


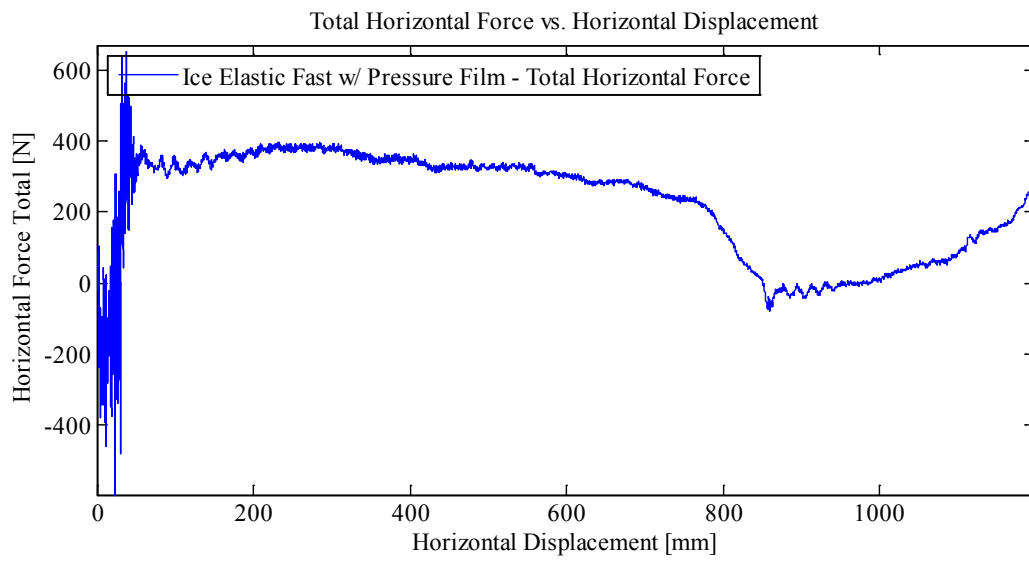
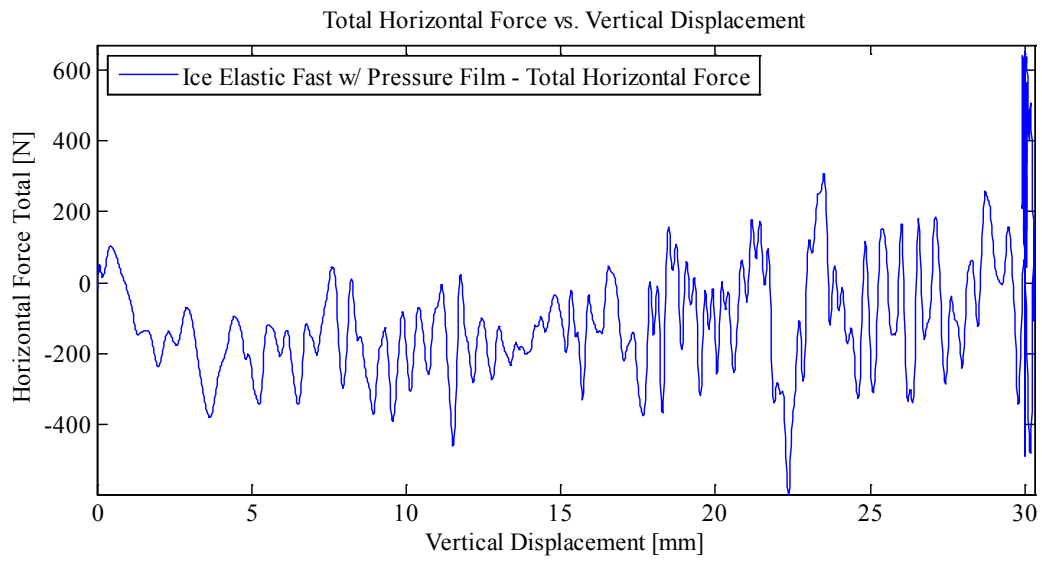


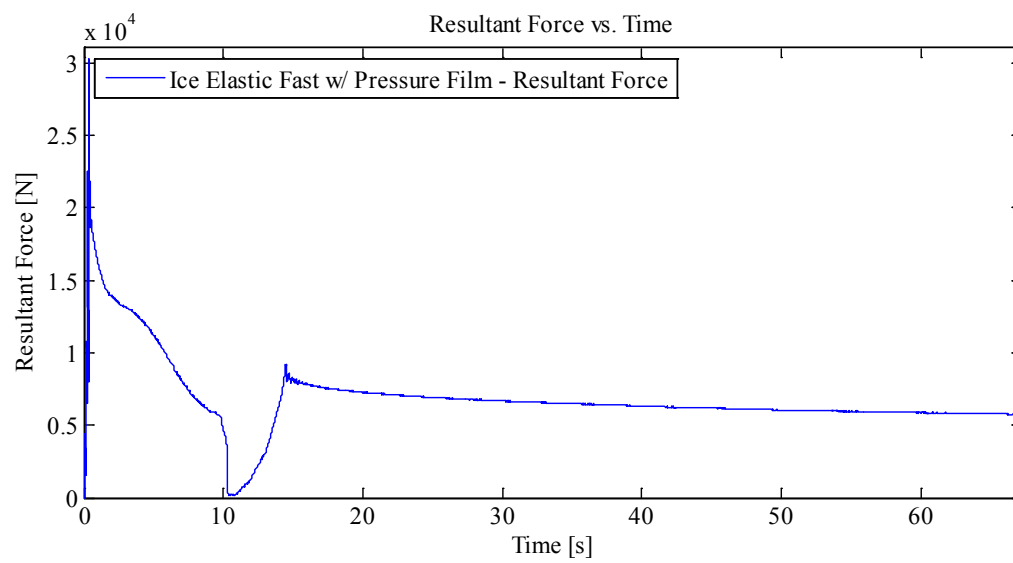
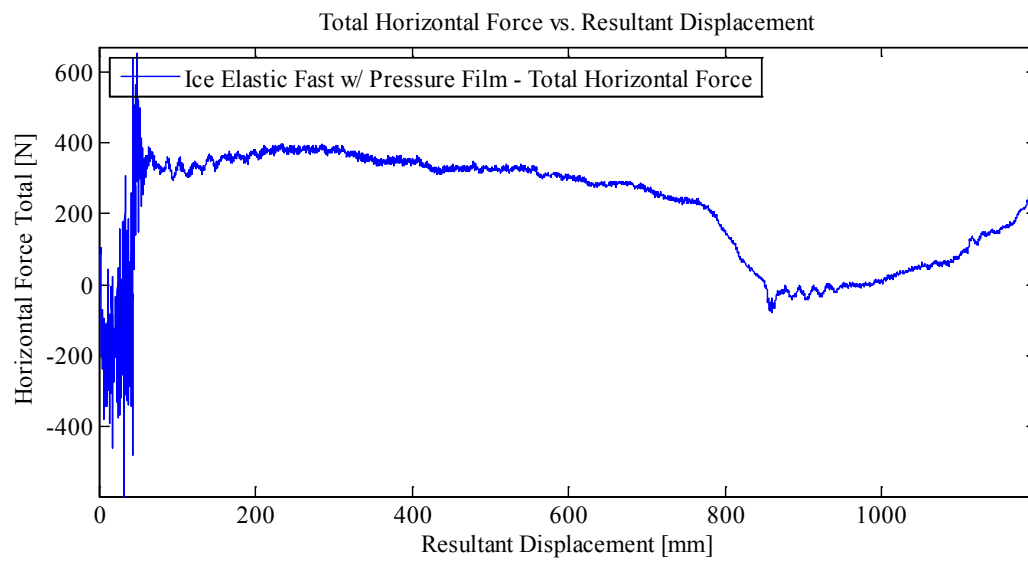


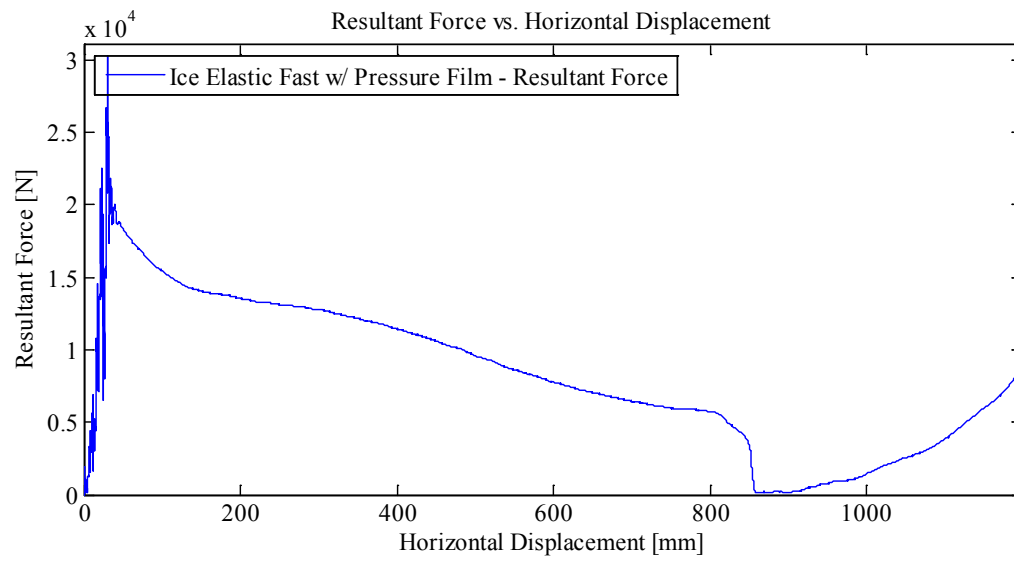
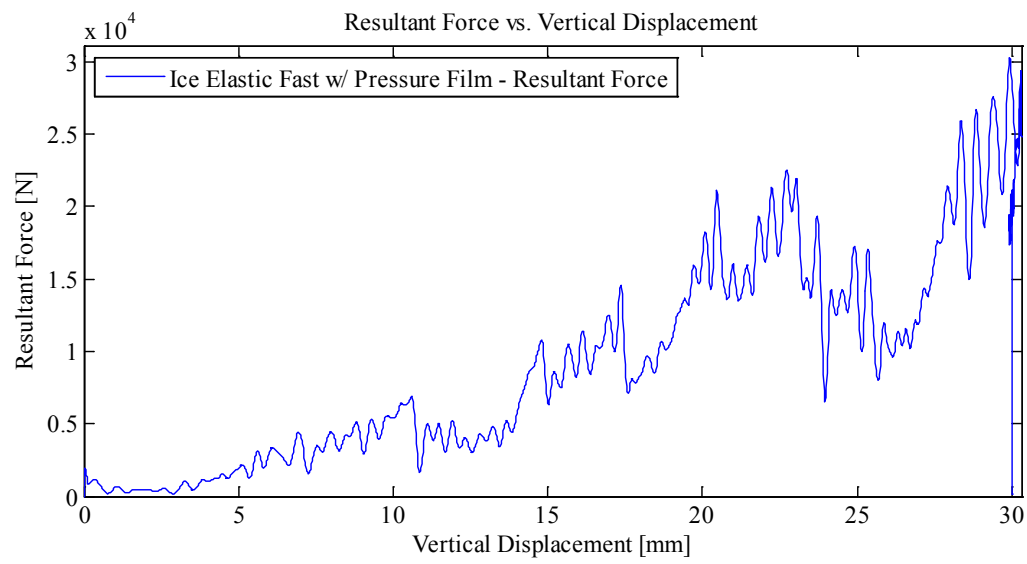


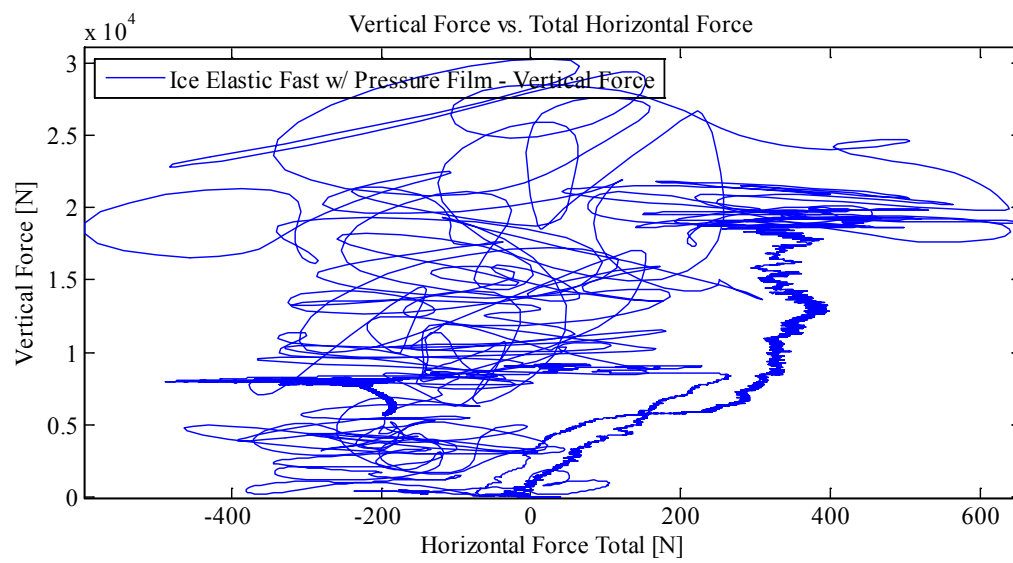
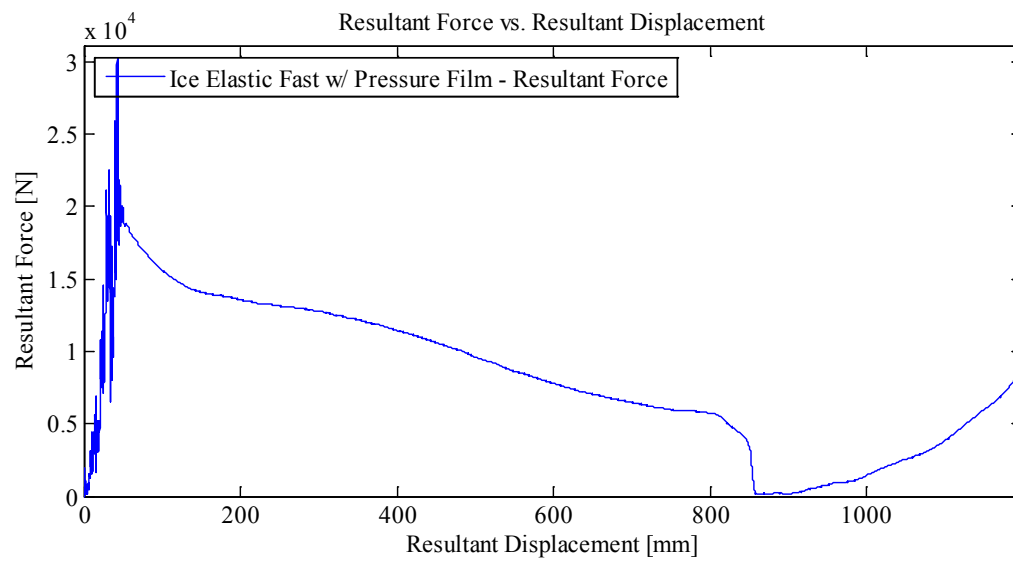


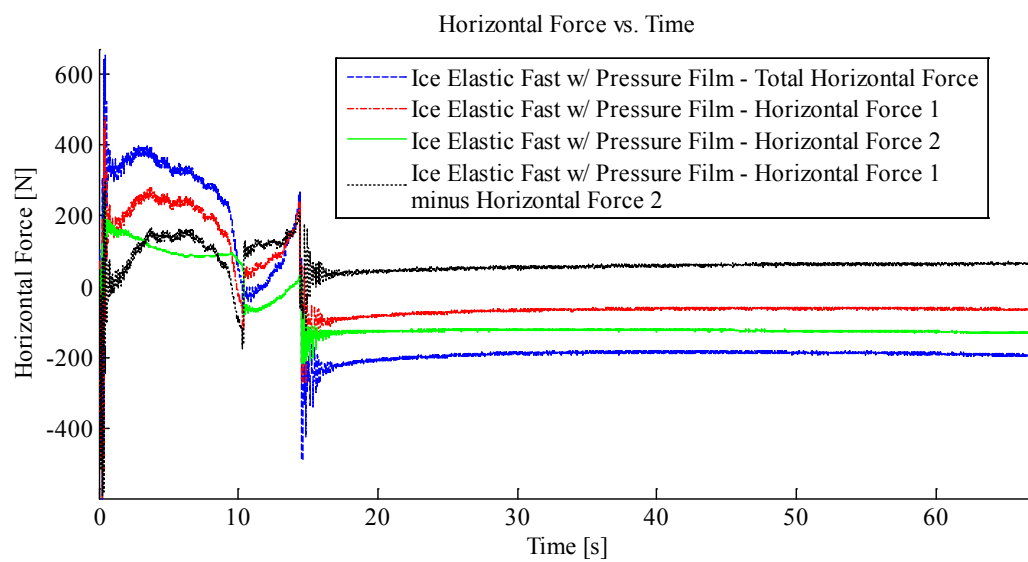






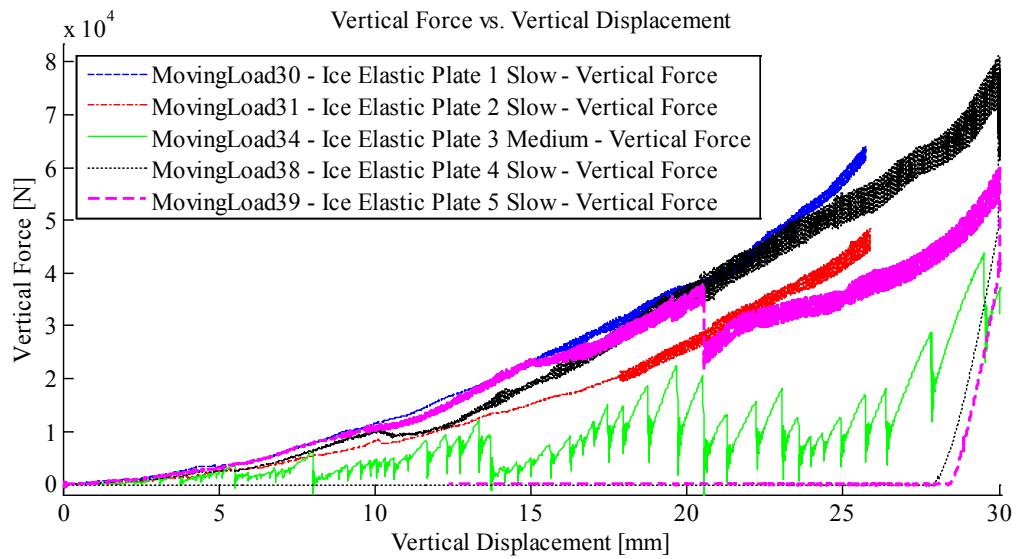
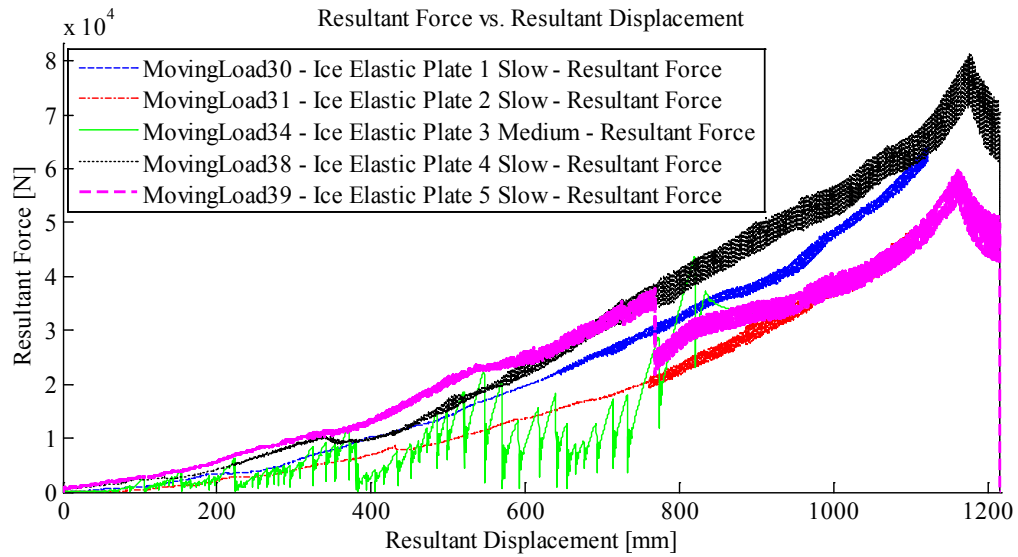


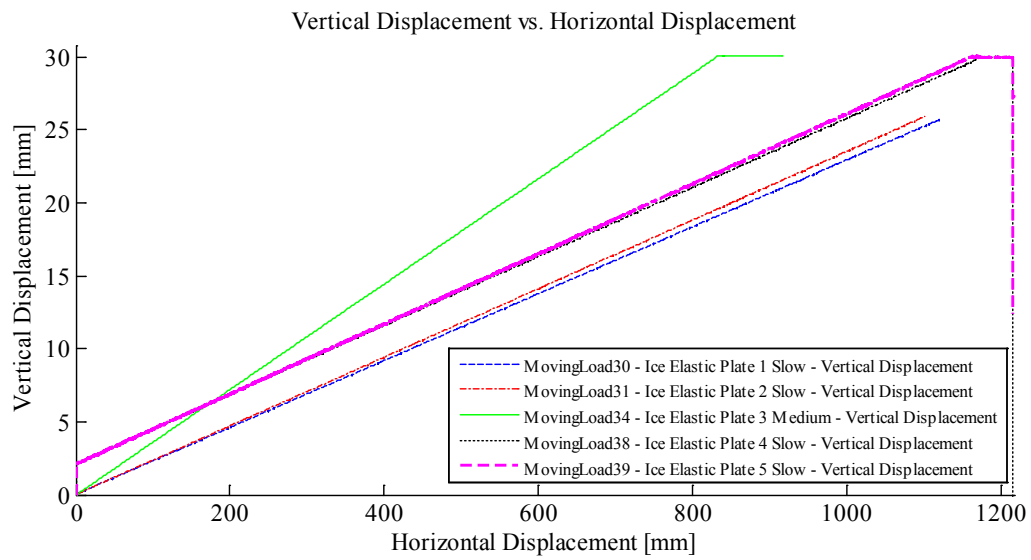
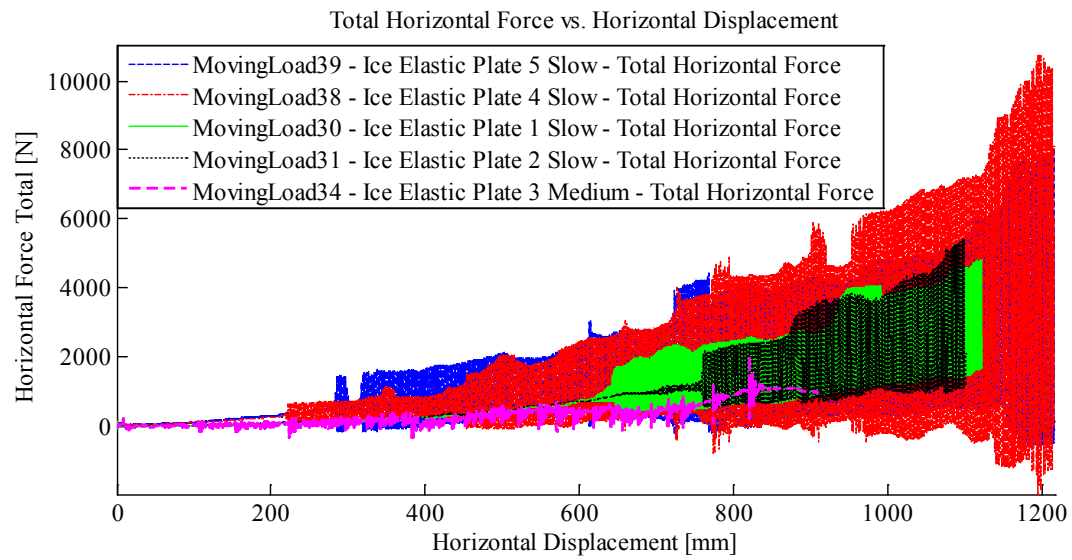


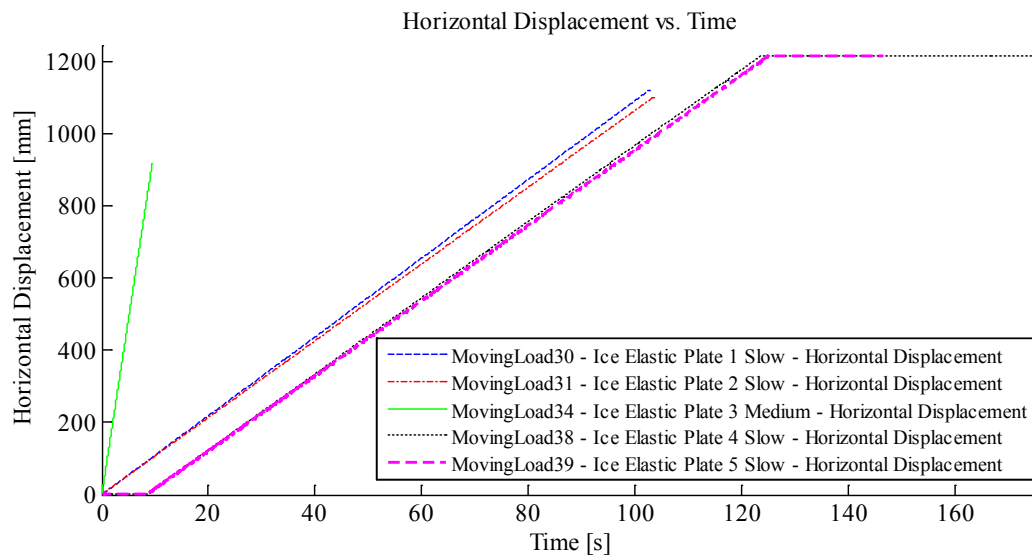
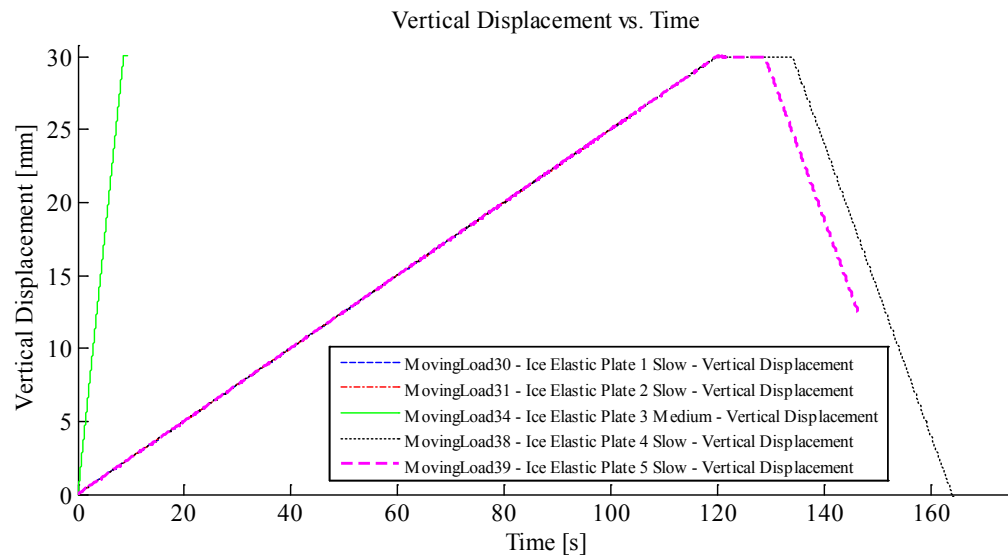


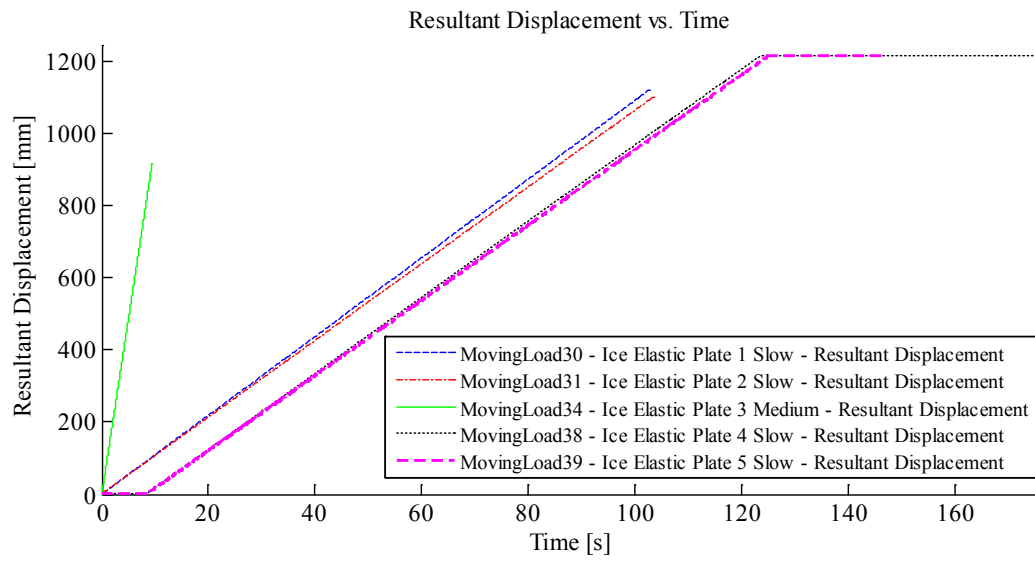
Appendix C3.2 – Ice Cone Tests Inducing Elastic Plate Response

Appendix C3.2.1 – Summary Plots for Experiments ML 30, 31, 34, 38, and 39









Appendix C3.2.2 – MovingLoad30

April 25, 2014 at ~1:00p.m.

Run # 23
Run Type: Ice Cone – Elastic Plate 1
Room-temperature: -7.6°C (Measured with thermocouple)
Sample Type: 1/2" Plate with Ice
Test Type: In-Along-Out End to End

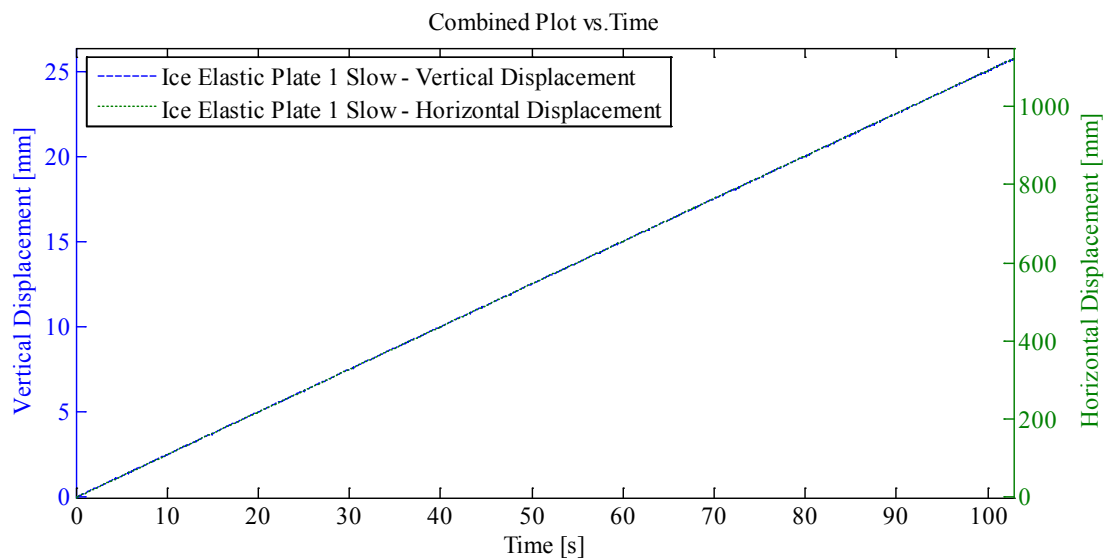
HStarting Point: End (-54.84 cm (-55 cm nominal))
HSpeed: 10mm/s (Nominal)
H Travel: End to End (110+ cm)

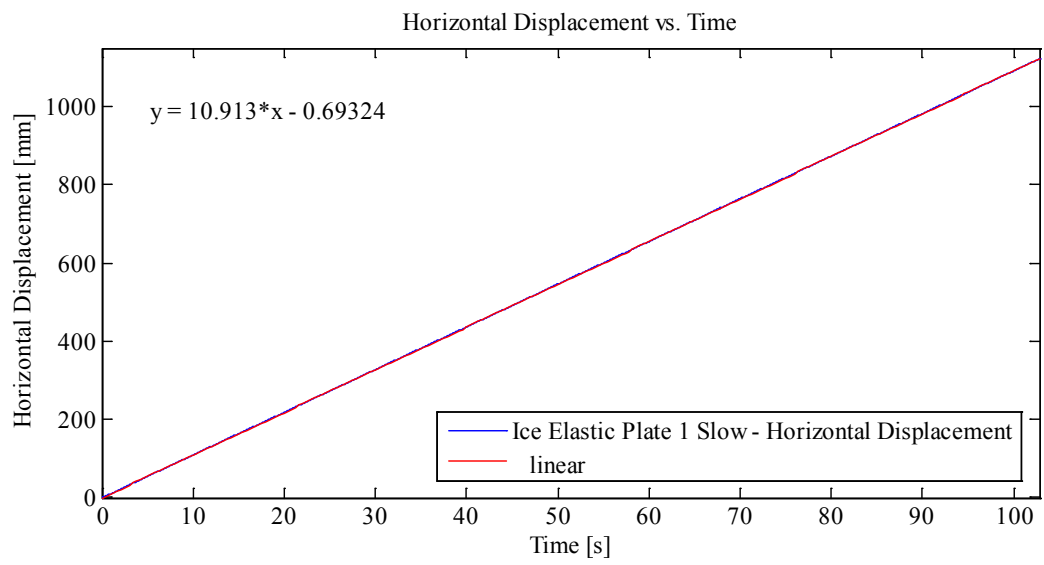
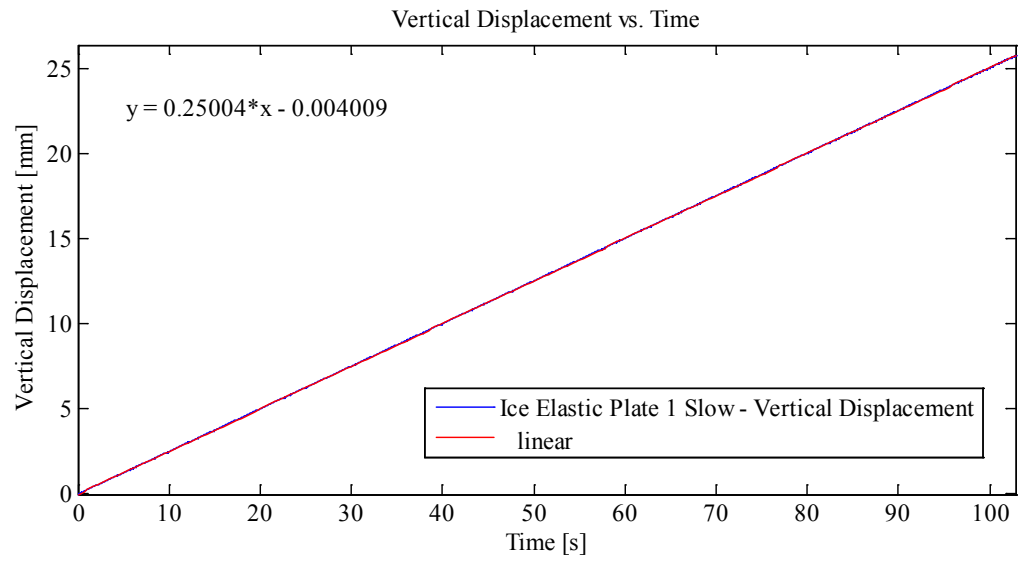
Vstarting Point: -1.45 mm
VSpeed: 0.25 mm/s
V Target: 30 mm
V Travel: 28.55 mm

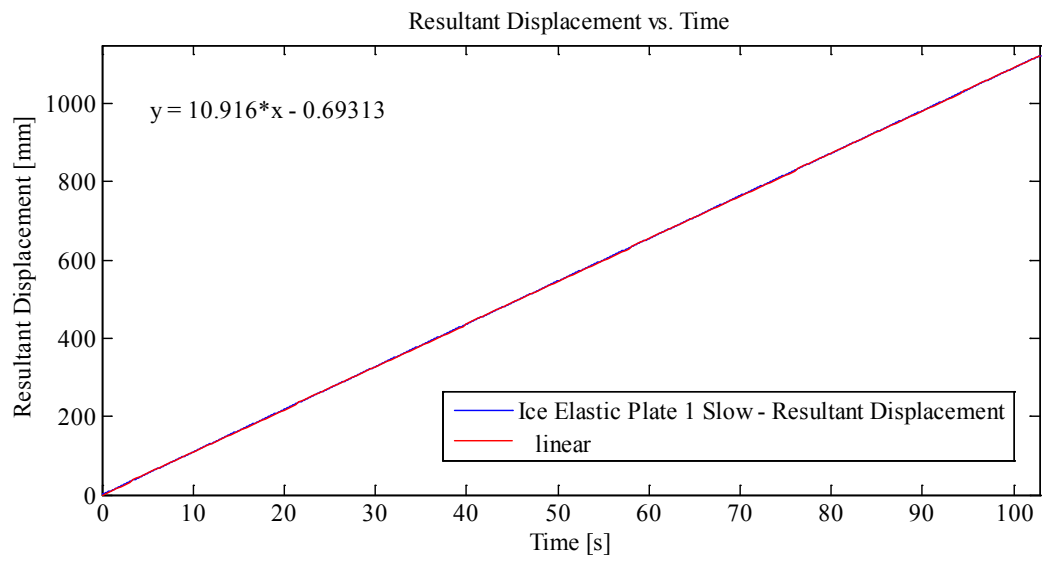
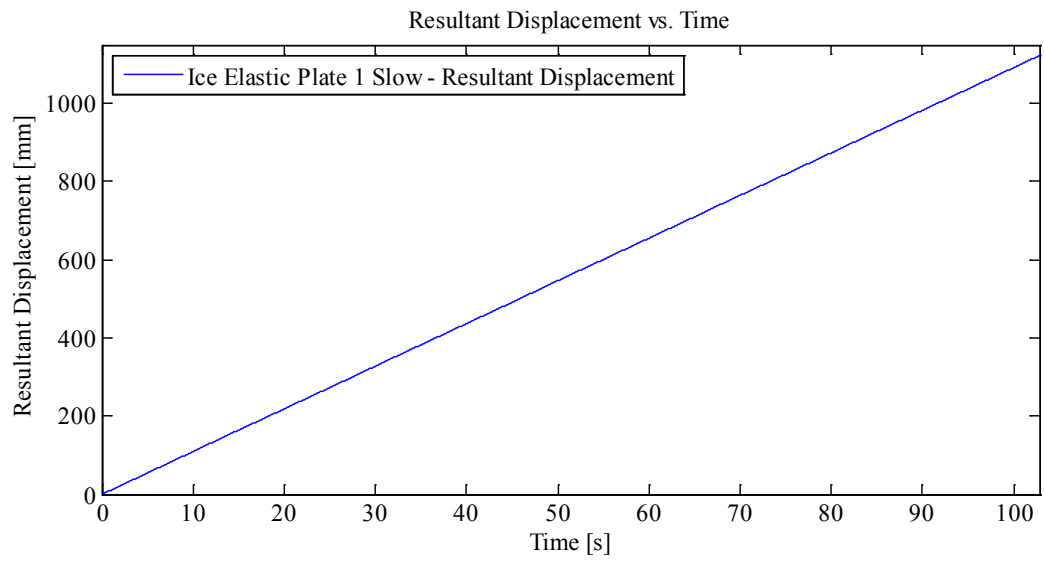
Notes:

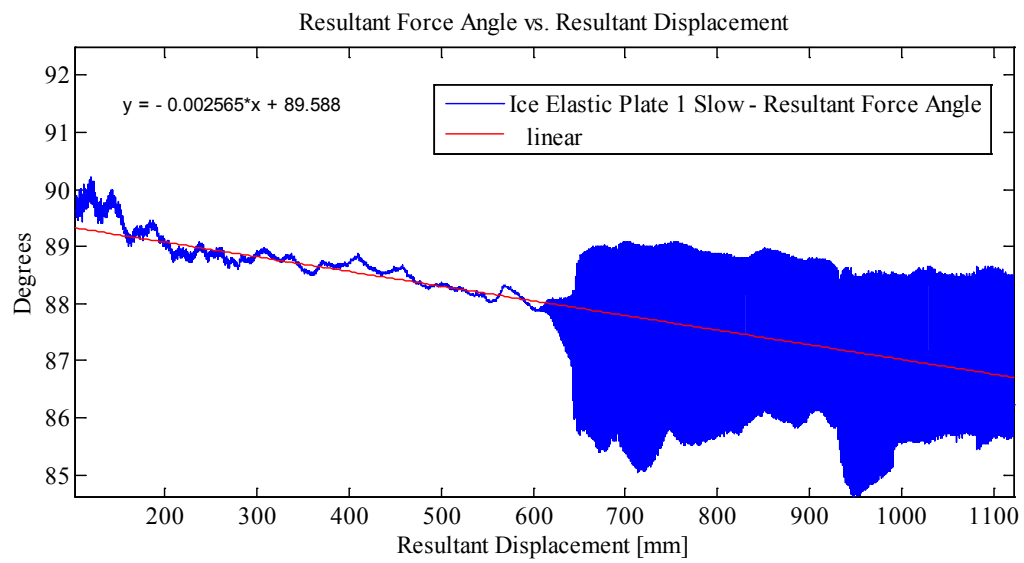
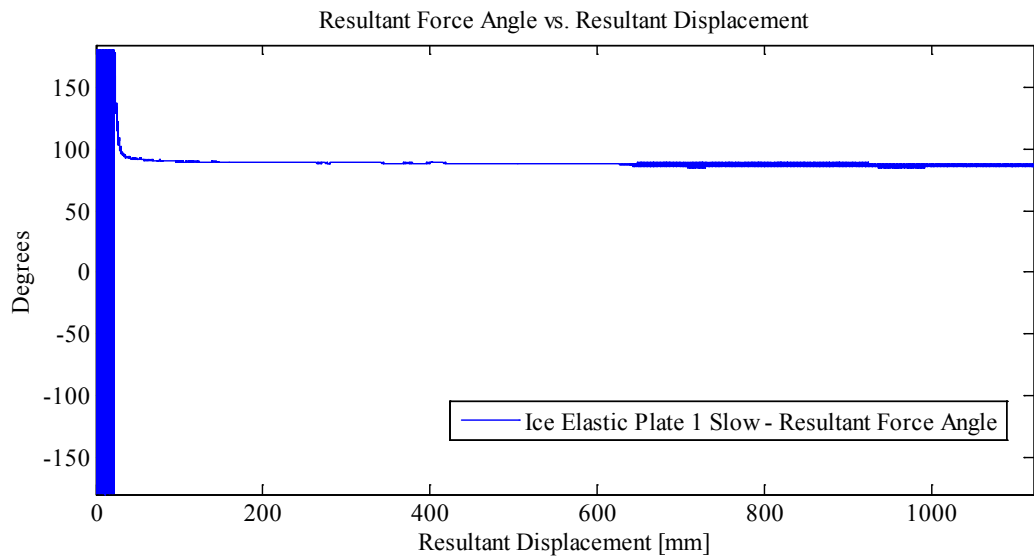
Force 1: 3 cm Ice Indentation In-Along-Out - End to End
Data from Indentation 1 saved as MovingLoad30
With Two Thermal Video Cameras and High Speed

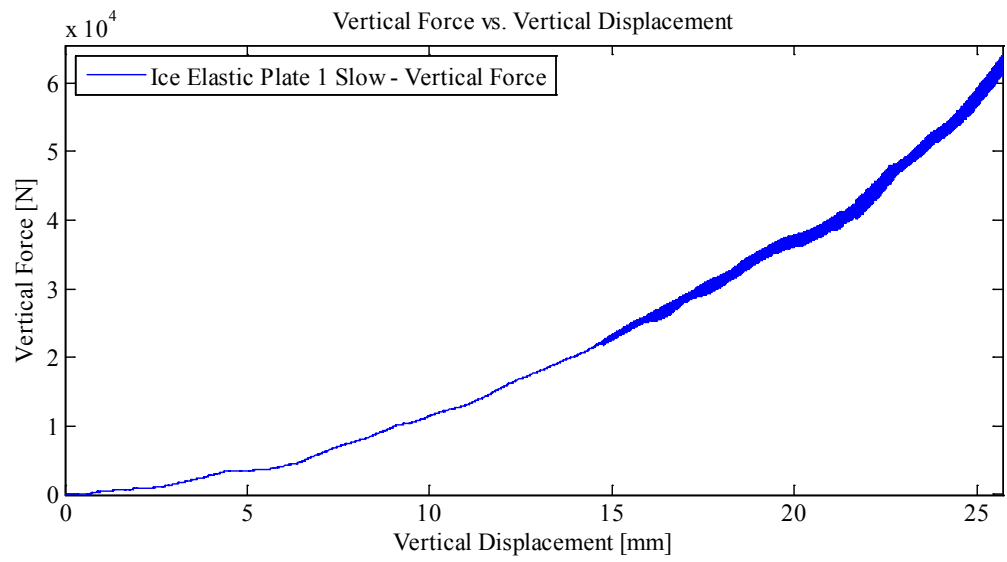
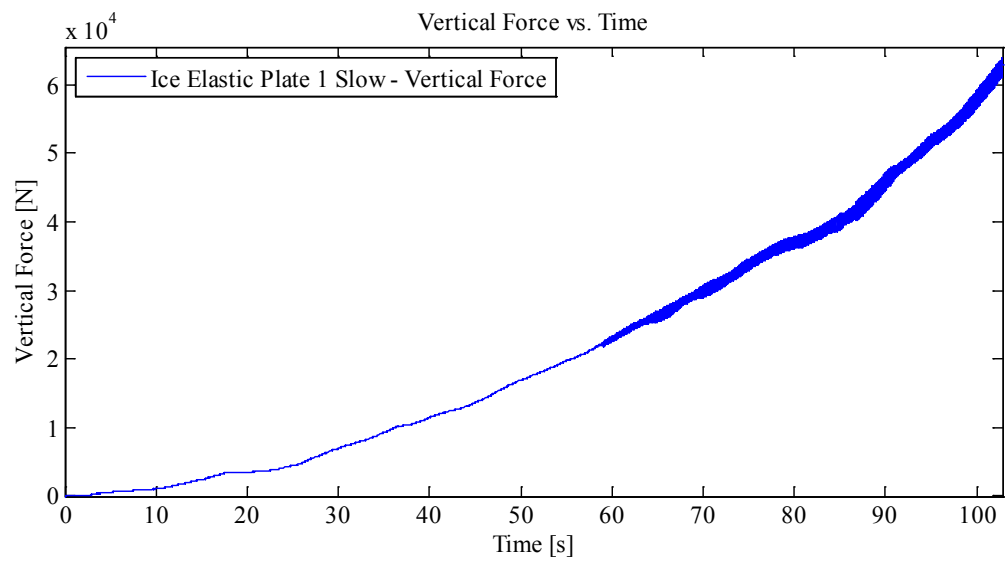
Plots:

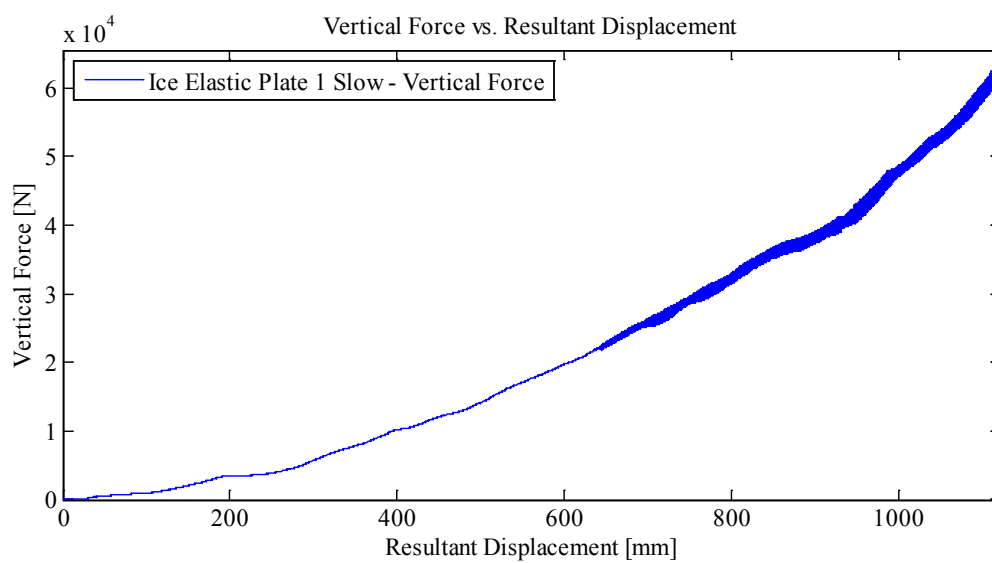
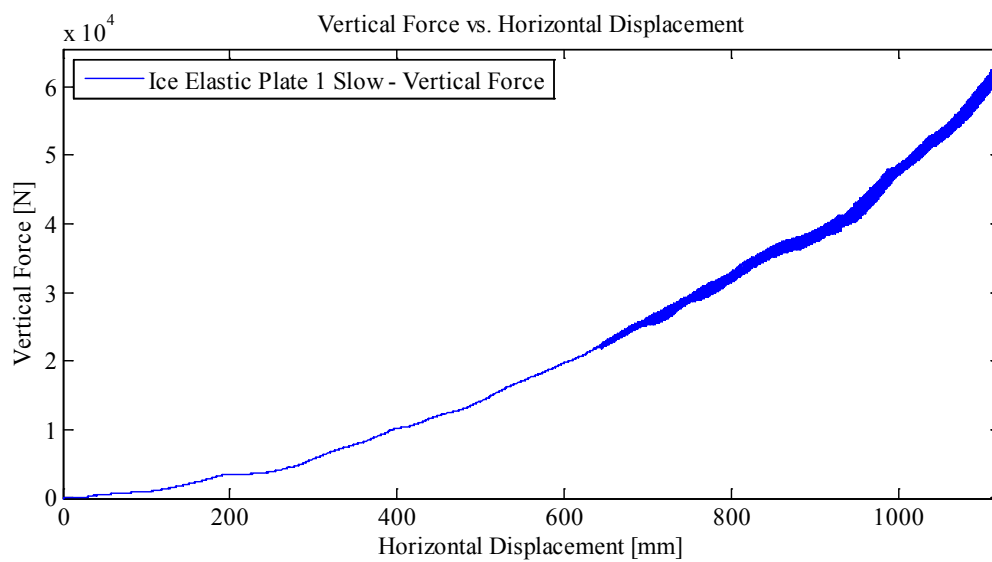


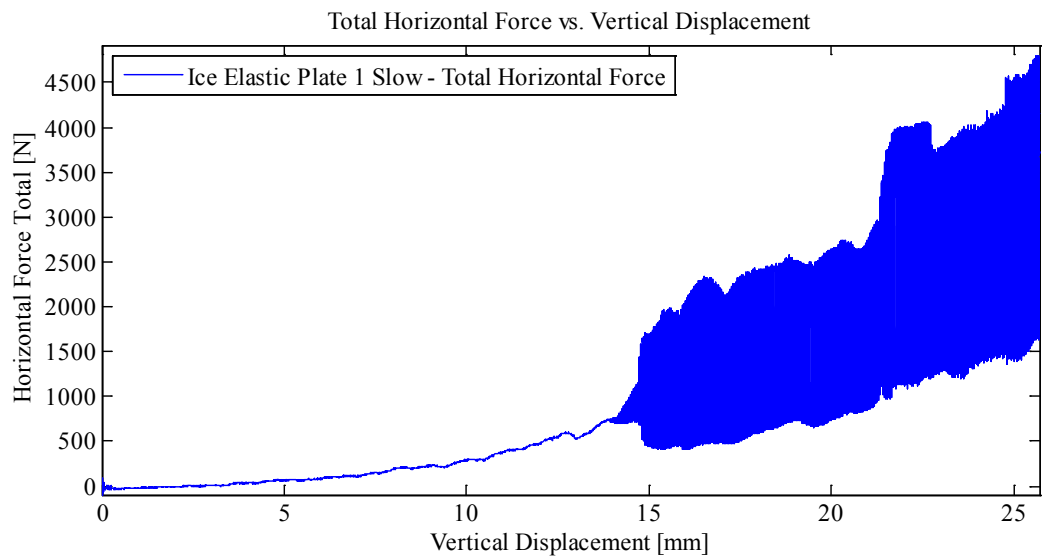
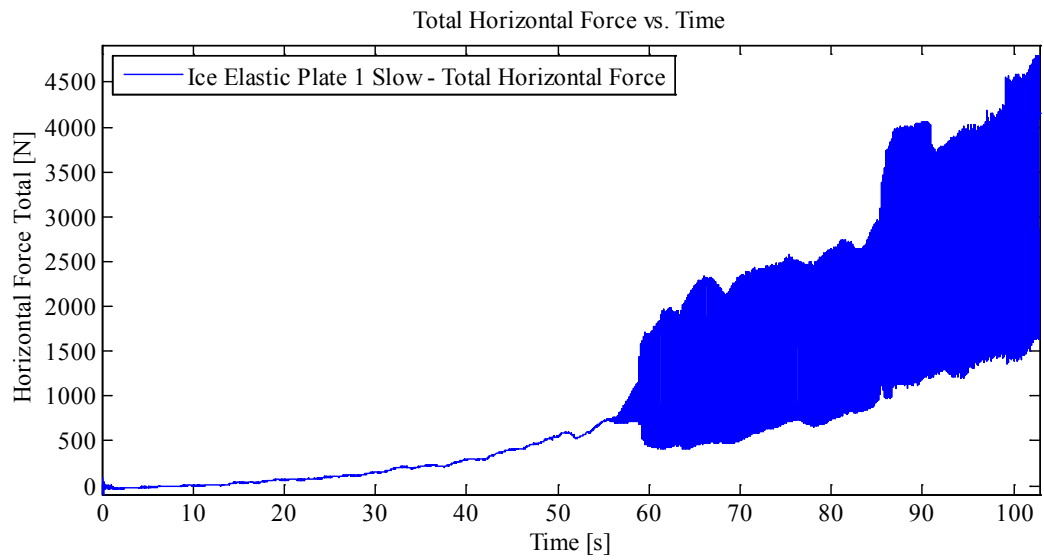


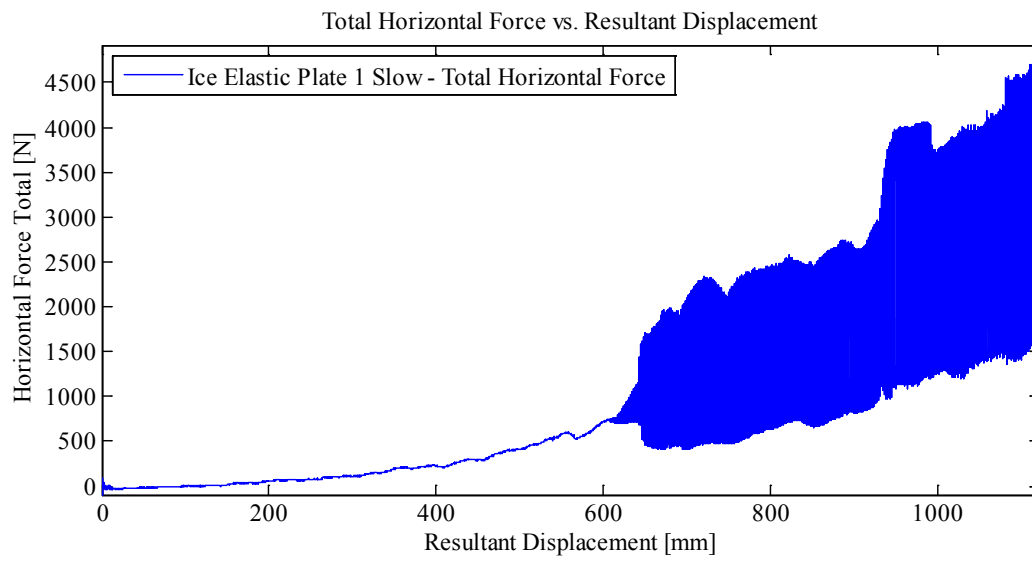
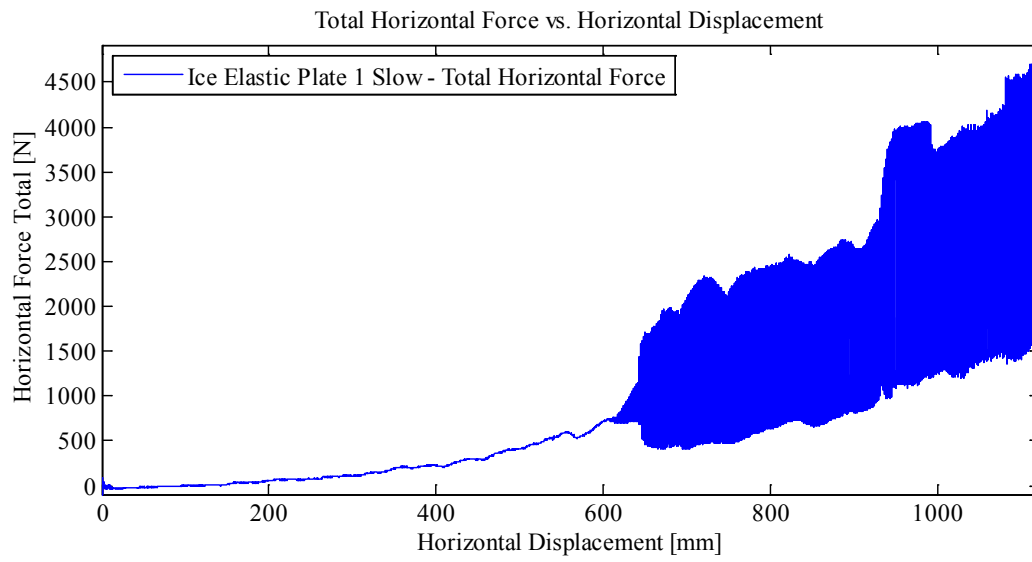


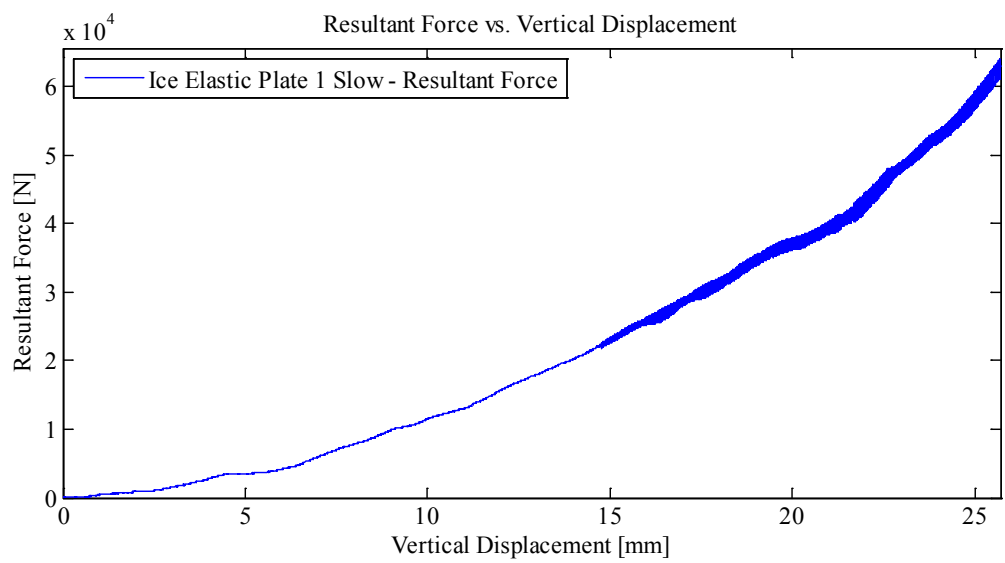
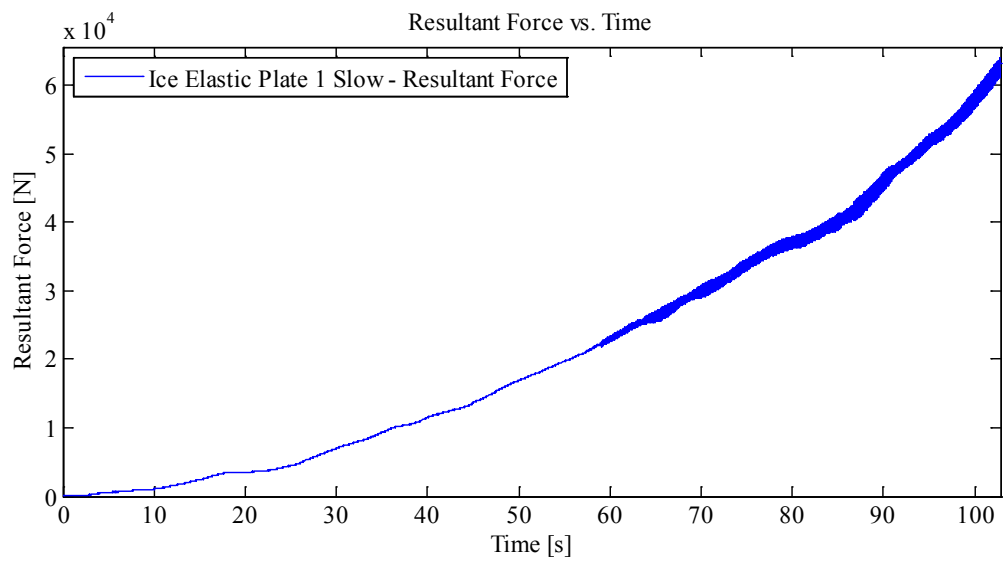


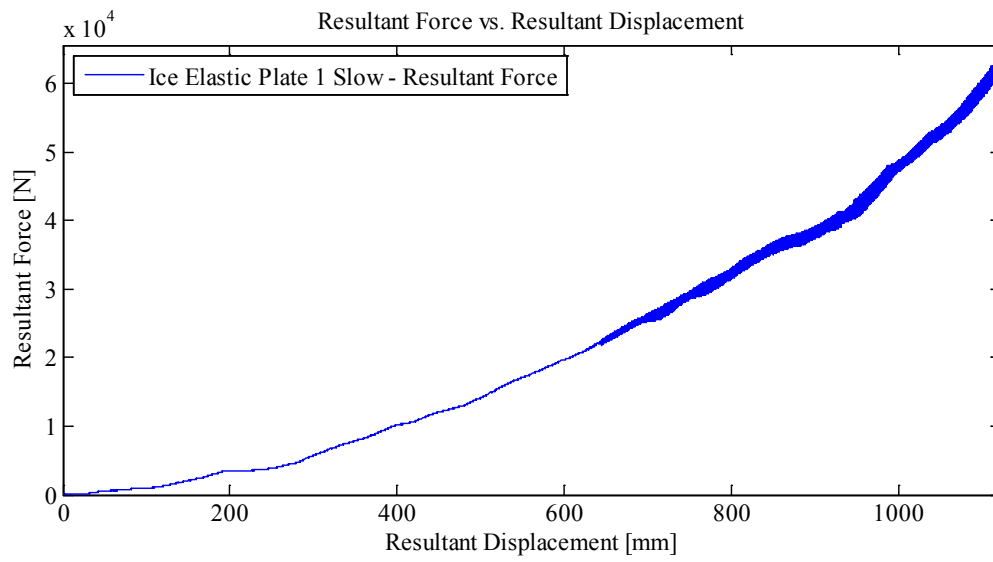
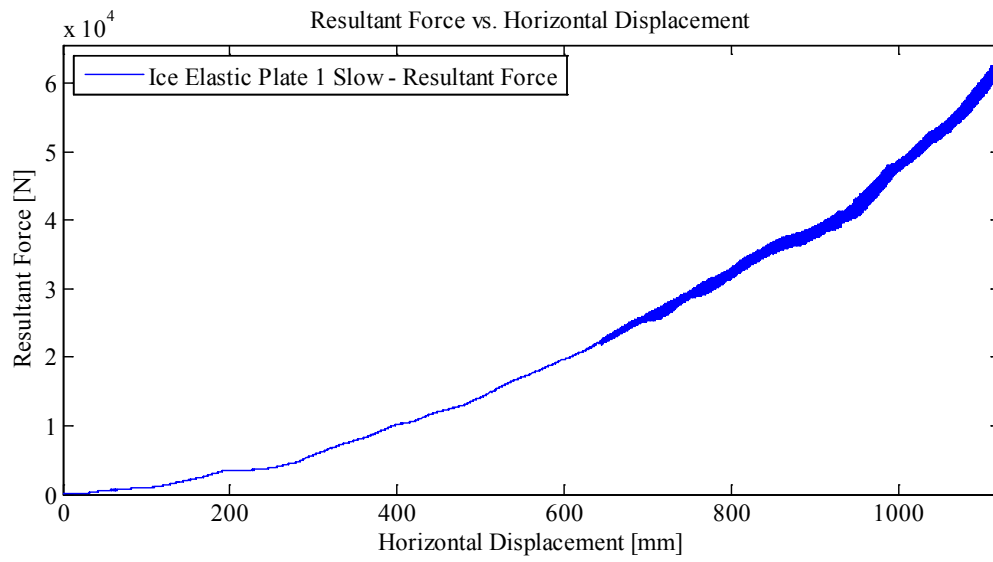


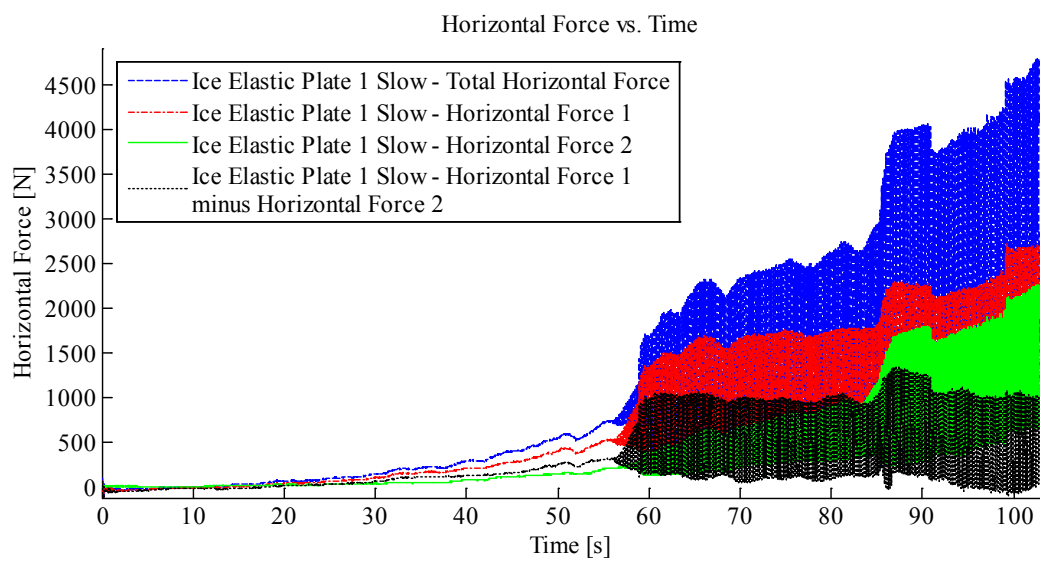
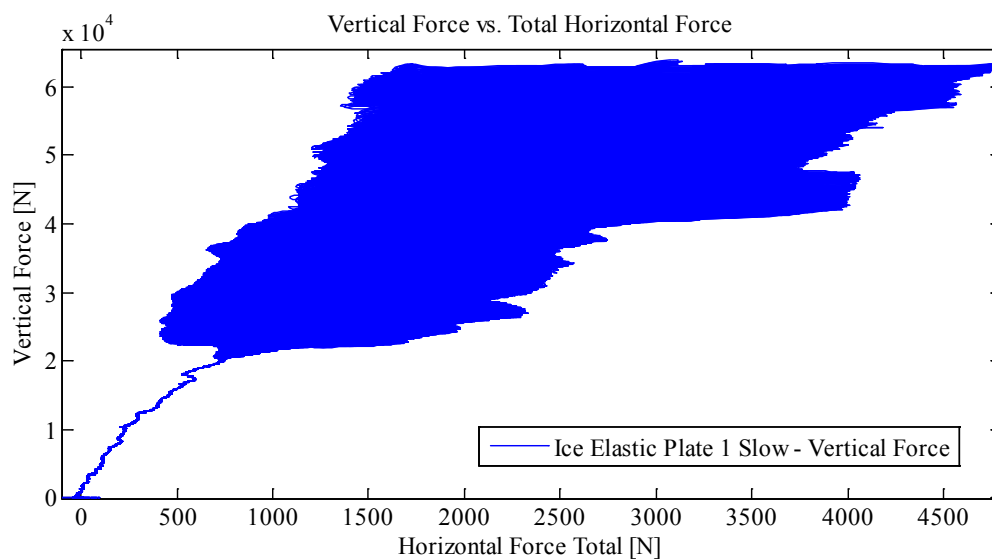












Appendix C3.2.3 – MovingLoad31

April 28, 2014 at ~11:45p.m.

Run #

Run Type: Ice Cone – Elastic Plate 2

Room-temperature: -9.4°C (Measured with thermocouple)

Sample Type: 1/2" Plate with Ice

Test Type: In-Along-Out End to End

HStarting Point: End (-54.73 cm (-55 cm nominal))

HSpeed: 10mm/s (Nominal)

H Travel: End to End (110+ cm)

Vstarting Point: +0.95 mm

VSPEED: 0.25 mm/s

V Target: 30.95 mm

V Travel: 30.0 mm

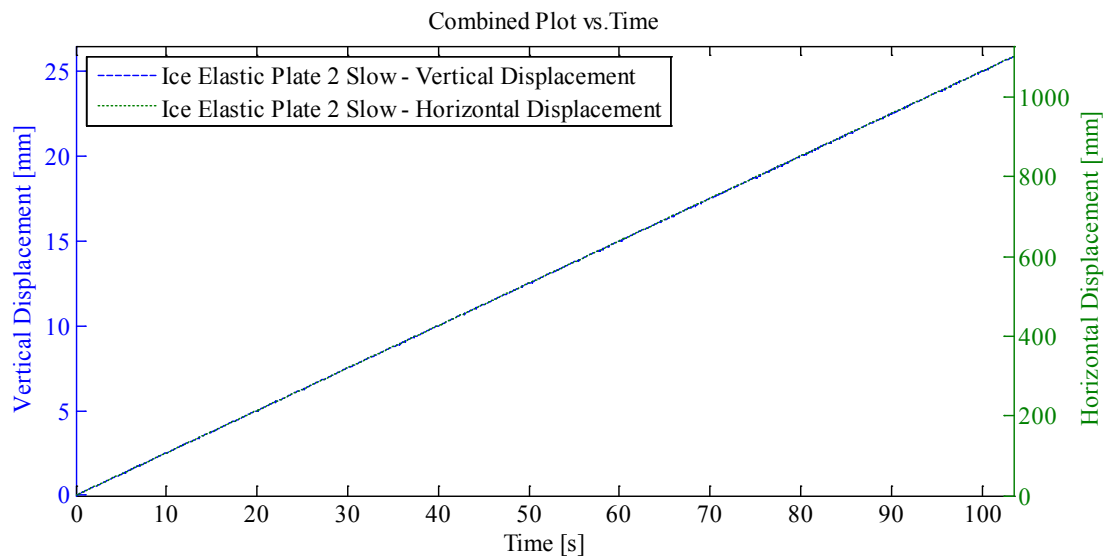
Notes:

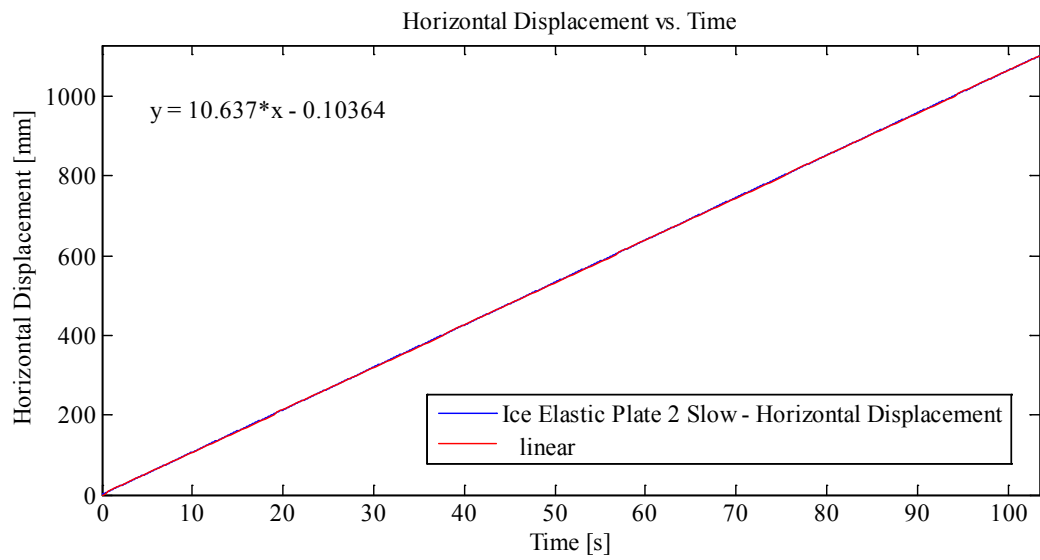
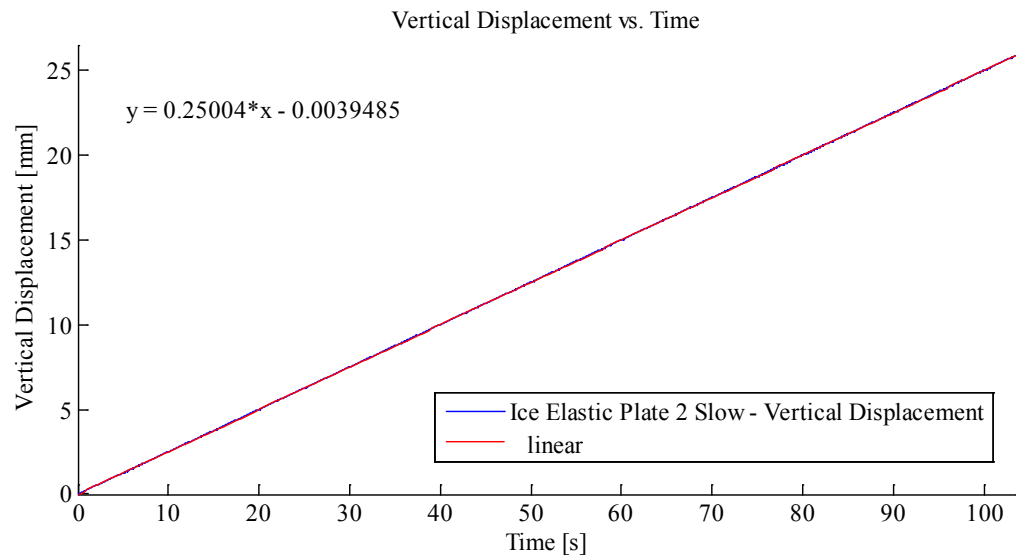
Force 1: 3 cm Ice Indentation In-Along-Out - End to End

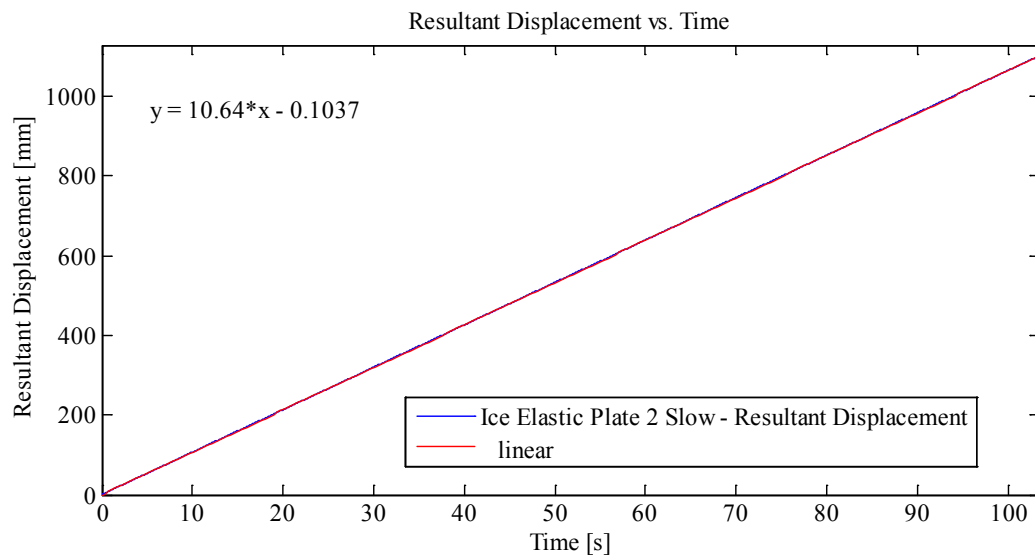
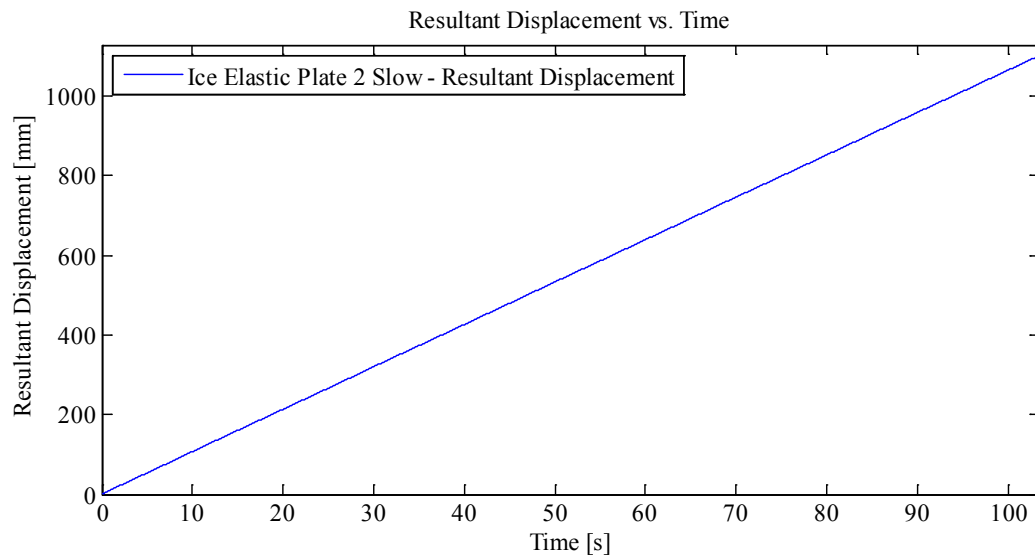
Data from Indentation 1 saved as MovingLoad31

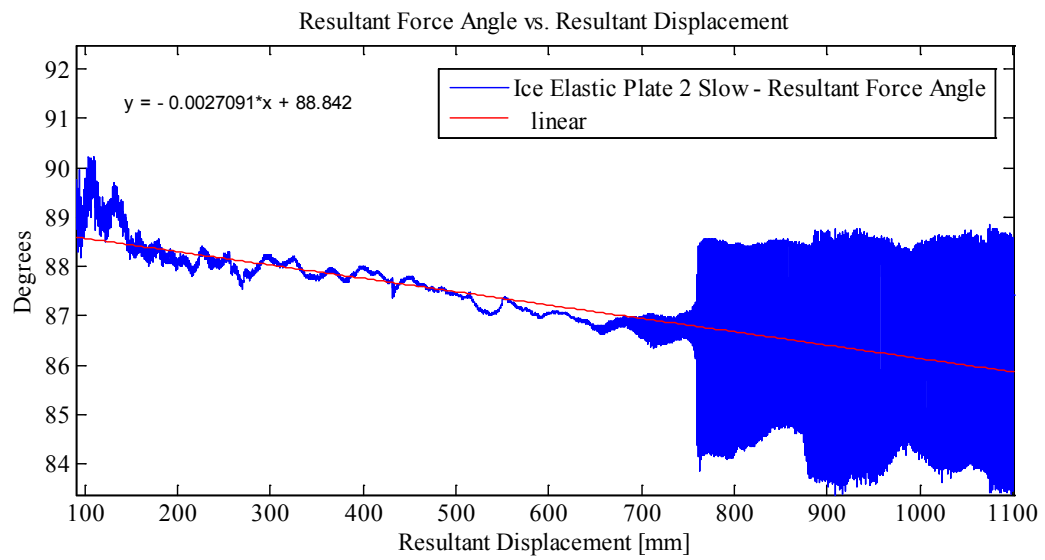
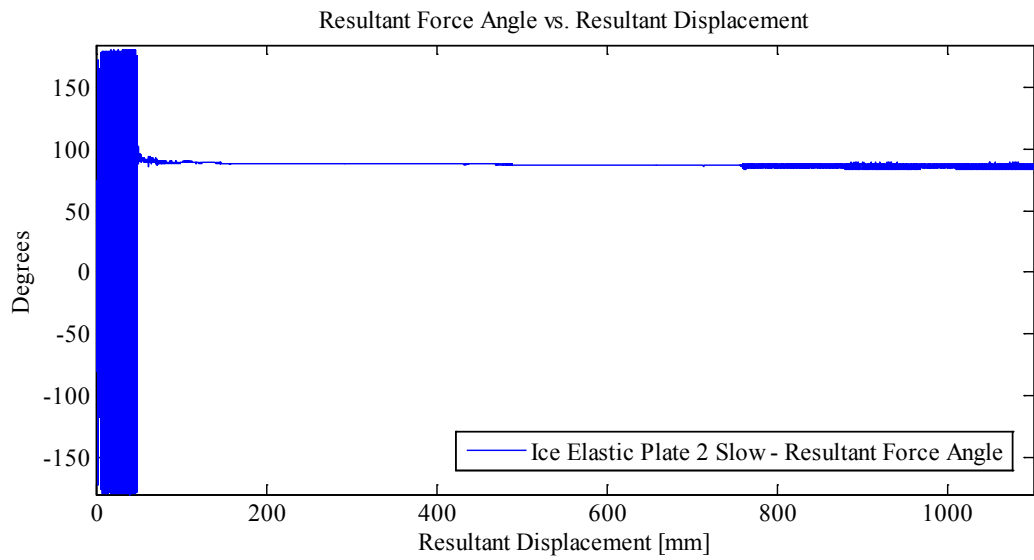
With Two Thermal Video Cameras and High Speed

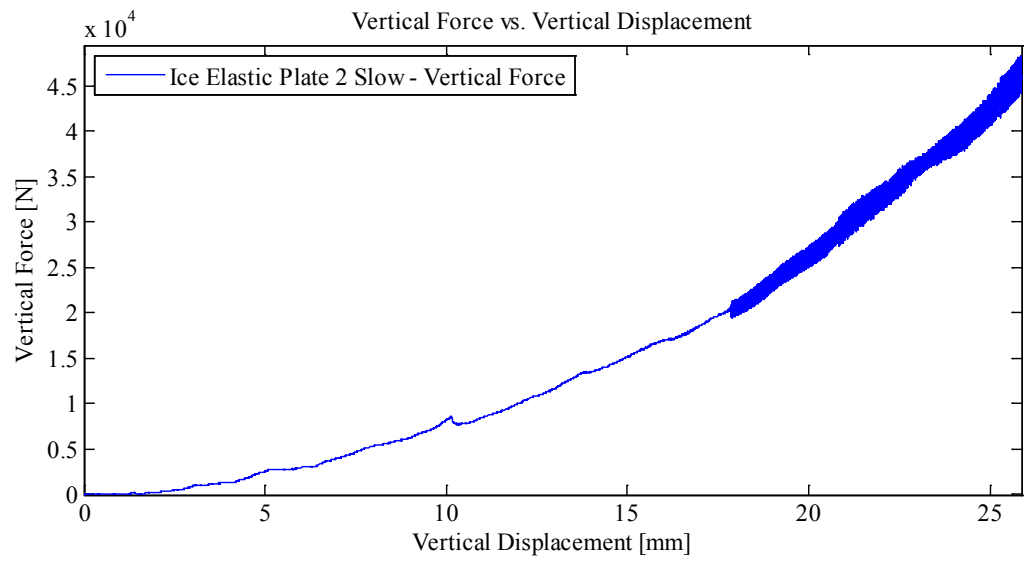
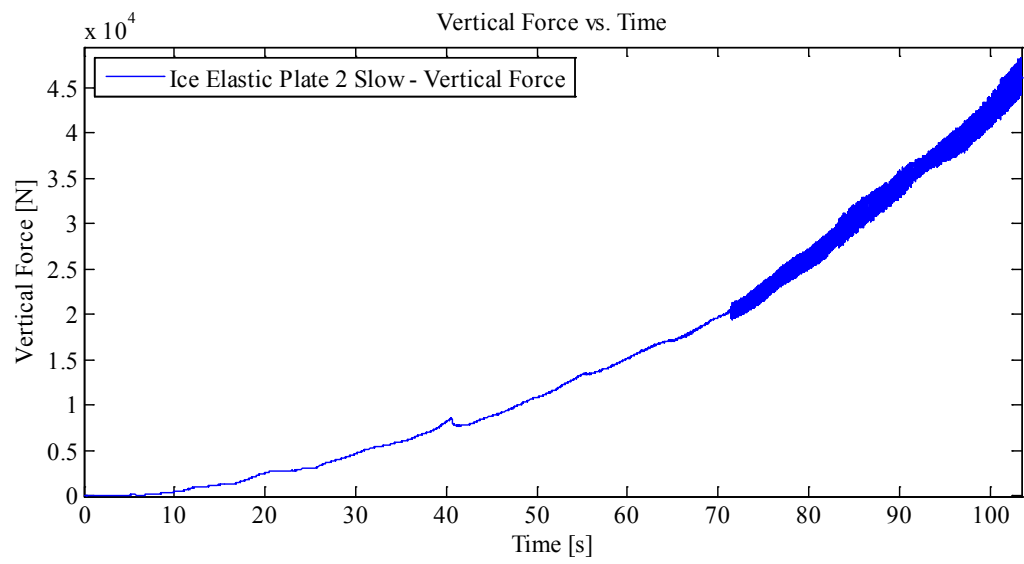
Plots:

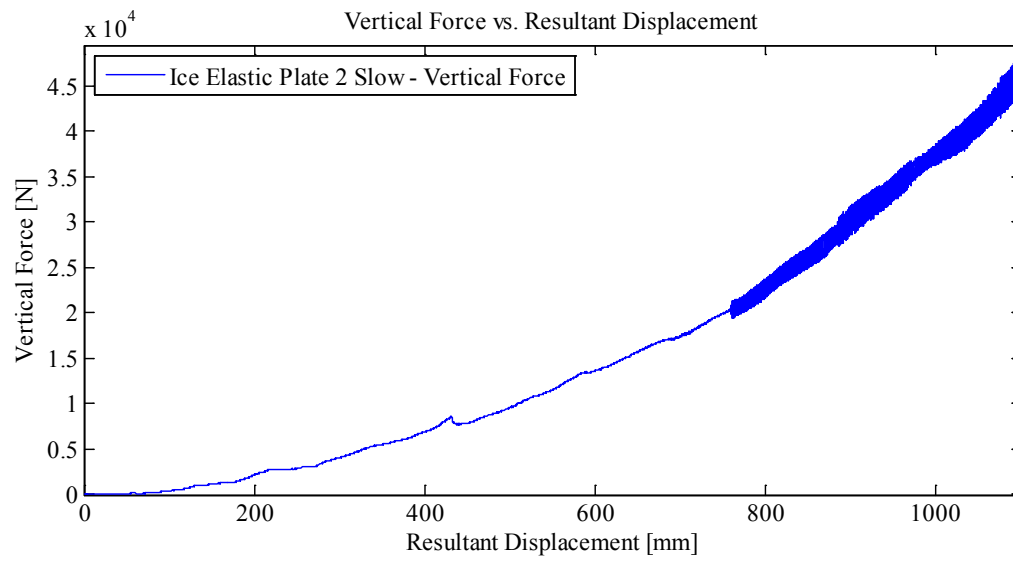
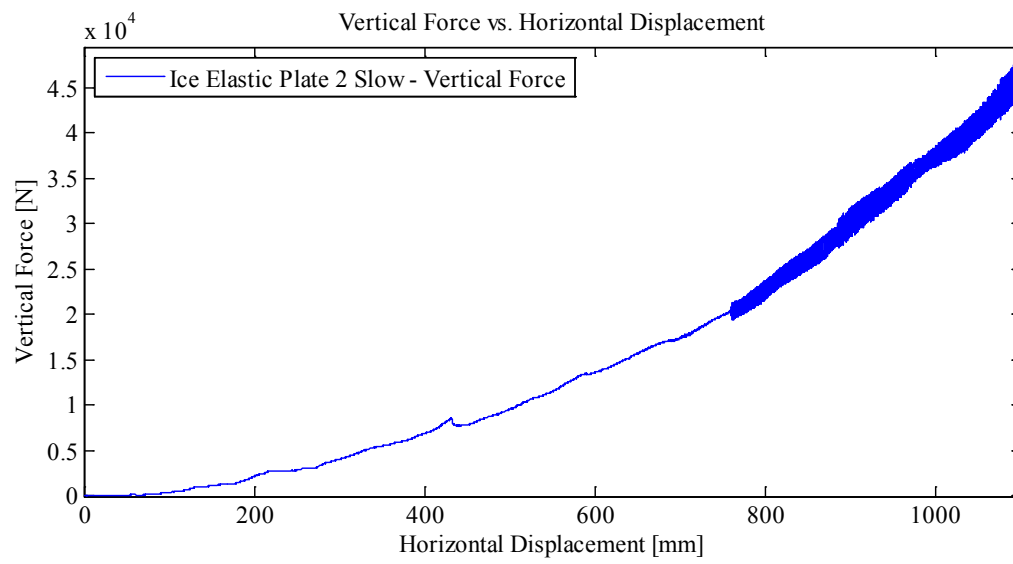


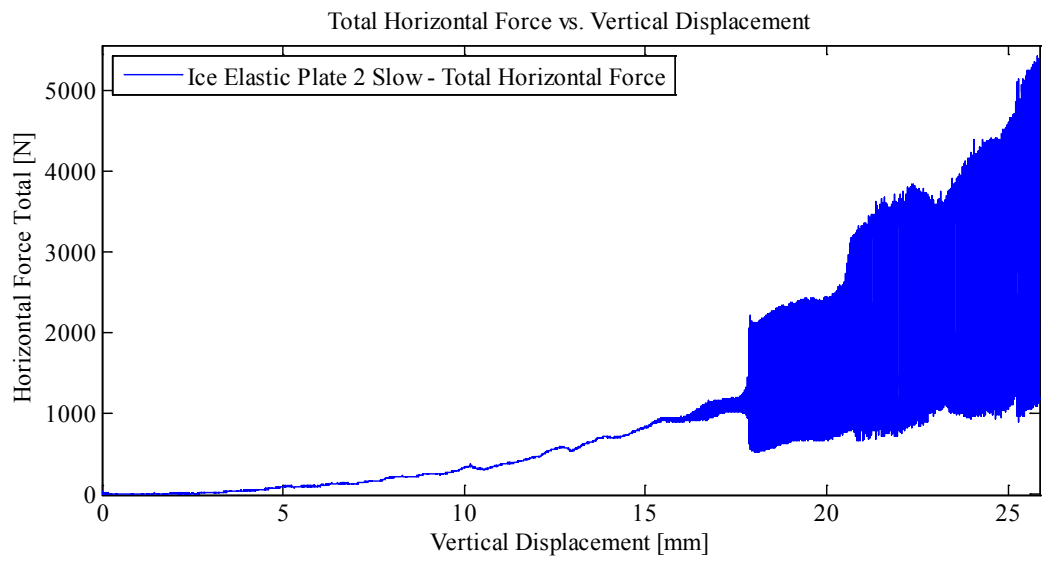
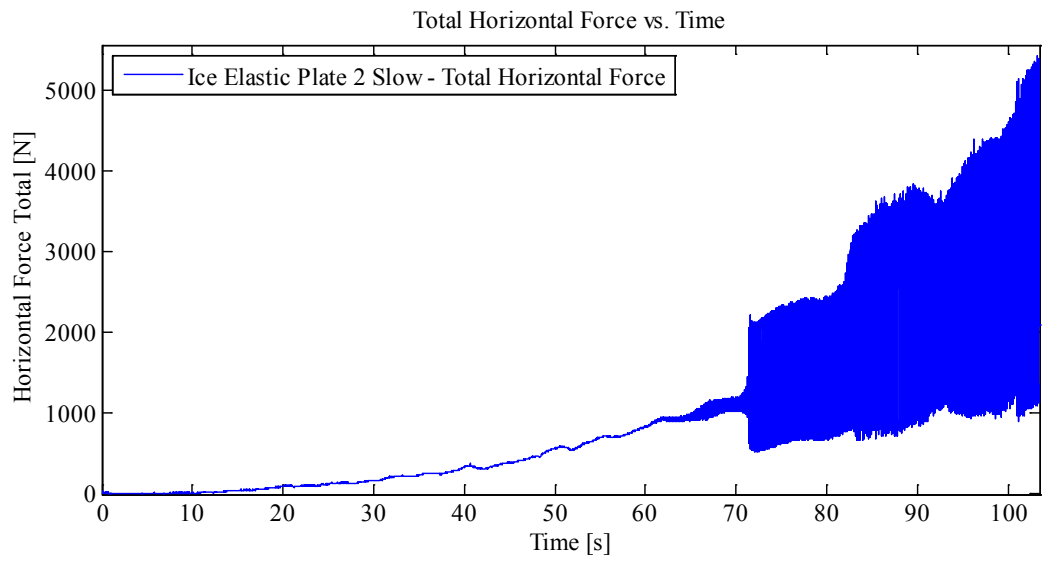


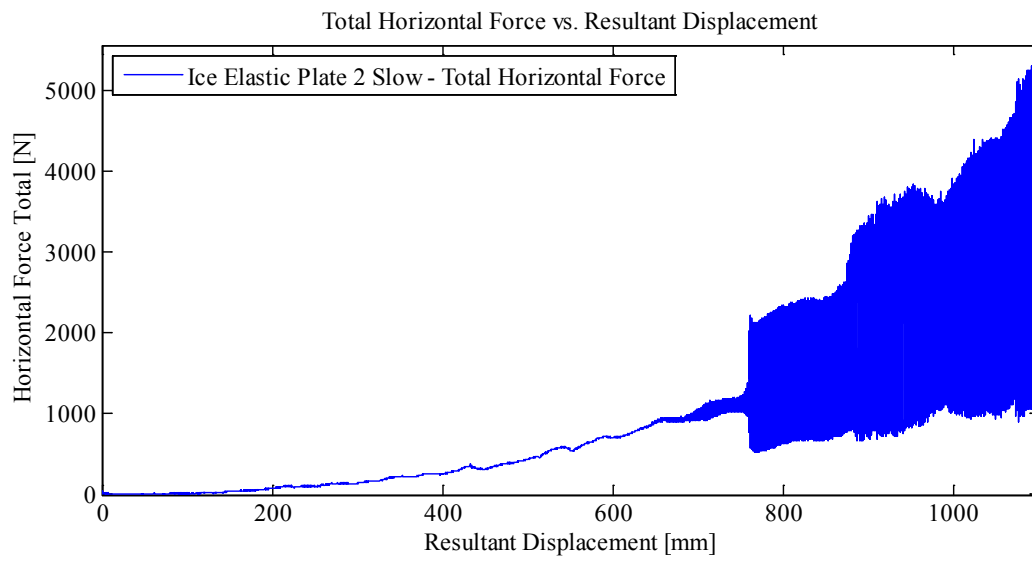
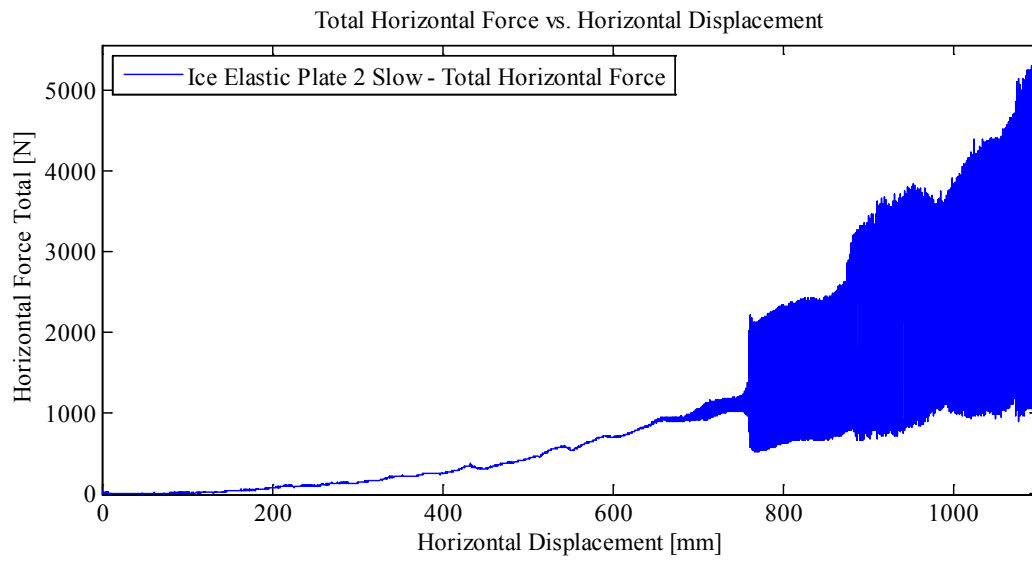


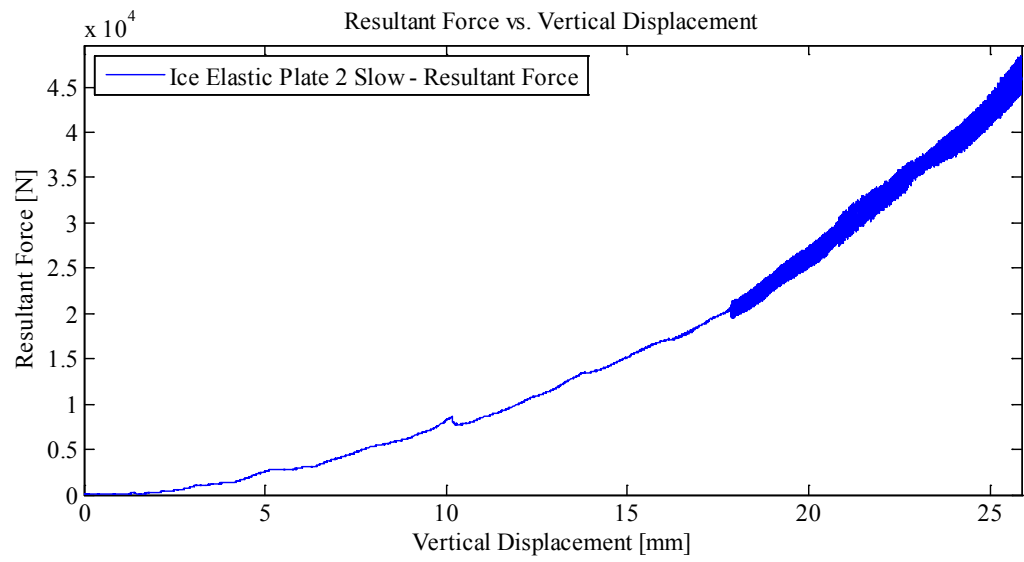
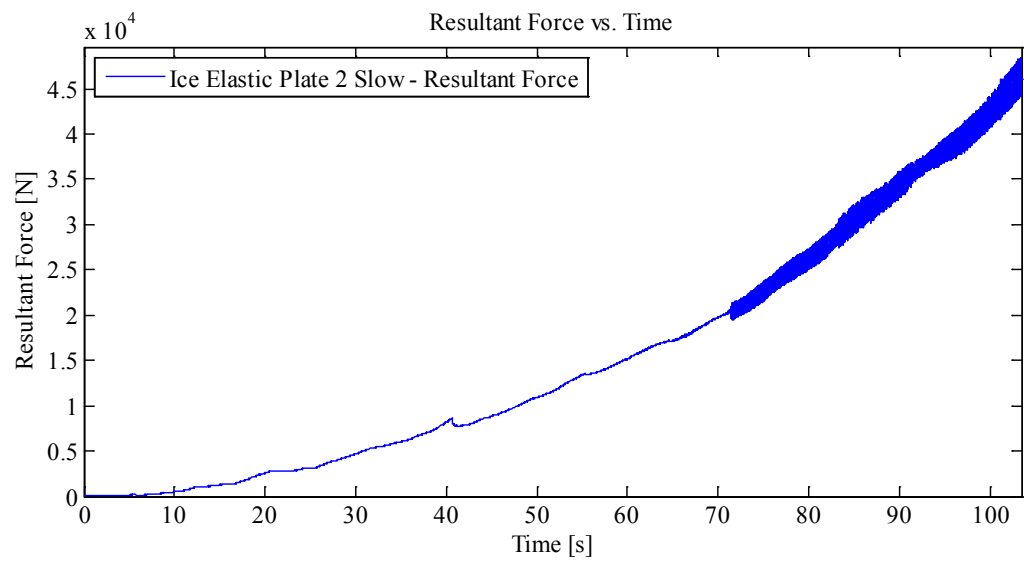


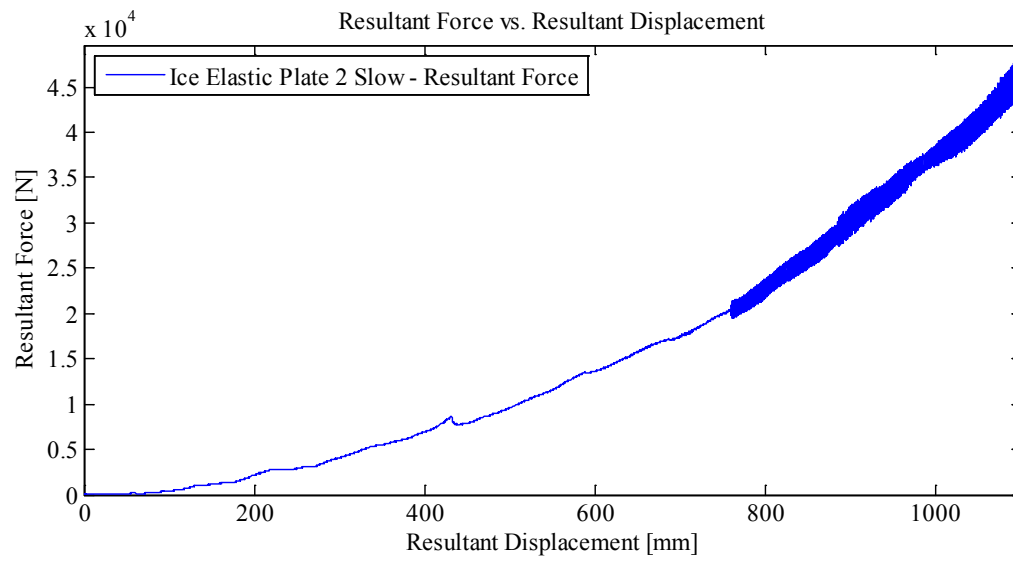
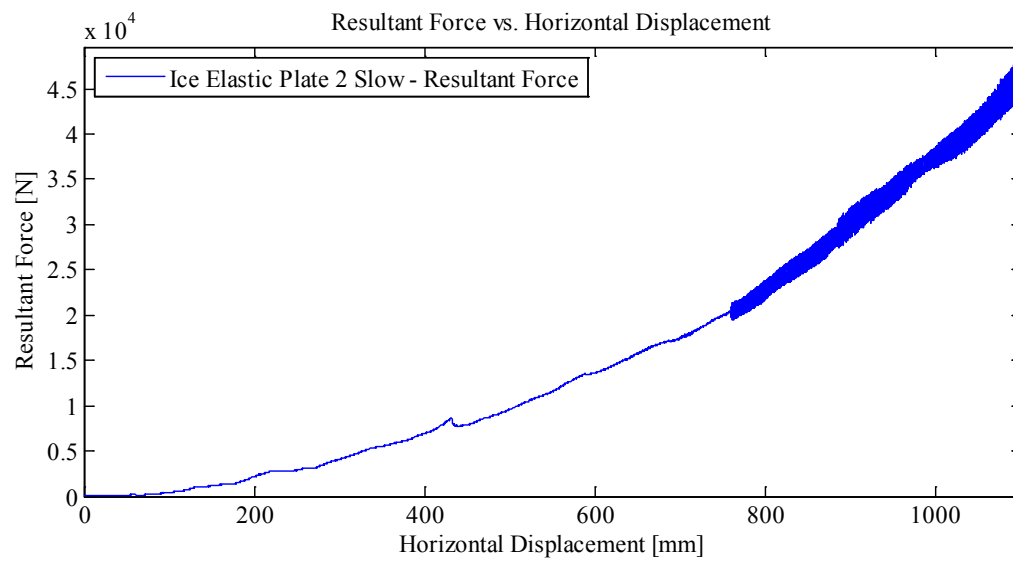


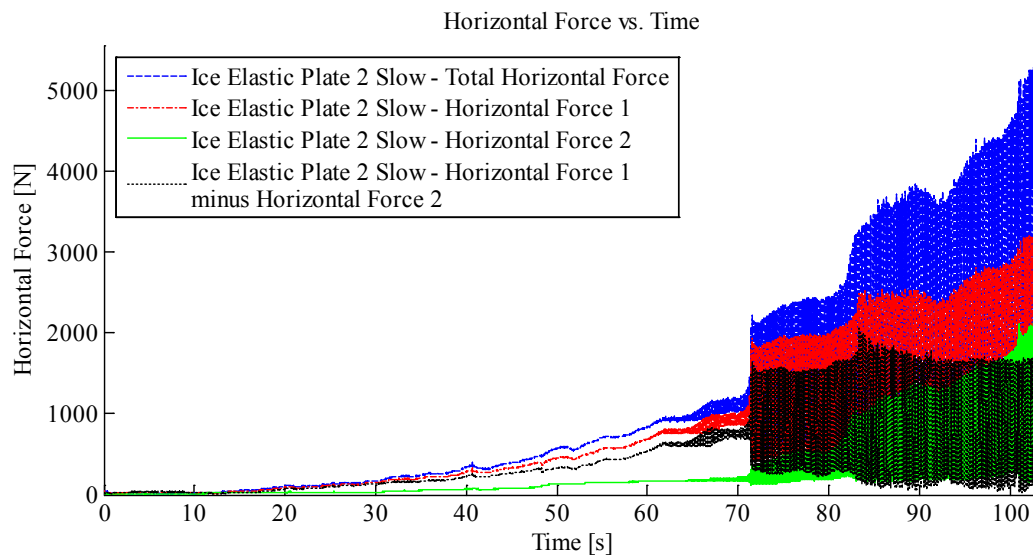
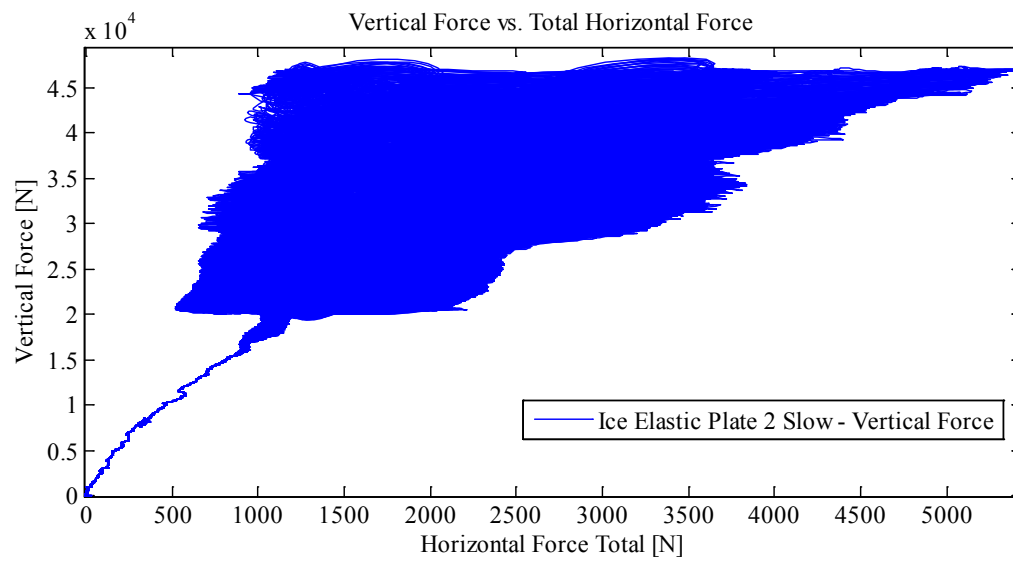












Appendix C3.2.4 – MovingLoad34

April 29, 2014 at ~2:40p.m.

Run #

Run Type: Ice Cone – Elastic Plate 3
Room-temperature: -8.9°C (Measured with thermocouple)
Sample Type: 1/2" Plate with Ice
Test Type: In-Along-Out End to roughly centre

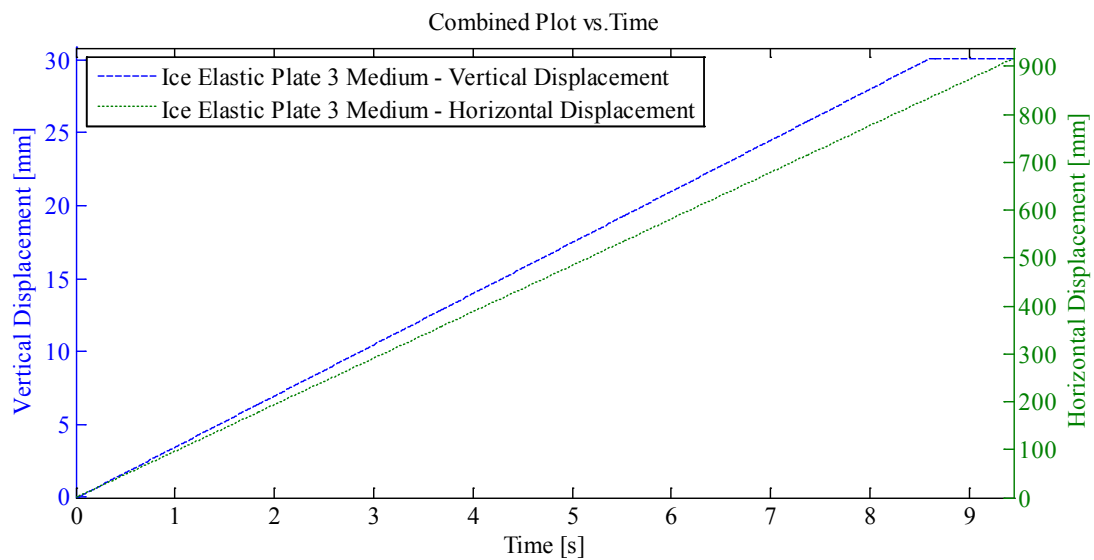
HStarting Point: End (-61.49 cm (absolute end))
HSpeed: 100mm/s (Nominal)
H Travel: Abs. End to roughly centre

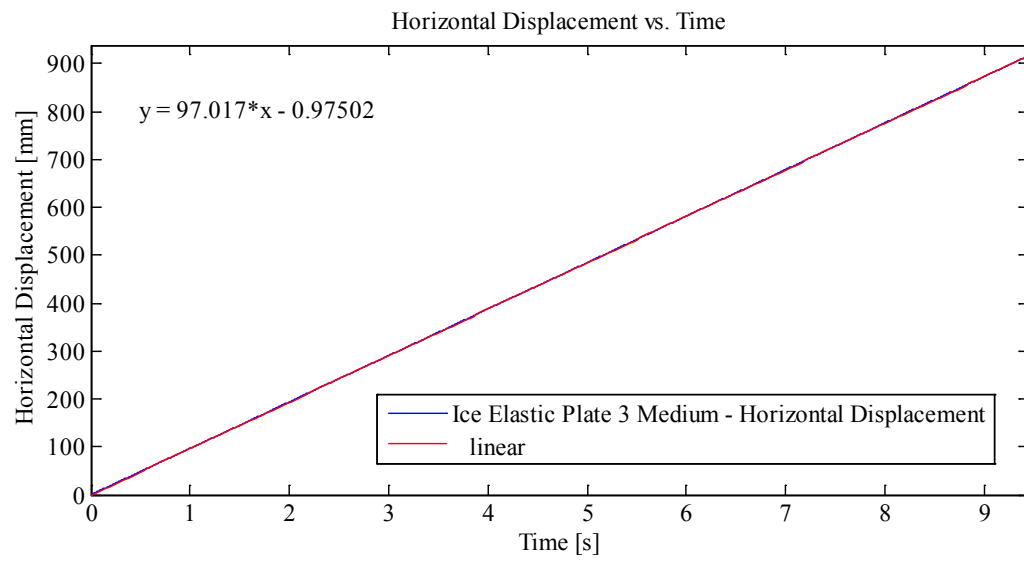
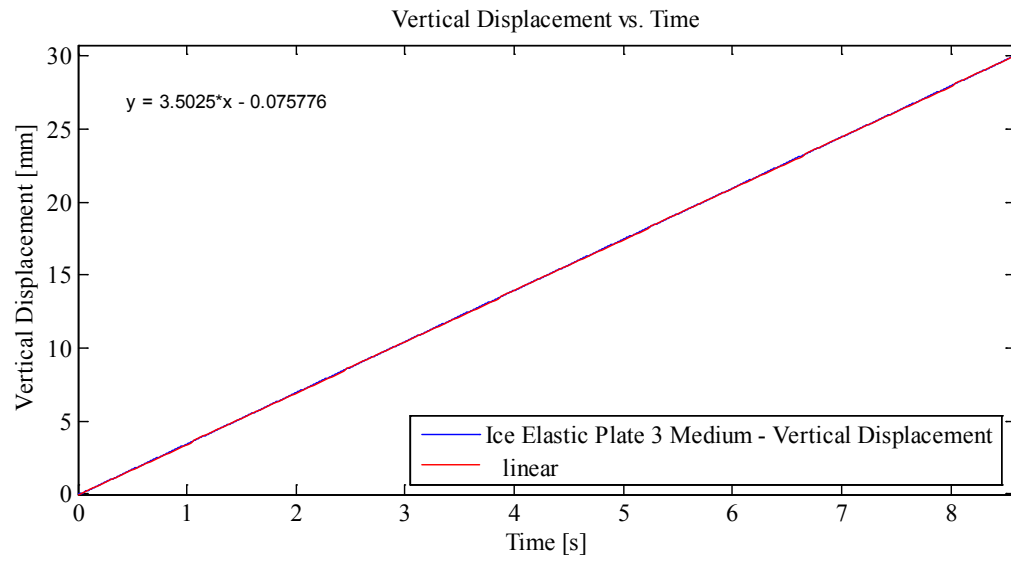
Vstarting Point: -1.38 mm
VSpeed: 3.5 mm/s
V Target: -31.38 mm
V Travel: 30.0 mm

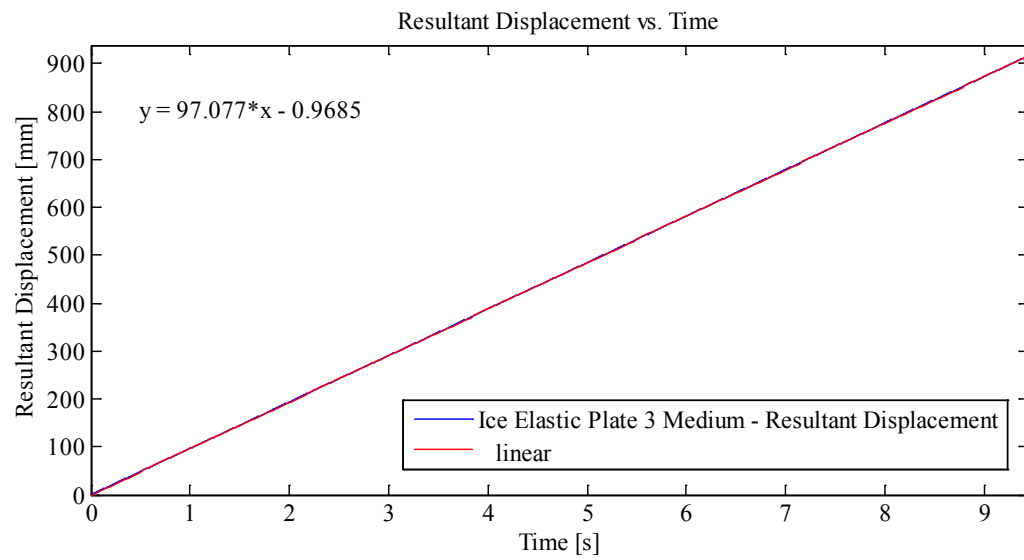
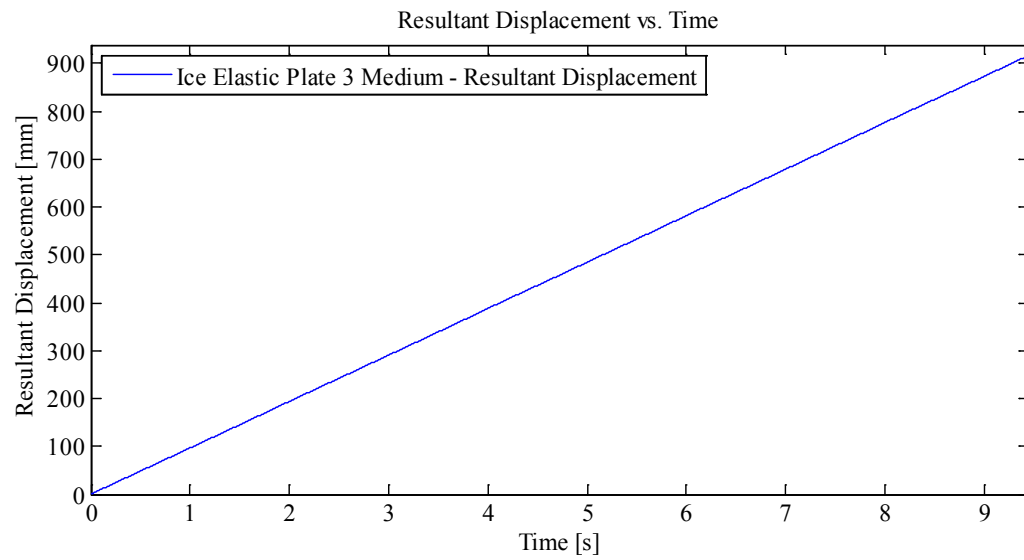
Notes:

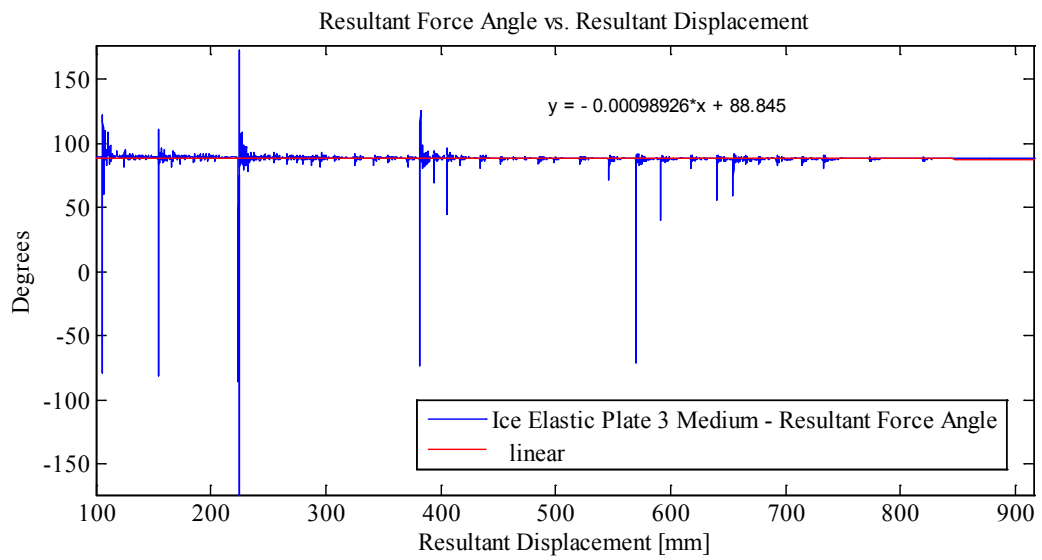
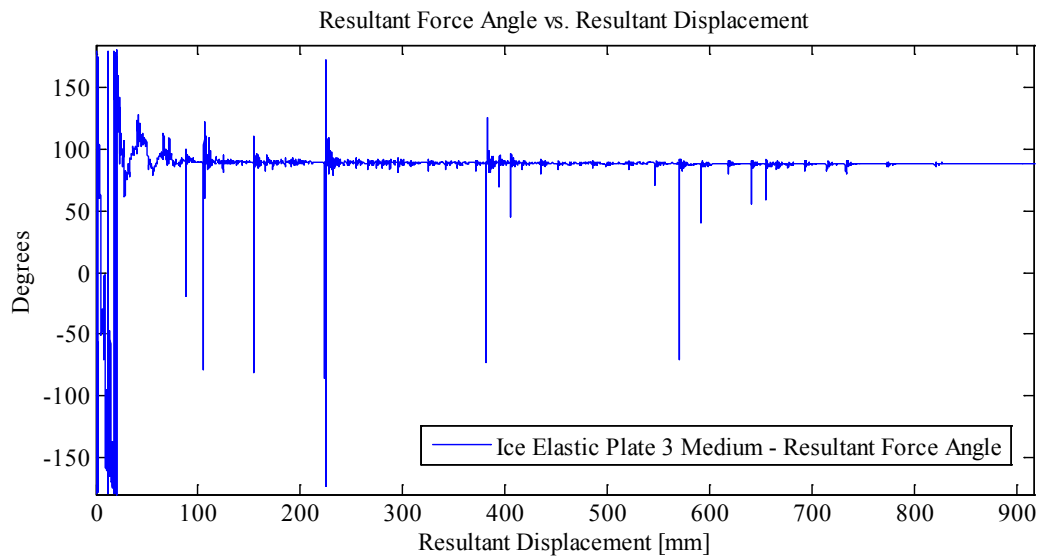
Force 1: 3 cm Ice Indentation In-Along-Out - End to roughly centre
Data from Indentation 1 saved as MovingLoad34
With Two Thermal Video Cameras and High Speed

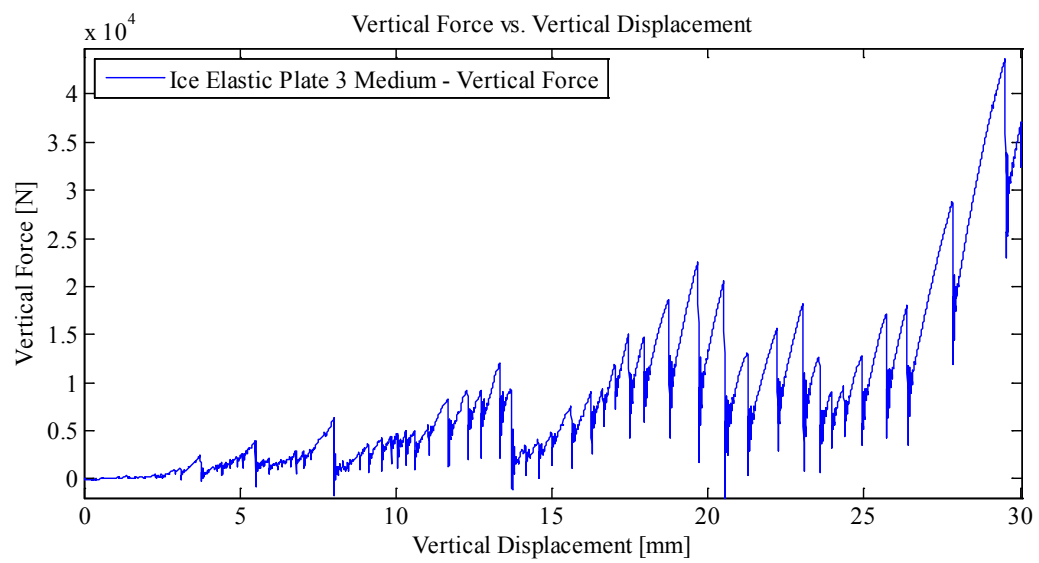
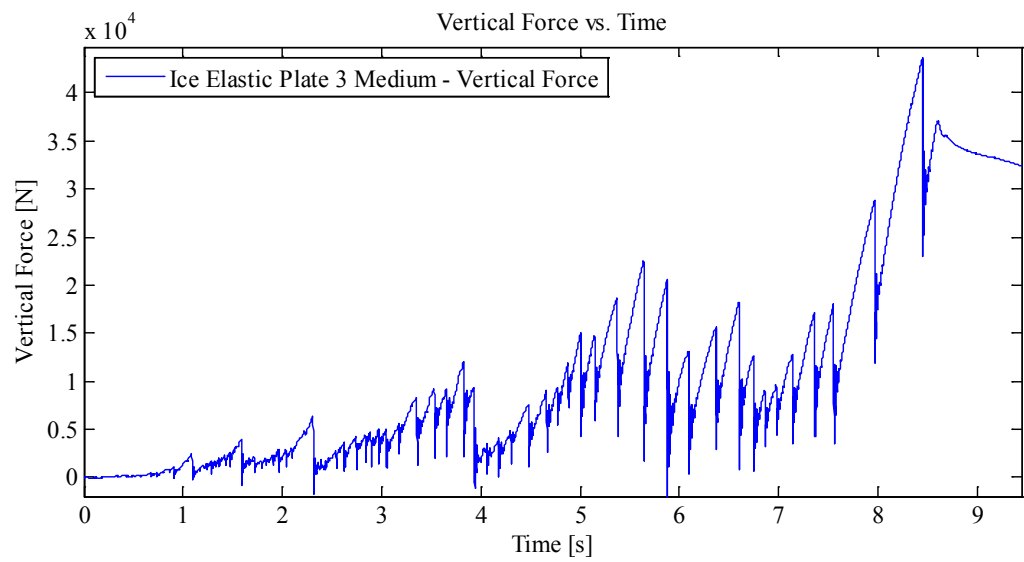
Plots:

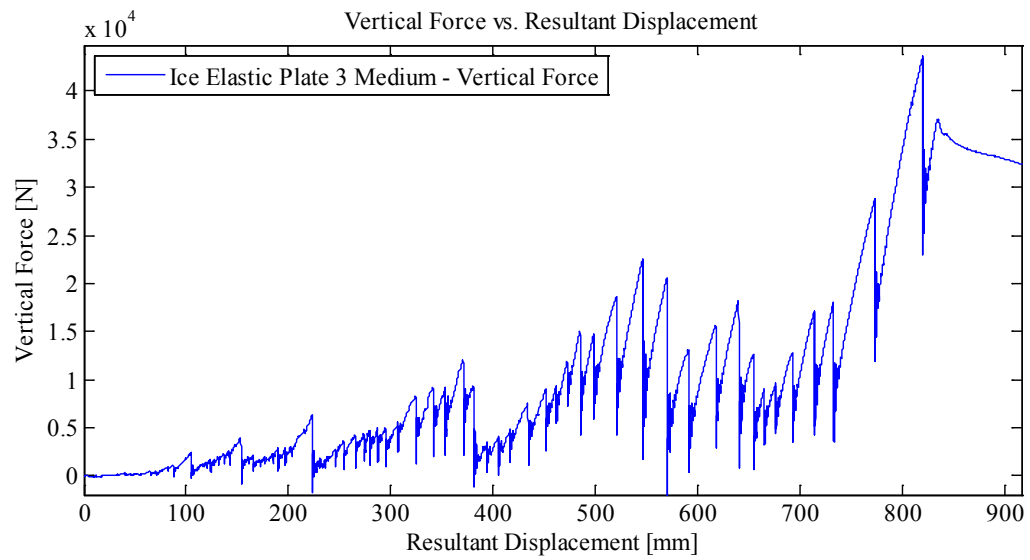
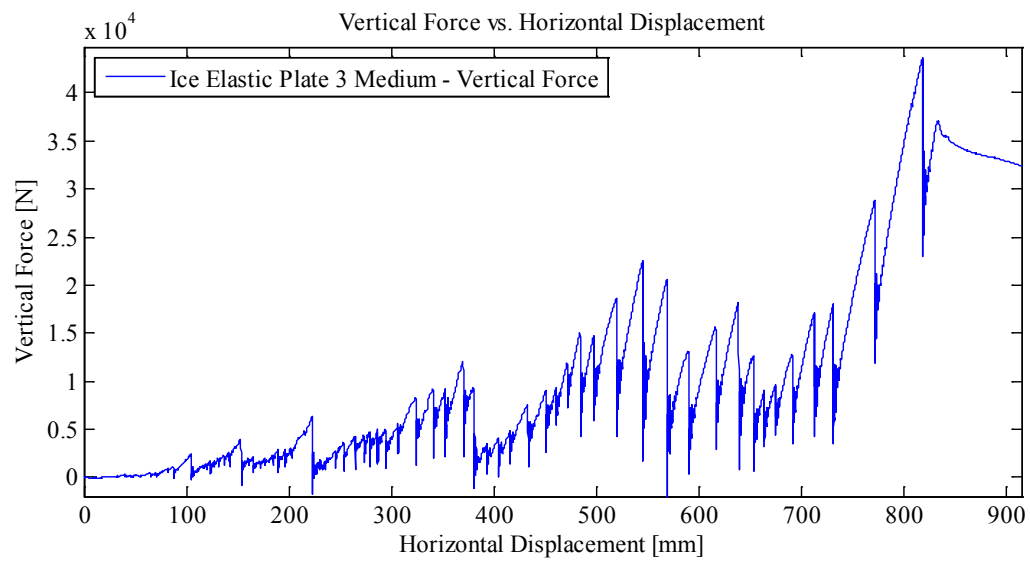


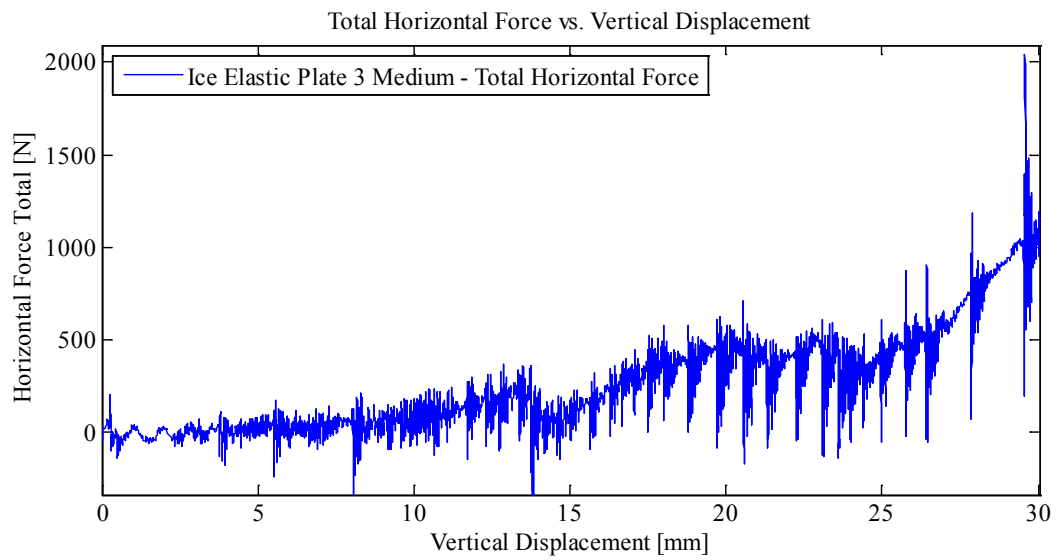
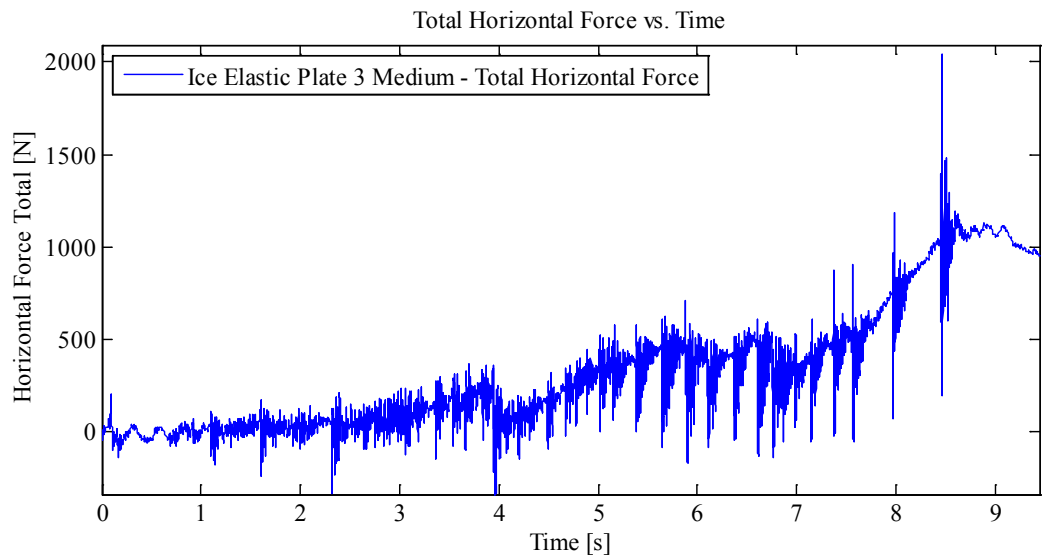


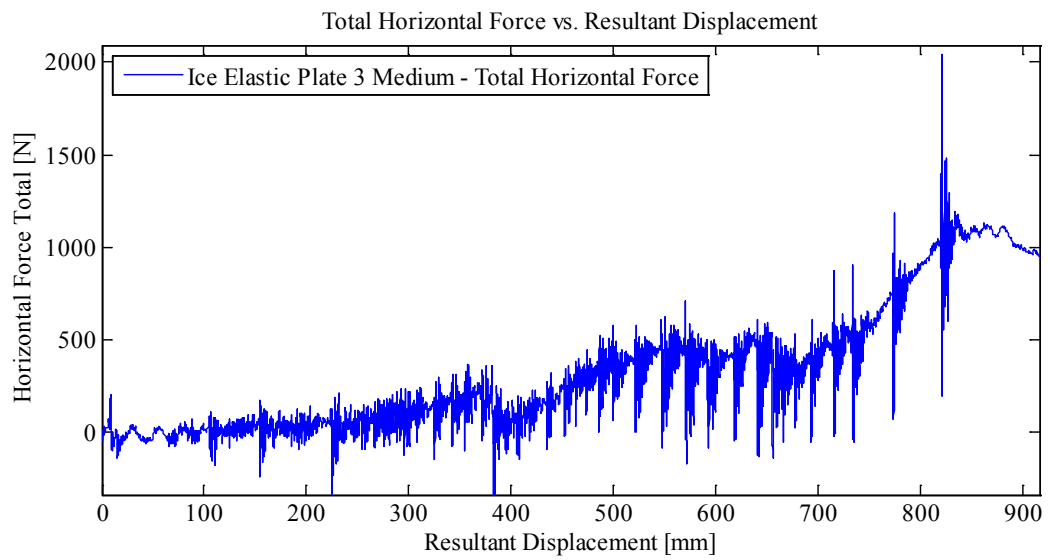
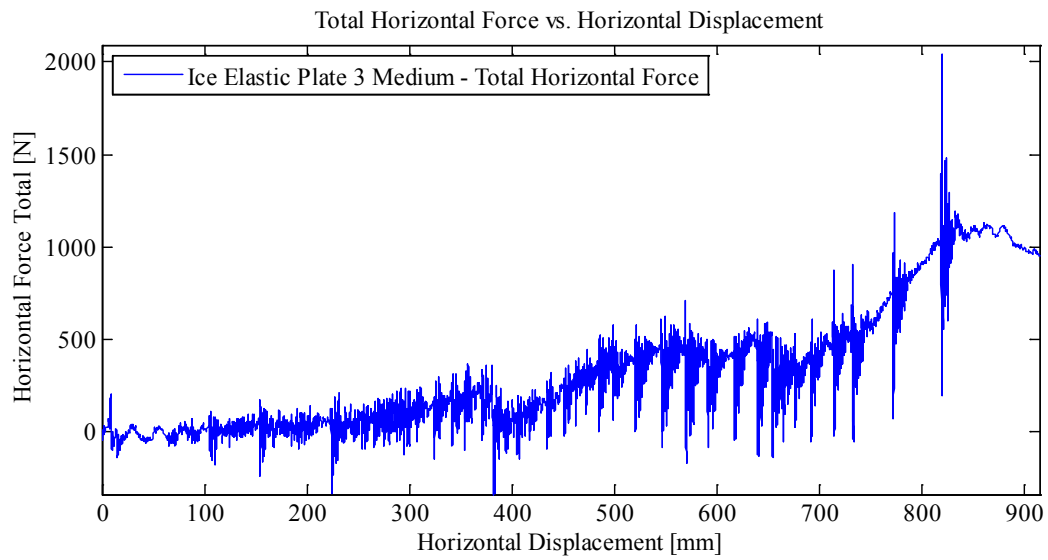


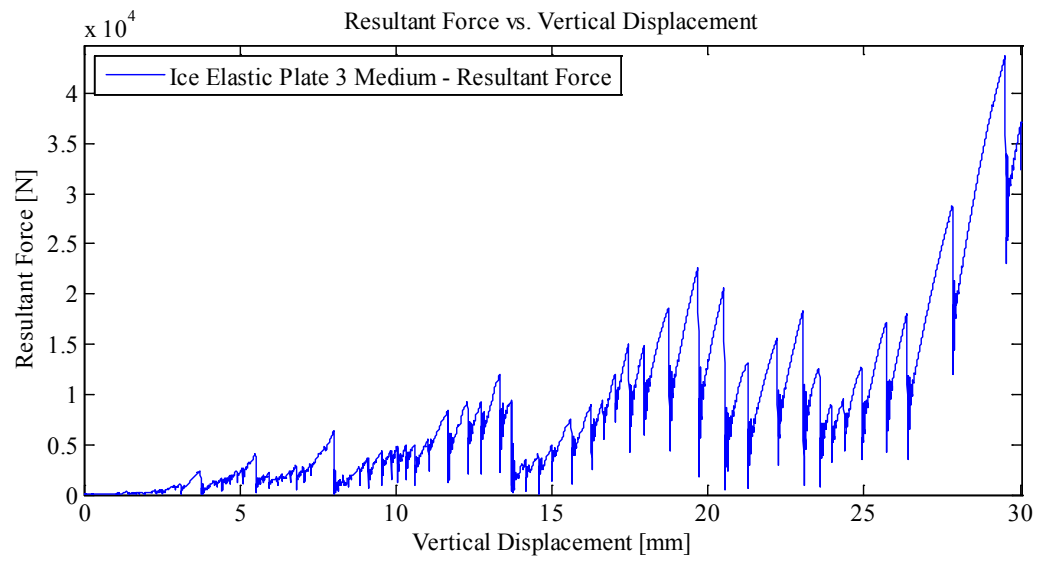
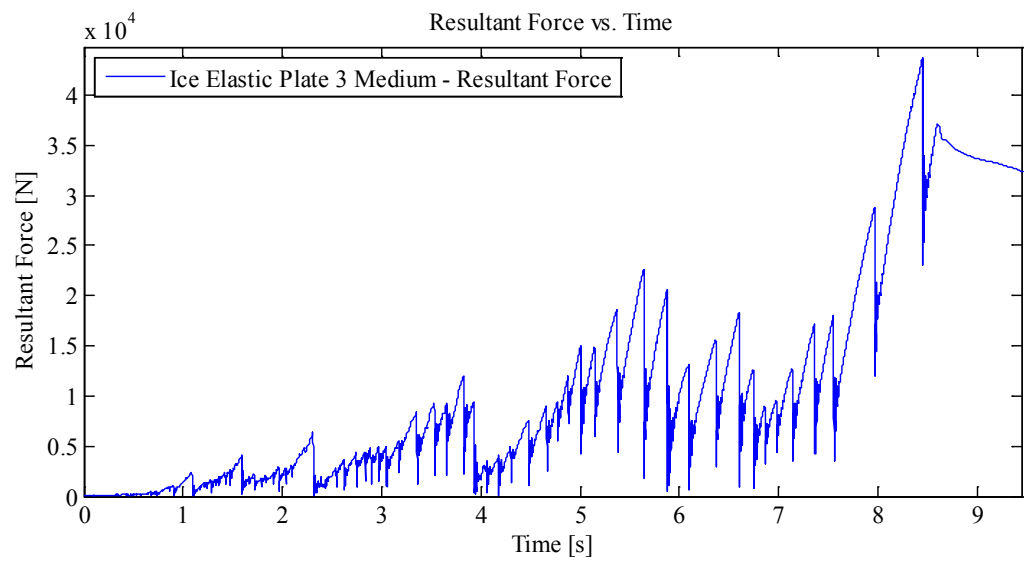


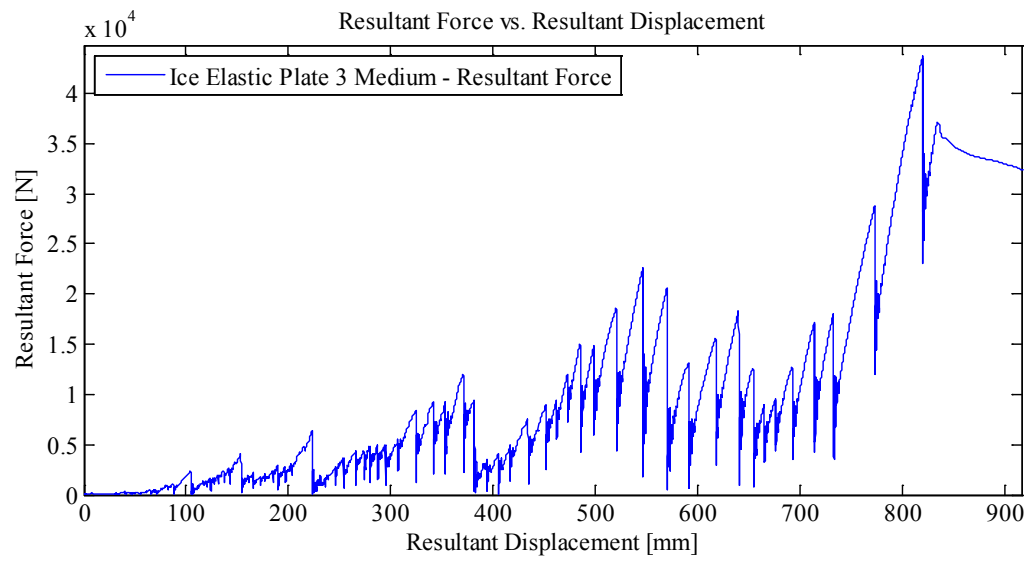
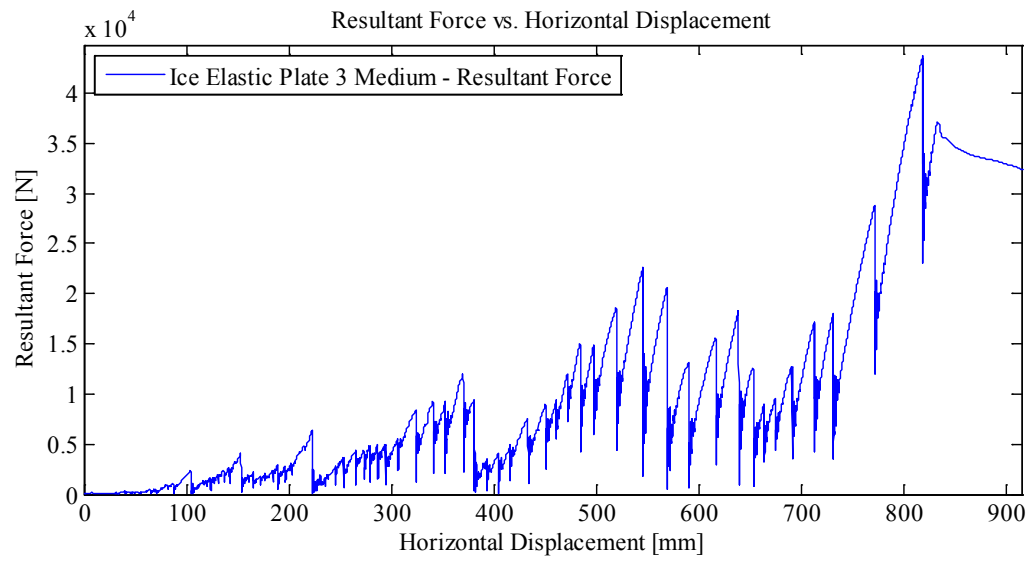


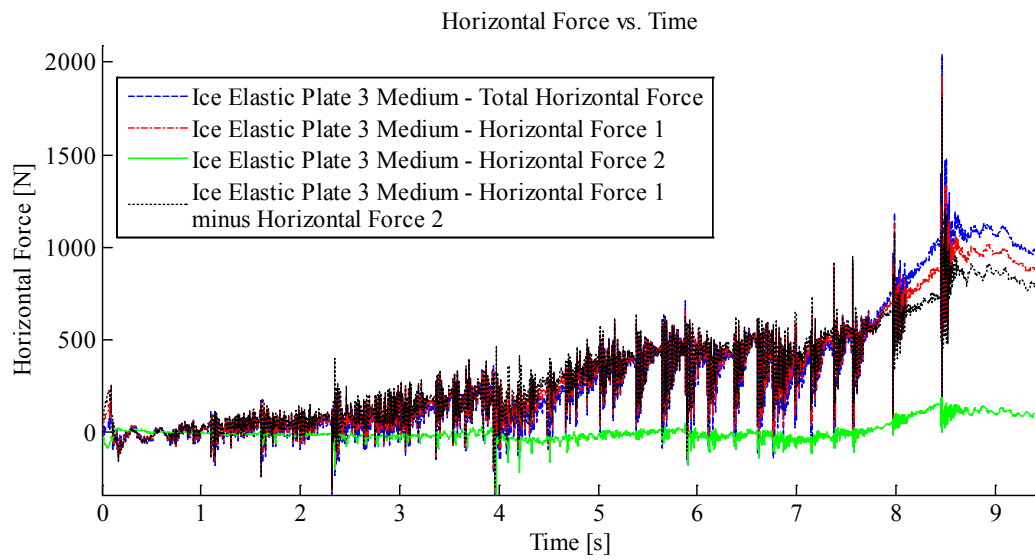
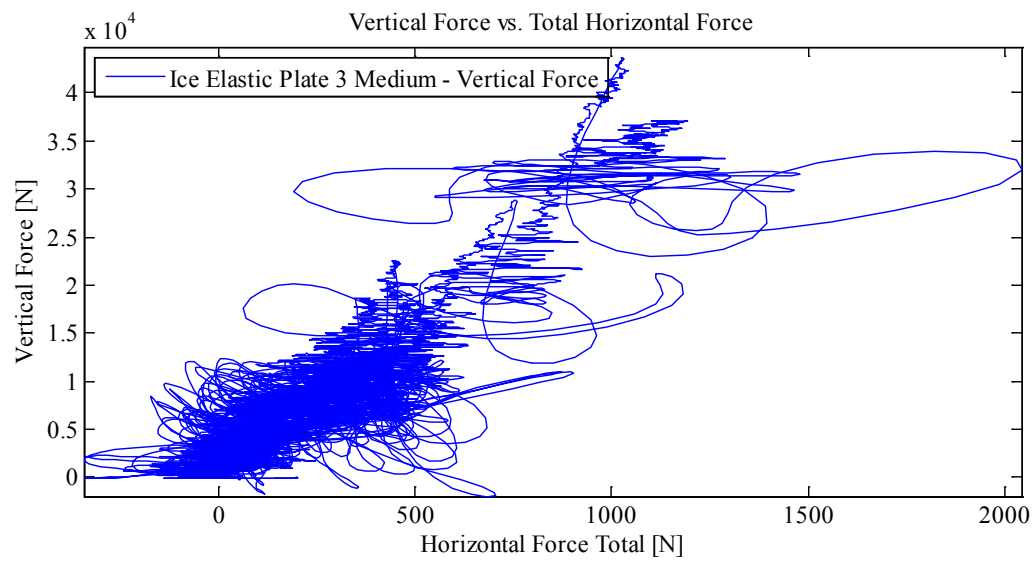












Appendix C3.2.5 – MovingLoad38

May 14, 2014 at ~2:45p.m.

Run # elastic 1/2" sample with ice
Run Type: Ice Cone – Elastic Plate 4
Room-temperature: -9.4°C (Measured with thermocouple)
Sample Type: Elastic 1/2" plate (again)
Test Type: In-Along-Out End to End

HStarting Point: End (-61.503 cm (-abs end))
HSpeed: 10mm/s (Nominal)
H Travel: End to End (110+ cm)

Vstarting Point: -1.84 mm
VSpeed: 0.25 mm/s (nominal)
V Travel: 30 mm
V Stopping Point: -31.840 mm

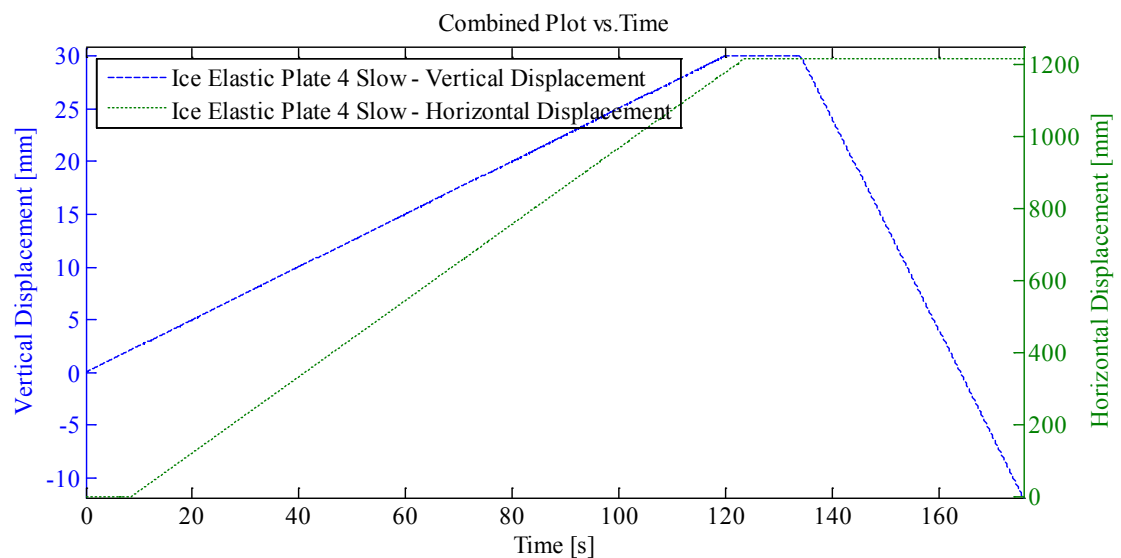
Notes:

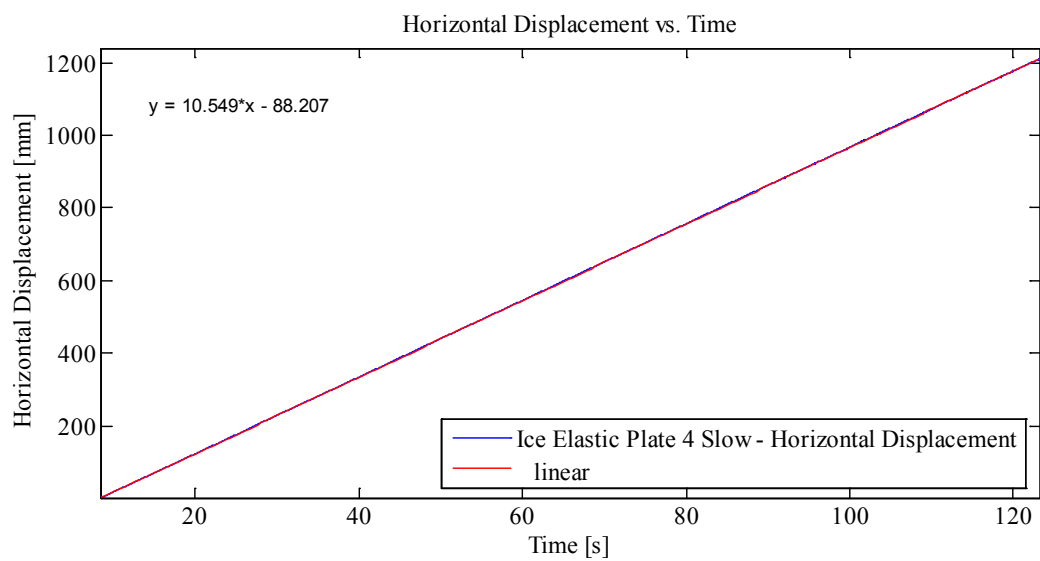
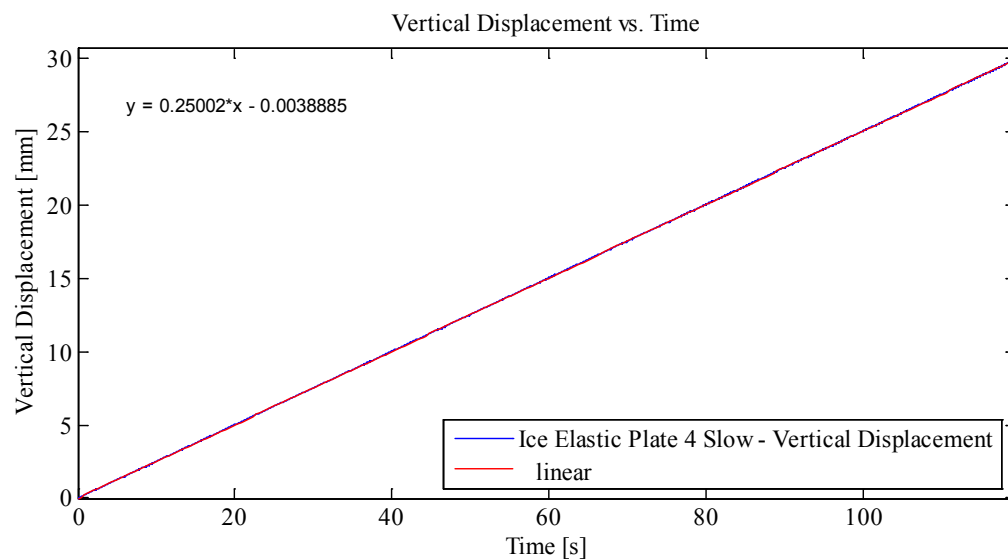
Disp Controlled: In-Along-Out - End to End

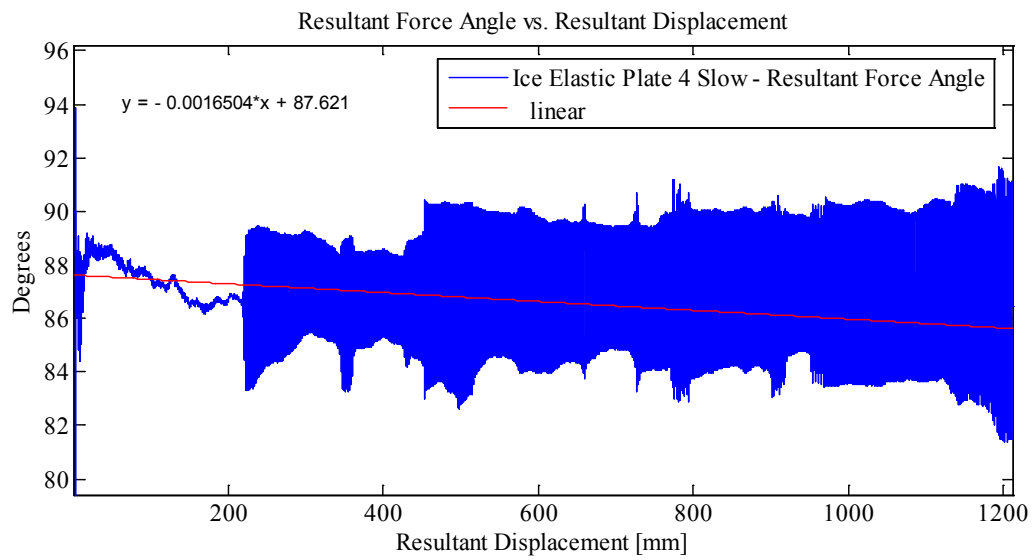
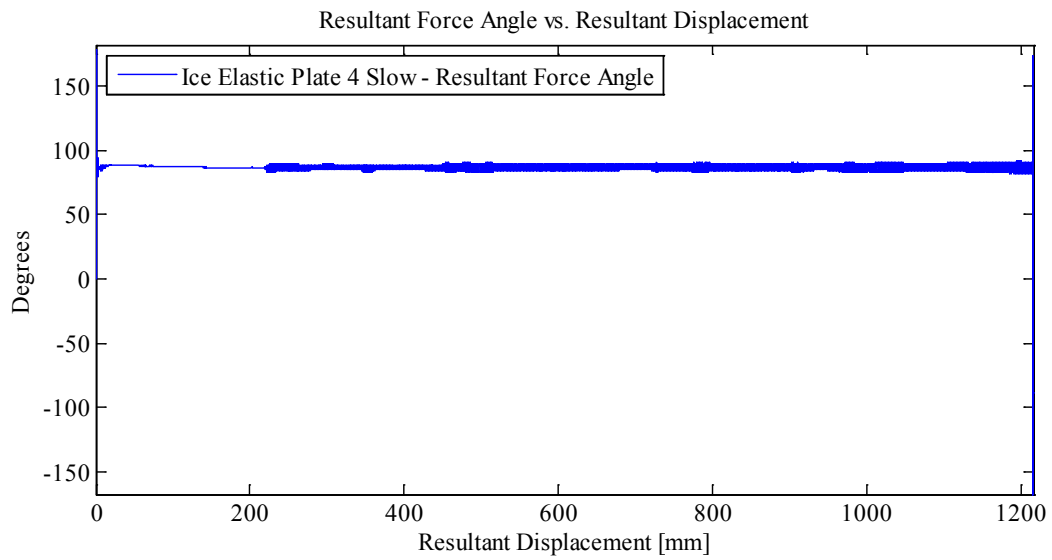
Data from Indentation 1 saved as MovingLoad38

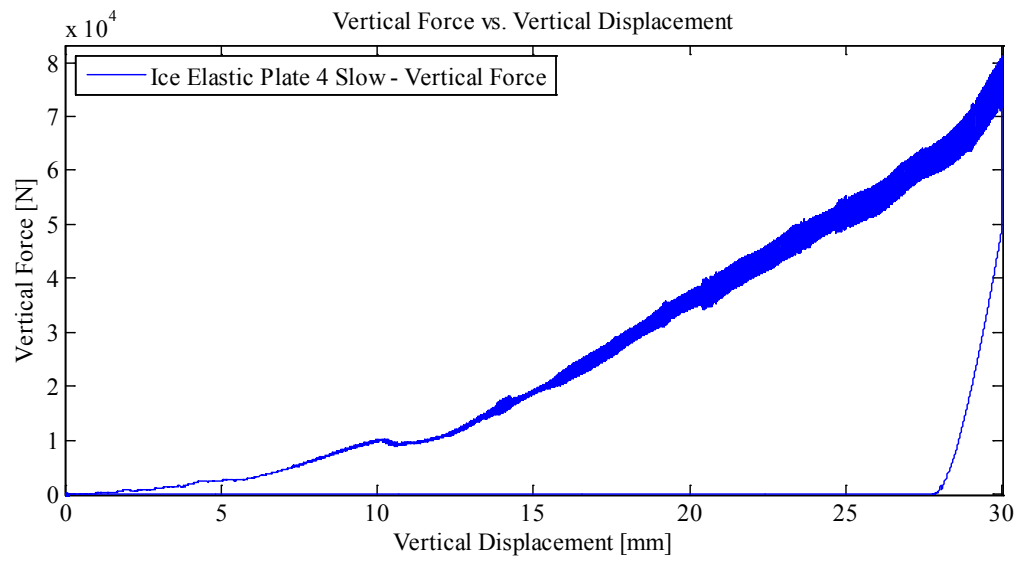
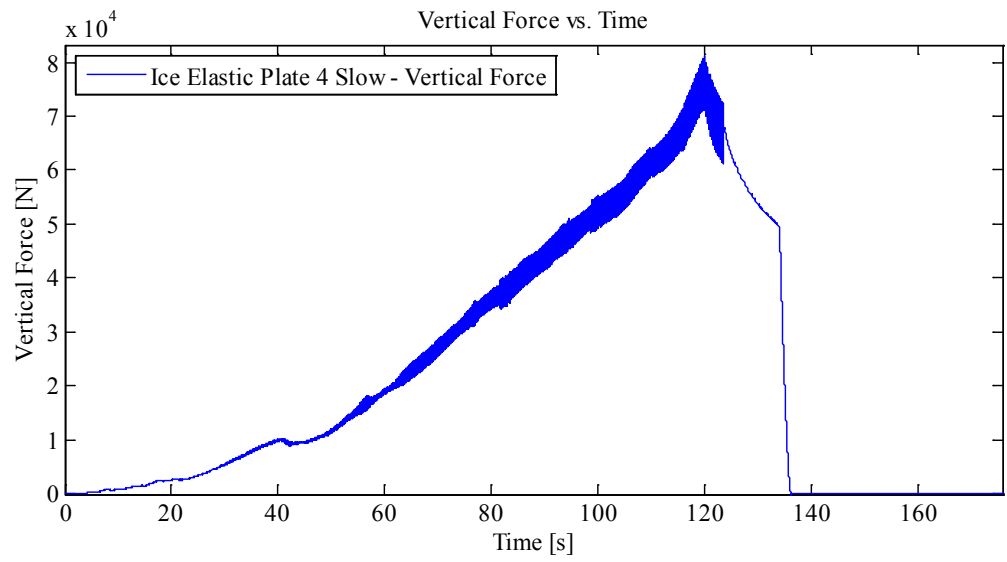
With one Thermal Video Camera and high speed video

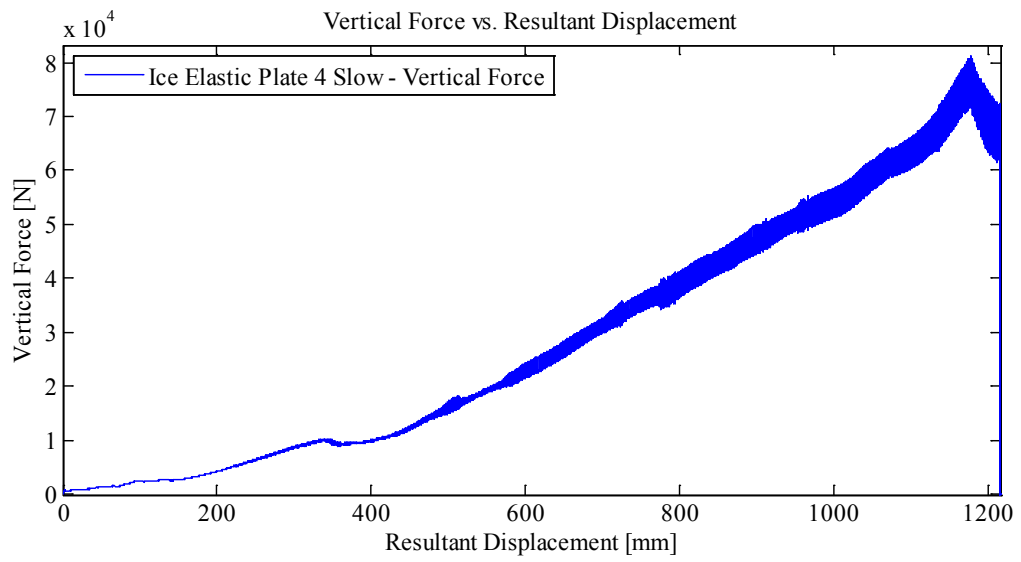
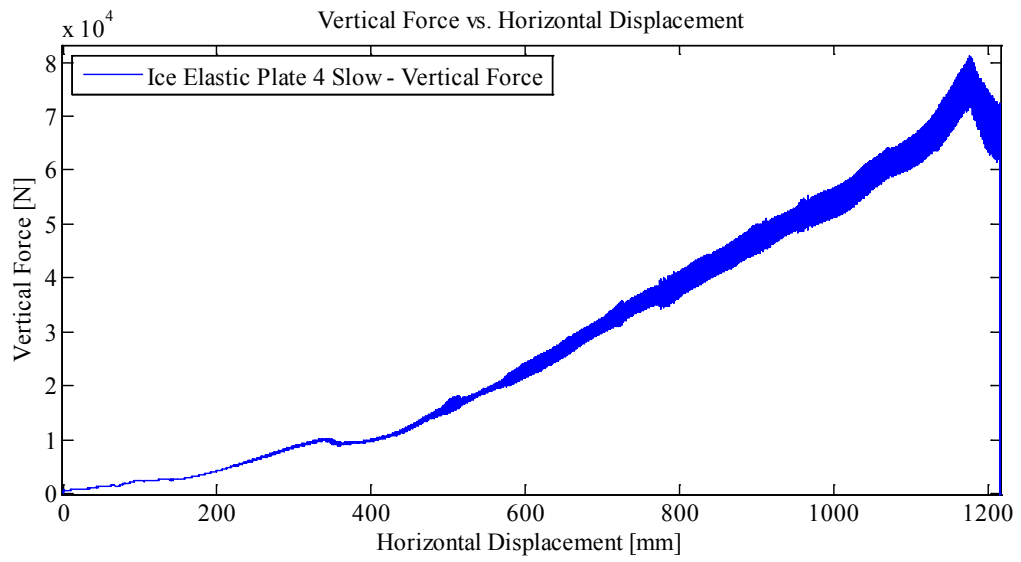
Plots:

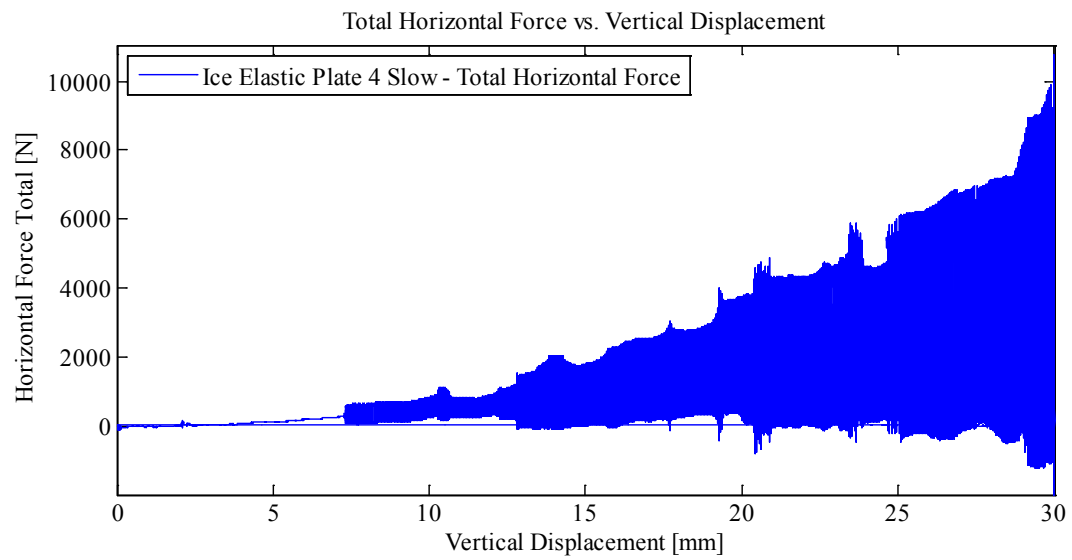
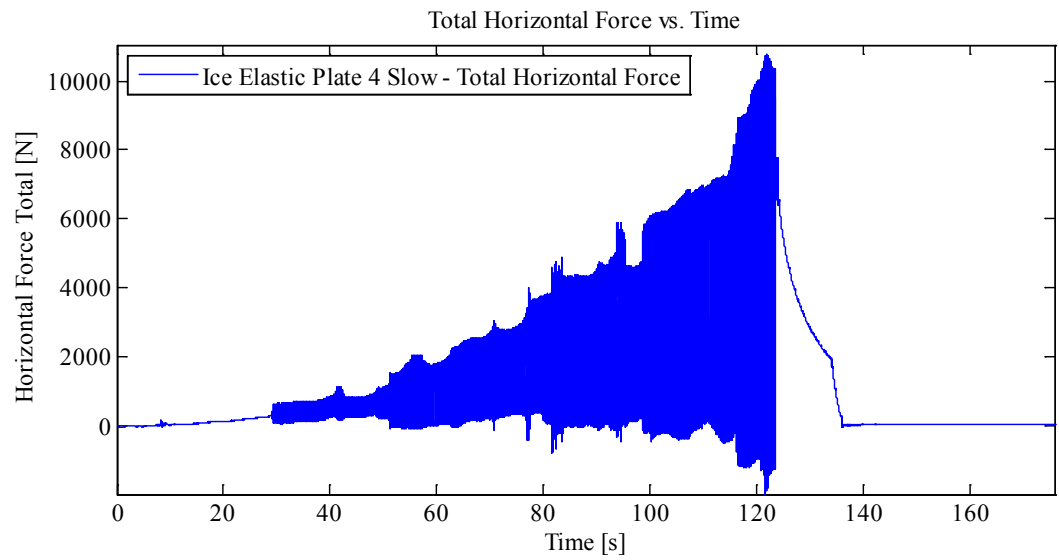


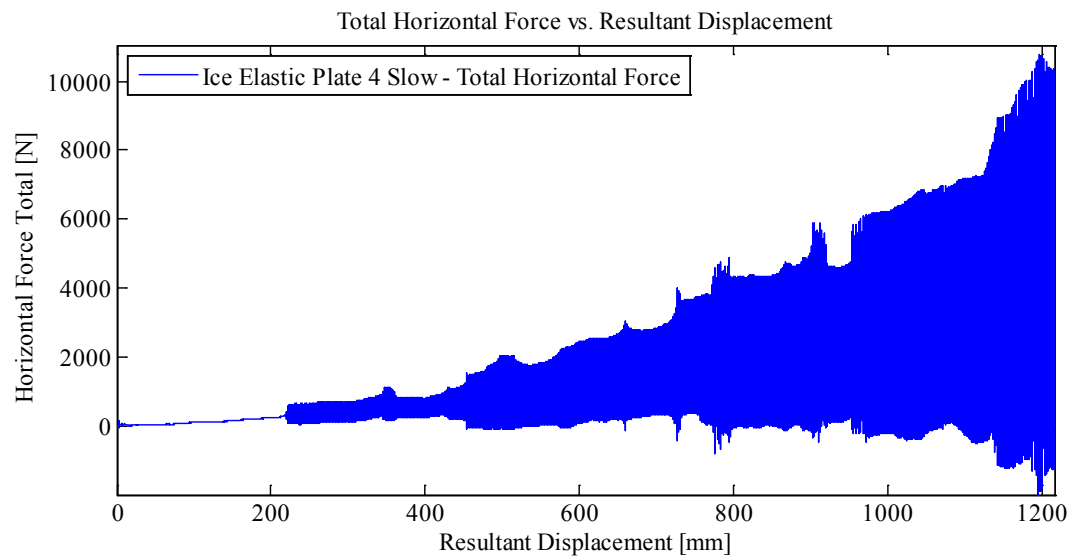
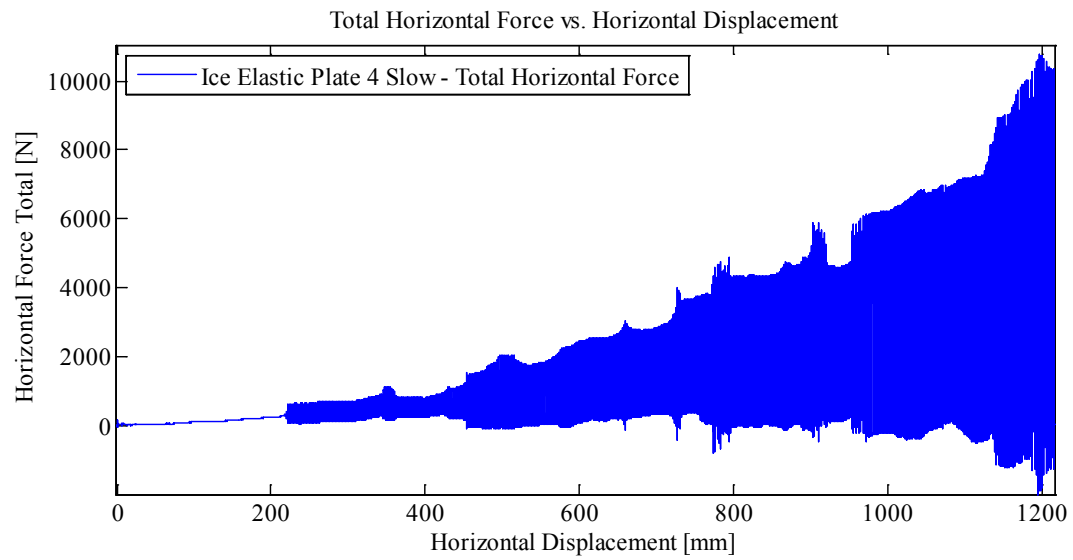


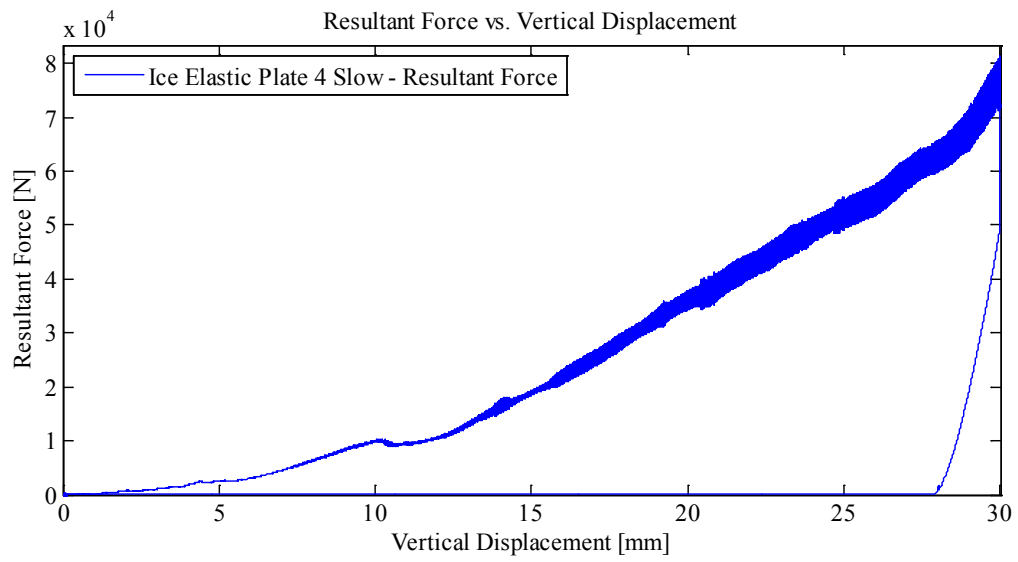
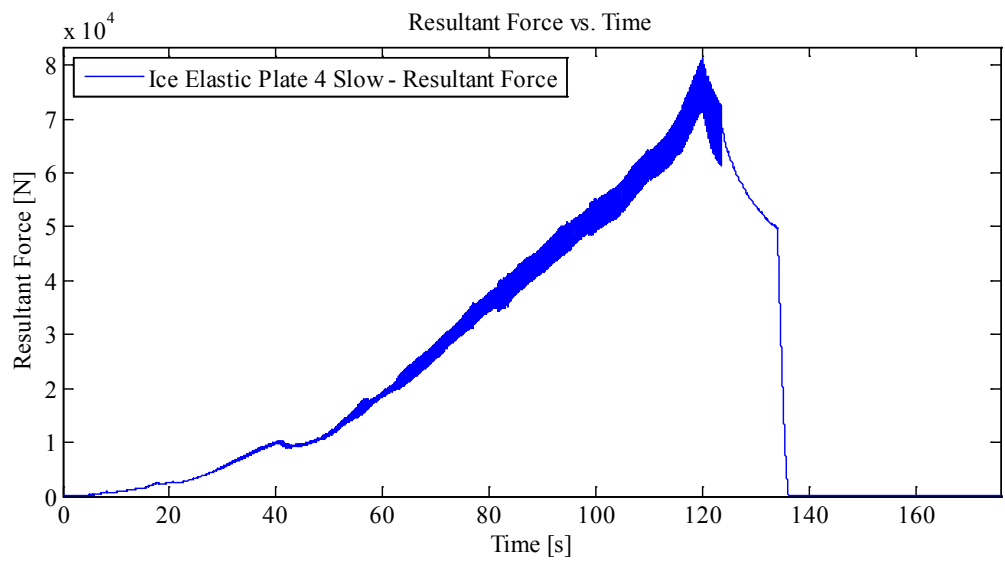


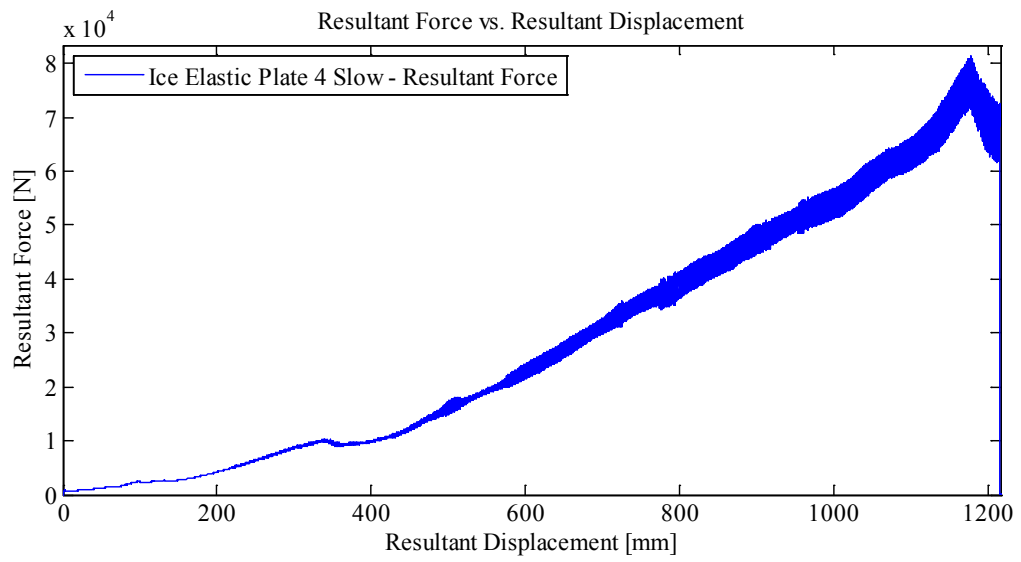
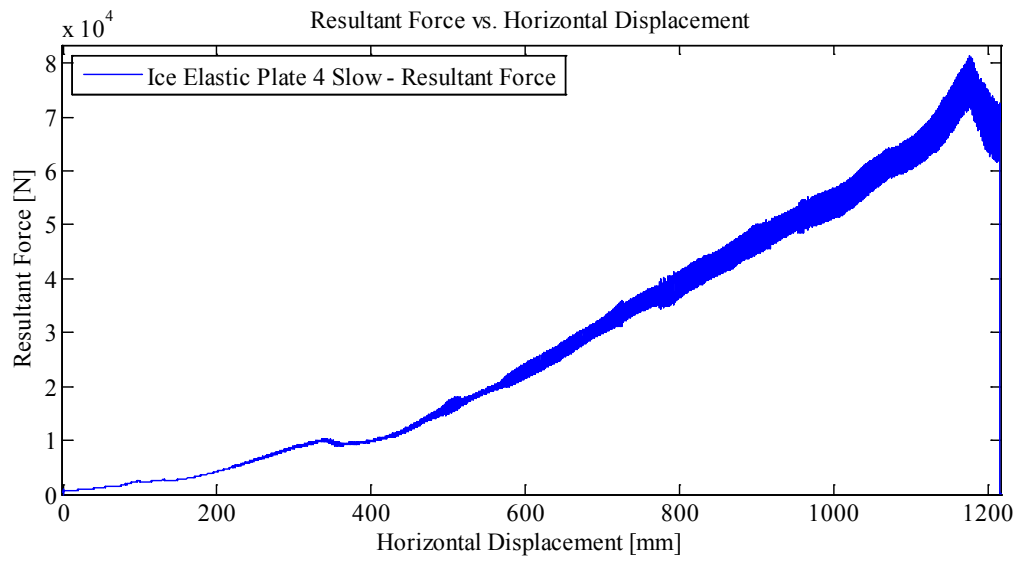


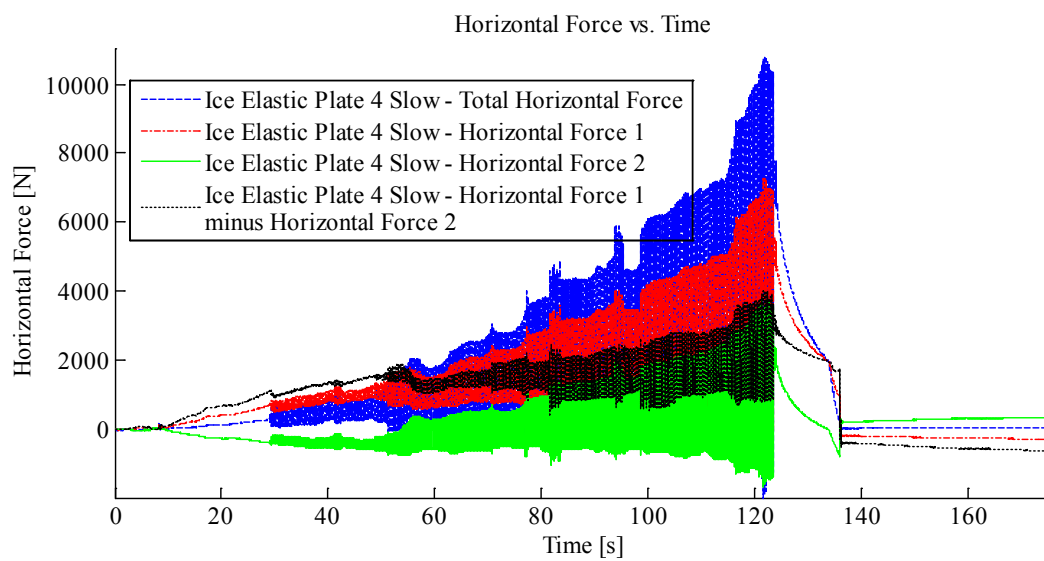
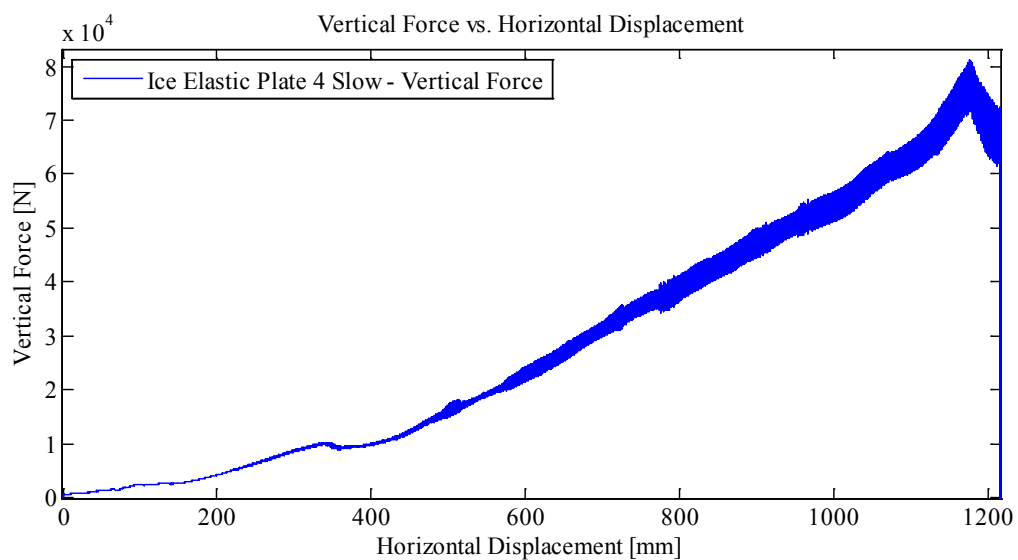












Appendix C3.2.6 – MovingLoad39

May 16, 2014 at ~10:50a.m.

Run # elastic 1/2" sample with ice
Run Type: Ice Cone – Elastic Plate 5
Room-temperature: -10.4°C (Measured with thermocouple)
Sample Type: elastic 1/2" plate (again)
Test Type: In-Along-Out End to End

HStarting Point: End (-61.503 cm (-abs end))
HSpeed: 10mm/s (Nominal)
H Travel: End to End (110+ cm)

Vstarting Point: -0.496 mm
VSpeed: 0.25 mm/s (nominal)
V Travel: 30 mm
V Stopping Point: -30.496 mm

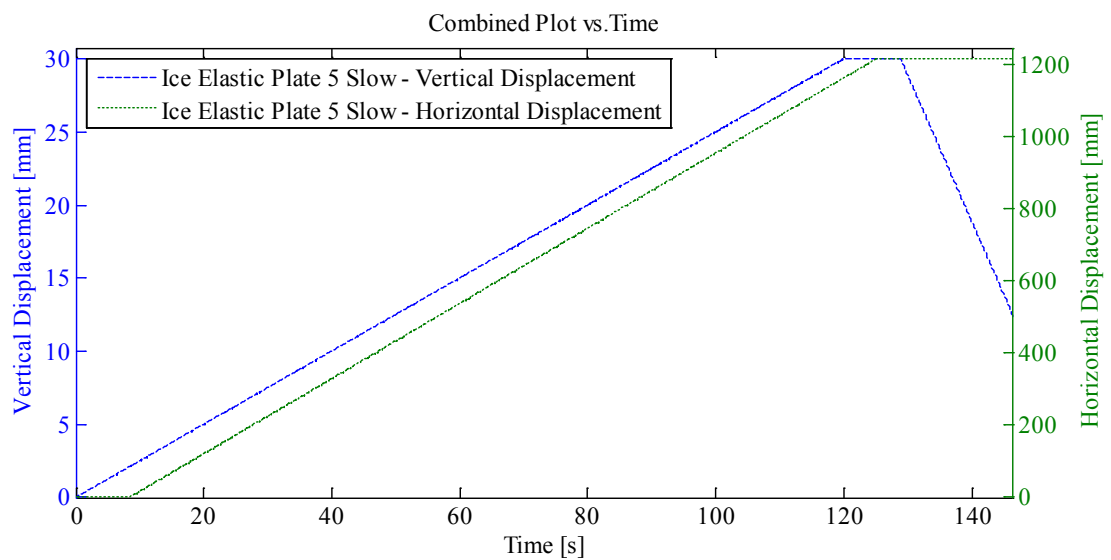
Notes:

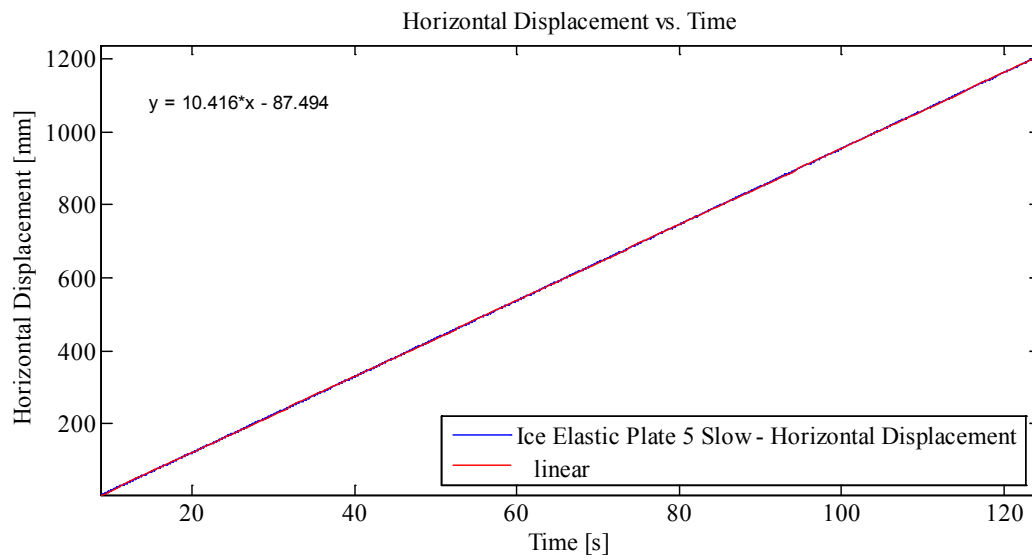
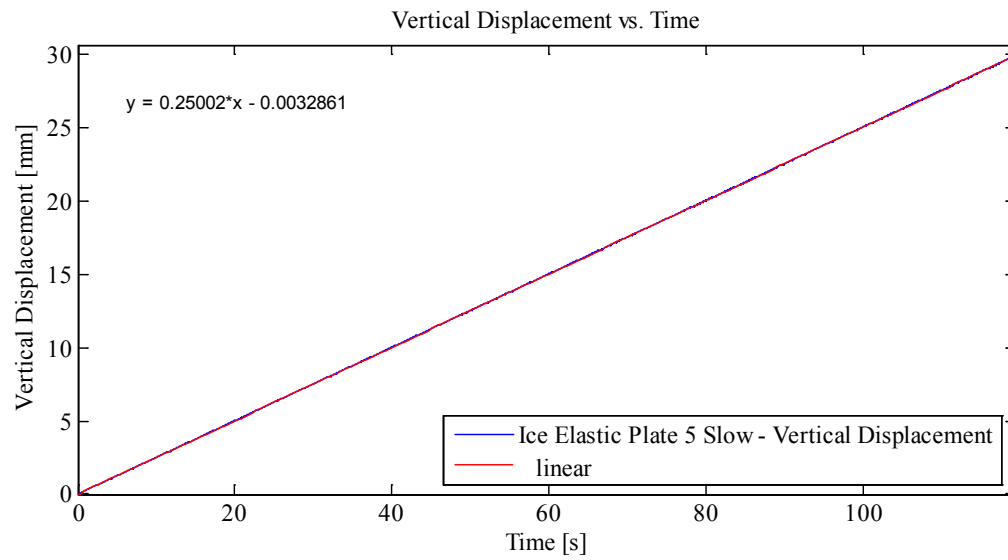
Disp Controlled: In-Along-Out - End to End

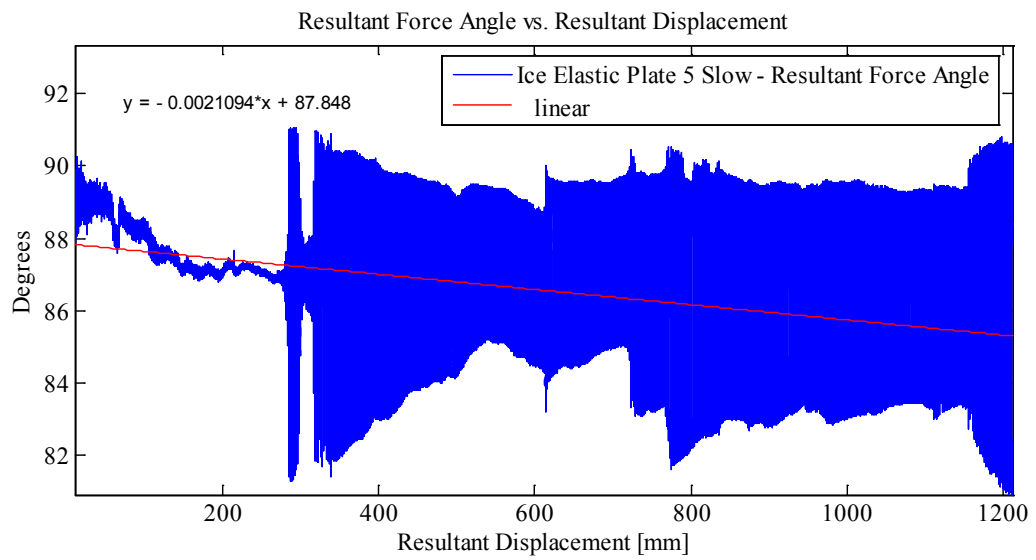
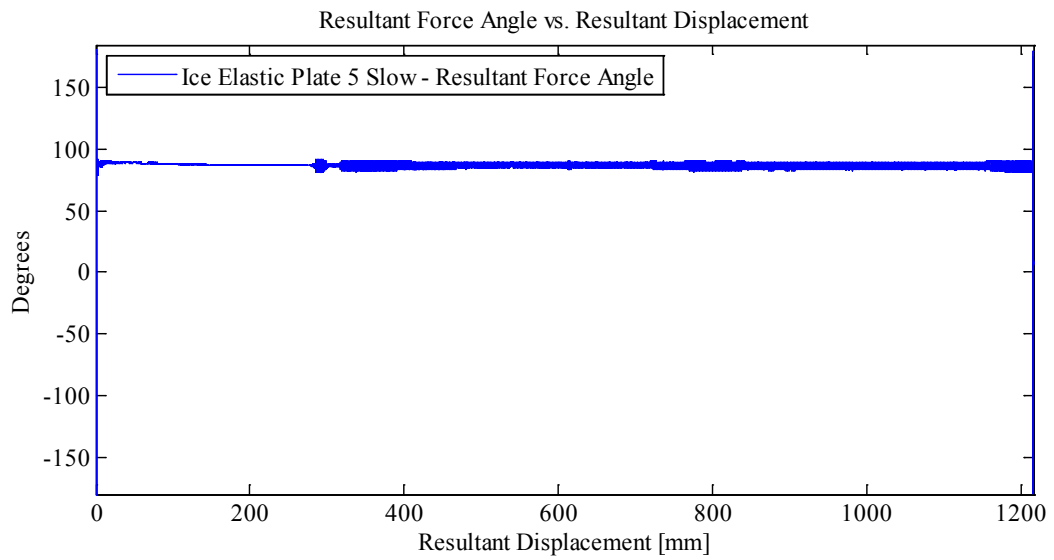
Data from Indentation 1 saved as MovingLoad39

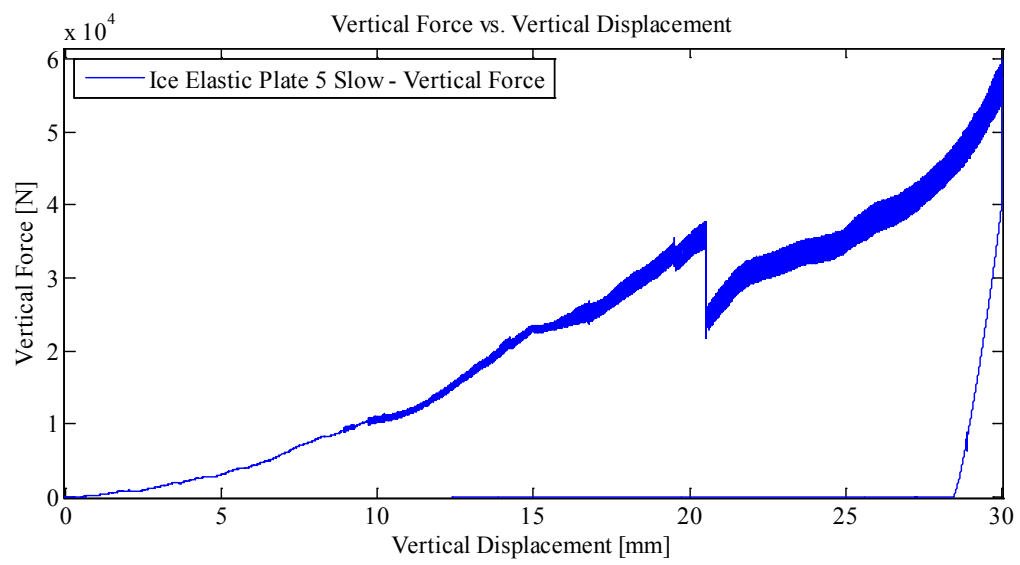
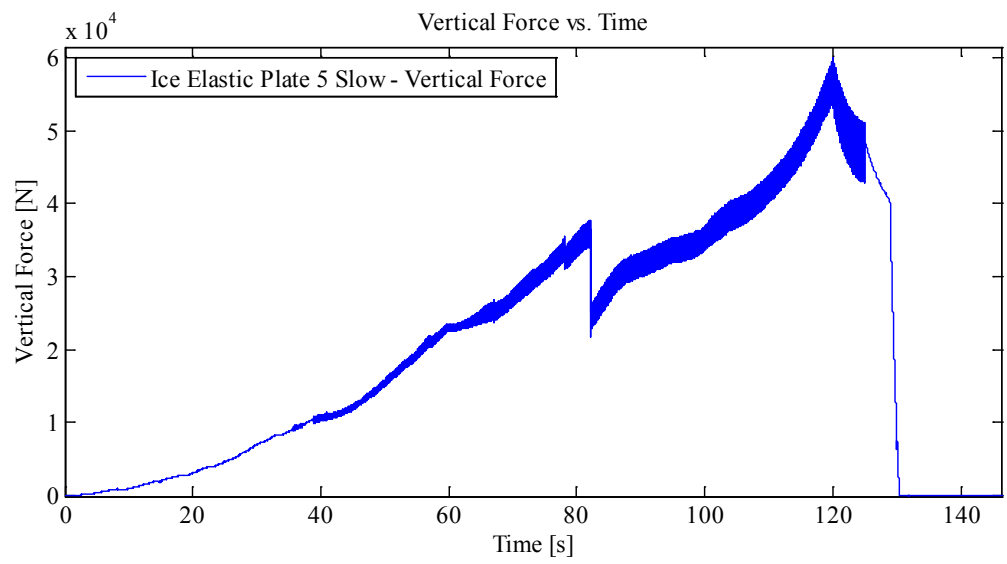
With one Thermal Video Camera and high speed video

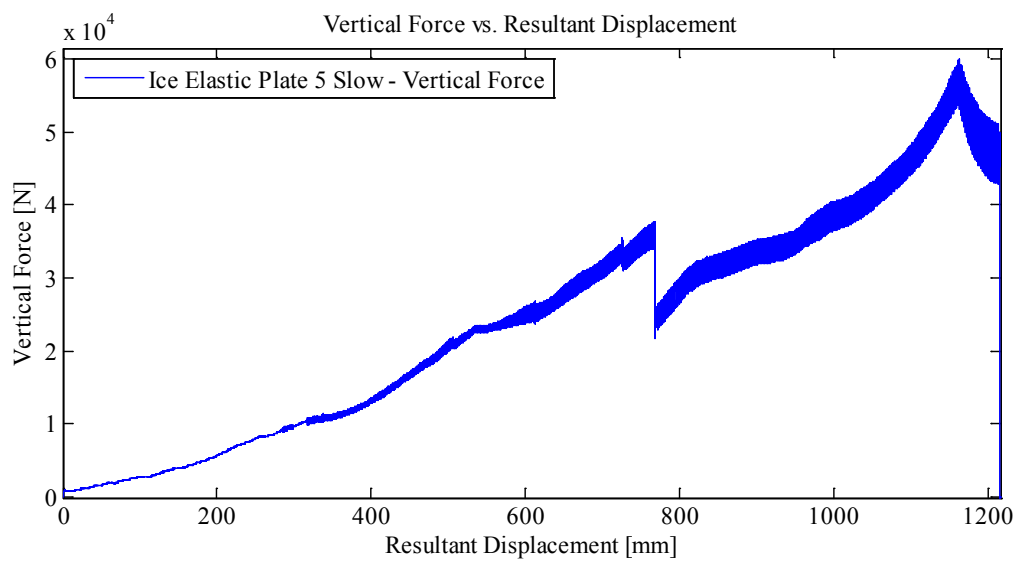
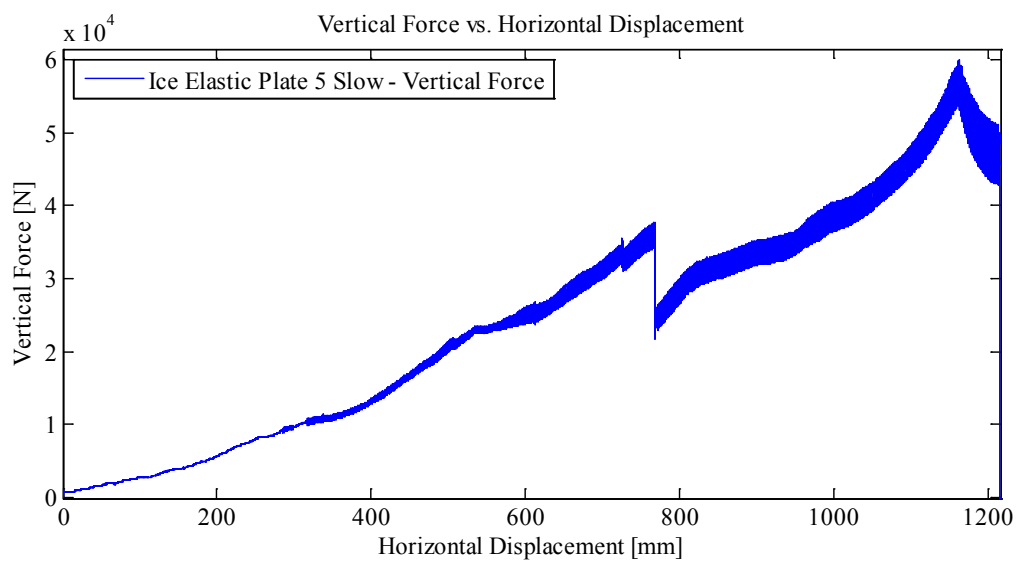
Plots:

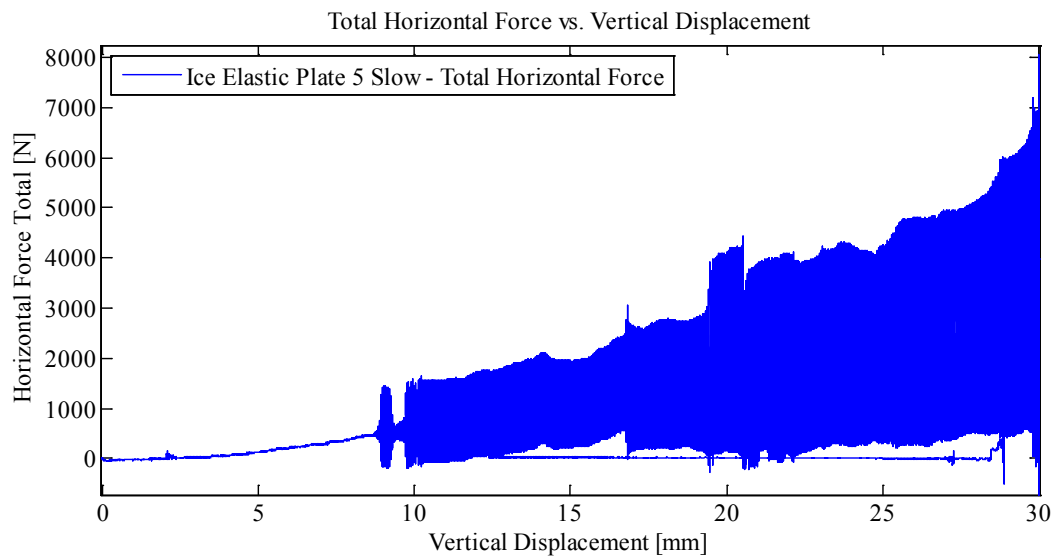
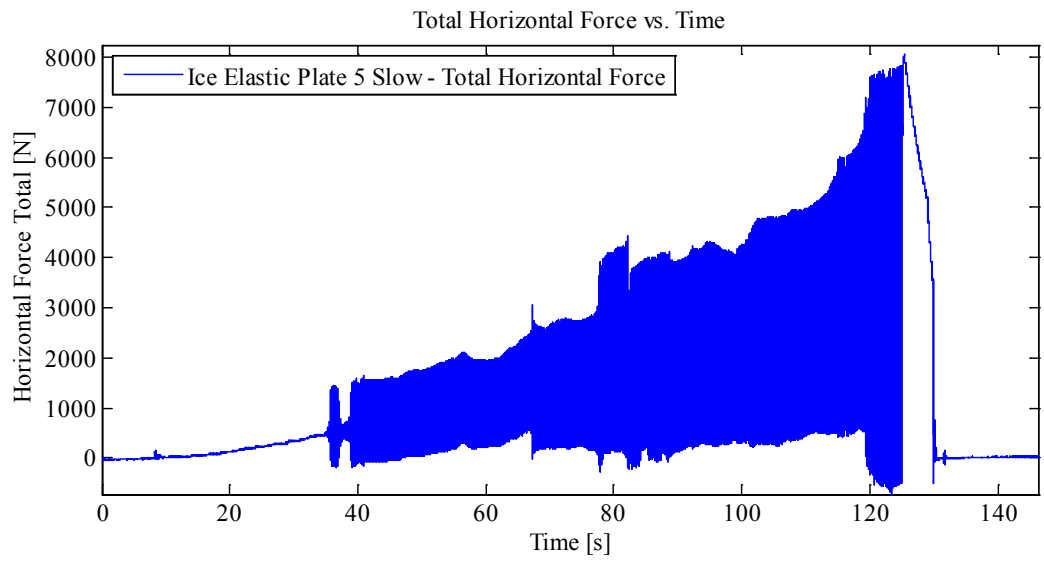


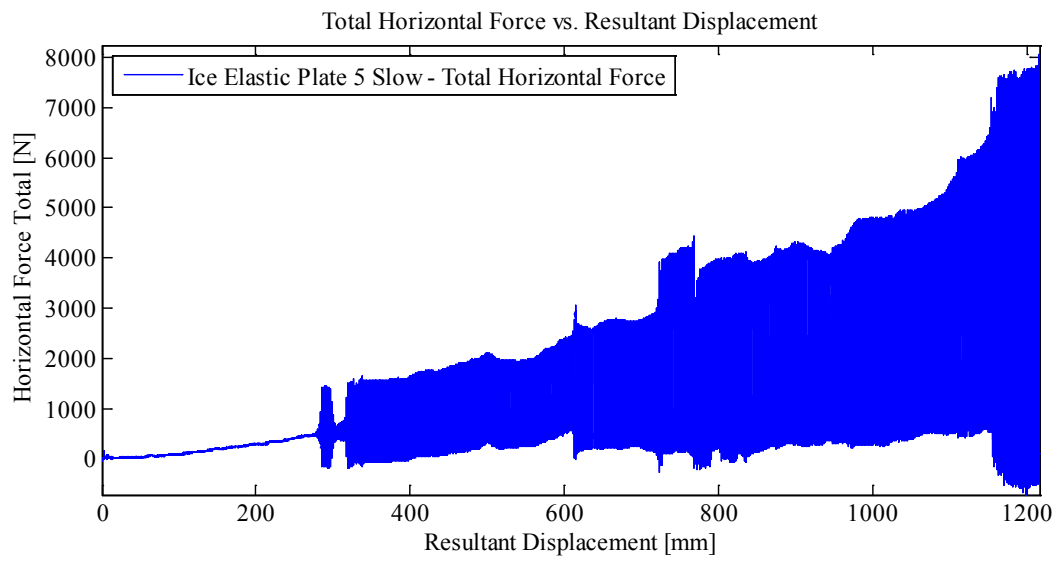
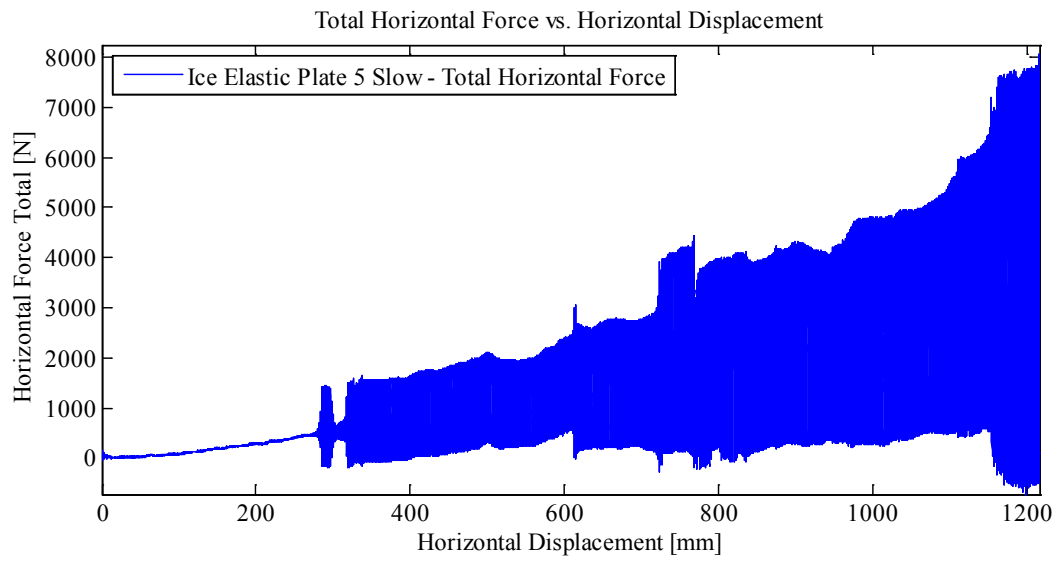


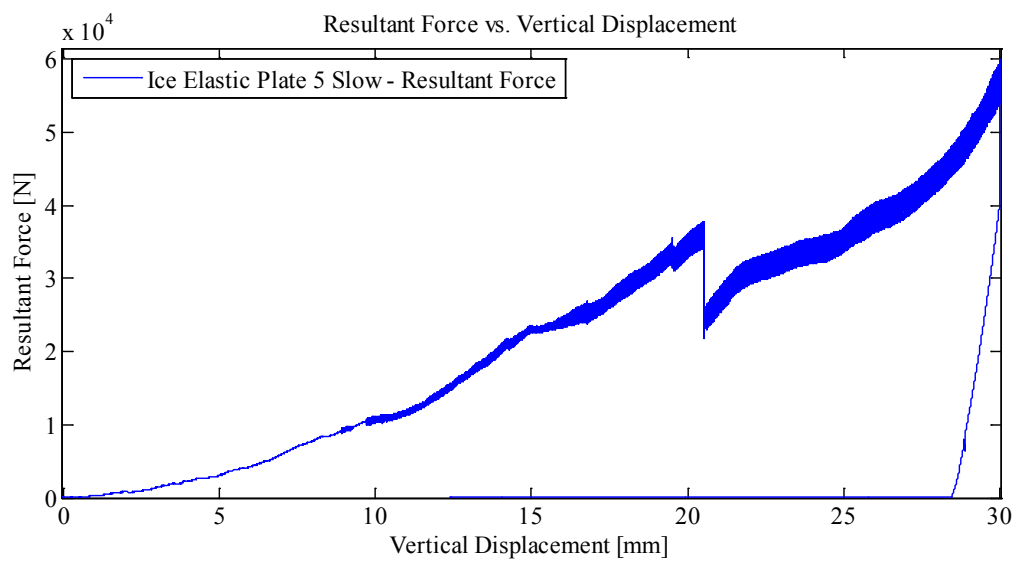
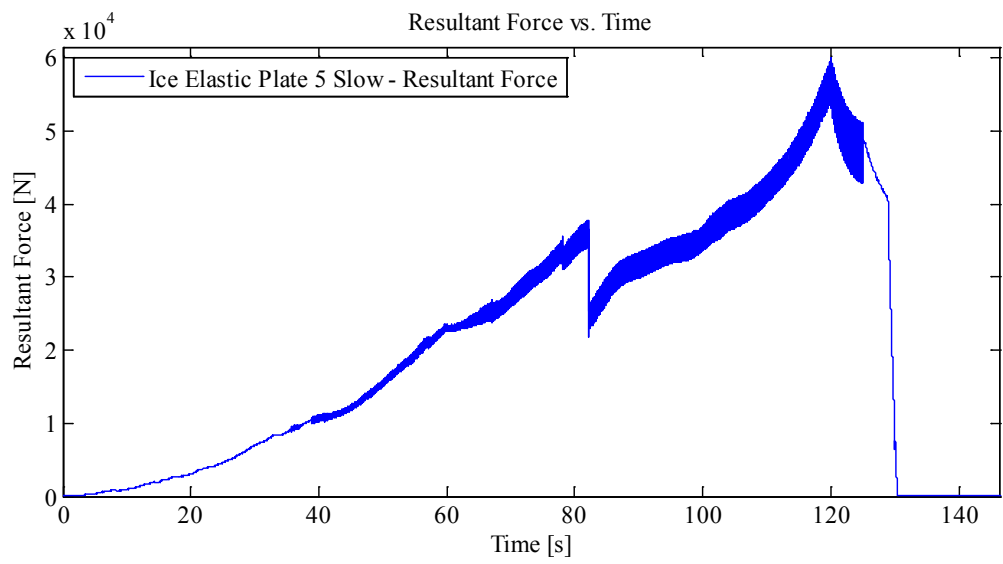


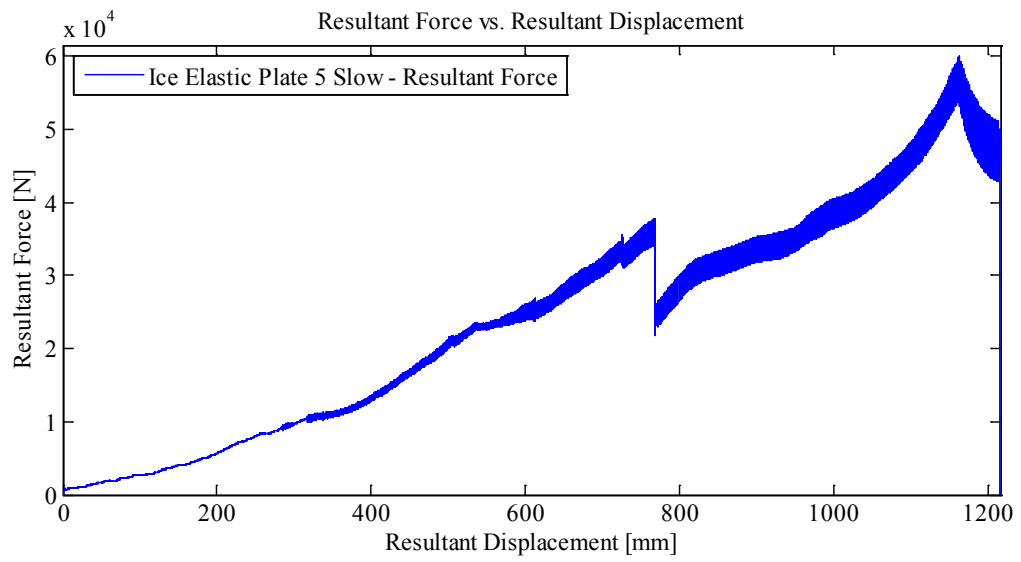
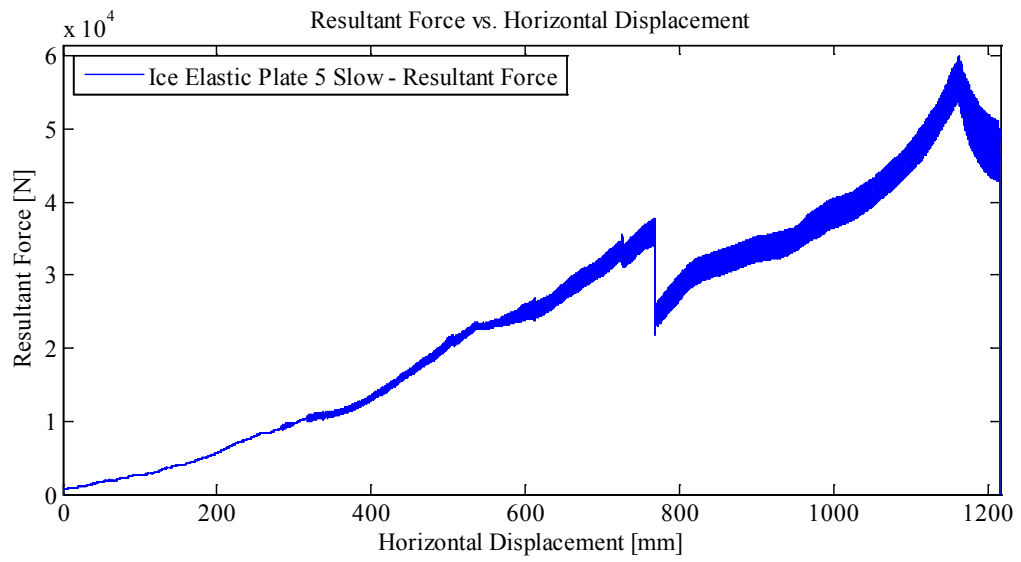


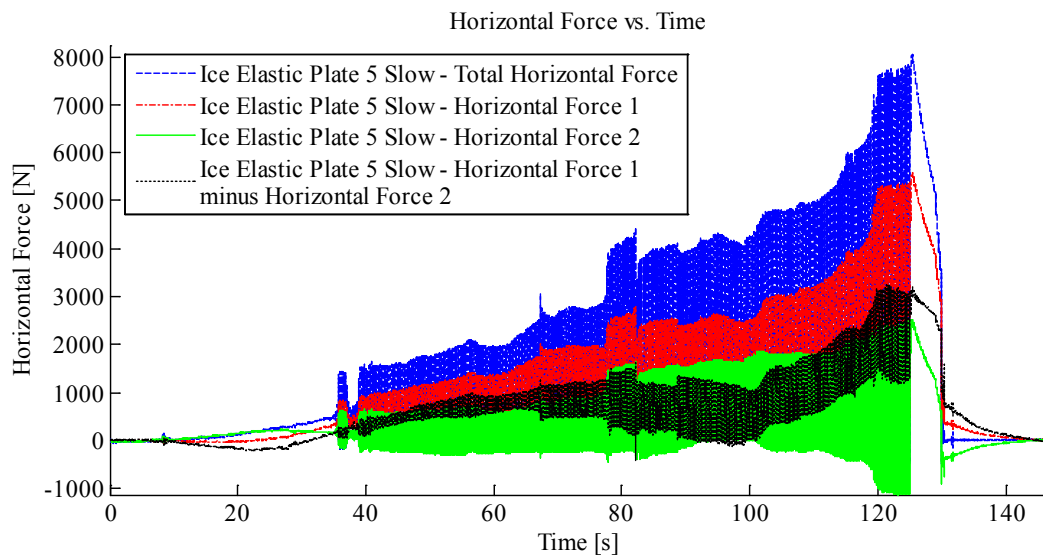
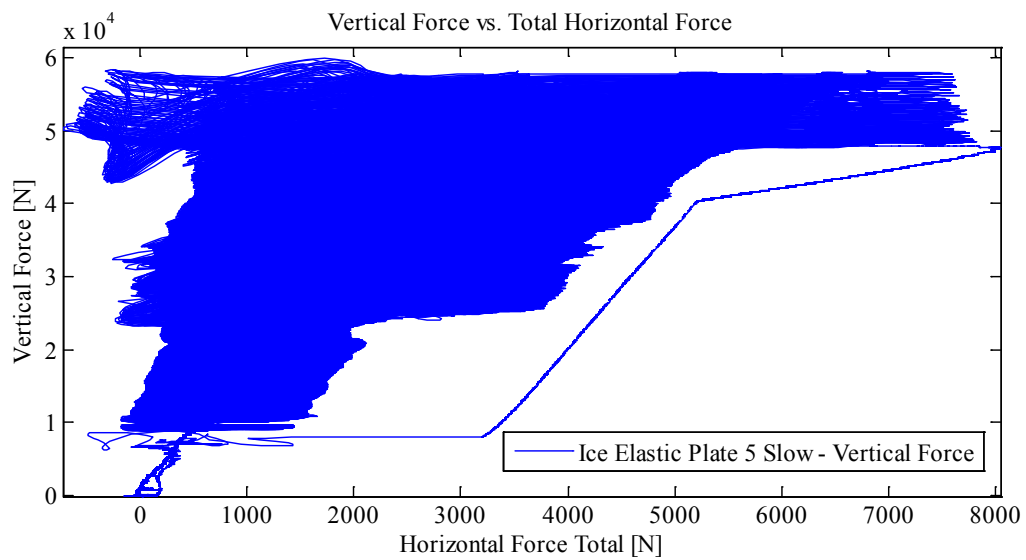








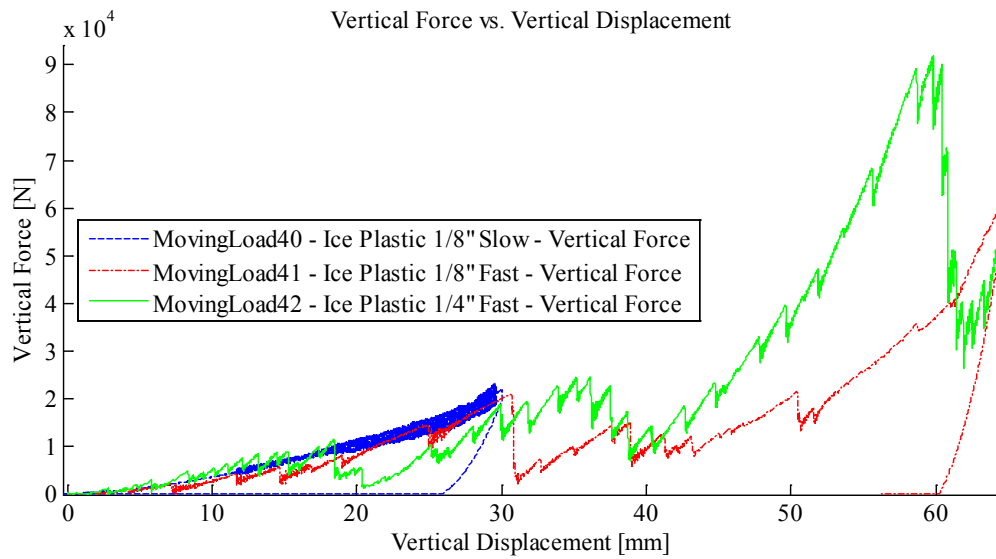
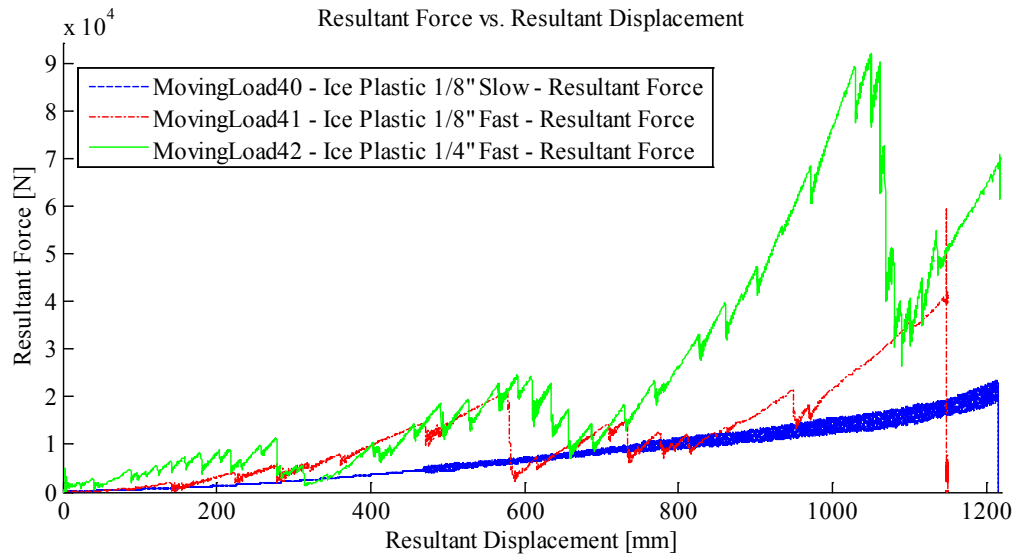


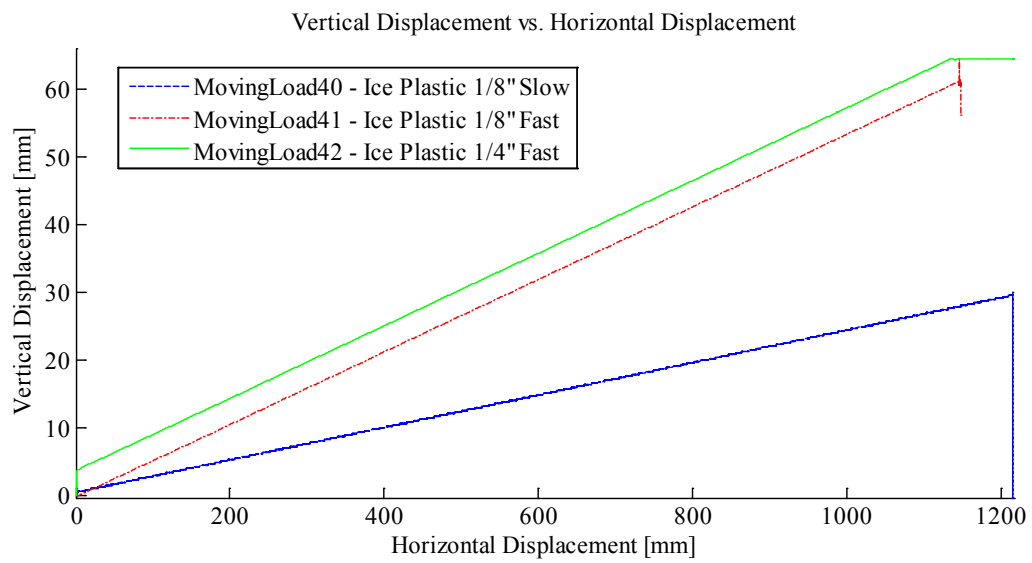
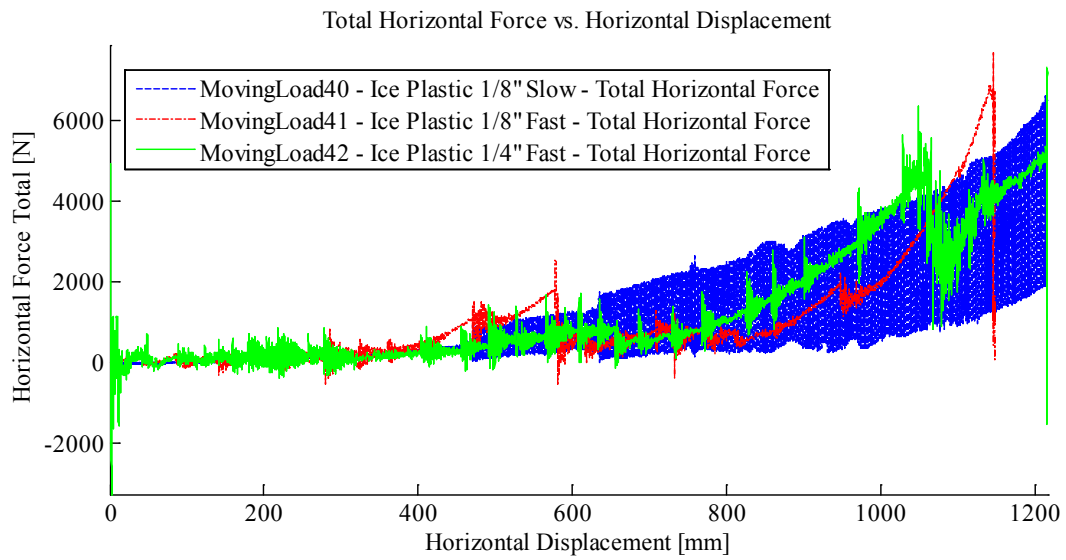


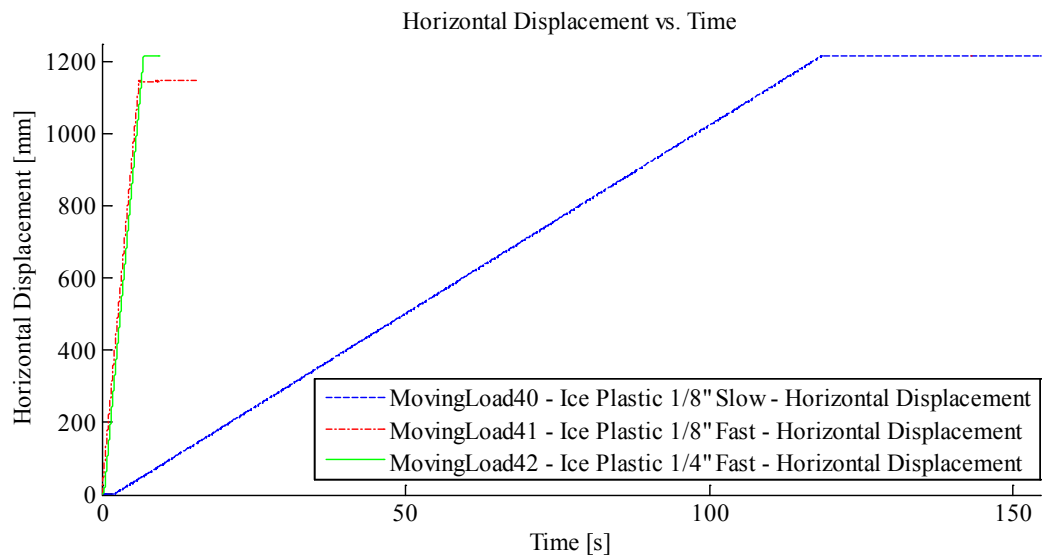
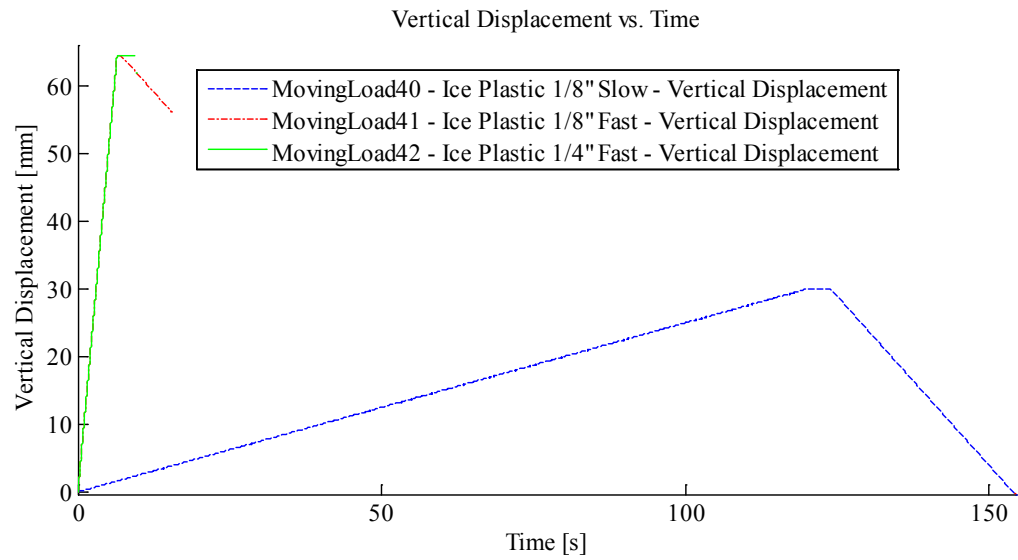
Appendix C3.3 – Ice Cone Tests Inducing Plastic Plate Deformation

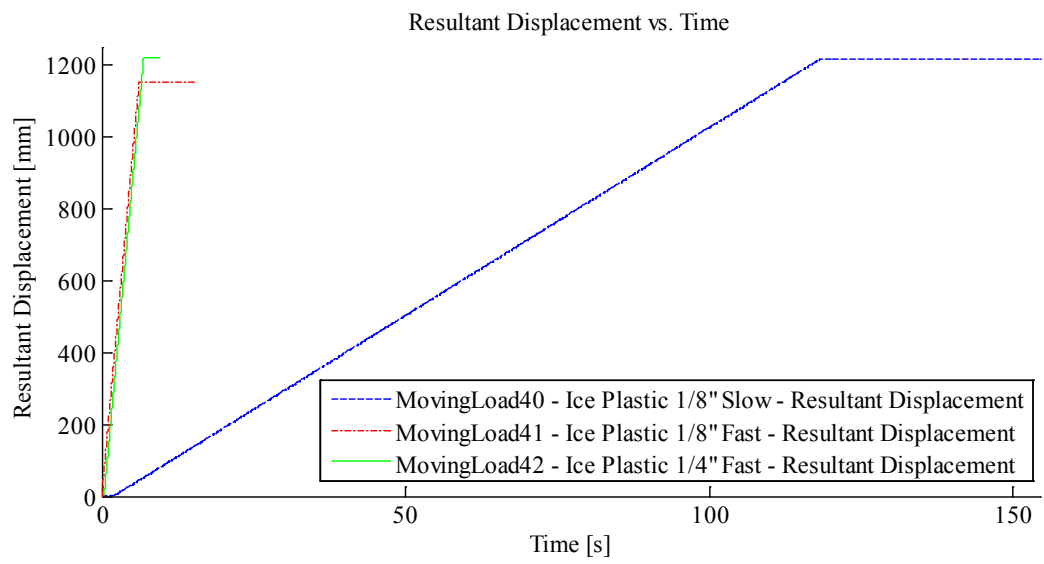
Appendix C3.3.1 – Summary Plots for Experiments ML 40, 41 and

42









Appendix C3.3.2 – MovingLoad40

May 16, 2014 at ~2:45p.m.

Run # 1/8" plate with ice (no keystack)
Run Type: Ice Cone – Slow – Plastic Plate 1
Room-temperature: -9.1°C (Measured with thermocouple)
Sample Type: 1/8" plate
Test Type: In-Along-Out End to End

HStarting Point: End (-61.503 cm (-abs end))
HSpeed: 10mm/s (Nominal)
H Travel: End to End (110+ cm)

Vstarting Point: -11.92 mm
VSpeed: 0.25 mm/s (nominal)
V Travel: 30 mm
V Stopping Point: -41.9 mm

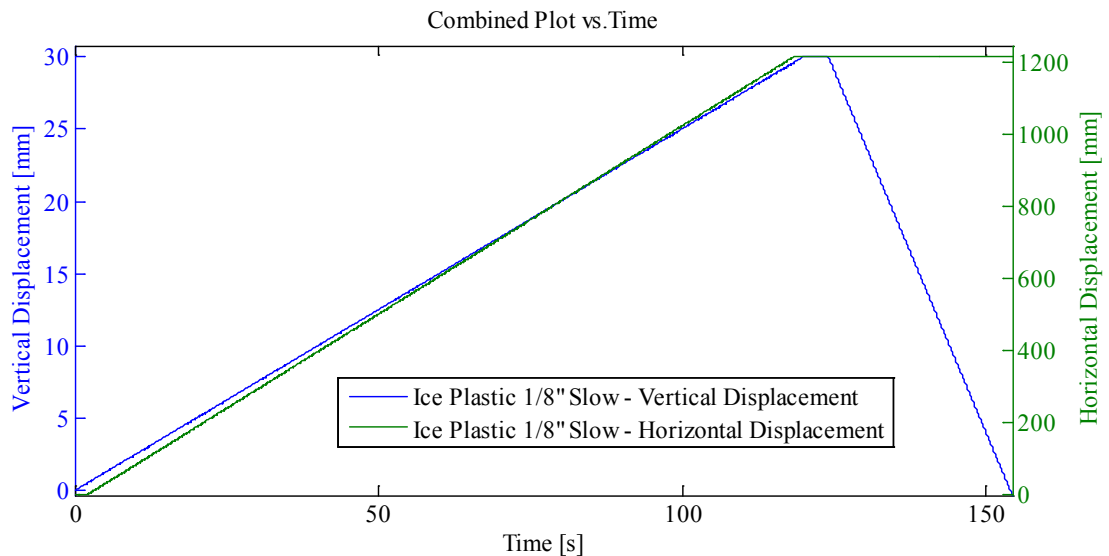
Notes:

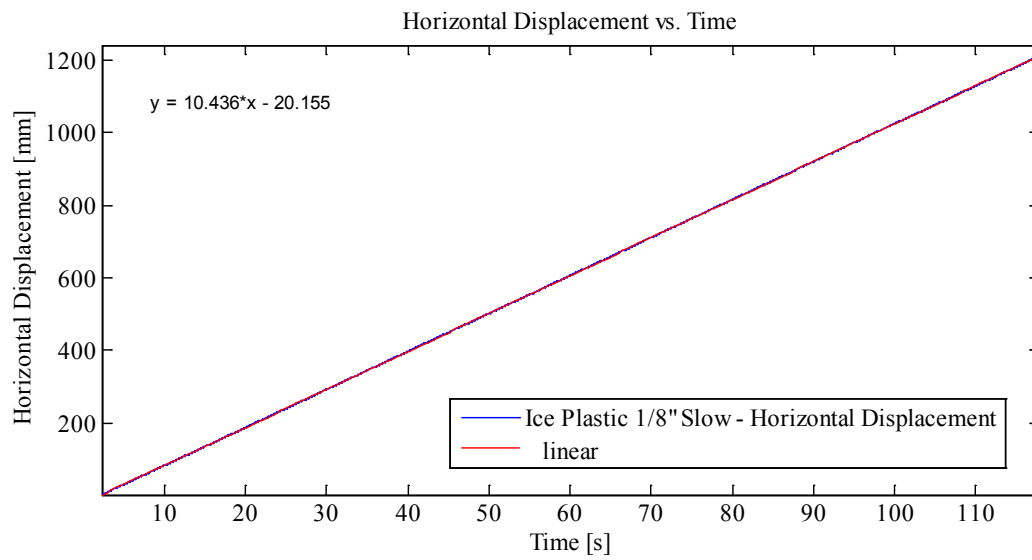
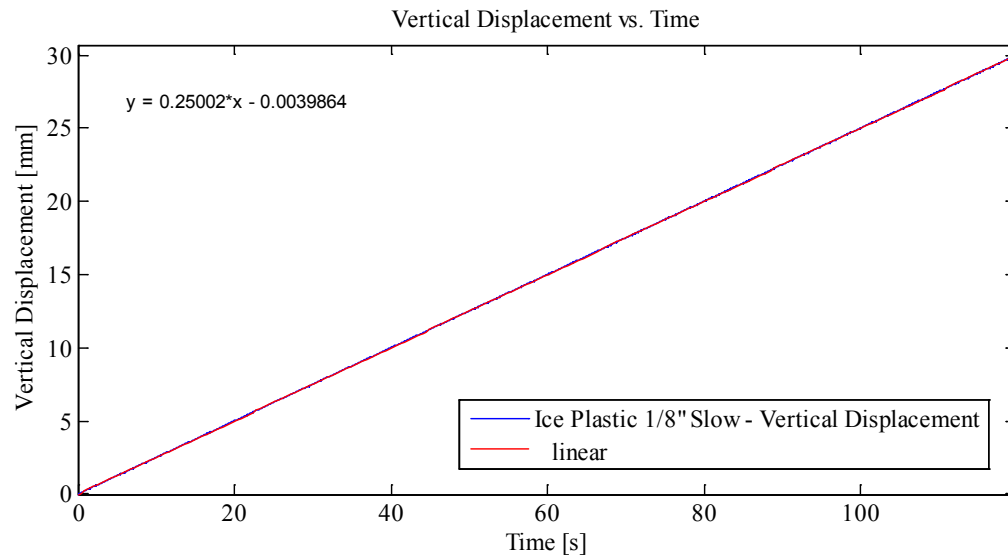
Disp Controlled: In-Along-Out - End to End

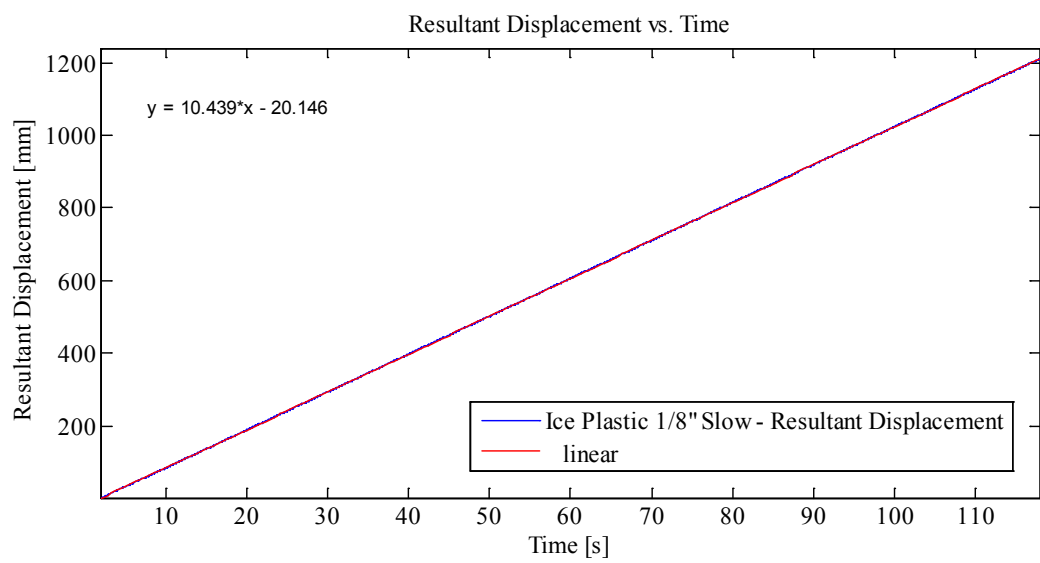
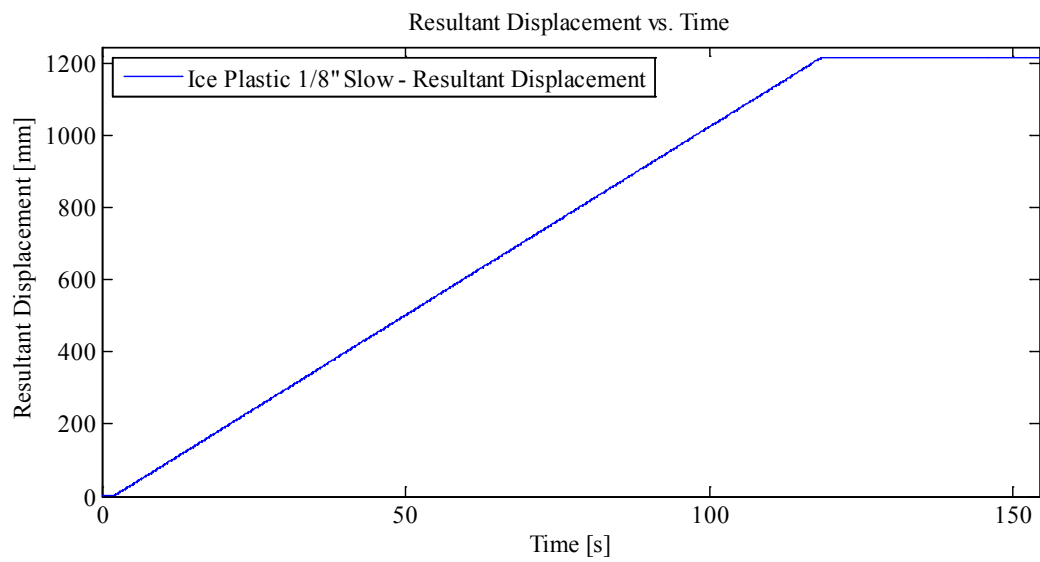
Data from Indentation 1 saved as MovingLoad40

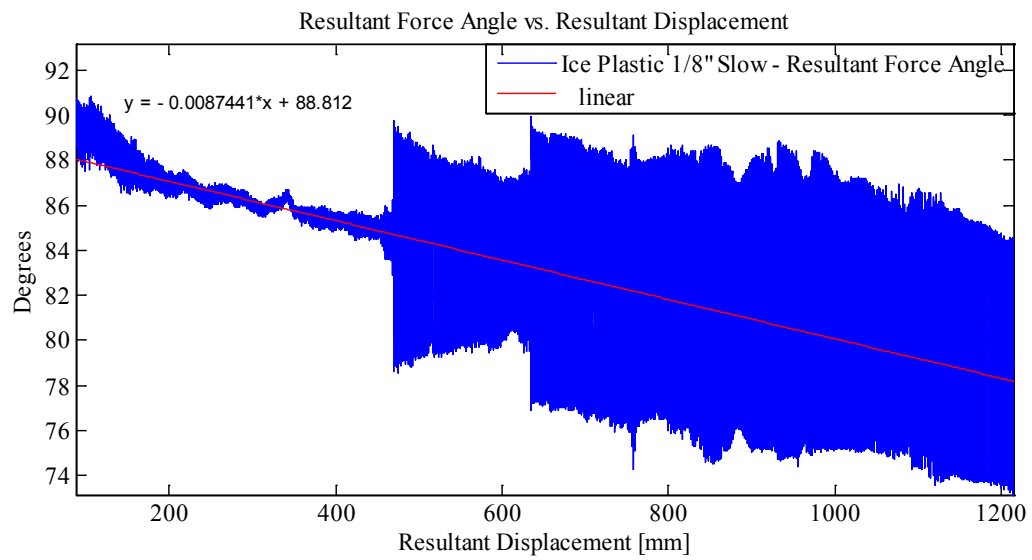
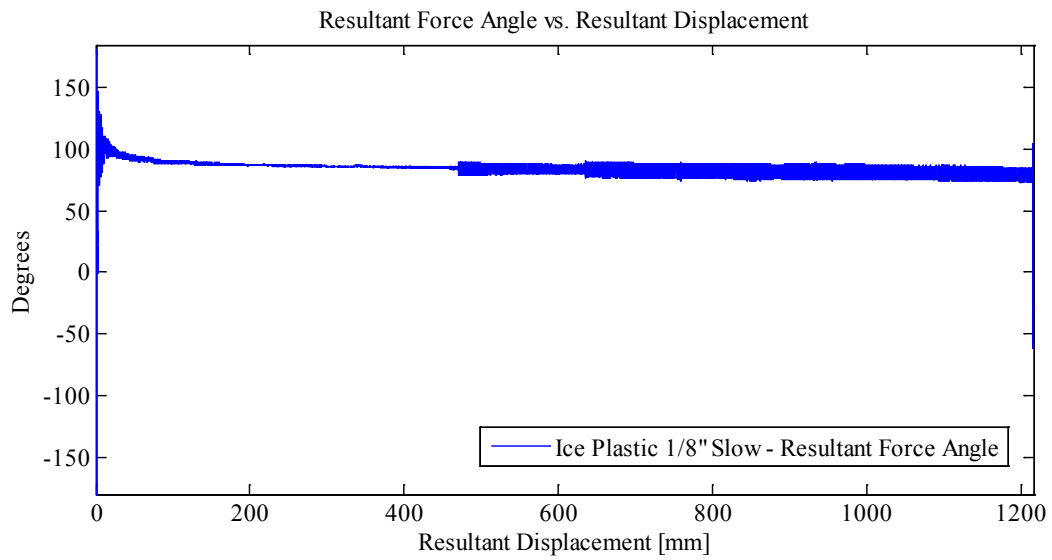
With one internal Thermal Video Camera and external high speed video

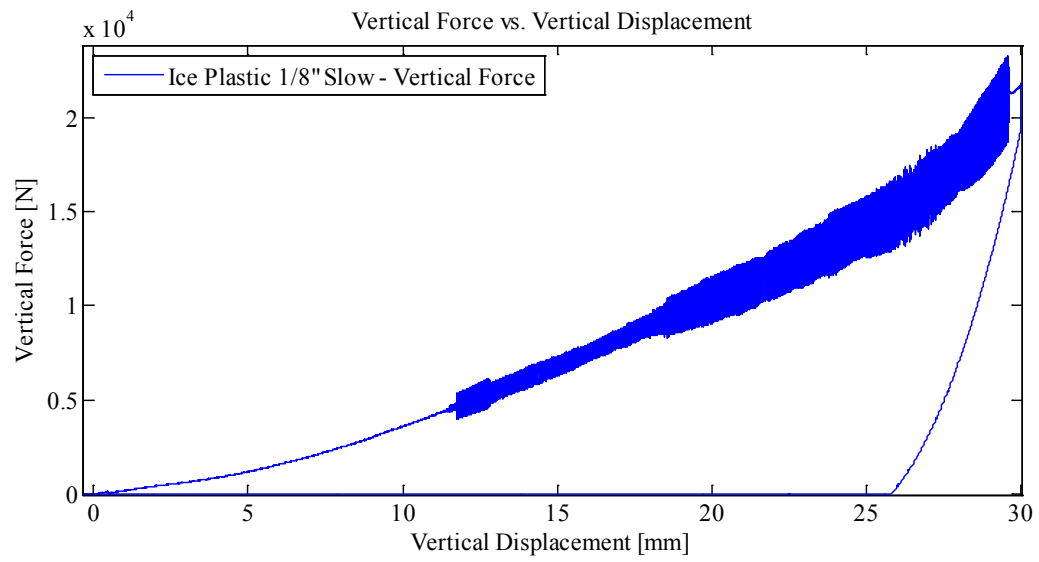
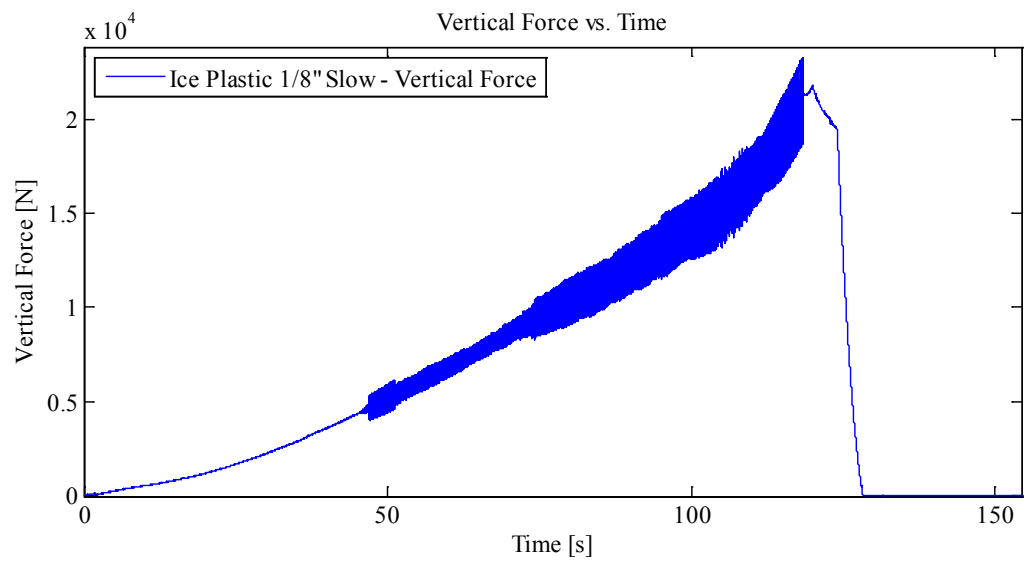
Plots:

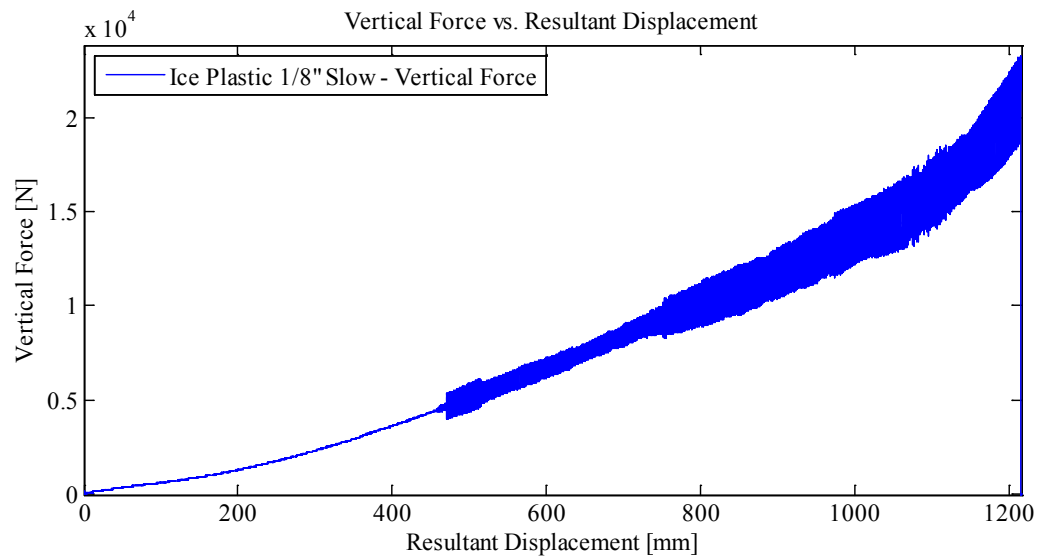
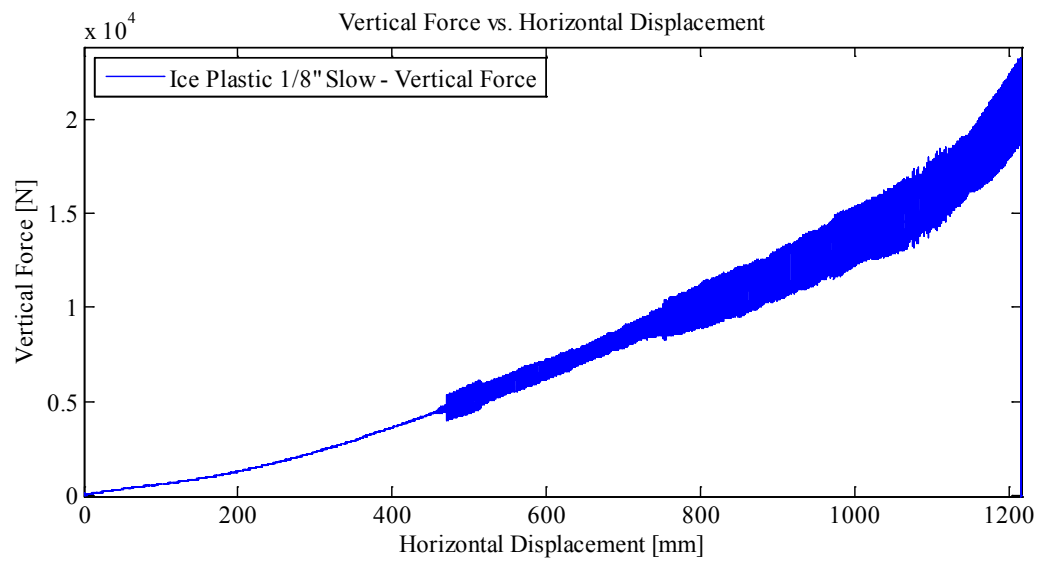


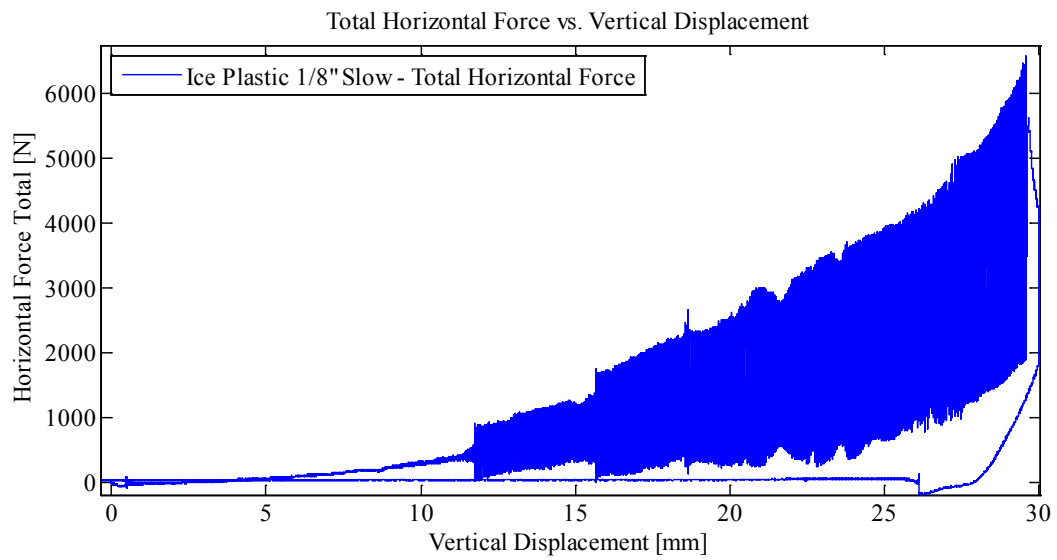
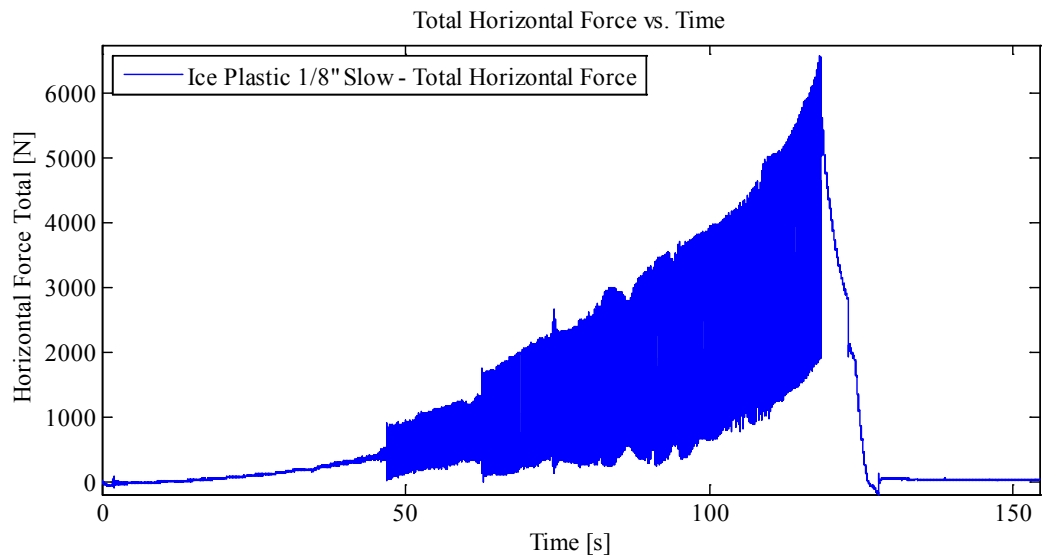


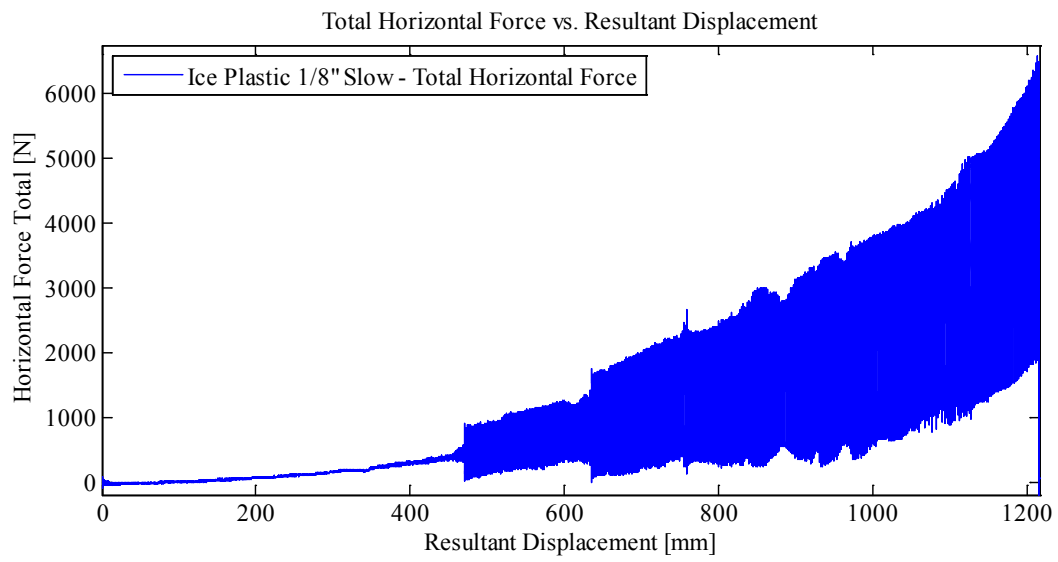
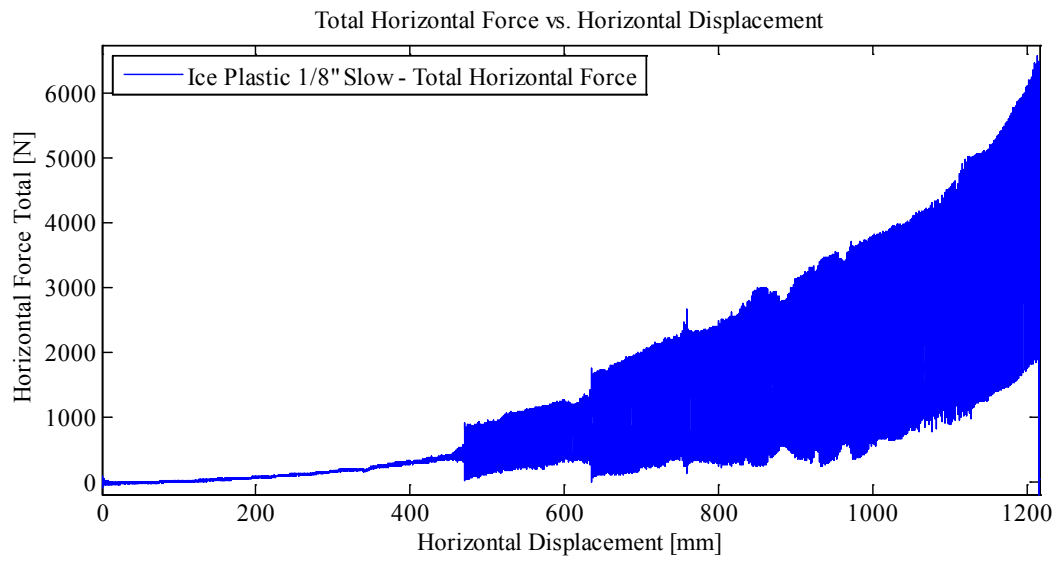


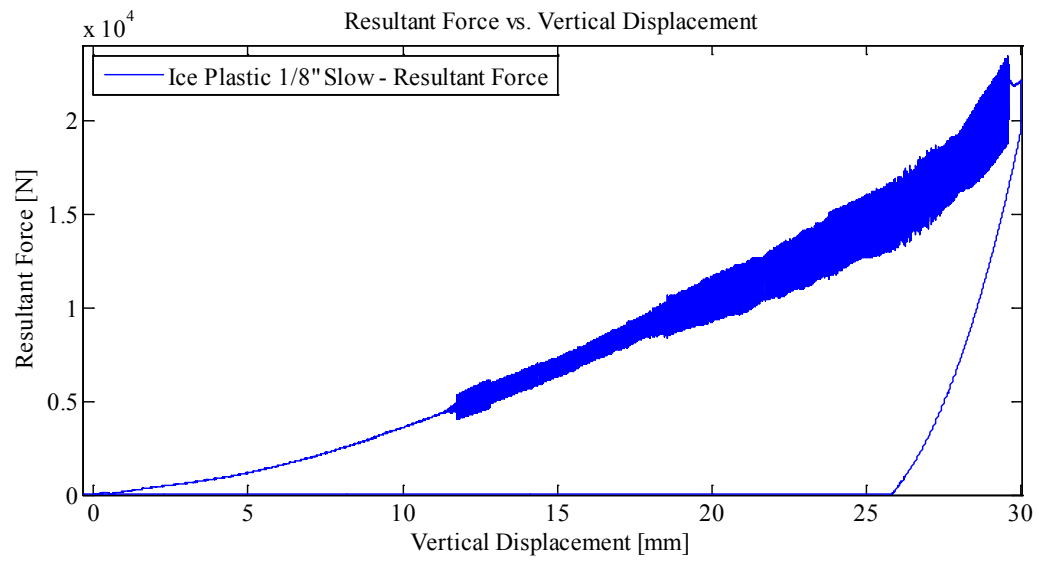
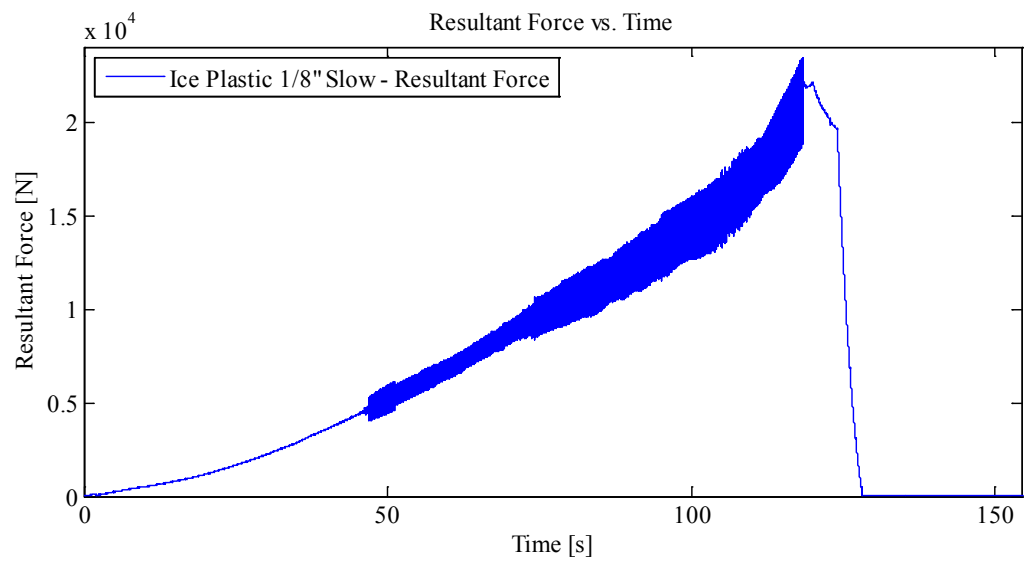


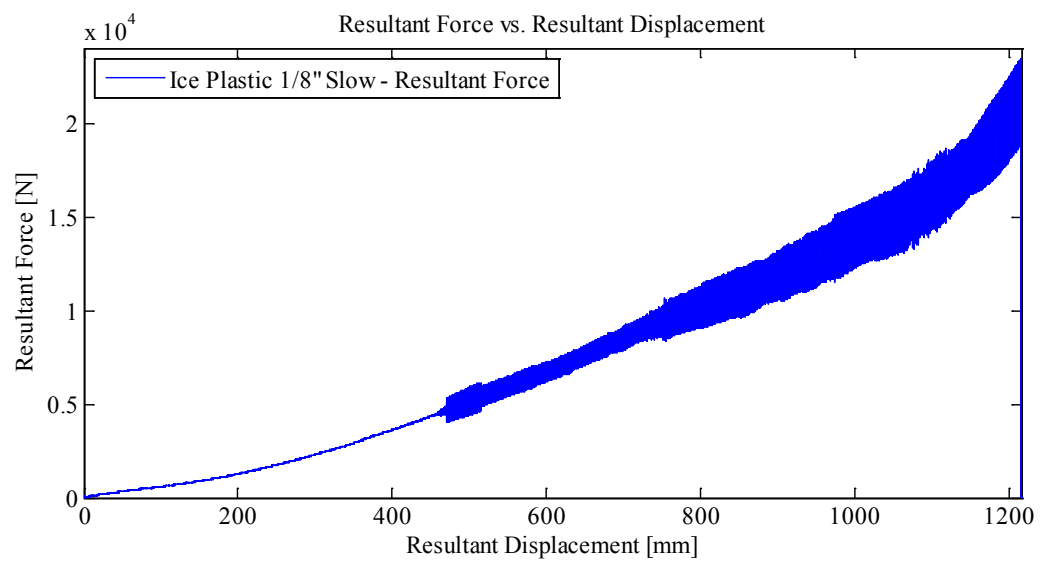
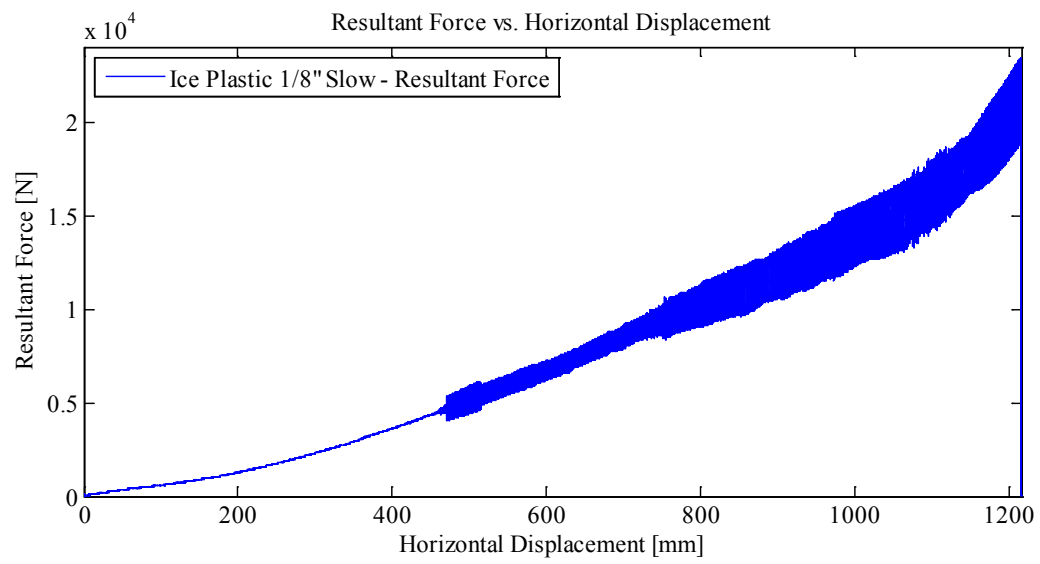


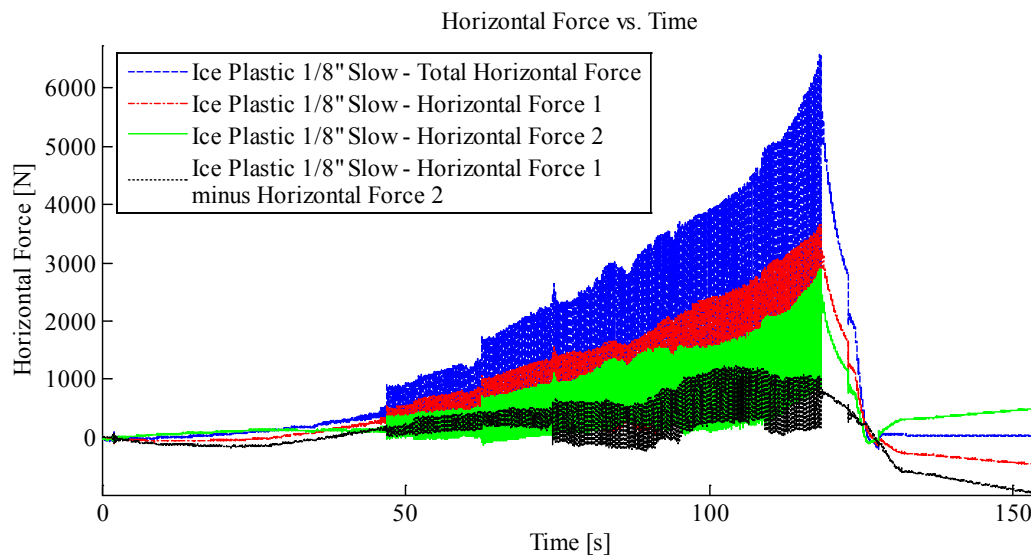
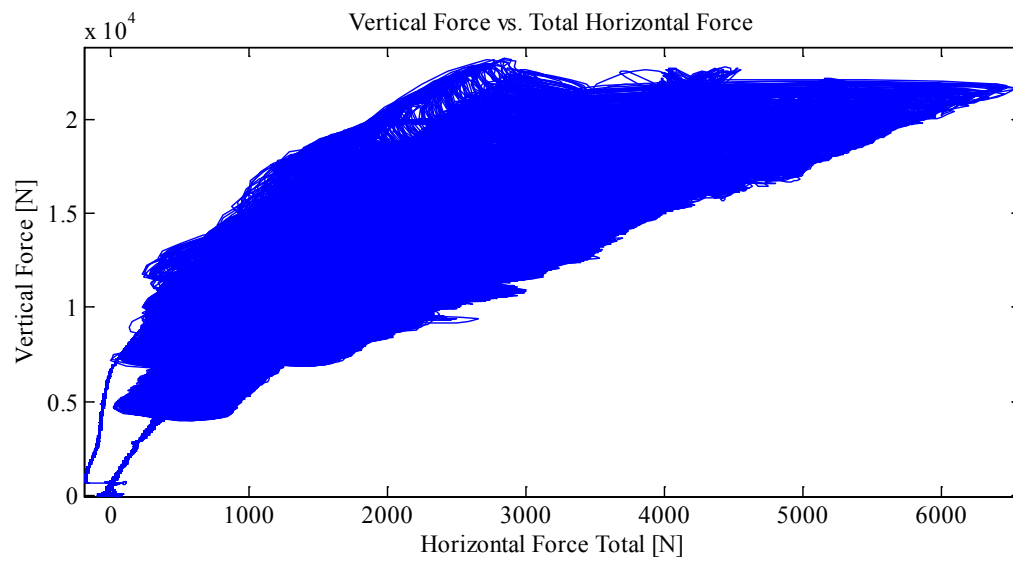












Appendix C3.3.3 – MovingLoad41

May 20, 2014 at ~12:00p.m.

Run # 1/8" plate with ice (no keystack)
Run Type: Ice Cone – Plastic Plate 2
Room-temperature: -9.3°C (Measured with thermocouple)
Sample Type: 1/8" plate
Test Type: In-Along-Out End to End

HStarting Point: End (-61.503 cm (-abs end))
HSpeed: Fastest
H Travel: Abs End to Abs End (110+ cm)

Vstarting Point: -11.621 mm
VSpeed: 10 mm/s
V Travel: 64.383 mm
V Stopping Point: -76.0 mm

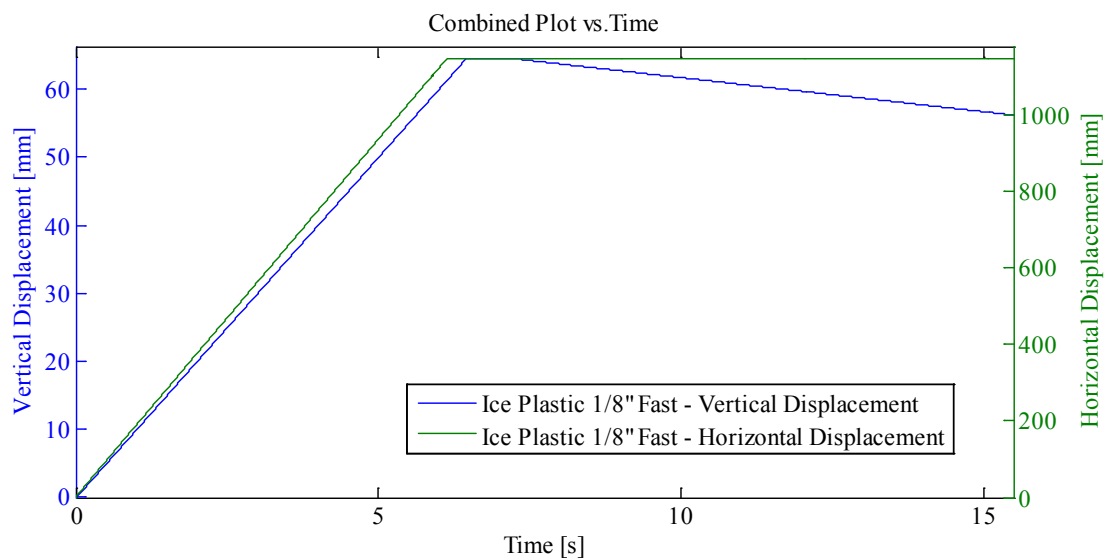
Notes:

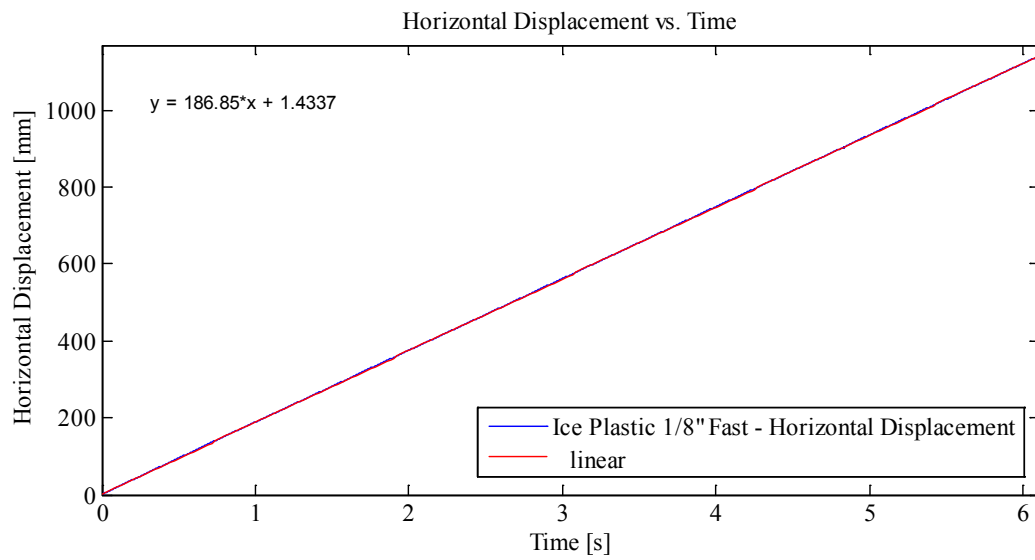
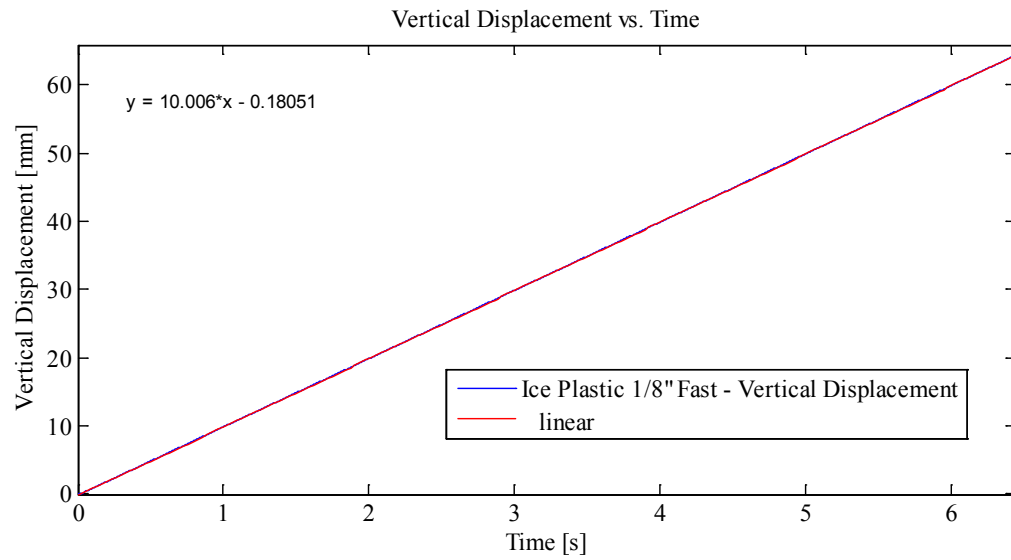
Disp Controlled: In-Along-Out - End to End

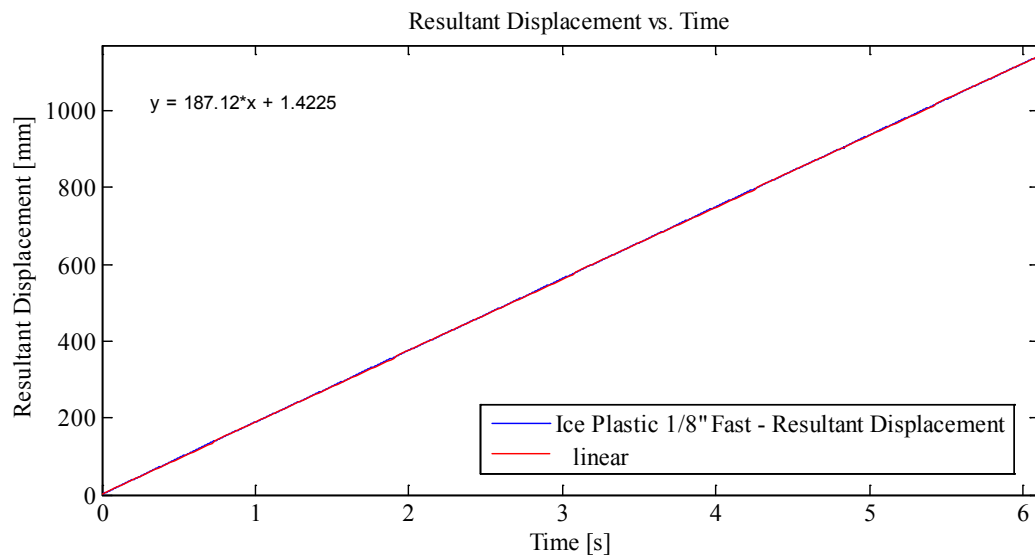
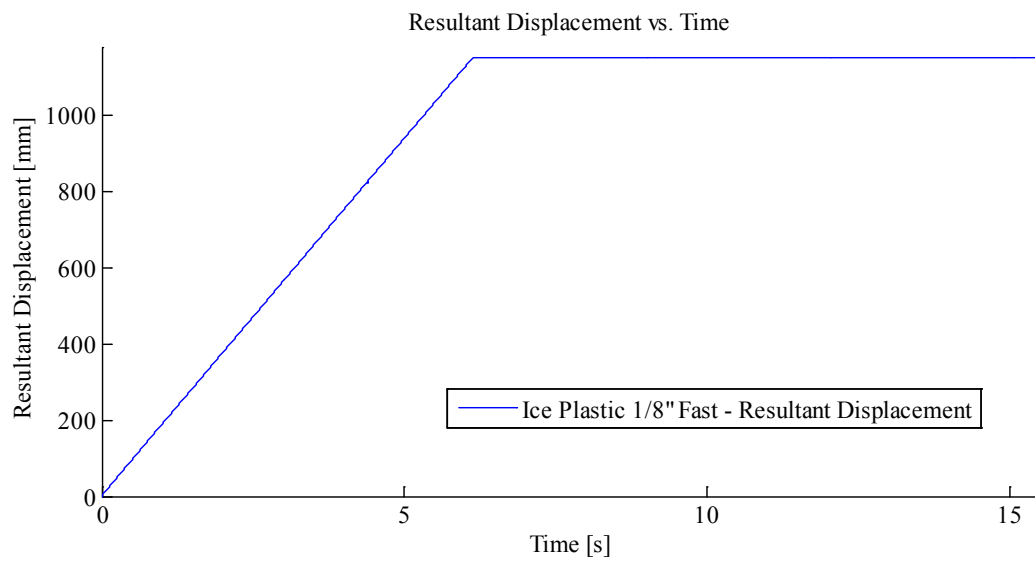
Data from Indentation 1 saved as MovingLoad41

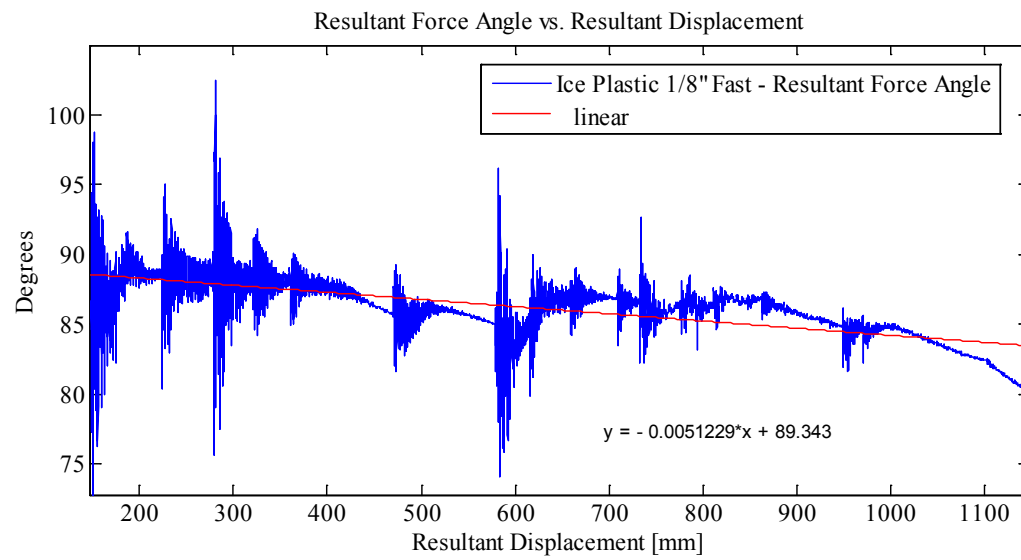
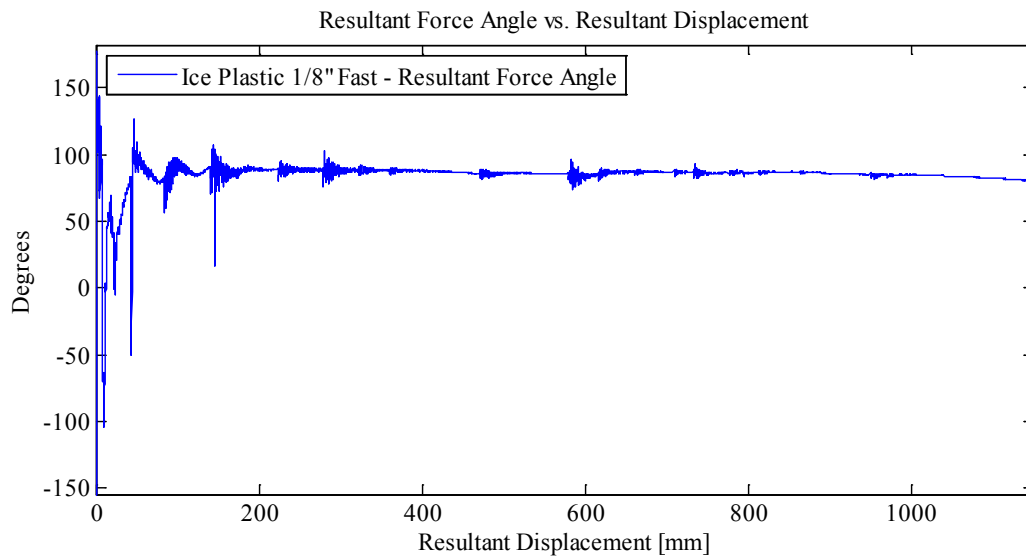
With one internal Thermal Video Camera and external high speed video

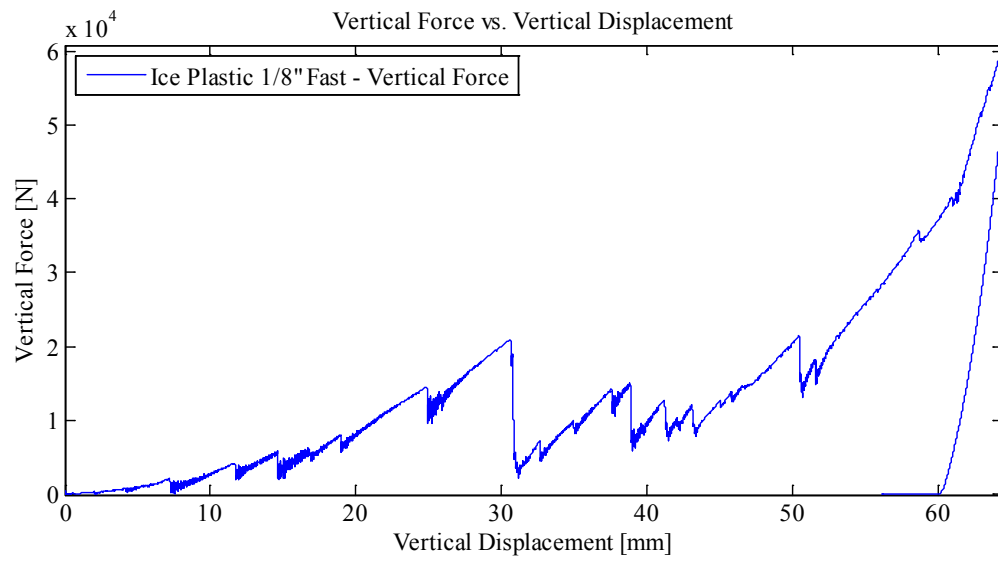
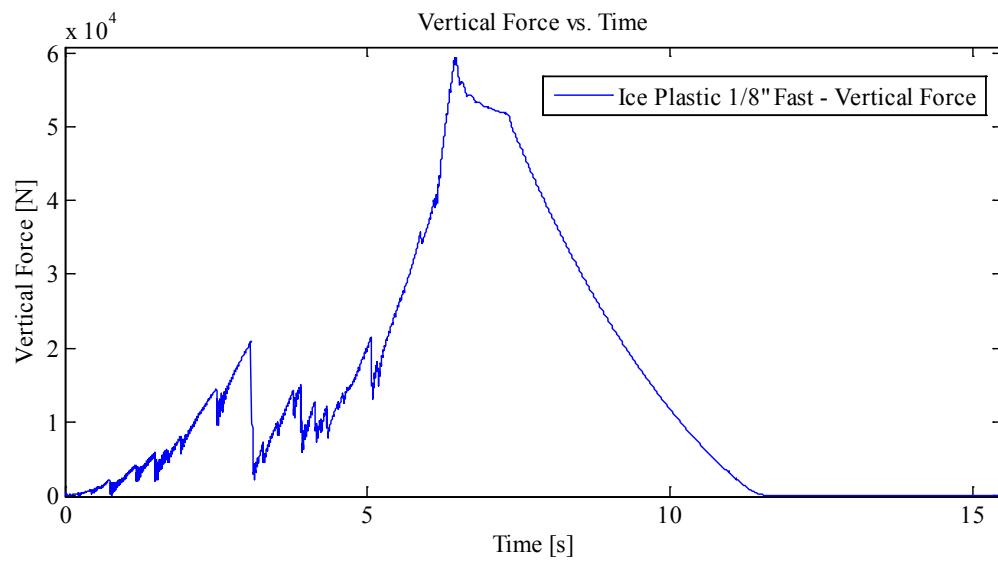
Plots:

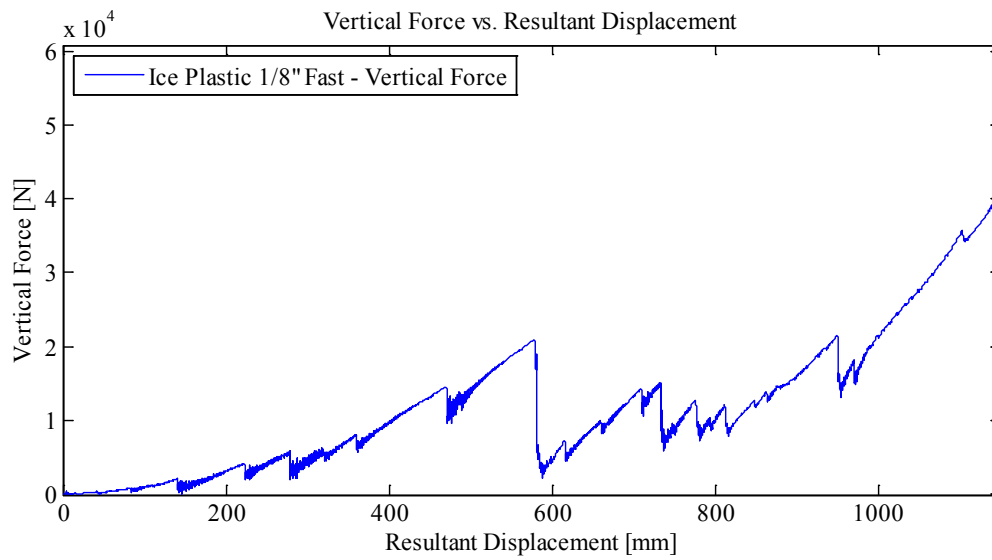
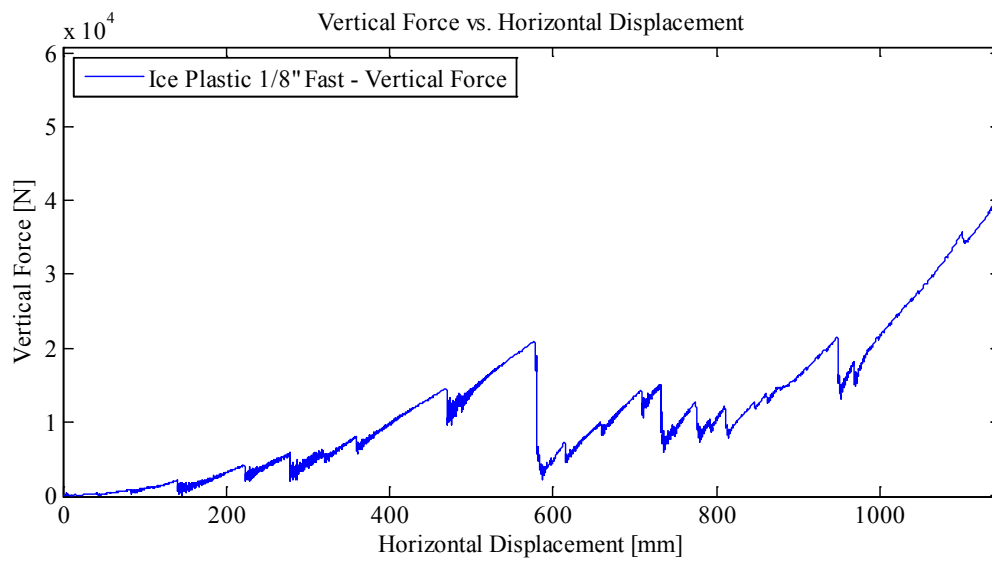


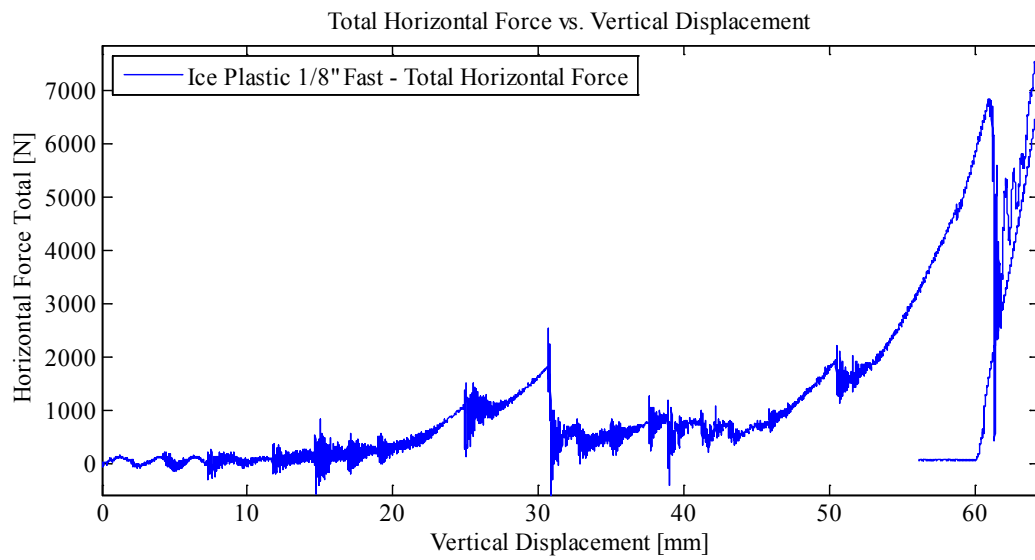
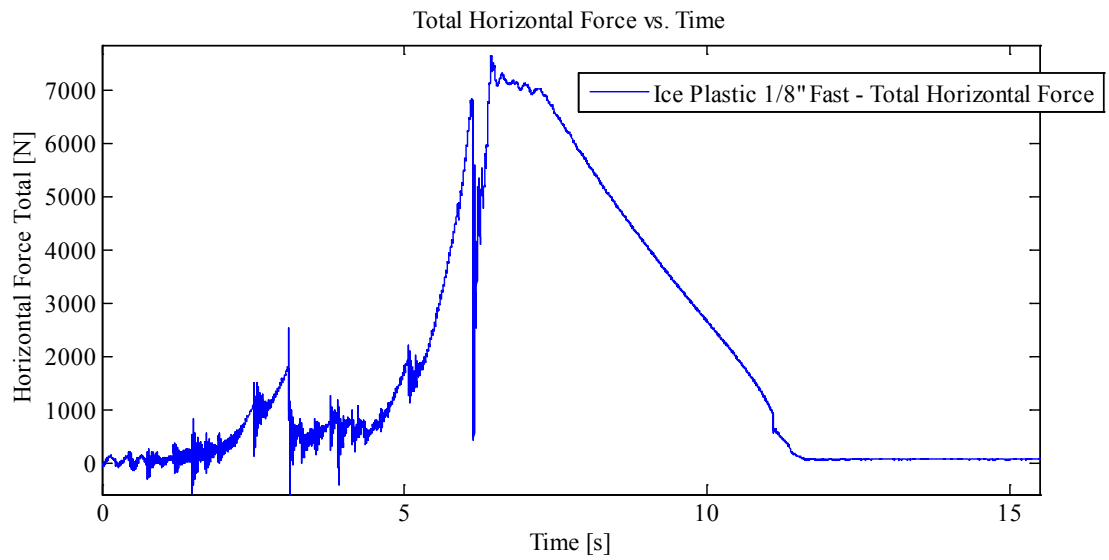


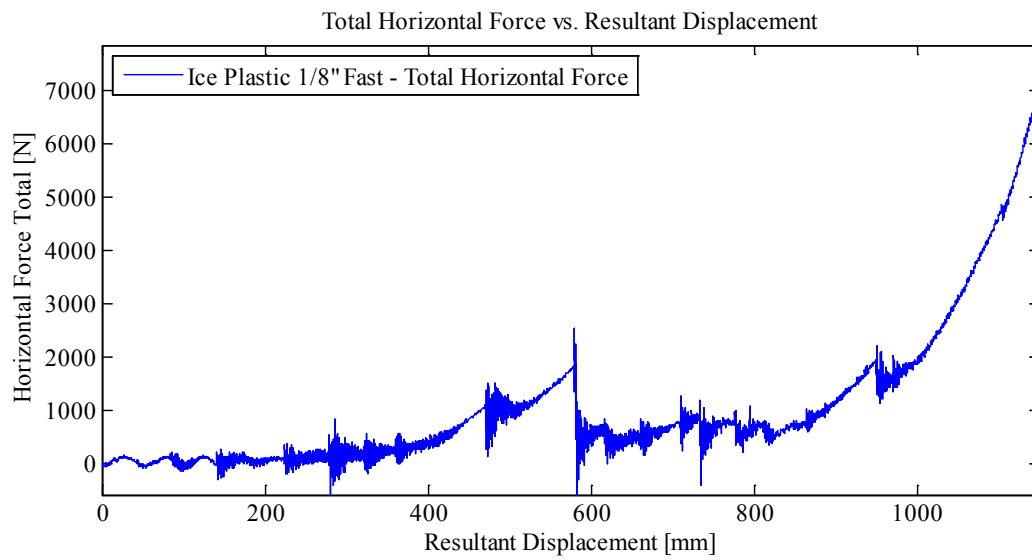
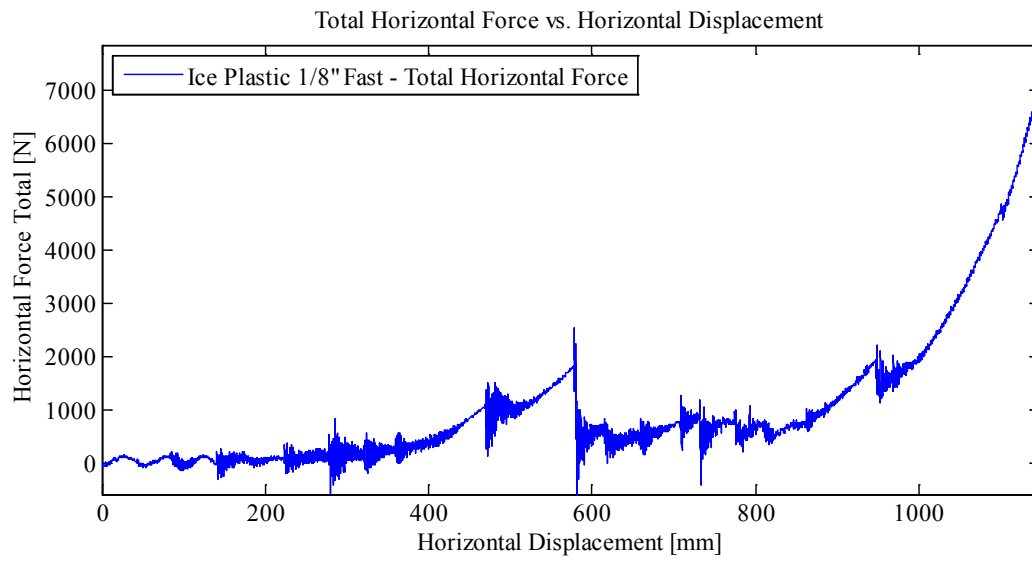


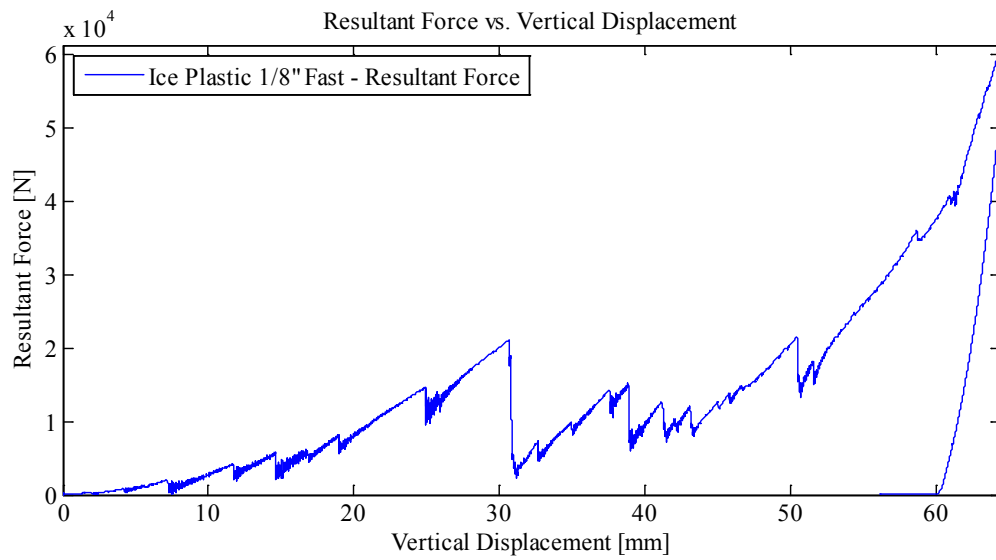
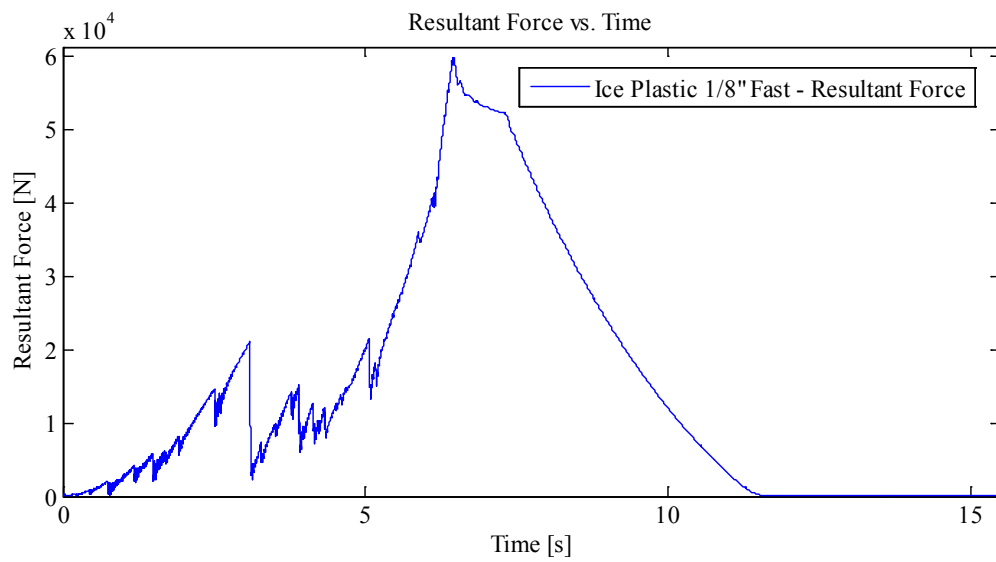


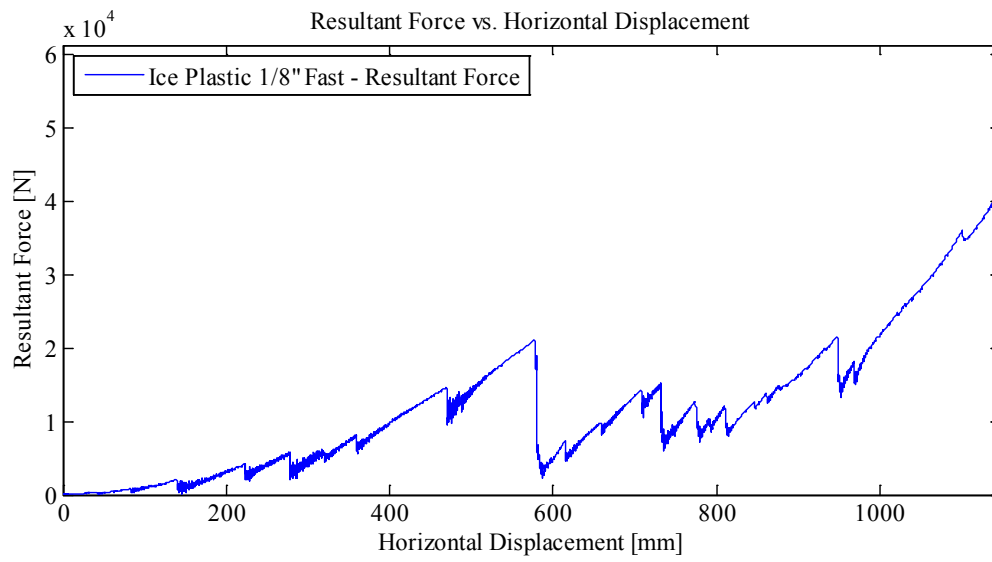
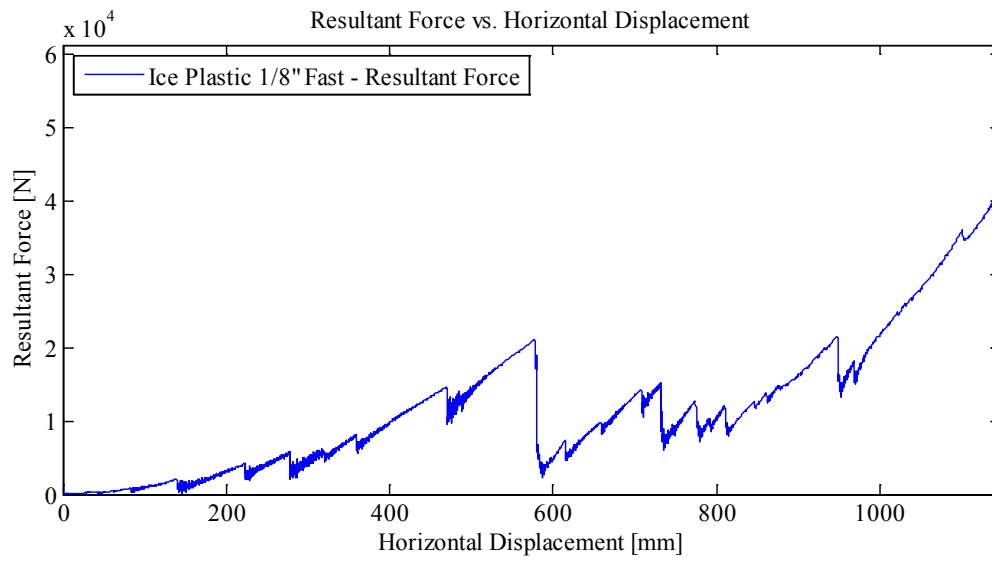


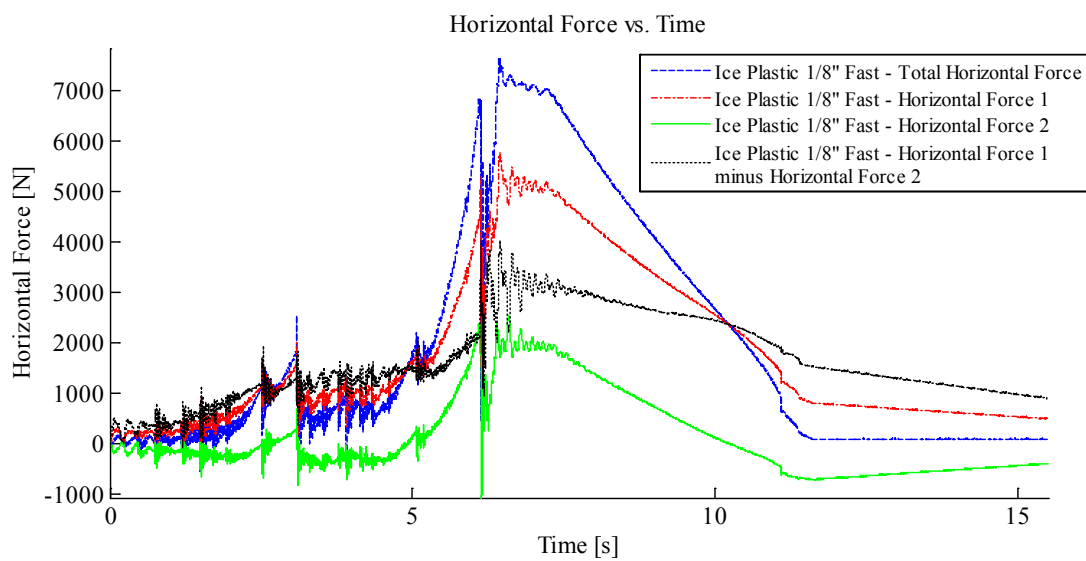
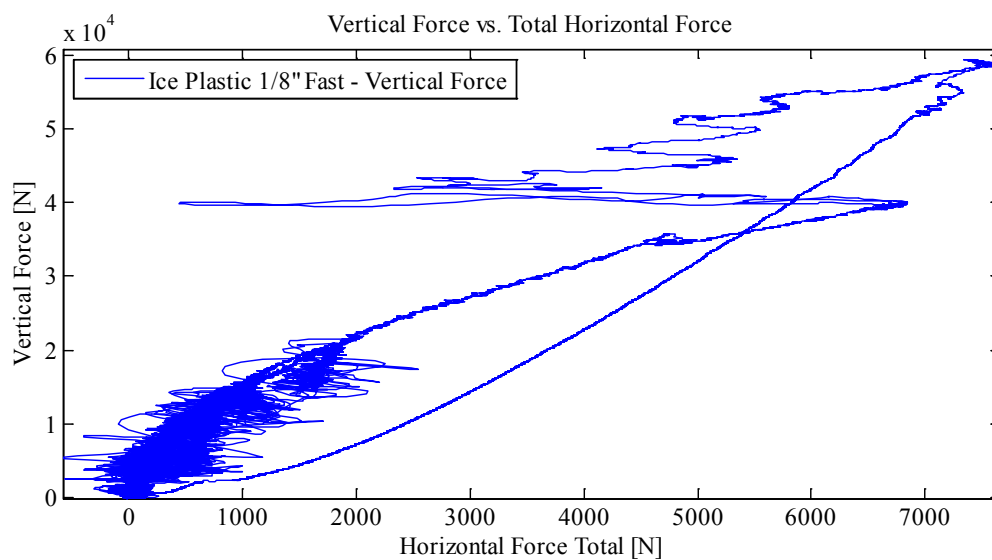












Appendix C3.3.4 – MovingLoad42

May 20, 2014 at ~3:25p.m.

Run # 1/4" plate with ice
Run Type: Ice Cone – Plastic Plate 3
Room-temperature: -9.3°C (Measured with thermocouple)
Sample Type: 1/4" plate
Test Type: In-Along-Out End to End

HStarting Point: End (-61.503 cm (-abs end))
HSpeed: Fastest
H Travel: Abs End to Abs End (110+ cm)

Vstarting Point: -8.992 mm
VSpeed: 10 mm/s
V Travel: 64.383 mm
V Stopping Point: -73.375 mm

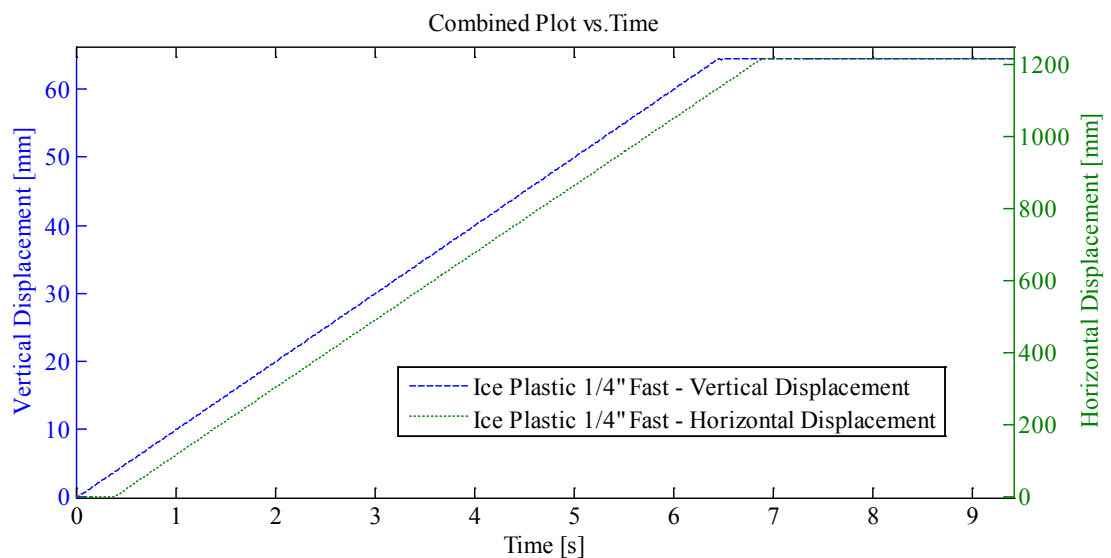
Notes:

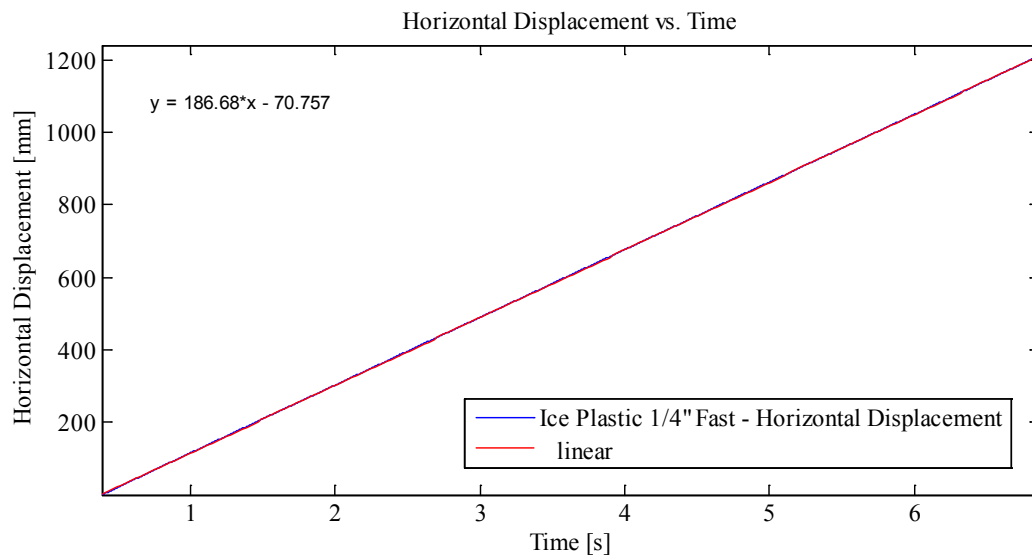
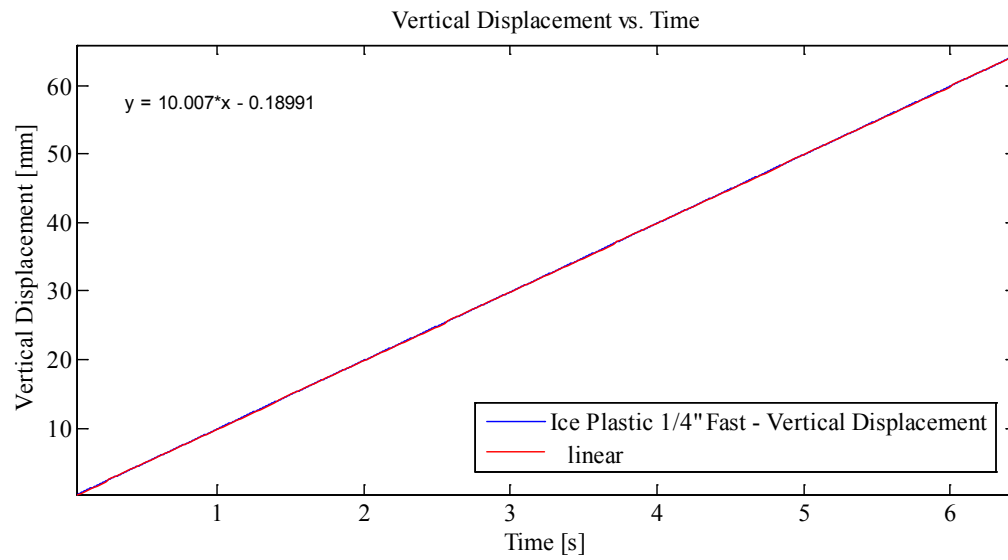
Disp Controlled: In-Along-Out - End to End

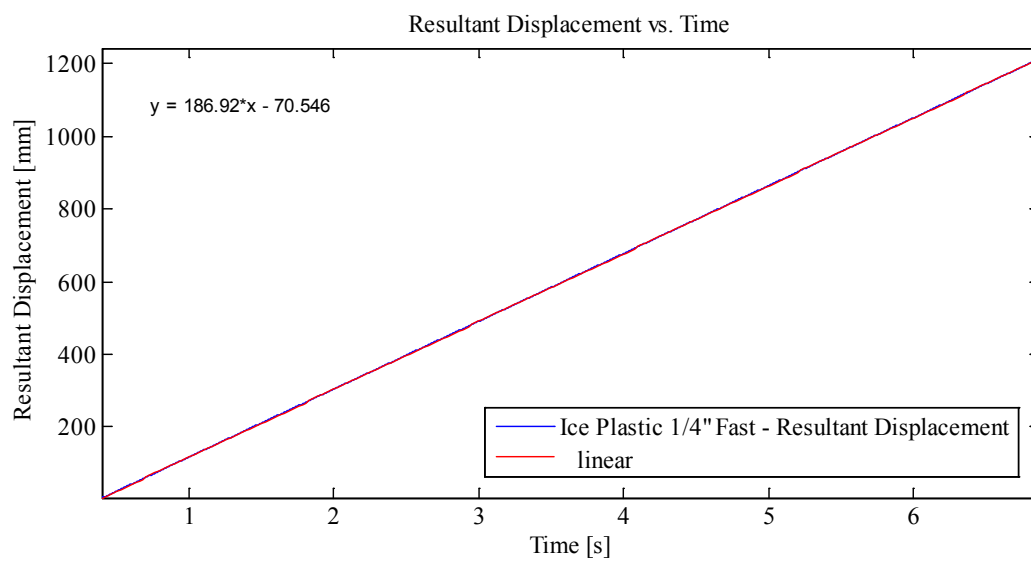
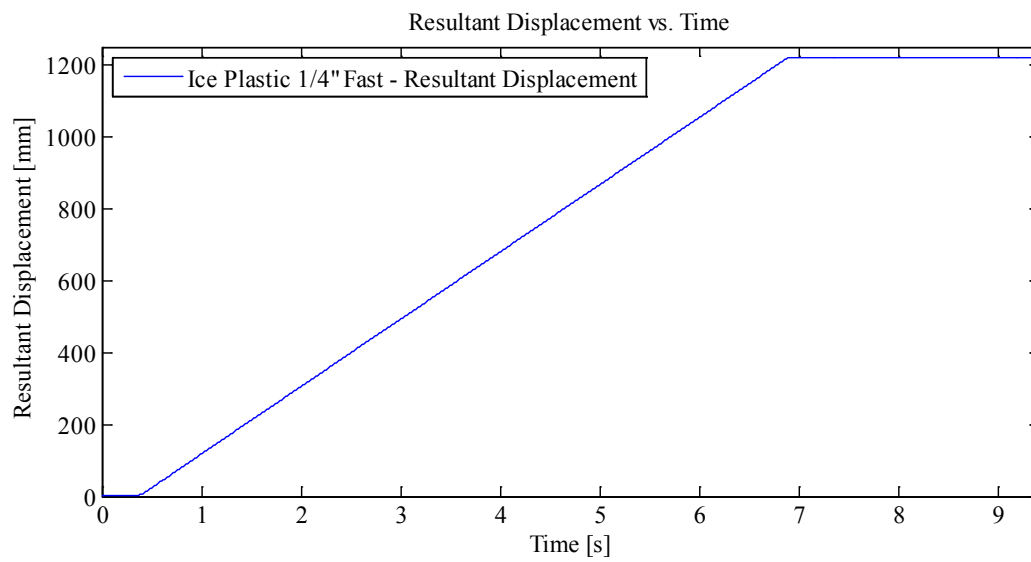
Data from Indentation 1 saved as MovingLoad41

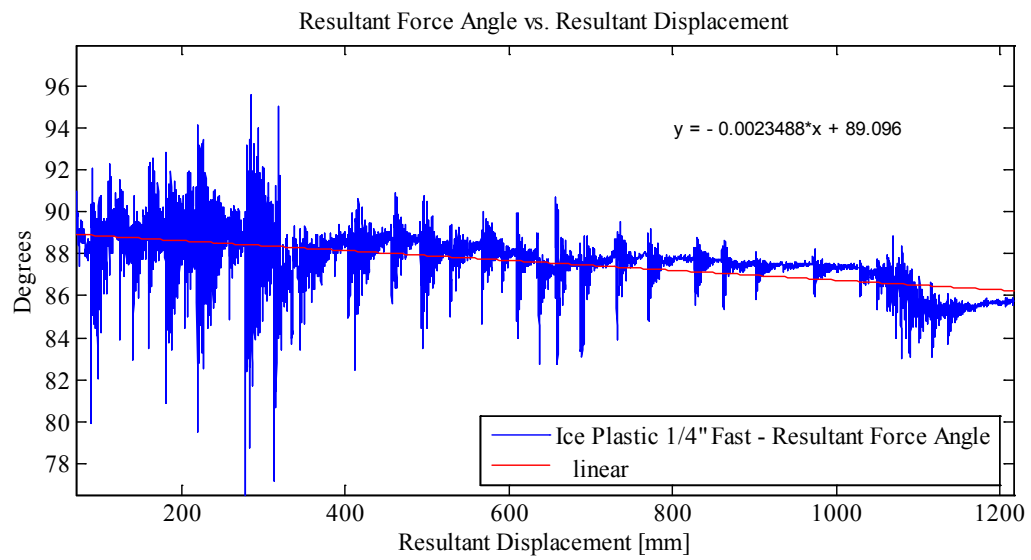
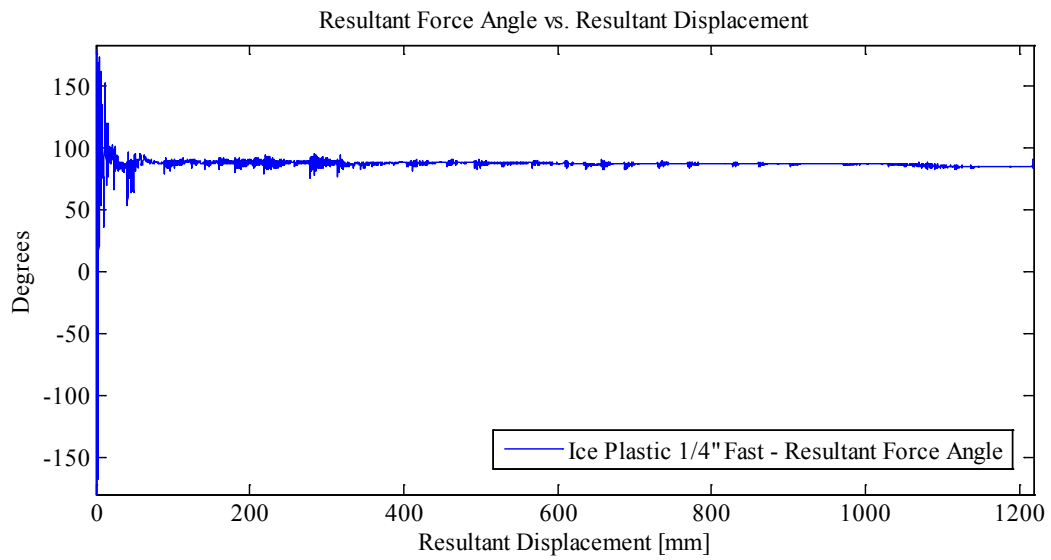
With one internal Thermal Video Camera and external high speed video

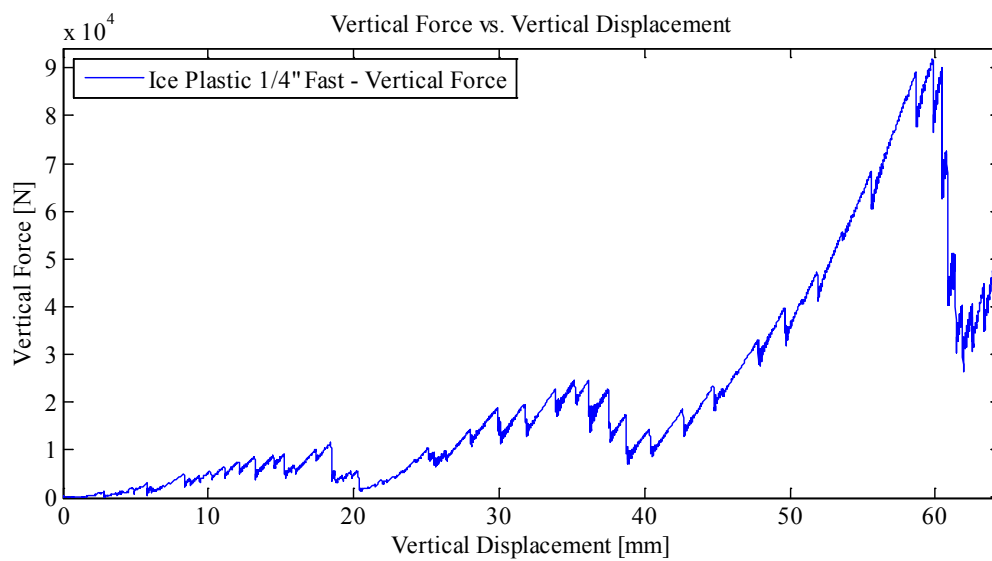
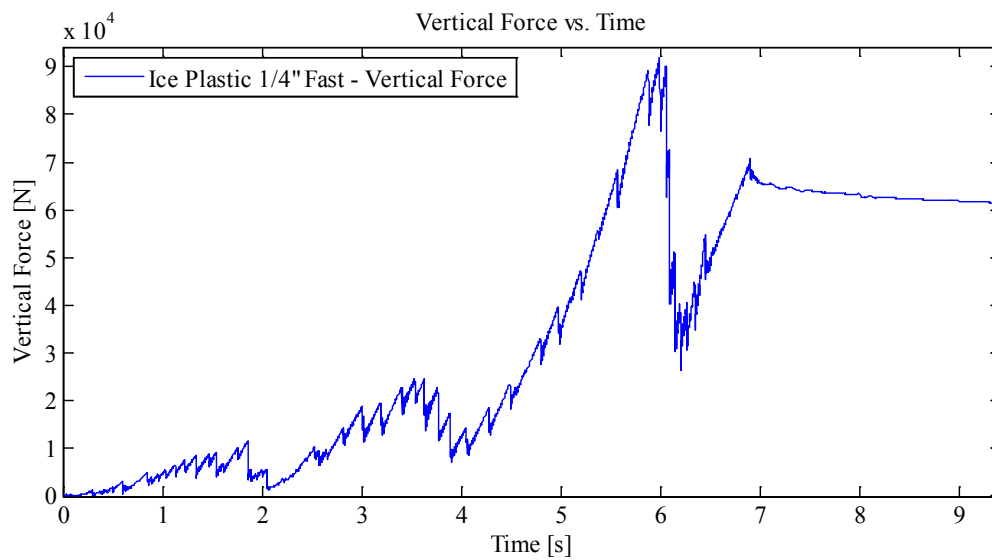
Plots:

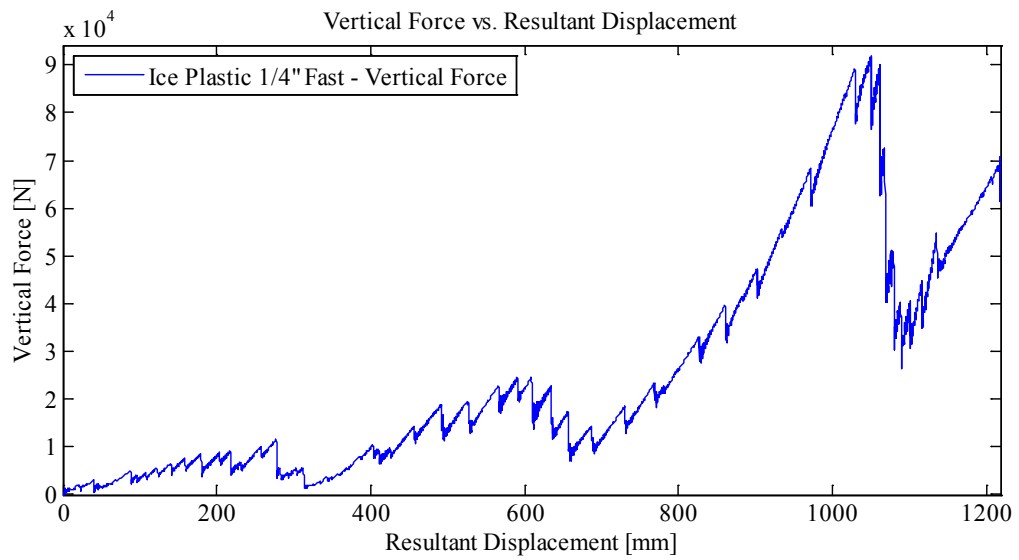
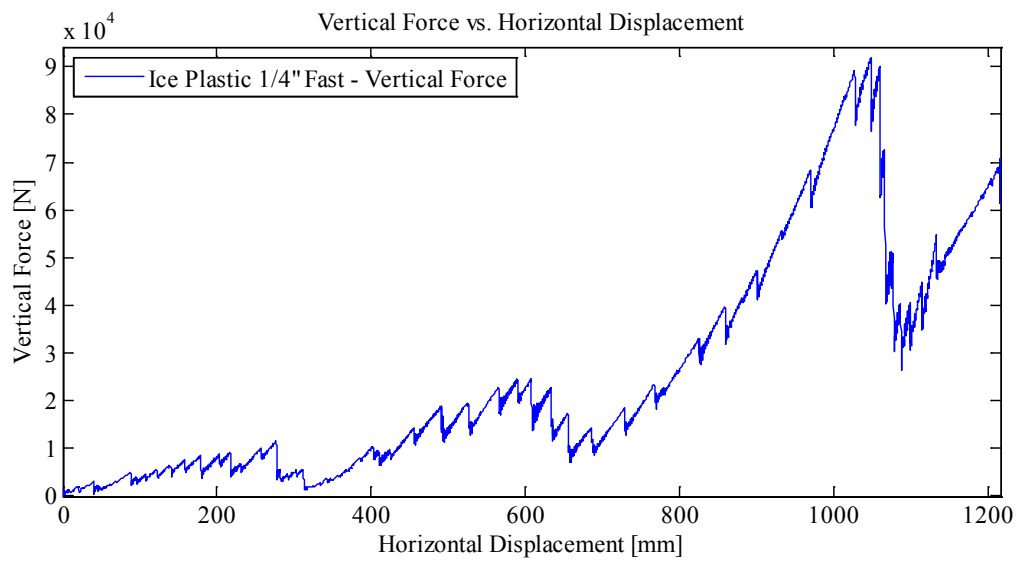


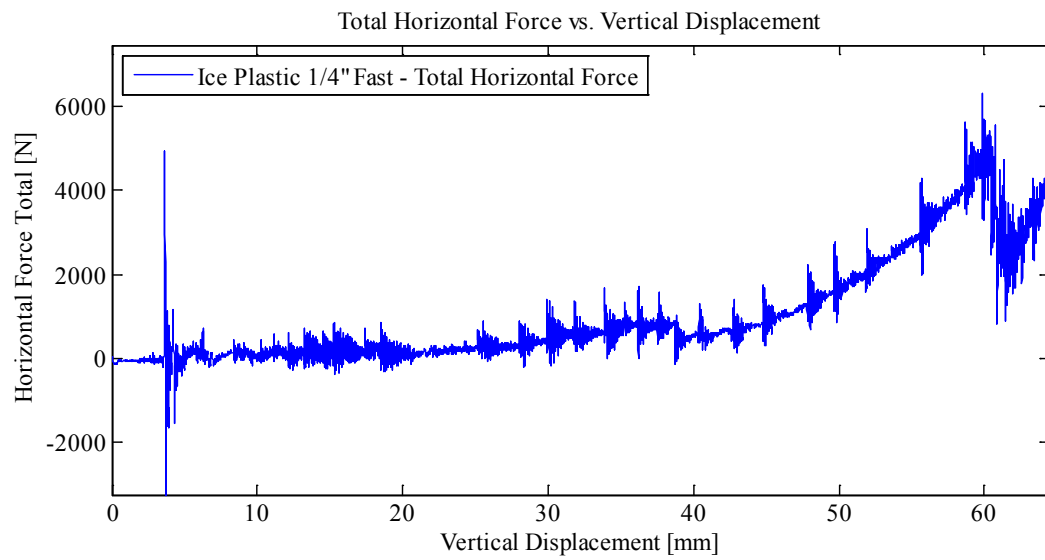
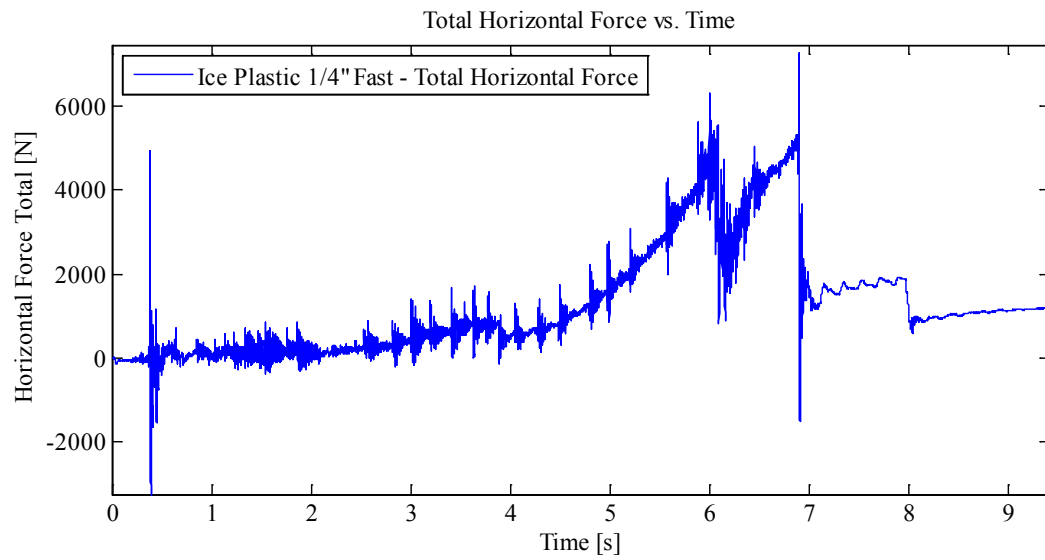


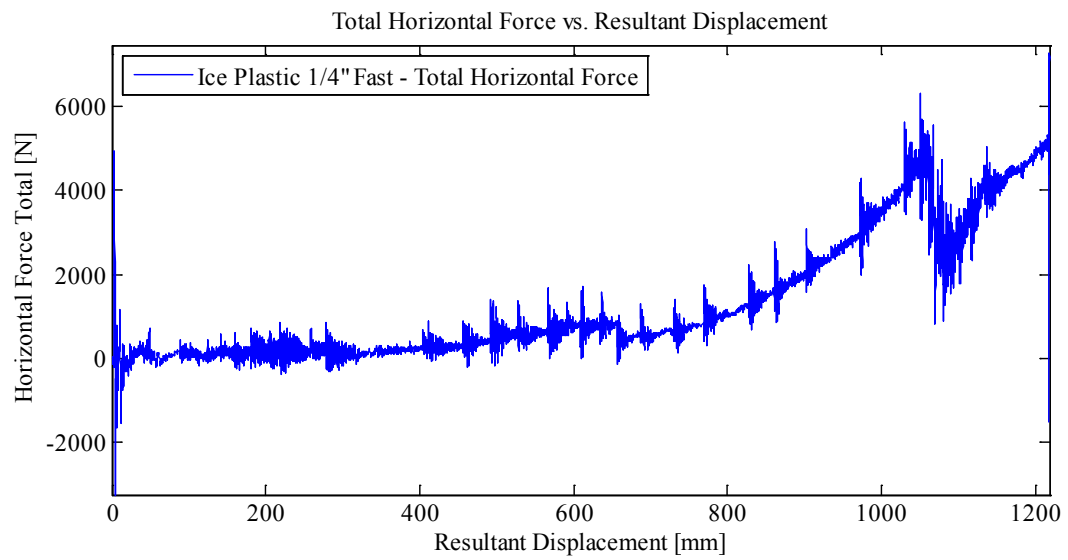
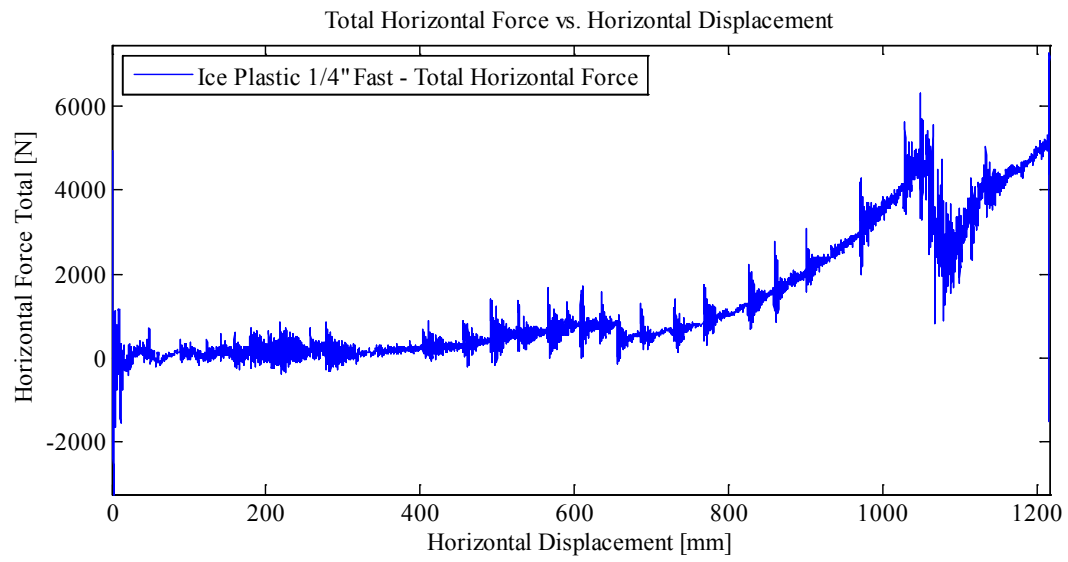


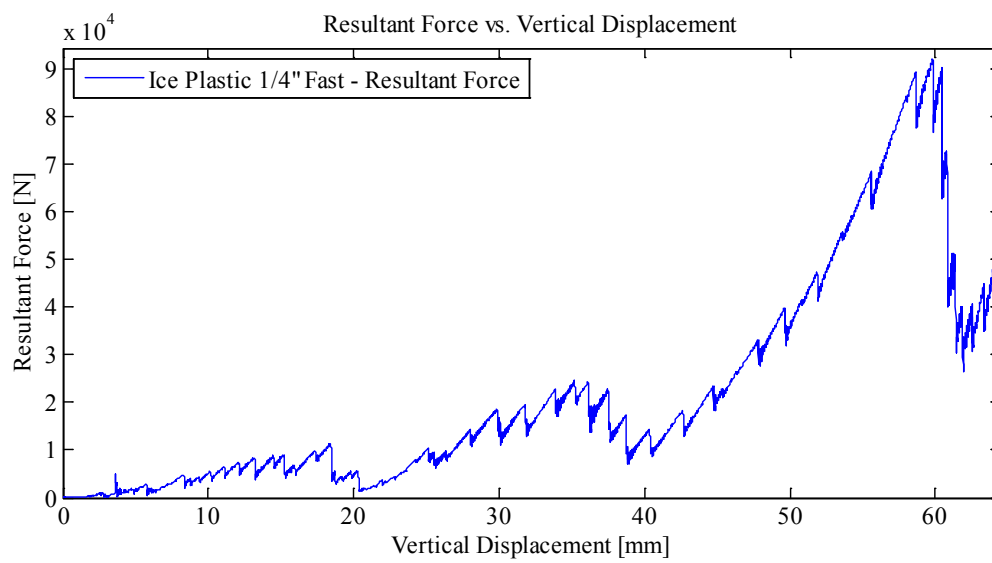
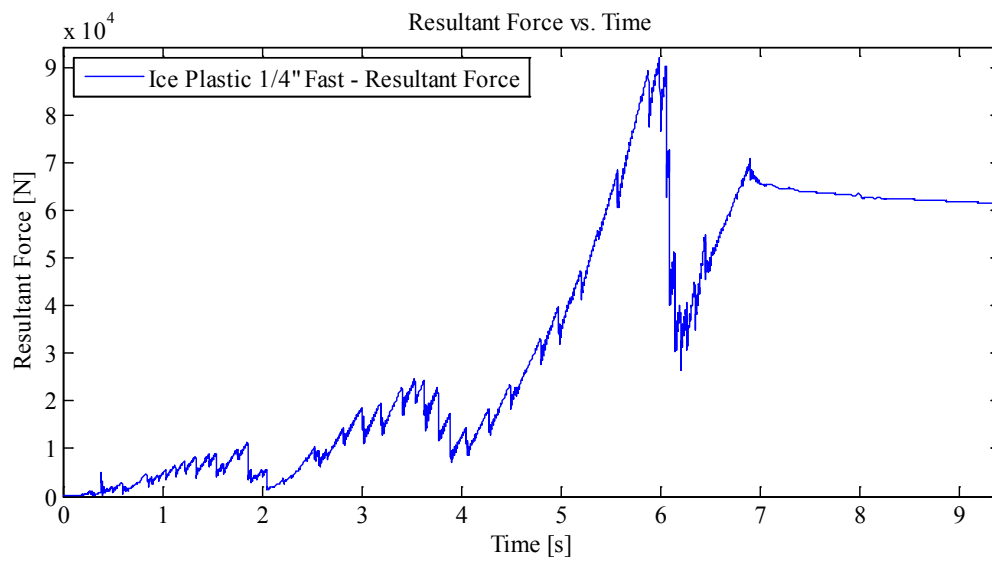


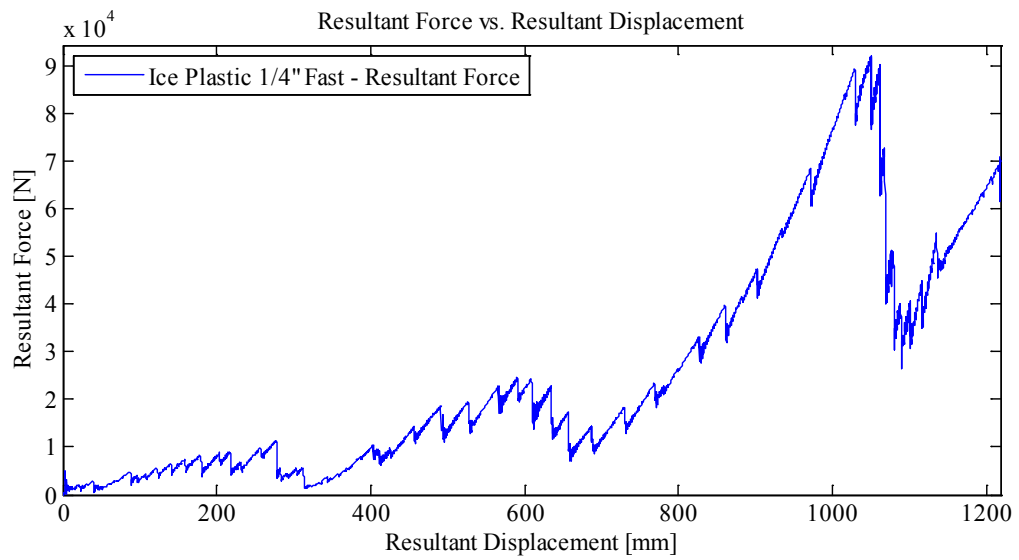
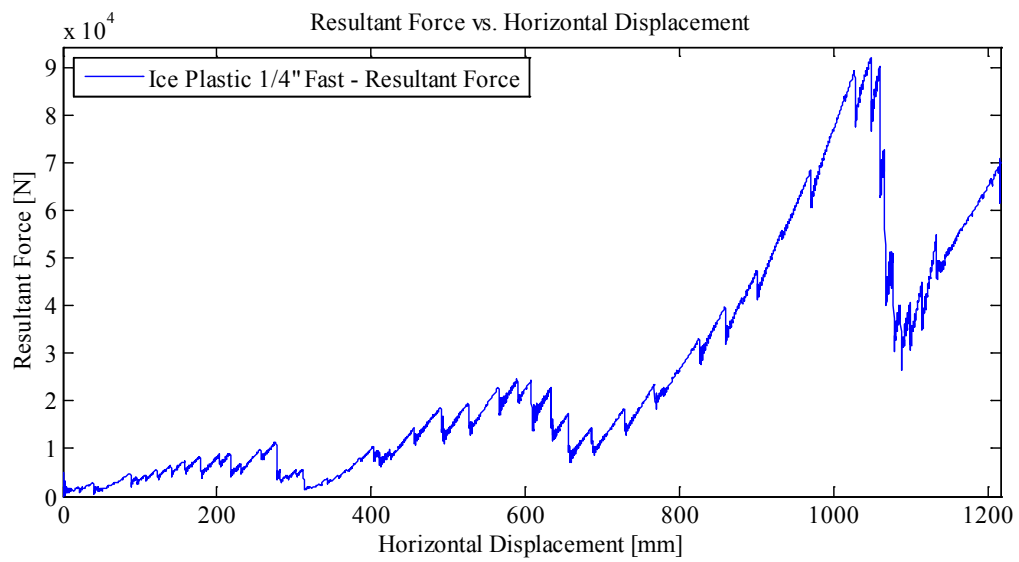


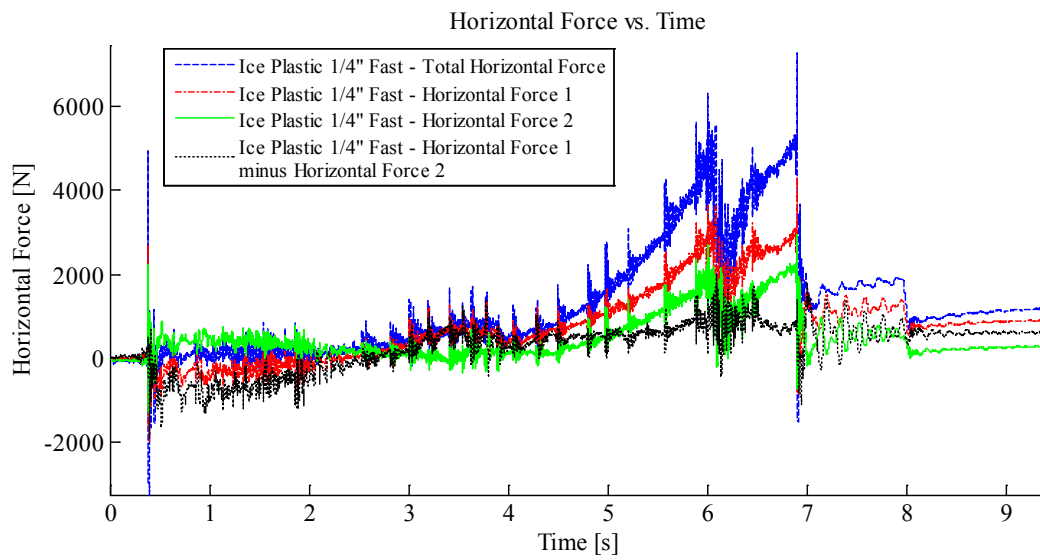
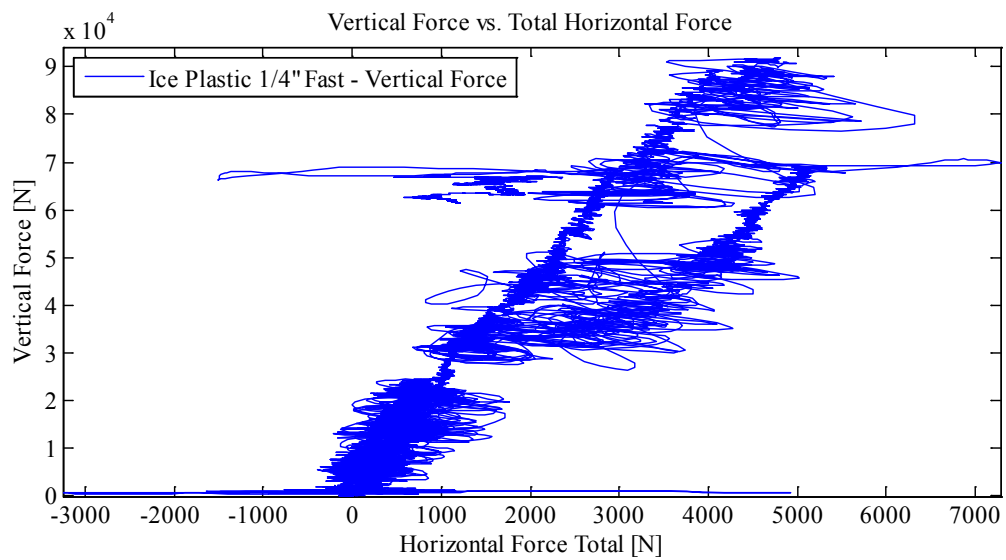












Appendix D – Custom Data Analysis and Plotting Script

As the data for all moving load experiments was recorded at either a 2048Hz or 4096 Hz resolution, the data files for the longer duration tests (some well over 100 seconds) were very large. In order to facilitate the analysis of this data, a custom data analysis script and accompanying graphical user interface was written in Matlab®. The following script was used to perform all data manipulations, and was used exclusively to interrogate, and create the plots for all of the moving load experimental data.


```

function varargout = Moving_Load_Data_Analysis2(varargin)
%=====
% Software License
% Copyright (c) 2014, Bruce W.T. Quinton
% All rights reserved.
%
% Redistribution and use in source and binary forms, with or without
modification, are permitted provided that the following conditions are met:
%
% 1. Redistributions of source code must retain the above copyright notice, this
list of conditions and the following disclaimer.
%
% 2. Redistributions in binary form must reproduce the above copyright notice,
this list of conditions and the following disclaimer in the documentation and/or
other materials provided with the distribution.
%
% 3. Neither the name of the copyright holder nor the names of its contributors
may be used to endorse or promote products derived from this software without
specific prior written permission.
%
% THIS SOFTWARE IS PROVIDED BY THE COPYRIGHT HOLDERS AND CONTRIBUTORS "AS IS"
AND ANY EXPRESS OR IMPLIED WARRANTIES, INCLUDING, BUT NOT LIMITED TO, THE
IMPLIED WARRANTIES OF MERCHANTABILITY AND FITNESS FOR A PARTICULAR PURPOSE ARE
DISCLAIMED. IN NO EVENT SHALL THE COPYRIGHT HOLDER OR CONTRIBUTORS BE LIABLE FOR
ANY DIRECT, INDIRECT, INCIDENTAL, SPECIAL, EXEMPLARY, OR CONSEQUENTIAL DAMAGES
(INCLUDING, BUT NOT LIMITED TO, PROCUREMENT OF SUBSTITUTE GOODS OR SERVICES;
LOSS OF USE, DATA, OR PROFITS; OR BUSINESS INTERRUPTION) HOWEVER CAUSED AND ON
ANY THEORY OF LIABILITY, WHETHER IN CONTRACT, STRICT LIABILITY, OR TORT
(INCLUDING NEGLIGENCE OR OTHERWISE) ARISING IN ANY WAY OUT OF THE USE OF THIS
SOFTWARE, EVEN IF ADVISED OF THE POSSIBILITY OF SUCH DAMAGE.
%=====
%
% MOVING_LOAD_DATA_ANALYSIS2 MATLAB code for Moving_Load_Data_Analysis2.fig
% MOVING_LOAD_DATA_ANALYSIS2, by itself, creates a new
MOVING_LOAD_DATA_ANALYSIS2 or raises the existing
% singleton*.
%
% H = MOVING_LOAD_DATA_ANALYSIS2 returns the handle to a new
MOVING_LOAD_DATA_ANALYSIS2 or the handle to
% the existing singleton*.
%
% MOVING_LOAD_DATA_ANALYSIS2('CALLBACK',hObject,eventData,handles,...)
calls the local
% function named CALLBACK in MOVING_LOAD_DATA_ANALYSIS2.M with the given
input arguments.
%
% MOVING_LOAD_DATA_ANALYSIS2('Property','Value',...) creates a new
MOVING_LOAD_DATA_ANALYSIS2 or raises the
% existing singleton*. Starting from the left, property value pairs are
% applied to the GUI before Moving_Load_Data_Analysis2_OpeningFcn gets
called. An
% unrecognized property name or invalid value makes property application
% stop. All inputs are passed to Moving_Load_Data_Analysis2_OpeningFcn via
varargin.
%
% *See GUI Options on GUIDE's Tools menu. Choose "GUI allows only one
% instance to run (singleton)".
%
% See also: GUIDE, GUIDATA, GUIHANDLES
% Edit the above text to modify the response to help Moving_Load_Data_Analysis2

```

```

% Last Modified by GUIDE v2.5 15-Dec-2014 19:03:04
% Begin initialization code - DO NOT EDIT
gui_Singleton = 1;
gui_State = struct('gui_Name',       mfilename, ...
                  'gui_Singleton',   gui_Singleton, ...
                  'gui_OpeningFcn',   @Moving_Load_Data_Analysis2_OpeningFcn, ...
                  'gui_OutputFcn',    @Moving_Load_Data_Analysis2_OutputFcn, ...
                  'gui_LayoutFcn',    [], ...
                  'gui_Callback',     []);
if nargin && ischar(varargin{1})
    gui_State.gui_Callback = str2func(varargin{1});
end
if nargout
    [varargout{1:nargout}] = gui_mainfcn(gui_State, varargin{:});
else
    gui_mainfcn(gui_State, varargin{:});
end
% End initialization code - DO NOT EDIT
% --- Executes just before Moving_Load_Data_Analysis2 is made visible.
function Moving_Load_Data_Analysis2_OpeningFcn(hObject, eventdata, handles,
varargin)
% This function has no output args, see OutputFcn.
% varargin    command line arguments to Moving_Load_Data_Analysis2 (see VARARGIN)
movegui(hObject, 'northwest')
% Clear data and reset parameters
axes(handles.axes1)
cla reset
[handles] = initializeGUI(handles);
% Choose default command line output for Moving_Load_Data_Analysis2
handles.output = hObject;
% Update handles structure
guidata(hObject, handles);
% UIWAIT makes Moving_Load_Data_Analysis2 wait for user response (see UIRESUME)
% uiwait(handles.figure1);
% --- Outputs from this function are returned to the command line.
function varargout = Moving_Load_Data_Analysis2_OutputFcn(hObject, eventdata,
handles)
% Get default command line output from handles structure
varargout{1} = handles.output;
% --- Executes on selection change in x_data_series.
function x_data_series_Callback(hObject, eventdata, handles)
% hObject     handle to x_data_series (see GCBO)
% Hints: contents = cellstr(get(hObject, 'String')) returns x_data_series
%           contents as cell array
%           contents{get(hObject, 'Value')} returns selected item from x_data_series
% --- Executes during object creation, after setting all properties.
function x_data_series_CreateFcn(hObject, eventdata, handles)
% hObject     handle to x_data_series (see GCBO)
if ispc && isequal(get(hObject, 'BackgroundColor'),
get(0, 'defaultUicontrolBackgroundColor'))
    set(hObject, 'BackgroundColor', 'white');
end
% --- Executes on button press in plot_button.
function plot_button_Callback(hObject, eventdata, handles)
% hObject     handle to plot_button (see GCBO)
% Get data series to plot
[handles] = get_xseries(handles);
[handles] = get_yseries(handles);
[handles] = get_y2series(handles);
% Set x_sliders ranges

```

```

[handles] = set_slider_values(handles);
% Plot data
[handles] = plot_data(handles);
guidata(hObject, handles);
% -----
function open_datafile_ClickedCallback(hObject, eventdata, handles)
% hObject handle to open_datafile (see GCBO)
% Clear old data
if isfield(handles.myvars, 'data') == 1
    handles.myvars=rmfield(handles.myvars, 'data');
end
axes(handles.axes1)
% cla reset % Clear axis
% set(handles.holdon_checkbox, 'Value', 0);
% Change to specimen directory
cd (handles.myvars.default_dir);
[handles.myvars.filename, handles.myvars.pathname] = uigetfile('*.dat', 'Please
choose a data file...');
% User "Cancel" button condition
if isequal(handles.myvars.filename, 0)
    disp('User selected Cancel')
    % return;
    clear all
    close all
else
    disp(['User selected: ', fullfile(handles.myvars.pathname,
handles.myvars.filename)])
    % Set Default Filename equal to lowest directory name
    a=strread(handles.myvars.pathname, '%s', 'delimiter', '\\');
    a=a{length(a)};
    handles.myvars.specimen_name=a;
    % Display default filename
    set(handles.specimen_popupmenu, 'Value', 43);
    handles=importDataFcn(handles);
end
guidata(hObject, handles);
% --- Executes on button press in reset_button.
function reset_button_Callback(hObject, eventdata, handles)
% hObject handle to reset_button (see GCBO)
% Clear data and reset parameters
[handles] = initializeGUI(handles);
guidata(hObject, handles);
% --- Executes on button press in exit_button.
function exit_button_Callback(hObject, eventdata, handles)
% hObject handle to exit_button (see GCBO)
cd (handles.myvars.program_dir); % Change to program directory
clear all % Clear all workspace
close all % Close all Figures
clc % Clear Command Window
% --- Executes on selection change in y_data_series.
function y_data_series_Callback(hObject, eventdata, handles)
% hObject handle to y_data_series (see GCBO)
% Hints: contents = cellstr(get(hObject, 'String')) returns y_data_series
contents as cell array
% contents{get(hObject, 'Value')} returns selected item from y_data_series
% --- Executes during object creation, after setting all properties.
function y_data_series_CreateFcn(hObject, eventdata, handles)
% hObject handle to y_data_series (see GCBO)
if ispc && isequal(get(hObject, 'BackgroundColor'),
get(0, 'defaultUiControlBackgroundColor'))

```

```

        set(hObject,'BackgroundColor','white');
    end
    % --- Executes on button press in plot_style_checkbox.
    function plot_style_checkbox_Callback(hObject, eventdata, handles)
    % hObject      handle to plot_style_checkbox (see GCBO)
    % Hint: get(hObject,'Value') returns toggle state of plot_style_checkbox
    % --- Executes on selection change in y2_data_series.
    function y2_data_series_Callback(hObject, eventdata, handles)
    % hObject      handle to y2_data_series (see GCBO)
    % Hints: contents = cellstr(get(hObject,'String')) returns y2_data_series
    % contents as cell array
    %      contents{get(hObject,'Value')} returns selected item from
    y2_data_series
    % --- Executes during object creation, after setting all properties.
    function y2_data_series_CreateFcn(hObject, eventdata, handles)
    % hObject      handle to y2_data_series (see GCBO)
    if ispc && isequal(get(hObject,'BackgroundColor'),
    get(0,'defaultUicontrolBackgroundColor'))
        set(hObject,'BackgroundColor','white');
    end
    % --- Executes on button press in spec_analysis_button.
    function spec_analysis_button_Callback(hObject, eventdata, handles)
    % hObject      handle to spec_analysis_button (see GCBO)
    if get(handles.use_all_data_checkbox,'Value')==1
        handles.myvars.templow = 1;
        handles.myvars.temphigh = size(handles.myvars.xseries,1);
    else
        [quick_x, quick_y]=ginput(2);                % Interactive user peak
        selection with mouse
        %      disp(quick_x);
        %      disp(min(handles.myvars.xseries));
        %      disp(max(handles.myvars.xseries));
        %      disp(quick_y);
        %      disp(min(handles.myvars.yseries));
        %      disp(max(handles.myvars.yseries));
        if (quick_x(1)<min(handles.myvars.xseries))    % Ensure selection is within
        data boundaries
            quick_x(1)=min(handles.myvars.xseries);
        else
            end
            if (quick_x(2)>max(handles.myvars.xseries)) % Ensure selection is within
            data boundaries
                quick_x(2)=max(handles.myvars.xseries);
            else
                end
            handles.myvars.start_x=quick_x(1);
            handles.myvars.end_x=quick_x(2);
            [I1 I2] = find (handles.myvars.xseries>=handles.myvars.start_x); % Find
            matrix coords less than 1st mouse click
            %      min(I1)
            %      handles.myvars.start_x
            %      handles.myvars.xseries(min(I1))
            handles.myvars.templow = min(I1);                % Get matrix
            coords of 1st mouse click
            [J1 J2] = find (handles.myvars.xseries<=handles.myvars.end_x); % Find
            matrix coords greater than 2nd mouse click
            %      max(J1)
            %      handles.myvars.end_x
            %      handles.myvars.xseries(max(J1))

```

```

        handles.myvars.temphigh = max(J1); % Get matrix
coords of 2nd mouse click
end
% Get Quick Stats
quick_min=min(handles.myvars.yseries(handles.myvars.templow:handles.myvars.temphigh));
I_min=find(handles.myvars.yseries==quick_min);
quick_x_min=min(handles.myvars.xseries(handles.myvars.templow:handles.myvars.temphigh));
quick_max=max(handles.myvars.yseries(handles.myvars.templow:handles.myvars.temphigh));
I_max=find(handles.myvars.yseries==quick_max);
quick_x_max=max(handles.myvars.xseries(handles.myvars.templow:handles.myvars.temphigh));
quick_mean=mean(handles.myvars.yseries(handles.myvars.templow:handles.myvars.temphigh));
quick_x_mean=mean(handles.myvars.xseries(handles.myvars.templow:handles.myvars.temphigh));
quick_y_spread=quick_max-quick_min;
quick_x_spread=quick_x_max-quick_x_min;
quick_min_loc=handles.myvars.xseries(I_min);
quick_max_loc=handles.myvars.xseries(I_max);
quick_min_time=handles.myvars.xseries_time(I_min);
quick_max_time=handles.myvars.xseries_time(I_max);
% Plot Refline
if get(handles.refline_checkbox,'Value') == 1
    h_refline=refline(0,quick_min);
    set(h_refline,'Color','k','LineWidth',2)
    handles.myvars.legend_title(end+1)={'Reference Line'};
    % Display Legend
    if get(handles.legend_checkbox,'Value')==1
        LEG=legend(gca,handles.myvars.legend_title,'Location','NorthWest');
        if get(handles.transparent_legend_checkbox,'Value') == 1
            set(LEG,'color','none')
        end
    end
end
end
% Display Quick Stats
set(handles.start_time_edit,'String',num2str(round(quick_x_min*100)/100));
set(handles.end_time_edit,'String',num2str(round(quick_x_max*100)/100));
set(handles.x_mean_edit,'String',num2str(round(quick_x_mean*100)/100));
set(handles.x_spread_edit,'String',num2str(round(quick_x_spread*100)/100));
set(handles.min_edit,'String',num2str(round(quick_min*100)/100));
set(handles.max_edit,'String',num2str(round(quick_max*100)/100));
set(handles.mean_edit,'String',num2str(round(quick_mean*100)/100));
set(handles.y_spread_edit,'String',num2str(round(quick_y_spread*100)/100));
set(handles.miny_xval_edit,'String',num2str(round(quick_min_loc*100)/100));
set(handles.maxy_xval_edit,'String',num2str(round(quick_max_loc*100)/100));
set(handles.miny_time_edit,'String',num2str(round(quick_min_time*100)/100));
set(handles.maxy_time_edit,'String',num2str(round(quick_max_time*100)/100));
if get(handles.FFT_checkbox,'Value')==1
    clear y t
    y=handles.myvars.yseries(handles.myvars.templow:handles.myvars.temphigh);
    t=handles.myvars.data.time(handles.myvars.templow:handles.myvars.temphigh);
    Fs=1/((t(2,1)-t(1,1))); % Sampling Frequency
    L = length(y); % Length of signal
    NFFT = 2^nextpow2(L); % Next power of 2 from length of y
    Y = fft(y,NFFT)/L;
    f = Fs/2*linspace(0,1,NFFT/2+1);
    % Plot single-sided amplitude spectrum.

```

```

figure
subplot(2,1,1)
plot(t,y)
title('Data Selection')
xlabel('Time [s]')
subplot(2,1,2)
plot(f,2*abs(Y(1:NFFT/2+1)))
title('Single-Sided Amplitude Spectrum of y(t)')
xlabel('Frequency (Hz)')
ylabel('|Y(f)|')
end
% % Tare data
% % Get mouse input for tare region
% [x, y]=ginput(2); % Interactive user peak selection with mouse
% if (x(1)<0) % Ensure time > 0
% x(1)=0;
% end
% % Get indicies of mouse selection and ensure they are inside the mouse
% % selection.
% ind(1)=max(find(handles.myvars.data.time<=x(1)))+1;
% ind(2)=min(find(handles.myvars.data.time>=x(2)))-1;
% vdisp_tare=mean(handles.myvars.data.vdisp(ind(1):ind(2)));
% handles.myvars.data.vdisp=handles.myvars.data.vdisp-vdisp_tare;
%
% vforc_tare=mean(handles.myvars.data.vforc(ind(1):ind(2)));
% handles.myvars.data.vforc=handles.myvars.data.vforc-vforc_tare;
%
% hdisp_tare=mean(handles.myvars.data.hdisp(ind(1):ind(2)));
% handles.myvars.data.hdisp=handles.myvars.data.hdisp-hdisp_tare;
%
% hforc1_tare=mean(handles.myvars.data.hforc1(ind(1):ind(2)));
% handles.myvars.data.hforc1=handles.myvars.data.hforc1-hforc1_tare;
%
% hforc2_tare=mean(handles.myvars.data.hforc2(ind(1):ind(2)));
% handles.myvars.data.hforc2=handles.myvars.data.hforc2-hforc2_tare;
if get(handles.fit_data_checkbox,'Value')==1
    fit_curve(handles);
end
guidata(hObject,handles);
function min_edit_Callback(hObject, eventdata, handles)
% hObject handle to min_edit (see GCBO)
% Hints: get(hObject,'String') returns contents of min_edit as text
% str2double(get(hObject,'String')) returns contents of min_edit as a
double
% --- Executes during object creation, after setting all properties.
function min_edit_CreateFcn(hObject, eventdata, handles)
% hObject handle to min_edit (see GCBO)
% Hint: edit controls usually have a white background on Windows.
if ispc && isequal(get(hObject,'BackgroundColor'),
get(0,'defaultUiControlBackgroundColor'))
    set(hObject,'BackgroundColor','white');
end
function max_edit_Callback(hObject, eventdata, handles)
% hObject handle to max_edit (see GCBO)
% Hints: get(hObject,'String') returns contents of max_edit as text
% str2double(get(hObject,'String')) returns contents of max_edit as a
double
% --- Executes during object creation, after setting all properties.
function max_edit_CreateFcn(hObject, eventdata, handles)
% hObject handle to max_edit (see GCBO)

```

```

% Hint: edit controls usually have a white background on Windows.
if ispc && isequal(get(hObject,'BackgroundColor'),
get(0,'defaultUicontrolBackgroundColor'))
    set(hObject,'BackgroundColor','white');
end
function mean_edit_Callback(hObject, eventdata, handles)
% hObject    handle to mean_edit (see GCBO)
% Hints: get(hObject,'String') returns contents of mean_edit as text
%          str2double(get(hObject,'String')) returns contents of mean_edit as a
double
% --- Executes during object creation, after setting all properties.
function mean_edit_CreateFcn(hObject, eventdata, handles)
% hObject    handle to mean_edit (see GCBO)
% Hint: edit controls usually have a white background on Windows.
if ispc && isequal(get(hObject,'BackgroundColor'),
get(0,'defaultUicontrolBackgroundColor'))
    set(hObject,'BackgroundColor','white');
end
function end_time_edit_Callback(hObject, eventdata, handles)
% hObject    handle to end_time_edit (see GCBO)
% Hints: get(hObject,'String') returns contents of end_time_edit as text
%          str2double(get(hObject,'String')) returns contents of end_time_edit as
a double
% --- Executes during object creation, after setting all properties.
function end_time_edit_CreateFcn(hObject, eventdata, handles)
% hObject    handle to end_time_edit (see GCBO)
% Hint: edit controls usually have a white background on Windows.
if ispc && isequal(get(hObject,'BackgroundColor'),
get(0,'defaultUicontrolBackgroundColor'))
    set(hObject,'BackgroundColor','white');
end
function start_time_edit_Callback(hObject, eventdata, handles)
% hObject    handle to start_time_edit (see GCBO)
% Hints: get(hObject,'String') returns contents of start_time_edit as text
%          str2double(get(hObject,'String')) returns contents of start_time_edit
as a double
% --- Executes during object creation, after setting all properties.
function start_time_edit_CreateFcn(hObject, eventdata, handles)
% hObject    handle to start_time_edit (see GCBO)
% Hint: edit controls usually have a white background on Windows.
if ispc && isequal(get(hObject,'BackgroundColor'),
get(0,'defaultUicontrolBackgroundColor'))
    set(hObject,'BackgroundColor','white');
end
% --- Executes on button press in plot_sep window checkbox.
function plot_sep_window_checkbox_Callback(hObject, eventdata, handles)
% hObject    handle to plot_sep_window_checkbox (see GCBO)
% if get(hObject,'Value')==1
%     handles.sep_figure=figure;
% end
% if get (hObject,'Value')==0
%     close(handles.sep_figure)
% end
% Hint: get(hObject,'Value') returns toggle state of plot_sep_window_checkbox
guidata(hObject,handles);
% --- Executes on button press in holdon_checkbox.
function holdon_checkbox_Callback(hObject, eventdata, handles)
% hObject    handle to holdon_checkbox (see GCBO)
% Hint: get(hObject,'Value') returns toggle state of holdon_checkbox
if get(hObject,'Value')==0

```

```

        if isfield(handles.myvars, 'plotcount') == 1
            handles.myvars=rmfield(handles.myvars, 'plotcount');
        end
    end
    guidata(hObject,handles);
    % --- Executes on button press in cla_pushbutton.
    function cla_pushbutton_Callback(hObject, eventdata, handles)
    % hObject    handle to cla_pushbutton (see GCBO)
    [handles]=clear_plot(handles);
    guidata(hObject,handles);
    % --- Executes on button press in tare_by_initial_checkbox.
    function tare_by_initial_checkbox_Callback(hObject, eventdata, handles)
    % hObject    handle to tare_by_initial_checkbox (see GCBO)
    % Hint: get(hObject,'Value') returns toggle state of tare_by_initial_checkbox
    if get(hObject,'Value')==1
        [handles] = clear_derived_data(handles);
        [handles] = tare_data(handles);
        [handles] = create_derived_data(handles);
    elseif get(hObject,'Value')==0
        [handles] = clear_derived_data(handles);
        [handles] = untare_data(handles);
        [handles] = create_derived_data(handles);
    end
    guidata(hObject,handles);
    % --- Executes on button press in use_all_data_checkbox.
    function use_all_data_checkbox_Callback(hObject, eventdata, handles)
    % hObject    handle to use_all_data_checkbox (see GCBO)
    % Hint: get(hObject,'Value') returns toggle state of use_all_data_checkbox
    if get(hObject,'Value') == 1
        set(handles.refline_checkbox,'Value',0)
        set(handles.refline_checkbox,'Enable','off')
    end
    if get(hObject,'Value') == 0
        set(handles.refline_checkbox,'Enable','on')
    end
    % --- Executes on button press in FFT_checkbox.
    function FFT_checkbox_Callback(hObject, eventdata, handles)
    % hObject    handle to FFT_checkbox (see GCBO)
    if get(hObject,'Value')==1
        set(handles.fit_data_checkbox,'Enable','off')
        set(handles.data_fit_popupmenu,'Enable','off')
        set(handles.refit_pushbutton,'Enable','off')
    else
        set(handles.fit_data_checkbox,'Enable','on')
        set(handles.data_fit_popupmenu,'Enable','on')
        set(handles.refit_pushbutton,'Enable','on')
    end
    guidata(hObject,handles);
    % Hint: get(hObject,'Value') returns toggle state of FFT_checkbox
    % --- Executes on selection change in curve_operations_popup.
    function curve_operations_popup_Callback(hObject, eventdata, handles)
    % hObject    handle to curve_operations_popup (see GCBO)
    % Hints: contents = cellstr(get(hObject,'String')) returns
    curve_operations_popup contents as cell array
    %         contents{get(hObject,'Value')} returns selected item from
    curve_operations_popup
    oper_val=get(hObject,'Value');
    oper_str=get(hObject,'String');
    switch oper_str{oper_val}
        case 'Addition'

```



```

        set(handles.curve_operations_curve2,'Enable','on');
        set(handles.text16,'String','Curve 1');
        set(handles.text17,'String','Curve 2');
    case 'Subtraction'
        set(handles.curve_operations_curve2,'Enable','on');
        set(handles.text16,'String','Curve 1');
        set(handles.text17,'String','Curve 2');
    case 'Division'
        set(handles.curve_operations_curve2,'Enable','on');
        set(handles.text16,'String','Numerator');
        set(handles.text17,'String','Denominator');
    case '1st Integral'
        set(handles.curve_operations_curve2,'Enable','on');
        set(handles.text16,'String','Integrate');
        set(handles.text17,'String','with respect to...');
    case '1st Derivative'
        set(handles.curve_operations_curve2,'Enable','off');
        set(handles.text16,'String','Curve 1');
        set(handles.text17,'String','Curve 2');
    case '2nd Derivative'
        set(handles.curve_operations_curve2,'Enable','off');
        set(handles.text16,'String','Curve 1');
        set(handles.text17,'String','Curve 2');
end
guidata(hObject,handles);
% --- Executes during object creation, after setting all properties.
function curve_operations_popup_CreateFcn(hObject, eventdata, handles)
% hObject    handle to curve_operations_popup (see GCBO)
if ispc && isequal(get(hObject,'BackgroundColor'),
get(0,'defaultUicontrolBackgroundColor'))
    set(hObject,'BackgroundColor','white');
end
% --- Executes on selection change in curve_operations_curve1.
function curve_operations_curve1_Callback(hObject, eventdata, handles)
% hObject    handle to curve_operations_curve1 (see GCBO)
% Hints: contents = cellstr(get(hObject,'String')) returns
curve_operations_curve1 contents as cell array
%     contents{get(hObject,'Value')} returns selected item from
curve_operations_curve1
% --- Executes during object creation, after setting all properties.
function curve_operations_curve1_CreateFcn(hObject, eventdata, handles)
% hObject    handle to curve_operations_curve1 (see GCBO)
if ispc && isequal(get(hObject,'BackgroundColor'),
get(0,'defaultUicontrolBackgroundColor'))
    set(hObject,'BackgroundColor','white');
end
% --- Executes on button press in curve_operations_button.
function curve_operations_button_Callback(hObject, eventdata, handles)
% hObject    handle to curve_operations_button (see GCBO)
% handle%    Set x series data
[handles] = get_xseries(handles);
[handles] = get_yseries(handles);
[handles] = get_y2series(handles);
% The above is unnecessarily necessary...
curve1_val=get(handles.curve_operations_curve1,'Value');
curve1_str=get(handles.curve_operations_curve1,'String');
handles.myvars.curve1_title=curve1_str{curve1_val};
switch handles.myvars.curve1_title
    case 'Time'
        handles.myvars.curve1=handles.myvars.data.time;

```

```

case 'Vertical Displacement'
    handles.myvars.curve1=handles.myvars.data.vdisp;
case 'Vertical Velocity'
    handles.myvars.curve1=handles.myvars.data.vvel;
case 'Vertical Acceleration'
    handles.myvars.curve1=handles.myvars.data.vacc;
case 'Vertical Force'
    handles.myvars.curve1=handles.myvars.data.vforc;
case 'Vertical Impulse'
    handles.myvars.curve1=handles.myvars.data.vimpulse;
    case 'Vertical Work'
        handles.myvars.curve1=handles.myvars.data.vwork;
case 'Horizontal Displacement'
    handles.myvars.curve1=handles.myvars.data.hdisp;
case 'Horizontal Velocity'
    handles.myvars.curve1=handles.myvars.data.hvel;
case 'Horizontal Acceleration'
    handles.myvars.curve1=handles.myvars.data.hacc;
case 'Horizontal Force 1'
    handles.myvars.curve1=handles.myvars.data.hforc1;
case 'Horizontal Force 2'
    handles.myvars.curve1=handles.myvars.data.hforc2;
case 'Total Horizontal Force'
    handles.myvars.curve1=handles.myvars.data.hforc_total;
case 'Horizontal Impulse'
    handles.myvars.curve1=handles.myvars.data.himpulse;
case 'Horizontal Work'
    handles.myvars.curve1=handles.myvars.data.hwork;
case 'Resultant Displacement'
    handles.myvars.curve1=handles.myvars.data.resultant_disp;
case 'Resultant Force'
    handles.myvars.curve1=handles.myvars.data.resultant_force;
case 'Resultant Force Angle'
    handles.myvars.curve1=handles.myvars.data.resultant_force_angle;
end
curve2_val=get(handles.curve_operations_curve2,'Value');
curve2_str=get(handles.curve_operations_curve2,'String');
handles.myvars.curve2_title=curve2_str{curve2_val};
switch handles.myvars.curve2_title
    case 'Time'
        handles.myvars.curve2=handles.myvars.data.time;
    case 'Vertical Displacement'
        handles.myvars.curve2=handles.myvars.data.vdisp;
    case 'Vertical Velocity'
        handles.myvars.curve2=handles.myvars.data.vvel;
    case 'Vertical Acceleration'
        handles.myvars.curve2=handles.myvars.data.vacc;
    case 'Vertical Force'
        handles.myvars.curve2=handles.myvars.data.vforc;
    case 'Vertical Impulse'
        handles.myvars.curve2=handles.myvars.data.vimpulse;
        case 'Vertical Work'
            handles.myvars.curve2=handles.myvars.data.vwork;
    case 'Horizontal Displacement'
        handles.myvars.curve2=handles.myvars.data.hdisp;
    case 'Horizontal Velocity'
        handles.myvars.curve2=handles.myvars.data.hvel;
    case 'Horizontal Acceleration'
        handles.myvars.curve2=handles.myvars.data.hacc;
    case 'Horizontal Force 1'

```

```

        handles.myvars.curve2=handles.myvars.data.hforc1;
    case 'Horizontal Force 2'
        handles.myvars.curve2=handles.myvars.data.hforc2;
    case 'Total Horizontal Force'
        handles.myvars.curve2=handles.myvars.data.hforc_total;
    case 'Horizontal Impulse'
        handles.myvars.curve2=handles.myvars.data.himpulse;
    case 'Horizontal Work'
        handles.myvars.curve2=handles.myvars.data.hwork;
    case 'Resultant Displacement'
        handles.myvars.curve2=handles.myvars.data.resultant_disp;
    case 'Resultant Force'
        handles.myvars.curve2=handles.myvars.data.resultant_force;
    case 'Resultant Force Angle'
        handles.myvars.curve2=handles.myvars.data.resultant_force_angle;
end
oper_val=get(handles.curve_operations_popup,'Value');
oper_str=get(handles.curve_operations_popup,'String');
handles.myvars.curve0_title=oper_str{oper_val};
switch handles.myvars.curve0_title
    case 'Addition'
        handles.myvars.yseries=handles.myvars.curve1+handles.myvars.curve2;
    case 'Subtraction'
        handles.myvars.yseries=handles.myvars.curve1-handles.myvars.curve2;
    case 'Division'
        handles.myvars.yseries=handles.myvars.curve1./handles.myvars.curve2;
    case '1st Integral'

handles.myvars.yseries=cumtrapz(handles.myvars.curve2,handles.myvars.curve1);
    case '1st Derivative'

handles.myvars.yseries=diff((handles.myvars.curve1)/(handles.myvars.data.time(2,
1)-handles.myvars.data.time(1,1)));
    s=size(handles.myvars.data.time);
    handles.myvars.yseries(s(1))=handles.myvars.yseries(s(1)-1);
    case '2nd Derivative'
        diff1=diff((handles.myvars.curve1)/(handles.myvars.data.time(2,1)-
handles.myvars.data.time(1,1)));
        handles.myvars.yseries=diff((diff1)/(handles.myvars.data.time(2,1)-
handles.myvars.data.time(1,1)));
        s=size(handles.myvars.data.time);
        handles.myvars.yseries(s(1)-1)=handles.myvars.yseries(s(1)-2);
        handles.myvars.yseries(s(1))=handles.myvars.yseries(s(1)-1);
end
handles.myvars.xseries=handles.myvars.data.time;
handles.myvars.xseries_title='Time';
handles.myvars.yseries_title=strcat(handles.myvars.curve0_title,{' of
'},handles.myvars.curve1_title,{' and '},handles.myvars.curve2_title);
handles.myvars.xlabel='Time [s]';
handles.myvars.ylabel=char(handles.myvars.yseries_title);
[handles] = plot_data(handles);
guidata(hObject,handles);
% --- Executes on selection change in curve_operations_curve2.
function curve_operations_curve2_Callback(hObject, eventdata, handles)
% hObject      handle to curve_operations_curve2 (see GCBO)
% Hints: contents = cellstr(get(hObject,'String')) returns
curve_operations_curve2 contents as cell array
%      contents{get(hObject,'Value')} returns selected item from
curve_operations_curve2
% --- Executes during object creation, after setting all properties.

```

```

function curve_operations_curve2_CreateFcn(hObject, eventdata, handles)
% hObject    handle to curve_operations_curve2 (see GCBO)
if ispc && isequal(get(hObject,'BackgroundColor'),
get(0,'defaultUicontrolBackgroundColor'))
    set(hObject,'BackgroundColor','white');
end
% --- Executes on button press in fit_data_checkbox.
function fit_data_checkbox_Callback(hObject, eventdata, handles)
% hObject    handle to fit_data_checkbox (see GCBO)
if get(hObject,'Value')==1
    set(handles.FFT_checkbox,'Enable','off')
else
    set(handles.FFT_checkbox,'Enable','on')
end
guidata(hObject,handles);
% Hint: get(hObject,'Value') returns toggle state of fit_data_checkbox
% --- Executes on selection change in data_fit_popupmenu.
function data_fit_popupmenu_Callback(hObject, eventdata, handles)
% hObject    handle to data_fit_popupmenu (see GCBO)
% Hints: contents = cellstr(get(hObject,'String')) returns data_fit_popupmenu
contents as cell array
%     contents{get(hObject,'Value')} returns selected item from
data_fit_popupmenu
% --- Executes during object creation, after setting all properties.
function data_fit_popupmenu_CreateFcn(hObject, eventdata, handles)
% hObject    handle to data_fit_popupmenu (see GCBO)
if ispc && isequal(get(hObject,'BackgroundColor'),
get(0,'defaultUicontrolBackgroundColor'))
    set(hObject,'BackgroundColor','white');
end
function x_spread_edit_Callback(hObject, eventdata, handles)
% hObject    handle to x_spread_edit (see GCBO)
% Hints: get(hObject,'String') returns contents of x_spread_edit as text
%     str2double(get(hObject,'String')) returns contents of x_spread_edit as
a double
% --- Executes during object creation, after setting all properties.
function x_spread_edit_CreateFcn(hObject, eventdata, handles)
% hObject    handle to x_spread_edit (see GCBO)
% Hint: edit controls usually have a white background on Windows.
if ispc && isequal(get(hObject,'BackgroundColor'),
get(0,'defaultUicontrolBackgroundColor'))
    set(hObject,'BackgroundColor','white');
end
function y_spread_edit_Callback(hObject, eventdata, handles)
% hObject    handle to y_spread_edit (see GCBO)
% Hints: get(hObject,'String') returns contents of y_spread_edit as text
%     str2double(get(hObject,'String')) returns contents of y_spread_edit as
a double
% --- Executes during object creation, after setting all properties.
function y_spread_edit_CreateFcn(hObject, eventdata, handles)
% hObject    handle to y_spread_edit (see GCBO)
% Hint: edit controls usually have a white background on Windows.
if ispc && isequal(get(hObject,'BackgroundColor'),
get(0,'defaultUicontrolBackgroundColor'))
    set(hObject,'BackgroundColor','white');
end
function x_mean_edit_Callback(hObject, eventdata, handles)
% hObject    handle to x_mean_edit (see GCBO)
% Hints: get(hObject,'String') returns contents of x_mean_edit as text

```

```

%         str2double(get(hObject,'String')) returns contents of x_mean_edit as a
double
% --- Executes during object creation, after setting all properties.
function x_mean_edit_CreateFcn(hObject, eventdata, handles)
% hObject    handle to x_mean_edit (see GCBO)
% Hint: edit controls usually have a white background on Windows.
if ispc && isequal(get(hObject,'BackgroundColor'),
get(0,'defaultUicontrolBackgroundColor'))
    set(hObject,'BackgroundColor','white');
end
% --- Executes on button press in plot_2nd_axis_pushbutton.
function plot_2nd_axis_pushbutton_Callback(hObject, eventdata, handles)
% hObject    handle to plot_2nd_axis_pushbutton (see GCBO)
% Check for plot to separate window
if get(handles.plot_sep_window_checkbox,'Value')==1
    handles.sep_figure=figure;
    set(0,'CurrentFigure',handles.sep_figure)
    set_axes_props(handles)
else
    axes(handles.axes1) % Forces the following plots to handles.axes1 axes
    cla reset
end
[handles] = get_xseries(handles);
[handles] = get_yseries(handles);
[handles] = get_y2series(handles);
[handles] = getPlotTickRanges(handles);
[hAx,hline1,hline2]=plotyy(handles.myvars.xseries,handles.myvars.yseries,handles
.myvars.xseries,handles.myvars.y2series);
% Apply Style
if get(handles.plot_style_checkbox,'Value') == 1
    set(hline1,'LineStyle','--')
    set(hline2,'LineStyle',':')
end
% Set xlimits
xlim(hAx(1),[min(handles.myvars.xseries) max(handles.myvars.xseries)]);
xlim(hAx(2),[min(handles.myvars.xseries) max(handles.myvars.xseries)]);
% Set ylimits
set(hAx(1),'YLim',[handles.myvars.yseries_range(1)
1.025*handles.myvars.yseries_range(2)]);
set(hAx(2),'YLim',[handles.myvars.y2_series_range(1)
1.025*handles.myvars.y2_series_range(2)]);
% Link both sets of x-axes so they do not show overlapping ticks,
% tickmarks, etc...
linkaxes(hAx,'x');
% Remove extra set of y1-axis tick marks on y2-axis (right-hand side)
set(hAx(1),'Box','off')
set(hAx(2),'Box','off')
% Replace x-axis on top of plot
set(hAx(2),'XTickLabel','', 'XAxisLocation','Top')
% Repair yticks
set(hAx(1),'YTickMode','auto')
set(hAx(2),'YTickMode','auto')
% Set xlabel
xlabel(handles.myvars.xlabel);
% Set y1-ylabel
ylabel(hAx(1),handles.myvars.ylabel);
% Set y2-ylabel
ylabel(hAx(2),handles.myvars.y2label);
% Set plot title
title(strcat('Combined Plot',' vs. ',handles.xstr{handles.xval}));

```

```

% Include Legend
if get(handles.inclspecattr, 'Value')==1
    val_1=get(handles.specimen_popupmenu, 'Value');
    if get(handles.run_no_checkbox, 'Value') == 0
        legend_title(1)={char(strcat(handles.myvars.specimen_attr(val_1-1,2),{'
- ',handles.myvars.yseries_title)});
        legend_title(2)={char(strcat(handles.myvars.specimen_attr(val_1-1,2),{'
- ',handles.myvars.y2series_title)});
    else
        legend_title(1)={char(strcat(handles.myvars.specimen_name,{'
- ',handles.myvars.specimen_attr(val_1-1,2),{'
- ',handles.myvars.yseries_title)});
        legend_title(2)={char(strcat(handles.myvars.specimen_name,{'
- ',handles.myvars.specimen_attr(val_1-1,2),{'
- ',handles.myvars.y2series_title)});
    end
else
    if get(handles.run_no_checkbox, 'Value') == 0
        legend_title(1)={char(handles.myvars.yseries_title)};
        legend_title(2)={char(handles.myvars.y2series_title)};
    else
        legend_title(1)={char(strcat(handles.myvars.specimen_name,{'
- ',handles.myvars.yseries_title)});
        legend_title(2)={char(strcat(handles.myvars.specimen_name,{'
- ',handles.myvars.y2series_title)});
    end
end
end
if get(handles.legend_checkbox, 'Value')==1
    LEG=legend([legend_title(1) legend_title(2)], 'Location', 'NorthWest');
    if get(handles.transparent_legend_checkbox, 'Value') == 1
        set(LEG, 'color', 'none')
    end
end
end
guidata(hObject, handles);
function [handles] = get_xseries(handles)
% Reset handles.myvars.xseries_time
handles.myvars.xseries_time=handles.myvars.data.time;
% Set x series data
handles.xval=get(handles.x_data_series, 'Value');
handles.xstr=get(handles.x_data_series, 'String');
% Set x Series Title
handles.myvars.xseries_title=handles.xstr{handles.xval};
switch handles.myvars.xseries_title
    case 'Time'
        handles.myvars.xseries=handles.myvars.data.time;
        handles.myvars.xlabel='Time [s]';
    case 'Vertical Displacement'
        handles.myvars.xseries=handles.myvars.data.vdisp;
        handles.myvars.xlabel='Vertical Displacement [mm]';
    case 'Vertical Velocity'
        handles.myvars.xseries=handles.myvars.data.vvel;
        handles.myvars.xlabel='Vertical Velocity [mm/s]';
    case 'Vertical Acceleration'
        handles.myvars.xseries=handles.myvars.data.vacc;
        handles.myvars.xlabel='Vertical Acceleration [mm/s^2]';
    case 'Vertical Force'
        handles.myvars.xseries=handles.myvars.data.vforc;
        handles.myvars.xlabel='Vertical Force [N]';
    case 'Vertical Impulse'
        handles.myvars.xseries=handles.myvars.data.vimpulse;

```

```

        handles.myvars.xlabel='Vertical Impulse [Ns]';
    case 'Vertical Work'
        handles.myvars.xseries=handles.myvars.data.vwork;
        handles.myvars.xlabel='Vertical Work [Nmm]';
    case 'Horizontal Displacement'
        handles.myvars.xseries=handles.myvars.data.hdisp;
        handles.myvars.xlabel='Horizontal Displacement [mm]';
    case 'Horizontal Velocity'
        handles.myvars.xseries=handles.myvars.data.hvel;
        handles.myvars.xlabel='Horizontal Velocity [mm/s]';
    case 'Horizontal Acceleration'
        handles.myvars.xseries=handles.myvars.data.hacc;
        handles.myvars.xlabel='Horizontal Displacement [mm/s^2]';
    case 'Horizontal Force 1'
        handles.myvars.xseries=handles.myvars.data.hforc1;
        handles.myvars.xlabel='Horizontal Force 1 [N]';
    case 'Horizontal Force 2'
        handles.myvars.xseries=handles.myvars.data.hforc2;
        handles.myvars.xlabel='Horizontal Force 2 [N]';
    case 'Total Horizontal Force'
        handles.myvars.xseries=handles.myvars.data.hforc_total;
        handles.myvars.xlabel='Horizontal Force Total [N]';
        case 'Horizontal Imuplse'
            handles.myvars.xseries=handles.myvars.data.himpulse;
            handles.myvars.xlabel='Horizontal Impulse [Ns]';
    case 'Horizontal Work'
        handles.myvars.xseries=handles.myvars.data.hwork;
        handles.myvars.xlabel='Horizontal Work [Nmm]';
    case 'Resultant Displacement'
        handles.myvars.xseries=handles.myvars.data.resultant_disp;
        handles.myvars.xlabel='Resultant Displacement [mm]';
    case 'Resultant Force'
        handles.myvars.xseries=handles.myvars.data.resultant_force;
        handles.myvars.xlabel='Resultant Force [N]';
    case 'Resultant Force Angle'
        handles.myvars.xseries=handles.myvars.data.resultant_force_angle;
        handles.myvars.xlabel='Degrees';
end
function [handles] = get_yseries(handles)
% Set y series data
handles.yval=get(handles.y_data_series,'Value');
handles.ystr=get(handles.y_data_series,'String');
% Set y Series Title
handles.myvars.yseries_title=handles.ystr(handles.yval);
switch handles.myvars.yseries_title
    case 'Time'
        handles.myvars.yseries=handles.myvars.data.time;
        handles.myvars.ylabel='Time [s]';
    case 'Vertical Displacement'
        handles.myvars.yseries=handles.myvars.data.vdisp;
        handles.myvars.ylabel='Vertical Displacement [mm]';
    case 'Vertical Velocity'
        handles.myvars.yseries=handles.myvars.data.vvel;
        handles.myvars.ylabel='Vertical Velocity [mm/s]';
    case 'Vertical Acceleration'
        handles.myvars.yseries=handles.myvars.data.vacc;
        handles.myvars.ylabel='Vertical Acceleration [mm/s^2]';
    case 'Vertical Force'
        handles.myvars.yseries=handles.myvars.data.vforc;
        handles.myvars.ylabel='Vertical Force [N]';
end

```

```

case 'Vertical Impulse'
    handles.myvars.yseries=handles.myvars.data.vimpulse;
    handles.myvars.ylabel='Vertical Impulse [Ns]';
case 'Vertical Work'
    handles.myvars.yseries=handles.myvars.data.vwork;
    handles.myvars.ylabel='Vertical Work [Nmm]';
case 'Horizontal Displacement'
    handles.myvars.yseries=handles.myvars.data.hdisp;
    handles.myvars.ylabel='Horizontal Displacement [mm]';
case 'Horizontal Velocity'
    handles.myvars.yseries=handles.myvars.data.hvel;
    handles.myvars.ylabel='Horizontal Velocity [mm/s]';
case 'Horizontal Acceleration'
    handles.myvars.yseries=handles.myvars.data.hacc;
    handles.myvars.ylabel='Horizontal Displacement [mm/s^2]';
case 'Horizontal Force 1'
    handles.myvars.yseries=handles.myvars.data.hforc1;
    handles.myvars.ylabel='Horizontal Force 1 [N]';
case 'Horizontal Force 2'
    handles.myvars.yseries=handles.myvars.data.hforc2;
    handles.myvars.ylabel='Horizontal Force 2 [N]';
case 'Total Horizontal Force'
    handles.myvars.yseries=handles.myvars.data.hforc_total;
    handles.myvars.ylabel='Horizontal Force Total [N]';
    case 'Horizontal Imuplse'
        handles.myvars.yseries=handles.myvars.data.himpulse;
        handles.myvars.ylabel='Horizontal Impulse [Ns]';
case 'Horizontal Work'
    handles.myvars.yseries=handles.myvars.data.hwork;
    handles.myvars.ylabel='Horizontal Work [Nmm]';
case 'Resultant Displacement'
    handles.myvars.yseries=handles.myvars.data.resultant_disp;
    handles.myvars.ylabel='Resultant Displacement [mm]';
case 'Resultant Force'
    handles.myvars.yseries=handles.myvars.data.resultant_force;
    handles.myvars.ylabel='Resultant Force [N]';
case 'Resultant Force Angle'
    handles.myvars.yseries=handles.myvars.data.resultant_force_angle;
    handles.myvars.ylabel='Degrees';
end
function [handles] = get_y2series(handles)
% Set y2 series data
handles.y2val=get(handles.y2_data_series,'Value');
handles.y2str=get(handles.y2_data_series,'String');
% Set y2 Series Title
handles.myvars.y2series_title=handles.y2str(handles.y2val);
switch handles.myvars.y2series_title
case 'Time'
    handles.myvars.y2series=handles.myvars.data.time;
    handles.myvars.y2label='Time [s]';
case 'Vertical Displacement'
    handles.myvars.y2series=handles.myvars.data.vdisp;
    handles.myvars.y2label='Vertical Displacement [mm]';
case 'Vertical Velocity'
    handles.myvars.y2series=handles.myvars.data.vvel;
    handles.myvars.y2label='Vertical Velocity [mm/s]';
case 'Vertical Acceleration'
    handles.myvars.y2series=handles.myvars.data.vacc;
    handles.myvars.y2label='Vertical Acceleration [mm/s^2]';
case 'Vertical Force'

```



```

        handles.myvars.y2series=handles.myvars.data.vforc;
        handles.myvars.y2label='Vertical Force [N]';
    case 'Vertical Impulse'
        handles.myvars.y2series=handles.myvars.data.vimpulse;
        handles.myvars.y2label='Vertical Impulse [Ns]';
    case 'Vertical Work'
        handles.myvars.y2series=handles.myvars.data.vwork;
        handles.myvars.y2label='Vertical Work [Nmm]';
    case 'Horizontal Displacement'
        handles.myvars.y2series=handles.myvars.data.hdisp;
        handles.myvars.y2label='Horizontal Displacement [mm]';
    case 'Horizontal Velocity'
        handles.myvars.y2series=handles.myvars.data.hvel;
        handles.myvars.y2label='Horizontal Velocity [mm/s]';
    case 'Horizontal Acceleration'
        handles.myvars.y2series=handles.myvars.data.hacc;
        handles.myvars.y2label='Horizontal Displacement [mm/s^2]';
    case 'Horizontal Force 1'
        handles.myvars.y2series=handles.myvars.data.hforc1;
        handles.myvars.y2label='Horizontal Force 1 [N]';
    case 'Horizontal Force 2'
        handles.myvars.y2series=handles.myvars.data.hforc2;
        handles.myvars.y2label='Horizontal Force 2 [N]';
    case 'Total Horizontal Force'
        handles.myvars.y2series=handles.myvars.data.hforc_total;
        handles.myvars.y2label='Horizontal Force Total [N]';
        case 'Horizontal Imuplse'
            handles.myvars.y2series=handles.myvars.data.himpulse;
            handles.myvars.y2label='Horizontal Impulse [Ns]';
    case 'Horizontal Work'
        handles.myvars.y2series=handles.myvars.data.hwork;
        handles.myvars.y2label='Horizontal Work [Nmm]';
    case 'Resultant Displacement'
        handles.myvars.y2series=handles.myvars.data.resultant_disp;
        handles.myvars.y2label='Resultant Displacement [mm]';
    case 'Resultant Force'
        handles.myvars.y2series=handles.myvars.data.resultant_force;
        handles.myvars.y2label='Resultant Force [N]';
    case 'Resultant Force Angle'
        handles.myvars.y2series=handles.myvars.data.resultant_force_angle;
        handles.myvars.y2label='Degrees';
end
% -----
function uipushtool2_ClickedCallback(hObject, eventdata, handles)
% hObject    handle to uipushtool2 (see GCBO)
% --- Executes on button press in refit_pushbutton.
function refit_pushbutton_Callback(hObject, eventdata, handles)
% hObject    handle to refit_pushbutton (see GCBO)
fit_curve(handles);
guidata(hObject,handles);
function fit_curve(handles)
if get(handles.fit_data_checkbox,'Value')==1
    clear x y
    y=handles.myvars.yseries(handles.myvars.templow:handles.myvars.temphigh);
    x=handles.myvars.xseries(handles.myvars.templow:handles.myvars.temphigh);
    data_fit_val=get(handles.data_fit_popupmenu,'Value');
    data_fit_str=get(handles.data_fit_popupmenu,'String');
    switch data_fit_str{data_fit_val}
        case 'linear'
            fit_type='poly1';

```

```

        case 'quadratic'
            fit_type='poly2';
        case 'cubic'
            fit_type='poly3';
        case 'exp1'
            fit_type='exp1';
        case 'exp2'
            fit_type='exp2';
        case 'power1'
            fit_type='power1';
        case 'power2'
            fit_type='power2';
        case 'poly4'
            fit_type='poly4';
        case 'poly5'
            fit_type='poly5';
    end
    [curve1, gof1]=fit(x,y,fit_type);
    % Plot Fit
    axes(handles.axes1) % Forces the following plots to handles.axes1 axes
    plot(curve1,x,y)
    LEG=legend('Location','NorthWest');
    if get(handles.transparent_legend_checkbox,'Value') == 1
        set(LEG,'color','none')
    end
    covals=coeffvalues(curve1);
    rsquared=gof1.rsquare;
    switch data_fit_str{data_fit_val}
        case 'linear'
            eq=strcat('Y',{ ' ' }, '=', { ' ' }, num2str(covals(1)), 'x +', { ' ' }, num2str(covals(2)), '\newlineR^2', { ' ' }, '=', { ' ' }, num2str(rsquared));
        case 'quadratic'
            eq=strcat('Y',{ ' ' }, '=', { ' ' }, num2str(covals(1)), 'x^2 +', { ' ' }, num2str(covals(2)), 'x +', { ' ' }, num2str(covals(3)), '\newlineR^2', { ' ' }, '=', { ' ' }, num2str(rsquared));
        case 'cubic'
            eq=strcat('Y',{ ' ' }, '=', { ' ' }, num2str(covals(1)), 'x^3 +', { ' ' }, num2str(covals(2)), 'x^2 +', { ' ' }, num2str(covals(3)), 'x +', { ' ' }, num2str(covals(4)), '\newlineR^2', { ' ' }, '=', { ' ' }, num2str(rsquared));
        case 'exp1'
            eq=strcat('Y',{ ' ' }, '=', { ' ' }, num2str(covals(1)), '*exp^', strcat('{', num2str(covals(2)), '*x)'), '\newlineR^2', { ' ' }, '=', { ' ' }, num2str(rsquared));
        case 'exp2'
            eq=strcat('Y',{ ' ' }, '=', { ' ' }, num2str(covals(1)), '*exp^', strcat('{', num2str(covals(2)), '*x)'), '\newlineR^2', { ' ' }, '=', { ' ' }, num2str(rsquared));
        case 'power1'
            eq=strcat('Y',{ ' ' }, '=', { ' ' }, num2str(covals(1)), '*x^', strcat('{', num2str(covals(2)), '}'), '\newlineR^2', { ' ' }, '=', { ' ' }, num2str(rsquared));
        case 'power2'
            eq=strcat('Y',{ ' ' }, '=', { ' ' }, num2str(covals(1)), '*x^', strcat('{', num2str(covals(2)), '}'), { ' ' }, '+', { ' ' }, num2str(covals(3)), '\newlineR^2', { ' ' }, '=', { ' ' }, num2str(rsquared));
        case 'poly4'
            eq=strcat('Y',{ ' ' }, '=', { ' ' }, num2str(covals(1)), 'x^4 +', { ' ' }, num2str(covals(2)), 'x^3 +', { ' ' }, num2str(covals(3)), 'x^2 +', { ' ' }, num2str(covals(4)), 'x +', { ' ' }, num2str(rsquared));
    end

```

```

'},num2str(covals(4)),'x +',{ ' '},num2str(covals(5)),'\newlineR^2',{ ' '},'={',{ '
'},num2str(rsquared));
    case 'poly5'
        eq=strcat('Y',{ ' '},'={',{ ' '},num2str(covals(1)),'x^5 +',{ '
'},num2str(covals(2)),'x^4 +',{ ' '},num2str(covals(3)),'x^3 +',{ '
'},num2str(covals(4)),'x^2 +',{ ' '},num2str(covals(5)),'x +',{ '
'},num2str(covals(6)),'\newlineR^2',{ ' '},'={',{ ' '},num2str(rsquared));
    end
end
text(handles.myvars.start_x+(handles.myvars.end_x-
handles.myvars.start_x)*.1,min(y)+(max(y)-min(y))* .9,eq);
function [handles] = create_derived_data(handles)
    % Create derived data

%=====
=====
    % Get Total Horizontal Force

handles.myvars.data.hforc_total=handles.myvars.data.hforc1+handles.myvars.data.h
forc2;
    % Get Resultant Displacement
    handles.myvars.data.resultant_disp=sqrt(handles.myvars.data.vdisp.^2 +
handles.myvars.data.hdisp.^2);
    % Get Resultant Force and Angle
    handles.myvars.data.resultant_force=sqrt(handles.myvars.data.vforc.^2 +
handles.myvars.data.hforc_total.^2);
    %
handles.myvars.data.resultant_force_angle=atan2(handles.myvars.data.vforc./handl
es.myvars.data.hforc_total);

handles.myvars.data.resultant_force_angle=atan2d(handles.myvars.data.vforc,handl
es.myvars.data.hforc_total);
    % Derive Data
    % Integrate Data

handles.myvars.data.vimpulse=cumtrapz(handles.myvars.data.time,handles.myvars.da
ta.vforc);

handles.myvars.data.vwork=cumtrapz(handles.myvars.data.vdisp,handles.myvars.data
.vforc);

handles.myvars.data.himpulse=cumtrapz(handles.myvars.data.time,handles.myvars.da
ta.hforc_total);

handles.myvars.data.hwork=cumtrapz(handles.myvars.data.hdisp,handles.myvars.data
.hforc_total);
    % Differentiate Data
    % Vertical Velocity

handles.myvars.data.vvel=diff((handles.myvars.data.vdisp)/(handles.myvars.data.t
ime(2,1)-handles.myvars.data.time(1,1)));
    s=size(handles.myvars.data.time);
    handles.myvars.data.vvel(s(1))=handles.myvars.data.vvel(s(1)-1);
    % Horizontal Velocity

handles.myvars.data.hvel=diff((handles.myvars.data.hdisp)/(handles.myvars.data.t
ime(2,1)-handles.myvars.data.time(1,1)));
    s=size(handles.myvars.data.time);
    handles.myvars.data.hvel(s(1))=handles.myvars.data.hvel(s(1)-1);
    % 2nd Derivative of Data

```

```

        % Vertical Acceleration
        diff1=diff((handles.myvars.data.vdisp)/(handles.myvars.data.time(2,1)-
handles.myvars.data.time(1,1)));
        handles.myvars.data.vacc=diff((diff1)/(handles.myvars.data.time(2,1)-
handles.myvars.data.time(1,1)));
        s=size(handles.myvars.data.time);
        handles.myvars.data.vacc(s(1)-1)=handles.myvars.data.vacc(s(1)-2);
        handles.myvars.data.vacc(s(1))=handles.myvars.data.vacc(s(1)-1);
        % Horizontal Acceleration
        diff1=diff((handles.myvars.data.hdisp)/(handles.myvars.data.time(2,1)-
handles.myvars.data.time(1,1)));
        handles.myvars.data.hacc=diff((diff1)/(handles.myvars.data.time(2,1)-
handles.myvars.data.time(1,1)));
        s=size(handles.myvars.data.time);
        handles.myvars.data.hacc(s(1)-1)=handles.myvars.data.hacc(s(1)-2);
        handles.myvars.data.hacc(s(1))=handles.myvars.data.hacc(s(1)-1);

%=====
=====
function [handles] = clear_derived_data(handles)
% Clear derived data
if isfield(handles.myvars.data,'vwork') == 1

%=====
=====
    % Clear Total Horizontal Force
    handles.myvars.data=rmfield(handles.myvars.data,'hforc_total');
    % Get Resultant Force and Angle
    handles.myvars.data=rmfield(handles.myvars.data,'resultant_disp');
    % Get Resultant Force and Angle
    handles.myvars.data=rmfield(handles.myvars.data,'resultant_force');
    handles.myvars.data=rmfield(handles.myvars.data,'resultant_force_angle');
    % Derived Data
    % Integrated Data
    handles.myvars.data=rmfield(handles.myvars.data,'vimpulse');
    handles.myvars.data=rmfield(handles.myvars.data,'vwork');
    handles.myvars.data=rmfield(handles.myvars.data,'himpulse');
    handles.myvars.data=rmfield(handles.myvars.data,'hwork');
    % Differentiated Data
    % Vertical Velocity
    handles.myvars.data=rmfield(handles.myvars.data,'vvel');
    % Horizontal Velocity
    handles.myvars.data=rmfield(handles.myvars.data,'hvel');
    % 2nd Derivative of Data
    % Vertical Acceleration
    handles.myvars.data=rmfield(handles.myvars.data,'vacc');
    % Horizontal Acceleration
    handles.myvars.data=rmfield(handles.myvars.data,'hacc');

%=====
=====
else
end
function [handles] = tare_data(handles)
    handles.myvars.data.time=handles.myvars.data.time-
handles.myvars.data.timetare;
    handles.myvars.data.vdisp=handles.myvars.data.vdisp-
handles.myvars.data.vdisptare;
    handles.myvars.data.vforc=handles.myvars.data.vforc-
handles.myvars.data.vforctare;

```

```

        handles.myvars.data.hdisp=handles.myvars.data.hdisp-
handles.myvars.data.hdisptare;
        handles.myvars.data.hforc1=handles.myvars.data.hforc1-
handles.myvars.data.hforc1tare;
        handles.myvars.data.hforc2=handles.myvars.data.hforc2-
handles.myvars.data.hforc2tare;
function [handles] = untare_data(handles)

handles.myvars.data.time=handles.myvars.data.time+handles.myvars.data.timetare;

handles.myvars.data.vdisp=handles.myvars.data.vdisp+handles.myvars.data.vdisptare;

handles.myvars.data.vforc=handles.myvars.data.vforc+handles.myvars.data.vforctare;

handles.myvars.data.hdisp=handles.myvars.data.hdisp+handles.myvars.data.hdisptare;

handles.myvars.data.hforc1=handles.myvars.data.hforc1+handles.myvars.data.hforc1tare;

handles.myvars.data.hforc2=handles.myvars.data.hforc2+handles.myvars.data.hforc2tare;
function set_axes_props(handles)
    % Change default axes fonts.
    set(handles.sep_figure,'DefaultAxesFontName', 'Times New Roman')
    set(handles.sep_figure,'DefaultAxesFontSize', 12)
    % Change default text fonts.
    set(handles.sep_figure,'DefaultTextFontname', 'Times New Roman')
    set(handles.sep_figure,'DefaultTextFontSize', 12)
    % Set up figure for paper printing
    set(handles.sep_figure,'PaperUnits','centimeters')
    xSize=16;
    ySize=8;
    xLeft=(21.6-xSize)/2;
    yTop=(27.9-ySize)/2;
    set(handles.sep_figure,'PaperPosition',[xLeft yTop xSize ySize])
    set(handles.sep_figure,'Position',[450 450 xSize*50 ySize*50])
    xAxisPos=1.5/xSize;
    yAxisPos=1.0/ySize;
    xAxisWidth=(xSize-3)/xSize;
    yAxisHeight=(ySize-1.75)/ySize;
    axes('position',[xAxisPos yAxisPos xAxisWidth yAxisHeight])
% --- Executes on button press in save_as_mat.
function save_as_mat_Callback(hObject, eventdata, handles)
% hObject    handle to save_as_mat (see GCBO)
fname=fullfile(handles.myvars.pathname,strcat(handles.myvars.specimen_name,'.mat'
));
save_data=handles.myvars.data;
f = fieldnames(save_data);
v = struct2cell(save_data);
for i=1:size(f,1)
    f(i)=strcat(cellstr(f(i)),'_',handles.myvars.specimen_name);
end
save_data = cell2struct(v,f);
disp(save_data)
save(fname, '-struct', 'save_data');
% --- Executes on button press in plot3_checkbox.
function plot3_checkbox_Callback(hObject, eventdata, handles)

```

```

% hObject    handle to plot3_checkbox (see GCBO)
% Hint: get(hObject,'Value') returns toggle state of plot3_checkbox
if get(hObject,'Value')==1
    set(handles.text23,'String','Applicate (z)')
    set(handles.plot_button,'String','Plot 3D')
    %     set(handles.plot_style_checkbox,'Value',0);
    %     set(handles.plot_style_checkbox,'Enable','off');
else
    set(handles.text23,'String','2nd Ordinate (y2)')
    set(handles.plot_button,'String','Plot')
    %     set(handles.plot_style_checkbox,'Enable','on');
end
guidata(hObject,handles);
% --- Executes on selection change in specimen_popupmenu.
function specimen_popupmenu_Callback(hObject, eventdata, handles)
% hObject    handle to specimen_popupmenu (see GCBO)
% Hints: contents = cellstr(get(hObject,'String')) returns specimen_popupmenu
%           contents as cell array
%           contents{get(hObject,'Value')} returns selected item from
%           specimen_popupmenu
if get(handles.x_origin_checkbox,'Value') == 1
    set(handles.x_origin_checkbox,'Value',0)
end
% Clear old data
if isfield(handles.myvars,'data') == 1
    handles.myvars=rmfield(handles.myvars,'data');
end
axes(handles.axes1)
% cla reset           % Clear axis
% set(handles.holdon_checkbox,'Value',0);
% Change to specimen directory
cd(handles.myvars.default_dir);
oper_val=get(hObject,'Value');
oper_str=get(hObject,'String');
handles.myvars.specimen_name=oper_str{oper_val};
handles.myvars.pathname=fullfile(handles.myvars.default_dir,handles.myvars.specimen_name);
handles.myvars.filename='specimen.dat';
handles=importDataFcn(handles);
guidata(hObject, handles);
% --- Executes during object creation, after setting all properties.
function specimen_popupmenu_CreateFcn(hObject, eventdata, handles)
% hObject    handle to specimen_popupmenu (see GCBO)
if ispc && isequal(get(hObject,'BackgroundColor'),
get(0,'defaultUiControlBackgroundColor'))
    set(hObject,'BackgroundColor','white');
end
function [handles] = importDataFcn(handles)
% Function to import data from specimen.dat files
try
    % Import ASCII data from the data file specimen.dat

datatemp=importdata(fullfile(handles.myvars.pathname,handles.myvars.filename));
% Place data in a struct
handles.myvars.data.time=datatemp.data(:,1);
handles.myvars.data.vdisp=datatemp.data(:,2);
handles.myvars.data.vforc=datatemp.data(:,3);
handles.myvars.data.hdisp=datatemp.data(:,4);
handles.myvars.data.hforc1=datatemp.data(:,5);
handles.myvars.data.hforc2=datatemp.data(:,6);

```

```

clear datatemp;
% Catch Error in data import
catch err
    % Display Error Message in Input Dir Edit Box
    set(handles.specimen_popupmenu,'String','Problem');
    errordlg('Either an internal error has occurred or the specimen.dat file is
missing or there is a problem with the specimen.dat file in this directory.
Please check them and try again.','Input Error');
    rethrow(err);
end
%=====
% Manipulate raw imported data
%=====
% Make vforc and vdisp positive
handles.myvars.data.vdisp=-1.*handles.myvars.data.vdisp;
handles.myvars.data.vforc=-1.*handles.myvars.data.vforc;
% Extract initial values
handles.myvars.data.timetare=handles.myvars.data.time(1,1);
handles.myvars.data.vdisptare=handles.myvars.data.vdisp(1,1);
handles.myvars.data.vforc tare=handles.myvars.data.vforc(1,1);
handles.myvars.data.hdisptare=handles.myvars.data.hdisp(1,1);
handles.myvars.data.hforc1tare=handles.myvars.data.hforc1(1,1);
handles.myvars.data.hforc2tare=handles.myvars.data.hforc2(1,1);
% Display Data Sampling Rate
handles.myvars.data_sampling_rate=round(1/(handles.myvars.data.time(2,1)-
handles.myvars.data.time(1,1)));
set(handles.sample_rate_statictext,'String',num2str(handles.myvars.data_sampling
_rate));
% Check for tare data
if get(handles.tare_by_initial_checkbox,'Value')==1
    [handles] = clear_derived_data(handles);
    [handles] = tare_data(handles);
    [handles] = create_derived_data(handles);
else
    % Create Derived Data
    [handles] = clear_derived_data(handles);
    [handles] = create_derived_data(handles);
end
%=====
% Change to program directory
cd(handles.myvars.program_dir);
function [handles] = plot_data(handles)
% Check for existing plotcount
test_plotcount=isfield(handles.myvars,'plotcount');
if test_plotcount==0
    handles.myvars.plotcount=0;
end
if get(handles.holdon_checkbox,'Value')==0
    [handles]=clear_plot(handles);
end
[handles] = getPlotTickRanges(handles);
% Plot Data
if get(handles.plot_sep_window_checkbox,'Value')==1
    handles.sep_figure=figure;
    set(0,'CurrentFigure',handles.sep_figure)
    set_axes_props(handles)
else
    axes(handles.axes1) % Forces the following plots to handles.axes1 axes
end
% Check for "hold on"

```

```

if get(handles.holdon_checkbox, 'Value')==1 && test_plotcount==0
    hold on
    handles.myvars.plotcount=0;
elseif get(handles.holdon_checkbox, 'Value')==1 && test_plotcount~=0
    hold on
    handles.myvars.plotcount=handles.myvars.plotcount+1;
else
    hold off
    cla reset
    set(handles.holdon_checkbox, 'Value', 0);
    handles.myvars.plotcount=0;
end
if handles.myvars.plotcount==0 || get(handles.holdon_checkbox, 'Value')==0
    line_color='b';
    line_style='--';
    line_width=1;
elseif handles.myvars.plotcount==1
    line_color='r';
    line_style='-.';
    line_width=1;
elseif handles.myvars.plotcount==2
    line_color='g';
    line_style='-';
    line_width=1;
elseif handles.myvars.plotcount==3
    line_color='k';
    line_style=':.';
    line_width=1;
elseif handles.myvars.plotcount==4
    line_color='m';
    line_style='--';
    line_width=2;
elseif handles.myvars.plotcount==5
    line_color='c';
    line_style='-.';
    line_width=2;
else
    line_color='y';
    line_style=':.';
    line_width=2;
end
if get(handles.plot3_checkbox, 'Value')==0
    if get(handles.plot_style_checkbox, 'Value')==1

plot(handles.myvars.xseries, handles.myvars.yseries, strcat(line_color, line_style)
, strcat('LineWidth'), line_width);
        else

plot(handles.myvars.xseries, handles.myvars.yseries, line_color, strcat('LineWidth'
), line_width);
        end
    else
        if get(handles.plot_style_checkbox, 'Value')==1

plot3(handles.myvars.xseries, handles.myvars.yseries, handles.myvars.y2series, strc
at(line_color, line_style), strcat('LineWidth'), line_width);
        else

plot3(handles.myvars.xseries, handles.myvars.yseries, handles.myvars.y2series, strc
at('LineWidth'), line_width);

```



```

        end
    end
    % Set xlims
    xlim([handles.myvars.xseries_range(1) handles.myvars.xseries_range(2)]);
    % Set ylims
    ylim([handles.myvars.yseries_range(1) 1.025*handles.myvars.yseries_range(2)]);
    % Set zlimits
    zlim([handles.myvars.y2_series_range(1)
1.025*handles.myvars.y2_series_range(2)]);
    % Set xlabel
    xlabel(handles.myvars.xlabel);
    % Set ylabel
    ylabel(handles.myvars.ylabel);
    % Set zlabel
    zlabel(handles.myvars.y2label);
    % Set plot title
    % title(strcat(handles.myvars.specimen_name,{'
'},handles.myvars.yseries_title,{' vs. '},handles.myvars.xseries_title));
    % title(strcat(handles.myvars.ylabel,{' vs. '},handles.myvars.xlabel));
    title(strcat(handles.myvars.yseries_title,{' vs.
'},handles.myvars.xseries_title));
    % Include Legend
    if get(handles.inclspecattr,'Value')==1
        val_1=get(handles.specimen_popupmenu,'Value');
        if get(handles.run_no_checkbox,'Value') == 0

handles.myvars.legend_title(handles.myvars.plotcount+1)={char(strcat(handles.myv
ars.specimen_attr(val_1-1,2),{' - '},handles.myvars.yseries_title));
            else

handles.myvars.legend_title(handles.myvars.plotcount+1)={char(strcat(handles.myv
ars.specimen_name,{' - '},handles.myvars.specimen_attr(val_1-1,2),{' -
'},handles.myvars.yseries_title));
            end
        else
            if get(handles.run_no_checkbox,'Value') == 0

handles.myvars.legend_title(handles.myvars.plotcount+1)={char(handles.myvars.yse
ries_title));
            else

handles.myvars.legend_title(handles.myvars.plotcount+1)={char(strcat(handles.myv
ars.specimen_name,{' - '},handles.myvars.yseries_title));
            end
        end
    end
    % Display Legend
    if get(handles.legend_checkbox,'Value')==1
        LEG=legend(gca,handles.myvars.legend_title{:},'Location','NorthWest');
        if get(handles.transparent_legend_checkbox,'Value') == 1
            set(LEG,'color','none')
        end
    end
end
% --- Executes on button press in raise_existing_plot_button.
function raise_existing_plot_button_Callback(hObject, eventdata, handles)
% hObject    handle to raise_existing_plot_button (see GCBO)
% Remove legend to avoid problem raising figure
if get(handles.legend_checkbox,'Value')==1
    legend('off')
end
h1 = findobj(gcf,'type','axes'); % Find the axes object in the GUI

```

```

h2=figure;
s = copyobj(h1,h2); % Copy axes object h into figure f1
set(gcf,'PaperUnits','centimeters')
set(gcf,'PaperPosition',[2.80000000000000,9.95000000000000,16,8])
set(gcf,'Position',[450,450,800,400])
set(gca,'FontName','Times New Roman')
set(gca,'Units','normalized')
set(gca,'OuterPosition',[-
0.0425403225806452,0.0150000000000000,1.04838709677419,0.963144171779141])
set(gca,'Position',[0.0937500000000000,0.125000000000000,0.812500000000000,0.781
250000000000])
set(findall(gcf,'type','text'),'FontName','Times New Roman')
% Reapply Legend
if get(handles.legend_checkbox,'Value')==1
    LEG=legend(gca,handles.myvars.legend_title{:},'Location','Best');
    if get(handles.transparent_legend_checkbox,'Value') == 1
        set(LEG,'color','none')
    end
    LEG_text=findobj(LEG,'type','text');
    %set(LEG_text,'FontSize',10);
end
% --- Executes on button press in legend_checkbox.
function legend_checkbox_Callback(hObject, eventdata, handles)
% hObject handle to legend_checkbox (see GCBO)
% Hint: get(hObject,'Value') returns toggle state of legend_checkbox
if get(hObject,'Value') == 1
    set(handles.transparent_legend_checkbox,'Enable','on')
    set(handles.inclspecattr,'Enable','on')
    set(handles.run_no_checkbox,'Enable','on')
else
    set(handles.transparent_legend_checkbox,'Enable','off')
    set(handles.inclspecattr,'Enable','off')
    set(handles.run_no_checkbox,'Enable','off')
end
guidata(hObject, handles);
function [handles] = clear_plot(handles)
axes(handles.axes1)
zoom off
cla
reset(handles.axes1)
if isfield(handles.myvars,'plotcount')
    handles.myvars=rmfield(handles.myvars,'plotcount');
end
if isfield(handles.myvars,'xseries_range')
    handles.myvars=rmfield(handles.myvars,'xseries_range');
    handles.myvars=rmfield(handles.myvars,'yseries_range');
    handles.myvars=rmfield(handles.myvars,'y2_series_range');
end
if isfield(handles.myvars,'legend_title')
    handles.myvars=rmfield(handles.myvars,'legend_title');
end
legend('off');
% set(handles.holdon_checkbox,'Value',0);
function [handles] = set_slider_values(handles)
data_range=size(handles.myvars.xseries);
set(handles.x1_index_slider,'Min',1);
set(handles.x1_index_slider,'Max',data_range(1));
set(handles.x1_index_slider,'Value',1);
set(handles.x2_index_slider,'Min',1);
set(handles.x2_index_slider,'Max',data_range(1));

```

```

set(handles.x2_index_slider, 'Value', data_range(1));
set(handles.x1min_slider_edit, 'String', num2str(get(handles.x1_index_slider, 'Min'
)));
set(handles.x1max_slider_edit, 'String', num2str(get(handles.x1_index_slider, 'Max'
)));
set(handles.x1val_slider_edit, 'String', num2str(get(handles.x1_index_slider, 'Valu
e')));
set(handles.x2min_slider_edit, 'String', num2str(get(handles.x2_index_slider, 'Min'
)));
set(handles.x2max_slider_edit, 'String', num2str(get(handles.x2_index_slider, 'Max'
)));
set(handles.x2val_slider_edit, 'String', num2str(get(handles.x2_index_slider, 'Valu
e')));
% --- Executes on button press in inclspecattr.
function inclspecattr_Callback(hObject, eventdata, handles)
% hObject    handle to inclspecattr (see GCBO)
% Hint: get(hObject, 'Value') returns toggle state of inclspecattr
% --- Executes on button press in refine_plot_pushbutton.
function refine_plot_pushbutton_Callback(hObject, eventdata, handles)
% hObject    handle to refine_plot_pushbutton (see GCBO)
if get(handles.refine_by_sliders_checkbox, 'Value')==0
    [quick_x, quick_y]=ginput(2);                % Interactive user peak
selection with mouse
    if (quick_x(1)<min(handles.myvars.xseries))    % Ensure selection is within
data boundaries
        quick_x(1)=min(handles.myvars.xseries);
    else
    end
    if (quick_x(2)>max(handles.myvars.xseries))    % Ensure selection is within
data boundaries
        quick_x(2)=max(handles.myvars.xseries);
    else
    end
    handles.myvars.start_x=quick_x(1);
    handles.myvars.end_x=quick_x(2);
    [I1 I2] = find (handles.myvars.xseries>=handles.myvars.start_x); % Find
matrix coords less than 1st mouse click
    handles.myvars.templow = min(I1);                % Get matrix
coords of 1st mouse click
    [J1 J2] = find (handles.myvars.xseries<=handles.myvars.end_x);    % Find
matrix coords greater than 2nd mouse click
    handles.myvars.temphigh = max(J1);                % Get matrix
coords of 2nd mouse click
else
handles.myvars.templow=floor(str2num(get(handles.x1val_slider_edit, 'String')))

handles.myvars.temphigh=floor(str2num(get(handles.x2val_slider_edit, 'String')))
end
handles.myvars.xseries=handles.myvars.xseries(handles.myvars.templow:handles.myv
ars.temphigh);
handles.myvars.yseries=handles.myvars.yseries(handles.myvars.templow:handles.myv
ars.temphigh);
% Create dummy time to match handles.myvars.xseries indices
handles.myvars.xseries_time=handles.myvars.data.time(handles.myvars.templow:hand
les.myvars.temphigh);
[handles] = set_slider_values(handles);
[handles] = plot_data(handles);
guidata(hObject, handles);
% --- Executes on slider movement.

```

```

function x1_index_slider_Callback(hObject, eventdata, handles)
% hObject      handle to x1_index_slider (see GCBO)
% Hints: get(hObject,'Value') returns position of slider
%           get(hObject,'Min') and get(hObject,'Max') to determine range of slider
set(handles.x1val_slider_edit,'String',floor(get(hObject,'Value')));
% --- Executes during object creation, after setting all properties.
function x1_index_slider_CreateFcn(hObject, eventdata, handles)
% hObject      handle to x1_index_slider (see GCBO)
% Hint: slider controls usually have a light gray background.
if isequal(get(hObject,'BackgroundColor'),
get(0,'defaultUicontrolBackgroundColor'))
    set(hObject,'BackgroundColor',[.9 .9 .9]);
end
% --- Executes on slider movement.
function x2_index_slider_Callback(hObject, eventdata, handles)
% hObject      handle to x2_index_slider (see GCBO)
% Hints: get(hObject,'Value') returns position of slider
%           get(hObject,'Min') and get(hObject,'Max') to determine range of slider
set(handles.x2val_slider_edit,'String',floor(get(hObject,'Value')));
% --- Executes during object creation, after setting all properties.
function x2_index_slider_CreateFcn(hObject, eventdata, handles)
% hObject      handle to x2_index_slider (see GCBO)
% Hint: slider controls usually have a light gray background.
if isequal(get(hObject,'BackgroundColor'),
get(0,'defaultUicontrolBackgroundColor'))
    set(hObject,'BackgroundColor',[.9 .9 .9]);
end
% --- Executes on button press in refine_by_sliders_checkbox.
function refine_by_sliders_checkbox_Callback(hObject, eventdata, handles)
% hObject      handle to refine_by_sliders_checkbox (see GCBO)
% Hint: get(hObject,'Value') returns toggle state of refine_by_sliders_checkbox
function x1min_slider_edit_Callback(hObject, eventdata, handles)
% hObject      handle to x1min_slider_edit (see GCBO)
% Hints: get(hObject,'String') returns contents of x1min_slider_edit as text
%           str2double(get(hObject,'String')) returns contents of x1min_slider_edit
as a double
set(handles.x1_index_slider,'Min',round(str2num(get(hObject,'String')));
% --- Executes during object creation, after setting all properties.
function x1min_slider_edit_CreateFcn(hObject, eventdata, handles)
% hObject      handle to x1min_slider_edit (see GCBO)
% Hint: edit controls usually have a white background on Windows.
if ispc && isequal(get(hObject,'BackgroundColor'),
get(0,'defaultUicontrolBackgroundColor'))
    set(hObject,'BackgroundColor','white');
end
function x1max_slider_edit_Callback(hObject, eventdata, handles)
% hObject      handle to x1max_slider_edit (see GCBO)
% Hints: get(hObject,'String') returns contents of x1max_slider_edit as text
%           str2double(get(hObject,'String')) returns contents of x1max_slider_edit
as a double
set(handles.x1_index_slider,'Max',round(str2num(get(hObject,'String')));
% --- Executes during object creation, after setting all properties.
function x1max_slider_edit_CreateFcn(hObject, eventdata, handles)
% hObject      handle to x1max_slider_edit (see GCBO)
% Hint: edit controls usually have a white background on Windows.
if ispc && isequal(get(hObject,'BackgroundColor'),
get(0,'defaultUicontrolBackgroundColor'))
    set(hObject,'BackgroundColor','white');
end
function x1val_slider_edit_Callback(hObject, eventdata, handles)

```

```

% hObject    handle to x1val_slider_edit (see GCBO)
% Hints: get(hObject,'String') returns contents of x1val_slider_edit as text
%          str2double(get(hObject,'String')) returns contents of x1val_slider_edit
as a double
set(handles.x1_index_slider,'Value',round(str2num(get(hObject,'String'))));
% --- Executes during object creation, after setting all properties.
function x1val_slider_edit_CreateFcn(hObject, eventdata, handles)
% hObject    handle to x1val_slider_edit (see GCBO)
% Hint: edit controls usually have a white background on Windows.
if ispc && isequal(get(hObject,'BackgroundColor'),
get(0,'defaultUicontrolBackgroundColor'))
    set(hObject,'BackgroundColor','white');
end
function x2min_slider_edit_Callback(hObject, eventdata, handles)
% hObject    handle to x2min_slider_edit (see GCBO)
% Hints: get(hObject,'String') returns contents of x2min_slider_edit as text
%          str2double(get(hObject,'String')) returns contents of x2min_slider_edit
as a double
set(handles.x2_index_slider,'Min',round(str2num(get(hObject,'String'))));
% --- Executes during object creation, after setting all properties.
function x2min_slider_edit_CreateFcn(hObject, eventdata, handles)
% hObject    handle to x2min_slider_edit (see GCBO)
% Hint: edit controls usually have a white background on Windows.
if ispc && isequal(get(hObject,'BackgroundColor'),
get(0,'defaultUicontrolBackgroundColor'))
    set(hObject,'BackgroundColor','white');
end
function x2max_slider_edit_Callback(hObject, eventdata, handles)
% hObject    handle to x2max_slider_edit (see GCBO)
% Hints: get(hObject,'String') returns contents of x2max_slider_edit as text
%          str2double(get(hObject,'String')) returns contents of x2max_slider_edit
as a double
set(handles.x2_index_slider,'Max',round(str2num(get(hObject,'String'))));
% --- Executes during object creation, after setting all properties.
function x2max_slider_edit_CreateFcn(hObject, eventdata, handles)
% hObject    handle to x2max_slider_edit (see GCBO)
% Hint: edit controls usually have a white background on Windows.
if ispc && isequal(get(hObject,'BackgroundColor'),
get(0,'defaultUicontrolBackgroundColor'))
    set(hObject,'BackgroundColor','white');
end
function x2val_slider_edit_Callback(hObject, eventdata, handles)
% hObject    handle to x2val_slider_edit (see GCBO)
% Hints: get(hObject,'String') returns contents of x2val_slider_edit as text
%          str2double(get(hObject,'String')) returns contents of x2val_slider_edit
as a double
set(handles.x2_index_slider,'Value',round(str2num(get(hObject,'String'))));
% --- Executes during object creation, after setting all properties.
function x2val_slider_edit_CreateFcn(hObject, eventdata, handles)
% hObject    handle to x2val_slider_edit (see GCBO)
% Hint: edit controls usually have a white background on Windows.
if ispc && isequal(get(hObject,'BackgroundColor'),
get(0,'defaultUicontrolBackgroundColor'))
    set(hObject,'BackgroundColor','white');
end
function miny_xval_edit_Callback(hObject, eventdata, handles)
% hObject    handle to miny_xval_edit (see GCBO)
% Hints: get(hObject,'String') returns contents of miny_xval_edit as text
%          str2double(get(hObject,'String')) returns contents of miny_xval_edit as
a double

```

```

% --- Executes during object creation, after setting all properties.
function miny_xval_edit_CreateFcn(hObject, eventdata, handles)
% hObject    handle to miny_xval_edit (see GCBO)
% Hint: edit controls usually have a white background on Windows.
if ispc && isequal(get(hObject,'BackgroundColor'),
get(0,'defaultUicontrolBackgroundColor'))
    set(hObject,'BackgroundColor','white');
end
function maxy_xval_edit_Callback(hObject, eventdata, handles)
% hObject    handle to maxy_xval_edit (see GCBO)
% Hints: get(hObject,'String') returns contents of maxy_xval_edit as text
%         str2double(get(hObject,'String')) returns contents of maxy_xval_edit as
a double
% --- Executes during object creation, after setting all properties.
function maxy_xval_edit_CreateFcn(hObject, eventdata, handles)
% hObject    handle to maxy_xval_edit (see GCBO)
% Hint: edit controls usually have a white background on Windows.
if ispc && isequal(get(hObject,'BackgroundColor'),
get(0,'defaultUicontrolBackgroundColor'))
    set(hObject,'BackgroundColor','white');
end
function miny_time_edit_Callback(hObject, eventdata, handles)
% hObject    handle to miny_time_edit (see GCBO)
% Hints: get(hObject,'String') returns contents of miny_time_edit as text
%         str2double(get(hObject,'String')) returns contents of miny_time_edit as
a double
% --- Executes during object creation, after setting all properties.
function miny_time_edit_CreateFcn(hObject, eventdata, handles)
% hObject    handle to miny_time_edit (see GCBO)
% Hint: edit controls usually have a white background on Windows.
if ispc && isequal(get(hObject,'BackgroundColor'),
get(0,'defaultUicontrolBackgroundColor'))
    set(hObject,'BackgroundColor','white');
end
function maxy_time_edit_Callback(hObject, eventdata, handles)
% hObject    handle to maxy_time_edit (see GCBO)
% Hints: get(hObject,'String') returns contents of maxy_time_edit as text
%         str2double(get(hObject,'String')) returns contents of maxy_time_edit as
a double
% --- Executes during object creation, after setting all properties.
function maxy_time_edit_CreateFcn(hObject, eventdata, handles)
% hObject    handle to maxy_time_edit (see GCBO)
% Hint: edit controls usually have a white background on Windows.
if ispc && isequal(get(hObject,'BackgroundColor'),
get(0,'defaultUicontrolBackgroundColor'))
    set(hObject,'BackgroundColor','white');
end
% --- Executes on button press in transparent_legend_checkbox.
function transparent_legend_checkbox_Callback(hObject, eventdata, handles)
% hObject    handle to transparent_legend_checkbox (see GCBO)
% Hint: get(hObject,'Value') returns toggle state of transparent_legend_checkbox
function [handles] = getPlotTickRanges(handles)
% Set plot tick ranges
x_range_temp(1)=min(handles.myvars.xseries);
x_range_temp(2)=max(handles.myvars.xseries);
y_range_temp(1)=min(handles.myvars.yseries);
y_range_temp(2)=max(handles.myvars.yseries);
y2_range_temp(1)=min(handles.myvars.y2series);
y2_range_temp(2)=max(handles.myvars.y2series);
test_seriesRange=isfield(handles.myvars,'xseries_range');

```

```

if test_seriesRange==0
    handles.myvars.xseries_range=x_range_temp;
    handles.myvars.yseries_range=y_range_temp;
    handles.myvars.y2_series_range=y2_range_temp;
else
    if handles.myvars.xseries_range(1) > x_range_temp(1)
        handles.myvars.xseries_range(1) = x_range_temp(1);
    end
    if handles.myvars.xseries_range(2) < x_range_temp(2)
        handles.myvars.xseries_range(2) = x_range_temp(2);
    end
    if handles.myvars.yseries_range(1) > y_range_temp(1)
        handles.myvars.yseries_range(1) = y_range_temp(1);
    end
    if handles.myvars.yseries_range(2) < y_range_temp(2)
        handles.myvars.yseries_range(2) = y_range_temp(2);
    end
    if handles.myvars.y2_series_range(1) > y2_range_temp(1)
        handles.myvars.y2_series_range(1) = y2_range_temp(1);
    end
    if handles.myvars.y2_series_range(2) < y2_range_temp(2)
        handles.myvars.y2_series_range(2) = y2_range_temp(2);
    end
end
% --- Executes on button press in run_no_checkbox.
function run_no_checkbox_Callback(hObject, eventdata, handles)
% hObject    handle to run_no_checkbox (see GCBO)
% Hint: get(hObject,'Value') returns toggle state of run_no_checkbox
function [handles] = initializeGUI(handles)
% Clear data and reset parameters
if isfield(handles,'myvars') == 1
    handles=rmfield(handles,'myvars');
end
axes(handles.axes1)
cla reset
set(handles.specimen_popupmenu,'Value',1);
set(handles.tare_by_initial_checkbox,'Value',1);
set(handles.x_data_series,'Value',1);
set(handles.y_data_series,'Value',5);
set(handles.y2_data_series,'Value',8);
set(handles.plot_style_checkbox,'Value',0);
set(handles.plot_sep_window_checkbox,'Value',0);
set(handles.holdon_checkbox,'Value',0);
set(handles.legend_checkbox,'Value',1);
set(handles.inclspecattr,'Value',1);
set(handles.transparent_legend_checkbox,'Value',1);
set(handles.run_no_checkbox,'Value',1);
set(handles.plot3_checkbox,'Value',0);
set(handles.refine_by_sliders_checkbox,'Value',0);
set(handles.curve_operations_popup,'Value',2);
set(handles.curve_operations_curve1,'Value',11);
set(handles.curve_operations_curve2,'Value',12);
set(handles.FFT_checkbox,'Value',0);
set(handles.fit_data_checkbox,'Value',0);
set(handles.use_all_data_checkbox,'Value',1);
set(handles.refline_checkbox,'Value',0);
set(handles.xlmin_slider_edit,'String','----');
set(handles.xlmax_slider_edit,'String','----');
set(handles.xlval_slider_edit,'String','----');
set(handles.x2min_slider_edit,'String','----');

```

```

set(handles.x2max_slider_edit,'String','----');
set(handles.x2val_slider_edit,'String','----');
set(handles.sample_rate_statictext,'String','----');
set(handles.x_origin_checkbox,'Value',0);
handles.myvars.variables={
    'Time'
    'Vertical Displacement'
    'Vertical Velocity'
    'Vertical Acceleration'
    'Vertical Force'
    'Vertical Impulse'
    'Vertical Work'
    'Horizontal Displacement'
    'Horizontal Velocity'
    'Horizontal Acceleration'
    'Horizontal Force 1'
    'Horizontal Force 2'
    'Total Horizontal Force'
    'Horizontal Imuplse'
    'Horizontal Work'
    'Resultant Displacement'
    'Resultant Force'
    'Resultant Force Angle'
};
set(handles.x_data_series,'String',handles.myvars.variables);
set(handles.y_data_series,'String',handles.myvars.variables);
set(handles.y2_data_series,'String',handles.myvars.variables);
set(handles.curve_operations_curve1,'String',handles.myvars.variables);
set(handles.curve_operations_curve2,'String',handles.myvars.variables);
% Set program and default specimen directories
handles.myvars.program_dir=pwd;
handles.myvars.default_dir='E:\MyDataDrive\2 - PhD Research\ColdRm-
MovingLoadApparatus\Experiments\MTSDData\';
% handles.myvars.default_dir='R:\Work\bruceq-svn-repo\MovingLoads\ColdRm-
MovingLoadApparatus\Experiments\MTSDData';
% Create Specimen Attributes table
handles.myvars.specimen_attr={
    'MovingLoad01'      ,      'Initialization-Test'
    'MovingLoad02'      ,      'Initialization-Test'
    'MovingLoad03'      ,      'Initialization-Test'
    'MovingLoad04'      ,      'Initialization-Test'
    'MovingLoad05'      ,      'Initialization-Test'
    'MovingLoad06'      ,      'Warm Fast Centre'
    'MovingLoad07'      ,      'Warm Slow Centre'
    'MovingLoad08'      ,      'Warm Slow Full-Length'
    'MovingLoad09'      ,      'Warm Fast Centre'
    'MovingLoad10'      ,      'Warm Slow Centre'
    'MovingLoad11'      ,      'Warm Slow Full-Length'
    'MovingLoad12'      ,      'Initialization-Test'
    'MovingLoad14'      ,      'Warm Fast Centre'
    'MovingLoad15'      ,      'Warm Slow Centre'
    'MovingLoad16'      ,      'Warm Slow Full-Length'
    'MovingLoad17'      ,      'Cold Fast Centre'
    'MovingLoad18'      ,      'Cold Slow Centre'
    'MovingLoad19'      ,      'Cold Slow Full-Length'
    'MovingLoad20'      ,      'Cold Slow Centre'
    'MovingLoad21'      ,      'Cold Slow Full-Length'
    'MovingLoad22'      ,      'Cold Fast Centre'
    'MovingLoad23'      ,      'Cold Fast Centre'
    'MovingLoad24'      ,      'Cold Slow Centre'

```



```

'MovingLoad25'      ,      'Cold Slow Full-Length'
'MovingLoad26'      ,      'Cold Fast Centre'
'MovingLoad27'      ,      'Cold Slow Centre'
'MovingLoad28'      ,      'Cold Slow Full-Length'
'MovingLoad29'      ,      '1/2" Plate Cold Force-Ctrl Full-Length'
'MovingLoad30'      ,      'Ice Elastic Plate 1 Slow'
'MovingLoad31'      ,      'Ice Elastic Plate 2 Slow'
'MovingLoad32'      ,      'Ice Elastic Slow w/ Pressure Film'
'MovingLoad33'      ,      'Ice Elastic Medium w/ Pressure Film'
'MovingLoad34'      ,      'Ice Elastic Plate 3 Medium'
'MovingLoad35'      ,      'Ice Elastic Fast w/ Pressure Film'
'MovingLoad36'      ,      '1/4" Plate Cold Force-Ctrl Full-Length'
'MovingLoad37'      ,      'Frame Cold Force-Ctrl Full-Length'
'MovingLoad38'      ,      'Ice Elastic Plate 4 Slow'
'MovingLoad39'      ,      'Ice Elastic Plate 5 Slow'
'MovingLoad40'      ,      'Ice Plastic 1/8" Slow'
'MovingLoad41'      ,      'Ice Plastic 1/8" Fast'
'MovingLoad42'      ,      'Ice Plastic 1/4" Fast'
'Other'             ,      'Other'
};

% --- Executes on button press in pushbutton20.
function pushbutton20_Callback(hObject, eventdata, handles)
% hObject      handle to pushbutton20 (see GCBO)
handles.sep_figure=figure;
set_axes_props(handles)
hold all;
plot(handles.myvars.data.time, handles.myvars.data.hforc_total, 'b--')
plot(handles.myvars.data.time, handles.myvars.data.hforc1, 'r-.')
plot(handles.myvars.data.time, handles.myvars.data.hforc2, 'g-')
plot(handles.myvars.data.time, handles.myvars.data.hforc1-
handles.myvars.data.hforc2, 'k:')
xlim([min(handles.myvars.data.time) max(handles.myvars.data.time)]);
ylim([min(handles.myvars.data.hforc_total)
max(handles.myvars.data.hforc_total)]);
% Include Legend
if get(handles.inclspecattr, 'Value')==1
    val_1=get(handles.specimen_popupmenu, 'Value');
    if get(handles.run_no_checkbox, 'Value') == 0
        legend_prepend={char(strcat(handles.myvars.specimen_attr(val_1-1,2),{' -
' })))};
    else
        legend_prepend={char(strcat(handles.myvars.specimen_name,{' -
' },handles.myvars.specimen_attr(val_1-1,2),{' - ' })))};
    end
else
    if get(handles.run_no_checkbox, 'Value') == 0
        legend_prepend='';
    else
        legend_prepend={char(strcat(handles.myvars.specimen_name,{' - ' })))};
    end
end
title('Horizontal Force vs. Time')
xlabel('Time [s]')
ylabel('Horizontal Force [N]')
legend_title(1)={char(strcat(legend_prepend, 'Total Horizontal Force'))};
legend_title(end+1)={char(strcat(legend_prepend, 'Horizontal Force 1'))};
legend_title(end+1)={char(strcat(legend_prepend, 'Horizontal Force 2'))};
legend_title(end+1)={char([legend_prepend 'Horizontal Force 1 minus Horizontal
Force 2'])};
% Display Legend

```

```

if get(handles.legend_checkbox,'Value')==1
    LEG=legend(gca,legend_title,'Location','NorthWest');
    set(LEG,'FontSize',9)
    if get(handles.transparent_legend_checkbox,'Value') == 1
        set(LEG,'color','none')
    end
end
end
% --- Executes on button press in refile_checkbox.
function refile_checkbox_Callback(hObject, eventdata, handles)
% hObject    handle to refile_checkbox (see GCBO)
% Hint: get(hObject,'Value') returns toggle state of refile_checkbox
if get(handles.use_all_data_checkbox,'Value') == 1
    set(hObject,'Value',0)
    set(hObject,'Enable','off')
else
    set(hObject,'Enable','on')
end
end
% --- Executes on button press in x_origin_checkbox.
function x_origin_checkbox_Callback(hObject, eventdata, handles)
% hObject    handle to x_origin_checkbox (see GCBO)
% Hint: get(hObject,'Value') returns toggle state of x_origin_checkbox
if get(hObject,'Value') == 1
    handles.myvars.data.hdisp=handles.myvars.data.hdisp-550;
end
if get(hObject,'Value') == 0
    handles.myvars.data.hdisp=handles.myvars.data.hdisp+550;
end
guidata(hObject, handles);

```

